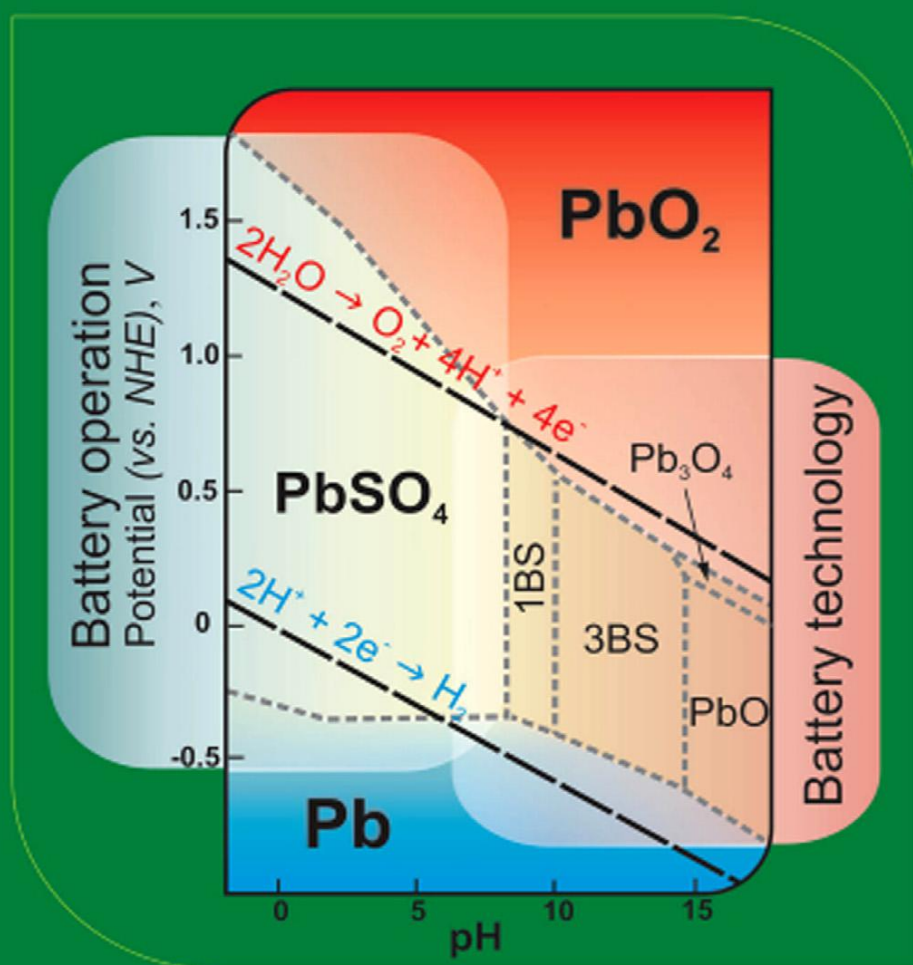




Detchko Pavlov

Lead-Acid Batteries Science and Technology

A handbook of lead-acid battery technology
and its influence on the product



Lead-Acid Batteries: Science and Technology

Lead—Acid Batteries: Science and Technology

*A Handbook of Lead—Acid Battery Technology
and its Influence on the Product*

Detchko Pavlov



ELSEVIER

AMSTERDAM • BOSTON • HEIDELBERG • LONDON • NEW YORK • OXFORD
PARIS • SAN DIEGO • SAN FRANCISCO • SINGAPORE • SYDNEY • TOKYO

Elsevier

Radarweg 29, PO Box 211, 1000 AE Amsterdam, The Netherlands
The Boulevard, Langford lane, Kidlington, Oxford, OX5 1GB, UK

First edition 2011

Copyright © 2011 Elsevier B.V. All rights reserved

No part of this publication may be reproduced, stored in a retrieval system or transmitted in any form or by any means electronic, mechanical, photocopying, recording or otherwise without the prior written permission of the publisher

Permissions may be sought directly from Elsevier's Science & Technology Rights Department in Oxford, UK: phone (+44)(0) 1865 843830; fax (+44)(0) 1865 853333; email: permissions@elsevier.com. Alternatively you can submit your request online by visiting the Elsevier web site at <http://elsevier.com/locate/permissions> and selecting *Obtaining permission to use Elsevier material*

Notice

No responsibility is assumed by the publisher for any injury and/or damage to persons or property as a matter of products liability, negligence or otherwise, or from any use or operation of any methods, products, instructions or ideas contained in the material herein.

Library of Congress Cataloging in Publication Data

A catalog record for this book is available from the Library of Congress

British Library Cataloguing in Publication Data

A catalogue record for this book is available from the British Library

ISBN: 978-0-444-52882-7

For information on all Elsevier publications
visit our website at www.elsevierdirect.com

Printed and bound in the Great Britain

11 12 13 11 10 9 8 7 6 5 4 3 2 1

Working together to grow
libraries in developing countries

www.elsevier.com | www.bookaid.org | www.sabre.org

ELSEVIER

BOOK AID
International

Sabre Foundation

*Dedicated to my mother Ekaterina,
my father Pavel and my wife Svetla*

This page intentionally left blank

Contents

<i>Preface</i>	ix
<i>Acknowledgements</i>	xi
 <i>Part 1: Fundamentals of Lead-Acid Batteries</i>	 1
<i>Chapter 1: Invention and Development of the Lead–Acid Battery</i>	3
<i>Chapter 2: Fundamentals of Lead–Acid Batteries</i>	29
 <i>Part 2: Materials Used for Lead-Acid Battery Manufacture</i>	 115
<i>Chapter 3: H₂SO₄ Electrolyte – An Active Material in the Lead–Acid Cell</i>	117
<i>Chapter 4: Lead Alloys and Grids. Grid Design Principles</i>	149
<i>Chapter 5: Lead Oxide</i>	223
 <i>Part 3: Processes During Paste Preparation and Curing of the Plates</i>	 251
<i>Chapter 6: Pastes and Grid Pasting</i>	253
<i>Chapter 7: Additives to the Pastes for Positive and Negative</i> <i>Battery Plates</i>	 311
<i>Chapter 8: Curing of Battery Plates</i>	363
 <i>Part 4: Plate Formation</i>	 405
<i>Chapter 9: Soaking of Cured Plates Before Formation</i>	407
<i>Chapter 10: Formation of Positive Lead–Acid Battery Plates</i>	443
<i>Chapter 11: Processes During Formation of Negative Battery Plates</i>	481
<i>Chapter 12: Technology of Formation</i>	501
 <i>Part 5: Battery Storage and VRLA Batteries</i>	 533
<i>Chapter 13: Processes After Formation of the Plates and During Battery</i> <i>Storage</i>	 535
<i>Chapter 14: Methods to Restore the Water Decomposed During Charge and</i> <i>Overcharge of Lead–Acid Batteries: VRLA Batteries</i>	 567

Part 6: Calculation of the Active Materials in a Lead–Acid Cell605

Chapter 15: Calculation of the Active Materials for Lead–Acid Cells607

Epilogue623

Appendices625

Index633

Preface

The lead–acid battery was invented at the advent of electricity. The discovery of electricity as a form of energy is the greatest achievement of mankind, which has changed human life dramatically. For over 150 years, the lead–acid battery technology has developed driven by the accumulation of new knowledge and the invention of new materials. The lead–acid battery has become one of the main portable sources of electric power with wide application in man's everyday life (transport vehicles, telecommunications, information technologies, etc.). It has won a dominating position in energy storage and load-levelling applications (reserve electric power supply and remote area energy systems). Lead–acid batteries are cheap, easy to produce and easy to recycle, and the resources for their manufacture are practically unlimited. This is why the lead–acid battery industry has reached annual turnovers of tens of billions of US dollars on a worldwide basis.

The lead–acid battery is a complex dynamic system, or shall I call it 'a complex dynamic world', in which various processes proceed continuously, at different rates, no matter whether the battery is on charge, discharge or open circuit. This 'living' organism exists due to the simultaneous operation of two electrochemical systems: the lead system (Pb/PbSO_4 and $\text{PbO}_2/\text{PbSO}_4$) and the water system ($\text{H}_2\text{O/H}_2$ and $\text{H}_2\text{O/O}_2$). The latter is thermodynamically supported, but kinetically suppressed. These two systems are in continuous competition with each other, the lead system playing the dominating role, which makes the lead–acid battery functional and useful to mankind.

This dynamic world is governed by the laws of chemistry and electrochemistry, physics and physical chemistry, metallurgy and corrosion science. This 'world' is a meeting point for the kinetics and thermodynamics of chemical and electrochemical reactions, crystal nucleation and growth with diffusion and migration processes, mechanical and corrosion processes in lead alloys, as well as a number of phenomena of efficient transformation of chemical energy into electrical energy and vice versa.

My collaborators and I have been studying this 'world' for many years now. We have advanced step by step, overcoming numerous barriers, towards identifying the processes and phenomena that proceed during lead–acid battery manufacture and operation, disclosing the mechanisms of these processes and elucidating the structures of the obtained intermediate and end products. It is really rewarding when you gain all this knowledge.

Sooner or later, every man comes to the end of his active professional carrier. Having reached this point in my life, with this book I want to share the knowledge and experience accumulated for over 44 years of research with my fellow scientists, battery designers, engineers and technologists in the battery industry. There are chapters in this book devoted to the fundamental theoretical background of lead—acid battery manufacture and operation, and others discussing more technological issues, thus allowing the reader to find more easily his/her specific topics of interest.

When writing this book, I rejoiced immensely at ‘the complex dynamic world’ that I was trying to describe. If it stirs up a similar feeling in you, too, dear reader, then I would believe that the book has accomplished its mission.

Acknowledgements

I would like to express my thanks to Mrs. Mariana Gerganska for her valuable help with the translation of this book and for her amicable criticism and useful remarks.

I also thank Ms. Dina Ivanova for her technical assistance with the graphical illustrations and all my collaborators from the Lead-Acid Batteries Department of IEES for their most generous support.

I am grateful to Mr. P. Kirubhakaran and Mr. B. Mageswaran and their team from Elsevier's book publishing division, Chennai, for their excellent work in converting my manuscript into a book. And last, but not the least, I sincerely thank Ms. Anita Koch, Associate Acquisition Editor at Elsevier, for her patience and understanding throughout the time of preparation and submission of my manuscript.

I would also like to express my sincere gratitude to the following organizations for their kindness to grant me permissions to reproduce copyright materials:

- Elsevier B.V.
- The Electrochemical Society, Inc.
- Springer Science and Business Media B.V.
- John Wiley & Sons, Ltd.

While every effort has been made to contact copyright holders or their agents, a few have remained untraceable. I would be interested to hear from any copyright holders who have not been acknowledged. I would be grateful if notified of any corrections that should be incorporated in future reprints or editions of this book.

This page intentionally left blank

PART 1

Fundamentals of Lead-Acid Batteries

This page intentionally left blank

Invention and Development of the Lead–Acid Battery

1.1. A Prelude

A scientific product is never born spontaneously in a researcher's mind. Normally, it is a result of the efforts of many scientists whose work and achievements have provided the background for and 'paved the way' to the invention of this new product. The person recognised as the inventor of the product is actually the one who has best understood its essence (fundamental principles) and has produced and convincingly demonstrated this product to the public. Such is the case with the invention of the lead–acid battery, too.

The discovery of electricity as a form of energy is, if not the greatest, definitely one of the greatest achievements of mankind. Electricity has changed human life dramatically, making it easier, more modern and sophisticated. It opened the door for rapid development of industry, transport, communications and other spheres of activity. In the initial period following the advent of electricity as a form of energy, electrochemical power sources played a major role. They were used to produce electric power or served as 'stores' of electric energy. So at the beginning of nineteenth century many chemists and physicists devoted their lives to the invention and enhancement of various chemical power sources. Some of these will be discussed in brief subsequently.

In 1801, the French physicist N. Gautherot connected the two electrodes of a Volta cell to two platinum wires immersed in saline solution and passed electric current through them [1]. Water decomposed to hydrogen and oxygen, and when the circuit was cut off and the platinum wires were connected to each other, electric current flowed in the opposite direction for a short time.

A year later in Germany, Johann Ritter (Fig. 1.1) connected a Volta cell to layered discs of copper and cardboard moistened with NaCl solution [2]. The charging voltage was 1.3 V. After the circuit was disconnected, a voltage of 0.3 V was measured between the two copper discs. Ritter conducted similar experiments with lead, tin and zinc plates. Different voltages were measured for the different types of plates. He called this voltage polarisation.

When electric current flows through lead electrodes immersed in H_2SO_4 solution, lead dioxide is formed on one of the electrodes. Such experiments were performed by Kästner in 1810, Nobili in 1828, Schönbein in 1838 and Wheatstone in 1843 [2].



Figure 1.1:
Portrait of Johann Wilhelm Ritter [2].

In 1854, the German medical officer Wilhelm Sinsteden (Fig. 1.2), while studying the electrical phenomena, observed that when electric current flowed through lead electrodes immersed in diluted H_2SO_4 solution the obtained cell delivered electric current and had a specific energy output of 0.1 Wh kg^{-1} for 15 min of discharge [2,3].

1.2. Gaston Planté — The Inventor of the Lead–Acid Battery

In 1859, the French physicist Gaston Planté studied the polarisation between two identical electrodes immersed in diluted aqueous solution of sulfuric acid. He investigated different electrodes including silver, lead, tin, copper, gold, platinum and aluminium electrodes. He established that, depending on the type of electrodes used, the cells were polarised to different levels when electric current flowed through the electrodes and the cells became generators of reverse current. He summarised the results of all these experiments in his paper entitled ‘Recherches sur la polarisation voltaïque’, which was published in Comptes Rendus of the French Academy of Sciences in 1859 [4].

Gaston Planté established that the secondary current (as was then called) that flowed through a cell with lead plates separated by rubber strips and immersed in 10% sulfuric acid solution



Figure 1.2:
Portrait of Wilhelm Joseph Sinstedden [2].

was the highest and flowed for the longest period of time as compared to all other cells under test. This cell had the highest voltage, too.

On 26 March 1860, Gaston Planté demonstrated before the French Academy of Sciences the first rechargeable lead–acid battery comprising nine cells connected in parallel and presented a lecture entitled ‘Nouvelle pile secondaire d’une grande puissance’ (Fig. 1.3) [5]. This was practically the birth certificate of the lead–acid battery.

1.2.1. Gaston Planté – The Scientist

Raymond-Louis Gaston Planté was born on 22 April 1834 in the town of Orthez, Basses-Pyrénées province in France.

The Planté family seems to have been born under a lucky star. All three brothers, Leopold (born 1832), Gaston (born 1834) and Francis (born 1839), gained national, and even international, fame. Leopold Planté was one of the leaders of lawyers in Paris; Francis Planté was a brilliant piano player who amazed the cultural world of his time with his talent. He was called ‘God of the piano’ and gave concerts until the age of 91. The Planté family was an old and highly respected family from Orthez [6]. The father of the three brothers, Pierre (Pedro), and their

(a)



(b)

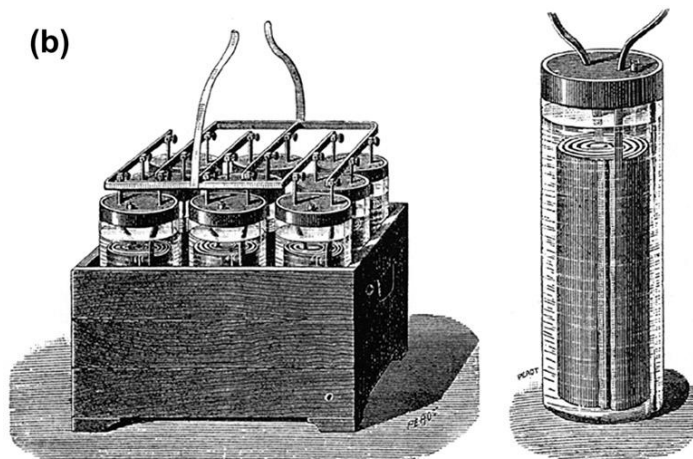


Figure 1.3:

(a) Portrait of Gaston Planté; (b) the first rechargeable lead-acid battery comprising a series of nine cells connected in parallel.

uncle Raymond had occupied high posts in the local administration of Orthez and of the Basses-Pyrénées district. In 1841, Pierre Planté and his family left Orthez and moved to Paris in order to assure better education for his sons.

Gaston Planté started his education at a private school and then went to the Lycée Charlemagne. At the age of 16, he became Bachelor of Letters and at 19, Bachelor of Science. Then he attended the most renowned university in Paris, La Sorbonne, and in 1855 he obtained the degree Master of Science.

During his university years Gaston impressed his professors with his analytic mind, practical skills and extraordinary dexterity in doing experimental work. Because of these qualities of the young student, Prof. Edmond Becquerel chose Gaston Planté as assistant in his laboratory at the Conservatory of Arts and Crafts.

Under Prof. Becquerel's tutorship, Gaston mastered the scientific approach to studying natural processes and demonstrated a lively interest in disclosing natural phenomena. As a result of this inborn curiosity of his, in 1855, Gaston discovered an unknown fossil bird in a quarry near Paris. The French Academy of Sciences, in agreement with the British Museum, gave this bird the name *Gastornis parisiensis*.

In the middle of the nineteenth century, laboratory experiments demonstrated ever more clearly the great potential of electricity to be of help to people and to change fundamentally their everyday life. Gaston Planté was among the first to realise this and started investigations of various electrical phenomena. His experiments were very impressive. On 28 March 1858, he was chosen to demonstrate before Emperor Napoleon the Third and the Empress, in Palais de Tuileries, the principal electrical experiments that were known at that time [7].

Gaston Planté was very active in the field of electrochemistry. He replaced the then used platinum electrode with lead electrode in the process of reproduction of full-relief figures in galvanoplastics. This method was employed for the fabrication of the sculptures decorating the front of the Opera house in Paris. In 1866, Gaston Planté explored the electrolytic production of ozone. He came to the conclusion that production of ozone should be performed using lead electrodes instead of platinum.

Despite his significant achievements in the field of electrochemistry, Gaston Planté remains essentially a physicist. Since 1873, he studied the difference between static and dynamic electricity as well as high-voltage phenomena.

In 1877, he constructed a machine (called the Rheostatic Machine) in which he used multi-cell battery and a bank of capacitors and, with the help of a series of commutators and contacts, alternately charged the capacitors connected in parallel and then discharged them connected in series (Fig. 1.4). The large-scale model of this machine comprised 80 capacitors and a series of

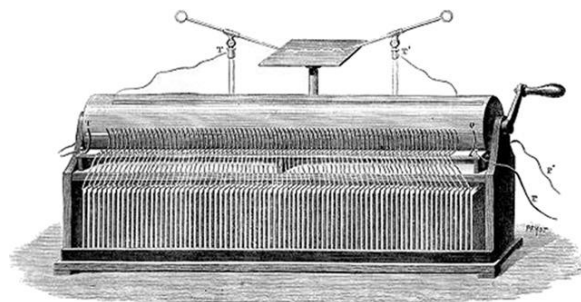


Figure 1.4:

G. Planté constructed a ‘Rheostatic Machine’ comprising multiple lead–acid Cells, a bank of capacitors and a series of commutators and contacts.

lead–acid batteries with 800 cells (1600 V). This machine was able to deliver voltages of up to 200,000 V. Planté used this machine to explore high-voltage electrical sparks. Based on the results of these experiments, he proposed hypotheses about the origin of spiral nebulae, globe lightnings and solar spots and even about the origin of the sun.

He performed systematic studies of electrical phenomena and summarised the results of these studies in the book *Recherches sur l’électricité* (*Research on Electricity*), which was published in 1879 but the information in it is still relevant today [8]. In this book Gaston Planté considers electricity as a very fast flow of electrically charged material, which may in some cases cause an electric spark or a voltaic arc and in others charge or discharge a battery. Atomic structure was not known to scientists at that time, but, based on scientific generalisations, Planté envisaged the involvement of electric charges in the structure of materials. Such was the scientist Gaston Planté — always ahead of time.

1.2.2. Gaston Planté — The Person

His contemporaries describe Gaston Planté as a very kind-hearted, modest and unselfish man, fully dedicated to his work — a real workaholic (Fig. 1.5).

Besides his deep interest in science, he loved music and was a virtuoso piano player. He wrote and spoke fluently English, German, Spanish and Italian. He was deeply religious and profoundly moral, which gained him sympathy, love and respect from all who knew him.

Gaston Planté never protected his inventions by patents and showed no interest in obtaining material benefits from them. He refused all kinds of privileges. Being a widely recognized scientist, when invited to run for Member of the French Academy of Sciences, he declined the offer saying that he would lose much time in preparation for the election and would rather prefer to spend this time working in his laboratory.



Figure 1.5:
Portrait of Gaston Planté.

He never accepted appointment at official remunerated positions, but did not decline invitations to perform honourable functions. He was:

- Professor of physics at the Polytechnic Association;
- Member of the Imperial Jury at the International Exhibitions held in London in 1863 and in Paris in 1867.

He received many distinctions and awards, including:

- Knight of the Order of the Rose — Brazil;
- Cavalier of the Legion of Honour of France, Italy and Austria;
- Lacaze Prize of the French Academy of Sciences;
- Golden Medal in Arts Economique;
- Golden Ampere Medal of the Society for Encouragement of National Industry.

When the President of the Society for Encouragement of National Industry, the renowned chemist Dumas, presented the Ampere Medal to Gaston Planté he said: 'I am happy to give you this medal bearing the effigy of Ampere and am sure that in the future our successors will give a medal with your effigy.' [6].

Gaston Planté donated the sum of 10,000 Francs, which he received with the Lacaze Prize, to the Friends of Science Society to help scientists in need, and he sold the two golden medals and gave the money to the poor.

In 1889, Gaston Planté's health deteriorated. He began to gradually lose his sight and on 22 May 1889 he died at the age of 55.

In his will, Gaston Planté donated three real estate properties to Friends of Science Society. The French Academy of Sciences received all his savings under the obligation to award a biannual monetary prize to scientists or inventors with an important contribution in the field of electricity. Pierre Curie was the second recipient of this award, which was presented to 21 scientists between 1893 and 1933.

Such a moral and highly ethical person was Gaston Planté.

In 1989, on the eve of the 130th anniversary of the invention of the lead–acid battery and in connection with the first LABAT international conference on lead–acid batteries, the Bulgarian Academy of Sciences, with the approval of the French Academy of Sciences, established an award, a medal, named after the great French scientist Gaston Planté (Fig. 1.6) [9].



Figure 1.6:
The Gaston Planté Medal.

The Gaston Planté Medal is presented every 3 years to prominent scientists who have made significant contributions to the development of lead–acid battery science and technology. The recipients of the award are elected by an international committee comprising 15 scientists from all over the world. Up to now the Gaston Planté Medal has been awarded to 11 scientists from 7 countries as well as to the Advanced Lead–Acid Battery Consortium for promoting research and development in the field of lead–acid batteries.

1.3. What Pains Had the Lead–Acid Battery to Go Through

1.3.1. In the Beginning Was the Planté Technology

The lead–acid battery was born some 10 years before the invention of the mechanical generators of electricity. Being a secondary power source, the lead–acid battery needed a cheap and easy-to-use charging device. At that time, the battery was charged by Daniell cells or Bunsen cells, which was not an easy procedure at all.

In 1869, Zénobe Gramme constructed the first direct current dynamo machine, which made battery charging easy. Mechanical energy was converted into electric energy, which was then stored in a lead–acid battery in the form of chemical energy.

In 1873, the Bréquet Company was the first to produce Planté lead–acid batteries and Gramme dynamo machines. Thus, a technical possibility was created to easily generate and store electric energy. At that time, the system dynamo and lead–acid storage battery was still only a curious scientific achievement. Electric energy had not yet found practical application in human life.

In 1879, Thomas Edison in the United States and Joseph Swan in England invented the incandescent lamp, thus making it possible to convert electric energy into light. The invention of the light bulb promoted the use of electricity in people's everyday life. Electricity entered human lives. Lead–acid battery demand increased. However, large-scale production of lead–acid batteries was constrained by the technology of their manufacture.

Immediately after its invention, the lead–acid storage battery attracted the interest of many researchers who looked for variants of Planté's cell.

In 1861, Charles Kirchoff in the United States proposed a cell comprising platinum electrodes immersed in a solution of $\text{Pb}(\text{NO}_3)_2$ and $\text{Pb}(\text{CH}_3\text{COO})_2$ [10]. At the same time, Wilhelm Siemens in Germany devised a secondary cell with carbon electrodes impregnated with lead salts and immersed in acid solution [11]. These, however, were rather curious attempts to create a novel secondary cell.

1.3.2. Development of New Technology for Lead–Acid Battery Manufacture

Application of lead–acid batteries was limited because of the slow process of manufacture of the electrodes and their low capacity. In the late 1870s there was an acute need of new technology for lead–acid manufacture.

In 1881, Camille Fauré coated the lead plates with a paste of red lead oxide, sulfuric acid and water, and then charged them to form Pb and PbO₂ active masses. The specific energy of the battery increased to 8 Wh kg^{−1} at 10 hours discharge rate [12].

The same year, Ernest Volckmar replaced the lead sheet with lead grid [13] and Scudamore Sellon [7] used lead–antimony grids instead of pure lead grids. S.C. Curie devised tubular positive plates for lead–acid batteries.

In 1882, Gladstone and Tribe disclosed the reactions that proceeded at the two electrodes during battery operation and proposed the double-sulfate theory [14].

In 1883, Hermann Aron studied in detail the processes on charge and discharge of a lead–acid battery [15]. He established a correlation between the specific density of H₂SO₄ electrolyte and discharge time, and first described the processes of battery sulfation.

1.3.3. First Applications of Lead–Acid Batteries in Human Life

Thus, in the early 1880s, a lead–acid battery of high capacity and relatively simple technology of manufacture was created. This battery rapidly found various practical applications. In 1881, Gustave Trouvé first used a lead–acid battery in his three-wheeled electric automobile, which reached a speed of 12 km h^{−1}. In 1886, the first submarine propelled by lead–acid batteries was launched in France. A lead–acid battery was mounted in a small dirigible balloon which was propelled at a speed of 4 m s^{−1}. In 1899, Camille Jenatzy reached a speed record of 109 km h^{−1} with his cigar-shaped electric car powered with lead–acid batteries.

The lead–acid battery was quickly adopted in the emerging telecommunications technologies: first, in Morse electric telegraph and later by the telephone companies in the United States, too.

In 1882, the city of Paris installed a system for the distribution of electricity for lighting comprising a combination of dynamos and lead–acid batteries. The first electrically lit street was Grands Magasins du Louvre in Paris (‘the city of lights’). In 1883, Planté supplied the Imperial Palace of Franz Josef in Vienna with stationary and portable equipment for lighting.

The lead–acid battery was gradually deployed in various sectors of the industry and became an important means of electric energy production and storage. Thus, the first stage in the development of the lead–acid battery system and the technology for its manufacture was completed.

1.4. The Lead–Acid Battery in the Twentieth Century – Second Stage in its Development

1.4.1. Leady Oxide Production Processes

In 1881, Camille Fauré developed a process for coating both sides of lead plates, and later lead grids, with a paste of lead oxide (litharge), red lead, sulfuric acid and water and then charging the plates to form Pb and PbO₂ active masses. This was a revolutionary breakthrough in battery technology, which opened the way for industrial production of lead–acid batteries. The lead oxide was produced by melting lead in a reverberatory furnace and then the molten lead was oxidised by a flow of air and water steam. The process was slow (about 30 hours per batch) and cumbersome, and the obtained oxide was coarse-grained and had to be mill ground to yield a product suitable for use in the battery industry.

Methods have been looked for to accelerate the process of lead oxide manufacture. Various technological processes have been proposed for the production of lead oxide from lead carbonate, lead acetate, etc., but they all proved to be too complicated and expensive.

In 1898, George Barton patented a new process where molten lead was rapidly stirred and atomised into small droplets, which were then carried away and oxidised by a humidified air stream drawn through the pot. The resulting oxide was passed through a series of cyclone classifiers where the larger particles were separated and returned back to the reaction pot for further processing, while the fine powder was collected in silos (drums or hoppers).

In a patent of 1926, G. Shimadzu described an adaptation of the ball-mill process used for grinding ores, pigments, etc., by using lead balls tumbling against one another in a mill. The friction created sufficient heat to oxidise the outside surface of the lead balls and the obtained oxide layer fell off continuously in the form of dust. An air flow of a definite speed and humidity carries away the oxide dust through inbuilt screens to separate the coarser fractions and return them to the mill. The fine lead oxide particles were collected in storage silos.

Both the methods (Barton pot and ball-mill) produced partially oxidised lead oxide containing between 20% and 40% free lead. Hence, this oxide was called ‘leady oxide’. The production time of this oxide was reduced substantially, which gave a strong impetus to the development of the lead–acid battery industry after 1926. Nowadays, these two processes are still the dominating methods for leady oxide production.

1.4.2. New Materials and New Technological Processes Are Adopted in the Production of Lead–Acid Batteries

The twentieth century was the time of invention and rapid development of many new materials and novel technological processes, which soon found practical application in the construction

and manufacturing technologies of lead–acid batteries. Let us mention some of these innovative developments.

The ebonite battery case was replaced by polypropylene and polyethylene copolymer or by acrylonitrile butadiene styrene.

The original wooden sheet separators evolved through sintered PVC to polyethylene or polypropylene and, in some battery types, to absorptive glass mat (AGM).

The first grid alloys used were lead alloys with 11% antimony content called ‘hard lead’. These alloys were replaced with low-antimony lead alloys with additions of Sn, As and Ag. Later, battery grid manufacturers switched to lead–calcium and lead–calcium–tin alloys.

At the end of the century, new methods of plate grid manufacture were introduced, parallel to casting. These include the expanding metal grid process and, more recently, the die-cut technology.

1.4.3. Solution to the Water Loss and Battery Maintenance Problem

The first and most important problem that battery researchers and engineers had to resolve was to eliminate or reduce substantially the maintenance of the battery during its exploitation.

In the first half of the twentieth century, lead alloys with high antimony content were used for the manufacture of the plate grids for lead–acid batteries. These batteries lost water during operation and hence they needed maintenance. Significant efforts of battery scientists and technologists in the twentieth century were focused on resolving the water loss problem.

During corrosion of the positive grids, antimony diffuses to the electrolyte and is deposited on the negative plates. Hydrogen evolution on antimony proceeds at low overpotentials. Hence, decomposition of water from the electrolyte is accelerated. The battery has to be topped up with water periodically.

In 1935, Haring and Thomas from Bell Laboratory replaced the lead–antimony grids with lead–calcium for their stationary batteries. The need for battery maintenance was reduced substantially [16,17].

In 1957, Otto Jache from Sonnenschein introduced the gel electrolyte and patented the sealed lead–acid battery [18]. In this battery construction, the oxygen evolved at the positive plates passes through cracks in the gel and reaches the negative plates, where it is reduced and thus restores the lost water and suppresses hydrogen evolution. The German company Sonnenschein started mass production of gel-sealed lead–acid stationary batteries.

In 1967, Donald McClelland and John Devitt of Gates Corporation in the United States used AGM separator which facilitated the transport of oxygen to the negative plates and also

absorbed the electrolyte [19]. Thus, the maintenance-free valve-regulated lead–acid battery (VRLAB) was invented. Lead–tin–calcium grids were used for VRLABs.

1.4.4. Premature Capacity Loss Problem and its Resolution

With the introduction of lead–calcium alloys for the plate grids, however, the life of the battery on deep discharge cycling declined dramatically to 20–25 cycles. This phenomenon was first called ‘Sb-free effect’ and later ‘premature capacity loss’ (PCL effect) [20]. It was established that the PCL effect was a result of certain processes that proceed at the positive battery plate, more precisely at the interface grid/positive active mass (PCL-1 effect) [21] and/or in the positive active mass volume (PCL-2 effect) [22].

The capacity-limiting effect of the interface was found to be due to the following reasons. During battery charge and over-charge, the oxygen evolved at the positive plate surface penetrates through the corrosion layer to the lead grid and oxidises its surface to PbO. The obtained PbO layer has high ohmic resistance. It is oxidised by the evolved oxygen to PbO_n ($1 < n < 2$) and the latter is further oxidised to PbO_2 . If the rate of PbO formation is higher than the rate of its oxidation to PbO_2 , a thick layer of PbO with high ohmic resistance forms on the grid surface which leads to high polarisation of the plate on discharge and eventually to capacity loss [23]. Tin and antimony additions to the grid alloy proved to increase the rate of PbO oxidation to PbO_2 and thus the PCL-1 effect was suppressed [24]. The PCL-2 effect is due to impaired electroconductivity of the contact between the PbO_2 particles (neck zones) of the positive active mass (Kugelhaufen theory) [22]. Tin and antimony added to the grid alloy improve this contact. So, it is imperative to introduce $\text{Sn} > 1.2\%$ to the lead–calcium positive grids of batteries for cycling duties in order to reduce or even avoid the PCL effect.

1.4.5. Basic Lead Sulfate Pastes

Another challenge that battery researchers had to face was to disclose the mechanism of the processes that take place during the manufacture of the plates and to find technological methods to control these processes.

During the second half of the twentieth century, intense research began into the processes during manufacture of lead–acid battery plates. J.J. Lander established the formation of tribasic lead sulfate (3BS) when the battery pastes were prepared at temperatures up to 60 °C (Fig. 1.7a) [25]. At higher temperatures the paste microstructure comprised big crystals of tetrabasic lead sulfate (4BS), as observed by H. Bode and E. Voss (Fig. 1.7b) [26]. John Pierson studied the formation of 4BS during high-temperature (83 °C) curing of positive battery plates [27]. The active mass obtained from 4BS paste proved to have longer cycle life than that produced from 3BS paste [28,29]. It was established that 4BS paste could be obtained only from an initial three-component mix of 3BS + orthorhomb-PbO + tet-PbO without organic

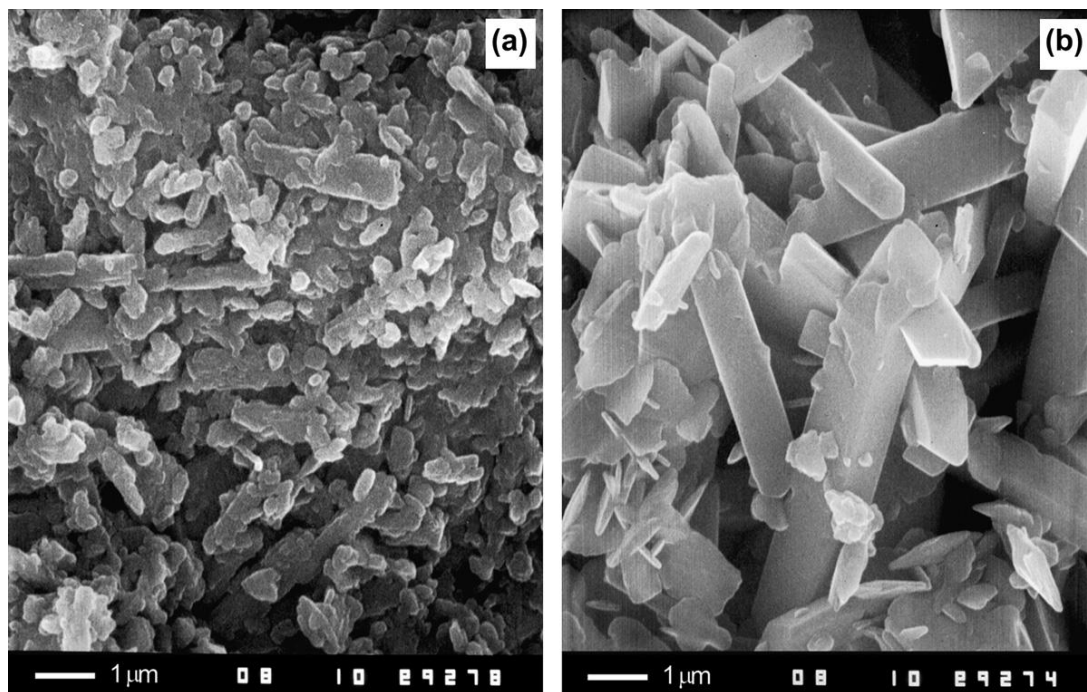


Figure 1.7:
SEM Images of (a) 3BS particles and (b) 4BS particles. Magnification: 10,000 \times .

capillary active substances, for example, the expander lignosulfonate [30,31]. The correlations between 3BS content and H_2SO_4 /lead oxide ratio [32], and 4BS content and lead oxide/red lead ratio [33] during paste preparation were determined.

1.4.6. Skeleton and Energetic Structure of Battery Active Masses

The capacity and cycle life of the battery depend greatly on the structure of the active materials. Hence, it was important to examine the structure of the two types of active masses and to elucidate how it was formed during the technological process of plate manufacture.

It was established that, during the formation of the positive active mass, both $\beta\text{-PbO}_2$ and $\alpha\text{-PbO}_2$ were formed [34,35]. Investigation of the formation processes proved that it proceeded in two stages [36,37]. During the first formation stage, 3BS (4BS) and PbO are oxidised yielding mostly $\alpha\text{-PbO}_2$ because the solution in the pores of the cured paste is neutral to slightly alkaline. Then, in the second stage of formation, the PbSO_4 formed during soaking prior to formation and during the first formation stage is oxidised to $\beta\text{-PbO}_2$ as the solution in the pores is acidic [37]. The $\alpha\text{-PbO}_2$ crystals form the active mass ‘skeleton’ which is less involved in the charge–discharge processes but conducts the current throughout the positive

active mass volume and is connected to the grid providing mechanical support to the active mass. The β - PbO_2 modification is electrochemically active and forms the ‘energetic structure of the positive active mass’, which determines the capacity of the positive plates [37,38].

Formation of the negative active mass (NAM), too, proceeds in two stages [39]. During the first stage, 3BS and PbO are reduced forming the ‘lead skeleton of NAM’ which is connected to the grid, and during the second stage of formation, reduction of PbSO_4 proceeds yielding small Pb crystals of large surface [40,41]. These crystals form the ‘energetic structure of NAM’ and determine its capacity.

A technological process of formation with circulating electrolyte was developed which shortened the duration of the formation procedure to 8–10 hours, sustaining optimum temperature and H_2SO_4 concentration and minimising air pollution [42,43].

1.4.7. Gel–Crystal Structure of the Lead Dioxide Active Mass

When the positive plates for lead–acid batteries are produced using chemically obtained lead dioxide, their capacity is improperly low. In contrast, when the lead dioxide plates are produced employing electrochemical methods, they have a high capacity. What is this correlation between the electrochemical activity of battery positive plates and the method of lead dioxide production due to?

When VRLABs were adopted for mass production, the volume of H_2SO_4 electrolyte in the battery was confined to the amount that the AGM separator could absorb. In order to preserve the quantity of H_2SO_4 as active material, its density was increased to 1.31 g cm^{-3} and even to 1.34 g cm^{-3} . This led to a dramatic drop in capacity of the positive plates.

But why does the electrochemical activity of electrochemically obtained lead dioxide depend on the acid concentration, whereby the plate capacity declines abruptly at higher H_2SO_4 concentrations? Researchers argued over the source of the electrochemical activity of lead dioxide. First, it was related to the formation of oxygen vacancies or of hydrogen ions in the lead dioxide crystal lattice [44–48]. No direct relation was established, however, between the electrochemical activity and these components [49–52]. Other researchers explained the electrochemical activity with the formation of coral-shaped structures of PbO_2 [53,54]. It was also suggested that the impeded contact between the PbO_2 crystals determined the electrochemical activity of PbO_2 [22,55].

Our team, too, carried out research aimed to find the answer to the question. Samples of chemically and electrochemically obtained lead dioxide were examined with a scanning electron microscope (SEM) and a transmission electron microscope (TEM). Figure 1.8 shows the SEM images obtained, and the TEM images are presented in Chapters 2 and 10 of this book.

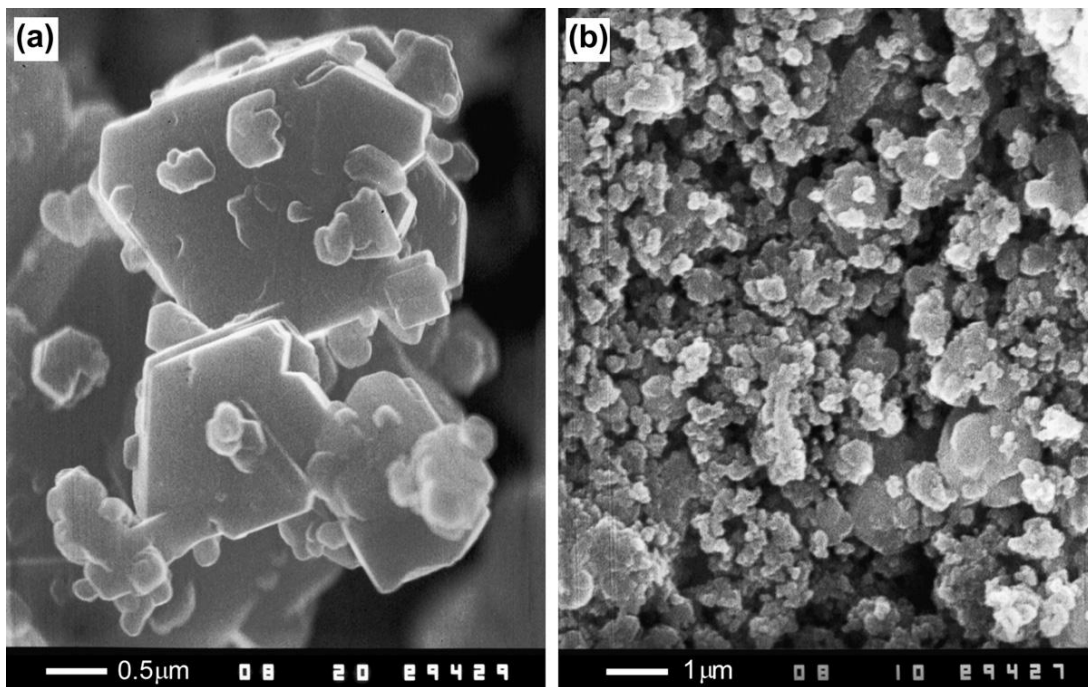
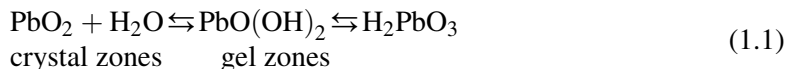


Figure 1.8:

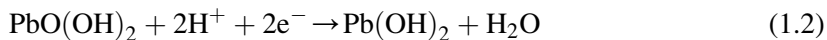
SEM images of (a) chemically obtained lead dioxide and (b) electrochemically obtained lead dioxide.

As evident from the SEM and TEM pictures, the electrochemically obtained lead dioxide particles comprise crystal (PbO_2) zones and hydrated (amorphous) zones [$\text{PbO}(\text{OH})_2$]. The two types of zones are in equilibrium [56–58].



When this lead dioxide was heated and dehydrated, its capacity declined abruptly. These results indicate that the electrochemical reaction of PbO_2 reduction proceeds in the hydrated (gel) zones of the particles and it is these gel zones that determine the electrochemical activity of the lead dioxide [59]. The gel zones of PbO_2 particles have both electron and proton conductivity due to the polymer chains of the lead dioxide structure [59].

For the electrochemical reaction of discharge to proceed:



equivalent amounts of electrons from the crystal zones and H^+ ions from the solution have to enter the gel zones so as to avoid charging of the gel zones and blocking of the electrochemical process. It has been established experimentally that gel zones exchange ions with the solution

and SO_4^{2-} ions are absorbed in the gel zones affecting the gel–crystal zones equilibrium [60]. SO_4^{2-} absorption in the gel zones of PbO_2 particles increases with increase of acid electrolyte concentration. At H_2SO_4 solution densities higher than 1.29 g cm^{-3} , a great number of SO_4^{2-} ions are absorbed in the gel zones, reducing both the electron and proton conductivity of these zones. During plate discharge, sulfate ions form immediately PbSO_4 in the gel zones, which leads to rapid electrode passivation. To keep up the capacity of the positive plates, the number of sulfate ions absorbed in the gel zones of the PbO_2 particles should be relatively small. Then, the reaction of PbO_2 reduction will pass through several stages, including first formation of $\text{Pb}(\text{OH})_2$ and water, and then the lead hydroxide will react with H_2SO_4 forming PbSO_4 [59]. In this way large amounts of PbO_2 will be involved in the reduction process, yielding high electrode capacity. It has been established that the H_2SO_4 electrolyte concentration should not exceed 1.28 g cm^{-3} . At these acid concentrations, 20–50% of the positive active mass (depending on the discharge current) may be involved in the capacity formation processes.

As to the electrochemical activity of chemically obtained lead dioxide, either it is composed of crystal zones only or, if hydrated, the gel zones in its structure are very small, which is the reason for the low specific capacity of such an electrode.

1.4.8. The $\text{Pb}|\text{PbO}|\text{PbSO}_4|\text{H}_2\text{SO}_4$ Electrode

Lander [61] and Burbank [62] applied the XRD method to analyse the substances formed during polarisation of a lead electrode in H_2SO_4 solution. Some unexpected results were obtained. Beside the diffraction peaks for PbSO_4 and PbO_2 , the XRD pattern featured other peaks, too, which were related to the formation of tetragonal PbO . This was a bit surprising and posed the question whether PbO formed electrochemically in H_2SO_4 solution? A counter-interpretation of the XRD data was immediately proposed, namely that those were diffraction peaks for $\alpha\text{-PbO}_2$ [63]. Many of the diffraction peaks for these two oxides do coincide. The formation of tet- PbO was refuted based on thermodynamic grounds as well [64].

This dispute in the international literature aroused our curiosity and we conducted combined XRD and chemical analysis of the products formed on polarisation of a lead electrode in H_2SO_4 solution. It was established that on polarisation between -0.400 and $+0.950 \text{ V}$ (vs $\text{Hg}|\text{Hg}_2\text{SO}_4$ electrode) in $0.5 \text{ M H}_2\text{SO}_4$ solution, a $\text{Pb}|\text{PbO}|\text{PbSO}_4|\text{H}_2\text{SO}_4$ electrode system was formed [65–67]. It was interesting to disclose the mechanism of formation of PbO in H_2SO_4 solution. Based on experimental investigations we have proposed the following mechanism for the formation of lead monoxide. First, a lead sulfate layer forms on the electrode surface comprising PbSO_4 crystals with pores of membrane sizes between them. The lead sulfate membrane is permeable for water and hydrogen ions, but does not let the larger SO_4^{2-} ions to get through. The diffusion potential of the PbSO_4 membrane was determined [68]. When electric current flows through the electrode, Pb^{2+} ions are formed at the interface $\text{Pb}|\text{PbSO}_4$ membrane. These ions react with water at this interface producing $\text{Pb}(\text{OH})_2$ and H^+ ions. In

order to preserve the electroneutrality of the anodic layer, the hydrogen ions migrate through the pores of the PbSO_4 membrane to the solution. $\text{Pb}(\text{OH})_2$ is dehydrated, as a result of which tet- PbO forms between the Pb and PbSO_4 layers. A mechanism of the growth processes of the tet- PbO layer on polarisation of the $\text{Pb}|\text{PbO}|\text{PbSO}_4$ membrane has also been proposed [69–71]. These membrane processes proceed sometimes in the lead–acid battery on deep discharge and sulfation of the negative plates.

1.4.9. Three-Component Expander Added to the NAM

What development did the utilization coefficient of the NAM go through?

The specific surface of NAM is between 0.6 and $1.0 \text{ m}^2 \text{ g}^{-1}$. The PbSO_4 formed as a result of lead oxidation during discharge would rapidly cover this surface and thus reduce substantially the capacity of NAM. In order to achieve high capacity of the negative plates, the discharge processes should involve not only the surface of the NAM but also layers from its volume. The passivating effect of the PbSO_4 layer became clearly obvious after the Second World War, when the wooden separators were replaced with polymers. The cold cranking ability and the capacity of the battery declined drastically. The negative plates were found to be responsible for this decline. It was established that lignosulfonate leached from the wooden separator to the H_2SO_4 solution and adsorbed onto the lead surface, thus retarding the formation of a passivating PbSO_4 layer, which eventually reduced battery capacity, especially at low temperatures.

As a remedy for this phenomenon, various additives (collectively called ‘expander’) are introduced in the NAM so as to prevent the formation of a passivating PbSO_4 layer and allow 20–50% of the lead (NAM) volume (depending on the current density) to participate in the oxidation reaction. The organic expander component (lignosulfonate), being a surface active polymer, is adsorbed on the Pb surface and prevents the formation of a continuous PbSO_4 layer on the electrode surface [72,73]. The other expander component, barium sulfate, provides nuclei for the growth of numerous small PbSO_4 crystals, forming a porous layer instead of the continuous PbSO_4 film [74]. Thus, the lead active mass volume, and not only its surface, can participate in the discharge reaction. Active carbon additives (the third expander component) increase the electrochemically active surface of the NAM on which the charge reaction $\text{Pb}^{2+} + 2\text{e}^- \rightarrow \text{Pb}$ proceeds, thus increasing further the NAM volume which is involved in the charge processes [75]. Moreover, carbon conducts the electric current when a great part of the lead phase has been oxidized to PbSO_4 [76]. That is why the three expander components (lignosulfonates, BaSO_4 and carbon) are indispensable attributes to NAM. However, their proportion in NAM should vary depending on the intended battery duty.

1.4.10. Conclusions

So the utilization of the active materials can be improved by involving greater volume of these materials, and not only their surface layers, in the charge–discharge processes. The proportion

between the skeleton and energetic microstructures of the positive and negative active masses exerts a strong influence on the capacity and cycle life performance of the battery. Therefore, it was essential to modify the technology of battery manufacture so as to guarantee formation of appropriate active mass structures with adequate utilization coefficients.

Any change in materials or technological processes used for lead–acid battery manufacture was associated with certain problems in battery operation. The research efforts aimed at resolving these problems resulted in disclosing new structures, processes and properties of lead–acid batteries. This comes to demonstrate that the lead–acid battery is a fairly complex system whose proper and effective functioning cannot be reduced to electrochemical reactions only.

Research into the processes that take place during the different technological procedures involved in the manufacture of positive and negative battery plates gave rise to the science of battery manufacturing technology.

1.5. Applications of Lead–Acid Batteries

1.5.1. Types of Lead–Acid Batteries

After World War II, production of lead–acid batteries increased immensely, stimulated by the rapid development of the automobile, transport and telecommunications industries, as well as by the increased demand for reserve (stand-by) energy, and most recently by the boom of information technology.

According to their application, lead–acid batteries can be classified into the following main types:

- *SLI (starting, lighting, ignition) batteries* used in automobiles.
- *Stationary batteries* are commonly used for backup power supply, i.e., to generate and store electric energy for use, on request, by telecommunication systems, electric utility centres, computer systems, etc.
- *Motive power (traction) batteries* are industrial batteries used to power in-house transport vehicles: fork-lift trucks, electric cars, mining equipment, etc.
- *Special purpose batteries* intended for use in aircraft, submarines, special military equipment.
- Currently, major scientific and engineering work is focused on the development of *batteries for hybrid or full electric vehicles*.

In terms of maintenance, batteries are classified as:

- *Flooded batteries* (with high-Sb grid alloys) — they require regular maintenance.
- *Maintenance-free batteries* (with PbCaSn or low Sb, As and Sn for the positive plates and PbCa grids for the negative plates).
- *VRLABs* (with PbSnCa grids and AGM separators).

1.5.2. Position of the Lead–Acid Battery Among the Secondary Electrochemical Power Sources

The lead–acid battery could be adequately evaluated only if compared to the other types of secondary power sources. A theoretical assessment can be made by comparing the electrical, energetic, power and economic parameters of the different sources of electricity, but the relative share of each battery chemistry in practical applications is the most objective evaluation criterion. Table 1.1 summarises the basic energy and power characteristics of six types of secondary power sources which are currently used most widely. Data from the studies of Wentzl [78] and Köhler [79] have been used. It can be seen that the lead–acid battery has inferior specific energy and power characteristics as compared to the other types of batteries.

Table 1.2 presents the unit cost (in Watt-hour per dollar) of the electric energy produced, as well as the advantages and disadvantages of the different power sources [77]. The lead–acid battery generates two to three times cheaper energy than all other battery types. Its only disadvantage is its low specific energy (Wh.kg^{-1}), due to the high atomic weight of lead.

But why, despite their unfavourably high atomic weight, have lead–acid batteries found such a wide application and occupy leading market positions?

It is because of their advantages, both with regard to performance and economic parameters, and technology of manufacture. It is not only the technical characteristics that matter for the mass adoption of a given product in practise. Very often, economic issues are more relevant.

Lead–acid batteries are capable to deliver very high power; they are reliable and easy to produce. The resources for their manufacture are practically unlimited. Almost 95% of the materials used in a lead–acid battery are recyclable. A lead–acid battery can store its energy for a very long time.

Table 1.1: Main characteristics of various batteries.

System	Voltage (V)	Specific Energy (Wh kg^{-1})	Energy Density (Wh L^{-1})	Power Density (W kg^{-1})	Specific Energy of Cell* (Wh kg^{-1})	Specific Energy of Battery* (100% SOC) (Wh kg^{-1})
Sealed lead–acid (LA)	2.1	30–40	60–75	180	20–35	20–35
Nickel–cadmium (Ni–Cd)	1.2	40–60	50–150	150	40–60	40–60
Nickel–metal hydride (Ni–MH)	1.2	30–80	140–300	250–1000	50–70	40–70
Lithium-ion LiCoO_2	3.6	160	270	1800		
Lithium polymer	3.7	130–200	300	3000		
Lithium-ion LiFePO_4	3.25	80–120	170	1400		

*Data from references [78] and [79] are used.

Table 1.2: Energy cost, advantages and disadvantages of various batteries [77].

System	Voltage (V)	Energy Cost (Wh \$ ⁻¹)	Advantages	Disadvantages
Sealed lead–acid (LA)	2.1	5–8	Cheap	Heavy
Nickel–cadmium (Ni–Cd)	1.2	2–4	Reliable, inexpensive, high discharge rate, good low temperature behaviour	Heavy, toxic material, memory effect
Nickel–metal hydride (Ni–MH)	1.2	1.4–2.8	High energy density, environment friendly	Higher internal resistance, gas formation, self-discharge
Lithium-ion LiCoO ₂	3.6	3–5	High specific energy, low self-discharge	Expensive, requires safety electronics
Lithium–polymer	3.7	3–5	High specific energy, low self-discharge	Expensive, requires safety electronics
Lithium-ion LiFePO ₄	3.25	0.7–1.6	Safe	Technology in development

The major disadvantage of the lead–acid battery is that Pb has very high atomic weight, which reduces the specific energy and power of the battery.

Nowadays, hundreds of millions of lead–acid batteries are produced worldwide, which makes the lead–acid battery the most successful power source of all times.

1.6. Challenges Calling for a New Stage in the Development of the Lead–Acid Battery

1.6.1. Hybrid Electric Vehicles

At the end of the twentieth century, consumption of petroleum fuels increased significantly on a worldwide basis and the first symptoms of a petrol crisis appeared. Automobile manufacturers decided to reduce petrol consumption by combining an electrical engine with an internal combustion engine to propel the vehicle. Thus, the hybrid electric vehicle (HEV) was devised. Depending on the involvement of the electric motor (battery) in the propulsion of the vehicle, several types of HEVs have been developed.

- Full HEVs.* An automobile driven by an electric motor alone can pass only a short distance. The electric battery system is used mainly when the internal combustion engine functions with low efficiency and when high power is demanded. The battery is partially discharged during operation of the electric motor and is recharged by the internal combustion engine. Regenerative braking, too, plays an important role in charging the battery. The electric system operates at over 200 V. Fuel consumption is reduced by 40%.
- Mild HEVs.* The electric system is called upon mainly during the accelerating phase and for starting the vehicle. Regenerative charging of the battery when the vehicle decelerates or

stops is essential for reducing the fuel consumption. The electric system in mild HEVs operates between 100 and 200 V and the fuel consumption savings range from 15% to 20% depending on the driving mode.

- c. *Micro HEVs*. These use the start–stop system which turns off the engine when the car stops and the battery takes over the electric supply needed for all accessories. In urban driving mode, the fuel consumption is reduced by about 8%.
- d. *Plug-in HEVs*. This hybrid vehicle version uses the mains power supply to charge the battery. It has the characteristics of both a full electric vehicle and a conventional automobile powered by an internal combustion engine. When the battery is exhausted, the combustion engine works as a backup power source.

Full electric vehicles are driven by electric motors only, powered by a battery pack that can be recharged from an external electric power source.

Figure 1.9 summarizes the energy and power demands of micro, mild and full HEVs, as well as of plug-in HEVs [79]. With the increase of the contribution of the electric motor to car propulsion, the power and energy demands to the battery increase abruptly. They are the highest for full and plug-in HEVs.

For the time being, only nickel-metal hydride batteries can perform the tasks and meet the energy and power demands for application in full HEVs. Intense research and development work has been carried out aimed to make lithium-ion batteries suitable for the HEV market.

Full HEVs are currently produced by Toyota (the Prius model and the Hybrid Synergy Drive series), Ford (Ford Escape and Ford Fusion models) and recently General Motors, too.

Mild HEVs also use NiMH batteries. Examples of this type of HEVs are Honda's Civic and Insight, Chevrolet's Silverado, General Motors' Saturn and Malibu series, BMW's Concept 7 series, etc.

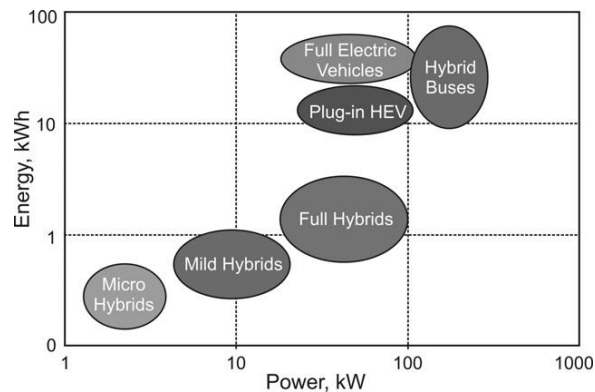


Figure 1.9:

Energy and power demands on batteries for various types of HEVs [79].

Lead–acid batteries are generally used in micro HEV applications. Models of these HEV types are produced mostly in Europe by BMW, Daimler and Citroen.

1.6.2. The Major Problem of Lead–Acid Batteries in HEV Applications

The problems faced by lead–acid batteries in HEV duties are mostly related to the negative plates:

- The negative plates cannot accept the high charging currents generated on regenerative braking.
- Batteries operate at partial state-of-charge (SOC), which leads to rapid sulfation of the negative plates.

Figure 1.10 shows the SOC regions of operation of HEV batteries, as summarised by Furukawa Corporation.

Batteries in conventional cars and micro HEVs operate at over 90% SOC with up to 5% depth of discharge. At these high SOC levels, the negative plates do not suffer from sulfation. Batteries in mild HEV duties operate from between 70% and 90% SOC. Under these conditions, the negative plates undergo slow sulfation and special treatment is needed to reverse this process. The heaviest duty is that of full HEV batteries. Batteries in these applications operate within the 30–80% SOC region, which facilitates rapid sulfation of the negative plates. These processes make lead–acid batteries unfit for these two HEV modes.

What approaches have been adopted to resolve these problems and make lead–acid batteries suitable for HEV applications?

The most logical approach is to look for alternatives to the conventional Pb negative plates or to reduce their contribution to battery operation. Carbon super-capacitors have been chosen for this purpose. Probably, there are other methods, too.

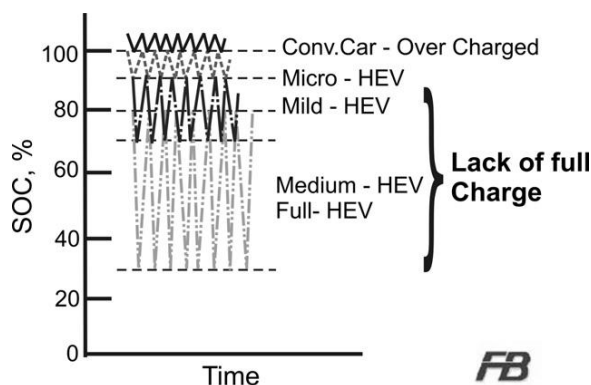


Figure 1.10:

SOC regions of battery operation in various HEV duties. Source: Furukawa Battery Corp.

Axion Power International (USA) has replaced entirely the negative plates of VRLABs with carbon super-capacitor plates [80]. CSIRO and Furukawa Battery have developed and tested a battery (called the Ultra Battery) with negative plates comprising half regular lead plate and half carbon super-capacitor plate [81].

Firefly Energy (USA) used carbon foam instead of a lead grid to hold the negative active material and to maintain a stable 3D structure of NAM with widely open pores [82]

Since 2004, the Advanced Lead–Acid Battery Consortium has been sponsoring research on addition of electrochemically active carbons to the NAM, thus increasing the reaction surface on which the charge processes proceed and hence accelerating these processes [83].

These innovations in battery design and technology are still in the process of development and testing. They are not yet commercially available. But it can be expected that they will mark the beginning of the third phase in the development of the lead–acid battery technology.

References

- [1] Mémoire des Sociétés savantes et littéraires de la République Française 1801, *J. Phys.* 56 (1802) 429.
- [2] J. Garche, *J. Power Sources* 31 (1990) 401.
- [3] W.J. Sinsteden, *Pogg. Ann. d. Physik u. Chemie* 92 (1854) 199, 1.
- [4] G. Planté, *C.R. Acad. Sci. XLIX* (1859) 402.
- [5] G. Planté, *C.R. Acad. Sci. L* (1860) 640.
- [6] An Conservatoire National des Arts & Métiers, ‘Gaston Planté et les accumulateurs électriques’, Conférence de M.L. Juman, 13 June 1934.
- [7] J.M. Schmidt, Gaston Planté: A Portrait of the Man, Planté Centennial Commemorative Issues, The Electrochemical Society Inc., Houston, Texas, October 1960.
- [8] G. Planté, *Recherche sur l’Électricité*, Gauthier-Villars, Paris, 1883.
- [9] D. Pavlov, *J. Power Sources* 30 (1990) 3.
- [10] E. Hoppe, *Die Akkumulatoren für Elektrizität*, second ed., Springer, Berlin, 1892, p. 162.
- [11] H. Samter (Ed.), *Das Reich der Erfindungen*, Urania, Berlin, 1896, p. 201.
- [12] S.A. Fauré, French Patent 141057, 1881.
- [13] E. Volckmar, German Patent 19928, 1881.
- [14] J.H. Gladstone, A. Tribe, *Nature* 25 (1882) 221.
- [15] H. Aron, *Elekt.-tech. Z.* (1883) 58.
- [16] H.F. Haring, U.B. Thomas, *Trans. Electrochem. Soc.* 68 (1935) 293.
- [17] E.E. Schumacher, G.M. Bouton, *Metals Alloys* 14 (1941) 865.
- [18] O. Jache, German Patent 1194015, 1958.
- [19] O.H. McClelland, J.L. Devitt, US Patent 3,862,861, 1975.
- [20] A.F. Hollenkamp, *J. Power Sources* 36 (1991) 567.
- [21] M.K. Dimitrov, D. Pavlov, *J. Power Sources* 46 (1993) 203.
- [22] A. Winsel, E. Voss, U. Hullmeine, *J. Power Sources* 30 (1990) 209.
- [23] D. Pavlov, *J. Power Sources* 48 (1994) 179.
- [24] D. Pavlov, B. Monakhov, M. Maja, N. Penazzi, *J. Electrochem. Soc.* 136 (1989) 27.
- [25] J.J. Lander, NRL Report No. C-3262, 22 March 1948.
- [26] H. Bode, E. Voss, *Electrochim. Acta* 1 (1959) 318.
- [27] J.R. Pierson, in: D.H. Collins (Ed.), *Power Sources* 2, Pergamon Press Ltd, Oxford, UK, 1970, p. 103.
- [28] J. Burbank, *J. Electrochem. Soc.* 113 (1966) 10.

- [29] R.V. Biagetti, M.C. Weeks, *Bell Syst. Tech. J.* 49 (1970) 1305.
- [30] V. Iliev, D. Pavlov, *J. Appl. Electrochem.* 9 (1979) 595.
- [31] D. Pavlov, V. Iliev, *Elektrokimia (Russ.)* 2 (1975) 1735 (in Russian).
- [32] D. Pavlov, G. Papazov, *J. Appl. Electrochem.* 6 (1976) 339.
- [33] D. Pavlov, N. Kapkov, *J. Power Sources* 31 (1990) 189.
- [34] V.H. Dodson, *J. Electrochem. Soc.* 108 (1961) 401.
- [35] A.C. Simon, E.L. Jones, *J. Electrochem. Soc.* 109 (1962) 760.
- [36] D. Pavlov, G. Papazov, I. Iliev, *J. Electrochem. Soc.* 119 (1972) 8.
- [37] D. Pavlov, G. Papazov, *J. Electrochem. Soc.* 127 (1980) 2104.
- [38] V.H. Dodson, *J. Electrochem. Soc.* 108 (1961) 406.
- [39] D. Pavlov, V. Iliev, G. Papazov, E. Bashtavelova, *J. Electrochem. Soc.* 121 (1974) 854.
- [40] D. Pavlov, V. Iliev, *J. Power Sources* 7 (1981) 153.
- [41] V. Iliev, D. Pavlov, *J. Appl. Electrochem.* 15 (1985) 39.
- [42] OMI Acid Recirculation Process, www.OMI-NBE.com
- [43] Battery Formation with Acid Circulation, www.inbatec.de
- [44] N.J. Maskalick, *J. Electrochem. Soc.* 122 (1975) 19.
- [45] H. Rickert, *Z. Phys. Chem. (NF)* 95 (1975) 49.
- [46] J.P. Pohl, H. Rickert, *J. Power Sources* 6 (1976) 59.
- [47] R.J. Hill, I.C. Madsen, *J. Electrochem. Soc.* 131 (1984) 1486.
- [48] J.R. Gavarri, P. Garnier, P. Boehr, A.J. Dianoux, G. Chedeville, B. Jacq, *J. Solid State Chem.* 75 (1988) 251.
- [49] A.C. Simon, S.M. Caulder, J.T. Stemmler, *J. Electrochem. Soc.* 122 (1975) 461.
- [50] P.T. Moseley, J.L. Hutchinson, C.J. Wright, M.A.M. Bourke, R.J. Hill, V.S. Rainey, *J. Electrochem. Soc.* 130 (1983) 829.
- [51] R.J. Hill, A.M. Jessel, *J. Electrochem. Soc.* 134 (1987) 1326.
- [52] J. Yamashita, H. Yutu, Y. Matsumaru, Yuasa-Jiho (Technical review) 64 (1983) 4.
- [53] S.M. Caulder, J.S. Murday, A.C. Simon, *J. Electrochem. Soc.* 120 (1973) 1515.
- [54] S.M. Caulder, A.C. Simon, *J. Electrochem. Soc.* 121 (1974) 1546.
- [55] U. Hullmeine, A. Winsel, E. Voss, *J. Power Sources* 25 (1989) 27.
- [56] D. Pavlov, E. Bashtavelova, V. Manev, A. Nasalevska, *J. Power Sources* 19 (1987) 15.
- [57] D. Pavlov, *J. Power Sources* 22 (1988) 179.
- [58] D. Pavlov, I. Balkanov, T. Halachev, P. Rachev, *J. Electrochem. Soc.* 136 (1989) 3189.
- [59] D. Pavlov, *J. Electrochem. Soc.* 139 (1992) 3075.
- [60] D. Pavlov, I. Balkanov, *J. Electrochem. Soc.* 139 (1992) 1830.
- [61] J.J. Lander, *J. Electrochem. Soc.* 98 (1951) 213; 103 (1956) 1.
- [62] J. Burbank, *J. Electrochem. Soc.* 103 (1956) 87.
- [63] P. Ruetschi, B.D. Cahan, *J. Electrochem. Soc.* 104 (1957) 406; 105 (1958) 369.
- [64] W.H. Beck, R. Lind, W.F.K. Wynne-Jones, *Trans. Faraday Soc.* 50 (1954) 147.
- [65] D. Pavlov, *Ber. Bunsen. Phys. Chem.* 71 (1967) 398.
- [66] D. Pavlov, C.N. Pouliouff, E. Klaja, N. Iordanov, *J. Electrochem. Soc.* 116 (1969) 316.
- [67] D. Pavlov, N. Iordanov, *J. Electrochem. Soc.* 117 (1970) 1103.
- [68] P. Ruetschi, *J. Electrochem. Soc.* 120 (1973) 331.
- [69] D. Pavlov, *Electrochim. Acta* 13 (1968) 2051.
- [70] D. Pavlov, R. Popova, *Electrochim. Acta* 15 (1970) 1483.
- [71] D. Pavlov, *Electrochim. Acta* 23 (1978) 845.
- [72] E. Willihganz, *Trans. Electrochem. Soc.* 92 (1947) 281.
- [73] E.J. Ritchie, *Trans. Electrochem. Soc.* 100 (1953) 53.
- [74] Y.B. Kasparov, E.G. Yampolskaya, B.N. Kabanov, *Zh. Prikl. Khimii (J. Appl. Chem.)* 37 (1964) 1936 (in Russian).
- [75] D. Pavlov, T. Rogachev, P. Nikolov, G. Petkova, *J. Power Sources* 191 (2009) 58.
- [76] K. Nakamura, M. Shiomi, K. Takahashi, M. Tsubota, *J. Power Sources* 59 (1996) 153.

- [77] H.J. Bergveld, D. Danilov, P.H.L. Notten, V. Pop, P.P.L. Regtien, in: J. Garche (Ed.), *Encyclopedia of Electrochemical Power Sources*, vol. 1, Elsevier, 2009, p. 459.
- [78] M. Wentzl, In: J. Garche (Editor-in-chief), *Encyclopedia of Electrochemical Power Sources*, vol. 1, Elsevier, 2009, p. 401.
- [79] U. Köhler, In: J. Garche (Editor-in-chief), *Encyclopedia of Electrochemical Power Sources*, vol. 1, Elsevier, 2009, p. 271.
- [80] Axion PbC® Technology, www.axionpower.com
- [81] L.T. Lam, R. Louey, *J. Power Sources* 158 (2006) 1140.
- [82] B. Monahov, K. Kelley, M. Alkhateeb, R. McDuff, *Proceedings of the 7th International Conference on Lead-Acid Batteries LABAT'2008*, Varna, Bulgaria (2008) 27.
- [83] P.T. Moseley, *J. Power Sources* 191 (2009) 134.

Fundamentals of Lead–Acid Batteries

2.1. Thermodynamics of the Lead–Acid Battery

2.1.1. General Notes

An electrochemical power source comprises two electrodes of different materials immersed in electrolyte, whereby electrode systems with different potentials are formed at the two electrodes. Electrochemical reactions proceed at the two interfaces which involve transfer of electrons between the electrode surface and ions from the solution. The difference between the potentials of the two electrodes generates the electromotive force of the electrochemical power source. When the two electrodes (anode and cathode) are connected to a conductor with a load, electric current which can do work flows between them, i.e., the chemical energy can be converted into an electrical one. Electric current flows due to changes of the valences of the materials at the two electrodes. Michael Faraday established that, when one gram equivalent of any substance takes part in an electrochemical reaction, the quantity of electricity that flows is always equal to 96,487 coulombs (C). This value is called Faraday constant, after the name of M. Faraday, and is denoted by the symbol F . The value of the constant is generally rounded to 96,500 C.

The electric energy, Q , that an electrochemical power source can deliver when one gram mole (atom) of material takes part in the electrochemical reactions at the two electrodes is equal to:

$$Q = nF(E_1 - E_2) \quad (2.E1)$$

where n is the number of valence electrons that take part in the electrochemical reactions, and E_1 and E_2 are the potentials of the two electrodes. F and n are numbers that determine the quantity of electricity. The electric energy depends on the difference between the potentials of the two electrodes made of different substances. Hence, the electric energy will depend on the selection of the materials for the two electrodes and for the electrolyte in which they are immersed.

Gaston Planté combined a Pb/PbSO₄ with a PbO₂/PbSO₄ electrode in sulfuric acid solution and obtained an electrochemical power source with high electromotive force. In 1860, he announced the invention of this power source as an electrochemical lead–acid cell of high power at a meeting of the French Academy of Sciences.

The lead–acid cell utilises the reactions of lead oxidation ($\text{Pb} \rightarrow \text{Pb}^{2+} + 2\text{e}^-$) and of lead dioxide reduction ($\text{Pb}^{4+} + 2\text{e}^- \rightarrow \text{Pb}^{2+}$). When the Pb and PbO₂ electrodes are immersed in

H₂SO₄ solution, PbSO₄ forms on both electrodes. The Pb/PbSO₄ electrode has a highly negative equilibrium potential as referred to the equilibrium potential of the hydrogen electrode, while the PbO₂/PbSO₄ electrode has a highly positive equilibrium potential. This potential difference generates one of the highest electromotive forces of all electrochemical power sources based on aqueous solutions.

The second factor that makes operation of the lead–acid cell possible is the high electron conductivity of PbO₂, which ensures involvement of the major part of the PbO₂ active material in the current generation process. The third beneficial factor is the reversibility of the electrochemical processes and of the structures formed in the lead–acid cell. PbO₂ and PbSO₄ are slightly soluble in H₂SO₄ solutions (of 1.10–1.28 relative density), which keeps them on the electrode surface where the electrochemical reactions proceed. In this way, the electrode structure remains intact during discharge and re-charge of the battery, and the latter has long cycle life as a re-chargeable power source. The electrode potentials E_1 and E_2 depend on the concentrations of the compounds that take part in the reactions and on the temperature in the cell. To quantitatively determine these dependences is an issue of electrochemical thermodynamics. The electrode potentials will be calculated, using thermodynamic data, further in this chapter.

2.1.2. Lead Sulfate Electrode (Pb/PbSO₄) Potential

The following electrochemical reaction proceeds at this electrode during discharge and charge:



The equilibrium potential of this electrode can be calculated using Nernst equation:

$$E_{\text{Pb/PbSO}_4} = E_{\text{Pb/PbSO}_4}^0 + (RT/nF)\ln k \quad (2.E2)^*$$

where k is the equilibrium constant for the electrochemical reaction. According to the law of mass action, the equilibrium constant is equal to the ratio between the concentrations, or more precisely the activities, a , of the oxidized and reduced products of the reaction:

$$k = a_{\text{PbSO}_4}/a_{\text{Pb}} \cdot a_{\text{SO}_4^{2-}} \quad (2.E3)$$

The activity of the solid phases (a_{PbSO_4} , a_{Pb}) is equal to 1.

T is the temperature in K. For 25 °C, $T = 298\text{K}$.

R is the universal (or ideal) gas constant; $R = 8.314$ Joules per kelvin per mole ($\text{J K}^{-1} \text{mol}^{-1}$)

To convert the natural logarithm into decimal logarithm, RT/nF should be multiplied by 2.303. Let us assume that $n = 1$.

$$2.303RT/nF = 8.314 \times 298 \times 2.303/96500 = 0.059 \quad (2.E4)$$

* The **E** in equation numbers stands for mathematical equations to differentiate them from reactions (chemical or electrochemical), which are labelled only with a number, e.g. (2.2).

$E_{\text{Pb/PbSO}_4}^0$ is the standard potential of the Pb/PbSO₄ electrode. It is equal to the electrode potential at $a_{\text{SO}_4^{2-}} = 1$. According to the principles of electrochemical thermodynamics, the standard electrode potential corresponds to the increase in Gibbs free energy (ΔG^0 cal), according to Eqn (2.1).

$$E_{\text{Pb/PbSO}_4}^0 = \Delta G^0 / nF \quad (2.E5)$$

The sign of ΔG^0 is determined by convention. It is negative when a reduction process takes place at the electrode.

If we substitute the free energy values for the reactants and the final products of reaction (2.1) in Eqn (2.E5), we obtain:

$$E_{\text{Pb/PbSO}_4}^0 = \left[-\Delta G_{\text{PbSO}_4}^0 - \left(\Delta G_{\text{SO}_4^{2-}}^0 + \Delta G_{\text{Pb}}^0 \right) \right] / nF \quad (2.E6)$$

Table 2.1 summarises the thermodynamic characteristics of the substances involved in the system Pb–H₂O–H₂SO₄. By substituting the values for $\Delta G_{\text{PbSO}_4}^0$, $\Delta G_{\text{SO}_4^{2-}}^0$ and ΔG_{Pb}^0 from Table 2.1 in Eqn (2.E6), we obtain:

$$E_{\text{Pb/PbSO}_4}^0 = 4.185 \cdot (-193.89 + 177.34) \cdot 1000 / 2.96500 = -0.358 \text{ V} \quad (2.E7)$$

4.185 is a coefficient of conversion of calories to Joules, multiplied by 1000 for kiloJoules.

Table 2.1: Thermodynamic characteristics of compounds in the system Pb–H₂SO₄–H₂O [1].

Compound	ΔG^0		ΔH^0		ΔS^0	
	kcal mol ⁻¹	kJ mol ⁻¹	kcal mol ⁻¹	kJ mol ⁻¹	kcal mol ⁻¹	kJ mol ⁻¹
Pb (crystal)	0.0	0.0	0.0	0.0	15.51	64.91
Pb ²⁺ (aq.)	–5.73	–23.98	0.3	1.26	4.587	19.20
Pb ⁴⁺ (aq.)	–72.3	–302.57	—	—	—	—
PbO (red)	–45.25	–189.37	–52.4	–219.29	16.2	67.80
PbO (yellow)	–45.05	–188.53	–52.07	–217.91	16.6	69.47
HPbO ₂ [–] (aq.)	–81.0	–338.98	—	—	—	—
Pb(OH) ₂	–100.6	–421.01	–123	–514.76	21	87.89
α-PbO ₂	–51.94	–217.37	–63.32	–264.99	—	—
β-PbO ₂	–52.34	–219.04	–66.12	–276.71	18.3	76.58
Pb ₃ O ₄	–147.6	–617.71	–175.6	–734.89	50.5	211.34
PbSO ₄	–193.89	–811.43	–219.5	–918.61	35.2	147.31
PbSO ₄ · PbO	–243.20	–1017.79	—	—	—	—
3PbO · PbSO ₄ · H ₂ O	–397.30	–1662.7	—	—	—	—
5PbO · 2H ₂ O	–336.35	–1407.62	—	—	—	—
Pb ₂ O ₃	–98.42	–411.89	—	—	—	—
SO ₄ ^{2–} (aq.)	–177.34	–742.17	–216.9	–907.73	4.1	17.16
HSO ₄ [–] (aq.)	–179.94	–753.05	–211.7	–885.96	30.32	126.89
H ₂ SO ₄	–177.34	–742.17	–216.9	–907.73	4.1	17.16
H ₂ O	–56.69	–237.25	–68.317	–285.91	16.72	69.97
H ⁺ (aq.)	0.0	0.0	0.0	0.0	0.0	0.0
H ₂ (gas)	0.0	0.0	0.0	0.0	31.21	130.61

Two electrons participate in the reactions at each of the two electrodes, i.e., $n = 2$.

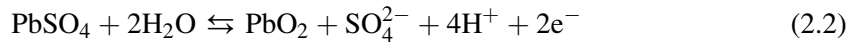
By substituting the values for k (Eqn 2.E3), RT/nF (Eqn 2E4) and E^0 (Eqn 2.E7) in Eqn (2.E2), we obtain the following equation for the equilibrium potential of the Pb/PbSO₄ electrode:

$$E_{\text{Pb/PbSO}_4} = -0.358 - 0.029 \lg a_{\text{SO}_4^{2-}} \text{ V} \quad (2.E8)$$

The increased activity (concentration) of SO_4^{2-} ions in the H_2SO_4 solution leads to an increase in the equilibrium potential of the Pb/PbSO₄ electrode in the negative direction (i.e., to higher negative values). At constant SO_4^{2-} ion concentration, the potential of the Pb/PbSO₄ electrode does not depend on the pH of the solution, but only on the temperature.

2.1.3. Lead Dioxide Electrode ($\text{PbO}_2/\text{PbSO}_4$) Potential

The following electrochemical reaction takes place at the positive electrode during charge and discharge:



The equilibrium potential of this electrode can be calculated by the following equation:

$$E_{\text{PbO}_2/\text{PbSO}_4} = E_{\text{PbO}_2/\text{PbSO}_4}^0 + (RT/2F) \ln a_{\text{PbO}_2} \cdot a_{\text{SO}_4^{2-}} \cdot a_{\text{H}^+}^4 / a_{\text{PbSO}_4} \cdot a_{\text{H}_2\text{O}}^2 \quad (2.E9)$$

The activities of the solid phases (a_{PbO_2} , a_{PbSO_4}) are equal to 1. a_{H^+} can be expressed in pH units. $E_{\text{PbO}_2/\text{PbSO}_4}^0$ can be determined in a similar way as $E_{\text{Pb/PbSO}_4}^0$:

$$E_{\text{PbO}_2/\text{PbSO}_4}^0 = \left(-\Delta G_{\text{PbO}_2}^0 - \Delta G_{\text{SO}_4^{2-}}^0 - 4\Delta G_{\text{H}^+}^0 + \Delta G_{\text{PbSO}_4}^0 + 2\Delta G_{\text{H}_2\text{O}}^0 \right) / 2.96500 \quad (2.E10)$$

By substituting the ΔG^0 values for the different reactants and products from Table 2.1, we obtain $E_{\text{PbO}_2/\text{PbSO}_4}^0 = 1.683 \text{ V}$.

Then Eqn (2.E9) for the dependence of the equilibrium potential of the $\text{PbO}_2/\text{PbSO}_4$ electrode on the concentration of the reactants in the electrochemical reaction becomes:

$$E_{\text{PbO}_2/\text{PbSO}_4} = 1.683 - 0.118 \text{ pH} - 0.059 \lg a_{\text{H}_2\text{O}} + 0.029 \lg a_{\text{SO}_4^{2-}} \quad (2.E11)$$

If we review the literature sources on lead–acid batteries, we will see that reported data about the value of the equilibrium potential of the $\text{PbO}_2/\text{PbSO}_4$ electrode differ by $\pm 5\text{--}6 \text{ mV}$ from the value in Eqn (2.E11). This difference comes from the different ΔG^0 values reported by the authors for the reactants and products of the electrochemical reaction, as well as whether a value of $F = 96500 \text{ C}$ is used or the more precise value of 96487 C .

The values of E^0 depend on the crystal modification of PbO_2 formed in the active material. PbO_2 exists in two crystal modifications: tetragonal ($\beta\text{-PbO}_2$) and orthorhombic ($\alpha\text{-PbO}_2$). For

β -PbO₂ a value of $E^0 = 1.687$ V has been determined [2], whereas the equilibrium potential for the α -PbO₂ modification is $E^0 = 1.697$ V [3].

Equation (2.E11) indicates that the equilibrium potential of the PbO₂/PbSO₄ electrode depends strongly on the pH of the solution. With increase in solution pH, the equilibrium potential of the PbO₂/PbSO₄ electrode changes by 0.118 V/pH. The value of $E_{\text{PbO}_2/\text{PbSO}_4}$ is less affected by the concentration of SO₄²⁻ ions.

2.1.4. Electromotive Force of the Lead–Acid Cell, ΔE

The electromotive force (EMF) is determined by the potential difference between the two electrodes: PbO₂/PbSO₄ and Pb/PbSO₄.

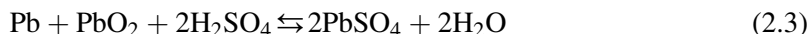
$$\Delta E = E_{\text{PbO}_2/\text{PbSO}_4} - E_{\text{Pb}/\text{PbSO}_4} \quad (2.E12)$$

By substituting the expressions for the two electrode potentials, $E_{\text{PbO}_2/\text{PbSO}_4}$ and $E_{\text{Pb}/\text{PbSO}_4}$, from Eqns (2.E8) and (2.E11) in Eqn (2.E12), we obtain the following equation for the electromotive force ΔE :

$$\Delta E = 2.041 - 0.118 \text{ pH} - 0.059 \lg a_{\text{SO}_4^{2-}} - 0.059 \lg a_{\text{H}_2\text{O}} \quad (2.E13)$$

It can be seen from the above equation that ΔE depends on the activity of the SO₄²⁻ ions and water. During battery discharge, H₂SO₄ is consumed and its concentration in the solution decreases. This leads to increase of the solution pH and, consequently, to decline in cell voltage. The slope of the curve ΔE vs discharge time depends on the changes in H₂SO₄ concentration in the solution filling the pores of the active materials of the two electrodes. This feature of the lead–acid battery is unfavourable as every battery user wants to rely on constant voltage during operation of the battery. When the cell voltage during discharge reaches a value of 1.70–1.80 V, the battery is considered to be fully discharged and should be subjected to re-charge.

The reactions that proceed at the two electrodes can be expressed by the following overall equation:



So the electromotive force for the lead–acid cell can be expressed by:

$$\Delta E = 2.041 + 0.059 \lg (a_{\text{H}_2\text{SO}_4}/a_{\text{H}_2\text{O}}) \quad (2.E14)$$

We can calculate the EMF for the different H₂SO₄ concentrations provided we know the activities of H₂SO₄ and H₂O at the respective concentrations.

What does activity of ions and molecules actually mean and how does the activity correlate to the concentration of given ions or molecules?

The law of mass action was first expressed in terms of concentration of ions and molecules that participate in the reactions. It was assumed that ions and molecules do not interact with each other, i.e., the solutions were assumed to be ideal. In actual solutions, however, ions and molecules do interact. In 1908, T. Lewis accounted for this interaction and introduced the term effective concentration or activity. The activity is a measure of how different molecules in a non-ideal gas or solution interact with each other. By substituting solution concentrations for activities it is possible to apply the law of mass action for ideal solutions to real solutions. The correlation between the activities of ions or molecules in a given solution and their concentrations is expressed by the following equation:

$$a_i = \gamma_i C_i \quad (2.E15)$$

where γ_i is the activity coefficient of a given ion (i) and C_i is its concentration in the solution. It is not possible to measure the activity coefficient of the individual ions in a solution, so a mean ionic activity coefficient is assumed, γ_{\pm} , which gives the activities of all ions of a given species in the solution.

Table 2.2 presents the mean activity coefficients for H_2SO_4 ions, the activities of water, $a_{\text{H}_2\text{O}}$, and H_2SO_4 , $a_{\text{H}_2\text{SO}_4}$, for solutions of different molalities (i.e., H_2SO_4 concentration in mol kg^{-1}), as reported by Robinson and Stokes [4] and Bullock [5].

Several sets of values have been reported in the literature for the above activities and activity coefficients, which differ by maximum 3–4%.

Table 2.2: Activity coefficients for H_2SO_4 ions and activities of H_2SO_4 and H_2O , as reported by Robinson and Stokes [4] and Bullock [5].

Concentration		γ	$a_{\text{H}_2\text{O}}$ (against molality)	$a_{\text{H}_2\text{SO}_4}$ (against molality)	EMF (ΔE), V
mol kg^{-1}	mol L^{-1}				
0.5	0.49	0.144	0.9819	0.00148	1.881
0.7	0.68	0.131	0.9743	0.00307	1.900
1	0.96	0.121	0.9618	0.00716	1.922
1.5	1.42	0.117	0.9387	0.0214	1.951
2	1.86	0.118	0.9126	0.0522	1.975
2.5	2.28	0.123	0.8836	0.1158	1.996
3	2.69	0.131	0.8516	0.2440	2.016
3.5	3.08	0.143	0.8166	0.4989	2.035
4	3.46	0.157	0.7799	0.9883	2.054
4.5	3.82	0.173	0.7422	1.888	2.072
5	4.17	0.192	0.7032	3.541	2.090
5.5	4.50	0.213	0.6643	6.463	2.106
6	4.83	0.237	0.6259	11.48	2.123
6.5	5.14	0.263	0.5879	20.02	2.139
7	5.44	0.292	0.5509	34.21	2.154

According to the electrochemical reaction (2.1), during battery discharge, a flow of electrons is generated at the negative electrode, which flows through the conductor towards the positive electrode. This leads to *loss of electric energy* out of the cell towards an external consumer. The reverse process occurs during charge, when under the action of an external power source, electrons produced by the electrochemical reaction (2.2) at the positive electrode flow through the conductor to the negative electrode and participate in the electrochemical reaction (2.1) in the reverse direction, whereby lead sulfate is reduced to lead. In this way, the lead–acid cell *is re-charged with electric energy*. The loss of electric energy per unit electric charge is the *cell voltage*. It is conventionally assumed that the electric current flows in the opposite direction to that of the electron flow. The product of cell voltage by current flowing through the electrical circuit gives the electrical power, $P_e = \Delta E \cdot I$, delivered by the cell for the particular consumer needs.

The lead–acid cell operates with H_2SO_4 solutions of concentrations up to 1.28 g cm^{-3} (at 25°C). At higher acid concentrations, the cycle life of the lead–acid cell is shortened.

As evident from the electrochemical reaction (2.3), during discharge, H_2SO_4 is consumed and water is produced. Hence, the acid concentration decreases from 1.28 to 1.11 g cm^{-3} on deep discharge. This leads to a decrease in cell voltage on open circuit from 2.15 to 1.95 V . The effect of cell voltage change with changes in acid concentration can be determined from Eqn (2.E14).

Depending on the quantity and physical state of the electrolyte, lead–acid batteries are classified into four types:

- a. batteries with flooded electrolyte (flooded batteries);
- b. low-maintenance batteries with large excess of electrolyte;
- c. batteries with electrolyte immobilised in absorptive glass mat (AGM) separators and equipped with a pressure valve (valve-regulated lead–acid batteries, VRLAB);
- d. batteries with gel electrolyte.

To improve the power output and the energy delivered by the battery, its electrodes are made of highly porous materials. Thus, greater amount of the plate mass is involved in the redox reactions. Highly porous plates are produced employing a complex technology based on a number of lead compounds and chemical and electrochemical reactions. This technology will be discussed in more detail in the following chapters of this book.

Having made an overview of the changes in H_2SO_4 consumption within one charge–discharge cycle, let us now see how does the volume of the solid phases at the two electrodes (plates) change during charge and discharge.

During discharge, part of the lead dioxide is reduced to lead sulfate at the positive plate. The molar volume of the new solid product (PbSO_4) is larger by 92% than the molar volume of

the initial PbO_2 phase involved in the reaction. At the negative plate, the process of discharge ($\text{Pb} \rightarrow \text{PbSO}_4$) leads to a 164% increase in volume of the newly formed solid phase as compared to the volume of the reacted Pb. During charge, the reverse process occurs, namely the plate volumes diminish by the above mentioned volume percents.

Thus, the plates in the lead–acid cell ‘pulse’ during cycling, expanding in thickness during discharge (because of the increased volume of the solid phases in the active masses, which reduces the pore volume at the same time), and then during re-charge, the plate thickness decreases and the active mass pore volume increases at that.

2.1.5. Brief Summary of the Lead Compounds Involved in the Manufacture and Operation of the Lead–Acid Cell

Prior to discussing the electrochemical reactions and the electrode potentials of the $\text{Pb}/\text{H}_2\text{O}$ and $\text{Pb}/\text{H}_2\text{SO}_4/\text{H}_2\text{O}$ systems, we will make a brief overview of the lead compounds involved in these systems.

Lead oxide (PbO)

This lead compound exists in two polymorphic forms: tetragonal ($\beta\text{-PbO}$) and orthorhombic ($\alpha\text{-PbO}$). The solubility of the two forms in water at 25 °C is 0.0504 g L^{-1} for $\alpha\text{-PbO}$ and 0.1065 g L^{-1} for $\beta\text{-PbO}$ [6]. Lead oxide forms lead hydroxides, $3\text{PbO} \cdot \text{H}_2\text{O}$ and $5\text{PbO} \cdot \text{H}_2\text{O}$ [7,8]. Lead oxide is hydrated forming $\text{Pb}(\text{OH})_2$, a compound of amphoteric nature. It dissociates to HPbO_2^- and $\text{Pb}(\text{OH})^-$ ions. In the battery industry, lead oxide is obtained by partial thermal oxidation of lead and is called ‘leady oxide’, as it contains between 73% and 85% PbO , the remaining part being non-oxidized lead. The basic constituent of leady oxide is tet- PbO , but orthorhombic PbO is also present, up to 5–6%. Leady oxide is used for the preparation of the pastes for lead–acid battery plate production.

Lead sulfate (PbSO_4)

At room temperature, this lead compound is usually orthorhombic, but at high temperatures (>800 °C), it acquires a cubic crystal form. Lead sulfate is isomorphic to BaSO_4 and SrSO_4 . It is poorly soluble in water: 0.0425 g L^{-1} at 25 °C and 0.056 g L^{-1} at 40 °C. Its solubility in sulfuric acid solution depends on the concentration of H_2SO_4 . Lead sulfate is formed during discharge and self-discharge of the positive and negative battery plates. It reacts with PbO to form basic lead sulfates.

Monobasic lead sulfate, $\text{PbO} \cdot \text{PbSO}_4$ (1BS)

It is a monoclinic crystalline substance built of long thin crystals. It is formed when PbO is mixed with H_2SO_4 solution during paste preparation, within a very narrow pH interval: 8–15 wt% H_2SO_4 /leady oxide. Monobasic lead sulfate is obtained also during soaking of the cured

plates in sulfuric acid solution prior to formation. 1BS is weakly soluble in water, 0.044 g L^{-1} at 0°C , but is more soluble in weak H_2SO_4 solutions.

Tribasic lead sulfate, $3\text{PbO} \cdot \text{PbSO}_4 \cdot \text{H}_2\text{O}$ (3BS)

This lead compound forms prismatic crystals with a length of $1\text{--}4 \mu\text{m}$ and $0.2\text{--}0.8 \mu\text{m}$ in cross section. Its density is 6.5 g cm^{-3} . It is poorly soluble in water, 0.0262 g L^{-1} . 3BS is obtained when leady oxide is mixed with sulfuric acid solution (up to 8 wt % $\text{H}_2\text{SO}_4/\text{PbO}$) and constitutes the basic component of the battery paste when the latter is prepared at temperatures below 70°C . Tribasic lead sulfate exerts an influence on the structure of the lead dioxide active mass and thus on some of the performance characteristics of the battery.

Tetrabasic lead sulfate, $4\text{PbO} \cdot \text{PbSO}_4$ (4BS)

It comprises prismatic crystals with a length from 10 to $100 \mu\text{m}$ and diameter from 3 to $15 \mu\text{m}$. 4BS is formed when leady oxide is mixed with sulfuric acid solution, $\text{H}_2\text{SO}_4/\text{PbO} < 6 \text{ wt\%}$, at temperature higher than 75°C , as well as during curing of the paste at high temperatures ($>85^\circ\text{C}$) in the presence of water steam. The structure of the active mass formed from 4BS ensures long battery cycle life.

Lead dioxide (PbO_2)

It exists in two polymorphic structural forms: orthorhombic ($\alpha\text{-PbO}_2$) and tetragonal ($\beta\text{-PbO}_2$). Lead dioxide is non-stoichiometric in composition, PbO_{2-x} , and contains oxygen vacancies. PbO_2 is an n-type degenerated semiconductor with a conductivity of $11,000 \text{ ohm}^{-1} \text{ cm}^{-1}$ [9]. With increase of temperature from 22 to 84°C , the conductivity of PbO_2 decreases by about 0.06% with each 1°C step. Lead dioxide is practically insoluble in water, while in sulfuric acid solution it has a solubility of 0.01 M L^{-1} at 22°C . PbO_2 is a strong oxidizer and is readily reduced to Pb_3O_4 and Pb_2O_3 , as well as to non-stoichiometric compounds of the general formula PbO_n ($1 < n < 2$). The surface layers of PbO_2 particles, when electrochemically obtained, are hydrated forming $\text{PbO}(\text{OH})_2$.

Red lead (in USA) or minium (in Europe), Pb_3O_4

This lead compound has spinel structure, similar to that of Fe_3O_4 . Its density is 9.1 g cm^{-3} . It is composed of 2PbO and 1PbO_2 and decomposes easily in acids. Red lead is virtually insoluble in warm and cold water ($10^{-7} \text{ mol L}^{-1}$). It reacts with H_2SO_4 to form 2PbSO_4 and PbO_2 . Red lead is used mostly (70–75% of the world production of Pb_3O_4) in the battery industry.

2.1.6. The $\text{Pb}/\text{H}_2\text{SO}_4/\text{H}_2\text{O}$ System

In acidic solutions, Pb^{2+} and Pb^{4+} ions are formed (though in low concentrations), whereas in neutral and weakly alkaline solutions, HPbO_2^- or PbO_3^{2-} ions form. The chemical and

Table 2.3: Chemical and electrochemical reactions involving lead ions in the Pb/H₂O system [10].

$\text{Pb}^{2+} + \text{H}_2\text{O} = \text{HPbO}_2^- + 3\text{H}^+ \quad \lg \frac{a_{\text{HPbO}_2^-}}{a_{\text{Pb}^{2+}}} = 28.02 + 3 \text{ pH}$	(2.4)
$\text{Pb}^{4+} + 3\text{H}_2\text{O} = \text{PbO}_3^{2-} + 6\text{H}^+ \quad \lg \frac{a_{\text{HPbO}_2^-}}{a_{\text{Pb}^{4+}}} = 23.06 + 6 \text{ pH}$	(2.5)
$\text{Pb}^{4+} + 2\text{e}^- = \text{Pb}^{2+} \quad E_h = 1.694 + 0.029 \lg \frac{a_{\text{Pb}^{4+}}}{a_{\text{Pb}^{2+}}}$	(2.6)
$\text{PbO}_3^{2-} + 6\text{H} + 2\text{e}^- = \text{Pb}^{2+} + 3\text{H}_2\text{O} \quad E_h = 2.375 - 0.177 \text{ pH} + 0.029 \lg \frac{a_{\text{PbO}_3^{2-}}}{a_{\text{Pb}^{2+}}}$	(2.7)
$\text{PbO}_3^{2-} + 3\text{H}^+ + 2\text{e}^- = \text{HPbO}_2^- + \text{H}_2\text{O} \quad E_h = 1.547 - 0.088 \text{ pH} + 0.029 \lg \frac{a_{\text{PbO}_3^{2-}}}{a_{\text{HPbO}_2^-}}$	(2.8)

electrochemical reactions involving these ions, and the equations representing their equilibrium state, are presented in Table 2.3 [10].

Except for the electrochemical reaction (2.6), all other reactions depend on the pH of the solution. A number of electrochemical reactions proceed in this system, which form different electrode systems, depending on lead ion valency, solution composition and pH, and electrode potential. These reactions cover a potential range of 2.0 V. Table 2.4 summarises the electrochemical reactions involving Pb, lead oxides, PbSO₄ and basic lead sulfates, and the equilibrium potentials of the respective electrode systems. The reactions and the equilibrium potentials for the hydrogen and oxygen electrodes are also given in the table. Several chemical reactions in which basic lead sulfates take part are also included in Table 2.4.

The reactions in Table 2.4 evidence that, with the increase of the PbSO₄ content in the initial compounds subject to reduction, the standard potential shifts to more negative values. When the oxidized lead phase is PbO₂, the increase in PbSO₄ content in the initial compounds subject to oxidation causes the standard potential to shift in the positive direction. Another important conclusion suggested by the reactions in Table 2.4 is that, with a few exceptions, the equilibrium potentials of the electrochemical reactions depend on pH of the solution. On grounds of the above dependencies, it is possible to plot an *E*/pH diagram, which would help us to determine the potential regions of operation of the different lead electrodes, as well as of the hydrogen and oxygen electrodes.

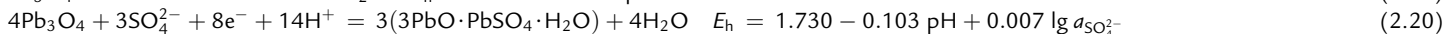
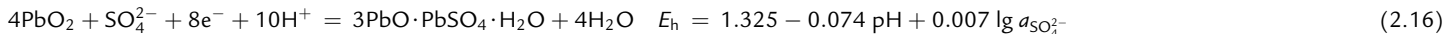
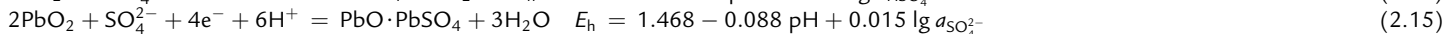
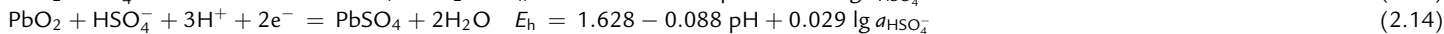
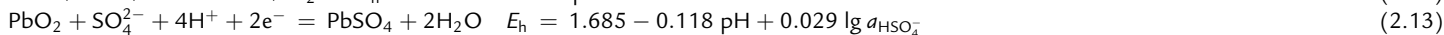
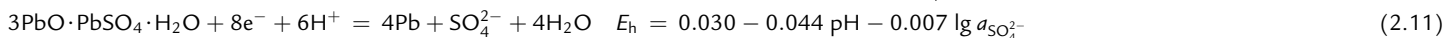
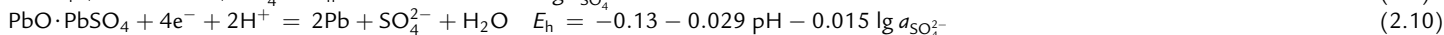
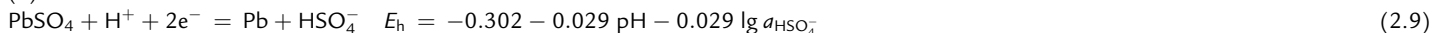
2.1.7. *E*/pH Diagram for the Pb/H₂SO₄/H₂O System

The *E*/pH diagram for the Pb/H₂O system was first proposed by Pourbaix [11], while Ruetschi and Angstadt [12] and Barnes and Mathieson [10] plotted the *E*/pH diagram for the Pb/H₂SO₄/H₂O system. Figure 2.1 shows the *E*/pH diagram proposed by Barnes and Mathieson.

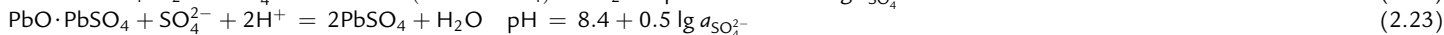
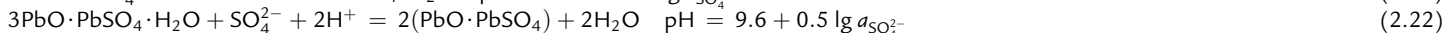
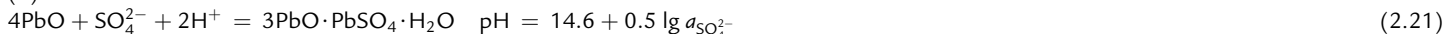
Since water participates in each electrode system, the equilibrium potentials of the hydrogen and oxygen electrodes must also be included in the system. The diagram neglects the

Table 2.4: Electrochemical and chemical reactions that proceed in the system Pb/H₂SO₄/H₂O [10].

(a) electrochemical reactions



(b) chemical reactions



(c) electrochemical reactions of H₂O decomposition



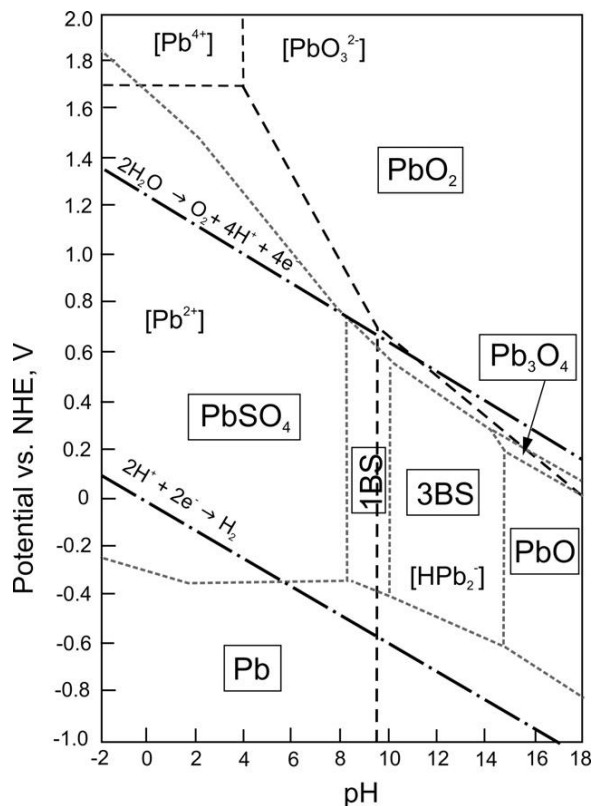


Figure 2.1:

Potential/pH diagram for the Pb/H₂SO₄/H₂O system at 25 °C in the presence of sulfate ions at unit activity [10].

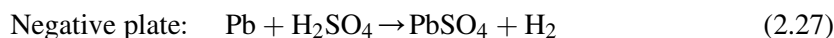
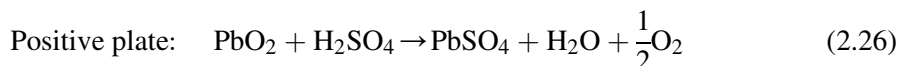
differences that appear for the two modifications of PbO and PbO₂. Although regions of α -PbO_n and β -PbO_n ($1 < n < 2$) are in fact located within the domain of Pb₃O₄, they are not shown in the figure. The areas delimited by continuous lines are the regions of stability of the solid phases. Each line represents the equilibrium potential of the electrochemical reaction that proceeds between the phases of two adjacent regions.

The E/pH diagram for the Pb/H₂SO₄/H₂O system is calculated for an overall activity of $a_{\text{HSO}_4^-} + a_{\text{SO}_4^{2-}} = 1$. The dashed lines delimit the regions of stability of Pb²⁺, HPbO₂⁻ and PbO₃²⁻ ions in the solution, and the dashed-and-dotted lines mark the dependencies of the equilibrium potentials of the hydrogen and oxygen electrodes on solution pH.

The potential/pH diagram shows that, at low pH values, the equilibrium potential of the H⁺/H₂ electrode has more positive values than that of the Pb/PbSO₄ electrode. It should be expected that H₂ will evolve first during battery charge. However, because of the high over-potential of hydrogen evolution on Pb, the above process does not proceed. Instead, PbSO₄ is reduced

to Pb first, and then, after the potential increases, evolution of H₂ starts. Similar processes occur at the H₂O/O₂ and PbO₂/PbSO₄ electrodes, too. Due to the high over-potential of O₂ evolution on PbO₂, first the reaction of PbSO₄ oxidation to PbO₂ proceeds and then oxygen evolution starts at more positive potentials.

The potential/pH diagram in Fig. 2.1 shows that the lead–acid cell is thermodynamically unstable on open circuit. Processes of self-discharge proceed on the two electrodes as a result of which water decomposes to H₂ and O₂, and discharge reactions commence at the positive and negative plates as follows:



The above reactions proceed at a low rate when the lead materials and H₂SO₄ in the cell are of high-purity grade. It has not been unequivocally established so far, which are the elementary processes that impede so strongly the processes of H₂ and O₂ evolution.

The *E*/pH diagram in Fig. 2.1 also shows that in strongly acidic solution, only Pb/PbSO₄ and PbO₂/PbSO₄ electrodes are formed within the Pb/H₂O/H₂SO₄ system and the reactions involve Pb²⁺, Pb⁴⁺ and PbO₃^{2–} ions.

Oxidation of PbO·PbSO₄, 3PbO·PbSO₄·H₂O and Pb₃O₄ to PbO₂, and of PbO to Pb₃O₄, proceeds at potentials more negative than the potential of oxidation of PbSO₄ to PbO₂. Therefore, in a mixture of PbO, basic lead sulfates and PbSO₄, PbSO₄ will be the last compound to convert to PbO₂, as the potential increases and the pH of the solution decreases. Such processes occur during formation of the positive (PbO₂) plates of the battery.

Figure 2.2 shows the potential/pH diagram of the Pb/H₂SO₄/H₂O system with marked regions of operation of the positive and negative electrodes during charge and discharge. The figure also shows the potential and pH regions within which the reactions of formation of the positive (PbO₂) and negative (Pb) active materials proceed during the technological process of lead–acid battery manufacture.

The paste for negative battery plates after curing consists of 3BS, PbO and small amounts of Pb. During formation, the basic lead sulfate is partially reduced to Pb and PbSO₄ forms (first formation stage). When the whole amount of basic lead sulfates is consumed, the electrode potential rises by absolute value and PbSO₄ is reduced to Pb (formation stage 2).

The paste for the positive plates is composed of 3BS, PbO and Pb plus small amounts of 1BS, or of 4BS, PbO and Pb. During plate formation, these compounds are oxidized to PbO₂ and sulfated to PbSO₄ (stage 1). When these compounds are exhausted, the potential of the positive plates increases and PbSO₄ is oxidized to PbO₂. This process occurs during the second stage of formation of the positive plates (Fig. 2.2).

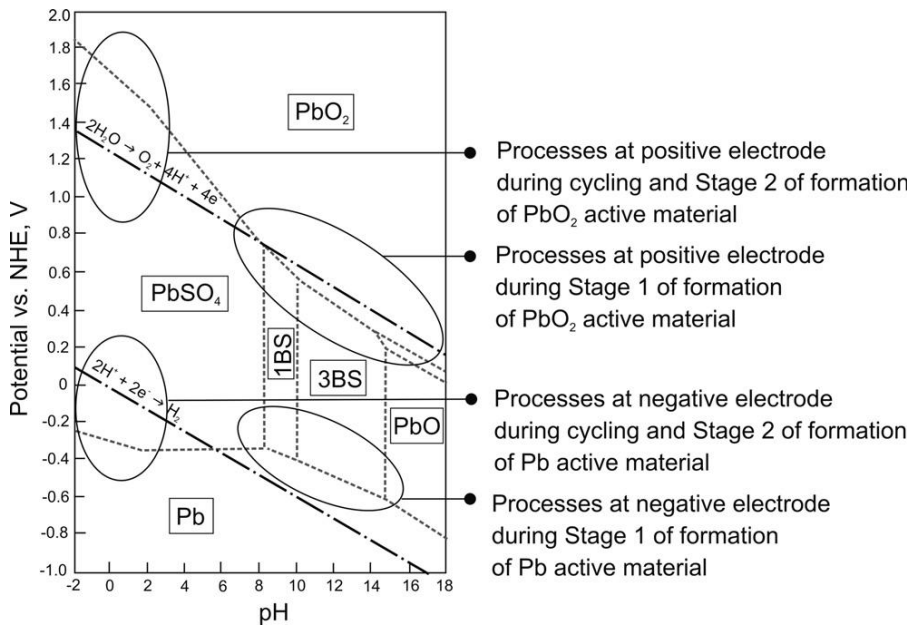


Figure 2.2:
Potential/pH diagram with marked regions of battery operation and of formation of the two electrodes.

2.1.8. Effect of Temperature on the EMF of the Lead–Acid Cell

Temperature is the second parameter that influences the electromotive force. The correlation between ΔE and temperature is expressed thermodynamically by the Gibbs–Helmholtz equation:

$$\Delta E = \Delta H/nF + T(\partial\Delta E/\partial T)_p \quad (2.E16)$$

where ΔH is the change in enthalpy of the overall reaction (2.3) for the lead–acid cell; ΔH gives the heat effect of the reaction and can be calculated using the thermodynamic data summarised in Table 2.1. The change in enthalpy related to acid dilution should also be taken into account when calculating ΔH . According to the overall reaction for the lead–acid cell (Eqn 2.3), ΔH is equal to:

$$\Delta H = \sum v_i \Delta H_e - \sum v_i \Delta H_i + 2\Delta H_w - 2\Delta H_a \quad (2.E17)$$

where $\sum \Delta H_e$ is the sum of the enthalpies of the end products of reaction (2.3), $\sum \Delta H_i$ is the sum of the enthalpies of the initial reactants, v_i are stoichiometric coefficients; ΔH_w is the change in enthalpy when 1 mol H_2O is added to the solution and ΔH_a is the change in enthalpy on addition of 1 mol H_2SO_4 to the solution. Since the enthalpies are given in

kilocalories per mole (Table 2.1), the value of ΔH should be multiplied by 4.185 to convert it to Joules.

$$\partial \Delta E / \partial T = -\Delta S / nF = \left(\sum v_e \Delta S_e - \sum v_i \Delta S_i \right) / nF \quad (2.E18)$$

where $\sum v_e \Delta S_e$ is the sum of the entropies of the end products of reaction (2.3) and v_e are the respective stoichiometric coefficients; $\sum v_i \Delta S_i$ is the sum of the entropies of the initial reactants that participate in reaction (2.3) and v_i stands for their stoichiometric coefficients. Using the data from Table 2.1, we obtain: $\Delta S = 61.81 \text{ cal mol}^{-1} \text{ } ^\circ\text{C}^{-1}$, and $\partial \Delta E / \partial T = 1.31 \text{ mV } ^\circ\text{C}^{-1}$ [1].

Bode [13] summarises the experimental data for the temperature coefficient of the EMF obtained by Harned and Hamer [14] and Craig and Vinal [15], and compares them to the thermodynamically calculated values. Figure 2.3 compares the curves for the temperature coefficient of EMF as a function of H_2SO_4 concentration based on the data reported by the above authors.

The temperature coefficient of the EMF increases with increase of acid concentration to 2.5 M H_2SO_4 , then it remains practically constant and equal to an experimentally measured value of about $+0.2 \text{ mV K}^{-1}$ within the acid concentration range from 2.5 to 5 M.

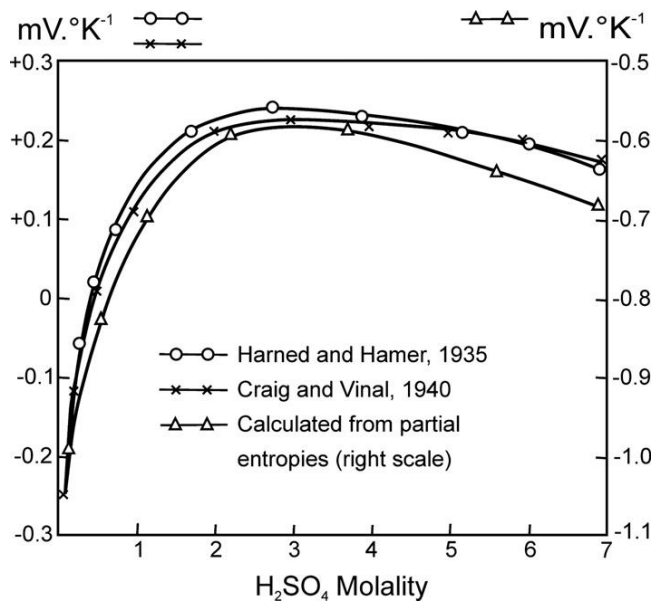


Figure 2.3: Temperature coefficient of the cell voltage of the lead–acid battery as a function of acid concentration $\text{Pb} + 2\text{H}_2\text{SO}_4 + \text{PbO}_2 = 2\text{PbSO}_4 + 2\text{H}_2\text{O}$ [13].

Harned and Hamer [14] determined experimentally the temperature dependence of the EMF of the lead–acid cell within the range from 0 to 60 °C for acid concentrations varying between 0.05 and 7.0 M H_2SO_4 , and represented it by the following empirical equation:

$$\Delta E = \Delta E_0 + aT + bT^2 \quad (2.E19)$$

where ΔE_0 is the EMF of the cell at 0 °C, and a and b are empirical constants. T is the temperature. Table 2.5 summarises the values of the EMF and of the empirical constants for various acid concentrations [14].

2.2. Electrode Systems Formed During Anodic Polarization of Pb in H_2SO_4 Solution

The most effective way to identify the different electrode systems has proved to be application of potentiostatic polarization followed by X-ray diffraction analysis of the obtained anodic deposit. Employing combined XRD and routine chemical analysis

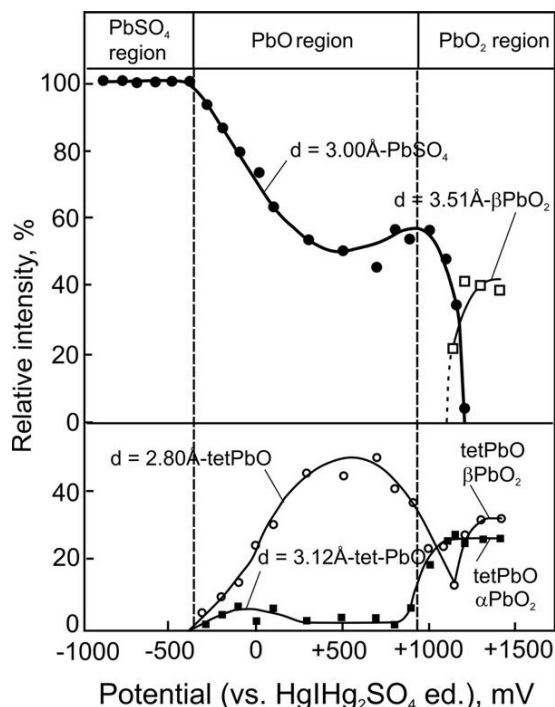


Figure 2.4:

Relative intensity of the diagnostic X-ray diffraction lines for different phases in the anodic layer formed on lead in 1 N H_2SO_4 solution as a function of the oxidation potential (vs $\text{Hg}/\text{Hg}_2\text{SO}_4$) [16–18].

Table 2.5: EMF of the cell $\text{Pb}/\text{PbSO}_4/\text{H}_2\text{SO}_4/\text{PbSO}_4/\text{PbO}_2$ at 0 °C, and constants for Eqn (2.E19) for the temperature range from 0 to 60 °C [14].

Concentration		E_θ^I, V	$a \times 10^4$	$b \times 10^4$
M (mol kg ⁻¹)	M (mol L ⁻¹)			
0.05	0.05	1.769	–310	134
0.1	0.1	1.802	–265	129
0.2	0.2	1.835	–181	128
0.5	0.49	1.879	–45	126
1	0.96	1.917	56.1	108
2	1.86	1.966	159	103
3	2.69	2.009	178	97
4	3.46	2.048	177	91
5	4.17	2.085	167	87
6	4.83	2.119	162	85
7	5.44	2.151	153	80

techniques, we have determined the phase composition of the anodic layer formed at different electrode potentials between the Pb/PbSO_4 and $\text{PbO}_2/\text{PbSO}_4$ regions [16–18]. Figure 2.4 presents the relationship between the relative intensity of the characteristic diffraction lines and the potential for each of the phases in the anodic layer formed during the potentiostatic oxidation of lead in 1 N H_2SO_4 solution. The characteristic diffraction lines of tet- PbO ($d = 3.12$ and 2.79 Å) coincide with those of α - PbO_2 ($d = 3.12$ Å) and β - PbO_2 ($d = 2.79$ Å). Therefore, the XRD analysis was combined with chemical analysis. The latter proved that PbO_2 formed at potentials more positive than $+0.95$ V (vs $\text{Hg}/\text{Hg}_2\text{SO}_4$ electrode) [16–18].

Based on the XRD data in Fig. 2.4 and the results of the chemical analysis, it has been concluded that three electrode systems form during the anodic polarization of a Pb electrode in H_2SO_4 solution, which are presented schematically in Fig. 2.5 [18].

- Lead sulfate electrode system (Pb/PbSO_4)* – stable at potentials from -0.97 to -0.40 V (vs $\text{Hg}/\text{Hg}_2\text{SO}_4$), an interval termed ‘the PbSO_4 potential region’.
- Lead oxide/lead sulfate electrode system ($\text{Pb}/\text{PbO}/\text{PbSO}_4$)* – which is stable in the potential range from -0.40 to $+0.95$ V, called ‘the PbO potential region’.
- Lead dioxide electrode system (Pb/PbO_2)* – formed above $+0.95$ V and containing α - and β - PbO_2 . This potential region is called ‘the PbO_2 potential region’.

Each of the above electrode systems has its own specific properties determined by the phases constituting the respective electrode system. The $\text{Pb}/\text{PbO}/\text{PbSO}_4$ system is formed both during potentiostatic and galvanostatic polarization of the electrodes, but the relative share of the PbO and PbSO_4 layers depends on the polarization mode.

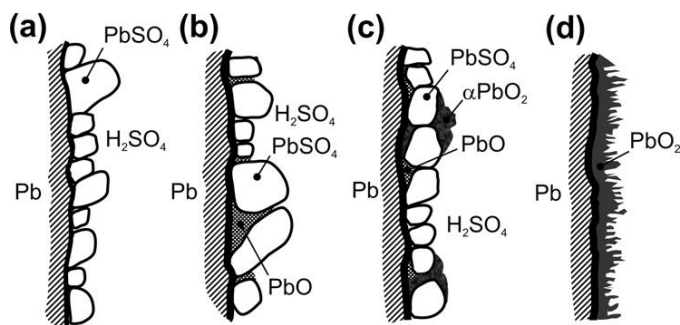


Figure 2.5:

Schematic representation of the anodic systems. (a) Pb/PbSO₄ electrode system formed in the PbSO₄ potential region; (b) Pb/PbO/PbSO₄ system formed in the PbO potential region; (c) electrode system formed at +0.95 V, i.e., between the PbO and PbO₂ potential regions; and (d) Pb/PbO₂ system formed in the PbO₂ potential region [18].

The existence of the above three potential regions has been confirmed by studies of the steady-state volt–ampere characteristics of a lead electrode in 1 N H₂SO₄ solution [19]. Figure 2.6 shows the experimental results obtained after potentiostatic polarization for 72 h. In acidic solution, the Pb/PbSO₄ and PbSO₄/PbO₂ electrode systems are thermodynamically stable, whereas in alkaline media the Pb/PbSO₄ system does not form. Formation of the Pb/PbO/PbSO₄ electrode system is therefore related to the specific structure of the anodic deposit. A lot of research efforts have been focused on studying this structure. The proposed mechanism of formation of the above electrodes and their specific properties will be discussed further in this chapter.

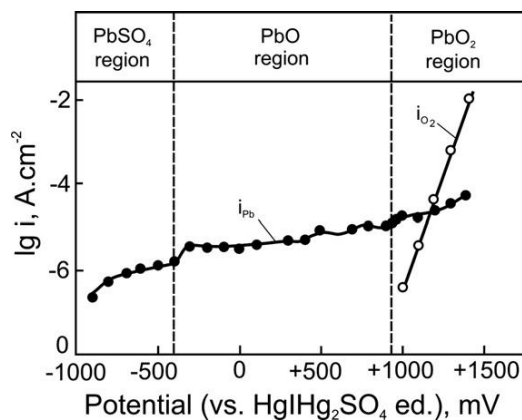


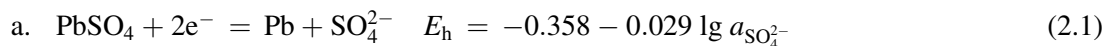
Figure 2.6:

Stationary voltage/current curve of a lead electrode in 1 N H₂SO₄ solution after 72 h of potentiostatic polarization at each potential [19].

2.3. The Pb/PbSO₄/H₂SO₄ Electrode

2.3.1. Electrode Processes on the Pb Surface

The following reactions proceed on a lead electrode immersed in H₂SO₄ solution (see Table 2.4):



b. Sulfuric acid dissociates in two steps which can be expressed by the following equations:

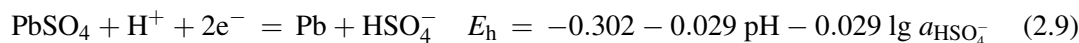


where

$$\lg(a_{\text{SO}_4^{2-}}/a_{\text{HSO}_4^-}) = -1.92 + \text{pH} \quad (2.E20)$$

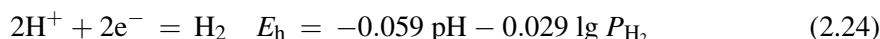
Eqn (2.E20) shows that at pH < 1, HSO₄[−] ions participate in the reaction with Pb²⁺, while at pH > 1, SO₄^{2−} ions are predominant in the solution.

c. Taking into consideration the HSO₄[−] ions, the equilibrium potential of the Pb/PbSO₄ electrode determined on the basis of thermodynamic data is:



The equilibrium potential depends on pH, as reflected in the E_h/pH diagram in Fig. 2.1.

d. The Pourbaix diagram in Fig. 2.1 shows that, in addition to the Pb/PbSO₄ reaction, evolution of hydrogen also takes place on the lead surface:



where P_{H_2} is the hydrogen pressure.

There is a potential difference of about 0.3 V between the Pb/PbSO₄ and H₂/H⁺ electrodes. This means that the potential of a lead electrode immersed in H₂SO₄ solution is a *steady-state potential*. The current/potential relationships for the above electrodes are presented in Fig. 2.7 [20].

Both the electrochemical oxidation of Pb and the reduction of PbSO₄ proceed with slight polarization, i.e., the electrode is nearly reversible. The hydrogen electrode is strongly polarized, so the H₂ evolution potential has more negative values than the potential of PbSO₄ reduction. This behaviour of the Pb/PbSO₄/H₂SO₄ (H₂/H⁺) electrode system has made it suitable for use as one of the electrodes in the lead–acid cell. In the subsequent discussion, the H₂/H⁺ electrode will be included (in parentheses) only when it affects the behaviour of the Pb/PbSO₄ electrode.

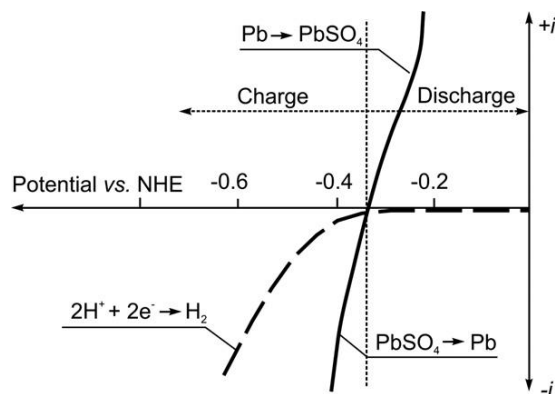


Figure 2.7:

Current/potential curves for polarization of Pb/PbSO₄ and H₂/H⁺ electrodes in H₂SO₄ solution [20].

The period during which the Pb/PbSO₄ electrode system may give or accept current depends on the ability of the Pb and PbSO₄ phases to exchange ions freely with each other. This time interval defines the capacity of the Pb electrode. In order to obtain high capacity, the Pb electrode is transformed into a porous mass with active surface of about 0.4–0.8 m² g⁻¹.

The Pb/PbSO₄/H₂SO₄ (H₂/H⁺) electrode system under open-circuit conditions is in a steady state when the partial currents between the Pb/PbSO₄ and H₂/H⁺ electrodes are equal. The mechanism of the reactions that proceed on the lead surface of the Pb/PbSO₄ and H₂/H⁺ electrodes is presented schematically in Fig. 2.8. The symbol V_a denotes the rate of the anodic reaction of lead oxidation and V_c stands for the rate of the cathodic reaction of hydrogen evolution. In the steady state, $V_c = V_a$.

Since the steady-state current is very low, the difference between the steady-state and equilibrium potentials of the Pb/PbSO₄ electrode is very small and can be neglected. If the electrode is kept at open circuit for a long period of time, the quantity of electricity that flows between the H₂/H⁺ and Pb/PbSO₄ electrodes will be substantial, despite the low steady-state current. The lead sulfate crystals formed during this time will reduce the free lead surface of the electrode system and thus decrease the capacity of the electrode, i.e., the negative plate will self-discharge. In order to avoid these processes the electrodes should sustain high over-potential of hydrogen evolution. The rate of the H⁺/H₂ reaction determines the rate of the self-discharge processes. If metals with low hydrogen over-potential (e.g., Sb, Ni) are deposited on the lead surface, the self-discharge processes will proceed at considerable rate and the plate will rapidly lose capacity on open circuit. Therefore, the purity of the materials used for lead–acid battery manufacture is essential.

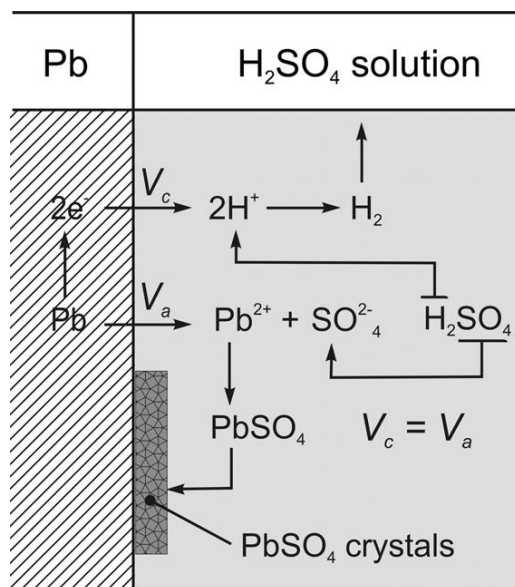


Figure 2.8:

Mechanism of the self-discharge processes on the negative plate at open circuit.

2.3.2. Elementary Processes of Anodic Oxidation of Pb and Formation of $PbSO_4$ Crystal Layer

To study the above processes a lead electrode was polarized by sweeping the potential linearly within a narrow potential interval on both sides of the equilibrium $Pb/PbSO_4$ electrode potential. Figure 2.9 shows the recorded cyclic voltammograms [21]. On the positive (anodic) potential scan, the current of Pb oxidation increases due to the electrochemical reaction of formation of Pb^{2+} ions. When the scan is taken to more positive potentials, a $PbSO_4$ layer forms on the electrode surface and a peak appears in the current curve. This lead sulfate layer exerts a passivating effect on the electrode and consequently the current rapidly declines. During the subsequent cathodic scan, the solid $PbSO_4$ layer is reduced to Pb, yielding a cathodic current peak (Fig. 2.9a).

What elementary processes occur before the formation of a $PbSO_4$ crystal layer? These processes were studied using a rotating lead disc electrode at low anodic polarization. The obtained curves are presented in Fig. 2.9b [21]. When the electrode is rotated during the anodic polarization, the current increases rapidly. No cathodic current flows when the anodic polarization is stopped and the direction of the potential scan is reversed. There are no Pb^{2+} ions to be reduced as they have been thrown out into the bulk of the solution as a result of the rotation of the electrode. Pb^{2+} ions survive in the solution for a certain period of time before reacting with SO_4^{2-} ions to form the $PbSO_4$ phase. This indicates that the

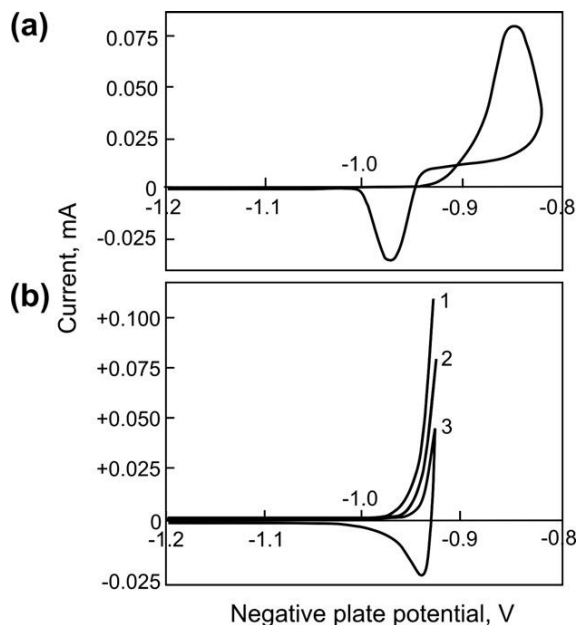


Figure 2.9:

Cyclic voltammograms recorded on polarization of a mechanically polished Pb rotating disc electrode (surface areas = 0.2 cm^2) in de-oxygenated $1 \text{ M H}_2\text{SO}_4$ solution at a scan rate of 30 mV s^{-1} . (a) rotation speed 24 rpm; (b) rotation speed 40 rpm (curve 1), 16 rpm (curve 2) and 0 rpm (curve 3). Potentials are measured vs $\text{Hg/Hg}_2\text{SO}_4$ reference electrode [21].

electrochemical oxidation of Pb in H_2SO_4 solution proceeds under diffusion control via a dissolution—precipitation mechanism. If lead sulfate is formed immediately after the oxidation of lead on the metal surface, it would form a thin amorphous PbSO_4 layer, which would passivate the electrode and hence reduce its capacity. The diffusion stage allows the Pb^{2+} ions to migrate to the solution and precipitate onto the PbSO_4 crystals. Thus, they form a porous lead sulfate layer and the reaction of lead oxidation can continue through diffusion of the Pb^{2+} ions through the pores of the PbSO_4 layer, which eventually leads to increase in electrode capacity. By the addition of polymer surface active substances to the negative active materials (e.g., lignosulfonate as one of the expander components), the time of diffusion of the Pb^{2+} ions is prolonged as they have to pass through the structure of the polymer. Thus, formation of the passivating PbSO_4 layer is impeded and the capacity of the negative plates increases, especially at low temperatures when the lead sulfate has but very low solubility.

A scanning electron micrograph of the anodic deposit formed in the PbSO_4 potential region and subjected to increase in potential to the PbO_2 region is shown in Fig. 2.10a. The observed crystals are PbSO_4 and the dark mass is PbO_2 phase. It can be seen from the micrograph that PbO_2 material sprouts among the PbSO_4 crystals.

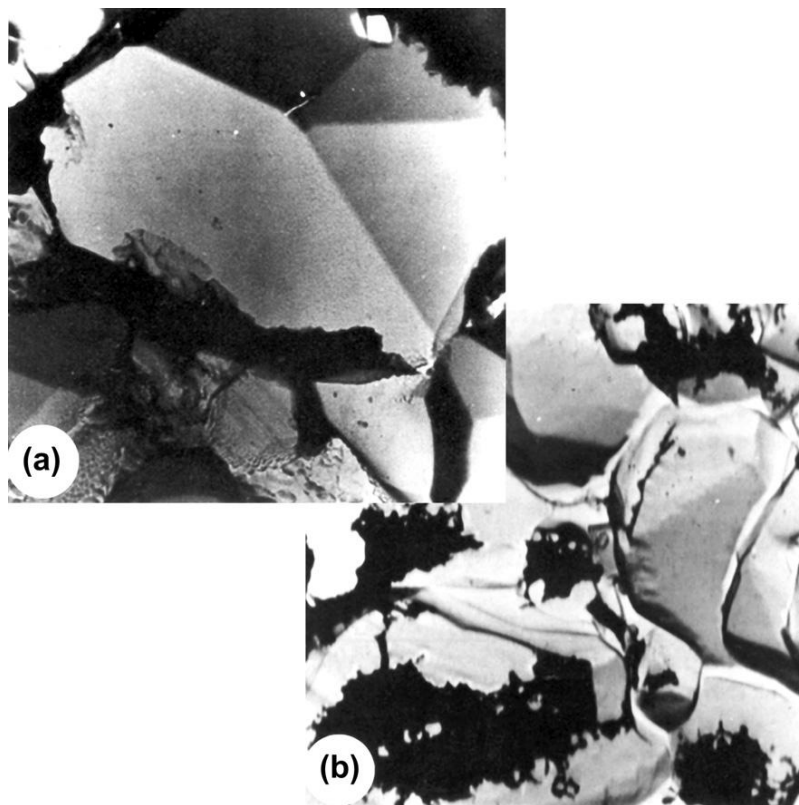


Figure 2.10:

SEM images of the lead sulfate layer formed on polarization of a Pb electrode in H_2SO_4 solution. (a) initial polarization in the PbSO_4 potential region and then, for a short time, in the PbO_2 potential region; (b) initial polarization in the PbSO_4 potential region, followed by increasing the potential to values within the PbO_2 potential region and then back to the PbSO_4 region.

The SEM image in Fig. 2.10b illustrates the situation when the anodic layer formed within the PbSO_4 potential region has been partially oxidized in the PbO_2 potential region and then reduced back to PbSO_4 . The micrograph evidences that the reduction process has proceeded in the inter-crystal spaces of the PbSO_4 layer and unreduced PbO_2 has remained on the outer faces of the PbSO_4 crystals. Based on such electron micrographic evidence, it has been demonstrated clearly that during polarization of a lead electrode, and after the initial build-up of the PbSO_4 layer, the reaction of lead oxidation continues between the lead sulfate crystallites [22]. The following elementary processes take place leading eventually to the formation of a porous PbSO_4 layer:

- electrochemical reaction of Pb oxidation to Pb^{2+} ions;
- diffusion of Pb^{2+} ions to the solution;
- concentration of Pb^{2+} and SO_4^{2-} ions reaches critical over-saturation level and they react forming PbSO_4 nuclei on the Pb surface;

- d. Pb^{2+} and SO_4^{2-} ions reach over-saturation level and precipitate on the already formed PbSO_4 crystals and thus contribute to their growth;
- e. as a result of the growth of adjacent PbSO_4 crystals the inter-crystal spaces get smaller and are transformed into pores;
- f. the electrochemical reaction of Pb oxidation continues on those sites of the lead surface which have access to electrolyte; the obtained Pb^{2+} ions move along the pores of the PbSO_4 layer to the solution and H_2SO_4 and H_2O flows move in the opposite direction; consequently, the composition of the solution in the pores of the PbSO_4 layer changes. These phenomena will be discussed in detail in the next section of this chapter.

2.3.3. Processes of Alkalization of the Solution in the pores of the PbSO_4 Layer

It is interesting to see what processes take place in the pores of the PbSO_4 layer. In an attempt to elucidate these processes, the electrochemical behaviour of a Pb/PbSO_4 electrode in 1 N H_2SO_4 solution has been investigated during galvanostatic polarization with low currents at potentials up to -0.2 V vs $\text{Hg}/\text{Hg}_2\text{SO}_4$ reference electrode [23,24]. Figure 2.11 presents a set of transients recorded under open-circuit conditions right after polarization of the electrode. The circuit was opened after reaching a definite potential.

It is evident from the curves in Fig. 2.11 that for polarization up to -0.50 V (curves 1–5) opening the circuit results in rapid drop of the electrode potential to the Pb/PbSO_4 equilibrium value. When the electrode potential is more positive than -0.50 V and the circuit is opened, a potential arrest is observed before reaching the Pb/PbSO_4 plateau. This difference in electrode behaviour is related to the alkalization of the solution in the pores of the PbSO_4 layer and the subsequent local formation of PbO and basic lead sulfates.

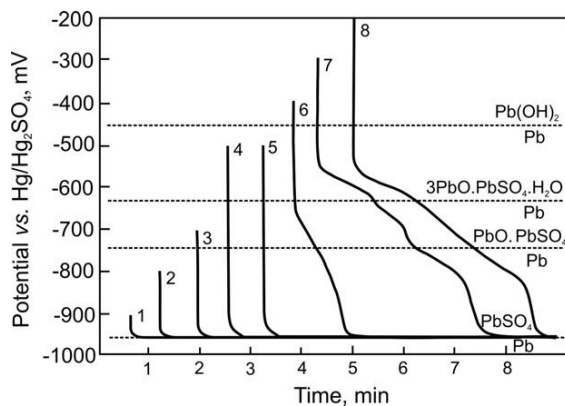


Figure 2.11:

Variation in electrode potential on open circuit after galvanostatic oxidation at $2.5 \mu\text{A cm}^{-2}$ up to continuously increasing potentials (vs $\text{Hg}/\text{Hg}_2\text{SO}_4$) [23].

During polarization of the electrode, PbSO_4 crystals are deposited on the metal surface. Since lead sulfate is a dielectric, the above electrochemical process stops in the areas covered by PbSO_4 crystal deposit. Thus, the only electrochemically active area is the metal surface between the PbSO_4 crystals. During the anodic polarization of the electrode, Pb^{2+} ions are formed at these active sites and flow between the crystals towards the bulk of the solution. A flow of SO_4^{2-} ions moves in the reverse direction. Thus, the components of the chemical reaction, Pb^{2+} and SO_4^{2-} ions, are separated by a porous dielectric layer of PbSO_4 crystals and the reaction between them must proceed at the site where the two opposite flows meet each other. Figure 2.12 illustrates the processes that take place in a pore between two PbSO_4 crystals [23].

The processes that occur in the solution of a pore, confined by the crystal planes of PbSO_4 , can be elucidated if the phenomena in a unit volume of the solution in the pore are considered. During oxidation, a flux of Pb^{2+} ions from the electrode side and a diffusion flux of SO_4^{2-} ions from the solution side will enter the unit volume. In case of equivalent fluxes of Pb^{2+} and SO_4^{2-} entering the unit volume, it will retain its electroneutrality. Soluble PbSO_4 will form. The maximum number of SO_4^{2-} ions entering the volume per unit time is determined by the bulk H_2SO_4 concentration, while that of Pb^{2+} depends on the rate of anodic dissolution, i.e. on the over-potential applied on the Pb/PbSO_4 electrode. Above a certain value of the over-potential (more positive than -0.5 V), the number of Pb^{2+} ions in the flux will surpass the equivalent number of SO_4^{2-} ions in the counter-flux and migration of positive charges starts in order to retain the electroneutrality of the volume. Since the mobility of H^+ is five times higher than that of Pb^{2+} , the principal part of the migrating cations are H^+ ions. This leads to water dissociation and increase of pH of the solution in the volume under consideration. The deeper the unit volume is located in the pore, the larger the difference between the fluxes of Pb^{2+} and SO_4^{2-} ions, and the higher the pH (Fig. 2.12a) [23].

At a definite polarization of the Pb/PbSO_4 electrode (-0.5 V vs $\text{Hg}/\text{Hg}_2\text{SO}_4$), the pH of the solution in the pore volume under consideration reaches values at which basic lead sulfates and $\text{Pb}(\text{OH})_2$ are formed. If the formation rates of lead oxide, basic lead sulfates and PbSO_4 are close, these compounds are ordered in the pores of the PbSO_4 layer according to their solubility product, i.e., PbSO_4 on the solution side and lead oxide near the lead surface (Fig. 2.12b). The sequence of compounds in the oxide layer obtained during the oxidation period will determine the processes to proceed after the polarization is interrupted. Then, diffusion of H_2SO_4 in the pores begins and the pH in the pores attains the bulk solution pH value. At this low pH, the basic lead sulfates and the lead oxide lose their thermodynamic stability and their conversion to PbSO_4 begins. These heterogeneous processes have a finite rate. The electrode potential reflects these chemical transformations through the Pb^{2+} activity. The value of the open-circuit potential established 2–5 s after switching off the polarization reflects this process of sulfation of the basic lead sulfates and the lead oxide. The potential/time curves in Fig. 2.11 illustrate the sulfation of $\text{Pb}(\text{OH})_2$, $3\text{PbO} \cdot \text{PbSO}_4 \cdot \text{H}_2\text{O}$ and $\text{PbO} \cdot \text{PbSO}_4$.

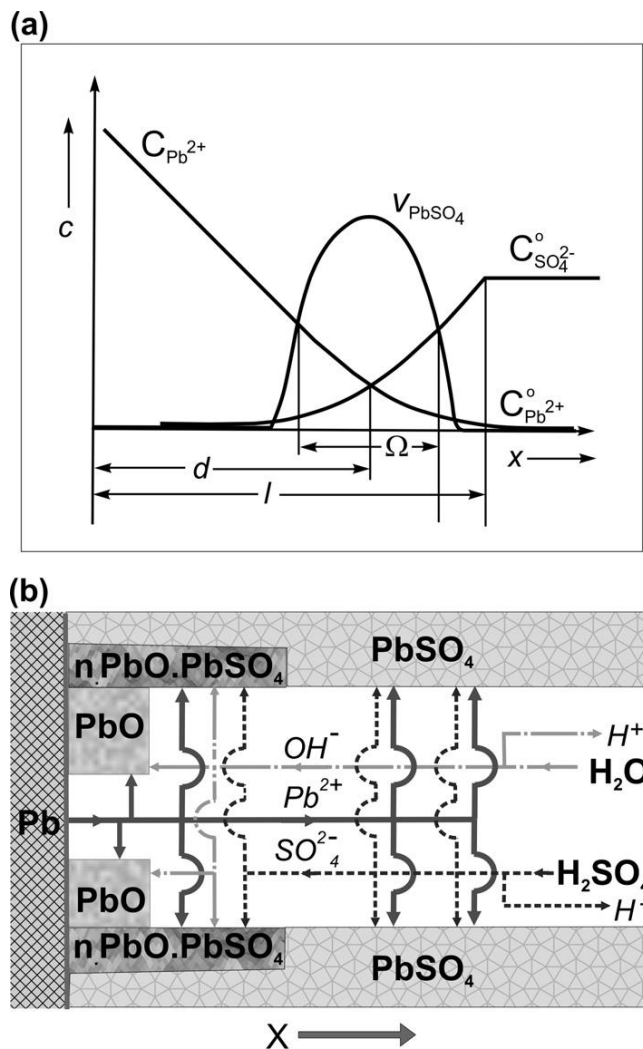


Figure 2.12:

(a) Schematic representation of the changes in concentration of Pb^{2+} and SO_4^{2-} ions in the pores of the $PbSO_4$ layer with distance from the grid. L , thickness of the diffusion layer; Ω , zone of $PbSO_4$ formation; d , distance at which the rate of $PbSO_4$ formation is highest [23]. (b) Schematics of the processes that proceed in the pores of the $PbSO_4$ crystal layer and lead to alkalization of the solution in the pores.

The actual pH of the solution in the pores on switching the current off is much higher, and hence the φ/t curves are arrested at more negative potentials than those presented in Fig. 2.11 due to sulfation of the lead oxides and basic lead sulfates [17,23]. The potentials of these compounds are a function of pH and shift to more negative values with decrease of the solution pH (Table 2.4).

2.3.4. The PbSO₄ Layer as a Selective Semipermeable Membrane — Pb/PbO/PbSO₄ Electrode Potential

It has been established that after a series of galvanostatic polarization runs with low currents, the Pb/PbSO₄ electrode is passivated permanently and its open-circuit potential remains within the range from -0.40 to -0.60 V [24]. It has been suggested that this behaviour is due to the transformation of the PbSO₄ layer into a *selective semipermeable membrane* by the process presented in Fig. 2.12 [24].

When the lead surface is covered by PbSO₄ crystals, the size of the inter-crystal spaces becomes commensurable with the diameter of the ions in the solution. In this case, only ions with small ionic radii enter the pores. The following equilibrium is established in the pore solution:



H^+ and OH^- ions have small radii, whereas SO_4^{2-} ions are relatively large and their diffusion into the PbSO₄ layer is difficult. Since the access of SO_4^{2-} ions into the pores is impeded or blocked altogether, the positively charged ions in the pores have to be neutralized by the negative charges of the OH^- ions, i.e., water in the pores dissociates and H^+ ions migrate to the bulk of the solution and OH^- ions remain in the pores (Fig. 2.12). Hence, the solution in the pores of the PbSO₄ layer becomes electroneutral at high pH [22–24] and the PbSO₄ layer is transformed into a selective ionic membrane with an established Donnan equilibrium potential [24].

According to the E_h/pH diagram in Fig. 2.1, when the pH value reaches the neutral or slightly alkaline region, the precipitation of basic lead sulfates and lead oxide starts. Ruetschi has simulated artificially prepared PbSO₄ membranes and has measured the Donnan equilibrium potential of the system Pb/PbO, Ba(OH)₂/Hg/Hg₂SO₄, 0.1 M H₂SO₄ [25]. The two electrodes were fixed on both sides of the membrane, and the experimentally determined potential was in agreement with the theoretically calculated Donnan potential, E_D , i.e.:

$$E_D = 0.059 \lg(a_{\text{H}_1^+}/a_{\text{H}_2^+})_{\text{PbSO}_4} \quad (2.E21)$$

where $a_{\text{H}_1^+}$ and $a_{\text{H}_2^+}$ are the activities of the H^+ ions at the bottom of the pores and in the bulk of the H₂SO₄ solution, respectively. Thus, it has been confirmed directly that the deposited PbSO₄ membranes are impermeable to SO_4^{2-} , HSO_4^- and Pb^{2+} ions, but lets H^+ and OH^- ions through. Therefore, the potential of the Pb/PbO/PbSO₄ electrode system is a sum of the equilibrium potential of the Pb/PbO electrode ($E_{\text{Pb/PbO}_{\text{H}^+}}$) at the local pH within the pores of the PbSO₄ membrane and the Donnan potential of the PbSO₄ membrane, namely:

$$E_{\text{Pb/PbO/PbSO}_4} = E_{\text{Pb/PbO}_{\text{H}^+}} + 0.59 \lg(a_{\text{H}_1^+}/a_{\text{H}_2^+})_{\text{PbSO}_4} \quad (2.E22)$$

To summarise, when a Pb electrode is covered with a PbSO₄ layer, depending on the diameter of the pores in the layer, two thermodynamically stable electrode systems can be formed [26]:

- a. *Wide pores*: all ions in the solution have free access to and move freely inside the PbSO₄ layer and can reach the metal surface. The electrode behaves as a classical Pb/PbSO₄ electrode, i.e., has a high electric capacitance and a potential of about -0.97 V (vs Hg/Hg₂SO₄). On polarization, the solution in the pores of the PbSO₄ layer is alkalized temporarily.
- b. *Pores with membrane dimensions*: only H₂O, H⁺ and OH⁻ ions can enter these pores and move inside. A pH gradient is formed (determined by the Donnan thermodynamic equilibrium), the solution becomes alkaline and PbO and basic lead sulfate are deposited. The potential of such an electrode is a sum of two components, namely, the equilibrium potential of the metal/oxide/solution at the bottom of the pores and the Donnan equilibrium potential of the PbSO₄ membrane determined by the difference in concentration of the H⁺ ions in the pores. The potential lies between -0.40 and -0.60 V depending on the pH of the solution in the pores and is stable with time.

2.4. H₂/H⁺ Electrode on Pb Surface

The E_h /pH diagram (Fig. 2.1) shows that an H₂/H⁺ equilibrium is established on the lead surface in H₂SO₄ solution:



The equilibrium potential of the hydrogen electrode is E_h . During polarization of this electrode to potential E_i , a current flows. The shift in potential, η_{H_2} , is equal to

$$\eta_{\text{H}_2} = E_i - E_h \quad (2.E23)$$

and is called ‘hydrogen over-voltage (over-potential)’. It is a function of the current density, i_C , as expressed by the Tafel equation

$$\eta_{\text{H}_2} = a + b \lg i_C \quad (2.E24)$$

where the constant a reflects the nature of the electrode and the constant b is related to the mechanism of the process of hydrogen evolution and is commonly known as the Tafel slope.

It has been established that the hydrogen over-voltage on Pb electrodes immersed in 0.5 M H₂SO₄ follows the Tafel equation, as illustrated in Fig. 2.13 [27]. It has been found experimentally that $b = 0.13$ V per decade, but its value depends greatly on the purity of the solution. Impurities at concentrations of 10^{-6} mol L⁻¹ cause an increase in the Tafel slope up to 0.24 V per decade.

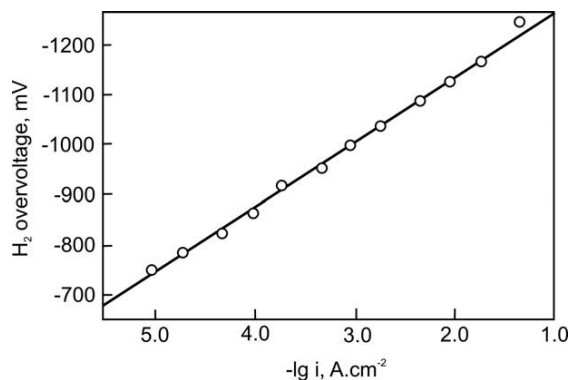


Figure 2.13:

Tafel plot of hydrogen evolution on a lead electrode in 0.5 M H_2SO_4 solution vs H_2/H^+ electrode [27].

The hydrogen over-voltage on lead at a given current density depends on the time of polarization and the nature of the anions in the solution [28]. Figure 2.14 shows the η_{H_2} vs $\lg i_C$ relationship at two different polarization rates. It can be seen that the Tafel curve displays hysteresis phenomena which depend on the speed with which the polarization is changed [28]. The observed hysteresis has been attributed: (a) to adsorption of anions on the Pb surface which alter both the distribution of the surface charges and the surface H^+ concentration [28,29] or (b) to dissolution of a certain amount of hydrogen in the Pb [30,31].

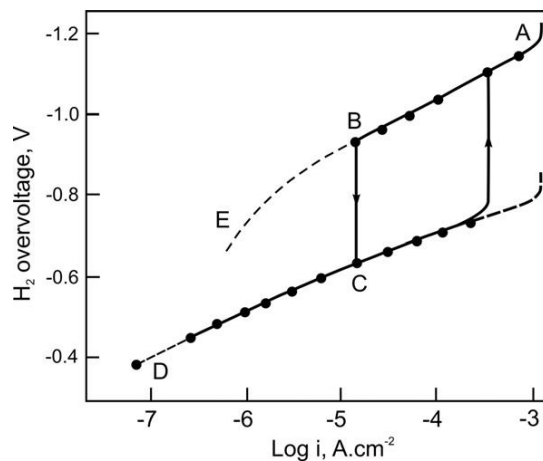


Figure 2.14:

Dependence of the hydrogen evolution rate on potential for a lead electrode immersed in 0.5 M H_2SO_4 solution during slow (continuous line) and fast (dashed line) polarization [28].

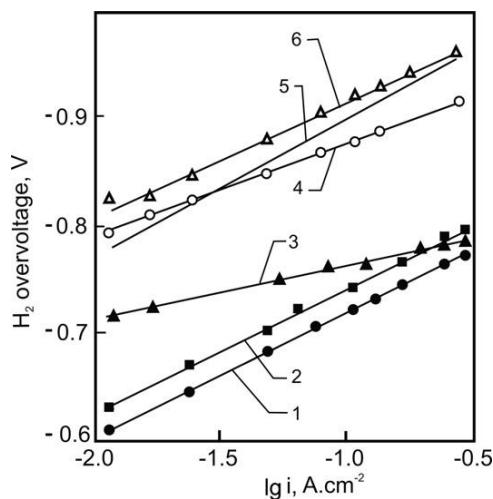


Figure 2.15:

Polarization relationships for hydrogen evolution on a porous lead electrode in 4.8 M H_2SO_4 solution: (1) no expander; (2) BaSO_4 ; (3) $\text{BaSO}_4 + \text{BNF} + \text{Al}_2(\text{SO}_4)_3$; (4) $\text{BaSO}_4 + \text{BNF}$; (5) $\text{BaSO}_4 + \text{Indulin}$; (6) $\text{BaSO}_4 + \text{DSV}$ [32].

The influence of different organic expander components on the hydrogen over-voltage on a porous lead electrode immersed in 4.8 M H_2SO_4 has been studied [32]. The obtained results presented in Fig. 2.15 indicate that the organic components contained in the expander increase the hydrogen over-voltage and the different compounds exert specific effects. Some of them have only a slight influence on the Tafel slope, while others cause it to increase or decrease markedly as compared to the b value of 0.12 V for a lead electrode in pure H_2SO_4 solution. In all cases, the value of the Tafel constant b is affected by the presence of organic expander components. It can be concluded, therefore, that while an organic expander compound will invariably alter the surface of the lead electrode, this will not necessarily lead to a change in the mechanism of the hydrogen evolution process.

Lead–antimony alloys are commonly used as grid material in lead–acid batteries. The effect of antimony on the hydrogen over-voltage has been studied intensively [33]. The polarization relationships for Pb–Sb, Pb–Ag and Pb–Sb–Ag alloys are given in Fig. 2.16. It can be seen from the data in the figure that both antimony and silver grid alloying additives lower the over-voltage of hydrogen evolution. In the three-component alloy, Pb–Sb–Ag, antimony plays the dominant role (curves 3 and 4). The observed changes in the Tafel slope have been attributed to the adsorption of SO_4^{2-} and HSO_4^- ions on the electrode surface.

The effect of both organic expander components and alloying additives on the hydrogen polarization characteristics is directly related to the charge and self-discharge processes on the negative plates, i.e., the higher the hydrogen over-voltage, the more efficient the charge and the lower the self-discharge of the plates.

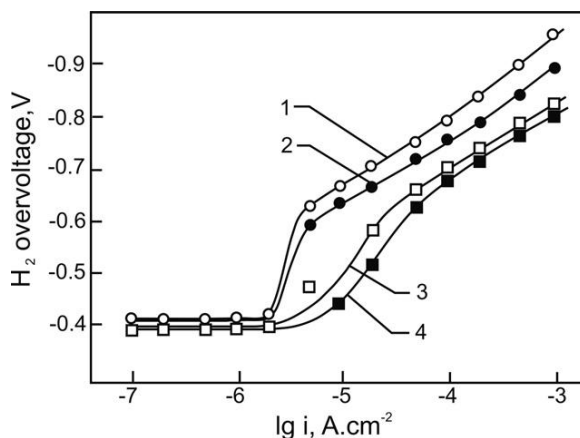


Figure 2.16:

Correlation between hydrogen over-voltage (over-potential) and alloy composition for a smooth electrode in 5.6 M H_2SO_4 at 25 °C: (1) Pb; (2) Pb–1%Ag; (3) Pb–4.5%Sb; (4) Pb–4.5% Sb–0.95%Ag [33].

2.5. The Pb/PbO/PbSO₄ Electrode System

2.5.1. Mechanism of PbO Growth

The Pb/PbO/PbSO₄ electrode system is formed when a lead electrode is immersed in H_2SO_4 solution and polarized within the potential range from -0.40 to $+0.95$ V vs Hg/Hg₂SO₄. What processes take place on the electrode after the solution in the PbSO₄ membrane is alkalinized? In our laboratory, we have studied the correlation between the thickness of the PbO and PbSO₄ layers and the quantity of electricity passing through the system [18]. It has been established that a PbSO₄ layer is initially formed and the more positive the potential, the shorter the period prior to the onset of formation of the tet-PbO and PbO·PbSO₄. These experimental findings confirm the assumption that a tet-PbO layer is located under the PbSO₄ layer and that the PbSO₄ membrane isolates the lead oxide from contact with the H_2SO_4 solution. After PbO has formed, its growth becomes the predominant process in the anodic layer. The amount of PbO·PbSO₄ does not change substantially, and its effect on the anodic deposition processes can therefore be neglected.

The basic issue in studying the growth of the oxide layer is to determine which ions carry the current through the oxide layer, i.e., Pb^{2+} or O^{2-} . Using X-ray diffraction analysis, i.e., measuring the relative content of the PbO vs PbSO₄ phases in the anodic layer as a function of the quantity of electricity passed, it has been established that in general the thickness of the tet-PbO layer steadily increases. Hence, it can be assumed that the ionic conductivity is provided by the O^{2-} ions [18].

The movement of O^{2-} ions through the dense PbO layer is made possible through the similarity in size of the ionic radii of Pb^{2+} and O^{2-} ions ($\sim 1.32 \text{ \AA}$). However, the Pb^{2+} ion has 13 times greater ionic weight than that of the O^{2-} ion. Due to their lower weight, O^{2-} ions have higher mobility than Pb^{2+} ions in the PbO crystal lattice.

The movement of O^{2-} ions through the PbO crystal lattice may proceed either by a vacancy mechanism or by an interstitial movement. The activation energy of the thermal oxidation of Pb was found to be approximately 1.0 eV [34]. This low value indicates that O^{2-} ions move through the oxide via a vacancy mechanism [34]. By measuring the temperature dependence of the current flowing through the Pb/PbO/PbSO₄ system during potentiostatic polarization, it was established that the energy of activation is about 0.5 eV [35]. This figure is extremely low, which gives grounds to assume that the transport of O^{2-} ions in the PbO layer formed by electrochemical oxidation proceeds via a vacancy mechanism [17,35]. A schematic representation of this mechanism is given in Fig. 2.17.

Pb is oxidized to Pb^{2+} ions and oxygen vacancies (O_{\square}^{2+}) are formed as a result. They move towards the membrane, through the PbO layer, under the driving force of the electric field. At the interface PbO|PbSO₄ membrane the oxygen vacancies react with water forming PbO and H^+ ions. The latter ions migrate towards the solution so that the electroneutral state of the membrane can be retained.

Since the molar volume of PbO is larger by about 23% than that of Pb, mechanical stresses are created at the interface with PbSO₄. Under the influence of these stresses some PbSO₄ crystals are displaced, pores between them are widened and H₂SO₄ penetrates into the PbSO₄ layer. When the acid comes in contact with the PbO surface, a reaction of H₂SO₄ with the oxide commences and PbSO₄ is deposited. The growing PbSO₄ crystals reduce the cross section of the pores and the solution becomes alkalized. Thus, the PbSO₄ crystals grow at the expense of partial dissolution of the PbO layer and its reaction with H₂SO₄ [18].

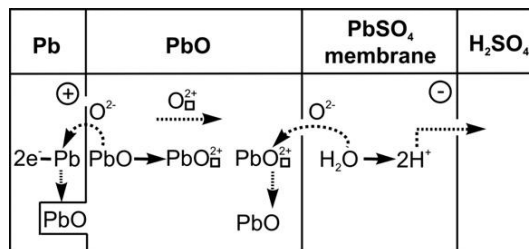


Figure 2.17:

Reaction scheme for the elementary processes that occur on current flow through the anodic layer formed in the lead oxide potential region during oxidation of lead in H₂SO₄ solution [17,35].

2.5.2. Intermediate Lead Oxides

Stoichiometry

Anderson and Sterns investigated the intermediate phases formed during oxidation of tet-PbO by oxygen at 310 °C for different reaction times, as well as during the disintegration of PbO₂ at 300–330 °C in vacuum or in nitrogen atmosphere [36]. These temperatures are relatively low and allow study of the slow structural alterations prior to establishment of equilibrium.

A schematic of the intermediate oxides is presented in Fig. 2.18.

At O:Pb ratios of $x = 1.08–1.42$, a two-phase system is formed, namely, tet-PbO + PbO_n. The latter compound is a non-stoichiometric oxide of variable composition and a pseudo-cubic elementary cell. During the thermal decomposition of PbO₂ within the region $x = 1.57–1.98$, the two-phase system PbO₂ + α -PbO_x is formed. It has been suggested that the elementary α -PbO_x cell is monoclinic with a formula in the ideal case of Pb₁₂O₁₉ (i.e., PbO_{1.583}) which contains a certain concentration of oxygen vacancies or three-valent lead ions.

The formation of the pseudo-cubic oxide PbO_n from tet-PbO is an interesting topochemical process. Figure 2.19 gives the relationship between the structure of the elementary cells of tet-PbO and PbO_n. Tet-PbO has a layered structure (Fig. 2.19a). The elementary cells contain both lead ion and oxygen ion layers as well as empty layers. In the case of PbO_n (Fig. 2.19b), the latter layers are partially filled with O^{2–} ions. In this case, the co-ordination around lead and oxygen ions is changed but slightly. The rearrangement of tet-PbO into PbO_n structure is illustrated in Fig. 2.19c [36].

The pseudo-cubic oxide is unstable. Under these conditions the thermodynamically stable compound should be Pb₃O₄. An equilibrium diagram of the oxides within the range

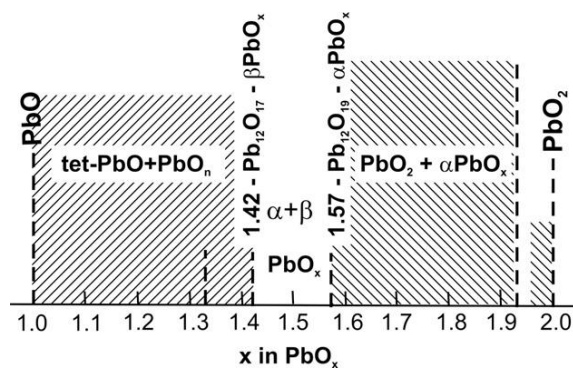
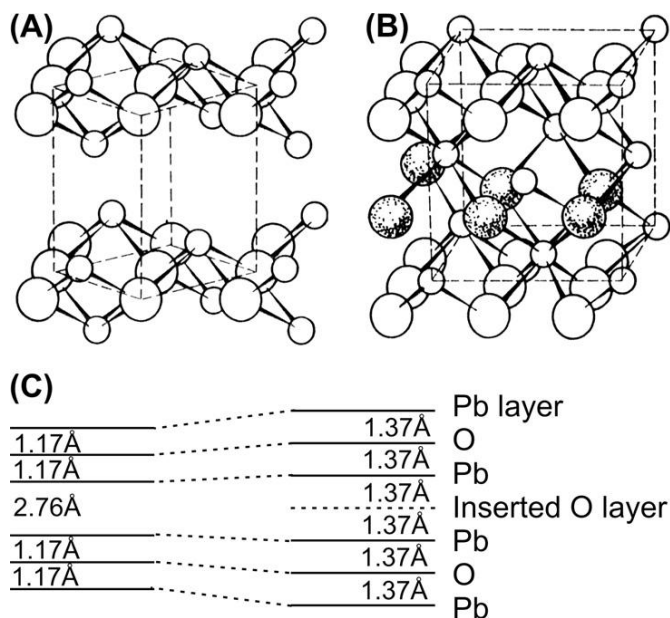


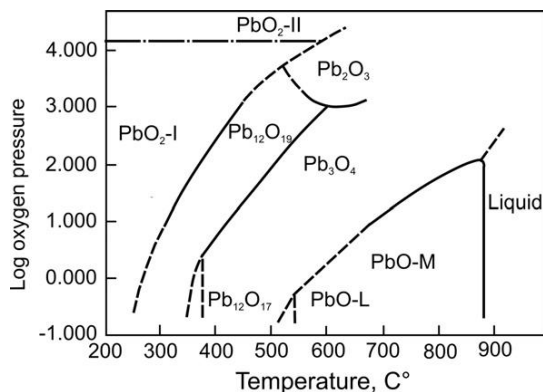
Figure 2.18:

Schematic diagram of the intermediate lead oxides formed within the PbO–PbO₂ potential region.

**Figure 2.19:**

Relationship between structures and unit cells of tet-PbO and pseudo-cubic oxides. (a) structure of tet-PbO; (b) Structure of pseudo-cubic oxide featuring intercalated oxygen layer and changed co-ordination around Pb and O; (c) Stacking sequence and principal dimensional changes [36].

PbO—PbO₂ as derived by Roy [37] is shown in Fig. 2.20. Pb₁₂O₁₉ has its own thermodynamic range of stability. An equilibrium exists between the rhombic (or tetragonal) PbO and Pb₃O₄. In order to reach this equilibrium, however, tens or in some cases hundreds of hours are required. The kinetics of this process depends on the experimental conditions and the history of the oxide.

**Figure 2.20:**

$\lg P_{O_2}$ vs temperature diagram of the phase equilibria in the PbO—PbO₂ range [37].

Within the $\text{PbO}_{1.40}$ to $\text{PbO}_{1.55}$ region, solid solutions are formed as well as some intermediate oxides. The difference in the O:Pb ratio is so small between the separate intermediate oxides, and the atomic weight of the lead atom is so much heavier than that of oxygen, that a precise analysis is not always possible. There is substantial disagreement in the literature on the nature of the intermediate oxide species [38].

Electrical conductivity

Lappe [39] prepared lead oxides with different oxygen content by electric arc sputtering in oxygen–argon atmospheres of different gas ratios. Figure 2.21 shows the relationship between the conductivity of the oxide and the oxygen content of the mixture. The results show that PbO_2 has a high conductivity of $10^2 \text{ ohm}^{-1} \text{ cm}^{-1}$. When the oxygen content in the gas mixture is reduced below 25%, lead oxides with a lower valency are formed and the conductivity decreases, reaching a value of $10^{-10} \text{ ohm}^{-1} \text{ cm}^{-1}$ in the case of tet-PbO. If the indicated change in the stoichiometric coefficient is assumed to be linear, it can be concluded that on reaching a stoichiometry of 1.4–1.5, PbO_n will have an electric conductivity close to that of PbO_2 .

Since lead oxides are semiconductors, their conductivity depends on the defects in their crystal lattice. These defects in turn depend on the method of oxide preparation, i.e., on the oxide

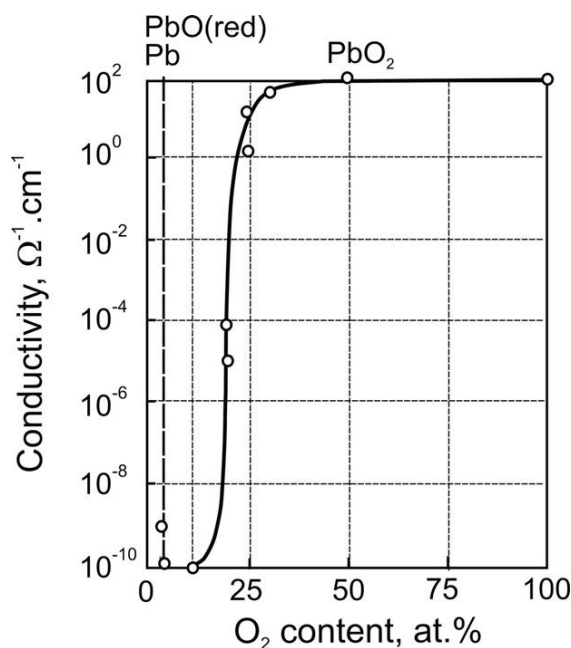


Figure 2.21:

Conductivity of a series of lead oxide layers (prepared by sputtering in different oxygen–argon mixtures) vs oxygen content of the gas mixture [39].

history. This fact has been neglected, which is the reason for the substantial differences in the literature data for the specific conductivity of lead oxides.

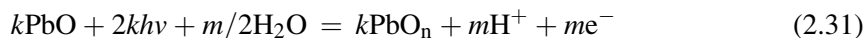
2.5.3. Photo-electrochemical Oxidation of Pb/PbO/PSO₄ to Pb/PbO_n/PbSO₄

Photo-activation

Tet-PbO is an n-type semiconductor with a bandgap energy, E_g , of 1.9–2.0 eV [40,41]. Other data claim this bandgap to be 2.7 eV [42,43]. These figures correspond to the visible light energy spectrum. Therefore, tet-PbO could be photoactive. Lead sulfate crystals are optically transparent so that the structure of a Pb/PbO/PbSO₄ electrode system allows light to reach the PbO layer and make the electrode photoactive.

Pavlov et al. [44] have investigated the photo-electrochemical properties of the above system during potentiostatic polarization. The system was formed at +0.40 V (vs Hg/Hg₂SO₄) in 0.5 M H₂SO₄ for a fixed period of time and then subjected to illumination with white light for 3 min. Figure 2.22 shows the change in current with time for five consecutive illuminations. During the first light pulse, it can be seen that the PbO formed in darkness is photo-inactive. However, after a certain amount of light energy falls on the electrode system, it becomes photoactive. This ‘photo-activation process’ continues when the electrode is polarized at potentials more positive than 0.0 V (vs Hg/Hg₂SO₄ electrode).

The photo-activation of PbO is a result of an increased oxide stoichiometric coefficient. This is possible if the chemical composition of the lead oxide is altered as a result of the photochemical processes, e.g.,



where $h\nu$ is the energy of a photon, and k and m are stoichiometry coefficients. PbO_n is non-stoichiometric lead oxide, where $1 < n < 2$.

The formation of PbO_n during the photo-electrochemical reaction can be considered to be a process similar to the chemical oxidation of tet-PbO by O₂ at elevated temperatures (300–350 °C). During the thermal process, non-stoichiometric PbO_n is formed with a pseudo-cubic crystal lattice and variable composition (Fig. 2.18) [36].

The formation of PbO_n can also be demonstrated during the polarization of the electrode at +0.40 V if the surface of the system is illuminated through a slot. Only the projection of the slot upon the electrode is illuminated. This region changes its colour from light grey to pale brown (Fig. 2.23).

In summary, these observations suggest that the process of photo-activation of the Pb/PbO/PbSO₄ system passes through a transformation into the Pb/PbO_n/PbSO₄

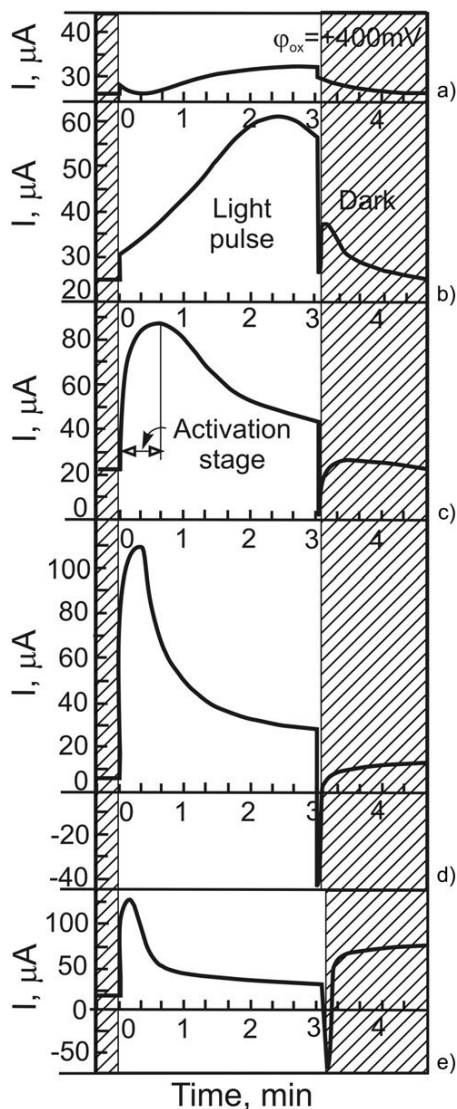


Figure 2.22:

Change in current during the five consecutive light pulses (3 min each) during the initial photo-activation period. Oxidation potential +0.40 V. Interval between two light pulses 30 min in the dark [44].

system. The photoelectrochemical behaviour of the Pb/PbO/PbSO₄ electrode has been studied by many researchers and different variants of the mechanism of the processes of photo-activation have been proposed, accounting for the semiconducting and chemical properties of PbO which lead to the formation of a non-stoichiometric lead oxide [45–49].

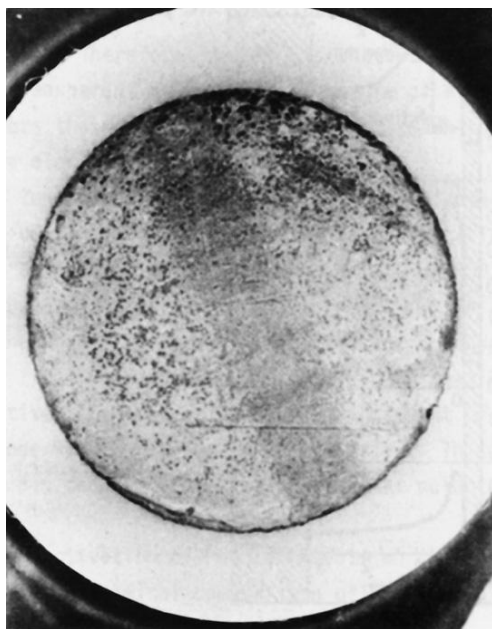


Figure 2.23:

Photograph of the electrode surface after illumination. The electrode is oxidized at +0.40 V for 4 h and illuminated through a slot for 40 min. The darker zone on the electrode surface results from formation of light brown PbO_n during the illumination [44].

2.5.4. Electrochemical Oxidation of Pb/PbO/PbSO₄ Electrode to Pb/PbO₂ Electrode

At potentials more positive than 1.10 V vs Hg/Hg₂SO₄, the Pb/PbO/PSO₄ electrode system is oxidized to Pb/PbO₂ electrode. A mechanism for these processes has been proposed including direct oxidation of PbO to α -PbO₂ and of PbSO₄ to β -PbO₂ [50,51]. This mechanism does not provide a clear physical picture of the initial stages of formation of the PbO₂ layer. If the electrode system is examined thermodynamically, the E_h /pH diagram (Fig. 2.1) and the phase diagram (Fig. 2.20) indicate that there exists a region, between the PbO and PbO₂ stoichiometric regions, where Pb₃O₄ and the non-stoichiometric lead oxides PbO_n and PbO_x are formed. This thermodynamic region, too, must be accounted for when studying the mechanism of oxidation of the Pb/PbO/PbSO₄ electrode system to Pb/PbO₂ electrode. Such an analysis is proposed in Ref. [52].

A Pb/PbO/PbSO₄ electrode system was prepared by potentiostatic oxidation of a Pb electrode in 0.5 M H₂SO₄ solution at +0.60 V vs Hg/Hg₂SO₄ reference electrode. After this, the system was subjected to potentiodynamic polarization at a scan rate of 10 mV s⁻¹. Figure 2.24 shows the potentiodynamic curves recorded during five potential runs up to 1.450 V [52].

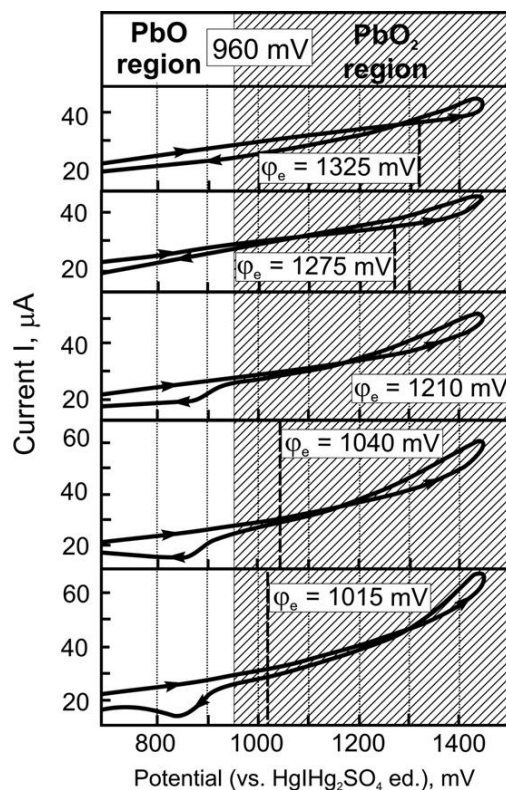


Figure 2.24:

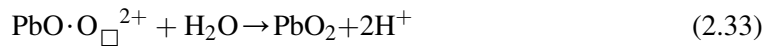
Cyclic voltammograms for a lead electrode in H_2SO_4 solution. Anodic potential limit 1.45 V (vs $\text{Hg}/\text{Hg}_2\text{SO}_4$); potential scan rate 10 mV s^{-1} [52].

During the first cycle, when the potential reaches 1.325 V, a new electrochemical process starts, and the anodic current increases slowly. For the first three cycles, no minimum is observed in the cathodic scan. This suggests that the product of the anodic reaction cannot be reduced and remains deep within the anodic PbO layer. Thus, the nature of the oxide is altered and during the next potential sweep, the anodic process commences at a more negative potential. A minimum appears in the cathodic scan only after five cycles. This minimum is associated with the reduction of PbO_2 . It is assumed that the anodic reaction (2.31) of formation of non-stoichiometric PbO_n proceeds in accordance with thermodynamic considerations (see Figs 2.1 and 2.20). Thus, the $\text{Pb}/\text{PbO}_n/\text{PbSO}_4$ system is formed.

Formation of PbO_n may proceed via the following mechanism. At potentials more positive than 1.30 V vs $\text{Hg}/\text{Hg}_2\text{SO}_4$, PbO at the Pb/PbO interface is oxidized and oxygen vacancies (O_{\square}^{2+}) are formed as a result. Let us assume that the PbO layer is built of PbO molecules. The following process will take place at the Pb/PbO interface:



Electrons enter the metal, while oxygen vacancies, driven by the electric field, move towards the $\text{PbO}|\text{PbSO}_4$ interface, where they react with H_2O and OH^- ions in the pores of the interface. 'PbO₂ molecules' are formed.



PbO₂ and PbO molecules form non-stoichiometric PbO_n ($1 < n < 2$). Hydrogen ions migrate through the pores of the PbSO₄ membrane to the solution. The non-stoichiometric oxide PbO_n has higher electro-conductivity. Hence, the potential drop in the PbO_n layer decreases and the potential at the interface PbO_n|PbSO₄ membrane increases and reaches the potential of the oxygen evolution reaction:



where O_{ad} and O_{ad}⁻ are oxygen atoms and radicals adsorbed on the PbO_n surface.

Electrons pass through the PbO_n layer and reach the metal. Hydrogen ions migrate through the pores of the PbSO₄ layer to the solution.

The concentration of O_{ad} atoms on the PbO surface increases and a concentration gradient is formed as a result. Under the influence of this gradient, oxygen species diffuse into the empty layers of the PbO_n crystal lattice (Fig. 2.19).

Let us consider the probability of O_{ad} to penetrate into the PbO_n crystal lattice. According to Anderson and Sterns [36] (Fig. 2.19), the width of the empty layers in tet-PbO is 2.76 Å, while the diameter of the oxygen atom is 1.22 Å. Hence, oxygen atoms move freely in the empty layers of the tet-PbO_n crystal lattice. Since they are efficient electron acceptors, they oxidize PbO_n to PbO₂, which leads to a significant increase in conductivity of the oxide layer. Thus, the PbO_n layer is oxidized to PbO₂ [49,52].

Electron microscopic studies of the anodic layer formed during potentiodynamic sweeps to 1.05 V at 1.0 mV s⁻¹ have been performed in an effort to disclose the mechanism of PbO₂ formation. Figure 2.25 shows micrographs of the electrode surface after oxidation. The PbO₂ phase (dark zones) is a shapeless mass sprouting from some of the pores. These SEM images show clearly that PbO₂ is formed as a new phase with nuclei initiated in the pores of the PbSO₄ layer and then growing to extend from the PbSO₄ membrane. X-ray diffraction analysis has provided clear evidence that PbO₂ formed under these conditions is of the α-modification. It has been suggested that the newly formed α-PbO₂ phase has a non-stoichiometric composition [52].

Figure 2.26 presents cyclic voltammograms recorded during oxidation of PbO_n and PbSO₄. During the first cycle, an anodic current maximum (C) is obtained, which corresponds to the formation of α-PbO₂ in the pores of the PbSO₄ membrane. When the α-PbO₂ phase gets in



Figure 2.25:
Electron micrograph of the initial stage of PbO_2 formation [52].

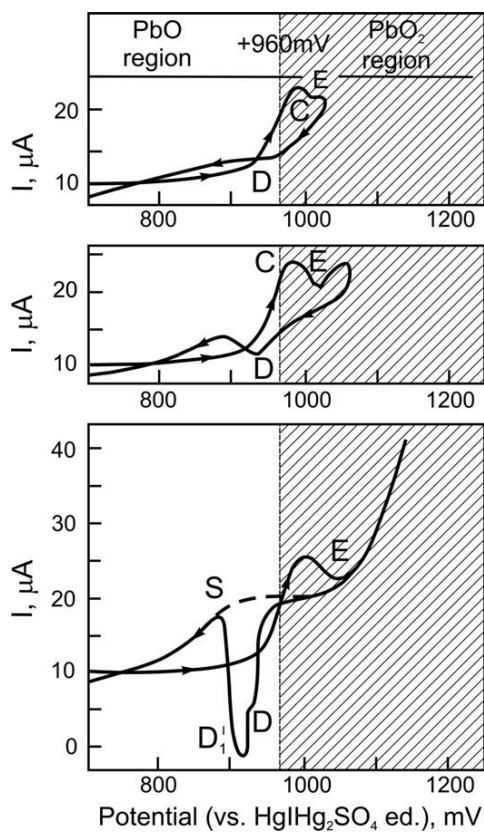
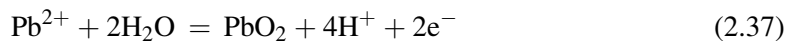
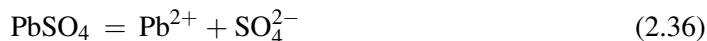


Figure 2.26:
Cyclic voltammograms for a lead electrode in H_2SO_4 solution on polarization to potentials of PbSO_4 membrane destruction.

contact with the H_2SO_4 solution, a new electrochemical process takes place on the PbO_2 surface, namely, the Pb^{2+} ions formed by the dissolution of PbSO_4 are oxidized to PbO_2 :



As a result of the above process, the anodic current increases after the minimum (Fig. 2.26b,c). Since this process proceeds in acidic medium, $\beta\text{-PbO}_2$ is formed. When the potential is reversed, a second minimum (D_1^i) appears in the cathodic part of the voltammogram. It is related to the reduction of $\beta\text{-PbO}_2$. Later on, the shape of the voltammogram depends on the disintegration processes in the PbSO_4 membrane.

The destruction of the PbSO_4 membrane is illustrated in Fig. 2.27a. The PbSO_4 layer is transformed into a shapeless mass, partially covered with a PbO_2 deposit. Figure 2.27b presents the profile of a PbSO_4 crystal covered with a PbO_2 layer, which provides evidence that the oxidation of PbSO_4 proceeds via the following mechanism:

Dissolution of a PbSO_4 crystal with formation of Pb^{2+} ions \rightarrow diffusion of Pb^{2+} ions (most often on the surface of the PbSO_4 crystal) to the PbO_2 phase \rightarrow oxidation of Pb^{2+} ions upon the PbO_2 surface \rightarrow deposition of PbO_2

Through polarization of a rotating ring-disc (Pb) electrode (2500 rpm) in the potential region between 0.8 and 1.7 V (vs $\text{Hg}/\text{Hg}_2\text{SO}_4$) at a scan rate of 10 mV s^{-1} it has been established that soluble unstable Pb^{4+} ions are generated during the anodic formation of PbO_2 in H_2SO_4 solution [53].

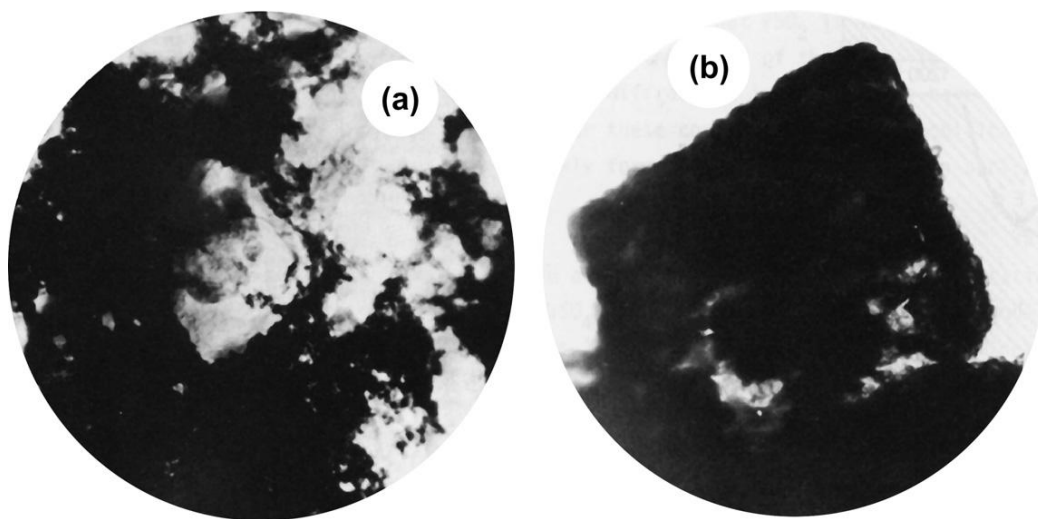


Figure 2.27:
Electron micrograph illustrating PbSO_4 membrane destruction [52].

When during the process of positive plate manufacture do the above processes take place? They occur during the technological process of plate formation, when the corrosion layer composed of PbO_n and PbSO_4 on the positive grid surface is oxidized to PbO_2 . At the beginning of the formation process, the polarization of the electrode increases abruptly. Then, after a certain time, gas evolution starts. The potential/time curve passes through a maximum and then declines rapidly. This profile of the potential curve is related to the conversion of the corrosion layer into a highly electron-conductive lead dioxide layer. The structure of this layer depends on the previously discussed processes. As evident from Fig. 2.27, if the anodic layer contains PbSO_4 crystals, they may be oxidized superficially. Such a structure of the anodic layer may impair the conductivity of the interface corrosion layer|active mass. So formation of PbSO_4 in the corrosion layer during plate soaking prior to formation should be avoided.

These are in brief the processes that take place during the transformation of the Pb/PbO/PbSO_4 electrode system into Pb/PbO_2 electrode.

2.6. The $\text{Pb/PbO}_2/\text{PbSO}_4$ Electrode System

2.6.1. Physico-chemical Properties of PbO_2

Polymorphism

Kameyama and Fukumoto established that, besides $\beta\text{-PbO}_2$, a second crystal modification of lead dioxide exists, too, namely, $\alpha\text{-PbO}_2$ [54]. The unit cell of $\alpha\text{-PbO}_2$ formed by anodic deposition from alkaline solutions is presented in Ref. [55]. Bode and Voss have established the presence of $\alpha\text{-PbO}_2$ in the active mass of the positive plates of lead–acid batteries [56]. Methods have been developed for the preparation of both PbO_2 crystal modifications in the pure state [57]. Figure 2.28 shows the unit cell models for $\alpha\text{-PbO}_2$ and $\beta\text{-PbO}_2$, respectively [58].

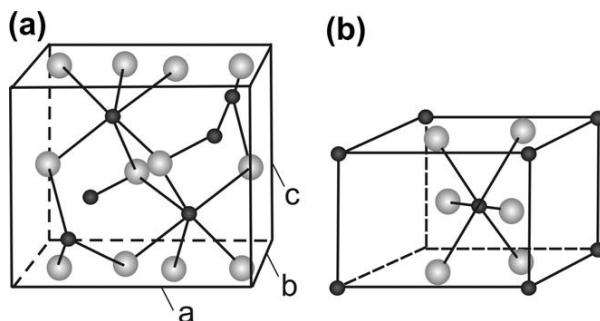


Figure 2.28:
Unit cells of (a) $\alpha\text{-PbO}_2$ and (b) $\beta\text{-PbO}_2$ crystals [58].

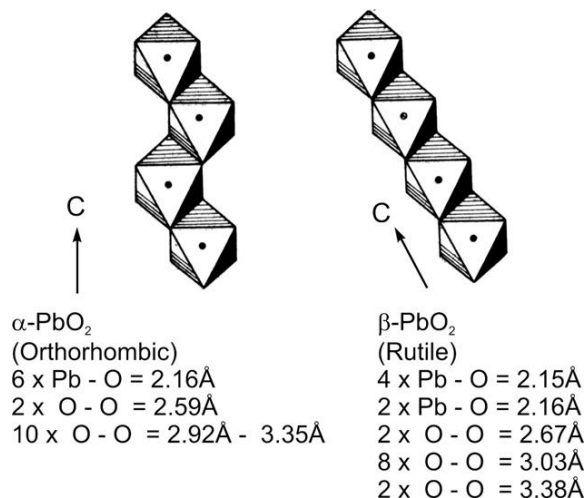


Figure 2.29:
Packing of octahedral in α -PbO₂ and β -PbO₂ crystals [60].

α -PbO₂ crystallises in the orthorhombic system with a structure similar to that of Columbite with lattice axes:

$$a = 4.938 \text{ Å}; b = 5.939 \text{ Å}; c = 5.486 \text{ Å}$$

The lead ions are fixed in the centres of the octahedron and are each surrounded by six oxygen ions at a distance of 2.16 Å (Fig. 2.29).

β -PbO₂ crystals have a tetragonal elementary cell of the rutile type with axes:

$$a = 4.945 \text{ Å}; b = 3.378 \text{ Å}$$

This structure, too, comprises lead ions positioned in the centres of distorted octahedra.

A close relationship exists between the two crystal lattices [59,60]. The difference is in the mode by which the octahedra of the two modifications are attached to each other. Figure 2.29 shows the respective packings [60]. In the β -PbO₂ crystal structure, neighbouring octahedra share opposite edges, which results in the formation of linear chains of octahedra. Each chain is connected to the next one by sharing corners. In α -PbO₂, neighbouring octahedra share non-opposing edges in such a way that zig-zag chains are obtained. As with β -PbO₂, each chain is connected to the next one by sharing corners. Both modifications have approximately equal Pb—O distance. This comparison between the crystal structures of the two PbO₂ modifications indicates that they differ mainly by the arrangement of the octahedral in the chains. In the case of tetragonal β -PbO₂, well-defined oxygen layers are observed, which obviously would result in higher mobility of the oxygen ions in this crystal lattice than in that of the α -PbO₂ modification.

Table 2.6: Density of α -PbO₂ and β -PbO₂ [26].

Author(s)	Reference No.	α -PbO ₂	β -PbO ₂	Form of PbO ₂
Zaslavskii and Tolkachev	[61]	9.53	9.37	Crystal deposit
Bode and Voss	[56]	9.87	9.70	
Bone and Fleischmann	[62]	9.76	9.65	
Burbank	[63]		9.63	Active mass
Fleischmann	[64]		8.6	Active mass
Bode, Panesar and Voss	[65]	9.87		
Micka, Svata and Koudelka	[66]		8.76	Active mass

Experimental values for the density of PbO₂ are given in Table 2.6 [26]. It can be seen that the density of α -PbO₂ is somewhat higher than that of β -PbO₂. The data in the table evidence also that PbO₂ in the active mass has a substantially lower density than that of the crystal deposit formed by electrochemical oxidation in the lead-ion-containing solutions. Micka et al. proposed the presence of amorphous PbO₂ in the active mass [66]. The formation of a third amorphous modification of PbO₂ in the positive active mass of lead–acid batteries has been established by many researchers [67–70].

Stoichiometry

Despite the fact that lead dioxide is represented nominally by the formula PbO₂, all researchers unanimously agree that it is a non-stoichiometric compound. Different authors give different values for the stoichiometric coefficient $x = \text{O}:\text{Pb}$, but they all agree that the actual oxygen to lead ratio is less than 2.00 [71–73]. The interval within which the stoichiometric coefficient x may vary without the initiation of a new phase (homogeneity region) is between 1.875 and 1.99 [73]. When x falls below the lower limit, formation of the pseudo-cubic phase starts (with composition PbO_{1.57}).

Butler and Copp established that PbO₂ contains water and suggested the following composition: PbO_{1.98}·0.04H₂O with a lower limit of homogeneity of PbO_{1.95} [74]. Other researchers have proved that the water in lead dioxide is very strongly bonded, which comes to support the conclusion that H₂O is included in the PbO₂ crystal lattice [36]. The latter authors suggest that in order to attain the ratio Pb:O = 1:2, part of the Pb⁴⁺ and O^{2–} ions are substituted by Pb²⁺ and OH[–] ions to give the formula PbO_{1.98}(OH)_{0.034}(H₂O)_{0.01}. The remaining water is adsorbed on the surface of the fine-grained deposit or in its pores [36].

Bagshaw et al. determined the chemical composition of PbO₂ as a function of the preparation method [57]. Table 2.7 summarised the obtained results. The obtained values for the stoichiometric coefficient of α -PbO₂ are lower than those for the β -PbO₂ modification.

Table 2.7: Composition of α -PbO₂ and β -PbO₂ prepared by different methods [57].

Preparation method	Chemical composition
α -PbO ₂	
1. Sodium chlorate/sodium nitrate oxidation	PbO _{1.83} (OH) _{0.14}
2. Chlorine dioxide oxidation	PbO _{1.81} (OH) _{0.26}
3. Ammonium persulfate oxidation	PbO _{1.83} (OH) _{0.23}
4. Alkaline electroformation	PbO _{1.80} (OH) _{0.16}
5. Alkaline/lead acetate electrodeposition	PbO _{1.82} (OH) _{0.19}
β -PbO ₂	
1. Lead tetra-acetate hydrolysis	PbO _{1.86} (OH) _{0.20}
2. Nitric acid oxidation of minium	PbO _{1.91} (OH) _{0.11}
3. Acid electroformation	PbO _{1.81} (OH) _{0.26}
4. Acid/lead perchlorate electrodeposition	PbO _{1.98} (OH) _{0.11}
5. Acid/lead acetate electrodeposition	PbO _{1.92} (OH) _{0.18}

Semiconductor properties

Lead dioxide is a degenerated n-type semiconductor. These types of semiconductors have such a high concentration of defects that the Fermi level lies within the conduction band. Mindt [60] determined that about 0.4 eV of the energy levels in the conduction band is occupied by free electrons, which makes the electrical properties of PbO₂ quite similar to those of metals. He has also investigated the electric properties of α -PbO₂ and β -PbO₂. Figure 2.30 presents the dependence of the specific electrical resistance (i.e., the resistivity, ρ), mobility (μ) and carrier density (n) on the thickness of the PbO₂ layer. The results indicate that the carrier density in

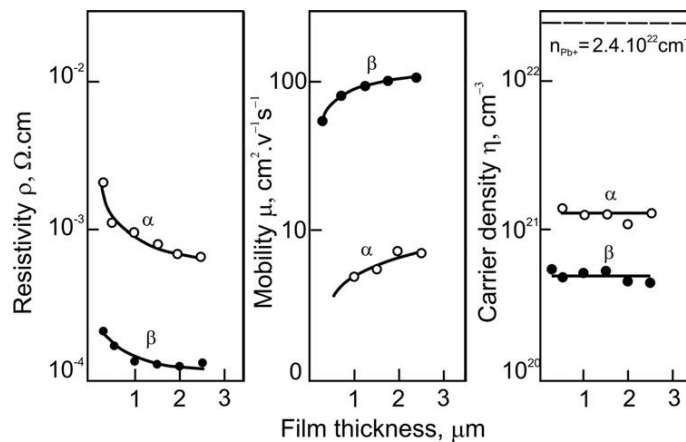


Figure 2.30:

Resistivity (ρ), mobility (μ) and carrier density (n) of α -PbO₂ and β -PbO₂ vs film thickness [60].

α -PbO₂ is higher than that in the β -PbO₂ crystal form. The carrier mobility of β -PbO₂ is about 1.5 orders of magnitude higher than that of α -PbO₂. Consequently, the specific resistance of α -PbO₂ is higher than that of β -PbO₂ by an order of magnitude. It has been established that mixtures containing α -PbO₂ and β -PbO₂ have slightly higher resistivities than pure β -PbO₂.

The concentration of Pb⁴⁺ ions in the crystal lattice of PbO₂ is $2.4 \times 10^{22} \text{ cm}^{-3}$. The electron concentration in PbO₂ is only 20 times less than the concentration of Pb⁴⁺ ions in the lead sub-lattice. Similar values for the density of carriers and their mobility in the β -PbO₂ crystal lattice are presented in Refs. [75] and [76] as well.

Mindt determined the width of the bandgap, the respective values being 1.45 eV for α -PbO₂ and 1.40 eV for β -PbO₂. These figures are quite similar to the values obtained by other researchers [39,77].

2.7. Electrochemical Preparation of the Me/PbO₂ Electrode

Platinum, gold and tantalum are chosen as substrates and PbO₂ is deposited from a Pb(II) solution of acetate, nitrate, perchlorate or alkaline plumbite.

2.7.1. Preparation of α -PbO₂ Layers

α -PbO₂ is formed electrochemically on foreign substrates under the following conditions:

- from saturated lead acetate solutions containing 6.5 M CH₃COONH₄ + 1.5 M NH₄OH at a current density of 5 mA cm⁻² [55];
- from solution containing 10 g L⁻¹ Pb(NO₃)₂ + 25 g L⁻¹ NaOH at 0.1 mA cm⁻² [56];
- from neutral solutions containing Pb(NO₃)₂ at 0.36 mA cm⁻² [78];
- from saturated PbO solutions in 2 M NaOH at 0.8–1.6 mA cm⁻² [79];
- from saturated PbO solutions in 0.2 M HClO₄ (pH = 5.5) at 0.1 mA cm⁻² [60].

2.7.2. Preparation of β -PbO₂

Deposition of β -PbO₂ on foreign substrates has been carried out in the following solutions containing Pb²⁺ ions:

- 0.03 M Pb(NO₃)₂ + 2.5 M HNO₃ at 3.0–5.0 mA cm⁻² [80];
- 0.5 M Pb(NO₃)₂ + 1 M HNO₃ at 3.0 mA cm⁻² [81];
- 195 g orthorhombic PbO in 500 mL 3 M HClO at 2.5 mA cm⁻² [57];
- 0.02 M PbO in 0.165 M HClO₄ (pH = 1) at 0.1 mA cm⁻² [60].

The two lead dioxide modifications can also be prepared by formation of battery plates in appropriate electrolytes. For example, battery plates have been formed in alkaline Na₂PbO₂ solutions [82], or in 3.5 M H₂SO₄ solution [57]. In the latter case, the active mass which

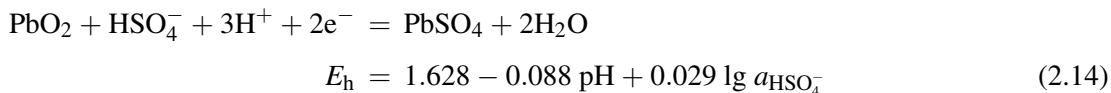
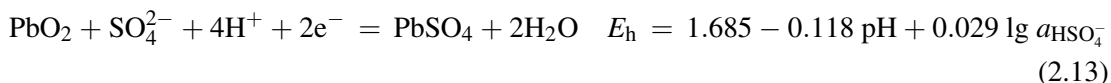
contained β -PbO₂ was boiled in 3 M HNO₃ for 45 min to allow the unoxidized divalent compounds to dissolve.

Bagshaw et al. [57] assumed that the type of the PbO₂ modification depends on the energy of nucleation and that the adsorption of certain ions on the surface of the PbO₂ crystals plays a role in the nucleation processes. The Pb⁴⁺ ions interact with the ions in the solution and form octahedra. This interaction is easiest with H₂O and OH⁻ ions. The nucleation process involves arrangement of these octahedra in the crystal lattice. When the octahedra are grouped, they liberate the surplus quantities of H⁺ and OH⁻ ions, or water. In terms of energy, the most favourable arrangement of the octahedra is following the diagram in Fig. 2.29, i.e., the α -PbO₂ and β -PbO₂ modifications. In H₂SO₄ solutions, SO₄²⁻ ions are probably included within the co-ordination sphere of the octahedra. Since SO₄²⁻ ions are big in size, they will occupy diametrically opposite sites in the octahedra. Hence, the bonding of the octahedra proceeds along those edges where SO₄²⁻ ions participate in the co-ordination. Thus, a linear chain of octahedra is formed, i.e., β -PbO₂ (Fig. 2.29). The chains first arrange parallel to each other, and then the β -PbO₂ crystal grows perpendicularly to the direction of the chain. In the presence of foreign cations (extrinsic cations, e.g., Co²⁺) adsorbed on the growing chain, the arrangement of the octahedra in a linear chain is disrupted and in this case α -PbO₂ is formed in acidic media.

2.8. Electrochemical Behaviour of the Pb/PbO₂/H₂SO₄ Electrode

2.8.1. Equilibrium Potentials

The Pourbaix diagram of the Pb/H₂O/H₂SO₄ system (Fig. 2.1) evidences a wide pH region within which PbO₂ and PbSO₄ are in thermodynamic equilibrium. Along the equilibrium line of the diagram the following reactions proceed:



Beck et al. [83] determined the following values for the equilibrium potentials of α -PbO₂ and β -PbO₂ vs SHE reference electrode:

$$\alpha\text{-PbO}_2 : E_{\text{h}} = 1.687 - 0.118 \text{ pH} + 0.029 \lg a_{\text{SO}_4^{2-}} \quad (2.E25)$$

$$\beta\text{-PbO}_2 : E_{\text{h}} = 1.697 - 0.118 \text{ pH} + 0.029 \lg a_{\text{SO}_4^{2-}} \quad (2.E26)$$

Figure 2.31 presents the dependences of α -PbO₂ and β -PbO₂ electrode potentials as a function of pH of solution pH [84].

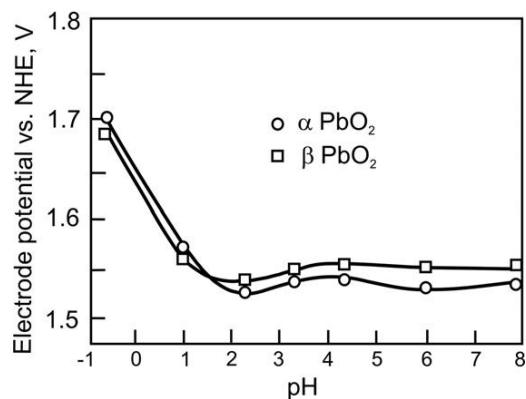


Figure 2.31:

Potentials of α -PbO₂ and β -PbO₂ electrodes as a function of solution pH [84].

2.8.2. Temperature Dependence

Figure 2.32 shows the relationship between the experimentally determined electrode potentials of α -PbO₂ and β -PbO₂ in H₂SO₄ solutions (3.90 M) as a function of temperature [85]. The results indicate that the temperature coefficients differ for the two modifications. The respective values at 25 °C are as follows:

$$\alpha\text{-PbO}_2 : (dE_h/dT)_p = -0.36 \text{ mV}^\circ \text{C}^{-1}$$

$$\beta\text{-PbO}_2 : (dE_h/dT)_p = -0.20 \text{ mV}^\circ \text{C}^{-1}$$

Based on these data, the difference in the enthalpies of the two lead dioxide modifications is:

$$\alpha\text{-PbO}_2 \rightleftharpoons \beta\text{-PbO}_2 \quad \Delta H = -2.6 \text{ kcal(at } 25^\circ \text{C)}$$

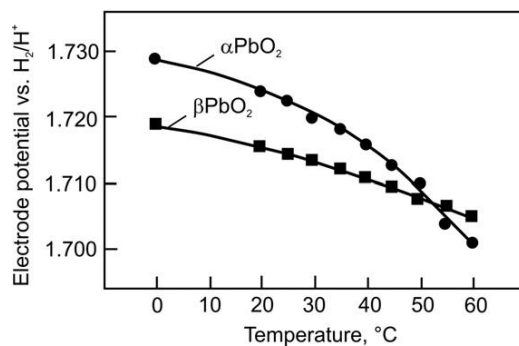


Figure 2.32:

Electrode potentials of α -PbO₂ and β -PbO₂ as a function of temperature [85].

2.8.3. Adsorption of H_2SO_4

Kiselova and Kabanov [86] studied the adsorption of H_2SO_4 on the surface of α - PbO_2 and β - PbO_2 layers prepared in different solutions and with various thicknesses. While H_2SO_4 is practically not adsorbed on the α - PbO_2 surface, adsorption on β - PbO_2 is quite substantial. The correlation between the quantity of adsorbed H_2SO_4 and the thickness of the PbO_2 layer indicates that adsorption proceeds also on the inter-grain surfaces. The irreversible adsorption of H_2SO_4 occurs during the crystal growth of β - PbO_2 crystals formed during the electrochemical oxidation of $PbSO_4$ in the H_2SO_4 solution. At high H_2SO_4 concentrations (e.g., 8 N), the PbO_2 particles formed are 100 times smaller than those formed during the oxidation of $PbSO_4$ in 0.01 N H_2SO_4 . This finding indicates that the adsorption of H_2SO_4 markedly decreases the growth rate of β - PbO_2 crystals.

2.9. Hydration and Amorphization of Active Mass PbO_2 Particles and Impact on the Discharge Processes

2.9.1. Gel–Crystal Structure of PAM Particles

The manufacture of positive battery plates is essentially a process of oxidation of $3PbO \cdot PbSO_4 \cdot H_2O$ or $4PbO \cdot PbSO_4$ and PbO to α - PbO_2 and β - PbO_2 . This technological process is called formation. Now let us discuss the structure of the PbO_2 active mass obtained as a result of formation.

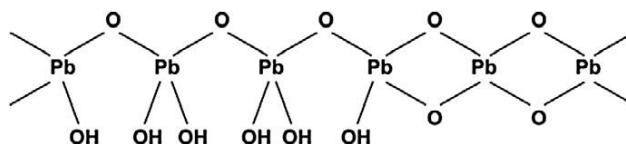
The positive active mass contains α - PbO_2 and β - PbO_2 crystal phases, as well as amorphous PbO_2 . Lead dioxide particles in turn contain considerable amounts of hydrogen. Caulder and Simon established that the hydrogen content in PbO_2 crystals formed as a result of electrochemical reactions is higher than that in chemically obtained lead dioxide [68,87]. At least two types of hydrogen are found in the electrochemically obtained PbO_2 . What is the amount of hydrogen? What are its functions in the electrochemical reactions? These are issues on which a number of scientists have been working for years. Hydrogen is found mainly at the crystal surface, part of it being in the form of mobile or adsorbed OH^- groups or H_2O molecules. The remaining hydrogen is firmly connected to the crystal lattice, which makes it less mobile [88,89].

It is generally assumed that the lead dioxide crystal comprises zones of ideal structures, $Pb_{24}O_{48}$ (octahedrons) with no protons, and strongly protonated zones, $Pb_{24}O_{40}(OH)_8$ [90,91]. These protons form $O-H \cdots O$ bonds with OH-type sensitivity. A correlation has been found between the oxide non-stoichiometry and the presence of protons in the crystal structure. The minimum Pb^{4+} content in the two PbO_2 modifications corresponds to a stoichiometric coefficient of 1.83. The latter corresponds to the maximum hydrogen amount that can be incorporated into the PbO_2 crystal lattice [90,91].

In our laboratory we have studied the structure of lead dioxide particles of the active mass formed from $3\text{PbO} \cdot \text{PbSO}_4 \cdot \text{H}_2\text{O}$ paste and subjected to five charge–discharge cycles [92,93]. Transmission electron micrographs (TEM) at high magnifications featuring lead dioxide particles in a sample of this active mass are presented in Fig. 2.33.

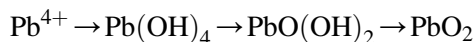
The images in Fig. 2.33a show that large zones in some of the PbO_2 particles are non-transparent for the electron beams (dark zones), while others let the electron beams through. The latter zones are heterogeneous in structure comprising fully transparent and less transparent zones. When the sample is heated in the microscope, it ‘boils’ and water is released, as a result of which the PbO_2 phase concentrates into a compact mass. This indicates that the electron transparent zones in the particles are composed of hydrated lead dioxide ($\text{Pb}(\text{OH})_4$ and $\text{PbO}(\text{OH})_2$).

Figure 2.33b shows a micrograph of the hydrated part of a PAM particle. Arranged planes are clearly seen in some regions. The distances between them range from 7 to 10 Å. These are values considerably higher than the interplanar distances in the elementary cells of PbO_2 crystals (Fig. 2.29), which indicates that there is water between the planes. Kassner suggested that high-valent lead oxides form linear polymer chains. We assumed that these polymer chains are hydrated [93]. Most probably, the arranged planes visible in Fig. 2.33b are namely these polymer chains of the type



The TEM pictures in Fig. 2.33 evidence that the lead dioxide active mass comprises particles with crystal (α - or β - PbO_2) or amorphous zones and hydrated (gel) zones. Figure 2.33c features PbO_2 particles with predominantly crystal structure. Only single surface zones are hydrated.

This highly heterogeneous structure of the PbO_2 particles obtained during the electrochemical formation of the lead dioxide active mass evidences that the processes of PbO_2 formation proceed through hydration and dehydration stages:



There is some kind of equilibrium between the dehydrated (crystal) and hydrated (gel) zones in the particles. That is why both types of zones are visible in the TEM pictures. Thanks to this equilibrium, the zones are stable under certain conditions.

The above-described structure of the lead dioxide particles is likely to exert an influence on the electrochemical and chemical processes that proceed in the positive active mass on charge and discharge, as well as on the behaviour of the positive plates in sulfuric acid solution.

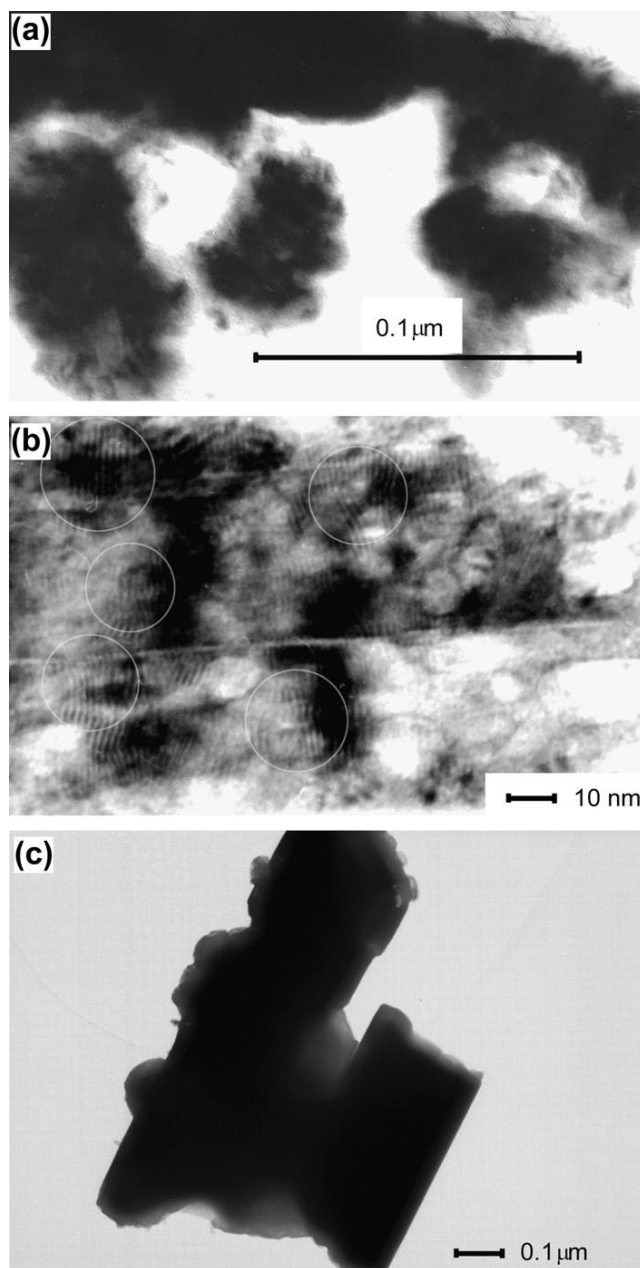


Figure 2.33:

TEM micrographs of lead dioxide particles of PAM. (a) PbO₂ particles with crystal and gel zones; (b) closer view of the gel zone of a PbO₂ particle; (c) PbO₂ particles with predominantly crystal zones.

Table 2.8: Binding energies for Pb4f and O1s calibrated with respect to the C1s peak at 284.4 eV [92].

Active mass	Pb 4f5/ 2 eV	Pb 4f7/ 2 eV	O1s eV		$S_{\text{OH}}/$ ($S_{\text{OH}} + S_{\text{PbO}}$)%
			Pb–O	O–H	
PAM from $3\text{PbO} \cdot \text{PbSO}_4 \cdot \text{H}_2\text{O}$					
1 st cycle	141.6	136.8	528.7	531.2	34
20th cycle	141.9	137.1	528.7	530.5	30.8
60th cycle	141.8	137.2	528.8	530.7	31.6
PAM from $4\text{PbO} \cdot \text{PbSO}_4$					
1 st cycle	142.2	137.2	529.0	531.0	30.7
20th cycle	141.9	137.1	528.8	530.6	28.8
60th cycle	142.1	137.1	528.8	530.9	39.4

Surface hydration of lead dioxide particles

This was determined by X-ray photoelectron spectroscopy (XPS). The O1s spectrum of oxygen, and Pb 4f5/2 and Pb 4f7/2 spectra of the lead ions in the particles of charged active mass were recorded [92].

Samples of active masses obtained from $3\text{PbO} \cdot \text{PbSO}_4 \cdot \text{H}_2\text{O}$ and $4\text{PbO} \cdot \text{PbSO}_4$ pastes subjected to 1, 20 or 60 charge–discharge cycles were investigated. The obtained binding energies for Pb 4f5/2 and Pb 4f7/2, the O1s values for the Pb–O and O–H bonds as well as the ratio of the peak area of the O–H bond to the peak area measured from the spectrogram and consisting of the areas of the Pb–O and O–H bonds are summarised in Table 2.8.

The data in the table indicate that the binding energies determined from the lead and oxygen peaks are almost equal for the active masses obtained from $3\text{PbO} \cdot \text{PbSO}_4 \cdot \text{H}_2\text{O}$ and $4\text{PbO} \cdot \text{PbSO}_4$, and do not change during cycling. The ratio between the peak areas, $S_{\text{OH}}/(S_{\text{OH}} + S_{\text{PbO}})$ indicates that 30% of the oxygen on the PbO_2 particle surface is bound to hydrogen ions. This hydrated (gel) part is only slightly influenced by the active mass origin and does not change much during cycling [92].

2.9.2. Equilibria Between the Crystal and Gel Zones in the Particles and Agglomerates of PAM, and the Ions in the Solution

The ion exchange between the crystal and gel zones and the solution can be followed through the changes in crystallinity of PAM as determined by X-ray diffraction analysis and reported in Ref. [94]. PAM was prepared employing the classical technology for positive battery plate manufacture. The active mass was removed from the grid, ground to powder, washed and dried. Figure 2.34 presents the relative intensities of the diffraction lines with interplanar distances of 3.50 and 2.80 Å, characteristic for $\beta\text{-PbO}_2$, as a function of the time of stay of PAM in: (a) 4.5 M H_2SO_4 , (b) 4.5 M $\text{H}_2\text{SO}_4 + 0.02$ M HCl and (c) 4.5 M $\text{H}_2\text{SO}_4 + 0.2$ M Li_2SO_4 solutions.

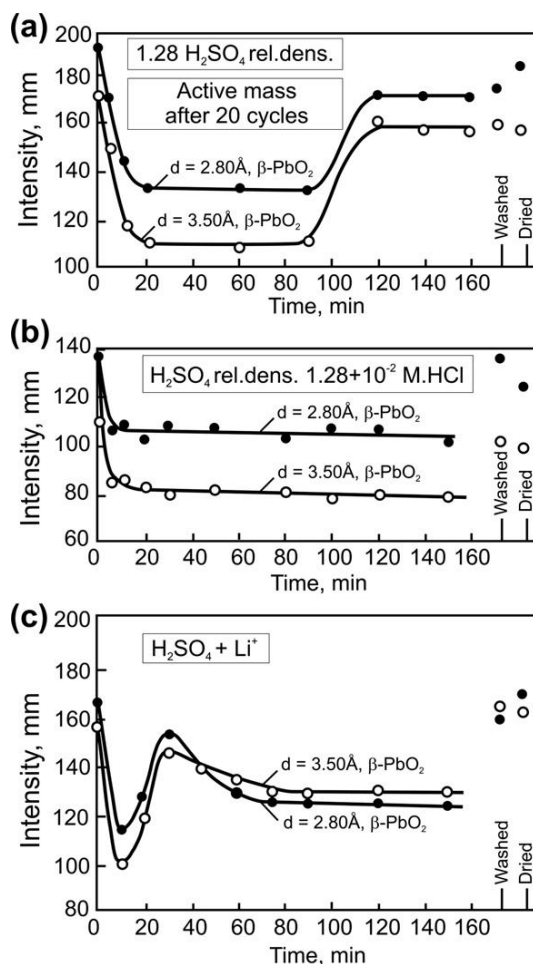


Figure 2.34:

Kinetic curves of the changes in intensity of the characteristic diffraction lines for β -PbO₂ with the time of stay in: (a) H₂SO₄, (b) H₂SO₄ + 10⁻² M HCl and (c) H₂SO₄ + 10⁻² M Li₂SO₄ solutions [94].

The experimental points on the ordinate give the X-ray data for dry PAM. The curves reflect the changes in crystallinity of PAM on its interaction with ions of the solution.

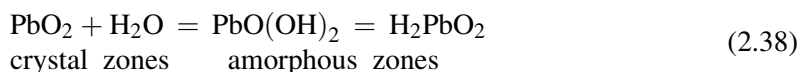
PAM samples with H₂SO₄ solution were X-rayed. After 160 min stay in the solution the positive active mass was washed and dried. The intensities of the diffraction lines after this treatment are presented on the right-hand side of the figure.

When PAM gets in contact with the solution, a decline in intensity of the characteristic diffraction lines for β -PbO₂ is observed. This implies that ions from the solution get into the particles and agglomerates, and change the ratio between the crystal and gel zones, thus

causing amorphization of the particles. For some ions of the solution, the kinetics of the ion exchange between PAM particles and the solution is related to the appearance of a maximum in the respective curves. Figure 2.34 evidences that the crystallinity of PAM depends on the composition of the solution, especially on the content of additives to the H_2SO_4 solution.

When PAM is washed with water, the reverse process takes place and it almost restores its initial crystallinity. It can be concluded that there is an equilibrium between the crystal and gel zones and the solution. When Li^+ cations from the solution enter the gel zones (Fig. 2.34c), an equivalent amount of H^+ ions should leave the particles in order to preserve their electroneutrality. Cl^- anions from the solution have to be exchanged with OH^- ions from the gel (Fig. 2.34b). This means that PAM has an amphoteric behaviour. Hydrated lead dioxide is known to have amphoteric properties [95,96].

These results indicate that the following equilibrium exists in the volume of PAM agglomerates and particles:



PbO(OH)_2 and H_2PbO_2 , on their part, stay in equilibrium with ions in the solution. The access of ions from the solution to the bulk of the particles and the relatively quick response of PAM crystallinity imply that the ions' processes that take place at the interfaces particle|solution and crystal zone|gel zone are almost reversible and relatively fast. These phenomena allow the electrochemical reactions in PAM to proceed in the bulk of the particles and agglomerates during discharge of the positive plates and thus increase the latter's capacity. This causes the current density and hence the polarization of the electrochemical reaction to decrease. As known, discharge of the positive lead–acid battery plates proceeds at low polarizations.

The data in Fig. 2.34 suggest that H_2SO_4 is absorbed in the gel zones of PbO_2 particles and alters the ratio gel/crystal zones, which will affect the capacity of the plates. It can be expected that the positive plate capacity will depend on the concentration of the H_2SO_4 electrolyte, especially at high concentration levels.

The ratio between gel and crystal zones in the PbO_2 particles depends also on the presence of Li^+ ions, too. The ions formed as a result of oxidation of the grid alloy would also have an impact on the electrochemical behaviour and the capacity of PAM, by affecting the crystal/gel zones equilibrium. Thus, the positive active mass is an open system.

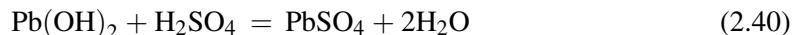
2.9.3. Proton–Electron Mechanism of Discharge of the Positive Active Mass

During discharge of the positive battery plate, the reduction of PbO_2 and PbO(OH)_2 to PbSO_4 proceeds in two steps [97]. The first one involves electrochemical reactions that

proceed in the bulk of the PbO_2 particles and agglomerates. It can be expressed by the equation:



When $\text{Pb}(\text{OH})_2$ gets in contact with ions from the H_2SO_4 solution, it interacts with the latter. During this second stage, PbSO_4 formation takes place:



Reactions (2.39) and (2.40) are separated in space, because of the limited access of H^+ , H_2O and H_2SO_4 to the different structural levels of PAM. H_2SO_4 cannot enter the micropores of the agglomerates because of the relatively large size of SO_4^{2-} ions (membrane effect).

Reaction (2.39) proceeds in the bulk of the agglomerates or particles through a ‘double-injection process’. This means that equivalent amounts of H^+ ions from the bulk of the electrolyte solution and electrons from the plate grid and the crystal zones of PbO_2 particles should enter the lead dioxide agglomerates for the reaction to proceed. In the gel zones, the electrochemical act of reduction can proceed very quickly. In this case, the rate of the reaction is determined by the rates of the electron and proton (H^+) flows in PAM. They differ for the different agglomerates. Consequently, some of the agglomerates are reduced quickly, others more slowly, and a third part of the agglomerates remain unaffected. The latter prevent the positive active mass from disintegration during discharge.

2.9.4. Processes During Anodic Polarization of Pb/PbO₂/PbSO₄ (O₂/H₂O) Electrode

On polarization of a Pb/PbO₂/PbSO₄ electrode immersed in H_2SO_4 solution, according to the E_{h} /pH diagram (Fig. 2.1), two redox reactions proceed on the electrode: one of these reactions is the evolution or reduction of oxygen ($\text{O}_2/\text{H}_2\text{O}$) and the other one is the oxidation of PbSO_4 or reduction of PbO_2 . At pH = 0, the oxygen electrode system has an equilibrium potential of ~1.25 V, and the lead dioxide electrode, ~1.50 V (vs NHE). The current/voltage curves of these two electrodes are presented in Fig. 2.35 [98]. The dotted line represents the oxygen evolution curve and the continuous line gives the rate of reduction and formation of PbO_2 .

Figure 2.35 shows that both the electrochemical oxidation of PbSO_4 and the electrochemical reduction of PbO_2 proceed at a low electrode polarization. In contrast, the oxygen evolution potential is much more positive than that of the PbSO_4 oxidation to PbO_2 . Therefore, during anodic polarization of the Pb/PbO₂/PbSO₄/H₂SO₄ (H₂O/O₂) system, oxidation of PbSO_4 takes place initially and then the evolution of oxygen commences. The H₂O/O₂ electrode will be

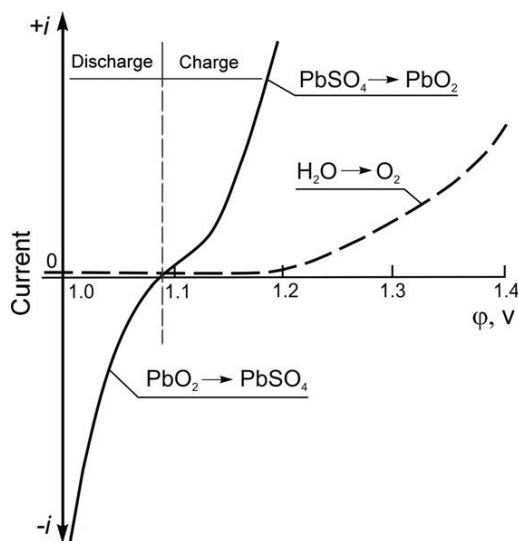


Figure 2.35:

Current/potential curves recorded on polarization of Pb/PbO₂/PbSO₄ and H₂O/O₂ electrodes in H₂SO₄ solution (Hg/Hg₂SO₄ reference electrode) [98].

given in parentheses in subsequent discussion when it affects the properties of the Pb/PbO₂/PbSO₄ system.

The time during which the above-mentioned system may generate current depends on the quantity and surface area of the PbO₂ phase. With increase of the amount of PbSO₄ phase covering the electrode surface, the free surface of the PbO₂ phase diminishes and the polarization of the electrode increases.

Under open-circuit conditions, the Pb/PbO₂/PbSO₄/H₂SO₄ (H₂O/O₂) system is in a steady-state condition. A current flows between the Pb/PbO₂/PbSO₄ and O₂/H₂O electrodes. Although the steady-state current is low, when the electrode rests for long periods of time, substantial quantity of electricity passes between the Pb/PbO₂/PbSO₄ and O₂/H₂O electrodes. Consequently, the amount of the PbO₂ phase decreases and hence the capacity of the electrode declines. This process is known as ‘self-discharge’ of the electrode.

The potential at which the rates of the oxygen evolution and the lead dioxide reduction processes become equal is the steady-state potential of the Pb/PbO₂/PbSO₄/H₂SO₄ (H₂O/O₂) system. Since the polarization of the H₂O/O₂ electrode is low, the steady-state current is very low, too. The difference between the steady-state potential and the equilibrium potential of the Pb/PbO₂/PbSO₄ electrode is negligible. This difference has often been ignored in published works.

2.10. The H₂O/O₂ Electrode System

2.10.1. Oxygen Over-voltage on Lead Dioxide

The oxygen electrode in acidic medium can be represented by the following overall reaction:



Based on thermodynamic data, the Nernst equation has been applied to calculate the equilibrium potential of this reaction:

$$E_{\text{h}} = 1.228 - 0.059 \text{ pH} - 0.029 \lg a_{\text{H}_2\text{O}} + 0.015 \lg P_{\text{O}_2} \quad (2.E27)$$

where P_{O_2} is the oxygen partial pressure.

Many researchers have tried to confirm experimentally the value of the equilibrium potential of the H₂O/O₂ system [99], but this has proved to be a difficult task. The oxygen reaction proceeds through several stages involving the formation of intermediate species, e.g., OH, O⁻, HO₂⁻, O. These species can interact with the defects in the lead dioxide crystal lattice and thus alter their properties, concentrations and charges. The surface of the PbO₂ phase may acquire different properties from those of the bulk of the degenerated semiconductor, which affect the value of the equilibrium potential of the H₂O/O₂ electrode on the PbO₂ surface.

The correlation between electrode potential and current density for α -PbO₂ and β -PbO₂ polarized in 4.4 M H₂SO₄ at 30 °C has been studied [84]. It has been established that the polarization behaviour follows the Tafel equation, with the following coefficients for the two modifications of the oxide:

$$\alpha\text{-PbO}_2 : \eta_{\alpha} = a_{\alpha} + 0.070 \lg i \quad (2.E28)$$

$$\beta\text{-PbO}_2 : \eta_{\beta} = a_{\beta} + 0.140 \lg i \quad (2.E29)$$

The value of the Tafel slope coefficient b for α -PbO₂ is half that for β -PbO₂. According to the principles of the general electrode kinetic theory, the coefficient b depends on the mechanism of the electrode reaction. The above equations show that the crystal structure of PbO₂ affects the mechanism of oxygen evolution [84]. Several authors have determined the value of b_{β} to be 0.118 (e.g., Refs. [100–102]), which is exactly equal to the figure for $b = 2.303 RT/\alpha F$ with $\alpha = 0.5$. Other researchers have established that η_{O_2} on α -PbO₂ formed by certain methods has a Tafel coefficient $b_{\alpha} = 0.118$ V, i.e., a value identical to that for β -PbO₂ [103].

To obtain reproducible polarization curves, the electrode must be subjected initially to preliminary polarization at the highest current density within the investigated polarization interval for a definite period of time [103]. Figure 2.36 illustrates the effect of pre-polarization on the Tafel relation.

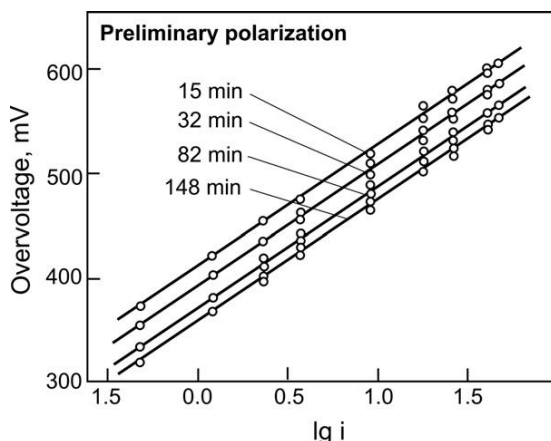


Figure 2.36:

Over-voltage vs $\lg i$ curves for oxygen evolution obtained after preliminary polarization of the electrode for different periods of time [103].

Based on general electrode kinetic theory, the constant a in the Tafel equation is found to depend on the nature of the electrode. Figure 2.36 shows that the preliminary polarization of the electrode affects the constant a , but it has no influence on the mechanism of the processes (constant b). This finding suggests that during pre-polarization of the electrode changes occur in the PbO_2 phase, which consequently lower the oxygen over-voltage.

It has been established that during the polarization of the $\text{Pb}/\text{PbO}_2/\text{H}_2\text{SO}_4$ electrode at potentials more positive than 2.0 V (SHE), formation of $\text{H}_2\text{S}_2\text{O}_8$ and O_3 occurs concurrently with oxygen evolution and the corrosion rate increases abruptly with increase in potential [104].

2.10.2. Oxygen Coverage of PbO_2 and Diffusion into the Lead Dioxide Layer

The increase in oxygen over-voltage during galvanostatic anodic polarization of the $\text{Pb}/\text{PbO}_2/\text{PbSO}_4/\text{H}_2\text{SO}_4$ ($\text{O}_2/\text{H}_2\text{O}$) electrode has been the subject of in-depth investigations [105]. The obtained results are presented in Fig. 2.37. From the slope of the linear region of the curves, a capacitance of $127 \mu\text{F cm}^{-2}$ (real surface) is obtained. This is a fairly high figure and suggests a strong adsorption and absorption of the oxygen participating in the reaction.

After polarization for a certain period of time, the circuit was opened and the decay in electrode potential with time was followed. Figure 2.38 shows the recorded changes in oxygen over-voltage and the amount of evolved oxygen during the potential decay. The slow increase in the amount of evolved oxygen indicates that the formation of molecular oxygen and its desorption from the PbO_2 surface is a heavily suppressed process. As a result of this, the electrode potential is sustained at values more positive than the steady-state value for long periods of time [105].

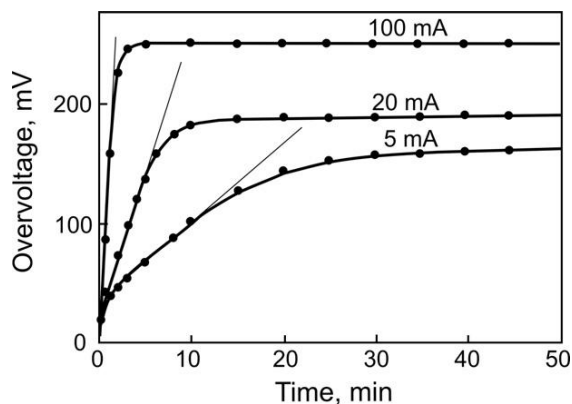


Figure 2.37:

Build-up of oxygen over-voltage on PbO_2 at constant current in 5 M H_2SO_4 solution at 30 °C [105].

The presence of atomic oxygen in the PbO_2 crystal lattice and its diffusion in this layer has been demonstrated directly by experiments conducted in a cell divided into two compartments by a PbO_2 membrane [106]. In the first compartment, the PbO_2 surface was polarized anodically and oxygen was evolved, while on the other side of the PbO_2 membrane (facing the unpolarized cell compartment) the potential was measured. After a certain period of polarization, the potential of the unpolarized side of the PbO_2 membrane was found to increase and reached a value characteristic of the $\text{H}_2\text{O}/\text{O}_2$ electrode. Since no pores were detected in the PbO_2 layer, it was concluded that the observed results could be attributed to the diffusion of atomic oxygen through the PbO_2 membrane [106].

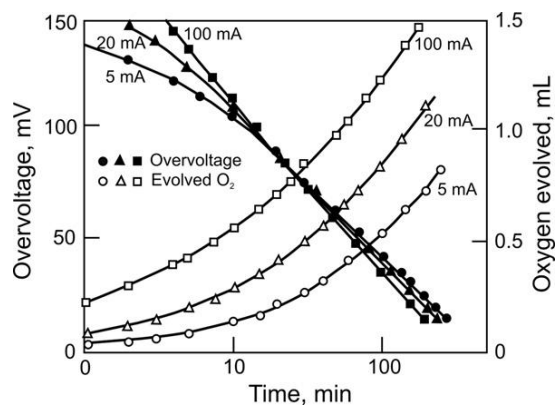


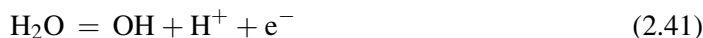
Figure 2.38:

Decay of oxygen over-voltage on PbO_2 for various pre-polarization currents and amount of oxygen gas desorbed; 30 °C [105].

2.10.3. Mechanism of Oxygen Evolution

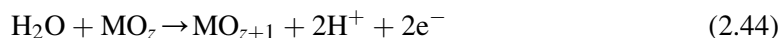
Several mechanisms have been proposed in the literature for the elementary reactions that proceed during oxygen evolution on the PbO_2 electrode in H_2SO_4 electrolyte. These were based on the current knowledge about the structure of the PbO_2 particles in PAM at that particular moment.

The first mechanism ignores involvement of the PbO_2 layer in the kinetics of the process of oxygen evolution. It assumes that the following elementary processes take place:



Some variants of this process have been proposed. The rate-limiting reaction has been assumed to be either the electrochemical reaction (2.41) [107] or the recombination of oxygen (2.43) [106].

The second mechanism of oxygen evolution on metal oxides can be expressed by the general equations given below. First, H_2O is decomposed forming an intermediate unstable oxide [108]:



Then this oxide is transformed into a stable one accompanied by oxygen evolution:

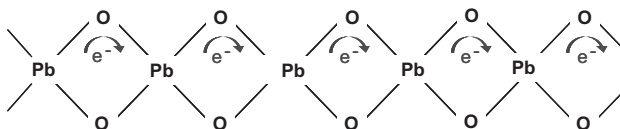


The composition of the unstable oxide depends on the potential of the electrode.

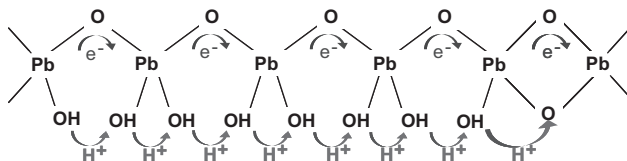
Both mechanisms assume that the PbO_2 layer is a crystal phase with electronic conductivity similar in behaviour to that of metals. Later, it has been established that electrochemically obtained PbO_2 , besides the crystal zones of α - and β - PbO_2 , comprises also hydrated (gel) zones of $\text{PbO}(\text{OH})_2$ [92–94,109]. Crystal and gel phases are in equilibrium. It has also been found that upon opening the circuit after polarization of the $\text{Pb}/\text{PbO}_2/\text{H}_2\text{SO}_4$ ($\text{O}_2/\text{H}_2\text{O}$) electrode, during which oxygen is evolved, the electrode potential decreases and the crystallinity of the $\text{PbO}_2/\text{PbO}(\text{OH})_2$ particles increases, i.e., the latter is dehydrated [93]. When the circuit is closed and electric current passes through the electrode causing oxygen evolution, the electrode potential increases up to a definite value, and the crystallinity of $\text{PbO}_2/\text{PbO}(\text{OH})_2$ particles decreases, i.e., the latter is hydrated again. It has been established that, when the positive plates of lead–acid batteries are charged to a 65–70% state of charge, PbSO_4 is oxidized to crystal PbO_2 . Upon further charging, an oxygen reaction proceeds parallel to the

reaction of lead sulfate oxidation, as a result of which a hydrated amorphous $\text{PbO}(\text{OH})_2$ lead dioxide is formed [94]. This electrode behaviour (i.e., increased degree of hydration of PbO_2 upon oxygen evolution) indicates that the hydrated zones in the $\text{PbO}_2/\text{PbO}(\text{OH})_2$ phase participate in the oxygen reaction.

On the other hand, it is well known that high-valent crystal lead oxides form polymer chains of the type given below [110]:



It is assumed that gel zones are built of similar polymer chains that are hydrated (Fig. 2.33) [93].

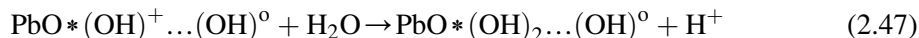


These chains keep the distances between the lead ions small enough for electrons to jump easily from one lead ion to the other along the chains. Hence, the gel structure has electron conductivity, too.

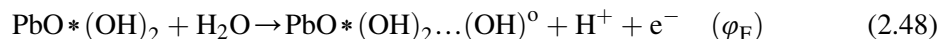
The oxygen evolution reaction proceeds at a certain number of active centres located in the hydrated (gel) zones. Based on this structure of the gel zones, the following mechanism has been proposed for the reactions of oxygen evolution, including two electrochemical and one chemical reaction [111]. An electron from one OH^- group of the polymer chain (active centre) jumps into the polymer network overcoming a certain potential barrier. Thus, the electron becomes common for the entire polymer network in the gel and moves along the chains reaching the crystal zones. The active centre is charged positively:



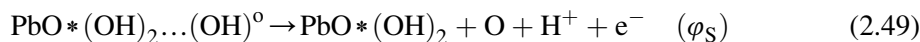
$\text{PbO}^*(\text{OH})_2$ is an active centre. The $(\text{OH})^0$ radicals formed remain bound to the active centre, and the bond is denoted by (\dots) . $\text{PbO}^*(\text{OH})^+ \dots (\text{OH})^0$ is electroneutralized through an interaction with a H_2O molecule in the hydrated layer. OH^- ions react with $\text{PbO}^*(\text{OH})^+$ forming $\text{PbO}^*(\text{OH})_2$. The hydrogen ions released from the H_2O molecule move out of the gel zone and thus the positive charge is carried to the bulk solution:



These processes represent the first anodic electrochemical reaction (FAER), which can be expressed by the following overall equation:



When this reaction proceeds, the active centres are blocked by $(\text{OH})^0$ radicals and the electrode is passivated. Upon increase of the potential above a value (φ_S) , the second anodic electrochemical reaction (SAER) begins:



Electrons enter the polymer networks. Hydrogen ions migrate into the bulk solution. Oxygen atoms leave the active centres and the latter are unblocked. Reaction (2.46) proceeds again in the vacant active centres. The oxygen atoms accumulate in the hydrated zones and recombine according to reaction (2.43):



Oxygen leaves the lead dioxide layer when its pressure becomes equal to atmospheric.

The above mechanism was confirmed by introducing additives to the solution which exert an influence on the activity of PbO_2 and on the oxygen reaction [112,113].

2.11. Anodic Corrosion of Lead and Lead Alloys in the Lead Dioxide Potential Region

2.11.1. Corrosion Layer Growth

The corrosion processes affecting lead when polarized within the PbO_2 potential region ($E_h > +0.95$ V vs $\text{Hg}/\text{Hg}_2\text{SO}_4$ electrode) are of major practical interest. Lead electrodes operate in this potential interval when used as positive electrodes in a lead–acid storage battery or as non-soluble anodes during the refining of some metals.

The dependence of the rate of oxidation upon the thickness of the PbO_2 corrosion layer is the first important relationship of the anodic kinetics. The correlation between corrosion rate and time of polarization of a lead electrode has been studied. The relationship between the weight of the oxidized lead (ΔP) per unit area has been determined as a function of the time of polarization at constant current density (6.5 mA cm^{-2}) [114–116]. The obtained results are given in Fig. 2.39. The shape of the curve suggests that the corrosion process comprises two stages:

a. non-steady-state stage, where

$$\Delta P = kt^x \quad (\text{for } t < 100 \text{ h}) \quad (2.E30)$$

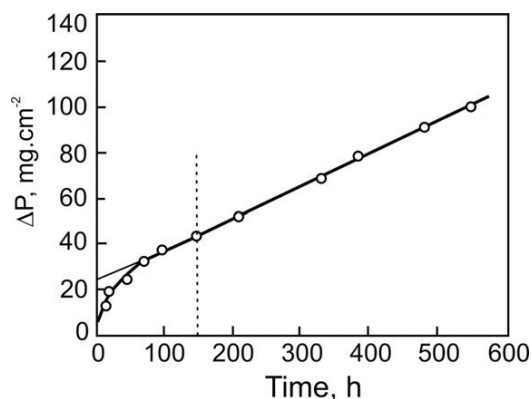


Figure 2.39:

Weight of oxidized lead metal per unit area as a function of polarization time; current density 6 mA cm^{-2} [114].

b. steady-state stage, where

$$\Delta P = P^0 + vt \quad (\text{for } t > 100 \text{ h}) \quad (2.E31)$$

where P^0 , k and x are constants (for Pb: $x = 0.47$) and v is the steady-state rate of lead oxidation. The values of the above constants depend on potential, temperature and alloying additives in the lead alloy. A similar dependence for different lead alloys is presented in Refs. [117–119] as well.

Microscopic studies of the anodic deposit show that it comprises two sub-layers [114]. Right on the metal surface there is a dense brownish layer, strongly adhering to the metal, that can be removed by chemical treatment only. Upon this layer, a dark brown loose layer is observed which can be easily removed mechanically. It is built of a shapeless mass of small crystals bonded into porous aggregates with large pores in between. It is the dense layer that determines the corrosion rate. The loose layer grows in thickness during the steady-state stage and sheds off. This finding suggests that the upper sub-layer does not affect the rate of metal oxidation. During the oxidation process, the dense layer is formed first and its thickness increases with increase of the quantity of electricity passed. The molar volume of PbO_2 is larger by 21% than that of lead. Since the PbO_2 layer is formed during the oxidation of Pb by a solid-phase reaction, internal mechanical stresses are created in the dense corrosion layer. The oxide layer at the PbO_2 /solution interface is partially dissolved and cracked, thus forming pores. When the rates of pore formation and of oxide formation become equal, the thickness of the dense corrosion layer no longer depends on the quantity of electricity passed and the corrosion rate reaches a stationary value.

By determining the steady-state corrosion rate, we can predict the life of the battery, provided the latter is limited by the corrosion rate of the positive grid.

2.11.2. Dependence of the Partial Currents of Lead Oxidation and Oxygen Evolution, as well as of the Composition of the Anodic Layer, on the Potential of the Pb/PbO₂/PbSO₄/H₂SO₄ Electrode

The Tafel equation for the lead oxidation reaction (i_C) and the evolution of oxygen (i_{O_2}) has been determined, and the obtained relationships are presented in Fig. 2.40 [116].

At potential $E_k = 1.530$ V, the two curves change slope. Both processes follow Tafel equation relationships:

$E < E_k$		$E > E_k$	
$E = a'_{O_2} + 0.056 \lg i_{O_2}$	(2.E32)	$E = a''_{O_2} + 0.114 \lg i_{O_2}$	(2.E33)
$E = a'_{Pb} + 0.094 \lg i_C$	(2.E34)	$E = a''_{Pb} + 0.160 \lg i_C$	(2.E35)

Since both processes proceed simultaneously, the ratios between their rates can be evaluated for each potential.

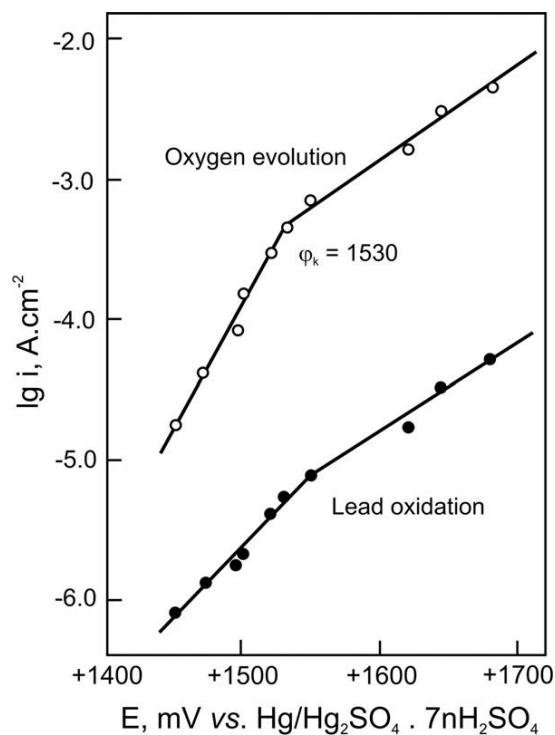


Figure 2.40:

Dependence of oxygen evolution current and corrosion current (i_C) on the potential of a lead electrode in H₂SO₄ solution [116].

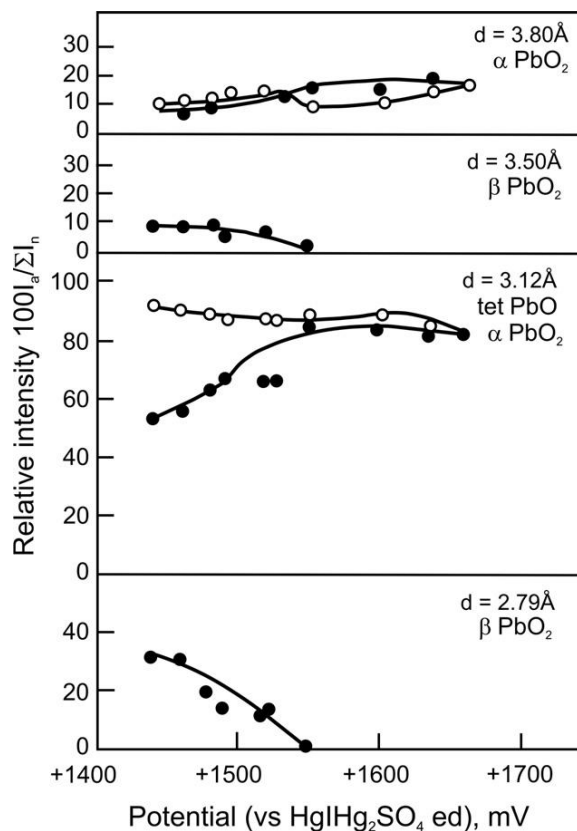


Figure 2.41:

Changes in phase composition of the anodic layer at the Pb|Oxide (o) and oxide|solution (●) interfaces as a function of oxidation potential; time of oxidation 72 h [116].

The phase composition of the anodic layer formed during the galvanostatic oxidation of Pb at current density 2.5 mA cm^{-2} has been investigated [120]. It is claimed that the metal surface is covered by a dense tet-PbO layer. With increase of the distance from the metal surface, formation of PbO_x ($1 < x < 2$) and $\alpha\text{-PbO}_2$ commences, and in the outermost layers $\beta\text{-PbO}_2$ is formed. The authors explain this sequence by diffusion of oxygen through the anodic layer [120].

A quantitative study of the above-mentioned relation has been performed and the phase composition of the anodic layer at the Pb| PbO_2 and $\text{Pb}_2|\text{H}_2\text{SO}_4$ interfaces has been determined using X-ray diffraction methods [116]. The relative intensities of the characteristic diffraction lines of the phases in the anodic layer are given in Fig. 2.41. The data in the figure show that $\beta\text{-PbO}_2$ is formed only at the $\text{PbO}_2|\text{H}_2\text{SO}_4$ interface at potentials more negative than 1.53 V. The line $d = 3.12 \text{ \AA}$ is common for both tet-PbO and $\alpha\text{-PbO}_2$. This is a very wide line

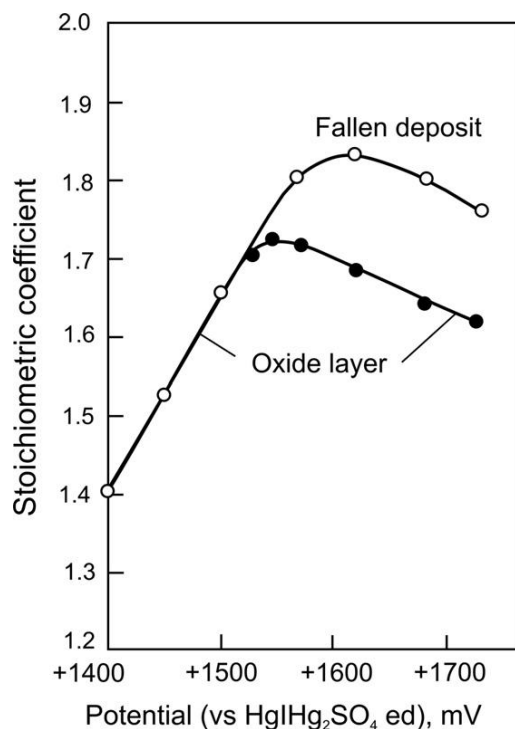


Figure 2.42:

Stoichiometric coefficient of the anodic oxide layer as a function of oxidation potential; lead electrode in H_2SO_4 solution [116].

suggesting the presence of a fine-grained crystal deposit. At potentials more negative than 1.53 V, the processes at the $\text{PbO}_2|\text{H}_2\text{SO}_4$ interface cause the intensity of this line to decrease. These processes are obviously related to the oxidation of tet-PbO to $\beta\text{-PbO}_2$. Since tet-PbO has high electric resistance (Fig. 2.21), it should display a high polarization under galvanostatic operational conditions. However, experimental studies have not confirmed this conjecture, so it can be concluded that tet-PbO is oxidized to PbO_x , retaining its crystal lattice. Hence, the oxide formed on the metal surface has been termed tet-PbO_x. At potentials more positive than 1.53 V, the anodic deposit consists of $\alpha\text{-PbO}_2$, and the inner region of the anodic layer is composed of tet-PbO_x and $\alpha\text{-PbO}_2$.

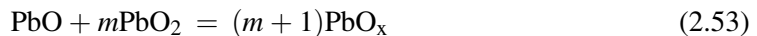
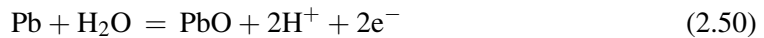
The stoichiometric coefficient of the oxide in the corrosion layer has been determined by conventional analysis to ascertain whether low valency oxides are formed at high potentials [116]. Figure 2.42 shows that, despite the high positive potential, the stoichiometric coefficient of the oxide layer does not reach values higher than 1.75. This is an integral value of the stoichiometric coefficient and refers to all oxides formed throughout the anodic layer, from the metal surface to the interface corrosion layer|solution. The lead oxidation process sustains this

relatively low value. At potentials more positive than 1.53 V, part of the oxide deposit sheds off and the stoichiometric coefficient of this material is higher than that of the oxide on the electrode. The shed-off oxide deposit is actually the porous part of the corrosion layer, which has been most oxidized. Thus, the degree of oxidation of the corrosion layer differs across its thickness.

2.11.3. Mechanism of Anodic Corrosion of Lead Within the PbO_2 Potential Region

The E_h/pH relationship (Fig. 2.1) indicates that lead is thermodynamically unstable within the PbO_2 potential region. Hence, the $\text{Pb}/\text{PbO}_2/\text{PbSO}_4$ system is subjected to continuous corrosion process under the action of a thermodynamic driving force. This corrosion process takes place through the oxide layer so the properties and structure of the latter will have a strong influence on the kinetics of the corrosion process. Different mechanisms of this process are proposed in the literature, depending on the composition and structure of the oxide layer:

- a. The first mechanism [117] assumes that the PbO_2 layer is porous throughout its cross section and water reaches the metal surface through the pores, where the following reactions proceed:



- b. The second mechanism presumes that the PbO_2 layer is composed of two parts: a dense sub-layer that covers the metal completely and isolates it from the solution and a porous sub-layer which is permeable to the solution.

Corrosion is a result of the reactions between lead and the oxygen which has diffused through the crystal lattice of the dense oxide layer [106,116]. A similarity has been established between the crystal lattices of Pb, tet-PbO and $\alpha\text{-PbO}_2$ (Fig. 2.43) [56]. Because of this similarity, relatively small amounts of energy are required for the steric alterations in the crystal lattice when it is transformed from one type to another.

Figure 2.41 evidences that the corrosion layer is built predominantly of tet-PbO and $\alpha\text{-PbO}_2$ phases [116]. This means that during the corrosion process, the lead oxides are transformed in two stages. Initially, the Pb crystal lattice is rearranged into tet-PbO_n lattice and then the crystal lattice of tet-PbO_n is transformed into an $\alpha\text{-PbO}_2$ lattice. This transformation is associated with the formation of fine-grained crystals. $\alpha\text{-PbO}_2$ has a sub-stoichiometric composition (Fig. 2.42).

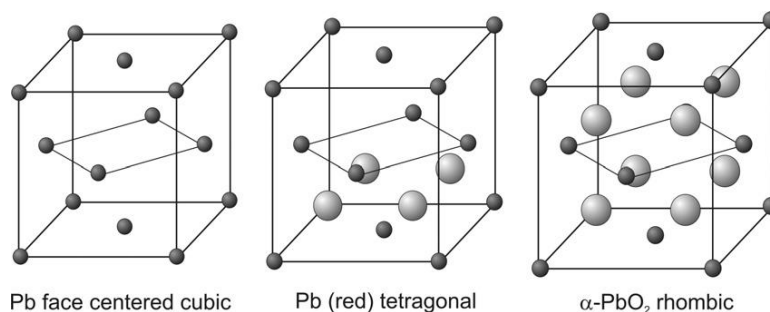


Figure 2.43:
Unit cells of Pb, tet-PbO and α -PbO₂ [56].

Figure 2.44 presents a model of the processes that take place on polarization of a lead electrode within the lead dioxide potential region and lead to corrosion of the lead grid.

The oxygen evolution reaction occurs at the anodic layer|solution interface, whereby oxygen atoms are obtained as intermediate products.



Some of the oxygen atoms diffuse into the anodic layer and on reaching the metal they oxidize it to tet-PbO [17].

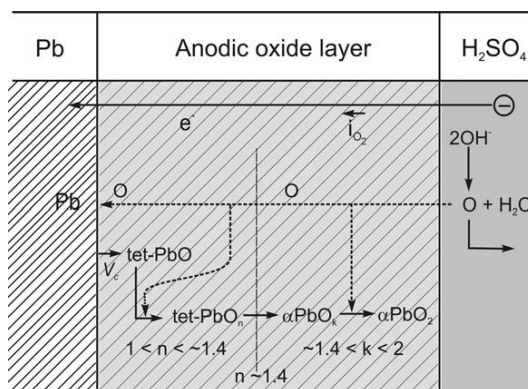


Figure 2.44:
Model of the processes in the Pb/non-stoichiometric PbO₂/O₂/H₂O/H₂SO₄ electrode system during polarization in the lead dioxide potential region [121].

The energy for the phase transformation of Pb to tet-PbO is comparatively low, so that naturally this crystal modification is obtained.

There are empty layers in the crystal lattice of tet-PbO where O can be easily inserted [56]. It oxidizes the tet-PbO phase to non-stoichiometric tet-PbO_n ($1 < n < 2$) without changing the crystal lattice parameters of tet-PbO [52].



The stoichiometric number n increases up to about 1.4, whereby the concentration of defects in the crystal lattice becomes so high that it is transformed into α -PbO₂ [52]. Since the crystal structures of tet-PbO and α -PbO₂ are quite similar, the energy of phase transformation is very low.



$\alpha\text{-PbO}_{(2-x)}$ is a non-stoichiometric oxide with the crystal lattice of $\alpha\text{-PbO}_2$ ($1.4 < (2-x) < 2$). Up to a certain potential, $\beta\text{-PbO}_2$ is formed at the oxide|solution interface (Fig. 2.41). This occurs probably when the solution participates in the oxidation of tet-PbO.

The data in Fig. 2.39 indicate that the corrosion process proceeds in two stages: non-stationary and stationary [114]. Bullock and Butler established that the corrosion rate is controlled by the rate of oxygen transport [122]. When the flux of oxygen to the Pb|tet-PbO interface equals the flux of oxygen to the tet-PbO| $\alpha\text{-PbO}_2$ interface, a steady-state corrosion rate is reached (Fig. 2.39). The thickness of the tet-PbO film will then remain constant. Under these conditions, the corrosion rate will be independent of potential and relatively insensitive to temperature.

2.11.4. Influence of Grid Alloying Additives on the Processes of Anodic Corrosion

The effects of alloying additives have been evaluated by adding Ag (an additive which reduces the rate of lead corrosion, i_C) or As (an additive which increases the corrosion rate). The above additives have been introduced either as components to the lead alloy or as additives to the solution, maintaining their constant concentration by periodically introducing additional amounts of the additive.

Figure 2.45 presents the current/voltage characteristics of the oxygen evolution and anodic corrosion reactions for pure lead electrodes immersed in an Ag⁺-containing H₂SO₄ solution as well as for a Pb–0.58% Ag electrode in pure H₂SO₄ solution. To understand the effect of Ag on the above-mentioned electrode systems, their volt–ampere relationships should be compared with those of a pure Pb electrode in H₂SO₄ solution. The latter relationships are given by dashed lines in Fig. 2.45 [121].

Introduction of silver in the lead electrode lowers the oxygen over-voltage. The polarization curve of the Pb–0.58% Ag electrode shifts by 30–40 mV in the negative direction. The

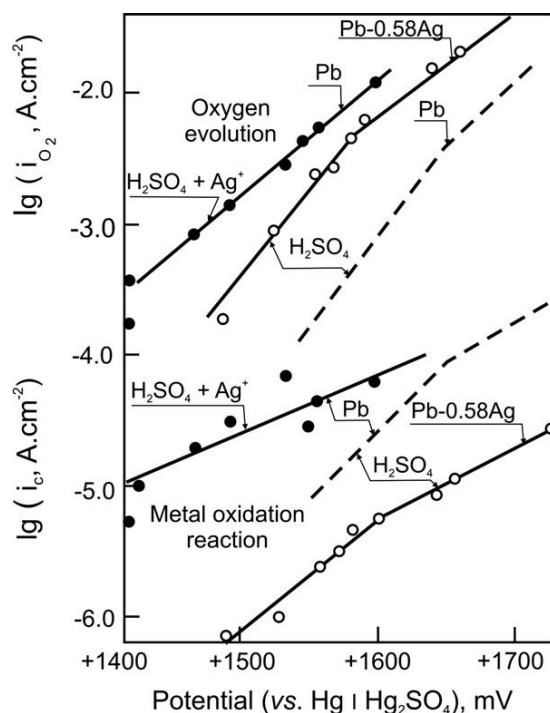


Figure 2.45:

Polarization curves of the oxygen evolution reaction and the corrosion reaction in the cases when Ag is introduced in the solution or in the metal [121].

addition of Ag^+ ions to the solution has an even stronger effect on this reaction, since the oxygen over-voltage is reduced by 50–70 mV. This difference in the polarization curves for the two methods of Ag introduction may be attributed to the different amounts of silver present in the electrode system.

What is the effect of silver on the anodic corrosion of lead? It is revealed by the rate of oxidation of the metal expressed in current density units (Fig. 2.45). Let us consider the case when the polarization is carried out at a constant potential (e.g., 1500 mV). When Ag^+ ions are introduced into the solution, the oxygen over-voltage decreases. When silver is alloyed in the metal, a weaker effect on the rate of oxygen evolution is observed, but the corrosion rate of the lead–silver alloy is considerably reduced. Hence, the introduction of silver by both methods accelerates the oxygen evolution reaction, but it affects differently the anodic corrosion of the metal.

The correlation between the rates of the two reactions (corrosion and oxygen evolution) can reveal the effect of Ag in a more clear-cut manner, eliminating the influence of the oxygen over-voltage decrease. Such a relationship is given in Fig. 2.46.

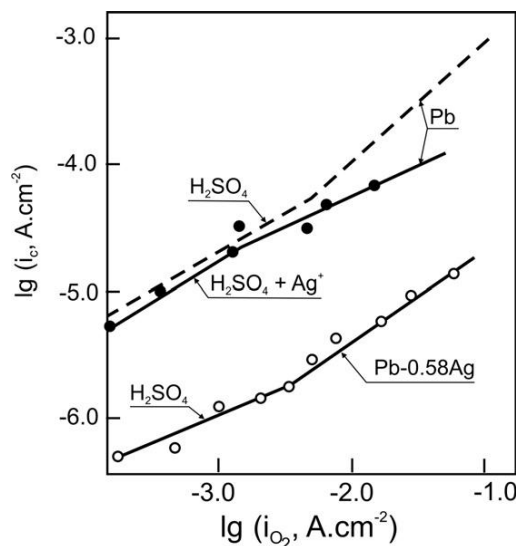


Figure 2.46:

Correlations between the corrosion currents in the cases when Ag is introduced in the solution or in the metal alloy. The dashed line represents the ratio between the rates of the two reactions for a pure Pb electrode in H_2SO_4 solution [121].

The effect of Ag^+ ions in the solution on the corrosion rate is within the range of the experimental error. Such a result would be accepted if we assume that the effect of Ag^+ ions is limited to the oxide|solution interface only. As the oxide|metal interface is isolated from the Ag^+ ions by the corrosion layer, the effect of these ions on the processes on the metal surface is negligible. When silver is alloyed in the metal, however, the corrosion rate is reduced by one order of magnitude. This experimental finding indicates that Ag in the alloy directly affects the corrosion process that occurs on the metal surface [121].

The effect of As on the electrode reactions of Pb has been studied by methods similar to those used in the case of Ag [121]. Lead electrodes have been polarized anodically in H_2SO_4 solutions containing 0.01 N $\text{As}_2(\text{SO}_4)_5$. The concentration of As in the solution has been kept constant by daily additions of As^{5+} ions in amounts as indicated by the chemical analysis.

Electrodes of Pb—As alloys have been polarized in pure H_2SO_4 solution. Figure 2.47 shows the potential/reaction rate relationships for both types of electrodes. The data in the figure evidence that As reduces the oxygen over-voltage as the polarization plots in both cases shift to more negative potentials.

The introduction of As affects the rate of the anodic corrosion reaction. If we look at the corrosion currents for the three electrodes at the same potential (e.g., 1500 mV), it becomes

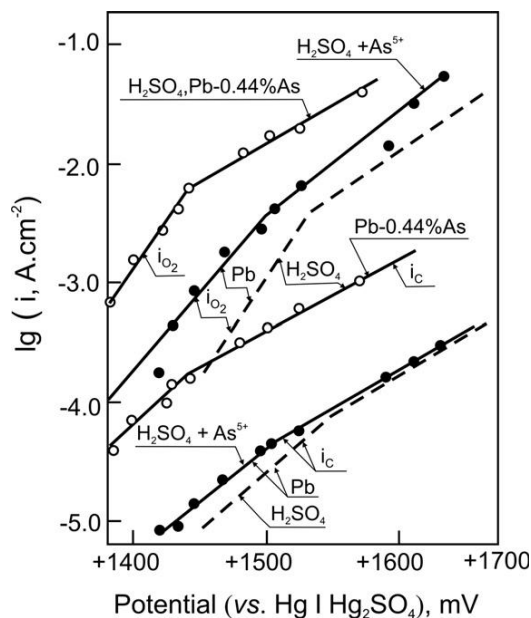


Figure 2.47:

Polarization curves of the oxygen evolution reaction and the corrosion reaction in the cases when as is introduced in the solution or in the metal alloy. The polarization curves of the two reactions for a Pb electrode in H_2SO_4 solution are represented by dashed lines [121].

apparent that As^{5+} ions added to the solution increase the corrosion rate, but very slightly (and not at all at higher potentials), whereas when introduced into the alloy ($\sim 0.5\%$), As enhances the corrosion rate by one order of magnitude.

Figure 2.48 juxtaposes the rates of the oxygen evolution and the anodic corrosion reactions for the above two types of electrodes. The addition of As^{5+} ions to the H_2SO_4 solution has practically no effect on the corrosion rate of the lead electrode. It is only at very high rates of oxygen evolution that these ions reduce the corrosion rate very slightly, as can be seen from the changed slope of the curves (Fig. 2.48). When introduced into the metal alloy, As accelerates the rate of anodic corrosion of the lead electrode.

Based on the above-discussed experimental results, it can be concluded that alloying additives influence the rate of the reaction of lead oxidation at the interface grid metal|corrosion layer. Probably, they induce changes in the structure of the interface as well and thus create conditions for the reaction of lead oxidation to proceed faster or slower. Since, this is a solid-phase reaction, the changes in volume of the newly formed phase will also play their role. Considering the unit cell structures presented in Fig. 2.43 and the presumed incorporation of oxygen in the crystal lattice of lead and formation of tet-PbO, it can be expected that alloying additives will affect this elementary process of transformation

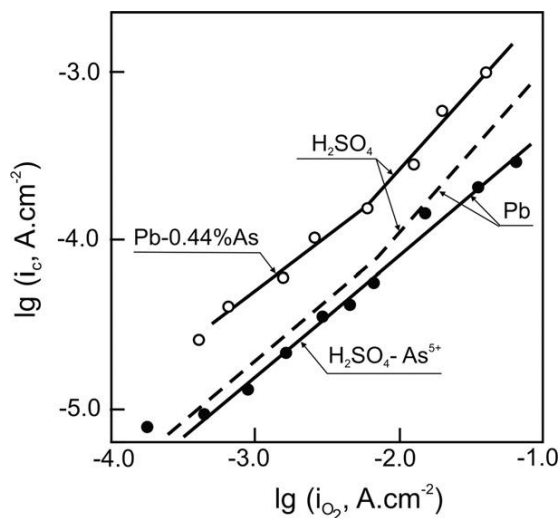


Figure 2.48:

Correlations between the corrosion currents for the electrodes when as is introduced in the solution or in the metal alloy. The dashed line represents the ratio between the rates of the two reactions for a pure Pb electrode in H_2SO_4 solution [121].

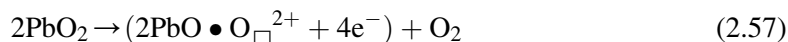
of one phase into another. Further studies are necessary to elucidate the effect(s) of additives on the mechanism of the corrosion process.

2.11.5. Stability of $\alpha\text{-PbO}_2$ and $\beta\text{-PbO}_2$ in Air

Mindt has investigated the changes in resistivity, mobility and carrier density of $\beta\text{-PbO}_2$ after long storage at room temperature in an air atmosphere (Fig. 2.49) [60]. Some battery plants often keep formed-positive plates in store awaiting battery orders from customers. During storage, the carrier density increases, the mobility decreases and the resistivity increases. X-ray inspection of the investigated samples evidences no structural alterations in the dioxide. The increase of carrier density indicates a change of the stoichiometry in the direction of decrease in oxygen content. The evolved oxygen has been determined by manometric techniques.

The loss of oxygen from both $\alpha\text{-PbO}_2$ and $\beta\text{-PbO}_2$ has been investigated, too, in dry and water-vapour saturated atmospheres (Fig. 2.50) [60]. Both types of oxides lose oxygen, the amount of lost O_2 from $\alpha\text{-PbO}_2$ being substantially smaller than that from $\beta\text{-PbO}_2$. The process is enhanced in humid atmospheres (curves (1) and (2) in Fig. 2.50).

The decomposition of the electroformed PbO_2 at room temperature can be interpreted in terms of generation of oxygen vacancies. Oxygen is evolved and the concentration of electrons increases. The stoichiometric equation is of the following type:



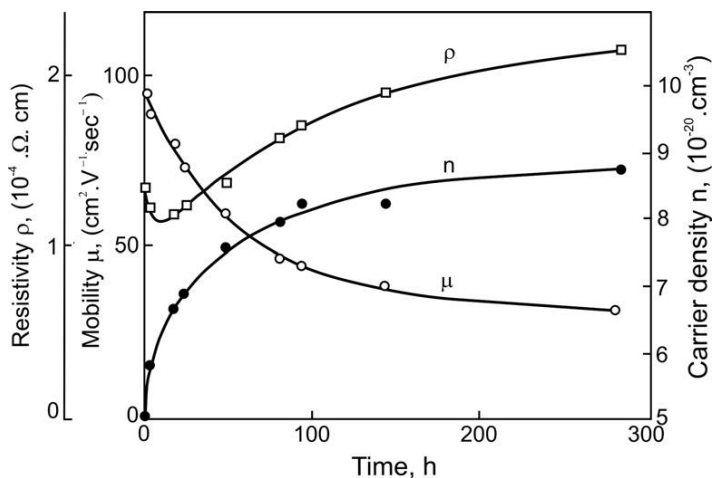


Figure 2.49:

Changes in resistivity (ρ), mobility (μ) and carrier density (n) of 1- μm -thick $\beta\text{-PbO}_2$ layer with time of stay in air at room temperature [60].

which corresponds to creation of defects in the PbO_2 structure, resulting in an increase of charge carrier density (Fig. 2.49).

$\beta\text{-PbO}_2$ is known to have higher electrochemical activity than $\alpha\text{-PbO}_2$, which means that the $\beta\text{-PbO}_2$ modification changes its valency more easily and is partially reduced. It is also known that the electrochemical reaction of reduction of lead dioxide proceeds in the hydrated zones of the PbO_2 particles. Hence, $\beta\text{-PbO}_2$ will evolve oxygen more easily in humid air

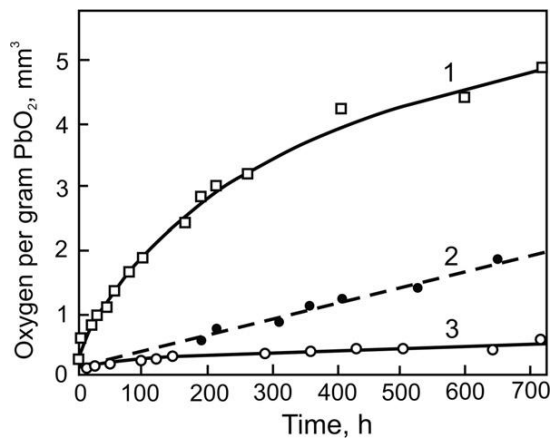


Figure 2.50:

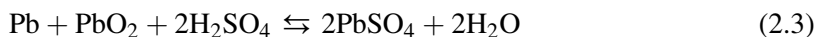
Loss of oxygen from PbO_2 vs time of stay at room temperature. (1) $\beta\text{-PbO}_2$ in air saturated with water; (2) $\beta\text{-PbO}_2$ in dry air; (3) $\alpha\text{-PbO}_2$ in air saturated with water [60].

atmosphere, which is actually observed in Fig. 2.50. On the other hand, α -PbO₂ is electrochemically less active and will release less oxygen, which again is demonstrated in Fig. 2.50. So during the process of hydration of the lead dioxide, it is also partially reduced preserving its crystal modification unchanged at that.

2.12. The Lead–Acid Cell

2.12.1. Specific Energy of a Lead–Acid Cell

The previous sections of this chapter made an overview of the types of electrodes and electrode systems in a lead–acid battery, their properties, electrochemical behaviour and the mechanisms of the processes that take place within the potential region from -1.30 to $+1.30$ V vs Hg/Hg₂SO₄ reference electrode. Let us now discuss in brief the lead–acid cell in which the processes expressed by the following overall equation proceed:



The active components (materials) in the cell are Pb, PbO₂, H₂O and H₂SO₄. The weight contributions (P_{LAC}) of these reactants are:

$$P_{\text{LAC}} = (207.2)_{\text{Pb}} + (239.2)_{\text{PbO}_2} + (196)_{2\text{H}_2\text{SO}_4} + (32)_{\text{H}_2\text{O}} = 674.4 \text{ g} \quad (2.E36)$$

Some authors do not include water as a reactant, though it takes part in reaction (2.3). If the weight of water is neglected, $P_{\text{LAC}} = 642.4 \text{ g}$.

According to Faraday's law, two gram-equivalents of these active components provide the following quantity of electricity, Q :

$$Q = 2(96500/3600) \text{ C} = 53.61 \text{ Ah} \quad (2.E37)$$

The specific energy of a cell is expressed in terms of watt-hours (Wh) that can be delivered per unit weight (kg) or unit volume (L) of the cell. The specific energy per unit weight (Wh kg⁻¹) is the more frequently used parameter. Its theoretical value can be calculated as follows.

If assumed that the discharge is carried out at the equilibrium voltage in 1 mol L⁻¹ acid ($\Delta E_e = 2.040 \text{ V}$) and that the components are completely consumed during the discharge, the theoretical specific energy, E_S , is given by:

$$E_S = (53.61 \times 2.040)/0.6744 = 162.2 \text{ Wh kg}^{-1} \quad (2.E38)$$

If water is excluded as a reactant, the E_S value is equal to 170.2 Wh kg⁻¹.

In some cases, the discharge voltage is assumed to be 2.0 V, which yields a theoretical specific energy of 167 Wh kg⁻¹. For comparison, petrol as a fuel delivers 12 kWh kg⁻¹ at a conversion efficiency of 100%.

The low theoretical specific energy of the lead–acid cell is a result of high atomic weight of lead, which is one of the heaviest natural products.

2.12.2. General Notes on Lead–Acid Cell Design

The theoretical specific energy is never delivered in practical cells. To transform the lead–acid cell into a practical power source, several design requirements must be met. Figure 2.51 shows the construction of a conventional SLI battery [123].

The plates (electrodes) of the lead–acid cell comprise grids (current collectors) and active mass. The active mass is built of two functional structures:

- energetic structure* — participates in the electrochemical reactions of transformation of the chemical energy into electrical energy and vice versa. The share of the energetic structure varies between 35% and 55%, depending on the design features of the battery and the discharge current.
- skeleton* — it supports mechanically the energetic structure and conducts the current to each point of the active mass.

The active mass is fixed in a lead-based grid that is chemically resistant to H_2SO_4 solution.

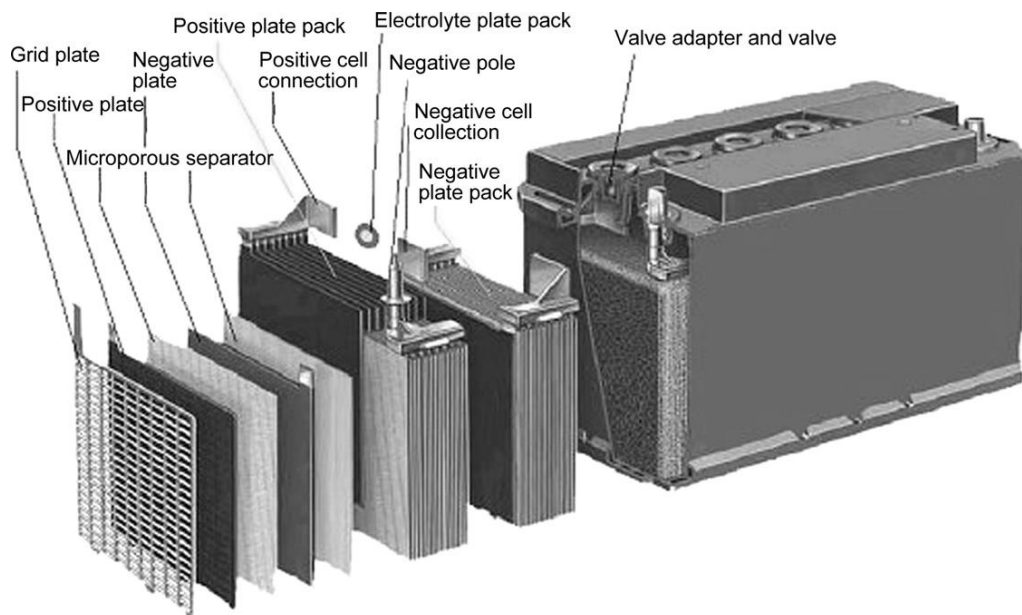


Figure 2.51:
Cut-away cell of SLI-Type lead–acid battery showing details of construction [123].

The positive and negative plates in a cell are separated by microporous separators that are ion permeable and resistant to H_2SO_4 , O_2 and H_2 attack.

The lead–acid cell uses approximately 36% H_2SO_4 solution as electrolyte. This has high electrical conductivity and a relatively low freezing point and corrosive attack of the lead grid is weak. On completion of discharge, a surplus quantity of H_2SO_4 must still remain to ensure ionic conductivity during the last stages of the discharge and at the beginning of re-charge.

The positive and negative plates, the separators and the intervening electrolyte form the ‘active block’ of the cell, which generates and accumulates the electric energy. Since the amount of H_2SO_4 in the active block is restricted, a reservoir of electrolyte is located above the active block and around the plate assembly. During discharge, H_2SO_4 is transported from the reservoir to the active block and the weight of the active block increases as a result of the formation of PbSO_4 . During charge, H_2SO_4 is generated inside the active block and diffuses back into the reservoir, thus reducing the active block weight.

The positive or negative plates are interconnected in ‘semi-blocks’ with terminal posts coming out of the cell.

At the end of charge, decomposition of water takes place and H_2 and O_2 gases are evolved. The cell is equipped with a valve to let these gases out. Electrolyte or water is added through this outlet, too. The cells are assembled in a container fitted with a cover. The cells are connected in series with lead connectors, over the cover or through the cell partitions.

The weight analysis of the components of a 40-Ah SLI battery is presented in Table 2.9 [124]. The data in the table give average component weight values for 2007.

As evident from these data, the electrochemically and chemically active components in a lead–acid battery account for about two-thirds of the total battery weight. Mass-produced SLI batteries have typical specific energy values of 34–40 Wh kg^{-1} , whereas traction EV batteries have a specific energy of between 28 and 34 Wh kg^{-1} .

Table 2.9: Battery component weight (%) [124].

12 V/40 Ah automotive battery	Average data for 2007
Total weight (kg)	11
Container/lid (wt%)	7
Separator (wt%)	1
Top lead (wt%)	9
Grid lead (wt%)	14
Active materials (wt%)	34
Electrolyte (wt%)	32

Source: Batteries for Automotive Use, John Wiley, New York, Table 2.2, p. 47.

Enormous research and engineering work has been carried out in the past decades aimed to reduce the share of the non-active components and increase the utilisation of the active materials. These efforts have resulted in an almost two-fold increase in the energetic characteristics of lead–acid batteries. Extensive R&D activities are currently focused on finding alternatives to part of the lead components in the plates, which do not take part in the reactions, and replacing them with carbon. Some promising results in this direction have been reported recently.

Besides improvement of the utilisation of active materials (lead and lead dioxide), another crucial issue that has been in the focus of battery researchers and design engineers for many years now is the immobilisation of battery electrolyte via its absorption in the glass mat separator or by converting it into gel state. Thus, the valve-regulated lead–acid (VRLA) battery was invented which requires minimum or no maintenance and has found wide application. In the VRLAB construction, the active block in the SLI cell is higher and occupies the upper electrolyte reservoir space, thus increasing the capacity of the cell within the same volume.

In an attempt to improve the power output of the lead–acid cell, its geometry was altered from prismatic to spirally wound. The specific energy and power characteristics of these batteries of the SLI type are summarised in Table 2.10 [124].

Table 2.10: Specific data for starter batteries according to European Norm (EN) (i.e., about 1 kWh of energy content, unless mentioned otherwise) [124].

	Flooded 12 V prismatic	AGM 12 V prismatic	AGM 12 V spirally wound	Gel 12 V Prismatic
Specific energy (Wh kg ^{−1}) 20 h, 25 °C threshold = 10.5 V	46	39	35	34
Energy density (Wh L ^{−1}) 20 h, 25 °C threshold = 10.5 V	95	95	70	71
Specific discharge power (Wh kg ^{−1}) 100% SoC; −18 °C; 10 s > 7.5 V	215 (according to EN)	235 (according to EN)	315 (CCA 750 A according to BCI)	155 (according to EN)
Power density (W L ^{−1}) 100% SoC; −18 °C; 10 s > 7.5 V	445	570	630	325
Integral charge throughput life (times nominal capacity) at ~20% DoD	~100	>300	~50 (deep cycles) (BCI)	>640 (to <60% initial capacity)

Cycle life calculated as possible integral charge throughput at 20% depth of discharge (DoC), unit capacity <50% of initial (unless other conditions are mentioned; cycle numbers should not be compared in that case).

Discharge power calculated from specified EN/CCA current, multiplied by threshold voltage (7.5 V, etc.).

Source: E. Meissner and G. Richter (2001). *Vehicle electric power systems are under change! Implications on design, monitoring and management of automotive batteries*. Journal of Power Sources, 95:11.

Batteries with free electrolyte (flooded batteries) are produced only with prismatic cell design with stacks of individual positive and negative plates. VRLA batteries with AGM separator are offered in both prismatic and spirally wound configurations. Spirally wound cells comprise one electrode of each polarity separated by AGM separator and wound in a cylindrical active block. In this cell design, the electrodes are under compression. The data in Table 2.10 indicate that this cell design is characterised by higher specific discharge power and power density as compared to prismatic cells. As regards the energetic performance parameters (specific energy and energy density), prismatic flooded and AGM-type batteries have better characteristics than spirally wound batteries. Table 2.10 shows also that gel prismatic batteries have inferior energetic and power characteristics than flooded and AGM batteries.

Lead–acid batteries have to meet a number of requirements, including the following: to deliver high power and energy output within a wide range of operation temperatures (from -25 to $+75$ °C), to have long service life (5–15 years), to undergo negligible self-discharge for long periods of storage, to be maintenance-free and fully recyclable, to have low cost, etc. Unfortunately, it is technically not possible to meet fully all the above requirements as claimed, but many of the above characteristics are steadily improved despite the insufficient financial support provided by governments and funding institutions for R&D activities in the field.

2.12.3. Technological Schemes for Battery Manufacture

Flat-plate batteries

The classical technological scheme for the manufacture of flat-plate lead–acid batteries is presented in Fig. 2.52. This technological process is basically used for the production of SLI, traction and stationary batteries. The process involves the following main production stages:

- a. *Grid casting.* Lead alloys are used for casting the positive and negative grids, as well as for small structural components (e.g., post straps, connectors, terminal posts). Highly automated and efficient casting machines are used.
- b. *Leady oxide manufacture.* Pure lead ingots are subjected to simultaneous grinding and surface oxidation (ball-mill method) or are melted and oxidized in humidified air (Barton pot method). A 60–80% oxidized lead powder (leady oxide) is obtained with a corresponding particle size distribution.
- c. *Paste preparation.* The leady oxide is charged in a mixing machine and then water and sulfuric acid solution are added under constant stirring. Basic lead sulfates are formed during this stage. After a definite period of mixing, the paste is used for the production of positive plates. The negative plates are produced in a similar way except that expanders are also added to the paste mix. In order to ensure proper completion of the subsequent technological procedures, the pastes should have definite density and consistency.
- d. *Grid pasting.* Grids are pasted in a specially designed machine. The pasted plates are then dried in a tunnel oven dryer and arranged on pallets.

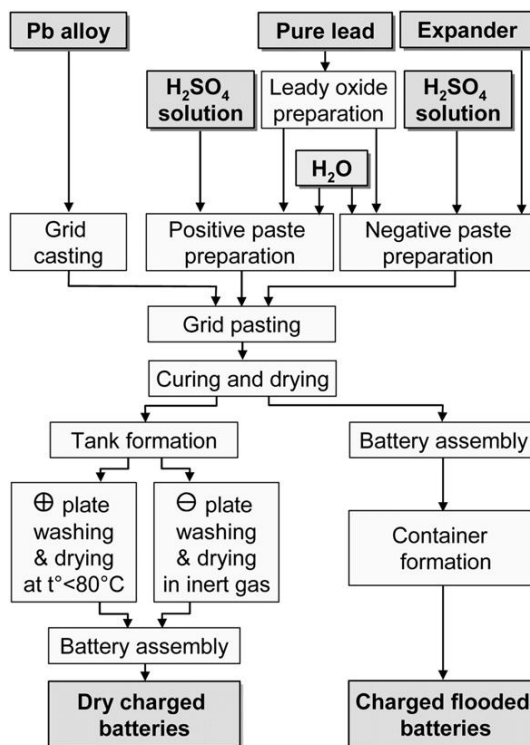


Figure 2.52:
Technological scheme for the manufacture of pasted-plate batteries.

- e. *Plate curing.* Pallets with plates are placed in a high humidity chamber and left to cure at 35 °C for 48–72 h. During the curing process, lead in the paste is oxidized, the basic lead sulfates recrystallize and the plates are then dried to moisture content <0.5%.
- f. *Plate formation.* The cured plates are loaded into large tanks containing sulfuric acid solution and electric current is passed through the plates (i.e., tank formation process). Spongy lead forms on the negative plates and lead dioxide on the positive plates. After formation, the positive plates are washed with water and dried at a temperature <80 °C. The negative plates are treated in the same way, but drying is done in an oxygen-free atmosphere.
- g. *Production of battery containers, covers, vents, etc.* Plastic battery components are manufactured by extrusion in appropriate moulds.
- h. *Battery assembly.* Dried plates are stacked in active blocks, so that positive and negative plates alternate with separators in between. Plates of like polarity are interconnected into semi-blocks by welding together through the plate lugs. The active blocks are then introduced into battery containers, the cells are connected and the batteries are covered with lids and tested for air-tightness. The vents are closed to eliminate access of air from the surroundings, and the batteries are packed and ready for delivery.

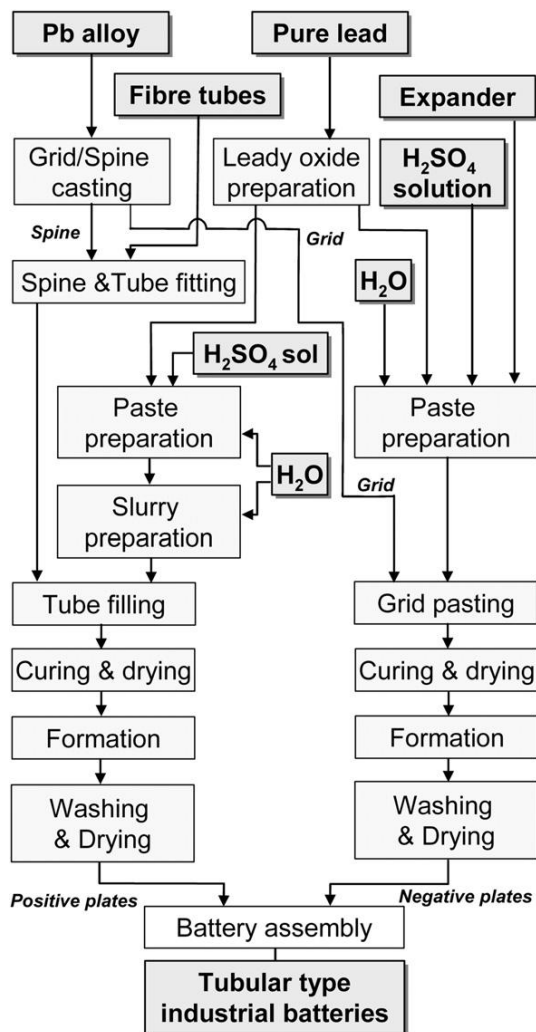


Figure 2.53:

Technological scheme for the manufacture of tubular-plate batteries.

This manufacturing process is employed for the production of dry charged batteries. These batteries are ready for use after adding the sulfuric acid solution with no need of preliminary charging. The shelf life of these batteries is more than 1 year.

Batteries intended to be used within 2 or 3 months after manufacture are produced with lead–calcium–tin alloys, filled with electrolyte and ready for use. In this case, the technological scheme in Fig. 2.52 is modified. The tank formation and plate drying steps are eliminated and plate curing is followed by battery assembly, the formation process being completed in the battery itself.

In the last decades, the basic scheme of battery manufacture has undergone a number of changes and improvements, which have resulted in acceleration, automation and computerisation of the individual technological processes and have led eventually to a several-fold increase in productivity, preserving the principal production stages at that.

Tubular-plate batteries

The tubular-plate technology is used in the manufacture of traction and stationary batteries. Figure 2.53 shows the main stages involved in the classical production process of tubular plates. Only the preparation of positive plates will be described briefly, since the other technological stages are identical to those discussed for flat-plate batteries.

- a. *Tube preparation.* Tubes (multi-tube gauntlets) are produced from chemically resistant glass or organic fibres (polyester, polypropylene, acrylonitrile co-polymers, etc.) by weaving, braiding or felting methods. The tubes are fixed into the required shape in an appropriate polymer solution and thermally treated.
- b. *Spine and grid casting.* This process is carried out by automatic casting machines. The spines are cast under high pressure.
- c. *Tube filling.* The tubular plates are filled, under pressure, with a slurry of 3BS or 4BS positive pastes diluted with water, or with a suspension obtained from leady oxide and red lead with the addition of sulfuric acid and water.
- d. *Curing.* Tubular plates are cured for several days under definite conditions.

The processes that occur during the manufacture of the plates will be discussed in detail in the next chapters of this book.

References

- [1] M.A. Dasoyan, I.A. Aguf, *Current theory of lead-acid batteries*, Technology, Stonehouse, England, 1979; 22.
- [2] B.N. Kabanov, *Sb. Rab. Khim. IstochNIKam Toka*, vol. 2 (in Russian), NIAI, Leningrad, 1938, p. 41.
- [3] A.K. Lorenz, *Sb. Rab. Khim. IstochNIKam Toka*, NIAI, Leningrad, vol. 4, Leningrad, 1939, p. 35 (in Russian).
- [4] R.A. Robinson, R.H. Stokes, *Electrolyte solutions*, second ed., Butterworths, London, 1959.
- [5] K.R. Bullock, *J. Power Sources* 35 (1991) 197.
- [6] A.B. Jarrett, S. Vellenga, C.M. Fontana, *J. Am. Chem. Soc.* 61 (1939) 367.
- [7] G. Todd, E. Parry, *Nature* 202 (1964) 386.
- [8] G.L. Clark, W.F. Tyler, *J. Am. Chem. Soc.* 61 (1939) 58.
- [9] U.B. Thomas, *Trans. Electrochem. Soc.* 94 (1948) 42.
- [10] S.C. Barnes, R.T. Mathieson, in: D.H. Collins (Ed.), *Batteries 2*, Pergamon Press, Oxford, G.B, 1965, pp. 41–52.
- [11] M. Pourbaix, *Atlas d'Equilibres Electrochimiques*, Gauthier-Villars, Paris, 1963, p. 485.
- [12] P. Ruetschi, R.T. Angstadt, *J. Electrochem. Soc.* 111 (1964) 1323.
- [13] H. Bode, in: R.J. Brodd, K. Kordesch (Eds.), *Lead-acid batteries*, John Wiley, Electrochem. Soc., New York, USA, 1977, p. 96.
- [14] H.S. Harned, W.J. Hamer, *J. Am. Chem. Soc.* 57 (1935) 27.

-
- [15] D.N. Craig, G.W. Vinal, J. Re. Nat. Bur. Stand. 24 (1940) 475.
- [16] D. Pavlov, C.N. Poullieff, E. Klaja, N. Iordanov, J. Electrochem. Soc. 116 (1969) 316.
- [17] D. Pavlov, Electrochim. Acta 23 (1978) 845.
- [18] D. Pavlov, N. Iordanov, J. Electrochem. Soc. 117 (1970) 1103.
- [19] D. Pavlov, S. Ruevski, Electrochem. Power Sources, Praha ZARI, C SSR (1975) 69.
- [20] D. Berndt, in: H.A. Kiehne (Ed.), Batterien, Band 57, Elektrotechnik, Expert Verlag, Markt und Technik, 1980, p. 29.
- [21] G. Archdale, J.A. Harrison, J. Electroanal. Chem. 34 (1972) 21.
- [22] D. Pavlov, Ber. Bunsenges. Phys. Chem. 71 (1967) 398.
- [23] D. Pavlov, Electrochim. Acta 13 (1968) 2051.
- [24] D. Pavlov, R. Popova, Electrochim. Acta 15 (1970) 1483.
- [25] P. Ruetschi, J. Electrochem. Soc. 120 (1973) 331.
- [26] D. Pavlov, in: B.D. McNicol, D.A.J. Rand (Eds.), Power sources for electric vehicles, Elsevier, Amsterdam, 1984, p. 162.
- [27] J.O'M. Bockris, S. Srinivasan, Electrochim. Acta 9 (1964) 31.
- [28] Y.M. Kolotyrkin, Trans. Faraday Soc. 55 (1959) 455.
- [29] J.P. Carr, N.A. Hampson, S.N. Holley, R. Taylor, J. Electroanal. Chem. 32 (1971) 345.
- [30] B.R. Wells, M.W. Roberts, Proc. Chem. Soc. London, UK (1964) 173.
- [31] M.W. Roberts, N.J. Young, Trans. Faraday Soc. 66 (1970) 2636.
- [32] E.G. Yampol'skaya, B. Edene, M.I. Martinova, U.A. Smirnova, Z. Prikl. Khimii (Sov. J. Appl. Chem.) 49 (1976) 2421 (in Russian).
- [33] I.A. Aguf, M.A. Dasoyan, Z. Prikl. Khimii (J. Appl. Chem.) 32 (1959) 2022 (in Russian).
- [34] B.A. Thompson, R.L. Strong, J. Phys. Chem. 67 (1963) 594.
- [35] D. Pavlov, S. Ruevski, CLEPS — BAS, Lead-acid annual report 1977, Bulgaria, Sofia, 1977.
- [36] J.S. Anderson, M. Sterns, J. Inorg. Nucl. Chem. 11 (1959) 272.
- [37] R. Roy, Bull. Soc. Chim. Fr. 113 (1965) 1065.
- [38] E.M. Otto, J. Electrochem. Soc. 113 (1965) 525.
- [39] F. Lappe, J. Phys. Chem. Solids 23 (1962) 1563.
- [40] V.A. Izvoztchikov, Sov. Phys. Solid State 3 (1961) 2060; 3229.
- [41] V.A. Izvoztchikov, Sov. Phys. Solid State 4 (1962) 2014.
- [42] V.A. Izvoztchikov, Sov. Phys. Solid State 4 (1962) 2747.
- [43] J. . van den Broek, Philips Res. Rep. 22 (1967) 36.
- [44] D. Pavlov, S. Zanova, G. Papazov, J. Electrochem. Soc. 124 (1977) 1522.
- [45] S. Fletcher, D.B. Matthews, J. Electroanal. Chem. 126 (1981) 131.
- [46] K.L. Hardel, A.J. Bard, J. Electrochem. Soc. 124 (1977) 215.
- [47] R.G. Barradas, D.S. Nadezhdin, J.B. Webb, A.P. Roth, D.F. Williams, J. Electroanal. Chem. 126 (1981) 273.
- [48] D. Pavlov, B. Monahov, CLEPS — BAS, Lead-acid annual report 1981, Bulgaria, Sofia, 1981.
- [49] D. Pavlov, J. Electroanal. Chem. 118 (1981) 167.
- [50] E.M. Valeriote, L.D. Gallop, J. Electrochem. Soc. 124 (1977) 370–380.
- [51] R.N. O'Brien, J. Electrochem. Soc. 124 (1977) 96.
- [52] D. Pavlov, Z. Dinev, J. Electrochem. Soc. 127 (1980) 855.
- [53] M. Skyllas-Kazakos, J. Electrochem. Soc. 128 (1981) 817.
- [54] N. Kameyama, T. Fukumoto, J. Soc. Him. Ind. Jap. 49 (1946) 1946.
- [55] A.I. Zaslavskii, Yu.D. Kondrashov, S.S. Talkachev, Dokl. Akad. Nauk SSSR 75 (1950) 559.
- [56] H. Bode, E. Voss, Z. Elektrochem. 60 (1956) 1053.
- [57] N.E. Bagshaw, R.L. Clarke, B. Halliwell, J. Appl. Chem. 16 (1966) 180.
- [58] M.A. Dasoyan, I.A. Aguf, Current theory of lead-acid batteries, Technology, Stonehouse, England, 1979; 115.
- [59] L. Pauling, J.H. Sturdivant, Z. Kristallchem. 68 (1929) 239.
- [60] W. Mindt, J. Electrochem. Soc. 116 (1969) 1076.

- [61] A.I. Zaslavskii, S.S. Talkachev, *Sov. J. Phys. Chem.* 26 (1952) 743.
- [62] S.J. Bone, M. Fleischmann, *Direct current* 1961 6 (1961) 53.
- [63] J. Burbank, *NRL report* 6345, Washington, 1964.
- [64] C.W. Fleischmann, *J. Electrochem. Soc.* 127 (1980) 664.
- [65] H. Bode, N. Panesar, E. Voss, *Chem. Ing. Tech.* 41 (1969) 878.
- [66] K. Micka, M. Svata, V. Koudelka, *J. Power Sources* 4 (1979) 43.
- [67] D. Kordes, *Chem. Ing. Tech.* 38 (1966) 638.
- [68] S.M. Caulder, A.C. Simon, *J. Electrochem. Soc.* 121 (1974) 1546.
- [69] P. Reinhardt, M. Vogt, K. Wiesener, *J. Power Sources* 1 (1976) 127.
- [70] D. Handtmann, K. Reuter, *Bosch Techn. Ber.* 2 (1967) 3.
- [71] J. Burbank, *J. Electrochem. Soc.* 106 (1959) 396.
- [72] J. Bystrom, *Ark. Kemi. Mineral. Geol.* 20A (1945) No.11.
- [73] T. Katz, *Ann. Chim. (Paris)* 5 (1950) 5.
- [74] G. Butler, J.L. Copp, *J. Chem. Soc.* (1956) 725.
- [75] A. Kittel, *de Beitrage zum Mechanismus der Elektrischen Leitung in PbO₂ and Se*, PhD Thesis, CSSR, Prague, 1944.
- [76] U.B. Thomas, *J. Electrochem. Soc.* 94 (1948) 42.
- [77] I.P. Shapiro, *Opt. i Spektrosk* 4 (1958) 256.
- [78] I.I. Astakhov, I.G. Kiselova, B.N. Kabanov, *Dokl. Akad. Nauk SSSR* 126 (1959) 1041.
- [79] V.H. Dodson, *J. Electrochem. Soc.* 108 (1961) 401; 406.
- [80] S. Ikari, S. Yoshizawa, S. Okada, *J. Electrochem. Soc. Jpn.* 27 (1959) E186–189; E223, E247.
- [81] P. Chartier, *Ber. Bunsenges. Phys. Chem.* 68 (1964) 404.
- [82] E. Voss, J. Freundlich, *Batteries*, in: D.H. Collins (Ed.), Pergamon Press, Oxford, 1967, p. 73.
- [83] W.H. Beck, R. Lind, W.F.K. Wynne Jones, *Trans. Faraday Soc.* 50 (1954) 136.
- [84] P. Ruetschi, R.I. Angstadt, B.D. Cahan, *J. Electrochem. Soc.* 106 (1959) 547.
- [85] R.T. Angstadt, C.J. Venuto, P. Ruetschi, *J. Electrochem. Soc.* 109 (1962) 177.
- [86] I.G. Kiselova, B.N. Kabanov, *Dokl. Akad. Nauk SSSR* 122 (1958) 1042.
- [87] S.M. Caulder, J.S. Murday, A.C. Simon, *J. Electrochem. Soc.* 120 (1973) 1515.
- [88] R.J. Hill, A.M. Jessel, I.C. Madsen, *Advances in lead-acid batteries*, *Proc.* vol. 84–14, in: K.R. Bullock, D. Pavlov (Eds.), *The Electrochem. Soc.*, Pennigton, NJ, 1984, p. 44.
- [89] R.J. Hill, I.C. Madsen, *J. Electrochem. Soc.* 131 (1984) 1486.
- [90] P. Boher, P. Garnier, J.R. Gavarri, *J. Solid State Chem.* 52 (1984) 146.
- [91] P. Boher, P. Garnier, J.R. Gavarri, D. Weigel, *J. Solid State Chem.* 55 (1984) 54.
- [92] D. Pavlov, I. Balkanov, T. Halachev, P. Rachev, *J. Electrochem. Soc.* 136 (1989) 3189.
- [93] D. Pavlov, *J. Electrochem. Soc.* 139 (1992) 3075.
- [94] D. Pavlov, I. Balkanov, *J. Electrochem. Soc.* 139 (1992) 1830.
- [95] J.W. Mellor, *A comprehensive treatise on inorganic and theoretical chemistry*, vol. 7, Longmans, London, 1960; 685.
- [96] G. Grube, *Zeit. Elektrochem.* 28 (1922) 278.
- [97] D. Pavlov, I. Balkanov, P. Rachev, *J. Electrochem. Soc.* 134 (1987) 2390.
- [98] D. Berndt, *Maintenance-free Batteries*, Research Studies Press Ltd, Taunton, UK, 1993; 95.
- [99] K. Feter, *Elektrokhimicheskaya Kinetika*, Khimia, Moscow, 1967, p. 646.
- [100] P. Jones, R. Lind, W.F.K. Wynne-Jones, *Trans. Faraday Soc.* 50 (1954) 972.
- [101] G.A. Kokarev, H.G. Bakhchisarait'syan, V.V. Panteleeva, *Tr. Mosk. Khim. Inst.* 54 (1967) 161.
- [102] J.E. Puzey, R. Taylor, in: D.H. Collins (Ed.), *Batteries* 2, Pergamon Press, Oxford, 1965, p. 29.
- [103] I.A. Aguf, M.A. Dasoyan, *Sb. Rab. Khim. Istochikam Toka* 4 (1969) 93.
- [104] S.O. Izidinov, E.H. Rahmatulina, *Elektrokhim.* 8 (1972) 864.
- [105] P. Ruetschi, J. Ockerman, R. Amlie, *J. Electrochem. Soc.* 107 (1960) 325.
- [106] B.N. Kabanov, E.S. Weisberg, I.L. Romanova, E.V. Krivolapova, *Electrochim. Acta* 9 (1964) 1197.
- [107] W. Feitknecht, A. Gaumann, *J. Chim. Phys.* 49 (1952) 135.

- [108] S. Trasatti, *J. Electroanal. Chem.* 182 (1985) 125.
- [109] B. Monahov, D. Pavlov, *J. Appl. Electrochem.* 23 (1993) 1244.
- [110] G. Kassner, *Arch. Pharm.* 228 (1890) 177.
- [111] D. Pavlov, B. Monahov, *J. Electrochem. Soc.* 143 (1996) 3616.
- [112] R. Amadelli, A. Maldotti, F.I. Danilov, A.B. Velichenko, *J. Electroanal. Chem.* 534 (2002) 1.
- [113] J. Cao, H. Zhao, F. Cao, J. Zhang, *Electrochim. Acta* 52 (2007) 7870.
- [114] D. Pavlov, M. Botton, M. Sotyanova, *Bull. Inst. Chim. Phys. BAS* 5 (1965) 55.
- [115] D. Pavlov, T. Rogachev, *Werkst. Korros.* 19 (1968) 677.
- [116] D. Pavlov, T. Rogachev, *Electrochim. Acta* 23 (1978) 1237.
- [117] N.J. Maskalick, *J. Electrochem. Soc.* 122 (1975) 20.
- [118] J.L. Weininger, E.G. Siwek, *J. Electrochem. Soc.* 123 (1976) 602.
- [119] E.M.L. Valeriotte, *J. Electrochem. Soc.* 128 (1981) 1423.
- [120] I.I. Astakhov, E.S. Vaisberg, B.N. Kabanov, *Dokl. Akad. Nauk SSSR* 154 (1964) 1414.
- [121] D. Pavlov, T. Rogachev, *Electrochim. Acta* 31 (1986) 241.
- [122] K.R. Bullock, M.A. Butler, *J. Electrochem. Soc.* 133 (1986) 1086.
- [123] A.C. Loynes, *Encyclopedia of electrochemical power sources*, vol. 4, in: J. Garche (Ed.), Elsevier B.V., 2010, p. 750.
- [124] E. Meissner, *Encyclopedia of electrochemical power sources*, vol. 4, in: J. Garche (Ed.), Elsevier B.V., 2010, p. 829.

Materials Used for Lead-Acid Battery Manufacture

This page intentionally left blank

H₂SO₄ Electrolyte — An Active Material in the Lead–Acid Cell

3.1. H₂SO₄ Solutions Used as Electrolytes in the Battery Industry

Sulfuric acid is one of the three active materials that take part in the generation and accumulation of electric energy in the lead–acid battery. As one of the top products of the chemical industry, commercially produced sulfuric acid is a clear, colourless, odourless, oily, viscous liquid with a density of 1.84 kg L^{−1}. Concentrated H₂SO₄ is an azeotropic mixture of 98.3% H₂SO₄ and 1.7% H₂O, which is obtained through distillation at 383 °C. Sulfuric acid is soluble in water at all concentrations, whereby substantial amounts of heat are generated, i.e., the dissolution reaction is highly exothermic. Therefore, when diluting H₂SO₄, the acid is added to water, under continuous stirring, and not the other way round.

Table 3.1 summarises the water solutions of sulfuric acid with concentrations expressed in mass percent (wt%), density (kg L^{−1}), molarity (mol L^{−1}) and temperature coefficient of density [1]. The range of acid concentrations used in lead–acid batteries is also marked in the table. If acid solutions of higher or lower concentrations than the battery operation range (battery acid window) are used, this would lead to a decline in performance parameters of the batteries.

Until recently, sulfuric acid concentration was referred to by battery experts by the term specific gravity (s.g.). This term gives the ratio of the density of H₂SO₄ solution in g cm^{−3} at a given temperature to the density of water at a reference temperature. Originally, the highest value of the density of water at 4 °C was taken as H₂O reference density. Nowadays, for the sake of simplicity, the density of water at 15 °C or at 25 °C is assumed as reference density. Several years ago, the term ‘specific gravity’ was replaced by ‘relative density’ (r.d.) in the IUPAC Compendium of Chemical Terminology.

Figure 3.1 illustrates the correlation between H₂SO₄ quantity expressed in g L^{−1} and H₂SO₄ relative density at 25 °C [2]. The relative density is a measureless unit as it represents the ratio between two densities. The temperature coefficient of the relative density of H₂SO₄ solutions is also given in the figure. The relative density of a given H₂SO₄ solution should be multiplied by the respective temperature coefficient to obtain the relative density of the H₂SO₄ solution at this particular temperature. Figure 3.1 shows also the H₂SO₄ concentration ranges of normal

Table 3.1: Relation of sulfuric acid concentrations [1].

	Mass percent (wt%)	Density (kg L ⁻¹)			Molality (mol kg ⁻¹)	Molarity (mol L ⁻¹)			Temperature coefficient of density (10 ⁻³ kg L ⁻¹ °C)
		0 °C	25 °C	50 °C		0 °C	25 °C	50 °C	
<i>Battery acid concentration window</i>	0	0.9998	0.9971	0.9981	0	0	0	0	0.236
	2	1.0147	1.0104	1.0006	0.208	0.2069	0.2060	0.2040	0.282
	4	1.0291	1.0234	1.0129	0.425	0.4197	0.4174	0.4131	0.324
	6	1.0437	1.0367	1.0256	0.651	0.6385	0.6342	0.6274	0.362
	8	1.0585	1.0502	1.0386	0.887	0.8634	0.8566	0.8472	0.398
	10	1.0735	1.0640	1.0517	1.133	1.0945	1.0849	1.0723	0.436
	12	1.0986	1.0780	1.0651	1.390	1.3319	1.3190	1.3032	0.470
	14	1.1039	1.0922	1.0788	1.660	1.5758	1.5590	1.5399	0.502
	16	1.1194	1.1067	1.0927	1.942	1.8261	1.8054	1.7825	0.534
	18	1.1351	1.1215	1.1070	2.238	2.0832	2.0583	2.0317	0.562
	20	1.1510	1.1365	1.1215	2.549	2.3471	2.3175	2.2870	0.590
	22	1.1670	1.1517	1.1362	2.875	2.6177	2.5834	2.5485	0.615
	24	1.1832	1.1672	1.1512	3.220	2.8953	2.8562	2.8170	0.640
	26	1.1996	1.1829	1.1665	3.582	3.1801	3.1358	3.0929	0.662
	28	1.2160	1.1989	1.1820	3.965	3.4715	3.4227	3.3745	0.680
	30	1.2326	1.2150	1.1977	4.370	3.7703	3.7164	3.6635	0.698
	32	1.2493	1.2314	1.2137	4.798	4.0761	4.0177	3.9600	0.712
	34	1.2661	1.2479	1.2300	5.252	4.3891	4.3260	4.2640	0.722
	36	1.2831	1.2647	1.2466	5.735	4.7097	4.6422	4.5757	0.730
	38	1.3004	1.2818	1.2635	6.249	5.0384	4.9663	4.8954	0.738
	40	1.3179	1.2991	1.2806	6.797	5.3749	5.2982	5.2228	0.746
	42	1.3357	1.3167	1.2981	7.383	5.7199	5.6385	5.5589	0.752
	44	1.3538	1.3346	1.3160	8.011	6.0735	5.9873	5.9039	0.756
	46	1.3724	1.3530	1.3343	8.685	6.4368	6.3458	6.2581	0.762
	48	1.3915	1.3719	1.3528	9.412	6.8101	6.7142	6.6207	0.774
	50	1.4110	1.3911	1.3719	10.196	7.1933	7.0918	6.9939	0.782
	55	1.4619	1.4412	1.4214	12.462	8.1980	8.0820	7.9709	0.810
	60	1.5154	1.4940	1.4735	15.294	9.2706	9.1397	9.0143	0.839

operation of the three types of lead–acid batteries (SLI, traction, stationary), in the charge and discharged state, as summarised by Barak [2]

3.2. Purity of H₂SO₄ Used in Lead–Acid Batteries

The lead–acid battery is a delicate electrochemical system in which the current generation electrochemical reactions involving lead compete with the electrochemical reactions of water decomposition (Fig. 2.1). A number of impurities exert strong effect on the above competition by accelerating the decomposition of water and, thus, may have a detrimental effect on battery performance. Therefore, the sulfuric acid solutions used for battery manufacture should have

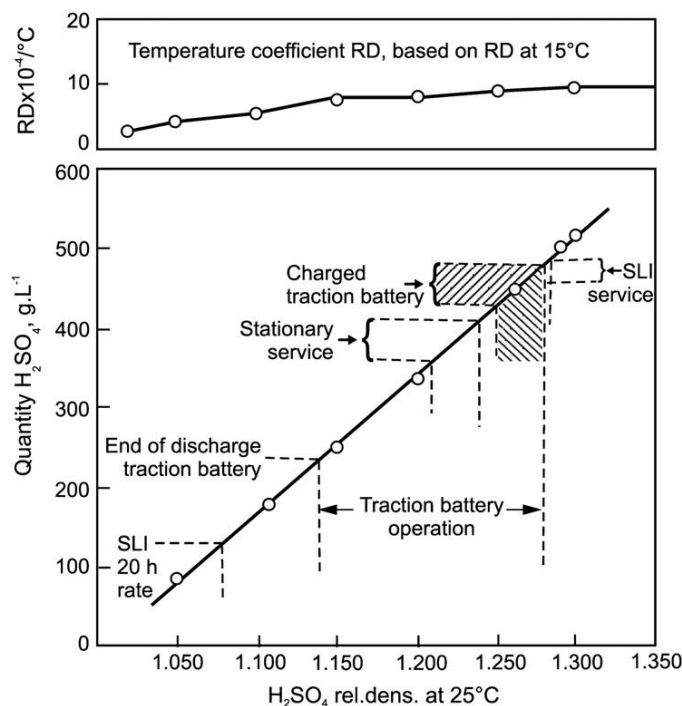


Figure 3.1:

Correlation between H₂SO₄ quantity in g L⁻¹ and H₂SO₄ relative density at 25 °C [2].

a definite purity grade. The maximum admissible impurities for the commercial product H₂SO₄ are summarised in Table 3.2. The table provides data about the most important impurities included in the US Federal Specification O-S801-b-4.14.65 and the British Standard Specification BS 3031.1972 [2].

Battery performance is adversely affected also by:

- multi-valent ions (Fe²⁺/Fe³⁺, Cu⁺/Cu²⁺, Cr³⁺/Cr⁵⁺, etc.), which change their valency at the two electrodes and thus accelerate the self-discharge processes in the battery;
- all noble metals, as they lower the over-potential of hydrogen and oxygen evolution, and thus reduce the efficiency of charge and accelerate battery self-discharge;
- oxidants such as ClO₃⁻, ClO₄⁻ and 4NO₃⁻ at low H₂SO₄ concentrations they form soluble salts, which leads to disintegration of the structures of PAM and NAM.

Bode accounted for the above-discussed factors and gave a more comprehensive list of impurities with their maximum admissible values [1]. These are presented in Table 3.3.

The water used for battery electrolyte preparation should be distilled or demineralized and have an electrical conductivity less than 10⁻⁵ ohm⁻¹ cm⁻¹ and pH between 5 and 7. Chlorine, nitrogen and sulfur compounds, as well as metal ions precipitated with H₂S or (NH₄)₂S, should

Table 3.2: Purity standards for sulfuric acid [2].

	BS 3031 Ref. 1.215 SG/20 °C	US O-S801-b (Max. wt%)
Fixed residue	0.015%	0.075
Chloride (Cl)	7 ppm	0.004
Sulfur dioxide (SO ₂)	5 ppm	0.0015
Nitrogen as ammonium (NH ₄)	50 ppm	0.0004
Nitrogen as oxides	5 ppm	0.0002
Iron (Fe)	12 ppm	0.003
Arsenic (As)	2 ppm	0.00004
Antimony (Sb)	Not stated	0.00004
Copper (Cu)	7 ppm	0.0025
Manganese (Mn)	0.4 ppm	0.000007
Zinc (Zn)	Not stated	0.0015
Selenium (Se)	Not stated	0.0007
Nickel (Ni)	Not stated	0.00004

Table 3.3: Purity requirements for battery acid [1]

Impurity	Maximum value, (mg.L ⁻¹)		
	VDE 0510	Fed.Spec. SO-801	
Density	1.17 to 1.30	1.40	1.28 (kg.L ⁻¹)
Platinum	0.05	(-) ^a	(-)
Copper	0.5	30	50
Other metals of the H ₂ S group:			
Singly	1	0.5	0.5
Total	2	(-)	5
Chromium, manganese, titanium,	0.2	1	0.2
Singly			
Iron	30	30	120
Other metals of the ammonium sulfide group:			
Singly	1	(-)	(-)
Total	2	(-)	(-)
Halogen, total	5	0.5	120
Nitrogen, as NH ₃	50	5	60
Nitrogen in combined form	10	3	(-)
SO ₂ or H ₂ S	20	(-)	(-)
Volatile organic acids:			
Acetic acid	20	(-)	(-)
Permanganate number	30	(-)	(-)
Residue on ignition at 700 to 800°C	250	150	(-)

^aNot specified

be in amounts below the detection threshold of any analytical technique. After evaporation of 1 L of water the obtained precipitate should be less than 100 mg (100 ppm), and when treated with permanganate, the reacted amount of impurities should be less than 20 mg L⁻¹ [1].

3.3. Dissociation of H₂SO₄

When mixed with water, sulfuric acid dissociates in two degrees. The first degree of dissociation of H₂SO₄ can be expressed by the equation:



The first dissociation constant is equal to:

$$k_1 = (a_{\text{H}^+} \cdot a_{\text{HSO}_4^-}) / a_{\text{H}_2\text{SO}_4} \approx 10^3 \quad (3.E1)$$

The value of k_1 has been determined experientially by Young [3]. Thus, the first dissociation sulfuric acid is a strong acid and the equilibrium maintains but a very small amount of non-dissociated H₂SO₄.

The second degree of sulfuric acid dissociation can be expressed by the equation:



The second dissociation constant $k_2 \approx 1.02 \times 10^{-2}$ [4–5]. This value indicates that the second degree of dissociation is incomplete and sulfuric acid behaves like a weak acid. The temperature dependence of k_2 within the temperature range 25–175 °C has been experientially determined and can be expressed by the following equation [4]:

$$\lg k_2 = 5.162 - 509/T - 0.01826T \quad (3.E2)$$

Figure 3.2 shows the concentration of HSO₄⁻ and SO₄²⁻ ions resulting from the dissociation of sulfuric acid vs H₂SO₄ concentration [3,5–8]. In the battery acid concentration range, the solution contains mainly HSO₄⁻ ions and small amounts of SO₄²⁻ ions and non-dissociated H₂SO₄. Obviously, the electrochemical processes of charge and discharge in the battery involve mostly HSO₄⁻ ions.

3.4. Electrical Conductivity of H₂SO₄ Solutions

The high value of the first dissociation constant maintains high concentration of H⁺ ions in the solution, and H⁺ ions have a several-fold higher mobility than all other ions in the solution. This guarantees high electrical conductivity of the H₂SO₄ electrolyte in the battery, which is a mandatory requirement for any chemical power source.

The specific electrical resistance (resistivity) of the H₂SO₄ electrolyte is one of the basic parameters that determines the inner resistance and power of a lead–acid cell. When the inner

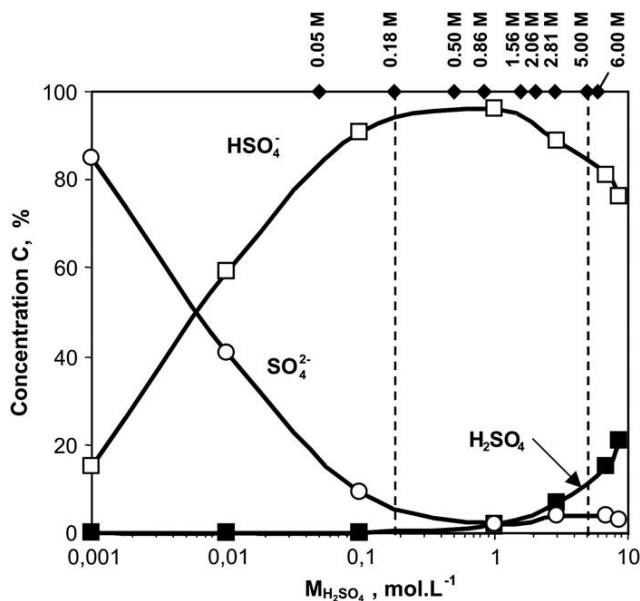


Figure 3.2:

Concentration of HSO_4^- and SO_4^{2-} Ions resulting from the dissociation of sulfuric acid vs H_2SO_4 concentration [8].

cell resistance is high, substantial part of the useful energy is consumed within the cell itself, i.e., energy is lost in the form of heat. The inner resistance of a cell, when electric current flows through it, depends on electrolyte concentration and temperature. The quantity that characterises the electrical resistance of a given material is the specific resistance (resistivity). This is the electrical resistance of a conductor of a unit cross-sectional area and unit length, and is measured in ohm-centimetres ($\Omega \text{ cm}$). The resistivity is an intrinsic property of the material and is temperature dependent.

Figure 3.3 shows the specific resistance (resistivity) of H_2SO_4 solutions as a function of H_2SO_4 concentration at different temperatures [2]. The acid concentration window of lead–acid battery operation is marked in the figure. It can be seen that within this window the specific resistance has the lowest values. Both decrease of $C_{\text{H}_2\text{SO}_4}$ below 1.10 and increase above 1.30 relative density cause the specific electrical resistance to increase. When the cell temperature falls below 0°C , the specific resistance increases rapidly and the battery loses both power and energy. The temperature window with sufficiently low electrical resistance is between 0 and 50°C . However, even at lower temperatures the battery is capable to deliver sufficient electric current to start the engine of an automobile.

Table 3.4 provides data about the specific and equivalent electrical conductivities of sulfuric acid solutions of various concentrations, expressed in different units [2].

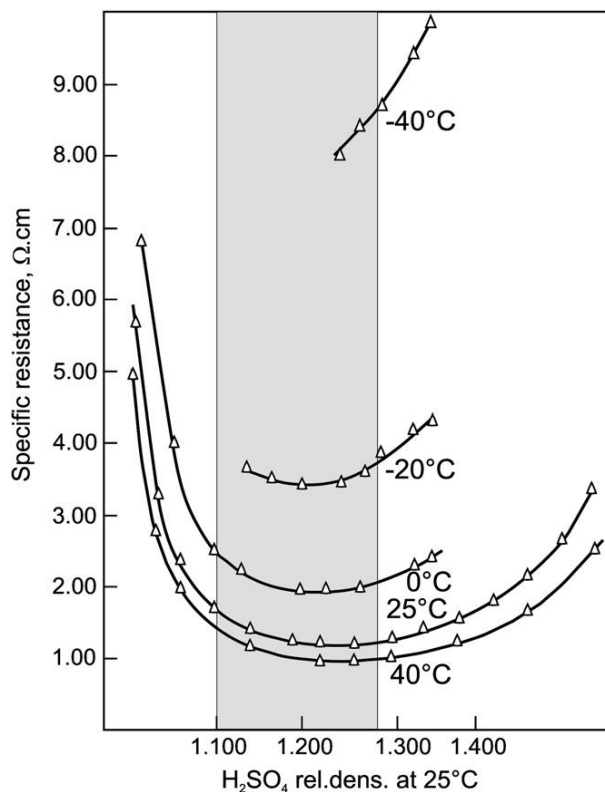


Figure 3.3:

Specific electrical resistance (resistivity) of various H₂SO₄ solutions as a function of concentration and temperature [2].

3.5. Dependence of the Electromotive Force of a Lead–Acid Cell on Electrolyte Concentration and Its Influence on Charge Voltage

Duisman and Giauque [9] calculated the EMF of the cell as a function of the molar concentration of H₂SO₄, within the range 0.1–14 M, based on the third law of thermodynamics. Following a period of stabilisation (generally several hours), the open-circuit voltage becomes equal to the EMF of the cell and is determined by the acid concentration in the cell and the temperature. Figure 3.4 shows the experimentally measured and the calculated values for the cell voltage as a function of H₂SO₄ relative density [9–13].

Within the H₂SO₄ relative density window from 1.10 to 1.28, the cell voltage at open circuit increases linearly as acid concentration augments. Based on this linear dependence a practical formula can be derived to be used for easy determination of the density of H₂SO₄ solutions, d , through measuring the open-circuit voltage of the cell, ΔE , in volts:

$$d = \Delta E - 0.845 \text{ rel. dens.} \quad (3.E3)$$

Table 3.4: Dependence of specific and equivalent conductivity on mass fraction and density for the water/sulfuric acid system. Temperature 25 °C [1].

Mass fraction (100 w)	Density, d (kg L ⁻¹)	Specific conductivity $10^2 \nu$ (ohm ⁻¹ m ⁻¹)	Equivalent conductivity $10^{-4} \Lambda_{eq}$ (m ² ohm ⁻¹ mol ⁻¹)
3.929	1.0229	0.1772	432.6
7.000	1.0434	0.3081	413.7
10.000	1.0640	0.4261	392.8
14.56	1.0962	0.5859	360.0
19.80	1.1351	0.7169	312.9
25.31	1.1774	0.7983	262.8
29.47	1.2107	0.8253	226.9
34.28	1.2503	0.8187	187.3
39.10	1.2913	0.7812	151.7
43.94	1.3340	0.7144	119.5
48.71	1.3787	0.6399	93.46
53.48	1.4258	0.5552	71.41
58.35	1.4762	0.4709	53.62

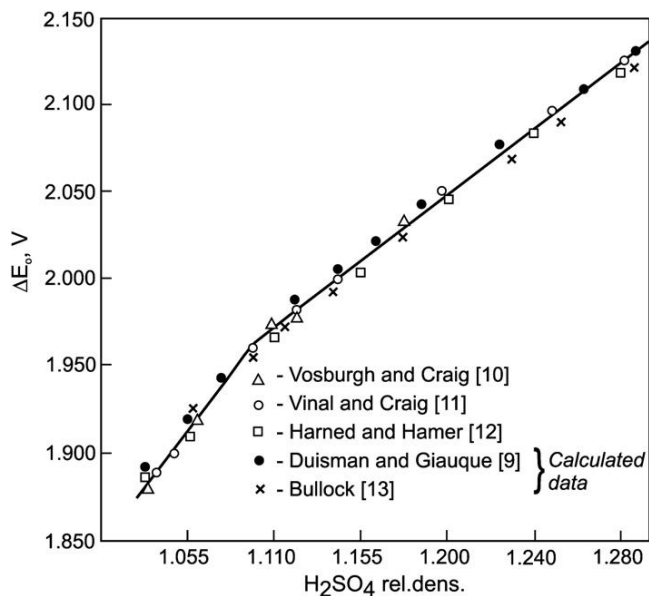


Figure 3.4:

Experimentally measured and calculated values for lead–acid cell voltage as a function of H_2SO_4 relative density, as reported by different authors.

This formula is correct when the cell voltage on open circuit is equal to the electromotive force of the cell, which is achieved when the cell has reached steady state and there are no more concentration or temperature gradients of the H₂SO₄ solution. The electrolyte in fully charged traction and SLI batteries has most often a relative density of 1.28. According to the data in Fig. 3.4, this H₂SO₄ relative density corresponds to an electromotive force of 2.125 V.

For the electrochemical reactions of charge to proceed at the two electrodes, the external voltage applied to the cell, U_{ch} , should be higher than the electromotive force of the cell, ΔE , at the given H₂SO₄ concentration. The difference between the two voltages is called polarization of the cell (battery), ΔU_{p} .

$$U_{\text{ch}} = \Delta E + \Delta U_{\text{p}} \quad (3.E4)$$

ΔE is a function of H₂SO₄ concentration and increases with increase of the state of charge of the cell (battery). This correlation should be taken into account when selecting the charge voltage for a particular battery type. The charge voltage, U_{ch} , should be higher than ΔE of a fully charged battery, i.e., on completion of battery charge, ΔU_{p} should have a value of 40–80 mV that would compensate for the inner resistance of the battery and a weak current would flow to compensate for battery self-discharge. Often, however, selection of the charge voltage, U_{ch} , is limited by the voltage of the charging device used. If the maximum voltage of the charging equipment is lower than the electromotive force of the fully charged battery, the concentration of the sulfuric acid electrolyte should be reduced so as to yield $U_{\text{p}} > 40$ mV in the charged state.

The above correlation can be illustrated by the example of lead–acid batteries for IT applications. Batteries (flooded type) have been assembled with sulfuric acid solutions of six different concentrations within the range from 1.15 to 1.33 relative density [14]. After initial capacity determinations, the batteries were set to cycling with a current corresponding to 4-h rate of discharge. Figure 3.5 shows the changes in battery voltage measured after 30 min open-circuit stay following charge (▲), after discharge followed by 30 min open-circuit stay (◆), and 5 min after the beginning of discharge (□). The charge voltage (13.62 V) and the end-of-discharge voltage (10.05 V) generally used for IT batteries are also marked in the figure [14].

The data in Fig. 3.5 indicate that batteries with H₂SO₄ concentrations higher than 1.26 relative density will not be fully charged at 13.62 V (2.27 V per cell) at 25 °C. If the H₂SO₄ concentration is 1.28 g cm^{−3}, the battery will be charged, but partially, and considerable amount of PbSO₄ will remain unreacted, i.e., not transformed into active material. The unreacted PbSO₄ in the plates will recrystallize and the plates will be sulfated. So, the electrolyte relative density should be kept below 1.26 to allow the battery to charge fully. Hence, selection of electrolyte concentration for a given battery type depends on the charge

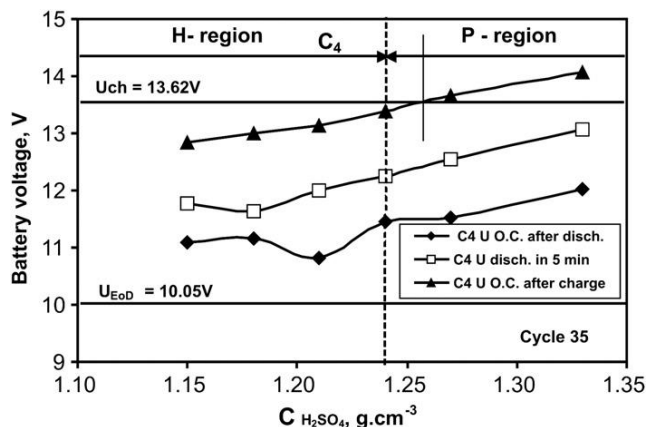


Figure 3.5:

Battery voltage measured after 30 min open-circuit stay following charge (\blacktriangle) after discharge followed by 30 min open-circuit stay (\blacklozenge); and 5 min after the beginning of discharge (\square), as a function of H_2SO_4 concentration [14].

voltage specified in the battery-operating specification. And vice versa, battery manufacturers should specify the minimum charge voltage to be employed for each battery type in accordance with the electrolyte concentration used.

Figure 3.5 also evidences that the three battery voltage vs H_2SO_4 concentration curves are more or less parallel. This means that the cell (battery) voltage depends on H_2SO_4 concentration both during and after the discharge.

3.6. Correlation Between H_2SO_4 Amount and Cell Capacity

Practically, sulfuric acid does not take part in the electrochemical processes of electron transfer through the electrode surfaces of both electrodes, which determines the capacity of the cell. However, H_2SO_4 reacts, in stoichiometric amounts, with the product (Pb^{2+} ions) of the preceding electrochemical reactions at the two electrodes, which makes it possible to determine indirectly the quantity of electricity delivered by the cell (battery) during discharge from the amount of reacted H_2SO_4 . Thus, although sulfuric acid participates in a chemical reaction, it is an active material in the lead–acid cell and participates in the reactions of charge and discharge according to Faraday’s law. When 1 Ah of electricity flows through the cell, the amount of H_2SO_4 that takes part in the reactions at the two types of plates is 3.666 g.

During discharge, only part of the H_2SO_4 contained in the solution in the cell reacts. Because of kinetic hindrances, part of the sulfuric acid is not involved in the reactions. On the other hand, the electrolyte should have a certain electrical conductivity for the next charge to be realised, i.e., it should contain a certain amount of unreacted H_2SO_4 to guarantee this electrical conductivity. Hence, only part of the total amount of H_2SO_4 in the cell participates in the

electrochemical reactions. The term ‘active material utilization coefficient’ has been generally adopted in the battery practice. The utilization coefficient gives what part of the total amount of active material is involved in the reactions of current generation.

From the range within which the concentration of H₂SO₄ changes during battery operation, it is possible to calculate the quantity of electricity the cell (battery) delivers. Figure 3.6 shows the correlation electric charge (in Ah per litre of H₂SO₄ solution) vs density and molality of the solution, and Table 3.5 gives the electrochemical equivalents (in Ah per litre of solution) of sulfuric acid solutions of different molality and density [1].

According to the data in Fig. 3.6, 1 L of H₂SO₄ electrolyte of 1.28 relative density ‘delivers’ 131 Ah of electricity. Let us assume that the electrolyte relative density has decreased to 1.15 at the end of discharge. Judging by the data in Fig. 3.6, this H₂SO₄ concentration corresponds to 68 Ah L⁻¹ specific capacity. This means that the sulfuric acid that has reacted with Pb²⁺ ions obtained by the electrochemical reactions at the two electrodes has ‘delivered’ 63 Ah of electricity. Hence, the coefficient of H₂SO₄ utilization during discharge is $\eta_{\text{H}_2\text{SO}_4} = 63 : 131 = 48.1\%$. It follows from the above considerations that it is possible to judge the state of charge of the battery from the H₂SO₄ concentration during discharge.

The total volume of H₂SO₄ solution in flooded batteries is distributed between the ‘active block’, comprising positive and negative plates and separators inbetween, and the ‘electrolyte ‘reservoir’ above the active block. In VRLA batteries, the whole electrolyte volume is contained in the active block, which is 96% saturated. Within the active block, the electrolyte fills the pores of the plates and separators, and the spaces between the positive and negative

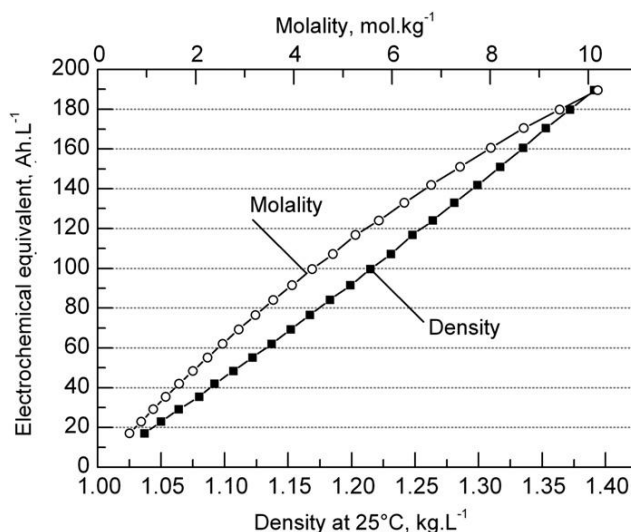
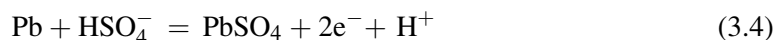


Figure 3.6:
Electrochemical equivalent of sulfuric acid solution vs solution density and molality.

Table 3.5: Electrochemical equivalents for sulfuric acid solutions in ampere-hours per litre of solution [1].

Mass Percent (wt%)	Density at 25 °C (kg L ⁻¹)	Molality M (mol kg ⁻¹)	Electrochemical Equivalent (Ah L ⁻¹)
6	1.037	0.651	17.0
8	1.050	0.887	22.9
10	1.064	1.133	29.1
12	1.089	1.390	35.4
14	1.092	1.660	41.9
16	1.107	1.942	48.4
18	1.122	2.238	55.1
20	1.137	2.549	62.0
22	1.152	2.875	69.3
24	1.167	3.220	76.5
26	1.183	3.582	84.0
28	1.199	3.965	91.5
30	1.215	4.370	99.5
32	1.231	4.798	107.2
34	1.248	5.252	116.8
36	1.264	5.735	124.0
38	1.281	6.249	133.0
40	1.299	6.797	141.9
42	1.317	7.383	151.0
44	1.335	8.011	160.5
46	1.353	8.685	170.5
48	1.372	9.412	179.8
50	1.391	10.196	189.5

plates. The volume of these spaces influences the capacity of the cell, the effect being determined by the reactions on both plates:



The above equations show that the mass of the electrolyte involved in the discharge of the positive plates is larger than that consumed at the negatives. Since the water formed during discharge at the positive plates dilutes the neighbouring H₂SO₄ solution, the volume of the positive electrolyte space has to be greater (by a factor of 1.6) than that of the negative space. This is achieved by placing the ribbed side of the microporous separator so as to face the positive plate.

For application in VRLA batteries, a special three-layer separator has been developed in this laboratory comprising one thin AGM sheet, which is in contact with the negative plate, one thick AGM sheet that contacts the positive plate and a modified AGM (MAGM) membrane between these two AGM sheets which separates the two electrode spaces [15]. This separator

design ensures higher reversibility of the processes during battery charge and discharge, and thus stable VRLA battery capacity on cycling.

3.7. Utilization of the Active Materials in the Lead–Acid Battery and Battery Performance

There are three active materials in the lead–acid battery: Pb, PbO₂ and H₂SO₄ electrolyte. One, or rarely two, of these active materials limit the cell capacity on discharge. Most often, the capacity-limiting active material is the one with the highest utilization coefficient. Let us assume that this rule holds for the three active materials in the lead–acid cell.

It is interesting to see what is the influence of sulfuric acid utilization, $\eta_{\text{H}_2\text{SO}_4}$ on the performance characteristics of the battery. The following investigation was performed with the aim to elucidate this influence [14,16]. Two series of 12 batteries each were assembled. Batteries of the first series had cells with outer negative plates and utilization coefficients of $\eta_{\text{PAM}} = 50\%$ for the positive active material and $\eta_{\text{NAM}} = 37\%$ for the negative plates. Let us denote this series of batteries P-series [14]. The 12 batteries of the second series had cells with outer positive plates and active material utilization coefficients of $\eta_{\text{PAM}} = 29\%$ and $\eta_{\text{NAM}} = 45\%$, respectively. Let us denote this series of batteries as N-series [16]. All batteries were of the flooded type and were filled with H₂SO₄ solutions of the same volume but of six different concentrations from 1.15 to 1.33 relative density. Two batteries were assembled with each of the above solutions.

Figure 3.7 shows the changes in sulfuric acid utilization, $\eta_{\text{H}_2\text{SO}_4}$, as a function of H₂SO₄ electrolyte concentration for the P- and N-series of batteries.

At H₂SO₄ relative densities lower than 1.25 (Fig. 3.7a) and 1.27 (Fig. 3.7b), the coefficient of H₂SO₄ electrolyte utilization is the highest. Within this acid concentration region, H₂SO₄ limits the capacity of the cells (batteries). Let us call this H₂SO₄ concentration region *H-region*. When $C_{\text{H}_2\text{SO}_4} > 1.25$ relative density (Fig. 3.7a), PAM has the highest utilization coefficient and hence the positive plates limit the capacity of the cell (battery). Let us call this H₂SO₄ concentration region *P-region*. At $C_{\text{H}_2\text{SO}_4} > 1.27$ relative density (Fig. 3.7b), the negative active mass is the capacity-limiting element, *N-region* of electrolyte concentrations. Depending on the acid concentration used for the manufacture of a given battery type, it will have different performance behaviour.

Sulfuric acid is consumed during battery discharge and is then restored during charge. These processes are reversible as far as H₂SO₄ is concerned because it does not change its structure as do the positive and negative active materials.

Figure 3.8 shows the maximum initial capacity (for the first 10 cycles) as a function of (a) H₂SO₄ concentration and (b) utilization of H₂SO₄ for 32-Ah batteries of the H- and

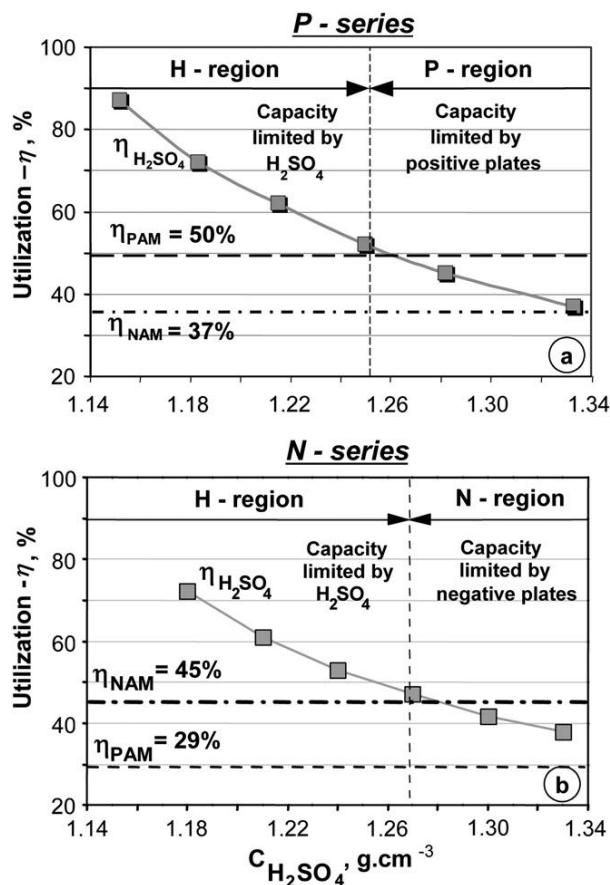


Figure 3.7:

Changes in sulfuric acid utilization, $\eta_{H_2SO_4}$, during discharge of the P- and N-series of batteries, as a function of H_2SO_4 electrolyte concentration.

P-types, i.e., with electrolytes within the H- and P-regions of H_2SO_4 concentrations, respectively.

Within the H-region of acid concentrations, the maximum initial battery capacity is lower than the rated value and increases with increase of electrolyte concentration to reach the rated capacity value at 1.22 relative density of the H_2SO_4 solution. This corresponds to 57% utilization of H_2SO_4 . Batteries with acid utilization higher than 57% do not reach their nominal capacity at 50% utilization of PAM. At $C_{H_2SO_4} > 1.22$ g cm⁻³, the electrolyte is not a capacity-limiting active material and the initial battery capacity is higher than the rated value, then it passes through a maximum at 1.24 relative density, followed by a decline in positive plate capacity at 1.33 rel.dens. These results indicate that, at electrolyte concentrations higher than 1.24 relative density, certain phenomena proceed at the positive plates, which cause their capacity to decline.

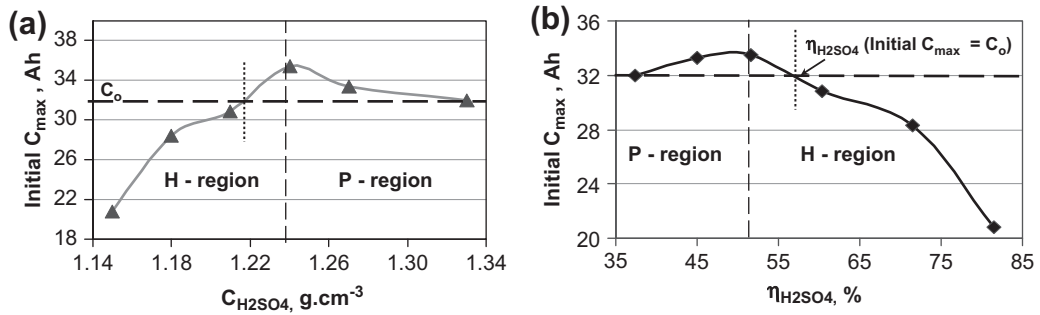


Figure 3.8:

Maximum initial capacity (for the first 10 cycles) of 32-Ah batteries with electrolytes of the H- and P-regions of H_2SO_4 concentrations as a function of: (a) H_2SO_4 concentration and (b) H_2SO_4 utilization coefficient [14].

Figure 3.9 presents the dependence battery cycle life vs H_2SO_4 concentration on cycling of 32-Ah batteries with 8 A (C_4) or 3.2 A (C_{10}) discharge currents. The end-of-life criterion is when the battery capacity falls down below 70% of the rated capacity, C_0 . Batteries with electrolytes within the H-region of acid concentrations (H-type batteries) have longer cycle life than those with H_2SO_4 concentration within the P-region (P-type batteries) [14]. With decrease of $C_{H_2SO_4}$ within the H-region of acid concentrations, the cycle life of the batteries increases. This means that the reversibility of the processes and of the active mass structures during charge and discharge improves at lower electrolyte concentrations within the H-region, and hence, the cycle life of the battery increases. However, the quantity of sulfuric acid in the diluted solutions of the H-region of H_2SO_4 concentrations seems to be insufficient to yield the required rated capacity of the battery. Or, at $C_{H_2SO_4} < 1.22$ g cm⁻³, kinetic difficulties (e.g., ion diffusion and crystal growth hindrances) occur in the plates, which limit the capacity of the cells, i.e., the ratio $\eta_{H_2SO_4} : \eta_{PAM} : \eta_{NAM}$ is of utmost importance.

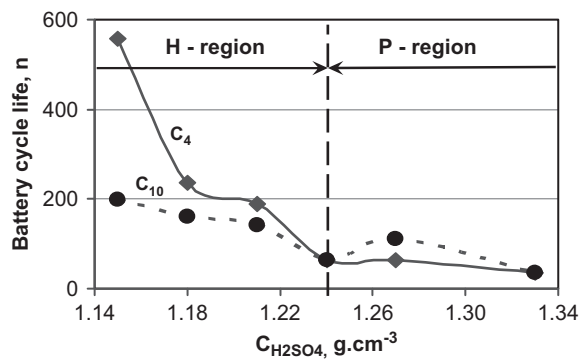


Figure 3.9:

Battery cycle life vs H_2SO_4 concentration on cycling of 32-Ah batteries with 8 A (C_4) or 3.2 A (C_{10}) discharge currents [14].

Figure 3.10 shows the dependences of (a) H_2SO_4 utilization, (b) measured initial capacity vs rated capacity and (c) battery cycle life as a function of H_2SO_4 concentration [16]. Batteries with $C_{\text{H}_2\text{SO}_4}$ within the H-region (H-type batteries) have lower initial capacity (above the rated value though) but longer cycle life and higher H_2SO_4 utilization on discharge. In the N-region of acid concentrations (N-type batteries), the utilization of H_2SO_4 decreases substantially, which results in higher initial capacity, but shortens battery cycle life.

The data in Fig. 3.10 evidence that the utilization of H_2SO_4 at a given electrolyte concentration depends on the discharge current and on the ratio $\eta_{\text{H}_2\text{SO}_4} : \eta_{\text{PAM}} : \eta_{\text{NAM}}$. Within the H-region of acid concentrations, the more diluted the H_2SO_4 solution, the stronger the influence of the discharge current.

The results presented in Figs 3.8–3.10 give grounds for the following conclusions. The different cycling behaviour of batteries with different electrolyte concentrations (within the P-, N- or H-regions) indicates that there is a difference in the elementary processes that limit the capacity of the three types of batteries. For batteries to meet the standard requirements for

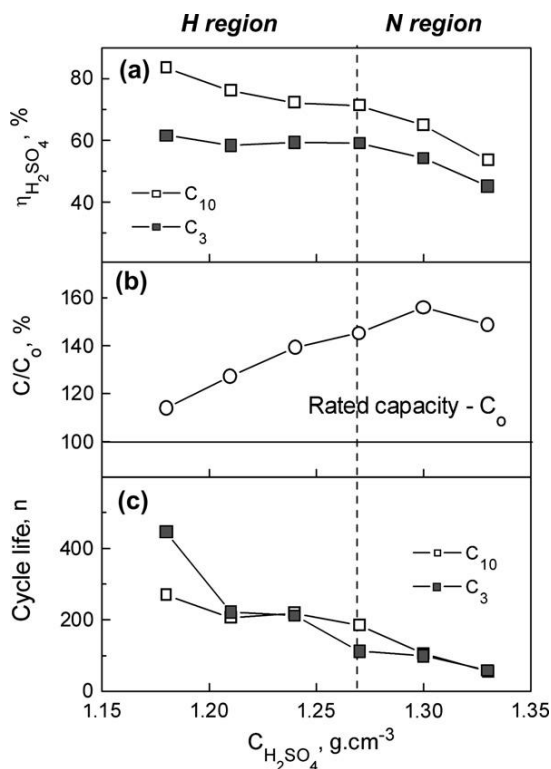


Figure 3.10:

Dependence of (a) H_2SO_4 utilization, (b) measured initial capacity C_{20}/C_0 and (c) battery cycle life on H_2SO_4 concentration [16].

initial capacity and cycle life performance, their active materials should have definite utilization coefficients, i.e., a definite ratio $\eta_{\text{H}_2\text{SO}_4} : \eta_{\text{PAM}} : \eta_{\text{NAM}}$ should be observed. Figure 3.10 evidences that within the H-region of acid concentrations, all batteries have long cycle life, but their initial capacity is far below the rated value, i.e., batteries of this type have an excess of PAM and NAM.

So on grounds of the above experimental data the following general conclusions can be drawn:

- a. When H₂SO₄ electrolytes with concentrations within the H-region (diluted solutions of H₂SO₄) are used for battery manufacture, the processes of charge and discharge proceed in a more reversible way, due to the reversible formation and disintegration of the PAM and NAM structures and of the PbSO₄ crystals, which eventually yields long battery cycle life. Hence, the H-region of acid concentrations can be used as a basis for determining the amounts of the other two active materials in the battery design process.
- b. The utilization coefficients for the positive and negative active materials should be selected in such a way as to ensure cell (battery) capacity higher than the rated value. This means that the ratio $\eta_{\text{H}_2\text{SO}_4} : \eta_{\text{PAM}} : \eta_{\text{NAM}}$ should guarantee that the discharge processes would be impeded by kinetic hindrances only after the rated capacity of the battery is reached.

If the above principles are observed in the battery design process, the battery will meet the standard performance requirements with optimum utilization of the three active materials.

3.8. Correlation Between the Electrochemical Activity of PbO₂/PbSO₄ Electrode and H₂SO₄ Electrolyte Concentration

Looking at the experimental data in Figs 3.8 and 3.9 the question arises: ‘Why does the increase in sulfuric acid concentration above 1.24 relative density lead to decrease in battery capacity and cycle life?’ Experiments were performed aimed to study the dependence of the electrochemical activity of a PbO₂/PbSO₄ electrode on H₂SO₄ concentration [8,17]. For the purpose, a PbO₂/PbSO₄ electrode was obtained by the Planté method, through cycling a smooth Pb electrode in H₂SO₄ solutions of different concentrations. After 1 or 16 h of cycling, the amount of PbO₂ reduced during the cathodic scan at a rate of 1 mV s^{−1}, was determined coulometrically. The obtained results are presented in Fig. 3.11.

Three acid concentration regions can be identified judging by the curve profiles:

- a. *Passive high-concentration region:* $C_{\text{H}_2\text{SO}_4} > 5 \text{ M H}_2\text{SO}_4$. The electrochemical activity of PbO₂ decreases with increase of H₂SO₄ concentration over 5 M (1.28 relative density).
- b. *Active medium-concentration region:* $0.86 \text{ M (1.05 rel. dens.)} < C_{\text{H}_2\text{SO}_4} < 5.0 \text{ M (1.28 rel. dens.)}$. In this acid concentration region, PbO₂ is electrochemically active and this is the electrolyte concentration region of normal lead–acid battery operation.

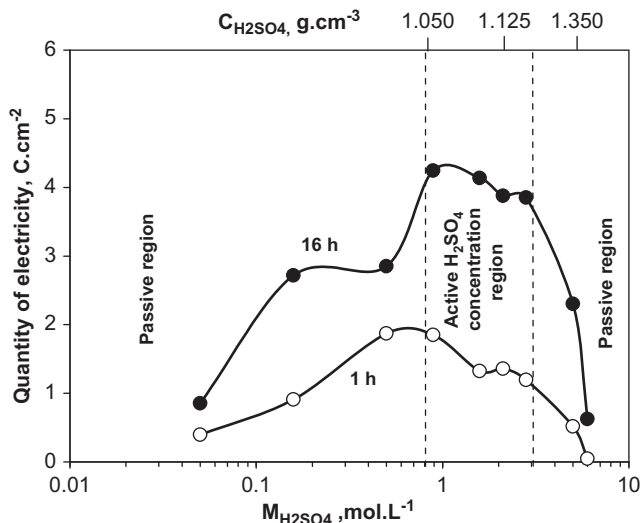


Figure 3.11:

Amount of active PbO_2 involved in the reduction process as a function of H_2SO_4 concentration [8].

- c. *Passive low-concentration region:* $C_{\text{H}_2\text{SO}_4} < 0.86 \text{ M}$ (1.05 rel. dens.). PbO_2 formed in this H_2SO_4 concentration region has low electrochemical activity that decreases further with decrease of $C_{\text{H}_2\text{SO}_4}$.

The data in Fig. 3.2 indicate that, within the active acid concentration region, sulfuric acid undergoes first degree of dissociation to H^+ and HSO_4^- ions. Figure 3.11 evidences that the PbO_2 obtained as a result of such a dissociation is electrochemically most active.

What is this increase in PbO_2 activity in the above acid concentration region due to? The phase composition of PbO_2 layers formed at different H_2SO_4 concentrations was determined by X-ray diffraction analysis. Figure 3.12 presents the areas of the characteristic X-ray diffraction peaks reflecting the content of the individual crystal phases for the anodic layers formed in H_2SO_4 solutions with concentrations varying between 6.0 and 0.05 M, after 1 and 16 h of cycling [8,17].

It is evident from Fig. 3.12 that, within the passive high-concentration region ($C_{\text{H}_2\text{SO}_4} > 5.0 \text{ M}$ H_2SO_4), the anodic layer contains mostly $\alpha\text{-PbO}_2$ and PbSO_4 , and small amounts of $\beta\text{-PbO}_2$.

In the active H_2SO_4 concentration region, the amount of $\beta\text{-PbO}_2$ in the anodic layer exceeds by several times that of the $\alpha\text{-PbO}_2$ phase. Below 0.86 M H_2SO_4 concentrations, the content of $\beta\text{-PbO}_2$ decreases on further dilution of the solution.

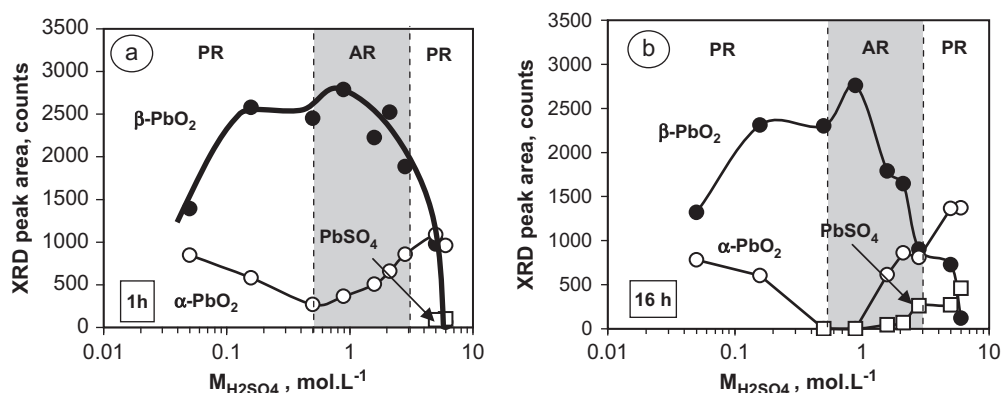


Figure 3.12:

Phase composition of the anodic layer formed for (a) 1h and (b) 16 h of cycling of a Pb electrode between 700 and 1600 mV at 100 mV s⁻¹ vs H₂SO₄ concentration [8,17].

In the passive region of low H₂SO₄ concentrations ($C_{\text{H}_2\text{SO}_4} < 0.5$ M), the amount of α -PbO₂ in the anodic layer increases, whereas that of β -PbO₂ decreases. Hence, the reaction of α -PbO₂ reduction to PbSO₄ is impeded.

Comparing the data for the two passive regions it is worth noticing that great amounts of α -PbO₂ form in both regions. In the active region mainly β -PbO₂ is formed. A comparison between Figs 3.11 and 3.12 suggests that the morphology of the PbO₂ crystals exerts an influence on its electrochemical activity. β -PbO₂ is electrochemically more active than the α -PbO₂ species. According to the data in Fig. 3.2, sulfuric acid solutions with concentrations within the active region contain predominantly H⁺ and HSO₄⁻ ions. So it is these ions that facilitate the formation of the β -PbO₂ crystal modification. Thus, through the crystal modifications of PbO₂ the sulfuric acid concentration affects the electrochemical activity of the positive plates of lead–acid batteries.

The decline in electrode capacity at higher acid concentrations may be a result of kinetic hindrances. At higher acid concentrations, the solubility of PbSO₄ decreases substantially. On cathodic polarization (discharge), the Pb²⁺ ions formed react immediately with the SO₄²⁻ ions, forming a passive PbSO₄ layer on the electrode surface. At low acid concentrations, too, some diffusion hindrances may occur, which would lead to decline in battery capacity. These kinetic hindrances, however, may also be associated with the phenomena involving α - and β -PbO₂.

With the introduction of VRLA batteries the volume of electrolyte in the cells was reduced. To compensate for the reduced amount of H₂SO₄ in the cells, its concentration was increased from 1.28 to 1.31, and even to 1.34 relative density. Consequently, the PbO₂ active material lost much of its electrochemical activity and hence the cell capacity on cycling declined. There is

a distinct H_2SO_4 concentration window of $\text{PbO}_2/\text{PbSO}_4$ electrode operation. Acid concentrations within this window should be selected in the battery design process so as to avoid capacity and cycle life decline.

3.9. Correlation Between Solubility of PbSO_4 Crystals and Electrolyte Concentration

The experimental data in Figs 3.9 and 3.10 raise the question as to why do batteries with electrolyte concentrations within the H-region, i.e., diluted H_2SO_4 solutions, have longer cycle life than batteries operating in the P- and N-regions of acid concentrations?

During discharge of lead–acid battery positive (PbO_2) and negative (Pb) plates PbSO_4 forms. This PbSO_4 should transform back into active materials (Pb and PbO_2) during charge. One of the elementary processes that takes place during battery charge is the process of dissolution of PbSO_4 particles (crystals). The solubility of PbSO_4 depends on H_2SO_4 concentration. This dependence has been disclosed by Vinal and Craig [11] and Danel and Plichon [18] and is presented in Fig. 3.13. The solubility of PbSO_4 crystals in H_2SO_4 solution of 1.28 relative density is 1.5 mg L^{-1} against 5.5 mg L^{-1} in acid solution of 1.10 relative density. It is within this acid concentration region that the lead–acid battery actually operates. With increase of H_2SO_4 concentration above 1.30 relative density, the solubility of PbSO_4 falls below 1.0 mg L^{-1} and the charge process will be impeded. In 0.5 M H_2SO_4 solutions, the solubility of PbSO_4 reaches a maximum of $6.0\text{--}6.5 \text{ mg L}^{-1}$, which decreases with further decrease of acid concentration.

On comparing Figs 3.11 and 3.13, it can be seen that PbSO_4 is most soluble within the active H_2SO_4 concentration region. There is a correlation between the maximum rate of PbO_2 formation and the maximum solubility of PbSO_4 . In the passive H_2SO_4 concentration region ($C_{\text{H}_2\text{SO}_4} > 1.28 \text{ rel. dens.}$), PbSO_4 is the least soluble. These facts give grounds to conclude that formation of the electrochemically active PbO_2 structure is affected by the concentration of Pb^{2+} ions in the solution, and this concentration depends on the solubility of PbSO_4 , which, in its turn, is determined by the H_2SO_4 concentration.

3.10. Influence of H_2SO_4 Electrolyte Concentration on Battery Performance

A summarized picture of the influence of H_2SO_4 electrolyte concentration on the performance of lead–acid batteries is presented diagrammatically in Fig. 3.14. There are no data available in the literature about the effect of $C_{\text{H}_2\text{SO}_4}$ on the processes in NAM.

H_2SO_4 electrolyte concentration exerts an influence on battery performance through four basic parameters:

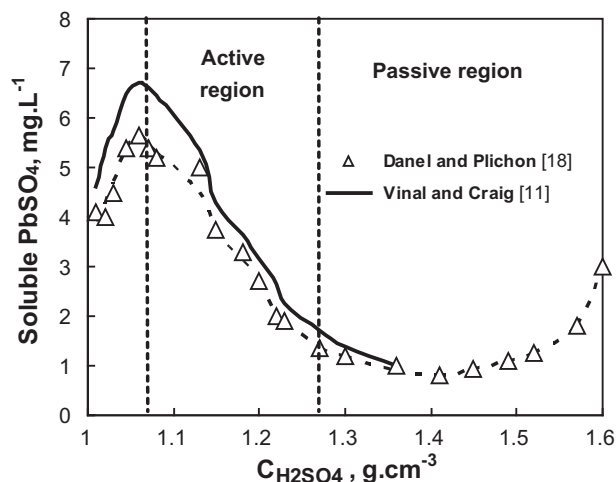


Figure 3.13:

Solubility of PbSO₄ crystals as a function of H₂SO₄ concentration.

- Open-circuit voltage (O.C.V.).* The O.C.V. of a battery is directly related to the electrolyte concentration. For the charge processes to proceed, the charge voltage should be at least 40–80 mV higher than the O.C.V. of a fully charged cell. If this requirement is not met, the cell will not charge fully and the charge acceptance of the cell, and hence its capacity, will be low, which may shorten its cycle life due to sulfation of the plates.
- Electrical resistivity.* At H₂SO₄ concentrations from 1.10 to 1.30 relative density, the electric conductivity of the electrolyte is high (i.e., low electrical resistivity), which guarantees high battery power output.

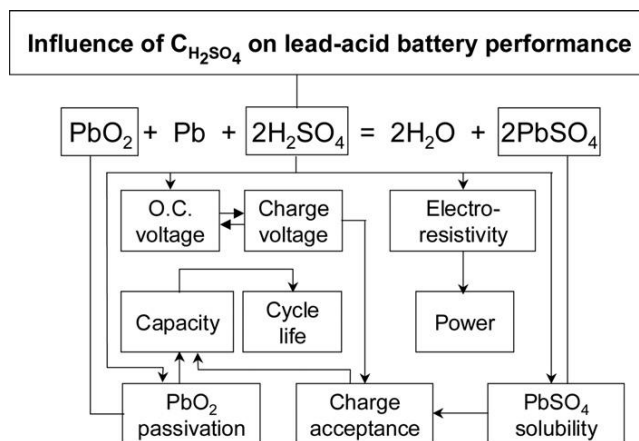


Figure 3.14:

Diagrammatic summary of the influence of C_{H₂SO₄} on lead–acid battery performance.

- c. *PbO₂ passivation.* At $C_{H_2SO_4} > 1.28$ relative density, the electrochemical activity of PbO₂ declines (PbO₂ is passivated), which results in decline of positive plate capacity and hence shortening of battery cycle life.
- d. *PbSO₄ solubility.* At high H₂SO₄ concentrations, ($C_{H_2SO_4} > 1.28$ relative density), the charge acceptance of the battery declines because of low PbSO₄ solubility, and the battery may not be fully charged, which will shorten its cycle life because of plate sulfation.

The ratio between the utilization coefficients of the three active materials in a lead–acid battery (Pb, PbO₂ and H₂SO₄) determines its performance characteristics. When the utilization of the H₂SO₄ electrolyte is higher than that of the Pb and PbO₂ active masses, the battery will have lower initial capacity, but the reversibility of the NAM and PAM structures on cycling will be higher and hence it will have longer cycle life. When PbO₂ or Pb is the capacity-limiting active materials, the initial capacity of the battery will be high, but its cycle life will be shorter.

The above-discussed phenomena and correlations should be taken into account in the battery design process, so as to allow the battery to exhibit its full potential.

3.11. Additives to Electrolyte

The lead–acid battery has a relatively low specific energy. One possible method to increase this parameter is by ‘increasing the utilization of the active materials’. For the purpose, additives to the three active materials are looked for to improve their utilization coefficient.

During battery discharge, the structures of the positive and negative active materials undergo partial disintegration and are then restored during charge. These processes should be reversible to guarantee long cycle life of the battery. This is not always the case, however. Irreversible processes, too, proceed slowly, which impair the structure of PAM and NAM. Attempts have been made to improve the reversibility of the crystallization processes on cycling by introducing various additives to the electrolyte.

Batteries for transport vehicle applications should have *high charge acceptance*. The latter is related to the reactions of PbSO₄ transformation to Pb at the negative plates and to PbO₂ at the positives. To maintain high rate of these reactions, the solubility of PbSO₄ should be sufficiently high. Additives are introduced into the H₂SO₄ solution or/and into NAM which increases the rate of PbSO₄ dissolution and facilitates the transfer of electrons at the negative plates during charge and thus improves their charge acceptance.

In order to minimise, or even eliminate, the need for maintenance, the battery should operate with *minimum water loss*. This is achieved when the *over-voltage of hydrogen and oxygen evolution* on Pb and PbO₂ surfaces, respectively, is very high. This is of utmost importance for VRLA and maintenance-free batteries. Hence, it is essential to reduce the rate of hydrogen evolution at the negative plates and to find appropriate methods to oxidize the evolved

hydrogen within the cell. Oxygen can readily recombine on the negative plates. The rate of hydrogen evolution on the lead surface can be slowed down by increasing the overvoltage of the hydrogen reaction. This can be achieved by introducing certain additives to the electrolyte or to NAM.

An oxygen cycle is operative in VRLA batteries. The O₂ evolved at the positive plates is reduced at the negatives. The rate of oxygen reduction depends greatly on the degree of sulfation of the lead surface. It is well known that, besides PbSO₄ crystals, SO₄²⁻ ions adsorbed on the lead surface can also form a PbSO₄ membrane (molecular films) on the Pb electrode surface. These films act as a barrier for the transfer of electrons to the oxygen molecules on the lead surface and thus retard the rate of its reduction. Some metal ions (Sn²⁺, Bi³⁺) added to the electrolyte are known to adsorb onto the lead surface and increase the oxygen conductivity of the lead sulfate layers, and thus eventually improve the efficiency of the closed oxygen cycle.

Additives should be chemically, thermally and electrochemically stable in H₂SO₄ solutions for prolonged periods of time, and also have low cost. Electrolyte additives can be classified into three groups: (a) inorganic compounds, (b) carbons and (c) polymer emulsions. A brief overview of the most widely used electrolyte additives and of their specific influence on battery performance will be made further in this chapter.

3.11.1. Inorganic Compounds

This group of additives includes phosphoric acid, boric acid, citric acid and some soluble metal sulfates.

(a) Phosphoric acid, H₃PO₄

Phosphoric acid has been used as additive to lead–acid batteries since 1920 and a number of patents have been issued claiming that H₃PO₄ improves the performance of batteries of different designs and applications [19]. Voss [20] and Meissner [21] have published comprehensive reviews of the effect of phosphoric acid and phosphate salts on the performance of lead–acid batteries. In general, addition of phosphoric acid to battery electrolyte has a diverse effect, e.g., it prolongs battery cycle life by reducing the shedding and irreversible sulfation of the positive active material but reduces the capacity of the battery. Many controversial effects of phosphoric acid have been reported in the literature. For this reason, much efforts have been put forth to elucidate the mechanism of action of phosphoric acid. Linear sweep voltammetry technique on smooth lead and lead alloy electrodes is mainly used to examine the influence of H₃PO₄ addition on the electrochemical kinetics of PbO₂/PbSO₄ reactions, as well as on oxygen evolution. It is established that, in the presence of phosphoric acid, the equilibrium potential of the positive electrode shifts to more positive values [22,23]. Phosphate ions reversibly absorb in the PbO₂ during charge and modify the nucleation and crystal growth of PbO₂. During discharge, H₃PO₄ is released. It has been found that phosphoric

acid is incorporated in the corrosion layer, too [24,25]. Experimental data evidence that H_3PO_4 has a beneficial effect on the performance of positive battery plates, when added in amounts of up to 0.8 wt%. Above this concentration, phosphoric acid has an adverse effect [25].

Generation of $\text{Pb}_3(\text{PO}_4)_2$ as an intermediate product of the process of PbO_2 formation at low H_3PO_4 concentrations has been established by Bullock [22,26]. Phosphoric acid increases the hydrogen and oxygen overpotentials [27–30]. Addition of H_3PO_4 to sulfuric acid electrolyte has been found to prevent the early capacity decline (premature capacity loss) of positive plates with Pb–Ca grids on deep discharge cycling [31–33]. It has been established that addition of H_3PO_4 to sulfuric acid electrolyte prevents passivation of positive plates with Sb-free grids on deep discharge cycling and facilitates formation of α - PbO_2 modification as well as of fine PbSO_4 crystals during discharge [34–35]. Most probably, the latter two effects are responsible for the decline in capacity of positive plates when phosphoric acid is added [36].

It has been found that H_3PO_4 prevents capacity decay of the positive electrode during cycling of gelled lead–acid batteries for electric vehicle applications [21]. Addition of phosphoric acid to VRLAB electrolyte yields stable capacity performance of these batteries in different solar power systems [37].

When phosphoric acid is added to the electrolyte in combination with H_3BO_3 , SnSO_4 and picric acid, corrosion of the positive grids is notably slowed down [38]. For standard automotive batteries, Torcheux et al. have patented an electrolyte additive formula containing 2.2% phosphoric acid and 4% colloidal silica [39]. The use of phosphoric acid in combination with colloidal silica prevents positive active mass softening, decreases acid stratification on cycling at high discharge rates and improves significantly the cycle life performance of lead–acid batteries [39].

(b) Other inorganic acids or salts

In an attempt to replace H_3PO_4 additive to sulfuric acid electrolyte, the effect of boric acid has been studied. It has been found that additions of H_3BO_3 in concentrations up to 0.4% inhibit the formation of hard PbSO_4 and decrease the self-discharge of the PbO_2 electrode [40]. Another alternative to phosphoric acid as electrolyte additive is citric acid. Its effect on the oxidation and reduction processes in the Pb/PbSO₄ and PbO₂/PbSO₄ potential regions has been studied through linear sweep voltammetry [41]. The presence of *citric acid has a beneficial effect on the charge/discharge processes*, but with the increase of its concentration, evolution of oxygen and hydrogen increases, too. The optimum effect of citric acid is achieved when added in amounts of about 2 g L^{−1} of electrolyte [41].

It has been found that addition of 0.1 g of SnSO_4 per 1 L of H_2SO_4 electrolyte improves substantially the re-chargeability of Planté batteries on deep discharge cycling [42]. When SnSO_4 is added to the electrolyte, Sn^{2+} ions are oxidized to Sn^{4+} ones, which are then incorporated into the PbO_2 phase, thus improving the latter's electro-conductivity [43].

Consequently, both the discharge capacity and the charge efficiency of the positive plates improve and the corrosion of the positive grids is reduced [43].

It has also been established that addition of 0.0225 M Al₂(SO)₄ to the sulfuric acid electrolyte increases significantly the rate of PbSO₄ reduction and thus prevents passivation of the negative plates of lead–acid batteries [44].

A commonly used electrolyte additive in AGM type of VRLA batteries is sodium sulfate (Na₂SO₄). This compound is introduced in batteries designed for deep discharge cycling and low temperature operation modes. Sodium sulfate acts as buffering agent and keeps up the conductivity of the electrolyte. As a result, the re-charge of batteries after deep discharge improves significantly. This electrolyte additive has proved especially appropriate for batteries in remote photovoltaic systems located on high mountain peaks. Unfortunately, sodium sulfate addition facilitates corrosion of the grids, especially of the negative plate lugs and of the connecting strap made of lead–tin alloy [45]. This adverse effect can be substantially mitigated by addition of Se to the grid alloy [45]. Moreover, addition of Na₂SO₄ accelerates the self-discharge processes in the battery, so this compound should be added only in combination with other additives which would suppress the self-discharge effect of sodium sulfate.

3.11.2. Carbon Suspensions

Kozawa et al. proposed the use of *ultra-fine carbon (UFC) and polyvinyl alcohol (PVA) composite colloid* as additive to electrolyte [46]. They demonstrated that UFC–PVA colloid converts inactive PbSO₄ accumulated in the negative electrode into an active one and improves its solubility. These effects are due to the influence of UFC colloid to reduce the size of PbSO₄ crystallites produced on discharge. The UFC–PVA colloid solution comprises carbon black particles 0.15 μm in size and PVA in a ratio of 10:4 by weight. Addition of 5 vol% of UFC–PVA colloid to the cell electrolyte has been recommended, i.e., the amount of colloid solid carbon is about 0.25 g per 100 mL of electrolyte. The UFC–PVA colloid reduces the self-discharge of negative plates and can act as an activator (de-passivator) of the sulfated lead electrode.

An aqueous solution of electrochemically *oxidized graphite* has been tested as an additive to the sulfuric acid electrolyte [47]. The carbon colloid addition improves the discharge capacity and extends the cycle life of the battery. This additive improves the electrical contact between PbO₂ particles in the positive plates and thus increases the discharge capacity and the charge acceptance of the lead–acid battery.

3.11.3. Polymer Emulsions

The effect of a wide variety of organic substances, *derivatives of benzaldehyde, benzoic acid and benzene, which act as inhibitors of hydrogen evolution*, has been studied. Dietz et al.

proposed *aldehydes and acetophenones* as appropriate electrolyte additives [48]. Application of these inhibitors in flooded lead–acid batteries reduces the water loss during cycling by 50%.

Recently, different *polymer materials* have attracted attention as possible additives to sulfuric acid electrolyte aimed to improve battery performance and to meet the ever-increasing demands for specific power and cycle life performance of lead–acid batteries.

An example of polymer additive to electrolyte is *FORAFAC 1033D (polyfluoroalkyl sulfonic acid)*. Addition of FORAFAC 1033D in a concentration of 0.1 wt% to the electrolyte immobilized in AGM VRLA batteries leads to a major improvement of battery cycle life [49]. Standby batteries containing FORAFAC have improved their service life by a factor of 1.5, suffering smaller water loss and reduced self-discharge.

The influence of *poly(N-vinylpyrrolidone) polymers (PVP)* as electrolyte additives on the performance of lead–acid batteries has been studied, but controversial results are reported by different research groups depending on the molecular weight and concentration of the polymer used. The application of PVP as additive to the positive or negative active materials is probably more effective than if added to the electrolyte.

The use of *polyaspartate (PASP)* as electrolyte additive has been found to control the crystallization process of lead sulfate by modifying the shape and size of the crystals [50]. Addition of PASP to electrolyte improves the utilization of the negative active material and reduces the internal resistance of the negative plates. A beneficial effect of PASP on the performance of lead–acid batteries is observed during high-rate partial state of charge (HRPSoC) operation, when the electrolyte contains 0.1% PASP. Addition of PASP prevents accumulation of ‘hard sulfate’ on the negative plates of batteries in the HRPSoC duty [50].

A great number of elementary processes of different nature occur during operation of the lead–acid battery, including transfer of electrons through phase interfaces, dissolution of PbSO_4 , diffusion of ions as well as crystallization and chemical processes of formation of PbSO_4 and PbO_2 . It would be hardly possible to find a single universal additive with beneficial effect on all these processes. It is necessary to search for appropriate composite additives to the sulfuric acid electrolyte, which would facilitate the capacity and life-limiting processes and thus improve the overall battery performance.

3.12. Contaminants (Impurities) in Electrolyte Solution

For adequate performance of VRLA and maintenance-free batteries it is of utmost importance to minimise the water loss during battery operation. Besides evaporation of water (more intense at higher temperatures), the major water loss is due to its electrolysis during charge, overcharge and self-discharge of the battery. Proper functioning of the lead–acid battery is possible thanks to the high over-potentials of oxygen evolution at the lead dioxide electrode and of hydrogen evolution at the lead electrode. However, during battery manufacture, some impurities are

introduced in the battery with the materials for its production. Decomposition of water on these contaminants may proceed at lower over-potentials as a result of which gas evolution in the cell is intensified, leading to increased water loss. Pierson et al. [51] studied the gas evolution in cells with H₂SO₄ electrolyte containing various contaminant ions (at 5000 ppm or saturation levels) on charging at 2.35 V for 4 h. Contaminants are deposited on the lead electrodes in the form of metals and/or are adsorbed on the lead dioxide electrodes. It is on their surface that electrolysis of water proceeds. Table 3.6 summarises the measured volumes of gas (in cm³) generated in cells with various contaminants [51].

Based on their effect on gassing in the cells, contaminants can be classified into three major groups:

- a. *accelerating substantially the electrolysis of water* (over 1000 cm³ of generated gas): anti-mony, cobalt, nickel, tellurium;
- b. *accelerating moderately the electrolysis of water* (from 500 to 1000 cm³ of generated gas): manganese, molybdenum, bismuth, vanadium;
- c. *exerting negligible effect on the electrolysis of water* (less than 500 cm³ of generated gas): all other contaminants from Table 3.6.

Obviously, special attention should be paid to the content of contaminants (impurities) from the first two categories in the source materials for battery manufacture (lead, lead alloys, H₂SO₄, expander, etc.). Impurities in these materials should be kept below definite maximum allowable limits so as to prevent them to influence the gassing rate in the cells. The maximum allowable concentrations of contaminants (impurities) in the sulfuric acid electrolyte according to the data reported in Ref. [51] are as follows:

- a. *below 1 ppm* for tellurium, antimony, arsenic, cobalt and nickel;
- b. *below 3 ppm* for manganese;
- c. *below 160 ppm* for iron;
- d. *below 500 ppm* for aluminium, bismuth, cerium, chromium, copper, molybdenum, silver and vanadium;
- e. *below 5000 ppm* for barium, cadmium, calcium, chlorine, lithium, mercury, phosphorus, tin and zinc.

The exact maximum allowable content of each contaminant should be determined for the electrolyte volume of each particular cell type based on the above classification of contaminants (impurities). It is important to know the content of impurities in the source materials used for battery manufacture and to calculate what part of these impurities will dissolve in the solution and deposit on the two types of plates. The lead used for leady oxide production should have very high degree of purity. The active materials (Pb and PbO₂) have large surfaces in contact with the electrolyte and about 25–40% of these surfaces will react with H₂SO₄ on battery cycling. The grids of the negative plates are not affected by corrosion, but those of the positive

Table 3.6: Total 4 h gas generation volumes at the 5000 ppm or saturation contaminant levels [51].

Contaminant	Gas generated (cm ³)	Contaminant	Gas generated (cm ³)
Aluminium	306.4	Iron	309.7
Antimony	2557.3	Lithium	258.4
Arsenic	626.2	Manganese	936.2
Barium	193.0	Mercury	194.2
Bismuth	916.0	Molybdenum	911.6
Cadmium	243.7	Nickel	1076.4
Calcium	172.5	Phosphorus	171.4
Cerium	286.4	Silver	285.8
Chlorine	266.4	Tellurium	1498.4
Chromium	571.8	Tin	179.2
Cobalt	5500.8	Vanadium	635.6
Copper	530.4	Zinc	218.4

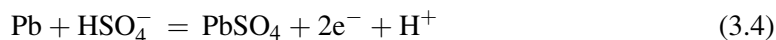
Note: The standard cells averaged a value of 230.5 cm³ of gas generated during the 4 h period.

plates undergo 20–25% corrosion. The additives and impurities in the gird alloys should be taken into account, too. Contaminants (impurities) introduced with the separators should also be known. Thus, adequate control of the contaminants (impurities) in the electrolyte is very important in order to guarantee insignificant gas evolution and hence minimum water loss of the cells, which will eventually ensure long service life of maintenance-free and VRLA batteries.

3.13. Influence of Electrolyte Stratification on Battery Performance

3.13.1. Processes Causing Electrolyte Stratification

The processes that take place at the two electrodes (plates) during charge and discharge are represented by the following overall equations:



When a flooded battery is discharged, sulfuric acid is consumed and water is produced in the positive plates. Sulfuric acid is consumed in the negative plates, too. Thus, electrolyte layers of low acid concentration are formed near the surfaces of both types of plates. These lighter layers rise to the electrolyte reservoir above the active block. The higher acid concentration in the reservoir forces a flow of heavier (more concentrated) H₂SO₄ electrolyte to move downwards between the plates. This movement of H₂SO₄ is illustrated in Fig. 3.15a [52]. During charge, sulfuric acid is produced in the two types of plates and the acid flow moves in the opposite direction (Fig. 3.15b). Thus, two layers of electrolyte are formed in the cell: a bottom layer of

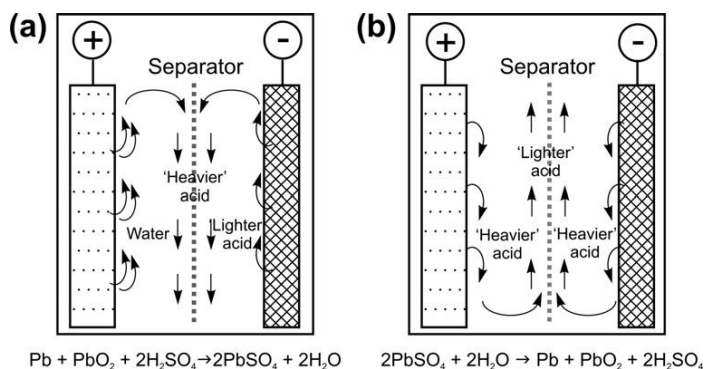


Figure 3.15:

Schematic representation of processes and electrolyte flow that contribute to acid stratification during (a) discharge and (b) charge [52].

higher H₂SO₄ concentration (with greater relative density) and an upper (top) layer of lower acid concentration (lower relative density). The development of a vertical concentration gradient of sulfuric acid was called ‘electrolyte stratification’ [53].

Figure 3.16 shows the changes in acid concentration in the top and bottom electrolyte layers on cell cycling, when there is no overcharge with gassing [54]. The data in the figure evidence that, after six cycles, the acid concentration in the bottom layer has reached 1.35 g cm⁻³, while in the upper layer it is only 1.22 g cm⁻³.

Sunu and Burrows [53] have investigated the development of the concentration gradient within the active block and its effect on cell capacity. Investigations were carried out on 400-Ah traction batteries which were charged with a current of 169 mA Ah⁻¹ up to 2.55 V per cell. The batteries were discharged at the same current rate to a cut-off-voltage of 1.7 V per cell (100% depth-of-discharge, DOD). The acid concentration was measured at the top, middle and bottom of the active block during the charge and discharge cycles. Figure 3.17 presents the changes in

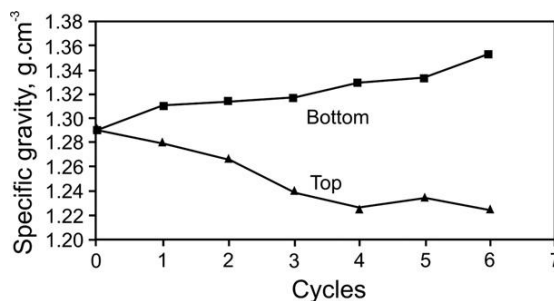


Figure 3.16:

Acid stratification in flooded batteries used in cycling application, when there is no overcharging with gassing and no electrolyte circulation [54].

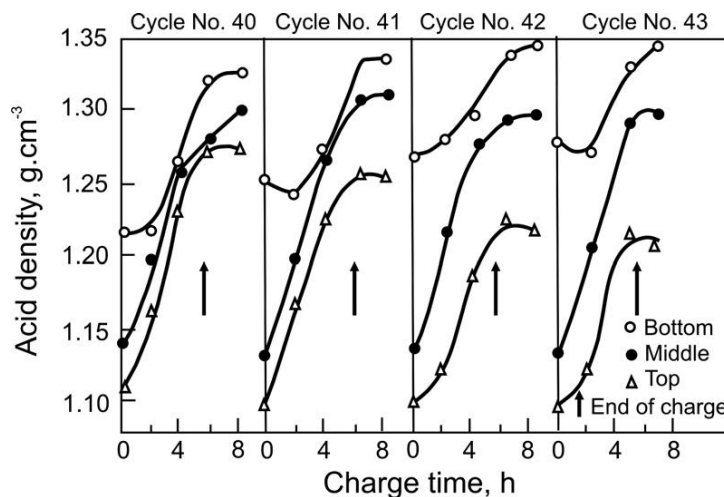


Figure 3.17:

Stratification of electrolyte measured during charging to 2% overcharge and after 100% DOD [53].

acid density during four consecutive cycles at 100% DOD and at charge/discharge coefficient $K_{ch/d} = 1.02$. The difference between the acid concentrations at the top and the bottom of the active block was used as a measure of the degree of electrolyte stratification, which reached a value of 0.15 specific gravity in the above studies.

As sulfuric acid is an active material, its stratification will affect cell capacity. Figure 3.18 shows this relationship. It can be seen that the capacity decreases by 1% per 0.01 sp gr. (rel.dens.) unit of stratification. This capacity loss also depends on the DOD and the charge/discharge coefficient.

How would electrolyte stratification affect the structure and composition of the active masses? The data in Figs 3.16 and 3.17 indicate that the electrolyte in the bottom part of the cells reaches a concentration of 1.35 g cm^{-3} . As evident from Fig. 3.11, the positive plates get progressively passivated at acid concentrations higher than 1.28 g cm^{-3} . Furthermore, Fig. 3.12 shows that lead sulfate is formed on lead dioxide electrodes immersed in H_2SO_4 solutions of concentrations within the passive region despite that polarization is conducted within the lead dioxide potential region [17]. At high H_2SO_4 concentrations, large amounts of HSO_4^- ions are absorbed in the gel zones of the lead dioxide particles which block the active centres where the electrochemical reactions of PbO_2 reduction proceed and thus the electrode capacity declines. HSO_4^- ions seem also to interrupt the polymer chains in the gel zones of the particles along which electrons and protons move in PAM. At these sites in the gel zones the discharge reaction proceeds yielding PbSO_4 instead of Pb(OH)_2 , which blocks the discharge process and eventually reduces the capacity of the positive plates.

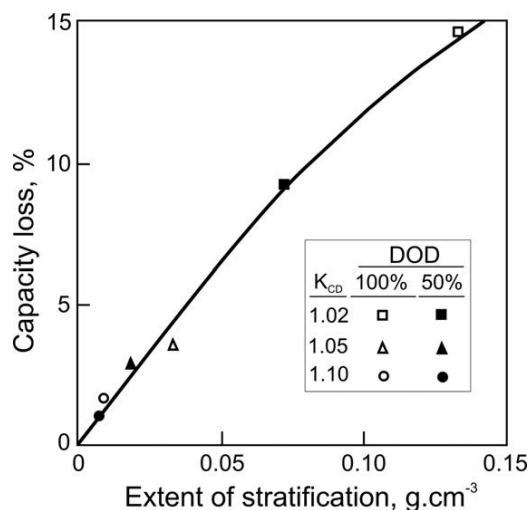


Figure 3.18: Capacity loss vs the extent of stratification for charge/discharge coefficients: 1.02, 1.05 and 1.10 [53].

Electrolyte stratification was studied by Sauer [55] and Mattera et al. [56]. These authors have established that electrolyte stratification appears during discharge and increases during charge. It decreases slightly at the beginning of discharge, but then increases again on further discharge. Experimental measurements have evidenced different local currents and potentials at different plate heights, which is an illustration of irregular electrochemical behaviour across the plates, leading to their progressive sulfation. Lead sulfate distribution in the positive plates follows a vertical gradient: the concentration of PbSO₄ is higher in the lower parts of the plates, where the acid concentration is the highest, and it decreases in the upper parts. The lower parts of the positive plates get more and more sulfated and these sulfated zones advance during cycling to the upper parts of the plates. Using isotope-labelled sulfur, a strong correlation has been found to exist between degradation of the positive active material because of sulfation and electrolyte stratification.

References

- [1] H. Bode, in: R.J. Brodd, K. Kordesch (Eds.), *Lead–acid batteries*, John Wiley, Electrochem. Soc., New York, USA, 1977, p. 42.
- [2] M. Barak, *Electrochemical power sources*, Peter Peregrinus Ltd., England, 1980, p. 159.
- [3] T.F. Young, *Rec. Chem. Prog* 12 (1951) 81.
- [4] L.A. Pavljuk, B.S. Smoljakov, P.A. Krjukov, *hr Izv. Sib. Otd. Akad., Nauk SSSR* 3 (1972) 3.
- [5] A.K. Covington, J.V. Dobson, W.F.K. Wynne-Jones, *Trans. Faraday Soc.* 61 (1965) 2050; 2057.
- [6] H.M. Dawson, *Proc. Leeds Soc.* 2 (1929–1934) 359.
- [7] A.J. de Bethune, T.S. Licht, N. Swendeman, *J. Electrochem. Soc.* 106 (1959) 616.
- [8] D. Pavlov, A. Kirchev, M. Stoycheva, B. Monahov, *J. Power Sources* 137 (2004) 288.

-
- [9] J.A. Duisman, W.F. Giauque, *J. Phys. Chem.* 72 (1968) 562.
- [10] W.S. Vosburgh, D.N. Craig, *J. Am. Chem. Soc.* 51 (1929) 2009.
- [11] G.W. Vinal, D.N. Craig, *J. Res. Nat. Bureau Stand.* 22 (1939) 55.
- [12] H.S. Harned, W.J. Hamer, *J. Am. Chem. Soc.* 33 (1991) 213.
- [13] K.R. Bullock, *J. Power Sources* 35 (1991) 197.
- [14] D. Pavlov, V. Naidenov, S. Ruevski, *J. Power Sources* 161 (2006) 658.
- [15] V. Naidenov, D. Pavlov, S. Ruevski, M. Cherneva, Three-layered absorptive glass mat separator for lead-acid batteries, *Bul. Pat.* 109755.
- [16] D. Pavlov, G. Petkova, T. Rogachev, *J. Power Sources* 175 (2008) 586.
- [17] B. Monahov, D. Pavlov, A. Kirchev, S. Vasilev, *J. Power Sources* 113 (2003) 281.
- [18] V. Danel, V. Plichon, *Electrochim. Acta* 27 (1982) 771.
- [19] R. Haase, P.F. Sauerma, K.H. Ducker, *Z. Phys. Chem.* 48 (1966) 206.
- [20] E. Voss, *J. Power Sources* 24 (1988) 171.
- [21] E. Meissner, *J. Power Sources* 67 (1997) 135.
- [22] K.R. Bullock, *J. Electrochem. Soc.* 126 (1979) 360.
- [23] S. Tudor, A. Weisstuch, S.H. Davang, *Electrochem. Technol.* 4 (1966) 406.
- [24] B.K. Mahato, *J. Electrochem. Soc.* 126 (1979) 365.
- [25] K.R. Bullock, D.H. McClelland, *J. Electrochem. Soc.* 124 (1977) 1478.
- [26] K.R. Bullock, *J. Electrochem. Soc.* 126 (1979) 1848.
- [27] S. Venugopalan, *J. Power Sources* 46 (1993) 1.
- [28] S. Venugopalan, *J. Power Sources* 48 (1994) 371.
- [29] S. Sternberg, V. Branzoi, L. Apateanu, *J. Power Sources* 30 (1990) 177.
- [30] O.Z. Rasina, I.A. Aguf, M.A. Dasoyan, *Z. Prokl. Khimii* 58 (1985) 1039.
- [31] S. Tudor, A. Weisstuch, S.H. Davang, *Electrochem. Technol.* 5 (1967) 21.
- [32] J. Burbank, *J. Electrochem. Soc.* 11 (1964) 112.
- [33] S. Tudor, A. Weisstuch, S.H. Davang, *Electrochem. Technol.* 3 (1965) 90.
- [34] J. Garche, H. Doering, K. Wiesener, *J. Power Sources* 33 (1991) 213.
- [35] H. Doering, K. Wiesener, J. Garche, W. Fischer, *J. Power Sources* 38 (1992) 261.
- [36] S. Sternberg, A. Mateescu, V. Branzoi, L. Apateanu, *Electrochim. Acta* 32 (1987) 349.
- [37] R. Wagner, de Dirk Uwe Sauer, *J. Power Sources* 95 (2001) 141.
- [38] A. Bhattacharya, I. Basumallick, *J. Power Sources* 113 (2003) 382.
- [39] L. Torcheux, P. Lailler, *J. Power Sources* 95 (2001) 248.
- [40] W.A. Badawy, S.S. El-Agamy, *J. Power Sources* 55 (1995) 11.
- [41] Guo-Lin Wei, es Jia-Rong Wang, *J. Power Sources* 52 (1994) 25.
- [42] E. Voss, U. Hullmeine, A. Winsel, *J. Power Sources* 30 (1990) 33.
- [43] G. Wei, J. Wang, *J. Power Sources* 52 (1994) 81.
- [44] Y. Guo, M. Wu, S. Hua, *J. Power Sources* 64 (1997) 65.
- [45] D. Pavlov, M. Dimitrov, G. Petkova, H. Giess, C. Gnehm, *J. Electrochem. Soc.* 142 (1995) 2919.
- [46] A. Kozawa, H. Oho, M. Sano, D. Brodd, R. Brodd, *J. Power Sources* 80 (1990) 12.
- [47] T. Kimura, A. Ishiguro, Y. Andou, K. Fujita, *J. Power Sources* 85 (2000) 149.
- [48] H. Dietz, G. Hoogestraat, S. Laibach, D. von Borstel, K. Wiesener, *J. Power Sources* 53 (1995) 359.
- [49] L. Torcheux, C. Rouvet, J.P. Vaurijoux, *J. Power Sources* 78 (1999) 145.
- [50] G. Petkova, P. Nikolov, D. Pavlov, *J. Power Sources* 158 (2006) 841.
- [51] J.R. Pierson, C.E. Weinlein, C.E. Wright, in: D.H. Collins (Ed.), *Power sources* 5, Academic Pres, London, UK, 1975, p. 97.
- [52] D.A.J. Rand, P.T. Moseley, in: J. Garche (Ed.), *Encyclopedia of electrochemical power sources*, vol. 4, Elsevier, 2009, p. 550.
- [53] W.G. Sunu, B.W. Burrows, in: J. Thompson (Ed.), *Power sources* 8, Academic Press, London, 1981, p. 601.
- [54] R. Wagner, *Encyclopedia of electrochemical power sources*, vol. 4, in: J. Garche (Ed.), Elsevier, 2009, p. 677.
- [55] D.U. Sauer, *J. Power Sources* 64 (1997) 181.
- [56] F. Mattera, D. Desmettre, J.L. Martin, Ph. Malbranche, *J. Power Sources* 113 (2003) 400.

Lead Alloys and Grids. Grid Design Principles

4.1. Battery Industry Requirements to Lead Alloys

Lead alloys are used for casting grids, straps, terminal posts and connectors for lead–acid batteries. The plate grids have two major functions:

- They are the ‘backbone’ that supports mechanically the active material of the two electrodes.
- They play the role of ‘blood system’ along which the current flows from and to every part of the plate.

In the above two roles plate grids do not take part in the electrochemical reactions that proceed in the cells.

Usually, the grid accounts for 40–50% of the total plate weight. Many attempts have been made to substitute the heavy lead alloy used for grid manufacture with a lighter material, but they all have failed because (i) the positive plates operate at very high potentials at which a few materials remain unoxidized; (ii) the electrolyte in the cells is highly corrosive, leading to the fast formation of a passive layer of high ohmic resistance; and (iii) the potential of water decomposition on these materials is low, thus making it impossible for the reactions in the lead–acid cell to proceed. In view of the above issues, battery manufacturers have formulated strict requirements to the physico-chemical properties of lead alloys to be used for plate grid manufacture. Some of these requirements will be discussed below.

- a. *Mechanical properties.* The grid must be of sufficient hardness and strength to support the mechanical and thermal strains incurred during the manufacturing process and throughout the subsequent service life of the battery; grid shape must be retained. The plate thickness increases during discharge and then decreases during re-charge, i.e., the plates ‘pulsate’ on battery cycling [1,2]. This leads to deformation of the plate grids. Moreover, the positive plates are subject to corrosion. The corrosion layer (CL) built of lead oxides has a 22–23% greater volume than that of unoxidized lead. Hence, it exerts mechanical stress on the metal and may deform the grid and impair its electrical contact with the active material.

To be able to endure the stresses caused by the above phenomena, the plate grids should have sufficient hardness, high yield strength (YS), high creep strength and low elongation. Table 4.1

Table 4.1: Required mechanical properties of lead–acid battery grids [3].

Grid Type	Brinell Hardness (kg mm^{-2})	Tensile Strength (kg mm^{-2})	Elongation (%)
EV batteries	12–15	4.5–6.5	4
SLI batteries	15–17	5–7	4

summarises some of the specific mechanical grid characteristics, based on experimentally obtained data [3].

- b. *Casting properties.* If grids are to be manufactured by casting, the alloys must have good castability so that the moulds can be adequately filled at relatively low temperatures and at the high production rate of the industrial casting machines.
- c. *Good weldability.* Since battery plates are assembled in positive and negative semi-blocks by welding the plate lugs to straps, the grid alloys must have good welding characteristics.
- d. *Corrosion resistance.* During battery operation, positive plate grids are subjected to high potentials at which they are thermodynamically unstable. Hence, the grids are continuously oxidized, i.e., suffer progressive corrosion. Lead dioxide is stable at these potentials. The formed CL reduces significantly the grid corrosion rate, but cannot stop the process altogether. Thus, positive plate grids are a crucial element of the lead–acid cell design which determines the durability and performance characteristics of the battery.
- e. *High electrical conductivity of the CL formed on positive grids.* The process of corrosion of the lead grid proceeds first through formation of PbO . The latter has very high specific resistance ($\sim 10^{12} \Omega \text{ cm}$). The formed lead oxide is further oxidized to a non-stoichiometric oxide, PbO_n ($1 < n < 2$). When the stoichiometric coefficient n reaches a value of 1.5, $R \approx 5 \times 10^2 \Omega \text{ cm}$ [4]. Oxidation of the CL proceeds further to the formation of PbO_2 (10^{-5} to $1.2 \times 10^{-6} \Omega \text{ cm}$ [4]). Additives to the grid lead alloys affect the oxidation rate of the oxides in the CL. Hence, alloying additives should be selected so as to retard oxidation of the lead grid (i.e., the grid corrosion process) and accelerate (facilitate) the processes of oxidation of PbO to PbO_2 .
- f. *Electrical properties.* Lead alloys used for plate grid manufacture must have high electrical conductivity so as to reduce ohmic energy loss.
- g. *Environmental and health aspects.* Alloys and grids must be produced by clean technologies with no detrimental effects on workers' health or on the environment.
- h. *Economic considerations.* Low content of inexpensive alloying additives as well as highly efficient technologies must be used in standard alloy manufacture so as to ensure production of low-cost grids.

Figure 4.1 presents schematically the basic properties of lead alloys which are essential for their applicability for casting battery grids. These alloy characteristics and their influence on battery performance parameters will be discussed in more detail in this chapter.

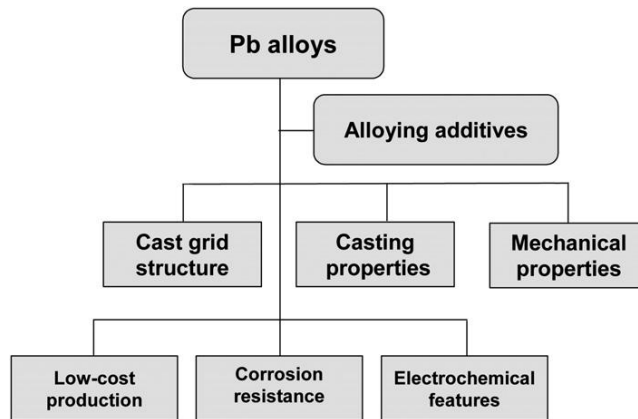


Figure 4.1:

Key properties of lead alloys to be used for casting battery grids.

Lead–acid batteries are mono-metallic. All active materials, plate grids, straps and connectors are made mostly of lead. Hence, recycling of lead from batteries is an easy process. Many countries have national lead pools (comprising production of primary lead and recycling of secondary lead). Schematics of the operation of a national lead pool is presented in Fig. 4.2.

Over 95% of failed lead–acid batteries are recycled in these pools, yielding secondary lead which is re-used for the manufacture of new lead–acid batteries. The secondary lead is purified to a degree, allowing its utilization in the production of leady oxide and lead alloys. A certain amount of primary lead extracted from lead ores is also added to the lead pool and used in the manufacture of leady oxide. Thanks to the high percentage of recycled secondary lead and the simple technology of manufacture, the lead–acid battery is the cheapest chemical power source available.

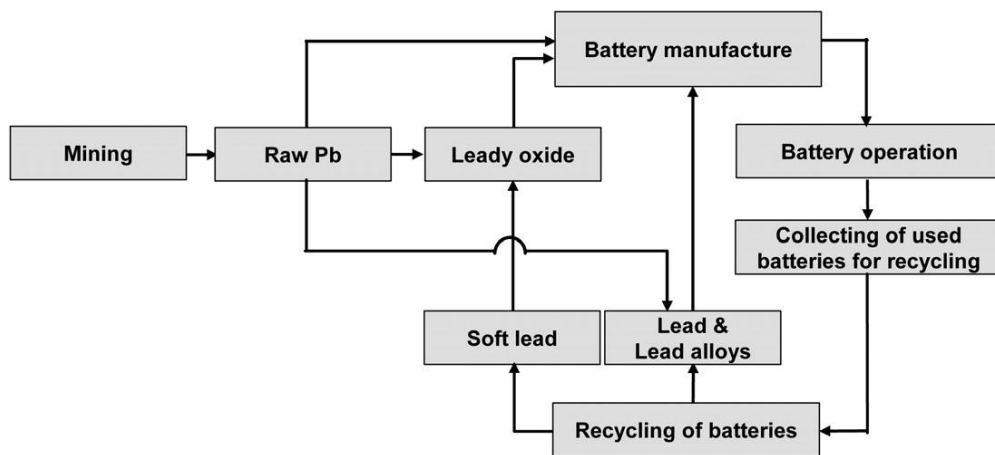


Figure 4.2:

Schematics of a national lead pool operation.

Table 4.2: Alloys used for lead–acid battery grids [5].

Alloying Additives	Application
Antimony alloys 4–11 wt% Sb, As, Sn, Cu (Ag)	Flat plates, tubular plates for traction batteries, older types of stationary batteries
Low-antimony alloys 0.5–3.0 wt% Sb, Se, Cu, S, As, Sn (Ag)	Flat plates, tubular plates for low-maintenance or maintenance-free batteries: SLI, traction, stationary
Lead–calcium alloys 0.05–0.07 wt% Ca, 0–3% Sn (Al), Ag, Bi	VRLA batteries
Pure lead Sn	Planté plates, Bell Syst. Batt. punched grids (Gates)
Antimony–cadmium alloy 1.5 wt% Sb, 1.5 wt% Cd	GNB ‘Absolyte battery’

Table 4.2 presents a summary of the lead alloys most widely used for the production of various types of lead–acid batteries [5]. Lead–antimony and lead–calcium grid alloys have dominating positions in the battery industry. The basic characteristics of these two types of alloys and their effects on battery performance will be discussed further in this chapter.

But before that, let us see what are the battery industry’s requirements for the purity of lead used in the manufacture of battery components.

4.2. Purity Specifications for Lead Used in the Battery Industry

In the battery industry, lead is used for the manufacture of:

- leady oxide* — the basic material used for the preparation of positive and negative pastes, resp. active materials;
- lead alloys* — for the positive and negative plate grids;
- battery straps* — which connect all positive or all negative plates in plate groups (semi-blocks), as well as for cell *terminal posts* and inter-cell *connectors*.

Lead of different purity is used for the manufacture of each of the above battery components. The lead used for the production of leady oxide and for the positive plate grids should be of the highest purity grade. During battery operation, the positive grids are attacked by corrosion (25–35%) and the additives and impurities contained in the grid alloy get into the CL, then become part of the composition of the formed active masses and thus affect the electrochemical processes. The negative grids are not subject to corrosion, but the alloy components and impurities on the grid surface get in contact with the electrolyte and may become active centres for the electrochemical reaction of hydrogen evolution and thus increase the water loss in the battery. To avoid this, the negative grid alloy should contain no impurities which facilitate gassing. Corrosion of the straps and connectors is a slower process. Hence, the additives and impurities in the lead alloys used for the manufacture of straps and connectors have the weakest effect.

Table 4.3: Impurity standards for primary and secondary lead (wt%) [10].

Element	Primary	Purified Secondary	Element	Primary	Purified Secondary
Al	<0.0001	<0.0001	Mn	<0.00005	<0.00005
Sb	0.0005	0.0003	Ni	0.0001	0.0001
As	<0.0001	0.0001	Se	<0.00005	<0.00005
Bi	0.006	0.018	Ag	0.0005	0.0017
Co	<0.00005	<0.00005	Sn	0.0001	0.0001
Cr	<0.00005	<0.00005	Te	<0.00005	<0.00005
Cu	0.0004	0.0003	S	<0.0001	<0.0001
Fe	<0.0001	<0.0001	Zn	0.0006	0.0001

As a rule, national battery standards stipulate only Pb purity grade of 99.99% without specifying the type and amount of allowable impurities. The specific influence of additives to and impurities in lead alloys has been in the focus of attention of many researchers [6–12]. Table 4.3 summarises the maximum allowable impurity levels for both primary and secondary lead for battery use [10]. Secondary lead comes from recycling batteries after purification. Lead of the purity grade presented in Table 4.3 can be used for the manufacture of leady oxide and lead alloys for both positive and negative grids.

The strongest effect on lowering the overpotential of hydrogen evolution and facilitating gassing on the negative plates has Se, Ni, Te and Mn impurities. Sb, Cu, As, Fe, Cd and others have a less pronounced accelerating effect on the hydrogen evolution reaction, and Bi, Ag and Zn, on the contrary, have a beneficial influence, i.e., they retard the evolution of hydrogen. Bismuth reduces the rate of the oxygen evolution reaction as well, whereas Ni, Se and Te accelerate this reaction. Hence, appropriate control of the content of the above impurities in the grid alloys is of utmost importance for battery performance.

4.3. Lead–Antimony Alloys

4.3.1. Some History

At the time of invention of the lead–acid battery, the compositions of the lead alloys for the manufacture of battery grids were developed empirically, through casting trials to test their castability, through mechanical tests to see whether the cast grids were hard enough to endure all technological procedures involved in the battery-manufacturing process and finally through evaluation of battery performance. Way back in 1880, it was established that lead–antimony alloys met all the above requirements and they occupied dominating positions in the battery industry for more than a century. Initially, battery grids were cast from Pb alloys with 10–12% Sb content, i.e., within the eutectic region. The high antimony content makes the alloy easy to cast at high casting rates, yielding hard castings and sustaining the reversibility of the structure of PAM on cycling, thus eventually improving battery cycle life. Besides, batteries with Pb–(10–12%)Sb

grids exhibit high charge efficiency and relatively stable discharge voltage. However, high corrosion rate of the positive plate grids is observed. Antimony ions get into the solution and are reduced to Sb on the negative plates. The overpotential of hydrogen evolution on antimony is much lower than that on lead, which facilitates gassing in the battery and thus increases water loss during battery charge and self-discharge. Hence, battery users have the responsibility to top up their batteries with water, i.e., maintain their batteries.

In the context of the ever-increasing role of automobiles as personal transport means, the battery industry was forced to develop low-maintenance and even maintenance-free batteries. The demand for such batteries was also supported by the users of stationary batteries. In an attempt to meet the above requirements, battery manufacturers reduced the content of antimony in the grid alloys to 4.5–6%. Quite expectedly, this posed serious casting problems. The mechanical properties of the cast grids deteriorated. In order to improve the flowability of lead–antimony alloys, 0.15–0.2% of tin was also added. To improve the hardness and accelerate the ageing process of the cast grids, As was introduced at a loading level of 0.15–0.2%. The grids' corrosion resistance was improved by the addition of 0.02–0.03% Ag.

The use of grids cast from the above multi-component alloys did reduce the need for battery maintenance but did not eliminate it altogether. So the battery industry chose two basic approaches to achieve the goal set by the automobile industry, i.e., to devise maintenance-free batteries.

- a. *Development of new lead alloy compositions.* Lead–calcium and lead–tin–calcium alloys were set to tests; some battery manufacturers even assembled batteries with pure Pb grids.
- b. *Development of lead alloys with low-antimony content (<2.5 wt%).* These alloys contained also additives improving their casting and mechanical properties. Batteries with low-antimony plate grids suffered negligible water loss and exhibited stable performance parameters. However, when these low-antimony alloys were used for casting battery grids they proved to be susceptible to hot cracking. The hot cracking problem was resolved by adding nucleants (grain refiners) to the alloy composition and thus exerting control over the crystallization processes during grid casting.

Depending on their properties the lead–antimony alloys adopted in the battery industry can be generally classified into four basic groups:

- a. *High-antimony alloys* with 9.0–12 wt% Sb content. These alloys comprise 85–100% eutectic phase. They have a narrow freezing range. They are used for pressure casting of long spine grids for tubular positive plates as well as for long grids for traction and stationary batteries.
- b. *Medium-antimony alloys* with 4.0–7.0 wt% Sb content. These alloys contain from 40% to 60% eutectic and have a much wider freezing range. They are used for positive grids for traction batteries.

- c. *Lead–antimony alloys for casting straps, posts and connectors* (2.9–4.0 wt% Sb). The eutectic phase in these alloys is from 25% to 40%. They contain large slushy regions, making them suitable for joining lead parts with different antimony contents and different melting points. As a rule, nucleants are added to these alloys.
- d. *Low-antimony alloys* with 1.0–2.7 wt% Sb content and various additives introduced to improve their mechanical (As, Sn), casting (Sn, Se, S, Cu), anti-corrosion (Ag) and electro-chemical (Sn, Bi) properties. These alloys contain but small amounts of eutectic (1–15%). They have a wide freezing range and are appropriate for continuous casting of grids or of metal strips which are then expanded and punched into grids.

4.3.2. Equilibrium Phase Diagram and Microstructure of the Lead–Antimony Alloy System

In the liquid state (melt) antimony is fully soluble in lead. On cooling the melt, formation of an α -Pb solid–solution starts whose composition depends on temperature and Sb content in the melt. Figure 4.3 presents the equilibrium phase diagram of the Pb–Sb system [13]. It reflects the thermodynamic state of the system when the phases are in equilibrium.

The diagram indicates the formation of a eutectic of Pb with 11.1 wt% Sb. As the battery industry uses pre-eutectic alloys (0–11 wt% Sb), only these alloys will be discussed in this chapter. The eutectic temperature is 252 °C. On cooling of the Pb–Sb melt, α -Pb grains form first as a result of which the melt is enriched with antimony. When the eutectic temperature of 252 °C is reached, the antimony content in the α -Pb crystals reaches $L_e = 3.45\%$. Formation of eutectic with 11.1% Sb starts. On further cooling, the solubility of Sb in α -Pb crystals declines

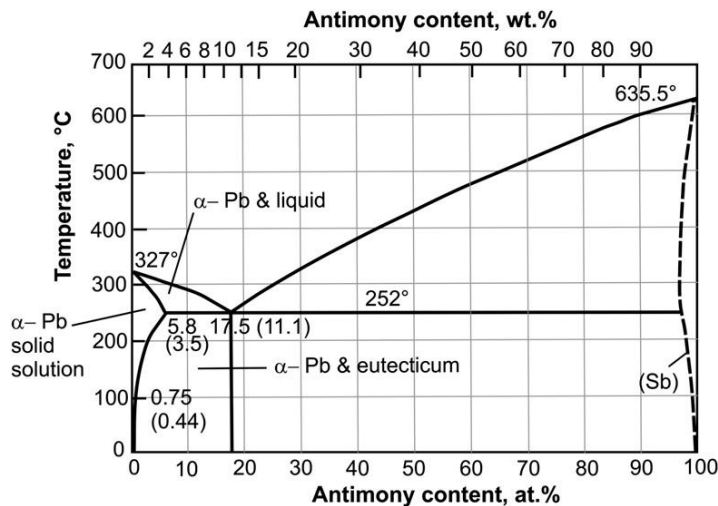


Figure 4.3: Equilibrium phase diagram of the Pb–Sb alloy system [13]. Values in parentheses are weight percent.

and coarse secondary β -Sb grains with dissolved Pb in them are formed [14]. When a temperature of 25 °C is reached, the solubility of Sb in α -Pb particles drops to 0.03% Sb, i.e., a 10 times lower value than that at the eutectic temperature. The thick line AB (Fig. 4.4) represents the equilibrium solubility of Sb in α -Pb as a function of temperature. At extremely slow cooling, the AB line represents the equilibrium composition of α -Pb particles. Maximum amount of coarse β -Sb grains is formed at 25 °C. These grains increase the hardness of the casting and it, too, reaches a maximum at 25 °C. This phenomenon of hardness change as a result of solid-phase processes is known as ‘age-hardening’ [15].

On fast cooling (e.g., quenching), α -Pb particles will be in non-equilibrium state, i.e., a supersaturated solution will form (Fig. 4.4). As diffusion of Sb atoms in α -Pb solid—solution is slow, the change in concentration of Sb atoms towards an equilibrium value will be a slow process, too. These processes result in the formation of sub-microscopic β -Sb particles which cause age hardening. However, the processes of β -Sb particle growth continue and the hardness of the casting increases reaching a maximum. The obtained β -Sb particles, too, are in non-equilibrium state and they tend to reach equilibrium, which reduces slightly the hardness of the casting, i.e., over-ageing occurs.

The above processes depend on the conditions of casting and on the subsequent temperature treatment. The extent and the rate of the solid-state processes depend on (a) the energy available to drive the processes, which depends on the over-saturation level, and (b) the energy available for solute atom diffusion, which depends on melt temperature [16]. These structural processes modify the mechanical properties, especially the hardness, of the alloy. The processes of age-hardening will be discussed in more detail later in this chapter.

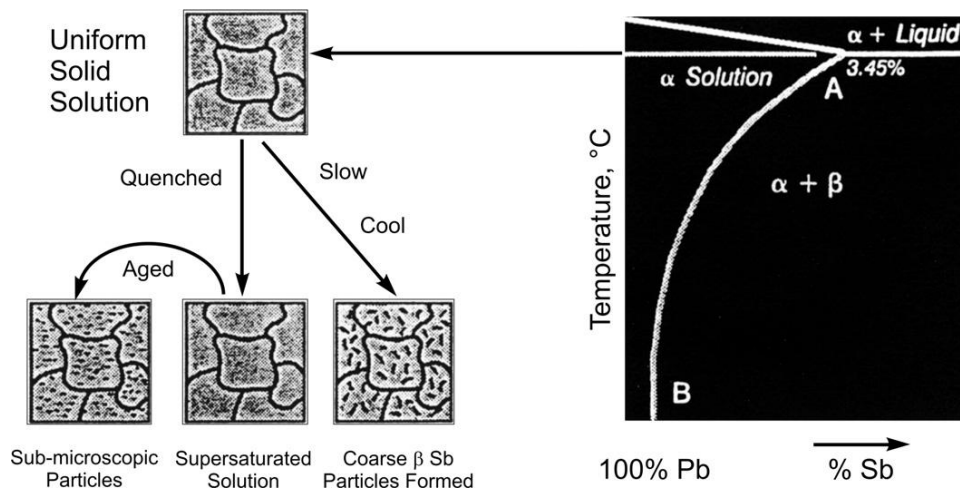


Figure 4.4:
Solubility of antimony in lead [15].

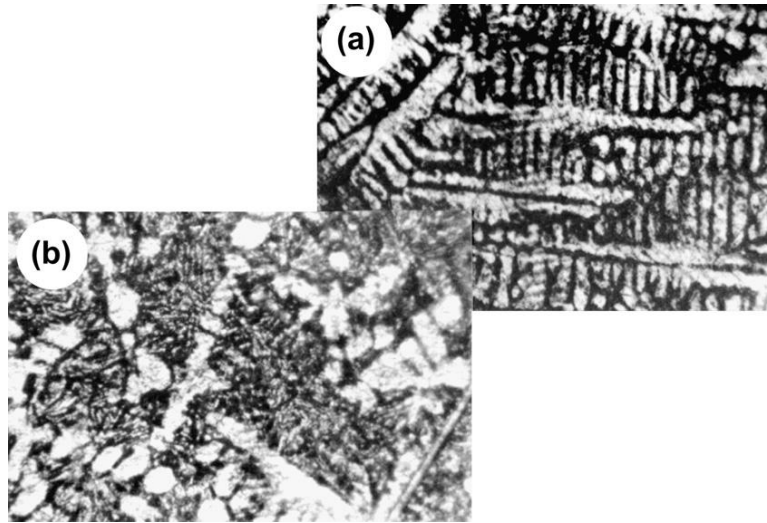


Figure 4.5:
Microstructure of (a) Pb—3.5 wt% Sb; and (b) Pb—11.7 wt% Sb alloys [17]. White dendrites are α -Pb particles.

Figure 4.5 shows pictures of the microstructure of (a) Pb—3.5 wt% Sb and (b) Pb—11.7 wt% Sb alloys [17].

The white dendrites are α -Pb particles. As evident from Fig. 4.5a for the Pb—3.5 wt% Sb alloy, the α -Pb dendrites are several hundreds of micrometres in size and are oriented along the cooling direction. These particles are surrounded by eutectic phase (dark grains). The crystallographic structure of the Pb—11.7 wt% Sb alloy (Fig. 4.5b) comprises mostly eutectic particles with only single α -Pb grains formed on cooling. These two phases (α -Pb and eutectic) have different mechanical properties and therefore the mechanical properties of the alloy will depend on its composition.

4.3.3. Properties of Pb—Sb Alloys with Different Antimony Contents

Castability and melting temperature of Pb—Sb alloys

Figure 4.6a shows the changes in melting temperature of Pb—Sb alloys as a function of Sb content within the pre-eutectic region. The melting point decreases by 7.1 °C with an increase of the antimony content in the alloy by 1.0 wt%. This is a fairly high sensitivity of alloy melting temperature to antimony content.

The relationship between alloy castability and antimony content is presented in Fig. 4.6b. It can be seen from the figure that the castability decreases markedly with decrease of antimony content from 13% to 8 wt%. Below 8 wt% Sb, the castability changes but slightly and the

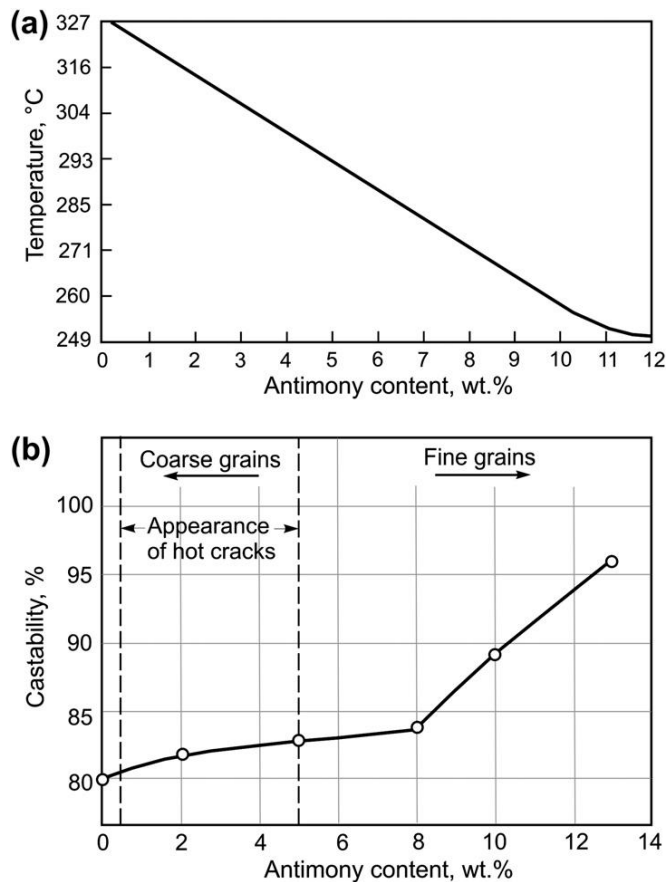


Figure 4.6:

(a) Dependence of melting point on antimony content for Pb–(0 ÷ 12) wt% Sb alloys (Grid Metal Manual IBMA 1975, p. 5). (b) Castability of Pb–Sb alloys [3].

casting process can be controlled by regulating the melt and mould temperatures [3]. At Sb content below 5 wt%, a tendency to form hot cracks is observed and the brittleness of the cast grids increases. The alloy solidifies into a coarse dendritic grain structure with cracks along the grain boundaries. Poor grid quality because of these cracks was one of the main reasons why low-antimony alloys were not used on a large scale in the battery industry in the past.

Hardness of Pb–Sb alloys

Antimony alloyed with lead improves the hardness of the alloy. The eutectic phase comprises alternating platelets of antimony and lead which increase the hardness of the alloy. Antimony platelets are much harder than lead ones. Hence, the overall alloy hardness depends on the content of antimony.

Figure 4.7 shows the hardness of natural air-cooled and thermal-treated Pb—Sb alloys as a function of antimony content [3]. Alloy hardness increases with increase of the eutectic/Pb solid—solution ratio. Low-antimony grids have been subjected to different thermal treatments in an effort to improve their hardness.

In the battery-manufacturing process, after pasting, the plates are subjected to flash drying and curing procedures. The temperature in the drying and curing chambers is fairly high and the duration of the curing process is long. During these procedures the plate grids may soften and cause technological problems. To avoid this, the grids should be sufficiently hard to endure the above technological treatments. Because of certain electrochemical considerations, the battery industry uses low-antimony alloys. These alloys, however, have low hardness. Thermal treatment methods have been developed to improve the hardness of low-antimony lead alloys.

Figure 4.8 presents the age-hardening curves for alloys with decreasing antimony content and small additions of Sn, As, Se, Cu and S [15]. The castings have been subjected to different modes of cooling (air cooling or quenching). The data in the figure indicate the following:

- With decrease of Sb content in the alloy from 3 to 0.8 wt% the Brinell hardness declines from 32 for the Pb—3 wt% Sb alloy to 13 for the Pb—0.8 wt% Sb alloy.
- Quenched, flash-dried samples have considerably higher Brinell hardness than the air-cooled ones. Figure 4.8b evidences that even air-cooled alloy samples with 1.5–1.7 wt% Sb content meet the hardness requirements (Table 4.1), if they contain additions of As, Sn, Se, Cu and S as well.

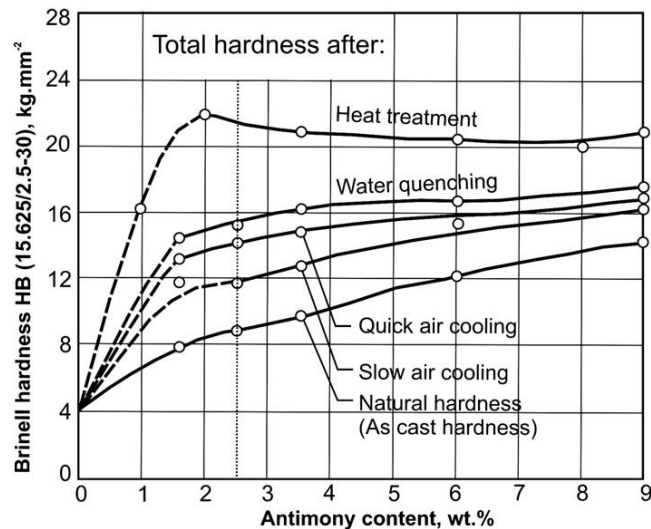
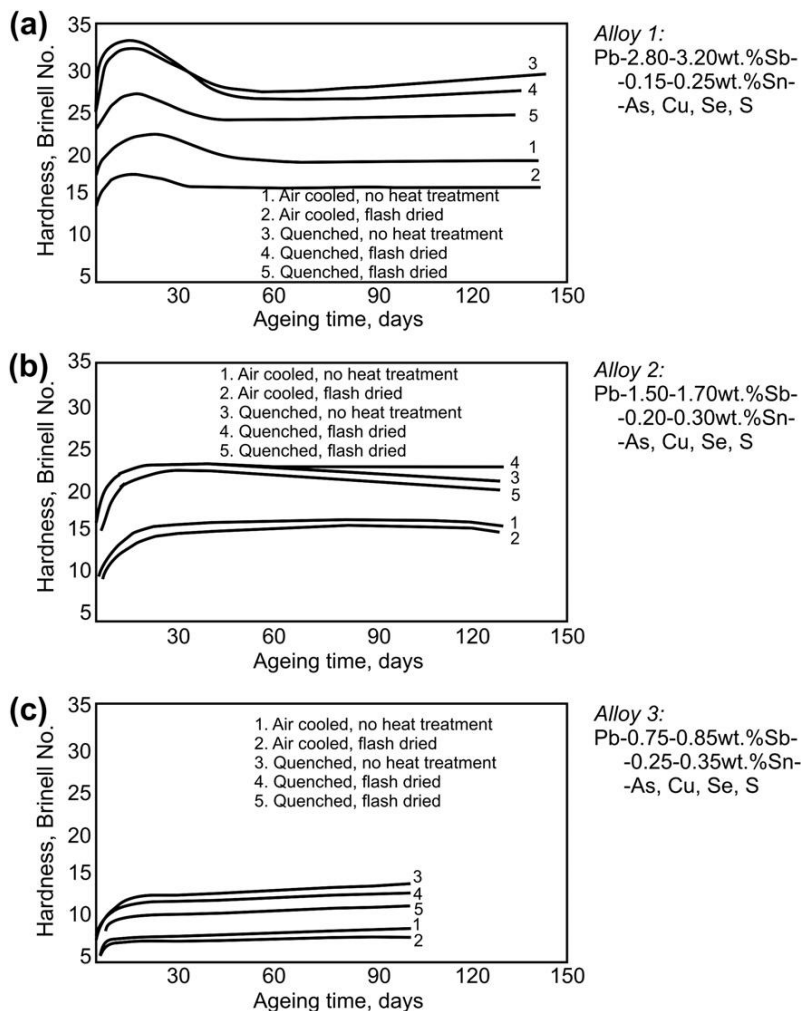


Figure 4.7:

Total hardness (natural hardness + age hardening) of Pb—Sb alloys. Cast temperature 500 °C, mould temperature 150–175 °C [3].

**Figure 4.8:**

Effect of cooling rate and subsequent heat treatment on the age-hardening behaviour of three types of Pb–Sb alloys with additions of different amounts of Sn, As, Se, Cu and S: (a) alloy 1; (b) alloy 2; (c) alloy 3 [15].

- c. The kinetic age-hardening curves for the Pb–3.0 wt% Sb alloy feature a maximum after 15 days of ageing, whereas the samples with 1.5 or 0.8 wt% Sb yield no such maximum, but the curves of these alloys reach saturation within 15 days.

The above results indicate clearly that, through the introduction of small amounts of alloying additives (Sn, As, Se, Cu and S) and a simple thermal treatment, grids cast from Pb–1.5 wt% Sb alloy may acquire a hardness level that meets fully the requirements of the battery industry.

Yield strength, ultimate tensile strength and elongation of Pb—Sb alloys

Figure 4.9 presents the dependences of YS, ultimate tensile strength (UTS) and elongation (EL) of cast and rolled lead—antimony alloys on the Sb content. Data from Ref. [18] are used to plot the curves in the figure. Two concentration zones can be distinguished in the influence of Sb on the mechanical properties of lead—antimony alloys: (a) low-antimony zone (up to about 3.0 wt% Sb in the alloy) in which the YS and UTS increase very rapidly, while the elongation decreases abruptly, and (b) high-antimony zone (3–11 wt% Sb content) where the curves of the above mechanical properties reach saturation, i.e., improve but very slightly with the increase of Sb content in the alloy.

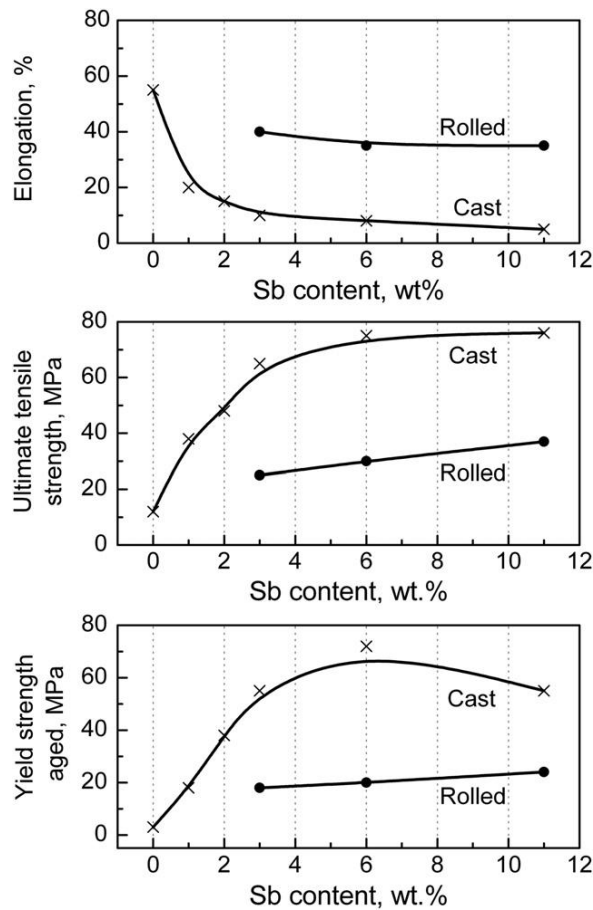


Figure 4.9:

Effect of antimony content on yield elongation, ultimate tensile strength and yield strength of Pb—Sb alloys. Data from ref. [18] are used.

A juxtaposition of the data in Fig. 4.9 with the equilibrium phase diagram of the Pb–Sb system presented in Fig. 4.3 indicates that, at 252 °C and up to 3.5 wt% loading level in the alloy, antimony has the highest solubility in α -Pb dendrites. On cooling, the dendrites get over-saturated with Sb and reorganisation of the structure of the solid phases starts, whereby the content of Sb in the α -Pb dendrites diminishes to 0.1% at room temperature. This improves the mechanical properties of the alloys. At Sb content between 3.0 and 11 wt%, the amount of the eutectic phase in the alloys changes but slightly, which results in minor improvement of their mechanical properties.

Figure 4.9 also evidences that in the high-antimony zone the mechanical properties of cast samples are several times higher than those of rolled samples. This is due to changes in the alloy microstructure on rolling [19]. Figure 4.10 shows the grain structures of cast and rolled Pb–6.0 wt% Sb alloy samples [18]. Rolling was conducted at a thickness reduction ratio of 10:1.

The microstructure of the cast sample (Fig. 4.10a) features well-pronounced α -Pb particles surrounded by eutectic phase. The latter is responsible for the high mechanical properties of the alloy. Figure 4.10b shows the microstructure of the same Pb–6.0 wt% Sb alloy but after rolling. The eutectic particles (platelets) are broken-apart and displaced in the rolling direction. As evident from Fig. 4.9, despite the relatively high Sb content (6.0 wt%) in the alloy, the disintegration of its eutectic structure impairs dramatically the mechanical properties of the alloy. Thus, the ability of the Pb–Sb grid to resist to deformation by stresses induced by the charge–discharge reactions of the active material during cycling depends not only on the antimony content, but also on the eutectic microstructure of the alloy.

Creep resistance of Pb–Sb alloys

Figure 4.11 presents the relationship between creep resistance as measured by the time of rupture of the samples at 27.6 MPa stress level. Data from Ref. [18] are used to plot the curves in the figure. This property of Pb–Sb alloys, too, depends very much on the Sb content. The creep resistance increases by almost two orders of magnitude with the increase of the Sb content from 1.0 to 11 wt%. Here again the microstructure exerts a very strong influence. Rolled Pb–11 wt% Sb samples rupture after 4.5 h of stress, whereas cast samples endure 12 h of stress before failure. Therefore, it is very important to study carefully the possible influence of any mechanical treatment of cast Pb–Sb grids on their mechanical properties, especially on the creep resistance, before adopting this treatment as part of the technological process of grid manufacture.

Corrosion resistance of Pb–Sb alloy

Figure 4.12 shows the correlation between the stationary value of the general corrosion rate at a current density of 6.3 mA cm^{-2} and the antimony content in the alloy [17]. The overall corrosion rate increases with the increase of the ratio eutectic/Pb solid–solution crystals.

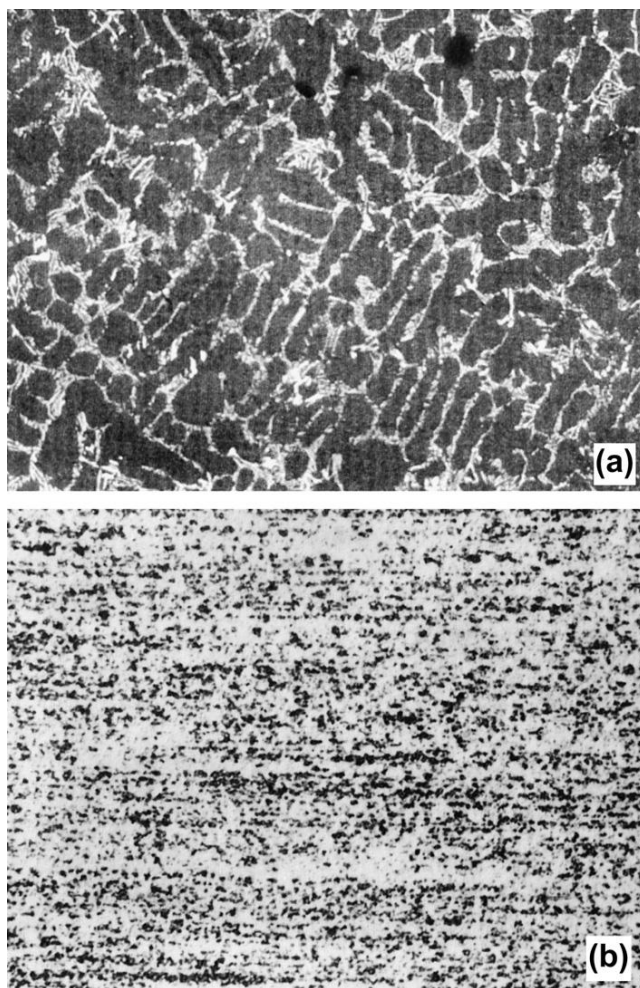
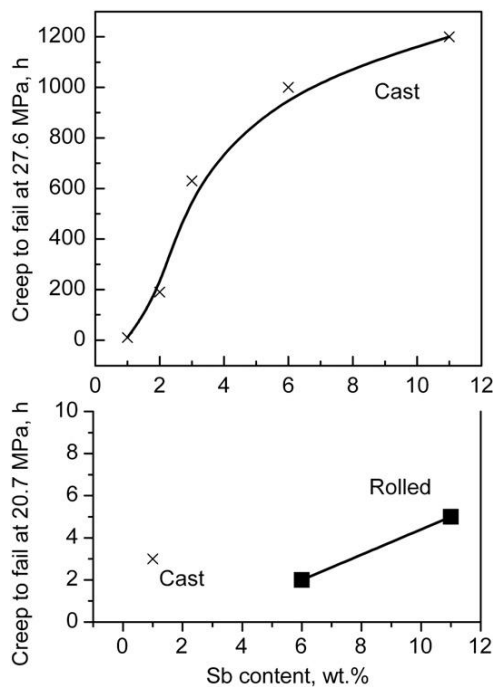


Figure 4.10:

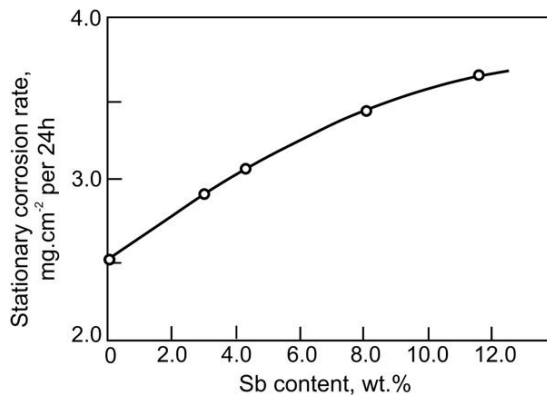
Grain structure of Pb—6.0 wt% Sb alloy: (a) cast, magnification 160 \times ; (b) rolled, magnification 120 \times [18].

During galvanostatic polarization under the above conditions, the basic reaction on the electrode is oxygen evolution. A $\text{Pb}(\text{Sb})|\text{PbO}_2(\text{Sb}^{5+})|\text{H}_2\text{SO}_4|(\text{O}_2/\text{H}_2\text{O})$ electrode system forms. As the corrosion reaction is a result of penetration of oxygen through the CL to the metal, it can be concluded that antimony ions incorporated into the corrosion oxide layer facilitate the transport of oxygen to the metal surface.

It has been established that low-antimony alloys are susceptible to inter-granular corrosion. At high antimony content levels (above 8.0 wt%), an overall (general) corrosion pattern prevails, whereas between 4.0 and 8.0 wt% Sb content both general and inter-granular corrosion occur [19,20].

**Figure 4.11:**

Effect of antimony content on the creep resistance of Pb—Sb alloys, cast and rolled samples. Data from ref. [18] are used.

**Figure 4.12:**

Stationary overall corrosion rate vs antimony content for Pb—Sb alloys [17].

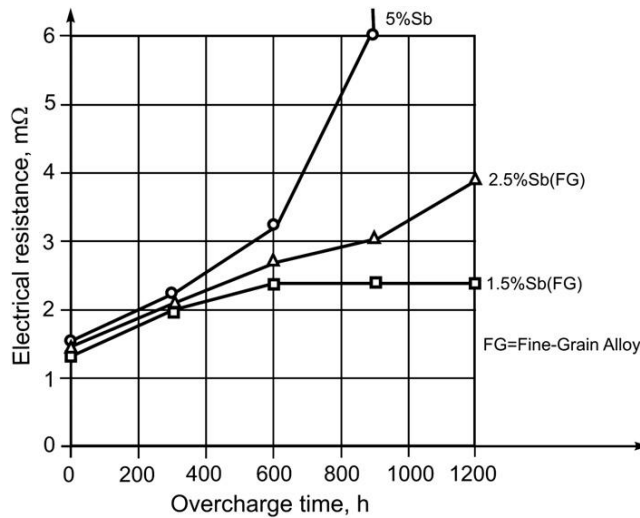


Figure 4.13:
Increase of electrical resistance due to grid corrosion [3].

The rate of corrosion affects the electrical resistance of the positive grids. This effect is illustrated in Fig. 4.13 [3]. The figure shows the electrical resistance of small test grids exposed to corrosion at 40 °C for different times of constant current overcharge. On completion of the corrosion process, the grid frames were cut at two opposite corners and the electrical resistance between the other two opposite corners was measured.

As evident from the data in Fig. 4.13, with time of battery operation, progressive corrosion of the positive grids increases their electrical resistance, which results in lower power and capacity performance. This process depends greatly on the content of antimony in the positive grids.

4.3.4. Additives to Pb–Sb Alloys

Arsenic

Table 4.4 summarises the effects of As on the mechanical properties of low-antimony lead alloys [21]. Arsenic improves the hardness and less so the UTS of the alloys. If these data are compared with the required grid alloy characteristics presented in Table 4.1, it can be seen that lead alloys with addition of arsenic meet the requirements of the battery industry with regard to hardness and their tensile strength is close to the required values.

The data in Table 4.4 evidence that the corrosion rate decreases with decrease of Sb content in the alloy. Appropriate additives to the Pb–Sb–As alloys should be looked for which would improve the tensile strength and the corrosion resistance of Pb–low Sb–As alloys. Table 4.4 shows also that small amounts of Ag (0.05 wt%) and Sn (0.02 wt%)

Table 4.4: Effect of arsenic, tin and silver additives on some parameters of low-antimony alloys [21].

Alloy Composition (wt%)				Corrosion Rate per day (mg cm^{-2})	Tensile Strength (kg mm^{-2})	Hardness 3 Days After Casting (kg mm^{-2})
Sb	As	Ag	Sn			
3.5				1.78	3.4	10.8
3.5	0.15			1.96	3.5	13.1
3.5 ^a	0.15			1.78	4.3	12.1
2.75 ^a	0.15			1.63	3.5	12.9
1.8 ^a	0.18			1.36–1.46	3.7	12.5
3.5	0.15	0.05	0.02	1.10	4.4	11.9

^aAlloy contains grain refiners.

added to the alloy reduce significantly the corrosion rate and improve the tensile strength, preserving the hardness of the alloy just above the lower limit required by the battery industry.

It has been established that, after 1 year of battery operation, the hardness of Pb–Sb grids diminishes, whereas that of cast Pb–Sb–As grids remains constant. Thus, addition of 0.1–0.2 wt% As is sufficient to prevent the ‘growth’ of the positive plates during battery service. It has been found that arsenic in amounts of up to 0.2 wt% reduces the size of the lead solid–solution particles [22]. Arsenic also accelerates dramatically the fast hardening of Pb–Sb–As alloys, this effect being more pronounced with high-antimony alloys. This effect of As offers a possibility to eliminate the required technological step of ageing of Pb–Sb–As grids prior to further processing. At concentrations above 0.1 wt%, arsenic reduces the rate of chemical oxidation of the melt and thus the amount of metal wasted in slag formation [23].

It has been established that an element will have high solubility in another element if their atomic radii differ by less than 15% [24]. The atomic radius of Pb is 1.746 (CN12) and that of As is 1.39 (CN12) [25]. The difference between these radii is more than 15%. Hence, arsenic has extremely low solubility in lead, viz., 0.05% As at the eutectic temperature of 291 °C and 0.01% at room temperature. Arsenic is to be found predominantly in the eutectic phase. When a Pb–As alloy is subjected to anodic polarization, attack by corrosion is confined mainly within the eutectic regions [23]. In Pb–Sb–As alloys, arsenic influences but slightly the rate of general corrosion (Table 4.4), but inhibits strongly the inter-granular corrosion [22].

Addition of 0.1–0.2 wt% As to Pb–Sb alloys reduces the melt flowability during casting. This effect is enhanced when the antimony content in the alloy is reduced. In order to improve the flowability of the melt during casting, some 0.15–0.20 wt% Sn is also added to the Pb–low Sb–0.15 wt% As alloy.

Tin

Addition of tin reduces the oxidation of immobilized Pb—Sb melts due to the formation of a protective SnO_2 film on the surface of the melt [26]. This effect is also retained during slight stirring of the melt, which results in reduced slag formation and hence less metal losses. During casting, and as a result of oxidation, the major part of the tin accumulates in the slag in the form of SnO_2 and only a small amount remains in the grid metal. The formation of a SnO_2 film increases the surface tension and thus improves the flowability of the melt [27]. Such melts can fill the grid moulds at low temperature and thus the casting rate is increased. This effect of tin is retained in both Pb—Sb—Sn and Pb—Sb—As—Sn alloys. Tin is added to the latter alloys in concentrations between 0.15 and 0.20 wt%. The mechanical properties and corrosion resistance of the above mentioned alloys are only slightly affected by tin concentrations of up to 0.4 wt%.

It has been established that, during hardening of the ternary Pb—Sb—Sn system, SbSn particles of lamellar shape and rounded Sn particles are formed [28]. These alloys harden through continuous precipitation. Cast Pb—Sb—<1.0 wt% Sn samples have a dendritic structure with segregation of tin to the sub-grain boundaries, which depends on the rate of melt cooling on solidification. Segregation reduces the over-saturation of dendrites and hence the hardness of the alloy when $\text{Sb} < 1.0$ wt%. Addition of tin slows down the segregation rate and thus improves the alloy hardness. This happens when the alloy contains 0.5–1.0 wt% Sn. At 1.5–2.5 wt% Sn content, the rate of age hardening of the alloy increases. Despite the segregation of Sb atoms to the grain boundaries in 2.5 wt% Sb-containing alloy, the remaining amount of Sb in the dendrites is sufficient to sustain over-saturation and to ensure adequate hardness of the alloy. In this case, small additions of Sn have an insignificant effect [28].

In an attempt to improve the properties of Pb—low Sb—Sn alloys and increase the productivity of the grid-casting process, different additives to these alloys have been tested. Selenium has proved to be one of the most efficient additives. Alloys with the composition Pb—3.0 wt% Sb—1.3 (or 1.5) wt% Sn—0.05 wt% Se have been in British Naval and British Rail use for over 20 years with very good results [29].

Silver

This element has proved to be most effective for reducing the corrosion rate of lead—antimony alloys and has therefore been intensively studied [17,30–32]. Alloy corrosion rate (evaluated by weight loss) and electrode potential have been measured vs Ag content for Pb—Ag and Pb—Sb—Ag alloys [33]. The obtained curves are presented in Fig. 4.14.

If the data in Figs 4.12 and 4.14 are juxtaposed, it can be noted that antimony increases the corrosion rate of lead, whereas silver not only neutralises this influence of Sb, but even improves the corrosion resistance of Pb—Sb—Ag alloys. Silver suppresses the inter-granular corrosion and hence overall corrosion is the main process in Pb—Sb—Ag alloys. Silver affects

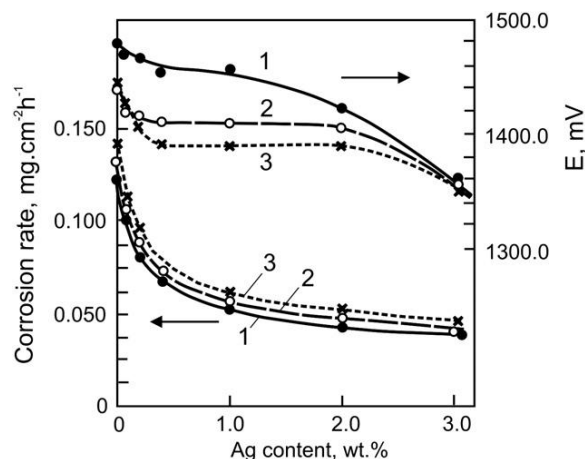


Figure 4.14:

Stationary overall corrosion rate and electrode potential as a function of silver content: 1 (•) Pb–Ag; 2 (○) Pb–5.7 wt% Sb–Ag; and 3 (×) Pb–10 wt% Sb–Ag alloy [33].

but slightly the oxygen evolution reaction. In Pb–Sb–Ag alloys, it is the antimony content that determines the oxygen evolution overpotential.

4.3.5. Effect of Antimony in the Grid Alloy on the Rate of Water Decomposition

The oxygen evolution reaction

Electrodes cast from alloys with different antimony content were subjected to polarization at a current density of 6.4 mA cm^{-2} [17]. The dependence electrode potential vs Sb content in the alloy was plotted on reaching stationary potential values. This dependence is presented in Fig. 4.15.

The over-potential of oxygen evolution decreases with the increase of the Sb content in the alloy. This indicates that Sb^{5+} ions incorporated in the PbO_2 CL participate in, or exert an influence on, certain elementary processes involved in the oxygen reaction. The data in Figs 4.14 and 4.15 evidence that, on the one hand, antimony increases the rate of corrosion and, on the other hand, it lowers the overpotential of oxygen evolution, which facilitates the decomposition of water both during the charge and self-discharge processes in the battery.

The hydrogen evolution reaction

Figure 4.16 shows the dependences of the rate of hydrogen evolution on electrode potential for pure Pb and Pb–Sb electrodes with different Sb content [8]. Addition of antimony to the alloy lowers substantially the potential of hydrogen evolution on electrode polarization at 2.0 mA cm^{-2} . Depending on the Sb content in the alloy, a reduction in hydrogen overpotential by 220 mV (Pb–2.2 wt% Sb) and by 380 mV (Pb–5.7 wt% Sb) is registered. These results speak

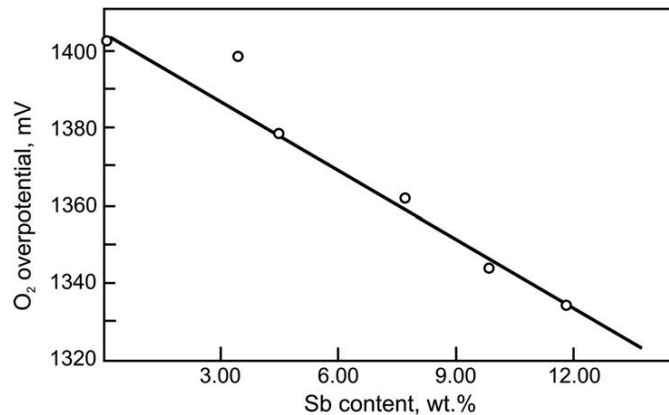


Figure 4.15:

Oxygen overpotential (vs. $\text{Hg}/\text{Hg}_2\text{SO}_4$) as a function of Sb content [17].

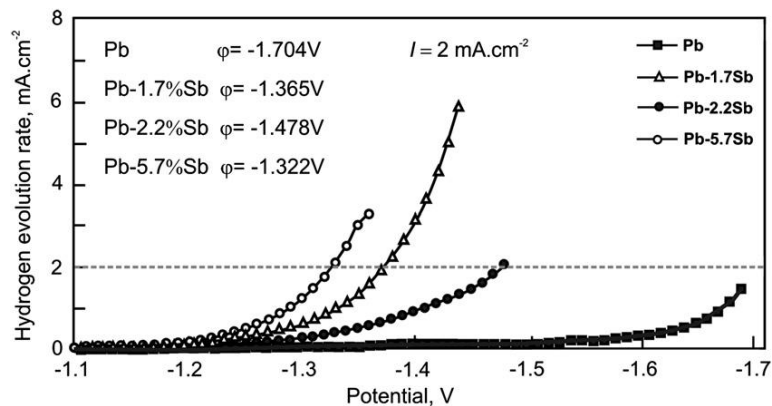
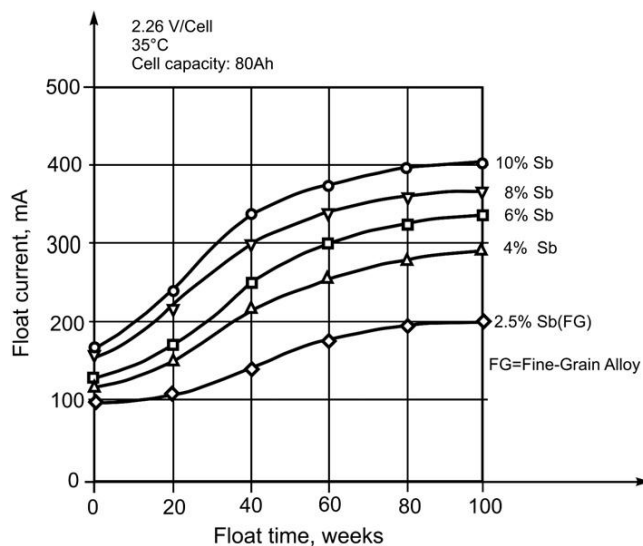


Figure 4.16:

Effect of antimony on the overpotential of hydrogen evolution [8].

of a very strong effect of Sb on the overpotential of hydrogen evolution, stronger than that on the evolution of oxygen (see Fig. 4.15).

During corrosion of the positive grids, antimony ions diffuse through the solution and Sb is deposited on the negative plates. Hydrogen is evolved on the Sb phase at a higher rate, which results in increased water loss in the cell. This process is illustrated in Fig. 4.17 in terms of changes in the float current with float time on polarization of 80-Ah batteries with Pb–Sb grids at 2.26 V per cell [3]. The higher the Sb content in the alloy the higher the float current of water decomposition to hydrogen and oxygen. Obviously, antimony plays an important role in the reactions of water decomposition.

**Figure 4.17:**

Changes in float current with float time on polarization of industrial batteries at 2.26 V per cell. Cell capacity 80 Ah [3].

4.3.6. Mechanism of Grid Hot Cracking

Attempts to improve the mechanical properties of low-antimony alloys by thermal treatment proved to be a technological failure. This method was rejected by the battery industry because it caused hot cracking of the grids and increased the inter-granular corrosion.

Heubner et al. [34,35] proposed the following mechanism of crack formation: when the liquid Pb–Sb alloy is poured into the mould, heat is dissipated through the walls of the mould to the surroundings. Because of the directional nature of heat extraction, the lead solid–solution dendrites grow with preferred orientation from the mould walls towards the melt. The melt is enriched with antimony and its volume decreases. During cooling, the dendrites start to shrink and the crystals may detach from one another forming micro-cracks. If the dendrites have a similar orientation, the contraction may be transferred to the grain boundaries and the grains may be separated. The rest of the melt is rich in antimony and tends to fill these cracks, but its quantity depends on the amount of antimony in the alloy.

Figure 4.18 shows the dependence of the share of eutectic phase in the grid alloy as a function of Sb content [36]. The curve in the figure indicates that the alloys with 2.5 wt% Sb content contain about 10% eutectic phase, whereas there is but very little eutectic in the alloy with 1.0 wt% Sb. The reduced eutectic volume allows the first α -Pb dendrites to crystallize in large highly oriented grains.

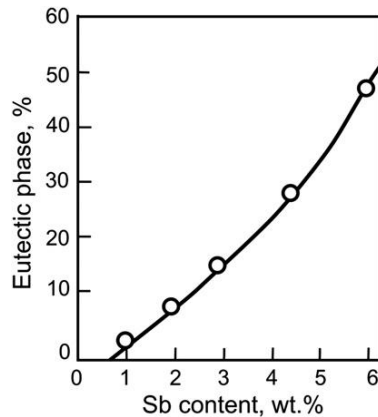


Figure 4.18:

Eutectic phase in grids as a function of antimony content [36].

When the grid alloy contains more than 5.0 wt% Sb, there is sufficient liquid molten phase to fill all cracks and sustain the continuity of the casting. If the Sb concentration is less than 4.0 wt%, many cracks remain empty (unfilled) and are responsible for the so-called 'hot cracking' of the grids (Fig. 4.19).

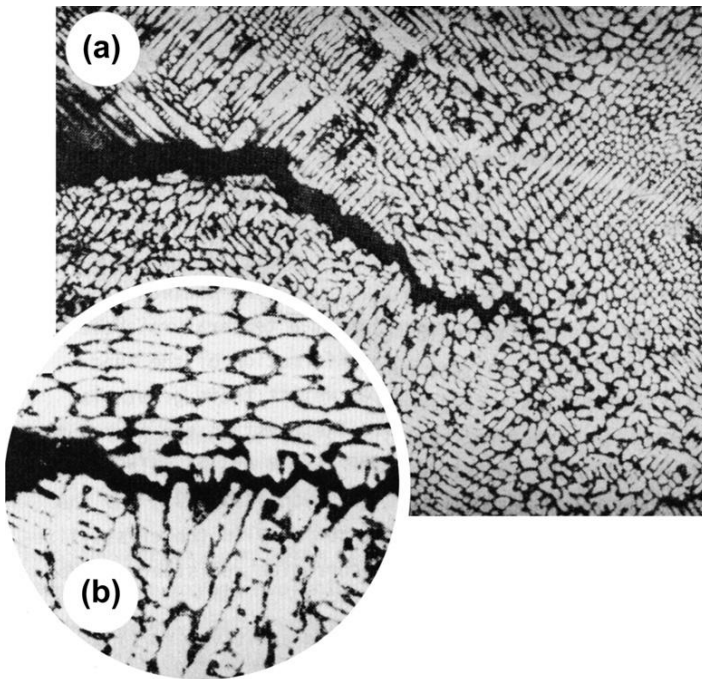


Figure 4.19:

Coarse dendritic cast structure with hot cracks (Pb–2.0 wt% Sb alloy) [3]. (a) general view of alloy structure; (b) closer view of a hot crack.

When a grid with such a structure is subjected to anodic polarization, the corrosion attack is faster along the inter-dendritic and grain boundaries. This leads to deeper inter-granular corrosion, which may eventually result in grid bar damage.

This hazard can be completely eliminated by the introduction of nucleants in the melt. These additives (grain refiners) crystallize in the melt at a temperature above the temperatures of lead dendrite formation. Thus, the growth of lead solid–solution crystals proceeds at a faster rate onto the already formed nuclei. As the latter are abundant in the melt, a fine-grain structure is obtained.

4.3.7. Nucleants (Refiners)

Selenium (Se) and sulfur (S)

These additives react with lead to form an inter-metallic lead–selenide compound, while sulfur forms a Pb–S phase which then acts as a nucleant. α -Pb grains grow readily on these nuclei up to 50–70 μm in size, thus preventing formation of large dendrites (700–1000 μm).

Figure 4.20 shows micrographs of the microstructure of a grid bar cast from Pb–2.5 wt% Sb–0.02 wt% Se alloy [3,37]. The pictures illustrate the fine-grain globulitic structure of the primary α -Pb solid–solution and the eutectic grain boundaries. Such an alloy structure prevents the hot cracking effect on casting.

The influence of selenium and sulfur as refiners on the grain size of low-antimony lead alloys has been studied. The obtained results are presented in Fig. 4.21 [34].

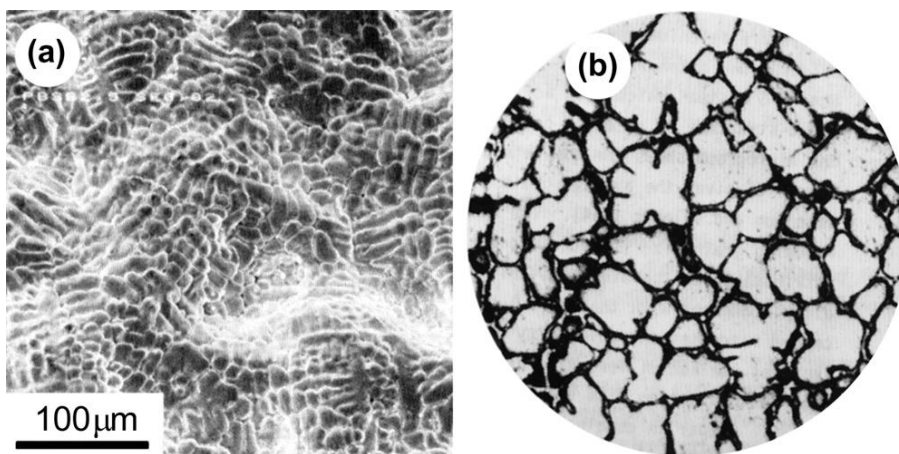


Figure 4.20:

Micrographs of the structure of cast Pb–2.5 wt% Sb–0.02 wt% Se alloy. (a) ref. [37]; (b) ref. [3].

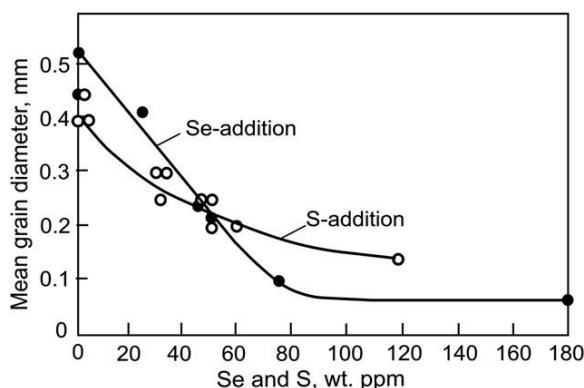


Figure 4.21:

Grain refinement of Pb–2.5 wt% Sb chill cast battery grids by means of Se and S additions. Casting temperature 500 °C, mould temperature 135 °C [34].

The specific effect of selenium in reducing grain size is much stronger than that of sulfur. This is attributed to the higher solubility of selenium in the Pb–Sb alloy as compared to sulfur. It has been established that copper increases the solubility of sulfur in the melt and hence improves its nuclei formation effect. For this reason, sulfur is used in combination with copper.

The grain refining effect of selenium exhibits within a wide range of antimony concentrations in the alloy (from 0.5 to 9.0 wt% Sb) [38]. However, the use of low-antimony alloys in the battery industry was made possible thanks to the addition of nucleants to the grid alloys. Alloys with nucleants are used not only for book-mould gravity casting and pressure die casting of battery grids, but also in the continuous drum casting process. Alloys with low-antimony content (e.g., Sb < 1.6 wt%) solidify very quickly. The small freezing range and the amount of eutectic phase in nucleants-containing alloys make them suitable for continuous casting, whereby a fine-grained structure is obtained which guarantees high mechanical properties and corrosion resistance of the grids. Nucleants play an important role not only in the crystallization processes during casting but also in the contribution to the improvement of the corrosion resistance of low-Sb battery alloys [39,40].

It has been established that at Sb content below 1.5 and 0.05 wt% Se in the grid alloy, water decomposition in the battery decreases substantially, but passivation of the positive plates occurs similar to that observed with Pb–Ca alloys. These passivation phenomena will be discussed in more detail in the section devoted to lead–calcium alloys later in this chapter. In order to overcome these phenomena, tin is added to the grid alloy in concentrations of 0.3–0.4 wt% [41].

Copper

Copper in combination with arsenic forms Cu_3As which exerts a nuclei-formation effect [14]. Copper at concentrations of 0.05–0.06 wt%, in combination with 0.006–0.007 wt% sulfur, also

acts as an efficient nucleant [14]. Besides, copper has a beneficial effect on the overall corrosion rate of lead and lead–antimony alloys [43]. The Pb–Cu eutectic alloy contains 0.06 wt% Cu. At this concentration level, a distinct minimum in the corrosion rate is observed. This minimum is even more pronounced when the antimony content in the alloy is reduced [42]. At 0.06 wt% Cu, both the castability and the hardness of Pb–Sb–Cu alloys exhibit a maximum. A wide variety of low-antimony alloys with nucleants are in current use, including Pb–(1.5–2.5) wt% Sb–(0.1–0.2) wt% As–(0.2–0.3) wt% Sn–(0.02–0.03) wt% Se and Pb–2.0 wt% Sb–(0.1–0.2) wt% As–(0.1–0.2) wt% Sn–(0.05–0.06) wt% Cu–(0.005–0.007) wt% S alloy systems. These low-antimony nucleant alloys require very precise control of the additives' content and of temperature during the casting process. During grid casting the temperature of both the melt pot and the metal delivery system should be sustained high (490–510 °C), so as to keep the nuclei dissolved in the melt. The temperature of the book mould should be 150–170 °C. Under such conditions there are no casting problems. If, however, the temperature of the melt is low, the nucleants in the alloy will have low solubility and will float out to the slag, i.e., they will have no effect on the alloy microstructure and the grids will be subject to intense hot cracking. In the presence of nucleants, the structure of low-antimony alloys depends on the amount and distribution of the nucleants (and hence on the precision of the temperature control during casting), rather than on the content of antimony in the alloy.

4.3.8. Influence of Sb, As and Bi on the Reversibility of the Lead Dioxide Active Mass Structure

Antimony and the alloying additives influence not only the rates of grid corrosion and of water decomposition, but also have a beneficial effect on the reversibility of the structure of the positive active mass (PAM). During discharge of the positive plate, 30–50% of the active mass is converted to PbSO₄. This results in a partial destruction of the PbO₂ active mass structure, which is then restored again during re-charge. Since these processes are not always reversible, the structure of the active mass gradually disintegrates and the capacity declines.

It has been established that antimony slows down the growth of PbO₂ agglomerates and reduces their crystallinity [43]. Sb⁵⁺ ions are adsorbed much more easily on the PbO₂ surface than Sb³⁺ ions [44]. The presence of antimony as a dopant in the PbO₂ crystal lattice increases electrode capacity, whereas when antimony is introduced into the electrolyte it has a passivating effect [45]. Bismuth and arsenic doped in the PbO₂ phase accelerate many reactions with oxygen transitions [46].

The influence of antimony, arsenic and bismuth on the reversibility of the PAM structure has been studied via cycling of cylindrical tubular electrodes filled with PAM powder to a density of 4.15 g cm⁻³ [47,48]. Current collectors (spines) of Pb or Pb–6.0 wt% Sb alloy are used. Figure 4.22 illustrates the effect of Sb³⁺, As³⁺ and Bi³⁺ ions in the electrolyte on the specific capacity of the tubular electrodes during the first 20 cycles.

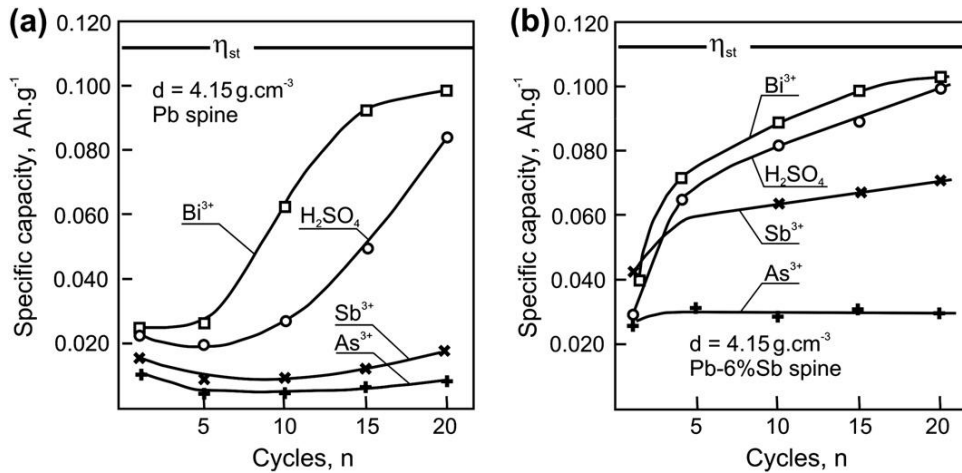


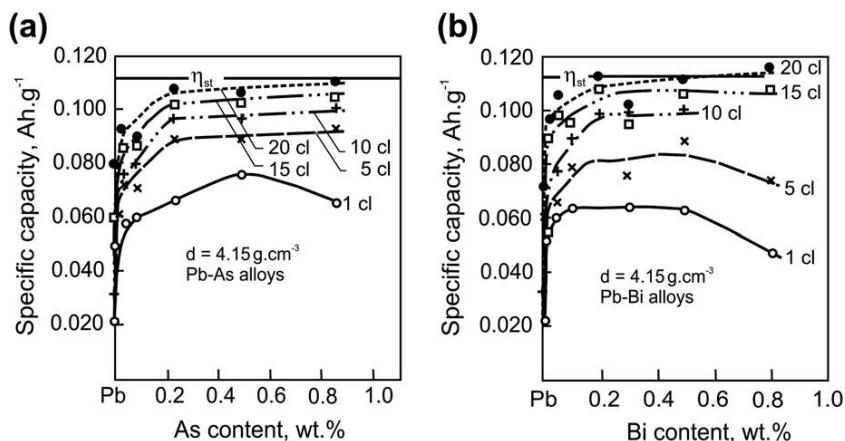
Figure 4.22:

Influence of As^{3+} , Bi^{3+} and Sb^{3+} ions in the electrolyte on the specific capacity/cycle life curve. tubular electrodes with (a) lead and (b) Pb–6.0 wt% Sb spines [47].

The data in the figure evidence that:

- Bi^{3+} ions accelerate the formation of the PAM structure, Sb^{3+} ions retard it, whereas As^{3+} ions stop the process altogether. These effects of the three additives are preserved irrespective of the type of spine used.
- Within the first five cycles, a CL is built up and formation of the PAM structure starts. This process is strongly affected by the presence of Sb in the alloy and all capacity curves are shifted towards higher values. Probably, during corrosion of the Pb–Sb spine, Sb ions are incorporated into the structure of the CL and improve the contact CL|PAM. This contact is affected by the ions in the solution and As^{3+} ions halt the process of building the PAM structure. The electrodes with Pb–Sb spines have 3.7 times higher capacity than those with pure Pb spines. The influence of antimony as alloying additive is stronger than that of Sb ions in the electrolyte. The beneficial effect of Sb in the spine alloy is enhanced further by the presence of Bi^{3+} ions in the electrolyte and formation of the PAM structure proceeds at the highest rate on these electrodes.

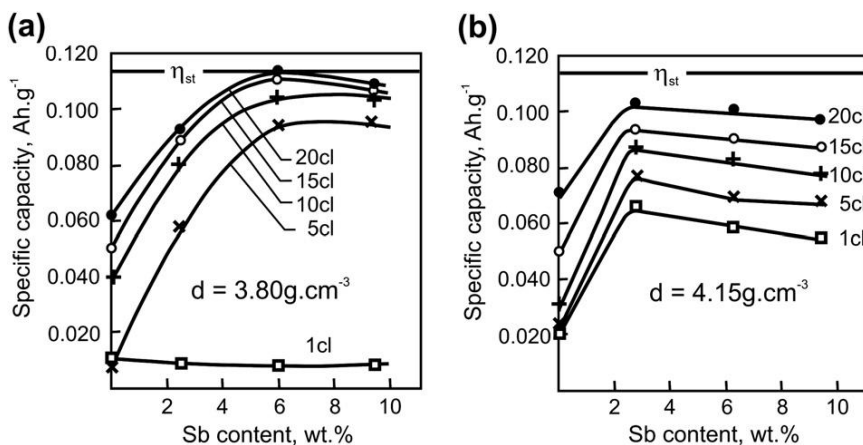
Figure 4.23 shows the specific capacity as a function of As and Bi content in the spine alloys during different cycles [48]. A comparison between the data in Figs 4.22 and 4.23 indicates that arsenic in the spine alloy has a highly beneficial effect on PAM formation, whereas As^{3+} ions in the solution block this process. As^{3+} ions incorporated in the CL improve the electrical properties of lead oxides and of the contact PAM|CL, and thus facilitate the formation of the PAM structure. Figure 4.23b evidences that, when the spine alloy contains 0.2–0.8 wt% Bi, the structure of PAM is built within the first 20 cycles, which ensures over 50% utilization of the PAM.

**Figure 4.23:**

Influence of (a) arsenic and (b) bismuth content in the alloy on tubular electrode specific capacity. PbO_2 powder density = 4.15 g cm^{-3} ; cl = cycle number [47].

Tests with tubular electrodes with different Sb content in the alloy and with different powder density (3.80 or 4.15 g cm^{-3}) have been performed in an attempt to study the effect of alloying additives on the CL|PAM interface [47,48]. The obtained results are presented in Fig. 4.24.

The electrode specific capacity depends on the antimony content in the spine alloy and on PAM density. This comes to indicate that antimony in the alloy exerts an influence not only on the structure of the interface CL|PAM but also on the PAM itself. Electrodes with lower PAM density reach maximum specific capacity at higher antimony concentrations in the spine alloy.

**Figure 4.24:**

Influence of antimony content in the alloy on tubular electrode specific capacity. PbO_2 powder density: (a) 3.80 g cm^{-3} , (b) 4.15 g cm^{-3} ; cl = cycle number [47].

This effect of antimony sustains the use of Pb—(5–10) wt% Sb alloys for casting grids and spines for the positive plates of traction batteries intended for deep discharge cycling duties. The performance characteristics of such batteries are more stable despite the higher water loss and hence the need for maintenance.

All these experimental data prove that the composition of the lead alloys for positive battery grids exerts an influence not only on the mechanical and electrochemical properties of the grids but also on the structure of the PAM and hence on the cycle life performance of the batteries.

4.3.9. Influence of Antimony on the Composition and Electrical Resistance of the Corrosion Layer Formed on Lead–Antimony Electrodes at Potentials Within the Lead Dioxide Region

On polarization at potentials within the lead dioxide potential region, the surface of the positive grids is oxidized and a CL forms which consists of a variety of oxides $\text{Pb|PbO|PbO}_n\text{|PbO}_2$ ($1 < n < 2$). While lead oxide is an electric insulator with ohmic resistance $r \sim 10^{12} \Omega \text{ cm}$, lead dioxide is a degenerated semiconductor with $r \sim 10^{-2} \Omega \text{ cm}$. High-power performance of the lead–acid battery can be achieved only if the CL formed on the positive grids is composed of high-valent lead oxides, i.e., the oxidation rate of PbO to PbO_2 should be higher than the rate of Pb oxidation to PbO. The influence of Sb in the grid alloy on these rates is illustrated in Fig. 4.25 [49].

A Pb|PbO|PbSO_4 electrode system was obtained by polarization of pure Pb, Pb–2.0 wt% Sb or Pb–12 wt% Sb electrodes immersed in H_2SO_4 solution at +0.6 V (vs $\text{Hg/Hg}_2\text{SO}_4$ electrode) for 16 h. Then, the PbO|PbSO_4 layer was further oxidized to PbO_2 via linear voltammetric sweeps between 0.6 and 1.3 V. The potential at which oxidation of PbO to PbO_2 commences is

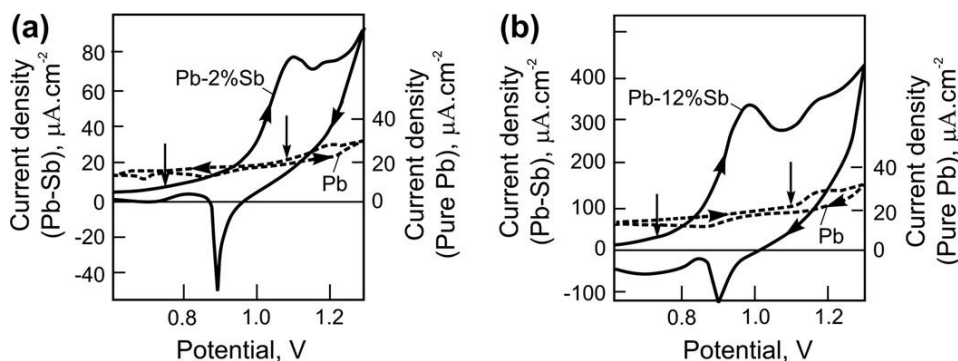


Figure 4.25:

Linear voltammetric sweeps: (a) Pb–2.0 wt% Sb and (b) Pb–12 wt% Sb electrodes performed after 16 h of potentiostatic polarization at +0.6 V in 0.5 M H_2SO_4 solution. Dashed lines show the voltammograms of a pure Pb electrode [49]. Left ordinate: current density for Pb–Sb electrodes. Right ordinate: current density for the pure Pb electrode.

marked by an arrow. A comparison between the obtained i/ϕ curves for the Pb–Sb and the pure Pb electrodes indicates that Sb lowers substantially the onset potential of PbO oxidation and accelerates greatly the formation of PbO₂, thus sustaining low-ohmic resistance of the CL. Hence, the influence of the electrical resistance of the interface CL|PAM on plate capacity is eliminated. The higher the Sb content in the grid alloy, the faster the oxidation of PbO to PbO₂. These experimental results suggest that Sb³⁺ and Sb⁵⁺ ions are incorporated into the structure of PbO, PbO_n and PbO₂ sub-layers forming Pb_{1-x}Sb_xO, Pb_{1-y}Sb_yO_n and Pb_{1-z}Sb_zO₂, respectively. These antimony ions will affect the properties of the respective lead oxides [49].

Based on the experimental results presented in Fig. 4.25, it can be concluded that antimony incorporated in the CL will improve the electrical and mechanical contact between the CL and the PAM, and eventually enhance the energetic performance of the lead–acid cell.

4.4. Lead–Calcium Alloys

4.4.1. How Were Lead–Calcium Alloys Widely Adopted in the Battery Industry

In an attempt to reduce water decomposition and thus battery maintenance, in 1935, Haring and Thomas [50] introduced lead–calcium alloys for casting the grids for stationary batteries for telecommunication centres. The content of calcium in the grid alloys was 0.03 wt%. This two-component (binary) alloy was also used in batteries for submarines. It has been established that, at Ca loading levels higher than the above value, the grids grow in size during battery operation [51]. Calcium contents in the alloy of less than 0.03 wt% result in inferior mechanical properties of the grids [52]. Grids with 0.03 wt% Ca are corrosion resistant and are suitable for casting both positive and negative grids for stationary batteries. Besides the alloy composition, the technology of casting lead–calcium grids also affects their microstructure and mechanical properties [53]. Lead–calcium alloys have won dominating position in the manufacture of grids for stationary and standby batteries intended for float service at constant voltage.

When lead–calcium alloys were employed for casting grids for traction batteries operating in deep-discharge cycling mode, the capacity of the batteries declined dramatically within the first 30–40 cycles. It seemed that the lack of antimony in the positive grids was responsible for this unexpected phenomenon [54–56]. This conjecture about the influence of antimony was verified by covering Pb–Ca positive grids with a layer of antimony. The battery with such positive grids behaved like Pb–Sb batteries until Sb was oxidized and dissolved in the solution, when its capacity dropped [57]. Because of the above-described ‘Sb-free effect’, the application of lead–calcium alloys was confined to stationary batteries for constant voltage float charge operation.

At the end of the twentieth century, maintenance-free VRLA batteries were invented. The first VRLA batteries employed lead–calcium grids. The antimony-free effect exhibited fully, which forced metallurgists to switch back to Pb–Sb alloys for the positive grids, minimising

the content of antimony in the grid alloy. Still, the Sb-free effect was not eliminated. This came to indicate that the observed rapid capacity loss was not a result of the lack of antimony, but rather of some physico-chemical phenomenon that occurred on the positive plates. This phenomenon was called ‘premature capacity loss’ (PCL effect) [58]. Two basic explanations of this effect were proposed:

- a. *PCL-1 effect related to processes at the interface grid|CL|PAM* [59–62]. During corrosion of the grids, a CL forms which is composed of PbO, PbO_n ($1 < n < 2$) and PbO₂. During cycling, the PbO sub-layer formed on Pb, Pb–Ca or Pb–low-Sb grids may quickly reach considerable thickness and create a high ohmic resistance interface. When the grid alloy contains considerable amounts of Sb or Sn additives, Sb and Sn ions accelerate the oxidation of PbO to oxides of higher valency and higher electrical conductivity, thus reducing the thickness of the PbO layer and hence the ohmic resistance of the interface.
- b. *PCL-2 effect related to changes in the active material itself* [63]. This effect is attributed to the inter-particle resistance of PAM. The PCL-2 effect has weaker influence on battery cycle life than the PCL-1 effect.

It was assumed that the two failure mechanisms were related to particular operating conditions and alloy compositions, and the PCL effect could be eliminated by adding a definite amount of tin to the Pb–Ca alloys. Lead–calcium–tin alloys occupied dominating positions in the industrial practice for casting negative grids for almost all types of lead–acid batteries, whereas the positive plates were produced with low-antimony grids, when intended for use in batteries for deep-cycling duties, or with lead–calcium grids with considerable tin content for other cycling applications.

The concentration of calcium in Pb–Ca alloys for battery grids varies between 0.03 and 0.15 wt%. Lead–calcium alloys have a narrow freezing range of 1–3 °C, which makes them suitable for high-speed permanent mould casting or continuous strip or grid casting. These alloys are appropriate for the manufacture of negative battery grids.

Depending on their properties, lead–calcium alloys can be classified as:

- a. *Low-calcium alloys (with 0.02–0.04 wt% Ca content)*, used for casting negative grids for standby batteries intended for float service. Very small amounts of aluminium are usually added to these alloys.
- b. *Medium-calcium alloys (0.06–0.10 wt% Ca)*, used for casting negative grids by the continuous casting process, for casting alloy strips for expanded and rolled grids for automotive batteries. Aluminium is also added to these alloys to sustain the content of Ca unchanged during the casting process. The narrow freezing range of these alloys allows casting at a high speed.
- c. *High-calcium alloys (0.10–0.15 wt% Ca)*. They contain high levels of aluminium as well and are used for casting negative grids for automotive batteries.

Let us now discuss in more detail the basic types of lead–calcium alloys used in the battery industry, their structure and properties, as well as the most common additives introduced in these alloys.

4.4.2. Equilibrium Phase Diagram of the Lead–Calcium Alloy System

It seems that only alloys with particular properties are suitable for casting grids for lead–acid batteries. Lead–calcium alloys, similar to lead–antimony alloys, belong to the age-hardening or precipitation-hardening group of alloys. With decrease of temperature, the solubility of calcium in the α -Pb solid–solution decreases and it precipitates in the form of small Pb_3Ca particles. A similar picture was described earlier for the Pb–Sb alloys.

Figure 4.26 shows the phase diagram of the equilibrium Pb–Ca alloys system [13,64]. A zone comprising (α -Pb + liquid) phases with maximum solubility of 0.1 wt% Ca in Pb is formed in the system at the peritectic temperature of 328 °C. At room temperature, the solubility of Ca is 0.01 wt%. This 10-fold difference in Ca content is a result of a solid-phase recrystallization process, which changes the microstructure of the alloys and hence its mechanical properties.

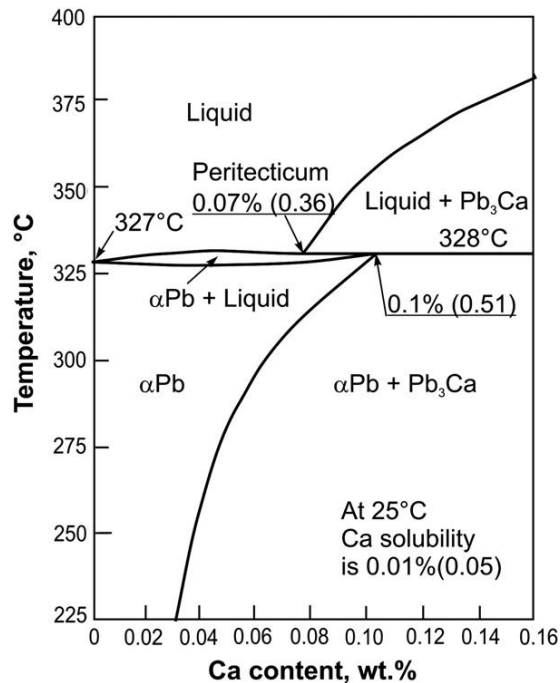


Figure 4.26:

Equilibrium phase diagram of the Pb–Ca alloy system [13]. Values in parentheses are atom percent.

The peritecticum (0.07 wt% Ca) divides the phase diagram of the Pb–Ca system into two regions:

- a. *Ca content* < 0.07 wt%, when significant amounts of supersaturated α -Pb solid–solution form. With time of alloy hardening, this solid–solution tends to reach an equilibrium state by precipitation of very fine Pb_3Ca particles. The latter deform the lead crystal lattice and thus increase the hardness of the alloy. The microstructure of a Pb–0.05 wt% Ca alloy sample is presented in Fig. 4.27a [65].
- b. *Ca content* > 0.07 wt%. Figure 4.27b shows the microstructure of the Pb–0.09 wt% Ca alloy [65]. It is possible to obtain solid–solution phase by fast cooling and thus prevent segregation of calcium. In this system, some recrystallization processes occur which lead to the formation of lead grains and dispersion of Pb_3Ca particles. The latter's amount depends on the alloy composition and the casting procedures employed, as for any age-hardening alloy system. At room temperature, Pb–Ca alloys harden much faster than do Pb–Sb alloys. The process of age-hardening may be further accelerated by keeping the cast grids at temperatures higher than room temperature.

4.4.3. Mechanical Properties of Lead–Calcium Alloys

The mean grain sizes of Pb–Ca alloys diminish with the increase of the Ca content in the alloy (Fig. 4.27), which induces changes in their mechanical properties. Figure 4.28

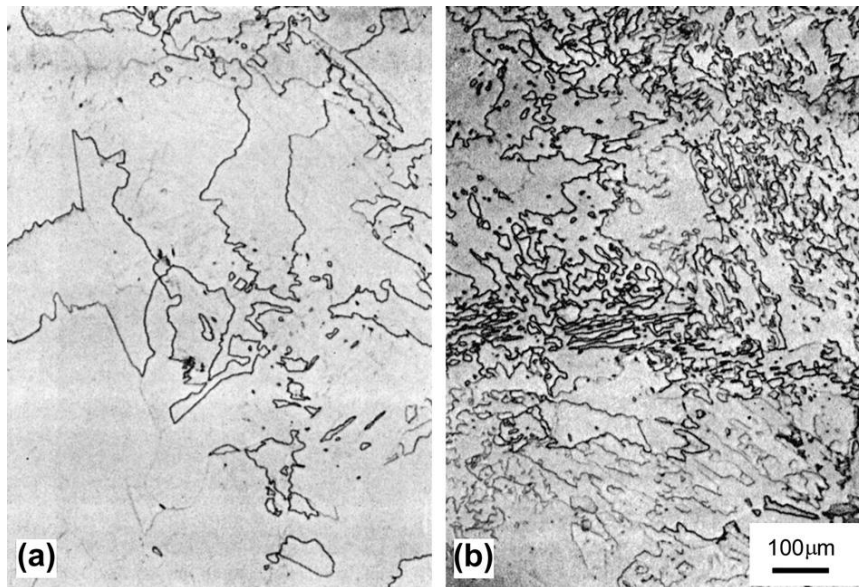


Figure 4.27:

Grain refinement with increasing Ca content in Pb–Ca alloys: (a) Pb–0.06 wt% Ca, (b) Pb–0.09 wt% Ca. Both at 90 \times magnification [65].

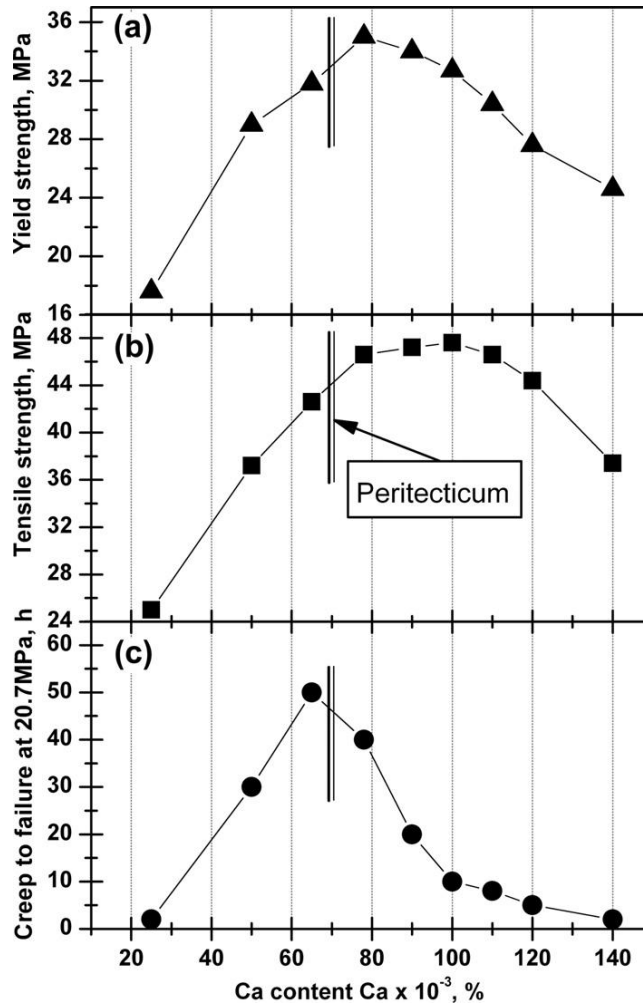


Figure 4.28:

Changes in (a) yield strength, (b) ultimate tensile strength and (c) creep to failure at 20.7 MPa as a function of calcium content in Pb–Ca alloys. Data from ref. [66] are used.

presents the dependences of YS, UTS and creep to failure (creep resistance) of Pb–Ca alloys with Ca contents of up to 0.14 wt%. Data reported in Ref. [66] are used to plot these dependences. The above mechanical properties improve with increase of the calcium content in the alloy up to 0.07 wt% (i.e., the peritectic Pb–Ca alloy composition) and then decline after this maximum. The creep resistance of alloys with $\text{Ca} > 0.08 \text{ wt}\%$ decreases abruptly, which results in significant growth of the positive grids on battery cycling. Hence, the contact grid|PAM is impaired and eventually the cycle life of the cells is shortened.

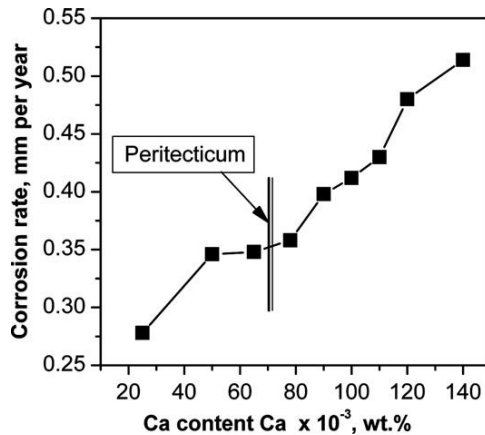


Figure 4.29:

Correlation between corrosion rate and Ca content in Pb—Ca alloys. Data from ref. [66] are used.

Figure 4.29 shows the corrosion rate of Pb—Ca alloys as a function of Ca content. Data from Ref. [66] are used. Increase of the Ca content in the alloy leads to rapid increase of the corrosion rate. This effect is the strongest on the rate of inter-granular corrosion because of Ca segregation to the grain boundaries. Calcium has a high affinity to oxygen, so the observed increase of the rate of inter-granular corrosion is quite logical. In order to suppress this effect, the content of calcium in the alloy should be reduced to no more than 0.05–0.07 wt%.

Battery-manufacturing practice has limited calcium concentration in the Pb—Ca alloys used in the battery industry to between 0.05 and 0.06 wt%. Plates with grids produced from such alloys cause negligible gassing and are suitable for application in maintenance-free batteries.

However, these alloys are susceptible to the PCL effect. Appropriate additives are looked for in order to suppress this effect of Pb—Ca alloys when used for the positive battery grids. A survey of these additives will be made further in this chapter.

4.4.4. Aluminium Addition to Pb—Ca Alloys

When casting grids for lead—acid batteries from lead—calcium alloys, the latter's composition should be controlled very precisely. If the content of calcium drops below 0.045 wt%, the grids will lose their mechanical properties, and if it exceeds the level of 0.07 wt%, they will have serious corrosion problems. During the casting process, calcium is easily oxidized and floats to the slug, thus causing casting problems as well. Various methods have been searched to reduce, or prevent altogether, the oxidation of Ca when casting Pb—Ca battery grids.

It has been established that aluminium added to the Pb—Ca alloy protects Ca from oxidation [67,68]. Aluminium is readily oxidized and the obtained oxide forms a thin film onto the

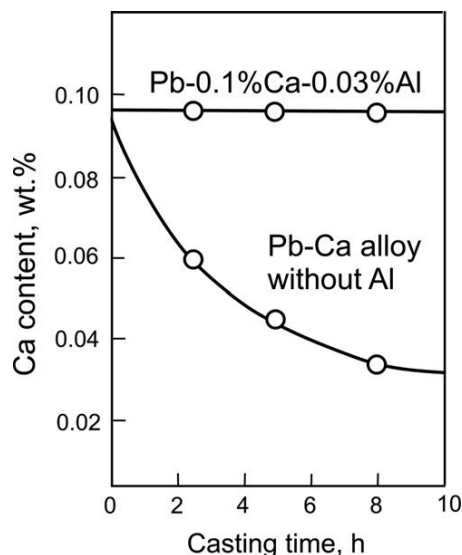


Figure 4.30:

Effect of aluminium on the loss of calcium in grid casting [36].

surface of the melt, thus blocking the access of oxygen to the bulk melt and preventing Ca oxidation. Figure 4.30 shows the changes in Ca content in the melt with time of casting grids from a Pb–0.1 wt% Ca alloy with or without the addition of Al [36]. The Al-free alloy loses about 15–20% of the Ca content on re-melting, and this loss reaches more than 60% after 8 h of casting. No such losses of Ca content are observed in the presence of Al in the alloy.

To be able to exhibit its anti-oxidation protective effect on Ca, the content of Al in the alloy should be above 0.03 wt% [36]. At lower concentrations, the amount of aluminium in the alloy would be insufficient to ‘repair’ the ruptured aluminium oxide skin on the melt surface during casting.

The solubility of aluminium in lead depends on temperature. Figure 4.31 illustrates this dependence based on data from Ref. [36]. In order to sustain the Al content in the Pb–Ca alloy above 0.03 wt%, the temperature of the melt should be kept above 500 °C. At lower temperatures part of the Al will be precipitated on the walls of the molten metal delivery system and Ca would remain unprotected from oxidation.

Grids cast from Pb–Ca–Al alloys are characterised by uniform mechanical properties, uniform fine-grain structure and delayed inter-granular corrosion. However, aluminium added to the Pb–Ca alloy does not eliminate the passivation phenomena that proceed in the CL formed on Pb–Ca grids; it resolves only a casting problem. There are some battery manufacturers who use Pb–Ca–Al alloys for casting the negative grids for their batteries.

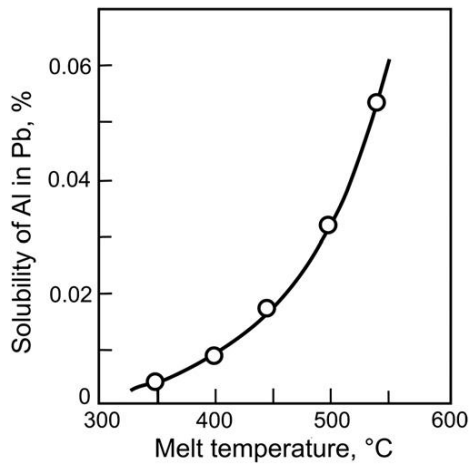


Figure 4.31:
Solubility of aluminium in lead as a function of temperature [36].

4.5. Lead–Calcium–Tin Alloys

4.5.1. Microstructure of Pb–Ca–Sn Alloys

Tin additions to lead–calcium alloys have changed dramatically the structure of the alloys and hence the mechanical, corrosion and electrochemical properties of the grids produced from these alloys, which have contributed to substantial increase of the market share of batteries using Pb–Ca–Sn or Pb–Sn grids, making it commensurate with that of batteries with Pb–Sb grids. These three types of batteries constitute the overall group of maintenance-free valve-regulated lead–acid batteries.

Let us see how tin used as an alloying element affects the microstructure and properties of the Pb–Ca–Sn alloy system.

Figure 4.32a,b,c shows pictures of the microstructure of parts of grid wires cast from Pb–0.06 wt% Ca alloys with increasing additions of tin to the alloy [69]. The grain sizes increase with the increase of the Sn content in the alloy. The coarse grains in alloys containing more than 0.8 wt% Sn may grow to such sizes that the cross section through the thin grid bars of SLI grids may comprise of several grains only.

The images in Fig. 4.32d,e,f illustrate the changes in microstructure of the Pb–0.3 wt% Sn–*X* wt% Ca alloy with changes in the calcium content from 0.09 to 0.13 wt% [69]. The grain sizes diminish with the increase of the Ca content.

The changes in grain diameter as a function of Sn content (*X*) in Pb–0.12 wt% Ca–*X* wt% Sn alloy are presented in Fig. 4.33 [70]. The grain diameter increases linearly with increase of tin content. As the grain diameter depends on both the Ca and Sn contents in the alloy, the ratio

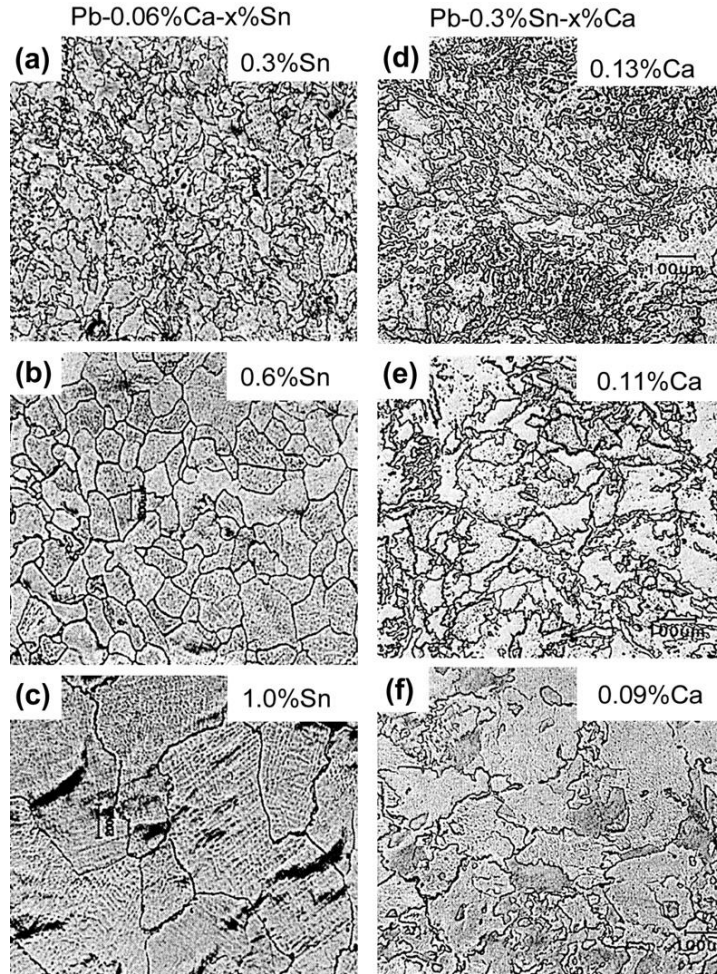


Figure 4.32:

Micrographs of Pb–Ca–Sn alloys after 1-week stay at room temperature. Alloy compositions: (a) 0.06 wt% Ca plus 0.3 wt% Sn, (b) 0.06 wt% Ca plus 0.6 wt% Sn, (c) 0.06 wt% Ca plus 1.0 wt% Sn; (d) 0.3 wt% Sn plus 0.13 wt% Ca, (e) 0.3 wt% Sn plus 0.11 wt% Ca, (f) 0.3 wt% Sn plus 0.09 wt% Ca [69].

$r = \%Sn/\%Ca$ was introduced in the literature [70–72]. The alloy microstructure is found to change at a critical value of about $r = 9$.

- At $r < 9$, the grains are small in size (30–100 μm) and the grain boundaries are serrated, which is explained in terms of the cellular precipitation of Pb_3Ca behind moving grain boundaries during solidification [73,74].
- At $r > 9$, the grains are well-defined and larger in size (100–150 μm), with a cellular substructure of segregated tin [69]. At higher r values, Sn segregates in inter-grain

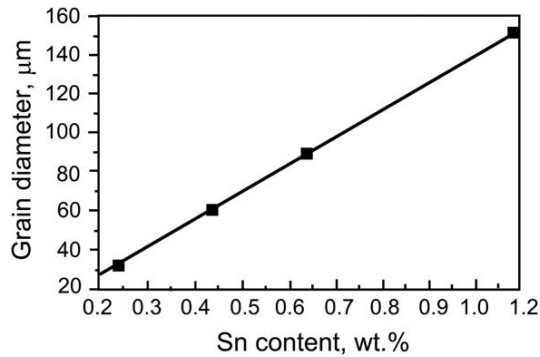


Figure 4.33:

Grain diameter as a function of Sn content (X) in Pb–0.12 wt% Ca– X wt% Sn alloys [70].

regions and calcium precipitation changes from cellular to continuous precipitation to form more stable $(\text{PbSn})_3\text{Ca}$ [69,70,74]. The size and type (morphology) of the particles exert an influence on the mechanical and corrosion properties of Pb–Ca–Sn alloys.

4.5.2. Mechanical Properties of Pb–Ca–Sn Alloys

Metallic lead has a low melting point ($T = 327^\circ\text{C}$). This allows diffusion of the alloying elements into the lead matrix at room temperature. These diffusion processes will result in the formation of inter-metallic compounds, which will alter the properties of the lead alloy with time. The changes in mechanical properties of lead alloys during ageing have been extensively studied. Some of the obtained results will be summarised below.

Figure 4.34 presents the age-hardening curves for Pb–Ca–Sn alloys with 0.06 wt% Ca content and two different concentrations of Sn [69]. The alloy with higher Sn content solidifies more

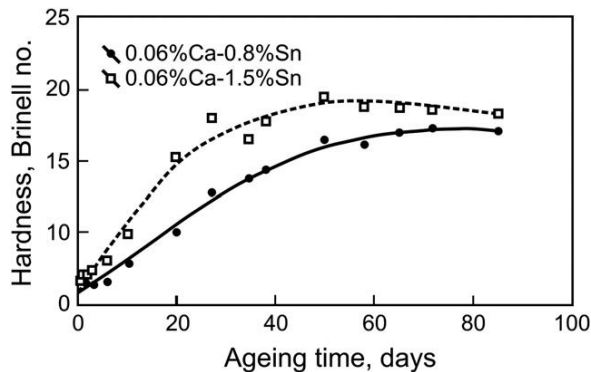
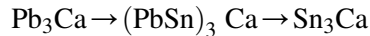


Figure 4.34:

Age-hardening of lead–calcium–tin alloys [69].

quickly and the casting has higher hardness as compared to the lower Sn counterpart. The mechanism of age-hardening is associated with structural transformation reactions:



After casting, the hardness of the Pb–Ca–Sn alloy increases rapidly with time through discontinuous precipitation of Pb_3Ca particles in the lead matrix, which then transform through continuous precipitation into very fine inter-metallic $(\text{Pb}_{1-x}\text{Sn}_x)_3\text{Ca}$ particles, thus leading to product *aged state*. The structural changes proceed further through a discontinuous precipitation process of lamellar and coarse $(\text{Pb}_{1-x}\text{Sn}_x)_3\text{Ca}$ particles, which leads to over-ageing of the precipitates and reduced hardness of the casting.

Figure 4.35 illustrates the different temperature–time zones of age-hardening of the Pb–0.11 wt% Ca–0.57 wt% Sn alloy. Zone A covers the discontinuous transformations; zone B is the zone of continuous precipitation of $(\text{Pb}_{1-x}\text{Sn}_x)_3\text{Ca}$ and zone C is the zone of discontinuous precipitation of lamellar $(\text{Pb}_{1-x}\text{Sn}_x)_3\text{Ca}$ phase [75].

The changes in mechanical properties, YS, UTS and creep resistance (CR), of fully aged cast lead–calcium–tin alloys with two different Sn concentrations (0.5 wt% Sn or 1.5 wt% Sn) as a function of Ca content are presented in Fig. 4.36. Data from Ref. [66] were used to plot these dependences. The alloys with low-Ca content (0.02 and 0.03 wt% Ca) have low mechanical properties which improve with an increase of the Ca content up to the peritectic concentration, pass through a maximum and decrease thereafter. All three measured parameters (YS, UTS and CR) have higher values when the alloys contain 1.5 wt% Sn (higher r value) than at the lower 0.5 wt% Sn level. Tin accelerates the precipitation reaction to completion. This holds for the whole range of calcium concentrations but proceeds at different rates.

The curves in Fig. 4.36 highlight clearly the peritectic region of the Pb–Ca system (0.07–0.08 wt% Ca) as the most appropriate for casting grids with high mechanical properties with the addition of considerable amounts of tin as well (above 1.0 wt% Sn). However, there is a second

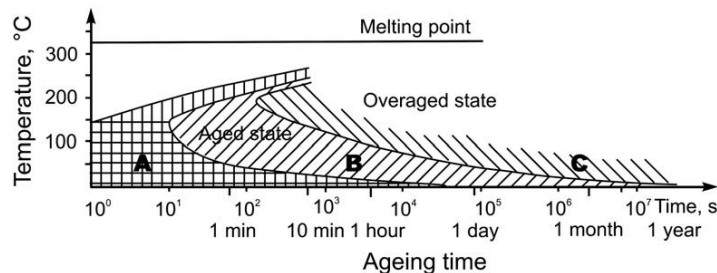


Figure 4.35:

Typical Temperature–Transformation–Time diagram (TTT diagram) of Pb–0.11 wt% Ca–0.57 wt% Sn alloy. Zone A: discontinuous transformation. Zone B: continuous precipitation of $(\text{Pb}_{1-x}\text{Sn}_x)_3\text{Ca}$. Zone C: discontinuous precipitation of lamellar $(\text{Pb}_{1-x}\text{Sn}_x)_3\text{Ca}$ [75].

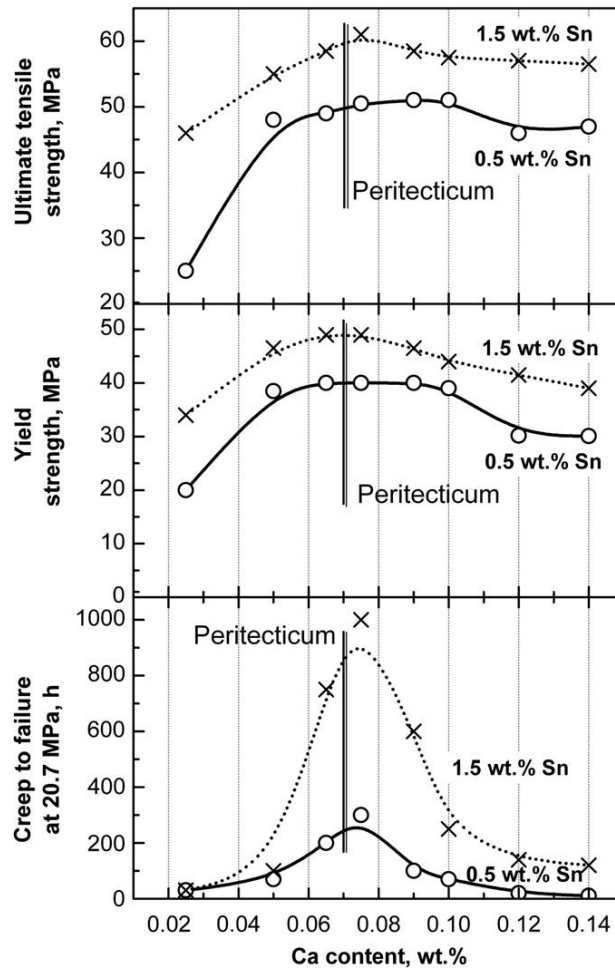


Figure 4.36:

Mechanical properties of cast lead–calcium–tin alloys with 0.5 or 1.5 wt% Sn contents. Data from ref. [66] are used.

important requirement to alloys to be used for casting grids, namely, to harden rapidly so that a high rate of the technological process of grid manufacture could be sustained. Alloys with 0.08–0.12 wt% Ca and 0.3–0.6 wt% Sn are most commonly used for VRLA batteries for stand-by and telecommunication service [66]. These alloys harden rapidly and the cast grids can be handled and processed further after a short ageing time at room temperature. Sometimes, battery manufacturers tend to make a compromise between grid parameters and production process duration. The mechanical properties of grids cast from Pb–Ca–Sn alloys depend very much on the technology of their manufacture and the subsequent treatment. One possible method to improve the mechanical parameters of Pb–Ca–Sn alloys is by rolling the

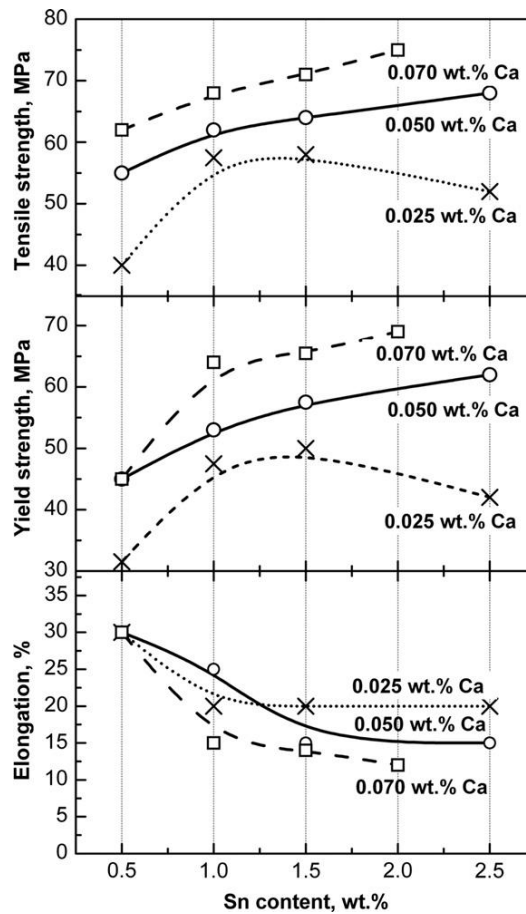


Figure 4.37:

Mechanical properties of wrought (rolled) lead–calcium–tin alloys with three different Ca concentrations. Data from ref. [18] are used.

material after casting. Figure 4.37 shows the dependences of YS, UTS and EL of Pb–Ca–Sn alloys with three different Ca concentrations below the peritectic value. The investigated samples were rolled at a reduction ratio of 10:1. Data from Ref. [18] are used.

The data in the figure indicate that rolling improves the mechanical properties of Pb–Ca–Sn materials. The alloys with a Ca content of 0.025 wt% reach maximum values of the mechanical parameters at 1.5 wt% Sn level. Alloys with higher Ca concentrations (0.05 and 0.07 wt% Ca) improve their mechanical properties with the increase of the Sn content up to 2.5 wt%. The mechanical parameters of rolled high-tin Pb–Ca–Sn alloys have values close to those of cast high-antimony lead alloys. Examinations of the microstructure of rolled Pb–Ca–Sn samples evidence particle orientation in the rolling direction.

The technological procedure of rolling is employed for the manufacture of expanded or die-cut (punched) grids from Pb–Ca–Sn alloys and yields high mechanical properties of the grids at high production rate.

4.5.3. Corrosion Resistance of Pb–Ca–Sn Alloys

Alloys with low r value (i.e., high concentration of calcium and low-tin content) have fine-grain structure. Figure 4.38 shows the correlation between corrosion rate and calcium content for Pb–Ca–Sn alloys with 0.5 or 1.5 wt% Sn content [18]. With increase of calcium content in the alloy, the r value decreases and the corrosion rate increases. When the Sn content is increased from 0.5 to 1.5 wt%, the r value increases from 7.1 to 21.4 at the peritectic phase composition of the ternary alloy and the corrosion rate decreases.

Figure 4.39 presents a micrograph of the CL formed on the spines of tubular plates cast from Pb–0.09 wt% Ca–0.3 wt% Sn alloy ($r = 3.33$) [18]. The battery suffered from PCL-1 effect and had low capacity. The picture features a thick CL with cracks parallel to the spine surface, which impair the contact CL|PAM. The appearance of these cracks can be attributed to the low creep resistance (30 h at 20.7 MPa). This is a value lower by more than a magnitude than the highest creep resistance measured for Pb–Ca–Sn alloys. The micrograph in Fig. 4.39

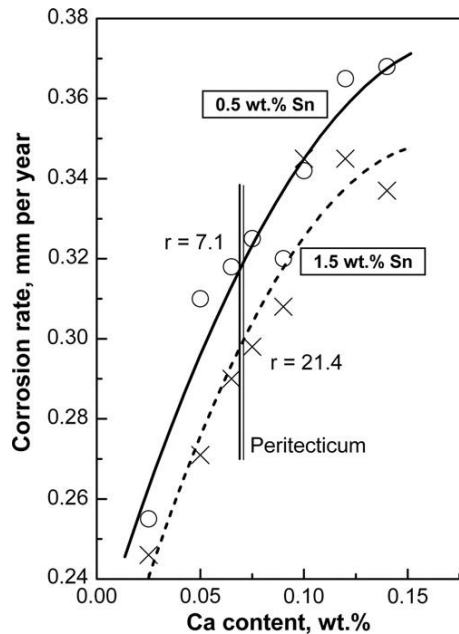


Figure 4.38:

Correlation between corrosion rate and Ca content for Pb–Ca–Sn alloys with two different Sn concentrations (0.5 or 1.5 wt% Sn). Data from ref. [18] are used.

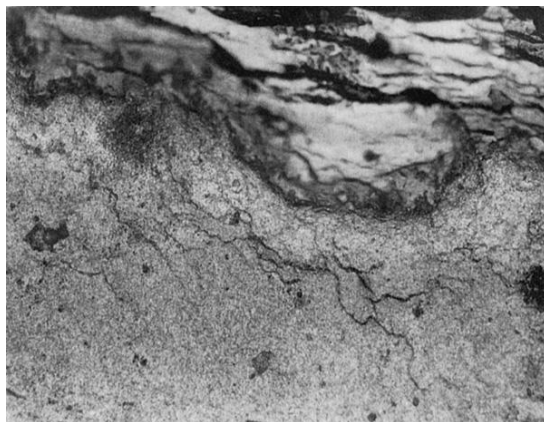


Figure 4.39:

Micrograph of the corrosion layer formed on a spine cast form Pb—0.09 wt% Ca—0.3 wt% Sn alloy. Magnification 160× [18].

evidences that the low creep resistance of the investigated alloy allows cracking not only of the CL but of the alloy itself, which opens the way for penetrating corrosion deep into the bulk metal. Thus, besides high corrosion resistance, grid alloys should have high creep resistance, too, to be able to ensure long battery cycle life. To achieve this, the alloys should have a higher r value.

Judging by the data in Fig. 4.36, the highest creep resistance is reached at the peritectic Ca composition. Figure 4.37 shows that at this concentration of Ca (0.07 wt%) the elongation is the lowest at Sn contents higher than 1.0 wt% for rolled products. The three-component alloy of such a composition will guarantee long battery cycle life if limited by the corrosion of the positive grids alone.

Figure 4.40 presents the changes in corrosion rate and oxygen evolution rate as a function of tin content in Pb—0.08 wt% Ca alloys on ageing [75]. With the increase of tin content, the rates of both corrosion and oxygen evolution decrease. The corrosion rate depends on the evolution rate of oxygen as the latter diffuses through the CL to the metal surface and oxidizes it. Figure 4.40 evidences that the presence of tin in the alloy increases the over-potential of oxygen evolution and thus reduces the rate of its evolution and hence the flow of oxygen accessing the metal.

It is evident from the data in Fig. 4.40 that ageing of the Pb—Ca—Sn alloys affects strongly the corrosion rate. Over-aged alloys suffer higher metal losses due to corrosion. The rate of the oxygen evolution reaction, too, increases in over-aged alloys. During overcharge, the content of tin in the precipitated $(\text{Pb}_{1-x}\text{Sn}_x)_3\text{Ca}$ particles increases at the expense of reduced tin concentration in the lead particles. This leads to reduction in the corrosion resistance of the particles during the over-ageing process. With the decrease of the Sn content in the lead

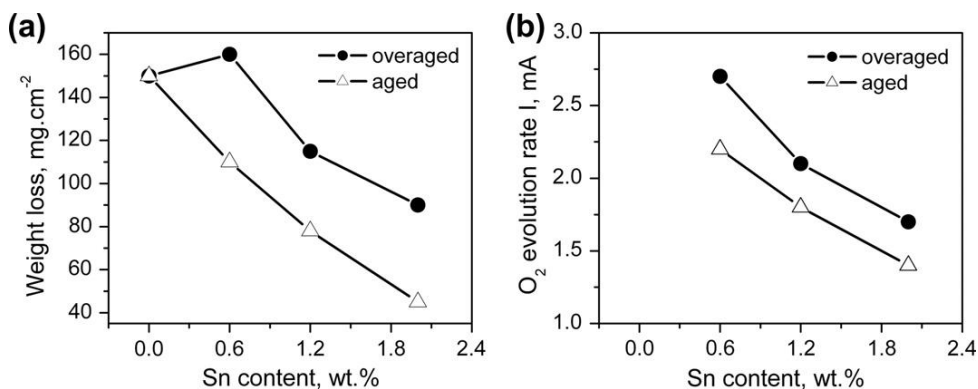


Figure 4.40:

(a) Weight loss and (b) Oxygen evolution as a function of Sn content (X) for Pb-0.08 wt% Ca-X wt % Sn alloys after 5 days of oxidation under overcharged conditions: +1.5 V (vs. Hg/Hg₂SO₄), 5 M H₂SO₄, 50 °C [75].

particles, the overpotential of oxygen evolution is lowered which facilitates the O₂ evolution reaction (Fig. 4.40b). Hence, the flow of oxygen into the CL is increased, inducing mechanical stresses which cause cracking or peeling of parts of the CL.

The above experimental results suggest that the evaluation of the corrosion resistance of lead alloys for battery grids should also account for the influence of ageing on the rate of corrosion as the lead-acid battery is a long-living product.

4.5.4. Electrochemical Properties of Pb-Ca-Sn alloys. Sn-Free Effect

When lead-calcium alloys were adopted for the manufacture of positive battery grids some unfavourable effects were observed, including (a) very low charge acceptance of the batteries during charge at constant voltage (1.1–1.3 V vs Hg/Hg₂SO₄); (b) significant reduction in battery discharge voltage when the positive plates were dried at temperatures higher than 80 °C after formation or when the batteries were stored for a longer period of time (i.e., thermopassivation or storage passivation); and (c) very low discharge power of the battery when kept under float conditions (at positive plate potentials of 1.1–1.3 V vs. Hg/Hg₂SO₄). These phenomena were found to be a result of the formation on the grid surface of a tet-PbO layer whose electrical properties determined the behaviour of the positive plates [76–78]. It was established that additions of tin to pure lead or to lead-calcium alloys improved substantially the charge acceptance of the positive plates. Therefore, this phenomenon was called Sn-free effect [77]. Tin additions to Pb-Ca and Pb-low Sb alloys suppressed significantly both thermopassivation and storage passivation [60,78,79]. This was found to be due to the fact that tin prevented the formation of a passive tet-PbO layer on the grid surface at potentials more positive than +1.0 V vs. Hg/Hg₂SO₄ electrode. An electro-conductive PbO_n layer formed instead.

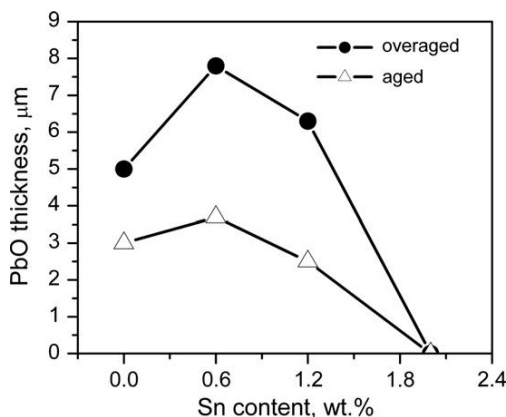


Figure 4.41:

Thickness of the PbO layer formed on Pb—Ca—Sn alloys after oxidation for 7 days under deep-discharge conditions: +0.7 V, 0.5 M H_2SO_4 , room temperature [75].

Figure 4.41 presents the thickness of the tet-PbO layer formed on aged and over-aged Pb—0.08 wt% Ca alloys, after 7 days of oxidation at +0.7 V (vs. $\text{Hg}/\text{Hg}_2\text{SO}_4$ electrode) in 1 M H_2SO_4 solution at room temperature, as a function of Sn content in the alloy [75]. The maximum thickness of the PbO layer is reached at 0.6 wt% Sn level and the rate of its formation decreases rapidly with further increase of the Sn content, to stop altogether in the alloy with 1.8 wt% Sn. The PbO layer formed on the over-aged electrodes is much thicker because this layer forms during the over-ageing time prior to polarization.

Basic conclusions about the effects of tin in Pb—Ca—Sn alloys

Tin improves the mechanical properties of Pb—Ca—Sn alloys. It reduces the passivation phenomena that proceed on the positive battery plates and improves the corrosion resistance of the positive grids. Tin increases also the creep resistance of the Pb—Ca—Sn alloys and thus sustains a good contact between the CL and the PAM. The combination of high corrosion resistance and high creep resistance of the grids prolongs the cycle life of the batteries.

Besides the above-mentioned effects, tin has also a beneficial influence on the casting process, reducing the metal losses during casting and contributing to the ease and stability of the process itself. The only disadvantage of tin is its fairly high price, but the expenditure is worth in view of the important beneficial effects of tin on the performance of the battery.

Lead—calcium—tin alloys with 0.06–0.08 wt% Ca and 0.6–1.5 wt% Sn are used for the manufacture of positive grids for maintenance-free, valve-regulated, automotive and stationary batteries. Cast grids have a coarse-grained structure and ensure stable battery operation. They are highly corrosion resistant and thus can guarantee long cycle life of the battery.

The above lead–calcium–tin alloys are suitable for rolling into thin strips. The strip is then expanded or punched into grids. Industrial production of such grids can be realised at a high rate and their properties yield battery life comparable to that of batteries with lead–high–antimony grids.

4.5.5. Additives to Pb–Ca–Sn Alloys

Barium

Albert et al. doped a Pb–0.07 wt% Ca–1.2 wt% Sn–0.009 wt% Al alloy with barium and investigated its mechanical, corrosion and electrochemical properties, as well as the changes in alloy microstructure with ageing [80,81]. This alloy was called Ba-Tech[®] alloy [81]. Negative grids produced by the continuous casting technology using Ba-Tech[®] alloy have enhanced mechanical properties (Fig. 4.42a), which allows manufacture of thinner but reliable grids. Positive grids, rolled or continuous cast, exhibit low growth rate (high creep resistance, Fig. 4.42b) even at high temperatures (60 °C), high mechanical properties, uniform corrosion at a very low rate and much longer battery cycle life at high temperatures (Fig. 4.43) than any other battery type [81].

Furukawa Battery Co. Ltd has also developed Pb–Ca–Sn–Ba alloy for battery grids. Figure 4.44 presents the correlation between the corrosion rate and the growth rate within one cycle for grids made from (a) Pb–0.06 wt% Ca–1.2 wt% Sn, (b) Pb–0.04 wt% Ca–0.60 wt% Sn–0.03 wt% Ag and (c) Pb–Ca–Sn–Ba alloy of optimized composition (called C-21 alloy) [82]. The batteries were tested at 75 °C employing the Hot SAE J240 standard. The C-21 alloy exhibits the highest corrosion resistance and the lowest growth rate as compared to the Pb–Ca–Sn and Pb–Ca–Sn–Ag grids.

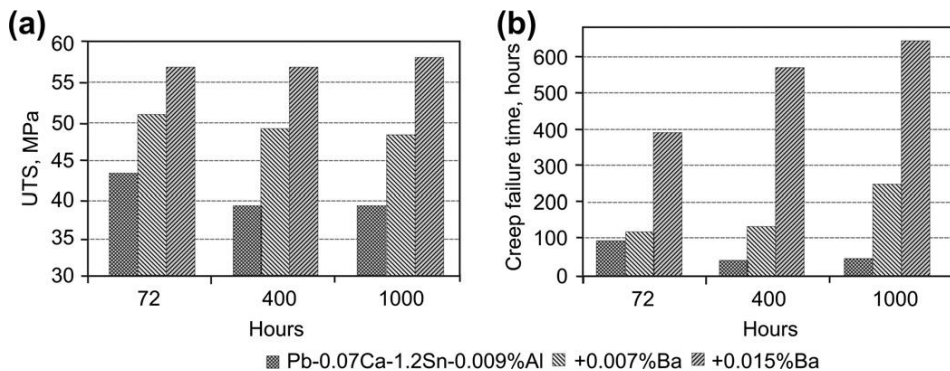


Figure 4.42:

- (a) Ultimate tensile strength (UTS) of expanded grids vs time at 60 °C, with or without barium doping;
 (b) creep resistance of expanded grids vs time at 60 °C, of undoped and doped alloys [80].

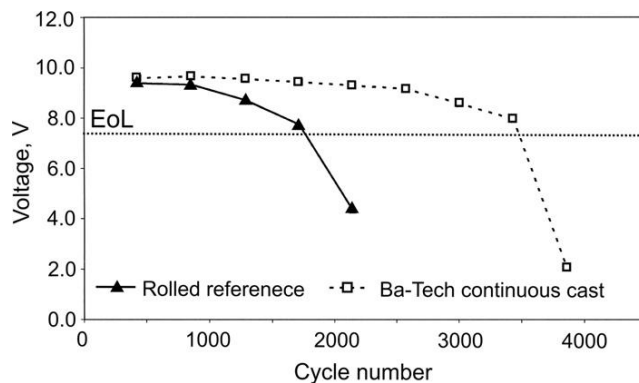


Figure 4.43:

Hot SAE J240 cycle-life test at 75 °C of batteries with rolled or Ba-Tech grids [81].

Batteries assembled with 1.30-mm-thick grids cast from C-21 alloy and others with 1.45-mm grids cast from conventional Pb–Ca–Sn alloy were set to cycling tests. The obtained results are presented in Fig. 4.45 [82]. The battery with C-21 alloy grids has longer cycle life despite the thinner grids. Obviously, addition of barium improves the mechanical, corrosion and electro-chemical properties of the grids, and extends battery life on cycling at high temperatures. Furukawa Battery Co. Ltd has employed this alloy in its ‘Gold Series’ SLI batteries with a 3-year warranty and 60,000 km driving range. Lead–calcium–tin–barium alloys tend to win important positions in the battery industry, especially for batteries intended for high-temperature duties.

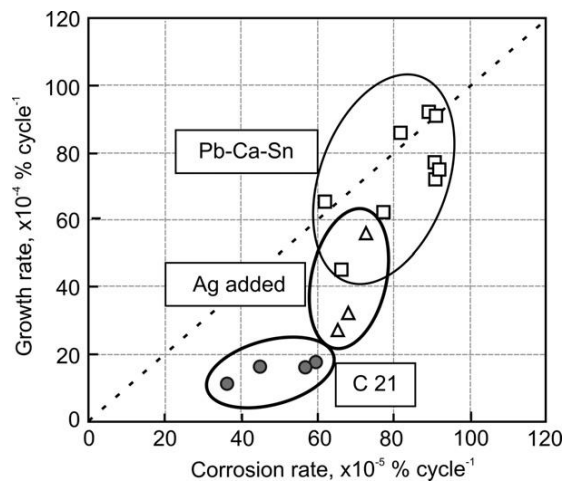


Figure 4.44:

Relationships between grid corrosion rate and growth rate under Hot SAE J240 cycling regimen for grids made from: Pb–Ca–Sn, Pb–Ca–Sn–Ag or Pb–Ca–Sn–Ba (C21) alloys [82].

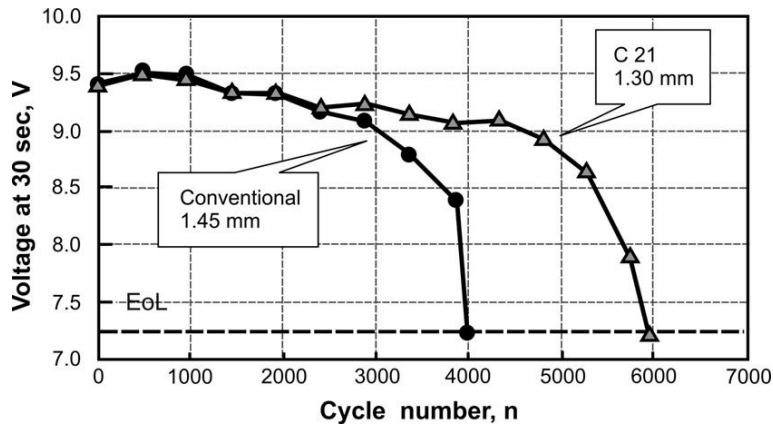


Figure 4.45:

Cycle lives of batteries with thicker conventional grids and thinner C21 grids under Hot SAE J240 cycling test [82].

Silver

It has been established that addition of silver in 0.05 wt% concentration improves the mechanical properties of Pb–Ca–Sn alloys and retards the ‘over-ageing processes’ [83]. Silver content in the alloy should be less than 0.1 wt% because higher amounts of Ag make the grid bars brittle due to decohesion at the grain and sub-grain boundaries [84]. Addition of Ag to the grid alloy above a definite concentration is known to lower the overpotential of hydrogen evolution and hence increase gassing [85].

Silver has long been known to reduce the corrosion rate of lead alloys. The effects of Ag on the behaviour of batteries with lead–calcium–tin–silver grids have also been studied. Table 4.5 presents the compositions of the alloys used for casting the grids for these test batteries. The batteries were set to the TC-96 cycling test at 100% depth of discharge. Figure 4.46 shows the obtained capacity curves [83]. The battery with Pb–0.077 wt% Ca–0.64 wt% Sn–0.048 wt% Ag grids (Ag-rich I alloy) has longer cycle life and sustains higher capacity values than the battery with 0.107 wt% Ag in the grid alloy (Ag-rich II alloy). The increased tin content from 0.64 to 1.20 wt% (Sn-rich alloy) extends most significantly the cycle life of the battery, but its

Table 4.5: Composition of test alloys [83].

Alloy	Ca (ppm)	Sn (wt%)	Ag (ppm)
Reference	790	0.64	30
Sn-rich	790	1.20	29
Ag-rich I	770	0.64	480
Ag-rich II	750	0.64	1070

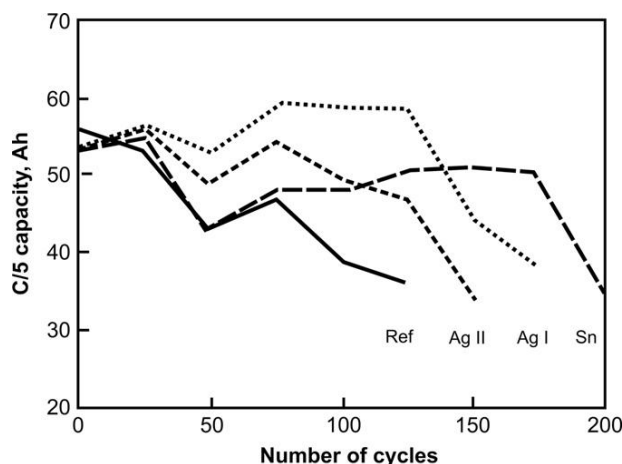


Figure 4.46:

C/5 capacity vs. cycle number during the TC-69 cycling test at 100% depth of discharge for batteries with lead–calcium–tin–silver grids. The grid alloy compositions are presented in Table 4.5 [83].

capacity is lower than that of the battery with 0.048 wt% Ag in the grid (Ag-rich I alloy) [83]. These experimental findings indicate that the effect of silver on battery performance parameters should be evaluated only in the context of the amount of tin in Pb–Ca–Sn–Ag alloys. At tin loading levels above 1.0 wt%, the beneficial effect of 0.05 wt% Ag in the alloy on battery cycle life is suppressed. Silver addition in concentration of 0.05 wt% has a pronounced positive effect on battery performance provided the content of tin in the alloy is less than 1.0 wt%.

Bismuth

Bismuth has properties similar to those of lead, which is the reason why it is very difficult and expensive to remove it during the manufacture of lead with 99.99% purity, especially when the Bi content is less than 250 ppm. It is therefore very important, for both lead manufacturers and battery manufacturers, to define the maximum admissible concentration of Bi in the lead alloys for the battery industry. Large-scale investigations of the effects of bismuth on the performance of lead–acid batteries have been performed. As evident from Figs 4.22 and 4.23, Bi improves significantly the bonds between the lead dioxide particles of the PAM and thus enhances the charge efficiency of the positive plates [47,48]. Bismuth at a concentration of 0.05 wt% is reported to improve the capacity and charge acceptance of VRLA batteries. It promotes the segregation in Ca-rich and Bi-rich regions and thus accelerates the movement of grain boundaries in the casting. These effects are observed in Pb–Ca–Sn alloys with high r values and are assumed to improve the re-chargeability of the battery after deep discharge [86]. At Bi levels below 0.08 wt%, it has no effect on the gassing rate in the battery [87]. Other experiments have proved that bismuth suppresses the evolution of hydrogen and enhances the oxygen reduction reaction [88]. On cycling according to the SAE J240 standard, batteries

with Pb–0.07 wt% Ca–0.7 wt% Sn–Bi grids exhibit extended cycle life performance when the Bi content in the four-component alloy is increased from 7 to 480 ppm [89]. At concentrations higher than 0.05 wt%, Bi may react with Ca to form Bi_3Ca_2 compound, which has a detrimental effect [90]. Incorporation of Bi in the Pb–Ca–Sn–Al alloy improves the electro-conductivity of the passive lead oxide CL formed on the positive grids, which has a beneficial effect on battery charge and suppresses the passivation phenomenon on the positive plates [47].

Aluminium

Aluminium can be alloyed in the molten lead via a tin–aluminium master alloy [89]. The simplest method to protect Ca in the Pb–Ca–Sn alloys from oxidation during the grid-manufacturing process is to add aluminium to the alloy. Figure 4.29 illustrates this effect of Al. A loading level of 0.015 wt% Al in the alloy is sufficient to prevent Ca loss during grid casting [36]. The influence of Al on the properties of lead–calcium alloys and on the process of their manufacture has already been discussed earlier in this chapter. It has an analogous effect on lead–calcium–tin alloys as well.

4.6. Lead–Tin Alloys

Lead–tin alloys with Sn content from 0.7 to 1.2 wt% Sn are used for casting grids for spirally wound and prismatic VRLA batteries for automotive, stationary and special purpose applications. Table 4.6 presents a summary of the mechanical properties of Pb–1.0 wt% Sn alloys with or without 0.06 wt% Ca [91].

The data in the table evidence that the Pb–1.0 wt% Sn alloy has catastrophically poor mechanical properties. As this alloy is easy to bend, it is used for casting grids for spirally wound batteries. Handling of Pb–Sn grids in the process of plate manufacture requires special attention and automated machines are used for the purpose. However, Pb–Sn grids are characterised by high corrosion resistance and tin ions incorporated in the CL of the positive plates improve significantly its electro-conductivity as they catalyse the formation of PbO_n ($1 < n < 2$). Through this influence of Sn on the CL composition it prevents the occurrence of the PCL-1 (Sn-free) effect [60]. Battery grids from Pb–Sn alloys are produced by the continuous cast technology or by rolling lead–tin sheets into strips which are then punched or expanded into grids.

Table 4.6: Mechanical properties of Pb–1.0 wt% Sn alloys with or without 0.06 wt% Ca [93].

Alloy	Yield Strength (MPa)	Tensile Strength (MPa)	Elongation (%)	Creep Hours to Failure at 20.7 MPa
Pb–1.0 wt% Sn	4.5	12.3	55	0
Pb–1.0 wt% Sn –0.06 wt% Ca	46.2	55.2	24	800

Lead–tin alloys are most widely used in the cast-on-strap technology for the manufacture of connector straps or for the production of terminals for maintenance-free VRLA batteries. The Sn content of alloys for these applications varies between 0.8 and 2.5 wt% Sn. If Pb–Sn alloys with low Sn concentration are used for the cast-on-strap process, it may yield unreliable strap-to-lugs connections. To avoid this, the grid lugs are previously plated with a lead–tin solder alloy (pre-tinning). Then they are placed on the mould for casting the strap and connecting it to the plate lugs.

A correlation has been found to exist between the conditions of thermal processing of the grids on casting and their mechanical properties and corrosion resistance. The thermal treatment parameters affect the sizes of the lead particles (grains) in the cast grids [92]. The coarser grain structure of Pb–(1–2.5) wt% Sn alloys yields improved corrosion resistance due to the reduction of cellular boundaries. The alloy microstructure depends on the rate of melt cooling. An optimum cooling rate of between 1.5 and 0.8 °C s⁻¹ has been established for the Pb–1.0 wt% Sn alloy and between 0.6 and 0.5 °C s⁻¹ for the Pb–2.5 wt% Sn alloy [92]. Such cooling rates yield cast grid microstructure that guarantees minimum corrosion and optimal mechanical properties [92].

In valve-regulated lead–acid batteries of the absorptive glass mat (AGM) type, the connecting strap (top lead) and the plate lugs are covered by a thin liquid film of H₂SO₄ solution [93]. The H₂SO₄ is consumed for the formation of a lead sulfate CL. The liquid film has high ohmic resistance and hence the strap and the plate lugs are cathodically unprotected. As a result of this, often the life of the battery is limited by corrosion of the negative semi-block (plate group) top lead. Lead–tin alloys are used for the production of the straps for the above battery type. It has been established that the potential of that part of the electrode immersed in H₂SO₄ solution controls the potential of the electrode up to a height of 1 cm above the solution level. The CL formed on the electrode surface above the solution (in the air space) features zones of different phase compositions. It is a common practice to add Na₂SO₄ to the electrolyte of batteries operating at remote locations (e.g., in the mountains) so as to improve the conductivity of the solution on deep discharge cycling.

Investigations have been carried out using Pb–2 wt% Sn electrodes (in the form of straps 6 cm long, 0.8 cm wide and 0.15 cm thick) partly inserted into AGM soaked in H₂SO₄ or (H₂SO₄ + Na₂SO₄) solutions. Figure 4.47 presents the measured weight losses of the electrodes with time of stay in oxygen atmosphere at 50 °C [93].

Additions of Na₂SO₄ to the sulfuric acid solution lead to a seven-fold increase of the corrosion rate. This is probably due to the increased solubility of PbSO₄ in the presence of Na⁺ ions in the solution and hence to the modified structure of the CL.

Figure 4.48a shows the corrosion transients for electrodes cast from Pb–2.0 wt% Sn or Pb–2.0 wt% Sn–0.03 wt% Se alloys and partly inserted in AGM soaked in H₂SO₄ solution. The transients obtained for electrodes immersed in AGM soaked in H₂SO₄ + Na₂SO₄ solution are presented in Fig. 4.48b.

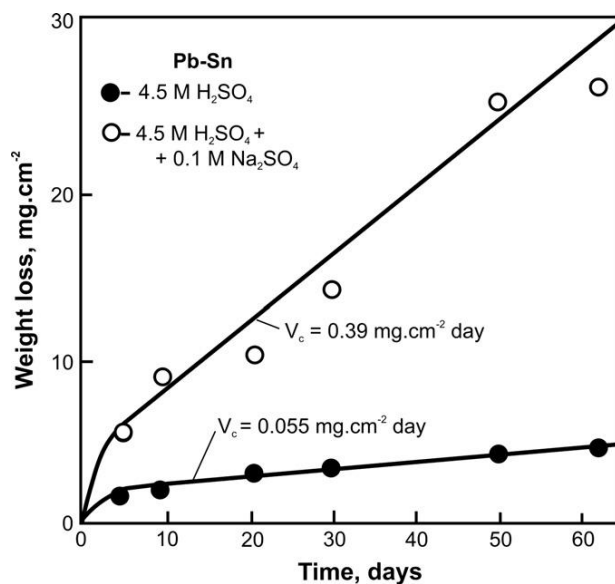


Figure 4.47:

Weight losses of Pb—2.0 wt% Sn electrodes with time of stay at 50 °C in oxygen atmosphere [93].

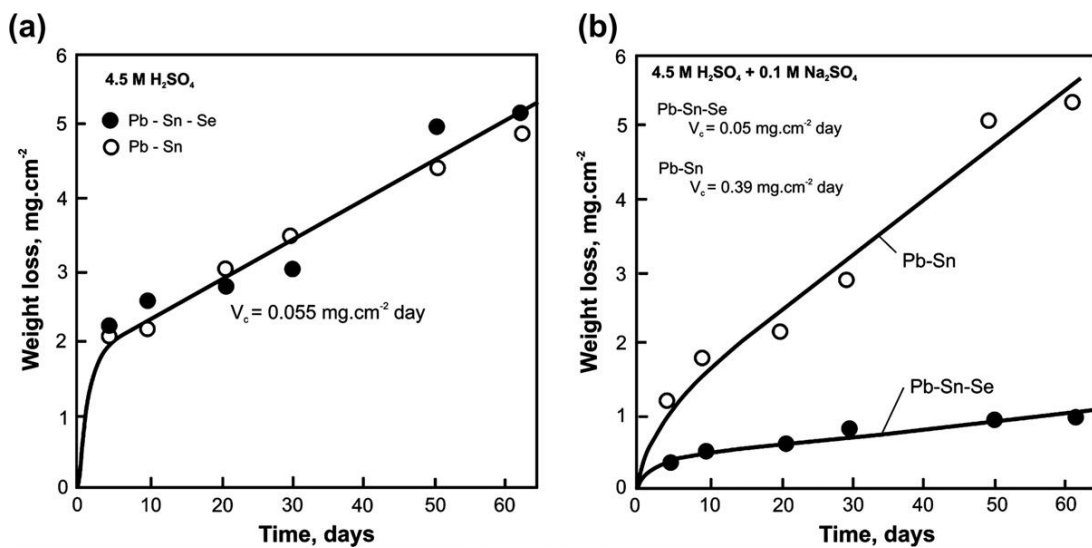


Figure 4.48:

Corrosion transients for Pb—2.0 wt% Sn and Pb—2.0 wt% Sn—0.03 wt% Se electrodes partly inserted in AGM soaked in (a) H₂SO₄ and (b) H₂SO₄ + Na₂SO₄ solution [93].

Additions of selenium to the electrode alloy do not have a notable effect on the rate of corrosion, when the Pb–2.0 wt% Sn electrodes are immersed in H_2SO_4 solution. The situation is different, however, when the AGM is soaked in $\text{H}_2\text{SO}_4 + \text{Na}_2\text{SO}_4$ solution. In this case, Se strongly reduces the corrosion rate of Pb–2.0 wt% Sn alloys. Hence, the detrimental effect of Na_2SO_4 addition on the corrosion rate of Pb–2.0 wt% Sn alloys is suppressed by adding Se to the alloy. Figure 4.48 indicates that the corrosion rate of Pb–Sn–Se alloys is about eight times lower than that of Pb–Sn alloys in $\text{H}_2\text{SO}_4 + \text{Na}_2\text{SO}_4$ solution.

It has also been established that Pb–Sn alloys with Sn content below 1.0 wt% are subject to higher corrosion rates. Selenium suppresses this effect, too, in alloys containing 0.6 wt% Sn. Selenium has an anti-corrosion effect and acts as grain refiner in Pb–Sn alloys, reducing also the size of PbSO_4 crystals and facilitating their nucleation [93].

4.7. Grid Design Principles

The grids for SLI, traction and stationary batteries are rectangular in shape. A conventional battery grid comprises a thick frame housing a network (mesh) of horizontal and vertical wires (current collectors), and a lug to carry the current into or out of the plate (Fig. 4.49). The grids support the positive and negative active materials of the plates, conduct the current throughout the plate volume, absorb the mechanical stresses incurred by the pulsation of the active masses on cycling (during discharge, the active masses expand in volume and then shrink during

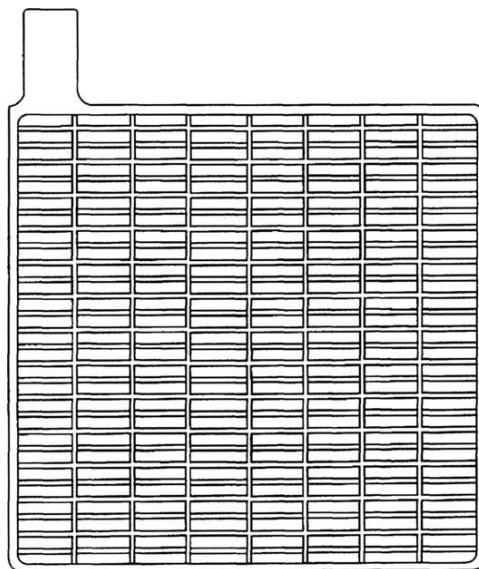


Figure 4.49:
Conventional flooded battery grid design.

re-charge). The positive grids should have high corrosion resistance to sustain the cross section of the grid wires and not limit battery power output. Besides, the grid design should ensure very good electrical and mechanical contact between the grid surface and the active material.

A basic requirement to the grid design is that its wires (current collectors) are positioned so as to cause minimum ohmic drop in the plate and to ensure uniform current distribution throughout the plate and thus guarantee that the electrochemical reactions proceed at a uniform rate.

Current is collected and drawn through the lug which is located on the upper plate frame bar. The grid design affects the ohmic drop in the plate at high current drains. Pasted plates (SLI, traction and stationary) generally have a rectangular structure of the grid wire network. Traction batteries use diamond-shaped grids. Current flow towards the lug, i.e., the current collecting ability, is improved in this grid design. The grid structure could be significantly improved by directing more vertical wires towards the plate lug, thus shortening the electric current path from each part of the plate to the plate lug and hence reducing the voltage drop. To achieve this, the plate lug should be positioned closer to the midpoint on the upper frame bar.

Figure 4.50a,b shows two variants of such battery grid designs. A grid pattern with a vertical lug passing along the whole plate height from bottom to top of the plate and collecting the current from the horizontal bars is also presented in the figure (Fig. 4.50c). The latter grid configuration is suitable for high-power batteries, but is heavier than conventional grids.

Besides the requirements for adequate electrical, mechanical and corrosion properties of the grids, the grid pattern should allow easy casting with no defects. The process of double-grid casting provides high productivity and has therefore been widely adopted in the battery industry.

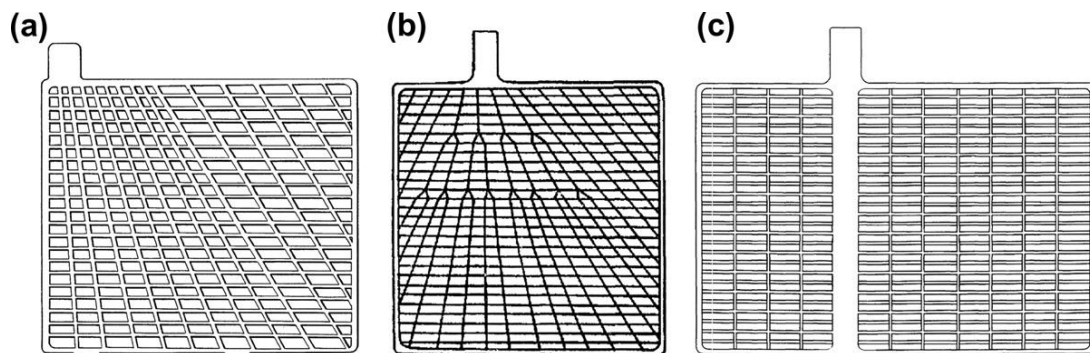


Figure 4.50:

Rectangular grids (a,b) with diagonal wires directed to the lug and (c) with a vertical lug crossing the grid from bottom to top and conducting (collecting) the current from the horizontal wires.

Positive plates are made thicker than their negative counterparts in order to compensate for corrosion and thereby extend battery service life. The negative semi-block (lead plate group) contains one plate more than the positive one. Only in special cases the number of plates in the two semi-blocks is equal. Current density and capacity of the cell is evaluated with regard to the positive semi-block. Typical plate thicknesses employed by the battery industry for SLI battery plates are 1.0–1.4 mm for negatives and 1.2–1.8 mm for positives. Heavy-duty batteries use 1.6–2.5-mm-thick plates, whereas traction plates are between 3 and 6 mm thick.

Both the lead and the lead dioxide active materials are electro-conductive and conduct electrons from the site of the electrochemical reaction to the nearest grid wire. During discharge, 30–50% of the active materials react forming PbSO_4 (which is an insulator). Consequently, the ohmic resistance of the active materials (i.e., of the active mass skeleton) increases, thus reducing their utilization, especially at high discharge currents. Therefore, the size of the active mass pellets confined between the grid wires is very important for the performance of the plates.

The correlation between grid design (geometry) and active material utilization was investigated using four types of plates with grids of different local geometry (Fig. 4.51): a conventional rectangular plate (A), expanded metal plate (C), tubular plate (B) and a plate with felt mat of fine titanium fibres (D) [94]. The right-hand part of the figure shows the dependence between the active mass utilization coefficient (at 5-h rate of discharge) and the distance between the grid wires. The utilization coefficient is found to increase from 25% to 80% with decrease of the distance between the grid bars from 6 mm to 0.1–0.2 mm. However, the corrosion rate of the positive grid increases with the decrease in grid bar cross section. Obviously, the efforts of grid designers should be aimed at finding a compromise between the

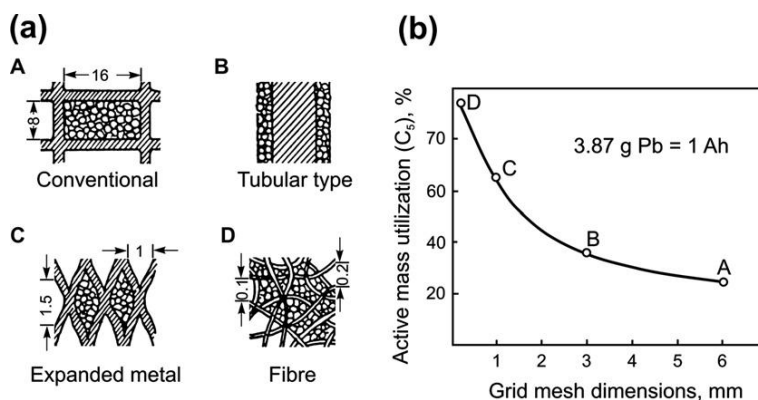


Figure 4.51:

(a) Grids of different local geometry: conventional rectangular plate (A), tubular plate (B), expanded metal plate (C), and felt mat of fine titanium fibres (D) [94]. (b) Active mass utilization vs local grid geometry [94].

active mass utilization coefficient and the corrosion rate, which limits battery service life. The negative plate does not suffer from such problems and hence even non-lead conductive materials may be used for the negative grids.

There are numerous patents in the literature proposing different methods to improve the electro-conductivity of the active materials at the end of discharge by adding various conductive materials to the active mass, such as graphite, active carbon, titanium oxides, glass fibres coated with tin dioxide. As evident from Fig. 4.51, the simplest way is to reduce the dimensions of the grid mesh openings (i.e., of the active mass pellets between the grid bars), which, however, makes the battery heavier and more expensive.

A positive SLI plate that contains 100 g PAM has an active surface of about 500–700 m² on which the electrochemical reactions take place, whereas the surface of the grid with rectangular geometry through which the current flows is only about 40–50 cm². That is, the current generated on the PAM surface area has to be concentrated to pass through the 1 million times smaller current collector surface. This requires an appropriate PAM structure with adequate contact to the grid that would ensure efficient and low-ohmic electron concentration during charge and electron distribution through the grid to PAM during discharge, causing no polarization of the plate. In this context, the skeleton of the PAM, which takes but a small part in the electrochemical reactions but serves mainly as current conductor in PAM, plays an important role [95]. A layer is formed in the PAM whose basic function is to collect the current from every point in PAM and conduct it to the CL during charge. During discharge, this layer collects the current from the CL and distributes it throughout the PAM. This layer has been denoted as ‘active mass connecting (collecting) layer’ (AMCL). Thus, the structure of the grid|PAM interface consists of two parts: CL and AMCL [95].

A key parameter in designing battery plates is the ratio (α) between the grid weight (W_{grid}) and the active mass weight (W_{PAM}), i.e.,

$$\alpha = W_{\text{grid}} / (W_{\text{PAM}} + W_{\text{grid}})$$

The value of α varies between 0.35 and 0.60, with a tendency to reduce this value as much as possible, as the plate capacity depends on the amount of active mass contained.

Battery designers should use also a second parameter (γ) which accounts for the critical role of the grid|PAM interface under deep-cycling duty. The γ coefficient reflects the amount of active mass per square centimetre of grid surface (S_{grid}) (g PAM cm⁻² grid collector surface) [95], i.e.,

$$\gamma = W_{\text{PAM}} / S_{\text{grid}}$$

The value of γ depends on the plate construction. This can be demonstrated by the cross section of two plates of different designs (Fig. 4.52).

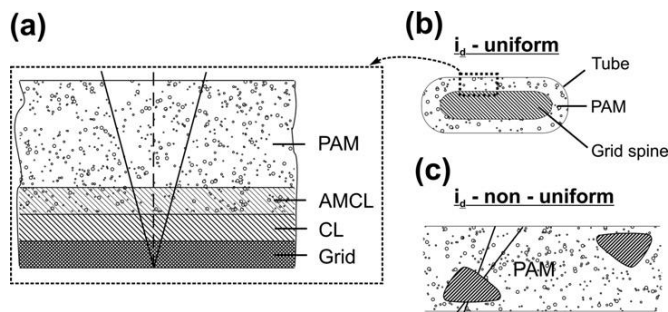


Figure 4.52:

Influence of grid and plate design on the uniformity of current distribution over the grid surface. (a,b) flat surface covered with a uniform PAM layer — uniform current density; (c) non-uniform current density at grid|PAM interface [95].

In the first type of plate design (Fig. 4.52a,b) a flat surface is covered with a uniform active mass layer and γ will have a constant value throughout the whole collector surface. This will allow a current of uniform density (i_d) to pass through the grid|PAM interface. In the second plate design, the collector consists of grid wires located asymmetrically in the plate cross section (Fig. 4.52c). The value of γ in this case will vary along the grid wire surface. This will result in a non-uniform current distribution over the grid surface. Thus, one of the basic principles in designing positive plates is to guarantee uniform distribution of the active mass over the grid wires.

For SLI positive plates, $\gamma = 2\text{--}2.5 \text{ g cm}^{-2}$, and for tubular plates, $\gamma = 1.6\text{--}1.8 \text{ g cm}^{-2}$. In an effort to improve PAM utilization, positive plates have been designed in the author's laboratory with $\gamma = 0.8 \text{ g PAM cm}^{-2}$ grid surface [95].

Besides the γ coefficient, the active mass utilization is also influenced by the specific resistance of the grid|PAM interface and it depends on the grid alloy composition. Hollenkamp et al. have measured the changes in the contact surface resistance (R_c) between the PAM and the grid during discharge of plates with grids cast from different alloys [96]. The obtained results for four types of plates are presented in Fig. 4.53. At the beginning of discharge, the R_c values are about $50 \text{ m}\Omega$ for all four grid alloys. Further during the discharge, an increase in the contact resistance (to $200 \text{ m}\Omega$) limits the capacity of the plates down to 53% for pure Pb or to 63% for Pb–0.1 wt% Ca, against 97% for the Pb–5.3 wt% Sb grids. The grid|PAM interface has no capacity-limiting effect on the Pb–2.2 wt% Sb–0.1 wt% Sn plates. These results indicate that the capacity of plates with pure Pb and Pb–Ca grids is limited by the electrical conductivity of the grid|PAM interface, whereas in the case of Pb–Sb and Pb–Sb–Sn plates the capacity is limited rather by the properties of PAM [96]. Addition of tin to the grid alloy contributes dramatically to increasing the electro-conductivity of the interface grid|PAM.

Stationary batteries for uninterruptible power supply (UPS) systems as well as some automobile batteries are demanded to be able to deliver high power. As the electrochemical

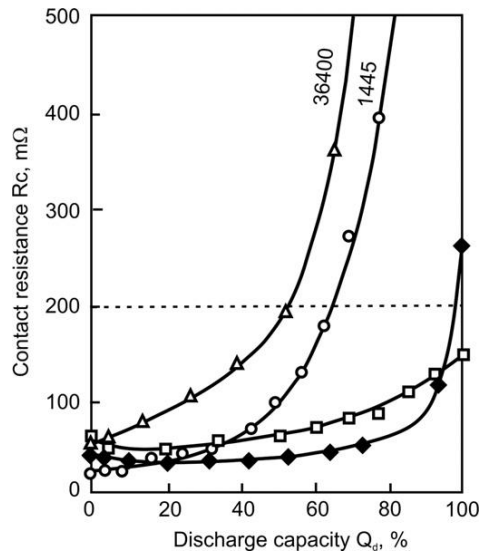


Figure 4.53:

Contact surface resistance (R_c) vs. % discharge capacity (Q_d) (100% DOD) for positive plates with grids cast from different alloys: (Δ) pure Pb; (\circ) Pb–0.1 wt% Ca; (\blacklozenge) Pb–5.3 wt% Sb; (\diamond) Pb–2.2 wt% Sb–0.1 wt% Sn [96].

reactions proceed on the electrode surface, it is important that the battery design provides high active surface. This can be achieved by the use of a great number of thin plates with thin grids. The latter should have high corrosion resistance as well. This is not always a realistic goal and the possible compromise is high battery power output at the expense of short service life (2 years).

4.8. Grid/Spine Casting

The quality of cast grids depends on the temperature regimen during casting and on alloy composition and crystallization. The process conditions should be adjusted to the specific alloy composition and grid design.

Battery grids are cast either by gravity or under pressure. The automatic casting machine should meet the requirements of the constant rhythm of the casting process, i.e., continuous movement of melt and grids, as well as constant temperature of the melt in the pot and in the different zones of the mould. A modern automatic casting machine operates at a speed of 10–16 castings per minute. One casting shot produces a double SLI or a single traction battery grid. The mould comprises two halves that are grooved to form the grid. The melt is poured into the closed mould and the latter is kept closed until the metal solidifies. Then the two halves of the mould are opened and the casting is ejected by a special system. The mould has a pouring lip for the distribution of the melt to the grooves, a temperature control system, a gas removal

system for the evacuation of air from the mould grooves, a mechanical system for the synchronous opening and closing of the mould, and a mechanism for ejecting the casting.

The heat released during solidification of the casting is released from the mould to a special cooling system comprising channels with running water, which allow faster cooling of the melt. There is also an electrical heating system in the mould. Thus, precise temperature control of both melt and mould is realised by the cooling and heating systems. The temperature in the mould depends on the freezing range of the alloy used.

To ensure high quality of casting at a high production rate, the surface of the mould must be covered with a heat-insulating coat. The function of this coat is to reduce the heat dissipation rate to a low level and reduce the friction during the movement of the melt in the casting mould. The coat has a porous structure to facilitate the separation of the casting from the mould.

Cork powder ($50\text{--}100\text{ g L}^{-1}$) and sodium silicate ($10\text{--}15\text{ g L}^{-1}$) are generally used for the mould coat, although other components are sometimes included, too, e.g., carboxy methyl cellulose (CMC). The cork suspension is sprayed onto the mould surface and heated to $80\text{--}90\text{ }^{\circ}\text{C}$. During casting, the cork powder gradually burns away, and a new coating is usually applied once or twice a shift.

The gravity method is used for casting grids for pasted plates, whereas the pressure-casting process is employed in the production of spines for tubular plates. The latter method yields castings with a stronger structure and is used especially for the production of long spines. The pressure-casting process has lower productivity as compared to the gravity-casting process, which makes the technological process of pressure casting more expensive.

Gas-tight moulds, with a buffer space for the compressed air, are used in the pressure casting process. The rated casting pressure is $6\text{--}8\text{ kg cm}^{-2}$ for alloys containing $8\text{--}11\text{ wt\% Sb}$ and is increased to $10\text{--}12\text{ kg cm}^{-2}$ for alloys with $5\text{--}8\text{ wt\% Sb}$.

The German company HADI Maschinenbau GmbH has developed high pressure-casting machines for casting spine grids from $\text{Pb}\text{--}1.8\text{ wt\% Sb}$ alloys. These grids have reduced substantially the need for maintenance of both traction and stationary batteries.

4.9. Continuous Plate Production Process

A medium-size automotive battery plant produces between 50 and 80 million plates a year. These huge production volumes require a great number of casting machines and numerous workers. During the 1970s and 1980s, the efforts to make the technology of battery grid manufacture more effective resulted in the development of the continuous plate production process, wherein a continuous grid strip was cast first which was then pasted and overlaid with paper on both sides. The pasted grid strip was cut into individual plates which were then oven cured and dried. The adoption of this technique in the battery industry lead to a 10-fold increase

in productivity. Several methods for continuous plate manufacture were developed for the production of SLI plates. Figure 4.54 presents a scheme of the existing technological processes for continuous production of battery grids and plates. These include the following principle techniques:

- a. *Continuous expanded grid production process.* One expansion method involves partial slitting of a rolled metal sheet cast from Pb—Ca—Sn or low-antimony alloy (0.8–1.22 mm thick) and then stretching (expanding) the wrought strips to form a diamond grid structure (Fig. 4.55) [97].

The expanded diamonds are formed symmetrically on both sides of the strip and comprise two components, nodes and strands (or wires), formed by three different processes: slitting, stretching and expanding (Fig. 4.56) [98]. In this technological process, slitting is carried out by two methods: reciprocation cut and rotary cut. The strands are transformed into wires by stretching, and the unaltered part of the strip forms the nodes. The next process is the formation of grid lugs in the central part of the strip that has not been subjected to expansion.

This technique was first used only for the manufacture of negative grids because expanded positive grids suffered from severe corrosion. However, with the improvement of the rolling

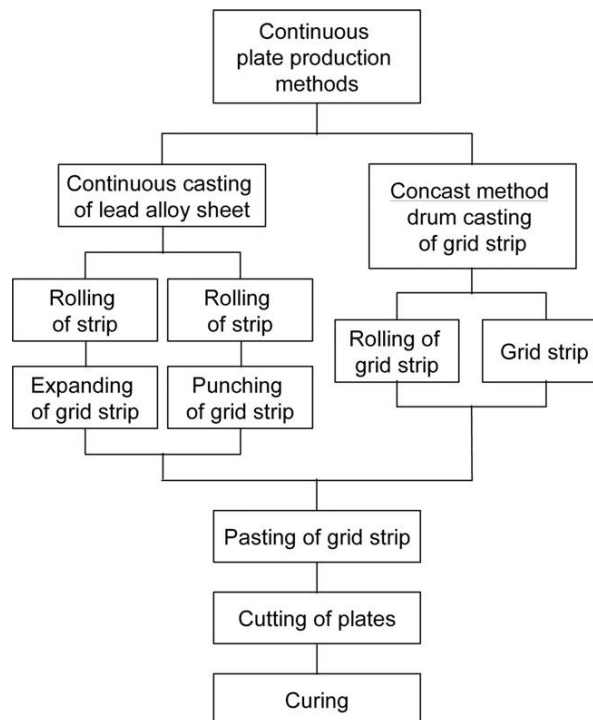
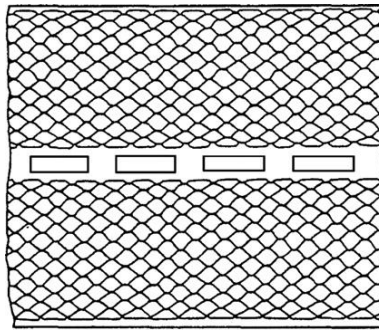
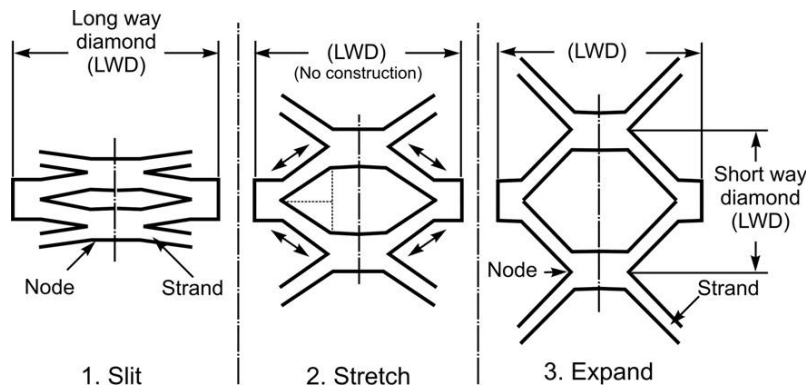


Figure 4.54:

General scheme of the most common methods for continuous grid and plate production.

**Figure 4.55:**

Expanded metal grid strip used for continuous plate production in the automotive battery industry [97].

**Figure 4.56:**

Scheme of metal grid expanding process [98].

process and optimization of the Pb–Ca–Sn alloy composition, the corrosion of the positive grids was suppressed to acceptable levels. Thus, the technological process of expanding grid strips and then pasting the strips and cutting them into individual grids quickly gained a significant share of the SLI and later of the AGM maintenance-free battery market, thanks to its low cost, high productivity and minimum waste production. However, this technology has some disadvantages as well. The diamond grid structure geometry depends on the expansion process. The current collecting wires are not oriented towards the plate lugs and hence the resistance of expanded grids is higher than that of conventional cast grids and cannot be optimized. But this method eliminates the time-consuming procedures of the batch grid casting process and their dependence on the personal skills of the operator. Another limitation of the continuous expanded grids production process is that it requires higher capital investments and would be effective only for the production of large series of grids of the same design.

- b. *Continuous punched grid production process.* In this process a metal strip is continuously cast first and is then die-cut into punched grids. Punched grids have a frame and may comprise wires of appropriate cross section, oriented towards the lugs, thus reducing the electrical resistance of the grids (Fig. 4.57).

Lead–calcium–tin alloys with low-Ca content are used for the manufacture of grids by the punching method. After casting, the metal strip is rolled before being punched. The rolling procedure allows manufacture of thin grids and improves the corrosion and creep resistance of the grid alloy. The major disadvantage of the punching method is that it produces considerable amounts of waste which is returned for re-melting. Thus, during the punched grid production process an ample quantity of melt circulates between the melting pot and the punching machine, which is associated with considerable energy consumption and loss of material. Punched grids are used for heavy-duty batteries.

The rolled Pb–Ca–Sn strips attain maximum mechanical and creep resistance properties during the reduction of the alloy strip thickness at a reduction ratio of 4:1 before expanding or punching. On further deformation of the metal sheet the mechanical parameters deteriorate, but still even at a thickness reduction ratio of 10:1 the rolled Pb–Ca–Sn alloy strip has superior mechanical properties than gravity cast grids.

- c. *Continuous drum-casting process for grid production (Concast process).* The lead alloy is poured into a casting shoe sliding on a rotating drum. The casting shoe is shaped to the contour of the drum surface and pressed against the drum. As in the case of book-mould grid casting, multiple grid patterns are engraved onto the drum surface. These grid engravings are filled with molten alloy through a slot in the casting shoe. The casting shoe is outfitted with cooling devices which very quickly cool the metal in the grooves on the drum surface and it solidifies. The drum rotates and the cast grid strip is

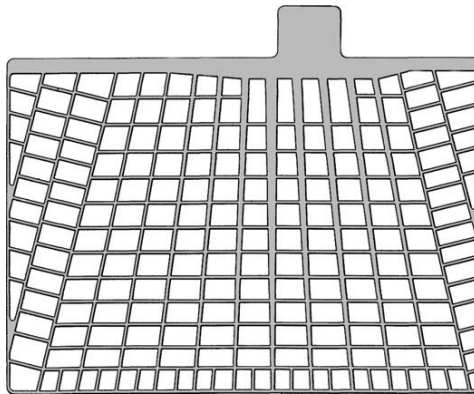


Figure 4.57:
Punched grid from cast or rolled metal strip.

detached from the drum surface and moves on for further processing. Application of this method is limited to the production of thin grids only because the lead/lead alloy melt in the grid moulds on the drum surface has to cool down very quickly and solidify before leaving the rotating drum.

WIRTZ Manufacturing Company offers the continuous casting—continuous rolling process (ConCast-Con-Roll), where after casting of the grid strip it passes between a series of compression rolls (rolling mills). Thus, the grain size structure is changed, which results in higher tensile strength and improved corrosion resistance. Besides, the contact surface of the grid with the active mass is increased.

After the manufacture of the grid strip by one of the above-described methods, the latter is pasted and cut into plates. An illustration of the continuous plate production process is presented in Fig. 4.58 [99]. The US company MAC Engineering and Equipment Co., Inc., was a pioneer in developing a continuous plate-making system. After casting, expanding and shaping the grid strips, the latter are pasted and coated with sheets of paper on both sides. Then the strips are cut into plates, which are then dried and stacked on pallets for curing. This continuous plate-making process is very efficient and labour saving. It reduces both production costs and pollution of the working areas and the environment. This process allows manufacture of plates with an active mass to grid ration of 2:1, which results in enhanced specific parameters of the battery. The system finds ever-increasing application in the manufacture of maintenance-free SLI batteries.

Contemporary continuous grid- and plate-manufacturing processes are highly improved and use optimized grid designs and fully automated machines and production lines.

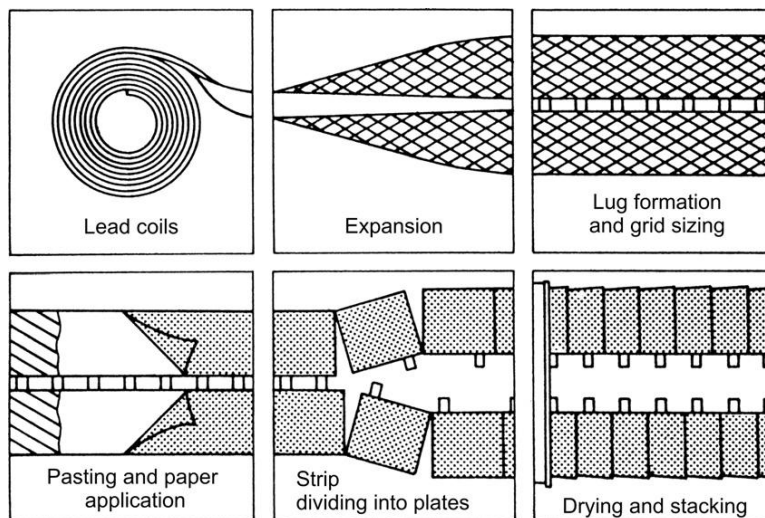


Figure 4.58:

Schematics of continuous process for manufacture of plates with expanded grids [99].

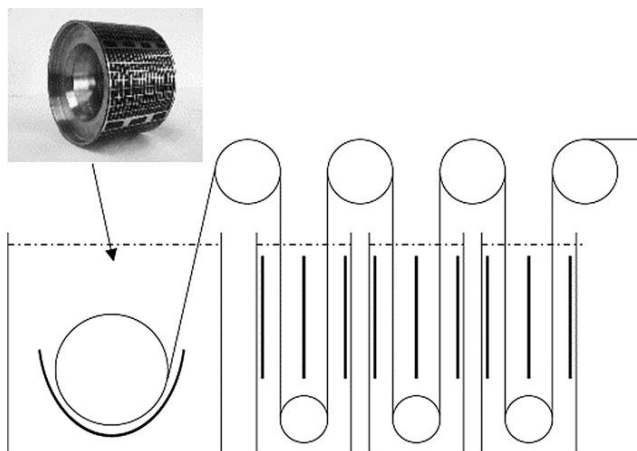


Figure 4.59:

Principle of grid production by continuous electroforming and strip galvanizing process. The structured cylinder (shown in insert), the strip passing through the equipment and the upper system of rolls form the cathode. The bold lines indicate the anodes [100].

There is no doubt that the continuous grid/plate production technology is most convenient for the manufacture of standard plates for SLI batteries and will certainly compete with the existing casting methods. However, the latter will preserve positions in the battery industry, provided the process is sufficiently flexible with regard to grid size/geometry.

A new continuous electroforming process to manufacture lead grids for automotive and industrial lead–acid batteries has been developed by DSL Dresden Material-Innovation GmbH [100,101]. A galvanic cell comprising a drum cathode for electro-forming and a subsequent series of galvanic cells which form a strip-galvanizing line are operating in a single continuous process (Fig. 4.59).

The cathode in the first cell, on which the electroforming of the grid takes place, is a cylinder with a surface comprising conductive and non-conductive areas according to the desired grid design. While the cylinder revolves at a pre-determined rate, an initial grid strip is deposited onto the conductive parts of the surface. The strip is about 50–150 μm thick. The deposit is stripped continuously from the cylinder surface. This thin grid strip is then immediately passed through a galvanizing line. The line consists of several cells in which the strip is plated further until it reaches a specified thickness, typically in the range from 0.4 to 2.0 mm. This method is still in the development phase.

4.10. Tubular Positive Plates

Tubular plates are used mainly for high-capacity long-cycle-life batteries. The latter find application in industrial in-house transport vehicles (forklifts, electric cars, etc.) as well as for

stationary reserve energy storage (thousands of Ah). Tubular plates are produced with low-antimony or Pb—Ca—Sn multi-spine grids with high tin content for flooded, VRLA and gel-type batteries. Tubular plates are designed to protect the active material from shedding during battery service. Tubes retain the active mass and secure its contact with the spine. Tubes should be resistant to both H_2SO_4 and strongly oxidizing media, and should be highly porous so as to allow electrolyte and ions to pass freely, but they should not be permeable to the PbO_2 and PbSO_4 crystals. Figure 4.60 illustrates a standard tubular plate design.

A series of parallel spines (current collectors) are connected at the upper end to a common connector bar (connector bus) which ends with a plate lug. The spines are positioned in the centre of tubes made of either woven, braided or felt acid-resistant glass wool or synthetic organic fibres. Depending on their shape (cross-sectional geometry), tubes may be cylindrical (round), elliptical (oval) or rectangular (square). Cylindrical tubes with the spines (current

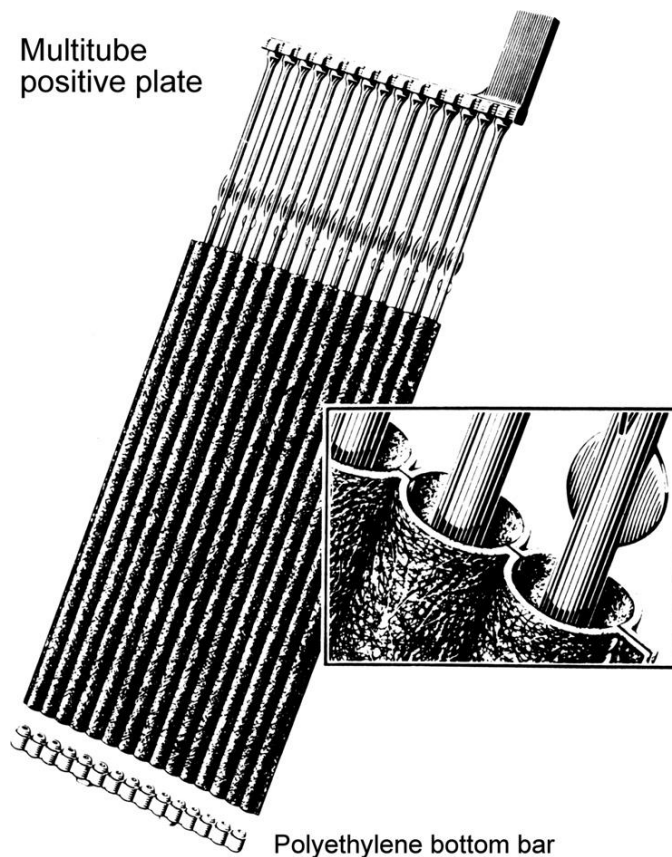


Figure 4.60:
Construction of a multi-spine gauntlet tubular plate.

collectors) positioned in the centre are most commonly used. The active material is contained in the tubes between the tube walls and the central spine. Tubes with a diameter of 8.0–8.4 mm are most frequently used and the layer of active material is 2.0–2.2 mm thick. The number of spines in a grid is between 15 and 19. The multi-spine (comb-like) grids are manufactured by book-mould pressure casting.

Tubular plates offer several advantages over the flat-plate grid design, the most important of which is that they prevent shedding of the PAM during battery service as it is held within the tubes. Thus, a lower density of the active material can be used. The typical active mass density for tubular plates is 3.6–4.0 g cm⁻³ (cf. 4.0–4.3 g cm⁻³ for flat-pasted plates). In addition, the enhanced porosity of the tubular plates improves the active mass utilization coefficient.

A further advantage is that the spine is coated with a layer of active material which protects it from corrosion. It has been experimentally established that tubular positive plates with 4-mm-diameter spines can complete 1500 charge/deep-discharge cycles, whereas flat-pasted plates with grids of the same thickness endure only 800 cycles before corrosive attack causes failure.

Figure 4.61 shows the correlation between the corrosion rate of the spines and the thickness of the positive active material for tubular electrodes with pure Pb, Pb–4.9 wt% Sb or Pb–10.6 wt% Sb spines [102]. The corrosion rate of spines covered with 1-mm-thick PAM layer is twice lower than that of the same spines when unprotected by PAM. On electrode polarization, oxygen is evolved mostly in the outer PAM layers and has to pass through thicker PAM and CLs before reaching the spine surface, i.e., its diffusion gradient decreases.

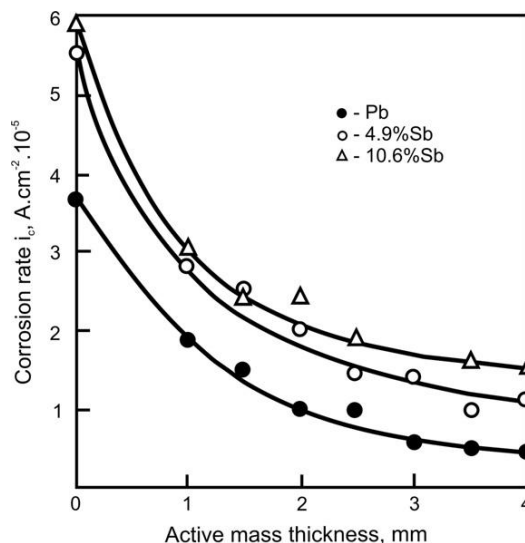


Figure 4.61:
Relationship between spine corrosion rate and active mass thickness [102].

However, tubular plates have some disadvantages as well. Their production is a bit more expensive. Furthermore, the contact area between the lead current collector and the active material is reduced when cylindrical spines are used. Thus, under continuous heavy current drains, the increased current density at the spine|active mass interface leads to higher polarization and local heating, which may cause cracking of the CL.

The conventional cylindrical tube design has a γ coefficient of 2.20–2.50 g PAM cm^{-2} of spine surface. At such a high γ coefficient, the current density at the interface spine|PAM is high and hence the plate polarization will be high, too. In order to increase the contact surface spine|PAM, the tube shape is changed to flattened elliptical and the spine is substituted for a strap [95,103]. Figure 4.62 presents schematics of a strap grid tubular plate. Cross-sectional views of cylindrical (Fig. 4.62a) and flattened elliptical (Fig. 4.62b) tubes are given in the figure. The thickness of the active mass layer between strap (current collector) and tube wall is 1.0–1.2 mm and the overall plate thickness is from 4.0 mm to maximum 5.0 mm. In this tubular plate design, $\gamma = 0.90\text{--}1.20$ g PAM cm^{-2} strap surface and batteries with strap grid tubular plates have higher power output than batteries with conventional cylindrical tubular plates, preserving the latter's long cycle life performance.

Round (cylindrical) tubes are generally used in flooded batteries, whereas the preferred tube shape for VRLAB is the rectangular (square) design because it ensures good contact of the AGM separator with the whole plate surface. The latter tube shapes are illustrated in Fig. 4.63.

Figure 4.64 shows the specific capacity of the PAM vs discharge current density for batteries with three types of plates: SGTP, SLI and cylindrical tubular plates [103]. Batteries with SGTP

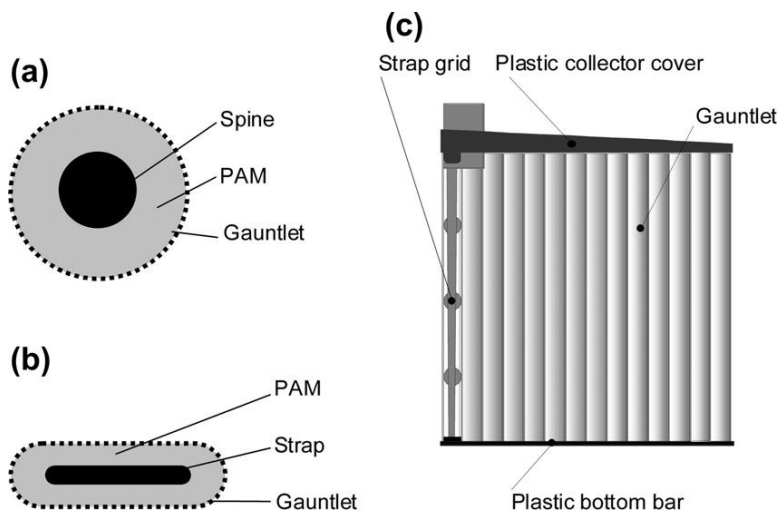
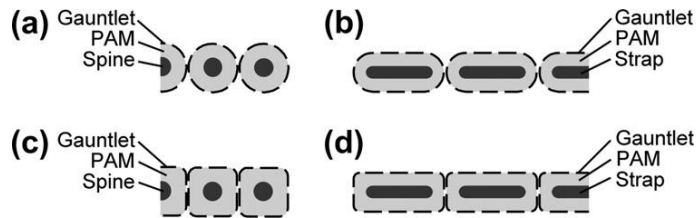
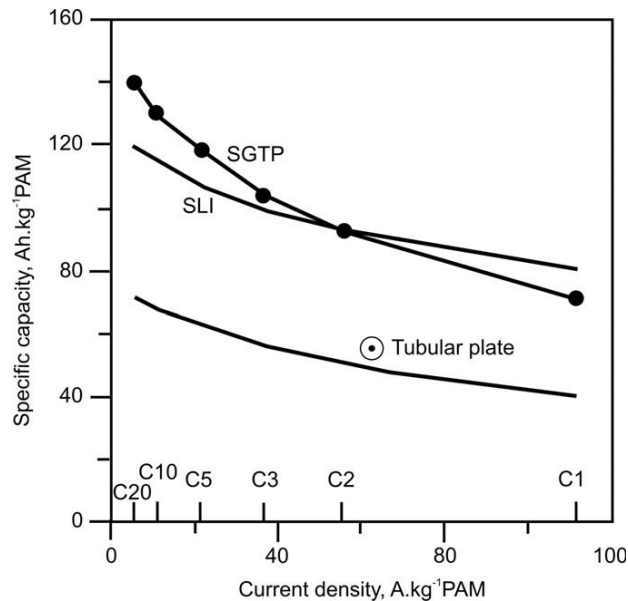


Figure 4.62:

Schematic representation of three tubular plate designs: (a) cylindrical tube cross section; (b) elliptical tube cross section; (c) strap grid tubular plate construction.

**Figure 4.63:**

Cross section geometry of four types of tubular plates: (a) cylindrical (round), (b) elliptical (oval), (c) square and (d) rectangular. Cylindrical and elliptical tubular plates are used for flooded batteries, whereas square and rectangular designs are preferred for VRLA batteries with AGM separators.

**Figure 4.64:**

Specific capacity of the positive active mass vs discharge current density for three types of batteries: SGTP, SLI and conventional cylindrical tubular plates [103].

plates have a Peukert dependence almost equal to that of SLI batteries [103]. This makes SGTP batteries suitable for use in both high-energy and high-power battery applications. The cycle life of these batteries reaches 900–1000 cycles.

4.11. Copper-Stretch-Metal Negative Grids

High-capacity batteries have tall cells (resp. tall plates). With increase of cell height the electrical resistance of the grids increases. As a result of this the plates undergo lower depth of discharge at

the bottom of the cell, which leads to a substantial potential difference between the top and bottom parts of the plates. Moreover, the higher grid resistance causes increased heat generation in the cell and hence increased energy loss. In an attempt to resolve these problems, the standard lead grids were replaced with copper grids for the negative plates. Copper has a specific electrical conductivity $\sigma = 59.6 \times 10^6 \text{ S m}^{-1}$ and that of lead is 10 times lower, $\sigma = 5.0 \times 10^6 \text{ S m}^{-1}$. Plates taller than 45–50 cm are produced with copper-stretch-metal (CSM) grids.

Copper strips are expanded to form grids with diamond-shaped structure of the grid wires. The expanded copper strip is then cut into individual grids. Top lead bars with lugs and bottom bars are cast, and the grids are covered with a thin layer of lead. Such a CSM grid design is presented in Fig. 4.65 [97]. The thus produced grids are then subjected to the subsequent technological procedures of pasting, curing and formation.

Negative plates with CSM grids ensure much more uniform proceeding of charge and discharge processes throughout the whole plate surface, which contributes to higher

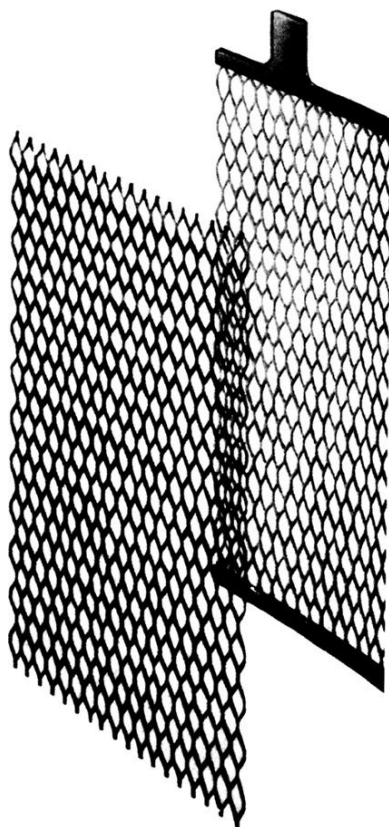


Figure 4.65:
CSM grid as basic material and after coating with a lead layer [97].

utilization of the active material. When conventional negative plates with lead grids are discharged at high currents, the local current density in the upper parts of the plates is much higher than that in the bottom parts. This non-homogeneity of current density may lead to sulfation of the bottom parts of the negative plates. It has been established that plates with CSM grids have about 17% lower electrical resistance than standard lead plates, which increases battery power output [104].

During charge, the copper grids ensure much more uniform current density distribution over the plate surface, and thus improve substantially the charge acceptance of the negative plates, which results eventually in improved energy performance of the battery. However, manufacture of negative plates with CSM grids involves a greater number of technological procedures and is therefore more expensive. The higher production costs of plates with CSM grids are worthwhile for the manufacture of batteries with high power and high capacity.

CSM grids are not suitable for positive plates because the corrosion will quickly 'eat up' the lead layer covering the grid and copper ions will diffuse to the solution and thus reduce the charge efficiency and accelerate greatly the self-discharge processes.

With this brief description of the CSM grid technology we will complete the overview of the most common grid alloys and grid design principles, and will continue further with the plate production processes.

References

- [1] D. Pavlov, E. Bashtavelova, J. Electrochem. Soc. 133 (1986) 241.
- [2] D. Pavlov, S. Ignatova, J. Appl. Electrochem. 17 (1987) 715.
- [3] D. Berndt, S.C. Nijhavan, J. Power Sources 1 (1976/77) 3.
- [4] H. Bode, in: R.J. Brodd, K.V. Kordesch (Eds.), Lead-acid batteries, translated, John Wiley & Sons, New York, 1977, p. 13.
- [5] D. Berndt, in: N.E. Bagshaw (Ed.), Maintenance-free batteries, Research Studies Press Ltd., John Wiley & Sons, New York, USA, 1993, p. 57.
- [6] D.M. Rice, J.E. Manders, J. Power Sources 67 (1997) 251.
- [7] J.R. Pierson, C.E. Weinlein, C.E. Wright, in: D.H. Collins (Ed.), Power sources 5, Academic Press, London, UK, 1975, p. 97.
- [8] L.T. Lam, J.D. Douglas, R. Pilling, D.A.J. Rand, J. Power Sources 48 (1994) 219.
- [9] M. Maja, N. Penazzi, J. Power Sources 22 (1988) 9.
- [10] K. Peters, in: D.A.J. Rand, P.T. Moseley, J. Garche, C.D. Parker (Eds.), Valve-regulated lead-acid batteries, Elsevier, 2004, p. 141.
- [11] L.T. Lam, O.V. Lim, N.P. Haigh, D.A.J. Rand, E.J. Manders, D.M. Rice, J. Power Sources 73 (1998) 36.
- [12] W. Brecht, Batteries International 30 (1997) 62.
- [13] M. Hansen, Constitution of binary alloys, McGraw-Hill Co., New York, 1958.
- [14] R.D. Prengaman, in: Proceedings of the 7th international lead conference, "Pb-80", Madrid, Lead Development Association, London, UK, 1980, p. 34.
- [15] W.F. Gillian, D.M. Rice, J. Power Sources 38 (1992) 49.
- [16] E.C. Rollason, Metallurgy for engineers, fourth ed., Edward Arnold Ltd., London, 1980, p. 96.
- [17] D. Pavlov, M. Botton, M. Stojanova, Bull. Inst. Chim. Phys. 5 (1965) 55.

-
- [18] R.D. Prengaman, *J. Power Sources* 53 (1995) 207.
 - [19] H. Borchers, W. Scharfenberger, *Metall* 20 (1966) 811.
 - [20] A.C. Simon, *J. Electrochem. Soc.* 114 (1967) 1.
 - [21] Z. Jiang, Y. Lu, S. Zhao, W. Gu, Z. Zhang, *J. Power Sources* 31 (1990) 169.
 - [22] G.W. Mao, J.G. Larson, *Metall. Dec.* (1968) 236.
 - [23] U. Heubner, A. Ueberschaer, *Metall.* 33 (1977) 963.
 - [24] W. Hume-Rothery, G.V. Raynor, *The structure of metals and alloys*, second ed., Institute of Metals, London, 1956.
 - [25] N.E. Bagshaw, *J. Power Sources* 33 (1991) 3.
 - [26] U. Heubner, *Erzmetall* 29 (1976) 41.
 - [27] S. Engler, Z.H. Lee, *Giessereiforschung* 28 (1976) 170.
 - [28] J.P. Hilger, *J. Power Sources* 53 (1995) 45.
 - [29] M. Torralba, *J. Power Sources* 1 (1976/77); 301.
 - [30] C.G. Fink, A.J. Dornblatt, *Trans. Electrochem. Soc.* 79 (1941) 269.
 - [31] V.P. Mashovets, A.Z. Lyandres, *Sov. J. Appl. Chem.* 21 (1948) 347.
 - [32] I.A. Aguf, M.A. Dasoyan, *Vestn. Elektroprom.* 10 (1959) 62.
 - [33] D. Pavlov, T. Rogatchev, *Werkst. Korros.* 19 (1968) 677.
 - [34] U. Heubner, A. Ueberschaer, in: *Proceedings of the 5th international lead conference*, Paris, 1974, 963.
 - [35] U. Heubner, I. Mueller, A. Ueberschaer, *Z. Metallkd.* 66 (1976) 74; 79.
 - [36] R.D. Prengaman, in: K.R. Bullock, D. Pavlov (Eds.), *Advances in lead–acid batteries*, The Electrochem. Soc. Inc., Pennington, NJ, USA, 1984, p. 201.
 - [37] B.E. Kallup, D. Berndt, in: K.R. Bullock, D. Pavlov (Eds.), *Advances in lead–acid batteries*, The Electrochem. Soc. Inc., Pennington, NJ, USA, 1984, p. 214.
 - [38] W.F. Gillian, *J. Power Sources* 19 (1987) 133.
 - [39] M.A. Dasoyan, *Dokl. Akad. Nauk. SSSR* 107 (1956) 863.
 - [40] M.A. Dasoyan, *Sov. J. Appl. Chem.* 29 (1956) 1827.
 - [41] W.F. Gillian, *J. Power Sources* 31 (1990) 177.
 - [42] A. Kirov, T. Rogatchev, D. Donev, *Metalloberflaeche* 26 (1972) 234.
 - [43] E.J. Ritchie, J. Burbank, *J. Electrochem. Soc.* 117 (1970) 357.
 - [44] J.L. Dawson, M.I. Gillibrand, J. Wilkinson, in: D.H. Collins (Ed.), *Power sources* 3, Oriel Press, Newcastle upon Tyne, 1970, p. 1.
 - [45] A. Boggio, M. Maja, N. Penazzi, *J. Power Sources* 9 (1983) 221.
 - [46] I.H. Yeo, D.C. Johnson, *J. Electrochem. Soc.* 134 (1987) 1973.
 - [47] D. Pavlov, A. Dakhouché, T. Rogachev, *J. Power Sources* 30 (1990) 117.
 - [48] D. Pavlov, A. Dakhouché, T. Rogachev, *J. Power Sources* 42 (1993) 71.
 - [49] B. Monahov, D. Pavlov, *J. Electrochem. Soc.* 141 (1994) 2316.
 - [50] H.E. Haring, U.B. Thomas, *Trans. Electrochem. Soc.* 68 (1935) 293.
 - [51] U.B. Thomas, F.T. Forster, H.E. Haring, *Trans. Electrochem. Soc.* 92 (1947) 313.
 - [52] E.E. Schumacher, G.M. Bouton, *Metals Alloys* 14 (1941) 865.
 - [53] G.W. Mao, J.G. Larson, P. Rao, *Metall* 1 (1969) 399.
 - [54] E.E. Schumacher, G.S. Phipps, *Trans. Electrochem. Soc.* 68 (1935) 309.
 - [55] E. Hoehne, *Z. Metallkd.* 30 (1938) 52.
 - [56] J. Burbank, A.C. Simon, E. Willihnganz, in: P. Delahay, C.W. Tobias (Eds.), *Advances electrochemical engineering*, vol. 8, Wiley Interscience, New York, 1971, p. 157.
 - [57] K. Fuchida, K. Okada, S. Hattori, M. Kono, M. Yamane, T. Takayama, et al., *Final Rep. ILZRO Project LE-276*, ILZRO, Research Triangle Park, NC, USA, 1982.
 - [58] A.E. Hollenkamp, *J. Power Sources* 36 (1991) 567.
 - [59] A. Kita, Y. Matsumaru, M. Shinpo, H. Nakashima; *International Power Sources Symposium*, in: L.J. Pearce (Ed.), *Power Sources*, 11, *Research and Development in Non-mechanical Electrical Power Sources*, Leatherhead, UK, 1986, p. 31.

- [60] D. Pavlov, B. Monakhov, M. Maja, N. Penazzi, J. Electrochem. Soc. 136 (1989) 27.
- [61] M.K. Dimitrov, D. Pavlov, J. Power Sources 46 (1993) 203.
- [62] D. Pavlov, J. Power Sources 42 (1993) 345.
- [63] A. Winsel, E. Voss, U. Hullmeine, J. Power Sources 30 (1990) 209.
- [64] E.E. Schumacher, G.M. Bouton, Metals Alloys 1 (1930) 405.
- [65] J. Perkins, G.R. Edwards, J. Mat. Sci. 10 (1975) 136.
- [66] R.D. Prengaman, in: D.A.J. Rand, P.T. Moseley, J. Garche, C.D. Parker (Eds.), Valve-regulated lead–acid batteries, Elsevier, Amsterdam, 2004, p. 15.
- [67] Sims R.J. US Patent 3,920,473, 1975.
- [68] N.E. Bagshaw, J. McWhinnie. US Patent 4,125,690, 1978.
- [69] C.S. Lakshmi, J.E. Manders, D.M. Rice, J. Power Sources 73 (1998) 23.
- [70] L. Bouirden, J.P. Hilger, J. Hertz, J. Power Sources 33 (1991) 27.
- [71] H. Borchers, H. Assmann, Z. Metallkd. 69 (1978) 43.
- [72] H. Borchers, H. Assmann, Metallurgia 33 (1979) 936.
- [73] H. Borchers, H. Scharfenberger, S. Henkel, Z. Metallkd. 64 (1973) 478.
- [74] R.D. Prengaman, J. Power Sources 33 (1991) 13.
- [75] E. Rocca, G. Bourguignon, J. Steinmetz, J. Power Sources 161 (2006) 666.
- [76] K.R. Bullock, M.A. Butler, J. Electrochem. Soc. 133 (1986) 1085.
- [77] H.K. Giess, in: K.R. Bullock, D. Pavlov (Eds.), Advances in lead–acid batteries, The Electrochem. Soc. Inc., Pennington, NJ, USA, 1984, p. 247.
- [78] D. Pavlov, B. Monakhov, M. Maja, N. Penazzi, Rev. Roumaine Chem. 34 (1989) 551.
- [79] K. Wiesener, J. Garche, N. Anastasijevich, J. Power Sources 9 (1983) 17.
- [80] L. Albert, A. Goguelin, E. Jullian, J. Power Sources 78 (1999) 23.
- [81] E. Jullian, L. Albert, J.L. Caillerie, J. Power Sources 116 (2003) 185.
- [82] J. Furukawa, Y. Nehyo, M.O.S. Takeshima, S. Shiga, Asian Batteries, Summer (2009) 28.
- [83] L. Albert, A. Chabrol, L. Torcheux, Ph. Steyer, J.P. Hilger, J. Power Sources 67 (1997) 257.
- [84] Ph. Steyer, J. Steinmetz, J.P. Hilger, J. Electrochem. Soc. 145 (1998) 3183.
- [85] R.D. Prengaman, Low gassing secondary soft lead, Eco-Bat Technology Ltd., 2009; Lecture.
- [86] R.D. Prengaman, J. Power Sources 42 (1993) 25.
- [87] T. Caldwell, V. Sokolov, L. Bocciarelli, J. Electrochem. Soc. 123 (1976) 1265.
- [88] M. Maja, N. Penazzi, J. Power Sources 22 (1988) 1.
- [89] J. Devitt, M. Myers, J. Electrochem. Soc. 123 (1976) 1769.
- [90] S. Zhong, H.K. Liu, S.X. Dou, M. Skyllas-Kazakos, J. Power Sources 59 (1996) 123.
- [91] R.D. Prengaman, in: J. Garche (Ed.), Encyclopedia of electrochemical power sources, vol. 4, Elsevier, 2009, p. 648.
- [92] L.C. Peixoto, W.R. Osorio, A. Garcia, J. Power Sources 195 (2010) 621.
- [93] D. Pavlov, M. Dimitrov, G. Petkova, H. Giess, C. Gnehm, J. Electrochem. Soc. 142 (1995) 2919.
- [94] P. Faber, in: D.H. Collins (Ed.), Power sources 4, Oriel Press, Newcastle upon Tyne, 1973, p. 525.
- [95] D. Pavlov, J. Power Sources 53 (1995) 9.
- [96] A.E. Hollenkamp, K.K. Constanti, M.J. Koop, L. Apateanu, M. Calabek, K. Micka, J. Power Sources 48 (1994) 195.
- [97] R. Wagner, in: J. Garche (Ed.), Encyclopedia of electrochemical power sources, vol. 4, Elsevier, 2009, p. 599.
- [98] G.H. Laurie, R.T. Sakauye, E.M. Valeriotte, in: Proceedings of the 156th ECS Meeting, Los Angeles, 1979, vol. 79–2, Ext. Abstr. No. 55, p.139.
- [99] D.C. Melnik, Battery Man 22 (1980) 2.
- [100] H. Warlimont, T. Hofmann, J. Power Sources 133 (2004) 14.
- [101] H. Warlimont, T. Hofmann, K. Jobst, J. Power Sources 144 (2005) 486.
- [102] T. Rogachev, G. Papazov, D. Pavlov, J. Power Sources 10 (1983) 291.
- [103] G. Papazov, D. Pavlov, J. Power Sources 62 (1996) 193.
- [104] R. Wagner, J. Power Sources 144 (2005) 494.

This page intentionally left blank

Lead Oxide

5.1. Physical Properties of Lead Oxide and Red Lead

5.1.1. Lead Oxide

Lead oxide (PbO) exists in two modifications (polymorphs): (1) red tetragonal lead oxide (tet-PbO) (also known as α -PbO or litharge) and (2) yellow orthorhombic lead oxide (orthorhomb-PbO) (also known as β -PbO or massicot). Tet-PbO is stable at low temperatures and low pressures. The transition temperature of tet-PbO to orthorhomb-PbO is 486–489 °C and the thermal effect of the transition is 1.35 kJ mol⁻¹. When orthorhomb-PbO is cooled rapidly, it may remain unchanged and continue to exist at low temperatures. Eventually, it is slowly transformed into tet-PbO under external physical action. Lead oxide exists also in amorphous form. The latter's amount depends on the method of manufacture of PbO.

The tet-PbO elementary (unit) cell is presented in Fig. 2.19. Tet-PbO has a well-defined layered structure. The bonds between the layers are a result of Pb–Pb interactions [1]. The layered structure is parallel to the (001) plane. The layers are arranged in a sandwich Pb–O–Pb structure. Within the sandwich, each Pb²⁺ ion is located at the top of a PbO₄ pyramid and all the Pb–O distances are identical and equal to 2.32 Å. To a first approximation, the Pb²⁺ ions can be considered as cubic packed. Oxygen ions use sp³ hybrid orbitals to form electron pairs with the lead atoms [2]. The bonds can be considered as approximately covalent. This localised electron distribution in PbO determines the latter's high electric resistance of 10¹² ohm cm [3].

Tet-PbO has a crystal lattice with the following parameters: $a = 3.976$ Å, $b = 3.976$ Å and $c = 5.023$ Å; density = 9.35 kg l⁻¹; specific volume = 0.107 l kg⁻¹; molar volume = 23.9 cm³ mol⁻¹ and molar heat capacity = 45.82 J mol⁻¹ K⁻¹.

Orthorhomb-PbO also has a layered structure; the layers are built of infinite Pb–O chains [2] as shown in Fig. 5.1. The surfaces of the layers are composed of Pb²⁺ ions and each oxygen ion is surrounded by four lead ions. The chain layers are stabilised by van der Waals bonds [2]. Therefore, the orthorhombic-PbO crystals are prone to flaking. In the covalent pattern, the electron pairs are localised and their delocalization requires excitation. This is responsible for the very low dark electric conductivity of orthorhomb-PbO. The following are the lattice parameters of the elementary cell: $a = 5.489$ Å, $b = 4.755$ Å and $c = 5.891$ Å. The melting point of orthorhombic PbO is 885 °C and the boiling point is 1480 °C.

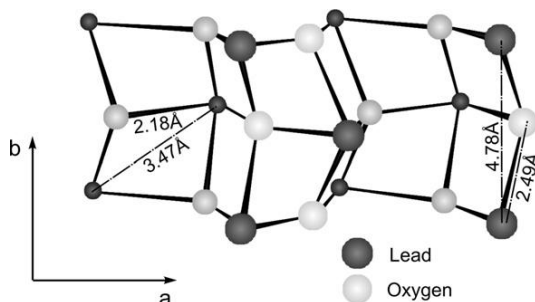


Figure 5.1:
Schematic representation of a layer of yellow PbO chains [2].

Soederquist and Dickens [4] have proposed a mechanism for the transition of orthorhomb-PbO into tet-PbO. It is based on the principle of minimum energy consumption and proceeds via a mechanism in which the nearest orthorhomb-PbO neighbours become the nearest tet-PbO neighbours. The transition then continues without drastic alteration to the ionic bonds. The oxygen ions shift further than the Pb^{2+} ions, since lighter ions have a more pronounced thermal vibration amplitudes. Thus, the lead sub-lattice is subjected to the least change and is similar in both PbO modifications.

Newly formed tet-PbO must be oriented to retain the disposition of the Pb^{2+} ions during the transition. This orientation must follow the conditions: (001) plane of tet-PbO parallel to the initial (001) plane of orthorhomb-PbO, and (110) plane of tet-PbO parallel to the (100) plane of orthorhomb-PbO. This can be achieved by a 13% contraction along the (001) plane and a 18% dilation along the (010) plane of orthorhomb-PbO. Under these conditions, the lattice remains unchanged along the (100) plane.

The specific resistivity along the direction perpendicular to the layers is 10^{12} ohm cm, whilst that along the length of the chain is 10^{10} – 10^{11} ohm cm [3]. Orthorhomb-PbO is an *n*-type semi-conductor with a forbidden energy gap of 2.66 eV [5].

The correlation between the ionic and electronic conductivity components of orthorhomb-PbO, oxygen pressure and dopant concentration (e.g. K and Bi) has been studied [7]. The electronic component depends on the pressure of oxygen; Bi addition creates *n*-type conductivity, whilst K dopant creates *p*-type conductivity. The transfer number of Pb^{2+} is only 0.01 and the ionic conductivity is due entirely to oxygen [6,7]. The exchange of oxygen between the gas and the surface of the oxide proceeds at a slow rate.

5.1.2. Red Lead (Pb_3O_4)

Red lead crystallizes as a tetragonal system and its elementary cell parameters are $a = 8.80$ Å, $c = 6.56$ Å. Figure 5.2 illustrates the coordination of ions in Pb_3O_4 crystal lattice. The latter

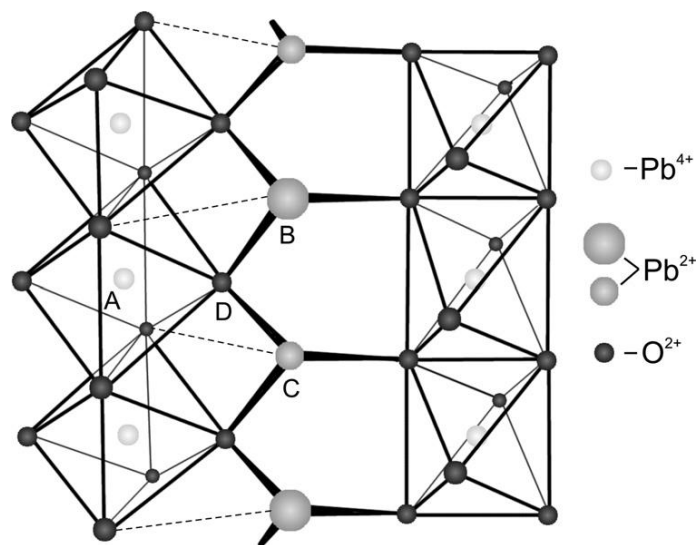


Figure 5.2:
Crystal structure of Pb_3O_4 [9].

contains PbO_6 octahedra with a Pb^{4+} ion in the centre and O^{2-} ions at the peaks which are bonded only at opposite edges. Infinite chains are formed along the c -axis, similar to those in $\beta\text{-PbO}_2$. The divalent Pb^{2+} ions link the chains to each other by coordination with three oxygen ions. The Pb^{2+} -oxygen bond is predominantly covalent (only 22–50% ionic character). This structure allows Pb_3O_4 to act as lead compound with Pb(II) and Pb(IV) valency. This behaviour is demonstrated on reaction with acid: red lead decomposes to $\beta\text{-PbO}_2$ (octahedral chains) and a Pb^{2+} salt.

Pb_3O_4 has usually been reported as a non-stoichiometric oxide. However, data reveal the presence of a region of homogeneity within the range $\text{PbO}_{1.31}$ to $\text{Pb}_{1.33}$. When heated to 550°C , Pb_3O_4 evolves oxygen and is converted into PbO . Red lead is characterised by the following properties: specific resistivity = 9.6×10^9 ohm cm at ~ 1000 bars, density = 9.1 kg L^{-1} , specific volume = 0.110 L kg^{-1} , molar volume = $75.3 \text{ cm}^3 \text{ mol}^{-1}$ and molar heat capacity = $45.82 \text{ J mol}^{-1} \text{ K}^{-1}$. Pb_3O_4 is a p -type semi-conductor with an energy gap of 2.18 eV [8].

5.2. Mechanism of Thermal Oxidation of Lead

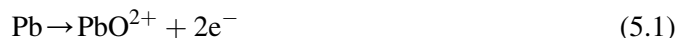
In humid medium, lead is oxidized by oxygen in the atmosphere even at room temperature. A PbO layer is formed on the metal surface, which separates the reactants. Later, the oxidation reaction proceeds via a solid-state mechanism. The basic issue is to determine which reactant passes through the PbO layer.

The diffusion of Pb^{2+} ions through the PbO layer requires an activation energy of 66 kcal mol^{-1} (2.86 eV) [10]. The energy of activation of the diffusion of oxygen ions is only 22.4 kcal mol^{-1} (0.97 eV) [7]. This marked difference between the two activation energies indicates that it is oxygen that is transported through the PbO layer.

The activation energy of diffusion in solids is generally considered to be a sum of the energies required for formation and for motion of defects. The energy for formation of defects is between 0.5 and 0.75 eV, depending on crystal type. These values, probably, hold also for oxygen defects. Hence, the energy of transportation of defects is 0.25–0.50 eV (6.9–11.5 kcal mol^{-1}). These figures are rather low and indicate that the movement of the O^{2-} ions through the PbO layer proceeds via a vacancy mechanism.

Anderson and Tare [11] have proposed a model for the oxidation processes which can be represented in a concise manner by the reactions presented in Fig. 5.3.

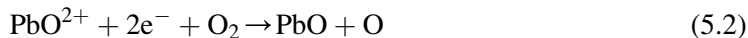
- a At the Pb/PbO interface the reaction



proceeds, during which oxygen vacancies and electrons are formed. These diffuse through the PbO layer and reach the PbO/air interface. The two types of particles have different mobility and an electric field may be created in PbO.

- b At the PbO/air interface, oxygen adsorbs initially upon separate adsorption centres. These centres may be the oxygen vacancies which have reached the surface of the PbO/air interface. Oxygen molecules enter the oxygen vacancies to fill the defects in the PbO crystal lattice and accept electrons to electroneutralize the adsorption centre.

Thus, the reaction



proceeds at the PbO/air interface. The oxygen atom interacts with another oxygen vacancy or reacts with another oxygen atom to form an oxygen molecule.

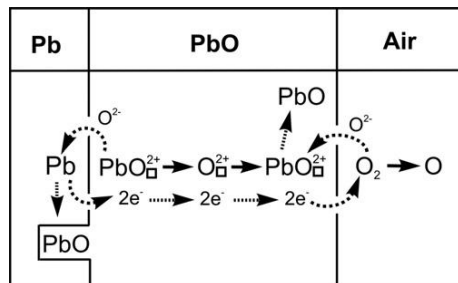


Figure 5.3:

Mechanism of the thermal oxidation of lead in air after formation of a PbO layer.

Within the different temperature intervals, any of the elementary processes (oxygen adsorption, disintegration of the O_2 molecule, surface processes at the Pb/PbO and PbO/air interfaces, transport of O^{2+} vacancies and electrons through the PbO layer) may become rate limiting and define a different kinetic equation for the oxygen process. In the presence of alloying additives in lead, the oxidation process may be further complicated, since the dopants affect not only the semi-conductor properties (n -, or p -type PbO conductivity), but also the mobility of ionic defects.

5.3. Production of Leady Oxide

In the earliest days of lead–acid battery production, lead monoxide (PbO) and red lead (Pb_3O_4) were used as starting materials for the preparation of battery plates. Pb_3O_4 was added in amounts from 25 to 70% by weight with the aim to accelerate the formation of the positive plates. PbO (litharge) was produced by melting lead in a reverberatory furnace. The molten lead was oxidized by the air flow and the water steam which catalysed the oxidation process. The lead oxide produced by this method was of rather coarse particle size and had to be subjected to further grinding in a roller or hammer mill. The obtained lead oxide powder was of the tetragonal structural modification. This method of lead oxide production was rather slow and cumbersome, so the need for a new and faster method became ever more evident. Such methods were developed at the end of the nineteenth and the beginning of the twentieth century, namely the Barton Pot and ball mill processes for the production of lead oxide. This oxide contains between 20 and 30 wt% unoxidized lead and is generally called *leady oxide*. Let us describe briefly the above two processes of lead oxide production which are currently employed in the lead–acid battery industry.

5.3.1. Barton Pot Method of Leady Oxide Production with Moderate Temperature Oxidation of Lead

In 1898, George V. Barton proposed a method that made the production process of lead oxide considerably faster and easier. This method yields partially oxidized lead powder (leady oxide) which ensures high battery performance.

Schematic of a typical unit for lead oxide production is presented in Fig. 5.4 [12]. The molten lead ($450^\circ C$) is fed via a pump into a large reaction pot equipped with rapidly rotating paddle to agitate the lead. The reaction pot is heated to about $470^\circ C$ and the molten lead is stirred and pulverised continuously. A stream of humidified air oxidizes the lead and carries the lead oxide particles to the classifier, where the coarse grains are separated from the fine particles and then returned to the reactor. The coarse particles are oxidized, dispersed and returned back to the classifier. A cleaning system (dust collector) for the escape of air ensures low emission levels.

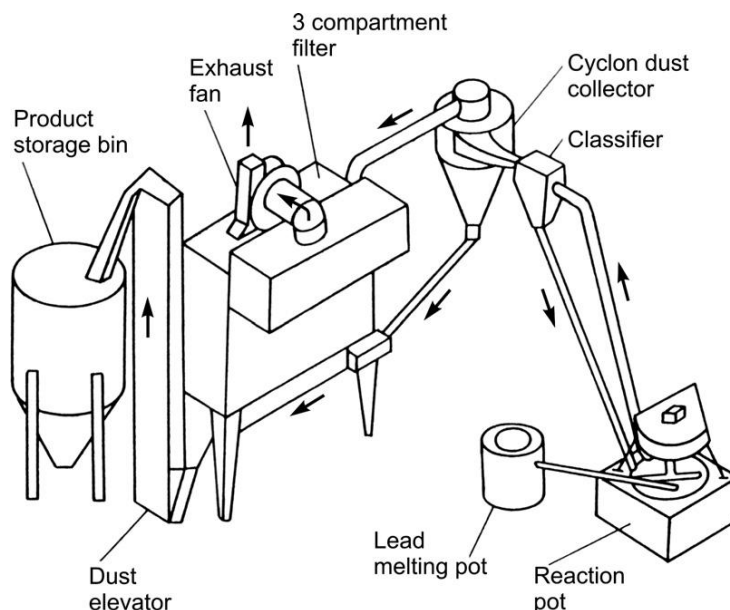


Figure 5.4:
Schematic of a Barton pot unit.

Since oxidation of lead is an exothermic reaction, considerable amounts of heat are produced in the reaction pot. The reaction temperature should be controlled carefully as it determines the type of the resulting leady oxide. The processing temperature should be kept below $487\text{ }^{\circ}\text{C}$ for the production of tet-PbO, which is the oxide modification preferred by the battery industry. Since the oxidation must be carried out at temperatures below the polymorphic transition temperature of $487\text{ }^{\circ}\text{C}$, the reactor pot is kept within the temperature range of $460\text{--}470\text{ }^{\circ}\text{C}$. Under these conditions, small amounts (less than 15%) of orthorhomb-PbO are formed and the subsequent parameters of the battery are virtually unaffected.

The temperature in the reaction pot depends on the amount and the speed of the humidified air flow blown through the reaction pot. Besides as catalyst of the reaction of lead oxidation, water lowers the temperature in the pot and supplies additional oxygen to the reaction chamber. Other parameters that affect the temperature in the reaction chamber are the amount and input speed of the lead stream fed into the reaction pot as well as the rate of the air flow drawn through the pot. These two flows guarantee sufficient heat generation during the oxidation of lead.

The obtained leady oxide with acceptable small particles and phase composition passes through a series of cyclone separators and a dust collector to remove the lead oxide dust from the air stream, and is then transported to a silo. The entire technological process is monitored by sensors and controlled by a computer.

The Barton method yields a 70–80% oxidized leady oxide. At high reactor temperatures, the oxide is entirely orthorhombic. At low temperatures, tet-PbO is formed along with orthorhomb-PbO. Small amounts of PbO_n and Pb_3O_4 can also be obtained by this method.

The influence of some of the Barton pot process parameters on the structure and properties of the obtained leady oxide can be summarised as follows:

- a *Effect of reactor pot temperature.* When the temperature in the reactor pot is increased the degree of oxidation of the lead powder increases, too, and so do the absorption of sulfuric acid and the productivity of the method. The amount of orthorhombic (yellow) lead oxide in the powder increases and small amounts of red lead may even be obtained. At the same time, the real density of the leady oxide is reduced and thus its poured (apparent) density decreases, too. The particle size and specific surface remain unchanged. The temperature in the reactor pot can be increased by increasing the amount and the speed of molten lead stream fed into the reactor. When the temperature in the reactor pot drops below a definite value, the molten lead fed into the reactor may solidify into a big ingot and block the system.
- b *Effect of air flow rate.* Higher air flow rates result in increased productivity of the Barton pot system and coarser particle sizes, as well as in higher real density of the leady oxide powder and hence higher poured density. At the same time, however, the absorption of water and sulfuric acid is reduced and so is the specific surface of the lead powder.
- c *Effect of air humidity.* Due to the catalytic effect of humidity on the oxidation process, when the humidity of the air flow is increased, the degree of oxidation of the lead powder increases, too, and consequently, its real and poured (apparent) density are reduced. The acid absorption increases. The particle size distribution and the specific surface of the leady oxide powder as well as the process productivity remain unchanged. The humidity of the air flow is increased usually by regular spraying of small amounts of water into the reactor pot.
- d *Effect of temperature in the melting pot.* The temperature in the melting pot should be maintained above the melting point of lead to prevent cooling and solidification of the lead melt before it is fed into the reactor pot. To achieve this, very often the supply pipe between the melting pot and the reactor pot is constantly heated. To prevent abrupt temperature drop in the melting pot simultaneous feeding of several lead ingots should be avoided. On the other hand, however, the temperature in the melting pot should not exceed 450 °C to avoid losses related to slag-formation.
- e *Effect of molten lead feed rate.* The lead feed rate is determined by the rate of feeding molten lead batches into the reactor pot. This is the basic method to control the required temperature level in the reactor pot, so any increase in the molten lead feed rate leads to a corresponding increase in reactor pot temperature and subsequent changes in the characteristics of the leady oxide. Obviously, the lead feed rate would determine directly the productivity of the equipment. The feed rate is controlled by an automatic control system and is varied as necessary depending on the current conditions at the moment.

In the production practice, interrelated variation of the different process parameters is applied to obtain the desired leady oxide powder quality. When the leady oxide powder is too coarse to be used directly in battery manufacture, it is subjected to further grinding in a mill.

About 75% of the total leady oxide production is realised by the Barton pot method. To bring the Barton pot process into operation at the desired reaction temperatures requires some 30 min each day. The required power for oxide manufacture is approximately 65 kW per ton of leady oxide.

Figure 5.5a and b presents scanning electron microscopic (SEM) images of Barton pot oxide particles and Fig. 5.5c and d shows micrographs of these particles mounted in resin and polished in cross-section [13]. Particles of two sizes can be identified in the pictures: fine lead oxide particles and coarse agglomerates of roughly spherical shape. When these particles are mounted in resin and polished, the unoxidized lead becomes visible. These are the large-sized particles obtained by solidification of the lead droplets and by surface oxidation of the lead particles. The pure lead oxide particles are small and fairly equal in size.

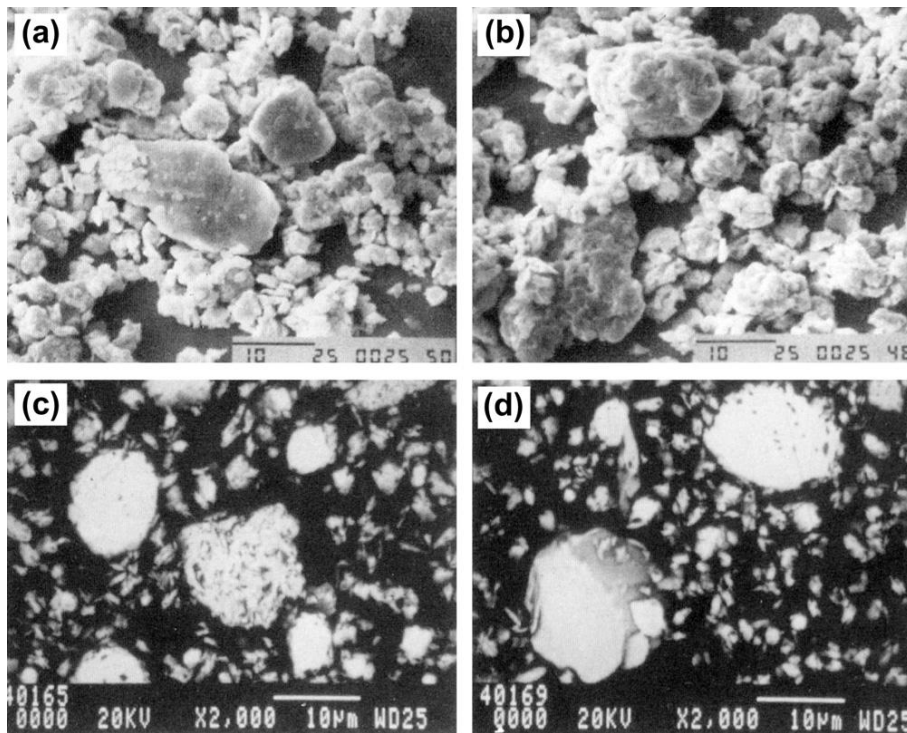


Figure 5.5:

(a,b) SEM micrographs of Barton pot oxides. (c,d) Lead oxide particles are mounted in resin and polished in cross-section [13].

5.3.2. ball mill Method of Leady Oxide Production with Low Temperature Oxidation of Lead

The ball mill method was first invented by Shimadzu in Japan in 1924. Nowadays, a great variety of mill designs are in use, but the basic principles applied by Shimadzu remains the same. The ball mill process is based on solid-phase reactions and operates within the temperature range between 70 and 180 °C. Schematic of a conical ball mill system is presented in Fig. 5.6 [15].

In the ball mill process, lead ball (cylinders) or ingots can be subjected to oxidation. The lead balls are fed into a large steel drum that rotates around its horizontal axis. Within the rotating drum the lead pieces (balls) rub and strike against each other. The heat generated by the friction between the

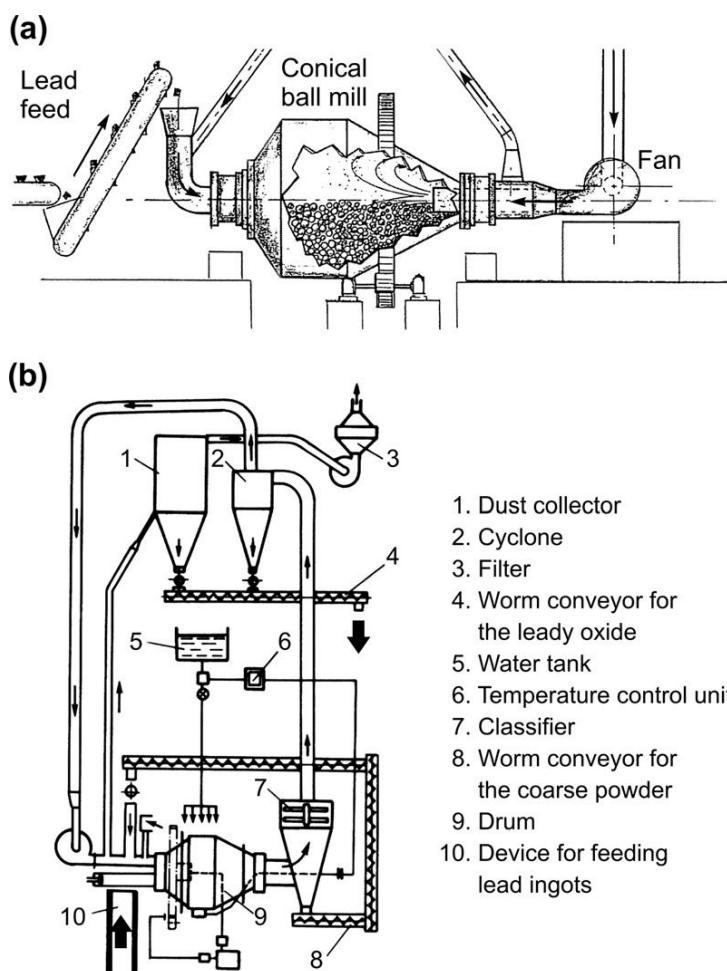


Figure 5.6:
(a) Conical ball mill [14]. (b) Chloride lead oxide mill [15].

lead pieces is sufficient to start the surface oxidation reaction. Since the latter reaction is exothermic, the evolved heat (983 kJ kg^{-1}) sustains the oxidation temperature and the excess heat has to be dissipated by cooling the drum by drawing cool air through it or spraying water over its outer wall. The drum temperature is kept at a value at which the lead surface oxidizes readily (i.e. about $90\text{--}100^\circ\text{C}$). The air flow drawn through the ball mill drum has a double function: to supply oxygen for the oxidation process and to entrain the lead oxide powder obtained. The air is usually supplied from two sources: through the inlet hole used for feeding the lead into the mill and through vents in the mill drum casing. The rate of the exothermic oxidation reaction should be carefully monitored and controlled by adjusting the water and air flows. After separation, the coarse lead oxide grains are returned to the mill for further grinding and oxidation. The cyclone separators and the dust collector are used to collect the lead oxide powder with the required grain particle size. The air is re-circulated and part of it is let out of the drum through a filter so as to keep the exhaust lead emission concentration below $1\text{--}2 \text{ mg m}^{-3}$.

The production rate of the ball mill process has been found to be proportional to the speed of the drum rotation. The energy needed for the production of 1 ton of lead oxide is fairly constant when the mill operates at between 55 and 90% of its critical rotation speed. The critical rotation speed is assumed to be the speed of drum rotation at which lead pieces stick to the drum walls under the action of centrifugal forces and do not rub against each other.

The productivity of the ball mill and the characteristics of the leady oxide obtained depend on the following parameters:

- drum rotation speed
- lead balls or ingots feed rate
- drum temperature
- air flow rate and humidity

The specific effect of each of these parameters, provided all the rest remain unchanged, is as follows:

- Effect of drum rotation speed.* With increase of the speed of drum rotation, the degree of oxidation of the lead powder, its specific surface and the degree of absorption of water and sulfuric acid increase, while the size of the particles and the real density, and hence its poured (apparent) density, decrease. The ball mill productivity remains unchanged as the feed rate is the same.
- Effect of lead balls feed rate.* When the feeding rate of lead balls into the mill is increased, the productivity of the system rises, the degree of powder oxidation is reduced, and hence its real density grows, which in turn leads to an increase in powder poured density. The particles grow in size, while their surface is reduced, and the degree of water and acid absorption decreases.
- Effect of temperature in the drum.* With increase of drum temperature, the degree of powder oxidation increases, which leads to lower real and poured (apparent) density,

accordingly. The acid absorption increases. The productivity of the ball mill equipment, the particle size and specific surface area of the powder remain unchanged. To maintain the desired temperature in the drum sometimes external water cooling is applied.

- (d) *Effect of air flow rate.* An increase in air flow rate through the system leads to an increase in degree of powder oxidation, and hence lower real and poured density of the obtained leady oxide powder. Higher air flow rate, however, may reduce the size of the particles, because their peripheral speed in the cyclone separator is increased and hence a greater number of particles are returned to the mill for further grinding. This reduces slightly the productivity of the ball mill system and leads to an increase in specific surface of the leady oxide obtained.
- (e) *Effect of air humidity.* Due to the catalytic effect of humidity on the oxidation process, an increase in humidity of the air drawn through the system results in higher degree of oxidation of the lead powder, and hence, its density (both real and poured) are reduced, while its capability to absorb sulfuric acid increases.

Most of the above-mentioned ball mill process parameters are continuously monitored with the help of sensors and the entire technological process is controlled by a computer.

The energy consumption for operation of the whole ball mill system is about 200 kW per ton of leady oxide. This is about three times the energy consumed by a Barton pot production unit of the same capacity [16].

The leady oxide produced by the ball mill process contains between 20 and 35% free (unoxidized) lead particles. The remaining phase being tet-PbO. The leady oxide particles form flake-shaped agglomerates. Figure 5.7 shows SEM images of leady oxide particles produced by the ball mill process [13]. Fairly large agglomerates can be seen which are built up of slices of lead (lead flakes) covered by oxide (Fig. 5.7c,d). These lead flakes are of various shapes and are surrounded by numerous fine oxide particles. This leady oxide particle shape is a result of the grinding effect in the ball mill process.

5.3.3. Comparison of Barton Pot and ball mill Leady Oxides

After the above brief description of the two methods of leady oxide production the question arises logically as to which of the two processes is better. Table 5.1 compares the characteristics of the leady oxides produced by the Barton pot and ball mill processes [17].

The three basic process parameters that are most often used to compare the two methods of leady oxide production can be summarised as follows:

1. reactivity of the leady oxide and its effect on battery performance
2. productivity (production rate), ease of operation (process control) and production costs
3. investments needed

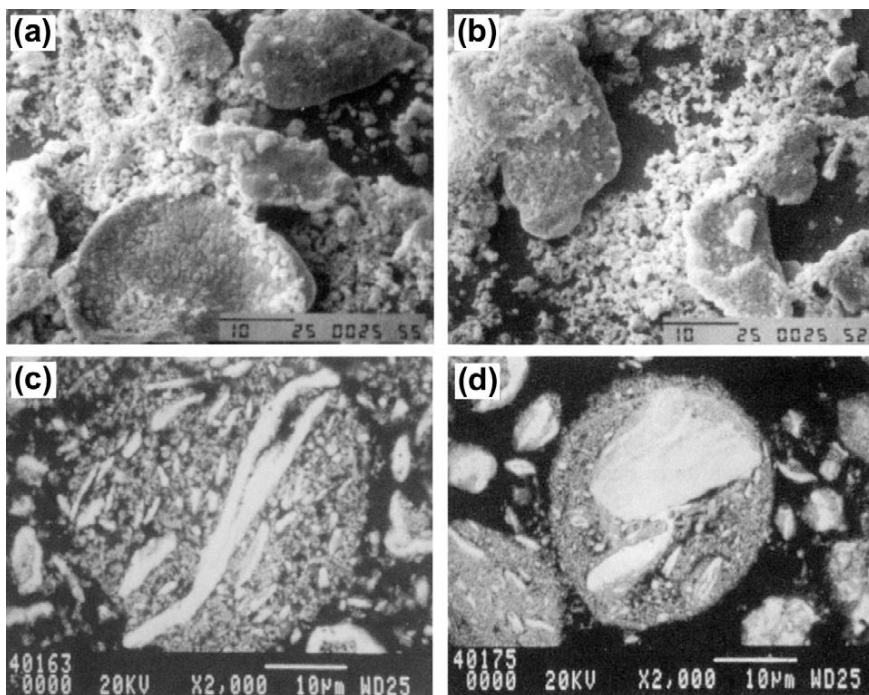


Figure 5.7:

(a,b) SEM micrographs of ball mill oxide particles. (c,d) SEM micrographs of polished cross-section of ball mill oxide mounted in resin [13].

A comparison between the reactivity and productivity of the two leady oxide production processes is presented graphically in Figure 5.8.

- (a) *Reactivity of leady oxide and its effect on battery performance.* In this respect, the ball mill method has an undeniable advantage. The powder produced by this method is much more active and facilitates the subsequent technological procedures ensuring better discharge performance and longer life, especially the positive plates of assembled batteries. The higher powder reactivity is probably due to the larger specific surface area of the particles in this type of leady oxide, and also to the absence of orthorhombic (yellow) lead oxide in it. This is the reason why some battery companies use mill oxide alone or a mixture of mill and Barton oxide for the production of positive pasted plates, and only Barton leady oxide for the negative plates, in both starter and traction battery applications.
- (b) *Productivity, ease of operation and production costs.* The Barton pot method has an obvious advantage with respect to these parameters. The production rate of the Barton systems is higher (up to 1000 kg leady oxide per hour), they are simple to operate, control and repair. The production costs related to the Barton pot method are lower. The difference in

Table 5.1: Comparison of Barton pot and ball mill oxides [17].

Characteristic	Barton Pot	ball mill
Particle size	3–4 mm median diameter	2–3 mm median diameter
Stability/reactivity in air	Generally more stable	Generally high. Can cause storage and long-distance transport problems
Oxide crystal structures (wt%)	5–30% β -PbO (typ.), remaining balance α -PbO	Essentially 100% α -PbO
Acid absorption (mg H ₂ SO ₄ g ⁻¹ oxide)	160–200 (unmilled, up to 240 with hammer milling)	240
Surface area (m ² g ⁻¹)	0.4–1.8	2.0–3.0
Free lead content (wt%)	Approx. 18–28	Approx. 25–35
Paste mixing characteristics	Makes a softer paste which can result in easier pasting	Makes a slightly stiffer paste which can require careful control
Battery performance	Enhances battery life, but can result in lower initial capacity	Batteries have good initial capacity, but possibly shorter life
Process control	Can be more difficult, but recent computer controls are helping	Easier, more consistent oxide
Typical production rate (kg h ⁻¹)	300–900	Possibly up to 1000
Investment considerations	Lower initial and operating costs; compact in size; relatively quiet; costs less to maintain; uses less energy to run	Higher initial and operating costs; requires more space; noisy; costlier to maintain
Energy use (kWh t ⁻¹)	Up to 100	100–300
Environmental aspects	With well-engineered environmental systems (including baghouse and storage), existing emissions standards can normally be met	

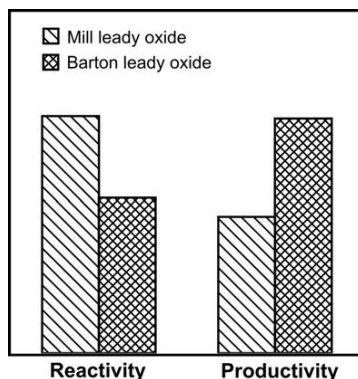


Figure 5.8:
Comparison of Barton pot and ball mill leady oxides.

production costs is mainly due to the different energy consumption for the production of 1 ton of lead powder, which is about 100 kWh t^{-1} for the Barton process, while the ball mill equipment may consume up to 350 kWh of energy for the production of 1 ton of leady oxide. Even in the latest milling systems developed recently, which may reach a productivity close to that of the Barton reactors (1000 kg of leady oxide per hour), the relative energy consumption is 150 kWh t^{-1} , a value much lower than that of traditional mills, but it is still much higher than the energy consumption of the Barton process.

- (c) *Investment costs.* Barton pot systems are significantly cheaper than the ball mill equipment, which makes them strong favourites in this respect, too. The lower price, the higher productivity and the lower operating and maintenance costs of Barton reactors have lead to a boom in their application by numerous battery companies worldwide after the 1960s.

5.3.4. Latest Advances in the Development of Barton Pot and ball mill Leady Oxide Processes

The major challenges that designers of Barton pot and ball mill systems have to cope with are to ensure adequate process control so as to guarantee the production of leady oxides with consistent and reproducible characteristics. A significant progress has been made recently in improving the control of the individual process parameters (variables) through the integration of enhanced computer control systems, sophisticated software designs, faster and more powerful interface, data collecting and networking systems, etc. Modern systems for the production of leady oxide are fully automated and programmable for the manufacture of products with specific pre-defined characteristics. The continuous monitoring of the technological process parameters and the automatic response to their fluctuations guarantee stable and consistent quality of the resultant leady oxide.

Operation of the Barton pot and ball mill leady oxide systems depends strongly on the surrounding ambient conditions such as temperature and humidity of the air. These conditions change daily and seasonally, and hence the operating settings of both types of systems should be adjusted accordingly in order to sustain the specified oxide characteristics. For the purpose, the air flow that is drawn through the Barton pot or the ball mill chamber should first be conditioned and then fed into the reaction chambers. This contributes greatly in improving the operating stability and the leady oxide consistency, and makes them less sensitive to ambient conditions fluctuations.

5.3.5. Production of Red Lead (Minium)

Red lead (Pb_3O_4) is prepared in mechanical furnaces by the oxidation of PbO batches (usually orthorhombic Barton oxide) within the temperature range 470–520 °C. The oxidation rate depends on the oxygen pressure, the surface of the oxide subjected to oxidation, and the temperature of the furnace. The latter is equipped with an automatic temperature control unit for continuous monitoring and control of the temperature throughout the entire red lead production process. The initial lead oxide (litharge) is ground prior to oxidation. Figure 5.9 illustrates the relationship between the degree of oxidation and the duration of the process. The percentage of Pb_3O_4 in the batch increases with time, while the oxidation rate remains constant up to 70–80% red lead and then slowly decreases. After the required content of Pb_3O_4 is reached, the process is stopped, the furnace is discharged and re-charged with fresh PbO . The red lead is ground before use in the battery industry. Two types of $\text{Pb}_3\text{O}_4/\text{PbO}$ mixtures are used for battery manufacture: (1) a mechanical mixture (blend) of Pb_3O_4 and tet- PbO and (2) a furnace product obtained when the oxidation of PbO is stopped at the required Pb_3O_4 content (e.g. 25%) in the oxide.

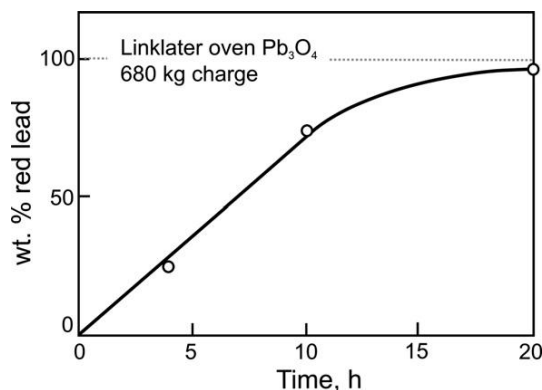


Figure 5.9:
Red lead content vs. oxidation time in a linklater furnace.

Red lead blended with leady oxide in the paste for the production of positive battery plates has two beneficial effects: (1) shortens the time for positive plate formation, which is, a rule, longer than the formation time of the negatives and (2) increases the initial capacity of the batteries.

Most often, high percentage (65 wt%) red lead and leady oxide blends are used for filling positive tubular plates for both traction and stationary batteries.

5.4. Characteristics of Leady Oxide

5.4.1. Purity of Lead for Lead Oxide Production

Especially important for proper operation of the battery are the impurities contained in the metal used for leady oxide manufacture. Lead for the battery industry is derived from ores mined in different parts of the world (primary lead) or is obtained by recycling of used up batteries that have reached their end of life (secondary lead). The recycling process is very often performed at the battery manufacturers' facilities. Purity standards have been adopted for the lead to be used for leady oxide production. These standards specify different maximum allowable amounts of impurities for flooded and valve-regulated lead-acid battery applications. Table 5.2 presents typical purity specifications for lead for making leady oxide for flooded batteries.

Special attention is being paid to bismuth in the lead as this element is difficult to remove during lead production. Bismuth has been found to contribute in the preservation of the lead

Table 5.2: Typical purity specifications for lead in oxide making for flooded batteries [18].

Material	Flooded Battery (max. wt%)
Lead	99.97–99.99
Trace elements	0.03–0.01
Antimony	0.001
Arsenic	0.001
Bismuth	0.03
Cadmium	0.001
Copper	0.0015
Iron	0.001
Manganese	0.0005
Nickel	0.0005 ^a
Selenium	0.0005
Silver	0.005
Tellurium	0.0005 ^a
Tin	0.001
Thallium	0.01
Zinc	0.001

^aQuantity can be crucial in some designs.

dioxide active mass structure and serves as a binder between the PbO_2 particles [19]. Its maximum allowable content in the lead for oxide production is up to 0.03 wt%.

The plate grids for flooded batteries are most often produced from lead-antimony alloy. Antimony lowers significantly the overpotential of hydrogen evolution and the latter is the predominating gas evolved in the battery. Hence, the effect of the other elements (impurities) is of minor importance. In valve-regulated lead–acid batteries, where antimony-free plate grids are used, the influence of impurities on the gassing processes increases substantially and it is essential to specify the maximum allowable concentrations of different elements in the starting lead for leady oxide manufacture in view of their effect on the rates of hydrogen and oxygen evolution. Such a specification is proposed by Lam and collaborators for 17 elements [20]. The authors have used field battery failure data and have performed screening determinations of different elements. The rates of hydrogen and oxygen evolution, and the float currents have been measured. Table 5.3 summarises the maximum acceptable levels (MAL) of residual elements in lead for leady oxide preparation.

Synergetic effects have been found during the determination of the MALs of individual elements. For hydrogen gassing, masking effects (‘beneficial synergetic effects’) arise mainly from the combined action of bismuth, cadmium, germanium, silver and zinc. A combination of bismuth, silver and zinc gives the greatest suppression of gassing, whereas nickel and selenium accelerate the gassing rate markedly. This indicates that nickel and selenium exert a ‘detrimental

Table 5.3: Maximum acceptable levels (MALs) for residual elements in leady oxide for VRLA batteries [20].

Elements	Level (ppm)			MAL (wt%)
	I_{float}	I_{hydrogen}	I_{oxygen}	
Ni	4	16	4	0.0004
Sb	6	15	6	0.0005
Co	4	7	4	0.0004
Cr	7	16	7	0.0007
Fe	—	—	—	0.0010
Mn	5	5	5	0.0005
Cu	33	13	34	0.0034
Ag	76	142	66	0.0066
Se	2	1	2	0.0001
Te	1.5	0.5	1.4	0.00005
Tl	25	25	25	0.0025
As	5	—	5	0.0005
Sn	41	—	40	0.0040
Bi	543	—	522	0.0500
Ge	673	250	658	0.0010
Zn	915	—	905	0.0500
Cd	756	—	722	0.0500

synergetic effect' on hydrogen evolution. For oxygen gassing, masking effects come from the combined action of antimony and iron. Again, nickel and selenium are found to enhance the gassing rate, but the effect is not as strong as that observed for hydrogen evolution [20].

5.4.2. Crystal Modification of the Lead Oxide

The crystal modification of the lead oxide depends on the conditions of its manufacture. At temperatures of oxidation below 470 °C (as is the case with ball mill PbO), the tetragonal polymorph is formed. If oxidation is performed in the temperature range of 460–470 °C through the Barton process, 60–70 wt% of the lead oxide formed is tetragonal (α -PbO), 15–20 wt% is orthorhombic (β -PbO) and the remaining balance is amorphous lead oxide.

Battery practice has proved that for batteries produced with 3BS pastes, the maximum allowable content of orthorhomb-PbO is 10 wt%. If 4BS pastes are used, however, this upper limit is increased to 20 wt%. The above limits hold for positive battery plates. The phase composition of the pastes for negative plates is practically of less importance, because no 4BS crystals are formed in the presence of expander. Here, the content of orthorhomb-PbO should not exceed 15 wt%.

The type of basic lead sulfate in the paste affects the structure of the active materials formed, especially of the lead dioxide active mass. And the active mass structure in turn determines the charge/discharge cycling performance of the battery. Thus, control of the α -PbO : β -PbO ratio is of fundamental importance for the quality of the batteries.

5.4.3. Chemical Composition of Leady Oxide

Leady oxide consists of lead oxide and free metallic lead. When produced by the ball mill method, the degree of oxidation of 65–75% is achieved, while the Barton process yields leady oxide powder with 70–80 wt% PbO content. When the leady oxide contains more than 30 wt% free lead, the material becomes very reactive. It is readily oxidized in humid air and the heat produced by this exothermic reaction may lead to combustion and damage the production equipment. Hence, effective control of the percent content of unoxidized lead in the leady oxide is very important, both during the production process and during the subsequent handling and storage of the leady oxide.

5.4.4. Absorption of Water and Sulfuric Acid

This characteristic gives useful information about the quality, and more precisely the reactivity of the leady oxide used for the manufacture of battery plates. Water absorption is determined by adding water, under constant stirring, to a sample of 100 g of leady oxide, until a paste of a given consistency is obtained. The quantity of absorbed liquid serves as a measure of the water absorption of the oxide. The typical value of H₂O absorption is between 7 and 13.7 mL

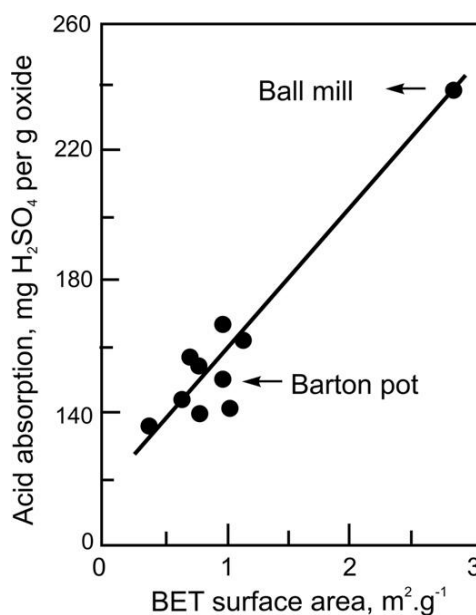


Figure 5.10:
Reactivity of ball mill and barton pot leady oxides [21].

per 100 g of leady oxide. It should be pointed out, however, that the consistency of the paste when prepared in small batches is determined fairly subjectively. It is recommended therefore that this determination is always performed by one and the same laboratory technician. The water absorption property provides an approximate measure of the surface area of the oxide which is in contact with water and is wetted by it. The water absorption depends on the number of particles and on their susceptibility to hydration.

The acid absorption of the leady oxide is determined by a method similar to that applied for determining the water absorption, but in this case sulfuric acid with 1.10 relative density is used instead of water. Depending on the method of leady oxide production and on the equipment used, the acid absorption value varies. Figure 5.10 presents the acid absorption (in mg H₂SO₄ per g oxide) as a function of the BET surface area for leady oxides produced by the Barton pot and ball mill methods [21].

ball mill leady oxide has higher acid absorption value, i.e. higher reactivity, than the oxide produced by the Barton pot process. This is due to the higher specific surface of the ball mill oxide which is composed of smaller particles.

5.4.5. Surface Area (Specific Surface)

The specific surface of leady oxide is determined by both particle size and shape. The leady oxide powder produced by the Barton pot process consists of spherical particles. So, in order to

achieve high specific surface, this powder should be ground to finer grains. Ball mill leady oxide comprises small mostly flake-like particles.

Most appropriate for determining the specific surface of powder materials of the above types is the adsorption method, or BET process. The average specific surface of leady oxide measured by BET is $0.7\text{--}1.4\text{ m}^2\text{ g}^{-1}$ for the Barton type and $2.4\text{--}2.8\text{ m}^2\text{ g}^{-1}$ for the ball mill type, respectively. It has been established that the BET surface area depends on the content of $\beta\text{-PbO}$ in the leady oxide [21]. A maximum area is obtained at 15 wt% $\beta\text{-PbO}$ level. It could be expected that the latter leady oxide would have the highest reactivity as well. The percent content of the $\beta\text{-PbO}$ crystal modification can be controlled by varying the temperature of the Barton pot. Process temperature of about 450°C yields the leady oxide with approximately 15 wt% $\beta\text{-PbO}$.

Leady oxides with ‘flat’ particles are generally preferred because of their higher surface area as compared to ‘spherical’ particles. Thus, many leady oxide manufacturers subject the Barton leady oxide to additional grinding in hammer mills.

5.4.6. Real Density, Poured (Apparent) Density and Packed Density

The *real density* is determined from the specific weight of only the solid phase in the powder particles or the density of the particles themselves. The real density of leady oxide is calculated on the basis of analytical data for the lead oxide and free lead contained, using their specific weights. The fine lead oxide fractions contain much more oxide than the larger-sized fractions in which metallic lead plays a major component.

The poured (apparent) density is an important technological parameter and should therefore be determined regularly to ensure production of leady oxide with stable characteristics. The apparent density is defined as the weight per unit volume of the leady oxide and includes not only the solid particles, but also the volume of the pores between them. There are standard methods and equipment for poured density determination. A popular device for measuring the poured density of leady oxide is the so-called Scott volumeter in which leady oxide is left to fall gently from an upper funnel with a mesh screen down a vertical box of rectangular cross-section with baffles arranged obliquely at intervals on either side of the box. A receiving cup (density cup) of a definite volume and weight is set under the baffle box. When the density cup is filled with powder and levelled, its weight is measured and the powder poured density is determined. The poured (apparent) density of the leady oxide is an important parameter used to monitor and control the operating conditions in the leady oxide mills, since its value is affected both by the ratio between fine and coarse grains, and by the amount of non-oxidized lead in the leady oxide powder. Table 5.4 gives some typical data for the poured (apparent) density of different leady oxides.

The packed density of leady oxides is also determined by applying standard methods. Each battery company uses, as a rule, its own method to determine the packed density of leady oxide.

Table 5.4: Poured (apparent) density data for different leady oxides (g cm^{-3}).

Cylindrical ball mill (15 mm dia. balls)	Conical ball mill (50 mm dia. bars)	Conical Mill + Subsequent Grinding	Barton Pot
1.9/2.0	1.1/1.7	1.6/1.8	1.4/2.3

These methods differ mainly by the technique used for packing (pressing) the powder into a vessel of a given volume and weight. The typical packed density of Barton pot oxide is about 3.6 g cm^{-3} and of ball mill leady oxide is it about 2.9 g cm^{-3} . This characteristic is very important for dry filling of tubular plates.

5.4.7. Particle Size Distribution

A definite amount of leady oxide is separated by a series of sieves of different mesh size placed above each other into fractions with different particle size distribution. The leady oxide is usually fed in the form of suspension. After a certain period of vibration of the sieve system, the weights of the different powder fractions are measured. A particle size distribution curve is plotted.

Besides sieve analysis, several other methods, too, have found wide application in leady oxide particle size determination as follows:

Sedimentation analysis. The distribution of the powder grains by size is calculated from the terminal velocity with which the grains fall, under the action of gravitation, into a liquid of a definite viscosity (settling velocity).

Nephelometric analysis (light scattering methods). This method is based on the difference in light reduction (scattering), caused by the presence of solid particles, when a light beam passes through a liquid column (optical nephelometry). Very high accuracy of the determination can be obtained by using laser beam instead of the light beam (laser nephelometry).

Microscopic method. The distribution of grains with sizes bigger than 5 microns is determined with the help of an optical microscope, and for particle sizes smaller than 5 microns, transmission or scanning electron microscopy is used. This is the only method that allows determination of the particle shape as well. All other methods assume that the grains are uniformly spherical in shape. The microscopic method determines both the size and number of grains, but the procedure is very slow and requires examination of a large area to obtain characteristic values. This method is not applicable for process monitoring of leady oxide production.

Figure 5.11 presents the particle size distribution curve for leady oxide produced by the ball mill method. The determination was performed by sedimentation analysis of the leady oxide in 0.1% NaPO_3 solution at 36°C . The obtained data evidence that all leady oxide particles are

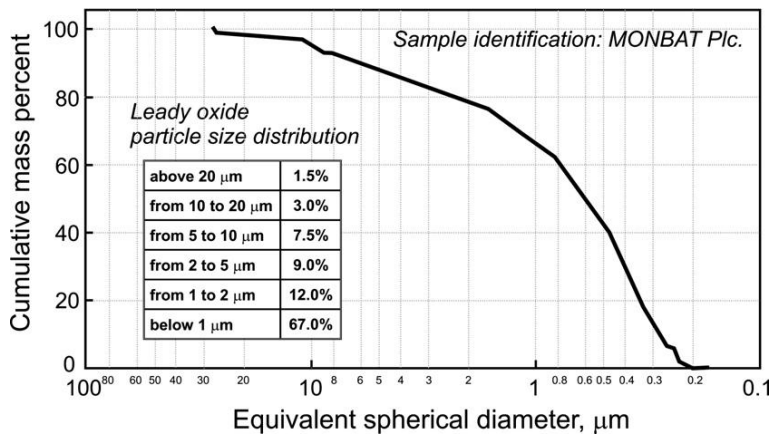


Figure 5.11:
Particle size distribution of ball mill lead oxide powder.

smaller than 20 μm in size, and 67% of them have a diameter less than 1 μm . This lead oxide has very high reactivity.

Logarithmic plots of the particle size distribution by diameter for ball mill and Barton pot lead oxides are presented in Fig. 5.12 [22]. The two curves differ significantly, indicating considerably higher percentage of particles with diameters less than 1 μm in the ball mill oxide as compared to the Barton pot oxide. This particle size distribution is responsible for the higher reactivity and the acid absorption of ball mill lead oxide, as well as for its lower apparent density.

The particle size distribution in the lead oxides produced by the two commercial processes can be controlled by varying the process parameters, as discussed in Sections 5.3.1 and 5.3.2. This, however, is not always sufficient to obtain the desired particle sizes which would ensure high battery performance characteristics. Hence, often Barton pot systems are coupled with a hammer mill to achieve higher degree of particle size control. In a hammer mill, a number of hammers are fitted to a rotating shaft with a variable speed drive. A stream of air is drawn through the mill at a controlled rate. Depending on the number of hammers and their speed of rotation, the air flow rate and the material feed rate, it is possible to produce lead oxides with desired particle size distributions. Flexible process settings can be developed which would allow the Barton pot systems with incorporated hammer mill to produce lead oxides of a wide range of particle size distributions, with strict control over the median particles size and the amount of fine particles in the end product.

Figure 5.13 shows a typical particle size distribution for lead oxides after different treatments in a hammer mill [23]. A decrease of the air flow rate through the mill leads to a decrease in median particle diameter from 5.3 to 2.1 μm and an increase of the percent share

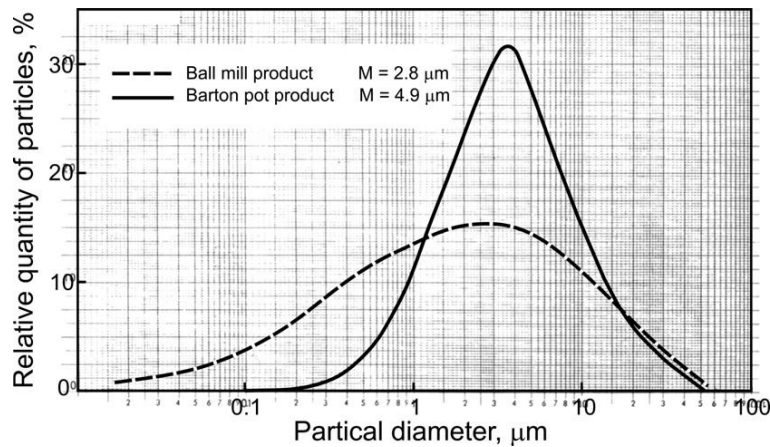


Figure 5.12:

Particle size distribution curves for ball mill and Barton pot leady oxides. Logarithmic plots [22].

of particles smaller than 1 μm from 1% to 24%. Of course, these changes in oxide particle size could also be achieved by varying the number of hammers in the mill and the speed of their rotation.

5.4.8. Stability of Leady Oxide

After its manufacture, leady oxide is stored in silos, but it should be used soon for battery manufacture, because its composition changes and some of its properties may deteriorate if it is

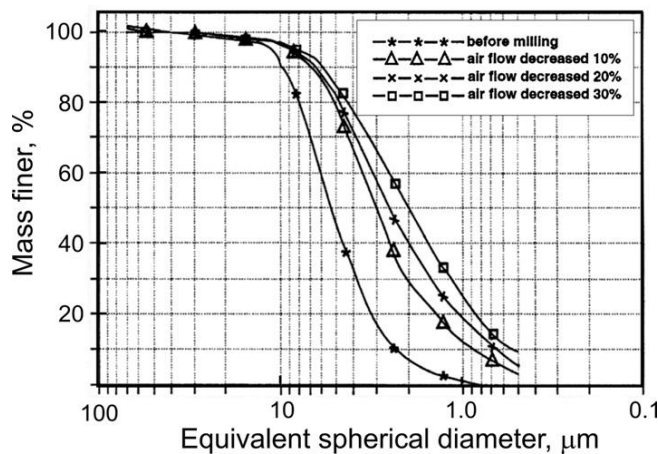


Figure 5.13:

Effect of mill conditions on the particle size distribution of leady oxide [23].

left in the air for too long, especially at high humidity. Figure 5.14a illustrates the changes in free lead content of Barton pot and ball mill leady oxides during storage.

After a 10-day stay, ball mill leady oxide contains half the free lead of the produced product and the decrease in metallic lead content is about 25% for Barton pot oxide. Since lead oxidation is an exothermic reaction and the generated heat accelerates further the oxidation process, the storage time of leady oxide should be reduced or the material should be stored in an isolated vessel (dry place) with no access of air. The storage temperature, too, exerts a strong influence on the rate of oxidation of free lead in the leady oxide. Figure 5.14b shows the changes in free lead content of ball mill leady oxide during storage at 2 °C and at room temperature of 23 °C [24]. At room temperature (23 °C), the content of free lead decreases at a rate of 0.5 wt% per day during the first three weeks of storage and continues to decrease at a rate of 0.2 wt% per day thereafter. When stored at 2 °C, the rate of Pb oxidation is

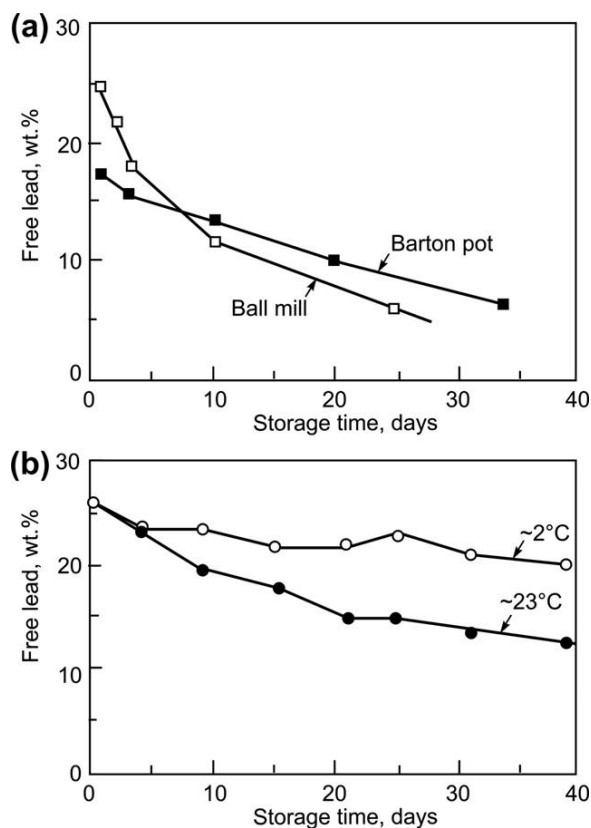


Figure 5.14:

- (a) Changes in free lead content of ball mill and Barton pot leady oxide during storage in air.
 (b) Free lead content of ball mill leady oxide as a function of storage time at 2 °C and at room temperature (~23 °C) [24].

significantly lower, about 0.15 wt% per day. The free lead in the Barton pot leady oxide oxidizes at a lower rate on storage than that of the ball mill oxide. Hence, Barton pot leady oxide has a longer shelf-life.

5.4.9. Environmental and Health Hazard Issues Related to Leady Oxide Production

Leady oxide manufacture is potentially very hazardous. It is therefore vital to take adequate measures to minimise, or even eliminate altogether, possible lead dust emissions out to the working environment and thus exposure of the personnel which would cause health problems. This is achieved by the use of a closed (isolated) leady oxide production equipment and transport pipes from the storage silos to the paste mixing unit. Special attention should be paid to the manufacture of tubular battery plates. Until recently, tubular plates were filled with a dry mixture of leady oxide and red lead powders.

5.5. Influence of Leady Oxide Properties on Battery Performance Characteristics

5.5.1. Cells Produced with Leady Oxide

As mentioned earlier in this chapter, the properties of the leady oxide affect eventually battery performance. Industrial experience has shown that the effect of leady oxide parameters is much stronger on the performance of positive plates than on the negatives. This is due mainly to the processes during formation of the plates, when metasomatic process take place in the positive active material as a result of which the structure of the cured paste is greatly reproduced into the formed lead dioxide active mass. Hence, the structure and morphology of the particles contained in the precursor paste are essential. These depend on the particle size distribution of the starting leady oxide. During formation of the negative lead active mass, the basic lead sulfates and PbSO_4 dissolve and the obtained Pb^{2+} ions are reduced to Pb. In this process, the structure of the cured paste is ‘forgotten’, i.e. it is not reproduced in the formed active mass, but rather a new structure forms, except for the non-oxidized lead from the leady oxide which is included in the negative active mass (NAM) structure.

The particle size of leady oxide exerts a major influence on the initial characteristics of lead–acid batteries (Fig. 5.15) [25]. Leady oxides with very fine-grained structure yield high initial capacity which then declines very soon (curve II for orthorhomb-PbO and curve IV for tet-PbO). On the contrary, when the powder is of coarse grain structure (curve III for orthorhomb-PbO and curve V for tet-PbO), the battery capacity during the initial cycles is low, but then increases gradually up to maximum and begins to decline slowly thereafter. This behaviour can be explained by incomplete formation of the plates produced with coarse leady oxides, which results in low initial capacity. A certain number of charge/discharge cycles are required for the unformed oxide to be converted into PbO_2 and thus yield the rated plate capacity.

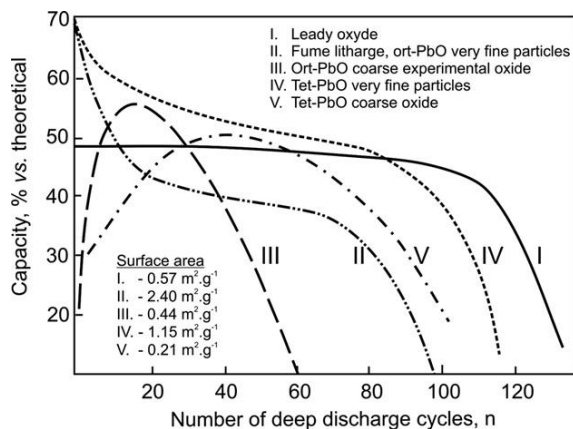


Figure 5.15:

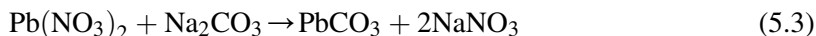
Alteration of the capacity of positive plates, prepared with different lead oxide powders, during the charge/discharge cycles [25].

Medium grain-sized leady oxide powders (5 μm to 50 μm) with predominant tet-PbO modification ensure typical capacity equal to 50% of the theoretical value and longest cycle life on deep-discharge cycling.

Based on the above information, it can be concluded that one of the technological ‘genetic codes’ that determines the performance characteristics of the positive plates is related to the properties of the leady oxide used, e.g. its phase composition, particle size distribution, etc. This genetic code is modified in the course of the subsequent manufacturing stages of paste preparation, curing and formation, but its influence on the capacity and cycle life of the positive plates remains noticeable throughout these stages, if the whole amount of PbO is not converted into basic lead sulfates. When leady oxides with different particle size distribution, specific surface and phase composition are used as starting material for paste preparation, they will require different amounts of sulfuric acid and different conditions of preparation of the pastes so as to yield active materials of high power and capacity performance characteristics, as demanded for the different battery applications.

5.5.2. Cells Produced with Nano-Structured Lead Oxide

During the past decade, nanotechnologies have found application in the manufacture of a number of products. Attempts have been made to obtain lead oxide with nano-sized particles under laboratory conditions. Synthesis of α -PbO with nano-crystal structure is achieved through two chemical reactions [26,27]. The first reaction is between solutions of $\text{Pb}(\text{NO}_3)_2$ and Na_2CO_3 :



The concentration of the solutions used is 0.1 M in [27] and 0.5 M in [26], respectively. The obtained PbCO_3 is washed and dried, and then calcinated at a temperature of 320 °C for 3–4 h, whereby PbCO_3 decomposes to $\alpha\text{-PbO}$ via the following reaction:



The obtained $\alpha\text{-PbO}$ particles are of median diameter of 0.530 μm [26]. Karami and collaborators [27] conducted the chemical reactions in the presence of ultrasonic waves (sono-chemical method) with the aim to reduce the size of the resultant particles. Under these conditions, $\alpha\text{-PbO}$ particles of 20–40 nm particle size are obtained. The thus synthesised PbO powder is used for the manufacture of positive plates for small laboratory test cells. Commercial negative plates are used as counter-electrodes. The test cells are set to cycling along with analogous cells assembled with commercial plates prepared with ball mill leady oxide. Figure 5.16 presents the obtained cycling test results for the two types of cells.

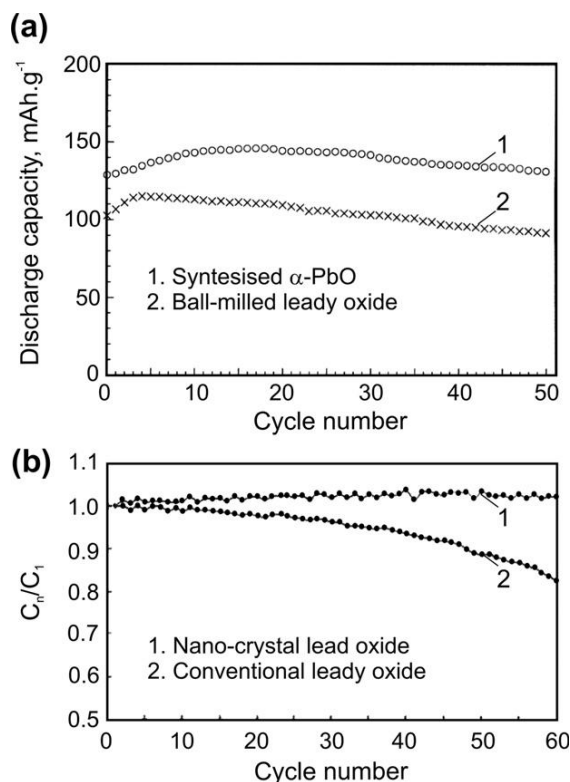


Figure 5.16:

(a) Discharge capacity vs. cycle number for (1) test cell with synthesised $\alpha\text{-PbO}$, and (2) test cell with ball-milled leady oxide [26]. (b) Comparing of cycling behaviours of a battery made with (1) lead oxide nano-powder and (2) by conventional leady oxide powder [27].

The results of both studies [26] and [27] evidence higher capacity values for the cells with chemically synthesised PbO, which change but slightly on cycling. There seems to be some kind of 'genetic code' in the lead oxide that exerts an influence on the end product.

The above investigations indicate that the physical and chemical properties of the lead oxide used as precursor material for the production of battery plates, though the lead oxide is only a starting compound for a number of chemical processes (paste preparation and plate formation, whereby PbO₂ and Pb are formed), exert an influence on the energetic and capacity performance parameters of lead-acid cells and batteries. Hence, it is essential to produce leady oxides with optimum and stable physico-chemical properties which would guarantee high battery performance.

References

- [1] B. Dickens, J. Inorg. Nucl. Chem. 27 (1965) 1503.
- [2] B. Dickens, J. Inorg. Nucl. Chem. 27 (1965) 1495.
- [3] L. Heyne, Phillips Res. Rept. Suppl. No. 4 (1961) 1.
- [4] R. Soederquist, B. Dickens, J. Phys. Chem. Solids 28 (1967) 823.
- [5] J. . van den Broek, Phillips Res. Rept. 22 (1967) 36.
- [6] L. Heyne, N.M. Beekmans, A. de Beer, J. Electrochem. Soc. 119 (1972) 77.
- [7] B.A. Thompson, R.L. Strong, J. Phys. Chem. 67 (1963) 594.
- [8] A.V. Panfilov, E.G. Evancheva, P.V. Drogomiretski, Sov. J. Phys. Chem. 41 (1967) 1072.
- [9] B. Dickens, J. Inorg. Nucl. Chem. 27 (1965) 1509.
- [10] R. Lindner, H.N. Terem, Ark. Kemi 4 (1952) 385.
- [11] J.R. Anderson, V.B. Tare, J. Phys. Chem. 68 (1964) 1482.
- [12] Globe Union, Balox leady oxide manufacturing equipment, 1980.
- [13] D. Hardy, R. Marx, J. Power Sources 38 (1992) 75.
- [14] T.L. Blair, J. Power Sources 73 (1998) 47.
- [15] G.G. Drachev, Y.P. Galuzin, Mechanization of battery production, Energy, Petersburg, Russia, 1969, p. 46.
- [16] The ABC's of oxide production, MAC Engineering and Equipment Company, Inc., USA, 2001.
- [17] M.G. Myer, D.A.J. Rand, J. Power Sources 59 (1996) 17.
- [18] R.D. Prengaman, J. Power Sources 42 (1993) 25.
- [19] D. Pavlov, A. Dakhouche, T. Rogachev, J. Power Sources 30 (1990) 117.
- [20] L.T. Lam, H. Ceylan, N.P. Haigh, T. Lwin, D.A.J. Rand, J. Power Sources 195 (2010) 4494.
- [21] D.A.J. Rand, L.T. Lam, The Battery Man, Nov (1992) 18.
- [22] H. Bode, in: R.J. Brodd, K. Kordesch (Eds.), Lead-acid batteries, John Wiley & Sons, New York, USA, 1977, p. 170.
- [23] D.P. Boden, J. Power Sources 73 (1998) 56.
- [24] G.L. Corino, R.J. Hill, A.M. Jessel, D.A.J. Rand, J.A. Wanderlich, J. Power Sources 16 (1985) 141.
- [25] T.G. Chang, J.A. Brown, Evaluation of battery oxides, ILZRO Project No. LE 272, International Lead Zinc Research Organization, July 1979.
- [26] J. Wang, S. Zhong, G.X. Wang, D.H. Bradhurst, M. Ionescu, H.K. Liu, et al., J. Alloys Compounds 327 (2001) 141.
- [27] H. Karami, M.A. Karimi, S. Haghdar, A. Sadeghi, Mater. Res. Bull. 43 (2008) 3054.

Processes During Paste Preparation and Curing of the Plates

This page intentionally left blank

Pastes and Grid Pasting

6.1. Introduction

The basic objective of the process of paste preparation for positive (PbO_2) and negative (Pb) battery plates is to produce particles of definite shape and composition. These particles are the basic building elements of the paste, which, after spreading onto the grids (current collectors), curing of the plates (during which process the particles are interlocked into porous mass) and formation (whereby the porous mass is converted electrochemically into active material), yield the electrodes (plates) of the lead-acid cell. The plates are characterised by definite porosity, active surface and hardness of the active mass and of its connection to the grid. It is the size of paste particles that determines the porosity of the active materials. Battery manufacturing practice has proved that the optimum paste particles should be needle-like (prismatic) in shape and have a length of 3–30 μm and a diameter of 0.4–5 μm . Particles of the above size yield positive active mass with appropriate porosity that ensures high specific active surface, adequate hardness of the porous mass and optimum pore distribution allowing easy access of ions of H_2SO_4 and H_2O molecules to every part of the plate volume. Tribasic lead sulfate ($3\text{PbO} \cdot \text{PbSO}_4 \cdot \text{H}_2\text{O} - 3\text{BS}$) and tetrabasic lead sulfate ($4\text{PbO} \cdot \text{PbSO}_4 - 4\text{BS}$) have crystals of the above-mentioned sizes. To improve the hardness of the porous mass built of these two types of particles, a certain amount of PbO and of its hydrated species are also needed. During paste preparation, water is used as a pore melding agent. 3BS and 4BS particles are formed as a result of reactions between leady oxide (LO) (containing 70–85% PbO) and H_2SO_4 solution. After nucleation and growth of 3BS and/or 4BS particles, the paste should have a definite density and moisture content.

In the present chapter, we will discuss the processes that occur during preparation of 3BS and 4BS pastes as well as the properties of the obtained pastes.

6.2. Fundamentals

6.2.1. Thermodynamics of the $\text{PbO}/\text{H}_2\text{SO}_4/\text{H}_2\text{O}$ System: Phase Composition of the Paste as a Function of Solution pH

Lander [1] has established that the paste is composed of basic lead sulfates, non-reacted lead oxides, hydrated lead oxides, free lead particles and basic lead carbonates. Some key thermodynamic data for basic lead sulfates, lead oxides and lead hydrates (hydroxides) are presented in Appendix 1 [2].

Table 6.1: Reactions for the PbO/H₂SO₄/NaOH system [3].

$5\text{HPbO}_2^- + 5\text{H}^+ = 5\text{PbO} \cdot 2\text{H}_2\text{O} + 3\text{H}_2\text{O}$	$\lg a_{\text{HPbO}_2^-} = -15.5 + 1.0 \text{ pH}$	A
$5\text{PbO} \cdot 2\text{H}_2\text{O} + 10\text{H}^+ = 5\text{Pb}^{2+} + 7\text{H}_2\text{O}$	$\lg a_{\text{Pb}^{2+}} = 12.6 - 2.0 \text{ pH}$	B
$\text{HPbO}_2^- + 3\text{H}^+ + \text{SO}_4^{2-} = \text{PbSO}_4 + 2\text{H}_2\text{O}$	$\lg a_{\text{HPbO}_2^-} = -36.0 + 3.0 \text{ pH} - \lg a_{\text{SO}_4^{2-}}$	C
$\text{PbSO}_4 = \text{Pb}^{2+} + \text{SO}_4^{2-}$	$\lg a_{\text{Pb}^{2+}} = -7.8 - \lg a_{\text{SO}_4^{2-}}$	D
$2\text{HPbO}_2^- + \text{SO}_4^{2-} + 4\text{H}^+ = \text{PbO} \cdot \text{PbSO}_4 + 3\text{H}_2\text{O}$	$\lg a_{\text{HPbO}_2^-} = -27.6 + 2.0 \text{ pH} - \frac{1}{2} \lg a_{\text{SO}_4^{2-}}$	E
$\text{PbO} \cdot \text{PbSO}_4 + 2\text{H}^+ = 2\text{Pb}^{2+} + \text{SO}_4^{2-} + \text{H}_2\text{O}$	$\lg a_{\text{Pb}^{2+}} = 0.5 - 1.0 \text{ pH} - \frac{1}{2} \lg a_{\text{SO}_4^{2-}}$	F
$4\text{HPbO}_2^- + 6\text{H}^+ + \text{SO}_4^{2-} = 3\text{PbO} \cdot \text{PbSO}_4 \cdot \text{H}_2\text{O} + 4\text{H}_2\text{O}$	$\lg a_{\text{HPbO}_2^-} = -22.8 + 1.5 \text{ pH} - \frac{1}{4} \lg a_{\text{SO}_4^{2-}}$	G
$3\text{PbO} \cdot \text{PbSO}_4 \cdot \text{H}_2\text{O} + 6\text{H}^+ = 4\text{Pb}^{2+} + \text{SO}_4^{2-} + 4\text{H}_2\text{O}$	$\lg a_{\text{Pb}^{2+}} = 5.3 - 1.3 \text{ pH} - \frac{1}{4} \lg a_{\text{SO}_4^{2-}}$	H

Bode and Voss [3] have investigated the system PbO/H₂SO₄/NaOH by adding H₂SO₄ to PbO suspension in 1N NaOH and measuring the pH of the solution. Precipitates are identified by XRD analysis. In alkaline solutions, lead takes the form of HPbO₂⁻ ions, whilst in acidic media it is present as Pb²⁺ ions. The activity of lead ions depends on the pH of the solution, according to the equations given in Table 6.1 [3].

Figure 6.1 shows the solubility curves for both types of lead ions (Pb²⁺ and HPbO₂⁻) in the system PbO/H₂SO₄/NaOH at 25 °C as a function of pH [3]. The least soluble compound is thermodynamically the most stable one. The figure shows the stability regions of the lead compounds at $a_{\text{SO}_4^{2-}} = 1$.

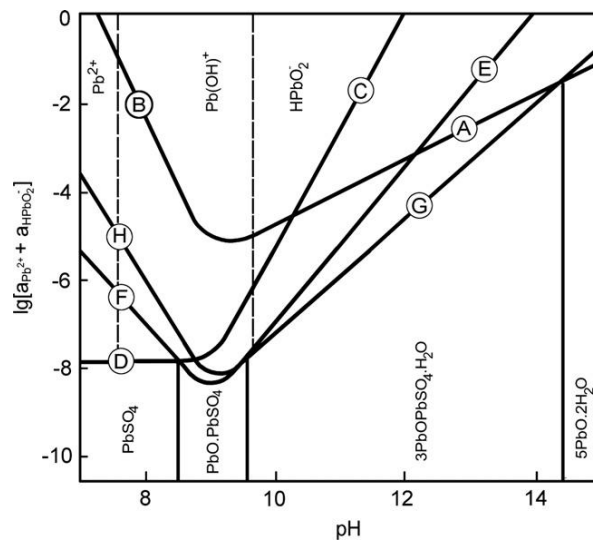


Figure 6.1:
Solubility vs. pH for lead compounds at 25 °C [3].

Table 6.2: Stability pH regions for PbSO₄, 1BS and 3BS at two different activities of SO₄²⁻ ions [3].

$a_{\text{SO}_4^{2-}} = 1 \text{ (M)}$	Stability pH Region		
	PbSO ₄	PbO·PbSO ₄	3PbO·PbSO ₄ ·H ₂ O
10 ⁻¹	up to 7.8	7.8–9.0	9.0–14.2
10 ⁻³	up to 6.8	6.8–8.1	8.1–13.2

From the data presented in Fig. 6.1, the stability pH regions for the individual phases at 25 °C and $a_{\text{SO}_4^{2-}} = 1$ can be determined as follows: pH < 8.4 for PbSO₄, pH = 8.4–9.6 for PbO·PbSO₄, pH = 9.6–14.4 for 3BS and pH > 14.4 for 5PbO·2H₂O, respectively.

Table 6.2 summarises the stability pH regions for PbSO₄, PbO·PbSO₄, 3PbO·PbSO₄·H₂O at two different activities of SO₄²⁻ ions, calculated using the data provided by Bode and Voss [3]. At lower activities of the SO₄²⁻ ions, the stability regions of PbSO₄, 1BS and 3BS shift towards lower pH values and vice versa.

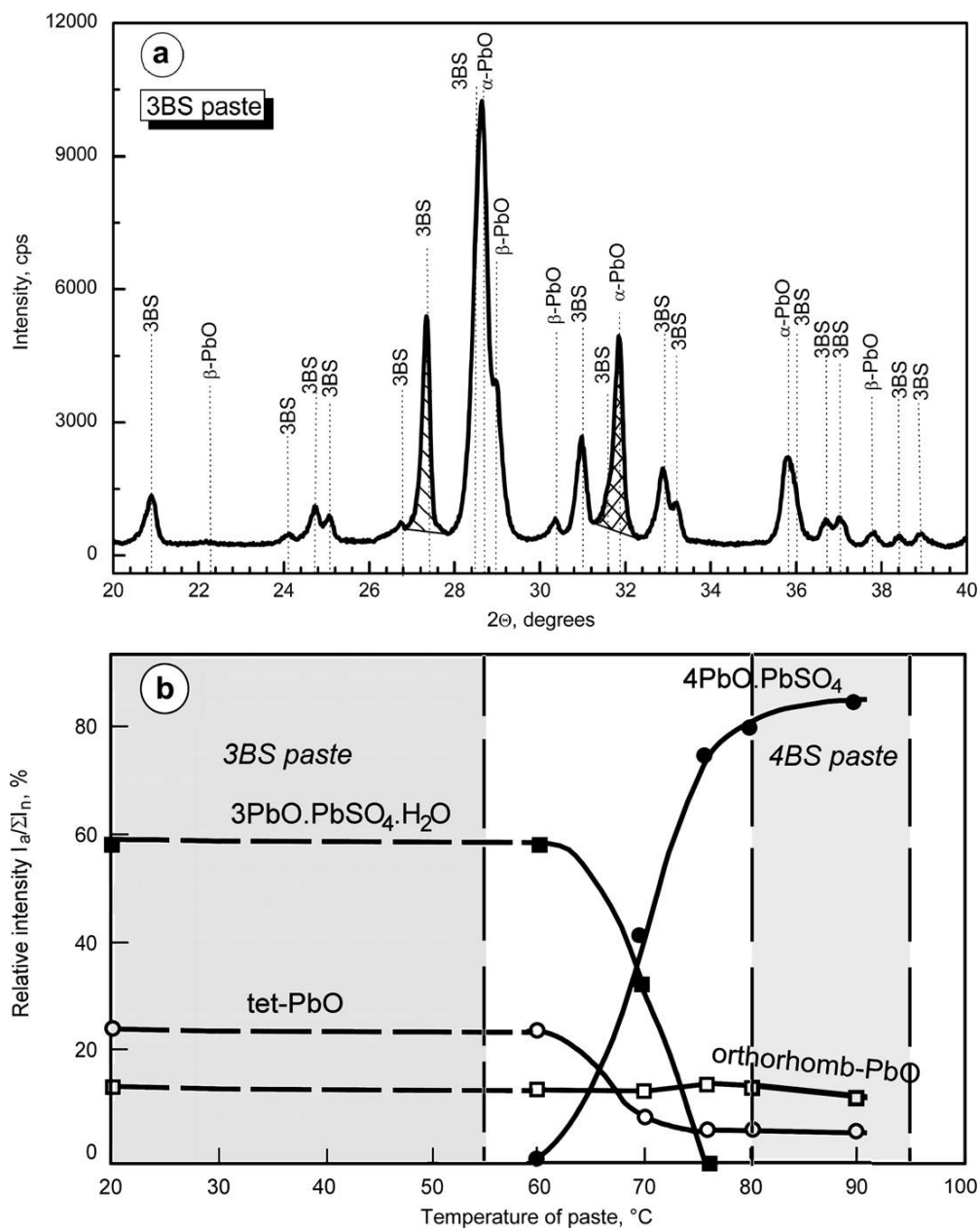
PbO·PbSO₄ and 3PbO·PbSO₄·H₂O form fine white prismatic crystals, whilst 4PbO·PbSO₄ crystallizes as coarse, pale yellow and prismatic crystals. Table 6.3 presents some of the physical characteristics of basic lead sulfates, PbO and PbSO₄ [2].

6.2.2. Phase Composition of the Paste as a Function of Paste Preparation Temperature

Figure 6.2a presents an X-ray diffraction pattern for 3BS paste. Each of the crystal phases contained in the paste has its own characteristic diffraction peaks. From the area (or height) of these peaks we can determine the amount of a given phase in the paste using the method of quantitative X-ray analysis. It is interesting to follow the changes in phase composition of the paste with changes in some of the parameters of paste preparation, e.g. amount of H₂SO₄ used, temperature, etc.

Table 6.3: Physical characteristics of basic lead sulfates, PbO and PbSO₄ [2].

Compound	Density (g cm ⁻³)	Molar Volume	m.p. (°C)	Elementary Cell				Ref.
				A	B	C	β	
PbO·PbSO ₄	6.92	76.79	975	13.75	5.68	7.05	116.2	[3]
2PbO·PbSO ₄	7.6	—	961	8.06	5.79	7.17	103	[5]
3PbO·PbSO ₄ ·H ₂ O	6.5	75		10.30	6.37	7.45	75	[4,2, p. 372]
4PbO·PbSO ₄	8.15	152	890	11.44	11.66	7.31	90.82	[5]
PbO tet	9.35	23.9		3.97		5.02		[2, p.372]
PbO orthorhomb	9.64			5.49	4.76	5.89		[2, p.372]
PbSO ₄ rhombic	6.29	48.2		8.52	5.39	6.99		[2, p.372]

**Figure 6.2:**

- (a) X-ray diffraction pattern for 3BS paste. Hatched peaks are characteristic for a given phase.
 (b) Phase composition of the paste as a function of temperature (revised) [6].

The crystal phase composition of the pastes and of the active masses is easily determined through X-ray diffraction analysis by measuring the relative intensities of the characteristic diffraction lines for the different phases in the pastes. The relative percent content of phase a in a mixture of crystal components is C_a and is equal to:

$$C_a = I_a / \sum I_n \%$$

where I_a is the peak area or intensity of the characteristic X-ray diffraction line for phase a, and $\sum I_n$ is the sum of peak areas or intensities of the characteristic diffraction lines for all phases in the paste.

X-ray powder diffraction data for some lead compounds are given in Appendix 2.

The phase composition of the system $\text{PbO}/\text{H}_2\text{SO}_4/\text{H}_2\text{O}$ depends strongly on temperature. This dependence has been investigated for various temperatures of paste preparation [6]. Pastes are prepared with 6% H_2SO_4 vs. LO by weight and stirred for 40 min at each temperature. The obtained results are presented in Fig. 6.2b. Within the temperature range 20–60 °C, the pastes contain the following crystal phases: $3\text{PbO} \cdot \text{PbSO}_4 \cdot \text{H}_2\text{O}$, tetragonal PbO and orthorhombic PbO. At temperatures within the range 65–80 °C, a reaction proceeds which results in the formation of $4\text{PbO} \cdot \text{PbSO}_4$. Hence, the paste contains all four phases: $3\text{PbO} \cdot \text{PbSO}_4 \cdot \text{H}_2\text{O}$, tet-PbO, orthorhomb-PbO and $4\text{PbO} \cdot \text{PbSO}_4$. When the paste is prepared at temperatures higher than 75 °C, the 3BS phase disappears and 4BS predominates in the paste with small amounts of orthorhomb-PbO and tet-PbO as well. The above investigations have been performed using ball mill LO with a fairly high chemical activity. When the chemical activity of the LO is low, the above temperature regions shift to higher temperatures.

The paste is a non-equilibrium system and Fig. 6.2b reflects only the crystal phases but not the amorphous components. It has been established that, when certain types of lead oxide are used, the strongest diffraction line for the $4\text{PbO} \cdot \text{PbSO}_4$ phase appears after one month shelf-storage of the paste at room temperature [7]. This indicates that nucleation of 4BS is a very slow process that depends strongly on temperature, initial materials (compounds) involved in the reaction and duration of the process of paste mixing.

During paste preparation, exothermic reactions proceed which cause the temperature in the paste mixer to rise. In order to obtain reproducibly a paste with definite phase composition and crystal morphology, which would ensure high and stable battery performance, the temperature in the mixer should be monitored and controlled continuously throughout the process of paste preparation.

Temperature exerts strong influence on the kinetics of 3BS formation. If the temperature of the reaction mix comprising stoichiometric amounts of H_2SO_4 and PbO is lower than 10 °C, the XRD results evidence that the rate of the reaction between PbO and H_2SO_4 yielding 3BS

is very low [8]. At temperatures between 20 and 60 °C, 3BS forms at a fairly high rate, but still some amount of unreacted PbO remains in the paste, which depends on the size of the particles in the initial PbO used.

6.2.3. Thermal Effects During Paste Preparation

The rise in temperature during paste preparation is a result of thermal effects of the chemical reactions that proceed and of the heat generated by the friction between particles caused by stirring.

Three types of reactions take place during paste preparation: (1) oxidation of lead, (2) formation of basic lead sulfates and (3) formation of hydrates. The thermal effects of the different reactions are calculated on the basis of thermodynamic data. The heat effects of the respective reactions of formation of basic lead sulfates and hydrates are given in Table 6.4.

An accurate evaluation of the heat evolved during stirring is quite complicated. It has been established that during preparation of a paste batch in a mixer with rated capacity of 600 kg lead powder, about 2.5 kWh of energy is introduced into the system to overcome the friction between particles on paste stirring [2, p. 228]. This energy is converted into heat. The latter heat energy plus the heat released by the chemical reactions give the total heat generated during the paste preparation process.

6.2.4. Tribasic Lead Sulfate Pastes, $3\text{PbO} \cdot \text{PbSO}_4 \cdot \text{H}_2\text{O}$ (3BS)

Kinetics of 3BS paste preparation

Tribasic lead sulfate pastes are most widely used in the battery industry for the production of both positive and negative plates. The reason for this preferential application of these pastes is the quick and easy formation (nucleation and growth) of 3BS, and the appropriate size and structure of the obtained 3BS particles and agglomerates.

Table 6.4: Thermal effects of formation of basic lead sulfates and hydrates [9].

Reaction	kcal mL ⁻¹	kJ mol ⁻¹
$\text{PbO} + \text{H}_2\text{O} = \text{Pb}(\text{OH})_2$	+2.64	11.05
$\text{Pb}(\text{OH})_2 + \text{PbSO}_4 = \text{PbO} \cdot \text{PbSO}_4 + \text{H}_2\text{O}$	+5.15	21.55
$\text{Pb}(\text{OH})_2 + \text{H}_2\text{SO}_4 = \text{PbSO}_4 + 2\text{H}_2\text{O}$	+38.66	161.75
$\text{PbO} + \text{H}_2\text{SO}_4 = \text{PbSO}_4 + \text{H}_2\text{O}$	+41.30	172.80
$5\text{PbO} + \text{H}_2\text{SO}_4 = 4\text{PbO} \cdot \text{PbSO}_4 + \text{H}_2\text{O}$	+46.19	193.26
$2\text{PbO} + \text{H}_2\text{SO}_4 = \text{PbO} \cdot \text{PbSO}_4 + \text{H}_2\text{O}$	+49.09	205.39
$4\text{PbO} + \text{H}_2\text{SO}_4 = 3\text{PbO} \cdot \text{PbSO}_4 \cdot \text{H}_2\text{O}$	+53.21	222.63

^a1 cal (cal) = 4.184 J

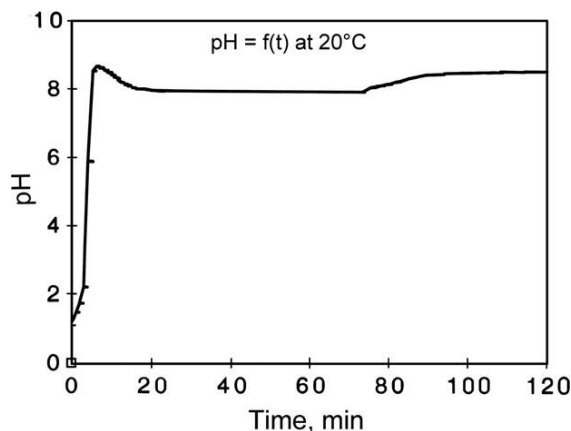


Figure 6.3:
pH curve obtained during mixing of PbO and H₂SO₄ solution at 20 °C [8].

At 20 °C, the kinetics of 3BS formation has been determined through measuring the pH of a suspension of H₂SO₄ solution and PbO, and through XRD analysis of its phase composition [8]. Figure 6.3 shows the changes in solution pH with time of paste preparation [8].

Two time intervals (stages) can be clearly distinguished in the curve. In the first interval, the solution pH increases from 1.0 to 8.0. This is related to consumption of H₂SO₄ for the formation of PbSO₄, 1BS and small amounts of 3BS. During the second interval, at pH round 8.0, 3BS forms at the expense of dissolution of PbSO₄ and 1BS. Hence, PbSO₄ and 1BS are intermediate products of the reactions of 3BS formation. During the second stage of 3BS formation, the solution pH is high and the solubility of PbO is low, so formation of 3BS proceeds only at the surface of the PbO particles thus isolating them from the solution. Diffusion of SO₄²⁻ ions through the 3BS layer that covers the PbO particles becomes the limiting stage in the kinetics of 3BS formation [9]. This is a very slow process and a certain amount of PbO remains unreacted despite the stoichiometric proportion between H₂SO₄ and PbO in the paste mix.

Figure 6.4 illustrates the changes in phase composition and temperature of the paste as a function of time of mixing [10]. Conditions of paste preparation: 5 kg batches are prepared using Barton leady oxide and H₂SO₄ solution of 1.40 relative density, at H₂SO₄/PbO ratio equal to 4.5% by weight, initial temperature 22 °C and time of mixing 30 min.

The process of 3BS crystal formation proceeds quickly. It is completed within 10 min of mixing. As the reactions between H₂SO₄ and PbO are exothermic, the temperature of the paste increases by about 5 °C vs. the initial temperature. Judging by the changes in intensity of the characteristic X-ray diffraction lines for tet-PbO and orthorhomb-PbO, it can be concluded that

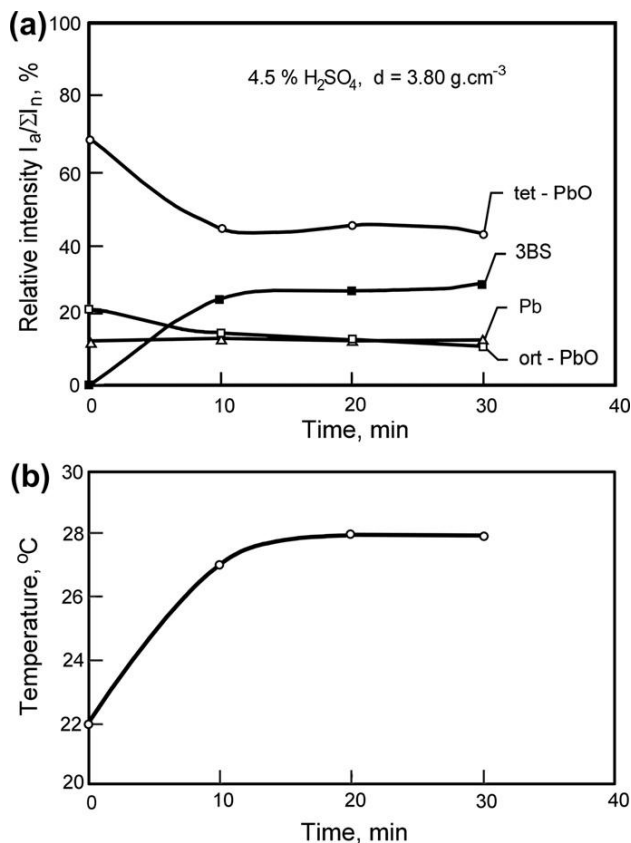


Figure 6.4:

Changes in (a) paste phase composition and (b) temperature during 30 min of paste mixing [10].

mainly tet-PbO is involved in the formation of 3BS crystals. The rate of sulfation of orthorhomb-PbO is considerably slower than that of tet-PbO. Hence, orthorhomb- β -PbO takes but a small part in the formation of 3BS.

Influence of H_2SO_4 /PbO ratio on phase composition and crystal morphology of the paste

Phase composition

In this investigation paste preparation is carried out at $35^{\circ}C$ [11]. The components are added in the following order: ball mill leady oxide, water, H_2SO_4 solution with 1.40 relative density. The content of H_2SO_4 is from 0 to 12% by weight vs. the leady oxide. The quantities of H_2SO_4 solution and water are selected so as to give pastes of equal density (4.00 g cm^{-3}). The duration of mixing is 40 min. On completion of the mixing process the phase composition of the pastes is determined through X-ray diffraction analysis. Paste consistency and density are also measured.

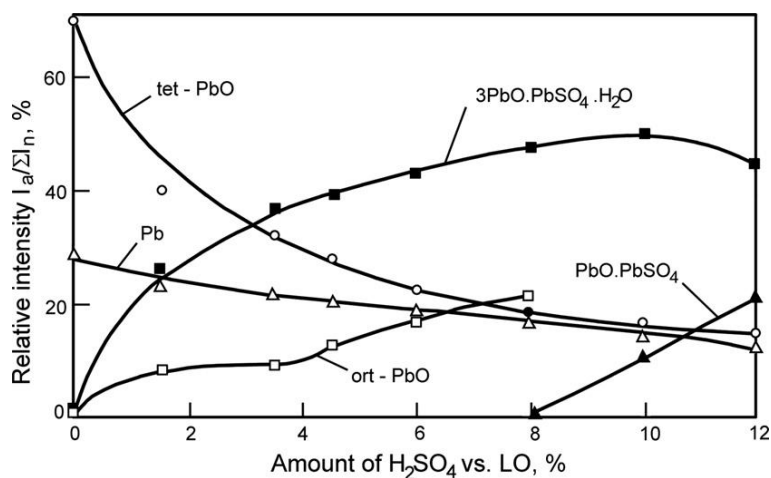


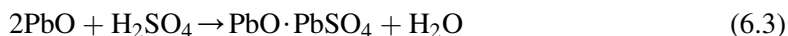
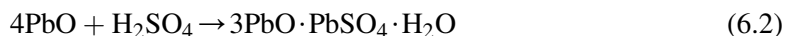
Figure 6.5:

Dependence of relative intensity of the characteristic diffraction lines for the different crystal phases in the paste on the H₂SO₄/LO ratio [11].

Figure 6.5 shows the changes in crystal phase composition of the paste as a function of H₂SO₄ content, represented by the changes in relative intensity of the characteristic diffraction lines for the different phases [11].

When the H₂SO₄ content is up to 10% by weight (vs. LO), the major phase formed is 3BS. Orthorhombic PbO is also detected in the paste. Above 8% H₂SO₄ vs. LO, PbO·PbSO₄ is formed, too. As the X-ray diffraction line with $d = 0.295$ nm reflects the formation of both PbO·PbSO₄ and orthorhomb-PbO, unambiguous identification of orthorhombic PbO species is very difficult when the H₂SO₄/LO ratio is higher than 8%. When leady oxide is mixed with H₂O, no orthorhomb-PbO is observed. The latter is formed only when a certain amount of H₂SO₄ is contained in the solution. This indicates that orthorhomb-PbO is formed at definite pH levels or in the presence of SO₄²⁻ ions [11].

Mixing of H₂SO₄ solution with leady oxide initiates heterogeneous reactions, which lead to the formation of lead hydroxides, crystalline basic lead sulfates and orthorhombic PbO. These reactions can be expressed by the following chemical equations:



From the above equations we can calculate the quantity of H₂SO₄ needed for the whole amount of PbO to be transformed into 3BS or 1BS.

It has been established that the size of 3BS crystals depends on the $\text{H}_2\text{SO}_4/\text{LO}$ ratio [12]. At high $\text{H}_2\text{SO}_4/\text{LO}$ ratios, the 3BS particles are smaller in size.

Figure 6.5 presents the changes in relative content (in percents) of the different crystal phases in the paste. If we assume that the whole amount of H_2SO_4 is consumed for the formation of 3BS, we can calculate the quantity of 3BS and of the residual non-reacted ($\alpha + \beta$) PbO in the paste. Such calculations have been made for $\text{H}_2\text{SO}_4/\text{LO}$ ratios up to 8%. Figure 6.6 compares the results of these calculations with the obtained XRD data.

The following conclusions can be drawn from the data in Fig. 6.6:

- At $\text{H}_2\text{SO}_4/\text{LO} = 4\%$ (LO is 80% oxidized), the calculated values for the amount of 3BS and PbO coincide with the relative content of these phases as determined by XRD.
- At $\text{H}_2\text{SO}_4/\text{LO} < 4\%$, the content of 3BS determined by X-ray diffraction is higher than the amount calculated on grounds of the H_2SO_4 quantity used for paste preparation. The reverse correlation is observed with the PbO phase. What is this difference due to? In the above range of $\text{H}_2\text{SO}_4/\text{LO}$ ratios, part of the PbO undergoes hydration:



$\text{Pb}(\text{OH})_2$ is an amorphous phase and cannot be detected by the XRD method. The obtained $\text{Pb}(\text{OH})_2$ reduces the amount of the crystal ($\alpha + \beta$)PbO phases in the paste. Hence, the relative content of the crystal phases changes: the amount of 3BS increases at the expense of a decrease in ($\alpha + \beta$)PbO content. The above results indicate that, at $\text{H}_2\text{SO}_4/\text{LO}$ ratios from 0 to 4% by weight, the process of hydration of PbO plays an important role, parallel to

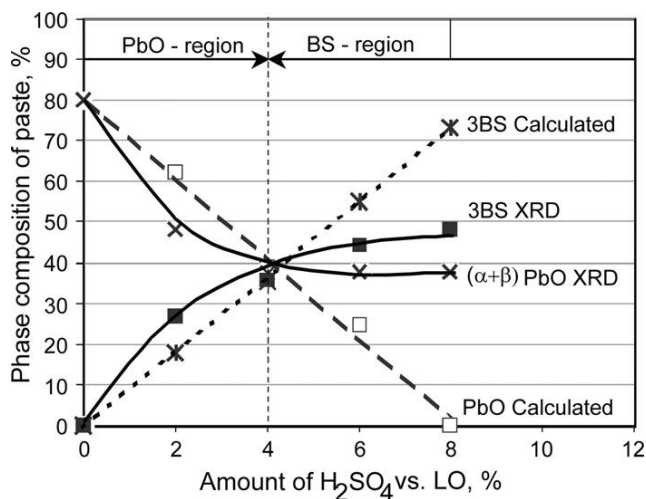
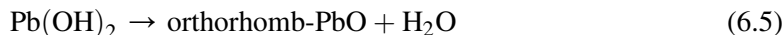


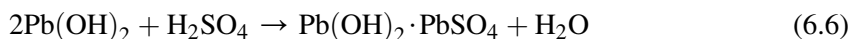
Figure 6.6:

Changes in phase composition of the paste as determined by XRD and as calculated from the $\text{H}_2\text{SO}_4/\text{LO}$ ratio.

that of 3BS formation. At $\text{H}_2\text{SO}_4/\text{LO} < 4\%$, the amount of PbO exceeds by almost 10 times that of H_2SO_4 , which means that the pH of the solution in the paste will be within the highly alkaline region. Hence, conditions will be created for hydration of PbO and subsequent formation of orthorhomb-PbO (reaction 6.5).



- (c) At $4\% < \text{H}_2\text{SO}_4/\text{LO} < 8\%$, according to Figs. 6.5 and 6.6, the content of 3BS increases but slightly, whereas that of $(\alpha + \beta)\text{PbO}$ remains almost unchanged despite that H_2SO_4 is introduced into the paste. This indicates that H_2SO_4 reacts with the hydrated Pb(OH)_2 whereby, most probably, an amorphous $\text{Pb(OH)}_2 \cdot \text{PbSO}_4$ phase is formed (reaction 6.6). This latter phase is not detected by the XRD analysis.



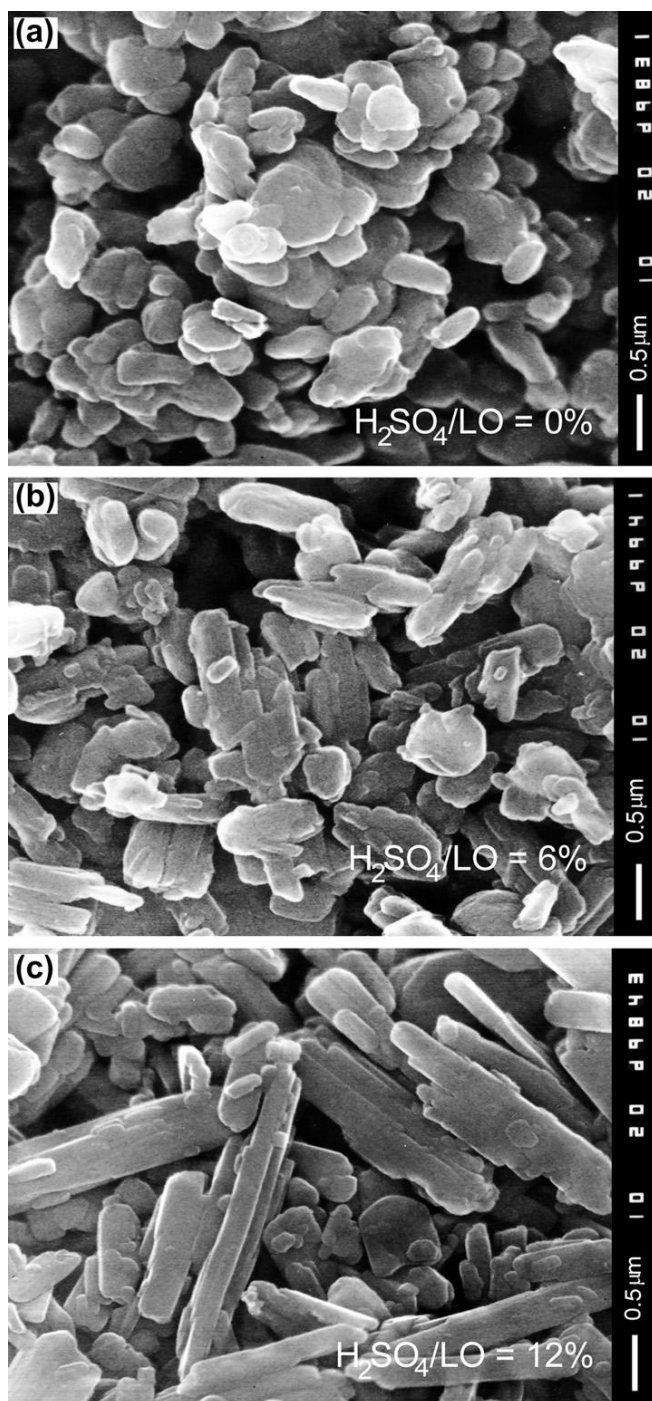
Only when a $\text{H}_2\text{SO}_4/\text{LO}$ ratio of 8% is reached, formation of the crystal phase $\text{PbO} \cdot \text{PbSO}_4$ starts, and the characteristic diffraction lines for this phase appear in the XRD pattern (Fig. 6.5). The relative percent content of 3BS increases but very slightly up to 10% $\text{H}_2\text{SO}_4/\text{LO}$.

Battery practice has proved that the content of 1BS in the paste should not exceed 5–8%. Otherwise, the battery performance declines. That is why the generally accepted $\text{H}_2\text{SO}_4/\text{LO}$ ratio in the battery industry is less than 6% by weight.

Crystal morphology of pastes prepared at different $\text{H}_2\text{SO}_4/\text{LO}$ ratios

Figure 6.7 presents SEM pictures of paste particles obtained at three different $\text{H}_2\text{SO}_4/\text{LO}$ ratios: 0%, 6% and 12%.

- When the LO is mixed with water instead of H_2SO_4 (i.e. $\text{H}_2\text{SO}_4/\text{LO} = 0\%$) the paste is composed mainly of PbO and Pb(OH)_2 particles. These are rounded particles sized about 1–2 μm and weakly connected to one another.
- At $\text{H}_2\text{SO}_4/\text{LO} = 6\%$ by weight, the paste comprises predominantly 3BS crystals (see Fig. 6.5). Well-shaped needle-like and rounded 3BS crystals are formed with dimensions of about 1–2 μm . In the temperature range 22–28 °C, the rate of 3BS crystal growth is probably low and hence even 30 min of mixing is not enough for the formation of well-pronounced 3BS crystals. Longer time of mixing or higher temperature should be applied to allow well-shaped 3BS crystals to grow in the paste.
- At $\text{H}_2\text{SO}_4/\text{LO} = 12\%$ by weight, the paste contains commensurable amounts of 1BS and 3BS. Mono-basic lead sulfate crystals are small in size (1–3 μm long and very thin). During plate formation they will be oxidized to βPbO_2 because of the high content of PbSO_4 in these crystals. Hence, the skeleton of PAM will be built of thin aggregates with large surface. This skeleton will disintegrate easily on cycling. That is why formation of 1BS during paste formation is avoided in the battery manufacturing practice by keeping

**Figure 6.7:**

SEM pictures of pastes prepared with different $\text{H}_2\text{SO}_4/\text{LO}$ ratios: (a) 0% (PbO , $\text{Pb}(\text{OH})_2$), (b) 6% (3BS) and (c) 12% (3BS, 1BS).

the proportion between H_2SO_4 and LO used for preparation of pastes lower than 6% by weight. When such a ratio is employed, even if 1BS does form, its content in the paste will be small (less than 5%) and will not affect the PAM structure.

Effect of expander added to the negative paste

Figure 6.8 illustrates the effect of BaSO_4 and of expander (1% of sodium lignosulfonate, SL) on the phase composition of pastes prepared using ball mill lead oxides with different $\text{H}_2\text{SO}_4/\text{PbO}$ ratios and mixed at 35 °C for 30 min [13].

A comparison between Figs. 6.6 and 6.8a shows that BaSO_4 alone exerts no effect on the phase composition of the paste. When 1% of SL expander is also added, formation of orthorhomb-PbO is suppressed. On comparing Figs. 6.8a and 6.8b, it can be seen that pastes produced with 2% H_2SO_4 vs. LO tend to contain more 3BS crystals when SL is also added, but on increasing the H_2SO_4 content in the paste, formation of 3BS crystals does

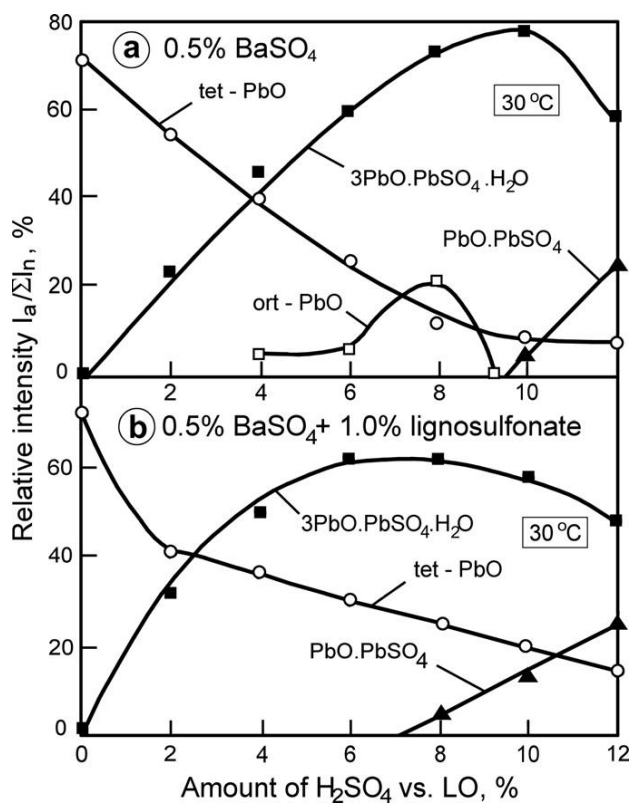


Figure 6.8:

Changes in crystal phase composition of the paste vs. $\text{H}_2\text{SO}_4/\text{LO}$ ratio: (a) with addition of 0.5% BaSO_4 , (b) with 0.5% BaSO_4 and 1% expander (lignosulfonate).

not follow a linear dependence. This indicates that SL affects the equilibrium between the 3BS crystal phase and the $3\text{Pb}(\text{OH})_2 \cdot \text{PbSO}_4$ amorphous phase. Secondly, small amounts of crystal $\text{PbO} \cdot \text{PbSO}_4$ are formed in pastes containing 8% of H_2SO_4 and SL. If no expander is added to the paste, $\text{PbO} \cdot \text{PbSO}_4$ is not formed at 8% $\text{H}_2\text{SO}_4/\text{LO}$. It can be concluded that lignosulfonate facilitates, to a certain extent, the formation of crystal $\text{PbO} \cdot \text{PbSO}_4$.

The above results imply that expanders exert an influence on the phase composition of the paste and, when one expander is to be replaced with another one, the manufacturer should know in advance how the new expander will affect the phases formed in the paste.

Effect of PbO modification on the rate of the reaction of 3BS formation [13]

The reactions between tet-PbO or orthorhomb-PbO and H_2SO_4 are followed for pastes prepared with $\text{H}_2\text{SO}_4/\text{LO} = 6\%$ at 80°C . In order to prevent formation of 4BS, 1% SL is added. The latter does not affect the formation of 3BS. The changes in phase composition (as determined by XRD analysis) of the paste prepared with tet-PbO and H_2SO_4 are presented in Fig. 6.9.

A reaction between tet-PbO and H_2SO_4 proceeds within the first several minutes already (Fig. 6.3 supports this assumption), as a result of which huge amounts of 3BS form ($d = 0.325$ nm), as well as small amounts of 1BS ($d = 0.333$ nm) and a bit more $5\text{PbO} \cdot 2\text{H}_2\text{O}$ ($d = 0.305$ nm). At this high temperature, the rates of the reactions are high, too, so they are completed within a very short period of time and, hence, the phase composition of the paste does not change for 120 min of stirring.

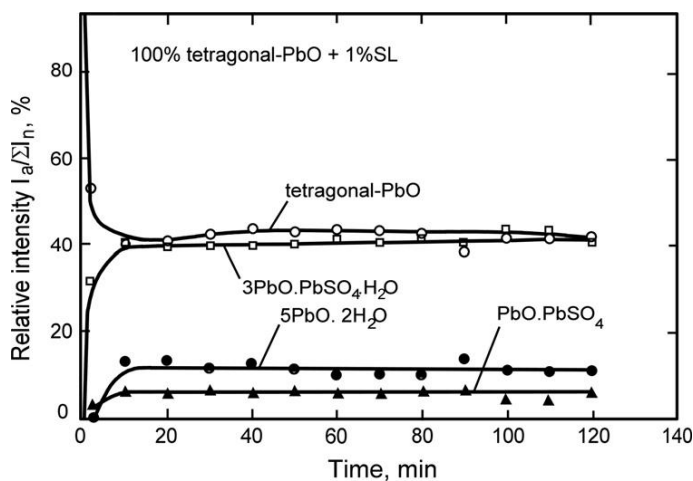


Figure 6.9:

Changes in phase composition of the paste during stirring. Initial oxide: 100% tetragonal PbO; H_2SO_4 solution and 1 wt% sodium lignosulfonate (SL) [13].

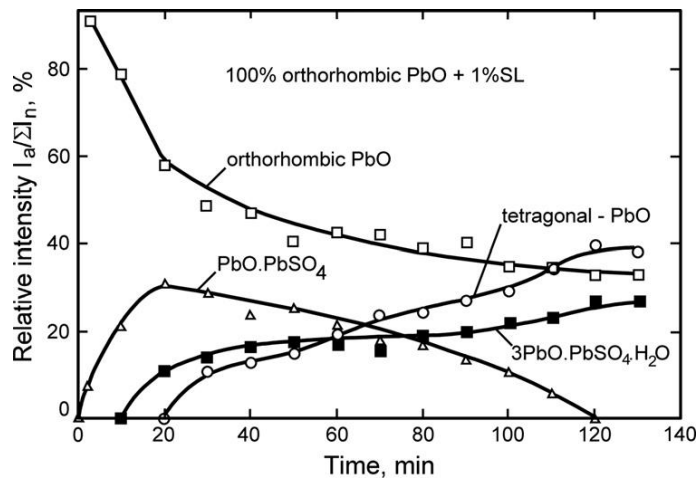


Figure 6.10:

Changes in phase composition during stirring of the paste. Initial oxide: 100% orthorhombic PbO; H₂SO₄ solution and 1 wt% sodium lignosulfonate [13].

This is not the case, however, with the reaction between orthorhomb-PbO and H₂SO₄.

Figure 6.10 shows the changes in phase composition (as determined by XRD analysis) of the paste prepared with orthorhomb-PbO, H₂SO₄/LO ratio 4.5% and addition of 1% SL, for 130 min of stirring [13].

1BS forms within the first several minutes already. Obviously, orthorhomb-PbO facilitates the nucleation of this crystal phase. After 10 min of paste stirring, formation of 3BS starts at the expense of diminishing quantities of 1BS and orthorhomb-PbO.



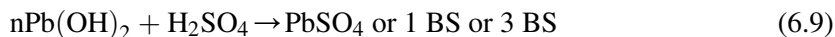
It is only after 20 min of stirring that formation of tet-PbO starts:



Reaction (6.7) is a slow process and it is completed after 2 h, whereby 1BS is converted into 3BS. Though at a slower rate, the amount of 3BS continues to increase, whereas orthorhomb-PbO decreases very slowly.

According to Fig. 6.1, formation of one or another type of basic lead sulfate depends on the pH of the solution. Table 6.2 presents the pH regions of stability of PbSO₄, 1BS and 3BS at two activity levels of the SO₄²⁻ ions. Which pH region will predominate in the paste depends on the rate of the reaction between PbO and H₂SO₄. Probably, this reaction passes through a hydration stage involving the following elementary reactions:





The rate of reaction (6.4) depends on the PbO modification used. Figure 6.9 evidences that tet-PbO undergoes quick hydration and reacts with H_2SO_4 , whereby 3BS is predominantly formed with small amounts of 1BS remaining in the paste. Figure 6.10 indicates that the reaction of hydration of orthorhomb-PbO is slow, which keeps the pH of the solution within the range between 7.0 and 9.0 for a long time, and hence, 1BS forms first. Only after the major part of orthorhomb-PbO has reacted with H_2SO_4 does the pH of the solution rise to over 9.0 and the formation of 3BS starts.

The PbO crystal lattice may influence the formation of one or another type of basic lead sulfate (reaction 6.9) through the rate of nucleation of the respective crystal phase. Nucleation of basic lead sulfates involves Pb^{2+} , OH^- , SO_4^{2-} and HSO_4^- ions. For the nucleation of a given basic lead sulfate, there should be over-saturation with the respective type of ions. The most favourable conditions for such an over-saturation are created on the surface of the hydrated $\text{Pb}(\text{OH})_2$ particles. There, the concentration of Pb^{2+} and OH^- ions is the highest and, hence, the reaction between these ions and H^+ and SO_4^{2-} ions will determine the type of hydrated basic lead sulfate to be formed and, later, the rate of nucleation of its dehydrated crystal form.

6.2.5. Tetrabasic Lead Sulfate Pastes, $4\text{PbO} \cdot \text{PbSO}_4$ (4BS)

Methods for preparation of $4\text{PbO} \cdot \text{PbSO}_4$ (4BS) pastes

Three essentially different methods for 4BS paste preparation are currently used in the battery manufacturing industry:

- From a slurry of lead oxide in water to which H_2SO_4 solution is added in stoichiometric proportion with regard to the PbO so as to form 4BS. Orthorhomb-PbO is used and the temperature of the slurry during paste preparation is 80 °C [4,14].
- By mixing leady oxide and H_2SO_4 solution at temperature higher than 80 °C for at least 30 min [11,13].
- By curing 3BS pastes at temperatures above 80 °C with purging water steam through the curing chamber for 3–5 h. The overall duration of the curing process is from 48 to 72 h. This method yields big 4BS crystals that form but very slowly [15].

The third method is the most widely used in the battery practice, followed by the second method of paste preparation.

Kinetics of 4BS crystal formation [10]

Figure 6.11 presents the changes in phase composition and temperature during preparation of two pastes at the initial temperature of 85 °C. The phase composition is determined from the relative intensity of the characteristic X-ray diffraction lines for the different phases.

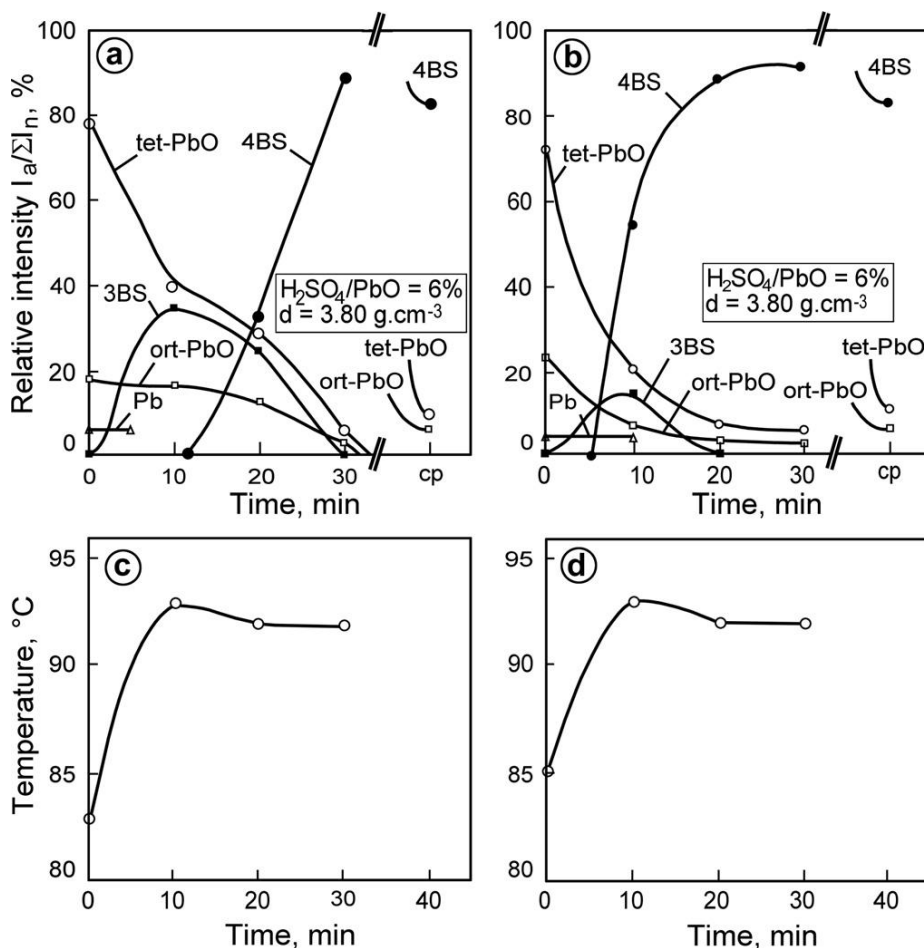


Figure 6.11:

(a,c) Changes in phase composition and temperature during preparation of two pastes with identical initial composition and conditions of preparation; (b,d) paste 2 contains 3% of paste 1 added at the beginning of preparation [10].

The two pastes are prepared one after the other using a H_2SO_4/LO ratio equal to 6% by weight. The initial materials used and the conditions of preparation are identical for the two pastes. The only difference is that a certain amount of the first paste (3%) is added to the second one, thus introducing some 4BS nuclei into the latter.

The initial leady oxide contains mostly tet-PbO. The latter facilitates the formation of 3BS nuclei first. On the other hand, part of the tet-PbO is converted into orthorhombic PbO. When tet-PbO, orthorhomb-PbO and 3BS crystals are present in the paste, formation of 4BS phase starts. This process begins between the 10th and 20th min of paste mixing and, within another 15 min, the whole paste is transformed into 4BS crystals (Fig. 6.11a).

The data in Fig. 6.11b suggest that the rate of 4BS nucleation may be increased significantly if formed 4BS nuclei are introduced into the paste. In this case, almost the whole paste is converted into 4BS crystals within 20 min. It can be concluded that the slowest elementary process involved in the preparation of 4BS pastes is the process of nucleation of this phase.

Figure 6.11 evidences that 3BS forms first on mixing of the leady oxide with H_2O and H_2SO_4 solution, but after 10–20 min it is converted into 4BS crystals. This indicates that 3BS crystals are thermodynamically unstable at 80 °C. At the same $\text{H}_2\text{SO}_4/\text{LO}$ ratio, but at temperatures lower than 60 °C, the rate of nucleation of 4BS is probably so slow that practically no 4BS crystals form.

The reactions of 4BS formation can be expressed by the following stoichiometric equations:

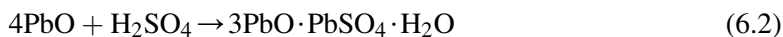


Figure 6.12 shows SEM micrographs of 4BS crystals obtained after 30 min of mixing of the second paste presented in Fig. 6.11.

Well-shaped 4BS crystals predominate in the paste. They differ in size because of the different times of nucleation and growth of each of these crystals. The largest 4BS crystals are between 15 and 30 μm in length and from 4 to 10 μm in diameter.

Effect of temperature on the preparation of 4BS pastes [10]

Barton leady oxide is used for paste preparation and the $\text{H}_2\text{SO}_4/\text{LO}$ ratio is equal to 6%. Figure 6.13 presents the kinetic curves of formation of 4BS pastes at three different temperatures.

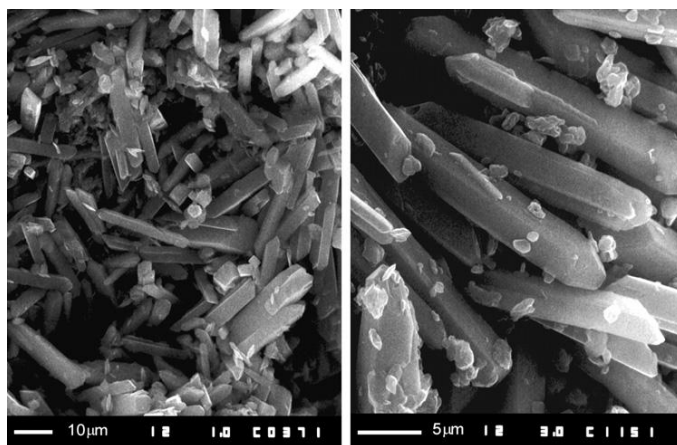


Figure 6.12:
SEM pictures of 4BS paste crystals at two magnifications.

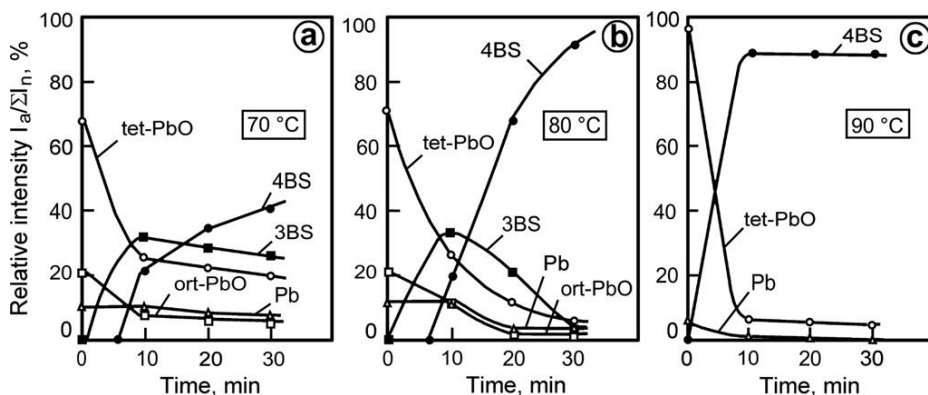


Figure 6.13:

Phase composition of three 4BS pastes, determined by XRD analysis, vs. time of paste mixing at three different temperatures: (a) 70 °C, (b) 80 °C, and (c) 90 °C [10].

When the paste is prepared at 70 °C, considerable amounts of 3BS crystals remain unreacted even after 30 min of mixing. The situation is different when the process of paste preparation is carried out at 90 °C. In this case, the whole paste is converted into 4BS crystals within the first 10 min. At 80 °C, the transformation of 3BS to 4BS is completed within 30 min. This indicates that the process of nucleation and growth of 4BS crystals is very sensitive to the temperature of paste preparation. In order to produce 4BS paste within 30 min the temperature of paste preparation should be above 90 °C.

Effect of H₂SO₄/LO ratio on phase composition of the paste [11]

Pastes are prepared at 80 °C using ball mill leady oxide (75% degree of oxidation). After 40 min of stirring, the phase composition is determined through XRD analysis. Figure 6.14 presents the obtained results [11].

When up to 8% of H₂SO₄ vs. LO is used, the basic product in the paste is 4BS. Maximum 4BS content is obtained when the paste is prepared using between 5 and 6% H₂SO₄ vs. LO. At H₂SO₄/LO ratios above 8%, the paste predominantly contains 3BS, its content reaching maximum values at 10% H₂SO₄ vs. LO. At H₂SO₄ levels above 8%, beside 3BS, 1BS forms, too.

The above sequence of formation of basic lead sulfates in the paste is related to the decreasing pH of the solution as a result of the increased H₂SO₄ concentration. According to the above reactions, at 6.5% H₂SO₄/LO, the whole amount of PbO should be converted into 4BS crystals. Indeed, the maximum content of the latter phase in the paste is registered within this region of H₂SO₄ concentrations (see Fig. 6.14). On increasing the H₂SO₄ content above 8% vs. LO, conditions are created, similar to those described in Section 6.2.4.2. for 3BS pastes, which favour the formation of sufficiently stable phases such as 1BS and 3BS at 80 °C.

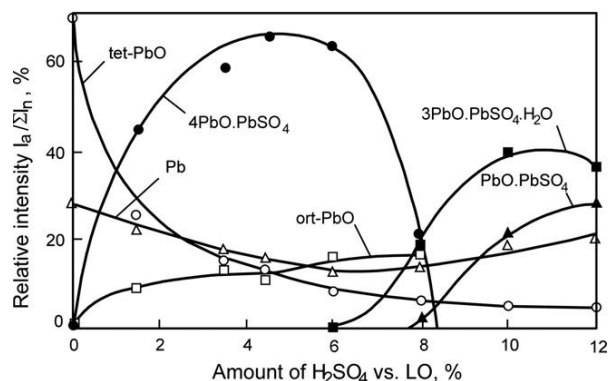


Figure 6.14:

Phase composition of a paste prepared at 80 °C vs. $\text{H}_2\text{SO}_4/\text{LO}$ ratio [11].

Effect of expanders or surface active materials on the preparation of 4BS pastes [16]

Figure 6.15 illustrates the correlation between phase composition of the paste and the $\text{H}_2\text{SO}_4/\text{LO}$ ratio used for its preparation [16]. Pastes are mixed for 30 min at 80 °C. The first series of pastes (Fig. 6.15a) are prepared with 0.5% BaSO_4 added to the lead oxide, and the second series of pastes (Fig. 6.15b) contain 0.5% BaSO_4 and 1% expander (sodium lignosulfonate). BaSO_4 exerts almost no influence on the phase composition of the pastes. The expander added to the paste blocks the formation of both orthorhombic PbO and 4BS. Processes similar to those proceeding at 30 °C occur in the pastes and lead to the formation of only 3BS and 1BS. No orthorhomb-PbO is formed.

In order to demonstrate the blocking effect of expander, the latter is introduced into the paste when the formation of 4BS has already started (i.e. after 20 min of stirring). Figure 6.16 presents kinetic curves reflecting the amounts of the different phases in a paste prepared at 80 °C using Barton lead oxide.

On adding the expander, formation of 4BS stops, orthorhombic PbO is probably converted into tet-PbO, which is associated with the formation of a certain amount of 3BS, too. As a result of these processes the paste contains no orthorhombic PbO. And, as the latter is one of the basic initial compounds needed for 4BS nucleation, this latter phase is no longer formed in the paste. Formation of 4BS is blocked as a result of lack of orthorhombic PbO in the paste. Hence, no 4BS crystals are formed in the pastes for negative plates containing expander.

Influence of PbO modification on the kinetics of 4BS formation [13]

Investigations into the kinetics of $4\text{PbO} \cdot \text{PbSO}_4$ formation have been carried out at 80 °C [13]. Tetragonal or orthorhombic PbO are used for preparation of the pastes. Figure 6.17 illustrates the changes in phase composition during stirring of pastes containing 6% $\text{H}_2\text{SO}_4/\text{tet-PbO}$.

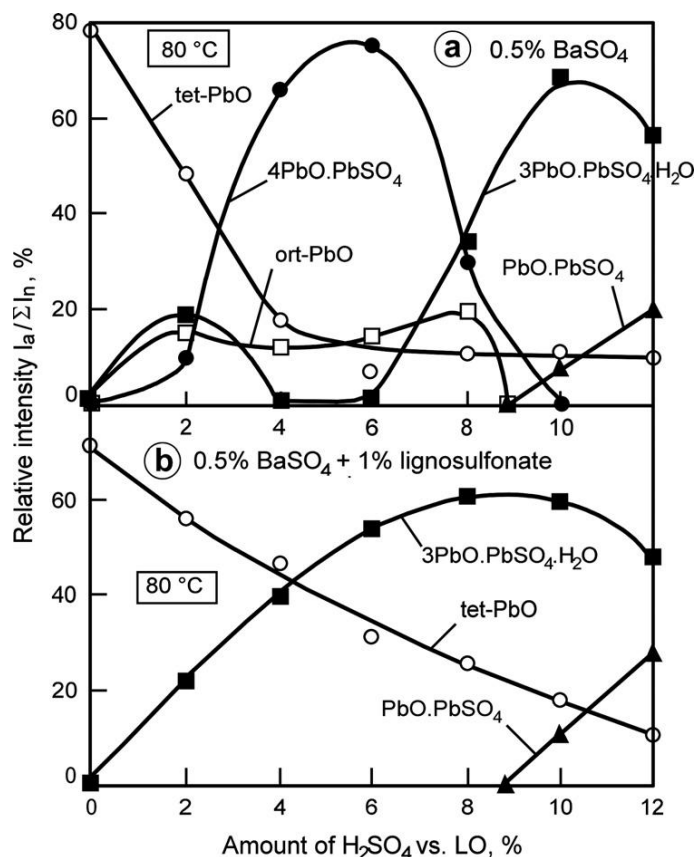


Figure 6.15:

Changes in phase composition of a paste prepared at 80 °C vs. $\text{H}_2\text{SO}_4/\text{LO}$ ratio. Additives to the paste: (a) 0.5% BaSO_4 ; (b) 0.5% BaSO_4 and 1% lignosulfonate [16].

Tetragonal PbO is a chemical product. It can be seen that first $3\text{PbO} \cdot \text{PbSO}_4 \cdot \text{H}_2\text{O}$ and orthorhomb-PbO are formed. After 30 min, the paste contains mainly $4\text{PbO} \cdot \text{PbSO}_4$.

The changes in relative intensity of the XRD lines for the phases formed during paste preparation from 100% orthorhomb-PbO and 6% $\text{H}_2\text{SO}_4/\text{LO}$ at 80 °C are given in Fig. 6.17b. The data in the figure evidence that PbSO_4 forms initially. Ten minutes later, the paste contains $\text{PbO} \cdot \text{PbSO}_4$, $3\text{PbO} \cdot \text{PbSO}_4 \cdot \text{H}_2\text{O}$, orthorhomb-PbO and tet-PbO. After 20 min of paste stirring, $\text{PbO} \cdot \text{PbSO}_4$ is completely transformed into $3\text{PbO} \cdot \text{PbSO}_4 \cdot \text{H}_2\text{O}$. Formation of $4\text{PbO} \cdot \text{PbSO}_4$ starts after 30 min and its content in the paste increases during the next 30 min. Figure 6.17 is analogous to Fig. 6.10. The main difference is that, in the case of 3BS paste preparation from orthorhomb-PbO, 1% SL is added to block the formation of 4BS. Without the addition of SL, as evident from Fig. 6.17b, beside 4BS also PbSO_4 forms at the beginning of paste preparation. Probably, the rate of the reaction between orthorhomb-PbO and H_2SO_4 is very

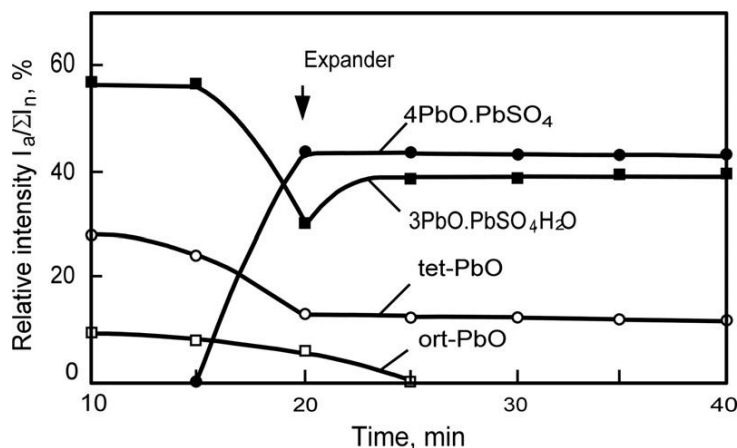


Figure 6.16:

Effect of expander (added at the 20th min of stirring) on phase composition of the paste. Introduction of expander stops formation of 4BS [27].

high and, when the H_2SO_4 solution gets in contact with the first orthorhomb-PbO particles, PbSO_4 forms locally. With gradual depletion of H_2SO_4 , the pH of the solution increases and, since PbSO_4 is unstable at $\text{pH} > 7.8$ (Table 6.2), it transforms into 1BS and 3BS.

Figure 6.17c shows that, when a mixture of 50% tet-PbO plus 50% orthorhomb-PbO is used, 3BS forms within the first couple of minutes already, while formation of 4BS starts after the 5th min of paste stirring. After 20 min, the content of 4BS is as high as 65% against 20% in the paste prepared from tet-PbO alone. Our investigations have proved that the maximum rate of 4BS formation is achieved when the leady oxide mix contains 75 to 80% tet-PbO. The recommended proportion of the two PbO modifications in the initial lead powder for preparation of 4BS pastes is 20% orthorhomb-PbO + 80% tet-PbO.

6.2.6. Amorphous Components as Indispensable Constituents of the Paste

Amorphous components of the paste

The basic components of the paste are crystal phases of 3BS or 4BS, small amounts of orthorhomb-PbO, tet-PbO and Pb. These are detected by X-ray diffraction methods. If a paste is prepared from crystal phases of 3BS and tet-PbO in the same proportion as in the paste prepared from leady oxide and H_2SO_4 , and then grids are pasted with this paste and set to curing and formation, the obtained PAM is mechanically unstable and difficult to form, and hence the plates have low capacity. Valeriotte has found that one of the reasons for the low energetic characteristics of positive plates is the lack of amorphous components in the paste [17]. The content of amorphous phases should amount to 15–10%. Such amorphous components in the paste are most often hydroxides. Some of the amorphous hydroxides are obtained as a result of oxidation of Pb in the leady oxide during paste preparation and plate curing. And the content

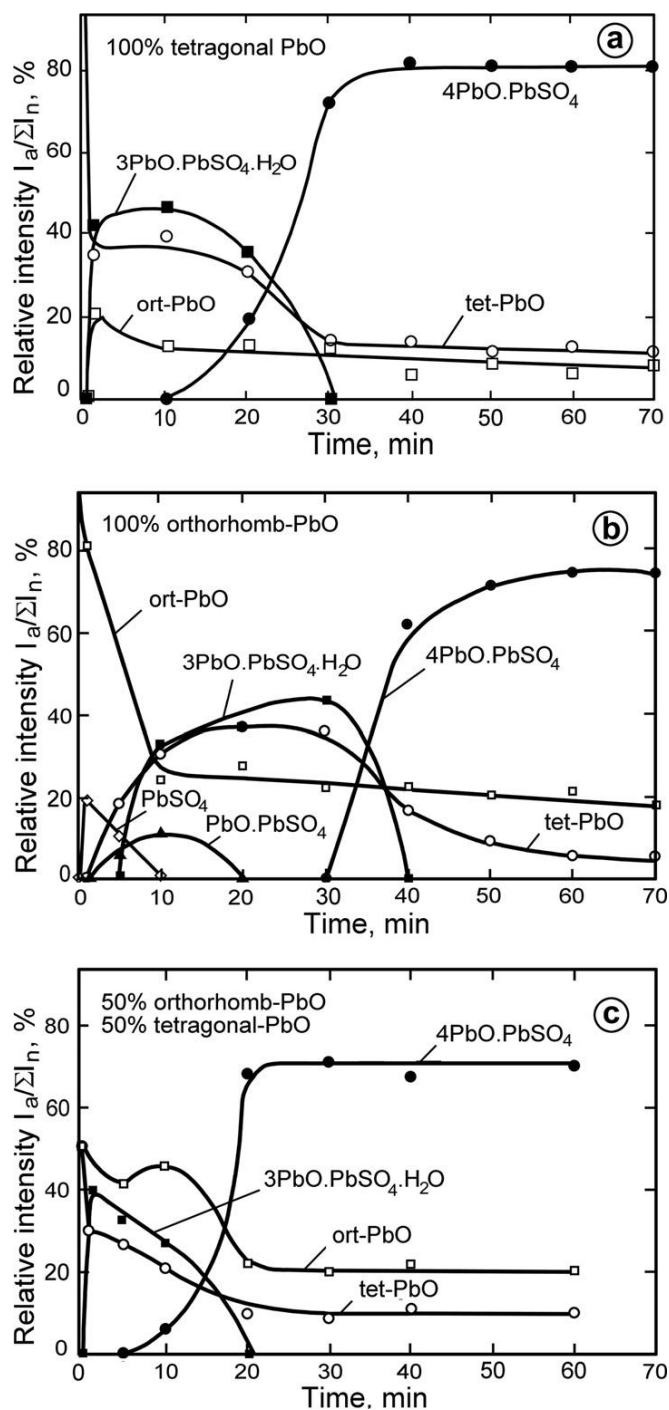


Figure 6.17:

Changes in phase composition of the paste during stirring at 80 °C. The paste is prepared from (a) 100% tet-PbO, (b) 100% orthorhomb-PbO and (c) 50% tet-PbO + 50% orthorhomb-PbO [13].

of elemental Pb in the leady oxide is of the order of 15–25%. During paste preparation, part of Pb is oxidized and its content in the paste diminishing to 10–15% and the products of this oxidation are lead hydroxide and hydrated basic lead sulfate [17]. These amorphous phases serve as binders (gluing agents) between the crystal particles of 3BS or 4BS. Thus, they improve the mechanical strength of the cured paste, facilitate its formation and prolong the life of the plates.

There are but scarce investigations into the role of amorphous components in the paste on battery performance.

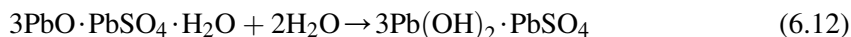
Reactions of hydration and carbonization of the paste, and oxidation of Pb

Parallel to the reaction of 3BS (or 4BS) formation, other reactions, too, proceed in the paste. First, a reaction of oxidation of Pb to PbO takes place:

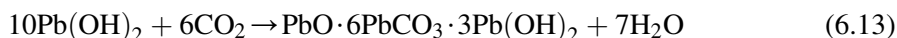


The relatively high temperature of paste preparation and mixing accelerate the above reaction.

The second reaction that proceeds is hydration of PbO, whereby lead hydroxide is formed. 3BS is also hydrated to some extent.



The third type of reactions is related to carbonization of the paste. The latter proceeds when there is considerable amount of CO₂ in the production facilities. Under such conditions lead hydrocarbonate is formed.



When the time of paste preparation is short and the paste mixer is isolated from the rest of the production premises, the reaction of carbonization is slowed down and only inconsiderable or even negligible amounts of hydrocarbonate will be formed.

The amorphous phases that cannot be detected by XRD can be determined from the difference between the calculated paste composition and the crystal content as determined by XRD. The hydrated and carbonated phases in the paste can be detected through differential scanning calorimetry (DSC) [18].

6.2.7. Cycle Life of Positive Plates as a Function of Phase Composition of the Paste [19]

It has been established experimentally that the phase composition of the paste exerts a stronger influence on the capacity and cycle life of positive plates than on negative ones.

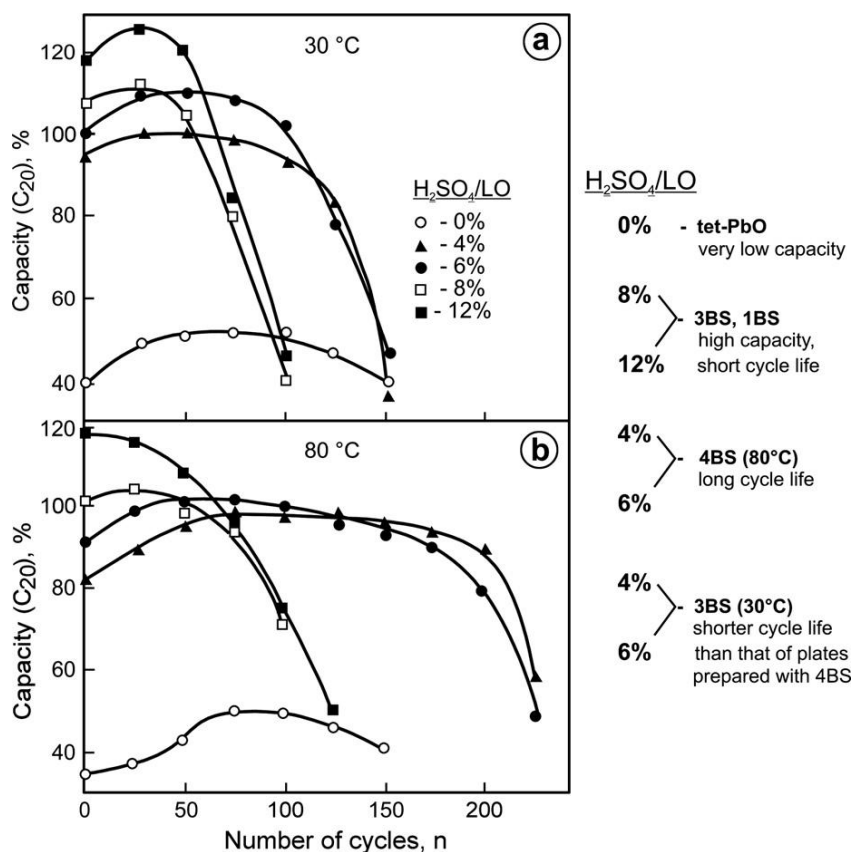


Figure 6.18: Capacity vs. number of cycles dependencies for batteries prepared with pastes of different phase composition at: (a) 30 °C and (b) 80 °C [19].

Figure 6.18 presents the cycle life test results obtained for positive plates pasted with pastes prepared at 30 °C and 80 °C using H₂SO₄ and LO in different proportions. As already mentioned above, pastes prepared at 30 °C with up to 10% H₂SO₄ content contain mainly 3BS crystals, and those with 8–12% H₂SO₄ vs. LO contain 1BS as well (see Fig. 6.5). Pastes prepared at 80 °C with 4–6% H₂SO₄ are composed mainly of 4BS (see Fig. 6.14). The paste prepared using 8% H₂SO₄/LO at 80 °C contains 3BS, 4BS, and 1BS, while that with 12% H₂SO₄ contains 3BS and 1BS. Positive plates expand in volume during battery cycling. In the above investigations, plate volume growth is not constrained by separators.

The active mass obtained from pastes containing no H₂SO₄ (0%) has very low capacity, irrespective of the temperature of paste preparation. That is why battery manufacturers use basic lead sulfate pastes, and not lead oxide ones, for the production of positive plates.

A very high initial capacity but rather short cycle life exhibit active masses obtained from pastes containing 3BS and 1BS (12% $\text{H}_2\text{SO}_4/\text{LO}$). The active masses with longest cycle life prove to be those obtained from 4BS pastes, but their initial capacity is lower than the rated value. It should be pointed out, however, that the size of the 4BS crystals in these pastes is from 30 to 40 μm . Pastes containing 3BS crystals have initial capacity equal or close to the rated one. Their life, however, is shorter than that of plates prepared with 4BS pastes.

The above results indicate unambiguously that the phase composition of the paste is very important for the performance characteristics of positive battery plates. The capacity and energetic parameters of the batteries as well as the span of their service life are predetermined already during the process of paste preparation.

The effect of phase composition of the pastes on the performance of lead-acid batteries has been studied by a number of authors.

Biagetti and Weeks [14] have established that plates produced with 4BS pastes have almost twice longer cycle life than 3BS plates. Culpin [20] has investigated SLI batteries with 4BS positive plates and has found that their cycle life at 20 h discharge rate and their CCA performance (at -18°C) are similar to those for SLI batteries with positive plates prepared with 3BS pastes. However, '4BS batteries' have longer cycle life (by 50%) than that of '3BS batteries' at 1 h and 5 h discharge rates.

Burbank [4] has proposed an explanation of the above test results. Lead dioxide aggregates, formed from the 4BS crystals as a result of the metasomatic processes of PAM formation, yield a mechanically more stable PAM resistant to expansion and shedding. Hence, 4BS batteries have longer cycle life. Burbank et al. [21] suggest that, during formation, 4BS cured pastes are converted partly into $\alpha\text{-PbO}_2$. This modification has a lower utilization coefficient on discharge and remains unreacted after the discharge. It builds a 3D network structure which provides a mechanical support to PAM preventing it from shedding and conducts the current to every point in PAM throughout the plate.

The explanation of the above described influence of phase composition of the paste on battery performance is reduced essentially to a structural problem. The positive active mass consists of (a) energetic structure, which is reduced during discharge and re-built during the subsequent charge; (b) skeleton structure, which conducts the current to all parts of PAM and provides mechanical support to the energetic structure. Only a small share of the skeleton structure participates in the charge and discharge processes. This share depends on several factors.

- (a) On the particular cycling mode. When the cycling schedule includes deep discharges, a greater share of the skeleton structure of PAM is involved in the discharge process and soon the skeleton structure will 'forget' its origin and vice versa. The variance in the results obtained by different authors about the influence of phase composition of the pastes on battery cycle life is due namely to the different cycling modes applied.

- (b) On the thickness of the skeleton branches which, in turn, depends on the morphology of the crystals and agglomerates in the paste as well as on the conditions of the subsequent technological procedures (soaking and formation). As evident from the SEM pictures in Figs. 6.7 and 6.12, the crystals of basic lead sulfates differ substantially in morphology from PbO particles. That is the reason for the higher performance characteristics of positive plates produced with basic lead sulfate pastes as compared to those produced only with PbO and H₂O. The difference in life span and in capacity performance of '3BS' and '4BS batteries' may also be related to the different crystal morphology of the two basic lead sulfates.
- (c) The content of α -PbO₂ in the skeleton structure also influences the process of restructuring of PAM skeleton on cycling. α -PbO₂ has a lower utilization coefficient than the β -PbO₂ modification and thus supports the skeleton structure (obtained during paste preparation, curing and formation) intact for a longer period of time during cycling, i.e. ensures longer battery life.

6.2.8. Technological Applicability of Basic Lead Sulfate Pastes in the Battery Industry

Three types of basic lead sulfates are obtained when mixing PbO with H₂SO₄ solution: 4BS, 3BS and 1BS.

Let us first discuss the applicability of 4BS pastes in the battery industry. Batteries produced with positive plates pasted with 4BS pastes have the longest cycle life, but their initial capacity is lower than the rated value and they need several preliminary cycles to reach the rated capacity.

What are the advantages of batteries produced with 4BS positive pastes? First, these batteries have the longest cycle life. The contact between grid and PAM is very good, which reduces or even eliminates the PCL-1 effect. The capacity vs. cycle number curve for such batteries features the longest horizontal segment (plateau), which means that the processes on charge and discharge are highly reversible. The positive active mass of such batteries does not soften on cycling.

What is the share of 4BS pastes in the battery manufacturing practice? The above features of batteries with 4BS positive plates have made them most widely used paste in stationary battery applications.

Why do battery manufacturers refrain from mass introduction of 4BS pastes? First, because the time for formation of 4BS plates is longer by some 30–50% and a more complex formation schedule should be employed, including charge and discharge steps. Secondly, the consumption of electric energy for the formation process is higher by 30–35%. Thirdly, the curing process of such plates needs higher temperatures, e.g. 3–5 h at 80–90 °C, which in turn requires a more complex curing chamber design and involves higher energy

consumption. And finally, 5 to 10 initial cycles are needed for the battery to reach its rated capacity.

Can these technological problems be solved? All above mentioned technological issues are related to the size of 4BS crystals in the paste. These crystals are between 20 and 80 μm in length and from 8 to 15 μm in diameter. Such crystals are oxidized but very slowly to PbO_2 and require a complex formation algorithm. On the other hand, large crystals yield a stable PAM structure with well organised system of macro and micropores ensuring long battery cycle life. However, if the size of 4BS crystals is reduced to 15–25 μm in length and 3–5 μm in diameter, formation of the plates will be accelerated without affecting the cycle life at that.

How can 4BS crystals with the above dimensions be obtained? Several methods have been developed for producing 4BS crystals between 15 and 25 μm long with diameters of up to 5 μm .

The first method includes addition of up to 5% ground 4BS crystals (powder) to the paste mix to serve as nuclei for the formation of larger 4BS crystals. These 4BS nuclei grow equally during paste preparation, which results in uniform crystal size distribution. As there are a great number of these nuclei in the paste mix, they will form small crystals. This can be achieved by limiting the time of paste mixing at high temperature to no more than 15–20 min and then cool down the paste so as to prevent subsequent recrystallization of larger 4BS crystals at the expense of disintegration of smaller ones. There are data in the commercial literature advertising specially developed additives that regulate the crystal growth of 4BS crystals to controlled sizes.

In our laboratory, we have developed a method for increasing the initial capacity of 4BS batteries by adding red lead (up to 30 wt%) to the paste mix. In the above concentration red lead has very strong beneficial effect on the initial performance characteristics of the battery without shortening its cycle life.

Let us now see what the effect of 1BS pastes on battery performance. Figure 6.18 evidences that batteries produced with 1BS pastes have the highest initial capacity, irrespective of the temperature of paste preparation. What is this high capacity due to?

In order to produce a paste with predominant 1BS composition, H_2SO_4 solution and LO should be used for paste preparation in a ratio higher than 10% by weight. When the $\text{H}_2\text{SO}_4/\text{LO}$ ratio is between 11 and 15%, the main component in the paste is 1BS. Mono-basic lead sulfate crystals are small in size (1–2 μm long and very thin). During plate formation, they are oxidized to $\beta\text{-PbO}_2$ and no $\alpha\text{-PbO}_2$ is formed. The skeleton of PAM is built of thin aggregates with large surface. This skeleton disintegrates easily on cycling.

The most common practice in the battery industry is to use 3BS pastes for the positive plates. As evident from Fig. 6.18, the cycle life of batteries produced with 3BS pastes is relatively long and the battery reaches its rated capacity within the first three cycles already.

The technology for preparation of this paste is simple, easy to implement and control. Batteries with 3BS positive plates are readily formed and require the least electric energy supply. All these advantages have made 3BS pastes preferable for all types of battery applications and unrivalled for SLI batteries.

To sum up, the performance parameters of the battery (capacity and cycle life) are greatly pre-determined by the type of paste used for plate manufacture, i.e. by the type of basic lead sulfate(s) it contains. The type and amount of basic lead sulfates in the paste influence both the initial capacity and the cycle life performance of the battery. Therefore, it is essential to know very well the processes that take place during paste preparation. The technological procedures of paste preparation should be conducted under strict control of the specified technological parameters.

6.2.9. Pastes Prepared From Leady Oxide and Pb_3O_4

It is useful to add red lead (RL), Pb_3O_4 , to the positive paste mix in the following two cases:

- (a) When the initial battery capacity is low, limited by the positive plates. If it is not possible to make other changes in the production technology, an addition of red lead will improve the capacity performance. Pb_3O_4 should be added in an amount of 20–33% by weight vs. LO.
- (b) When the duration of plate formation has to be shortened. As is well known, negative plates for automotive batteries are formed for 10–12 h, while positive plates require over 18 h of formation. Addition of red lead to the paste mix will reduce appreciably the formation time for positive plates.

The above effects of RL can only be achieved provided the PbO_2 formed as a result of decomposition of Pb_3O_4 in H_2SO_4 remains non-reduced. Decomposition of Pb_3O_4 in H_2SO_4 proceeds through the following chemical reaction:

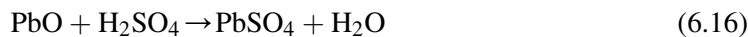


The obtained PbO_2 may diminish as it reacts with Pb in the LO according to the reaction:



Thus, the influence of red lead on the formation process and on the initial capacity is reduced substantially. To avoid this the above reaction should be suppressed.

The PbO formed by reaction (6.15) reacts with H_2SO_4 forming $PbSO_4$:



In order to increase the beneficial effect of Pb_3O_4 , the influence of reaction (6.15) should be reduced by reducing the amount of Pb, i.e. by reducing the content of LO in the paste (or slurry

for wet filling) and increasing the degree of LO oxidation. Thus a greater amount of PbO_2 will remain in the paste, which will facilitate the formation process.

The rate of reaction (6.14) depends strongly on the amount of H_2SO_4 used for paste or slurry preparation. Depending on the pH of the medium, $3\text{PbO} \cdot \text{PbSO}_4 \cdot \text{H}_2\text{O}$, $\text{PbO} \cdot \text{PbSO}_4$ and PbSO_4 will form at temperature $T < 60^\circ\text{C}$, or $4\text{PbO} \cdot \text{PbSO}_4$, $\text{PbO} \cdot \text{PbSO}_4$ and PbSO_4 at $T > 70^\circ\text{C}$, respectively. So the ratio $\text{H}_2\text{SO}_4/(\text{LO} + \text{RL})$ is a key parameter for this technology. It should be borne in mind that the presence of $\text{PbO} \cdot \text{PbSO}_4$ crystals in the paste (or slurry) will yield a PAM structure with short cycle life. To avoid this, the content of $\text{PbO} \cdot \text{PbSO}_4$ should be less than 5%. Therefore, the influence of $\text{H}_2\text{SO}_4/(\text{LO} + \text{RL})$ ratio on the phase composition and crystal morphology of the paste (slurry) is of utmost importance.

Pb_3O_4 contains two ‘molecules’ of PbO and one ‘molecule’ of PbO_2 . Stoichiometric calculations of a mixture of LO-40% plus RL-60% show that it contains 72% PbO , 20% PbO_2 and 8% Pb . PbO from LO and Pb_3O_4 will react with H_2SO_4 , and PbO_2 with Pb . Figure 6.19 presents the changes in phase composition of the paste as a function of $\text{H}_2\text{SO}_4/(\text{LO} + \text{RL})$ ratio [22].

Based on the data in Fig. 6.19 it can be concluded that the range of $\text{H}_2\text{SO}_4/(\text{LO} + \text{RL})$ ratios used for paste or slurry preparation can be divided in three regions with regard to the phase composition of the obtained pastes:

(a) From 4 to 8% $\text{H}_2\text{SO}_4/(\text{LO} + \text{RL})$: yielding 3BS (4BS) pastes

Within this region of $\text{H}_2\text{SO}_4/(\text{LO} + \text{RL})$ ratios, the basic product of the sulfation processes is 3BS, if the temperature of paste preparation is lower than 60°C , or a mixture of 3BS and 4BS at temperatures between 60 and 80°C . The obtained paste consists of unreacted Pb_3O_4 (about 53%), 3BS (from 23 to 15%), PbO_2 (2–3%) and $\alpha\text{-PbO}$ (from 23 to 15%). 3BS is

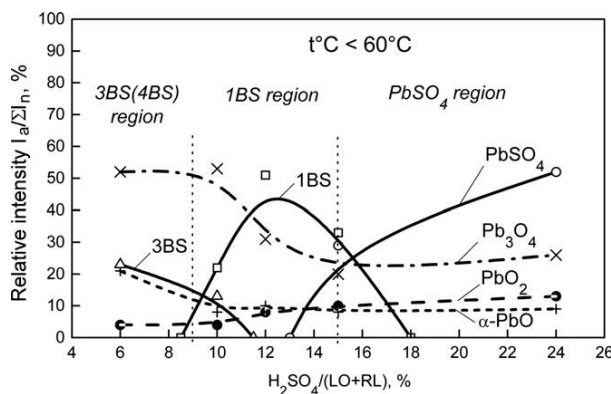


Figure 6.19:

Phase composition of pastes as a function of $\text{H}_2\text{SO}_4/(\text{LO} + \text{RL})$ ratio used for slurry preparation [22].

formed in solutions with pH higher than 9.5. In this pH region, Pb_3O_4 does not decompose. That is the reason why Pb_3O_4 has long been considered as an inert additive to the paste [23]. Probably, only the Pb_3O_4 particles that get in direct contact with H_2SO_4 when the latter is introduced into the mixer decompose. That is the reason for the insignificant amount of PbO_2 formed during paste or slurry preparation. The basic reaction that proceeds within this region is the reaction between PbO of the LO and H_2SO_4 .

(b) From 8 to 15% $\text{H}_2\text{SO}_4/(\text{LO} + \text{RL})$: yielding 1BS paste or slurry

1BS forms in solutions with pH between 8.2 and 9.5. Such pH values are reached when $\text{H}_2\text{SO}_4/(\text{LO} + \text{RL}) = 9\text{--}15\%$ are used for paste or slurry preparation. The main product of sulfation of such pastes or slurries is 1BS. When the above quantity of H_2SO_4 is introduced into the $(\text{LO} + \text{RL})$ mix, more Pb_3O_4 particles get in direct contact with the acid and hence greater amount of Pb_3O_4 will decompose. Consequently, the unreacted RL in the paste decreases from 53 to 20% (see Fig. 6.19), while the obtained PbO_2 increases from 4 to 10%. The content of unreacted $\alpha\text{-PbO}$ diminishes from 15 to 8%. 1BS crystals are needle-like in shape. The obtained paste is coloured in brown by the PbO_2 formed as a free phase. As pastes or slurries produced with 9–15% H_2SO_4 vs. $(\text{LO} + \text{RL})$ contain large amounts of 1BS, they should not be used for manufacture of positive plates.

(c) From 15 to 24% $\text{H}_2\text{SO}_4/(\text{LO} + \text{RL})$: yielding PbSO_4 pastes

Within this region of $\text{H}_2\text{SO}_4/(\text{LO} + \text{RL})$ ratios, the main product of sulfation of the $(\text{LO} + \text{RL})$ mix is PbSO_4 . The latter's content in the paste may reach up to 53% at $\text{H}_2\text{SO}_4/(\text{LO} + \text{RL}) = 24\%$. The paste (slurry) contains also some unreacted Pb_3O_4 (see Fig. 6.19). Pastes with such high content of PbSO_4 will form into PAM with predominantly $\beta\text{-PbO}_2$ structure. However, to ensure long battery life, the PAM after formation should contain considerable amounts of $\alpha\text{-PbO}_2$ (30–50%). Hence, it is essential to limit the content of Pb_3O_4 during the manufacture of pasted positive plates.

Figure 6.20 presents pictures of particles formed within the above three regions of $\text{H}_2\text{SO}_4/(\text{LO} + \text{RL})$ ratios [22]. The obtained pastes differ substantially in terms of both crystal morphology and structure. As a rule, Pb_3O_4 is added when pastes are prepared with H_2SO_4 and $(\text{LO} + \text{RL})$ in proportions within the first (3BS, 4BS) and third (PbSO_4) regions described above.

The reaction between H_2SO_4 and Pb_3O_4 proceeds at the surface of the Pb_3O_4 particles and the obtained products, depending on solution pH, are 3BS, 1BS, PbSO_4 and PbO_2 phases, which isolate the H_2SO_4 from the remaining unreacted part of the Pb_3O_4 particle. Hence, the concentration of the H_2SO_4 solution influences the processes of Pb_3O_4 decomposition. The latter reaction has been investigated through introducing 10 g of Pb_3O_4 into 100 mL of H_2SO_4 solutions of various concentrations [24–26]. After 40 min of stirring, the chemical composition of the suspension is determined. Figure 6.21 presents the dependence of the

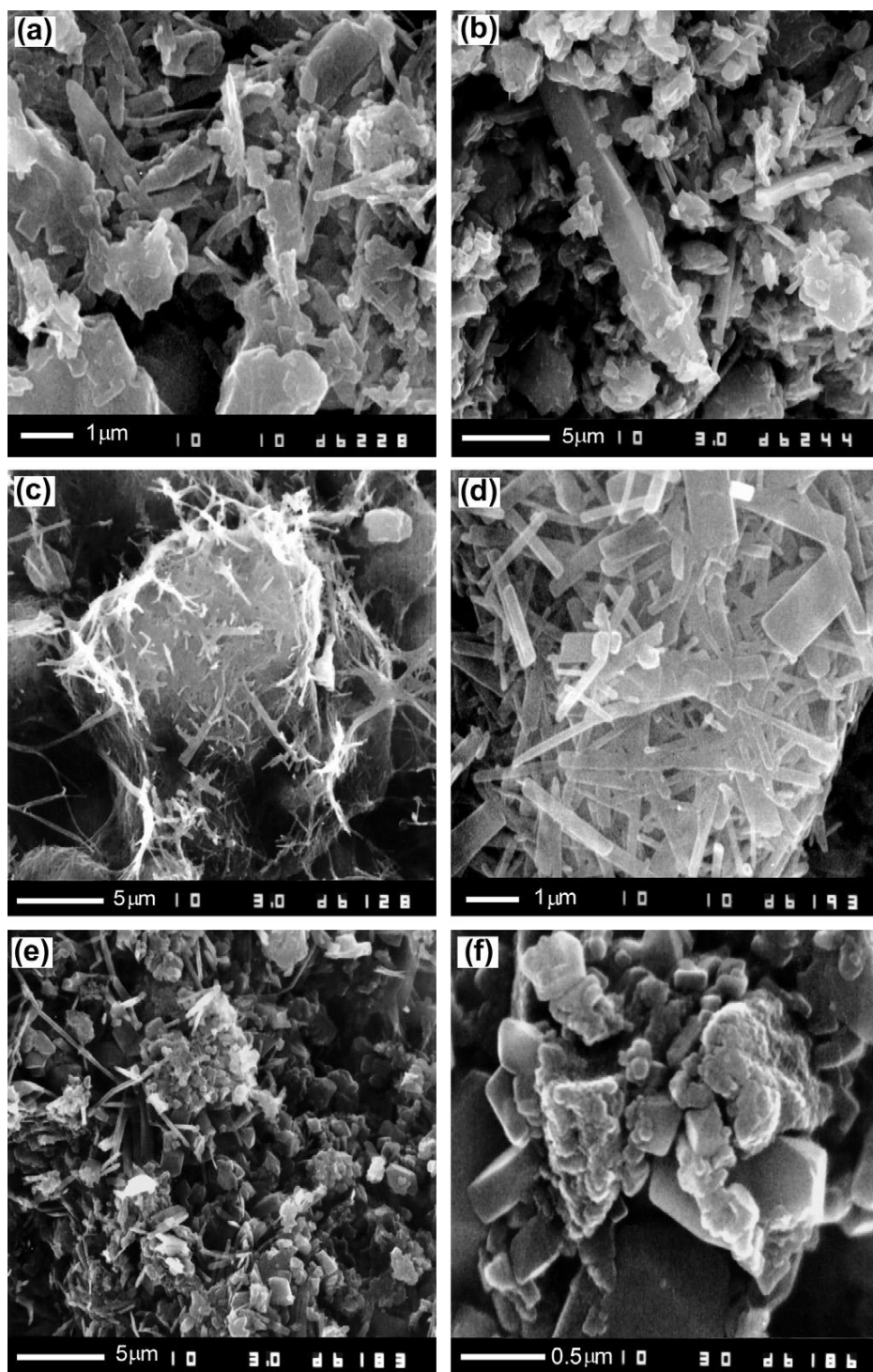


Figure 6.20:

SEM pictures of paste particles obtained in the three $\text{H}_2\text{SO}_4/(\text{LO} + \text{RL})$ regions: (a,b) 4–8% $\text{H}_2\text{SO}_4/(\text{LO} + \text{RL})$; (c,d) 8–15% $\text{H}_2\text{SO}_4/(\text{LO} + \text{RL})$ and (e,f) 15–24% $\text{H}_2\text{SO}_4/(\text{LO} + \text{RL})$ [22].

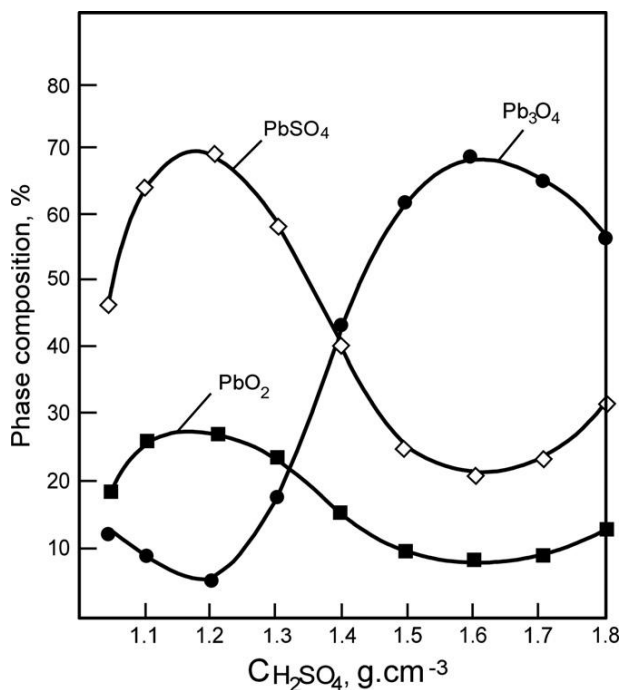


Figure 6.21:

Reactivity of Pb_3O_4 with H_2SO_4 — paste composition after 40 min of mixing [26].

content of PbSO_4 , PbO_2 and unreacted Pb_3O_4 as a function of H_2SO_4 concentration. The rate of Pb_3O_4 decomposition is the highest when H_2SO_4 solution of 1.20 relative density is used. At higher acid concentrations, the decomposition rate decreases substantially and considerable amounts of red lead remain unreacted in the paste.

Pastes prepared with 4BS yield active masses with low initial capacity and the batteries need some 10 charge-discharge cycles to reach their rated capacity. A method has been proposed for overcoming this drawback by adding Pb_3O_4 to the paste during its preparation [24–26]. The introduction of Pb_3O_4 in the paste mix creates a new system in which new processes occur leading to the formation of new phases in the paste and new structures of the paste particles, which eventually influence the performance of the battery.

Another important factor determining the morphology of paste particles is the technology of Pb_3O_4 decomposition [26]. Various methods can be used, including the following:

- Pb_3O_4 is decomposed with the whole amount of H_2SO_4 and H_2O , the mixture is stirred for 20 min and then the LO is added. Stirring continues for another 10 min.
- Another variation is to mix Pb_3O_4 with the LO in the dry state and then add H_2O and H_2SO_4 solution. In this case, PbSO_4 forms in the paste and some unreacted Pb_3O_4 remains as well.

Table 6.5: Cycling test results for batteries with Pb_3O_4 addition to the paste prepared by different technologies [26].

Batteries with active mass prepared from	Initial Capacity $C_{\text{measured}}/C_{\text{rated}}$ (%)	Cycle Life (Number of Cycles)
(a) Mix of $4\text{PbO} \cdot \text{PbSO}_4$ and Pb_3O_4	100–106	170
(b) $4\text{PbO} \cdot \text{PbSO}_4$ paste prepared with addition of Pb_3O_4	100–107	180
(c) Pb_3O_4 pre-decomposed with H_2SO_4 and then used for paste preparation	104–109	160
(d) Classical paste containing $3\text{PbO} \cdot \text{PbSO}_4 \cdot \text{H}_2\text{O}$	110–113	120

In an attempt to improve the initial capacity performance of batteries produced with 4BS pastes, various options for 4BS paste preparation with addition of Pb_3O_4 have been tried:

- 4BS paste is prepared from leady oxide and H_2SO_4 at $T^\circ > 80^\circ\text{C}$ and then Pb_3O_4 is added to the paste under continuous stirring for some time.
- Leady oxide and Pb_3O_4 are mixed in the dry state first and then hot water and H_2SO_4 are added in sequence under continuous stirring. The paste temperature reaches $90\text{--}95^\circ\text{C}$.
- Pb_3O_4 is decomposed with part of the H_2SO_4 and then the leady oxide and the remaining H_2SO_4 solution is added. The paste is stirred at $T^\circ > 80^\circ\text{C}$. With this method, the time period before the onset of 4BS formation is the shortest.
- For comparison, batteries with classical 3BS paste are also assembled and tested.

Table 6.5 summarises the cycling test results for batteries prepared by the above four methods [26].

It can be seen from the data in the table that Pb_3O_4 added to the paste, irrespective of the method used, improves the initial capacity performance of the batteries and prolongs their cycle life.

6.3. Technology of Paste Preparation

6.3.1. General Requirements to the Pastes

Pastes for positive and negative plates should meet the following requirements with regard to their technical characteristics:

- Adequate chemical and phase composition comprising particles of appropriate size and structure which, after formation, would yield stable skeleton and optimum energetic structure of the active masses. This is achieved by using a mixture of 3BS (or 4BS) and tet-PbO (with small amounts of orthorhomb-PbO) for preparation of the pastes. Some battery manufacturers add also Pb_3O_4 to the pastes for positive plates.

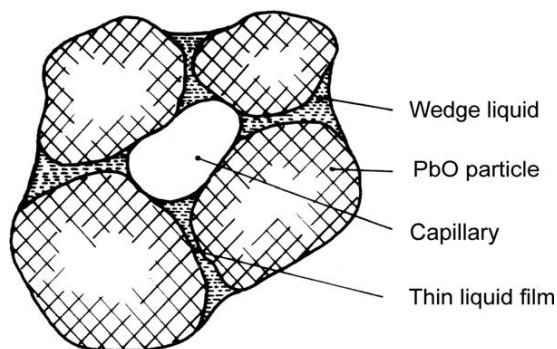
- (b) Definite paste density. The paste density is responsible for the porosity of the formed active masses, which in turn ensures large active surface and affects the capacity of the battery. The density of pastes for pasted positive plates should be within the range from 3.90 to 4.40 g cm⁻³. Pastes with lower densities (e.g. 3.70–3.80 g cm⁻³) could be used for tubular plates when high capacity is required rather than long cycle life performance. When battery life is of basic concern, however, the paste density should be between 4.30 and 4.60 g cm⁻³.
- (c) Adequate moisture content of the paste: 11–12%. This moisture level is needed for the processes of plate curing to proceed efficiently. The moisture content of the paste is determined from the weight loss after 1 h of heating at 110 °C.
- (d) Good plasticity (plastic flow properties). The latter characteristic is measured by the penetration of the penetrometer cone into the paste and its value should be between 20 and 35 readings of the penetrometer scale, depending on the angle of the cone penetrating into the paste. Paste plasticity is important for easy and uniform spreading of the paste onto the grids as well as for preventing the paste from shedding off the grids during the subsequent plate manufacturing procedures (i.e. paste/grid adhesion).
- (e) Homogeneity of the paste. It depends on the technology of paste preparation and on the design and technical characteristics of the paste mixer, i.e. its capability to mix uniformly the paste throughout its volume. The dispersivity of the initial materials used for paste preparation is also of importance. This feature is assessed by rinsing a pasted plate with water over a sieve with a definite mesh size. The paste is brushed off the grid into the sieve and then water is poured over it. No paste residue should remain in the sieve.

6.3.2. Paste Density

Liquid/particle system

If the thermodynamic properties of the thin liquid films formed between particles and the subsequent chemical reactions are ignored, the phenomena that occur when water is added to leady oxide can be explained simply as follows: (a) initially, PbO particles are hydrated and their surface is covered by absorbed water; (b) at the sites of contact between the particles a wedge of liquid is formed; (c) this wedge forms water rings on the surface of partially wetted particles in the contact regions; (d) these rings exert cohesion forces which hold the separate particles together in a rather loose system (Fig. 6.22) [27].

Particles held together by the wedge liquid form capillary spaces. The forces acting in these spaces flood the capillaries with liquid. A plastic state is reached characterised by a definite density and consistency, which allows the paste not only to be spread uniformly onto grids but also to be retained there. If the added water exceeds a certain critical amount, the liquid film between particles grows in thickness, the bonding between particles is weakened, and the entire system is transformed into a suspension.

**Figure 6.22:**

Liquid/particle system in the paste with capillaries not flooded by the liquid [27].

Density and consistency are parameters characterising the paste: density determines the bonding between particles under static conditions, whilst consistency does the same under dynamic conditions. Both parameters are functions of the water and H_2SO_4 content in the paste.

Paste density and parameters it depends on

Paste density is the weight per unit volume of battery paste. Paste density is measured by dividing the weight of paste contained in a cylinder by the cylinder volume. Most often, the paste used for positive plates has a density between 3.90 and 4.40 g cm^{-3} and that for negative plates, between 4.10 and 4.50 g cm^{-3} . Pastes based on red lead have densities higher by $0.20\text{--}0.30 \text{ g cm}^{-3}$.

As mentioned above, the phase composition of the paste depends on the ratio between sulfuric acid and leady oxide used for paste preparation. Pastes with identical quantities of liquid components, but with variable amounts of H_2SO_4 , have been prepared in an effort to determine the effect of the different phases upon paste density. In these experiments, the total liquid volume ($\text{H}_2\text{SO}_4 + \text{H}_2\text{O}$) is maintained constant varying the volumes of H_2SO_4 solution ($d = 1.20 \text{ g cm}^{-3}$) and of H_2O per 1 kg LO . The obtained results are presented in Fig. 6.23 [11]. The volume of H_2SO_4 solution used for paste preparation is given on the abscissa.

The data in the figure indicate that paste density does not depend on the proportion between the different phases (tet-PbO , $3\text{PbO} \cdot \text{PbSO}_4 \cdot \text{H}_2\text{O}$ and orthorhomb-PbO) in the paste, but rather on the proportion between the solid and liquid phases.

The changes in paste density have but a slight effect on phase composition of the cured paste and of the formed active mass as well as on capacity performance, but they exert a strong influence on battery cycle life. The life span is extended with increase of paste density, especially for pastes prepared with low $\text{H}_2\text{SO}_4/\text{LO}$ ratio.

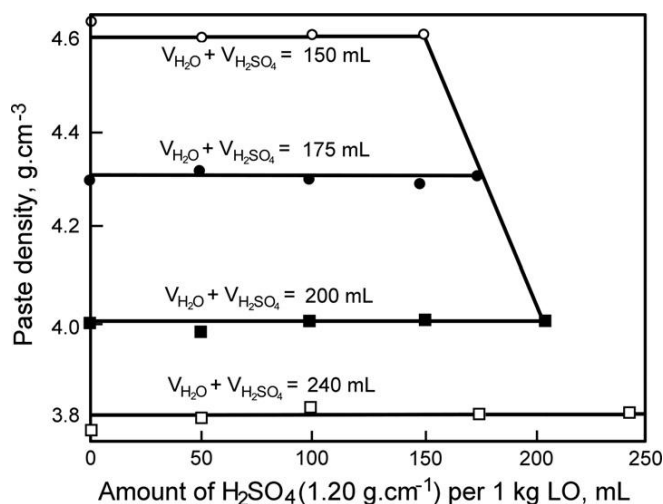


Figure 6.23:

Paste density vs. amount of H₂SO₄ per kg lead oxide at constant total amount of liquid components [11].

Beside the type of LO and the H₂SO₄/LO ratio used for paste preparation, the mixing technique (stirring or kneading) is of importance, too [28]. Adjustment of paste density is usually done by adding water, when the paste density is higher than desired, or by prolonged stirring and purging air through the paste, or vacuum treatment (to remove part of the water), or when the paste density is low. These adjustment procedures could be avoided by precise specification of the paste recipe, strict monitoring and control of the individual procedures performed by the mixer and continuous control of the temperature of paste mixing. The mixing process is completed when a definite paste density and moisture content is achieved.

Paste density critical values

Paste density determines the density of the active masses after formation. There is a lower critical value for the paste density, below which the structure of the formed active mass disintegrates, and an upper critical value above which the pore system in the formed active mass is not capable to transport ions to all parts of the active mass.

The above mentioned critical values for paste density have been determined by an indirect method [29]. Tubular electrodes are prepared with various PbO₂ powder masses of density, (d), between 3.40 and 4.50 g cm⁻³. These electrodes are subjected to cycling so as to allow the PbO₂ powder to be converted into porous PAM mass. Electrode cycling is conducted under the following conditions: discharge at 15 mA cm⁻² and recharge up to 200% of the preceding discharge capacity. Figure 6.24 presents the capacity/cycle number dependence for electrodes with lead spines. The capacity value calculated at 50% utilization of the active mass (C_0) is given for comparison.

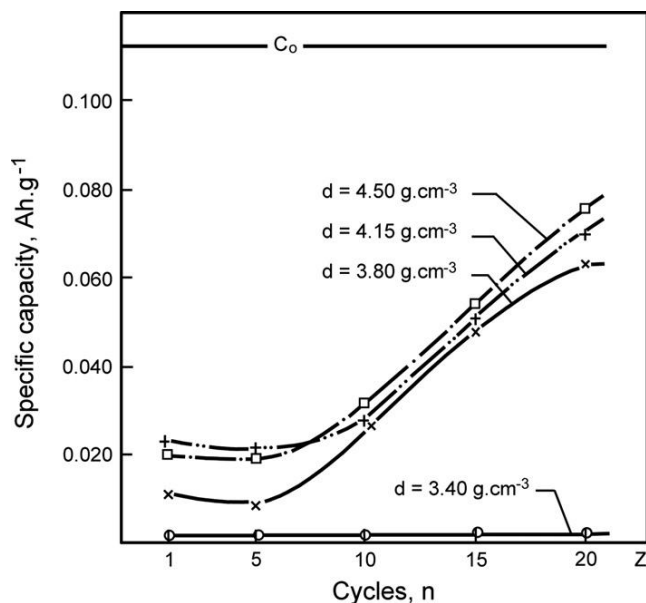


Figure 6.24:

Specific capacity of tubular electrodes with different PbO_2 powder densities vs. cycle number [29].

There is a lower critical value of the PbO_2 powder density above which restoration of the active mass commences. For a pure lead electrode this critical density is slightly less than 3.80 g cm^{-3} . Figure 6.24 evidences that there is but a very small difference between the capacity curves at $d = 4.15$ and $d = 4.50 \text{ g cm}^{-3}$. This means that, at $d = 4.15 \text{ g cm}^{-3}$, the PbO_2 particles have reached their full capacity to interconnect into an active mass skeleton.

After cycling, the polyester tubes are cut open. The active mass of electrodes prepared with PbO_2 powder with a density of 3.40 g cm^{-3} disintegrates into powder. Electrodes with 3.80 g cm^{-3} powder density also disintegrate easily under slight pressure. On the other hand, the active mass preserves its cylindrical shape in electrodes with 4.15 and 4.50 g cm^{-3} PbO_2 powder densities, i.e. the skeleton structure of the active mass of these latter electrodes has been built during the cycling process through interconnection of PbO_2 particles into a porous skeleton mass.

So the lower critical paste density limit is 3.80 g cm^{-3} . Densities above this value guarantee integrity of the active mass skeleton structure on cycling. Interlocking between PbO_2 particles and agglomerates into PAM skeleton is influenced by Bi^{3+} , Sb^{5+} and As^{3+} ions, which adsorb onto the surface of PAM particles and play the role of binders [29,30]. These ions are introduced mainly as additives to the grid alloys. On corrosion of the grid they are absorbed by the active mass.

There are literature data reporting of the practice of some battery manufacturers to introduce these additives into the paste through the leady oxide, by using lead powders containing certain amounts of these binders [31,32]. Thus for example, the maximum allowable content of Bi in the lead for LO production is up to 0.05%.

Semi-suspension technology for preparation of 4BS pastes

The German company Maschinenfabrik Gustav Eirich has adopted a new method for continuous temperature control of the paste preparation process, namely through evaporation (under vacuum) of the water contained in the paste [33]. This technology is called the Evactherm[®] technology. Utilization of vacuum treatment during preparation of battery pastes has much greater technological potential than simply to control the temperature of paste preparation.

One of its major advantages is that it allows the reaction between lead oxide and H_2SO_4 to proceed in a semi-suspension state (i.e. at densities between 3.20 and 3.50 g cm^{-3}). This method has been developed in our laboratory [34,35]. On completion of the crystallization process of basic lead sulfate, the semi-suspension can be concentrated through removal of the excess water (by evaporation under vacuum) until a paste of a desired density is obtained.

The semi-suspension has a much lower viscosity than that of the paste. This would allow the chemical reaction between H_2SO_4 and PbO to proceed uniformly throughout the whole mixer volume. This, in turn, would yield a homogeneous paste. Secondly, the ion transport between PbO in the powder and the growing basic lead sulfate crystals is much faster in the semi-suspension than in the paste and hence the chemical reaction is facilitated, which reduces the time for preparation of high-quality pastes.

It has been established from the battery practice that, in order to obtain pastes with densities from 3.90 to 4.40 g cm^{-3} , the total volume of H_2SO_4 solution and water should be between 180 and $216 \text{ mL kg}^{-1} \text{ LO}$. Let us assume the upper limit value ($216 \text{ mL kg}^{-1} \text{ LO}$) as the base volume of $\text{H}_2\text{SO}_4 + \text{H}_2\text{O}$ for paste preparation (denoted as V_0). The following method for 4BS preparation from semi-suspension has been developed [34,35]. First, leady oxide is loaded into the paste mixer. Then the total amount of H_2SO_4 solution and water, pre-heated to a temperature higher than 70°C , is added under stirring for a few minutes. The heat released by the chemical reaction between PbO and H_2SO_4 causes further temperature rise to $88\text{--}92^\circ\text{C}$ and the semi-suspension is stirred at this temperature for about 15 min . Then, vacuum is applied as a result of which the paste density increases and the temperature drops down to 30°C . Water is removed from the semi-suspension in an amount as to obtain a paste of the desired density.

Table 6.6 presents sample data about the excess water over the base volume $V_0 = 216 \text{ mL}$ ($\text{H}_2\text{SO}_4 + \text{H}_2\text{O}$), expressed both in $\text{mL kg}^{-1} \text{ LO}$ and in % vs. V_0 [34]. The water content in the semi-suspensions varies between 11 and 44% . The volume of the removed water is also given

Table 6.6: Quantity of water added to or removed from the semi-suspension during paste preparation^a [34].

Paste #	V_{H_2O} in (mL kg ⁻¹ LO)	in (% V_0)	out (mL kg ⁻¹ LO)	d (g cm ⁻³)	Pen (mm)
0	0	0	0	4.1	32
11	24	11	18	4.1	29
22	48	22	40	4.1	27
33	72	33	62	4.1	31
44	96	44	94	4.1	28

^a $V_0 = 216 + (\text{mL kg}^{-1} \text{ LO})$

in the table. All pastes have a density of 4.10 g cm⁻³. The penetration of the pastes is also measured and the obtained values are given in the last column under the heading 'Pen (mm)'. Pastes with higher water content (33 and 44%) have to be heated additionally during the vacuum treatment to accelerate water evaporation and remove the excess water from the semi-suspension. Hence, 260 mL of (H₂SO₄ + H₂O) solution per 1 kg LO is the technological upper limit for the semi-suspension method with no need for additional heating of the paste mixer.

Figure 6.25 illustrates the results from the initial three capacity and two CCA tests of batteries with positive plates prepared with pastes obtained from semi-suspensions with various densities. The numbers 0, 11, 22, 33 and 44 give the amount (in %) of the extra water added to the paste [34].

It can be seen that with increase of water content in the semi-suspension the capacity of the plates increases. The CCA performance of all batteries under test is the same, as it is limited by the negative plates.

Figure 6.26 presents the Peukert dependences for the above batteries. With increase of the water content in the semi-suspension, the Peukert curves shift towards higher specific capacity values.

The above batteries are set to cycle life tests. The discharge is conducted with a current equal to 2 h rate of discharge. The voltage after 1h of discharge is measured. Figure 6.27 shows the end-of-discharge voltage vs. the number of cycles for the batteries under test. The reference battery reaches its end of life after 28 cycles. The batteries produced with semi-suspension pastes have more than twice longer cycle life.

It is interesting to examine the relationship between discharge current density and specific capacity for batteries produced with semi-suspension pastes of various densities. For the purpose, let us draw a straight line at 110 Ah kg⁻¹ (Fig. 6.26) and read the intersection points of this line with the Peukert curves for the different batteries. These points give us the values of the discharge current densities at which the above specific capacity is delivered by the respective batteries. These values can be used for estimating battery power output at

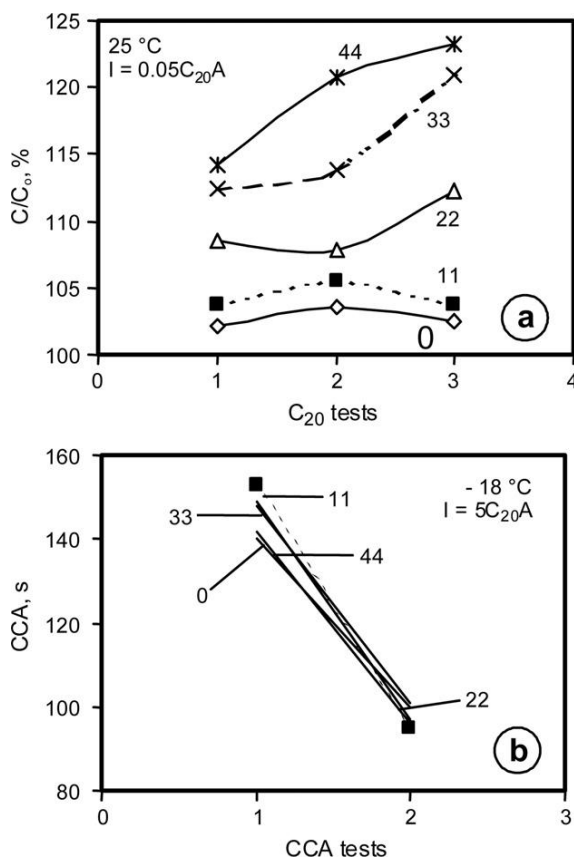


Figure 6.25:

a) Initial capacity and (b) cranking time on CCA test (with $I = 5 C_{20}$ at $t = -18^\circ\text{C}$) of batteries produced using semi-suspensions of various densities [34].

110 Ah kg^{-1} PAM specific capacity. What is the relation between these ‘power characteristics (markers)’ and the cycle life of the batteries? Figure 6.28 presents battery cycle life (in number of cycles until 10 V end-of-discharge voltage) vs. discharge current density at 110 Ah kg^{-1} PAM specific capacity.

The data in the figure indicate that batteries with positive plates prepared by the semi-suspension method have longer cycle life and higher power output as compared to batteries with positive plates produced with pastes. Another interesting finding is that on diluting the suspension, battery ‘power’ increases and its life remains unaffected at that. These results suggest that the conditions of 4BS(3BS) crystal formation and growth affect their structure. The latter influences the conductivity and stability of PAM, and thus the ‘power’ of the battery.

The obtained results evidence that the vacuum semi-suspension technology has a beneficial effect on the performance of positive plates, improving their service parameters.

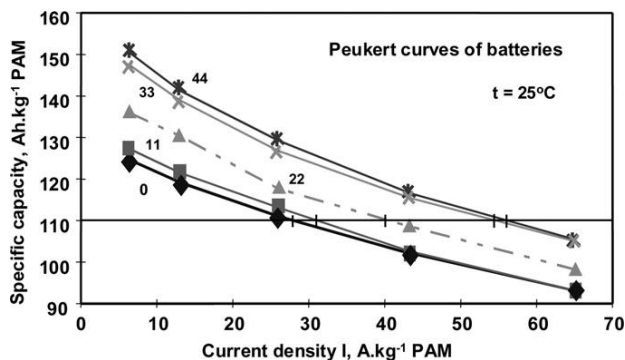


Figure 6.26:

Peukert curves for batteries with positive plates produced with 4BS pastes prepared by the semi-suspension technology [34].

6.3.3. Paste Consistency

Paste consistency is measured with the help of penetrometers, i.e. by checking the penetration depth into the paste of a cone with a given angle at the apex and a given weight. Paste consistency is inversely proportional to the penetration depth value. Figure 6.29 presents the results obtained from consistency measurements on pastes with identical densities vs. H_2SO_4 content. All pastes are prepared at 35 °C with 4 different densities and variable H_2SO_4 content (0–6%) [11].

Paste consistency, Q , increases linearly with increase of the H_2SO_4 content in the paste:

$$Q = A_0 + B \cdot C_{\text{H}_2\text{SO}_4}$$

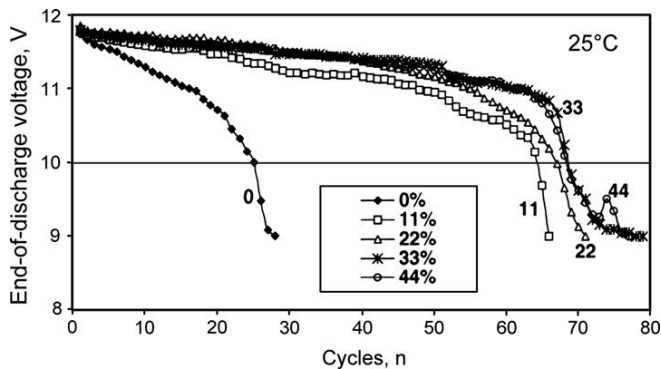


Figure 6.27:

End-of-discharge voltage reached for 1 h with discharge current equal to 2 h rate of discharge as a function of number of cycles [34].

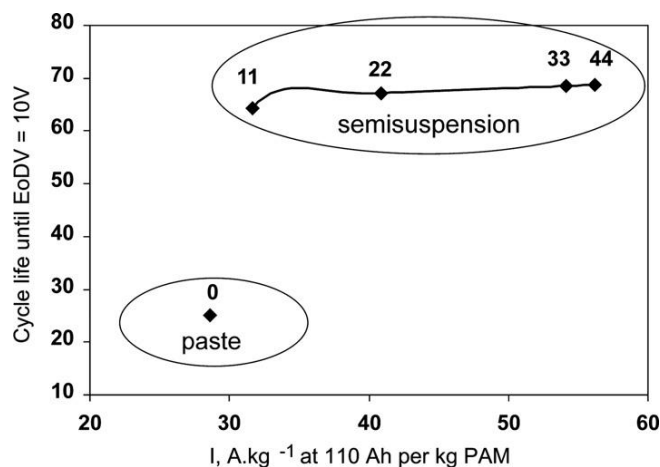


Figure 6.28:

Current density at 110 Ah kg^{-1} PAM (data from Fig. 6.26) vs. battery cycle life. The amounts of additional water in percent of the initial liquid volume ($V_0 = 216$ mL ($H_2SO_4 + H_2O$) per 1 kg LO) are also given in the figure.

where A_0 is the consistency of a paste prepared only with water, and B is a constant which depends on paste formulation. The linear increase in consistency reflects the linear increase of the 3BS content in the paste.

Figure 6.30 illustrates the correlation between the consistency of pastes prepared at 30 or 80 C and the content of $3PbO \cdot PbSO_4 \cdot H_2O$ or $4PbO \cdot PbSO_4$ in the paste [11].

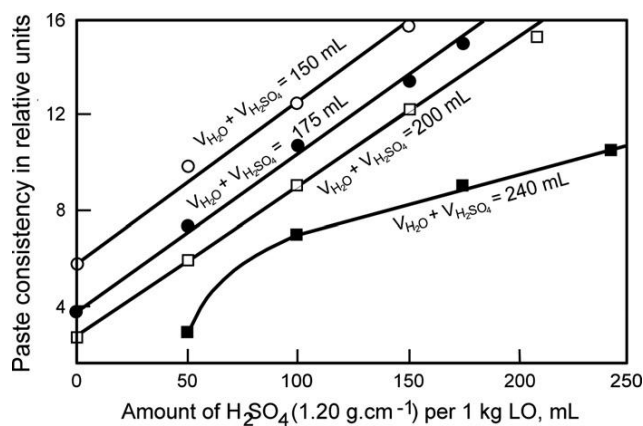


Figure 6.29:

Paste consistency vs. amount of H_2SO_4 at constant quantity of the liquid components per 1 kg leady oxide [11].

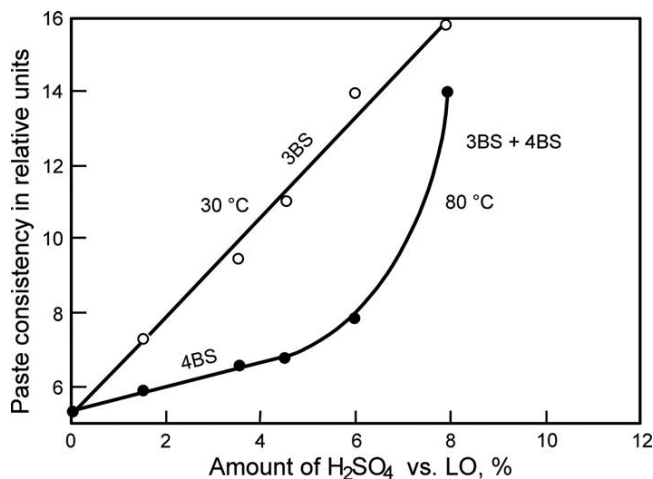


Figure 6.30:
Paste consistency vs. H_2SO_4 /LO ratio [11].

A comparison between Figs. 6.14 and 6.30 indicates that with increase of $4PbO \cdot PbSO_4$ content (curve at 80 °C), the paste consistency increases linearly up to 6% H_2SO_4 /LO, but with a less pronounced slope than that observed for the paste containing $3PbO \cdot PbSO_4 \cdot H_2O$ (35 °C).

Figures 6.29 and 6.30 evidence that paste consistency depends on the nature and amount of basic lead sulfates contained in it, i.e. on the friction between paste particles. When identical amounts of H_2SO_4 are used for paste preparation, displacement of the small $3PbO \cdot PbSO_4 \cdot H_2O$ crystals is associated with higher friction than that of the large prismatic $4PbO \cdot PbSO_4$ crystals (as the friction surfaces of 4BS crystals are considerably smaller).

The consistency of the negative paste depends not only on its phase composition, but also on the type of expander added, and especially on the organic capillary active component in the paste formulation. This relationship has been studied using two types of lignin, namely lignin M and hydrolyzed lignin (Fig. 6.31) [36]. All pastes are prepared with identical LO and H_2SO_4 /LO ratio, and differ only in the type of expander used. Water is then added to the thus prepared pastes in amounts as given on the abscissa and the paste consistency is measured after stirring.

As evident from the data in Fig. 6.31, lignin M reduces the consistency of the paste as compared to that of the expander-free formulation, whilst hydrolysed lignin increases paste consistency. In order to prepare a paste with the consistency required by the pasting machine, it is also necessary to select an adequate density and phase composition for the paste. If a given expander increases the consistency of the paste (i.e. the cone penetrates to a lesser depth into the paste), then the water content must be increased accordingly to retain the required paste consistency, but naturally the paste will have a lower density.

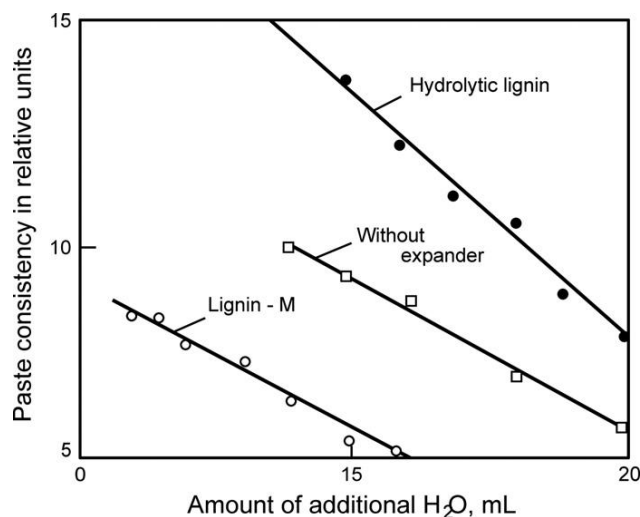


Figure 6.31:
Effect of expander upon paste consistency [36].

In summary, penetration depends on: moisture content, crystal morphology and time of paste mixing. Moisture content of the paste is of vital importance for both its density and consistency.

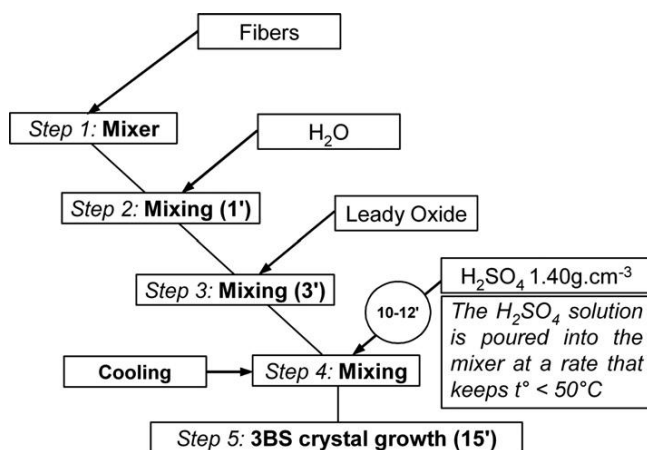
6.3.4. Technological Process and Equipment for Paste Preparation

Sequence of the technological procedures of paste preparation

Preparation of 3BS pastes for positive plates

A sample scheme of the successive technological procedures involved in the process of 3BS paste preparation is presented in Fig. 6.32. An example of a formulation for 3BS paste preparation could be: LO (78% PbO) – 500 kg, H₂O – 65 L, H₂SO₄ (1.4 g cm⁻³) – 39 L, fibres – 0.35 kg. For the conversion of the 3BS paste into 4BS during the plate curing procedure, some 6–7 kg of tetrabasic lead sulfate nucleants should also be added to the initial paste mix.

Paste preparation starts with the introduction of fibres or (fibres + 4BS nucleants) in the paste mixer. Then water is added and the suspension is mixed for 1 min. The next step is to add the leady oxide (LO) and mix for another 3–4 min until a homogenous mass is obtained. Then the sulphuric acid solution is added slowly, for about 10–12 min. The temperature is monitored continuously and kept below 50 °C. If needed, the cooling system of the paste mixer is activated. After adding the whole amount of H₂SO₄ solution, the paste is mixed for 15 more minutes to allow the 3BS crystals to grow. Finally, samples are taken from the paste to measure its density and consistency. If these parameters meet the technological requirements, the paste

**Figure 6.32:**

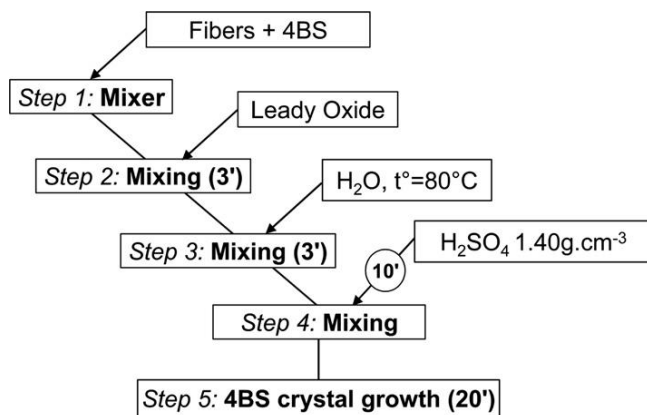
Preparation of tribasic lead sulfate (3BS) pastes for positive plates.

can be used for pasting grids. If not, they are adjusted by adding water in case the paste density is higher than required or by continuing mixing to allow the excess water to evaporate.

Preparation of 4BS pastes for positive plates

A technology for preparation of 4BS pastes has been developed in the author's laboratory [10]. Figure 6.33 presents schematically the sequence of technological procedures involved in this technological process.

First, fibres and 4BS nucleants are introduced into the paste mixer and mixed for 1 min, then the leady oxide is added. The dry mix is homogenized for 3 min and then water heated to 80 °C

**Figure 6.33:**

Preparation of tetrabasic lead sulfate (4BS) pastes for positive plates.

is added. The obtained paste is mixed for 3 more minutes before adding slowly (for 10 min) the H_2SO_4 solution to the heated and hydrated paste mass. The paste temperature rises to above 85°C , whereby 4BS crystals are formed and grow. Mixing is continued for 20 min more to allow the 4BS crystals to grow to $15\text{--}20\ \mu\text{m}$ in size. The final density and consistency of the paste are measured and if their values are within the technological norms, the paste can be used for pasting grids. If, however, they do not meet the requirements, the paste density is adjusted accordingly.

Preparation of 3BS pastes for negative plates

The technological procedures involved in the preparation of pastes for negative plates (Fig. 6.34) are similar to those for positive 3BS paste preparation described above. However, in the case of negative pastes, expanders (BaSO_4 , lignosulfonates and carbon additives) are also introduced into the paste mixer. Here again, first a suspension of fibres and expanders is prepared and mixed for 1 min. Then the leady oxide is added and the suspension is mixed for 3 min to homogenize. After that the sulphuric acid solution is added slowly (for 10 min), whereby 3BS crystals are formed. The paste is mixed for 15 more minutes to allow the 3BS crystals to grow. If the dry charged batteries are to be stored for several months (storage time), the lead plates get oxidized and the batteries lose capacity. In order to slow down the rate of lead oxidation, certain inhibitors are added to the paste formulation. One of the most widely used inhibitors is colophony. It is introduced into the paste in the form of 25% alcohol solution. The latter is poured into the paste mixer before the sulphuric acid solution. With these pastes, too, the temperature is monitored and kept below 50°C to prevent disintegration of the expanders. There are various commercially available expanders. The particular expander composition depends on the specific battery type and application. As of today, the major supplier of expander products is Hammond Expanders, USA.

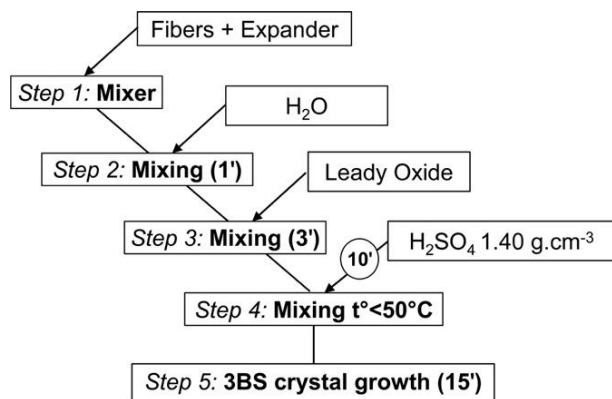


Figure 6.34:
Preparation of tribasic lead sulfate (3BS) pastes for negative plates.

The paste formulations and the durations of the various procedures given in the schemes are only illustrative. They vary depending on mixer type and design, paste batch volume, degree of oxidation of the LO as well as on the quality of the initial materials used for paste preparation, the temperature of mixing, etc.

Technological scheme for paste preparation and grid pasting

Figure 6.35 presents a scheme of the technological procedures, initial raw materials, machining conditions and controlled paste characteristics during paste preparation. The manufacturing steps of grid pasting and drying of the plates are also included. The basic technological parameters that should be monitored and controlled after pasting and drying of the plates are given in the figure, too.

Paste preparation equipment

Pastes for positive and negative plates are prepared in separate mixers so as to avoid contamination of the positive paste with BaSO_4 and expander from the negative paste. Such ‘impurities’ would impair the performance of positive plates.

Figure 6.36 shows a block scheme of the equipment for paste preparation incorporating vacuum system for paste cooling. This paste preparation system is produced by Maschinenfabrik Gustav Eirich, Germany [33]. The following are the main components of the system:

- leady oxide storage unit
- transport system
- fully automatic weighing and batching units for all components of the paste formulation, including additives (dry or in the form of suspension), fibres, and also lead sludge recycled from waste water
- reactor (mixer)
- paste feeder (hopper) for delivery to the pasting machine.

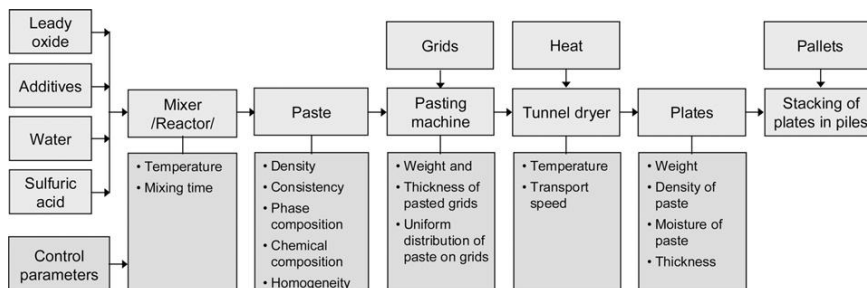


Figure 6.35:
Technological scheme for paste preparation and grid pasting.

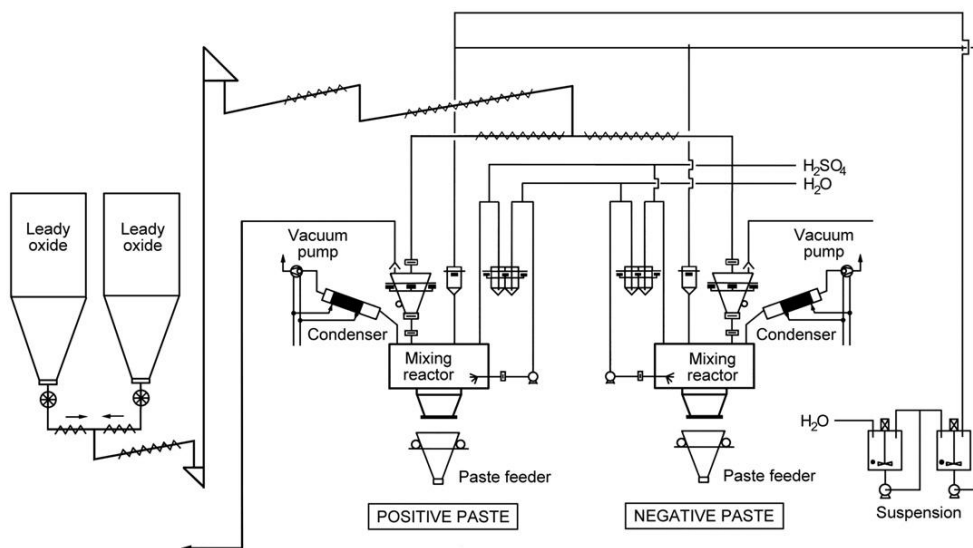


Figure 6.36:
Block scheme of paste preparation equipment [33].

Operation of the paste preparation station is under continuous hardware and software control. The sequence of the various procedures of paste preparation, weighing and dosing of the individual paste formulation components and the duration of mixing (of each component of the dry mix and of the paste) are controlled automatically. The changes in temperature and viscosity of the paste are also under continuous control.

Another widely used paste mixer is the one produced by Oxmaster, USA.

The reactor (mixer) is the basic component in every paste preparation equipment. The reactor (mixer) should ensure uniform stirring of the dry paste mix and of the wet paste throughout the mixer volume, leaving no 'dead' volumes that may result in inhomogeneity of the final paste. In order to produce a good paste, the whole paste volume should be stirred repeatedly for several minutes. It is very important to ensure continuous temperature control of the paste. Contemporary paste mixers use three types of cooling systems: (1) by purging air through the paste mixer, (2) by vacuum treatment and (3) through enclosing the mixer in a water jacket. The best quality of mixing is achieved when the pan and the mixing tools (agitators) rotate in opposite directions at a rate of 9 to 11 rounds per minute.

It is traditionally accepted in the battery manufacturing industry to call the equipment for paste preparation 'paste mixer'. This term is not quite accurate, however, as different reactions proceed in the mixer resulting in new products. Hence, it would be more precise to call the paste preparation equipment reactor.

When the paste is ready, it is poured into an intermediate paste feeder (hopper) from where it is charged periodically (in batches) into the pasting machine mounted under the hopper. The paste is stirred in the hopper to maintain its homogeneity and to allow recrystallization of basic lead sulfates to reach an advanced stage.

The next step is spreading the paste onto grids in high-speed automatic pasting machines. The most widely used pasting machines in current battery manufacturing practice are those supplied by MAC Engineering and Equipment Company (USA). There is a great variety of pasting machine designs, but almost all constructions comprise the following basic components: (a) warehouse for grid storage (dumped over each other in stacks) and grid picking device; (b) transportation system conveying grids, and then plates, through the subsequent technological steps; (c) paste container (hopper); (d) unit for paste application to grids (either by pressing or spreading) and (e) paste pressing and levelling device. A schematic of a belt-type pasting machine is presented in Fig. 6.37.

The pasting rate for grids for SLI battery applications is between 10 and 16 double plates per minute. Grids for traction batteries are pasted at a lower rate. During grid pasting the following parameters should be controlled: pasted plate thickness, applied paste weight, uniformity of paste distribution onto grids.

Pasted grids are then transported through a tunnel dryer. Paste particles are covered by a hydrated layer and a thin liquid film (Fig. 6.22), which impairs the contact between the particles themselves, and between paste and grid. Through the drying procedure, part of the water from the thin liquid film is removed and thus the contact between particles is improved.

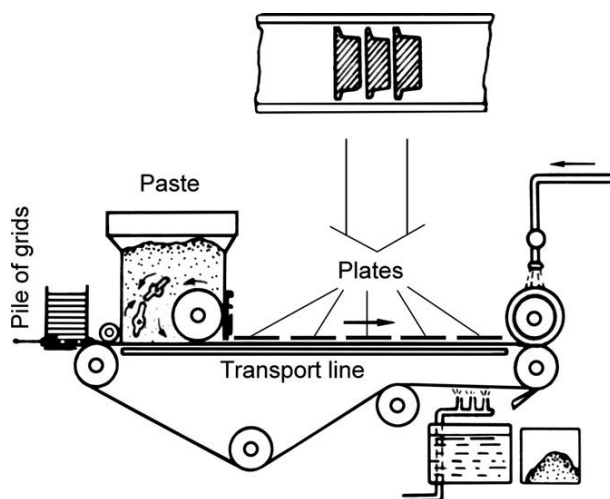
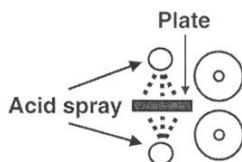
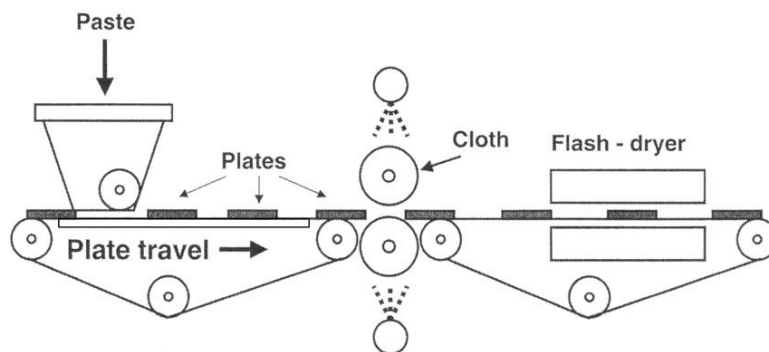


Figure 6.37:
Schematic of belt-type pasting machine.

Method 1



Method 2

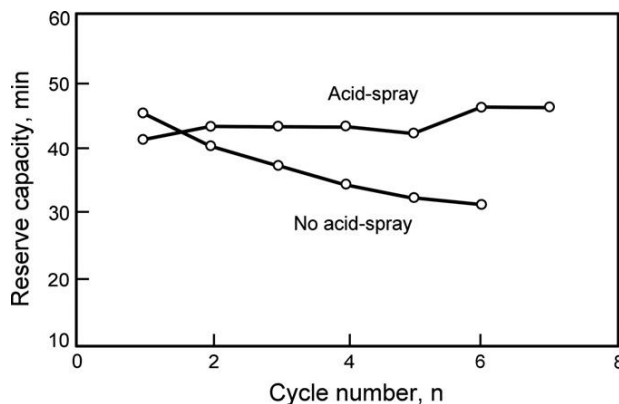
**Figure 6.38:**

Procedures for acid spray treatment of pasted battery plates [37].

During this process, both pore diameters and paste volume decrease, which results in paste shrinkage. Extensive shrinkage may lead to paste cracking or may even detach paste from grid. If cracks occur in the paste, they will disrupt the contact between paste and grid, and hinder the formation of the active mass. These cracks gradually disappear with battery service life. Two methods are commonly employed to avoid paste cracking: use of adequate plate drying mode or chemical processing of plates with 1.10 relative density H_2SO_4 solution. There are two different techniques for applying H_2SO_4 solution onto paste. The most widely used method is to fine-spray H_2SO_4 solution of 1.10 relative density onto both plate surfaces (Fig. 6.38, method 1) [37]. The second technique of applying H_2SO_4 solution is with the help of two rollers covered with a band of polymer mat or fabric (textile) (Fig. 6.38, method 2) [37]. First, the mat (fabric) is impregnated with H_2SO_4 solution (by spraying or soaking) and then the rollers apply the solution onto both surfaces of the pasted plates (conveyed on a transport belt). Thus, a layer of the paste surface, some 30–40 μm deep, is enriched in PbSO_4 or basic lead sulfate crystals. As the molar volume of PbSO_4 and nBS is larger than that of PbO , the diameters of the pores in the surface paste layers will diminish. Hence, drying of the plate interior will be slowed down.

Acid spray treatment of pasted plates improves the plate manufacturing processes in the following ways:

- (a) Reduces, or prevents altogether, cracking of the paste or its detachment from the grids after flash drying

**Figure 6.39:**

Influence of acid-spray treatment on reserve capacity of automotive batteries [37].

- (b) Reduces dust emission during the subsequent operations
- (c) Improves the homogeneity of the curing processes throughout the plate volume.

Figure 6.39 presents capacity curves for batteries produced with and without acid spraying of plates after pasting [37]. Plates subjected to acid-spray treatment preserve their reserve capacity, whereas the reserve capacity of untreated plates declines.

Transportation of pasted plates in the tunnel dryer results not only in removal of excess moisture from the paste, but also in drying the plate surfaces. Thus sticking of plates to one another is avoided when they are arranged in piles (stacked). At the outlet of the tunnel dryer the plates have a temperature of 40–45 °C and moisture content 9.5%. They are then piled (stacked) on palettes to be transported to and loaded into the curing chamber. The controlled parameters of the plates after drying are plate weight, moisture content of the paste and paste density.

There are three types of continuous process drying ovens, depending on the mode of operation:

- (a) Tunnel ovens (dryers) with through-circulation and cross-circulation air flow. Air is heated either by gas burners or by electric heaters. These ovens are multi-zone, with separate air circulation for each zone. The temperature in the highest-temperature zone is 160–180 °C and the drying time is about 5 min. Plates are usually arranged vertically on the transport conveyor system.
- (b) Tunnel ovens (dryers) with direct drying of the plates by a gas flame. These are, as a rule, shorter than those described in (a) above. The highest temperature in these dryers is about 360 °C and plates stay no longer than 1 min in this zone. In some designs plates are horizontally positioned during the drying process.
- (c) Contact ovens (dryers) in which plates pass between several successive pairs of rollers, heated to 550–600 °C. This drying method results in good surface drying of the plates.

The grid in a plate has but a very small heat capacity and much higher heat conductivity than the paste. When a plate passes through the flash-drying oven, the grid is heated to higher temperature than the paste. Water at the interface grid/paste evaporates forming gas bubbles which may form caverns or cracks, especially if the drying temperature in the oven is set to higher values or if the speed of the transport conveyor system is low. The thus formed cracks in the paste disrupt the integrity of the plate and increase its electrical resistance and inhomogeneity.

Dried plates are then arranged in piles, stacked in palettes and transferred to the curing chambers.

6.3.5. Manufacture of Positive Tubular Plates

Tubular plate filling

An overview of the general design and the properties of tubular plates is presented in Chapter 4.10. Here, we will discuss the process of filling tubular plates with lead oxides or suspension.

First, let us describe in brief the types of tubes used for tubular plate manufacture. Multi-tube assemblies (gauntlets) are produced from chemically resistant glass or organic fibres (polyester, polypropylene, acrylonitrile co-polymers, etc.). Manufacturing technologies include weaving, braiding or felting methods that are currently used in the textile industry.

Multiple-section tubes (gauntlets) are produced by weaving. Two fabrics are simultaneously woven, and are linked to each other at a given distance (half the circumference of the tubes). Aluminium spits are inserted into the formed sleeves (transversal to the fabric length) and the sleeves with the spins in them are then immersed in impregnating solution. After heating and curing of the resin, whereby the tubes acquire the desired shape, they are cut to the desired length. Automatic machines for continuous impregnation are used. Multi-tube gauntlets can also be produced from mat. Layers of impregnated mat of the required thickness and porosity are prepared. Two layers are overlapped and stitched together (with a multi-head sewing machine) at distances equal to half the circumference of the tube. The double-layered fabric, after sewing, is subjected to impregnation and curing by the above method.

Multi-tube gauntlets are set to the following tests: (a) bursting pressure, (b) tensile strength, (c) resistance to air and water flow, (d) displacement volume and porosity, (e) electrical resistance, (f) hot acid tests and (g) impurity tests.

Depending on their shape (cross-section geometry), tubes may be cylindrical (round), elliptical (oval) or rectangular (square) (Fig. 4.63). Round (cylindrical) tubes are generally used in flooded batteries, whereas the preferred tube shape for VRLAB is the rectangular (square) design, because it ensures good contact of the AGM separator with the whole plate surface.

The first technology for filling tubular plates used dry powders. This filling technology is still being employed in some battery plants. The above technology of tubular plate filling is costly and slow (despite that 5–8 plates are filled simultaneously) and it presents health hazards. The process requires extensive ventilation and cleaning of large volumes of air. Complete filling of the tubular plates is not always achieved and this causes variability in plate capacity.

New technologies for the production of tubular plates have been developed based on the following principles:

- (a) Automatic paste filling of tubular plates (Hadi Offermann Maschinenbau GmbH). The multi-spine grids, inserted in tubular gauntlets, are charged horizontally in the filling machine and the paste is filled into the tubes under pressure by means of a special device comprising multiple metallic filling tubes. The filling tubes slide into the tubular gauntlets and the paste is fed under pressure, while simultaneously the filling tubes slide back. When filled with paste, the tubular plates are closed with bottom bars, washed with water and weighed. In case of plate weight deviation from the technological tolerance limits, the filling device should be adjusted accordingly. Tubes to be filled using this technology should have high mechanical strength characteristics.
- (b) Tubular plate filling with paste slurry. Figure 6.40 shows schematic of this filling process. 3BS or 4BS paste is prepared in paste mixer (1). The paste is transferred to hopper (2) where stirring continues. Batches of paste are charged by pump (3) into mixing tank (4). The paste is diluted with water, under continuous stirring, until a density of $2.00\text{--}2.10\text{ g cm}^{-3}$ is achieved. The volume of the thus obtained slurry (suspension) is maintained constant and equal to 65% of the total mixing tank volume. The density of the paste is measured continuously by a densitometer, and it is adjusted automatically by adding paste or water and filtrate, if a deviation of slurry (suspension) density from the technological requirements is observed. The mixing tank is the basic reservoir supplying all filling modules with suspension (slurry). Each filtration fill module is equipped with an intermediate slurry tank (5). The latter is charged with slurry from the mixing tank and then pumps the slurry, under pressure, to the slurry filtration fill module (6). The filling module comprises two filling heads (7) and a filtrate tank (8). The filtrate is returned periodically to the mixing tank (4). If more than one filling modules are used, the filtrate is collected in a separate tank and is then fed back to the mixing tank. After end of work shift, the whole system is washed with water and this waste water is collected in a special station for further processing. The filled tubular plates are closed with bottom bars. Then they are washed with water and weighed for filling quality control. The above described slurry filling module is designed and constructed by Chloride Motive Power (UK) and the technology for filling tubular plates with slurry from 3BS or 4BS paste was developed by the Lead-Acid Battery Department of Institute of Electrochemistry and Energy Systems (former CLEPS), Bulgarian Academy of Sciences. The slurry is filled into the plates under pressure so as to obtain final density of the filled paste between 4.0 and 4.4 g cm^{-3} . During

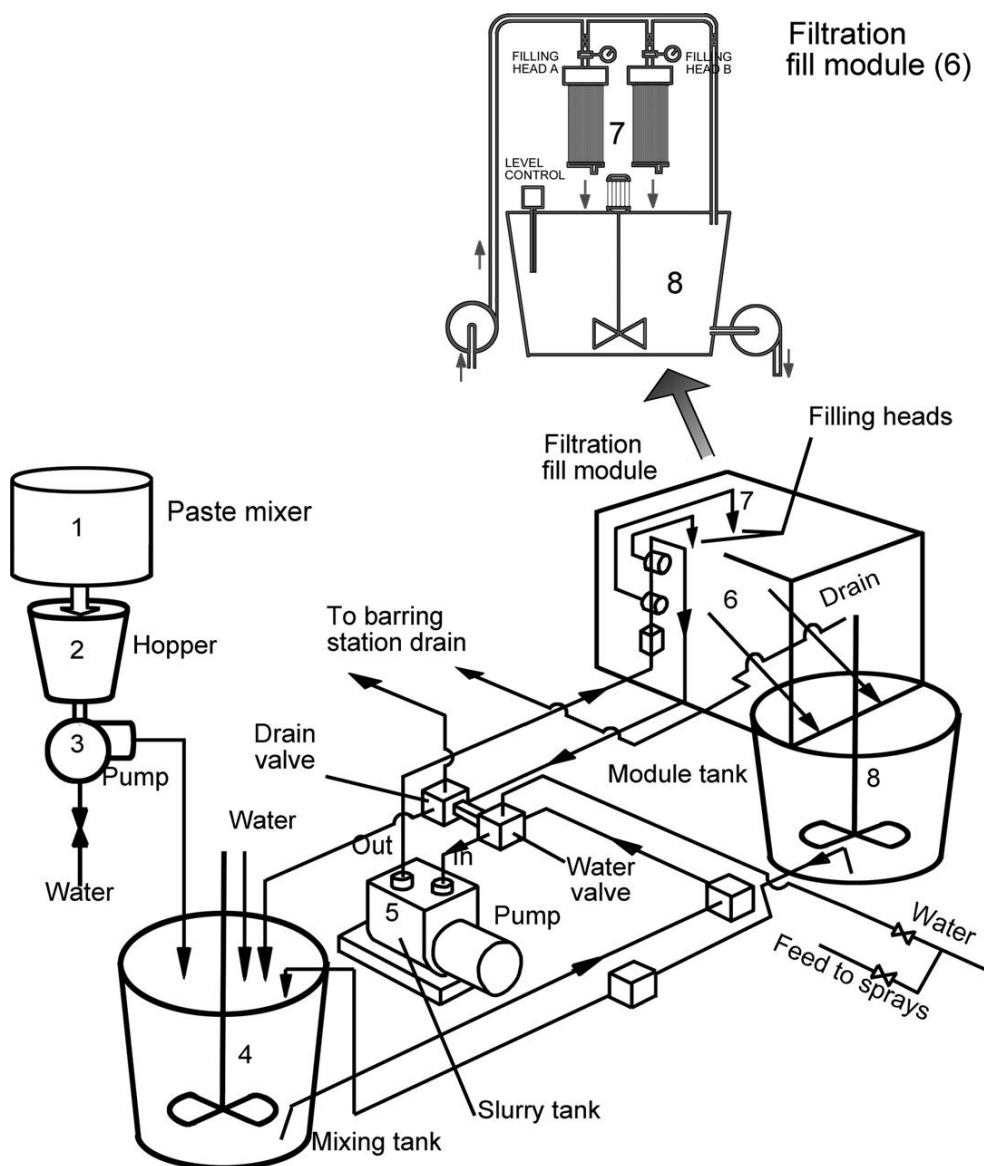


Figure 6.40:

Block scheme of the process of filling tubular plates with slurry obtained from paste.

preparation of the paste, the latter should be stirred for some 20–40 min to allow growth of bigger 3BS or 4BS crystals. For better efficiency of the filling process, the tube fabric should have smaller pores so as to retain even smaller 3BS or 4BS particles inside the tubes. The filled tubular plates are then transferred to the curing chamber for further processing.

- (c) Slurry filling method using ($\text{Pb}_3\text{O}_4 + \text{LO}$) slurry (chloride). In fact, this was the first technology developed for wet filling of tubular plates. It comprises the following procedures: first, a mixture of $\text{Pb}_3\text{O}_4 + \text{LO}$ (60% : 40%) is prepared and collected in a powder mixer. Batches of this mix are introduced into the main slurry mixer. Definite amounts of water and H_2SO_4 solution are also added. The proportion of H_2SO_4 solution should be selected so as to yield 3BS from PbO of the LO without causing decomposition of Pb_3O_4 (i.e. $\text{H}_2\text{SO}_4/\text{LO} \sim 2\%$ by weight). The filtrate from the filling modules, too, is returned to the slurry mixer. The thus obtained slurry is delivered to the filling modules (Fig. 6.40) and filled into the tubes. The filled tubes are closed with bottom bars, then the plates are washed and weighed. The next technological procedure is pickling of the plates. For the purpose the filled tubular plates are immersed in a tank with H_2SO_4 solution of 1.40 or 1.28 relative density, where sulfation of Pb_3O_4 and of the residual unreacted PbO proceeds. The pickling step takes 6 h. After that plates are taken out of the tank, washed with water to remove the remaining H_2SO_4 and then charged in drying chambers with high temperature. Then, the technological process of formation follows.

References

- [1] J.J. Lander, J. Electrochem. Soc. 95 (1949) 174.
- [2] H. Bode, Lead acid batteries, John Wiley, Electrochem. Soc. 1977, pp. 367, 372.
- [3] H. Bode, E. Voss, Electrochim. Acta 1 (1959) 318.
- [4] J. Burbank, J. Electrochem. Soc. 113 (1966) 10.
- [5] H.W. Billhard, J. Electrochem. Soc. 117 (1970) 690.
- [6] D. Pavlov, V. Iliev, G. Papazov, Annual report 1977, CLEPS, Bulg. Acad. Scis., Sofia, Bulgaria.
- [7] T.G. Chang, M.M. Wright, J. Electrochem. Soc. 128 (1981) 719.
- [8] F. Vallat-Joliveau, A. Delahaye-Vidal, M. Figlarz, A. de Guibert, J. Electrochem. Soc. 142 (1995) 2710.
- [9] ILZRO Project LE82-84, Final Report Dec.31, 1971, p. 2/27
- [10] S. Ruevski, D. Pavlov, T. Rogachev, Annual report 1992, CLEPS, Bulg. Acad. Scis., Sofia, Bulgaria.
- [11] D. Pavlov, G. Papazov, J. Appl. Electrochem. 6 (1976) 339.
- [12] H. Ozgun, L.T. Lam, D.A.J. Rand, S.K. Bhargava, J. Power Sources 52 (1994) 159.
- [13] V. Iliev, D. Pavlov, J. Appl. Electrochem. 9 (1979) 555.
- [14] R.V. Biagetti, M.C. Weeks, Bell Syst. Tech. J. 49 (1970) 1305.
- [15] J.R. Pierson, in: D.H. Collins (Ed.), Power sources 2, Pergamon Press, Oxford, 1969, p. 103.
- [16] D. Pavlov, V. Iliev, Elektrokhim. (Russ.) 2 (1975) 1735 (in Russian).
- [17] E.M. Valeriote, J. Power Sources 59 (1996) 199.
- [18] M. Matrakova, D. Pavlov, J. Power Sources 158 (2006) 1004.
- [19] G. Papazov, D. Pavlov, Annual report 1975, CLEPS, Bulg. Acad. Scis., Sofia, Bulgaria.
- [20] B. Culpin, J. Power Sources 25 (1989) 305.
- [21] J. Burbank, A.C. Simon, E. Willihnganz, in: P. Delahay, C.W. Tobias (Eds.), Advances in electrochemistry and electrochemical engineering 8, Wiley Interscience, London and New York, 1971, p. 157.
- [22] G. Papazov, D. Pavlov, Annual report 2005, IEES, Bulg. Acad. Scis., Sofia, Bulgaria.
- [23] H.B. Stephenson, C.L. Hixson, H.S. Long, J.S. Bryson, J.D. Purdum, E.J. Richie, Pastes and grids for lead-acid battery, ILZRO, Project LE-83/LE84, Final Report, Dec. 1971.
- [24] D. Pavlov, N. Kapkov, J. Electrochem. Soc. 137 (1990) 16.
- [25] D. Pavlov, N. Kapkov, J. Electrochem. Soc. 137 (1990) 21.

- [26] D. Pavlov, N. Kapkov, J. Power Sources 31 (1990) 189.
- [27] D. Pavlov, in: B.D. McNicol, D.A.J. Rand (Eds.), Power sources for electric vehicles, Chapter 5, Elsevier, Amsterdam, 1984.
- [28] W.R. Kitchens, R.C. Osten, D.W.H. Lambert, J. Power Sources 53 (1995) 263.
- [29] D. Pavlov, A. Dakhouche, T. Rogachev, J. Power Sources 30 (1990) 117.
- [30] D. Pavlov, J. Power Sources 33 (1991) 221.
- [31] L.T. Lam, N.P. Haigh, D.A.J. Rand, J. Power Sources 88 (2000) 11.
- [32] L.T. Lam, N.P. Haigh, D.A.J. Rand, J.E. Manders, J. Power Sources 88 (2000) 2.
- [33] H.J. Vogel, J. Power Sources 48 (1996) 71.
- [34] D. Pavlov, S. Ruevski, J. Power Sources 95 (2001) 191.
- [35] D. Pavlov, S. Ruevski, P. Eirich, A.C. Burschka, The Battery Man (April 1998) 16.
- [36] D. Pavlov, V. Iliev, G. Papazov, Annual report 1976, CLEPS, Bulg. Acad. Scis., Sofia, Bulgaria.
- [37] D.A.J. Rand, J. Power Sources 88 (2000) 130.

This page intentionally left blank

Additives to the Pastes for Positive and Negative Battery Plates

Let us first define the term ‘additive’. When the technology of manufacture of a given product is developed certain substances are added, in different amounts, to the basic constituents, which have positive effect(s) on the properties of the final product.

- (a) *Components*: These are substances used as basic ingredients for the manufacture of the product. They are used in quantities higher than 2.0% of the total amount of all initial reactants. These substances yield the major mass and basic properties of the final product.
- (b) *Additives*: These are substances that improve some of the properties of the final product or facilitate and accelerate the technological process of its manufacture. The content of additives in the product’s formulation is from 0.02 to 2.0% of the total weight balance of the initial materials.
- (c) *Impurities*: Their content is less than 0.01% by weight. They have no, or rather an unfavourable, effect on the properties of the final product, or on the processes of its manufacture, by initiating or accelerating some secondary or undesirable reactions.

In this chapter we will make an overview of the influence of additives to the pastes for positive and negative plates on the processes of plate manufacture and on the performance of lead–acid batteries.

7.1. Additives to the Pastes for Negative Plate Manufacture

7.1.1. Expander

What do the capacity, energy and power output of a lead–acid battery depend on? Conversion of electrical energy into chemical one and vice versa proceeds through electrochemical reactions at the interface solid phase/solution. Hence, the answer to the above question is: *the performance of the lead–acid battery depends on the surface of the active materials of the two types of electrodes.*

The reactions on the two types of electrodes of a lead–acid battery produce Pb^{2+} ions which react with H_2SO_4 forming a PbSO_4 film on the surface of the active materials, thus passivating the electrodes. Hence, the performance characteristics of the battery are determined by the surface area of the active materials where the reactions proceed.

However, the active mass surface is relatively small, so the capacity and power performance of the battery will be low.

In order to improve the performance parameters of the battery, formation of a continuous passivating PbSO_4 layer should be avoided. The lead sulfate layer formed on the surface of the active materials should be highly porous to sustain the progress of the electrochemical reactions into the depth of the electrode and thus to involve a thick layer of active material not only its surface. This will eventually improve the performance characteristics of the battery.

How can formation of a passivating PbSO_4 layer on the fairly small surface of the negative active material (NAM) be prevented? Practice has proved that this can be achieved by the addition of the so called ‘expander’ to the paste. This is a mixture of a surface active substance (e.g. lignosulfonate) + BaSO_4 + carbon additives. These substances are adsorbed on the lead surface and thus prevent the deposition of a continuous PbSO_4 passivating layer during battery discharge, but contribute to the formation of a porous sulfate layer instead.

The term ‘expander’ has been used lately to label the above three-component mixture. The reason for this was the launch of a commercial product named Expander comprising these three substances (lignosulfonate + BaSO_4 + carbon). Earlier, the term expander was used only for the organic component (lignosulfonate). The latter was introduced into the battery manufacturing practice by necessity. After the Second World War, when wood separators were replaced by synthetic materials, it was established that negative plates suffered a drastic decrease in capacity during cycling at low temperatures. Investigations revealed that this phenomenon resulted from the absence of lignosulfonic acids leached from the wooden separator into the electrolyte. So it became necessary to add lignosulfonic acid to the negative active mass. A wide variety of commercially available lignosulfonates, humic acid and tanning agents were tested in the battery industry, but only a few of these additives have found wide application.

As lignosulfonate disintegrates slowly during battery operation and hence, the negative plates lose capacity, a small amount of wood flour is also added to the expander formulation. During battery operation this wood flour decomposes gradually producing lignin, which compensates partially for the lignin lost as a result of disintegration of the initially introduced lignosulfonate.

Barium sulfate (BaSO_4) acts as a nucleation agent (nucleant) for PbSO_4 crystal formation and growth, and ensures uniform distribution of these crystals throughout the active mass pore surface. This function of BaSO_4 is a result of the isomorphism between PbSO_4 and BaSO_4 crystals.

Carbon additives are introduced in the paste mainly to improve the electric conductivity of the lead active mass at the end of discharge, when the content of PbSO_4 crystals in NAM increases substantially. When hybrid electric vehicles were launched on the market and lead–acid batteries tried to gain a share in this application, it turned out that the negative plates of these

batteries could not accept electric charges at high current rates. These plates have fairly low surface area ($0.5\text{--}0.7\text{ m}^2\text{ g}^{-1}$). Carbon was added to the negative pastes with the aim to increase the electrochemically active surface of the negative active material. Addition of carbon black or activated carbon improves the charge acceptance of the negative plates on high-rate cycling.

A well-balanced expander formulation, containing the above three components, guarantees good performance of the negative active material, especially at low temperatures. A typical expander formulation used in the battery industry is 0.2–0.3% lignosulfonate, 0.8–1.0% BaSO_4 , 0.1–0.3% carbon black, all calculated in weight percent vs. the leady oxide used for paste preparation.

Polymer fibres improve the consistency of the paste and reduce the production waste during plate manufacture.

Inhibitors of lead oxidation reduce the rate of the self-discharge reactions and prolong battery storage life.

Inhibitors of hydrogen evolution slow down the self-discharge processes and improve the charge acceptance of the negative plates.

Lignin structure

For the sake of brevity, further in this section, the term ‘expander’ will be used for the organic component of the expander only.

Wood is primarily composed of cellulose, hemi-celluloses and lignin. Lignins are most commonly derived from wood pulp. They are extracted from the pulp in the manufacture of paper and then purified by removing sugars and metal ions. Lignin molecules are formed from three precursors. The ratio between the latter depends on the type of wood pulp used to derive lignin and this ratio has an impact on battery performance. Lignin molecules can be sulfonated, to various degrees, using sulfurous acid.

Lignin is a polymer containing phenylpropane groups building a three-dimensional mesh-like structure. A number of structural models have been proposed for lignin, but the one that has found the strongest support is Freudenberg model of 1964. Freudenberg’s formula for lignin is presented in Fig. 7.1.

Lignin is not a single substance, but rather a mixture of several substances with similar chemical composition, but different structure. The structure of lignin comprises various structural groups with micropores in-between. These micropores allow transfer of ions through the layer of lignin adsorbed on the metal surface.

High molecular weight (HMW) lignins behave like flexible polyelectrolytes, whereas low molecular weight (LMW) lignins behave like colloids and dissociate or form micelles. The molecular weight of lignins used as expander components exerts an influence on battery

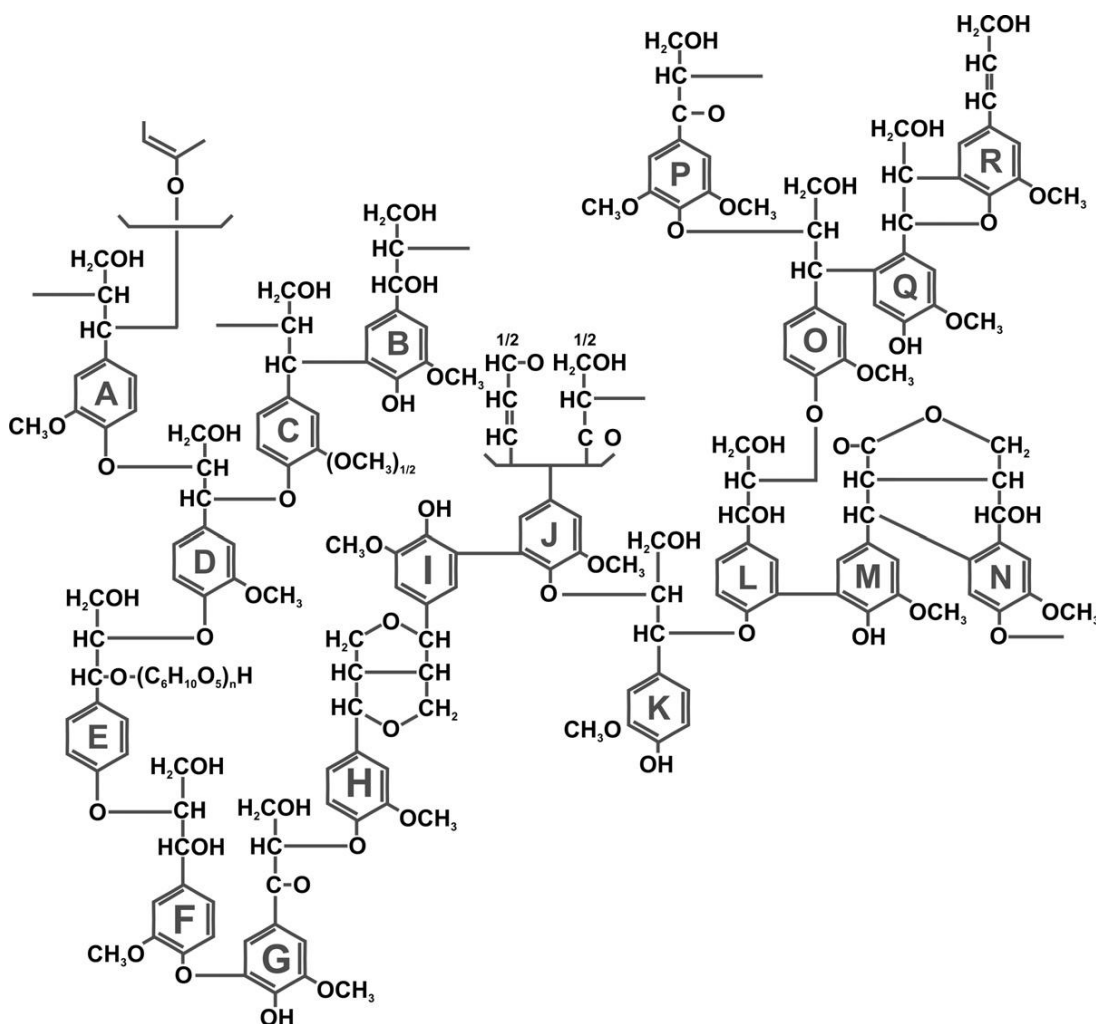


Figure 7.1:
Freudentberg formula for lignin.

performance. Lignins form a layer of polyelectrolyte on the lead surface, which impedes the formation of a passivating PbSO_4 layer on the negative electrode. Thus, through their structural properties, lignins protect the negative plates from passivation.

The activity of lignosulfonates changes during battery service life. Less effective lignins are those with more stable structure. Such lignins are preferred for traction battery applications, where long service life is demanded. They are not appropriate, however, for application in SLI batteries. Batteries with different expanders reach different states of charge when charged at 14.5 V, because of the different charge acceptance determined by the lignins contained in the expander.

Influence of the organic expander component on the processes of nucleation and growth of Pb and PbSO₄ crystals

Effect of expander on the electrochemical processes

The Pb|PbSO₄ electrode is very sensitive towards organic surfactants. Some of these capillary active substances completely inhibit the oxidation of the Pb electrode. Others have just the opposite effect and suppress passivation of the Pb electrode. Such effects are observed with lignosulfonates, some humic acids, tannic derivatives, etc. The influence of organic expanders has been demonstrated by the following experiment. Lead electrode is polarized in 5 M H₂SO₄ solution, with or without addition of organic expander, at a sweep rate of 3 mV s⁻¹ near the Pb|PbSO₄ equilibrium potential [1]. The resulting current density changes during anodic polarization are shown in Fig. 7.2.

When a maximum current value i_{\max} is reached, passivation of the electrode starts due to the formation of a PbSO₄ layer (curve A, Fig. 7.2). The presence of organic expander in the solution leads to a multifold increase in the quantity of electricity required for electrode passivation (curve B) and shifts the passivation potential at i_{\max} to more positive values. A shift of the Pb dissolution processes to more positive potentials is suggested by the appearance of an additional overvoltage in the Pb²⁺ dissolution processes. These phenomena have been related

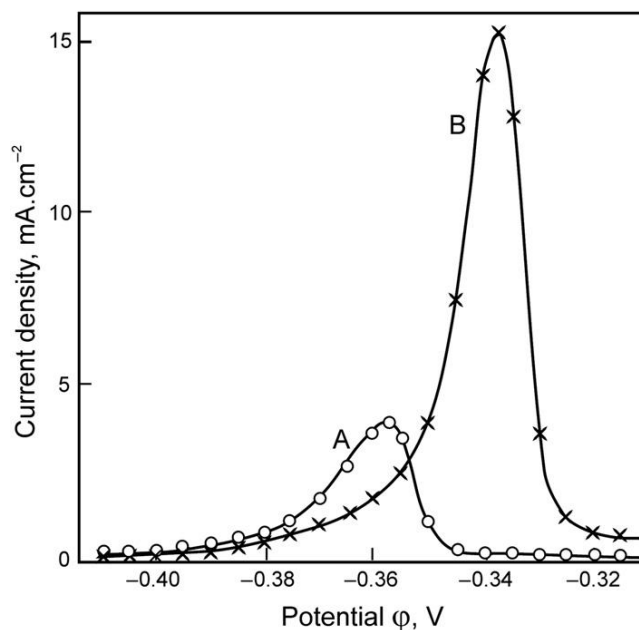


Figure 7.2:

Polarization curves for a stationary Pb electrode in 5 M H₂SO₄ solution: A — no expander; B — with 0.3 g L⁻¹ Lignosol C16 [1].

to the adsorption of organic substances onto the lead surface. Pronounced adsorption of expander on the metal surface has been observed by many authors [2–9].

A correlation has been found between expander activity and the rate of reduction of lead sulfate to lead [5]. For example, the curves presented in Fig. 7.3 evidence that the current of PbSO_4 reduction and H_2 evolution decreases with increase of expander activity. The observed decrease in cathodic current is attributed to adsorption of the additives on the electrode surface and on the surface of PbSO_4 crystals.

It follows from the above said that the organic expander improves the capacity of $\text{Pb}|\text{PbSO}_4$ plates in lead–acid cells, but it has a negative effect on battery charge

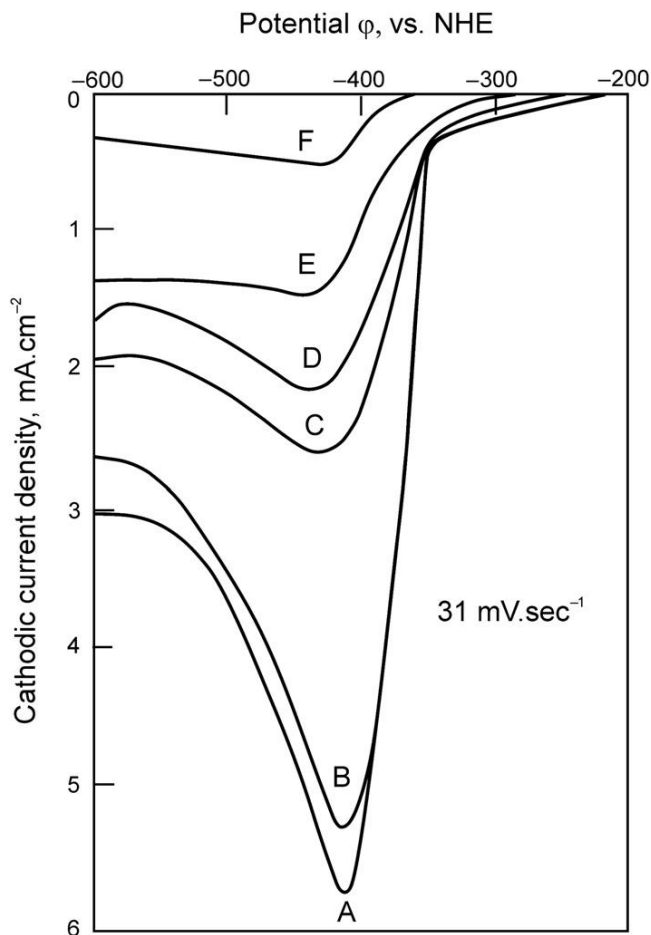


Figure 7.3:

Voltammograms for PbSO_4 reduction to Pb in 1.25 rel. dens. H_2SO_4 : A — no additive; B — rhodamine B; C — pyrogallolsulfonephthalein; D — gallein; E — ammonium lignosulfonate; F — coerulein. All additives were tested at 10 ppm [5].

acceptance as it slows down the reduction of PbSO_4 to Pb. Therefore, selection of the type and amount of expander to be added to NAM is always a matter of rational compromise between these two very important battery characteristics. The influence of expander depends on its molecular weight, chemical structure, purity of components and chemical stability.

Impact of the organic expander component on Pb and PbSO_4 crystal morphology and size

Yampolskaya *et al.* have established that PbSO_4 crystals are substantially larger when formed electrochemically from H_2SO_4 solutions containing expanders D-4 or BNF, than when formed in pure H_2SO_4 solutions [3,10]. The same effect is also observed with PbSO_4 obtained via chemical precipitation by gradual addition of saturated solution of $\text{Pb}(\text{NO}_3)_2$ to H_2SO_4 .

The reverse influence of expander on PbSO_4 crystal size has also been observed [11]. For example, expander REAX 80C causes a substantial decrease in the size of PbSO_4 and Pb crystals. Expander MARACELL E is found to suppress the growth of Pb crystals [12,13]. In the latter case, Pb crystals have small diameters and no long Pb dendrites form in NAM containing this expander. Such expander materials yield NAM structure of high capacity.

Figure 7.4 shows a schematic representation of the interface Pb/solution during formation of PbSO_4 crystals. When no expander is contained in NAM, the Pb surface is covered by a film of PbSO_4 crystals which dissolve partially, whereby Pb^{2+} ions (or PbSO_4 molecules) precipitate onto the PbSO_4 nuclei or crystals and thus contribute to their growth (Fig. 7.4a).

It has been established that the organic expander component forms a three-dimensional netlike (reticulate) layer on the metal surface and this layer is colloid-like [16]. Lead ions pass through this reticulate layer, though their transfer is impeded (Fig. 7.4b,c) [14]. Lead sulfate crystals form over this layer (rather than directly on the lead surface), thus no compact PbSO_4 layer forms on the electrode surface to passivate it. Consequently, the quantity of oxidized lead increases and hence the electrode capacity increases, too.

At lower temperatures ($T < 0^\circ\text{C}$), the solubility of PbSO_4 decreases substantially, which leads to faster formation of a passive PbSO_4 layer on the Pb surface and hence the electrode capacity declines abruptly. The expander prevents formation of such a passive layer at low temperatures, thus ensuring higher electrode capacity.

These phenomena suggest that the effect of different organic expanders upon the rate of nucleation and growth of Pb and PbSO_4 crystals is inherently specific. Nevertheless, all above mentioned expanders increase the quantity of electricity required for passivation of the electrode by the PbSO_4 layer. There is no unambiguous correlation between the de-passivation effect of expanders and their influence on the size and morphology of PbSO_4 crystals.

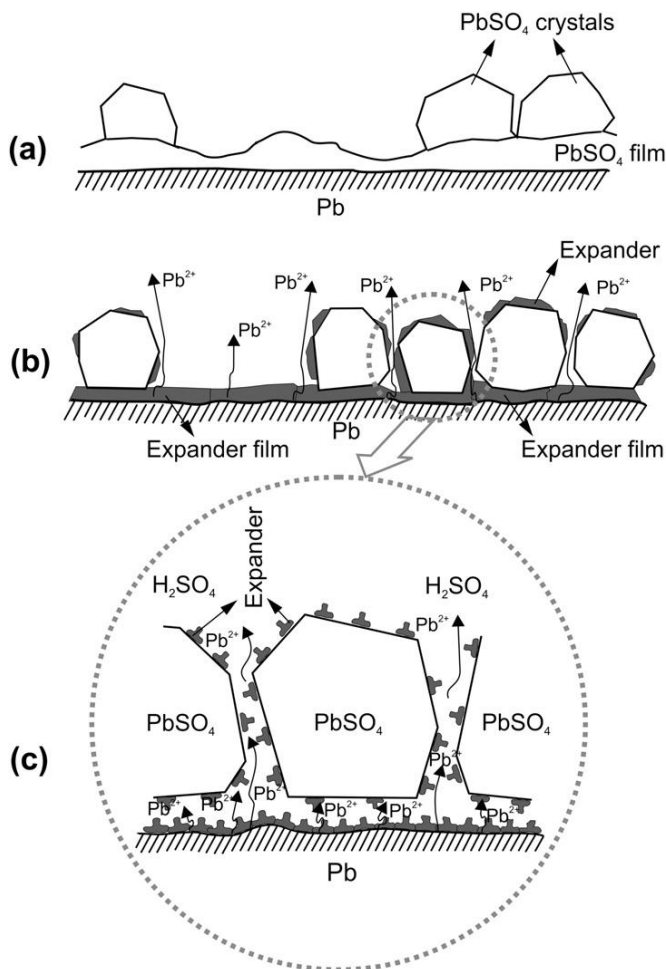


Figure 7.4:

Schematic of the structure of the PbSO₄ layer: (a) with no expander; (b,c) with expander [14].

Mechanism of action of the organic expander component on the charge and discharge processes [14]

Discharge processes

On anodic polarization of a Pb electrode in H₂SO₄ solution, a PbSO₄ layer forms which passivates the electrode (Fig. 7.4a). When expander is introduced into the above electrode system, the structure of the anodic layer changes (Fig. 7.4b). The expander is also adsorbed upon the PbSO₄ surface and, when two PbSO₄ crystals approach each other, an interaction occurs between the adsorbed layers, especially between the electrically charged groups in the expander molecules. Normally, organic expanders contain several types of active (structural) groups, e.g. —COOH, —Ar·OH, —O·CH₃, —SO₃H, etc. Some of these active groups are

adsorbed upon the Pb or PbSO₄ surface, whilst others are in direct contact with the solution and can thus dissociate and/or interact with the water molecules of the solvent. In the limiting case, when the adsorption layers of two particles get in contact (e.g. Pb surface and PbSO₄ crystal, or two PbSO₄ crystals), a 'bi-adsorption layer' is created between the particles (Fig. 7.4b) [14]. The bi-adsorption layer contains active groups and H₂O molecules that form a thin liquid film (Fig. 7.4c). The latter contains ions that are able to move within the thin liquid film. This phenomenon is similar to the one observed with thin-liquid-film containing surfactants [15]. After all, expander materials have the properties of surfactants.

No strong chemical bonds exist between the expander structural groups and the lead particles [16]. There is rather an intermolecular interaction, which is weaker than chemical bonding and this fact is of key importance.

In summary, the above described passivation model suggests that the composition and structure of the adsorbed expander layer, its affinity to Pb and PbSO₄ surfaces and its electric charge all exert strong influence on the delay of the passivation phenomena caused by the PbSO₄ layer.

Charge processes

Based on the above proposed mechanism of action of organic expanders on the discharge processes of Pb|PbSO₄ electrode, it can be concluded that the rate of these processes depends on the diffusion and migration of Pb²⁺ ions through the porous PbSO₄ layer (Fig. 7.4c). The diffusion rate, in turn, depends on the concentration gradients of Pb²⁺ ions in the pores of the PbSO₄ layer. On oxidation of lead (i.e. on discharge), the concentration gradient will be $(C_0 - C_s)/l$, where C_0 is the concentration of Pb²⁺ ions at the Me/PbSO₄ layer interface (it is very high); C_s is the concentration of Pb²⁺ ions determined by the solubility of PbSO₄ crystals (the smallest ones) at the PbSO₄/solution interface and l is the thickness of the PbSO₄ layer, including the adsorbed expander layer. During charge, the concentration gradient of Pb²⁺ ions is $(C_s - C_0)/l$. Since the electrode is cathodically polarized, the flow of Pb²⁺ ions reaching the metal surface reacts there forming Pb and hence the concentration of Pb²⁺ ions at the metal surface is $C_0 \approx 0$. During charge, the cathodic process of reduction of Pb²⁺ ions is retarded because of their slow diffusion through the PbSO₄ layer and the adsorbed expander layer. Consequently, the electrode charge acceptance will decrease. This is actually observed in practice. The more efficient the expander is during discharge, thus maintaining high electrode capacity (i.e. increasing the thickness of the PbSO₄ layer), the lower the charge acceptance of the Pb|PbSO₄ electrode.

Correlation between expander structural group composition and negative battery plate performance

The organic components of expanders are mainly chemically treated lignins or derivatives of the latter. These are complex polymer substances containing different functional groups such as methoxyl, phenolic, carboxylic, ketonic, carbinol structural groups, etc. The correlation

between the structural groups building the different expander molecules and the performance of the negative plates (e.g. capacity, CCA, cycle life, self-discharge, charge acceptance) has been in the focus of research carried out by many scientists [17–24]. This is a very complex correlation because, on the one hand, lignosulfonates themselves contain quite a great number of structural groups occupying different positions in their structure and, on the other hand, these active groups affect in different ways the physiochemical, electrochemical and crystallization processes involved in the formation and disintegration of the NAM structure. Phenolic groups have been found to have a beneficial effect on negative plate characteristics, the substitution of the second hydroxyl group enhancing their effect in the order ortho, meta and para [17]. This effect of phenolic groups is also confirmed in reference [21].

Carboxylic and ketonic groups have little effect on expander behaviour, whereas additives containing aldehyde groups increase its efficiency. SO₃H groups also exert a beneficial effect. Quinones and their derivatives (benzoquinone, quinhydrone, cyclohexanol, etc.) have well pronounced expander properties [19]. Structural groups of the pyrocatechol type, which are a constituent part of the lignin structure, exert a beneficial influence on the performance of the battery [22].

A joint research performed by our laboratory and the Norwegian company Borregaard LignoTech has disclosed the influence of the different functional groups, contained in different amounts in 8 lignosulfonate products, on the performance of batteries when tested following the DIN 43539/2 test protocol for SLI batteries [20–22]. It has been established that with increase of the content of carboxylic (–COOH) and phenolic (Ar–OH) groups and of lignin purity (expressed by K_{solid}), the life of batteries, when limited by the negative plates, improves, but their charge acceptance declines and the self-discharge increases. With increase of the content of methoxyl groups (–O·CH₃) and of organic sulphur (–S), the cycle life of the batteries decreases. Hence, the type and amount of active structural groups contained in the lignosulfonate's macromolecule have a strong effect on battery performance.

Influence of grid alloy composition on expander efficiency [22]

Batteries of equal capacity were assembled with the same organic expander added to the negative paste, but with different grids: PbSnCa or PbSb grid alloys were used for both the positive and negative plates. These batteries were set to cycle life tests according to the requirements of the German test standard DIN 43539/2. The end-of-discharge battery voltage at the 10th charge–discharge cycle (i.e. after one week of cycling) is presented in Fig. 7.5 vs. week-cycle number. By measuring the changes in potential of the negative half-cell it was established that the cycle life of the batteries under test was limited by the negative plates. Batteries with PbSnCa grids have longer cycle life than batteries with PbSb grids.

In order to evaluate the effect of grid alloy composition on expander action, two series of batteries were assembled with PbSb or PbSnCa grids, but with different amount of phenolic

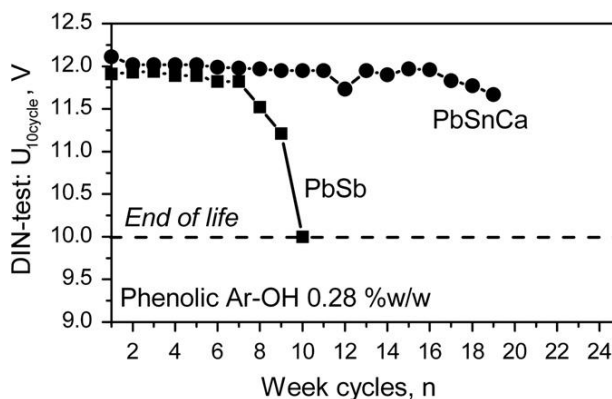


Figure 7.5:

DIN cycle life test results: $U_{10\text{ Cycle}}$ voltage as a function of the number of week-cycles for batteries with PbSb and PbSnCa grids [22].

groups in the expander. These batteries were set to cycling following the DIN 43539/2 test protocol. The obtained cycle life results are presented in Fig. 7.6.

Battery cycle life depends on the content of phenolic groups in the expander and on grid alloy composition. With increase of the content of phenolic groups in the expander, the cycle life of the batteries with PbSb grids increases. Probably, part of the phenolic groups reacts with Sb ions and hence their effect decreases. With increase of the phenolic group content their beneficial effect increases, because most of these groups do not react with Sb and hence they fully exhibit their beneficial effect on battery performance. The influence of phenolic group content on battery cycle life is considerably weaker in batteries with PbSnCa grids, because most probably phenolic groups react but less readily, or do not react at all, with Sn and Ca ions.

The above results indicate clearly that grid alloying additives interact with the organic expander. The thus formed organometallic compounds exert an influence on the performance characteristics of negative battery plates.

Impact of hydrogen and oxygen on expander stability [25]

Other substances that can interact with the organic expander are hydrogen and oxygen. In an attempt to determine their influence, charged negative plates were subjected to hydrogen or oxygen attack between two Pb|PbO₂ cells. Two charged lead–acid cells, with one positive and one negative plate per cell, were placed in a cell case filled with 1.28 rel. dens. H₂SO₄ solution. The plate to be investigated was inserted in the space between the two cells. When the effect of H₂ on expander properties had to be evaluated, the negative plates of the two cells faced the plate under test. Then the cells were set to polarization as a result of which hydrogen was evolved and saturated the electrolyte in the space between the two cells, thus attacking the plate under test. After a certain period of polarization (2–3 days), the negative plate was charged and

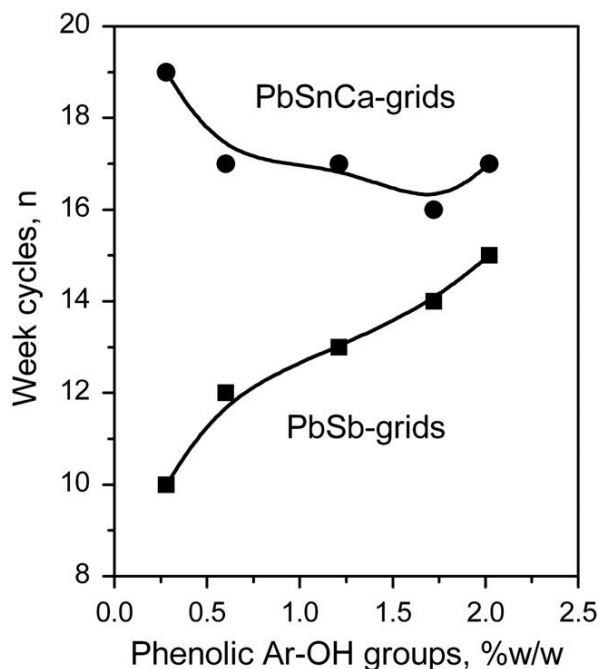


Figure 7.6:

Cycle life as determined by the voltage at the 10th week-cycle vs. phenolic —OH group content in the lignin [22].

its capacity was measured at $I = C_4$ A in another cell. To evaluate the impact of oxygen on expander stability, the cells were rotated so that their positive plates faced the plate under test. Consequently, the electrolyte in the inter-cell space was saturated with O_2 . In this way, the plate under test was subjected to oxygen attack. These experiments were conducted at 50 °C in an attempt to accelerate the reactions leading to expander disintegration.

Experiments were performed using plates with expanders Quebraco and EZE-Skitan. The resulting capacity curves, as a function of the time of oxidation or reduction, are presented in Fig. 7.7. Besides the plates subjected to oxidation or reduction, reference negative plates with the same expanders were left in the test cells with no hydrogen or oxygen attack.

The data in Fig. 7.7 give grounds for the following conclusions:

Quebraco disintegrates when attacked by hydrogen and even more rapidly under oxygen attack. EZE-Skitan reacts with H_2 and O_2 , but the resulting changes in expander structure improve its activity and thus the capacity of the negative plate increases.

Figure 7.8 presents the capacity curves for cells assembled with negative plates with different expanders. It is evident from the data in the figure that expanders Mimosa and VeleX have but a weak effect on battery cycle life. SNK and especially EZE-Skitan and Quebraco, improve

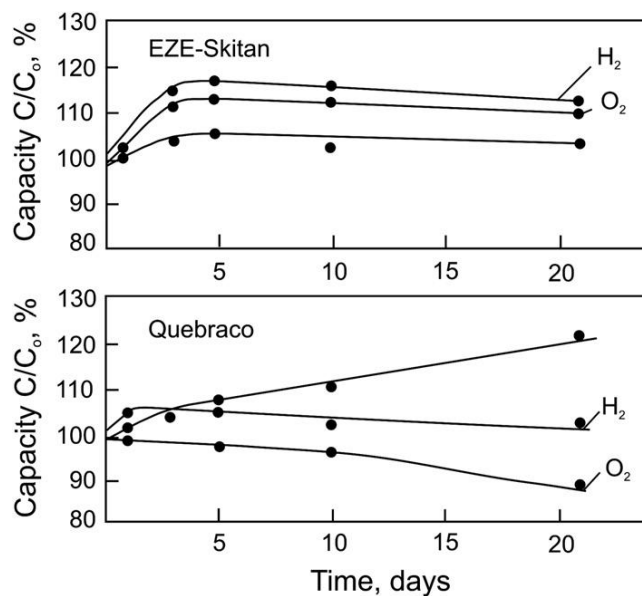


Figure 7.7:

Capacity curves as a function of time of oxygen and hydrogen attack for plates with quebraco or EZE-Skitan and for reference plates not subjected to such attack [25].

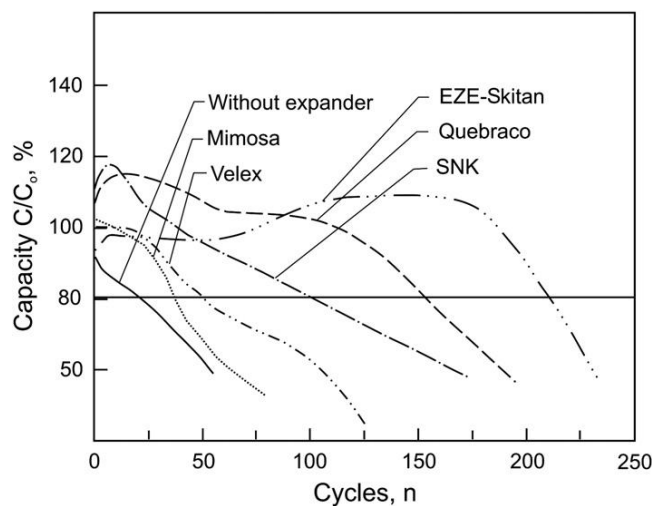


Figure 7.8:

Changes in capacity during cycling of cells with negative plates with five different expanders or without expander [25].

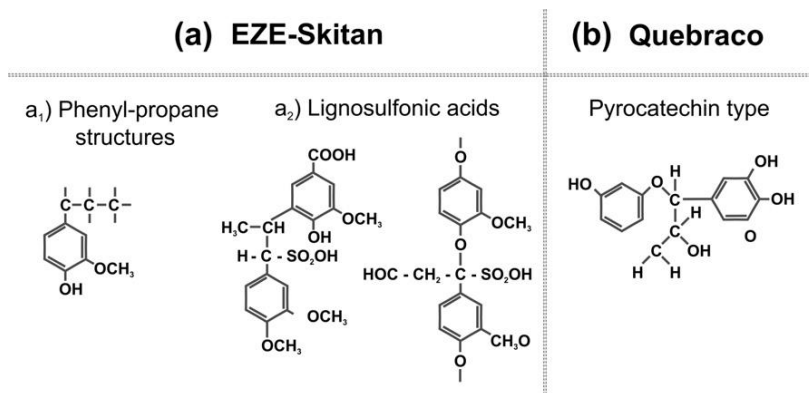


Figure 7.9:
Structural units of expander molecules [25].

substantially the life of the batteries. An interesting finding is that, after 50 cycles, EZE-Skitan disintegrates partially, which results in formation of more active structural groups in the lignosulfonate molecule, and hence both the capacity and the cycle life of the batteries increase.

Figure 7.9 shows the basic structural groups in Quebraco and EZE-Skitan [25].

On comparing the experimental data presented in Figs 7.7–7.9 it can be seen that expanders containing structural groups of the pyrocatechin type have beneficial effect on the electrical parameters and the life of negative battery plates. Pyrocatechin groups in EZE-Skitan are connected in more complex spatial structures and, hence, the initial plate capacity is considerably lower than that of plates containing Quebraco. Only after 50 to 60 cycles, when partial disintegration of the molecules of EZE-Skitan occurs, the effect of pyrocatechin structural groups is displayed more clearly.

Influence of temperature on expander stability during battery cycling [26]

For the purpose of these investigations, pastes for negative plates were prepared using a variety of the most efficient organic expander components currently used in the battery industry on a worldwide basis, such as Indulin AT (In) and Vanisperse A (VS-A), as well as a mixture of Indulin and Vanisperse. Indulin AT with kraft lignin is used as expander material mostly for industrial batteries, whereas Vanisperse A is employed mainly in SLI battery applications. Tests were also performed with the experimental expander products UP-393 and UP-414, produced by Borregaard LignoTech, Norway. All battery tests were conducted following the requirements of the European cycling test protocol ECE-15, for electric vehicle batteries [26].

The influence of temperature on the cycle life of negative plates containing the above discussed expanders is illustrated in Fig. 7.10 [26]. As all above tests were performed with VRLA cells, the effect of oxygen (during operation of the oxygen cycle) on the expander should also be added to the temperature effects.

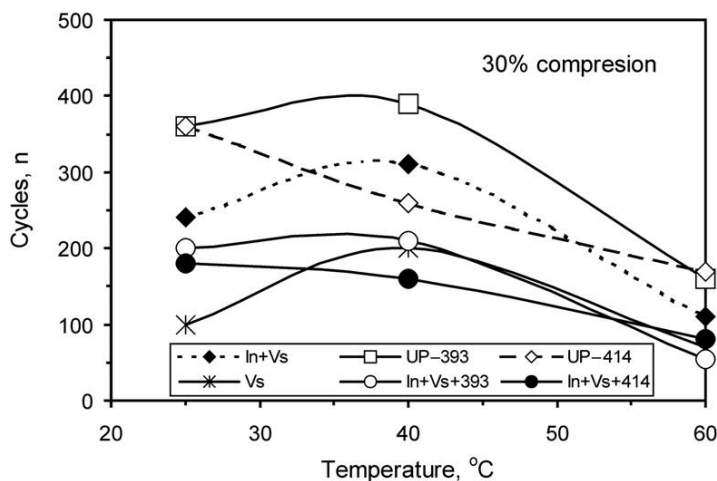


Figure 7.10:

Capacity changes on cycling of cells with different expanders at different temperatures [26].

The following conclusions can be drawn on grounds of the data in Fig. 7.10. Expanders UP-393 and In+VS ensure the longest cycle life at 40 °C. The product UP-414 can also be added to this group.

When the battery is cycled at 60 °C and is of the VRLA type, expanders containing lignin and its derivatives disintegrate, as a result of which the battery cycle life is reduced almost twice. In order to improve the cycle life performance of the negative plates, the battery temperature should be kept equal to about 40 °C.

7.1.2 Carbon Additives

Types of carbon additives to the negative plates and their influence on the structure of NAM

Two forms of carbon materials are used as additives in the battery industry: carbons and graphites. Carbons, in turn, are: carbon blacks, activated carbon, etc. Graphites are also available in several forms: purified natural flake graphites, expanded graphites, synthetic spherical graphites, etc. Table 7.1 summarises the basic characteristics (particle size, specific BET surface area, trade name) of some of the commercially available carbon and graphite materials.

The data in the table, as specified by the manufacturers, show that graphite particles are mostly of micron sizes (from 10 to 28 μm) and have a specific surface area from 9 to 24 $\text{m}^2 \text{g}^{-1}$. Carbon blacks comprise nano-sized particles (from 12 to 100 nm) and their specific surface area varies from 45 to several hundreds and even over thousand, of square meters per gram. Because of these differences in size and surface area of the various carbon and graphite

Table 7.1: Some commercially available carbon and graphite additives to NAM.

Product	Manufacturer	Type of Material	Bet Surface (m ² g ⁻¹)	Particle Size
Graphites				
FG1 Formula BT 2939APH	Superior Graphite	Purified natural flake graphite	9	10 µm (d50)
EG1 Formula BT ABG1010	Superior Graphite	Expanded graphite	24.0	10 µm (d50)
EG2 Formula BT ABG1025	Superior Graphite	Expanded graphite	18.0	28 µm (d50)
Carbons				
AC4 PRINTEX [®] XE2	Degussa	Carbon black	910	30 nm
AC3 Black Pearls 2000	Cabot Corporation	Carbon black	1475	12 nm
AC2 VULCAN XC72R	Cabot Corporation	Carbon black	257	30 nm
CB2 PUREBLACK – 205	Columbian Chemicals	Carbon black	50	42 nm
CB3 Denka black	Denki Kagaku	Carbon black	68	35 nm
PRU Printex [®] U	Evonik Industrie	Carbon black	100	25 nm
PR90 Printex [®] 90	Evonik Industrie	Carbon black	300	14 nm
AC1 NORIT AZO	NORIT	Activated carbon	635	100 µm
TDA SO-15A	TDA Research Inc.	Activated carbon	1615	< 44 µm
MWV Purified WV-E105	Mead Westvaco Corp.	Activated carbon	2415	8.7 µm

materials, they will have different impact on the electrochemical behaviour of the negative active material of a lead–acid battery.

Nakamura *et al.* [27,28] have established that introduction of carbon black to the negative active material retards substantially the sulfation of the negative plates during the simulated high-rate partial-state-of-charge (HRPSoC) test of batteries for hybrid electric vehicle (HEV) applications. This specific mode of operation is fairly indicative of the reversibility of the processes at the negative plates during battery cycling. That is why we have employed the HRPSoC cycling test to evaluate the effect of carbons on the performance of the negative plates. Most of the experimental results presented further in this Chapter and the conclusions drawn are based on this cycling mode.

Several mechanisms of the effect of carbons, on the processes at the negative plates of lead–acid batteries operated under HRPSoC conditions, have been proposed. Moseley *et al.* [29] have summarised the hypotheses proposed in the literature for the action of carbons on the HRPSoC performance of the batteries as follows: (a) carbon enhances the overall conductivity of NAM [27,30]; (b) carbon facilitates the formation of small isolated PbSO₄ particles that are easy to dissolve and restricts PbSO₄ crystal growth [28]; (c) some carbon forms contain impurities which impede the reaction of hydrogen evolution and hence improve the efficiency of charge [31,32]; (d) carbon acts as an electro-osmotic pump that facilitates acid diffusion in the inner NAM volume at the high rates of charge and discharge

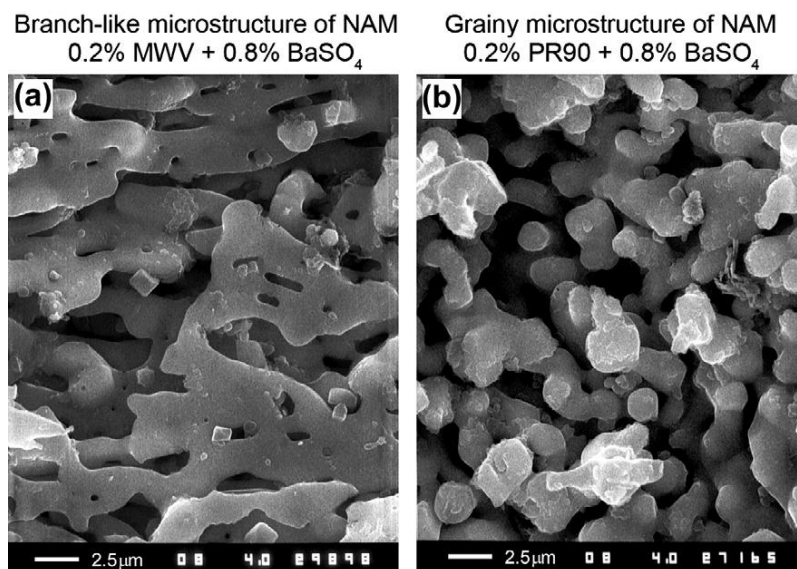


Figure 7.11:
SEM micrographs of NAM structure [35].

[29] and (e) high-surface-area carbon black particles have a supercapacitive effect in NAM [33]. A comprehensive survey of the influence of a wide spectrum of carbon materials introduced as additives to NAM on the HRPSoC cycling performance is provided in reference [34].

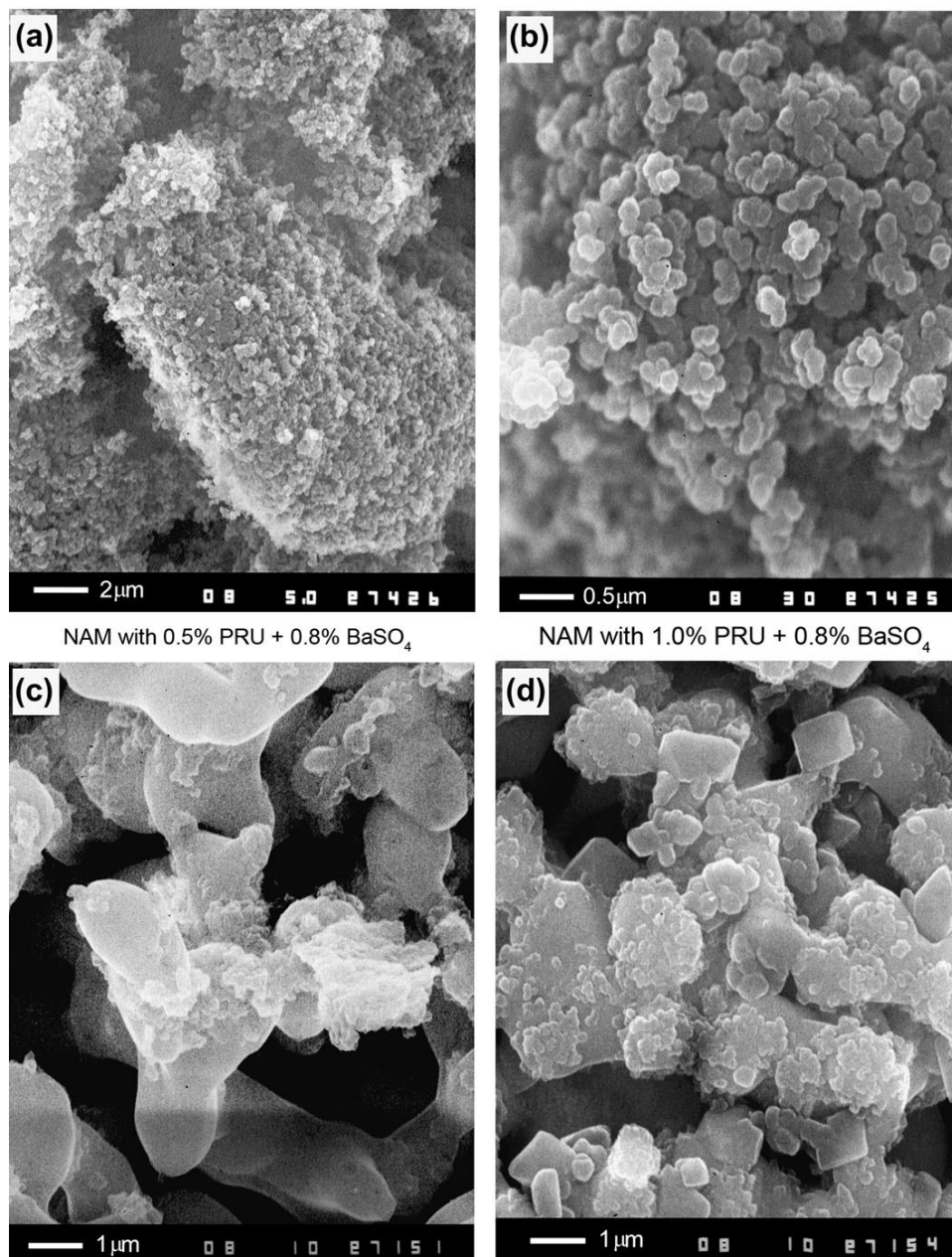
Let us first see how carbon additives affect the structure of the negative active mass.

Figure 7.11 presents SEM images of the microstructure of NAM with carbon and BaSO₄ additives. These images feature a lead skeleton or network. The skeleton in the left hand micrograph (Fig. 7.11a) consists of numerous interconnected branches of different thickness and various lengths. The right hand micrograph (Fig. 7.11b) shows spheroidal lead grains also interconnected in a network [35].

During discharge, parts of the lead skeleton are oxidized to PbSO₄ and they determine the capacity of the negative plates. The skeleton is then restored during re-charge. These parts form the *energetic structure of NAM*. The remaining non-oxidized part of the lead skeleton plays the role of *current-conducting structure*. It conducts the electric current from the plate grid to each point of the active mass even when the plate is being discharged.

Where and how are carbon particles included in the structure of NAM? Figure 7.12 presents SEM micrographs of Printex[®] U (PRU) carbon black particles [35]. The two SEM images evidence that PRU carbon black particles are fine grains of nanometer size, which are

PRU carbon particles

**Figure 7.12:**

(a,b) Microstructure of printex[®] U carbon black particles and agglomerates; (c,d) microstructure of NAM with 0.8 wt% BaSO₄ and 0.5 wt% Printex[®] U (c), or 1.0 wt% Printex[®] U (d) [35].

interconnected in porous formations (aggregates). Due to friction between the particles during the process of paste preparation, these formations have fallen apart to separate grains or small groups of grains (Fig. 7.12 a,b).

Let us now see how the structure of the negative active mass looks like when it contains both BaSO_4 and carbon black additives. Figure 7.12 c and d shows SEM images of NAM with 0.8 wt% BaSO_4 and two different concentrations of PRU carbon black. The carbon black particles are adsorbed on the lead surface and it is strongly folded. The surface area of NAM has increased.

The question arises logically: are these carbon grains adsorbed on the surface of NAM only or are they incorporated into the bulk of the lead skeleton branches? In order to find the answer to this question, cells with negative plates containing 0.2, 1.0 or 2.0 wt% PRU carbon black were discharged down to 100% DOD and samples of the formed active mass were examined by scanning electron microscopy. The obtained SEM micrographs of samples of the discharged active masses are presented in Fig. 7.13 [35]. With increase of the content of PRU carbon black the latter is involved in the growth of the PbSO_4 crystals. While at 0.2 wt% PRU level the PbSO_4 crystals have well shaped crystal faces and edges, at the higher concentration of 2.0 wt% the PbSO_4 crystals are rounded due to the embedded carbon particles. The latter create defects in the crystal lattice of PbSO_4 which would enhance the solubility of the lead sulfate and thus improve the efficiency of charging with high currents.

In an attempt to examine the structure of the bulk (interior) of the lead skeleton branches after discharge, the PbSO_4 crystals were dissolved in ammonium acetate. Figure 7.14 presents micrographs of the lead skeleton that has remained after dissolution of the PbSO_4 phase [35]. The nature of this skeleton strongly depends on the concentration of the carbon particles. At 0.2 wt% PRU, almost no carbon grains can be distinguished in the bulk of the skeleton, whereas at higher PRU concentrations (1.0 wt% and especially 2.0 wt%), the skeleton is strongly folded. This is a clear indication that the *grains of this type of carbon are incorporated in the bulk of the lead skeleton branches*. The extent of their inclusion in the bulk of the lead phase depends on the concentration of carbon blacks in NAM. Obviously, this will have an impact on the reversibility of the processes during HRPSOC cycling [35].

The inclusion of the PRU grains in the bulk of the lead skeleton branches indicates that this carbon black type has *high affinity to lead*. During formation of the negative active material, the carbon particles are adsorbed on the lead surface of the growing lead branch. As these particles are electroconductive, the electrochemical reaction of lead ion reduction proceeds on their surface. The newly formed lead surrounds the carbon grains and thus the latter are incorporated into the bulk of the lead branch of NAM skeleton.

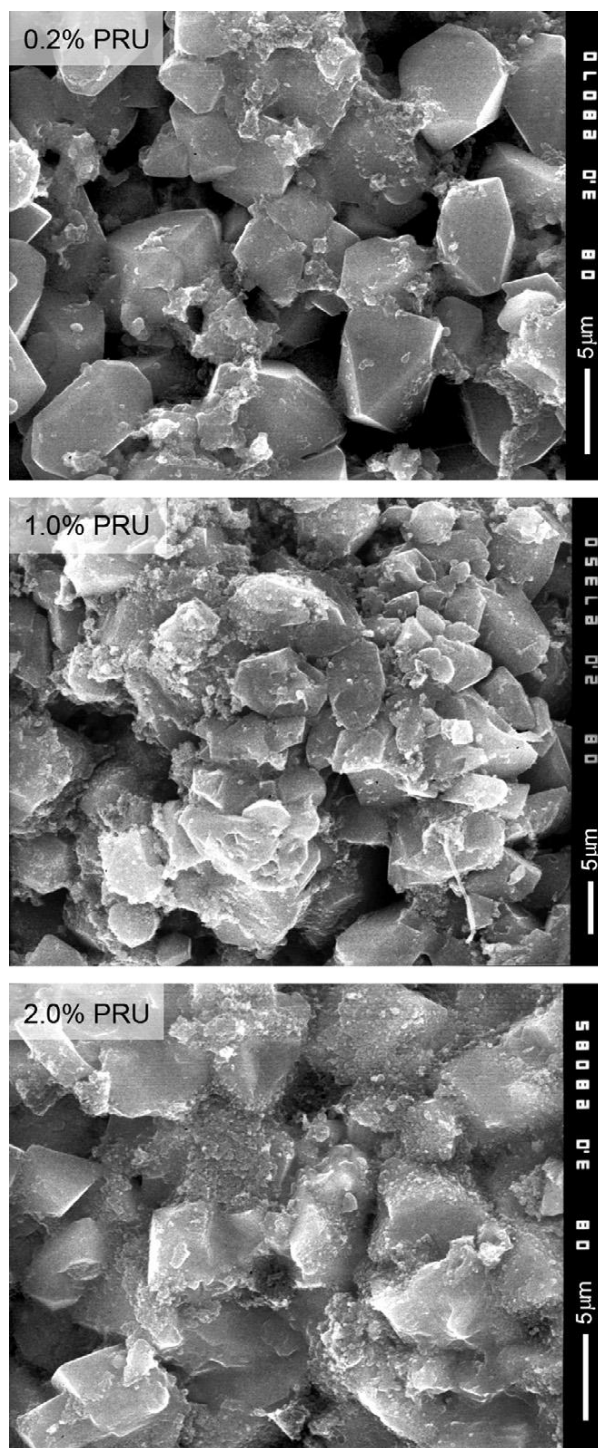


Figure 7.13:

Microstructure of NAM with different printex[®] U carbon black contents after deep discharge (100% DOD) of the negative plates [35].

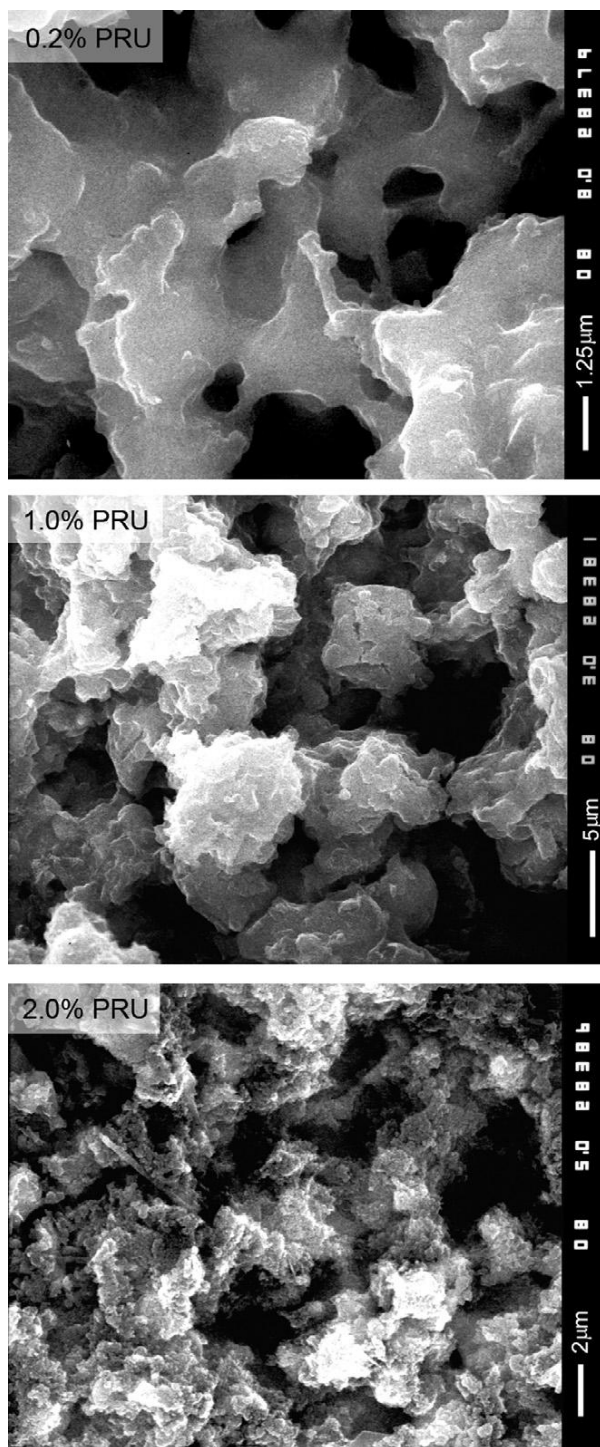


Figure 7.14:

Microstructure of parts of the inner volume of the current conducting branches of NAM lead skeleton after dissolution of the PbSO_4 phase. NAM contains 0.2 wt%, 1.0 wt% or 2.0% printex[®] U carbon black [35].

Hence, for the carbon grains to be incorporated into the bulk of the skeleton branches they should meet the following two requirements:

- carbon particles should have high affinity to lead, be electroconductive and electrochemically active;
- carbon particles should have a volume (size) much smaller than the cross-section of the lead branches of NAM skeleton.

If carbon particles are incorporated into the bulk of the lead skeleton branches, they will inevitably alter the macrostructure of NAM. This structure is characterised in terms of median pore radius and specific NAM surface and the changes in these parameters induced by carbons and graphites. Figure 7.15 illustrates the relationship between NAM median pore radius and carbon (graphite) content [36]. The investigated NAM samples contained also 0.2 wt% lignosulfonate and 0.8 wt% BaSO₄. It is evident from the data in the figure that the median pore radius of NAM diminishes below 1.0 μm with increase of the concentration of carbon blacks (AC4, AC3, AC2, CB2) above 0.5 wt%. Graphites (EG2 and FG1) have almost no effect on the median pore radius of NAM or cause but a small increase [34].

Figure 7.16 illustrates the changes in specific surface area of NAM as a function of the loading level of carbon black (AC2, AC3, AC4 and CB2) and graphite (EG2 and FG1) additives in the negative active material [36]. The specific surface area of NAM with addition

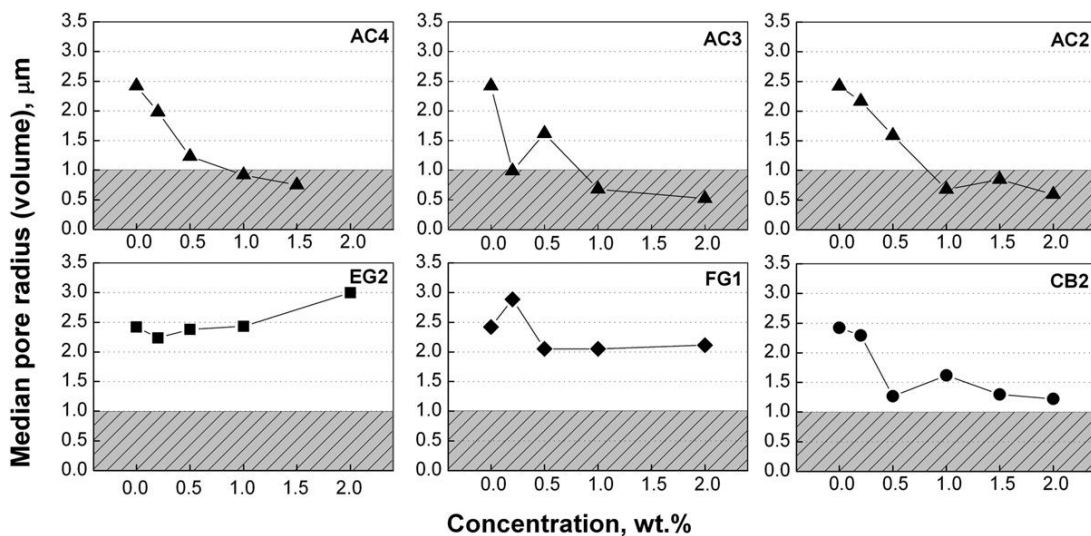


Figure 7.15:
Correlation between median pore radius of NAM and content of carbon or graphite additives [36].

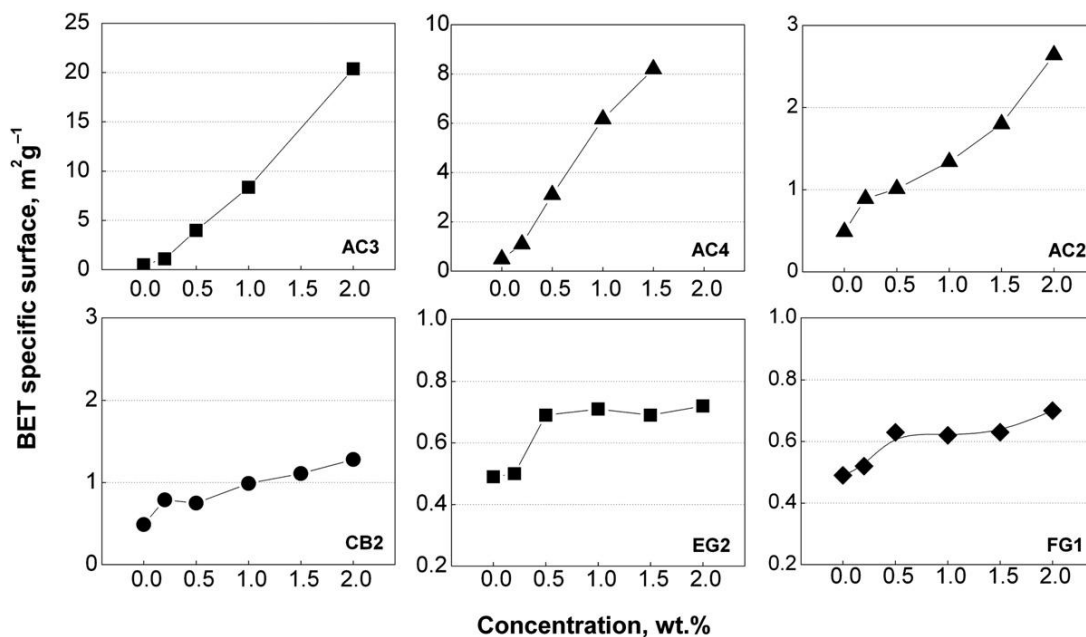


Figure 7.16:

Correlation between specific BET surface area of NAM and content of carbon or graphite additives [36].

of barium sulfate and lignosulfonate but no carbon is of the order of $0.5 \text{ m}^2 \text{ g}^{-1}$. When carbon is also added, the specific surface area increases with increase of the carbon content, this increase being most pronounced with AC3 and AC4 carbon blacks, while graphites (FG1 and EG2) have but the least contribution.

It follows from all above said that carbon particles interact with the lead active mass, being adsorbed on its surface and/or incorporated in the bulk of the lead skeleton branches. This results in macrostructural changes (reduced median pore radius and increased specific surface area of NAM). Thus, carbon additives alter the very nature of the lead electrode, converting it into a *lead-carbon electrode*, which will inevitably affect its electrochemical behaviour. The latter will depend on the affinity of carbon to lead, on the electrical conductivity of the carbon additive and on the electrochemical properties of the carbon surface.

Influence of carbon and graphite additives on the processes of charge of negative plates at high rates [36,37]

When batteries are set to deep discharge cycling the charge current reaches maximum values of $0.5 C_{20}$ A (usually it is $0.2 C_{20}$ A). At these current rates the negative plates charge efficiently. Batteries for hybrid electric vehicle applications, however, have to be

charged and discharged with very high currents ($I > 2 C_0$ A) and to operate from a partially charged state, 40–60% SOC, i.e. high-rate-partial-state-of-charge (HRPSoC) regime. Under these operating conditions, the efficiency of charge of the negative plates proves to be low. That is the reason why lead–acid batteries have been considered unfit for hybrid electric vehicle applications. In an attempt to overcome this limitation, methods have been looked for to improve the charge acceptance of negative plates on HRPSoC cycling.

The electrochemical behaviour of the lead–carbon electrodes were studied by subjecting cells to a simulated hybrid electric vehicle (HEV) cycling test comprising short (60 s) charge–discharge pulses with high currents ($I = 2 C_0$ A). The cells are cycled until a pre-set upper limit (e.g. end-of-charge voltage of 2.83 V per cell) or lower limit (e.g. end-of-discharge voltage of 1.83 V per cell) is reached. The above described cycling steps comprise one cycle-set of the test. The cells are then fully re-charged (to 100% SoC), their discharge (C_{20}) capacity is measured and they are again subjected to HRPSoC cycling between 50 and 53% state of charge.

The relationship between the end-of-charge cell voltage vs. cycle life for cells with carbon or graphite additives was investigated. The cells comprised of 3 positive and 2 negative plates, i.e. the positive plates were oversized as compared to the negatives, thus their potential changed but very slightly during cycling. The changes in cell voltage of the test cells on HRPSoC cycling are presented in Fig. 7.17 [28].

Polarization of the reference cell with no carbon in NAM increases by 400 mV within the first 300 cycles. This indicates that the electrochemical reaction of Pb^{2+} reduction on the Pb surface is very much impeded. The short cycle life of this cell implies that a PbSO_4 layer has accumulated rapidly on the negative plate during the charge/discharge processes leading to considerable cell polarization and hence shortening of its life to only 1300 HEV cycles. The cycle life of the cell is limited by reaching the upper voltage limit of 2.83 V.

Polarization of the cells with AC2 or AC4 carbon blacks depends on the concentration of the carbon added to NAM and is less than 50 mV for the cells with AC2 or with low concentrations of AC4 carbon blacks, respectively. The cells with CB2 or CB3 carbon black additives undergo higher polarization than the cells with AC additives, but it decreases significantly at higher CB concentrations in NAM, which means that carbon black participates in the charge processes. The end-of-charge voltage curves on HRPSoC cycling of cells with FG1 or EG2 graphites in the negative active mass indicate that the cells with graphite additives undergo significantly higher polarization than do cells with carbon blacks. Moreover, the end-of-charge voltage of cells with expanded graphite (EG2) exhibits small oscillations, which may be ascribed to poor contact between EG2 and lead particles.

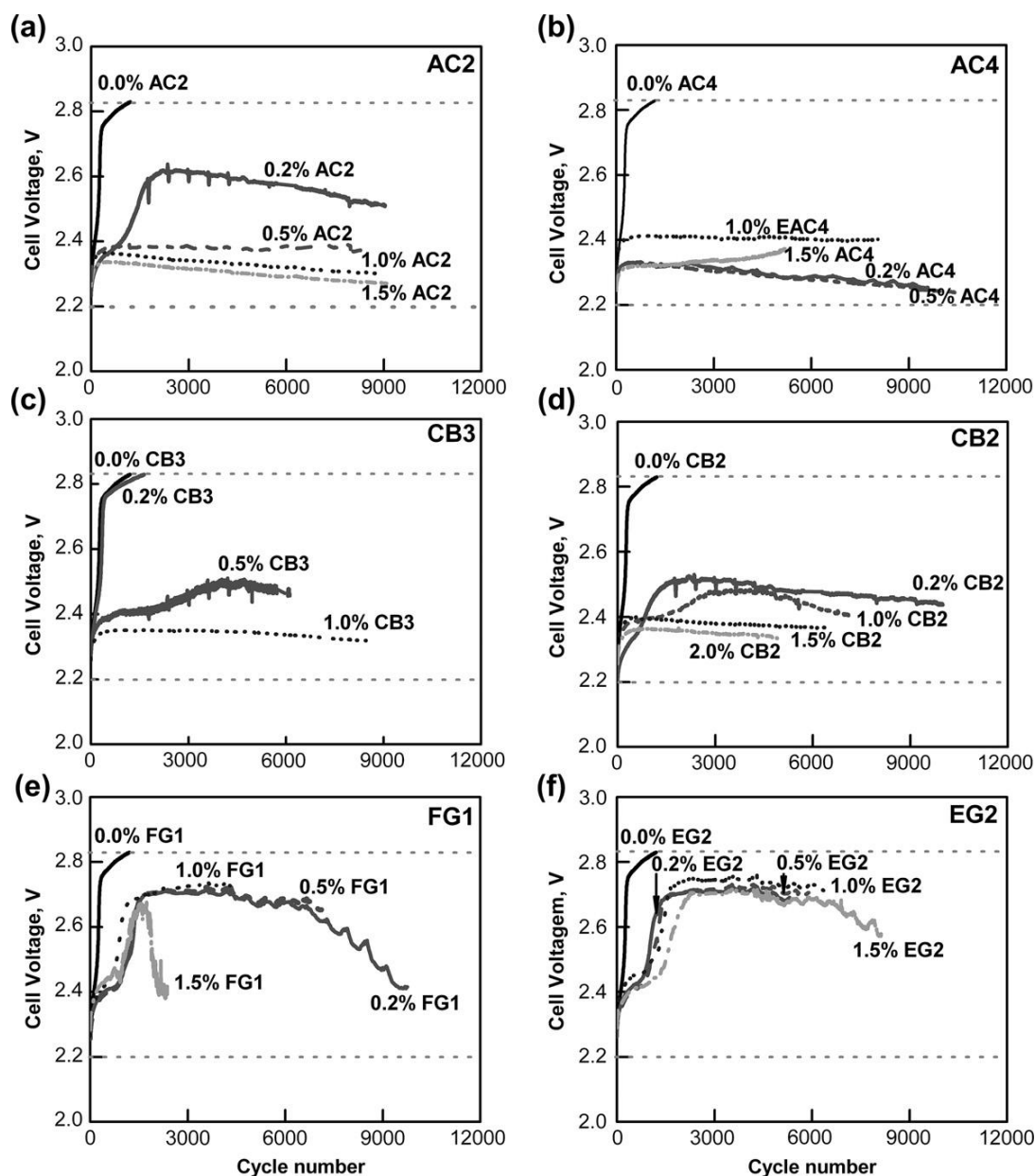


Figure 7.17: Changes in cell charge voltage during HRPSOC cycling as a function of carbon or graphite content in NAM with: (a) AC2; (b) AC4; (c) CB3; (d) CB2; (e) FG1; (f) EG2 [36].

Parallel mechanism of the charge reactions on negative plates containing carbons or graphites [36]

As evidenced by the data in Fig. 7.17, the carbon and graphite additives lower the polarization of negative plates on HRPSoC cycling. The polarization of the electrode on which the electrochemical reaction proceeds depends on the current density, i.e. the current per unit area of the electrode. The experimental data presented in Fig. 7.17 were obtained at constant current density. The lower polarization of the negative plates containing carbon or graphite additives must be due to increased surface on which the electrochemical reaction of Pb^{2+} reduction proceeds. This means that the latter reaction proceeds not only on the lead surface, but also on the surface of carbon and graphite particles. A schematic representation of the proposed parallel electrochemical mechanism is presented in Fig. 7.18. Reduction of PbSO_4 to Pb and subsequent oxidation of Pb proceed at the carbon surface parallel to the processes at the Pb surface [36,37].

Involvement of the carbon phase in the electrochemical process alters substantially the elementary reactions and the physico-chemical processes that occur during reduction of PbSO_4 to Pb. First, the access of Pb^{2+} ions to the surface on which the electrochemical reaction of charge proceeds is greatly facilitated. Secondly, the lead surface is covered by an adsorbed polymeric layer of expander, which increases the potential barrier for the transfer of electrons from the metal phase to Pb^{2+} ions and thus maintains low charge current. It can be assumed that the polymeric expander adsorbs but less readily on the carbon surface. Hence, electron transfer from the carbon phase to the adsorbed Pb^{2+} ions proceeds with less resistance, which lowers the polarization of the electrode on charge. Thus, the charge reactions proceed via a parallel mechanism, increasing the reversibility of the processes at the negative plates during cycling and eventually the cycle life of the cells. Cycling test results have proved that plates with no carbon additives endure 1300 charge-discharge cycles within one cycle-set of the HRPSoC test against over 5000 cycles for cells with carbon black in NAM.

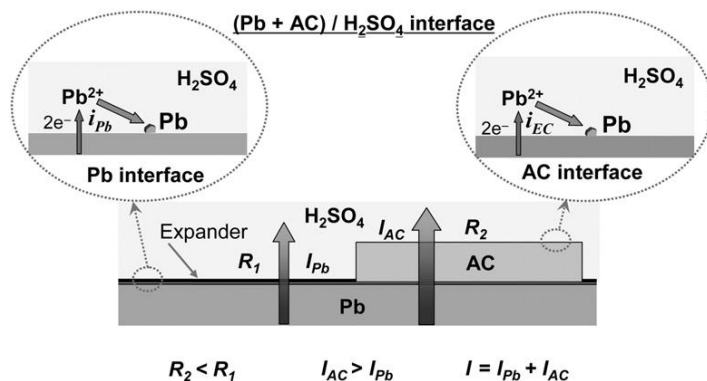


Figure 7.18:

Diagrammatic representation of the charge transfer through the Pb/solution and AC/solution interfaces according to the parallel mechanism of charge of negative plates.

The cycle life within one cycle-set depends strongly on the nature and properties of the carbon or graphite additives used. These materials differ in particle size, structure and affinity to lead and to the expander. Of special importance is the interface between carbon and lead particles, and its area as it determines the resistance that electrons have to overcome when transferred between these two phases and thus affects the potential and the rate of the electrochemical reactions at the carbon/solution interface. Only a limited number of carbon and graphite materials have optimum structural characteristics and may improve substantially the cycle life performance of the cells. It is of crucial importance to identify the most effective carbon (graphite) additives, i.e. with most beneficial effect on the parallel mechanism of charge of the negative plates.

Influence of type and concentration of carbon and graphite additives to NAM on the cycle life of cells in HRPSoC duty [35,36]

The effect of carbon content in NAM on the cycle life (within the first cycle-set) of lead–acid cells cycled under HRPSoC conditions is illustrated in Fig. 7.19.

Cells with carbon black (AC2, AC4, CB2) or graphite additives (FG1) in NAM have a cycle life of between 9200 and 11,300 cycles, at concentrations of the carbon additives between 0.2 and 0.5 wt%. On further increase of the carbon content, the cycle life within the first cycle-set decreases. Hence, these carbon additives should be introduced into the negative pastes in

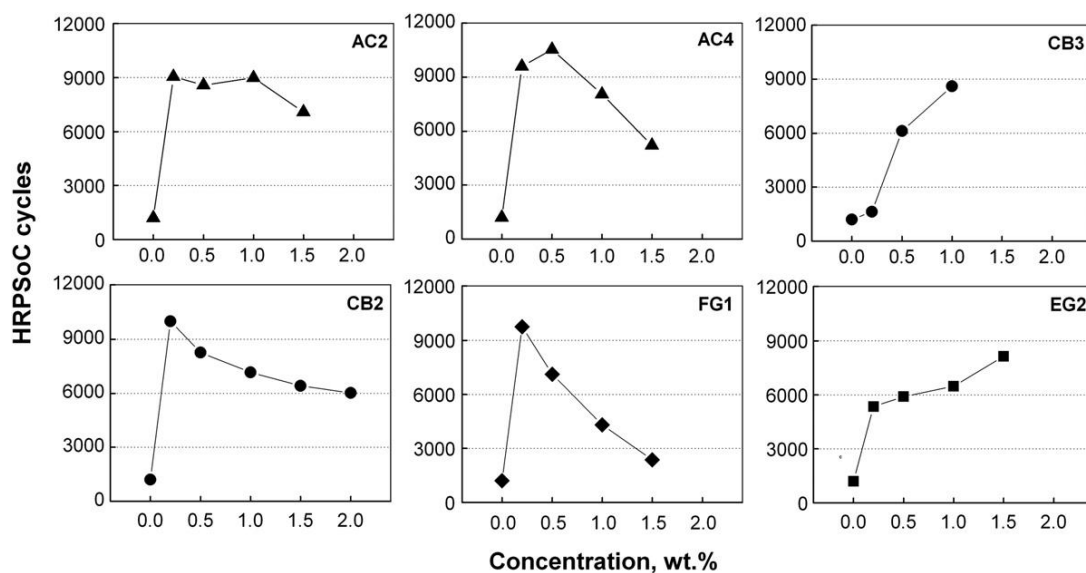


Figure 7.19: HRPSoC cycle life within the first cycle-set as a function of carbon black or graphite content in NAM [36].

concentrations ranging from 0.2 to 0.5 wt% so as to achieve maximum beneficial effect on cell (battery) performance. Flake graphite (FG1) additive guarantees the longest cycle life of the cells when its content in NAM is between 0.2 and 0.5 wt%, too. Expanded graphite (EG2), however, yields this effect when added in higher concentrations (e.g. 1.5 wt%).

The data in Figs. 7.19 demonstrate clearly that the cycle life of the cells in HRPSoC duty is affected by the type and amount of carbon or graphite additives to NAM. Hence, optimum cell performance could be achieved when an optimum proportion between the surfaces of lead and carbon (graphite) particles is reached.

Influence of carbon particle size and its affinity to lead on the electrochemical behaviour of NAM

SEM micrographs of AC1 activated carbon particles are given in Fig. 7.20a [35]. There is a variety of carbon particles of different sizes varying within the micron and down to the sub-micron range. These particles differ in shape, too, the elongated shape being the predominating one. The structure of NAM with incorporated AC1 carbon particles is presented in Fig. 7.20b, c. The SEM images show that the AC1 activated carbon particles are included in the lead active mass, but the contact with it is not very 'intimate'. They look rather like some foreign inclusions in the Pb active mass. Lead nuclei are formed at some sites on the surface of the big carbon particles, but these nuclei grow slowly. This is, probably, due to the low affinity of lead towards carbon. If this affinity were high, the lead nuclei formed on the carbon surface would grow rapidly and connect to the NAM skeleton.

The microstructure of TDA activated carbon particles (upper left SEM micrograph) and the sites of their inclusion in the lead skeleton of NAM (the other three SEM images) are illustrated in Fig. 7.21. The TDA activated carbon particles have micron or sub-micron dimensions (Fig. 7.21a). The micrographs of NAM evidence clearly that the carbon particles have become an ingredient part of the lead skeleton and participate in its build-up. The picture in Fig. 7.21b features lead branches grown from one big carbon particle. The lower two photos (Fig. 7.21c,d) show numerous lead nuclei formed on the surface of the carbon particle which tend to grow as new branches, thus being incorporated in the lead skeleton. These micrographs demonstrate clearly that there exists a great affinity between TDA activated carbon and lead particles, and that they can form together a lead skeleton.

How do these NAM structures affect the capacity and cycle life of the cells in the HRPSoC regime? Figure 7.22 summarises the cycling test results for cells with increasing amounts of AC1, MWV or TDA activated carbons and 0.8 wt% BaSO₄ in NAM [35]. No lignosulfonate was added to the negative plates.

Figure 7.22a illustrates the influence of AC1 activated carbon content on the number of HRPSoC cycles and on cell capacity. A well expressed peak in the number of completed cycles within the first cycle set is observed at the low carbon concentrations from 0.2 wt% to 0.5 wt%

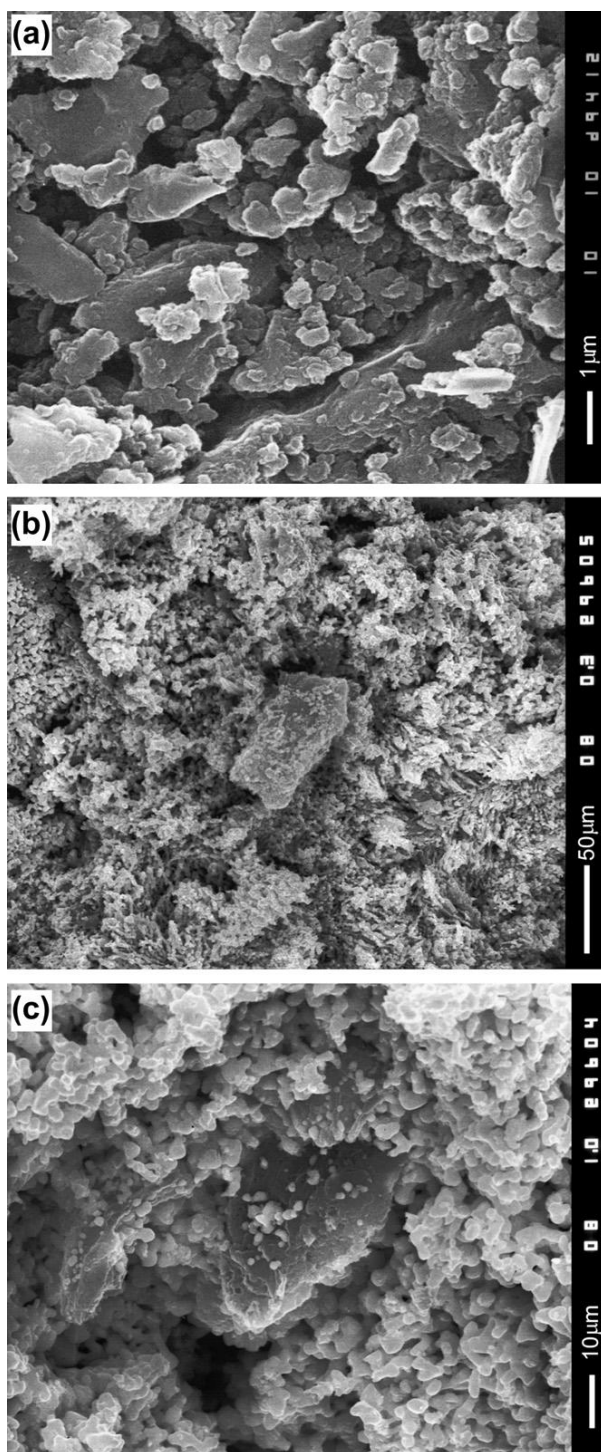


Figure 7.20:

(a) Microstructure of AC1 activated carbon particles; (b,c) microstructure of NAM with incorporated AC1 activated carbon particles [35].

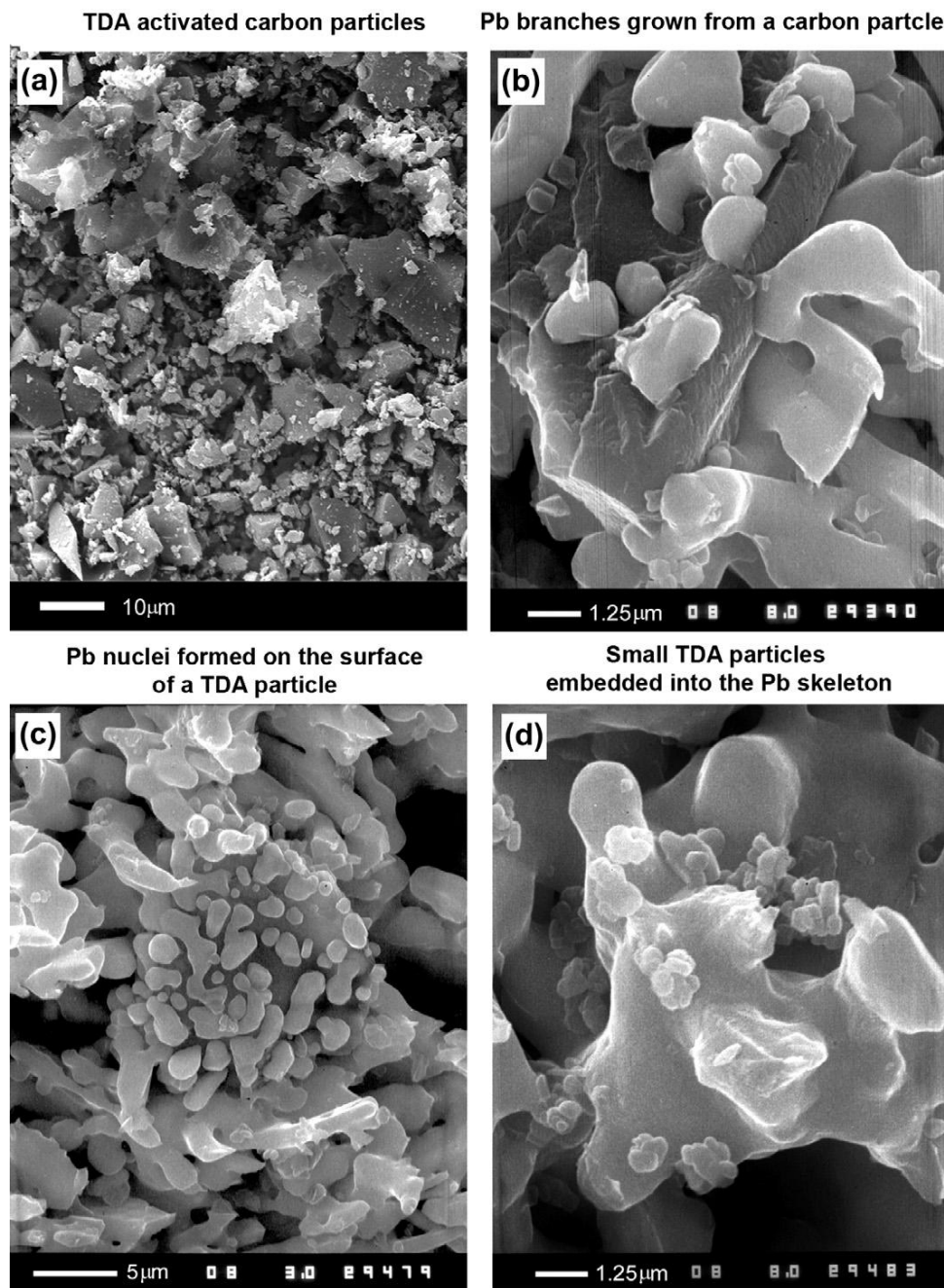


Figure 7.21:

(a) Microstructure of TDA activated carbon particles; (b,c,d) microstructure of NAM with TDA activated carbon and BaSO_4 [35].

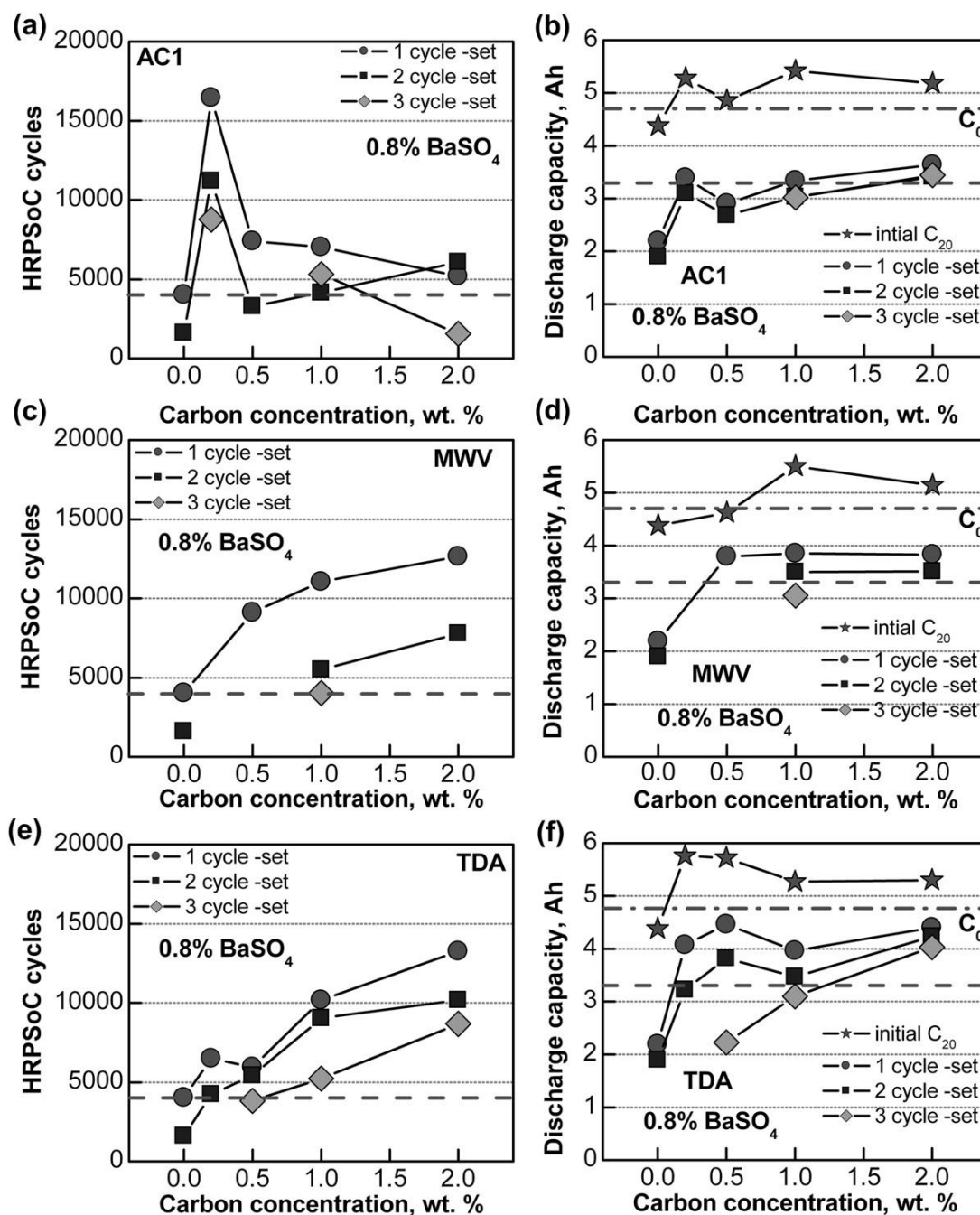


Figure 7.22:

Influence of (a,b) AC1, (c,d) MWV and (e,f) TDA activated carbons on the number of completed cycles and on cell capacity for three consecutive HRPSoC cycle sets [35].

AC1. After this maximum, further increase of the AC1 carbon load reduces the number of completed cycles per cycle set. Figure 7.22b shows the initial (C_{20}) capacities and the discharge capacities of the cells after each cycle set. All cells with AC1 activated carbon have initial capacity higher than the nominal value (C_0), which then declines down to the end-of-life limit value within the first cycle set already. This tendency is observed even with the cells with low carbon concentration.

The graphs in Fig. 7.22c illustrate the correlations between the number of completed HRPSoC cycles and the content of MWV activated carbon in NAM. The test cells complete increasing number of cycles with increase of the MWV carbon content. The initial capacities and the discharge capacities of the cells after each cycle set are presented in Fig. 7.22d as a function of MWV carbon content in NAM. All cells yield initial capacity close to or higher than the nominal capacity. The discharge capacity of the cells after the HRPSoC cycling declines significantly as compared to the initial capacity values, but remains above the end-of-life limit of 70% of the nominal capacity [35].

The effect of various concentrations of TDA activated carbon in NAM on the HRPSoC cycleability and the capacity of the cells is illustrated in Fig. 7.22e,f. Increase of TDA carbon content leads to an increase in the number of completed cycles per cycle set. At 2.0 wt% TDA level, the cells complete 13,500 cycles per cycle set, with only a small decrease in the number of completed cycles during each subsequent cycle set. An analogous trend in the behaviour of the cell capacity on HRPSoC cycling is also observed, which suggests that TDA activated carbon loads higher than 2 wt% may improve the cycleability of the cells within one cycle set and thus yield maximum overall cell cycle life [35].

The experimental data presented in Figs. 19 and 22 indicate that the degree of involvement of carbon additives in the electrochemical processes at the negative plates on cycling with high currents depends on their size and affinity to lead. If carbon particles have high affinity to lead, the contact carbon/lead will be mechanically stable and have low ohmic resistance (if the carbon added is highly electroconductive). The second characteristic with strong impact on the electrochemical behaviour of NAM is the size of carbon particles. If the latter are of nanosizes, i.e. they are much smaller than the cross-section of the lead skeleton branches, they may be incorporated into the bulk of the lead phase. This happens at carbon concentrations in NAM higher than 0.5 wt%. Such a structure of the skeleton branches is not quite stable mechanically and has high ohmic resistance, hence NAM with such a microstructure yields about 4000–5000 HRPSoC cycles. If, however, the carbon load in NAM is below 0.5 wt%, carbon particles will be pushed towards the surface of the NAM skeleton branches during formation and/or cycling and will increase the electrochemically active surface of NAM, thus eventually the number of completed cycles per cycle set may exceed 10,000.

When the dimensions of carbon particles are of the order of tens of micrometers (i.e. a size larger than the cross-section of NAM lead branches) and have high affinity to lead, the carbon

particles get integrated into the lead skeleton and become integral components of this skeleton. During formation, lead nuclei will form on the surface of these carbon particles and will grow into new branches, thus forming a *lead–carbon active mass skeleton*. Carbon particles have high surface area and microporous structure. When their pores are filled with water, they acquire the properties of a super-capacitor. SO_4^{2-} ions are big in size and would hardly pass through the pores of the carbon particles. Hence, only water and H^+ ions penetrate into the carbon pores. During charging, these carbon particles act as super-capacitors. Electric charges are concentrated in them and then they are distributed along the branches of the lead skeleton with the lowest ohmic resistance. This makes the lead skeleton a more dynamic electric system, which will be charged and discharged easier, which will improve the charge acceptance of the negative plates [35].

7.1.3. Barium Sulfate

Properties, structure and influence of BaSO_4 on PbSO_4 crystallization

Barium sulfate (BaSO_4) is highly insoluble in sulfuric acid solutions and electrochemically inactive in water and aqueous solutions. It does not participate in the chemical and electrochemical reactions at the negative plates during the operation of a lead–acid battery, but it affects the latter’s performance characteristics via some crystallization processes. Barium sulfate is isomorphous with lead sulfate (PbSO_4) and strontium sulfate (SrSO_4). All three compounds belong to the orthorhombic crystal structure group. The structural characteristics of the three sulfates are presented in Table 7.2 [38].

Due to its isomorphism with PbSO_4 , BaSO_4 affects the crystallization process of PbSO_4 during discharge of the battery. A new phase is formed through formation of nuclei which then grow to form the crystals of the new solid phase. Nucleation occurs when the solution is oversaturated with ions which participate in the formation of the new phase or with molecules of this phase. Oversaturation exhibits in increase of electrode potential (i.e. overpotential of nucleation). No such overpotential occurs in the presence of nuclei. Figure 7.23 presents the changes in potential of a fully charged negative plate (with no BaSO_4) at the beginning of discharge, when the PbSO_4 nuclei are formed (Fig. 7.23a) [38]. The initial potential increase

Table 7.2: Structural characteristics of PbSO_4 , BaSO_4 , SrSO_4 .

	PbSO_4	BaSO_4	SrSO_4
Dimensions of the orthorhombic crystal lattice, Å			
(a)	8.45	8.85	8.36
(b)	5.38	5.44	5.36
(c)	6.93	7.13	6.84
Cation–O bond length, Å	2.87	2.95	2.83
S–O bond length, Å	1.49	1.48	1.47

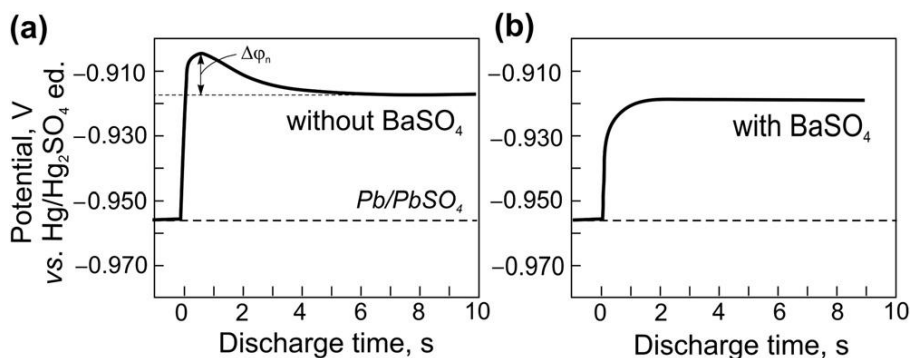


Figure 7.23:

Initial changes in potential on high rate anodic polarization of negative plates: (a) without BaSO₄ and (b) with BaSO₄ in NAM. $\Delta\phi_n$ is the nucleation overpotential [38].

is due to oversaturation of the solution with dissolved PbSO₄ molecules. This is the nucleation overpotential, $\Delta\phi_n$. With nucleation of the PbSO₄ phase the solution oversaturation decreases and so does the plate potential. Figure 7.23b shows the changes in potential at the beginning of discharge of a fully charged negative plate containing BaSO₄. Addition of barium sulfate to the negative paste reduces the oversaturation of the solution in the pores of NAM as BaSO₄ crystals serve as nucleation centres over which crystals of PbSO₄ grow. No overpotential of nucleation occurs. This is the isomorphism of BaSO₄ and PbSO₄ in action. Conjectures have been made such that mixed crystals of (Pb_(1-x)Ba_x)SO₄ are formed. Thus, by facilitating the crystallization process, BaSO₄ nuclei facilitate the formation of a porous layer of small PbSO₄ crystals on the lead surface, thereby preventing the deposition of a continuous PbSO₄ passivating film, which would impede the discharge process and reduce the capacity of the plate. The porous PbSO₄ layer facilitates the transfer of Pb²⁺ ions through this layer, thus sustaining the electrochemical reaction of discharge ($\text{Pb} \rightarrow \text{Pb}^{2+} + 2\text{e}^-$) and increasing the capacity of the plate.

The SEM micrographs in Fig. 7.24 show BaSO₄ particles (Fig. 7.24a) and their location in the structure of NAM with only barium sulfate added (Fig. 7.24b) [35]. Barium sulfate particles are mostly adsorbed at the sites of contact between the Pb particles. These are the sites in the NAM structure with the highest concentration of defects, causing higher concentration of structural energy which goes for the adsorption of BaSO₄ particles.

Two forms of barium sulfate are used for preparation of negative pastes: Blanc Fix and Barytes [39]. Blanc Fix is produced by precipitating BaSO₄ from solutions of barium salts and H₂SO₄ and is characterised by mean particle size of about 1 μm . Barytes is ground and purified natural mineral ore. Its particles are sized between 3 and 5 μm . The larger size of Barytes particles makes it less efficient as negative paste additive. It is presumed, however,

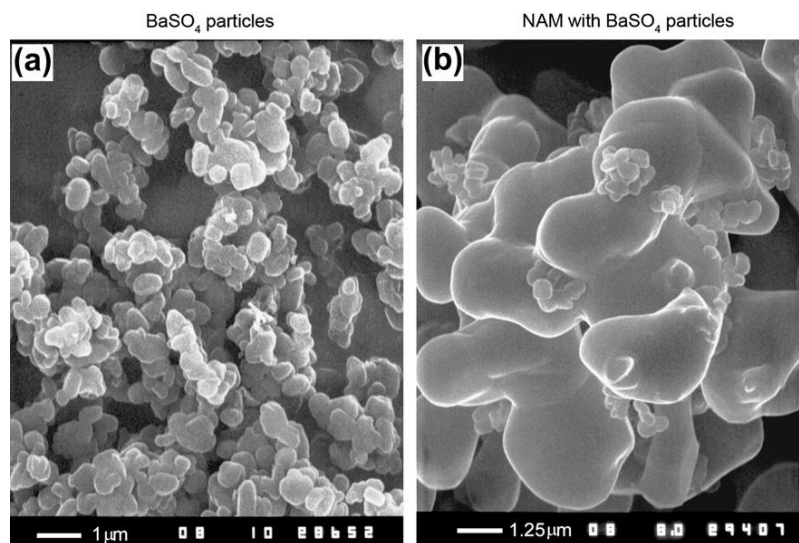


Figure 7.24:

- (a) SEM images of the microstructure of BaSO₄ particles; (b) BaSO₄ particles adsorbed on the NAM surface. they are embedded mainly at the sites of contact between the Pb particles of NAM.

that during battery operation the big Barytes particles disintegrate to smaller ones and thus its efficiency improves.

Influence of BaSO₄ on negative plate performance

The influence of BaSO₄ and of the organic expander component on the performance of cells on high rate (3C A) cycling and at temperatures between +30 °C and –18 °C has been investigated [38]. The latter study has proved that there is an interaction between BaSO₄ and the organic fraction of the expander and this interaction affects the capacity of the negative plates on cycling. Figure 7.25 presents the obtained capacity curves for cells with and without additives to NAM [38].

It can be seen from the data in the figure that cells and batteries with no additives to NAM (curve 1) have the lowest capacity and it declines rapidly on cycling. The plates (cells) with addition of BaSO₄ only (curve 2) have higher capacity than the blank cells, whereas those with organic expander but without BaSO₄ (curve 3) exhibit even higher capacity. However, the capacity of the three types of cells (batteries) declines fairly quickly on cycling. This is not the case with the cells and batteries containing both BaSO₄ and organic expander (curve 4). These cells (batteries) sustain high capacity performance for more than 150 cycles. These results indicate that there is some kind of interaction between the two additives to NAM. It has been assumed that BaSO₄ particles adsorb molecules of the organic expander. During discharge,

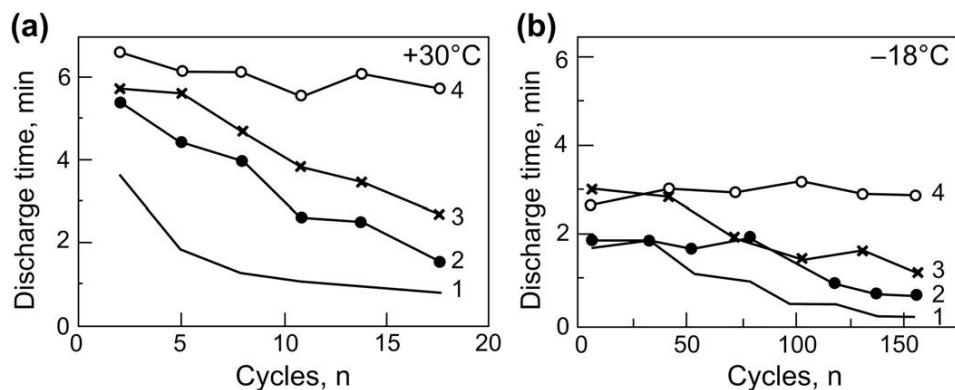


Figure 7.25:

Changes in discharge time (capacity) at (a) +30 °C; (b) -18 °C, on cycling cells with negative plates containing: (1) no additives; (2) 0.3% BaSO₄; (3) 1.0% humic acid (the organic expander component) and (4) 0.3% BaSO₄ + 1.0% humic acid. Fig. 7.25a presents the test results for cells and Fig. 7.25b for batteries [38].

BaSO₄ particles hold the organic molecules and prevent them from diffusing to the electrolyte and thus get oxidized on the positive plates.

The influence of BaSO₄ concentration in NAM on the performance of battery negative plates has been studied [40]. Figure 7.26 presents the results of the three initial capacity measurements on 20 h discharge at 25 °C of batteries with negative plates containing four different amounts of BaSO₄ (0.1, 0.4, 0.8 or 1.2 wt%). The capacities of a reference battery with no addition of BaSO₄ are also given for comparison [40]. All negative plates contain also 0.15 wt% Vanisperse A and 0.2 wt% carbon black.

The data in the figure evidence a rapid decline in capacity of the batteries with no barium sulfate or with 0.1 wt% BaSO₄. Batteries with BaSO₄ content higher than 0.4 wt%

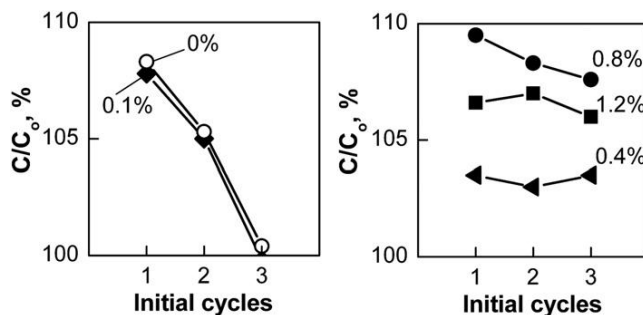


Figure 7.26:

Influence of BaSO₄ content in NAM on the initial capacity performance of cells on cycling at 20 h discharge rate [40].

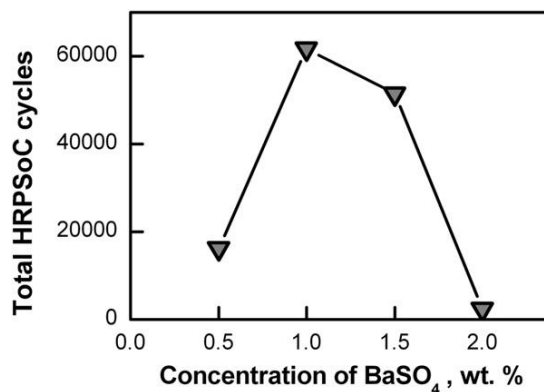


Figure 7.27:

Total number of completed HRPSoC cycles as a function of BaSO₄ content in NAM [41].

sustain almost constant capacity during the three initial capacity measurements. The highest and most stable capacity performance is registered for the batteries with 0.8 wt% BaSO₄ in NAM.

The optimum BaSO₄ loading level with most beneficial effect on the cycling performance of cells has been determined via the simulated HRPSoC test comprising short (60 s) charge-discharge pulses with high currents [41]. The obtained results are summarised in Fig. 7.27. In this cycling mode, too, the cells with 1.0 wt% BaSO₄ content in NAM exhibit the best cycle life performance.

Expander compositions for the various types of batteries

Lead–acid batteries are used in three main applications: automotive (starting, lighting and ignition, SLI), for motive power and for standby (reserve) power. A fourth type of lead–acid batteries is trying to gain a market segment, too, i.e. batteries for hybrid electric vehicle applications. In view of the particular battery function and the specificity of the operation mode in the above four applications, the amounts of the three expander components should differ for the different battery types, depending on their effect on the processes that occur in the battery. Boden [39] proposes typical expander formulations for the different battery applications as summarised in Table 7.3.

Table 7.3: Typical expander formulations for different battery applications [39].

	Automotive	Motive Power	Standby
Barium sulfate (%)	40–60	70–90	90–95
Lingosulfonate (%)	25–40	3–10	0
Carbon (%)	10–20	5–15	5–10

Besides the three basic components, the expanders for motive power batteries also contain small amounts of wood flour and soda ash. The wood flour decomposes slowly during battery operation producing lignin, which compensates for the lost lignin as a result of degradation of the lignosulfonate. The amount of expander added to the negative paste is 1.0–1.5 wt% for automotive batteries and about 2 wt% for industrial batteries. The high content of lignosulfonate in the expander for automotive batteries is needed to guarantee high power output of the battery at low temperatures (cold-cranking ability). The high content of BaSO_4 in motive power (industrial) batteries prevents the negative plates from passivation on deep discharge.

In standby (reserve) energy applications, a great number of cells are connected in a string. It is very important that the resistance of all cells is equal for many years of service of the battery. As was discussed above in Section 7.1.1.6, the expander is subjected to O_2 and H_2 attack and degrades at high temperatures. These processes progress at different rates in the different cells, as a result of which the overpotential of hydrogen evolution decreases and the float current increases. Consequently, the string is unbalanced. To avoid these phenomena, standby battery designers reduce substantially, or even exclude, the organic component (lignosulfonate) from the expander formulation at the expense of increased amount of BaSO_4 .

It can be concluded from all above said that the proportion of the three expander components should be selected skilfully, depending on the type of application and the specific conditions of operation of the battery.

7.1.4. Other Additives to the Negative Paste

Structural stabilizers of the lead active mass: Fibres, dynel flock, carboxymethylcellulose

Fibres of the above types (3 mm in length) and polypropylene fibres are introduced into the paste with the aim to provide mechanical stability to the structure of NAM. Because of the poor adhesion between lead and fibre particles, the role of mechanical strengthener of the NAM structure is not always very pronounced. Beyond any doubt, however, fibre additions reduce substantially the waste during the pasting process and throughout the technological process of negative plate manufacture, which provides very important economical effect.

The other paste components mentioned in the subtitle of this section have analogous effects. Moreover, they promote formation of macropores in NAM, thus facilitating the movement of ions into the plate interior. All these functions of the additives stabilizing mechanically the structure of NAM make them an indispensable component of the paste formulations for negative battery plates. Usually, polypropylene fibres with a length of 3 mm are introduced in amount within the range 0.075–0.08 wt% versus the lead oxide used for paste preparation.

Additives creating hydrophobic channels in NAM and accelerating the rate of oxygen reduction at the negative plates of VRLAB

It is generally assumed that oxygen electrochemical reduction (OEchR) is limited by the diffusion of oxygen through the separator and within NAM. The rate of the OEchR at the negative plate may be accelerated if the reaction surface on which the OEchR process proceeds is increased by increasing the depth to which oxygen can penetrate into the plate interior. This has been achieved by creating partially hydrophobic channels in NAM using Teflon emulsion [42]. Addition of 1.0 wt% of Teflon emulsion to the negative paste has proved to accelerate greatly the rate of the OEchR at the end of charge and during overcharge and thus improves the efficiency of the oxygen cycle. The content of Teflon in NAM, however, should not exceed the above level because it will reduce the capacity of the plates.

Inhibitors of hydrogen evolution at the negative plates

The driving force for an electrochemical reaction to proceed is polarization of the electrode, i.e. the potential difference between the equilibrium potential of the reaction and the electrode potential. The rate of the electrochemical reaction depends on the hindrances that have to be overcome by the reacting particles for the reaction to proceed. The hydrogen reaction on lead proceeds with great hindrances, i.e. at high overpotential. Hence, the competing reaction of lead sulfate reduction to lead proceeds with high coulombic efficiency and kinetic stability. This, in turn, ensures stable performance of the lead–acid battery.

The plate grids for lead–acid batteries are produced from lead alloys containing Sb, Sn, As, Ca, Cu, Ag, Se, etc. During battery operation, the grids corrode and alloying additives are released and deposit on the lead surface in the form of free metal particles. On all above metal substrates, the hydrogen reaction proceeds at lower, or even at very low, overpotentials. Thus, centres with catalytic effect on the hydrogen evolution reaction are formed on the negative plates and hence the decomposition of water is accelerated substantially. In order to avoid this undesired phenomenon, additives to the negative paste or to the electrolyte are looked for, which would adsorb on the catalytic centres and thus block, or retard, the hydrogen evolution reaction and eventually reduce water loss. These additives, however, should have no poisoning effect on the basic lead reactions during charge and discharge, and should not impair the integrity of the structure of NAM or reduce its surface area. Some of the investigated hydrogen evolution inhibitors are mentioned below, though their effect on all battery performance characteristics has not been fully studied yet.

- 3–5 Diaminobenzoic acid, *n*-dodecylamine, 2-benzimidazolethiol and nicotinic acid have inhibiting effect on the hydrogen evolution reaction and catalytic effect on the reaction of oxygen reduction [43].

- Anisaldehyde, in combination with Indulin-C and Na-1-naphthol-1-sulfonate in amounts of 700 ppm, is a highly efficient inhibitor of the hydrogen evolution reaction and increases the capacity of the negative plates. It can be introduced during operation of the battery, when the water loss increases [44].
- Benzaldehyde, benzoic acid and benzene also exhibit substantial inhibiting effect on the hydrogen reaction [45–47]. The hydrogen evolution inhibitors are adsorbed at the protons that are mainly present on the antimony sites (catalytic centres) of the electrode surface. Boehnsted *et al.* [45] propose a mechanism of the specific adsorption of aromatic aldehydes on these sites [45].
- Vanilline has been tested as inhibitor of the hydrogen evolution reaction on lead–antimony alloys at 47 °C. The water loss is reduced by 50% on battery cycling [48].
- α - and β -naphthol, α -nitroso- β -naphthol also act as inhibitors of the hydrogen reaction [49,50].

Comprehensive investigations in this direction are of utmost importance, especially for maintenance-free batteries. The inhibiting effect should be studied in correlation with the effects of expanders as both substances are adsorbed on the lead surface and may mutually facilitate or impede their influence.

7.2. Additives to the Positive Paste

The lead dioxide active mass has a fairly complex structure, sensitive to foreign substances, which may degrade or get passivated under the action of even small amounts of additives to the positive paste, respectively to PAM. That is why the number of additives to the positive paste is limited and their effect is not always unambiguous.

McGregor [51], Moseley [52], Bullock and Dayton [53] have published comprehensive surveys on the most common additives to the positive paste and their influence on the performance of lead–acid batteries. Additives to the paste for positive plates can be classified in the following major groups.

7.2.1. Additives Accelerating the Formation of the Positive Plates

Positive plates need much more time to form than negatives. The reason for this is the dielectric behaviour of the cured positive paste. Oxidation of the bivalent lead compounds in the paste and formation of the PbO_2 positive active mass passes through a number of chemical reactions, some of which proceed at a low rate, which retards the technological process of formation of the positive plate. In an attempt to accelerate the formation process, additives to the positive paste have been looked for, which are characterised by electro-conductive properties and stability in sulfuric acid. These additives create an electro-conductive network in the paste and the process of oxidation proceeds simultaneously within a large paste volume, thus accelerating plate formation.

Three basic types of additives that shorten the time for formation of positive plates are currently used in the battery manufacturing practice. The effect of these additives can be summarised as follows:

- (a) Additives with electron conductivity. These are mostly fibres and powder particles which are in contact with each other or with the electro-conductive PbO_2 zone in the paste and thus conduct the current into the plate interior, thereby increasing the surface on which the reactions of formation proceed.
- (b) Additives which oxidize PbO to PbO_2 and thus create electro-conductive zones in the paste, again increasing the reaction surface for the formation processes.
- (c) Red lead (Pb_3O_4) is added as paste component. On soaking and formation of the plates, Pb_3O_4 reacts with H_2SO_4 producing PbO_2 and PbSO_4 . The PbO_2 formed contributes to the conductivity of the paste and thus accelerates the formation process.

7.2.1. Electro-Conductive Additives

Barium plumbate (BaPbO_3) [54–56]

This is a ceramic with the perovskite structure. Addition of 10 wt% BaPbO_3 creates a conductive network in the plate which facilitates the oxidation of PbO and 3BS to PbO_2 , and the formation process is significantly accelerated. During battery operation its charge acceptance increases. However, BaPbO_3 decomposes in diluted H_2SO_4 to BaSO_4 and PbO_2 . BaSO_4 loads higher than 0.3 wt% in PAM shorten battery cycle life. Hence, the amount of BaPbO_3 added to the positive paste should not exceed 1 wt%. At such loading levels, however, the beneficial effect of BaPbO_3 on the conductivity of the cured paste decreases.

Magneli phases of titanium oxide (Ti_4O_7) [57–59]

This oxide has conductivity similar to graphite. The overpotential of hydrogen and oxygen evolution on these oxides is high. Titanium oxides are stable in the potential region of the $\text{PbO}_2|\text{PbSO}_4$ electrode operation. Chemically they are stable in H_2SO_4 solution and have good adhesion to the PbO_2 particles of PAM. Introduced into the paste in the form of fibres, they enhance the formation of positive plates.

Analogous behaviour have also other conductive metal oxides such as $\text{WO}_{(3-x)}$, $\text{MoO}_{(3-x)}$ and $\text{V}_2\text{O}_{(5-x)}$ ($0 \leq x \leq 1$) [60–61]. Titanium nitride-coated porous silica powder has also been tested as additive to the positive paste enhancing its conductivity [62], but there are no data available about its effect on the performance parameters of the battery.

Tin dioxide (SnO_2) coated glass flakes and fibres [63–64]

The SnO_2 coating is 0.3 μm thick. This oxide is stable in the potential region of operation of the $\text{PbO}_2|\text{PbSO}_4$ electrode. Negligible amounts of SnO_2 from the coated glass flakes leach into the

battery electrolyte within a long period of battery operation at high temperature. This additive improves the efficiency of the formation process and the utilization of the positive active mass. The load of SnO_2 coated glass flakes in the positive paste is 2 wt%. Flakes of different length and weight are added.

Carbon, carbon fibres, isotropic graphite, graphite fibres [65–67]

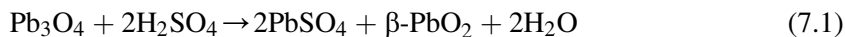
Addition of about 1.5 wt% of carbon fibres or graphite fibres to the paste significantly accelerates formation of the plates, but half of the carbon or graphite fibres are oxidized during this process. Consequently, the porosity of the positive active mass increases, which eventually leads to improvement of the utilization coefficient of PAM [66]. When the paste contains 0.1–0.5 wt% graphite fibre (3 mm long, 0.05 mm in diameter) produced from acrylonitrile, the formation process is enhanced substantially at lower energy input [65]. Carbon promotes the formation of $\alpha\text{-PbO}_2$ as greater amounts of PbO and 3BS are oxidized to PbO_2 during the first stage of formation, thus PbO and 3BS react with H_2SO_4 producing PbSO_4 [66]. During the second formation stage, the solution in the plates becomes acidic and $\beta\text{-PbO}_2$ is formed. Thus, carbon affects the $\alpha\text{-PbO}_2$: $\beta\text{-PbO}_2$ ratio in PAM [67]. On battery cycling, the remaining carbon (about 40% after formation) is further oxidized to CO_2 and soon disappears. As this process changes the porosity of PAM, the carbon content in the paste should not be too high (recommended load about 1 wt%) so that its oxidation would not impair the mechanical strength of the structure of PAM.

Conductive polymers [68–70]

Polyaniline, polypyrrole, polyparaphenylene and polyacetylene (doped with SO_4^{2-} , HSO_4^-), added to the positive paste as powders or fibres, enhance the formation process and increase the capacity of the cells. The amount of polymers added to the paste should be within the range 0.8–2.0 wt%. Higher polymer loads impair the mechanical stability of PAM and hence the life of the battery is shortened dramatically. Polymers disintegrate on overcharge. Polyaniline has proved to be most stable on battery overcharge.

Red lead (RL), Pb_3O_4 (25–100 wt% in the paste)

This lead compound reacts with H_2SO_4 forming PbSO_4 , $\beta\text{-PbO}_2$ and H_2O :



The extent to which this reaction proceeds depends on the ratio H_2SO_4 : (LO + RL) in the paste. The influence of this ratio was discussed in Chapter 6 of this book. Here, we will consider only the effect of red lead content in the paste on the composition of PAM.

- When the content of red lead in the paste is less than 30 wt%, the lead dioxide produced by the above reaction reacts with Pb in the leady oxide and the following reaction proceeds:



Depending on the amount of H_2SO_4 , the above reaction may progress further to formation of PbSO_4 . At the above loading levels, Pb_3O_4 does not affect the rate of the formation process.

- When more than 80 wt% Pb_3O_4 vs. the total paste amount is used for paste preparation, the formed PAM contains mostly $\beta\text{-PbO}_2$. Such a structure of PAM is rather brittle and easily disintegrates, which shortens the life of the battery substantially. Therefore, the use of high percent loads of Pb_3O_4 in the paste is acceptable only for tubular positive plates, where PAM is enclosed in tubes.
- The optimum content of red lead in the paste is about 2/3 of the total paste amount. In this case, some $\beta\text{-PbO}_2$ remains unreacted in the paste, which enhances the formation process. The formed PAM also contains certain amount of $\alpha\text{-PbO}_2$ phase, which sustains the stability of the PAM structure on cycling.

Ozone (O_3) treatment of the plates [71,72]

Cured positive plates are treated with ozone gas in a chamber, as a result of which PbO is oxidized to PbO_2 , which forms a thin coating on the surface of unformed plates. During formation, the lead dioxide layers on the two plate surfaces grow simultaneously towards the plate's interior. Consequently, the formation time and the energy input are reduced substantially. However, this method is too expensive and requires special corrosion-resistant chambers.

7.2.2. Additives Improving the Capacity, Energy, Power Output and Cycle Life of the Battery, When These Performance Characteristics are Limited by the Positive Plates

When the positive plates limit the performance of a lead—acid cell (battery), the above characteristics depend on the processes that take place:

- at the interface grid/corrosion layer/active mass (i.e. on the transfer of electrons from the grid to PAM) or
- within PAM itself (i.e. on the diffusion of ions within PAM, the electro-conductivity of PAM, the kinetics of electron transfer, etc.)
- in the grid (i.e. on the electro-conductivity of the grid, which at the end of battery life depends on its non-corroded part).

In order to understand the mechanism of action of additives to the positive plates and their influence on the performance parameters, it is necessary to identify the elementary processes which are affected by these additives.

The elementary process limiting the rate of discharge at a given site in the plate depends on plate and battery design, and on the discharge current density. At a site located deep in the

cross-section of a thick plate, the diffusion of ion flows along the pores into the plate interior is the elementary process that limits plate performance. Conversely, if a given site is located in the surface plate layers, the transfer of electrons from the current collector (grid) to this site may become the limiting elementary process for the discharge rate and the capacity of the plate. This dependence of the elementary process limiting the discharge rate on the distance from the current collector is more pronounced at higher discharge currents. This affects the overall utilization of the positive active mass. The stronger this dependence is, the lower the utilization of PAM and hence the lower the energy output of the cell. In an attempt to reduce the role of this dependence, additives to PAM have been looked for which would increase its electro-conductivity and other additives to facilitate and enhance the movement of ion flows through the plate pores. The third type of elementary processes limiting cell performance are those related to the transfer of electric charges through the surface of PAM. The kinetic difficulties of these processes may reduce the capacity and power output of the cells.

Moseley has made a survey of all investigated additives improving the conductivity of PAM and has summarised them in Table 7.4 [52].

Most of these materials were described as additives to the paste enhancing the formation process. It has been established that these compounds are most efficient when added in the form of fibres which form a conductive network that provides electric connection of every point across the PAM volume with the current collector [79].

The influence of Ti_4O_7 , as well as of two types of SnO_2 coated flakes on the specific capacity, specific energy and utilization of PAM has been studied for plates with 2 wt% of the above materials added to the paste with 3.9 g cm^{-3} density [63]. Table 7.5 summarises the obtained battery test results and the calculated specific capacity, specific energy and PAM utilization values [63]. The data in the table evidence that the plates with addition of Ti_4O_7 or SnO_2 -coated flakes (1/64 in) have higher specific capacity, specific energy and PAM utilization than the

Table 7.4: Materials proposed to enhance the conductivity of the positive active mass [52].

Material	Loading wt%	Conductivity at $300^\circ \text{K S m}^{-1}$ ^a	Density (g cm^{-3})	References
BaPbO ₃	~1	2×10^3	8.5	[54,73]
Ti ₄ O ₇	1–2	10^3	4.2	[74]
Ti ₅ O ₉	1–2	$\sim 10^2$	4.2	[75]
SnO ₂ (F)	2		6.9	[51]
SnO ₂ (Sb)	1–2	10^2 – 10^4	6.9	[76]
Graphite	0.5	10^5	2.2	[77]

Other transition metal oxides and a variety of forms of tin dioxide have been proposed in patents as reviewed in [51].

^aFor comparison the specific electrical resistance (in Ohms per meter) of α - and β -PbO₂ is 10^{-5} and $4 \times 10^{-5} \Omega \text{ m}$, respectively [78].

Table 7.5: Specific capacities, specific energies and positive active-material utilizations for cells with and without 2 wt% loadings of conductive additives [63,51].

Additive	Specific Capacity, Ah kg^{-1} (2 V cell)		Specific Energy, Wh kg^{-1} (12 V battery)		Positive Mass Utilization (%)	
	Reserve capacity	$C_5/5$	Reserve capacity	$C_5/5$	Reserve capacity	$C_5/5$
Untreated	89.8	110.0	24.9	32.4	38	48
SnO_2 -coated flakes, 1/64 in	90.8	124.9	25.6	35.5	39	55
SnO_2 -coated flakes, 1/8 in	83.8	119.2	24.3	34.9	36	52
Powdered Ti_4O_7	105.1	125.8	33.3	38.6	46	55

plates with no additive. During discharge, the positive plates with Ti_4O_7 have higher discharge voltage than the plates without additives.

Appel and Edward [80] have proposed a model for the correlation between positive plate capacity and the ratio between conductive and non-conductive particles in PAM during discharge at different rates. The model combines Fick's law of diffusion with 'critical volume fraction', which gives the proportion of the conductive and non-conductive material at which PAM becomes non-conductive. Plates containing conductive particles have higher utilization of PAM than the plates with non-conductive particles at all discharge rates. However, the difference between the utilization of the positive active masses of the two types of plates decreases with increase in the discharge current. This indicates that at higher discharge currents, another elementary process limits the capacity of the plates (cells). At higher discharge rates, the utilization of PAM is limited by the diffusion of the ionic flows in the PAM pores rather than by the electric conductivity of PAM. Hence, selection of the type and amount of additives to the positive paste should be made in view of the discharge rate. Batteries operating at low discharge currents should have positive plates containing additives that improve the electric conductivity of PAM, whereas batteries for high rate discharge duties should contain additives that facilitate the diffusion of ionic flows in the pores of PAM.

A brief overview of the additives enhancing the capacity, energy and power performance of lead–acid batteries will be presented below.

- (a) *Polyolefin (ES-100)* [81–83]. The average size of its particles is 150 μm . They are elongated in shape and porous in structure. Polyolefin is added to the paste in amounts between 1.5 and 2 wt% versus the leady oxide used. The additive increases the porosity of PAM and hence the power output of the battery. Addition of ES-100 improves the initial capacity by 15% on discharge with low currents and much more significantly at high discharge rates. Flooded batteries maintain this higher capacity throughout their service life, which is a bit longer than that of batteries with no additive. VRLA (AGM) batteries, too, have improved performance when 2 wt% of polyolefin (ES-100) vs. the

leady oxide is added. A 17% increase in capacity is registered with these batteries when discharged with low currents and 47%, on high rate discharge. Similar effects have also been observed with VRLAB (gel type) [83].

- (b) *Pore-forming additives: Carboxymethyl cellulose (CMC), silica, carbon black, Dynel flock* [84,85]. The effect of these additives, at loading levels from 0.2 to 2.0 wt% vs. the leady oxide, has been investigated. They facilitate the oxidation of Pb to PbO on plate curing. During formation, almost half of the added carbon black is oxidized thus opening large pores, whereas CMC forms small pores in PAM. The initial capacity of the battery increases by 5% on discharge with low currents or by 10% on high rate discharge. Within the potential region of operation of the $\text{PbO}_2|\text{PbSO}_4$ electrode, both CMC and carbon black are unstable. They are oxidized thus reducing the mechanical stability of the positive active mass, which eventually shortens the life of the battery. Batteries with CMC or carbon black in PAM have shorter cycle life than batteries without these additives.

Silica (0.2 wt%) is a porous material, which provides local reservoir of H_2SO_4 solution; thus improving the capacity of the plates on discharge without affecting their cycle life performance. Synthetic fibres 'Dynel flock' improve the mechanical stability of the cured paste, respectively of PAM. There are literature data available evidencing that they improve the cycle life of the battery, both at high and low discharge rates. Battery manufacturers, however, dispute the latter effects. The influence of anisotropic graphite on the performance of flooded and valve-regulated batteries has been studied [86,87]. The utilization of PAM in the current generation process increases on discharge with currents between 0.2 C and 1 C A. An interesting finding is that plates with the above additive have uniform distribution of PbSO_4 throughout the volume of PAM, unlike the plates with no additive, where PbSO_4 is deposited mostly in the surface plate layers. Addition of graphite increases the mean pore diameter to 2 μm . The increase in utilization of the active material is proportional to the increase in PAM porosity. At the potentials of operation of the $\text{PbO}_2|\text{PbSO}_4$ electrode, sulfate ions (HSO_4^-) intercalate into the graphite grains and increase the inter-layer distance from 1.5 to 2 times, thus accelerating the disintegration of the graphite lattice. Addition of 0.5 wt% graphite does not affect the cycle life of the cells, but the capacity of the plates is higher by 10% as compared to the plates with no graphite. VRLA batteries with PbCaSn grids and graphite additive have 5 to 10% higher capacity when discharged with 0.2 C A than the batteries without graphite [86] high rate discharge ($I = 5 \text{ C A}$), graphite additions (1 wt%) increase the capacity by more than 10%. During battery service life, graphites are oxidized to CO_2 gas and consequently their effect gradually diminishes, whereby the connection between PAM particles weakens and the positive mass becomes brittle. Baker et al. [88] assume that the enhanced transport of ions in the porous PbO_2 mass containing graphite is due to an electro-osmotic pumping effect. Electro-osmosis is the movement of a flow of ions or liquid along thin capillaries under the action of the potential between the capillary walls. HSO_4^- ions intercalate between the graphite crystal

layers and charge the particle's surface. Under the action of this potential a flow of H_2SO_4 solution moves along the pores of PAM. The rate of this flow is inversely proportional to the concentration of the H_2SO_4 solution. During discharge, H_2SO_4 is gradually consumed. Its concentration in the PAM pores decreases, which leads to increase of the rate of acid flow in the pores. Forced by the potential of the pore walls, an electro-osmotic flow starts moving in the pores together with the diffusion H_2SO_4 flow initiated by the concentration gradient. These driving forces assist the access of H_2SO_4 to the interior of the positive plates and thus improve their capacity. However, graphite disintegrates with time and the electro-osmotic pumping effect weakens.

Polymer additives of the *benzene sulfonate groups* have been searched which are stable in H_2SO_4 environment and also have electro-osmotic action. A fairly large number of polymer materials with electro-osmotic effect have been proposed in the patent literature [51].

- (c) *Binders* [89,90]. These additives improve the cycle life of the positive plates. During discharge, a certain amount of the PbO_2 particles in PAM are reduced, as a result of which the connections between the other PbO_2 particles near the reduction site change. Under the action of surface forces some processes of re-structuring of the particles in agglomerates start. It has been established that Sb, Bi and As ions exert an influence on these processes, facilitating the re-structuring of the PbO_2 particles in agglomerates. This effect of binders has been studied on cycling of tubular electrodes filled with PbO_2 powder with additions of salts of the above three elements. The capacity of the electrodes under test increases with increasing the number of cycles, the fastest increase being registered in the presence of Sb_2O_5 or Bi^{3+} ions. Batteries with 0.05 wt% Bi^{3+} in PAM have 18% longer cycle life than the batteries with no bismuth [91,92].
- (d) *Calcium sulfate (CaSO_4)* [93,94]. Added in the paste mix in amounts from 0.25 to 2.0 wt%, CaSO_4 improves the cold-cranking ability of SLI batteries. Moreover, it has been established through cycling tubular electrodes filled with PbO_2 powder, that calcium sulfate (0.8 wt%) acts as binder and improves the life of the positive plates on cycling.
- (e) *Fillers and nanotubes* [95]. These additives are characterised by high specific surface, chemical stability and adsorption ability. They are adsorbed onto the growing PAM crystals and change their morphology. Introduced in the paste, they modify the shape of its particles, too. Positive plates produced with pastes containing such additives have higher capacity and longer cycle life.

7.2.3. Additives to the Positive Pastes which Retard Sulfation of the Active Mass

The lead–acid battery may operate from full or partial state of charge, depending on the specific duty. On partial-state-of-charge cycling, a certain amount of small PbSO_4 crystals

remain in PAM not converted into active material. Part of these small crystals recrystallize into larger sulfate crystals (hard PbSO_4). The latter crystals have small surface and low solubility. Consequently, the plates get sulfated slowly. Additives have been searched that would retard or suppress the recrystallization process at the two electrodes and thus slow down battery sulfation. Two of these additives will be discussed below.

Phosphoric acid (H_3PO_4) and lead phosphate salts [96–103]

H_3PO_4 is introduced into the paste in amounts from 10 to 40 g per 1 kg of leady oxide [96]. Lead phosphates are formed which are more stable than basic lead sulfates [100]. These phosphates in the positive paste change the structure and reactivity of the formed lead dioxide active mass as well as of the grid corrosion layer. Consequently, the initial capacity of the plates is reduced by 13–18%. However, the discharge voltage of lead–acid cells with phosphate additives increases by 15–25 mV. Besides, the adhesion of PAM to the grids is much stronger when it contains phosphates. The contact between the particles and agglomerates in PAM is improved and hence PAM shedding is reduced. All these effects prolong the cycle life of the battery when it is limited by the positive plates.

Phosphoric acid (H_3PO_4) creates a second chemical system parallel to the lead–acid one [53,96]. Phosphate ions react with lead dioxide and their concentration in the electrolyte is low when the battery is fully charged. During discharge, the amount of lead dioxide that absorbs phosphate ions decreases and the concentration of H_3PO_4 in the solution increases. The reverse processes occur during re-charge. The incorporated phosphate ions retard the process of reduction of PbO_2 to PbSO_4 [100]. The type of phosphate ions in the solution depends on the H_2SO_4 concentration and more precisely on the concentration of H^+ ions. H_3PO_4 dissociates in three degrees: H_2PO_4^- , HPO_4^{2-} and PO_4^{3-} . In a charged battery, the H_2SO_4 concentration is high and H_3PO_4 undergoes weak dissociation. On battery discharge, the acid concentration decreases and the dissociation of H_3PO_4 increases. This change in solution composition affects the morphology and properties of the PbO_2 and PbSO_4 crystals formed, which, in turn, retards significantly the sulfation of the plates in partial state of charge and on open circuit state of a discharged battery. The presence of H_3PO_4 promotes the formation of small PbSO_4 crystals and slows down the recrystallization process. Self-discharge of the battery is also retarded. The rate of corrosion of the positive grids is reduced, too. However, mossing may occur. The positive plate lugs and the strap that connects them corrode and phosphate ions are incorporated in the PbO_2 particles altering their morphology. As these parts of the cell are more or less isolated from the solution, lead oxides with high phosphate content accumulate, which form a mossy layer. Flakes from this layer may peel off and fall onto the active block thus creating short circuits. The cycle life of the battery is shortened. In the battery design process measures should be taken to prevent the above phenomenon by covering the plates (or the whole active block) with separator.

Sodium sulfate (Na_2SO_4) [104,105]

When the battery is partially charged or fully discharged the concentration of H_2SO_4 is low. As evident from Fig. 3.13 in Chapter 3, lead sulfate is highly soluble, which accelerates the process of its recrystallization through dissolution of the small crystals and growth of larger PbSO_4 crystals. Consequently, a layer of 'hard lead sulfate' accumulates causing sulfation of the plates. Through the introduction of sodium sulfate (up to 2 wt%) in the paste for positive plates, or in the electrolyte, the solubility of PbSO_4 is significantly reduced at all acid concentrations, due to the common ions SO_4^{2-} and HSO_4^- in the two sulfates. Hence, the recrystallization process is retarded and so is the sulfation of the plates. Na_2SO_4 may be added to the electrolyte (see Chapter 3) or to the positive paste. The effect of Na_2SO_4 is enhanced in VRLA batteries, where the electrolyte volume is smaller than that in flooded batteries and at the end of discharge the concentration of the H_2SO_4 solution decreases to values at which the solubility of PbSO_4 is high.

When sodium sulfate is added to the paste in amounts up to 0.05 wt% of the leady oxide, it dissolves during formation and opens larger pores, thus facilitating the transport of sulphuric acid and eventually increasing the utilization of PAM. The increased porosity of PAM ensures higher capacity by some 4–8%. This high capacity is further sustained during cycling of the cells. It has been established, however, that Na_2SO_4 is more effective when introduced in the electrolyte.

References

- [1] M.P.J. Brennan, N.A. Hampson, J. Electroanal. Chem. 48 (1973) 465.
- [2] E.G. Yampol'skaya, B.N. Kabanov, Sov. J. Appl. Chem. 37 (1964) 2530.
- [3] E.G. Yampol'skaya, M.I. Ershova, V.V. Surikov, I.I. Astahov, B.N. Kabanov, Elektrokhim. 8 (1972) 1209.
- [4] E.G. Yampol'skaya, A.I. Smirnova, M.I. Ershova, S.A. Sapoonitskii, L.I. Kryukova, Elektrokhim. 8 (1972) 1289.
- [5] T.F. Sharpe, J. Electrochem. Soc. 116 (1969) 1639.
- [6] T.F. Sharpe, Electrochim. Acta 14 (1969) 635.
- [7] G. Archdale, J.A. Harrison, J. Electroanal. Chem. 47 (1973) 93.
- [8] A. Le Mehaute, J. Appl. Electrochem. 6 (1976) 543.
- [9] E.M. Strochkova, K.V. Rybalka, Elektrokhim. 13 (1977) 62.
- [10] E.G. Yampol'skaya, M.I. Ershova, I.I. Astahov, B.N. Kabanov, Elektrokhim. 2 (1966) 1327.
- [11] B.K. Mahato, J. Electrochem. Soc. 127 (1980) 1679.
- [12] J.R. Pierson, P. Gurlusky, A.C. Simon, S.M. Caulder, J. Electrochem. Soc. 117 (1970) 1463.
- [13] A.C. Simon, S.M. Caulder, P.J. Gurlusky, J.R. Pierson, J. Electrochem. Soc. 121 (1974) 463.
- [14] D. Pavlov, in: B.D. McNicol, D.A.J. Rand (Eds.), Power sources for electric vehicles, Elsevier, Amsterdam, 1984, p. 135.
- [15] D. Platicanov, N. Rangelova, Comp. R. Acad. Bulg. Sci. 21 (1969) 91.
- [16] D. von Borstel, G. Hoogenstraat, W. Ziechmann, J. Power Sources 50 (1994) 131.
- [17] E.J. Ritchie, J. Electrochem. Soc. 100 (1953) 53.
- [18] A. Hayeshi, Y. Namura, Tappi 21 (1967) 393.
- [19] A.C. Zachlin, J. Electrochem. Soc. 98 (1951) 325.
- [20] B.O. Myrvold, D. Pavlov, J. Power Sources 85 (2000) 92.

- [21] D. Pavlov, B.O. Myrvold, T. Rogachev, M. Matrakova, *J. Power Sources* 85 (2000) 79.
- [22] M. Matrakova, T. Rogachev, D. Pavlov, B.O. Myrvold, *J. Power Sources* 113 (2003) 345.
- [23] J. Burbank, A.C. Simon, E. Willihnganz, in: P. Delahay, C.W. Tobias (Eds.), *Advances electrochem engineering*, Vol. 8, Wiley Interscience, New York, 1971, p. 229.
- [24] Specification of Test Procedures for Electric Vehicle Traction Batteries, EUCAR, December 1996.
- [25] D. Pavlov, S. Gancheva, P. Andreev, *J. Power Sources* 46 (1993) 349.
- [26] G. Papazov, D. Pavlov, B. Monahov, *J. Power Sources* 113 (2003) 335.
- [27] K. Nakamura, M. Shiomi, K. Takahashi, M. Tsubota, *J. Power Sources* 59 (1996) 153.
- [28] M. Shiomi, T. Funato, K. Nakamura, K. Takahashi, M. Tsubota, *J. Power Sources* 64 (1997) 147.
- [29] P.T. Moseley, R.F. Nelson, A.F. Hollenkamp, *J. Power Sources* 157 (2006) 3.
- [30] A.F. Hollenkamp, W.G.A. Balasing, S. Lau, O.V. Lim, R.H. Newnham, D.A.J. Rand, et al., ALABC project N1.2, final report 2002, Advanced Lead-Acid Battery Consortium, Research Triangle Park, NC, USA, 2002.
- [31] P.T. Moseley, *J. Power Sources* 191 (2009) 134.
- [32] L.T. Lam, C.G. Phylant, D.A.J. Rand, D.G. Vella, L.H. Vu, ALABC project N3.1, final report 2002, Advanced Lead-Acid Battery Consortium, Research Triangle Park, NC, USA, 2002.
- [33] M. Fernandez, J. Valenciano, F. Trinidad, N. Munos, *J. Power Sources* 195 (2010) 4458.
- [34] D.P. Boden, D.V. Loosemore, M.A. Spense, T.D. Wojcinski, *J. Power Sources* 195 (2010) 4470.
- [35] D. Pavlov, P. Nikolov, T. Rogachev, *J. Power Sources* 196 (2011) 5155.
- [36] D. Pavlov, T. Rogachev, P. Nikolov, G. Petkova, *J. Power Sources* 191 (2009) 58.
- [37] D. Pavlov, P. Nikolov, T. Rogachev, *J. Power Sources* 195 (2010) 4444.
- [38] Y.B. Kasparov, E.G. Yampolskaya, B.N. Kabanov, *Zh. Prikl. Khimii (J. Appl. Chem.)* 37 (1964) 1936 (in Russian).
- [39] D.P. Boden, *J. Power Sources* 73 (1998) 89.
- [40] Ruevski S, Pavlov D. in: Ext. Abstr. LABAT'96 International Conference, Varna, Bulgaria, 1996, p. 46.
- [41] D. Pavlov, P. Nikolov, T. Rogachev, *J. Power Sources* 195 (2010) 4435.
- [42] Y. Kamenev, N. Chunts, N. Yakovleva, V. Nikitin, A. Kiselevich, E. Ostapenko, *J. Power Sources* 114 (2003) 303.
- [43] M. Maja, N. Penazzi, G. Clerici, in: Proc. 16th Intl. Power Sources Symp., Bournemouth, UK, 1988, p. 8.
- [44] M. Saakes, P.J. van Duin, A.C.P. Ligtoet, D. Schmall, *J. Power Sources* 47 (1994) 149.
- [45] W. Bohnstedt, M. Radwan, H. Dietz, J. Garche, K. Wiesener, *J. Power Sources* 19 (1987) 301.
- [46] H. Doring, M. Radwan, H. Dietz, J. Garche, K. Wiesener, *J. Power Sources* 28 (1989) 381.
- [47] S. Gust, E. Hameenoja, J. Ahl, T. Laitinen, A. Savonen, G. Sundholm, *J. Power Sources* 30 (1990) 185.
- [48] H. Dietz, G. Hoogestraat, S. Laiback, D. von Borstel, K. Wiesener, *J. Power Sources* 53 (1995) 359.
- [49] E.V. Parshikova, I.A. Aguf, M.A. Dasoyan, M.L. Ratner, *Sov. Elektrotehnika* 11 (1964).
- [50] E.V. Parshikova, I.A. Aguf, M.A. Dasoyan, *Sov. Elektrotehnika* 10 (1964).
- [51] K. McGregor, *J. Power Sources* 59 (1996) 31.
- [52] P.T. Moseley, *J. Power Sources* 64 (1997) 47.
- [53] K.R. Bullock, T.C. Dayton, in: D.A.J. Rand, P.T. Moseley, J. Garche, C.D. Parker (Eds.), *Valve-regulated lead-acid batteries*, Elsevier, 2004, p. 109.
- [54] W.H. Kao, K.R. Bullock, *J. Electrochem. Soc.* 139 (1992) L41.
- [55] N.K. Bullock, W.H. Kao, US Patent No. 5 045 170, 1991.
- [56] W.H. Kao, N.K. Bullock, R.A. Peterson, US Patent No. 5 302 476, 1994.
- [57] K.R. Bullock, *J. Power Sources* 51 (1994) 1.
- [58] N.E. Bagshaw, R.L. Clarke, K. Kendall, Ext. Abstr. Fall Meeting Electrochem. Society, Seattle, USA, 1990, Vol. 90-2, p. 2.
- [59] P.C.S. Hayfield, U.S. Patent No. 4 422 917, 1981.
- [60] B. Reichman, I.L. Strebe, WO Patent No. 91 06 985, 1991.
- [61] B.T. Tekkana, A.A. Kovacich, US Patent No. 5 106 709, 1992.
- [62] T. Inoe, Jap. Patent No. 0 322 355, 1991.
- [63] L.T. Lam, O. Lim, H. Ozgun, D.A.J. Rand, *J. Power Sources* 48 (1994) 83.

- [64] G.L. Wei, J.R. Wang, *J. Power Sources* 52 (1994) 81.
- [65] J.L. Weininger, C.R. Morlock, *J. Electrochem. Soc.* 122 (1975) 1161.
- [66] E. Hojo, J. Yamashita, K. Kishimoto, N. Nakashima, Y. Kasai, *Yuasa-Jiho* 72 (1992) 23 (in Japanese).
- [67] A. Tokunaga, M. Tsubota, K. Yonezu, *Proc. Fall Meeting of the Electrochemical Society, Honolulu, USA, 1987, Vol. 87-2, Abs. 129, p. 187.*
- [68] M. Matsumoto, S. Ito, *Jap. Patent No. 61/455 565 A2, 1986.*
- [69] P. Mirebean, G. Chedeville, E. Genies, *French Patent No. 2 553 581, 1985.*
- [70] P. Mirebean, *French Patent No. 2 519 191, 1983.*
- [71] B. Mahato, W. Delany, *US Patent No. 4 656 706, 1987.*
- [72] K.R. Bullock, B.K. Mahato, W.J. Wruck, *J. Electrochem. Soc.* 138 (1991) 3545.
- [73] W.H. Kao, S.L. Haberichter, P. Patel, *J. Electrochem. Soc.* 141 (1994) 3300.
- [74] K. Nagasawa, Y. Kato, Y. Bando, T. Takada, *J. Phys. Soc. Japan* 29 (1970) 241.
- [75] M. Marezio, D. Tranqui, S. Lakkis, C. Schlenker, *Phys. Rev. B* 16 (1977) 2811.
- [76] K. Uesmatsu, N. Mitzutami, M. Kato, *J. Mat. Sci.* 22 (1987) 915.
- [77] S. Wang, B. Xia, G. Yin, P. Shi, *J. Power Sources* 55 (1995) 47.
- [78] H. Bode, *Lead-acid batteries*, translated, in: R.J. Brodd, K.V. Kordesch (Eds.), Wiley, New York, 1977, p. 13.
- [79] H. Metzendorf, *J. Power Sources* 7 (1982) 281.
- [80] P.W. Appel, D.B. Edwards, *J. Power Sources* 55 (1995) 81.
- [81] J.A. Wertz, T.J. Clough, *Proc. 13th Annual battery conference on applications and advances, Long Beach, CA, USA, 1998, p. 311.*
- [82] J.A. Wertz, T.J. Clough, *Proc. 14th Annual battery conference on applications and advances, Long Beach, CA, USA, 1999, p. 189.*
- [83] J.A. Wertz, T.J. Clough, *Proc. 15th Annual battery conference on applications and advances, Long Beach, CA, USA, 2000, p. 77.*
- [84] H. Dietz, J. Garche, K. Wiesener, *J. Power Sources* 14 (1985) 305.
- [85] H. Dietz, J. Garche, K. Wienseer, *J. Appl. Electrochem.* 17 (1987) 473.
- [86] A. Tokunaga, M. Tsubota, K. Yonezu, K. Ando, *J. Electrochem. Soc.* 134 (1987) 525.
- [87] A. Tokunaga, M. Tsubota, K. Yonezu, *J. Electrochem. Soc.* 136 (1989) 33.
- [88] S.V. Baker, P.T. Moseley, A.D. Turner, *J. Power Sources* 27 (1989) 127.
- [89] D. Pavlov, A. Dakhouche, T. Rogachev, *J. Power Sources* 30 (1990) 117.
- [90] D. Pavlov, *J. Power Sources* 33 (1991) 221.
- [91] L.T. Lam, N.P. Haigh, D.A.J. Rand, *J. Power Sources* 88 (2000) 11.
- [92] L.T. Lam, H. Ceylan, N.P. Haigh, J.E. Manders, *J. Power Sources* 107 (2002) 155.
- [93] C.S. Ramanathan, *J. Power Sources* 35 (1991) 83.
- [94] T. Rogachev, D. Pavlov, *J. Power Sources* 64 (1997) 51.
- [95] Y. Kamenev, N.I. Chunz, A.V. Kiselevich, B.N. Leonov, *Elektrokhimicheskaya energetika* 7 (2007) 188 (in Russian).
- [96] E. Voss, *J. Power Sources* 24 (1988) 171.
- [97] E. Meissner, *J. Power Sources* 67 (1997) 135.
- [98] K.R. Bullock, D.H. McClelland, *J. Electrochem. Soc.* 124 (1977) 1478.
- [99] K.R. Bullock, *J. Electrochem. Soc.* 126 (1979) 360.
- [100] K.R. Bullock, *J. Electrochem. Soc.* 126 (1979) 1848.
- [101] J.P. Carr, N.A. Hampson, *J. Electroanal. Chem.* 28 (1970) 65.
- [102] S. Tudor, A. Weisstuch, S.H. Davang, *Electrochem. Technol.* 3 (1965) 90.
- [103] S. Tudor, A. Weisstuch, S.H. Davang, *Electrochem. Technol.* 5 (1967) 21.
- [104] G.W. Mao, A. Sabatino, *US Patent No. 3 988 165, 1976.*
- [105] J.S. Chen, *J. Power Sources* 90 (2000) 125.

This page intentionally left blank

Curing of Battery Plates

8.1. Introduction

The process of plate curing has been investigated both for practical purposes, with the aim to improve the performance parameters of battery plates, and for purely fundamental purposes, namely to disclose the mechanism of the elementary processes involved [1–15]. Based on the results of these investigations the essence of the curing process can be summarised as follows.

During the process of curing, paste particles are interconnected to form an uninterrupted strong porous mass (skeleton) which, in its turn, is tightly bound to the grid (Fig. 8.1).

The following basic processes take place during plate curing:

- (i) The skeleton (hard porous mass) of the cured paste is built. Small crystals in the paste dissolve and big ones grow in size. Water contained in the thin liquid films between the particles evaporates as a result of which 3BS or 4BS crystals and PbO particles interconnect into a strong skeleton.

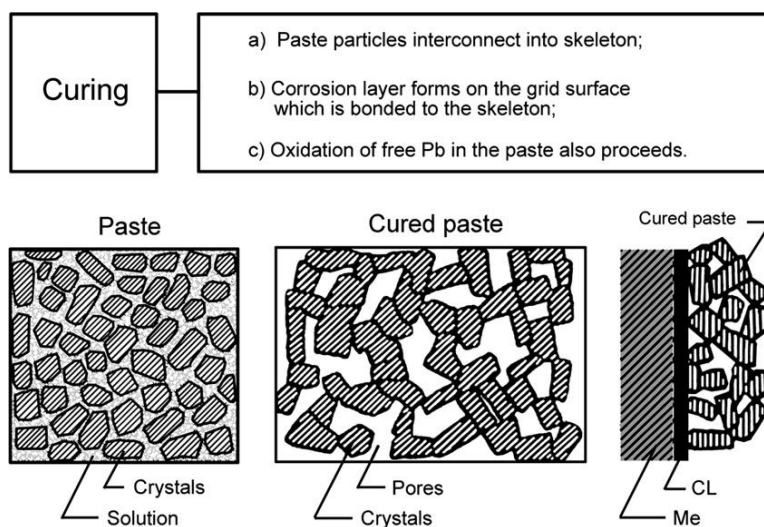


Figure 8.1:
Basic processes during plate curing.

- (ii) When curing is conducted at temperatures higher than 80 °C, 3BS paste is converted into 4BS cured paste.
- (iii) Residual free lead in the paste is oxidized. This is the lead in the leady oxide that has remained unoxidized during the process of paste preparation.
- (iv) The grid alloy is oxidized and a corrosion layer (CL) forms on the grid surface, which is tightly bound to the cured paste.

The plate curing processes are influenced by two types of parameters:

- Internal, i.e. paste characteristics: phase composition, density and moisture content of the paste.
- External, i.e. characteristics of the surrounding medium: air temperature, relative humidity (RH) and air flow rate; the processes of plate curing are atmosphere dependent.

The above parameters determine the water content (moisture) of the paste. The latter, in turn, determines the rates of the basic curing processes as described above. Depending on the amount of water contained in the paste (moisture), the curing process can be divided into two stages: (a) curing at over 5% moisture content of the paste and (b) drying at less than 5% moisture content. Formation of positive plates proceeds through metasomatic processes. The matrix of the cured paste is preserved to some extent and it builds the structure of the lead dioxide active mass. Hence, the processes that take place during preparation of positive pastes and during positive plate curing exert a strong influence on battery performance. During formation of negative plates, a new structure of the negative active mass is formed, which is the reason why the curing of the negative plates has a weaker effect on battery performance characteristics.

8.2. Fundamentals

8.2.1. Formation of a Hard Porous Mass (skeleton) in the Cured Paste

Changes in phase composition and crystallinity of the paste on curing

During the technological procedure of plate curing, some processes of recrystallization proceed whereby small particles (most often amorphous) dissolve and big crystals grow in size according to Ostwald–Freundlich equation. For this to happen, the moisture content of the paste should be between 6 and 11%. To keep up the moisture content during the curing process, the RH of the air in the curing chamber should be maintained at a level of 100%. Changes in crystal phases in the paste are examined through X-ray diffraction analysis.

The X-ray diffraction patterns for a 3BS paste before and after curing (40 °C, 100% RH, 48 h) are presented in Fig. 8.2a [16].

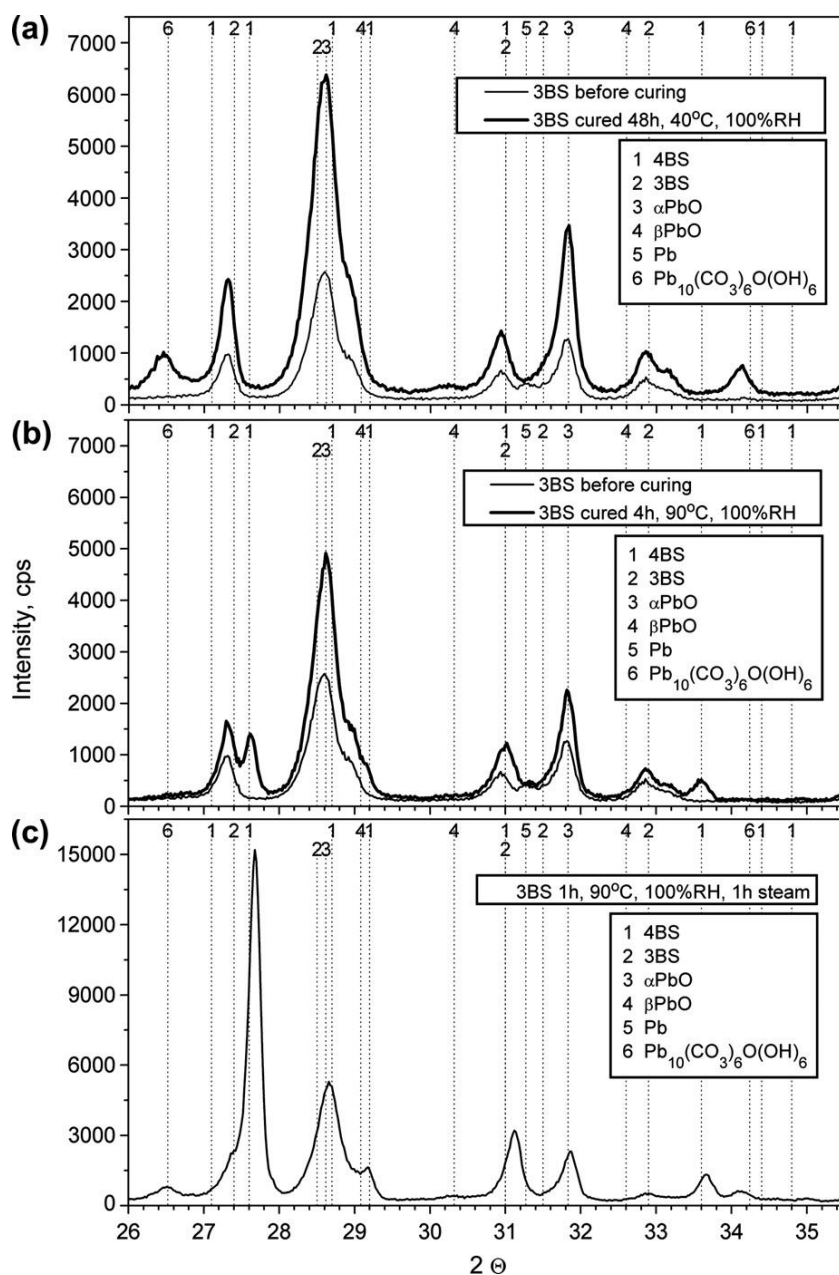


Figure 8.2:

Changes in phase composition of 3BS pastes on curing at (a) 40 °C for 48 h, (b) 90 °C for 4 h and (c) 90 °C for 1 h, followed by 1 h of steam treatment [16].

As a result of curing, the area of the characteristic peak for 3BS ($2\theta = 27.18^\circ$) increases 2.43 times against a 2.44-fold increase of that of the αPbO peak ($2\theta = 31.90^\circ$). These findings indicate an increased crystallinity of the 3BS and αPbO phases during plate curing. The X-ray diffractogram in Fig. 8.2a evidences the presence of plumbonacrite, $\text{Pb}_9(\text{CO}_3)_6(\text{OH})_6$. The latter is formed as a result of interaction between $\text{Pb}(\text{OH})_2$ from the paste and CO_2 from the air during the curing process.

Figure 8.2b shows the X-ray diffraction patterns for 3BS pastes cured at 90°C and 98% RH for 4 h. Under these conditions, 3BS is converted into 4BS but only partially. The ratio between the crystal phases formed is $3\text{BS}/4\text{BS} = 0.83$.

Figure 8.2c presents the X-ray diffraction patterns for the paste cured at 90°C for 1 h and then steam treated for another hour. This paste contains a well pronounced 4BS crystal phase. Hence, introduction of steam into the curing chamber facilitates the conversion of 3BS particles into 4BS ones. With this technology, a small quantity of $\text{Pb}_9(\text{CO}_3)_6(\text{OH})_6$ is also formed in the paste.

Figure 8.3 presents X-ray diffraction patterns for 4BS pastes before and after curing at 90°C for 4 h [16].

An increase by about 1.38 times is observed in the intensities of the 4BS characteristic diffraction lines on curing. This cannot be a result of formation of new quantities of 4BS crystals as no H_2SO_4 is introduced into the paste during the curing process. The observed changes in intensity result from the changed proportion between crystal and amorphous

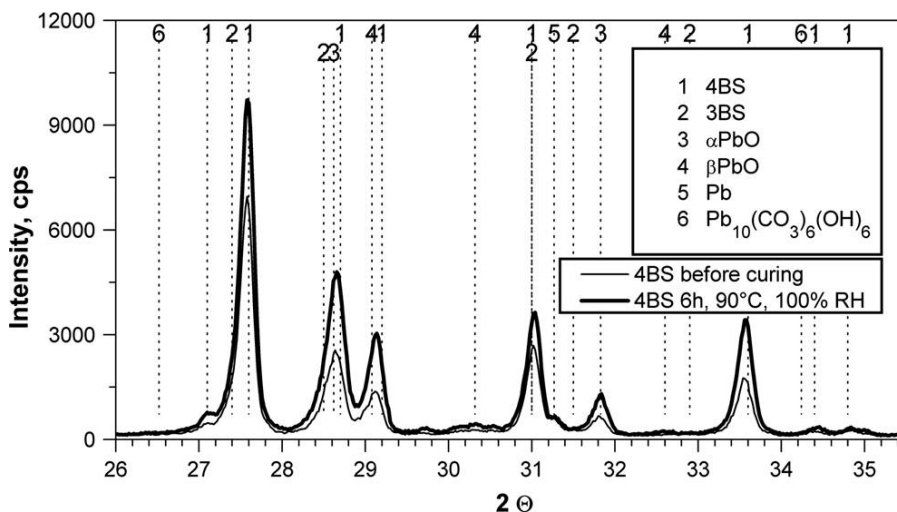


Figure 8.3:

X-ray diffraction patterns for 4BS pastes before and after curing at 90°C for 4 h [16].

parts (zones) in the 4BS particles. It has been established that 4BS particles comprise crystal and amorphous zones [17]. The intensity of the characteristic diffraction line for tet-PbO is 1.83 times higher after curing than before curing, which is partially due to the oxidation of Pb.

Phase composition of the cured paste as a function of H_2SO_4/LO ratio used for paste preparation

The correlation between phase composition of cured pastes and initial H_2SO_4/LO ratio is presented in Fig. 8.4 for curing at 30 °C and 80 °C [5].

The amount of crystal 3BS phase increases slightly due to crystallization of its amorphous zones. In pastes prepared at 80 °C with $H_2SO_4/LO > 8\%$ by weight, small amounts of $PbO \cdot PbSO_4$ are transformed into $3PbO \cdot PbSO_4 \cdot H_2O$.

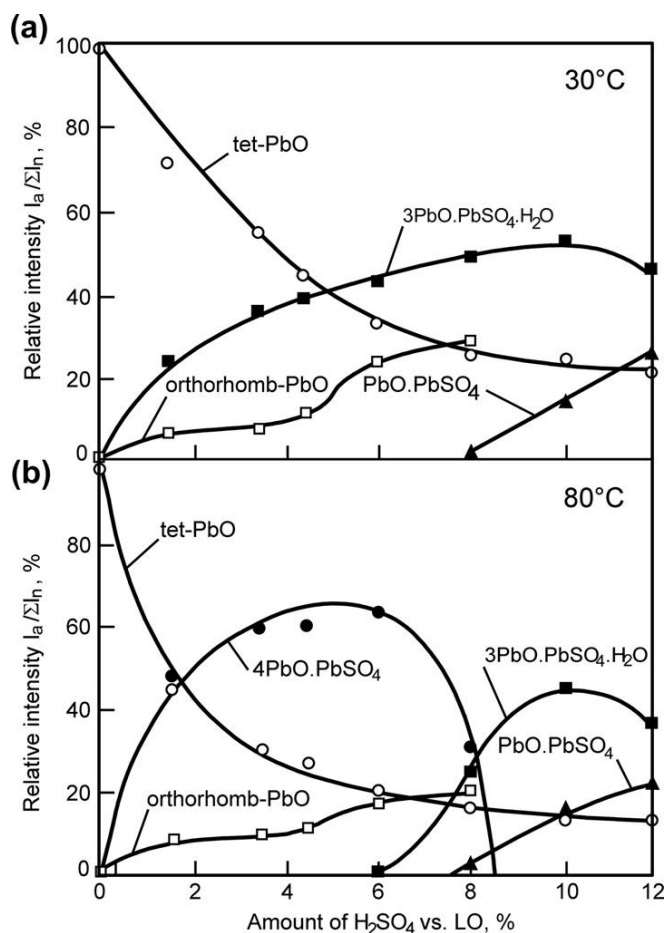


Figure 8.4:

Phase composition of cured pastes prepared at (a) 30 °C and (b) 80 °C as a function of H_2SO_4/LO ratio [5].

Structure and crystal morphology of cured 3BS and 4BS pastes

Figure 8.5 shows micrographs of the structure and crystal morphology of cured 3BS (Fig. 8.5a,b) and 4BS (Fig. 8.5c,d) pastes. The 3BS paste is cured at 50 °C and 100% RH for 24 h and then dried at 40 °C and 10% RH for another 24 h. The 4BS paste is cured at 90 °C and 100% RH for 2 h, then treated with water steam for 2 h and finally dried at 60 °C and 40% RH for 12 h and at 30 °C and 10% RH for another 12 h.

3BS particles are 1–2 μm long and tightly interconnected. Several particles form agglomerates. 4BS particles are 15–20 μm in length and 4–5 μm in diameter. A certain number of small particles (probably PbO) can be distinguished among the larger 4BS ones. The contact between 4BS particles is very good.

Processes of conversion of 3BS pastes into 4BS ones

Depending on the temperature of paste preparation and plate curing two types of cured pastes are obtained:

- (a) *Pastes built of 3BS particles.* These are obtained when paste preparation is performed at temperature from 30 to 60 °C and plate curing is conducted within the same temperature range.
- (b) *Pastes built of 4BS particles.* When the paste is prepared at temperatures between 80 °C and 95 °C, it is composed of 4BS crystals. Curing of such pastes involves mainly the processes of growth of large 4BS crystals at the expense of dissolution of smaller ones. These processes occur within 6–8 h of curing at 80–95 °C. When the paste is prepared at 50 °C, it contains 3BS crystals. The latter may be converted into 4BS ones if the paste is cured at 80–95 °C and 100% RH for 24 h, or at temperatures above 95 °C for 2–3 h with purging of water steam through the curing chamber. In both cases, the basic problem is the rate of 4BS nucleation. It should be sufficiently high to ensure uniform distribution of 4BS nuclei throughout the paste volume and hence the formation of roughly equal-sized 4BS crystals. This is achieved when a certain quantity of 4BS particles (nucleants) is introduced to the paste mix, together with the leady oxide, during paste preparation.

Figure 8.6 illustrates the changes in phase composition of the paste during curing at 93 °C for 8 h under continuous flow of water steam through the curing chamber [6].

The initial paste contains 3BS, tet-PbO and Pb at the beginning of the curing process. Within 6 h of curing, the 3BS crystals convert into 4BS ones. The latter keep growing until the 10th hour of curing. The amount of tet-PbO decreases as it is involved in the formation of 4BS and orthorhombic PbO.

The onset of 4BS crystal formation on curing of 3BS paste at 90 °C for 2 h steam treatment is illustrated in the micrograph presented in Fig. 8.7 [16]. The formation of a 4BS crystal

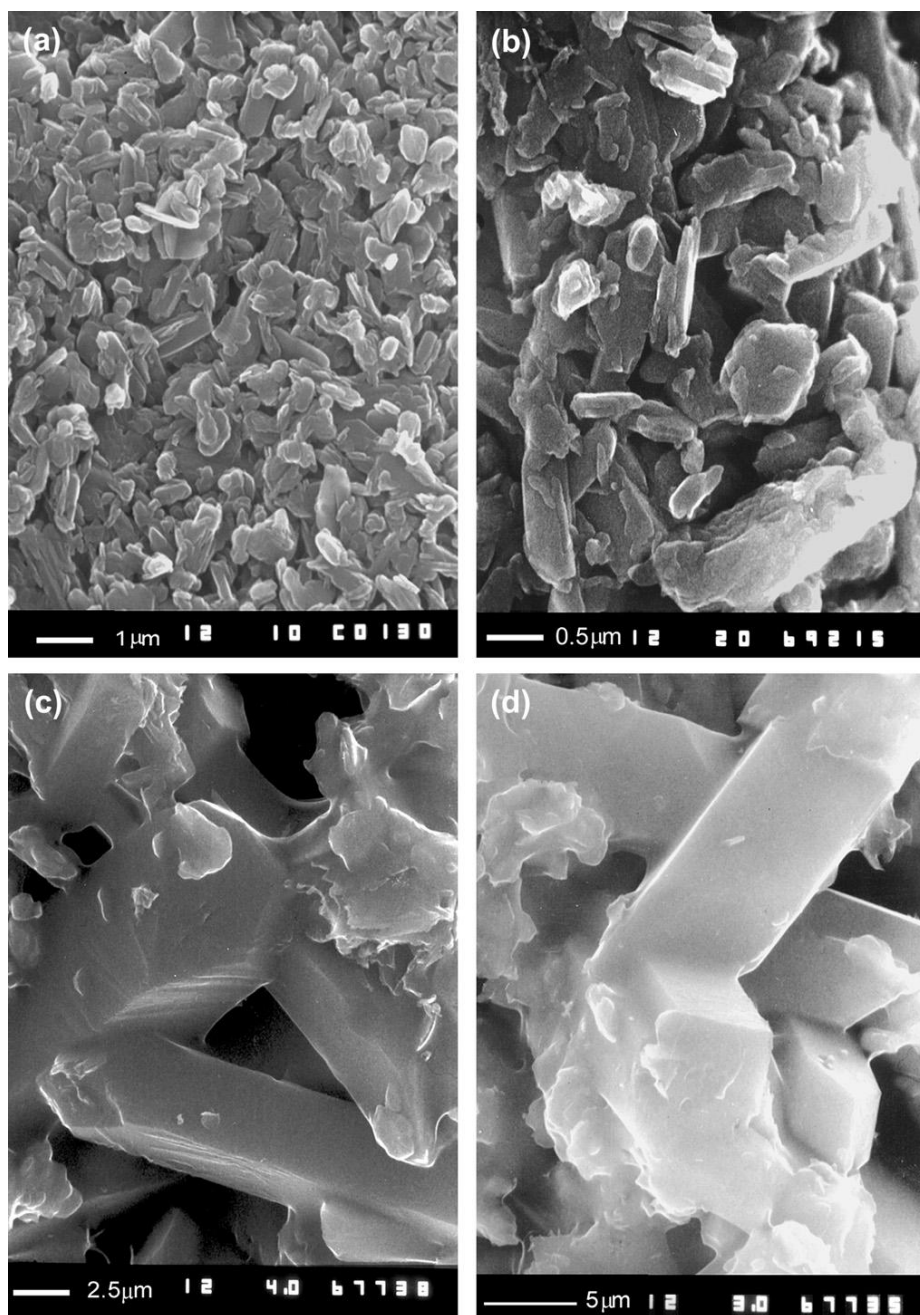


Figure 8.5:
SEM micrographs of the structure of cured pastes: (a,b) 3BS and (c,d) 4BS.

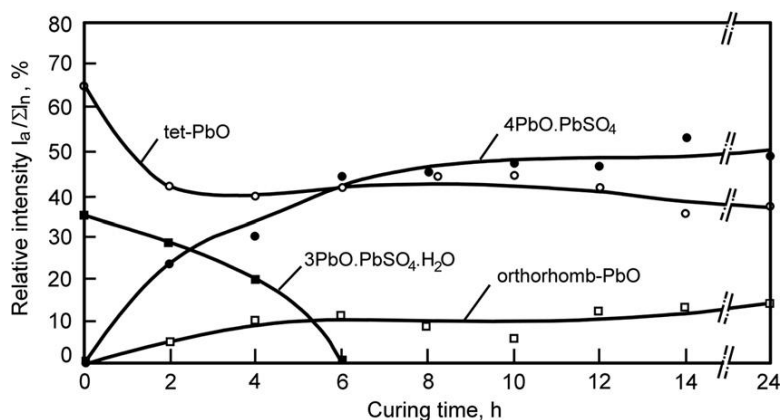


Figure 8.6:

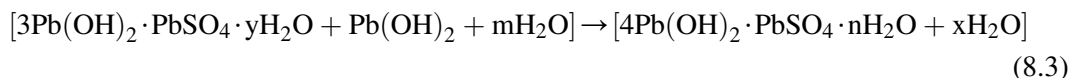
Changes in phase composition of the paste on curing at 93 °C under continuous water steam flow [6].

through merger of many 3BS particles can be seen in the right hand side of the picture in Fig. 8.7.

The above picture suggests the following mechanism of 4BS formation [16]. First, PbO and 3BS particles are hydrated



Neighbouring hydrated particles coalesce into a hydrated complex, involving also the hydrated $\text{Pb}(\text{OH})_2$. Processes of self-organization of the $\text{Pb}(\text{OH})_2$ molecules proceed in this complex and a hydrated 4BS complex forms.



Within this latter complex, formation of a 4BS crystal lattice starts through dehydration:



The density of the paste at this curing stage is 6.5 g cm^{-3} , which is a value lower than the density of 4BS paste (8.15 g cm^{-3}) [7]. This low paste density is a result of the hydrated 4BS phase formed.

The above processes require water steam and high temperature (above 90 °C). To accelerate the process of 3BS conversion into 4BS steam, it should be purged through the curing chamber.

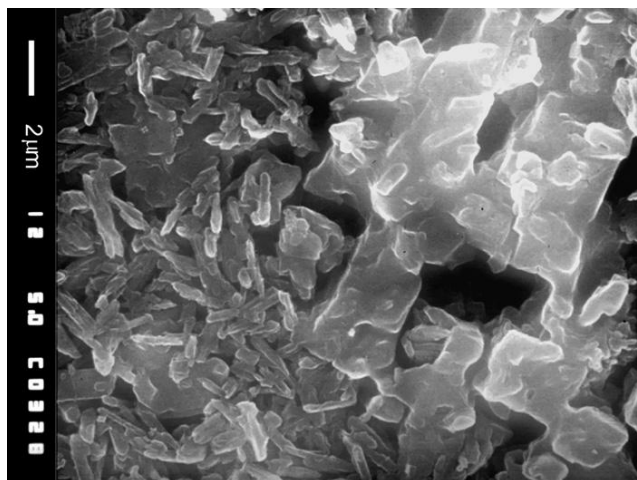


Figure 8.7:

Structure and crystal morphology of 3BS paste (3BS → 4BS) after curing at 90 °C for 2 h with steam treatment [16].

Influence of curing conditions on the size of 4BS particles

Tetrabasic lead sulfate particles obtained during the curing process are sized from 5 to 10 μm in diameter and from 30 to 100 μm in length. Such big particles are difficult to form, especially those with large diameter. A crust of PbO_2 (1.5 μm thick) forms on the surface of 4BS particles thus impeding the formation of PbO_2 in their interior [18]. Torcheux et al. have proposed a model implying that the diameter of 4BS particles should not exceed 5–6 μm so that the whole crystal volume could be formed [19]. It has been established that the size of 4BS particles depends on the conditions of plate curing and on the type and amount of additives to the paste [20]. Curing temperature affects the length of 4BS particles. At $T < 95^\circ\text{C}$, 4BS particles are less than 70 μm long. The phase composition of the paste before the curing process is of significance for 4BS particle size, because all cases of 4BS formation pass through 3BS and α and βPbO phases. Hence, the size of 3BS particles is also important. Addition of 2.5% PVP polymer to the paste reduces the diameter of 4BS particles to less than 7 μm and has a beneficial effect on the kinetics of the process of 4BS growth, and later of PbO_2 formation [20].

Pore volume, BET surface area and solid phase density of cured pastes

During the process of curing, a system of pores is created in the cured paste which determines the pore system of the active masses during the subsequent plate formation phase. The pore system is the second element (beside the structure of Pb and PbO_2 active masses) that determines the capacity and power performance of the battery.

During plate curing, the pore distribution in the paste changes due to recrystallization and chemical conversion processes. Figure 8.8 illustrates the pore volume distribution by

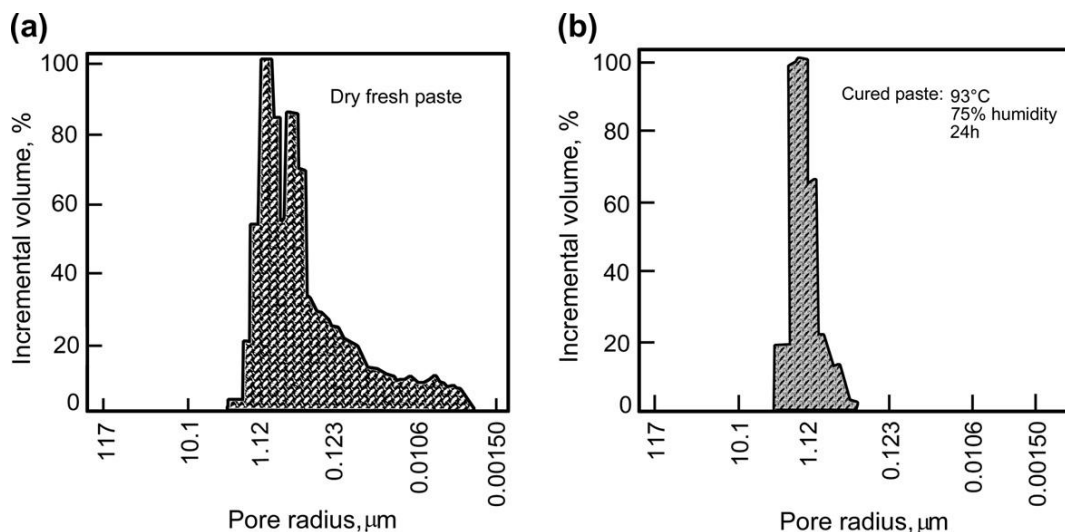


Figure 8.8:

Pore volume distribution by radius in (a) 4BS paste prepared at 80 °C and (b) same paste cured at 93 °C for 24 h.

radius for 4BS paste prepared at 80 °C and for the same paste after curing at 93 °C for 24 h.

With time of curing, the pores with small radii disappear and the cured paste contains pores with radii between 0.6 and 4 μm. This indicates that the small crystals vanish (or their number decreases abruptly) at the expense of the growth of big 4BS crystals forming large pores.

Figure 8.9 presents the pore distribution diagrams for cured pastes prepared with 6% H₂SO₄ vs. LO at 30 °C and 80 °C, respectively. These porograms evidence that the pore size distribution is confined within a very narrow range of radii [5].

If the inflection point of these curves is accepted as the mean pore radius, the relationship between this radius and the composition of the paste can be represented as shown in Fig. 8.10 [5].

In pastes prepared at 30 °C, the mean pore radius does not depend on the phase composition of the cured paste. This is due to the almost identical size of 3PbO·PbSO₄·H₂O, tet-PbO and PbO·PbSO₄ crystals. When the cured paste contains 4PbO·PbSO₄ (80 °C), the mean pore size is a function of paste composition. At 6% H₂SO₄/LO by weight, both the amount of 4PbO·PbSO₄ and the mean pore radius reach maximum values. Pastes containing 4PbO·PbSO₄ have larger pore volume and mean pore radius than those with 3PbO·PbSO₄·H₂O, because 4BS crystals are much bigger in size than 3BS ones. The pore size is determined by the size of the particles building the porous mass.

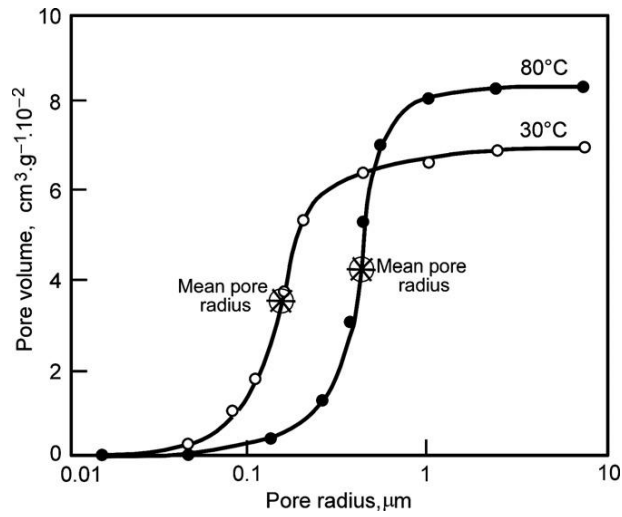


Figure 8.9:

Pore size distribution diagrams for cured pastes prepared at 30 ° and 80 ° c with 6% $\text{H}_2\text{SO}_4/\text{LO}$ by weight [5].

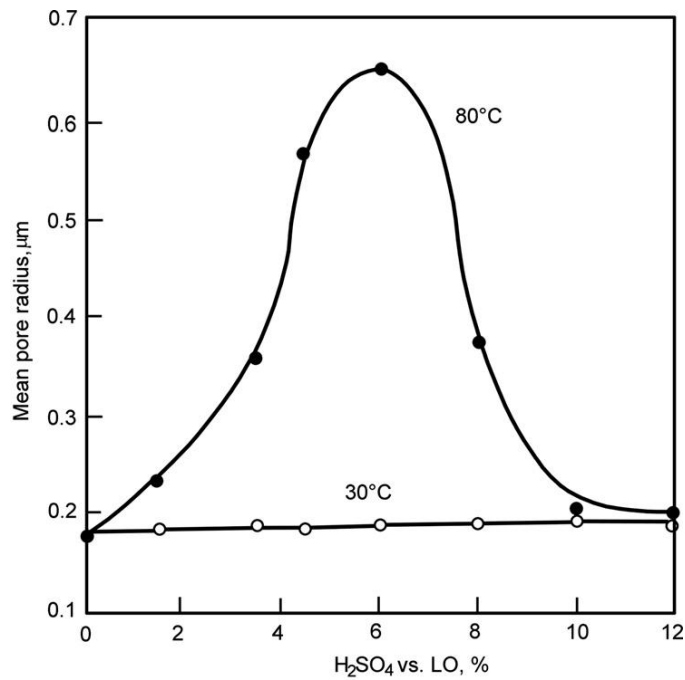


Figure 8.10:

Average (Mean) pore radius vs. $\text{H}_2\text{SO}_4/\text{LO}$ ratio in the paste [5].

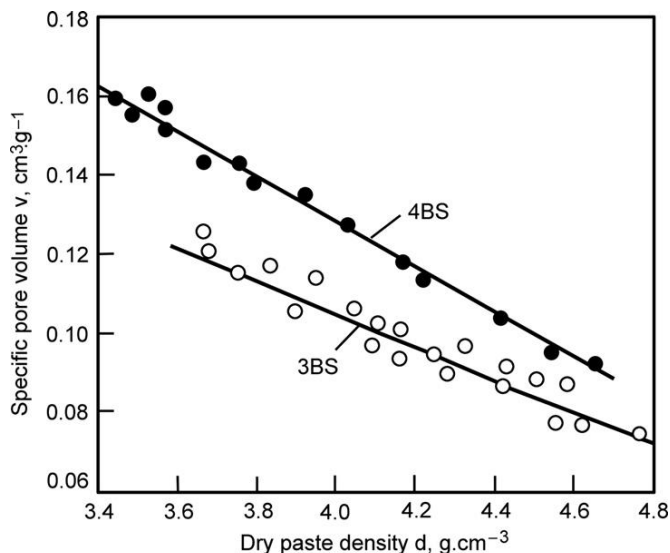


Figure 8.11:

Specific pore volume of cured pastes vs. paste density for pastes containing 4BS or 3BS [8].

A linear dependence has been established between specific pore volume ($\text{cm}^3 \text{g}^{-1}$) and paste density for 3BS and 4BS pastes (Fig. 8.11) [8]. This is a further proof that pastes containing $4\text{PbO} \cdot \text{PbSO}_4$ have larger pore volume per gram cured paste than those containing $3\text{PbO} \cdot \text{PbSO}_4 \cdot \text{H}_2\text{O}$.

Investigations have been carried out into the pore systems formed on curing 3BS and 4BS pastes as well as in 3BS pastes converted into 4BS during plate curing [16]. Some of the obtained porograms for 4BS cured pastes are presented in Fig. 8.12a. Figure 8.12b shows the porograms for 3BS paste as well as for 3BS pastes converted into 4BS ones during plate curing [16].

The following conclusions can be drawn from the porometric data:

- In the case of 4BS pastes, only the paste cured at 90°C for 24 h has larger total pore volume. All 4BS cured pastes have almost the same pore volume distribution by radius.
- The 3BS paste cured at 35°C for 48 h contains fairly small pores with the largest total pore volume. The total pore volume vs. pore radius curves for pastes undergone two-step $3\text{BS} \rightarrow 4\text{BS}$ conversion feature 2 inflection points, which suggests formation of two groups of pores with pronounced mean pore radii. This is related to the formation of large- and small-sized 4BS crystals, respectively.

The obtained porometric data are summarised in Table 8.1 [16].

The pore volume for seven of the cured pastes is about $0.096 \pm 0.03 \text{ cm}^3 \text{g}^{-1}$. The mean pore radius does not depend on curing time for Group I of pastes, whereas the BET surface

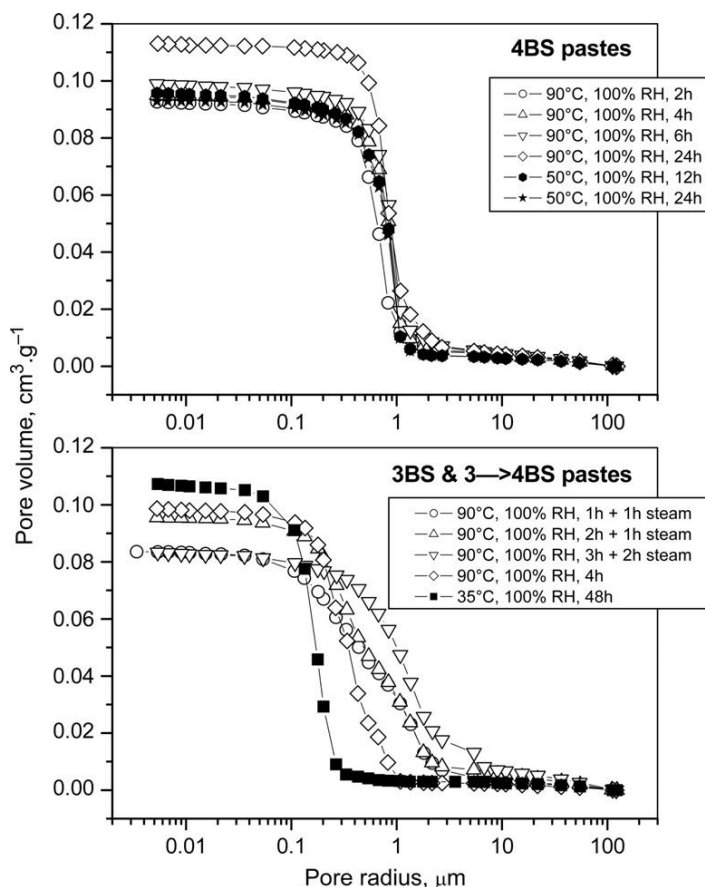


Figure 8.12:

Pore volume distribution by radius for 3BS and 4BS pastes cured under different conditions [16].

increases slightly. For Group II (4BS pastes cured at 90 °C) both the mean pore radius and BET surface values increase with increasing curing time. The smallest mean pore radius of 0.17 μm and the largest BET surface and total pore volume are measured for the 3BS paste (Group IV). The pastes of Group III subjected to two-step curing at 90 °C (first step without steam, followed by a second step with steam treatment) have mean pore radii varying from 0.65 to 1.25 μm and their BET surface decreases with increase of curing time.

All pastes contain a certain amount of PbO with a density of 9.3 g cm⁻³ and free lead ($d = 11.3$ g cm⁻³). So the solid phase paste density values should be higher than those for pure 3BS ($d = 6.50$ g cm⁻³) and 4BS ($d = 8.15$ g cm⁻³).

Judging by the solid phase densities the cured pastes can be divided in two groups: one with a solid phase density of around and above 7.9 g cm⁻³ and the other one with a density of about 6.5 g cm⁻³. The latter group refers mainly to 3BS pastes treated with water steam during

Table 8.1: Pore volume, mean pore radius, BET surface area and solid phase density of cured pastes as well as discharge current densities yielding specific capacity of 80 Ah kg⁻¹ PAM [16].

Paste Group	Battery Number	Phase Composition of Paste	Curing Conditions	Pore Volume (cm ³ g ⁻¹)	Mean Radius (μm)	BET Surface (m ² g ⁻¹)	Solid Phase Density (g cm ⁻³)	I, A kg ⁻¹ at 80 Ah kg ⁻¹ PAM
I	B13	4BS	12 h – 50 °C	0.096	0.84	0.331	8.35	17.77
	B14	4BS	24 h – 50 °C	0.093	0.83	0.363	8.02	20.50
II	B10	4BS	2 h – 90 °C	0.093	0.68	0.263	8.29	20.50
	B11	4BS	4 h – 90 °C	0.095	0.86	0.341	8.40	22.00
	B12	4BS	6 h – 90 °C	0.099	0.89	0.363	8.09	28.70
	B04	4BS	24 h – 90 °C	0.113	0.82	0.363	7.85	25.20
III	B05	3BS → 4BS	4 h – 90 °C	0.099	0.35	1.080	8.08	55.47
	B15	3BS → 4BS	1/1 h steam, 90 °C	0.084	0.65	0.850	6.47	36.05
	B06	3BS → 4BS	2/1 h steam, 90 °C	0.096	0.53	0.590	6.59	39.86
	B07	3BS → 4BS	3/2 h steam, 90 °C	0.083	1.25	0.280	6.46	43.23
IV	B08	3BS	48 h – 40 °C	0.110	0.17	1.620	7.97	—
		3BS	[8.9]	—	—	—	6.50	—
		4BS	[8.7]	—	—	—	8.15	—

the curing process. Though in these pastes 3BS crystals have converted into 4BS ones, their solid phase density is close to that of the pure 3BS phase.

The 3BS cured paste has higher solid phase density than that of the pure 3BS phase. Such a high value can be obtained if the paste contains considerable amounts of PbO and Pb. Except for the paste cured at 90 °C for 4 h the pastes of Group III (Table 8.1), produced from the same initial 3BS paste by two-step curing with steam treatment, have densities about 6.50 g cm^{-3} after curing. The decrease in solid phase density indicates that conversion of 3BS crystals into 4BS ones occurs through incorporation of water in the crystals. There is no other substance in the paste that would reduce the crystal density.

8.2.2. Oxidation of Residual Free Lead in the Paste

Rate of oxidation as a function of moisture content of the paste

Figure 8.13 shows the changes in lead and water content in the paste during plate curing [1]. The rates of the two processes change during curing, because they are interrelated. Water acts as catalyst for the exothermic reaction of lead oxidation, while the heat released during this latter process causes the moisture to evaporate from the paste.

Figure 8.14 presents the relationship between oxidation rate of free lead in the paste and moisture content [2].

The highest oxidation rate is observed within the humidity range 7–9%. On curing, the paste moisture content remains within this range only for a short period of time. The process of

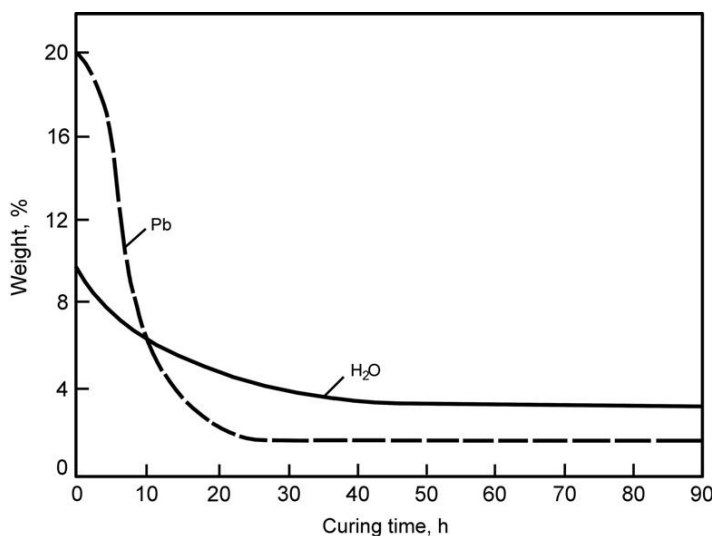


Figure 8.13:
Metallic lead and moisture content of the paste vs. curing time [1].

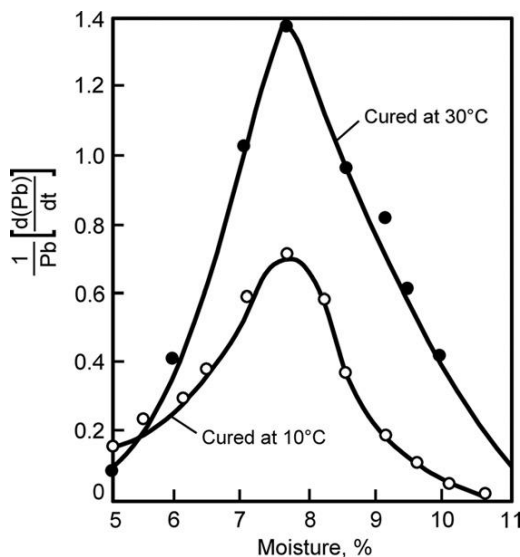


Figure 8.14:

Oxidation rate of residual free metallic lead vs. paste moisture content [2].

lead oxidation may be prolonged or its rate may reach a maximum if the initial moisture content of the paste is from 9.5 to 10%. At the beginning of the process, the rate of lead oxidation will start to increase, though slowly, due to the decrease in moisture content. When the latter reaches a value of 8.5%, the oxidation rate features a maximum.

By introducing curing chambers with independent temperature and humidity control in the battery manufacturing practice, the problems related to moisture content of the pastes after tunnel drying have been solved. Humidity and temperature in the curing chamber are continuously monitored and controlled, and the moisture content of the paste varies in accordance with the selected humidity profile.

Rate of oxidation of free Pb in the paste as a function of air humidity and temperature

This dependence has been established through measuring the residual unoxidized lead on curing pastes at 25 °C in curing chambers with various humidity levels. The obtained results of these experiments are presented in Fig. 8.15 [14].

The rate of lead oxidation is the highest at humidity levels between 55 and 86%. Hence, to facilitate oxidation of the residual free lead in the paste, the RH in the curing chamber should be reduced to values within the above range, after the process of recrystallization has been completed. The data in Fig. 8.15 indicate also that oxidation of lead at air humidity within the range from 55 to 86% proceeds most quickly during the first 6 h of curing. So the plate curing algorithm should include a period of 6 h during which the RH in the curing chamber should be kept between 55 and 85%.

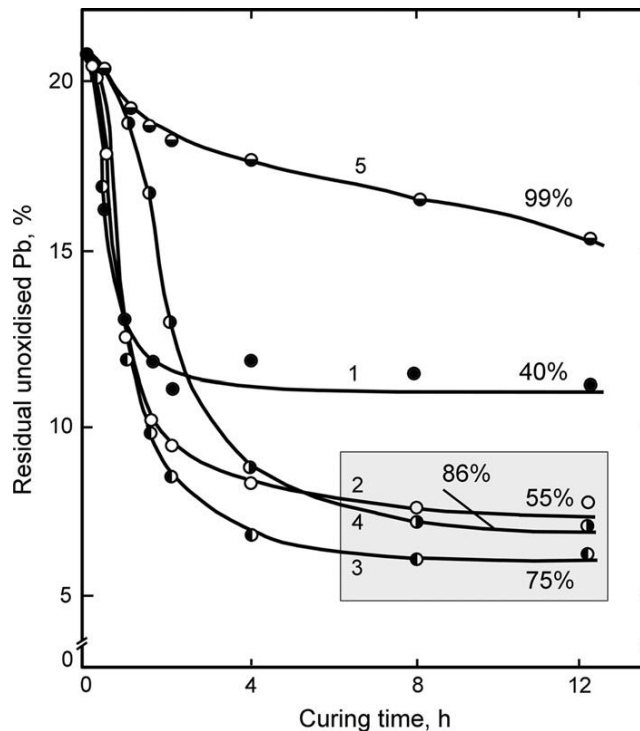


Figure 8.15:

Amount of residual unoxidized lead as a function of curing time for plates cured at 25 °C and different relative humidity in the curing chamber [14].

The second parameter that affects the rate of lead oxidation is temperature. This effect is illustrated in Fig. 8.16 presenting the amount of unoxidized lead in the paste after 1 h of curing at different relative humidities and temperatures [14]. The initial lead content in the paste is 21%.

With increase of temperature in the curing chamber the rate of lead oxidation increases, irrespective of the RH. However, at $RH > 81\%$ this increase is insignificant, whereas at $RH = 55\text{--}75\%$ it is substantial. For 1 h of curing at 50 °C in air atmosphere with RH between 55 and 75%, the content of residual free lead in the paste diminishes from 21 to 11–12%.

The rate of lead oxidation is influenced also by the moisture content of the paste prior to curing. The amount of water in the paste pores should be reduced so as to open the pores for access of oxygen from the air needed to oxidize the residual free lead in the paste. The rate of water evaporation from the paste pores depends on the RH in the curing chamber. This dependence is illustrated in Fig. 8.17 for plate curing at 25 °C and various relative humidities [14].

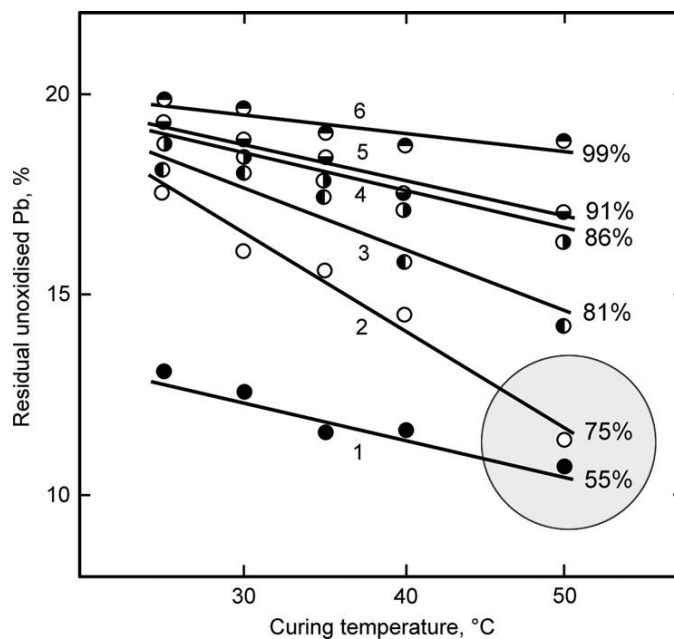


Figure 8.16:

Amount of residual unoxidized lead in the paste after 1 h of curing as a function of relative humidity and temperature in the curing chamber [14].

At 99% RH of the air in the curing chamber, almost no water evaporates from the paste. With decrease of the RH below 86%, the rate of water evaporation increases and at $RH = 40\%$, the paste pores open fully for about 4 h, whereas at $RH = 86\%$ it takes about 8 h for the paste pores to be completely evacuated.

Water evaporates from the paste pores quickly when the initial moisture content of the paste is less than 15% and the RH in the curing chamber is between 40 and 75%.

Figure 8.15 evidences that at the above humidity levels, the rate of Pb oxidation is the highest during the first 2 h. Within this time period, evaporation of water from the paste is most intense at RH between 40 and 55% (the slope of curves 1 and 2 in Fig. 8.17 is the highest). These results suggest that the time for reaching optimum moisture content of the paste that ensures highest rate of Pb oxidation, as well as the time during which this maximum rate of oxidation is maintained, depend on the rate of water evaporation from the paste, on the humidity and temperature in the curing chamber.

Mechanisms of Pb oxidation and role of water in these processes

Oxidation of lead during plate curing proceeds through two mechanisms: a chemical and an electrochemical one with formation of local microelements involving conjugated reactions.

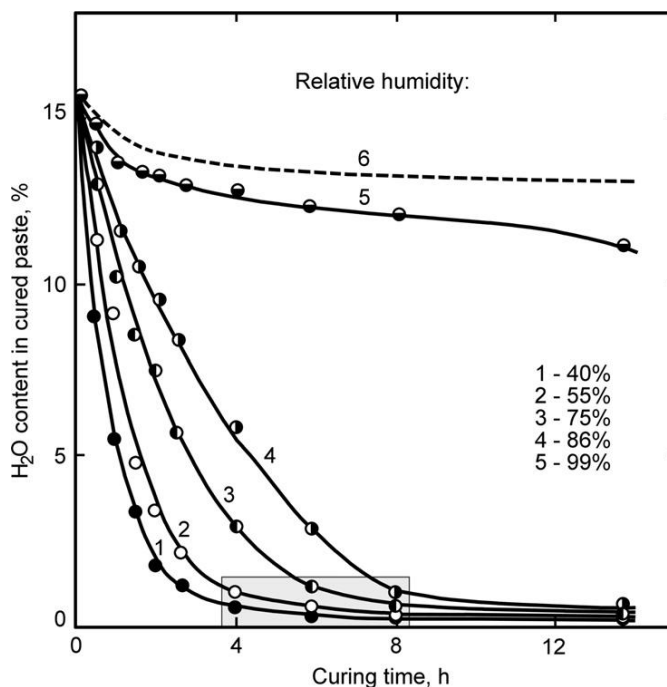
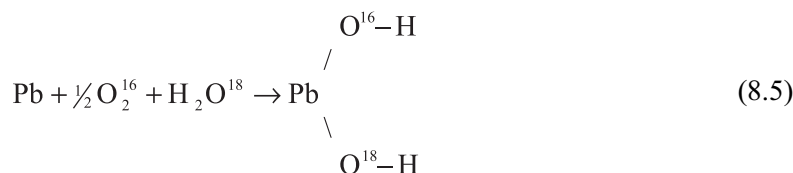


Figure 8.17:

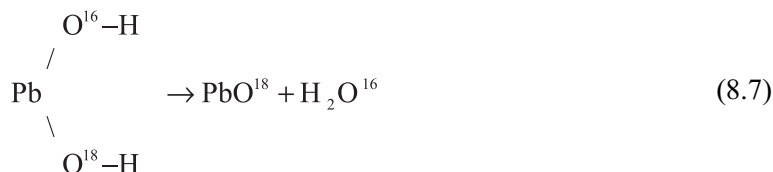
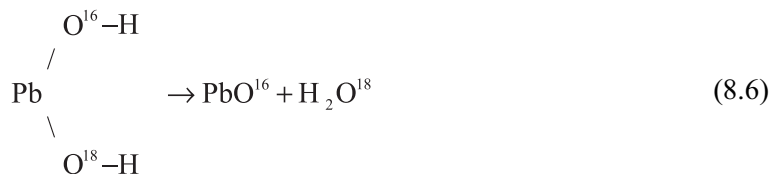
Content of residual water in the paste as a function of curing time for plates cured at 25 °C and different relative humidity in the curing chamber [14].

Mechanism of Pb oxidation through chemical reactions

Boden has investigated the mechanism of Pb oxidation and the role of water through isotope-exchange experiments [21]. He has used deuterium oxide instead of water. In the presence of D_2O , the rate constant of the reaction of Pb oxidation diminishes almost twice. This indicates that water takes part in the reactions of lead oxidation. The bond D—O is stronger than the bond H—O. Isotope-exchange experiments have been conducted with H_2O^{18} and H_2O^{16} isotopes. It has been established that almost 50% of PbO obtained as a result of Pb oxidation contains O^{18} isotope. On grounds of these results, the following mechanism of Pb oxidation with involvement of H_2O has been proposed:



This intermediate lead hydroxide has a short life and is dehydrated. It has been assumed that the bonds $O^{16}-H$ and $O^{18}-H$ have equal strengths, which allows formation of PbO with 50% O^{18} and 50% O^{16} , according to the following reactions:



Thus, Pb oxidation proceeds through a reaction in which water is directly involved, whereby an intermediate product (a hydroxide) is formed which is then dehydrated, rather than through a simple reaction between Pb and oxygen from the air to form PbO . In case of direct involvement of H_2O in the reaction of Pb oxidation by O_2 , its amount influences the oxidation rate. The ratio between 1 g mol of H_2O and 1 g atom of Pb is $18/207 = 8.7\%$. It is at this H_2O/Pb proportion that the rate of Pb oxidation is the highest, which indicates that one water molecule reacts with one lead atom. This ratio supports the above proposed mechanism of Pb oxidation with direct participation of H_2O .

The above described mechanism is incomplete. It does not explain how the bond between oxygen atoms in the O_2 molecule break. And this is a very important process as this bond is very strong. In gas-diffusion oxygen electrodes this bond is dissociated through formation of an intermediate product, H_2O_2 [22].

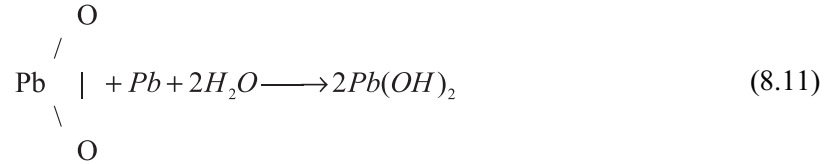


It has been established that the rate of H_2O_2 reduction to H_2O on Pt substrate is twice higher than that of O_2 reduction to H_2O_2 . Hence, no H_2O_2 accumulates in the solution.

It can be assumed that breaking of oxygen bonds in the O_2 molecule during plate curing proceeds through a similar mechanism, where electrons come from Pb oxidation and lead peroxide forms.



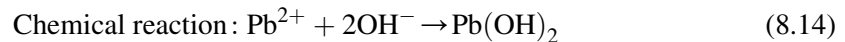
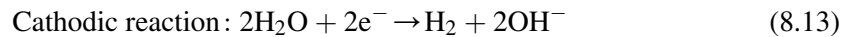
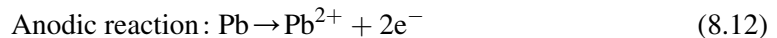
Lead peroxide is a strong oxidizer and has short life. It reacts with lead atoms and water forming $\text{Pb}(\text{OH})_2$.



This reaction changes the structure of the metal surface transforming it to lead hydroxide structure. Most probably, the above process is facilitated by water. $\text{Pb}(\text{OH})_2$ releases water, which then participates in reaction (8.11) involving other peroxide molecules. Thus, water plays an important role as catalyst for Pb oxidation. Oxygen from the water molecules contributes to the formation of lead hydroxide, which is in agreement with the result of Boden's isotope experiments.

Mechanism of Pb oxidation in the paste through electrochemical micro-galvanic elements

This mechanism has been proposed by Hung et al. [14]. These authors have investigated oxidation of Pb powder in an ampoule with humid air in the absence of O_2 . Despite the lack of oxygen, lead is oxidized and H_2 is formed in the ampoule. Galvanic microelements form on the lead particle surface where the following reactions proceed:



Reactions (8.12) and (8.13) are conjugated reactions and proceed at the same rate which is limited by the rate of the slower one. The rates of these reactions are determined through measuring the amount of unoxidized lead in the ampoule. However, in the presence of O_2 , a second conjugated reaction may proceed at the cathode:



The electromotive force of the micro-galvanic cell generated by reactions (8.12) and (8.15), and calculated using thermodynamic data, is equal to $U = 1.01 \text{ V}$ at $a_{\text{SO}_4^{2-}} = 10^{-4}$ and

pH = 10 [14]. At this pH, formation of basic lead sulfates is possible. Both reactions (8.13) and (8.15) consume water. When the water content of the paste drops below 5% (Fig. 8.13), the rates of reactions (8.13) and (8.15) are strongly impeded and oxidation of Pb practically stops.

Besides by reactions (8.13) and (8.15), water is also lost through evaporation. Consequently, water content falls rapidly below the critical value and oxidation of Pb stops. Water evaporation can be reduced by keeping relatively high humidity levels in the curing chamber (e.g. 55–75%). Thus, the reaction of Pb oxidation will proceed at a high rate for a longer period of time and the moisture content of the paste will be maintained above the critical value of 5%.

Evaporation of water from the plate is facilitated also by the temperature rise resulting from the heat effect of the exothermic reaction of Pb oxidation (Fig. 8.13).

The conjugated electrochemical processes that take place in galvanic microelements on the Pb surface are influenced by pH of the solution that covers the surface of Pb particles. With increase of pH of this solution, the overvoltage of hydrogen evolution (reaction (8.13)) increases and hence these reactions are slowed down. Thus, formation of a layer of $\text{Pb}(\text{OH})_2$ and PbO on the surface of Pb particles suppresses oxidation of lead through the galvanic microelement electrochemical mechanism.

8.2.3. Corrosion of PbSnCa Grids During Plate Curing and Formation of Corrosion Layer

Segregation of Sn and Ca during plate curing and its effect on grid corrosion

Let us now see what are the phenomena that occur at the grid/paste interface during plate curing. First, the changes in grid alloy structure during curing will be considered. Then, we will discuss the structure and properties of the corrosion layer formed at the grid/paste interface during the curing process. The phenomenological study will be exemplified by PbCaSnBiAg grids, produced by WIRTZ Manufacturing Co., employing their Concast (C-grid) or Conroll (R-grid) technologies and pasted with 3BS or 4BS pastes [16].

Figure 8.18 presents micrographs of the structure of the grid surface before and after curing as well as formation of intergrain layer during the curing process.

Figure 8.18a features the microstructure of the grid surface before curing. Large-sized grains are distinguished with smooth boundaries oriented in the direction of heat transfer during the cooling process. Darker zones can be interpreted as defects in the structure of the grains to which Sn has segregated forming most probably phases of an intermetallic compound, $(\text{Pb}_{(1-x)}\text{Sn}_x)_3\text{Ca}$, and α -solid solution [3,24,25].

Figure 8.18b shows the microstructure of the grid bar surface after curing. A segregation process occurs which results in formation of a thin layer along the grain boundaries composed of $(\text{Pb}_{(1-x)}\text{Sn}_x)_3\text{Ca}$ and α -solid solution according to [23]. In addition, Sn_3Ca , Sn–Ag and

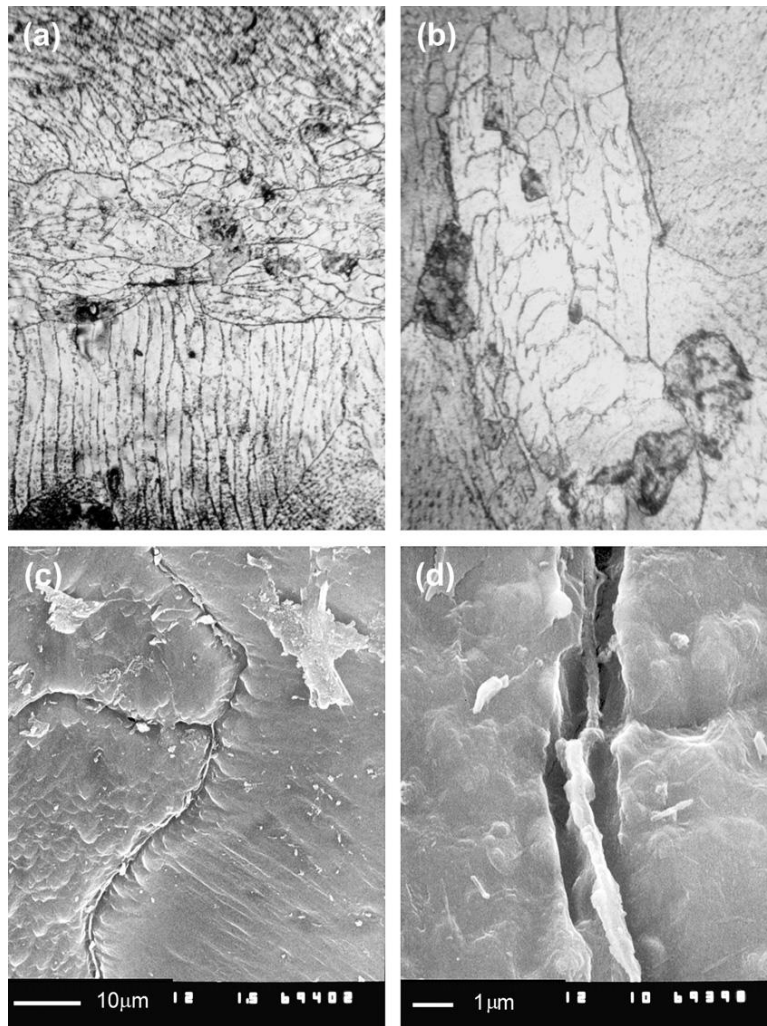


Figure 8.18:

(a,b) Microstructure of PbSnCaAg alloy before and after curing. (c,d) SEM pictures of the interface between grains feature formation of thin intergrain layer, probably of $(\text{Pb}_{(1-x)}\text{Sn}_x)_3\text{Ca}$ [16].

Sn—Pb compounds are formed at the subgrain boundaries [23,24]. The grain and the subgrain volumes are depleted of Sn and Ca. The presence of Ag in the alloys with high Sn content slows down the above process [25].

Figures 8.18c and 8.18d show SEM micrographs featuring interfaces between grains and formation of intergrain layer [16]. The latter forms a separate phase at most grain boundaries. This phase is rich in Ca, which has high affinity to oxygen and is readily oxidized. Hence, corrosion of the intergrain layer will proceed at higher rate, both during grid storage in air after manufacture, and especially during plate curing.

Table 8.2: Sn/Pb and Ca/Pb ratios at the surface and in the bulk grid alloy for C(concast) and R(conroll) grids [16].

Grid type	Sn/Pb		$\text{Sn}_{\text{surf}} / \text{Sn}_{\text{bulk}}$	Ca/Pb		$\text{Ca}_{\text{surf}} / \text{Ca}_{\text{bulk}}$
	Bulk	Surface		Bulk	Surface	
C – grid	0.0189	0.0330	1.75	0.0031	0.158	51.2
R – grid	0.0182	0.0628	3.45	0.0036	0.208	58.4

Segregation of Sn and Ca advances from the bulk grid alloy towards its surface. This process has been studied by examining the elemental composition of the grid surface layer (10 nm thick) by X-ray photoelectron spectroscopy (XPS) and that in the bulk grid alloy by atomic absorption spectroscopy (AAS) [16].

Table 8.2 presents the Sn/Pb and Ca/Pb ratios in the grid surface layer (XPS) and in the bulk alloy (AAS), as well as the ratios between the Sn and Ca contents at the grid surface vs. that in the bulk grid alloy [16].

The following are the conclusions from Table 8.2:

- The surface layer (~10 nm) of the R-grid contains about 3.5 times more Sn and about 58 times more Ca than the bulk R-grid alloy. For the C-grid, these values are about 1.7 times for Sn and 51 times for Ca, respectively. During stay of the grid in the air prior to curing, Ca is oxidized forming CaO and/or CaCO_3 , parallel to the processes of SnO and PbO formation.
- Higher Sn and especially Ca segregation at the grid surface is observed with R-grids than with C-grids. Sn enrichment of surface oxide on PbSnCa grids has been proved together with the formation of basic lead carbonates [23].

Figure 8.19 presents micrographs of the surface of a concast grid from 3BS plate cured at 40 °C for 48 h. The oxidized intergrain layer was dissolved using a solution of glucose and NaOH.

The above pictures indicate that corrosion has affected most strongly the intergrain layer. The metal grains can be clearly distinguished. The closer to the grain boundary, the faster the metal oxidation. That is the reason for the ‘hilly’ surface of the metal. The impact of intergranular corrosion can be reduced by integrating grid manufacture and pasting into a single technological process. Such plate manufacturing technologies have been developed and implemented in the battery practice, which not only increase productivity rates, but also inhibit intergranular corrosion as the grid surface is covered with paste.

Corrosion layer and its interfaces with PbSnCa grid and paste

Corrosion layer structure

The micrographs in Fig. 8.20 show the corrosion layer formed on the surface of PbSnCaBiAg concast grids pasted with (a) 4BS paste and (b) 3BS paste, after curing at

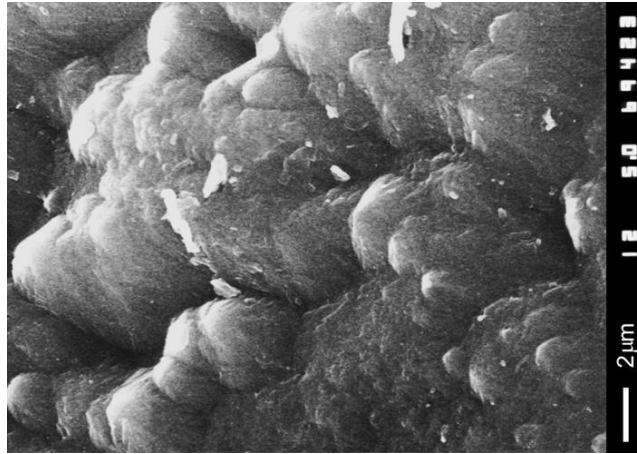


Figure 8.19:

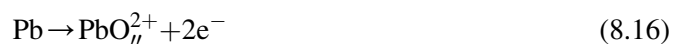
SEM micrographs of the surface of PnSnCaBiAg grid after curing and dissolution of corroded phases using a solution of glucose and NaOH [16].

50 °C for 24 h [16]. The upper picture evidences that the corrosion layer consists of two sub-layers: a thin compact sub-layer covering the metal grains (denoted by CL₁) and a second sub-layer denoted by CL₂ (bottom part of Fig. 8.20b). The CL₁ layer consists of PbO particles obtained during oxidation of Pb. Part of the CL₂ layer is hydrated comprising grains closely packed together. The evolution of the structure of the CL₂ layer is a result of intercalation of H₂O into its interior and subsequent hydration of PbO to Pb(OH)₂.

Oxygen vacancies mechanism of grid corrosion during plate curing

During the curing process, a corrosion layer forms on the grid surface, which is thin at the beginning and then grows thicker with time of curing. This is realized by ion diffusion through the corrosion layer. It has been established that the activation energy of thermal oxidation of Pb to PbO is about 1 eV [26]. This low value indicates that the movement of O²⁻ ions through the oxide layer is realized by an oxygen vacancies (O_{''}²⁺) mechanism [27]. An analogous mechanism has been found also for the electrochemical oxidation of Pb to PbO in the lead oxide potential region [28]. An oxygen vacancies (O_{''}²⁺) mechanism of chemical oxidation of the lead grid during curing can be accepted, too. It can be represented by the following reactions:

- Pb oxidation proceeds at the metal/PbO corrosion layer interface with formation of oxygen vacancies (O_{''}²⁺) and electrons:



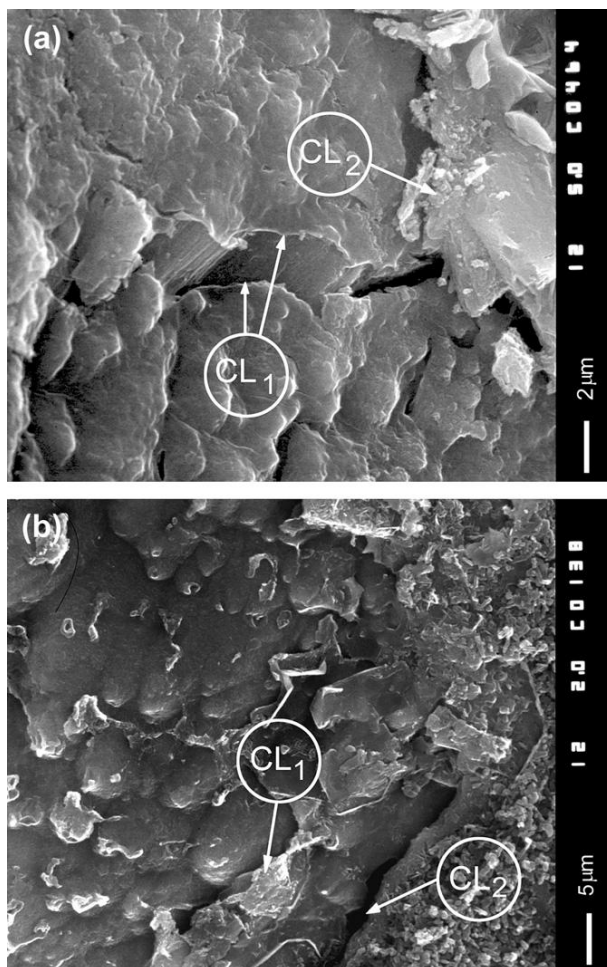
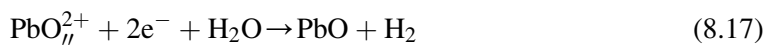
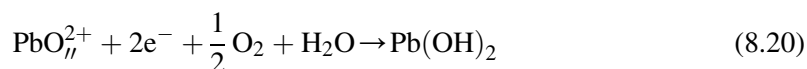


Figure 8.20:

Corrosion layers formed on the surface of PbSnCaBiAg concast grids pasted with (a) 4BS paste and (b) 3BS paste, after curing at 50 °C for 24 h [16].

- Oxygen vacancies and electrons move through the corrosion layer (CL) to the CL/paste interface, where they react with H₂O and O₂ in the pores forming possibly PbO, or more probably Pb(OH)₂:





The above reactions proceed in the solid state, i.e. at slow rate. It is known that the duration of the curing process at 30–40 °C is between 48 h and 72 h, including the drying procedure. Water loss, due to formation and growth of corrosion layer, should be compensated for. That is why a RH from 40 to 75% should be maintained and air should be introduced in the curing chamber.

Bonding of paste crystals to the CL₂ layer

Tribasic and tetrabasic lead sulfate crystals (3PbOPbSO₄·H₂O and 4PbOPbSO₄·xH₂O) contain water and are partly hydrated (*x* in the 4BS formula is a variable with a value between 0.18 and 0.16, i.e. 4BS crystals are superficially hydrated) [17]. PbO in the CL₂ layer is hydrated, too. It can be expected that bonding between 3BS or 4BS particles of the paste and of the corrosion layer will occur by an interaction between their hydrated layers.

A SEM picture of the bonds between 4BS crystals and the CL₂ layer formed in a plate cured at 50 °C for 24 h is presented in Fig. 8.21. 4BS crystals are “welded” to the CL₂ surface at the points of contact with the latter.

At high temperatures, 4BS crystals absorb water forming a soft hydroxide mass which interacts with the Pb(OH)₂ surface of the CL₂ corrosion layer. Thus, non-interrupted bonds are formed (Fig. 8.21). Probably, the dissolved Pb(OH)₂ from the CL₂ layer keeps up the higher alkalinity of the solution in the paste pores at the interface, which facilitates hydration of 4BS crystals.

The bonding between 3BS crystals and the CL₂ layer of a plate with C-grid cured at 40 °C for 48 h is presented in Fig. 8.22. Many 3BS particles are incorporated partly into the CL₂ surface layer [16].

Formation of hydrocarbonates at the paste/corrosion layer interface

Figure 8.23 shows the interface paste/CL₂ layer of a plate prepared with 3BS paste cured at 90 °C for 3 h and then treated with steam for another 2 h. Carbon dioxide is introduced into the curing chamber with the water steam [16]. The shape of the crystals formed under these conditions is typical of plumbonacrite and cerussite crystals. Obviously, the technology of 3BS conversion into 4BS through purging with water steam, i.e. introduction of CO₂ from the air, leads to formation of hydrocarbonates at some sites of the paste/CL₂ interface.

Figure 8.23a illustrates the steps of oxidation of the (Pb_{1-x}Sn_x)₃Ca layer and formation of hydrocarbonates. The figure evidences onset of oxidation of the (Pb_{1-x}Sn_x)₃Ca layer. Probably, lead hydroxide and calcium hydroxide are formed. A more advanced stage of this process is observed in some zones, where crystallization of some oxides occurs. Well-pronounced crystals can be distinguished in other zones. These crystals look very much like plumbonacrites, Pb₃(CO₃)₆(OH)₆.

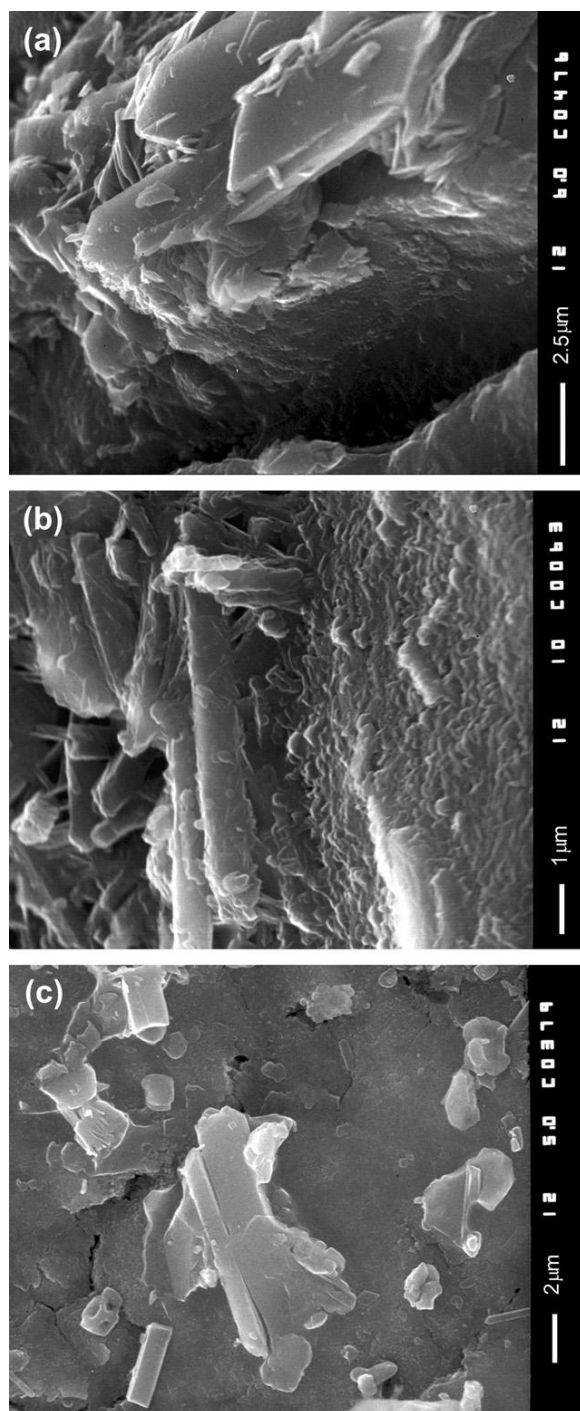


Figure 8.21:

Bonding of 4BS particles to the CL₂ layer (a) for plate cured at 50 °C for 24 h and (b) for plate cured at 90 °C for 4 h [16].

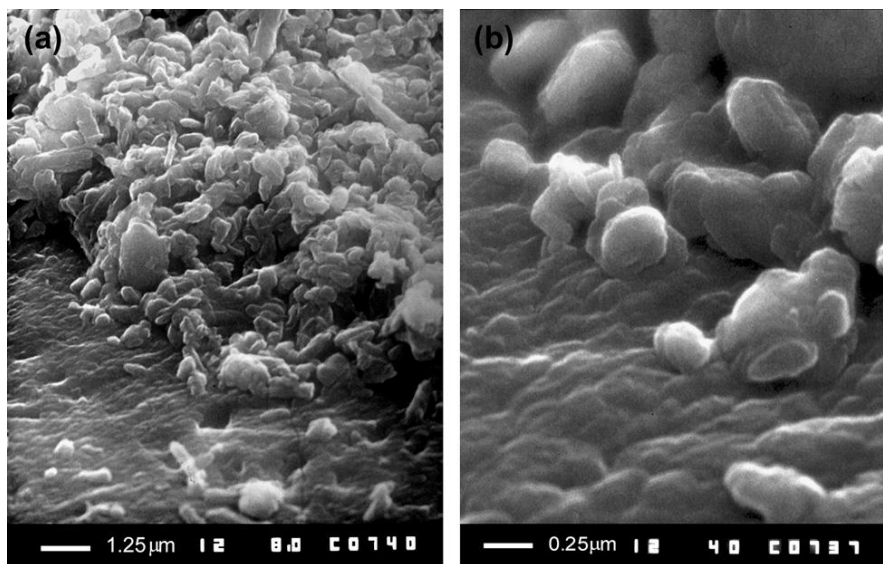


Figure 8.22:

Bonding of 3BS particles to the CL_2 layer for plates cured at 40 C for 48 h. (a) and (b) SEM images of the CL macrostructure with bonded particles from the cured paste at different magnifications [16].

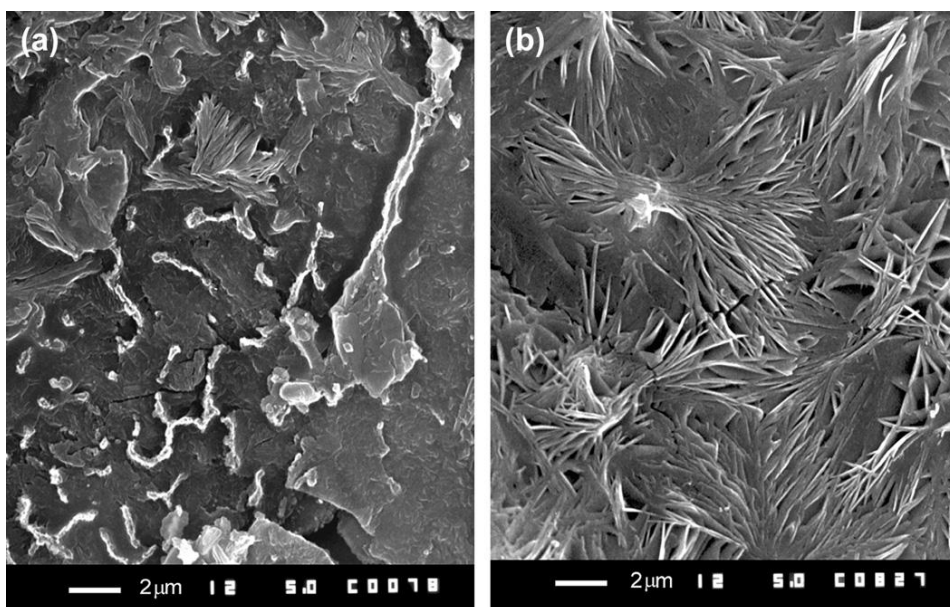


Figure 8.23:

(a) Initial stages of hydration of the intergrain layers and formation of hydrocarbonates and (b) Microstructure of plumbonacrites and hydrocerrusites formed at the paste/ CL_2 interface [16].

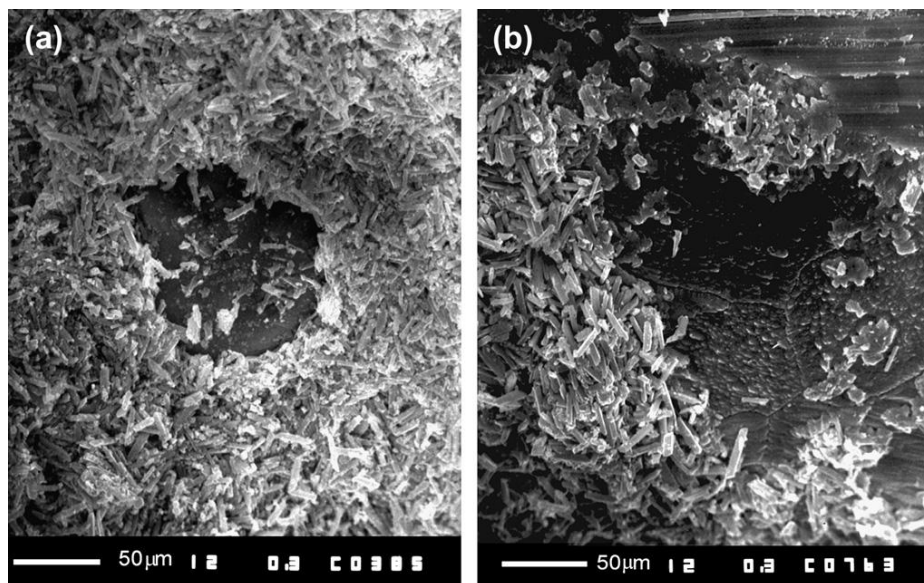


Figure 8.24:

Bare grid surface areas on 4BS plates cured at 90 °C for 2 h. Water vapour bubbles, formed during heating of the grid, have displaced the 4BS crystals and detached them from the grid surface.

(a) macrostructure of the grid/paste interface with a cavern; (b) closer view of the cavern with boundaries between the lead grains.

Formation of gas bubbles at the paste/CL₂ layer interface

Figure 8.24 presents a SEM picture of paste cured at 90 °C for 2 h. 4BS crystals are clearly visible in the cured paste. A certain bare grid surface area is observed. The crystals around this area are tightly packed. These bare areas on the grid surface have, most probably, resulted from formation of gas bubbles which exert pressure on the neighbouring 4BS particles and thus cause them to pack around the bubble walls. Gas bubbles form on heating of plates to 90 °C. The grid metal has lower specific heat than the paste and its temperature rises first. The water at the grid surface evaporates forming bubbles, which displace the nearest 4BS crystals of the paste away from the grid surface. Thus, caverns form at the CL/paste interface and are preserved during the subsequent formation process, too.

8.2.4. Processes During Plate Drying

Decrease in moisture content of the paste on drying

Even after recrystallization of 3BS and 4BS is completed, the residual free lead in the cured paste is oxidized and a corrosion layer is formed on the grid surface, the structure of the plate is still mechanically weak. A great number of the paste particles are interlocked through their

hydrated layers or through the thin liquid films formed between them. In order to improve the hardness and strength of the plates, they are subjected to drying and aimed to reduce the moisture content to 0.2–0.1%. The changes in total pore volume and in pore distribution by radius with decrease in moisture content of the paste are presented in Fig. 8.25 [29].

When the moisture content of the paste is 11.8%, the pores with radii larger than 11 μm are evacuated. At 8.6% moisture content, the pores with diameter $d > 1.5 \mu\text{m}$ are open for air access, and at 3.9% moisture content of the paste, this happens also to the pores with diameter $d > 0.24 \mu\text{m}$. On drying the paste after curing, the pores with the largest radii are evacuated first and then the smaller ones. Such behaviour indicates that evaporation of moisture from the paste follows a pattern opposite to the process of wetting the lead oxide powder.

Figure 8.26 presents diagrammatically the physical picture of the system particles/liquid at different stages of the drying process.

Paste drying proceeds in two stages: during the first stage, water filling the capillaries is least tightly bound to the particles and evaporates first. Large void pores are formed. On further drying, water from the thin liquid layers between particles also evaporates and the plate shrinks. The only liquid phase that remains in the paste is in the form of rings, wedge liquid (Fig. 8.26c). The latter is retained by the surface forces. During the second drying stage, the wedge water evaporates, too, as a result of which the lead hydroxides contained in the wedge liquid precipitate between the particles and interconnect them into a continuous porous mass (Fig. 8.26d).

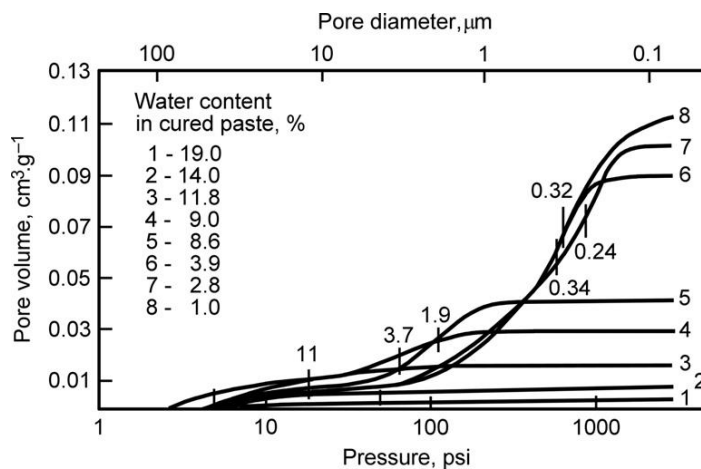
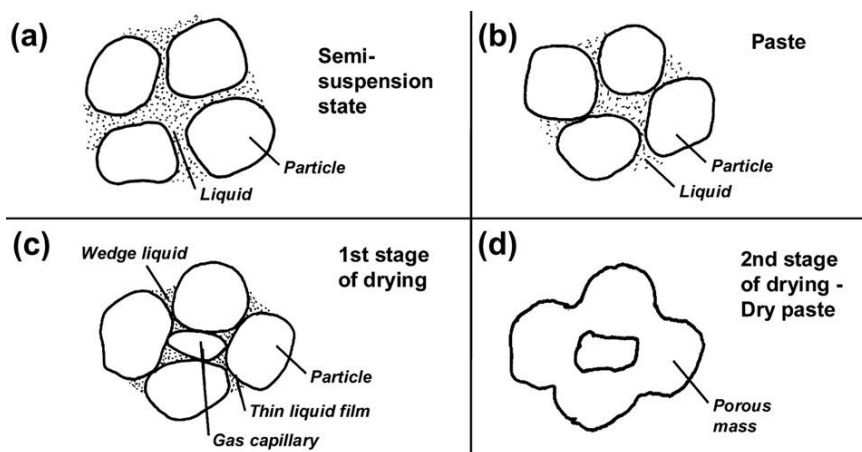


Figure 8.25:

Total pore volume and pore size distribution for paste samples taken at different stages of curing [29].

**Figure 8.26:**

Physical picture of the system particles/liquid at different stages of the drying process.

Paste curing and drying: Atmospherically dependent processes

Moisture content of the surface plate layers depends on water vapour or steam pressure in the atmosphere above the plate. With decrease of air access to the plates, the moisture in the surface plate layers begins to evaporate thus opening the capillaries. Water from the inner plate parts diffuses towards the plate surface in an attempt to restore the moisture equilibrium throughout the plate volume (Fig. 8.27a). Consequently, the largest capillaries in the plate interior are evacuated, too. Thus, the processes illustrated in Fig. 8.26c and 8.26d proceed across the whole plate volume.

Sometimes, water evaporation from the surface plate layers may proceed at a much higher rate than the diffusion of capillary water from plate interior to its surface. In these cases, the radii of the pores in the plate surface layers will diminish more quickly than those in the interior of the plate. Hence, inner tensions will be created in the cured paste and the latter will crack. To avoid this, the air humidity in the curing chamber should be reduced slowly accounting for the speed of capillary water movement through the plate cross-section.

In battery manufacturing practice, after passing through the paste dryer at the exit of the pasting machine, pasted plates are arranged in piles (Fig. 8.27b). The latter are stacked on pallets, thus forming a batch of plates to be loaded into the curing chamber. The above arrangement in stacks reduces the contact surface of plates with the ambient atmosphere. The exchange of moisture and oxygen between paste and curing chamber atmosphere is inhibited. That is the reason why the processes of paste curing and drying are the slowest technological processes in the manufacture of battery plates.

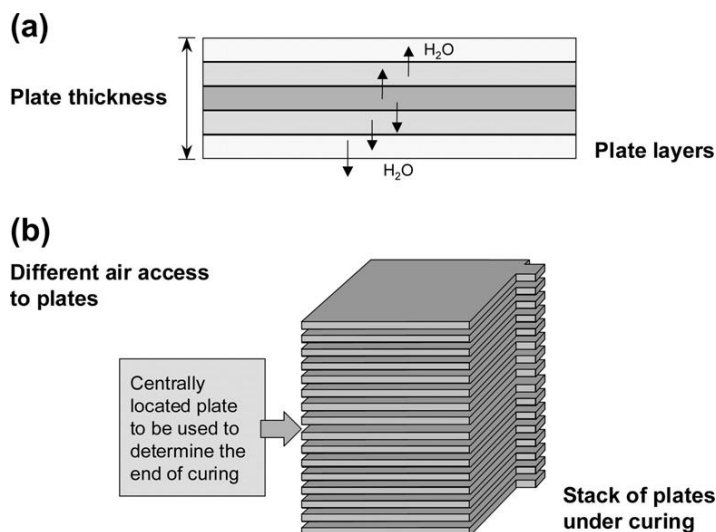


Figure 8.27:

(a) Scheme of movement of water from the inner plate layers towards the surface as a result of water evaporation from the surface layers and opening of paste capillaries and (b) stack of plates under curing.

For progress control of the processes of plate curing and drying, a plate should be taken from the most unfavourable position in the stack and from the center of the pallet, where air and water exchange is the slowest (Fig. 8.27).

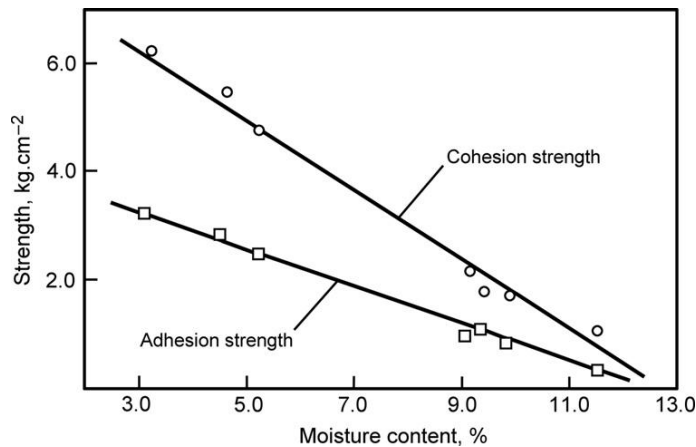
Paste adhesion and cohesion strengths

The bonding strength between crystals (particles) of the paste is cohesion strength and that between paste and grid is adhesion strength. Figure 8.28 presents these strengths as a function of moisture content of the paste [2].

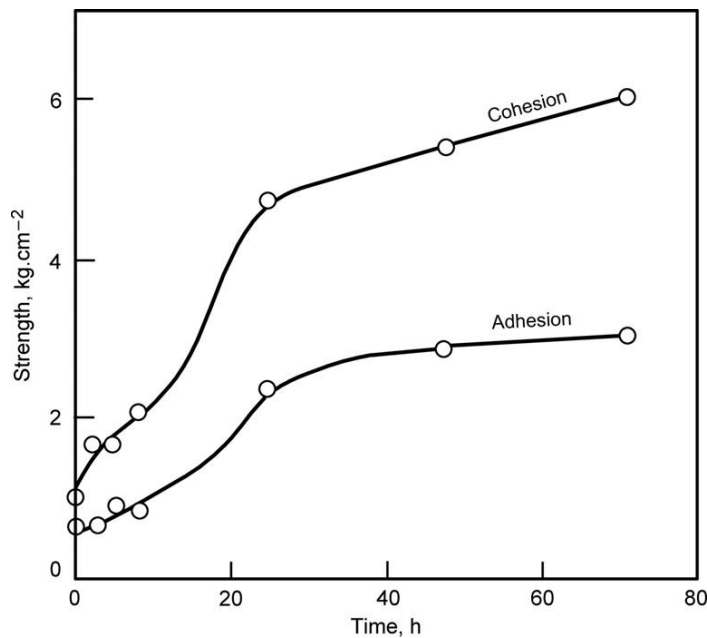
A linear increase is observed in both strengths with decrease in moisture content. The adhesion strength is associated with the formation of corrosion layer on the grid surface. Formation of a well-defined corrosion layer (2–3 μm thick) improves the bond between cured paste and grid, which later provides a reliable grid/active mass contact.

Figure 8.29 illustrates the changes in cohesion and adhesion strengths during plate curing [2].

Within the first 8 h of curing, a recrystallization process occurs, which increases slightly the strength of cohesion (up to 2 kg cm^{-2}). After that, capillary water and water from the thin liquid films between particles evaporates and the latter are interlocked into a porous mass, as a result of which the cohesion strength increases from 2 to 4.8 kg cm^{-2} . Then, evaporation of the wedge water and subsequent hardening of the porous mass follow. Consequently, the cohesion forces increase from 4.8 to 6.0 kg cm^{-2} .

**Figure 8.28:**

Changes in adhesion and cohesion strengths as a function of moisture content of the cured paste [2].

**Figure 8.29:**

Changes in adhesion and cohesion strengths during plate curing and drying [2].

The change in adhesion strength is related to the formation of corrosion layer. As can be seen from Figure 8.29, it starts after the 8th hour of paste drying, when the pores are open and oxygen can enter them. Cohesion and adhesion strengths grow most rapidly between the 10th and 24th hour of drying, because by that time there is enough

moisture needed for lead oxidation and the grid surface is open to access of O_2 from the air.

There are two interesting findings in this figure that deserve special mention:

- (a) The adhesion strength is lower than the cohesion strength, which implies that the connection grid/paste may become a capacity-limiting factor.
- (b) Both adhesion and cohesion strengths increase but slowly during the second stage of paste drying. If this process is accelerated the duration of the curing procedure can be shortened.

8.3. Technology of Plate Curing

8.3.1. Air Curing

In the actual battery manufacturing practice the pallets with stacked pasted plates are not always charged into the curing chamber(s) immediately after pasting. Some smaller battery plants do not even have a curing chamber. Pasted plates are left in the air under uncontrolled conditions. The curing processes that have started in the plates during drying in the tunnel dryer (after pasting) continue. This process is known as air curing. Evaporation of water from the plates is accelerated in the tunnel dryer and the percent of moisture content of the paste decreases. Hence, oxidation of Pb is enhanced. The amount of heat released by this exothermic process increases. The temperature of the plates rises thus accelerating further water evaporation from the plates. The moisture content of the paste drops below 5% and the curing processes stop before being completed. Depending on their position in the stacks, the plates will reach different stages of curing. Hence, air cured plates yield batteries with poorer performance.

In order to slow down water evaporation from the plates during stay in the air, the pallets with stacked plates are wrapped with plastic (polyethylene) foil. Thus, a small closed space is formed which is quickly saturated with humidity and further moisture loss from the plates stops or is substantially slowed down. In the summertime, when the temperature in the production premises is relatively high, the stacked plates on the pallets are sprayed with water before being wrapped. Thus, the curing processes proceed more homogeneously across the plate stacks and in the plates themselves.

Table 8.3 illustrates the influence of curing conditions on the physico-chemical parameters and the capacity of positive plates cured by three different air curing methods [30].

With the first curing method water will evaporate from the paste most quickly and the curing process will stop at a very early stage. The degree of active mass formation and the capacity of the positive plates will be low (Table 8.3). In the second method of curing, with increase of temperature to 55 °C and RH = 80%, water evaporation from the plates will be slowed down

Table 8.3: Influence of air curing conditions on the physico-chemical parameters of cured and formed positive plates, and on capacity [30]

Curing Method	Cured Paste		Formed Plate			Capacity (Ah kg ⁻¹)
	Free Pb (%)	Porosity (%)	PbSO ₄ (%)	PbO ₂ (%)	BET Surface (m ² g ⁻¹)	
2 days, air curing	6.7	43	13.7	85.4	4.8	50
1 day, curing at 55°C, 80%RH	4.7	51	8.1	89.9	5.0	77
1 day, drying						
Plates covered with polyethylene sheet,	2.0	63	1.4	97.3	6.2	96
1 day, curing at 55 °C						
1 day, air drying						

and the curing process will advance faster in the presence of higher moisture content. Hence, the characteristics of the plates cured by the second method will improve as compared to the first one. When, however, the plates are air cured at 55 °C but in a closed hood at 100% RH, and these conditions are maintained for 24 h, the curing processes will be most advanced and these positive plates will have the most developed active mass and the highest capacity performance (Table 8.3). So the key parameters of the curing process are RH and temperature of the surrounding air and moisture content of the paste.

8.3.2. Curing in a Curing Chamber

Plate curing can be conducted under optimum conditions in a curing chamber with independent (autonomous) temperature and humidity control. In this case it is essential to devise the optimum curing algorithm (profile) for each particular plate type and size. The pre-set parameters are temperature and RH for each of the two stages: curing and drying.

With the financial support provided by the Advanced Lead-Acid Battery Consortium within the ALABC Programme of ILZRO, our team has investigated the influence of curing conditions on the performance of plates prepared with 4BS pastes or with 3BS pastes cured at 90 °C so as to convert into 4BS during plate curing. All pastes were dried under identical conditions: drying temperature 60 °C and 60% RH for 4 h, followed by drying at the same temperature but at 40% RH for another 4 h and finally, 12 h at 10% RH. PbCaSn concast grids were used. Table 8.1 summarises the pore volume, mean pore radius, BET surface area and solid phase density of cured pastes as well as the discharge current densities yielding specific capacity of 80 Ah kg⁻¹ PAM [16].

The plates described in Table 8.1 were assembled in 12V/34 Ah batteries that were set to tests at 42% utilization of the positive active mass. Beside the initial capacity at 20 h discharge rate (all batteries met the requirements of this test), the Peukert dependences for these batteries

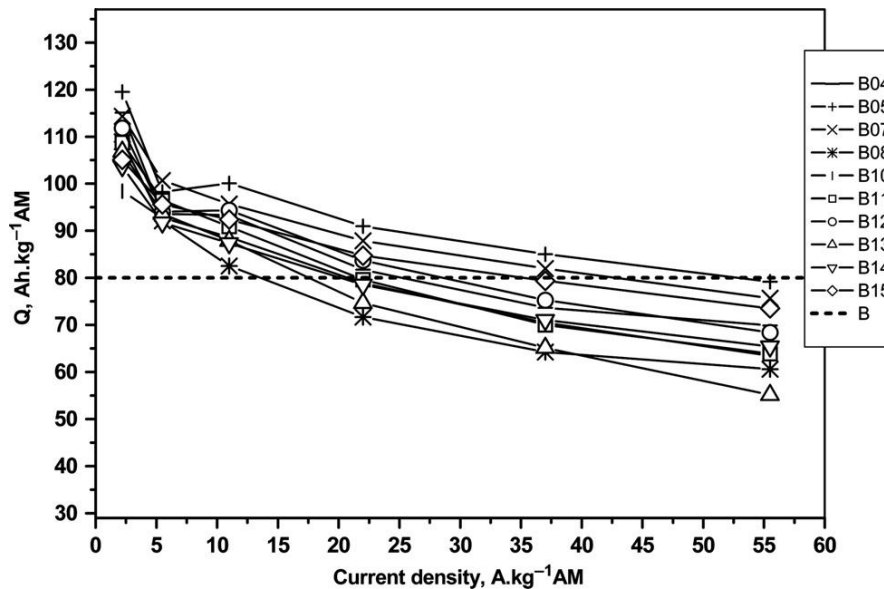


Figure 8.30:
Peukert dependences for batteries with positive plates produced by the curing methods presented in Table 8.1 [16].

were also determined. Figure 8.30 shows the Peukert dependences in terms of specific capacity delivered on battery discharge with different current densities.

It is evident from the figure that the Peukert curves differ for the different types of plates depending on the employed curing algorithm. The Peukert dependence allows for predictive assessment of the power that can be delivered by the plates, as follows: all batteries deliver a specific capacity of $80 \text{ Ah kg}^{-1} \text{ PAM}$. The latter specific capacity is delivered by the different types of batteries when discharged at different current densities, I_d . The discharge current densities, I_d , yielding specific capacity of $80 \text{ Ah kg}^{-1} \text{ PAM}$ were determined for the various batteries under test. The obtained I_d results are presented in Table 8.1 and can be used for estimating battery power output.

The above batteries were then subjected to cycling tests at 1 h discharge rate. The end-of-life criterion was $80\% C_{20}$. Figure 8.31 compares the number of cycles (i.e. battery cycle life) and the current density at $80 \text{ Ah kg}^{-1} \text{ PAM}$ for the different battery types.

The data in Fig. 8.31 give grounds for the following conclusions:

- Batteries produced with 3BS positive pastes cured at 90°C , whereby the 3BS paste converts into 4BS, have good power output performance. However, the cycle life of these batteries is shorter by about 30% than that of the batteries with 4BS pastes.
- Batteries with 4BS plates cured at 50°C and at 90°C have long cycle life, but fairly low power output.

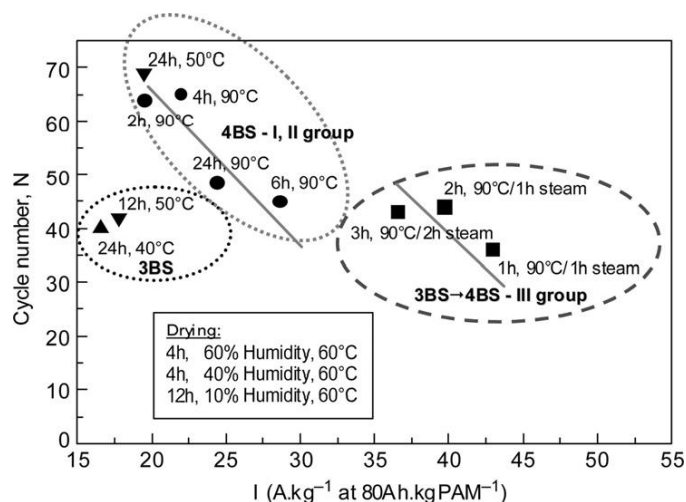


Figure 8.31:
Influence of curing schedule on battery life and power performance.

The above results provide an evidence of the influence of positive plate curing schedule on battery performance characteristics.

Curing schedules for 3BS and 4BS pastes

Plate curing algorithms should be designed for each particular paste type (3BS or 4BS) accounting for plate size and grid alloy used. The latter determines the rate of grid corrosion. When PbSb alloys are used the duration of the second (corrosion) curing stage can be shortened, as the rate of corrosion of these alloys is fairly high. PbSnCa grids are characterised by lower corrosion rate, so when such grids are used the duration of the corrosion stage should be prolonged. Curing schedules should take into account the thickness of the plates and the manner of their arrangement in the curing chamber (stacked on pallets or racked in cassettes at a distance from one another). The processes of curing depend also on the ratio between curing chamber volume and number of plates loaded to cure.

Figure 8.32 presents a model schedule for curing 3BS SLI plates and Fig. 8.33 shows an analogous scheme for curing 4BS plates. The conditions to be maintained in the curing chamber during each of the three curing stages are also given in the figures. These model curing schedules provide an example for designing working technological algorithms for plate curing.

The characteristics of the plates on completion of the curing process should be:

- moisture content $< 0.2\%$
- $Pb < 1\%$ in positive plates
- $Pb < 5\%$ in negative plates

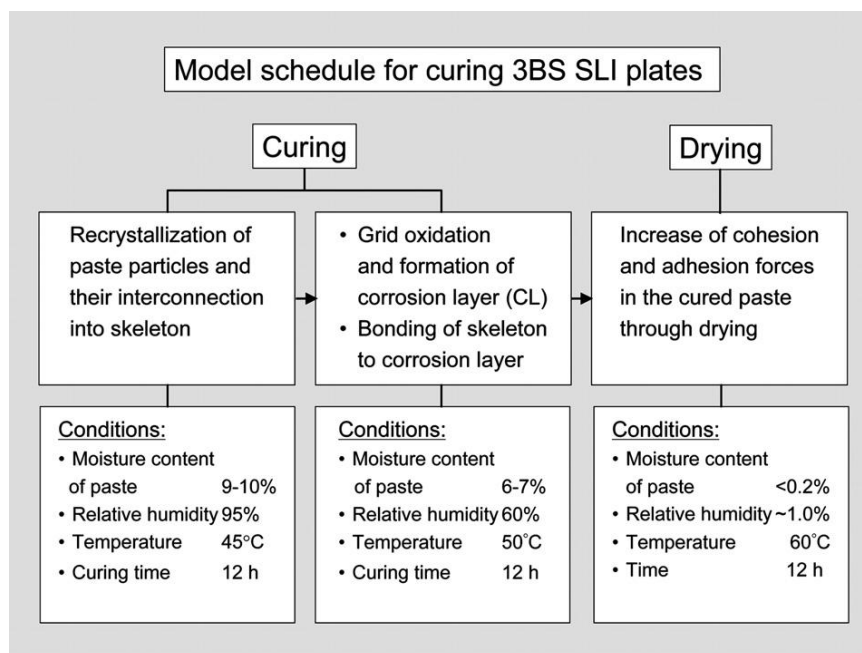


Figure 8.32:
Model curing schedule for 3BS SLI plates.

Cured plates should have no cracks and should be hard enough to endure falling from a height of 0.8 m with no shedding off or cracking of the paste.

Plate curing equipment

Typically, in battery plants, a batch-type system of curing is employed, i.e. a shift's worth of plates is loaded in large curing chambers (batch curing). Pasted plates are partially dried after pasting and then arranged in piles (stacked) on pallets. Pallets are transferred with a fork-lift to the curing chambers and arranged, horizontally or vertically, in the chamber. Sufficient vacant space should be left around the pallets to allow free air circulation. Usually, plates located in the middle of the curing chamber are heated to higher temperatures than those in the periphery (near the chamber walls). This would result in non-homogeneous curing and drying of the plates in the curing chamber. To avoid this, some free space should also be left between the pallets to allow free air circulation.

Free air circulation throughout the curing chamber is as essential as temperature and humidity for uniform curing of the plates in all parts of the chamber. Uniform distribution of air flows within the chamber is complicated by uneven loading of the chamber. Best air circulation can be achieved if air is introduced through inlets on one side of the chamber, forced to flow across its length and height and carried out of the chamber through outlet

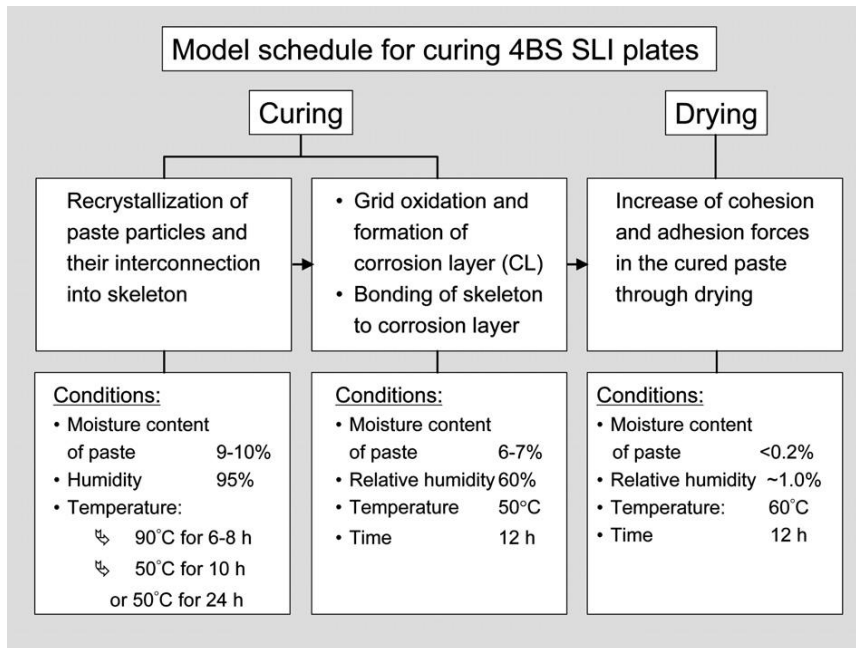


Figure 8.33:
Model curing schedule for 4BS SLI plates.

on the opposite side. In this case, air will flow almost uniformly over the pallets with stacked plates. The even distribution of air flows in the curing chamber depends also on air flow rate. Typical air flow rates for large curing chambers are 220–280 m³ per a shift's production [13]. All curing chambers have fans mounted on the ceiling of the chamber. The humidity and temperature control system is usually fixed in the air revert channels. The RH in the chamber can be increased using atomized water or steam [13]. Oxygen needed for oxidation of Pb and atomized water are supplied by introducing compressed air. Heating is switched on when the temperature in the curing chamber drops below the pre-set value and during the subsequent drying step. Air temperature and humidity levels should be controlled independently. Curing programs (algorithms) should also account for the level of plate loading and for the types of plates and their arrangement in the chamber.

Methods to accelerate the plate curing process

Plate curing is one of the slowest procedures in the technology of battery plate manufacture. Methods are looked for to accelerate this process to rates commensurable with those of the other automated technological processes. In his analysis of curing, Glascock [31] points out that plate stacking in piles and arrangement of these piles on large pallets (batch curing) is

the main reason for the long duration of curing and drying. Various methods have been proposed to accelerate the curing process as for example:

- Pasted plates do not pass through a tunnel flash dryer. They are arranged vertically in cassettes with a small distance between them. The free access of air to all plates facilitates substantially all curing and drying processes.
- Cassettes are arranged at a distance from one another and these cassettes are loaded in a curing chamber. The US company General Thermal, Inc. (Concure System) and the German company Muenstermann arrange the cassettes vertically in the curing chamber so as to save production space.

It is important to ensure continuous control of the following parameters in the curing chamber during plate curing and drying:

- RH of the air in the chamber.
- Temperature of the air in the curing chamber. Oxidation of Pb to PbO is an exothermic process and the released heat keeps up the temperature of plates higher than that of the air in the chamber. The magnitude of this temperature difference depends on the amount of free Pb in the paste.
- Rate, RH and oxygen content of incoming and outgoing air flows in the different zones of the curing chamber.

Trials of the above mentioned variants of curing and drying have reduced the overall time for plate curing and drying to 12 h for thin SLI plates [31] and to 24 h for thicker plates.

References

- [1] J.R. Pierson, in: D.H. Collins (Ed.), *Power sources 2*, Pergamon Press, London, UK, 1970, p. 103.
- [2] M.E.D. Humphreys, R. Taylor, S.C. Barnes, in: D.H. Collins (Ed.), *Power sources 2*, Pergamon Press, London, UK, 1970, p. 55.
- [3] C.S. Lakshmi, J.E. Manders, D.M. Rice, *J. Power Sources* 73 (1998) 23.
- [4] S. Fouache, A. Charbol, *J. Power Sources* 78 (1999) 12.
- [5] D. Pavlov, G. Papazov, *J. Appl. Electrochem.* 6 (1976) 339.
- [6] D. Pavlov, N. Kapkov, *J. Electrochem. Soc.* 137 (1990) 21.
- [7] H.W. Billhard, *J. Electrochem. Soc.* 117 (1970) 690.
- [8] C.W. Fleischman, W.J. Schlöter, *J. Electrochem. Soc.* 123 (1976) 969.
- [9] J. Burbank, *J. Electrochem. Soc.* 113 (1966) 10.
- [10] R. De Marco, A. Rochliadi, J. Jones, *J. Appl. Electrochem.* 31 (2001) 953.
- [11] B.A. Thompson, R.L. Strong, *J. Phys. Chem.* 67 (1963) 594.
- [12] N. Yamasaki, Jia-jun Ke, *J. Power Sources* 36 (1991) 95.
- [13] E.S. Napoleon, *J. Power Sources* 19 (1987) 169.
- [14] N. Duc. Hung, J. Garche, K. Wiesener, *J. Power Sources* 17 (1986) 331.
- [15] D.A.J. Rand, R.J. Hill, M. McDonagh, *J. Power Sources* 31 (1990) 203.
- [16] D. Pavlov, M. Dimitrov, T. Rogachev, L. Bogdanova, *J. Power Sources* 114 (2003) 137.
- [17] D. Pavlov, S. Ruevski, *J. Power Sources* 95 (2001) 191.

- [18] S. Grugeon-Dewaele, J.B. Leuche, J.M. Tarascon, A. Delahaye, L. Torcheux, J.P. Vaurijoux, F. Henn, A. de Guibert, J. Power Sources 64 (1997) 71.
- [19] L. Torcheux, J.P. Vaurijoux, A. de Guibert, Proceedings of LABAT'96 Conference, Varna, Bulgaria, 1996, p. 153.
- [20] S. Laruelle, S. Grugeon-Dewaele, L. Torcheux, A. Delahaye-Vidal, J. Power Sources 77 (1999) 83.
- [21] D.P. Boden, in: D.H. Collins (Ed.), Power sources-2, Pergamon Press, London, UK, 1970, p. 66.
- [22] J.P. Hoare, The electrochemistry of oxygen, John Wiley & Sons, New York, 1968, p. 124.
- [23] L. Bouirden, J.P. Hilger, J. Hertz, J. Power Sources 33 (1991) 27.
- [24] R.D. Prengaman, J. Power Sources 95 (2001) 224.
- [25] Ph. Steyer, J. Steinmetz, J.P. Hilger, J. Electrochem. Soc. 154 (1998) 3183.
- [26] R. Lindner, H.N. Terem, Arkiv from kemi 7 (1954) 31; 273.
- [27] R.A. Thompson, R.L. Strong, J. Phys. Chem. 67 (1963) 594.
- [28] D. Pavlov, Electrochim. Acta 23 (1978) 845.
- [29] H. Bode, in: R.J. Brodd, K. Kordesch (Eds.), Lead-acid batteries, John Wiley, Electrochem. Soc., New York, USA, 1977, p. 243.
- [30] A. Sahari, L. Zerroual, J. Power Sources 32 (1990) 407.
- [31] Battle Glascock, Batteries International, April 1998, 43.

Plate Formation

This page intentionally left blank

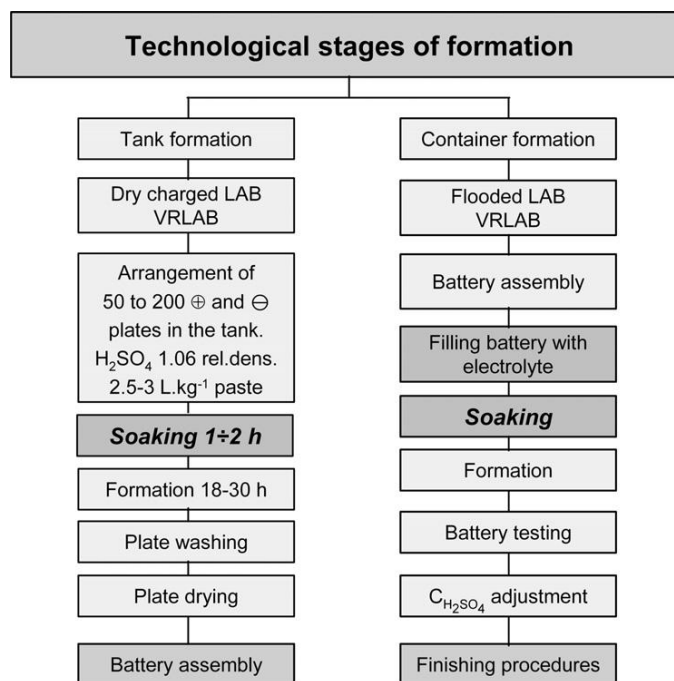
Soaking of Cured Plates Before Formation

9.1. Technological Procedures Involved in the Formation of Lead–Acid Battery Plates

The cured pastes of both positive and negative plates comprise identical mixtures of bivalent lead compounds (3BS, 4BS, PbO, Pb), which cannot create electromotive forces when the pasted plates are assembled into cells. The purpose of the technological process of formation is to convert the cured pastes into electrochemically active porous materials: PbO₂ in the positive plates and Pb in the negative plates, which are connected mechanically and electrically to the grids. The process of formation can be conducted via two basic technological schemes.

Figure 9.1 presents the technological steps involved in the two types of formation processes: tank formation and container (jar) formation.

- (a) *Tank formation* is used for the production of dry-charged and VRLA batteries. In this technological process, 50–200 single or coupled positive and negative cured plates are arranged in a tank containing H₂SO₄ solution of 1.06 rel. dens. Plates of similar polarity are connected to each other. The amount of electrolyte is calculated on the basis of 2.5–3 L of electrolyte per 1 kg of dry paste. The plates are left to soak in this solution for 1–2 h and then the current is switched on for the formation proper to start. The formation temperature is monitored and controlled within the range from 25 to 50 °C. For the conventional technology, the formation current varies between 0.7 and 2.5 mA cm⁻² throughout the different stages of the formation process. The duration of this formation process is from 48 to 72 h for traction battery plates and from 18 to 30 h for SLI battery plates. The quantity of electricity that flows through the plates is between 1.7 and 2.3 times the theoretical capacity of the plates. On completion of the formation procedure, the plates are taken out of the tank, rinsed with water to remove the H₂SO₄ and dried under appropriate conditions. Negative plates are dried either in oxygen free atmosphere or under vacuum. Then, positive and negative plates with separators between them are assembled into dry-charged batteries. This technology is employed for manufacture of batteries with more than 6 months of storage time before exploitation.
- (b) *Container (jar) formation* is used mainly for the production of SLI batteries to be put into operation within 6 months after their production date. These may be flooded or VRLA batteries. In the jar formation process, cured positive and negative plates,

**Figure 9.1:**

General scheme of the procedures involved in the technological process of formation of lead–acid batteries.

with separators between them, are assembled into ‘plate groups’, which are then placed in the battery containers. For VRLA batteries with absorptive glass mat (AGM) separators, the plate groups should be compressed to a definite pressure and then fastened with polymer tapes before the insertion into the battery containers (for both traction and stationary cells). If the cells are small and the container is designed to maintain the required compression, the plate groups are placed in the containers without fastening. The next step is to fill the containers with electrolyte. This is a rather delicate procedure for VRLA batteries with AGM separators or gelled electrolyte. After a period of 1 to 2 h of soaking, the battery is connected to the power source and formation proper starts. The batteries are then tested, recharged, the electrolyte concentration is adjusted, if necessary, and after some finishing procedures the batteries are ready for sale and use.

In this chapter we will discuss the processes that take place during soaking. This is the first stage of the technological process of formation, during which reactions of sulfation and hydration proceed in the plates, which affect the subsequent formation processes.

9.2. H_2SO_4 Electrolyte During Soaking and Formation

9.2.1. Concentration of H_2SO_4 Solution During Soaking and Formation

As the amount and concentration of H_2SO_4 solution play an important role in the soaking and formation processes, we will start with a short overview of these technological parameters for the different types of formation (Fig. 9.2).

Tank formation is usually conducted in H_2SO_4 solutions with concentrations between 1.05 and 1.08 rel. dens., most often 1.06 rel. dens. What is the criterion for selecting the appropriate acid concentration?

Since H_2SO_4 reacts with the lead oxides and basic sulfates in the paste, its concentration decreases. The lower acceptable limit of H_2SO_4 concentration is 1.025 rel. dens., so when selecting the number of plates to be loaded in the formation tank, the above parameter should be taken into account. Usually, 2.5–3 L of electrolyte with 1.06 rel. dens. are used per 1 kg of dry paste.

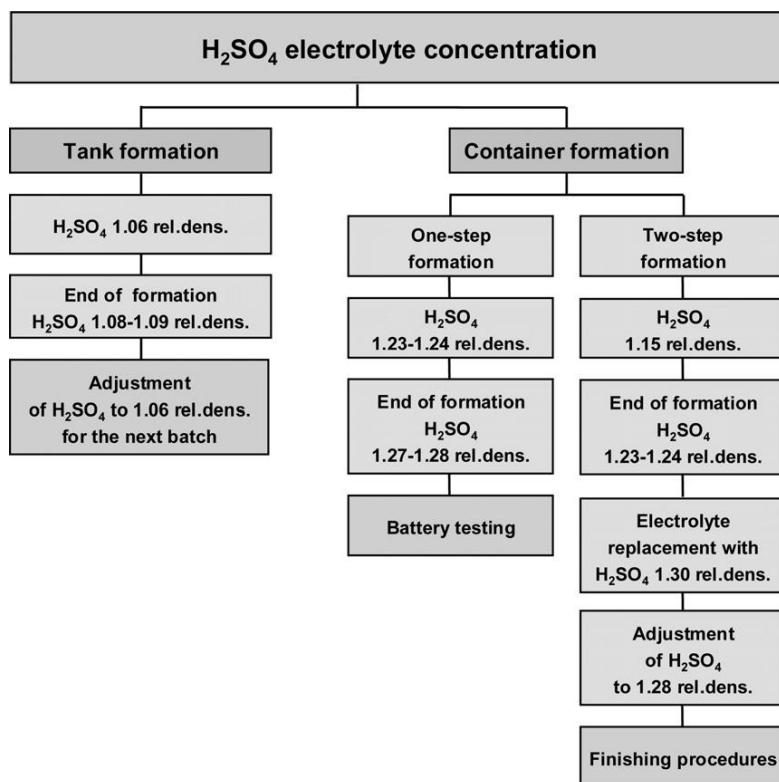


Figure 9.2:
Concentration of H_2SO_4 formation electrolyte.

The second important technological parameter is the temperature in the formation tank, which should not exceed 50 °C nor fall down below 15 °C. The optimum temperature range for the soaking and formation steps is between 25 and 50 °C.

The H₂SO₄ used for paste preparation is released from the plates during formation, as a result of which the electrolyte concentration increases to 1.08–1.09 rel. dens. at the end of the formation process. Hence, it is necessary to adjust the concentration of the H₂SO₄ solution in the formation tank before charging the next batch of plates into the tank. As part of the electrolyte is carried away with the plates when taken out of the tank, it is necessary to add water in order to maintain the electrolyte level in the tank. This additional water dilutes the electrolyte and the acid concentration decreases. The actual decrease in H₂SO₄ concentration in the tank depends on its balance with the H₂SO₄ released by the plates during formation. In any case, the acid concentration in the tank should be adjusted to the starting level of 1.06 rel. dens. before the next batch of plates is immersed in the tank for formation.

In the container (jar) formation process there are two options depending on the electrolyte used: one-step formation and two-step formation. In the one-step formation process, batteries are filled with H₂SO₄ electrolyte with 1.23–1.24 rel. dens., which increases to 1.27–1.28 rel. dens. at the end of the formation process. This is the acid concentration of normal battery operation. Then the batteries are tested and, after some finishing procedures, are ready for use.

In the two-step formation process, batteries are filled with H₂SO₄ of 1.15 rel. dens. and set to formation. At the end of the formation process the acid concentration rises to 1.23 rel. dens. Then this electrolyte is poured out of the batteries and replaced with acid solution of 1.30 rel. dens. This solution is diluted by the residual electrolyte in the plates and separators, and its concentration eventually reaches values of 1.28–1.27 rel. dens.

The question arises as to which formation method to choose?

Figure 9.3 shows the dependence of the content of α -PbO₂ in PAM as a function of electrolyte relative density during soaking and formation [1]. It is evident from the figure that PAM contains between 45 and 55% α -PbO₂ when battery soaking and formation are conducted in electrolytes of 1.14–1.15 rel. dens. The proportion β/α -PbO₂ in the formed plates should be equal to or a bit higher than 1:1 for the battery to have high capacity and long cycle life. Figure 9.3 shows also that the initial capacity of the batteries is above 90% when soaking and formation are conducted in H₂SO₄ electrolyte with concentration lower than 1.15 rel. dens. At this acid concentration the efficiency of the formation process is high. To achieve this, however, the two-step formation process should be used, which is more expensive and involves some unattractive technological procedures. So the choice of formation process to be employed is actually a choice between battery price and performance.

For VRLA batteries tank formation is preferred to jar formation (Fig. 9.4). The latter formation process should not be used for tall VRLA batteries, for battery applications requiring long

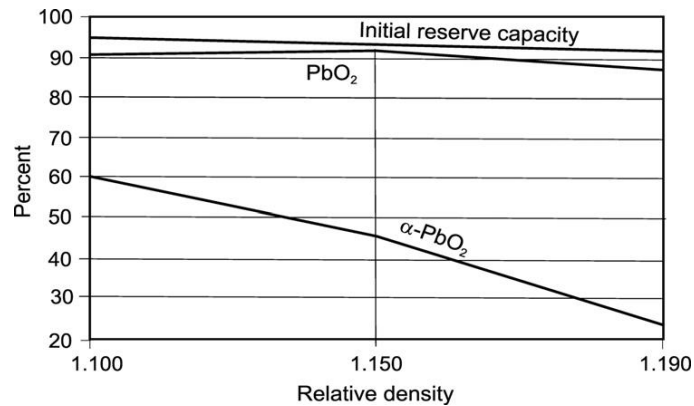


Figure 9.3:

Content of α -PbO₂ in PAM and initial battery capacity as a function of electrolyte relative density during soaking and formation [1].

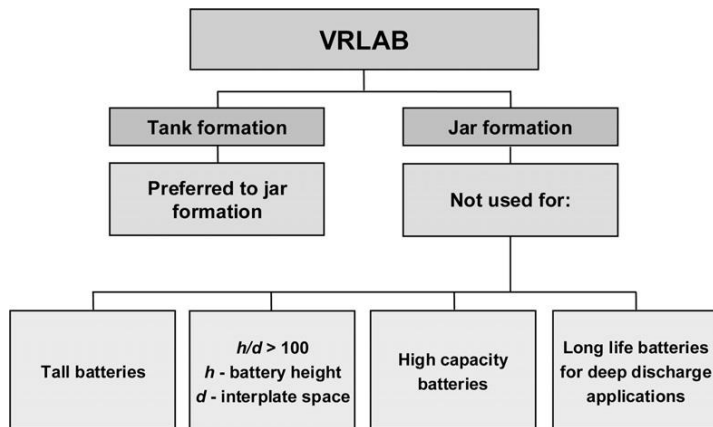


Figure 9.4:

Formation options preferred for VRLA batteries.

cycle life and high capacity performance, as well as for battery designs in which the ratio between cell height and inter-plate distance (i.e. thickness of the AGM separator) is greater than 100 [2].

9.2.2. Electrolyte Filling Process for Container Formation of Flooded and VRLA Batteries

Since the plate groups in VRLAB are under compression, filling with electrolyte is a rather delicate process in two aspects. First, addition of acid solution initiates exothermic chemical reactions which result in heat generation and the temperature in the cells rises rapidly. During

the soaking step, the temperature may exceed 60 °C, which is undesirable. The second critical moment in the jar formation process is that during the curing procedure, the plates undergo partial carbonization and the obtained lead hydrocarbonate reacts with H_2SO_4 , whereby CO_2 gas is released. This intense gassing should be taken into account when filling the cells (batteries) with electrolyte.

The efficacy of the filling process depends on the following parameters:

- (a) *Pore system in AGM and plates.* Both plates and AGM separators have a porous structure. The transport of H_2SO_4 solution through the pores is strongly impeded. It depends on the total pore volume and the pore-size distribution by radius as well as on the hydrophilicity of pore walls, in both AGM separators and plates.
- (b) *Plate-group design and dimensions.* A very important design parameter is the ratio between plate height (h_p) and separator thickness (d_{AGM}) [2]. For $h_p/d_{\text{AGM}} < 50$, filling the plate group with electrolyte is easy. If this ratio is between 50 and 100, there are some difficulties with filling and the process is strongly impeded at ratios between 100 and 200. At ratios greater than 200, the access of H_2SO_4 solution to some parts of the plate group may be blocked and hence ‘dry zones’ may be formed.
- (c) *Phase composition of cured paste.* The heat released by the reactions of sulfation causes the temperature of the plate group to rise. As the acid concentration is not the same in all parts of the plate group, the temperature in the different zones will also be different. In some zones, it may rise so much that water vapour may form. Through heat exchange between the different zones in the plate group, and between the plate group and the surrounding medium, the temperature will be equalised after a certain period of time (0.5–1.0 h). The rates of the above reactions of sulfation are most often reduced by cooling the H_2SO_4 solution to temperatures between 0 °C and 10 °C before pouring it into the cells. In order to maintain the temperature in the battery below 50 °C, batteries are immersed in baths full of cold water. The water baths have high heat capacity and hence the heat exchange between battery and water in the bath proceeds at a high rate.

The most widely used filling techniques are presented in Fig. 9.5.

Gravity filling (top or bottom-up), which is a multi-step procedure, is fairly slow and takes about 10–30 min. This method can be used for filling VRLAB with a ratio between cell height and inter-plate distance smaller than 50. The second method for filling cells with electrolyte is the *vacuum method*. There are two modifications of this method. ‘Soft vacuum’ filling, when a vacuum of 20 mm Hg column is applied in combination with push/pull steps. This method allows the filling procedure to be completed within 1–2 min. The second modification is the ‘hard vacuum’ filling method, where the applied vacuum is lower than 10 mm Hg column. Both filling methods cause intense heat generation, because all pasted plates get immediately in contact with the H_2SO_4 solution and the exothermic reactions of

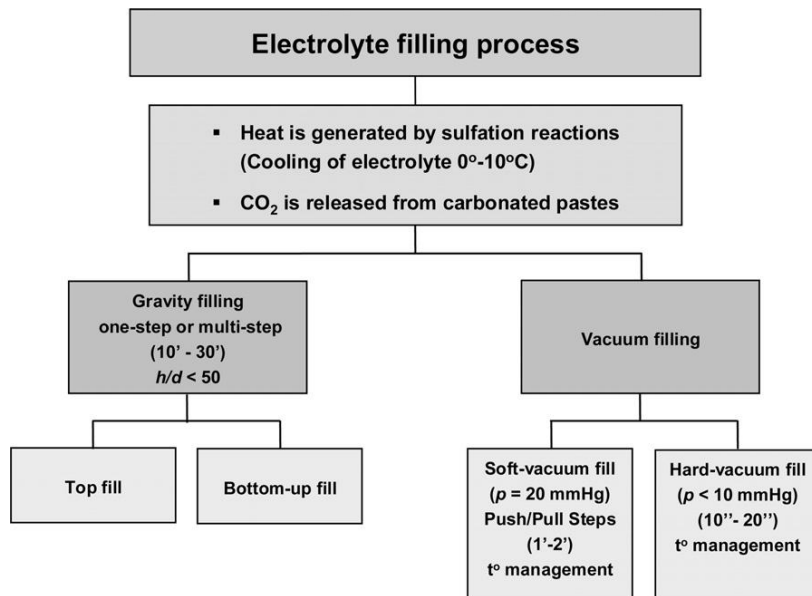


Figure 9.5:
Electrolyte filling techniques.

sulfation proceed at a high rate throughout the cured pastes of all plates. Hence, both these methods require thermal management.

VRLA cells are filled with H₂SO₄ electrolyte until a layer of electrolyte is formed over the plate groups. On completion of the formation process, the excess solution is removed from the cells. A mirror-like electrolyte surface, interrupted only by the tops of the separators, forms in the plate group. This corresponds to 100% saturation of the AGM separator with electrolyte. At the beginning of cycling, the oxygen cycle operates with low efficiency, which leads to water loss. When the electrolyte saturation drops below 96%, the efficiency of the oxygen cycle increases thus reducing water loss. When considerable part of the water in the electrolyte has decomposed, water should be added to the cells, if possible, to compensate for the loss.

9.3. Processes During Soaking of 3BS Cured Plates

9.3.1. Changes in Chemical and Phase Composition of the Paste and in H₂SO₄ Concentration During Soaking

After flooding the cured plates with H₂SO₄ solution in the battery container (for jar formation) or immersing the plates into the tank filled with H₂SO₄ solution (for tank formation), reactions proceed between H₂SO₄ and the cured paste as a result of which new solid phases are formed at both plate surfaces.

A study has been conducted for the chemical processes that take place on soaking 3BS cured pastes in three H_2SO_4 solutions of different relative densities [3]. In these investigations, 1.425 g of cured paste (both positive and negative) reacts with 1 cm^3 of electrolyte. The changes in chemical and phase composition of 3BS pastes, when soaked in H_2SO_4 solutions of 1.05, 1.15 and 1.25 rel. dens., have been studied. The resulting changes in electrolyte rel. dens. are shown in Fig. 9.6. The highest rate of sulfation is observed during the first hour of soaking.

The changes in PbO and PbSO_4 content in the paste (determined by wet chemical analysis) during soaking of positive plates are presented in Fig. 9.7. Similar changes in chemical composition have also been observed with the negative plates. After 8 h, the amount of PbSO_4 in the positive paste increases by 22, 47 or 60% for acid solutions of 1.05, 1.15 or 1.25 rel. dens., respectively.

The cured paste contains $\alpha\text{-PbO}$ (tetragonal), $\beta\text{-PbO}$ (orthorhombic) and 3BS. During soaking, $\text{PbO}\cdot\text{PbSO}_4$ (1BS) and PbSO_4 are formed. The changes in intensity of the characteristic X-ray diffraction lines for these phases on soaking are shown in Fig. 9.8. During the first 15 min, the content of $\alpha\text{-PbO}$ and 3BS decreases rapidly. The reaction between $\beta\text{-PbO}$ and H_2SO_4 is strongly impeded. This is not the case with $\alpha\text{-PbO}$, which reacts readily with H_2SO_4 .

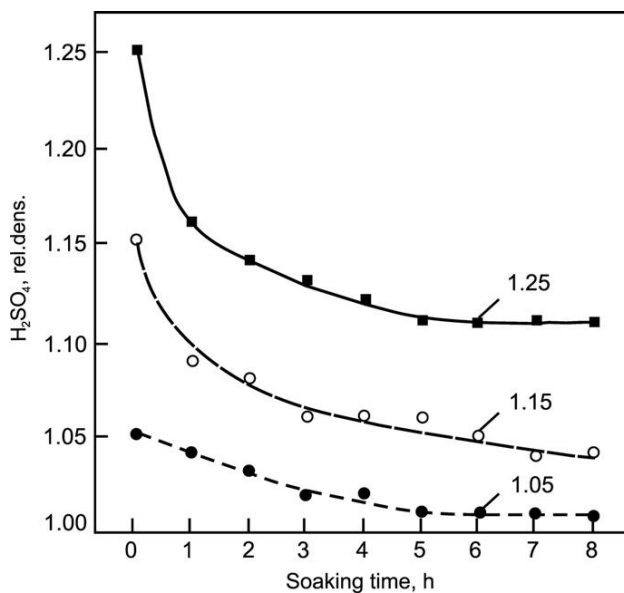
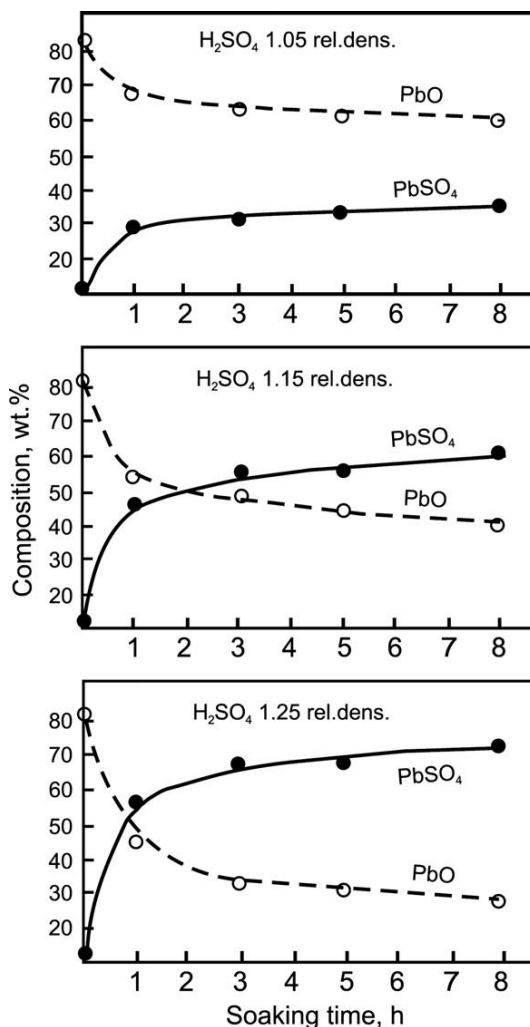


Figure 9.6:

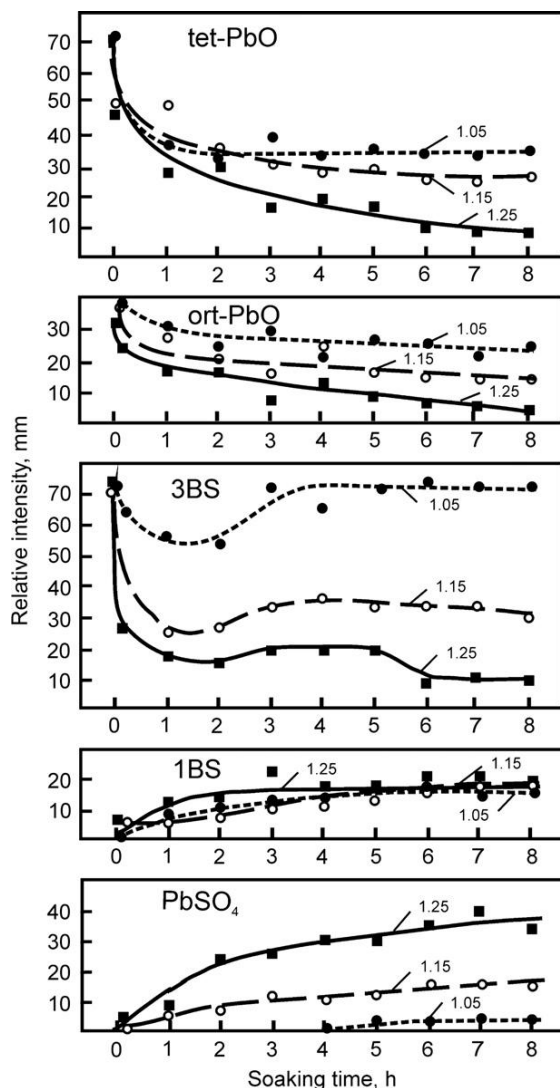
Changes in electrolyte concentration of cells during soaking in 1.05, 1.15 or 1.25 rel. dens. H_2SO_4 solution [3].

**Figure 9.7:**

Changes in chemical composition of cured positive plates during soaking in H_2SO_4 solution of 1.05, 1.15 or 1.25 rel. dens. [3].

On soaking in H_2SO_4 of 1.05 rel. den., the principal crystal products of sulfation are 1BS and 3BS, with small amounts of $PbSO_4$ formed after 4 h of soaking. 1BS is formed at the beginning of soaking and the 3BS phase 1–2 h later. The higher the H_2SO_4 concentration, the greater the amount of $PbSO_4$ formed in the paste.

Figure 9.9 presents electron micrographs of paste crystals after 1 and 3 h of soaking in H_2SO_4 solution of 1.05 rel. den. [3]. The paste structure at the plate surface and in its interior is examined.

**Figure 9.8:**

Changes in relative intensity of characteristic XRD lines for different phases in pastes during soaking in 1.05, 1.15 or 1.25 rel. dens. H₂SO₄ solution. PbSO₄, 1BS and some 3BS are formed during soaking [3].

Needle-like crystals, typical of 1BS, form at the plate surface during the first hour of soaking. The 1BS crystals in the plate interior are much smaller in size. After 3 h of soaking, small prismatic crystals characteristic for 3BS are also observed.

Figure 9.10 presents micrographs of a paste soaked in H₂SO₄ solution of 1.25 rel. den. [3]. Needle-like 1BS crystals are detected at the surface of the plate only during the first hour.

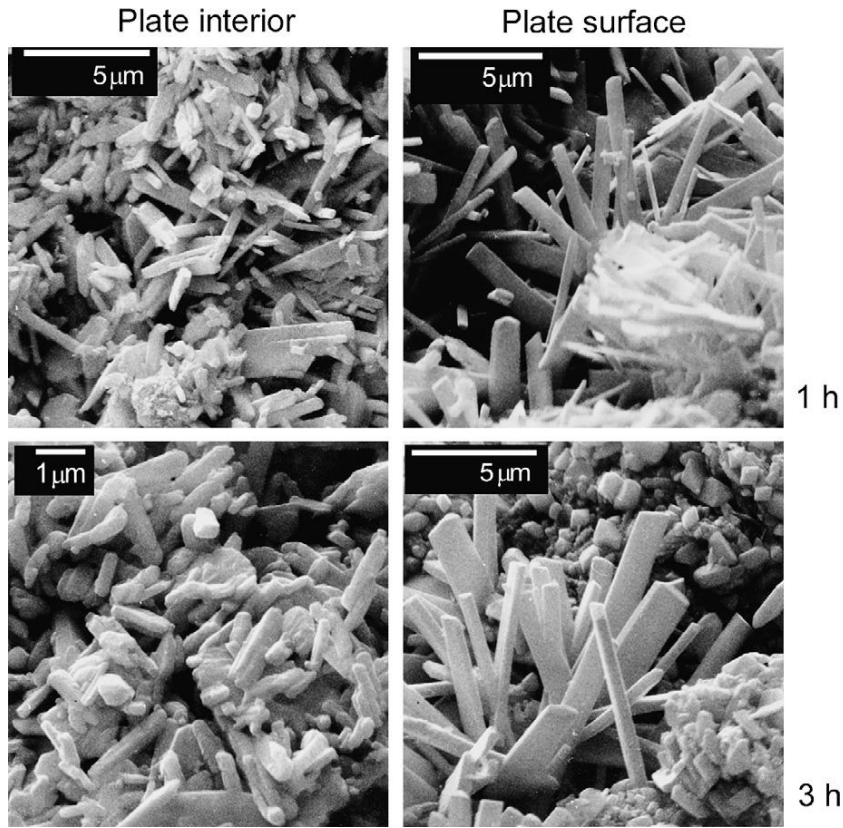


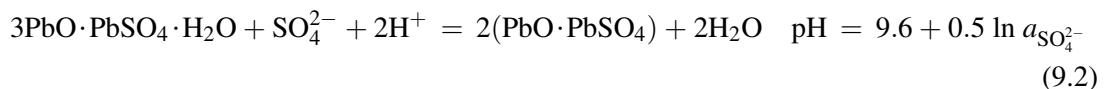
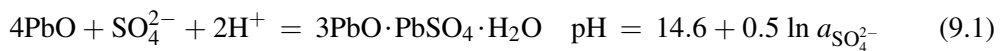
Figure 9.9:

SEM micrographs of paste structure and crystal morphology at the surface and in the interior of a plate soaked in H_2SO_4 solution of 1.05 rel. den.

These crystals disappear after 3 h of soaking and are converted into well-pronounced PbSO_4 crystals. Shapeless particles and amorphous mass are formed in the plate interior, which recrystallize later into well-shaped PbSO_4 crystals.

The data in Figs. 9.6 and 9.7 indicate that, despite the presence of PbO and H_2SO_4 , the reaction between them proceeds at a very low rate after the first hour of soaking.

The chemical processes that take place during soaking of the plates result in sulfation of the basic lead sulfates and of PbO as follows:



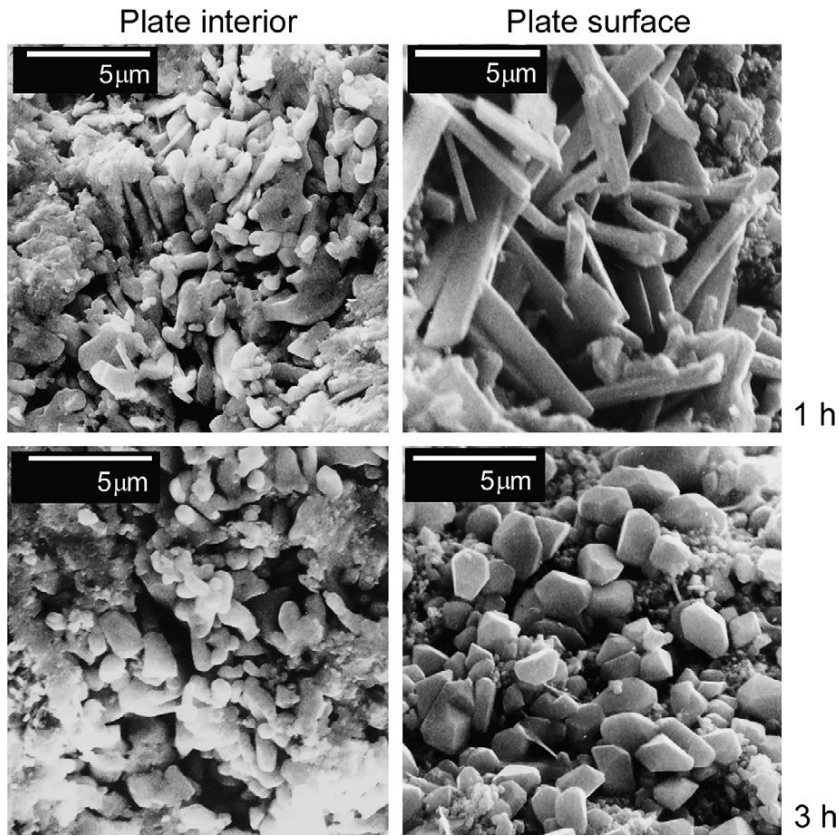
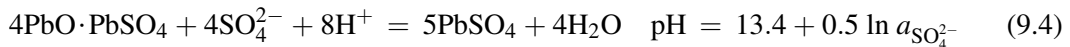
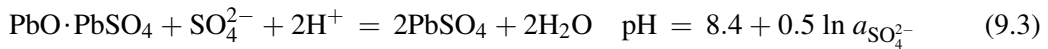


Figure 9.10:

SEM micrographs of paste structure and crystal morphology at the surface and in the interior of a plate soaked in H_2SO_4 solution of 1.25 rel. den.



The above reactions start at the two surfaces of the plates and form two zones rich in PbSO_4 , which grow towards the core of the plate. Cured pastes are yellow in colour (basic lead sulfates and PbO), while sulfated zones are grey. This difference in colouring allows easy determination of the growth rate of sulfate zones towards the plate interior. The rate of movement of the reactions of sulfation (V_{sul}) into the bulk of the cured paste depends on the following parameters:

$$V_{\text{sul}} = f(\text{CH}_2\text{SO}_4, T, C_{\text{paste}}, d, l, \text{H}_2\text{SO}_4/\text{PbO})$$

where T is the temperature; C_{paste} is the phase composition of the paste; d is the density of the cured paste; l is the thickness of the plate; $\text{H}_2\text{SO}_4/\text{PbO}$ is the acid-to-oxide ratio and PbO is the amount of free and bonded PbO .

9.3.2. Zonal Processes During Plate Soaking Forming Different Sub-Layers Across the Plate Thickness [4]

Figures 9.6–9.8 evidence that reactions of sulfation proceed most quickly within the first hour of soaking. After that, the rate of sulfation declines substantially and even after 8 h of soaking in the most concentrated H_2SO_4 solution considerable amounts of α - and β - PbO , and 3BS remain un-reacted, despite the presence of un-reacted H_2SO_4 . During the first hour of soaking, the structures formed in the plates impede both the contact of PbO and 3BS with H_2SO_4 , and the movement of H_2SO_4 inside the plate.

Figure 9.11 presents micrograph through the cross-section of a plate prepared with 3BS paste after soaking in 1.06 rel. dens. H_2SO_4 for 4 h. Three layers or zones can be distinguished which differ in colour [4]:

- A — outer layer: dark grey in colour; close to the plate surface contacting the electrolyte;
- B — intermediate layer: grey coloured with sporadic light spots;
- C — central layer (zone): light grey in colour with a great number of relatively large white spots; in the centre of the plate.

The above layered structure of the cross-section of soaked plates must be due to different chemical processes and different reaction products formed in the different parts across the plate thickness. These products can be identified by SEM examination of segments (fractions) of the above plate layers (zones) at higher magnifications.

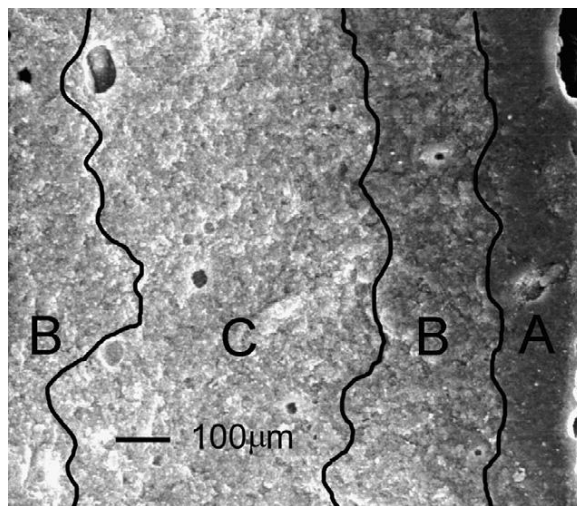


Figure 9.11:

Plate layers with different density and different chemical composition after soaking: (A) layer rich in PbSO_4 ; (B) intermediate layer; (C) central layer of un-reacted paste [4].

A – Outer layer[4]

Figure 9.12 shows a SEM picture of the outer layer A close to the plate surface contacting the bulk of electrolyte after 4 h of soaking in 1.10 rel. dens. H_2SO_4 solution. This layer consists of PbSO_4 crystals and residual un-reacted paste particles. PbSO_4 crystals differ in size. The big crystals have well pronounced walls, edges and apexes. Such well-shaped crystals may be formed as a result of recrystallization processes. The prolonged time of soaking facilitates recrystallization of PbSO_4 and formation of 1–1.5 μm sized PbSO_4 crystals. Crystals of the above size do not impede the reactions of PAM formation.

B – Intermediate layer [4]

Penetrating into the pores of the cured paste, H_2SO_4 flows react with PbO and 3BS forming PbSO_4 and 1BS (Fig. 9.8), and H_2O (eqn. (9.1)–(9.4)). Hence, part of H_2SO_4 is consumed and its concentration in the pore solution decreases.

As evident from the above reactions, water is produced as a result of paste sulfation. This water dilutes further the H_2SO_4 solution in the pores of the A and B layers. Thus, the pH of the solution filling the pores increases in the inner plate parts and a neutral zone may be formed in the plate interior. This would lead to onset of reactions of hydration of PbO and $3\text{PbO} \cdot \text{PbSO}_4$ crystals, and to formation of $\text{Pb}(\text{OH})_2$, $3\text{Pb}(\text{OH})_2 \cdot \text{PbSO}_4 \cdot \text{H}_2\text{O}$ and $\text{Pb}(\text{OH})_2 \cdot \text{PbSO}_4$.

Figure 9.13 presents SEM micrographs of the structure of the B layer in the paste after soaking and the morphology of its particles. After hydration, compounds of the type $3\text{Pb}(\text{OH})_2 \cdot \text{PbSO}_4 \cdot \text{H}_2\text{O}$ and $\text{Pb}(\text{OH})_2$ interact with each other as a result of which the boundaries

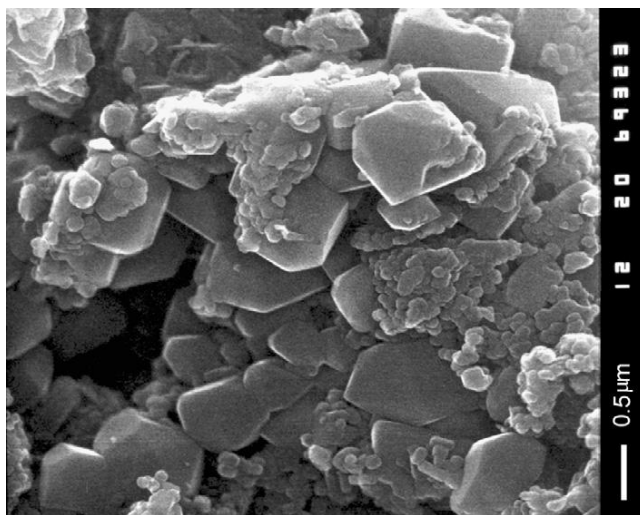


Figure 9.12:
Structure of outer plate layer a and morphology of PbSO_4 crystals.

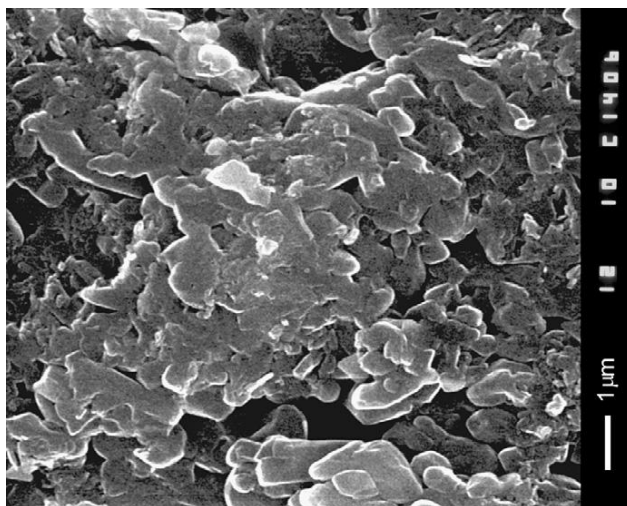


Figure 9.13:

Microstructure of the intermediate plate layer B containing hydrated and crystalline particles.

between the individual particles may disappear, completely or partially (Fig. 9.13). Thus, beside the crystal zones, also lead hydroxide and hydrated lead sulfate zones are formed in the particles and agglomerates. It can be expected that the partly hydrated compounds will be a bit larger in volume than crystal basic lead sulfates and, consequently, the total pore volume will decrease and the mean pore radius will be reduced; small pores will disappear and the radii of the larger ones will decrease. This is actually observed in Fig. 9.13.

Figure 9.14 presents SEM pictures of the structure of the intermediate layer evidencing advanced sulfation. It can be seen that the walls of the large pore have undergone sulfation. A membrane layer of PbSO_4 crystals has formed which impedes access of H_2SO_4 to the interior of 3BS and PbO particles and agglomerates, and thus stops their further sulfation. The slower sulfation rate in the *B* and *C* layers manifests in changes of the H_2SO_4 concentration (Fig. 9.6.) and of the chemical and phase composition (Figs. 9.7 and 9.8) after the first hour of soaking.

In some plate regions, thin needle-like particles are formed. They look very much like 1BS crystals (maybe their hydrated species). Such a structure of the intermediate layer is presented in Fig. 9.14b (right hand and bottom parts). The mono-basic lead sulfate crystals are formed within a definite pH interval between the pH regions for PbSO_4 and 3BS formation. The solution in the pores of the *B* layer where these needle-like particles are formed has probably a pH corresponding to the 1BS pH region.

C — Central layer (zone) [4]

Figure 9.15 shows SEM micrograph featuring the structure and crystal morphology of the cured paste in the central *C* zone of the plate after 2 h of soaking in H_2SO_4 solution of

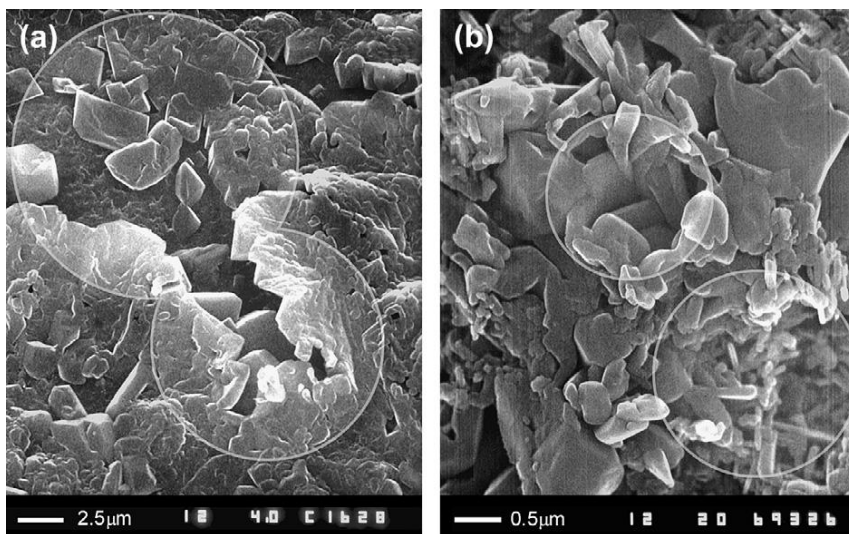


Figure 9.14:

Sulfation of lead hydroxides, lead hydroxy-sulfate *B* layer. (a) PbSO_4 crystals (encircled) are formed on the surface of the large pore in the lead hydroxy-sulfate agglomerate; (b) small 1BS crystals can be seen in the right hand bottom part of the picture [4].

1.06 rel. den. Most of the 3BS particles have remained unaffected by the processes of hydration and sulfation. However, bonding of the particles has started at some sites and the first aggregates with hydrated surface can be seen. Some of them have incorporated a couple of particles and have reached sizes of 1–2.5 μm .

Tribasic lead sulfate ($3\text{PbO} \cdot \text{PbSO}_4 \cdot \text{H}_2\text{O}$) contains water in its molecule. On heating the paste samples during the differential thermal gravimetric (DTG) measurements, this water evaporates and the samples lose weight.

Figure 9.16 presents the obtained DTG curves giving the differential weight losses on temperature increase for the outer (*A*), intermediate (*B*) and central (*C*) layers of paste samples taken after 1 and 4 h of soaking in H_2SO_4 of 1.06 and 1.25 rel. den.

The following conclusions can be drawn from Figure 9.16:

- The DTG curve for the 3BS paste immediately after curing features a high low-temperature (200–300 $^{\circ}\text{C}$) and a small high-temperature (300–400 $^{\circ}\text{C}$) characteristic peaks. Within the former temperature interval two peaks can be distinguished clearly: at 240 $^{\circ}\text{C}$ and at 270 $^{\circ}\text{C}$. These peaks are indicative of different types of water bonding in the 3BS particles of the paste.

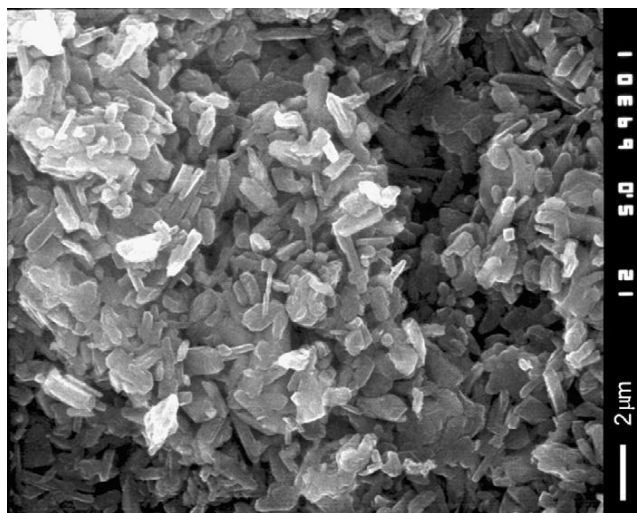


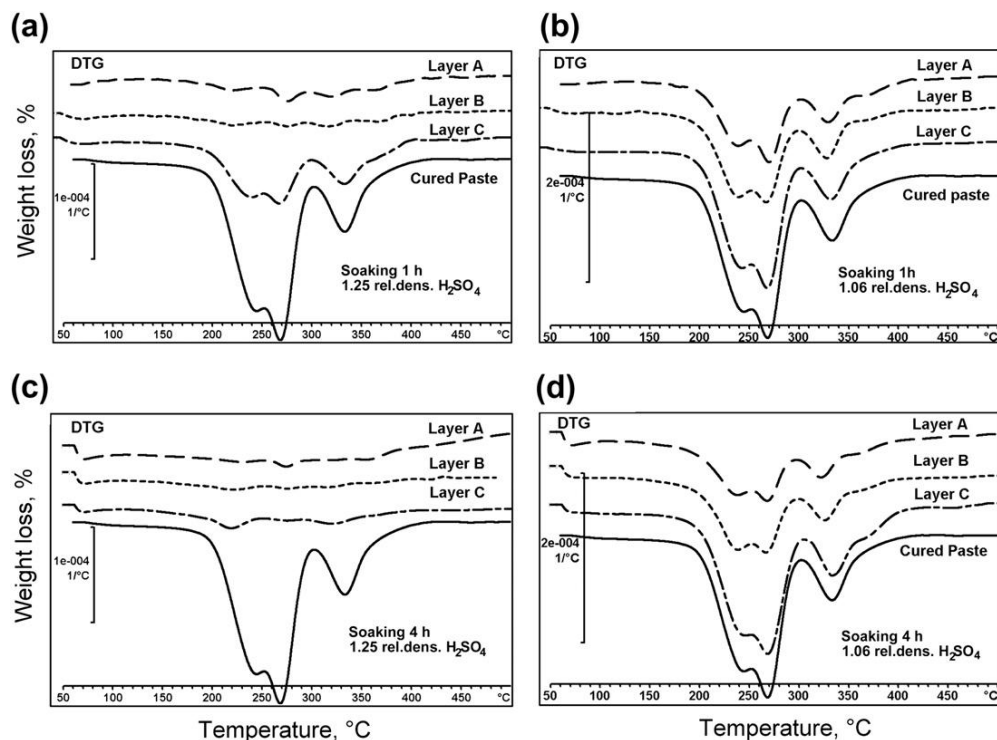
Figure 9.15:

Structure and crystal morphology of cured paste in the central plate zone after 2 h of soaking in 1.06 rel. dens. H_2SO_4 solution.

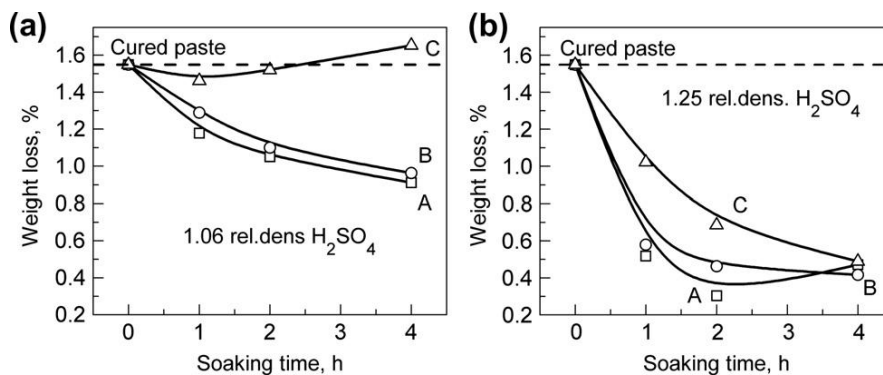
- On soaking in H_2SO_4 solution of 1.25 rel. dens., the endothermic characteristic peaks for 3BS decrease considerably in the DTG curves for the *A* and *B* layers within the first hour of soaking. The *C* layer contains substantial amounts of 3BS. Only after 4 h of soaking, the 3BS content in the *C* layer decreases to negligible amounts.
- When soaking is conducted in H_2SO_4 solution of 1.06 rel. dens., the characteristic peaks for 3BS are preserved, though less intensive, even after 4 h of soaking. 3BS crystals remain not much affected by sulfation.

Figure 9.17 shows the weight losses (as measured by thermal gravimetry, TG) on heating samples from the three paste layers after different times of soaking [4]. When plates are soaked in H_2SO_4 solution of 1.06 rel. dens. (Fig. 9.17a), the weight losses of layers *A* and *B* decrease slightly. After 4 h of soaking, the weight loss measured for the central layer *C* is even greater than that for the cured paste. This indicates that some hydration processes take place in the central layer of plates during soaking. Probably, the PbO and $3\text{PbO} \cdot \text{PbSO}_4 \cdot \text{H}_2\text{O}$ phases undergo hydration.

Figure 9.17b presents the weight losses on heating samples from the three plate layers soaked in H_2SO_4 solution of 1.25 rel. dens. After 4 h of soaking, the weight losses for the three layers are almost the same (0.4%). Despite the still high H_2SO_4 concentration, no sulfation of PbO proceeds or, if any, it proceeds at a very low rate. Figure 9.17 indicates that all three layers contain H_2O , though in very small amounts. Hence, the oxides and basic lead sulfates in the soaked pastes have undergone hydration and some of the hydrated particles have been isolated from direct contact with the H_2SO_4 solution.

**Figure 9.16:**

Differential thermogravimetric (DTG) curves of sample weight loss with temperature increase for the outer (A), intermediate (B) and central (C) plate layers after 1 and 4 h of soaking in: (a,c) 1.25 rel. dens. H₂SO₄ solution; and (b,d) 1.06 rel. dens. H₂SO₄ solution [4].

**Figure 9.17:**

Weight losses for the three sub-layers of the plate (A–C), determined through TGA measurements after different times of soaking in 1.06 and 1.25 rel. dens. H₂SO₄ solutions [4].

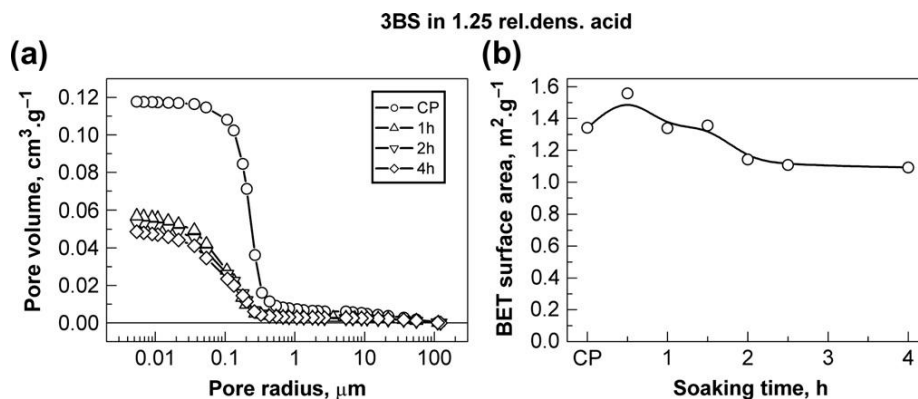


Figure 9.18:

(a) Pore volume distribution by pore radius for pastes immediately after curing and after soaking in H_2SO_4 solution of 1.25 rel. dens. for 1, 2 or 4 h. (b) Changes in BET surface of pastes immediately after curing (CP), and after soaking in H_2SO_4 solution of 1.25 rel. dens. for different periods of time [4].

Figure 9.17 suggests that, when soaking is conducted in more concentrated H_2SO_4 solutions (e.g. 1.25 rel. dens.), the processes of sulfation change radically the structure of the cured paste. After plate formation, the structure of PAM and NAM is determined by the paste structure formed during soaking and it is less influenced by the preceding technological procedures. On the contrary, if soaking is conducted in diluted H_2SO_4 solutions (e.g. 1.06–1.10 rel. dens.), the structure of PAM depends strongly on the technological procedures preceding soaking, as considerable amounts of 3BS and PbO particles and agglomerates are involved in the formation processes and thus affect the structure of PAM and NAM.

The changes in BET surface and porosity of the 3BS paste during soaking in H_2SO_4 solution of 1.25 rel. den. are summarised in Fig. 9.18 [4]. After 4 h of soaking, the BET surface area decreases by 35% and the total pore volume by almost 60%, the mean pore radius being reduced from 0.20 to 0.07 μm . As the molar volume of PbSO_4 is greater than that of the compounds in the cured paste, and especially of PbO , sulfation will reduce the total pore volume of the paste.

It has been established that the processes of soaking are affected by the density of the 3BS paste. Thus, at paste density of 3.89 g cm^{-3} , the amount of H_2SO_4 that reacts during the soaking step is greater than that for pastes with density 4.39 g cm^{-3} [5].

9.3.3. Changes in Structure of the Interface Cured Paste/Corrosion Layer/Grid during Plate Soaking [4]

H_2SO_4 flows penetrate into the volume of the cured paste and reach the interface corrosion layer/paste. They react with the corrosion layer surface and the adjacent cured paste. Since

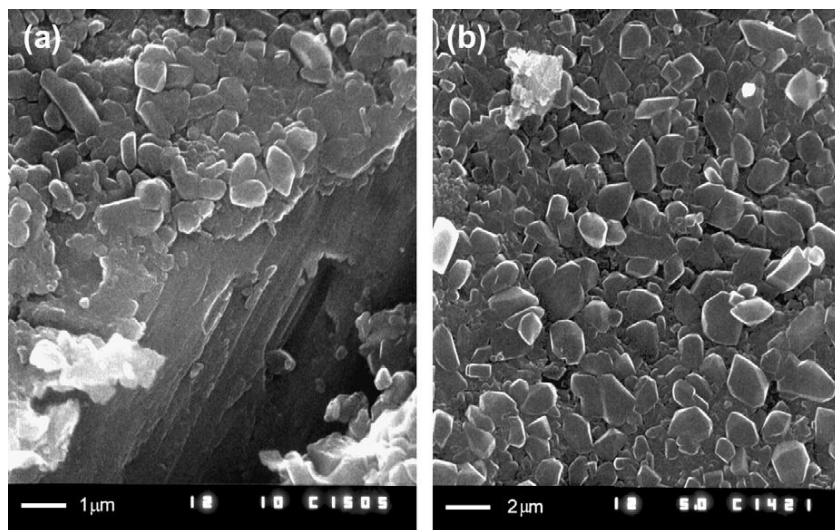


Figure 9.19:

Corrosion layer formed on the grid surface after 1 h of soaking in H_2SO_4 solution of 1.10 rel. dens. (a) The grid has been stretched to allow a better view of the CL cross-section; (b) Formation of PbSO_4 crystals on the surface of the corrosion layer [4].

paste particles do not cover entirely the corrosion layer surface, H_2SO_4 reacts with the bare corrosion layer forming PbSO_4 . Such is the case illustrated in Fig. 9.19, which shows a cross-section and an en face view of the corrosion layer formed on the plate grid after 1 h of soaking in H_2SO_4 solution of 1.10 rel. den.

Part of the bulk CL (close to the metal) has remained unaffected after soaking, i.e. it has not reacted with the H_2SO_4 solution (Fig. 9.19a). Most probably, a PbSO_4 membrane film has formed on the surface of the CL, which has isolated it from the H_2SO_4 solution. Figure 9.19b evidences that the surface of the CL is covered with a layer of PbSO_4 crystals.

During soaking, H_2SO_4 flows are highly diluted when they reach the corrosion layer that is formed on the grid in the centre of the plate. This diluted H_2SO_4 participates in reactions of hydration of the corrosion layer and of the adjacent cured paste, as well as in further sulfation of these hydrated agglomerates with formation of PbSO_4 on their surface. Such a structure is presented in Fig. 9.20. The corrosion layer and the adjacent paste are partially hydrated and sulfated.

Figure 9.21 presents SEM pictures of the corrosion layer of plates with PbSnCa grids. The CL has become thinner during curing, thus revealing the microstructure of the grid metal.

The pictures imply that the inter-grain layer, formed as a result of Sn and Ca segregation at the metal grain boundaries, is more reactive and PbSO_4 crystals form over it. This layer has

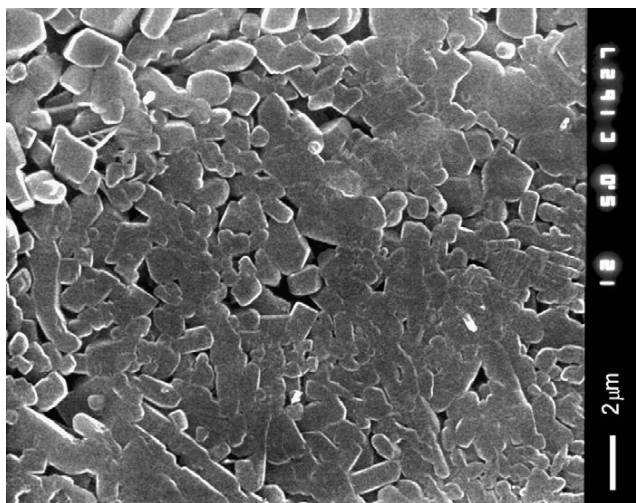


Figure 9.20:
Partially hydrated and sulfated corrosion layer.

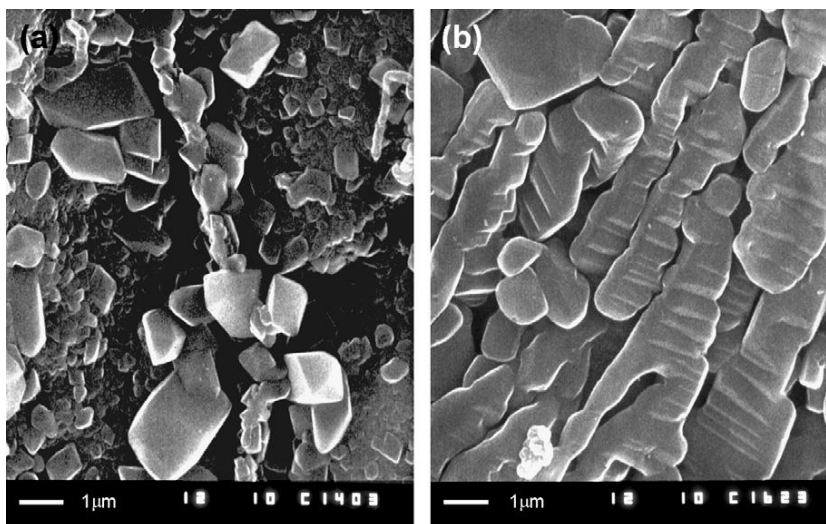


Figure 9.21:
(a) H_2SO_4 flows react with the thin CL over the metal grains and with the inter-grain layer of $(\text{Pb}_{1-n}\text{Sn}_n)_3\text{Ca}$. PbSO_4 crystals grow faster on sulfation of the inter-grain layer. (b) Sulfation of the hydrated CL by concentrated H_2SO_4 flows [4].

a composition of the type $(\text{Pb}_1 - x\text{Sn}_x)_3\text{Ca}$. Calcium reacts with H_2SO_4 forming CaSO_4 . The latter serves as a nucleus for the growth of PbSO_4 crystals over the inter-grain layer (Fig. 9.21a). PbSO_4 also forms on the surface of the corrosion layer that covers the metal grains, but these PbSO_4 crystals are considerably smaller in size (Fig. 9.21a).

Figure 9.21b shows a picture of the interface featuring continuous sulfation of the lead hydroxides of the corrosion layer along the direction of the H_2SO_4 flows close to the CL. The H_2SO_4 flows cause formation of chains of elongated PbSO_4 particles. The length of these particles may reach up to 4–5 μm with a thickness of about 0.3–0.5 μm . Such PbSO_4 particles are formed when the amount of one type of the reaction ions exceeds substantially that of the other type [6]. These PbSO_4 particles lack the typical crystal forms and walls, and have rounded edges.

9.3.4. Mechanism of the Reactions that Proceed During Soaking of 3BS Pastes

G. Liptay and Sors [7] mixed a given amount of leady oxide with increasing amounts of H_2SO_4 . They determined continuously the phase composition of the obtained pastes until a stoichiometric ratio of $\text{H}_2\text{SO}_4/\text{PbO} = 1$ was reached. The phase composition of the paste was determined immediately after its preparation and 24 h later. Based on the data presented in [7], the dependence of phase composition of the paste as a function of the increasing $\text{H}_2\text{SO}_4/\text{PbO}$ ratio (from 3 to 100%) is plotted (Fig. 9.22).

The data in Figure 9.22 indicate that on increasing the amount of H_2SO_4 vs. that of PbO , the successive reactions represented by chemical equations (9.1), (9.2) and (9.3) proceed. The maximum amount of 3BS is formed at $\text{H}_2\text{SO}_4/\text{PbO} = 33\%$, whereas at $\text{H}_2\text{SO}_4/\text{PbO} = 75\%$, mostly 1BS is formed. Even at $\text{H}_2\text{SO}_4/\text{PbO} = 100\%$, the paste does not transform completely to PbSO_4 . That is the picture of the processes that take place during paste preparation.

The cured paste is a porous mass composed of PbO and 3BS, and when soaked, H_2SO_4 penetrates into the pores of this mass. Reactions of sulfation proceed between the surface of PbO and

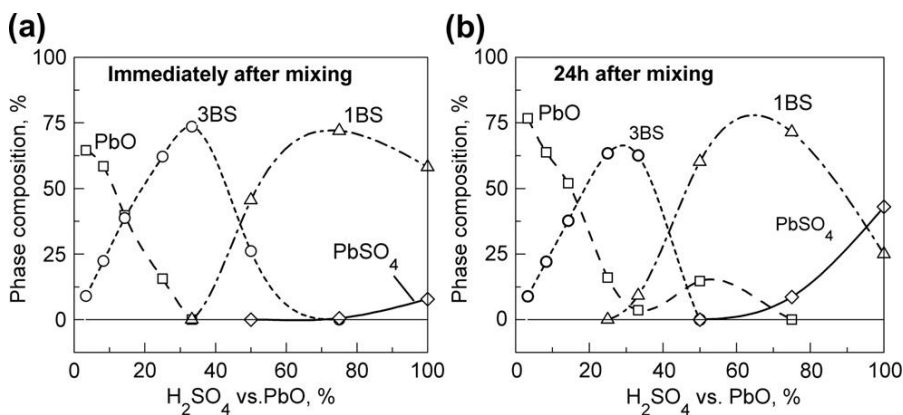
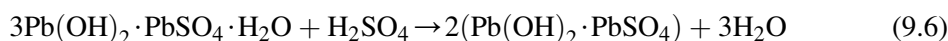
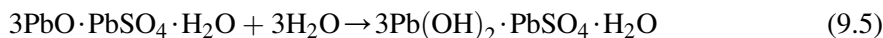


Figure 9.22:

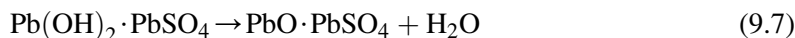
Phase composition of pastes prepared with different amounts of H_2SO_4 vs. PbO . The values on the abscissa give the $\text{H}_2\text{SO}_4/\text{PbO}$ ratio in % (100% corresponds to $\text{H}_2\text{SO}_4 : \text{PbO} \frac{1}{4} 1$). The curves are plotted using data reported in [7]. Phase composition of the paste: (a) immediately after paste preparation; (b) after 24 h of mixing.

3BS particles, and H_2SO_4 in the paste pores. These processes are similar to the ones illustrated in Fig. 9.22. The $\text{H}_2\text{SO}_4/\text{PbO}$ ratio decreases in the plate interior, because part of the H_2SO_4 reacts and water is produced as a result of sulfation of the PbO , 3BS and 1BS phases. The SEM pictures (Figs. 9.12–9.15 and 9.19–9.21) evidence that the processes of sulfation of the paste and of the paste/grid interface proceed at different rates in the different parts of the plate volume, and lead to the formation of different phases in the different micro-regions of the paste.

The TGA curves in Figs. 9.16 and 9.17 indicate that some processes of hydration proceed during paste soaking. Probably, PbO , 3BS and 1BS are hydrated first, and the obtained hydrated products undergo sulfation, e.g. through the following reactions:



Part of the $\text{Pb}(\text{OH})_2 \cdot \text{PbSO}_4$ is dehydrated, the 1BS phase being registered by X-ray diffraction:



and another part is sulfated further:



The great amount of PbSO_4 in the *A* and *B* layers, even after soaking in H_2SO_4 of 1.06 rel. dens., indicates that the reaction of sulfation of $\text{Pb}(\text{OH})_2 \cdot \text{PbSO}_4$ proceeds faster than the dehydration reaction.

The rates of the reactions of hydration and sulfation of the lead oxide and of the basic sulfates depend on the radii of the paste pores. If the mean pore radius is smaller than a certain critical value, the diffusion flow of H_2SO_4 in the pores is very small and the reactions of hydration will proceed at a higher rate than the sulfation reactions. Hence, micro-volumes of hydrated oxides and basic lead sulfates will be formed (Fig. 9.20). On the contrary, when the pores have large radii, more intense diffusion flows of H_2SO_4 will enter them and the rate of the reactions of sulfation of the various hydrates will be much higher. PbSO_4 will form in these micro-regions of the paste and of the paste/grid interface (see Fig. 9.14).

On comparing the phase composition of the paste immediately after mixing and 24 h later (see Fig. 9.22), it becomes evident that some recrystallization processes take place in the paste, as a result of which the content of crystal PbSO_4 increases from 8 to 42%. Such recrystallization processes proceed also during soaking of the plates.

9.3.5. Influence of Soaking Processes on Battery Cycle Life Performance [4]

Three capacity tests were performed at 20 h rate of discharge. All batteries exhibited over 100% of the rated capacity calculated at 50% utilization of the PbO_2 active mass. Figure 9.23

presents the capacity vs. cycle number dependencies for batteries produced with conroll PbSnCa grids and 3BS positive pastes.

The concentration of the H_2SO_4 solution on soaking and formation exerts a stronger influence than the duration of soaking, when longer than 1 h. Batteries soaked in H_2SO_4 solution of 1.06 rel. dens. have longer cycle life than those soaked in 1.25 rel. dens. H_2SO_4 . The time of soaking has a weaker effect on battery life as the basic processes are completed within the first hour of soaking. During this time, the three zones across the plate thickness are formed.

What is the influence of soaking on positive plate performance due to?

Figure 9.11 shows a picture of the sulfated plate surfaces and the formation of three layers of different chemical composition across the plate thickness. During formation, as a result of oxidation of PbSO_4 crystals, the solution in the paste pores becomes acidic and $\beta\text{-PbO}_2$ is formed. The latter is reduced at high rate on discharge of the plate and hence contributes greatly to its capacity [8–11]. However, $\beta\text{-PbO}_2$ does not form mechanically strong and stable structure that would endure the mechanical and electrical loads on charge and discharge for a long time. That is why, positive plates composed only of $\beta\text{-PbO}_2$ have short cycle life.

On the other hand, $\alpha\text{-PbO}_2$ is reduced to PbSO_4 at a low rate and yields but low capacity on discharge as considerable amounts of $\alpha\text{-PbO}_2$ do not take part in the discharge processes. It is assumed that the surface of $\alpha\text{-PbO}_2$ particles is quickly covered by PbSO_4 crystals [8–12]. These regions of PAM comprise its skeleton structure, which conducts the current and on which PbO_2 is deposited during plate charge, i.e. $\alpha\text{-PbO}_2$ contributes mainly to the formation of the PAM skeleton that provides mechanical support to PAM and conducts the current to all parts of the plate volume.

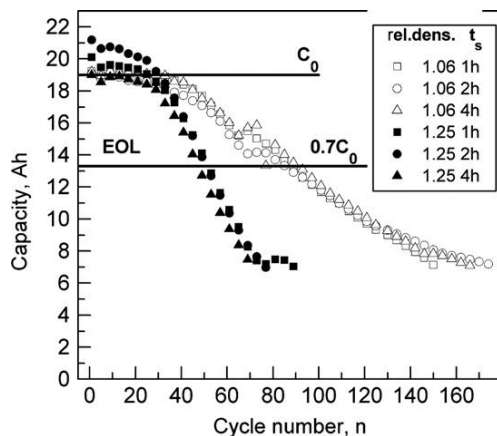


Figure 9.23:

Battery capacity vs. number of charge-discharge cycles for batteries soaked and formed in H_2SO_4 solution of 1.06 or 1.25 rel. den. [4].

During the soaking procedure, part of the cured paste is sulfated. Through this procedure the proportion between the α - and β - PbO_2 modifications is controlled. If soaking is conducted in highly concentrated H_2SO_4 solutions for a long time, all three layers of the cured paste undergo sulfation and the main product of the subsequent formation process will be β - PbO_2 , i.e. the plate (battery) will have high capacity but short cycle life. If soaking is conducted in more diluted H_2SO_4 solutions (e.g. 1.06 rel. dens.) for 1–2 h, mainly the surface plate layer A, and partially the intermediate layer B, are sulfated. Partially hydrated cured paste, composed of PbO and 3BS (4BS), remains in the central plate zone C. In this latter zone, and partially in the B layer, α - PbO_2 is predominantly formed during plate formation. As mentioned earlier, the α - PbO_2 modification forms the skeleton of PAM and ensures longer cycle life, provided there is no other irreversible process that would limit battery life. The above proposed picture is supported by the capacity curves presented in Fig. 9.23. Hence, the technological process of soaking has its own specific contribution to the performance parameters of battery positive plates.

9.4. Soaking of 4BS Cured Pastes

9.4.1. Sulfation Rates of 3BS and 4BS Pastes in H_2SO_4 Solution

Figure 9.24 presents the amount of PbSO_4 , formed on soaking 10 g of 3BS or 4BS paste in H_2SO_4 solution of 1.23 rel. dens., as a function of soaking time [13]. The experimental conditions are identical for both types of pastes.

The 4BS paste reacts with H_2SO_4 much more slowly than its 3BS counterpart, because of the smaller surface area and the bigger size of the crystals in the 4BS paste. Therefore, the industrial approach to soaking 3BS and 4BS pastes should be different. 4BS pastes require sufficient soaking time and temperature to reach adequate growth of the PbSO_4 content. In contrast, 3BS pastes should be soaked at lower temperature and for shorter period of time.

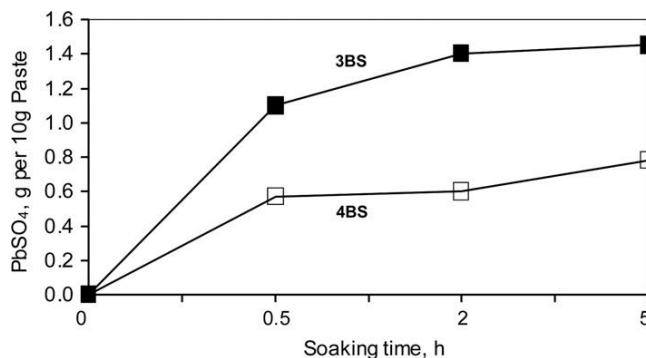


Figure 9.24:

Changes in PbSO_4 content formed on soaking 3BS and 4BS pastes as a function of soaking time [13].

Both curves (for 3BS and 4BS) in Fig. 9.24 are similar in profile, which implies that similar processes occur on soaking 4BS pastes as those described for 3BS pastes (see Section 9.3.2.) leading to formation of different layers (zones) across the plate thickness. However, the volume of 4BS crystals is much bigger than that of 3BS crystals. Therefore, sulfation of 4BS particles requires special consideration.

9.4.2. Processes of Sulfation of 4BS Crystals During Soaking

Tetrabasic lead sulfate crystals are big in size (10–100 μm in length and 1–10 μm in diameter). The processes of sulfation of 4BS crystals have been studied by many scientists and the obtained results are summarised in [9,14–17]. Conjectures about the processes that occur on soaking 4BS pastes are made on grounds of the obtained phases across the 4BS crystal cross-section as a result of soaking (see Fig. 9.25).

Two layers can be distinguished on the surface of 4BS crystals after soaking in H_2SO_4 solution of 1.23 rel. dens. [13,16]:

- (a) A superficial layer of PbSO_4 crystals sized from 1.5 to 2.0 μm . Let us denote this layer as ‘ $\text{PbSO}_4(\text{s})$ layer’ (s = surface).
- (b) Inner layer of granules (nodules) and crystals up to 0.2 μm in size [14,16]. Let us denote this layer as ‘i-layer’ (i = inner).

The $\text{PbSO}_4(\text{s})$ layer is formed through a dissolution/recrystallization mechanism. When the 4BS crystal gets in contact with H_2SO_4 solution, a film of PbSO_4 particles forms on its surface. PbSO_4 ‘molecules’ from this film dissolve and precipitate onto the PbSO_4 nuclei already formed on this surface. Thus, the nuclei grow with time of soaking into big crystals. These

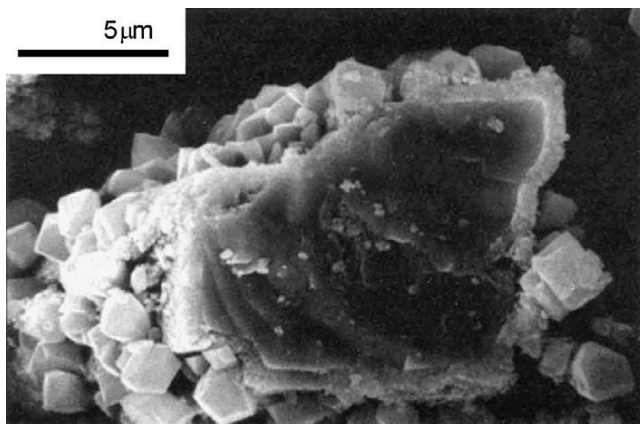


Figure 9.25:

Photograph of cross-section of a broken 4BS crystal with PbSO_4 layer on surface [15].

processes proceed at the solution/crystal interface, so the PbSO_4 crystals formed have well-pronounced walls and edges. The free space between the PbSO_4 crystals diminishes and may reach membrane sizes. Hence, the H_2SO_4 solution is isolated from the surface of 4BS crystals by the PbSO_4 membrane. The dimensions of pores in this membrane layer will determine the composition of the ion flows that can reach the 4BS surface.

Formation of the 'i-layer' starts after the membrane $\text{PbSO}_4(\text{s})$ layer has formed. Initially, while the pores between PbSO_4 crystals are large enough, H_2SO_4 flows reach the surface of 4BS crystals and sulfate it, though at a low rate. With time of soaking, the spaces between PbSO_4 crystals diminish and diffusion of H_2SO_4 through the pores of the $\text{PbSO}_4(\text{s})$ layer is strongly impeded. The pores contain water with dissolved 4BS ions. Consequently, the pH of the solution in the pores increases on reaching the pH zone of formation of basic lead sulfates (1BS, 3BS). So it can be assumed that the i-layer is composed of a mixture of PbSO_4 and small quantity of basic lead sulfates.

The evolution of the i-layer formed at different temperatures as a function of soaking time is presented in Fig. 9.26. [13].

The curves in Fig. 9.26 confirm the evolution of the soaking processes of 4BS crystals through two stages. The first stage covers the period of formation and growth of the s-layer until a critical thickness is reached. During the second stage, flows of H_2O and H^+ , OH^- and SO_4^{2-} ions pass through the $\text{PbSO}_4(\text{s})$ membrane layer at a very low rate and hence the thickness of i-layer grows very slowly. This stage depends on the temperature of soaking. At higher temperatures the rates of ion flow diffusion are higher and, hence, a thicker i-layer is formed.

The degree of sulfation of 4BS cured pastes depends also on the size of the 4BS crystals [13]. If the crystals are bigger than 3–4 μm in diameter, part of their volume will remain isolated from

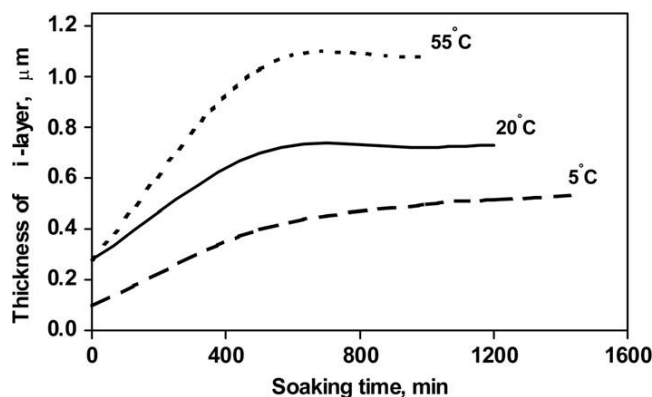


Figure 9.26:
Changes in thickness of the i-layer on 4BS crystal during soaking at three different temperatures [13].

Table 9.1: Phase composition of formed 4BS plates (250% charge at C/20 rate) after different soaking time

Conditions	Analytical Method	Phase Composition (%)		
		β -PbO ₂	PbSO ₄	4BS
Without soaking		51.3	43.3	5.4
Soaking time 0.5 h	XRD	52.1	27.7	20.2
	Chem.	52.3	34.5	13.2
Soaking time 2 h	XRD	63.2	28.7	8.1
	Chem.	68.8	13.8	16.9
Soaking time 4 h	XRD	64	8.8	27.1
	Chem.	68.8	21.3	9.9

the H₂SO₄ flow by the PbSO₄(s) membrane layer and hence unaffected by the soaking processes. This will influence the efficiency of subsequent formation of PbO₂. Hence, the processes that take place during the technological step of soaking depend not only on the conditions of soaking, but also on the size of the 4BS crystals in the cured paste. The latter, in turn, are determined by the method of 4BS crystal formation, i.e. by the technological procedures of 4BS paste preparation preceding the soaking process.

It has been established that, during the formation of 4BS pastes, the i-layer is oxidized first followed by the PbSO₄(s) layer [15,16]. Lead oxides and basic lead sulfates, as well as their hydrated forms, are oxidized at lower potentials than the potential of PbSO₄ oxidation. This is an indirect proof of the presence of hydroxides and basic lead sulfates in the i-layer. As the i-layer grows with time of soaking, it is to be expected that soaking time will exert an influence on the efficiency of the formation process. Table 9.1 presents the phase composition of formed 4BS plates after 250% charge at C/20 rate, after different times of soaking [13]. The composition of the formed PAM is determined through X-ray diffraction and chemical analyses. The results of both determinations are given in the table.

With increase of the time of soaking the amount of β -PbO₂ formed increases, too. According to the data in Fig. 9.26, 4 h of soaking belong to the stage of s-layer growth. Most probably, the observed increase of β -PbO₂ content in formed plates is a result of the increased thickness of the s-layer. The data of the chemical analysis give higher values for the PbO₂ content in PAM as it registers not only its crystal but also its amorphous (hydrated) part as established in r[18,19].

9.4.3. Changes in Macro and Microstructure of 4BS Pastes on Soaking

The technology of plate preparation for this investigation is as follows: paste prepared with H₂SO₄/LO = 6% by weight; 4BS paste; paste density 4.32 g cm⁻³; curing at 90 °C or 50 °C and soaking in H₂SO₄ solution of 1.10 or 1.25 rel. dens. [4,20].

SEM examinations (at small magnifications) of the 4BS plates after soaking do not show distinctly the individual layers across the plate thickness as is the case with the 3BS plates. In order to be able to follow the changes in paste structure, paste samples are taken from the surface of the plate and from its interior and set to scanning electron microscopy [20].

Figure 9.27 presents SEM pictures of the paste layer close to the plate surface. The 4BS crystals are preserved, but they are covered by a thin film of small particles (Fig. 9.27a). Big PbSO_4 crystals of regular shape are formed here and there on the surface of the 4BS crystals (Fig. 9.27b). Probably, they have formed as a result of recrystallization of the small PbSO_4 particles. These PbSO_4 crystals reduce the cross-section of the pores in the surface plate layer [20].

The structure of the 4BS paste at a distance of about $250\text{ }\mu\text{m}$ from the plate surface changes after 2 h of soaking in 1.25 rel. dens. H_2SO_4 solution (see Fig. 9.28). Figure 9.28a shows a picture of a 4BS crystal with hydrated and then partially sulfated surface. At a certain pH level, 4BS crystals react with water forming hydroxy-sulfates in the form of small particles (Fig. 9.28b). The latter may merge with the hydrated layers of the adjacent 4BS crystals (Fig. 9.28a). Thus, a continuous hydrated porous structure is formed, which is then sulfated.

H_2SO_4 flows penetrate along the pores of the hydrated paste zones and formation of PbSO_4 crystals starts. These phenomena are manifested in the SEM pictures at high magnification

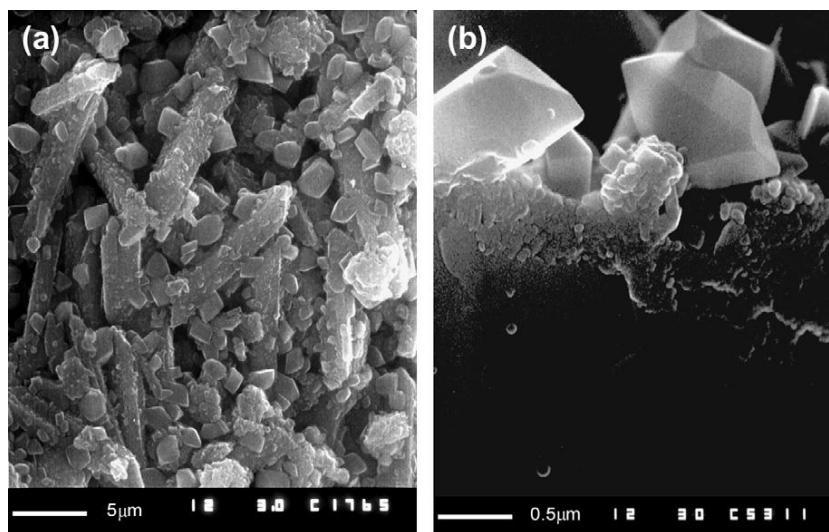


Figure 9.27:

(a) Macro and microstructure of soaked 4BS paste sample from the surface layer of the plate. (b) $\text{PbSO}_4(\text{s})$ and i-layers can be distinguished over the surface of the 4BS crystal [20].

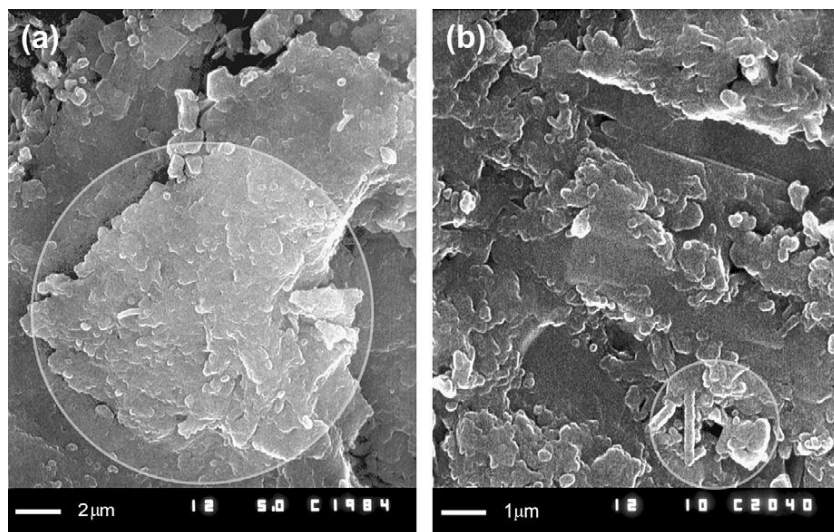


Figure 9.28:

Hydrated 4BS crystals in the central layers of the plate after soaking featuring onset of sulfation of these layers and formation of: (a) PbSO_4 crystals (encircled), and (b) $\text{PbO} \cdot \text{PbSO}_4$ (1BS) crystals (encircled) [20].

presented in Fig. 9.29. The pictures illustrate the stages of conversion of the hydroxide mass into a well-shaped crystal. H^+ and SO_4^{2-} ions penetrate into the hydroxy-sulfate crystal layer and gradual growths of PbSO_4 crystals starts within the hydroxy-sulfate layer. Water is released and a PbSO_4 crystal is formed. These phenomena are similar to the sulfation processes that occur in the hydrated zones of 3BS plates on soaking.

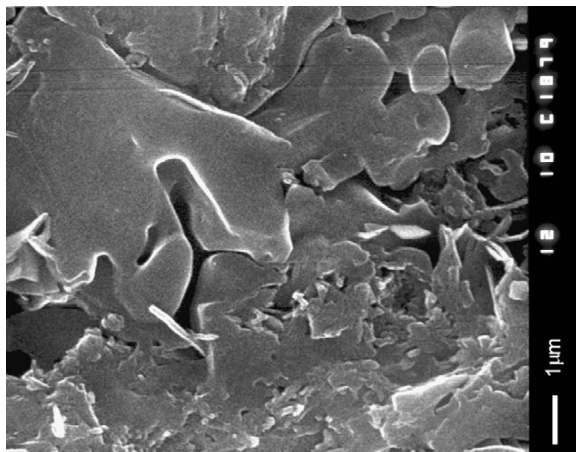


Figure 9.29:

Sulfated 4BS crystals that have first been hydrated. The sample is taken from the central plate layer [20].

9.4.4. Structure of the Interface Paste/Corrosion Layer After Soaking of 4BS Plates

Figure 9.30 shows pictures of the corrosion layer after 1 h of soaking in H_2SO_4 solution of 1.25 rel. den.[20]. Similar processes of sulfation of the corrosion layer in 4BS plates proceed as in the case of 3BS plates. A layer of well-shaped PbSO_4 crystals is formed as a result of the reaction of $\text{Pb}(\text{OH})_2$ in the CL with H_2SO_4 . These crystals are located so close to each other that the pores between them may reach membrane sizes. This PbSO_4 layer blocks the access of H_2SO_4 to the $\text{Pb}(\text{OH})_2$ in the corrosion layer and hence the reaction of sulfation of the latter is strongly impeded.

Figure 9.30b shows the sites of contact of the corrosion layer with 4BS crystals of the paste not much affected by the H_2SO_4 flows. A reaction of hydration of the 4BS crystals proceeds and the obtained particles interconnect with the hydroxide in the corrosion layer, after which their surface undergoes partial sulfation by the H_2SO_4 flows of low concentration, and small PbSO_4 crystals are formed.

9.4.5. Porometric and BET Surface Measurements of Soaked 4BS Pastes

Figure 9.31 presents porograms for 4BS paste samples taken after different times of soaking in H_2SO_4 solution of 1.25 rel. den. [20].

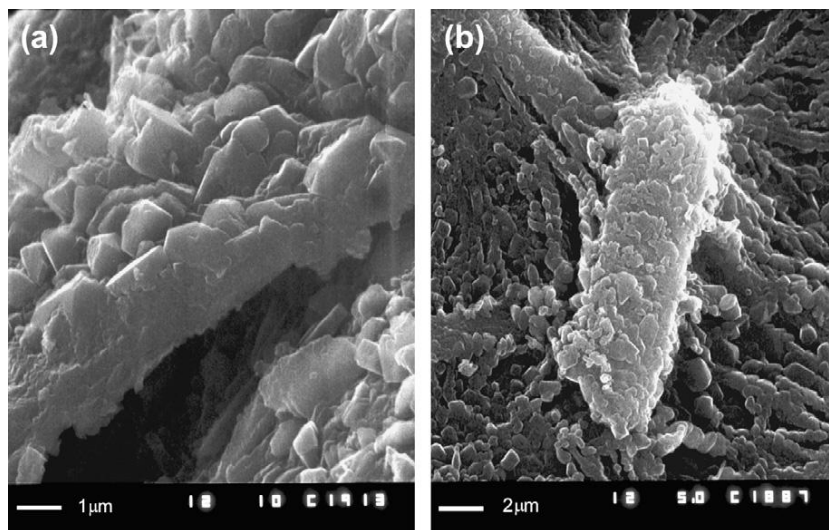


Figure 9.30:

Structure of the corrosion layer after soaking in H_2SO_4 solution of 1.25 rel. dens. for 1 h.

(a) The grid has been stretched so that the corrosion layer would crack and thus allow examination of its cross-section; (b) Sulfated corrosion layer and a hydrated and sulfated 4BS crystal [20].

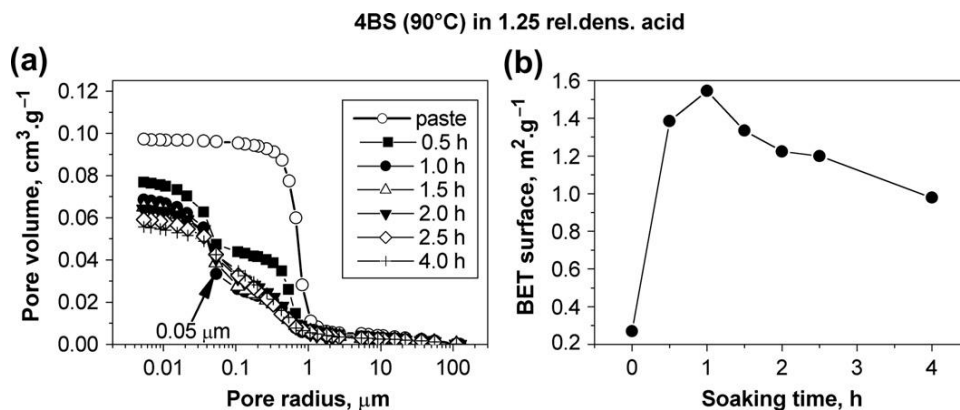


Figure 9.31:

(a) Pore volume distribution vs. pore radius for 4BS plates after soaking in H₂SO₄ solution of 1.25 rel. dens. for different periods of time; (b) Changes in BET surface area of 4BS pastes as a function of soaking time [20].

Within the first 30 min already the pore system of the paste changes substantially: the total pore volume decreases and pores with small radii (0.05 μm) are formed. The cured paste comprises big crystals forming medium-sized pores with radii of about 0.8 μm. On plate soaking, the surface of the 4BS crystals is sulfated, which reduces the cross-section of the pores, but they still preserve a mean radius of about 0.3–0.4 μm. The interior of the plate undergoes hydration. The hydrated zones cause the pore system to change dramatically due to disintegration of the 4BS crystals and a new pore system is formed with mean pore radius of less than 0.05 μm. On further soaking, the degree of sulfation of the 4BS crystals in the sulfated zone increases and this zone grows in size, thus reducing the volume of the micropores. These phenomena are clearly manifested in Fig. 9.31b. They are associated with an increase of BET surface area during the first hour of soaking. After that, sulfation of the pore walls in the hydrated zone reduces the BET surface.

9.4.6. Differential Scanning Calorimetric (DSC) Measurements of Soaked Pastes Cured at 90 °C

Figure 9.32 presents DSC curves for 4BS paste (cured at 90 °C) after soaking in 1.05 or 1.25 rel. dens. H₂SO₄ solution for 0, 1, 2, 3 and 4 h [20].

Three endothermic peaks occur when the cured paste samples are heated. These peaks are a result of evaporation of the bonded water from the paste, which is incorporated in different structures. The sharp peak at 330 °C is related to melting of the metallic lead in the paste. When the plates are soaked in H₂SO₄ solution of 1.05 rel. den., the peak C disappears and the energy of the endothermic peak A increases, i.e. this type of hydration increases. The height of peak B diminishes slightly.

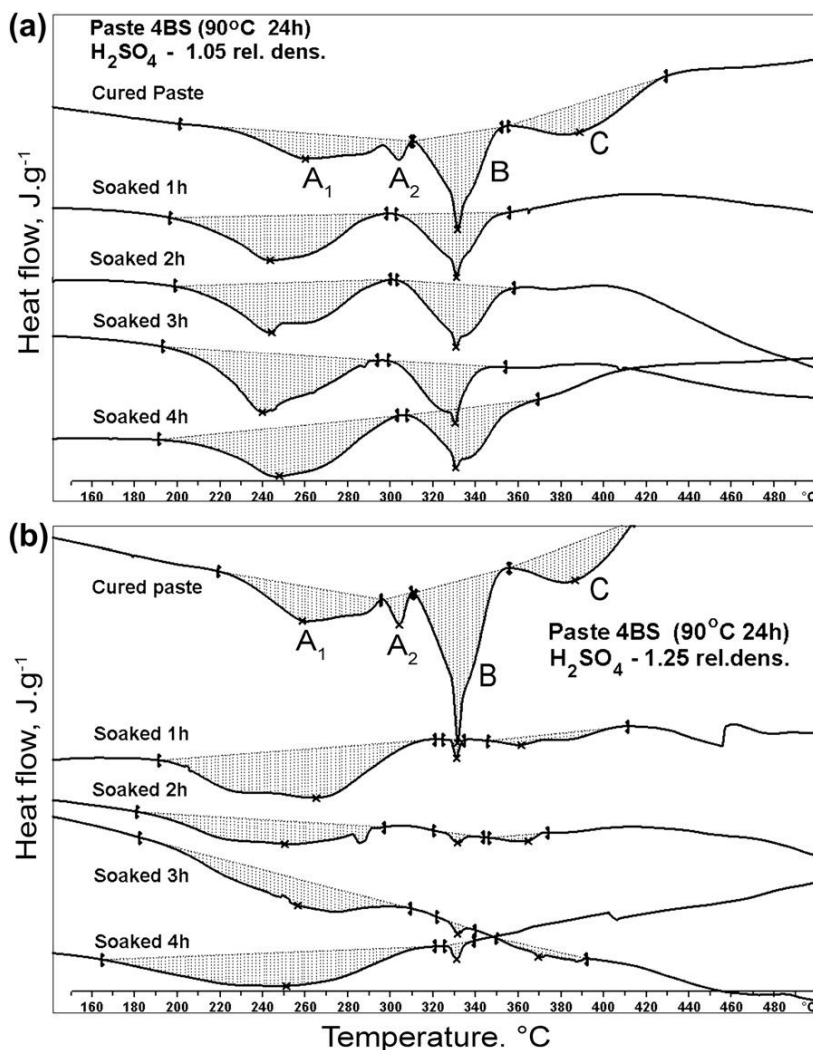
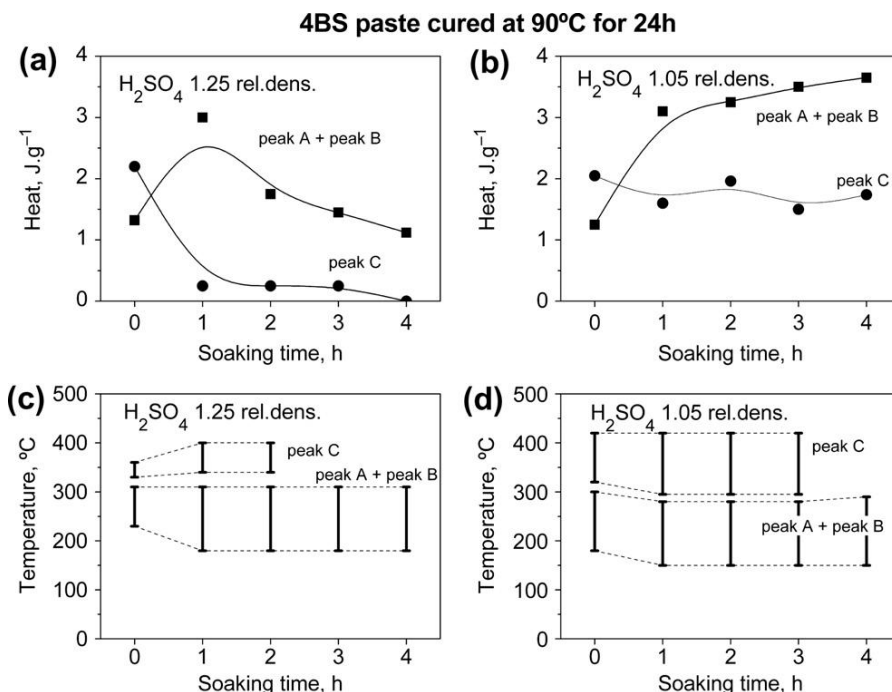


Figure 9.32:

DSC curves for 4BS paste cured at 90 °C immediately after curing and after soaking in (a) 1.05 rel. dens. H₂SO₄; (b) 1.25 rel. dens. H₂SO₄ for 1, 2, 3 and 4 h [20].

Figure 9.33 shows quantitatively the heat effects of dehydration as a function of time of soaking in the two types of electrolytes as determined by differential scanning calorimetry (DSC). The temperature ranges within which these processes occur are also given in the figure [20].

When the plates are soaked in 1.05 rel. dens. H₂SO₄ solution, the 4BS paste undergoes intense hydration during the first hour of soaking and then further hydration increases but slowly within the next 3 h. The opposite tendency is observed when the plates are soaked in 1.25 rel.

**Figure 9.33:**

(a,b) Heat effects, and (c,d) temperature ranges of dehydration of 4BS pastes cured at 90 °C as a function of soaking time, as determined by the DSC curves presented in Fig. (9.32) [20].

dens. H_2SO_4 solution, namely the (A + B) endothermic peaks decrease after 1 h of soaking because of sulfation of the paste in the inner parts of the plate.

Figure 9.33 shows also the temperature ranges within which the endothermic dehydration peaks appear for the pastes soaked in H_2SO_4 solution for different periods of time. Dehydration of the paste soaked in H_2SO_4 of 1.25 rel. dens. proceeds at a bit higher temperature than when soaked in 1.05 rel. dens. H_2SO_4 solution. The temperature ranges within which the endothermic peaks appear are almost independent of the time of soaking.

9.5. Influence of the Soaking Process on Battery Performance

The influence of time on soaking of positive plates prior to formation on the initial battery capacity has been studied [13]. Batteries are formed with a quantity of electricity corresponding to 250% of their theoretical capacity. The results of the first discharge at 20 h rate are presented in Fig. 9.34.

It can be seen from the figure that the first discharge capacity increases with increase of soaking time, which is quite logical as the content of $PbSO_4$, and hence the amount of β - PbO_2 formed in the positive plates increases.

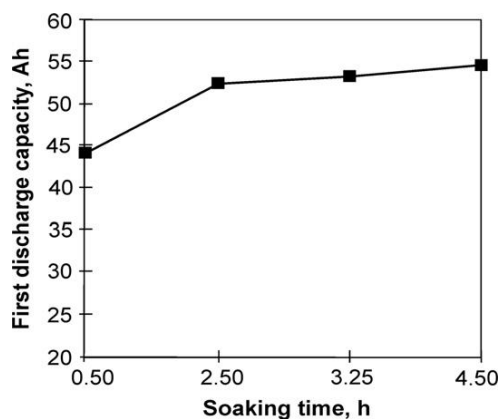


Figure.9.34:

Evolution of the first discharge capacity of a battery in relation to the soaking time before formation [13].

Figure 9.35 presents cycle life curves for SLI batteries produced with positive plates with PbSnCa grids and 4BS pastes, and soaked in H_2SO_4 solution of 1.25 or 1.06 rel. den. for 1, 2 or 4 h [4]. All batteries are of the flooded type. The batteries are subjected to deep discharge cycling at 50% utilization of PAM. The obtained test results indicate that batteries soaked in 1.06 rel. dens. H_2SO_4 solution have longer cycle life than batteries soaked in 1.25 rel. dens. H_2SO_4 . These batteries require tank or two-step formation.

The above-discussed cycling test results evidence that soaking, in the case of 4BS pastes, has its own effect not only on the initial performance parameters of the battery, but also on its

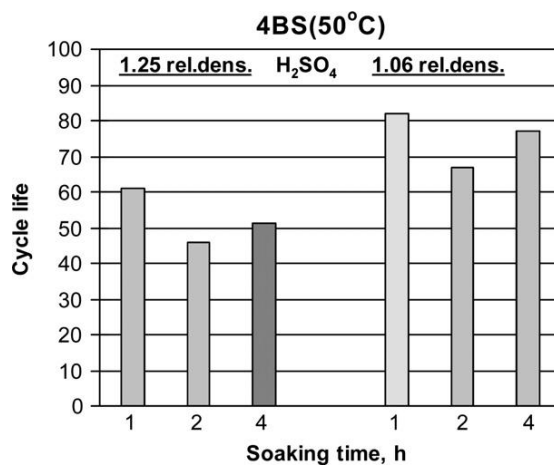


Figure 9.35:

Cycle life of SLI batteries produced with positive plates with the same 4BS paste, but soaked in H_2SO_4 solution of 1.06 or 1.25 rel. dens. for 1, 2 or 4 h [4].

cycle life. Hence, soaking should be regarded as an independent technological procedure in the process of lead–acid battery manufacture.

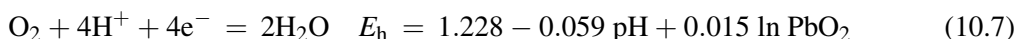
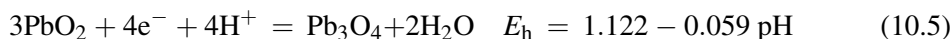
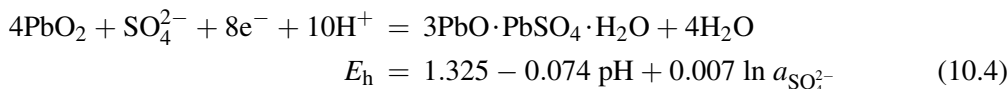
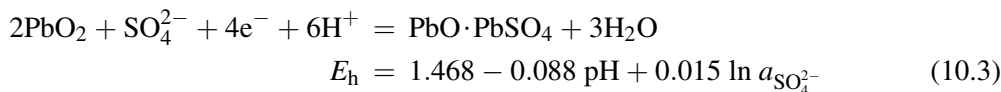
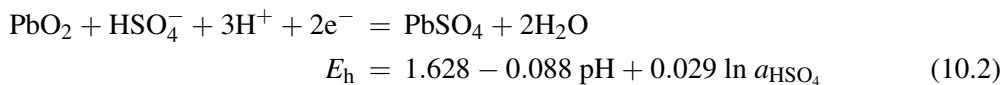
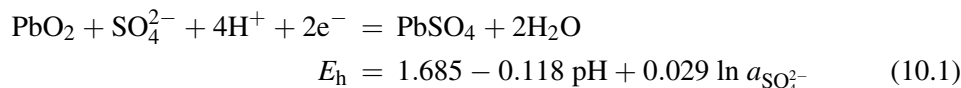
References

- [1] N.R. Eisenhut, E.M. Kseniak, *J. Power Sources* 33 (1991) 77.
- [2] R. Nelson, in: Lecture course on VRLAB, LABAT'99 conference, Sofia, Bulgaria, June 1999.
- [3] D. Pavlov, S. Ruevski, T. Rogachev, *J. Power Sources* 46 (1993) 337.
- [4] M. Dimitrov, D. Pavlov, T. Rogachev, M. Matrakova, L. Bogdanova, *J. Power Sources* 140 (2003) 168.
- [5] I. Drier, F. Saez, P. Scharf, R. Wagner, *J. Power Sources* 85 (2000) 117.
- [6] D. Pavlov, I. Pashmakova, *J. Appl. Electrochem.* 17 (1987) 1075.
- [7] G. Liptay, L. Sors, *Thermochim. Acta* 14 (1976) 279.
- [8] D. Berndt, E. Voss, in: D.H. Collins (Ed.), *Batteries – 2*, Pergamon Press, Oxford, 1965, p. 17.
- [9] I.J. Astakhov, I.G. Kiseleva, B.N. Kabanov, *Dokl. Akad. Nauk USSR* 126 (1959) 1041.
- [10] R.I. Angstadt, C.J. Venuto, P. Ruetschi, *J. Electrochem. Soc.* 109 (1962) 177.
- [11] E. Voss, F. Freundlich, in: D.H. Collins (Ed.), *Batteries*, Pergamon Press, London, 1963, p. 73.
- [12] H.B. Mark, *J. Electrochem. Soc.* 109 (1962) 634.
- [13] S. Grugeon-Dewaele, J.B. Leriche, J.M. Tarascon, H. Delahaye-Vidal, L. Torcheux, J.P. Vaurijoux, F. Henn, A. de Guibert, *J. Power Sources* 64 (1997) 71.
- [14] L. Torcheux, J.P. Vaurijoux, A. de Guibert, *J. Power Sources* 64 (1997) 81.
- [15] S. Grugeon-Dewaele, S. Laruelle, L. Torcheux, J.M. Tarascon, H. Delahaye-Vidal, *J. Electrochem. Soc.* 145 (1998) 3358.
- [16] L.T. Lam, A.M. Vecchio-Sadus, H. Ozgun, D.A.J. Rand, *J. Power Sources* 38 (1992) 87.
- [17] L.T. Lam, H. Ozgun, L.M.D. Craswick, D.A.J. Rand, *J. Power Sources* 42 (1993) 55.
- [18] D. Pavlov, I. Balkanov, T. Halachev, P. Rachev, *J. Electrochem. Soc.* 136 (1989) 3189.
- [19] D. Pavlov, *J. Electrochem. Soc.* 139 (1992) 1830.
- [20] D. Pavlov, M. Dimitrov, T. Rogachev, L. Bogdanova, *J. Power Sources* 114 (2003) 137.

Formation of Positive Lead–Acid Battery Plates

10.1. Equilibrium Potentials of the Electrode Systems Formed During the Formation Process

The electrochemical reactions that proceed during the formation of positive plates can be represented by the following equations. E_h represents the equilibrium potential for the reaction at 298.15 K. These reactions were already presented in Chapter 2 of this book, but we will repeat them once again in this chapter for the sake of readers' convenience.



All equilibrium potentials are referred to a standard hydrogen electrode. The $\text{Hg}|\text{Hg}_2\text{SO}_4$ electrode is widely used in lead–acid battery investigations. This electrode has a potential which is 0.620 V more positive than that of the standard hydrogen electrode at pH = 0 [1].

The above reactions involve bivalent lead compounds with different PbO and PbSO₄ contents. The higher the content of PbO in a given compound, the more negative is the potential of its oxidation to PbO₂. Thus, on oxidation of a mixture of PbSO₄, 1BS, 3BS and Pb₃O₄ in the cured

paste after soaking, first PbO and then the basic lead sulfates will be oxidized. When the amount of the starting compounds diminishes, the potential of the positive plates will increase and when it exceeds the equilibrium $\text{PbO}_2|\text{PbSO}_4$ potential, oxidation of PbSO_4 will start. Consequently, different potential plateaux will be observed during formation of the soaked paste, depending on the phase composition of the paste. The development of potential plateaux for the different paste phases in the potential–time curve depends on the kinetics of the redox reactions. For purely kinetic reasons, some of the phases in the paste may not manifest themselves by a specific plateau in the potential curves. This is most often the case with formation of cured pastes, where, due to kinetic difficulties, the plateaux for the different basic lead sulphate electrodes merge.

10.2. Formation of PAM from 3BS-Cured Pastes

10.2.1. Influence of H_2SO_4 Concentration on the Reactions of PAM Formation from 3BS Pastes [2,3]

Pastes are prepared at 30 °C using H_2SO_4 and LO in a ratio of 4.5% by weight, and adding water until a paste density of 4.0 g cm^{-3} is obtained. H_2SO_4 solutions of 1.15 or 1.05 rel. den. are used as formation electrolyte and the time of soaking is 10 min. Small regions of the pasted plates are sulfated during the soaking step. The formation current density is 5 mA cm^{-2} .

The reactions that proceed during positive-plate formation have been identified by the accompanying changes in phase and chemical composition of the plates, as well as by the changes in both open-circuit and charge potentials of the plates. The phase composition is determined by X-ray diffraction analysis (XRD) and the chemical composition through conventional analytical methods; the potentials are measured vs. a $\text{Hg}|\text{Hg}_2\text{SO}_4$ reference electrode.

Figure 10.1 presents the changes in phase and chemical composition of the paste and of the active mass during formation of cells with 1.05 or 1.15 rel. dens. H_2SO_4 solution. The characteristic diffraction line with $d = 0.312 \text{ nm}$ is common for tet-PbO and $\alpha\text{-PbO}_2$ until the 6th hour of formation, but after that it reflects the content only of the $\alpha\text{-PbO}_2$ phase.

Depending on the phase and chemical composition of the paste and of the active mass, the formation process may be divided in two stages, as follows:

- (i) *Stage 1.* Lead oxide and basic lead sulfates are oxidized to $\alpha\text{-PbO}_2$ and small amounts of $\beta\text{-PbO}_2$. During this stage, the solution filling the paste pores is of neutral to slightly alkaline pH. The paste reacts with H_2SO_4 to form PbSO_4 (reaching approximately 25% on formation in H_2SO_4 solution of 1.05 rel. dens., or 52% in formation electrolyte of 1.25 rel. dens., at the end of the first stage); the potential is low, both under load and on open-circuit.

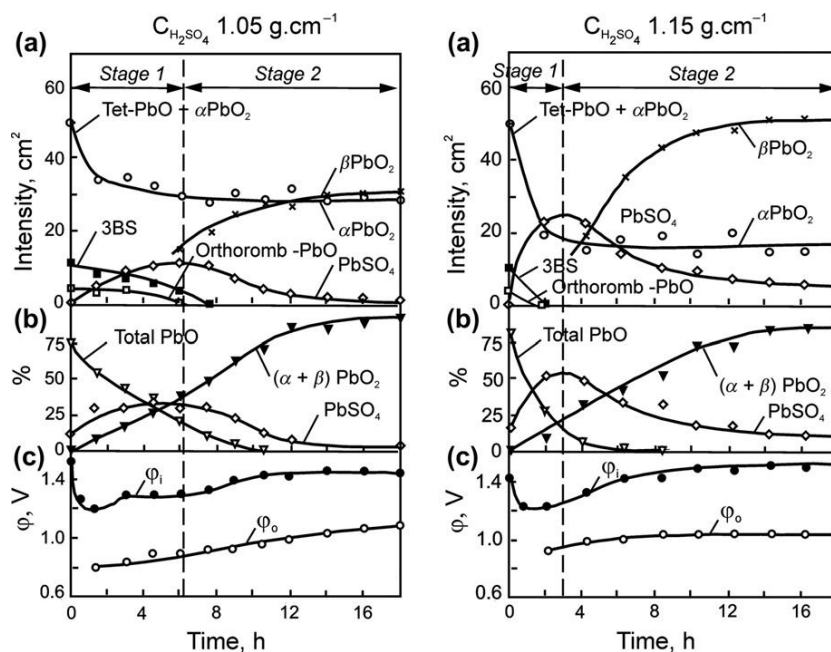


Figure 10.1:

Changes in (a) phase composition, (b) chemical composition, (c) potentials on open circuit (ϕ_0) and under current load (ϕ_i) during plate formation in two H_2SO_4 concentrations [2].

- (ii) *Stage 2.* The PbSO_4 formed on soaking and during the first stage of formation is oxidized to $\beta\text{-PbO}_2$. The pH of the pore solution is highly acidic. The potentials under load and on open circuit increase.

Figure 10.1 evidences that the short time of soaking and the low H_2SO_4 concentration on formation (1.05 rel. dens.) yield approximately equal amounts of $\alpha\text{-PbO}_2$ and $\beta\text{-PbO}_2$. On formation in 1.15 rel. dens. electrolyte, the phases formed are 71.6% $\beta\text{-PbO}_2$ and 28.4% $\alpha\text{-PbO}_2$. The duration of the first formation stage depends on the concentration of H_2SO_4 in the formation electrolyte: it is 6 h at $C_{\text{H}_2\text{SO}_4} = 1.05$ rel. dens. and only 3 h at $C_{\text{H}_2\text{SO}_4} = 1.15$ rel. den.

It follows from all above said that the increase in H_2SO_4 concentration on formation results in:

- shorter duration of the first stage of the formation process;
- formation of more PbSO_4 in the paste during the first formation stage;
- increased content of $\beta\text{-PbO}_2$ in PAM.

10.2.2. Evolution of the Pore System in the Paste During Formation

The changes in material volume during formation of PbO_2 from several lead compounds contained in the cured paste are summarised in Table 10.1 [4]. The data in Table 10.1 show that

Table 10.1: Material volume changes during formation of PbO₂ [4].

Compound	Moles PbO ₂ per Mole Compound	ΔV^a (cm ³)	% ΔV^a per Pb Atom
PbSO ₄	1	−23.12	−48.12
β -PbO	1	1.69	7.18
α -PbO	1	0.96	4.02
Pb ₃ O ₄	3	−0.72	−2.81
PbO·PbSO ₄	2	−12.66	−33.77
3PbO·PbSO ₄ ·H ₂ O	4	−13.00	−34.00
4PbO·PbSO ₄	5	−4.51	−15.38

^a ΔV is volume change upon conversion to β -PbO₂ per gram atom of Pb in compound.

oxidation of PbO to PbO₂ leads to an increase by 4 to 7% in the volume of the solid phase. By contrast, oxidation of basic lead sulfates to PbO₂ causes shrinkage of the solid phase volume by 15–34% per Pb atom. Thus, plates containing only basic lead sulfates may have cracks after formation. To reduce plate cracking, the paste should contain PbO and basic lead sulfates in an appropriate ratio. The overall material volume change will depend on the phase composition of the paste.

The changes in porosity of pastes, prepared with 6% H₂SO₄ vs. LO at 30 °C and containing 3BS, during formation with a current density of 2 mA cm^{−2} are presented in Fig. 10.2 [5]. The pore size distribution curves for the surface layers and for the interior of the plate are plotted and compared with those for an unformed plate.

The cured paste in the plate interior is hydrated and at the plate surface it is sulfated, which is the reason for the smaller pore volume in the surface plate layers. During the first formation stage (12 Ah, 18 Ah), the average pore radius (determined from the inflection point of the curves) remains practically unchanged: the number of fine pores increases whilst that of large pores decreases. The total volume of the pores decreases, which indicates that sulfation and hydration processes have a predominant effect on pore volume during this stage. During the second stage of formation (28 Ah, 60 Ah), PbSO₄ is oxidized to PbO₂ and the average radius of the pores increases from 0.15 to 0.80–1.00 μm , whereas the total pore volume of the active mass increases from 0.065 to 0.085 cm³ g^{−1} PAM.

The above results indicate that the pore system of PAM is determined by the phase composition of the paste and by the processes of its sulfation during the soaking step and the first formation stage.

10.2.3. Chemical and Electrochemical Reactions during Formation of Lead–Acid Battery Positive Plates

Based on the analytical data for the changes in phase and chemical composition of the plates during formation, a general scheme has been proposed for the chemical and electrochemical

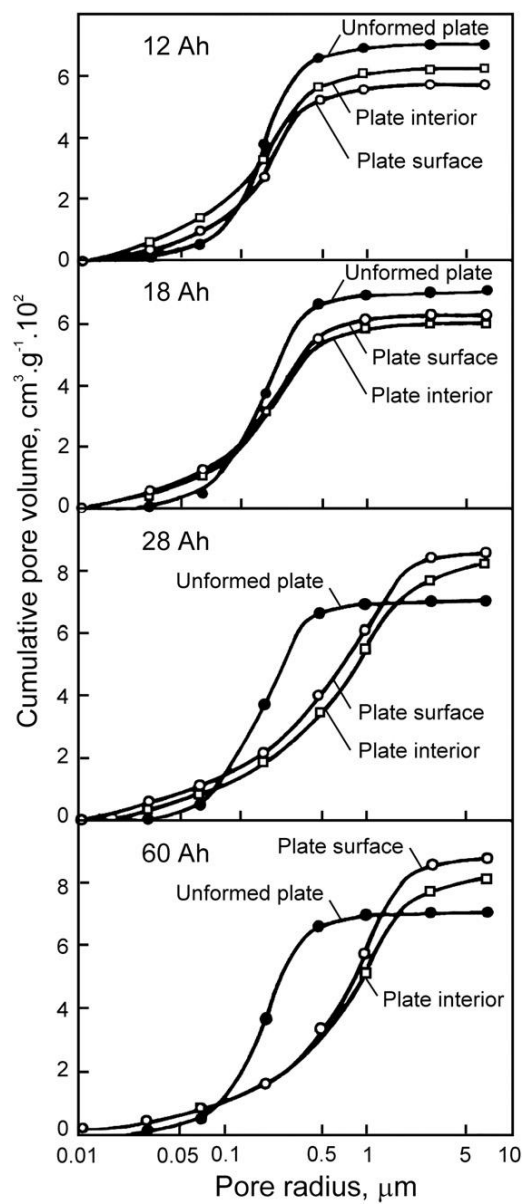


Figure 10.2:

Changes in total pore volume and pore-size distribution by radius for 3BS paste and active mass during formation [5].

reactions that proceed during the two stages of formation (see Fig. 10.3) [5]. The reactions of formation of PbO_2 from the basic lead sulfates during the first formation stage are represented by a general formula of the stoichiometric coefficients in Fig. 10.3. The parameter θ gives the amount of Pb^{2+} ions that participate in the electrochemical process (B) leading to the formation of PbO_2 according to reaction (C); $(1-\theta)$ stands for the remainder of the lead ions that react to form PbSO_4 (reaction D).

The coefficient m accounts for the PbO ‘molecules’ in the basic lead sulfate. When the paste consists solely of PbO , $m = \infty$. The corresponding values of m for PbO and PbSO_4 are 1 and 0,

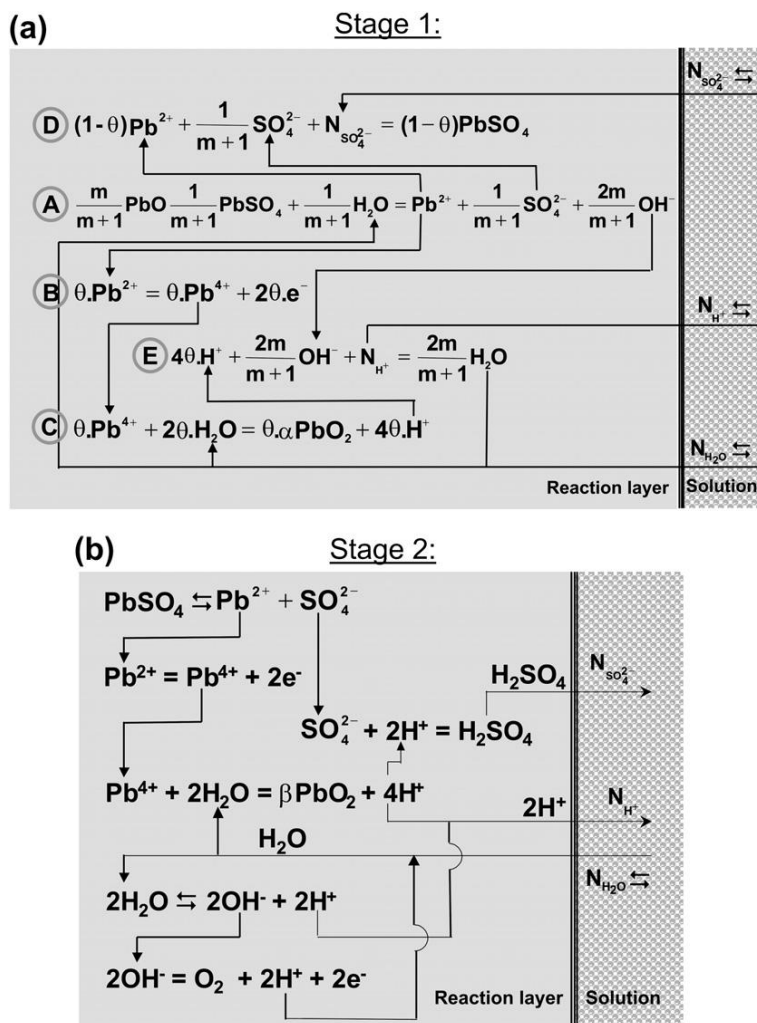


Figure 10.3:

General scheme of the reactions during (a) the first and (b) the second stages of PAM formation [5].

respectively. When the paste consists solely of PbSO_4 , $m = 0$, and the corresponding coefficient values are 0 and 1. In the case of $3\text{PbO} \cdot \text{PbSO}_4 \cdot \text{H}_2\text{O}$ pastes, $m = 3$. The electrochemical and chemical reactions proceed in a reaction layer located between the formed PbO_2 zone and the unformed paste.

It can be seen from the reaction scheme in Fig. 10.3 that an exchange of H^+ and SO_4^{2-} ions, and H_2O flows (signified by N_{H^+} , $N_{\text{SO}_4^{2-}}$ and $N_{\text{H}_2\text{O}}$) is needed between the reaction layer and the bulk of electrolyte for the reactions to proceed. Let us assume that the water exchange is very rapid and does not control the processes in the reaction layer. The flows of H^+ and SO_4^{2-} ions may enter or leave the reaction layer, depending on phase composition of the paste, current density, electrolyte pH, etc. [6]. The process of formation will advance in the direction where the H^+ and SO_4^{2-} ion flows move at the highest rate.

Due to the different colouring of the initial and final products of the reactions of formation, it is easy to follow the progress of the formation processes throughout the plate volume.

The grid is the only electron conductor in the cured plate. The paste is a semi-conductor with high ohmic resistance. PbO_2 has electron conductivity. Hence, the process of formation commences from the grid bars yielding PbO_2 phase, which grows into the bulk paste volume. During plate formation, the reaction layer moves in the paste volume, increasing the volume of the formed PAM.

Lead oxides and basic lead sulfates are white or yellow in colour, whereas PbO_2 is dark brown or black. This difference in colour allows the formed and unformed zones in the plate to be clearly distinguished during the first formation stage. Photographs of the plate cross-section during different stages of formation in H_2SO_4 of 1.15 rel. dens. are shown in Fig. 10.4 [2]. The growth of PbO_2 starts at the grid bars and can be clearly seen as a dark-brown zone. Phase analysis shows that this zone consists of PbO_2 and PbSO_4 crystals. During formation, the $\text{PbO}_2 + \text{PbSO}_4$ zone grows first in the interior of the plate. White zones of PbSO_4 crystals, which are formed on both surfaces of the plate during the soaking step and during the first formation stage, grow into the plate core. The $\text{PbO}_2 + \text{PbSO}_4$ zones of two adjacent grid bars advance towards each other until they coalesce and then the PbSO_4 is oxidized to $\beta\text{-PbO}_2$. As this second stage of formation the electrode potential is highly positive (Fig. 10.1), the PbSO_4 formed in the interior of the plate during the first stage is also oxidized to $\beta\text{-PbO}_2$. The direction of growth of the $\text{PbO}_2 + \text{PbSO}_4$ zone during stage 1 is determined by the transport hindrances that the H^+ and SO_4^{2-} ion flows have to overcome and by the water transfer between the reaction layer and the bulk electrolyte, as well as by the paste composition and the formation current density [6].

Zonal processes are slow processes. They are responsible for the long duration of plate formation. Hence, it is important to find methods to by-pass the zonal processes. In order to accelerate the formation of positive plates, some conductive additives have been added to the

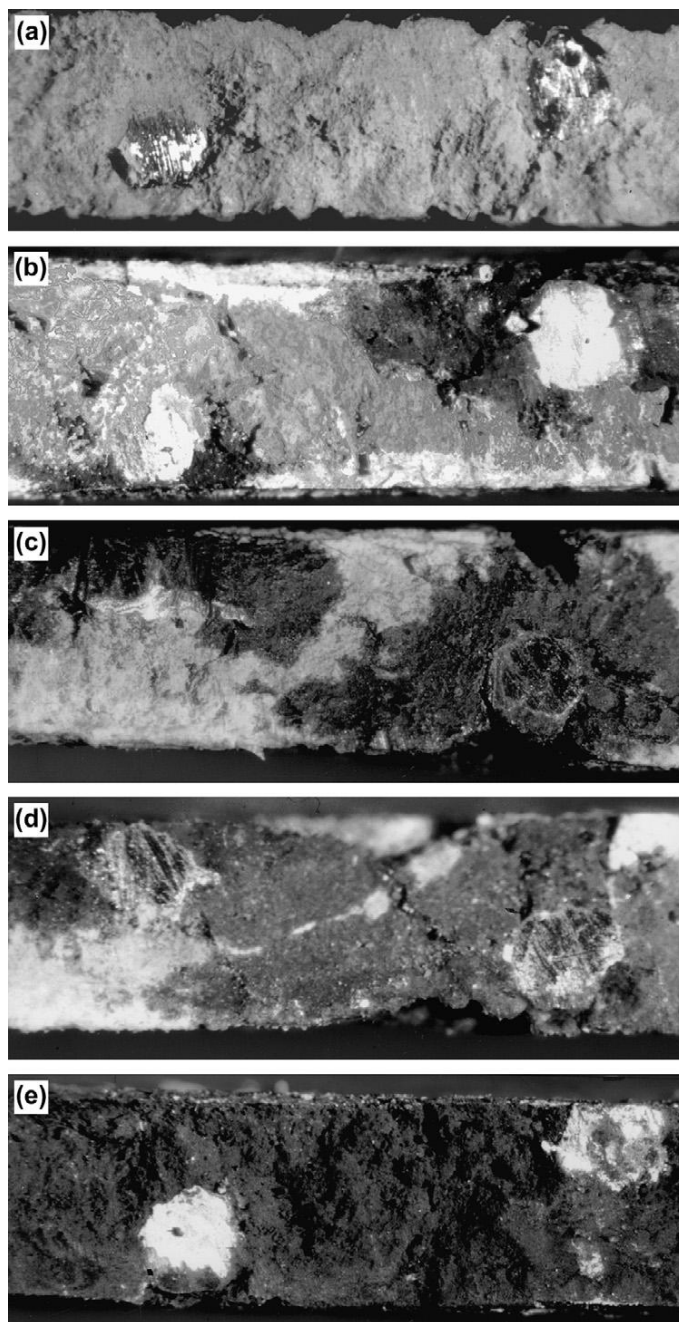


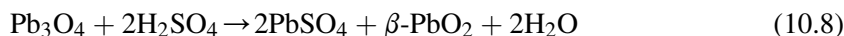
Figure 10.4:

Photomicrographs of cross-sections of a plate portion between two grid bars at different stages of formation in H_2SO_4 of 1.15 rel. dens: (a) unformed plate; (b–d) the dark portions are PbO_2 Zones, while the light ones are zones of unformed cured paste; (e) completely formed plate [2].

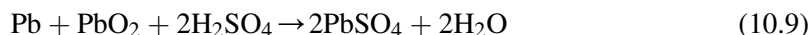
positive pastes [7,8]. These additives increase the conductivity of the cured paste and the electric current flows along the conductive additive network, thus formation proceeds almost uniformly throughout the whole plate volume. The additives should be chemically stable in H_2SO_4 solution. Data have been reported about successful attempts to reduce the duration of the formation procedure to 8 h.

Conductive additives proposed in the literature as formation catalysts include the following:

- (i) Carbon, anisotropic graphite and graphite.
- (ii) Conductive polymers, i.e. polyaniline, polypyrrole, polyparaphenylene and polyacetylene, in the form of powders or fibres. These polymers are added to the positive paste. The maximum amounts of these additives should not exceed a few percent by weight. As of today, there are no data evidencing wide use of these polymers in the battery industry.
- (iii) Glass fibres coated with SnO_2 have been developed and used in lead–acid battery positive plates with the aim to improve the process of plate formation and the performance of the plates.
- (iv) Barium plumbate is a relatively stable conductive ceramic having the perovskite structure. Addition of this material to PAM improves significantly the formation efficiency [9,10].
- (v) Lead dioxide or red lead (25–50%) are widely used by many major battery manufacturers. When H_2SO_4 is added to red lead the following reaction proceeds:



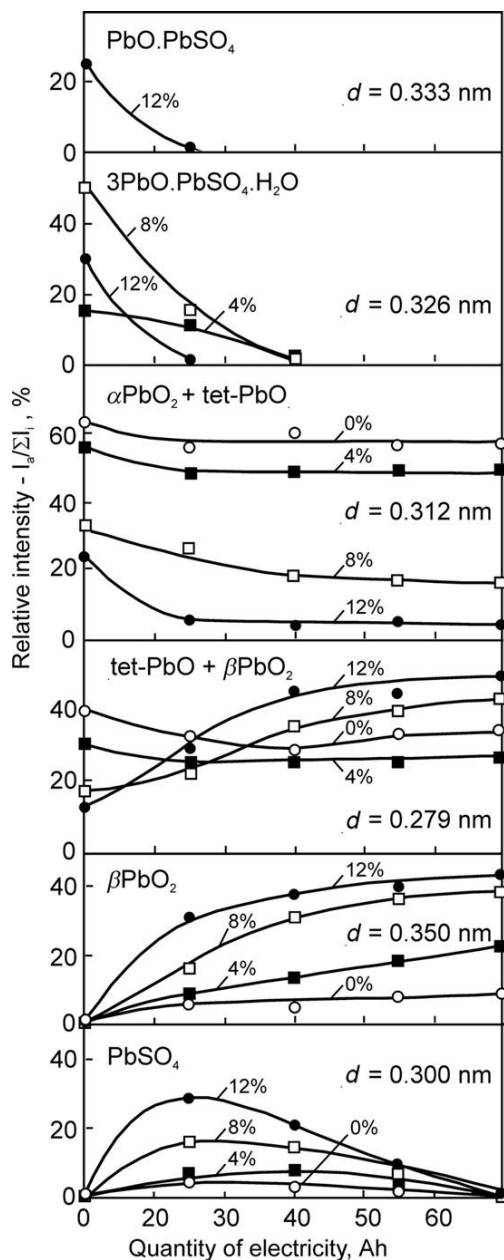
$\beta\text{-PbO}_2$, when present in sufficient amounts, may suppress the zonal processes and thus improve substantially the efficiency of the formation process. This can be achieved, however, only if the leady oxide does not contain much lead. In the opposite case, the following reaction proceeds:



and the role of Pb_3O_4 as an additive that suppresses the zonal processes is eliminated.

10.2.4. Influence of the Ratio $\text{H}_2\text{SO}_4/\text{LO}$ on the Reactions of Formation of 3BS Pastes [5]

Figure 10.5 illustrates the changes in phase composition during formation of pastes prepared with different proportions of H_2SO_4 and LO ($\text{H}_2\text{SO}_4/\text{LO} = 0, 4, 8$, or 12% by weight). The first formation stage is completed when the 3BS, 1BS and PbO phases in the paste are used up, and it is marked by the maximum content of PbSO_4 in the plate. The characteristic X-ray diffraction lines with $d = 0.312$ nm and $d = 0.279$ nm (though common for tet- PbO and PbSO_4 as well) are assumed to be characteristic lines for α and $\beta\text{-PbO}_2$. At the end of the formation process, when tet- PbO and PbSO_4 are oxidized to PbO_2 , the relative intensities of the above

**Figure 10.5:**

Relative intensity of the characteristic diffraction lines for the different phases in the paste during formation of plates with pastes prepared with different $\text{H}_2\text{SO}_4/\text{LO}$ ratios: 0, 4, 8 or 12% by weight [5].

diffraction lines reflect only the contents of α and β -PbO₂. Hence, it is possible to determine the proportion between β and α -PbO₂ in PAM. With increase of H₂SO₄/LO ratio the α/β -PbO₂ ratio decreases rapidly.

The influence of paste composition on the direction of growth of the PbO₂ + PbSO₄ zones is illustrated in Fig. 10.6 [5]. The data are for cross-sections of partially formed plates prepared with pastes containing 0, 2, 4, 6, 8, 10 or 12% H₂SO₄. Examinations have been carried out after 8 h of formation of 12 Ah battery plates.

In all cases, formation starts at the grid bars and the growth of the zones depends on the amount of H₂SO₄ in the paste. If the paste is prepared with water alone (i.e. 0% H₂SO₄), the zones advance initially along the surface of the plate and then into its interior. With pastes containing more than 8% H₂SO₄, the growth of the zones proceeds in the reverse direction. On formation of pastes prepared with 2–6% H₂SO₄, the growth may follow different patterns depending on the acid-to-oxide ratio in the paste and the density of the formation current [6]. Hence, the phase composition of the active mass (α -PbO₂ or β -PbO₂) will differ for the different regions within the cross-section of the plate and will depend on the direction of PbO₂ + PbSO₄ zone growth during formation. At low H₂SO₄/LO ratios, the N_{H⁺} and N_{SO₄²⁻} ion flows will enter the reaction layer. Their movement will be most facilitated if the PbO₂ + PbSO₄ zone grows along the plate surface, as this is the shortest distance between the reaction layer and the bulk of the solution. At H₂SO₄/LO > 8%, the N_{H⁺} and N_{SO₄²⁻} ion flows will move in the opposite direction, i.e. out of the reaction layer located between the paste and the PbO₂ + PbSO₄ zone. These ion flows will leave the reaction layer most rapidly if they penetrate into the paste, as they will react with it as a result of which a high acid concentration gradient will be created. This is actually observed in Fig. 10.6, the PbO₂ + PbSO₄ zone grows into the paste interior.

10.3. Formation of Plates Prepared with 4BS Cured Pastes

The size of 4BS crystals varies from 10 to 100 μ m in length and from 2 to 15 μ m in diameter. The changes in phase and chemical composition of the plate during formation of 4BS pastes are illustrated in Fig. 10.7 [11]. The cured paste is initially composed of 4PbO·PbSO₄, tet-PbO and orthorhomb-PbO. The data in Fig. 10.7 give grounds for the following conclusions:

- (i) The basic product of the electrochemical reaction is β -PbO₂. The results of the chemical analysis and the XRD data for β -PbO₂ indicate that oxidation of the paste to PbO₂ proceeds at a fairly high rate until the PbO₂ content reaches ~70 wt%, and then slows down.
- (ii) At the beginning of the formation process, it is virtually impossible to prove the presence of α -PbO₂ by XRD analysis. This is because the characteristic diffraction lines for α -PbO₂ coincide with those for other lead compounds. After 30 h of formation, however, the 3.12 Å line is pretty well expressed and, hence, it can be concluded with confidence that the line signifies the presence of α -PbO₂.

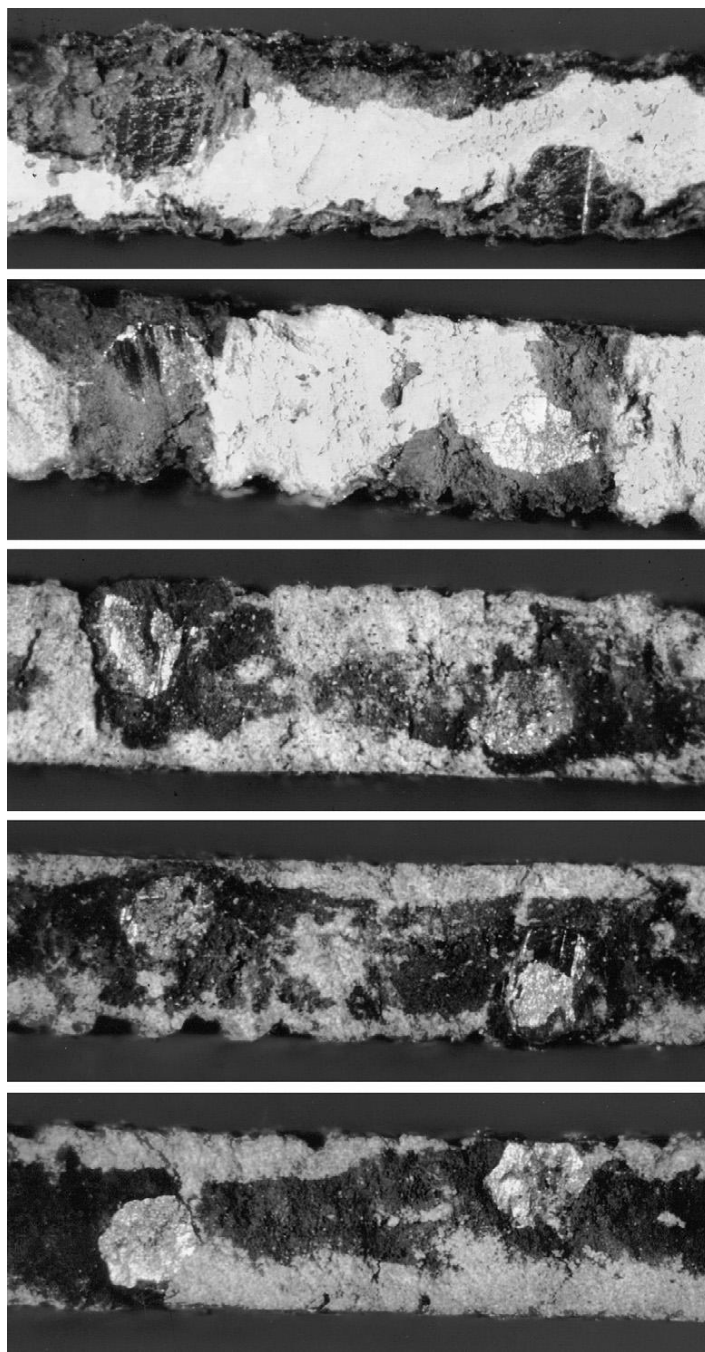


Figure 10.6:
 $\text{PbO}_2 + \text{PbSO}_4$ zones in partially formed plates prepared with pastes of different acid-to-oxide ratio (wt%). Plate thickness is 1.8 mm [5].

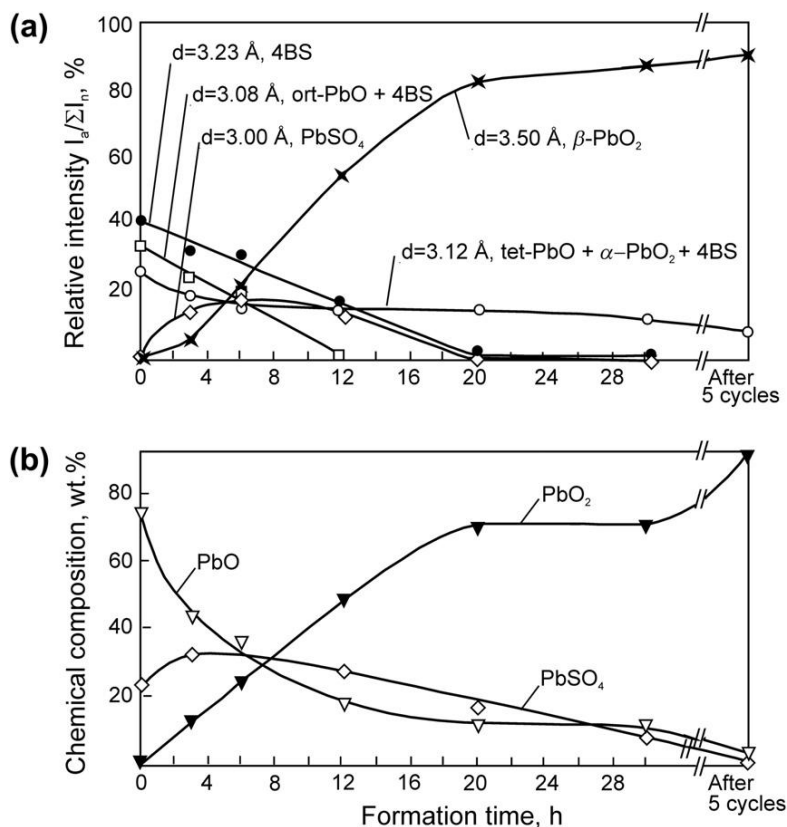


Figure 10.7:

Changes in (a) phase and (b) chemical composition of 4BS pastes during active mass formation. Maximum degree of formation is 70% after 30 h [11].

- (iii) During plate formation, H_2SO_4 reacts with PbO and $4\text{PbO} \cdot \text{PbSO}_4$ to yield PbSO_4 . The amount of PbSO_4 reaches a maximum after about 6 h of formation and decreases slowly thereafter. After 20 h, broad peaks appear at interplanar distances of 3.00 \AA and 3.33 \AA that differ slightly from the noise signal. This suggests that the PbSO_4 phase is most probably present in the form of very fine crystals.
- (iv) The amount of $4\text{PbO} \cdot \text{PbSO}_4$ decreases gradually during formation and, after 20 h, the 3.23 \AA line is very wide and differs but slightly from the noise signal.

The remaining unformed 4BS crystals can be easily identified by immersing a piece of PAM in a mixture of $\text{H}_2\text{O}_2 + \text{HNO}_3$. Lead dioxide dissolves in this solution and the remaining core consists of 4BS and PbSO_4 phases, as confirmed also by the XRD data. A scanning electron micrograph of the plate core is presented in Fig. 10.8 [11]. The remnants of unformed 4BS in the interior of particles are marked by circles.

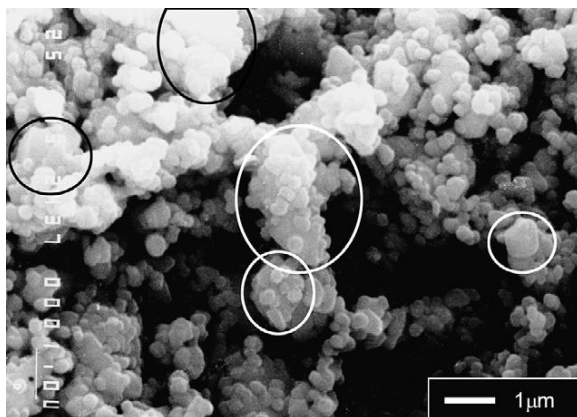


Figure 10.8:

Scanning electron micrograph of non-formed parts of particles in the interior of PbO_2 agglomerates after 30 h of formation. PbO_2 is dissolved in $\text{H}_2\text{O}_2 + \text{HNO}_3$. X-ray diffraction analysis evidences presence of PbSO_4 crystals [11].

As mentioned earlier in Chapter 9 devoted to soaking, only a superficial layer of 4BS crystals (1–2 μm thick) is sulfated during the soaking procedure. Further sulfation stops thereafter. If the diameter of 4BS crystals is kept constant (about 10 μm), their length does not influence the efficiency of the formation process [12]. The formation efficiency depends very strongly on the diameter of the 4BS crystals [12,13].

The formation of 4BS crystals is influenced by the conditions of soaking, which determine the thickness of the PbSO_4 layer formed on the surface of 4BS crystals. The stages of formation of a partially sulfated 4BS crystal are shown schematically in Fig. 10.9 [13].

First, the superficial PbSO_4 layer is oxidized to PbO_2 (Fig. 10.9b). As a result of the electrochemical and chemical reactions involved in formation of the latter compound, H_2SO_4 is formed which reacts partially with the 4BS crystals to produce more PbSO_4 , and the remaining unreacted part of H_2SO_4 leaves the crystals. Consequently, a layer of 4BS + PbSO_4 is formed in the crystal interior (Fig. 10.9c). The unoxidized interior of the large 4BS crystals can be easily dissolved by treating the formed PAM with ammonium acetate solution at 80 °C. The bivalent compounds dissolve and only PbO_2 remains in the PAM. An electron micrograph of a treated sample of PAM after 6 h of formation is shown in Fig. 10.10 [11].

The PbO_2 surface layer consists of small agglomerates with micropores in-between. During formation, H_2O and H^+ ions have to penetrate through these pores into the interior of the 4BS crystal and SO_4^{2-} ions have to escape. These flows have to overcome some transport hindrances on their way. The data in Fig. 10.7 evidence that formation of the remaining part of the 4BS crystals cannot be completed even after 30 h of formation. Ion transport difficulties are the

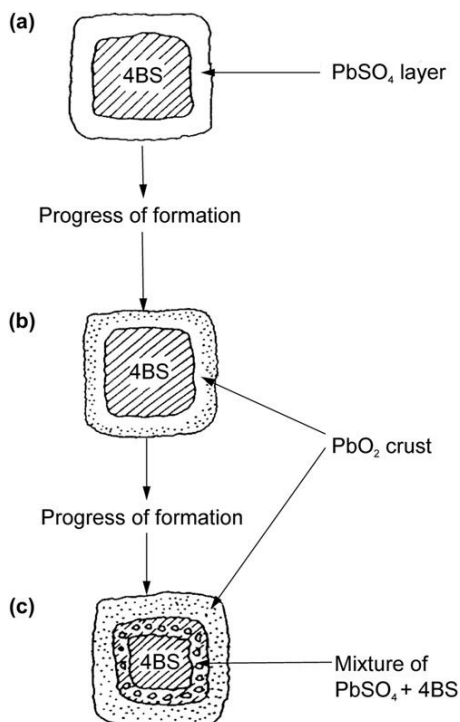


Figure 10.9:
Schematic of conversion of 4BS crystals to PbO_2 after a short soaking period [13].

reason for the low efficiency of formation of the 4BS crystals. The interior of the aggregates is formed only after 5–10 deep discharge–charge cycles.

10.4. Mechanisms of the Crystallization Processes During Formation of Positive Plates with 4BS Paste

The chemical alteration of one solid material into another one, through chemical and electrochemical reactions involving import and export of chemical components (mass transfer), with no changes in the outer matrix of the solid materials is called ‘metasomatism’. Burbank [4] has observed metasomatism on transformation of 4BS cured paste into PbO_2 active mass. Figure 10.11 shows SEM pictures of 4BS crystals of the paste as well as of PbO_2 aggregates in PAM.

The matrix of 4BS crystals is transformed into aggregates of PbO_2 particles, which preserve the shape of the initial substance. PbO_2 aggregates interconnect to form a skeleton with a structure similar to that of the initial cured paste. The strength of this skeleton depends on the length and thickness of its branches as well as on the strength of their connections. In the case of PAM

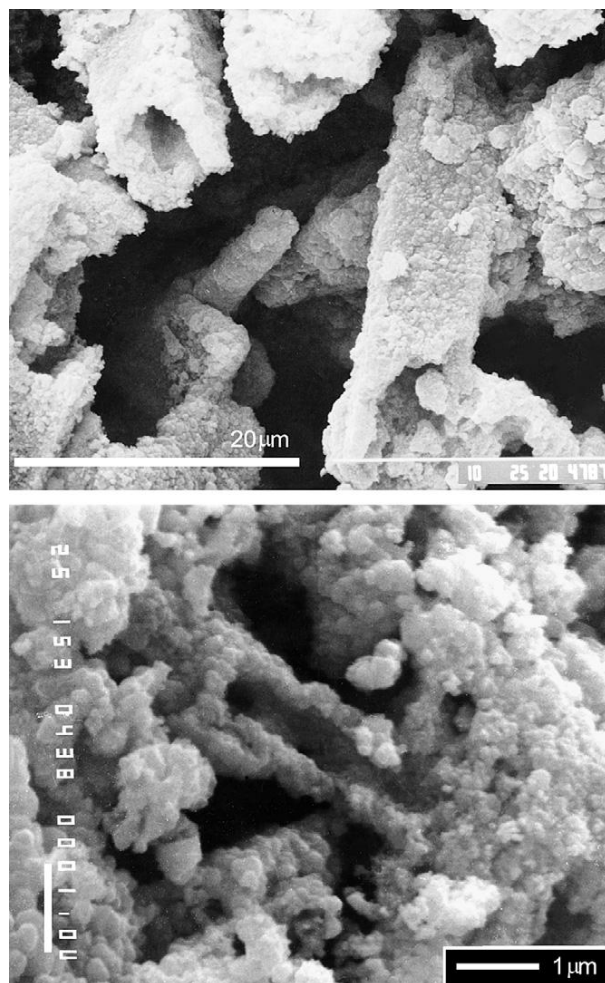


Figure 10.10:

Electron micrographs of PbO_2 aggregates, treated with ammonium acetate, after 6 h of formation. Inner parts of aggregates have dissolved [11].

formed from 4BS pastes, the size of the skeleton branches is predetermined by the size of the 4BS crystals of the paste and by the connections between them formed during the process of curing. Hence, the PAM skeleton formed is stable and batteries with 4BS positive plates have long cycle life.

On formation of 4BS pastes, the reactions between H_2SO_4 and the surface of 4BS crystals proceed at a very high rate and a porous PbSO_4 forms on the 4BS crystal surface. Later during the formation process, this layer is oxidized as the plate potential exceeds the equilibrium potential of the $\text{PbO}_2/\text{PbSO}_4$ electrode. This happens through formation of a thick layer of PbO_2 within the matrix of the 4BS crystal. Thus, metasomatic

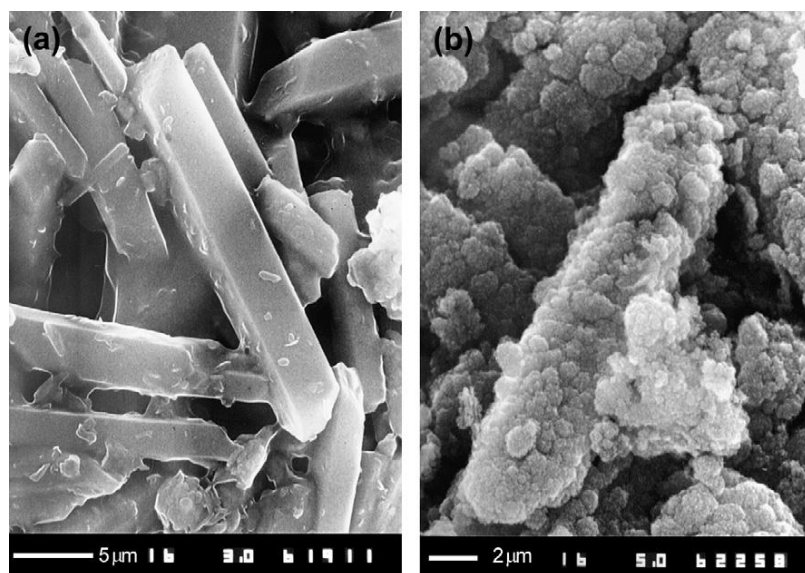


Figure 10.11:

SEM micrographs of the structure of (a) cured 4BS paste and (b) PAM obtained from 4BS paste.

transformation of the paste structure into PAM structure occurs. If, however, oxidation of 4BS proceeds through a dissolution mechanism and Pb^{2+} ions enter the solution, i.e. oxidation proceeds somewhere else on the PbO_2 surface, PAM will not ‘remember’ the initial structure of the cured paste.

In the case of 3BS pastes, the skeleton is built of branches of aggregates and agglomerates of 3BS and PbO particles. The size of aggregates depends on the number and size of the 3BS particles building it (2–4 μm in length and 0.2–1.0 μm in diameter), as well as on the area of the contact surfaces between the particles and the strength of these contacts. If the 3BS and PbO aggregates are less than 8–10 μm long and 3–4 μm wide, they will react with H_2SO_4 on soaking and the shape of the PbSO_4 crystals will become dominating. No metasomatic processes will occur and hence the 3BS skeleton matrix will not be reproduced. If, however, the aggregates and agglomerates are larger than 15–20 μm in length and 8–10 μm in diameter, the superficial process of sulfation will ‘seal’ their shape without changing it and formation will proceed through metasomatic processes.

It can be expected that PAM obtained from 3BS paste will comprise aggregates of both above types. However, judging by the initial capacity and cycle life performance of 3BS positive plates, the latter type of aggregates predominates in cured 3BS pastes of higher density. The transfer of the cured paste structure to the structure of PAM depends on the PbSO_4 layer formed on the surface of the paste aggregates and on its thickness and continuity.

10.5. Structure of the Formed Interface Grid/Corrosion Layer/Active Mass [14]

As discussed in Chapter 7 of this book, the interface paste/corrosion layer comprises lead hydroxide after curing. During plate soaking, part of the $\text{Pb}(\text{OH})_2$ undergoes sulfation. It is interesting to see what is the structure of the formed corrosion layer. In an attempt to examine this structure after 1 Ah of electricity has passed through the plate, the paste was removed from the grid and grid surface beneath it was examined. The surface was black in colour due to the PbO_2 deposited on it. Part of the grid was processed with ammonium acetate to dissolve the bivalent compounds and then the corrosion layer was examined by scanning electron microscopy.

Figure 10.12 shows SEM pictures of formed corrosion layer [14]. It is heterogeneous in structure. This heterogeneity of the oxidized corrosion layer may be a result of the presence of SnO_2 in this layer (the grid alloy used was PbSnCa), which has dissolved or parts of the corrosion layer have remained un-oxidized and these bivalent compounds dissolve during the acetate treatment. This appearance of the corrosion layer implies that oxidation of this layer occurs without dissolution, i.e. through a solid state reaction.

The hydrated corrosion layer is readily oxidized to lead dioxide. The latter is ion conductive and is in contact with the PbSO_4 and basic lead sulfate particles of the paste. These particles have to be oxidized to PbO_2 . Oxidation of PbSO_4 proceeds by two mechanisms: without

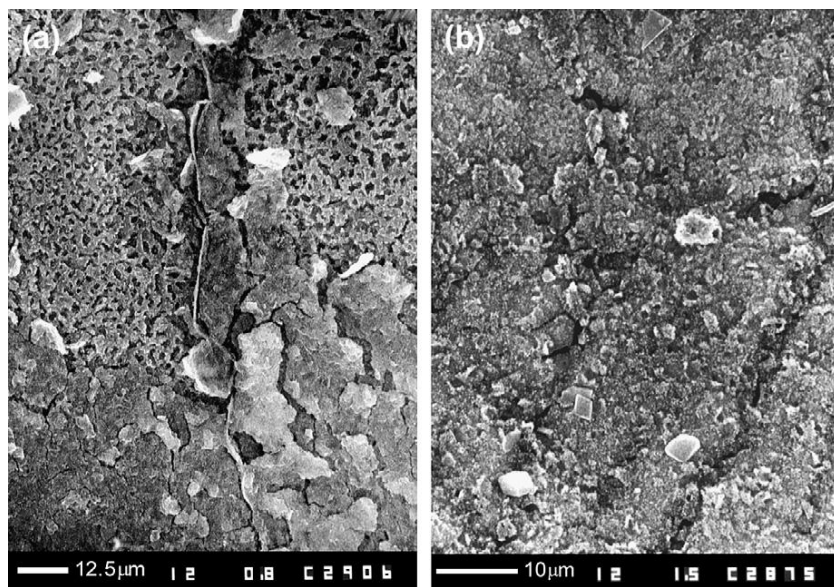


Figure 10.12:

SEM pictures of the formed part of the corrosion layer. (a) corrosion layer with visible intergranular layer, (b) the intergranular layer in the corrosion layer has dissolved (dark lines).

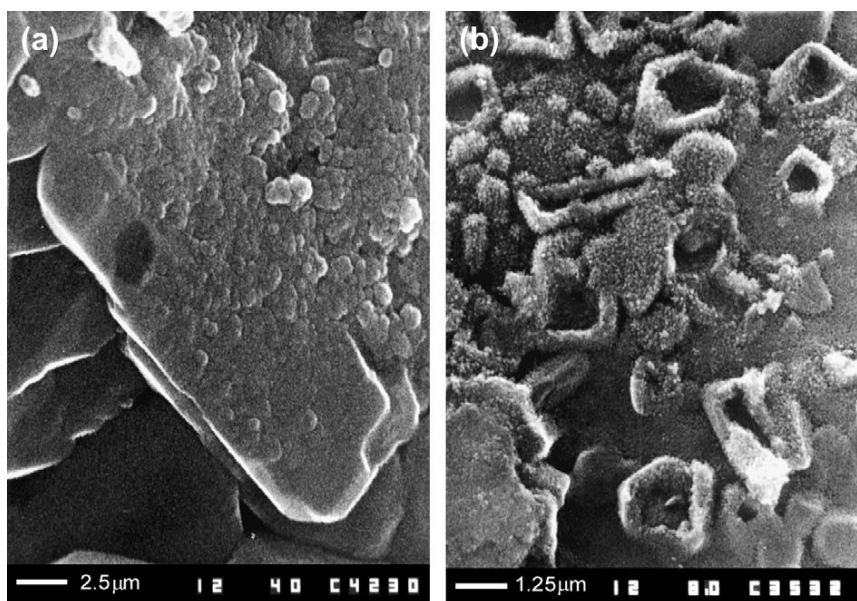


Figure 10.13:

PbSO₄ crystals of the interface partially oxidized by (a) reactions on the surface of the PbSO₄ crystal without dissolution of the latter and (b) oxidation of Pb²⁺ ions after dissolution of the PbSO₄ crystal.

dissolution and with dissolution in the pore solution. In the former mechanism PbSO₄ crystals on the CL surface are oxidized without destroying the PbSO₄ matrix. This reaction is illustrated in Fig. 10.13a. The matrix of the PbSO₄ crystals is transferred to the PbO₂ aggregates. This oxidation is not always completed within the technological process of formation and proceeds further during battery cycling.

The second mechanism of PbSO₄ crystal oxidation is through dissolution of these crystals. This mechanism is similar to the mechanism of oxidation during charge of the positive plates. The hydrated corrosion layer is oxidized to PbO₂ first. Then, the PbSO₄ crystals dissolve and Pb²⁺ ions diffuse to the solution surrounding the PbSO₄ crystal. Pb²⁺ ions are oxidized on the PbO₂ surface of the corrosion layer near the PbSO₄ crystal. The formed PbO₂ particles build a layer that surrounds the dissolving PbSO₄ crystal. These PbO₂ particles are clearly seen in the micrograph in Fig. 10.13b.

Now, let us consider the formation of 4BS crystals bonded to the corrosion layer. This interface is presented in Fig. 10.14a. The SEM pictures in the figure feature the structure of the 4BS/CL interface before and after acetate treatment. The 4BS crystals are tightly connected to the CL by hydration processes (Fig. 10.14a). After oxidation of the CL, solid state oxidation of the hydrated layer in the 4BS crystals starts. When the bivalent lead compounds are fully dissolved

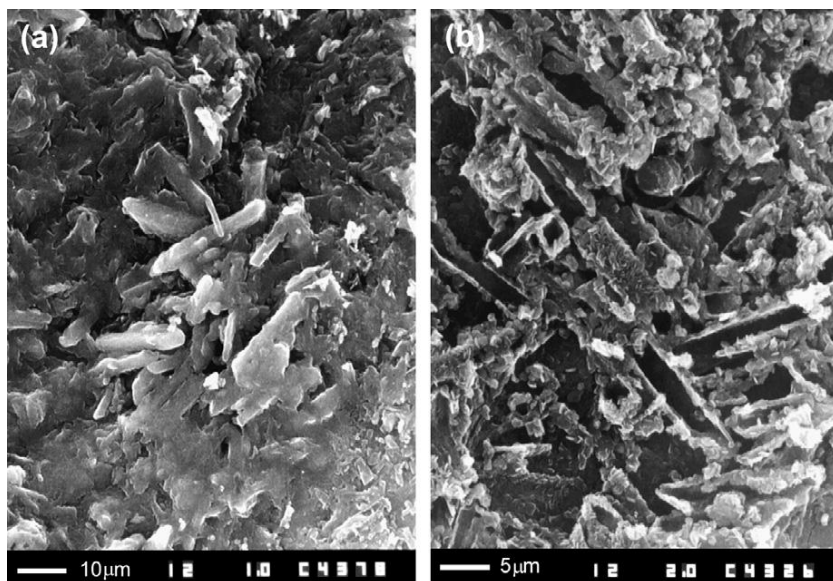


Figure 10.14:

Formation of 4BS crystals connected to the corrosion layer: (a) before and (b) after acetate treatment.

by the acetate treatment, the oxidized hydrated parts of the 4BS crystals can be seen. These are presented in the photograph in Fig. 10.14b. They feature clearly the matrix of the 4BS crystals.

10.6. Influence of the H_2SO_4/LO Ratio on the Proportion Between β - and α - PbO_2 in PAM and on Plate Capacity

The influence of the H_2SO_4/LO ratio on the capacity of positive plates has been studied by the following method. Pastes are prepared at 30 °C (3BS) or 80 °C (4BS) using H_2SO_4 and LO in different proportions from 0 to 12% by weight [15]. Formation of the plates is conducted in H_2SO_4 solution of 1.05 rel. dens., so that only a small part of the paste is sulfated during soaking and formation. These plates are assembled in 14 Ah cells (comprising one positive and two negative plates per cell), which are set to formation, followed by determination of the β/α - PbO_2 ratio in PAM and capacity tests at two discharge currents, 0.7 A and 42 A. The results of these investigations are summarised in Fig. 10.15 [15].

The following conclusions can be drawn from the data in Fig. 10.15:

- (a) The β/α - PbO_2 ratio increases with increase of the H_2SO_4/LO ratio for PAM produced from both 3BS and 4BS pastes. At H_2SO_4/LO ratios up to 8%, the content of β - PbO_2 vs. that of α - PbO_2 increases but slightly, whereas at H_2SO_4/LO ratios above 8 and up to 12%, when 1BS forms, the β/α - PbO_2 ratio increases rapidly.

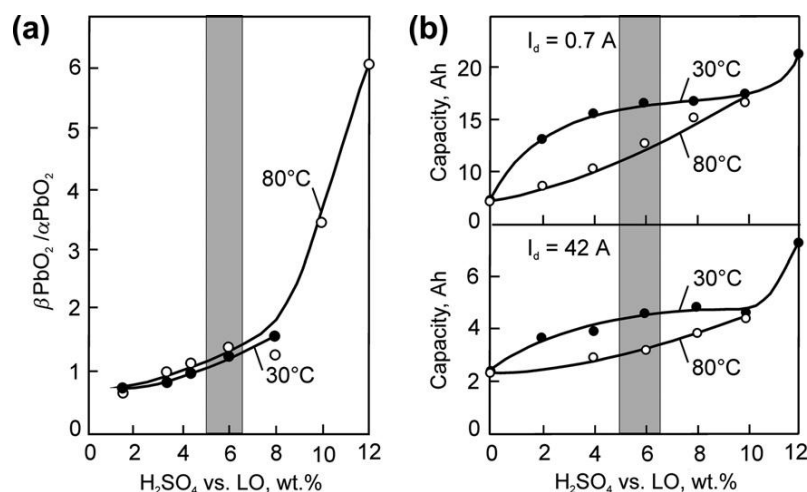


Figure 10.15:

(a) Experimentally determined $\beta/\alpha\text{-PbO}_2$ ratio in PAM and (b) cell capacity, as a function of $\text{H}_2\text{SO}_4/\text{LO}$ ratio in the paste [15].

- (b) With increase of the content of $\beta\text{-PbO}_2$ in PAM, the capacity of the positive plates increases, but this is not an unambiguous correlation. The capacity increase depends on the type of basic lead sulfate in the paste: a greater capacity increase is measured for plates prepared with 3BS pastes as compared to those produced with 4BS pastes. The most significant capacity increase is registered when the PAM is formed from a paste with high 1BS content ($\text{H}_2\text{SO}_4/\text{LO} = 12\%$).
- (c) The correlation between cell capacity and $\text{H}_2\text{SO}_4/\text{LO}$ ratio is influenced also by the discharge current. At high discharge current ($I = 3 C_{20} \text{ A}$), the effect of the $\beta/\alpha\text{-PbO}_2$ ratio is reduced substantially. Probably, this dependence is also affected by the type of pore system formed in PAM.

The distribution of the $\alpha\text{-PbO}_2$ and $\beta\text{-PbO}_2$ phases through the cross-section of the plate depends on the local pH of the solution that fills the pores of the reaction layer. It has been established that $\beta\text{-PbO}_2$ predominates in the outer layers of the plate, whereas $\alpha\text{-PbO}_2$ is found mostly in the plate core [16–21]. This phase distribution is determined greatly by the zonal processes that occur in the plate.

10.7. Structure of the Positive Active Mass

10.7.1. Micro and Macrostructure of PAM

Having made an overview of the processes that take place during formation of the plates, the question arises as to what kind of structure is formed as a result of these processes?

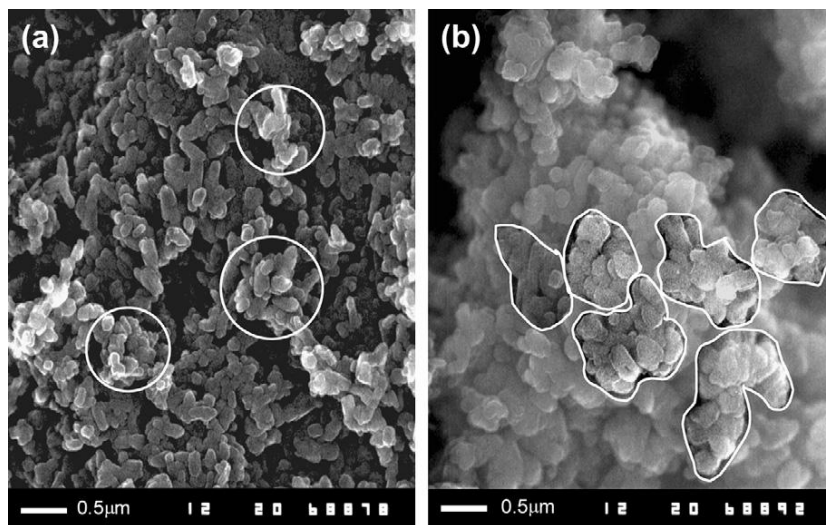


Figure 10.16:

SEM pictures of PAM: (a) PbO_2 particles, and (b) PbO_2 agglomerates.

Employing scanning electron microscopy and porometry we have examined the structure of the positive active mass after formation and during cycling of the plates and have proposed a model for this structure [22–25]. Figure 10.16 presents SEM pictures of PAM at high magnifications.

Microstructure of PAM

The smallest building element of PAM structure is the *PbO₂ particle* (Fig. 10.16a). These particles interconnect in different ways. When a certain number (10–20) of PbO_2 particles interlock so tightly that the boundaries of the individual particles are hardly visible, an *agglomerate* is formed. Several agglomerates are marked by circles in the SEM picture in Figure 10.16b. A huge number of agglomerates and particles interconnect into an *aggregate or branch* (see Fig. 10.16b) with micropores in-between. Particles, agglomerates and micropores form the local *microstructure of PAM*. The aggregate volume is microporous and, hence, ions of the solution can access it. Micropores have large surface where the electrochemical and chemical reactions proceed, provided the aggregate surface is highly porous. In certain PAM structures, however, the aggregate surface is but slightly porous. A superficial membrane layer forms, which slows down the rate of the electrochemical and chemical reactions in these aggregates or localises them in some sites only. Consequently, the utilization of PAM during the current generation process is restricted. So the porosity of the surface of PAM aggregates exerts an influence on the capacity performance of positive plates.

Macrostructure of PAM

A huge number of aggregates interconnect to form a *skeleton or porous mass*, which is connected to the plate grid through an interface. Micrographs of PAM skeleton and porous

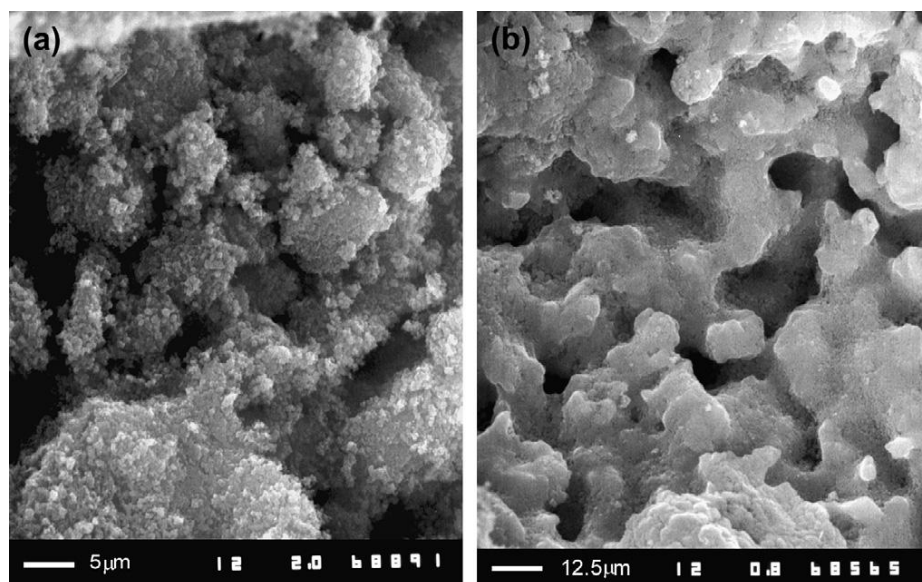


Figure 10.17:

SEM pictures of PAM skeleton with macropores between the aggregates. (a) and (b) SEM images at different magnifications.

mass are presented in Fig. 10.17. Macropores are formed between the skeleton branches (aggregates) along which H^+ and SO_4^{2-} ions and water move. Depending on the radii of these macropores, the acid and water flows will have different access to aggregates in the plate core.

Figure 10.18 shows a model for the micro- and macro- levels of the PAM structure. The microlevel comprises structures sized up to 800–1000 nm, whereas the formations at the macrolevel are larger than 1000 nm in size. The type of macrostructure to be formed in PAM depends on the size of the crystals in the cured paste. Crystals and particles of 3BS, 4BS, PbO and $PbSO_4$ are converted into agglomerates and aggregates, which build up the macrostructure of the PAM. It should be noted that 3BS and 4BS crystals, as well as PbO particles, vary in size. Consequently, different types of macrostructures are formed. They may comprise well pronounced branches (as on formation of 4BS pastes, Fig. 10.11) or porous mass (see Fig. 10.17b). These structures evolve during the discharge and charge cycles, whereby the density of PAM may decrease or increase, depending on the cycling mode. It is interesting to follow the influence of PAM macrostructure on the porosity and the capacity performance of positive plates.

10.7.2. Transport and Reaction Pores in the Microstructure of PAM and Their Influence on Plate Capacity [23]

The dependences of pore volume and pore surface-area on pore radius for an active mass formed from 3BS paste on lead–antimony grids are presented in Fig. 10.19a and 10.19b, respectively.

Model for the structure of lead dioxide active mass

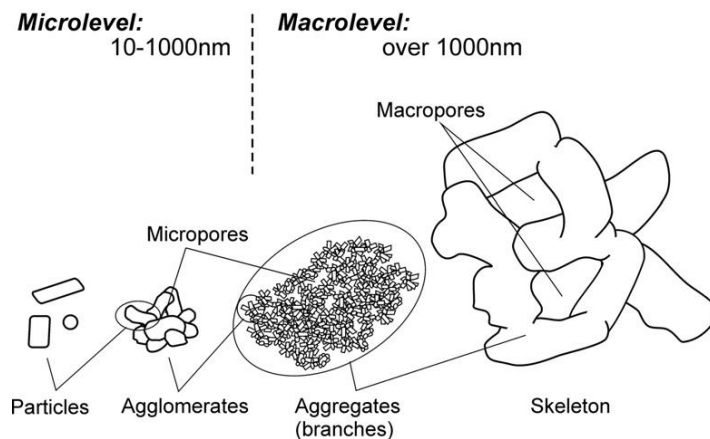


Figure 10.18:
Model for PAM structure [25].

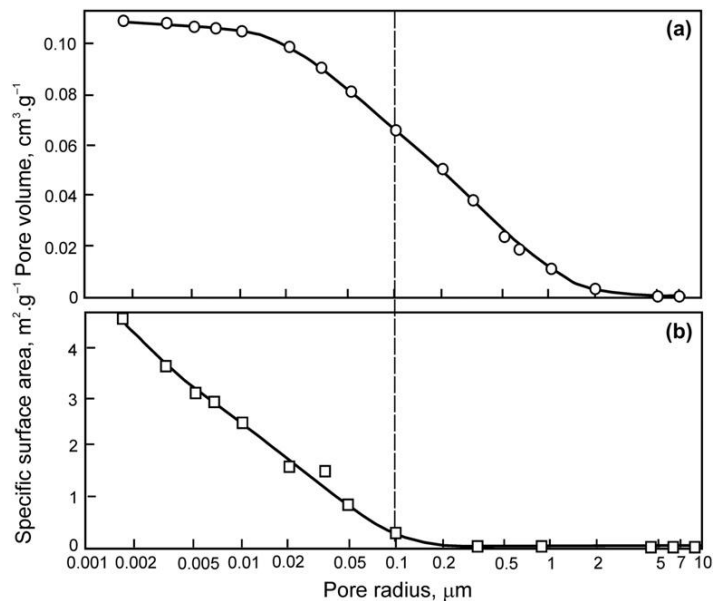


Figure 10.19:

(a) Pore volume and (b) pore surface-area distribution for PAM formed from 3BS paste. Pore radius of $\sim 0.1 \mu\text{m}$ is assumed to be the boundary between micro- and macro- (transport) pores [23].

The pore volume begins to increase at a pore radius of 1 μm and the surface area at a pore radius of 0.1 μm . Pores with 0.1 μm radius have a specific pore volume of $0.065 \text{ cm}^3 \text{ g}^{-1}$, which is about 62% of the total pore volume. The surface area of the pores of this same size is only 6% of the total surface area of the PAM. These results indicate that the macrostructure of PAM contains mostly pores with radii larger than $\sim 0.1 \mu\text{m}$ (*macropores*) and these pores serve as the *main transport system* for the flows of ions and H_2O between the bulk of the solution and the aggregates inside the plate. Pores with radii smaller than $\sim 0.1 \mu\text{m}$ (*micropores*) are located inside the aggregates, between the lead dioxide particles and agglomerates. The electrochemical processes of discharge take place on the surfaces of these small *reaction pores* [23].

The pore volume and surface area distribution *vs.* pore radius for PAM formed from pastes with various phase compositions and densities are given in Fig. 10.20 [23]. The curves for chemically prepared PbO_2 are also provided for comparison. When the PAM is obtained by formation of basic lead sulfate pastes, the pore volume grows gradually within a wide range of radii (0.05 to 1.2 μm). For chemically prepared PbO_2 , the total pore volume attains its maximum value within a very narrow range of radii. A steep rise in the surface area curve for

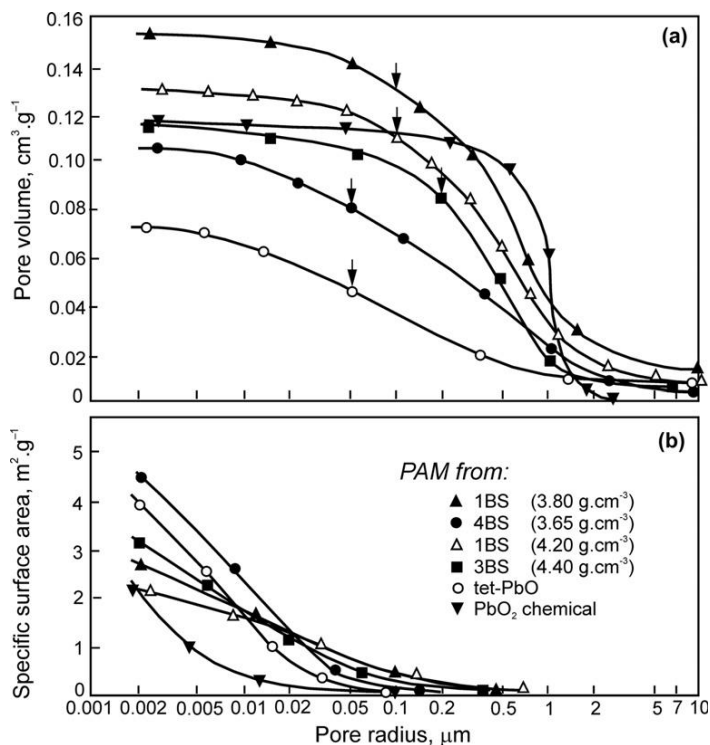


Figure 10.20:

(a) Pore volume and (b) pore surface-area distribution for PAM formed from pastes with various phase composition. Arrows mark the assumed boundary between micro- and macro-pores [23].

PAM prepared from basic lead sulfate pastes is observed for pore radii smaller than 0.5–0.1 μm . In the case of chemical PbO_2 , this rise starts at radii ten times smaller (0.01 μm). Both the pore volume and the surface area are strongly dependent on the phase composition and density of the paste. These experiments suggest that the porosity of the PAM can be controlled through the phase composition and the density of the initial paste.

The boundary between micro- and macropores is marked by an arrow on the porograms in Fig. 10.20. The surface area of the PAM is determined mainly by the surface of the micropores with a negligible contribution from the macropores. Hence, the boundary between the macro- and micropores is determined by the pore radius above which the PAM surface area starts to increase rapidly (Fig. 10.20b). As the agglomerates and particles that surround the micropores differ in size for PAMs obtained from different pastes, the macropore/micropore boundary varies between 0.05 and 0.2 μm (Fig. 10.20b). In the literature, it is often assumed that the boundary micropore radius has an average value of $\sim 0.1 \mu\text{m}$.

The correlation between the total pore volume (V_p) and the micropore volume ($V_{\mu p}$), on the one hand, and the capacity of the plate at the fifth cycle, on the other hand, is given in Fig. 10.21 [23]. The capacity increases with increase of the total pore volume and does not depend on the volume of micropores. The difference $V_p - V_{\mu p}$ gives the volume of the transport pores. Hence, the volume of the transport pores is the capacity-limiting parameter for positive plates with lead–antimony grids.

Figure 10.22 presents the capacity of cells with positive plates, produced with lead–antimony grids and pastes with different phase composition and density, as a function of the BET surface area of the PAM (at the fifth cycle) [23]. The general tendency is for the plate capacity to

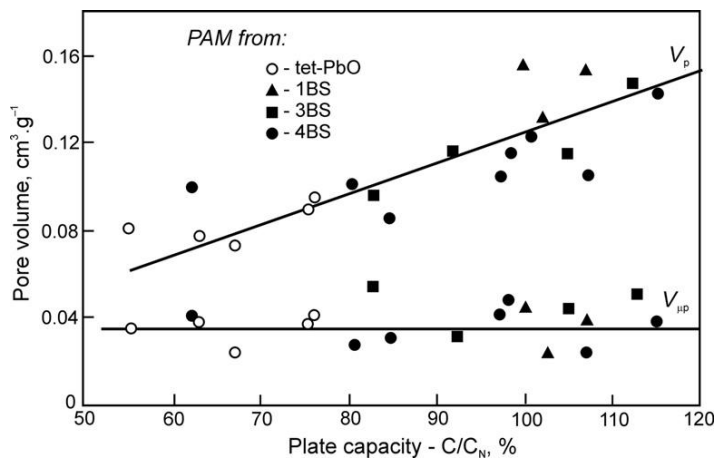


Figure 10.21:

Dependence of cell capacity on total pore volume (V_p) and on volume of micropores ($V_{\mu p}$) for PAM prepared from pastes with various phase compositions [23].

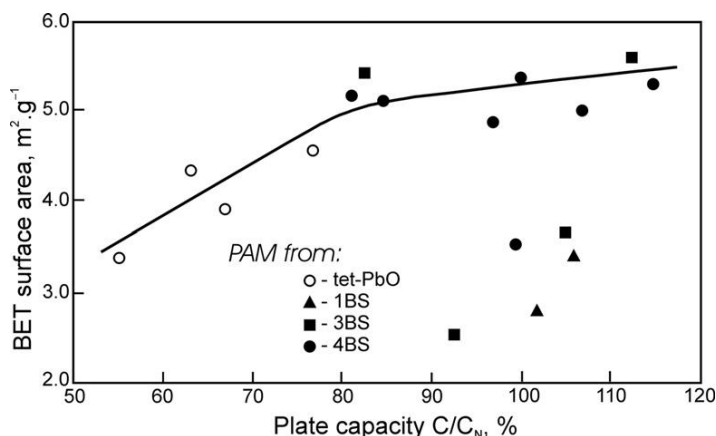


Figure 10.22:

Plate capacity as a function of BET surface area for PAM prepared from pastes with various phase compositions [23].

increase with increase in BET surface area. Several plates have comparatively low BET surface area, but high capacity. Hence, the BET surface area of the PAM is not the sole parameter that determines plate capacity.

The above porosity, BET surface area and capacity measurements have been carried out at the fifth cycle, i.e. when the structure of the PAM is determined by the formation process. On further cycling, the PAM structure undergoes changes, as a result of which one or more of the above parameters may become capacity limiting.

10.7.3. Gel—Crystal Forms of PbO_2 Particles

The following types of particles can be distinguished from electron micrographs of PbO_2 particles interconnected in agglomerates (Fig. 10.23) [25]:

- Spherical or egg-shaped formations as if obtained from a liquid phase (Fig. 10.23a,b), in which PbO_2 particles have coalesced into small agglomerates (Fig. 10.23a) or individual particles with good contact between them (Fig. 10.23b).
- PbO_2 crystal particles, which are relatively small in size but are in contact with each other or large crystallites with well-shaped faces, apexes and edges (Fig. 10.23c). Some of the crystallites have partially built faces of prismatic form. These forms are a result of metasomatic oxidation of undissolved parts of the PbSO_4 crystals, which have converted into PbO_2 during charge. Several small particles feature heterogeneous structures (Fig. 10.23d). The contact surface area between these particles is not so large.
- Needle-like particles, possibly with a common base (Fig. 10.23e) or individual needle-like particles, possibly with contacts between them (Fig. 10.23f).

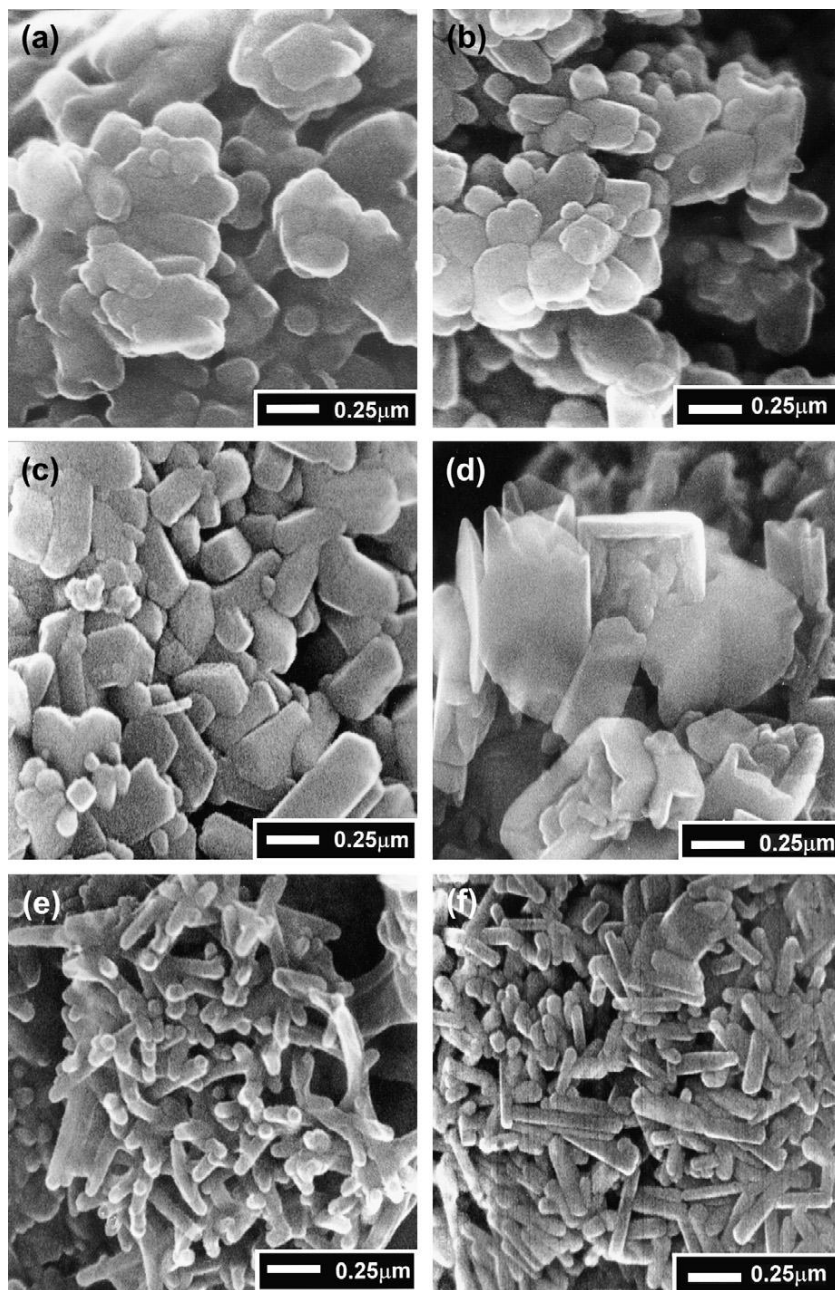


Figure 10.23:

Scanning electron micrographs of PbO_2 particles of various shapes formed during plate formation and cycling [25]. (a,b) rounded PbO_2 particles coalesced into agglomerates; (c,d) PbO_2 crystal-shaped particles; (e,f) needle-like PbO_2 particles.

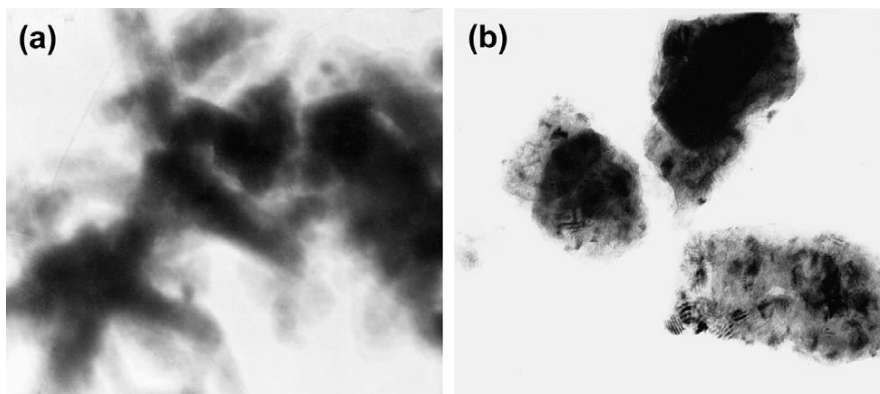


Figure 10.24:

Transmission electron micrograph of PbO_2 particles. The particles have a non-homogeneous composition. (a) PbO_2 particles with hydrated surface layers; (b) hydrated PbO_2 particles with crystal nuclei (dark spots) in their volume.

The images of PbO_2 particles obtained by means of transmission electron microscopy are presented in Fig. 10.24. They evidence that lead dioxide particles consist of zones of different composition.

A transmission electron micrograph and a diagrammatic representation of the phase composition (as determined by micro electron diffraction analysis) of a particle of formed PAM are presented in Fig. 10.25 [26]. The electron diffraction analysis evidences predominance of zones with $\beta\text{-PbO}_2$ structure in the central part of the particle. By contrast, the uppermost and bottom parts, which are far more electron-transparent, have amorphous structure. A PbSO_4 nucleus is also detected in the bottom part near the amorphous zone.

It has been established, through XRD analysis, that the average dimensions of PbO_2 crystals in PAM are between 25 and 60 nm [27–32]. The micrographs in Figs. 10.23 and 10.24 show that the size of some PbO_2 particles exceeds 200 nm. This implies that PbO_2 particles comprise several crystallites whose size is measurable by XRD and amorphous zones that cannot be detected by the XRD method.

Most probably, amorphous zones are highly hydrated. To verify this conjecture, PbO_2 particles have been subjected to heating inside a scanning electron microscope. Micrographs of particles, prior to and after heating, are presented in Fig. 10.26 [32]. The small particle contains only a small amorphous zone; the longer one, contains several amorphous zones (Fig. 10.26a). When heated at 100 °C for 20 min, the long particle boils for a short time and water evaporates from inside the particle. The material concentrates in several zones, mainly around the crystal part of the particle (Fig. 10.26b). Empty zones (voids) also appear. It follows then that the lighter zones in the particle are hydrated and are of an amorphous nature. These regions are referred to as ‘gel zones’.

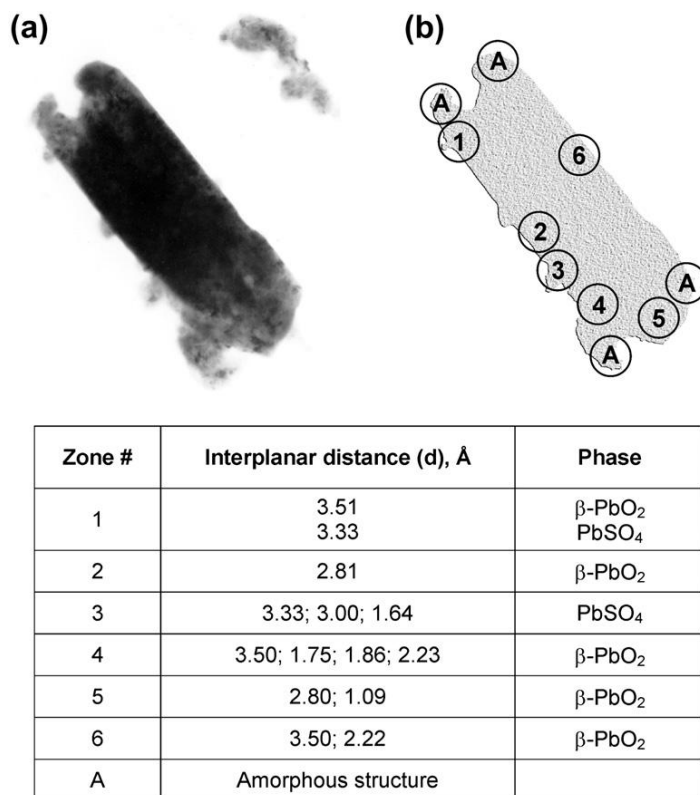


Figure 10.25:

Transmission electron micrograph of a PbO₂ particle and distribution of structural zones, as determined through electron diffraction analysis [26]. (a) PbO₂ particle, (b) labelled sites on the surface of the PbO₂ particle which were subjected to electron diffraction analysis, (c) summary of the obtained results.

Studies with X-ray photoelectron spectroscopy have established that the formed PAM contains 34% OH⁻ groups, when obtained from 3BS pastes and 31% OH⁻ groups, when the PAM is formed from 4BS pastes [26]. Hydrothermogravimetric analysis has shown that in the temperature range from 260 to 450 °C, water evaporates from the PAM in an amount of 0.00323 cm³ per g PAM [33,34].

When the size of the crystal zones substantially exceeds that of gel zones, the particles have a recognizable crystal habit (Fig. 10.23c,d). If the gel zones occupy a relatively thick layer on the surface of the particles, the latter have rounded shape (Fig. 10.23a,b). When, however, the particles are completely hydrated (which is usually the case with small particles, see Fig. 10.23b,c), their shape is drop-like or egg-like. It has been found that there is equilibrium between gel zones and crystal zones, and this equilibrium depends on the temperature, the types of ions in the solution and the alloying additives used [32]. The influence of ions in the solution on the equilibrium gel/crystal zones was discussed in Section 2.9.2.

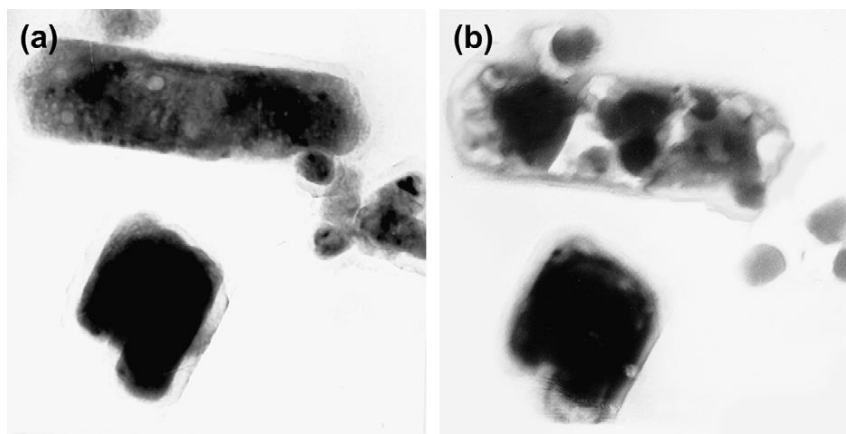
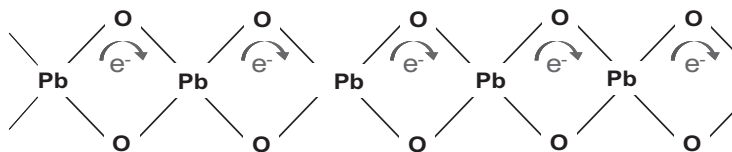


Figure 10.26:

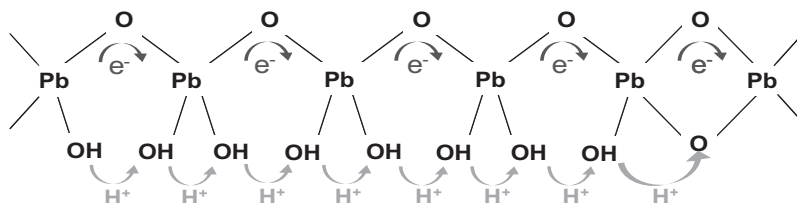
Transmission electron micrographs of PbO₂ particles: (a) before and (b) after heating inside microscope [32].

10.7.4. Electrochemical Reactions Which Proceed in the Gel Zones of the PbO₂ Active Mass

Kassner suggests that high-valent lead oxide (PbO₂) forms linear polymer chains of the type

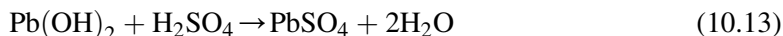


which are responsible for the high mobility of electrons in the PbO₂ crystals [35]. We assume that gel zones in PbO₂ particles contain polymer hydrated chains, and H⁺ ions and electrons can easily move along these chains [36]. These chains have both electron and proton conductivity, which is a necessary condition for the reactions of PbO₂ discharge and O₂ evolution to proceed. Electrons and protons move along the polymer chains overcoming low potential barriers, thus facilitating the above reactions by maintaining the electro-neutrality of gel zones. The reactions of oxygen evolution were discussed in Section 2.10.3.



When a potential more negative than the equilibrium potential of the $\text{PbO}_2|\text{PbSO}_4$ electrode is applied to the positive plate, electric current flows through the plate. Electrons enter the hydrated zones along the polymer chains and reduce Pb^{4+} ions to Pb^{2+} ones. The zones are charged with the negative electric charge of the O^{2-} ions. This charge is electro-neutralized through diffusion and migration of H^+ ions from the solution into the gel zones of the particles. Thus, H_2O and $\text{Pb}(\text{OH})_2$ are formed. Water dilutes the gel zones and H_2SO_4 penetrates into these zones and reacts with the lead hydroxide forming PbSO_4 and water. PbSO_4 molecules diffuse in the solution and contribute to the growth of the PbSO_4 crystals.

The above processes can be expressed by the following equations representing the discharge reactions at the positive battery plates.



The reaction of discharge involves both electrons and protons (Eqn. 10.12). When these two types of charged particles reach a given point in the gel zone of the lead dioxide particle simultaneously, the discharge reaction proceeds. When the PAM has high electron conductivity but low proton conductivity, the capacity of the plate will be low. If the PAM exhibits high proton conductivity but low electron conductivity, the plate capacity will be low again. By contrast, if the PAM is a gel-crystal system with high electron and proton conductivities, the plate will have high capacity [32,36].

Not all PbO_2 particles have a structure with adequate electron and proton conductivity. Hence, the above reactions proceed only in some particles of PAM. The sites where these reactions proceed are *active centres* with a definite structure and are connected, via the polymer chains, with the crystal zones and the solution.

The effect of hydration on the electrochemical activity of PbO_2 has been investigated [33]. For the purpose, samples of charged PAM taken after the plate capacity tests, are ground to powder and filled into tubular electrodes at a density of 4.0 g cm^{-3} . PAM obtained from 3BS and 4BS pastes, as well as chemical PbO_2 (Merck), are used for these investigations. Other tubes are filled with the same PAM, but heated to 260°C . The tubular electrodes are set to capacity tests. The obtained results are presented in Table 10.2.

The lower capacity of tubular electrodes is a result of the poor ohmic contacts between agglomerates and between PAM and spine. Discharge is conducted at low current. It has been established that dehydration of PbO_2 particles as a result of heating causes a dramatic decline in electrode capacity. So the hydrated layers in PbO_2 particles determine their electrochemical activity. This may mean that *the electrochemical reactions of PbO_2 reduction proceed in the hydrated layer.*

Table 10.2: Effect of hydration on PAM capacity [33].

PAM Obtained From	PAM Capacity in Pasted Plates (Ah g^{-1} PAM)	PAM Capacity in Tubular Powder Electrodes (Ah g^{-1} PAM)	
		PAM as taken from plate	PAM heated at 260°C
$3\text{PbO} \cdot \text{PbSO}_4 \cdot \text{H}_2\text{O}$	0.1177	0.0231	0.00156
$4\text{PbO} \cdot \text{PbSO}_4$	0.0896	0.0175	0.00146
Chemical PbO_2	—	0.0013	—

Chemical PbO_2 contains no hydrated zones [36] and hence its capacity is extremely low and falls down to zero after heating. It can be concluded that the electrochemical activity of PbO_2 is determined by the degree of its hydration.

10.8. Influence of Grid Alloying Additives on the Electrochemical Activity of PbO_2 Binders

When the lead–antimony alloy commonly used for the positive grids of lead–acid batteries was substituted for lead–calcium alloy, the cycle life of the batteries decreased dramatically. Obviously, antimony influenced the electrochemical behaviour of PbO_2 . One of the hypotheses was that it affected the hydration of $\text{PbO}_2 \cdot \text{PbO}(\text{OH})_2$ particles. This hypothesis was verified through oxidation of Pb–Sb alloys with different content of antimony and determining the water content in the anodic PbO_2 layer formed. The obtained results of these investigations are presented in Fig. 10.27 [34].

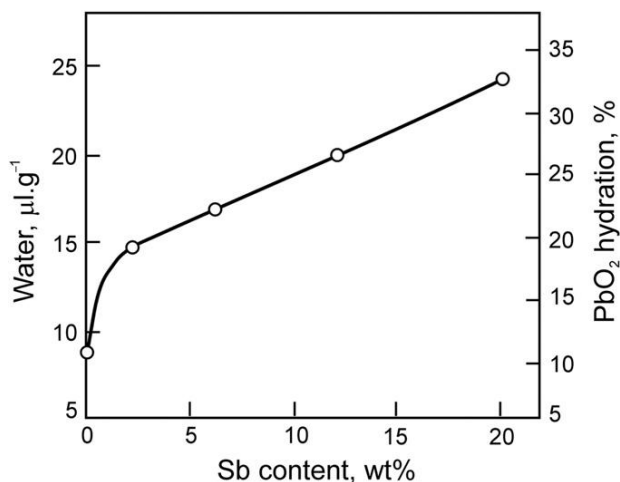


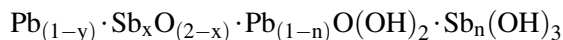
Figure 10.27:

Water content in the anodic layer (measured in microlitres of water per gram of sample), formed at $+1.50\text{ V}$ potentiostatic polarization on flat electrodes, as a function of antimony content in the alloy [34].

The higher the antimony content in the alloy, the higher the degree of hydration of the corrosion layer obtained, i.e. the volume of the gel zones in the lead dioxide layer increases due to incorporation of antimony ions in its structure. These results indicate that antimony increases the degree of amorphization of the PbO_2 layer, which is also confirmed by the XRD data for the anodic layer [34].

The water content of some of the commercially available lead and antimony oxides was determined and the obtained results are presented in Table 10.3 [34].

Chemically obtained PbO_2 contains far less water than the electrochemically obtained oxide. This finding is in good agreement with the TEM data for the structure of chemical and electrochemical oxides [35,36]. TEM observations show that chemically obtained PbO_2 consists of well shaped crystals with no gel zones in them. It has low electrochemical activity. Antimony oxides are strongly hydrated, especially Sb_2O_5 . Consequently, the introduction of Sb ions into the lead dioxide particles and agglomerates will increase the latter's degree of hydration. Based on this assumption, lead–antimony dioxide can be represented by the following general formula:



As mentioned earlier, antimony ions are incorporated into the structure of PbO_2 particles. Most probably, these ions enter the gel zones of the particles and contribute to binding the polymer chains to one another. Antimony ions improve the connections between the linear chains that form a network. A schematic representation of these connections is presented in Fig. 10.28 [38].

Antimony ions have high affinity towards water (Table 10.3). Polymer chains of PbO_2 particles and agglomerates, on the other hand, are hydrated. Consequently, antimony ions would be readily bonded to hydrated polymer chains to form a polymer network. It is therefore appropriate to term these dopants ‘binders’. Binders support the polymer chains and prevent the polymer network from disintegration on decrease of the PAM density. When there is no binder, the polymer network exhibits high conductivity only with a high density of polymer chains in the gel. On decreasing PAM density, the polymer chains disintegrate

Table 10.3: Water content of lead and antimony oxides [34].

Substance	Water Content ($\mu \text{ L g}^{-1}$)
tet- PbO_2	1.7
β - PbO_2 chem.	1.9
β - PbO_2 el.chem.	5.9
Sb_2O_3	5.4
Sb_2O_5	46.6

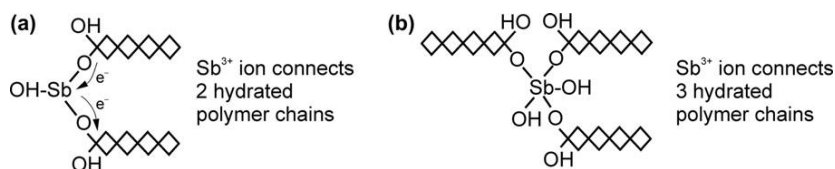


Figure 10.28:

Connections between hydrated polymer chains in gel zones, through (a) Sb^{3+} and (b) Sb^{5+} ions, into an integral system with electron and proton conductivity [38].

rapidly and the conductivity of the gel zones declines abruptly. This happens on plate cycling. The same effect is also observed when the concentration of binders in the gel is low. Most sensitive to these changes are the regions near the CL/PAM interface. Fortunately, these regions are saturated with ions of the binder that are formed as a result of oxidation of the grid alloy.

The above discussion can be summarised as follows: antimony improves the electron conductivity of the gel zones of PbO_2 particles, and the tendency of antimony towards hydration both stabilises the gel concentration and improves the proton conductivity. Similar properties are exhibited by tin, bismuth and probably other metal ions as well (see Fig. 4.23).

In order to verify experimentally the mechanism of action of antimony, a lead dioxide (PAM) sample from a plate with Pb grid was ground to powder and this powder was mixed with small amounts of Sb_2O_3 or Sb_2O_5 . Tubular electrodes were filled with the above two mixtures ($\text{PbO}_2 + \text{Sb}_2\text{O}_3$ or $\text{PbO}_2 + \text{Sb}_2\text{O}_5$). A third type of electrodes were filled with the ground PAM powder only with no addition of antimony oxide. The powders filled in all three types of electrodes had identical density, 4.10 g cm^{-3} . Two tubular electrodes of each type were set to cycling so that the powders would be formed to active masses. Figure 10.29 presents the specific capacity/cycle number curves for the three types of electrodes under test [39].

During the first few cycles, Sb_2O_3 and Sb_2O_5 cause an abrupt rise in electrode capacity. These oxides have a similar effect to that of antimony added to the grid alloy. Sb_2O_5 has a more beneficial influence than Sb_2O_3 . It follows, therefore, that the valency of antimony also plays a role in the processes of building up the structure of PAM. The data in Table 10.3 evidence that Sb_2O_5 is more hydrated than Sb_2O_3 . Probably, the higher affinity to hydration of Sb_2O_5 as compared to Sb_2O_3 contributes to the more beneficial effect of Sb_2O_5 .

The above experimental data indicate that the alloy composition plays an important role during the formation processes as it determines the conductivity of the PAM layer that is in contact with the corrosion layer. This PAM layer is formed electrochemically and contains gel zones.

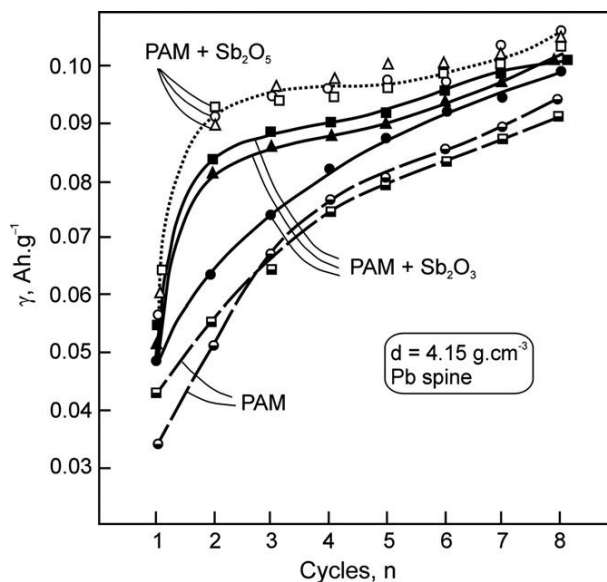


Figure 10.29:

Changes in specific capacity on cycling tubular powder electrodes prepared with PAM containing 50 mg of Sb_2O_3 or Sb_2O_5 , or with no additives [39].

References

- [1] P. Ruetschi, R.T. Angstadt, *J. Electrochem. Soc.* 111 (1964) 1323.
- [2] D. Pavlov, G. Papazov, V. Iliev, *J. Electrochem. Soc.* 119 (1972) 8.
- [3] D. Pavlov, in: B.D. McNicol, D.A.J. Rand (Eds.), *Power sources for electric vehicles*, Elsevier, Amsterdam, 1984, p. 328.
- [4] J. Burbank, *J. Electrochem. Soc.* 113 (1966) 10.
- [5] D. Pavlov, G. Papazov, *J. Electrochem. Soc.* 127 (1980) 2104.
- [6] G. Papazov, *J. Power Sources* 18 (1986) 337.
- [7] P.T. Moseley, *J. Power Sources* 64 (1997) 47.
- [8] K.R. Bullock, T.C. Dayton, in: D.A.J. Rand, P.T. Moseley, J. Garche, C.D. Parker (Eds.), *Valve-regulated lead-acid batteries*, Elsevier, Amsterdam, 2004, p. 109.
- [9] K.R. Bullock, W.H. Kao, US Patent 5,045,170, September 1991.
- [10] W.H. Kao, K.R. Bullock, *J. Electrochem. Soc.* 139 (1992) 41; 4L.
- [11] D. Pavlov, E. Bashtavelova, *J. Power Sources* 31 (1990) 243.
- [12] S. Grugeon-Devaelle, S. Laruelle, L. Torcheux, J.-M. Tarascon, A. Delahaye-Vidal, *J. Electrochem. Soc.* 145 (1998) 3358.
- [13] L.T. Lam, H. Ozgun, L.M.D. Craswick, D.A.J. Rand, *J. Power Sources* 42 (1993) 55.
- [14] M. Dimitrov, D. Pavlov, T. Rogachev, M. Matrakova, L. Bogdanova, *J. Power Sources* 140 (2005) 168.
- [15] D. Pavlov, G. Papazov, *Electrochemical power sources*, Proc. First Symposium EPS, Praha, 1975, p. 49.
- [16] V.H. Dodson, *J. Electrochem. Soc.* 108 (1961) 406; 401.
- [17] A.C. Simon, E.L. Jones, *J. Electrochem. Soc.* 109 (1962) 760.
- [18] J.R. Pierson, *Electrochem. Technol.* 5 (1967) 323.
- [19] J. Armstrong, I. Dugdale, W.J. McCusker, in: D.H. Collins (Ed.), *Power sources 1966, research and development in non-mechanical electric power sources*, Pergamon Press, Oxford, 1965, p. 163.

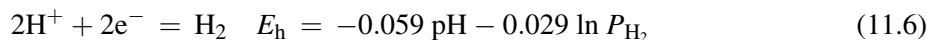
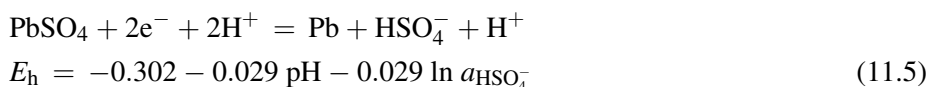
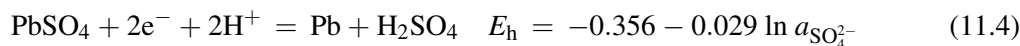
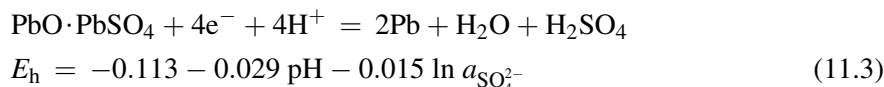
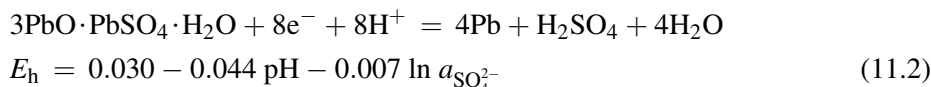
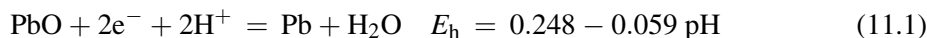
- [20] S. Ikari, S. Yoshizawa, S. Okada, *Denki Kagaku* 27 (1959) 487.
- [21] B. Culpin, *J. Power Sources* 25 (1989) 305.
- [22] D. Pavlov, E. Bashtavelova, *J. Electrochem. Soc.* 131 (1984) 1468.
- [23] D. Pavlov, E. Bashtavelova, *J. Electrochem. Soc.* 133 (1986) 241.
- [24] D. Pavlov, E. Bashtavelova, D. Simonson, P. Ekdunge, *J. Power Sources* 30 (1990) 77.
- [25] M. Dimitrov, D. Pavlov, *J. Power Sources* 93 (2001) 234.
- [26] D. Pavlov, I. Balkanov, T. Halachev, P. Rachev, *J. Electrochem. Soc.* 136 (1989) 3189.
- [27] A.C. Simon, S.M. Caulder, *J. Electrochem. Soc.* 118 (1971) 659.
- [28] I. Kim, S.H. Oh, H.Y. Kang, *J. Power Sources* 13 (1984) 99.
- [29] T.G. Chang, *J. Electrochem. Soc.* 131 (1984) 1755.
- [30] A. Santoro, P. D'Antonio, S.M. Caulder, *J. Electrochem. Soc.* 130 (1983) 1451.
- [31] K. Kordes, *Chem. Ing. Tech.* 38 (1966) 638.
- [32] D. Pavlov, I. Balkanov, *J. Electrochem. Soc.* 139 (1992) 1830.
- [33] D. Pavlov, E. Bashtavelova, V. Manev, A. Nasalevska, *J. Power Sources* 19 (1987) 15.
- [34] B. Monahov, D. Pavlov, *J. Electrochem. Soc.* 141 (1994) 2316.
- [35] G. Kassner, *Arch. Pharm.* 228 (1890) 177.
- [36] D. Pavlov, *J. Electrochem. Soc.* 139 (1992) 3075.
- [37] P. Faber, *Electrochim. Acta.* 26 (1981) 1435.
- [38] D. Pavlov, *J. Power Sources* 46 (1993) 171.
- [39] D. Pavlov, A. Dakhouch, T. Rogachev, *J. Power Sources* 42 (1993) 71.

This page intentionally left blank

Processes During Formation of Negative Battery Plates

11.1. Equilibrium Potentials of the Electrochemical Reactions of Formation

The paste of cured negative plates is composed of 3BS, PbO and residual Pb as well as additives including expanders, carbon, etc. The lead compounds are reduced to Pb through electrochemical reactions. We can judge about the sequence of these reactions by the respective equilibrium potentials (E_h) of their reduction at 298.15K [1]. All equilibrium potentials are referred to a standard hydrogen electrode.



P_{H_2} is the pressure of hydrogen in the cell. It is generally assumed in electrochemistry that the standard potential of the hydrogen electrode is equal to zero volts at all temperatures. Hence, there is no numerical term in Eqn. (11.6). On comparing the values of the numerical terms in Eqns. (11.1) to (11.6), it can be expected that after the reduction of PbO and 3BS, water decomposition would start with evolution of hydrogen. Due to kinetic limitations, however, this does not actually happen. The hydrogen overpotential on lead is one of the highest observed for different metals. Hence, basic lead sulfates (BS) and PbSO₄ are reduced to lead first and then, on increase of the potential, the hydrogen reaction commences.

The above sequence of reactions indicates that formation of negative plates will proceed in two stages. The difference of 300mV between the equilibrium potentials of the PbO|Pb and 3BS|Pb

electrodes on the one hand and $\text{PbSO}_4|\text{Pb}$ on the other suggests that during the first stage, reduction of PbO and 3BS will proceed and then, after the potential increases by over 300 mV, the second stage of formation will start with reduction of PbSO_4 .

The electrochemical equations (11.1–11.6) give grounds for two more interesting conjectures. The first one refers to the rates of the electrochemical reactions of reduction in different parts of the plate volume. All electrochemical reactions involve H^+ ion flows. The latter carry the current through the solution. The larger the H^+ flow the higher the rate of the electrochemical reaction in the respective part of the plate. The H^+ ion flow is most intense in the surface plate layers, because the latter are in direct contact with the bulk H_2SO_4 solution. Hence, during the formation process, lead will be formed first on the plate surface and then in its interior.

Secondly, reduction of PbO and BS results in the formation of water. The latter will dilute the solution in the plate pores and thus maintain high pH in the pores. This happens during the first stage of formation. When reduction of PbSO_4 starts, it leads to the production of H_2SO_4 and hence the pH of the pore solution decreases substantially reaching the highly concentrated H_2SO_4 acid region. Obviously, these two different solution pH regions will affect the structure of the obtained lead active mass.

11.2. Reactions During Formation of Negative Plate

The changes in phase composition of negative plates (12 Ah) when formed in H_2SO_4 solution of 1.05 rel. dens. at a current density of 5mAcm^{-2} , after a 10-min soaking period, are presented in Fig. 11.1 [2]. The XRD data show that the formation process can be divided into two stages. During the first stage (approx. 6h), the amounts of PbO and 3BS decrease, whilst those of Pb

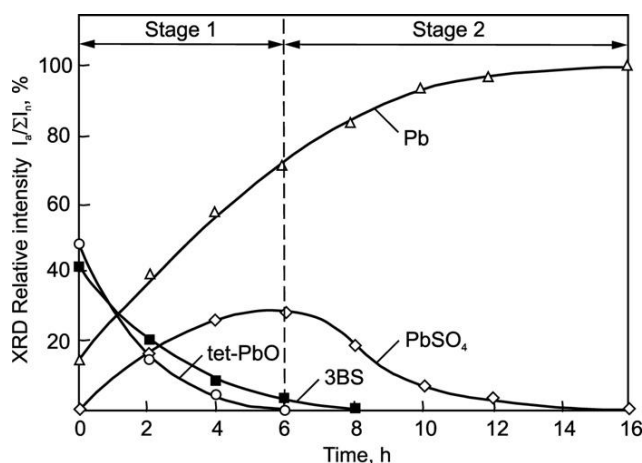


Figure 11.1:

Changes in phase composition of paste and active mass of negative plates during formation [2].

and PbSO_4 increase. This suggests that PbO and 3BS are partly reduced to Pb , and partly react with H_2SO_4 to form PbSO_4 . During the second stage, the XRD lines for PbSO_4 indicate a decrease in the amount of PbSO_4 and an increase in Pb content.

Based on the above XRD data, a general scheme has been proposed for the electrochemical and chemical reactions that proceed during the first formation stage, including lead oxide and all basic lead sulfates (Fig. 11.2 [2]). This scheme represents only the stoichiometry of the reactions during the first stage of formation, but not the elementary processes that occur. The coefficient m stands for the 'PbO molecules' in the basic lead sulfates. When the paste consists of PbO only, m is equal to infinity. The corresponding values of the coefficients preceding PbO and PbSO_4 are 1 and 0, respectively. When the paste consists of $3\text{PbO} \cdot \text{PbSO}_4 \cdot \text{H}_2\text{O}$, $m = 3$.

The first reaction involves hydration and dissolution of basic lead sulfate to Pb^{2+} , SO_4^{2-} and OH^- ions. Part of the Pb^{2+} ions (let us mark them with q) are reduced to Pb . The remaining part $(1 - q)$, together with the SO_4^{2-} ions, participate in the formation of PbSO_4 . The OH^- ions are neutralized by H^+ ions coming from the bulk solution and form H_2O molecules. Thus, during the first stage of formation of negative plates Pb , PbSO_4 and H_2O are formed.

To preserve the electro-neutrality of the plate, an exchange of H^+ and SO_4^{2-} ions has to proceed between the reaction layer (located between the paste and the formed $(\text{Pb} + \text{PbSO}_4)$ zone and the bulk of electrolyte, so that the above reactions may occur.

Figure 11.3 shows a scheme of the reactions that occur during the second stage of formation. Beside Pb , H_2SO_4 forms as well, which diffuses from the plate to the bulk solution.

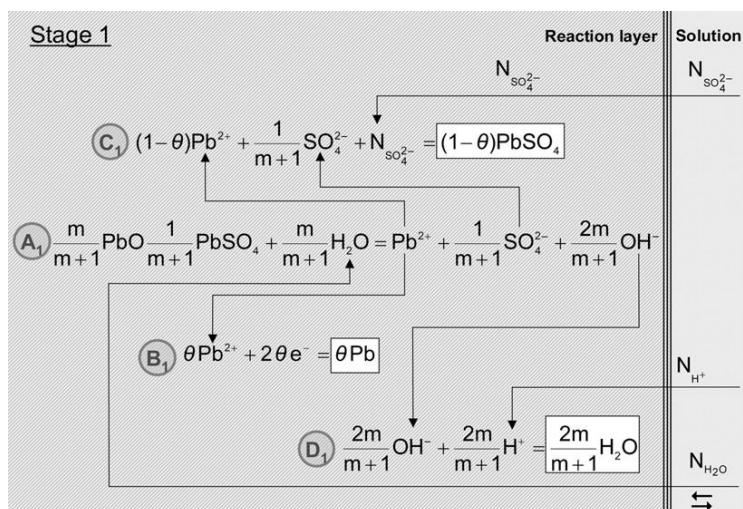


Figure 11.2:

Electrochemical and chemical reactions during the first stage of NAM formation from BS pastes [2].

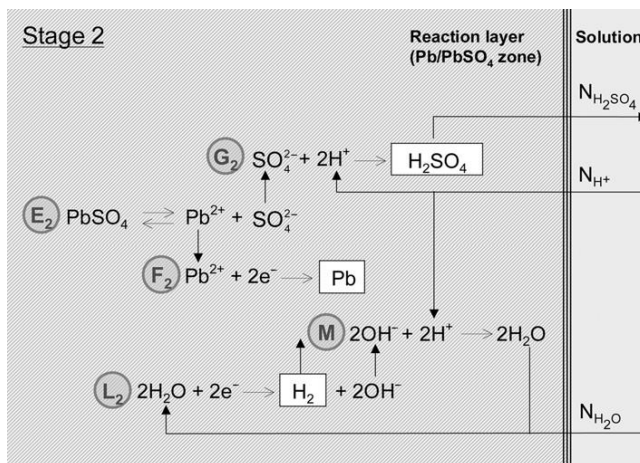


Figure 11.3:
Reactions during the second stage of NAM formation [2].

If we compare the two reaction schemes, it becomes evident that the growth of lead crystals proceeds at different pH during the two stages of formation. Thus, *during the first stage*, the solution in the reaction layer has a pH within the neutral or weakly alkaline regions. At this pH, the following reaction proceeds in the solution filling the paste pores:



When the solution pH becomes higher than 9.5, HPbO_2^- ions will form in the pore solution. These ions are then reduced to Pb.

Let us call the lead structure formed during the first stage of plate formation ‘primary structure’. During the second stage, H_2SO_4 forms. In H_2SO_4 solutions, lead exists in the form of Pb^{2+} ions. The lead crystals grow in acidic medium. Let us call this lead structure ‘secondary’. It can be expected that the morphology of the lead crystals in the primary and secondary structures would be different.

11.3. Zonal Processes

How do the formation processes proceed through the cross-section of the plate? Photographs of the plate cross-section prior to formation as well as during different stages of formation are presented in Fig. 11.4 [3]. Formation starts on the grid surface. A grey zone is formed, which grows along the two surfaces of the plate. According to the X-ray data and the results of the chemical analysis, this zone is composed of Pb and PbSO_4 . After covering the whole surface of the plate, the $(\text{Pb} + \text{PbSO}_4)$ zones grow towards the interior of the plate until the entire cross-section is formed.

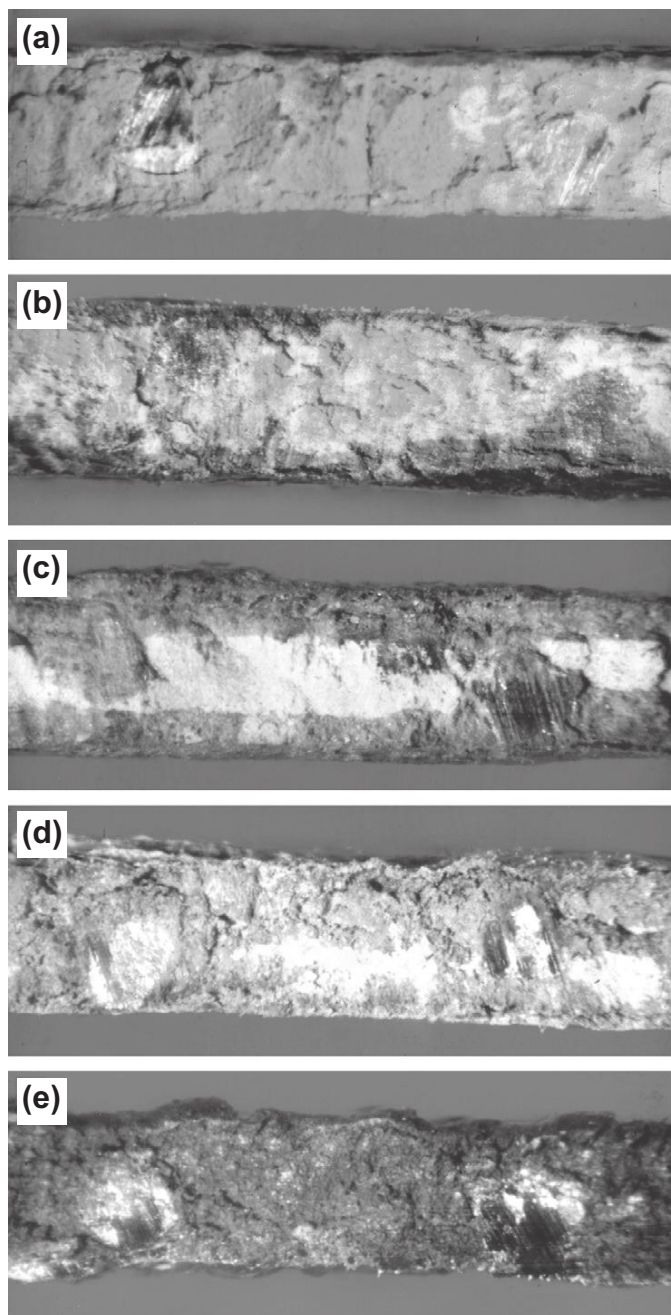


Figure 11.4:

Photographs of cross-section of negative plate during formation: (a) prior to formation; (b–d) during different formation stages, dark regions are $(\text{Pb} + \text{PbSO}_4)$ zones; (e) completely formed plate. Plate thickness is 1.8 mm [3].

According to the reaction scheme in Fig. 11.2, an exchange of H^+ , SO_4^{2-} ions and H_2O occurs between the bulk of electrolyte and the reaction layer located between the $(\text{Pb} + \text{PbSO}_4)$ zone and the non-formed paste. The electrochemical reaction $\text{Pb}^{2+} + 2e^- \rightarrow \text{Pb}$ decreases the concentration of the positive charges in the reaction layer. The charges of OH^- and SO_4^{2-} ions in this layer remain uncompensated. In order to preserve the electrical neutrality of the solution in the reaction layer, H^+ ions must migrate from the bulk of electrolyte into the reaction layer and SO_4^{2-} ions must move in the reverse direction. The rates of these flows control the rate of the electrochemical reactions in the reaction layer. Since H^+ ions are much more mobile than SO_4^{2-} ions, they will maintain the electric neutrality of the reaction layer. The H^+ ions experience the least transport difficulties when passing along the shortest paths between the surface plate layers and the bulk of electrolyte. Therefore, the $(\text{Pb} + \text{PbSO}_4)$ zones will first grow in the plate surface layers and, after the plates are fully covered by the $(\text{Pb} + \text{PbSO}_4)$ zones, the latter will progress towards the interior of the paste [4]. These zonal processes are illustrated in Fig. 11.4.

The question arises as to when does the second stage of formation commence? Does this occur when PbO and 3BS in the plate are completely depleted, or does it start earlier? In an attempt to find the answer to this question, the changes in PbSO_4 content (free and bonded in basic lead sulfate) have been determined with a Hitachi XMA-5 electron microprobe during the formation process. The obtained results are presented in Fig. 11.5 [3]. The values on the abscissa give the distance l of a given point in the plate from the plate surface vs. the total plate thickness l_d , i.e. the relative plate thickness. The PbSO_4 distribution across the plate cross-section after 2 h of formation shows that the surface plate layers undergo sulfation. During the first 4 h of formation, PbSO_4 is formed in substantial amounts only in the surface layers of the plate. After 6h, the PbSO_4 content in the surface layers begins to decrease, i.e. the reaction $\text{PbSO}_4 \rightarrow \text{Pb}$ proceeds, though the PbO and 3BS phases in the inner plate layers have not yet fully reacted. This indicates that two reaction layers have formed: one in the interior of the plate where Pb is produced as a result of the electrochemical reduction of PbO and 3BS (first stage), and a second reaction layer near the plate surface where PbSO_4 is reduced to Pb [4]. With time of formation, the first reaction layer disappears as the amounts of PbO and 3BS are exhausted, and the second reaction layer grows towards the interior of the plate. Through model investigations, it has been established that these phenomena are a result of impeded transport (diffusion and migration) of the H^+ and SO_4^{2-} ions into the plate interior [4].

11.4. Structure of Negative Active Mass

11.4.1. Influence of the Two Stages of Formation on NAM Structure

The morphology of the crystals in the $(\text{Pb} + \text{PbSO}_4)$ zone during the first stage of negative-plate formation has been investigated by means of scanning electron microscopy [2]. An electron micrograph of the crystal structure of a $(\text{Pb} + \text{PbSO}_4)$ zone is shown in Fig. 11.6. The PbSO_4 crystals exhibit miscellaneous morphology. Part of the negative plate has been

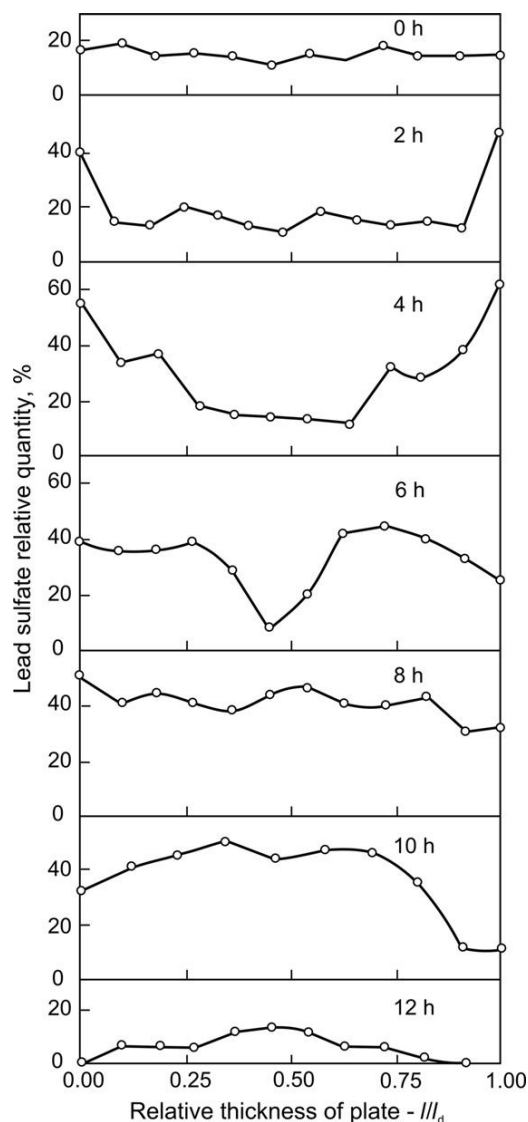


Figure 11.5:

Changes in PbSO_4 distribution through plate cross-section during formation [3,4].

immersed in a boiling saturated solution of ammonium acetate for 30min to allow all divalent compounds to dissolve and leave only the lead phase.

The structure of this lead phase (Fig. 11.7) consists of a network (skeleton) of bonded particles of irregular shape. The length and width of the separate branches is 3 to 10 and 2 to 5 μm , respectively. If Figs. 11.6 and 11.7 are compared, it becomes evident that the $(\text{Pb} + \text{PbSO}_4)$ zone is composed of a network of Pb particles covered with PbSO_4 crystals.

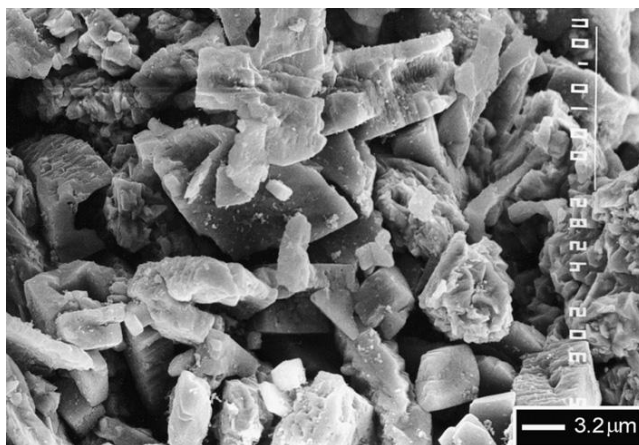


Figure 11.6:

Scanning electron micrograph of crystals within (Pb + PbSO₄) zone during the first stage of formation of negative plate [2].

The lead structure of a completely formed plate is presented in Fig. 11.8. Small, dendrite-shaped lead crystals are formed from PbSO₄ during the second formation stage. These crystals grow on the lead skeleton surface. Therefore, it can be assumed that the negative active-mass consists of a *skeleton of primary lead crystals* that are bonded to each other and to the plate grid, and are covered with small *secondary lead crystals*. The presence of two types of lead structures poses the question about their function during operation of the negative plates. The lead crystals in a completely charged plate, after 10 charge–discharge cycles at a current density of 5 mAcm^{−2}, are shown in Fig. 11.9. A comparison between Figs. 11.8 and 11.9 shows

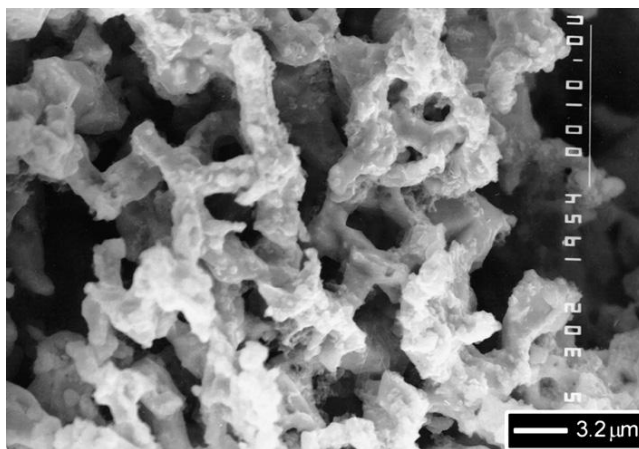


Figure 11.7:

Scanning electron micrograph of lead skeleton obtained during the first formation stage [2]. PbSO₄ crystals in the (Pb + PbSO₄) zone have been dissolved.

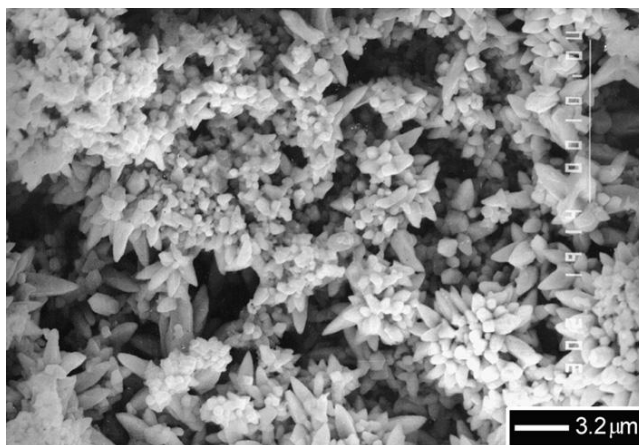


Figure 11.8:

Scanning electron micrograph of lead crystals in a completely formed negative plate [2]. Formation was conducted in H_2SO_4 solution of 1.05 relative density [2].

that the overall appearance of the lead crystals after cycling is different from that after formation. This difference is due to the different H_2SO_4 concentrations in which the lead crystals have formed during plate formation and cycling.

The structure of the discharged active mass is shown in Fig. 11.10. Densely packed PbSO_4 crystals (1–4 μm) are observed in the micrograph. It is interesting to see how does the skeleton change during deep discharge. The morphology of the lead skeleton has been examined after

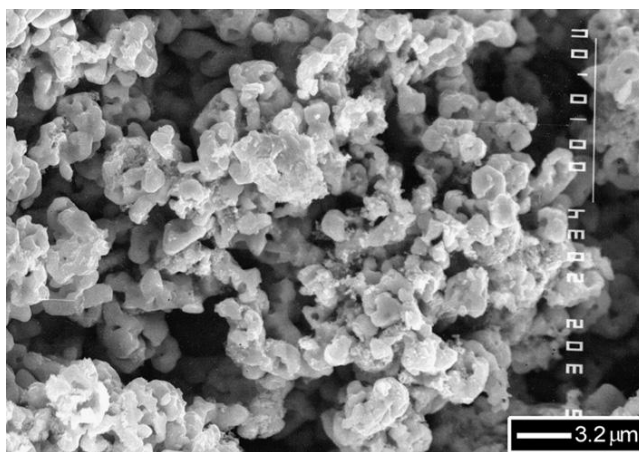


Figure 11.9:

Scanning electron micrograph of lead crystals in charged negative plate after 10 charge-discharge cycles. The small Pb crystals form an energetic zone with large surface and high capacity. These crystals have formed during cycling, i.e. in H_2SO_4 solution of 1.28 relative density [2].

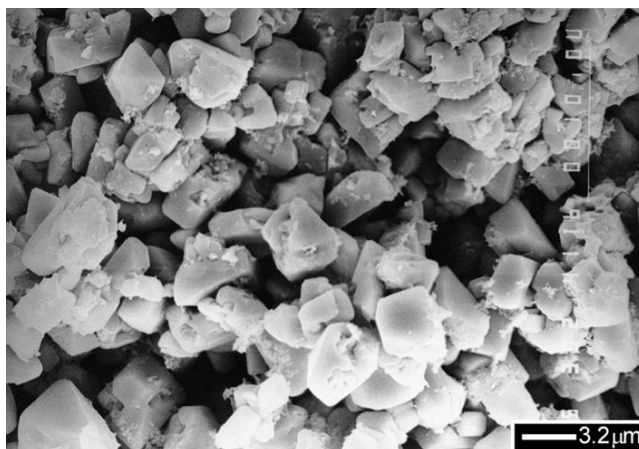


Figure 11.10:

Morphology of crystals in fully discharged plate [2]. The well shaped crystals are those of PbSO_4 .

dissolving the PbSO_4 in ammonium acetate solution. An electron micrograph of this lead sub-structure is given in Fig. 11.11. A comparison of Figs. 11.7 and 11.11 reveals that the lead structure obtained during the first formation stage has been but slightly affected during charge—discharge cycling. Hence, the skeleton formed during the first formation stage is practically preserved unchanged during the subsequent charge-discharge cycles.

The lead skeleton has a double function: it serves as a current-collector for all parts of the active mass and provides mechanical support to the lead crystals which participate in the current generation process. Based on this fact it can be presumed that the capacity of

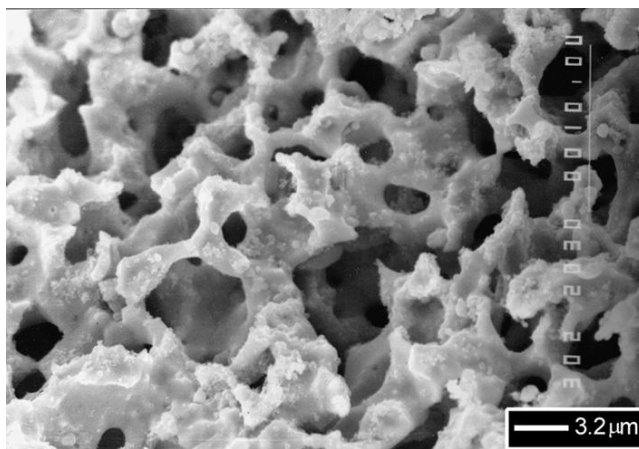


Figure 11.11:

Scanning electron micrograph of skeleton of discharged negative plate after dissolving PbSO_4 crystals [2]. The lead skeleton is unchanged after cycling.

the negative plate is determined mainly by the secondary lead crystals, which we will call 'energetic structure'. In an attempt to prove this assumption, chemical analytical methods have been applied to determine the amount of lead in the active mass obtained during the first and the second stages of negative plate formation. This amount was compared to the quantity of lead oxidized during discharge of the plate. A summary of the data obtained, as judged by the quantity of electricity delivered, is given in Table 11.1. The data in the table indicate that during discharge, the entire secondary lead structure, together with 15% of the lead skeleton, are involved in the current generation process.

During pasting of the grids, the paste is homogeneous in all parts of the plate. During formation, however, electrochemical processes occur in two stages. Due to the different equilibrium potentials of the divalent lead compounds contained in the paste, different products are formed during these processes. Micro-heterogeneity is thus created by the occurrence of a primary and a secondary structure [2]. These two structures play different roles during battery operation (charge—discharge cycling). It may be expected that the capacity, power and cycle-life of the plate will depend on the relative proportions of these structures. By keeping an optimum ratio between these two structures, it is possible to maintain stable performance parameters of the negative plates.

The above described structure of the lead active mass (NAM) suggests that the ratio between the skeleton and the energetic structures will determine the performance of the negative plates. If the share of the skeleton structure exceeds by far that of the energetic structure, the NAM will have small active surface area and hence the capacity of the plates will be low. On the contrary, when the share of the energetic structure is much bigger than that of the skeleton structure, the plate capacity at low discharge currents will be high, but their power output will be low because the skeleton structure will comprise branches of small cross-section and hence high Ohmic resistance. Most probably, some parts of NAM will have such a high Ohmic resistance that these parts will be excluded from the current generation process.

What does the proportion between skeleton and energetic NAM structure depend on? The skeleton structure forms as a result of reduction of the PbO and the basic lead sulfates in the paste. Hence, the paste composition ($\text{H}_2\text{SO}_4/\text{LO}$ ratio) plays a major role. This composition changes

Table 11.1: Comparison of the amount of lead obtained during the second stage of formation and the lead oxidized during discharge of the plate.

Formation Stage	Pb Produced per Plate During Formation		Discharge Capacity Ah
	G	Ah	
Stage 1	46	11.9	13.5
Stage 2	45	11.6	
Total	91	23.5	

during soaking and formation, depending on the concentration of the H_2SO_4 solution during these two technological procedures. So the technology of plate manufacture should be selected so as to yield 48–55% skeleton structure during the first formation stage, which proportion would guarantee optimum capacity, power and cycle life performance of the negative plates.

The secondary structure of the negative plate builds up and disintegrates during each charge–discharge cycle. On the other hand, the skeleton structure changes slowly throughout the cycle-life of the battery. Hence, the primary structure created during the first stage of formation constitutes the ‘memory’ for the technology of negative-plate manufacture [2].

11.4.2. Evolution of Pore Structure of Negative Plates During Formation

The changes in molar volume on conversion of one lead compound into another one or on reduction to Pb are given in Table 11.2 [5]. The molar volume increases during the reactions of sulfation and decreases during the electrochemical reaction of reduction of lead compounds to lead. Changes in pore-volume distribution by radius during formation of a negative plate have been determined for both the surface layers (o) and the interior of the plate (x). The obtained results are presented in Fig. 11.12 [2]. Prior to formation, the pore radii vary between 0.1 and 0.3 μm ; after formation, they are in the range from 0.6 to 4 μm . The two stages of formation can be clearly distinguished by the behaviour of the programs. During the first formation stage (first 6h), the total pore volume in the surface plate layers decreases slightly. This indicates that the rate of the chemical reaction of PbSO_4 formation is higher than that of the formation of Pb. After 8h, the reaction of Pb formation becomes dominating both in the surface layers and in the interior of the plate, whilst the rate of the reaction of paste sulfation decreases abruptly or ceases altogether as the 3BS and PbO phases are exhausted. The total pore volume increases and so does the average pore radius after 10, 12 and 14 h of formation (Fig. 11.12).

The above results indicate that the pore system of NAM depends on the degree of paste sulfation during the different steps of the technological process of plate manufacture.

Table 11.2: Volume changes during formation of lead [5].

Reaction		Relative Volume Change vs. Initial Product (%)
Starting Product	End Product	
PbO	Pb	–23
	$3\text{PbO} \cdot \text{PbSO}_4 \cdot \text{H}_2\text{O}$	+60
	PbSO_4	+100
$3\text{PbO} \cdot \text{PbSO}_4 \cdot \text{H}_2\text{O}$	Pb	–52
	PbSO_4	+23
PbSO_4	Pb	–60

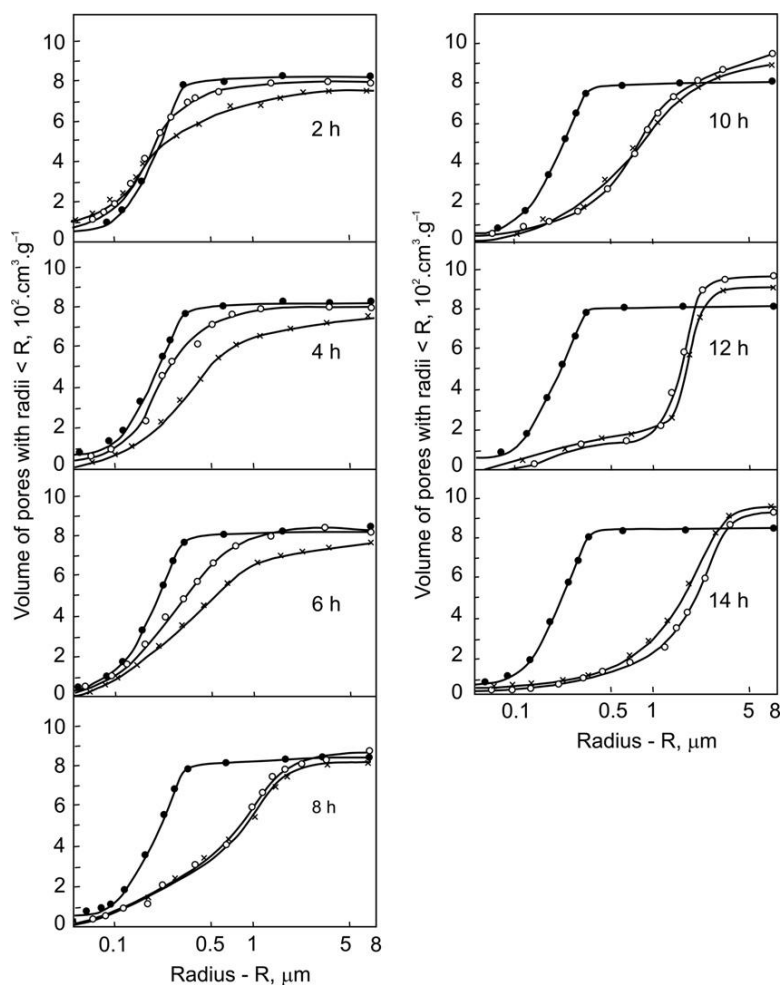


Figure 11.12:

Changes in pore volume and pore-size distribution on formation of NAM: (•) unfurmed plate; (○) plate surface layers; (×) plate interior [3].

11.5. Effect of Expander on the Processes of Formation of NAM Structure and Factors Responsible for Expander Disintegration

11.5.1. Influence of Expander on the Processes of Plate Formation

Further in this chapter, the term ‘expander’ will be used to designate only the organic expander component, i.e. the lignosulfonate additive to the negative active material. Expanders exert a strong influence on the crystallization processes of Pb on charge and of PbSO₄ on discharge [6–16]. They also suppress the formation of β-PbO and 4BS crystals [14,17].

How does the organic expander affect the skeleton and the secondary NAM structure?

Negative plates with or without expander (lignosulfonate) have been investigated. The changes in potential (vs. $\text{Hg}|\text{Hg}_2\text{SO}_4$ electrode) and the content of PbSO_4 during plate formation are presented in Fig. 11.13 for negative plates with and without expander [14]. Formation of the plates containing expander is completed within 10h, while those without expander require 12 h of formation. Hydrogen evolution starts on plates with expander at an overpotential by 160 mV more negative than on plates with no expander.

The dependence of plate potential on current density during the first and the second formation stages is presented in Fig. 11.14 [14]. The processes of PbO and 3BS reduction during the first stage of formation proceed at a lower potential in the plates without expander. The same tendency is observed with the reduction of PbSO_4 to Pb . This indicates that expanders impede all electrochemical reactions involved in the formation process.

Figure 11.15 shows the morphology of the Pb crystals that build up the NAM skeleton of plates with or without expander. A more pronounced roughness of the skeleton surface is observed in expander-containing plates. Different expanders yield different NAM skeletons, which may serve as ‘memory’ of the technology of plate manufacture [14].

The secondary lead structure of completely formed plates with or without expander is shown in Fig. 11.16. In NAM without expander, the secondary lead structure covers the skeleton in the

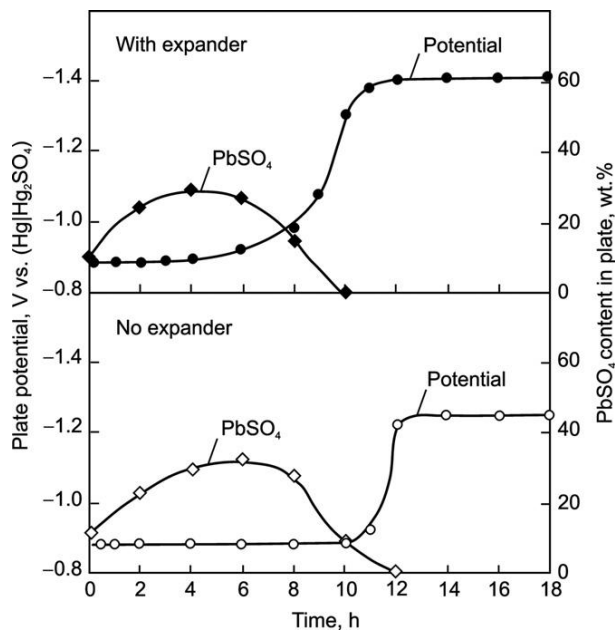


Figure 11.13:

Changes in plate potential and PbSO_4 content on formation of NAM with or without expander [14].

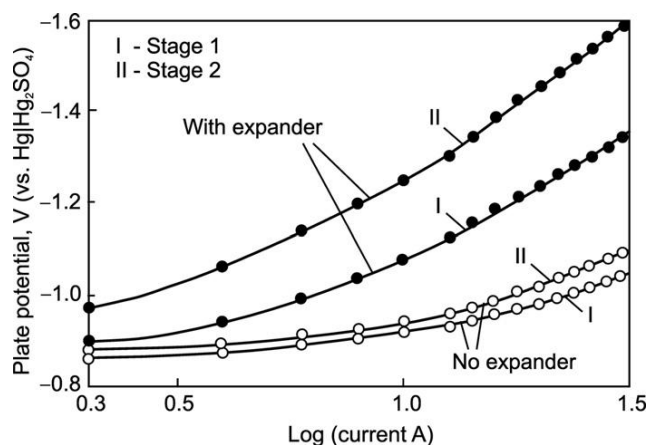


Figure 11.14:

Polarization curves during the second hour (stage 1) and seventh hour (stage 2) of formation of negative plates with or without expander [14].

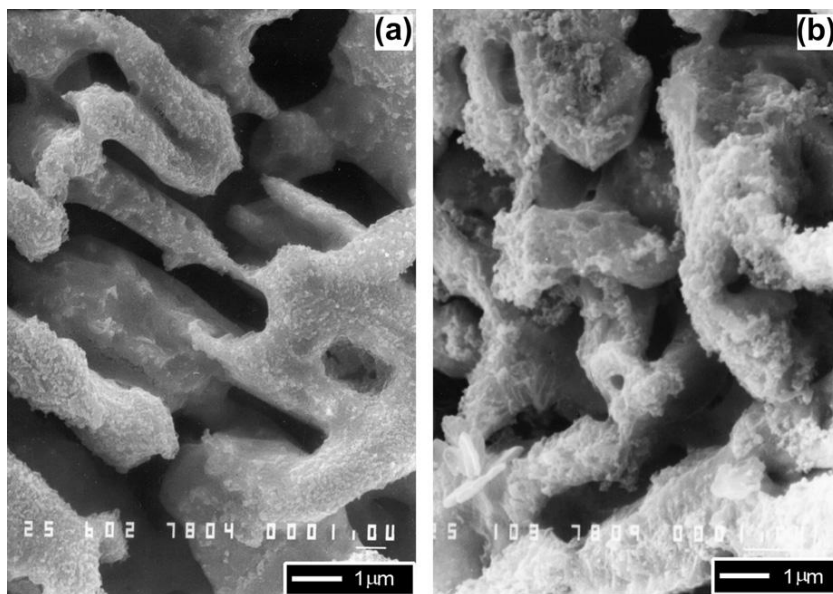


Figure 11.15:

Scanning electron micrographs of skeleton structure of NAM formed during the first formation stage: (a) no expander and (b) with expander [14].

form of a smooth layer, whereas the secondary lead structure in the NAM of expander-containing plates comprises individual Pb crystals over the skeleton structure. Hence, organic expanders regulate the processes involved in the formation of both types of structure in the lead active-mass during formation of negative plates. They have a greater contribution to the

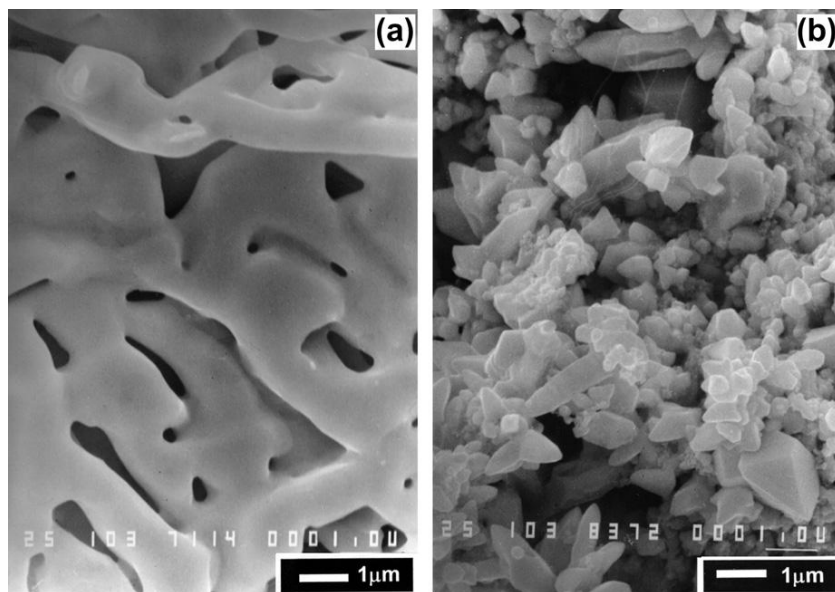


Figure 11.16:

Crystal morphology of secondary lead structure formed in plates during the second formations stage: (a) no expander and (b) with expander [14].

formation of the energetic structure built of small Pb crystals yielding large NAM surface and thus high plate capacity (Fig. 11.16b). So the capacity performance of the negative plates depends on the nature of expander(s) used and on its(their) stability as they determine the surface area of the energetic structure.

The most widely used expander material for automotive batteries is Vanisperse A (VS-A) produced by Borregaard LignoTech (Norway). By contrast, a great variety of expanders is used by manufacturers of industrial and standby batteries. In batteries for cycling applications, the use of an expander blend of Indulin and VS-A guarantees a much longer cycle-life than when the two organic substances are used alone [18]. The choice of an appropriate expander for a given type of battery is very important for the overall performance of the battery.

11.5.2. Changes in NAM Structure on Cycling Limiting Battery Cycle Life

The question arises logically as to what changes in NAM structure are responsible for the capacity decline of negative plates? In an attempt to answer this question we compared the skeleton and energetic structures of NAM after plate formation and on completion of the cycling test. The SEM picture in Fig. 11.17 features the particles building up the energetic structure of NAM before and after cycling of plates produced with the three most efficient expanders [18]. It can be seen that the size of the particles depends on the type of expander used. Secondly, the Pb particles of the energetic structure almost disappear on plate cycling at

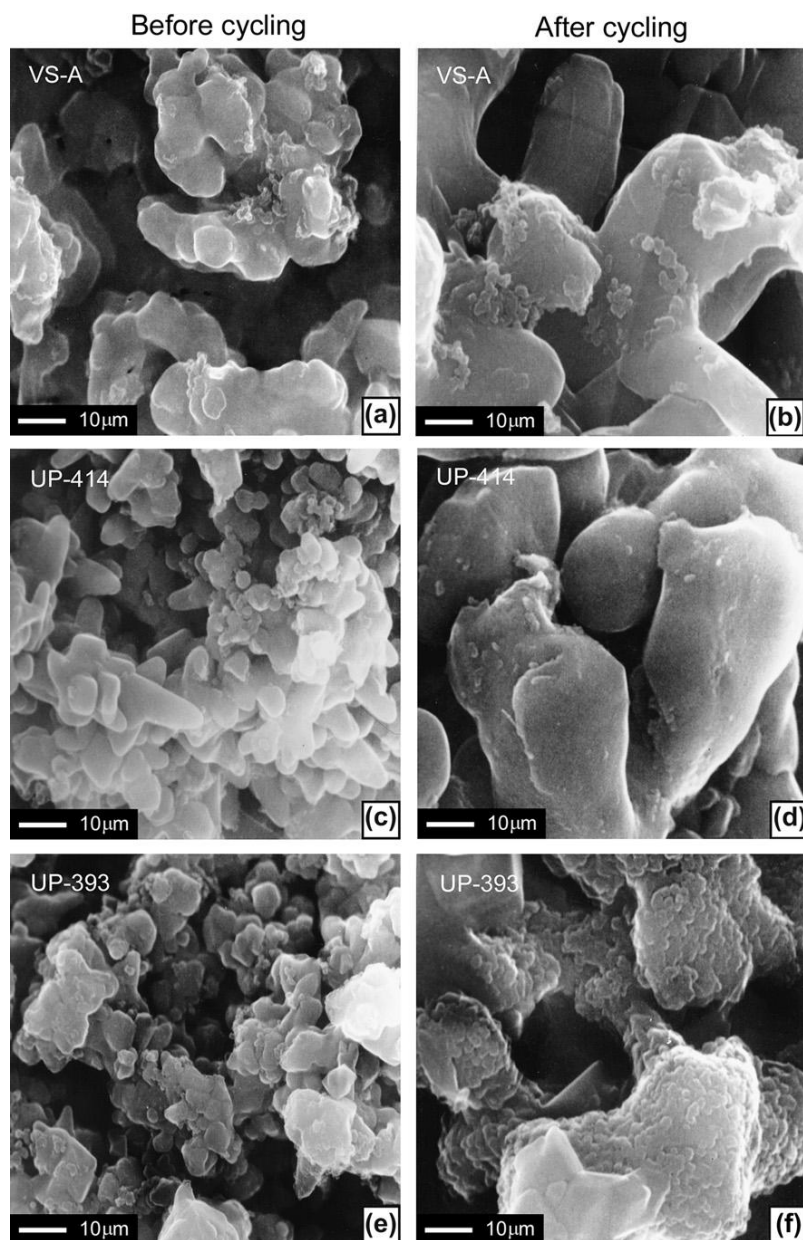


Figure 11.17:
Changes of the energetic structure of NAM on DIN cycle life tests. (a,c,e) energetic structure of NAM after plate formation; (b,d,f) NAM structure after cycling.

the expense of visible growth of the skeleton structure. Consequently, the active surface of NAM decreases, which will lead to capacity decline.

So it can be concluded that expanders contribute to building the energetic structure of NAM which comprises small Pb crystals with large surface area. Depending on the type and amount of structural groups contained in the expander molecule, the particles of the energetic NAM structure differ in morphology. The stability of the energetic structure on cycling will depend on the stability of the expander used. The expander stability, in turn, is influenced by the temperature of battery operation as well as by the type of ions and compounds contained in the solution which may get into a chemical interaction with the expander and thus change its composition, structure and properties.

Figure 11.18 shows the energetic and skeleton structures of plates with (In+Vs) expander blend at the end of battery life, when cycled at 60 °C.

There is no difference between the two types of structure. If we compare the two micrographs in Figs. 11.18, it can be seen that the skeleton structure (as also the whole NAM structure) consists of thin branches interconnected into a highly porous mass. The expander has disintegrated under the action of the high temperature, as a result of which the NAM skeleton has transformed into small thin Pb particles similar to those of the energetic structure. The NAM at the end-of-plate-life is very soft and highly expanded in volume. These results imply that in order to guarantee high negative plate capacity, the negative active mass should have large surface but also skeleton structure comprising thick branches with low Ohmic resistance.

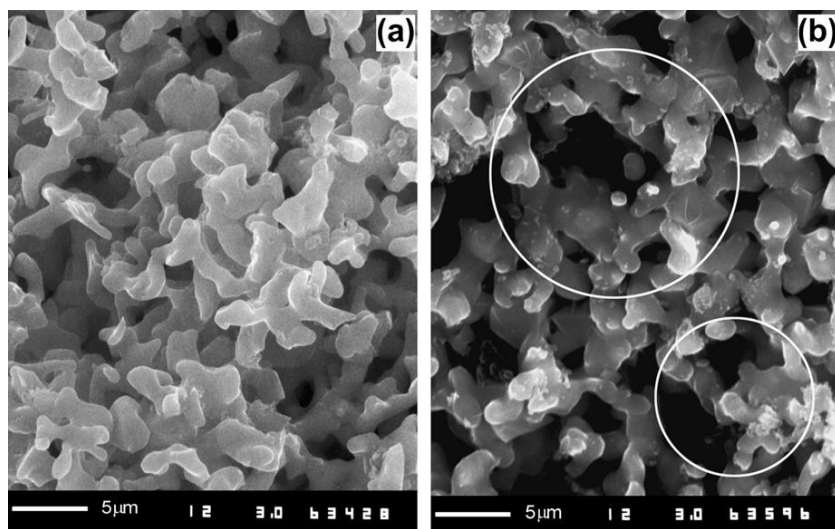


Figure 11.18:
SEM micrographs of NAM cycled at 60 °C. (a) skeleton and (b) energetic structure [18].
Magnification $\times 3000$.

References

- [1] S.C. Barnes, R.T. Mathieson, in: D.H. Collins (Ed.), *Batteries 2*, Pergamon Press, Oxford, 1965, p. 41.
- [2] D. Pavlov, V. Iliev, *J. Power Sources* 7 (1981/82) 153.
- [3] D. Pavlov, V. Iliev, G. Papazov, E. Bashtavelova, *J. Electrochem. Soc.* 121 (1974) 854.
- [4] D. Pavlov, *J. Electroanal. Chem.* 72 (1976) 319.
- [5] J. Burbank, *J. Electrochem. Soc.* 113 (1966) 10.
- [6] A.C. Simon, S.M. Caulder, P.J. Gurlusky, J.R. Pierson, *Electrochim. Acta* 19 (1974) 739.
- [7] J. Burbank, A.C. Simon, E. Willihnganz, in: P. Delahay, C.W. Tobias (Eds.), *Advances Electrochemical Engineering*, vol. 8, Wiley Interscience, New York, 1971, p. 229.
- [8] A.C. Zachlin, *J. Electrochem. Soc.* 98 (1951) 321.
- [9] E. Willihnganz, *Trans. Electrochem. Soc.* 92 (1947) 148.
- [10] E.G. Yampol'skaya, M.I. Ershova, I.I. Astakhov, B.N. Kabanov, *Elektrokhim.* 2 (1966) 1211; 8 (1972) 1209.
- [11] B.K. Mahato, *J. Electrochem. Soc.* 127 (1980) 1679.
- [12] T.F. Sharpe, *Electrochim. Acta* 1 (1969) 635.
- [13] G.I. Aidman, *J. Power Sources* 59 (1996) 25.
- [14] V. Iliev, D. Pavlov, *J. Appl. Electrochem.* 15 (1985) 39.
- [15] D. Pavlov, S. Gancheva, P. Andreev, *J. Power Sources* 46 (1993) 349.
- [16] D. Pavlov, in: B.D. McNicol, D.A.J. Rand (Eds.), *Power sources for electric vehicles*, Elsevier, Amsterdam, 1984, p. 273.
- [17] D. Pavlov, V. Iliev, *Elektrokhim.* 11 (1975) 1627.
- [18] G. Papazov, D. Pavlov, B. Monahov, *J. Power Sources* 113 (2003) 335.

This page intentionally left blank

Technology of Formation

12.1. Introduction

12.1.1. Changes in Temperature, H_2SO_4 Concentration and Open Circuit Cell Voltage During Active Mass Formation

The changes in temperature during tank and battery (container) plate formation are presented in Fig. 12.1.

When the plates are immersed into the solution, chemical reactions proceed between PbO , basic lead sulfates and H_2SO_4 . Since these reactions are exothermic, the temperature in the tank or battery rises. The temperature rise differs for the two formation methods.

In the *battery (container) formation method*, the heat capacity of the battery is small, the concentration of H_2SO_4 is high (1.15 or 1.23 rel. den.) and considerable amounts of paste are sulfated, hence, a great amount of heat energy is generated. All this leads to a rapid increase of battery temperature, which may exceed $60^\circ C$. Such a temperature rise is undesirable and could be avoided by immersing the batteries in tanks (baths) filled with cold water thus facilitating the heat exchange between battery and water in the tank (bath), and preventing temperature rise above $50^\circ C$.

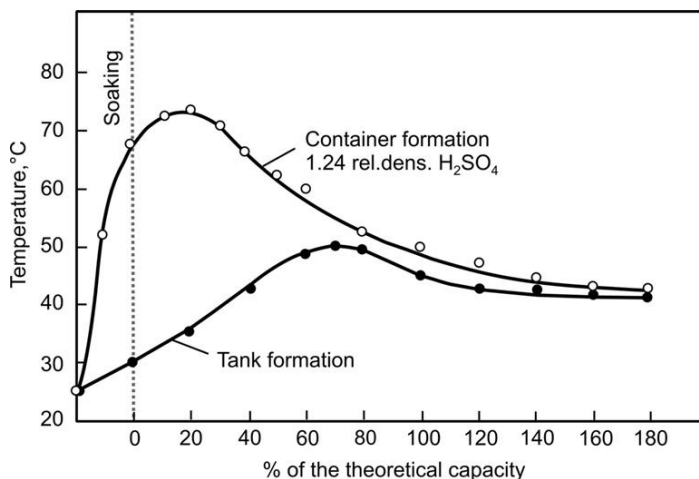


Figure 12.1:

Changes in temperature during soaking and formation of battery plates. Based on data from [1].

In the *tank formation method*, the heat capacity of the tank is great and the concentration of the H_2SO_4 solution is low (1.06 rel. dens.), so a small quantity of paste is sulfated and less heat is generated (and at a lower rate) during the formation process. Hence, the temperature reaches a maximum after the PbO and basic lead sulfates in the surface paste layers have reacted with most of the H_2SO_4 solution.

During the technological process of formation, electrochemical reactions of formation of Pb and PbO_2 proceed which also contribute to the overall thermal balance. These reactions, however, are endothermic.

Industrial practise has shown that the optimum temperature range for the formation process is between 35 and 50 °C.

Figure 12.2 shows the changes in H_2SO_4 concentration and cell voltage during plate formation [1]. Two stages can be distinguished judging by the curves. During the first stage, the reactions of sulfation predominate, as a result of which the concentration of H_2SO_4 in the bulk solution decreases and the temperature in the cells rises (Fig. 2.1). The cell voltage decreases because

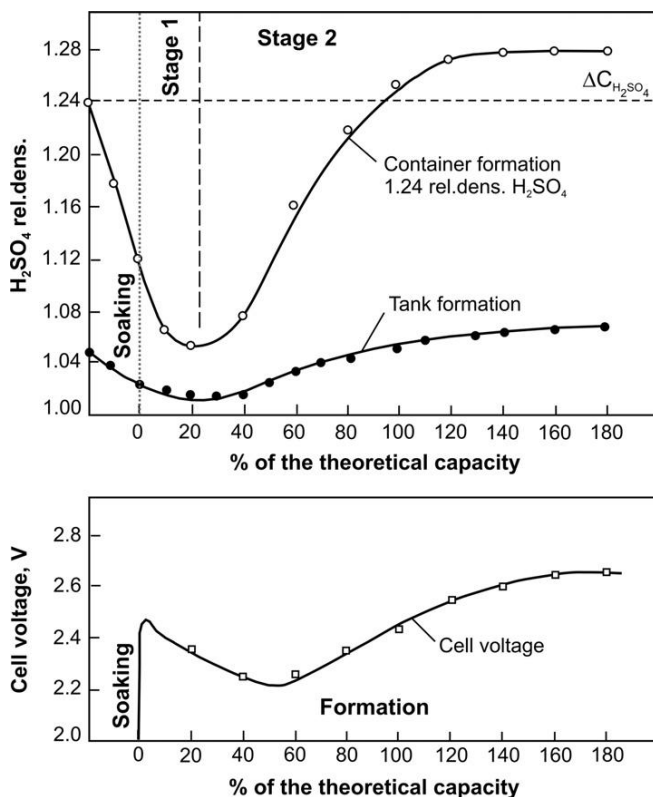


Figure 12.2:

Changes in H_2SO_4 concentration and cell voltage during plate formation. Based on data from [1].

the electrode systems, formed by Pb (or PbO₂) and PbO and basic lead sulfates of the paste, have low equilibrium potentials (see Chapter 2).

During the second stage of formation, H₂SO₄ is released from the plates and diffuses into the bulk electrolyte. The latter's concentration rises. This indicates that PbSO₄ is reduced to Pb at the negative plates and oxidized to PbO₂ at the positive ones. The electrochemical reactions of oxidation and reduction of PbSO₄ proceed at high potentials and hence the cell voltage increases during this second stage of formation. Hence, the concentration of H₂SO₄ electrolyte at the end of the formation process is higher than the initial concentration, because the sulphuric acid used for paste preparation is released during the formation of Pb and PbO₂. The greater the amount of H₂SO₄ used for paste preparation, the higher the electrolyte concentration at the end of the formation process. So frequent adjustment of the formation electrolyte concentration is required when the tank formation method is employed.

12.1.2. Technological Parameters of the Formation Process

The following parameters play an essential role in the technology of formation:

- (a) *Formation current.* It determines the rates of the electrochemical reactions as well as those of the chemical reactions caused by the electrochemical ones that proceed on both types of plates. The formation current algorithm takes account of the different stages during which the various structural elements (i.e. corrosion layer, adjacent PAM layer, two types of active material) are formed. An appropriate current profile should yield optimum performance parameters of the plates, but should also shorten the duration of the formation procedure and minimise the amount of water that decomposes during this step (i.e. ensure high efficiency of formation). The maximum admissible current density is limited by temperature and voltage restrictions. Normally, a current density of 2–10 mA per cm² of plate surface is applied. Accelerated formation is conducted with 10–15 mA cm⁻² current density. Recently, some innovative formation techniques have been proposed allowing completion of the formation process within 6–8 h. These methods involve periods during which current densities of 40–50 mA cm⁻² are applied.
- (b) *Temperature.* The temperature of formation should not exceed 50 °C. This temperature limit should be taken into account when designing the formation current algorithms. When formation is conducted at temperature lower than 60 °C, the content of α-PbO₂ in PAM is significant, which results in lower initial capacity but stronger and more stable active mass yielding longer cycle life. The efficiency of the formation process during the second stage is low, which means that the overall duration of the formation process will be longer. When formation is performed at temperatures higher than 60 °C, the obtained PAM contains considerably more β-PbO₂ than α-PbO₂. Then the initial capacity of the battery is higher, but soon the PAM begins to shed off and hence the battery capacity

starts to decline. The elevated temperature reduces the capacity of the negative plates, too, due to expander degradation. Temperatures higher than 60 °C reduce the voltage of water decomposition and, hence, the efficiency of the formation process decreases. Moreover, the higher temperature accelerates the corrosion of the positive grids.

- (c) *Battery voltage.* Battery voltage should be lower than that causing intense hydrogen and oxygen evolution, as such gassing would increase energy losses and harmful emissions to the environment. The voltage limit for formation depends on the temperature, the type of grid alloy used, the H_2SO_4 concentration and the phase composition of the paste. An upper formation voltage limit of 2.60–2.65 V per cell is generally accepted.
- (d) *Quantity of electricity flowing through plates.* The theoretical quantity of electricity needed for formation of 1 kg of PbO to Pb or to PbO_2 is 241 Ah. In the battery practise, 1 kg of PbO is formed with between 1.5 and 2.2 times the theoretical quantity of electricity (i.e. 360–530 Ah per 1 kg of PbO). This quantity may drop below 330 Ah kg^{-1} dry paste for formation of negative plates, where some unoxidized Pb remains. The quantity of electricity depends on the thickness of the plates, the phase composition of the cured paste, the size of the particles that constitute the individual phases, and the employed current and voltage algorithms of formation.
- (e) *H_2SO_4 concentration.* The sulfuric acid concentration exerts an influence on the processes of sulfation of the plates during soaking and formation, and hence on the structure and phase composition of the active materials. The influence of H_2SO_4 concentration on the structure of PAM and NAM was discussed in detail in the previous two chapters.

Each of the above parameters exerts an influence on the formation of the structure of the active masses and on the nature of their interfaces with the grids. Thus, these parameters affect the performance of the battery. The algorithm of the formation process should take account of the zonal processes that occur on both types of plates so as to ensure the formation of appropriate active-mass structures, which would guarantee high battery performance characteristics.

Let us now make an overview of the above parameters during formation of the grid/paste interface and during formation of the active materials.

12.2. Influence of Active Mass Structure on Plate Capacity

Numerous attempts have been made to produce positive and negative plates by pressing chemically obtained PbO_2 or Pb powders onto the grids. These attempts have always led to the conclusion that such plates have small capacity and low electrochemical activity. These results have been attributed to poor contact of the chemically prepared active materials with the grid, oxidation of the lead powders, etc.

How do chemically prepared active materials differ from electrochemically obtained ones? The chemically obtained active mass has homogeneous structure comprising interconnected particles of identical morphology and structure. The electrochemically obtained active mass,

on the other hand, is built of skeleton and energetic structures comprising particles of different morphology and structure, or even different phase composition (α - and β -PbO₂) and different surface area and reactivity, as is the case with positive plates. These structures are formed separately from different initial materials. The skeleton structure creates the conducting network that spreads throughout the whole plate volume and supports mechanically the energetic structure, thus conducting the electric current to and from each part of the plate. The above structures are built during the process of formation. Hence, the technology of plate formation is very important for the performance characteristics of the battery. The different stages during formation of the active mass structures will be discussed further in this chapter.

12.3. Initial Stages of Formation of Lead–Acid Batteries

12.3.1. Processes During the Initial Stage of Corrosion Layer Formation

Formation of lead–acid batteries is usually performed by connecting the batteries in strings. Prior to starting the formation process and switching the formation current on, it is necessary to check the ‘continuity of the strings.’ The electrical (ohmic) resistance of each string is measured with the help of an ohmmeter. It should be within definite limits. Resistance higher than the specified values is an indication of break in connections. The latter has to be identified and fixed. Otherwise, the string will be disconnected from the formation circuit and the batteries will not be formed, but will rather undergo severe sulfation. Moreover, when one string is excluded from the electric circuit system, the formation current in the parallel strings will increase, which is undesirable, too.

Let us now see what happens at the beginning of the formation process.

The grid/paste interface comprises a corrosion layer formed during the curing step and then partially sulfated and hydrated during the soaking process. Besides, as a result of soaking, the surface layers of the plate are rich in PbSO₄, whereas the plate interior contains hydrated PbO and basic lead sulfate layers.

The only electron conductor in the plate is the grid. Hence, on switching the formation current on, first the corrosion layer and the paste layer adjacent to it will be formed.

Several formation current algorithms are used in the battery practise. The simplest one is to apply constant formation current, e.g. equal to 0.3 C A. Figure 12.3 shows the changes in cell voltage during the first several hours of formation.

At the beginning of formation, the ohmic resistance of the cell is high as the corrosion layer is composed of PbO and Pb(OH)₂. The interface resistance depends on the sulfation of the corrosion layers formed on the positive and negative grids. Cells set to longer soaking which results in high sulfation of the corrosion layer, will have high resistance of both types of plates. When formation current flows through such plates, substantial quantities of Joule heat will be

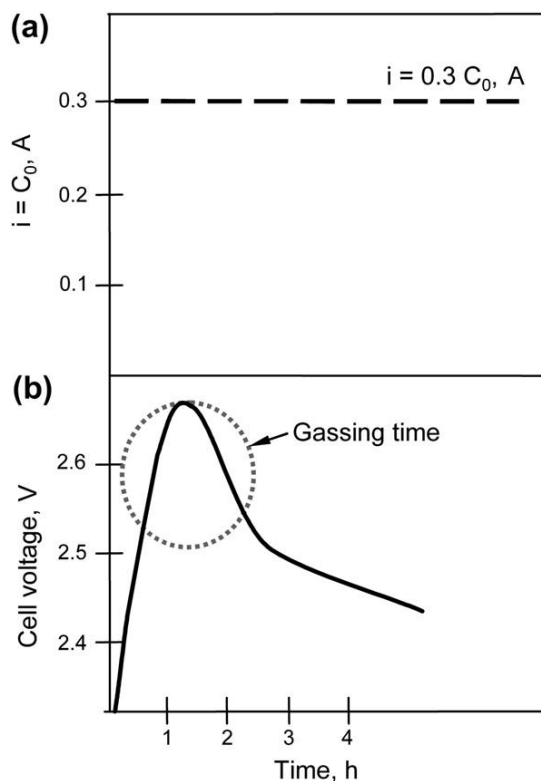


Figure 12.3:

Changes in cell voltage during the initial stage of formation of a lead–acid cell with formation current equal to $0.3C_0 A$.

generated in the interface layer. For electric current to flow through the cell, it should be highly polarized. Depending on the formation current, the cell voltage may reach values of the order of 2.7–2.9 V. These voltage levels exceed the voltage of water decomposition and hence intense gassing starts at both types of plates. After oxidation of the corrosion layer and of the adjacent paste layer is completed, the rise in cell voltage stops, it passes through a maximum and begins to decrease thereafter with increase of the volume of $(PbO_2 + PbSO_4)$ zones in the positive plates and $(Pb + PbSO_4)$ zones in the negative ones.

The above cell voltage profile and the observed intense gassing at the interface create serious problems. The gas bubbles evolved on the grid surface exert substantial pressure on the skeleton branches in the paste that connect it to the corrosion layer and these branches may crack. Consequently, caverns may form between paste and grid. The ample amount of local Joule heat generated at the interface, too, contributes to the formation of such caverns.

Figure 12.4 presents SEM pictures of the interface corrosion layer/PAM with the formed caverns and channels (pores) along which the gas from the caverns has left the plate [2]. These

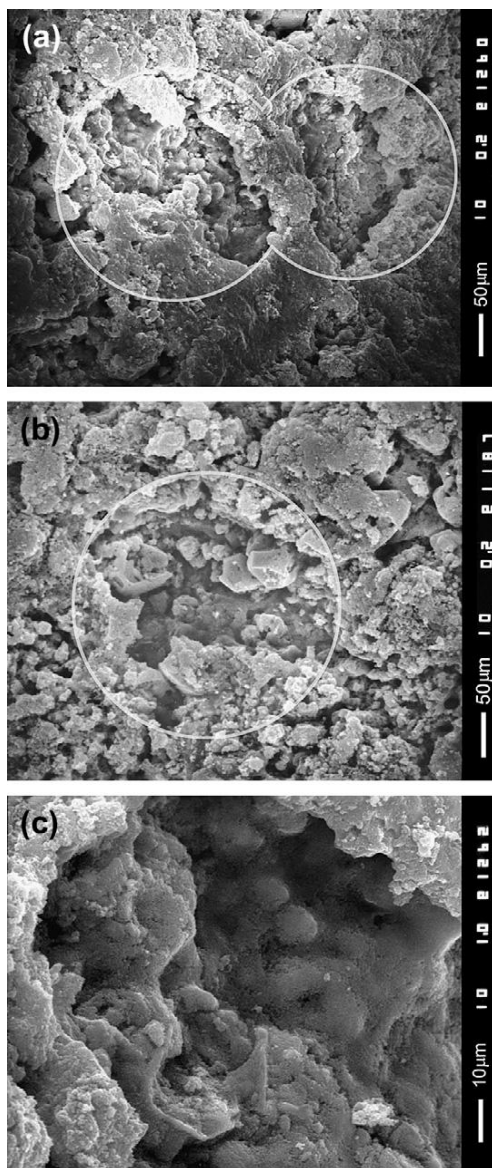


Figure 12.4:

Corrosion layer/PAM interface with gas caverns and pores along which the gas from the caverns leaves the plate [2]: (a,b) images of gas caverns and channels (pores) at different interface sites; (c) closer view of a gas cavern.

caverns and gas channels are preserved even after formation of PAM and NAM is completed, and thus reduce the contact area PAM/corrosion layer (resp. NAM/grid). Consequently, the current density through the interface, and thus the polarization of the positive and negative plates, increases during charge and discharge. Caverns are formed in substantial amounts in

plates thicker than 2 mm. So it is important to avoid gassing during the first stage of the formation process. This can be achieved by reducing the time of soaking, using formation electrolyte of moderate H_2SO_4 concentration and limiting the cell voltage to maximum 2.55 V during the initial stage of formation.

The lead dioxide active material layer that is in contact with the corrosion layer has the function to collect the current from the whole volume of PAM and conduct it to the corrosion layer during charge and, vice versa, to collect the current from the corrosion layer and distribute it throughout the whole PAM volume during discharge. That is why this layer was called 'Active Mass Connecting Layer' (AMCL) [3]. Figure 12.5 shows SEM pictures of the structure of the interface metal (grid) surface/corrosion layer/AMCL [2]. The corrosion and

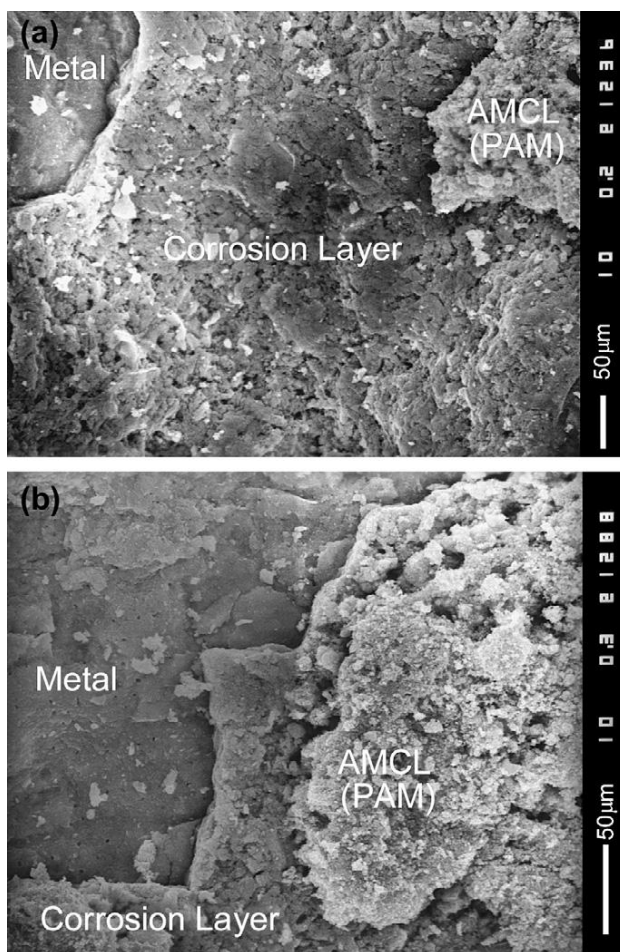


Figure 12.5:

Grid/corrosion layer/AMCL/PAM interface [2]: (a), (b) images of different parts of the interface.

AMCL layers have different structure and the connection between them is very delicate. Moreover, pores are formed between them (Fig. 12.5b). It is through these macropores that the H_2SO_4 solution reaches the AMCL forming PbSO_4 during discharge. The sulfate crystals formed reduce the cross-section of the PbO_2 branches of the skeleton structure of the AMCL and thus the ohmic resistance of the interface increases and so does the polarization of the plate. These processes often limit the capacity of the positive plates.

12.3.2. Current and Voltage Algorithms for the Initial Stage of Formation [4]

To avoid gas evolution at the beginning of formation, the current should be increased gradually, in 4 or 5 steps of 15–20 min each, so as to allow the formation and growth of sufficiently large ($\text{PbO}_2 + \text{PbSO}_4$) and ($\text{Pb} + \text{PbSO}_4$) zones round the grid bars. Thus, the surface on which the electrochemical reactions of paste oxidation on the positive plates and paste reduction on the negative plates proceed will increase substantially and the potential of water decomposition with gas evolution will not be reached. Possible current steps may include: $I_1 = 0.02 \text{ C A}$, $I_2 = 0.04 \text{ C A}$, $I_3 = 0.08 \text{ C A}$, $I_4 = 0.15 \text{ C A}$ and $I_5 = 0.3 \text{ C A}$ [4].

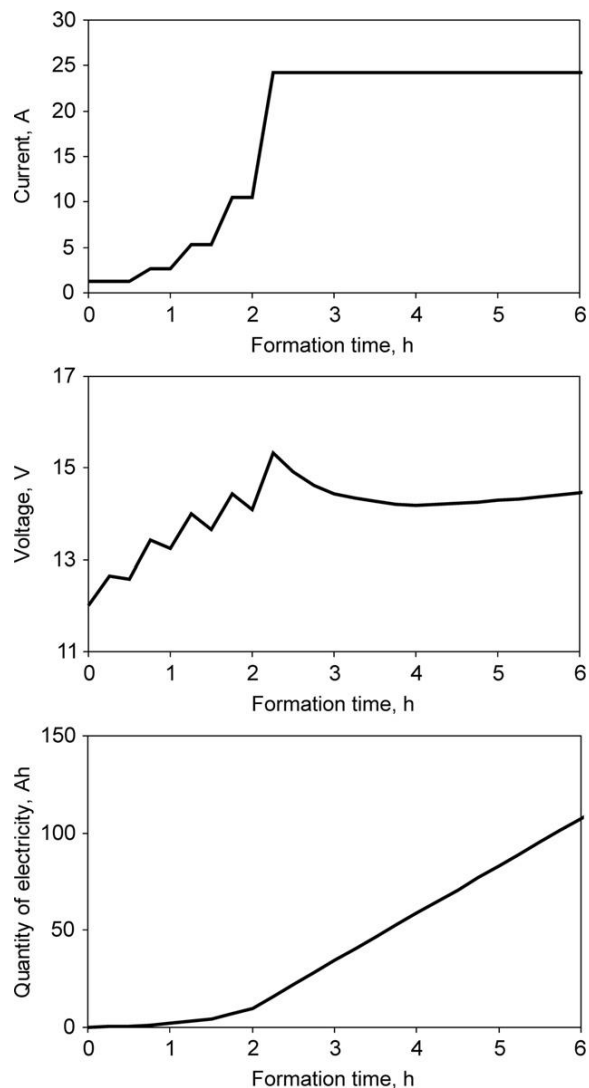
Figure 12.6 shows an example of a multi-step current increase during formation. The changes in battery voltage during the different steps and the quantity of electricity flowing through the battery are also given in the figure. For complete formation of the grid/PAM interface of a 50 Ah battery, an electric charge of 5–8 Ah should flow through the battery during the initial stage of formation [4].

12.4. Formation of Positive and Negative Active Materials from Cured Pastes

12.4.1. Distinction Between Formation and Charging of Lead–Acid Batteries

After PbO_2 (resp. Pb) have formed at the grid/corrosion layer/cured paste interface of positive (resp. negative) plates, formation of PbO_2 (PAM) and Pb (NAM) active materials from the cured pastes starts at the two types of plates. As discussed earlier in Chapters 10 and 11, formation of PAM and NAM proceeds in two stages. During the first stage, PbO_2 and Pb are formed through electrochemical reactions involving PbO and basic lead sulfates. During the second formation stage, only PbSO_4 participates in the electrochemical reactions of PAM and NAM formation. The above two types of processes create different structures in the different parts of PAM and NAM. The specific processes that occur during the different formation stages should be accounted for when designing the formation algorithms.

It is often assumed in the literature that formation is actually the first charge of the battery and, based on this assumption, charging schedules are automatically transferred to the formation algorithms. This is not quite correct, however. The processes that take place during formation differ substantially from the charge processes.

**Figure 12.6:**

Changes in current, voltage and quantity of electricity flowing through a 50 Ah battery during the initial formation stage [4].

First, during the initial stage of battery charging, it is advisable that strong currents are applied. This is not the case with the initial stage of formation. The initial formation current should be low as the grid surface is small and it is during this stage of formation that the non-conductive corrosion layer, formed on the surface of both types of grids and composed of PbO and Pb(OH)_2 , is converted into Pb and PbO_2 , respectively. Only with progress of this latter process and increase of the volumes of Pb and PbO_2 formed should the formation current be increased.

Second, during the first stage of formation of the negative plates, the Pb skeleton structure of NAM is built, whereas at the positive plates, an α -PbO₂ skeleton forms round the grid bars, which then advances towards the plate interior until the whole amount of PbO and BS in the cured paste is exhausted. After that, β -PbO₂, produced as a result of oxidation of the PbSO₄ formed in the plate interior, also contributes to skeleton formation. During battery charge, the skeleton structures of PAM and NAM have been built already, and formation of the energetic structures of PAM and NAM starts over the skeletons. These latter processes proceed in strongly acidic medium.

Third, during the second stage of formation of the negative plates, PbSO₄ is reduced to Pb crystals, which differ in morphology from the Pb phase obtained during the first stage. At the positive plates, PbSO₄ is oxidized to β -PbO₂. These reactions proceed in acidic medium at both types of plates during formation and only these processes are analogous to the ones that proceed during battery charge.

On grounds of the above considerations, it can be concluded that the current and voltage algorithms employed for battery charging should not be used for the formation process.

12.4.2. Formation Algorithms

Ritchie claims that formation of lead—acid batteries could reach close to the theoretical electric charge, 241 Ah kg⁻¹ PbO, if conducted with weak current for a period of at least two weeks. However, battery manufacturers cannot afford such a long formation time. The general strive is to complete the formation process within 15–30 h, and even less. This is associated with 1.7–2.5-fold increase in electricity consumed per 1 kg of dry paste. New formation current and voltage algorithms are aimed to reduce substantially the above energy consumption.

The rates of the electrochemical reactions that proceed at the two types of plates depend on current density. Increase of formation current is associated with increase of the heat effects of the reactions and of the Joule heat released. This causes the temperature in the battery to rise. And battery temperature is one of the technological parameters that should be kept within definite limits to ensure high battery performance characteristics. So the basic dependencies that have to be monitored and controlled during the formation process are current, battery voltage and temperature as a function of formation time.

In tank formation, the tank full of electrolyte has great heat capacity, so substantial amount of heat has to be generated for the temperature in the tank to rise (Fig. 12.1). This is not the case with container formation, however. There is a small volume of electrolyte in the battery and hence the latter's heat capacity is small. The heat capacity of a system is the measure of the heat energy required to increase the temperature of the system by 1 °C. The heat capacity of 1 g of mass is called specific heat. The electrolyte has the highest specific heat as compared to the specific heats of the other battery components. During soaking, the temperature in the battery increases rapidly

to fairly high values (Fig. 12.1). It is necessary to cool the battery down to below $50\text{ }^{\circ}\text{C}$ before switching the formation current on. This requires quite a long time of open circuit rest, which may lead to excessive plate sulfation. To accelerate the heat exchange of the battery with the surroundings and thus shorten the soaking time, the batteries are immersed in cold water bath. Thus, the heat exchange is facilitated and the water bath has great heat capacity, i.e. it can absorb substantial amount of heat before its temperature rises. In this way, the open circuit rest period before switching on the formation current can be shortened. This requires continuous monitoring of the temperature in the water bath during the formation process.

The basic principles in designing the formation algorithms should include the following:

- Electrolyte temperature in the battery or in the formation tank should be kept within the range from 30 to $50\text{ }^{\circ}\text{C}$.
- Cell voltage increase should be limited to a definite upper limit so as to avoid excessive gassing in the battery.
- Formation current profile should account for the specific processes that occur in the battery during the different formation stages, depending on electrolyte temperature and rate of gas evolution.
- Negative plates are formed more quickly than positives. So the progress of the formation process should be monitored and controlled by the state of the positive plates.

12.4.3. Constant-Current Formation Algorithms

This is the simplest formation program, i.e. a constant current is applied throughout the formation process, irrespective of electrolyte temperature and battery voltage. Figure 12.7 shows the changes in battery voltage, temperature and gassing rate during formation of a 12 V/20 Ah VRLA battery [5]. Formation is conducted with constant current of 2.2 A for 36 h ,

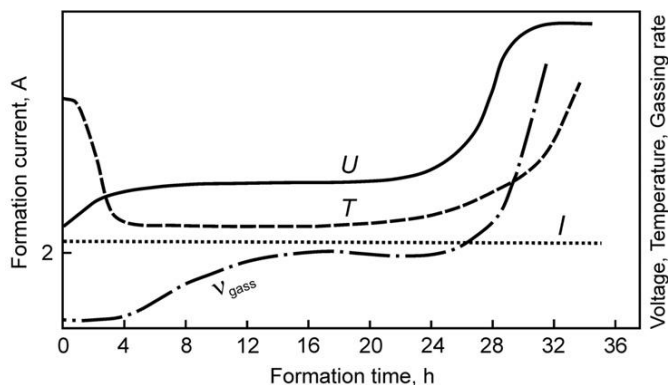


Figure 12.7:

Changes in voltage, temperature and gassing rate during formation of a 12 V/20 Ah battery with a constant current of 2.2 A [5].

i.e. 80 Ah of electricity is charged (twice the theoretical capacity). During the first 24 h, the electricity flowing through the battery is equal to 1.2 times its theoretical capacity. A rapid increase in battery voltage starts thereafter and a fast rise in temperature and in gassing rate is also observed. This results in intense evolution of oxygen at the positive plates and hydrogen at the negative ones. The evolved gases push the electrolyte out of the pores in PAM and NAM, and the contact surface of the two active materials with the electrolyte is reduced leading to an increase in ohmic resistance. Polarization of the battery increases and so does the gas evolution. The efficiency of formation declines. Moreover, the evolved gases absorb H_2SO_4 fumes and dissipate them to the atmosphere thus creating human health and environmental hazards.

During the first 6 h of formation, when PbO and basic lead sulfates are involved in the reactions at the two types of plates, the gassing rate is low and the efficiency of formation is high. Within this period, the cell (battery) voltage increases slowly and the temperature reaches a definite value which remains constant thereafter. If the battery electrolyte temperature is below 50°C after the corrosion layer has been formed, the current may be increased and kept constant at a level that does not allow the temperature to exceed 50°C .

12.4.4. Mutli-Step Formation Current Algorithms

Chen et al. [7] propose an algorithm for tank formation of batteries including many steps of current increase and decrease. This algorithm (presented in Fig. 12.8) is assessed as optimum, in terms of energy consumption and battery performance, but the formation process is rather too long.

Various techniques have been developed for temperature control of the formation process [8,9]. Batteries are immersed in cold water baths and the temperature of both battery electrolyte and water (coolant) in the bath is monitored. The applied formation current is changed

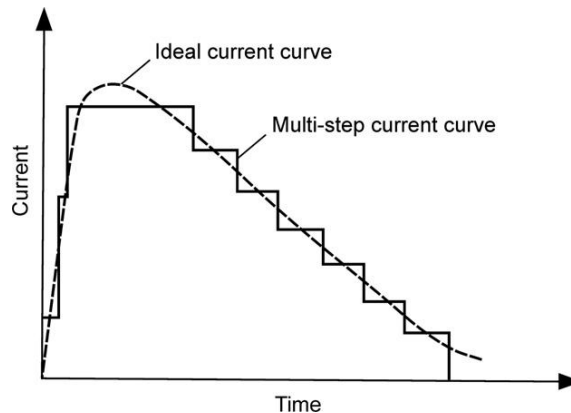


Figure 12.8:
Multi-step current profile for tank formation [7].

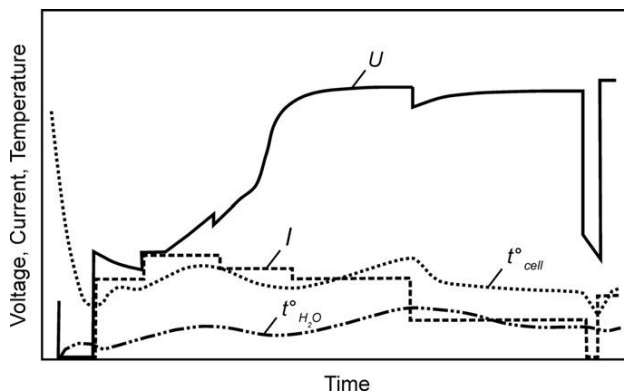


Figure 12.9:

Changes in current, battery voltage, battery temperature and coolant temperature during battery formation. The cooling water in the bath is not flowing [5].

depending on battery voltage and temperature. Figure 12.9 shows a formation current algorithm with programmed multi-step changes in current. The changes in battery voltage and temperature, as well as in coolant temperature, are also given in the figure [5]. The overall duration of the formation process is 50 h. The current is switched on for start of formation when the battery temperature falls down below the specified upper temperature limit. As battery voltage is not controlled, it may reach very high values and set off intense gassing, which would reduce notably the efficiency of formation.

There are techniques employing automatic control of the formation current, depending on battery temperature and voltage. A formation algorithm based on such a technique is presented in Fig. 12.10 [8]. Battery voltage and temperature are monitored continuously. When the voltage

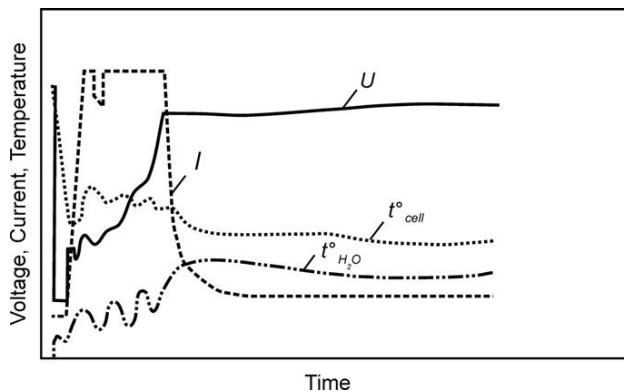


Figure 12.10:

Changes in formation current, battery voltage, battery temperature and flowing coolant temperature during formation [5].

reaches the specified upper technological limit, the formation current is automatically switched to lower value. A sensor measures the temperature in the battery. When the temperature reading reaches the specified upper temperature limit, the formation current is reduced again. As a rule, the working temperature and voltage limit values are kept lower than the specified technological limits for the formation process. The electrolyte temperature is not uniform throughout the battery. In order to prevent temperature rise above the technological upper limit in some parts of the battery, the formation current is reduced before this technological limit is reached.

12.4.5. Formation of the Active Mass Connecting Layer (AMCL)

If we draw an analogy between the structure of battery plates and the structure of a tree with a large crown, the plate grid would play the role of the tree trunk. The trunk splits into several thick branches, which develop further into a system of thinner branches from which the leaves and buds grow. In the case of a battery plate, the AMCL plays the role of the thick branches from which the tree crown grows. That is why the skeleton of the AMCL should be built of thick branches so as to have low ohmic resistance. Otherwise, the AMCL of the plates will get strongly polarized when the high formation current is switched on.

For the formation of a great number of thick skeleton branches in the AMCL, the rate of the electrochemical reactions that yield Pb or PbO₂ should be high, i.e. after formation of the corrosion layer is completed, the current should be increased. Such an algorithm for formation of 12 V/60 Ah batteries is proposed by Ruevski [6] and is presented in Fig. 12.11.

In this algorithm, the formation current is increased gradually in four steps to allow formation of the corrosion layer, and then the process is conducted further with a current $I = 0.3 C_{20}$

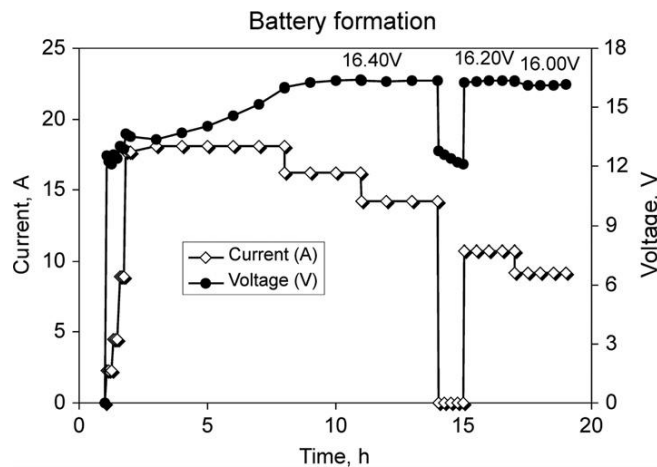


Figure 12.11:

Changes in current and battery voltage during formation of a 12 V/60 Ah battery [6].

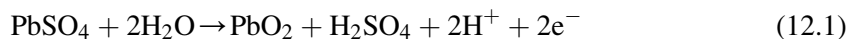
A for the cured paste to be formed, which takes 7 h. During this latter period, the AMCL and the skeleton structures of PAM and NAM are formed. At the beginning of this period, the current density is high and hence the rate of nucleation and growth of the Pb and PbO₂ phases will be high, too. As a result of this process, thick branches will be formed in the AMCL. With increase of the (Pb + PbSO₄) and (PbO₂ + PbSO₄) zones formed in the negative and positive plates, the conductive surface on which the electrochemical reactions proceed grows in area and hence the current density decreases. However, during the initial period of AMCL formation, the current density has been high and a great number of Pb and PbO₂ nuclei have formed, which then grow rapidly at the expense of the PbO and BS phases in the cured paste.

When the battery voltage reaches 16.4 V, the formation current is reduced by 10%. The electric charge until this point of the formation process is almost equal to the theoretical capacity of the battery. The battery electrolyte temperature is kept at about 45 °C. In order to maintain the above battery voltage, another current reduction step of 12% is done, followed by 1 h rest period. The total quantity of electricity charged into the battery before the rest period is equal to 1.8 times the theoretical capacity. Two more steps of current reduction follow after the rest period, during which the battery voltage is kept below 16.0 V, and the electric charge for the whole formation period is 2.15 times the theoretical capacity of the battery. The overall time of formation is 19 h.

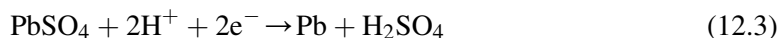
12.4.6. Rest and Discharge Periods in the Formation Algorithms

After a few hours of polarization, the PbO and basic lead sulfates in the cured paste are used up and the second stage of formation commences. When the formation process is conducted galvanostatically, the potentials of the two types of plates begin to increase and other electrochemical reactions have to proceed to keep the current constant. These reactions involve PbSO₄ and H₂O.

At the positive plates:



At the negative plates:



The data in Fig. 12.7 evidence that the beginning of the second stage of formation is marked by an increase in battery voltage and intense gassing. Reactions of water decomposition proceed, parallel to the reactions of Pb and PbO₂ formation from PbSO₄, for a considerable period of time. During this period, H₂SO₄ is produced in the plate pores, which then diffuses to the bulk electrolyte thus increasing its concentration. Water enters the pores of the positive plates to compensate for the water consumed by the electrochemical reaction (12.2). Bubbles of

hydrogen and oxygen leave the pores of both negative and positive plates. This process continues until a quantity of electricity equal to the theoretical capacity of the battery is charged. Actually, the battery is formed only about 70%, because part of the electric current is consumed for water decomposition during this period.

With increase of the H_2SO_4 concentration in the plate pores, the solubility of PbSO_4 decreases, which impedes the electrochemical reactions. This can be clearly seen in Fig. 12.7 after 24 h of formation. The evolved gases (H_2 and O_2) change the overall dynamics of the movement of H_2O , H_2SO_4 and H^+ ions through the plate pores. First, H_2 and O_2 gases fill a significant part of the pore volume in the plate core. Consequently, the pore cross-section through which the flows of H_2SO_4 and H_2O pass is reduced and so is the surface on which the electrochemical reactions proceed. The rates of the reactions of Pb and PbO_2 formation are slowed down substantially.

Besides, water decomposition proceeds at the highest rate in the surface plate layers, where the access of H_2O and H^+ ions is most intense. This keeps up the gas pressure in the interior of the plate. In order to accelerate the reactions of formation of Pb and PbO_2 , the gases filling the pores in the plate volume should be evacuated. This can be achieved by two methods:

1. *Evacuation of gases from the plates by opening the electric circuit* (Fig. 12.12). This allows electrolyte that enters the plate pores to push the gases out. This is a slow process and takes about 1–2 h. To reduce the rate of water decomposition, after the OC rest period, further formation should be conducted with weaker currents (Fig. 12.11), keeping the battery voltage below 16.0 V at that. If gassing is still intense, the rest period should be repeated one or two more times.

Figure 12.13 shows the changes in formation current, battery voltage and quantity of electricity during formation of a 40 Ah battery with a 2 h rest period during the second stage of formation

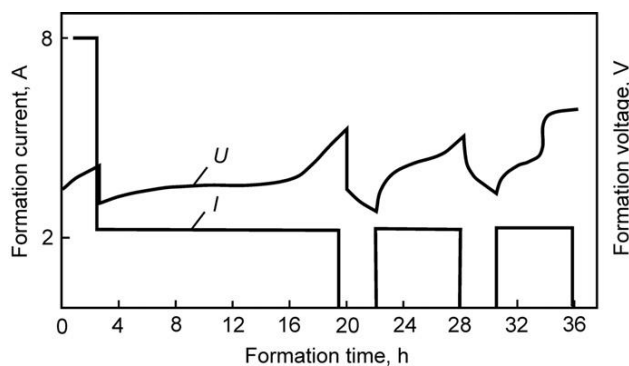


Figure 12.12:

Current and voltage formation algorithms including two open-circuit rest periods.

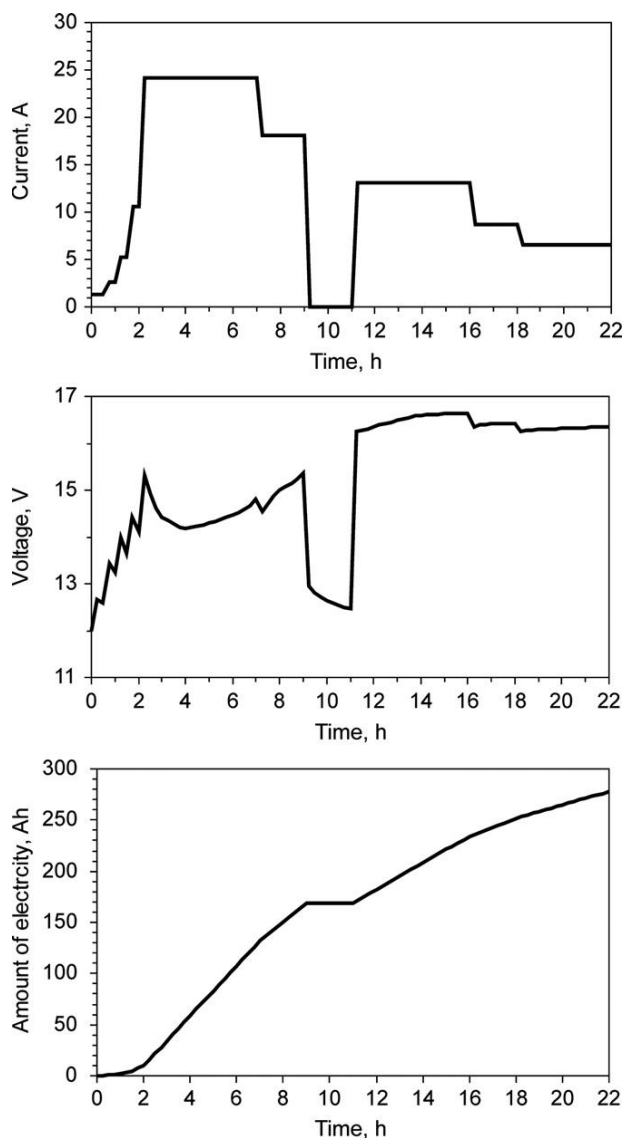


Figure 12.13:

Changes in current, voltage and quantity of electricity during formation of a lead—acid battery [10].

[10]. When the battery voltage exceeds 16.0 V after the rest period, the formation current is reduced so that the maximum battery voltage is kept below 16.0 V.

The rest periods have a second function, too, to reduce battery temperature. During the OC rest periods, no heat is generated in the battery and the heat exchange between battery and water in the cooling bath is intense leading to decrease in battery temperature.

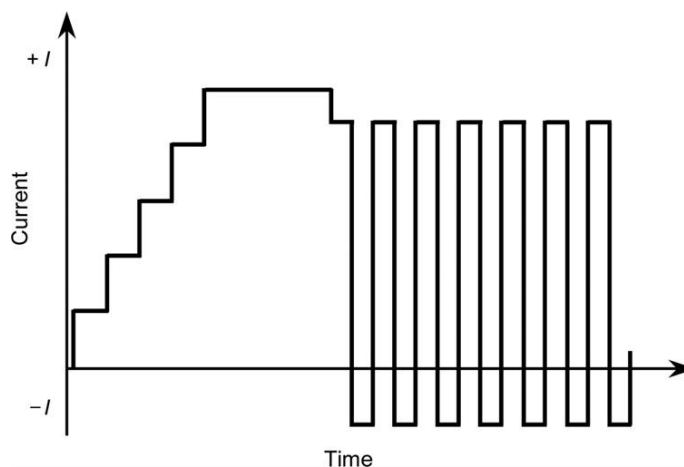


Figure 12.14:

Formation current algorithm including discharge pulses for gas evacuation during the second stage of formation.

2. *Evacuation of gases from the plates through discharge pulses.* In this method, the hydrogen evolved at the negative plates is oxidized to H^+ ions, and the oxygen at the positive plates is reduced to H_2O . Thus the pores are evacuated to allow electrolyte to fill them. Figure 12.14 presents a formation current algorithm with discharge pulses for gas evacuation.

The duration of the discharge pulses, and the discharge current to be employed, depend on formation current and plate thickness. The discharge pulses lead to slight discharge of the battery, too.

When positive plates are produced with 4BS cured pastes, at the end of the formation process the battery is set to one discharge followed by a recharge. The aim of this discharge is to uncover the non-formed parts of the 4BS crystal volume, which will then be formed during the subsequent recharge, thus allowing formation of a greater volume of the 4BS crystal. This preliminary discharge cycle increases significantly the initial capacity of the battery.

12.5. Influence of PbO_2 Crystal Modifications on the Capacity of Positive Plates. Formation Parameters that Affect the α/β - PbO_2 Proportion

12.5.1. Electrochemical Activity of α - PbO_2 and β - PbO_2

Dodson [11] has determined the capacity of positive active materials (435 g) containing β - PbO_2 or α - PbO_2 alone as a function of discharge current. The results obtained are presented graphically in Fig. 12.15.

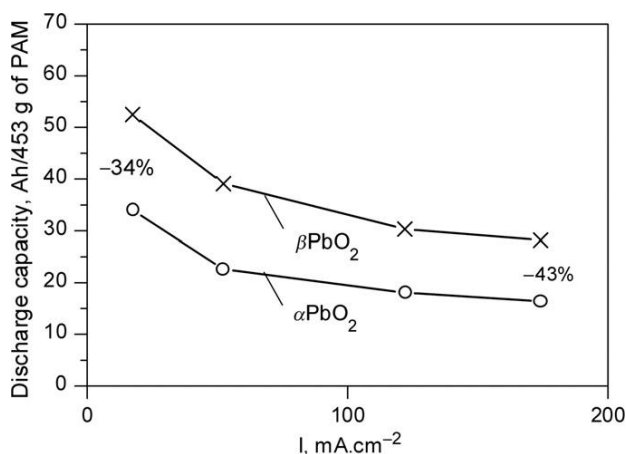


Figure 12.15:

Capacity of positive plates with α -PbO₂ or β -PbO₂ active materials as a function of discharge current density [11].

At weak discharge currents, α -PbO₂ delivers 34% less electricity than the β -PbO₂ modification. This difference is 43% in favour of the β -PbO₂ modification if strong discharge currents are applied. These results indicate that, when a mixture of the two crystallographic forms is present in the active mass, the major amount of electricity is delivered by the electrochemical reactions that proceed on β -PbO₂ with a small contribution by the reactions on the α -PbO₂ crystal form. Hence, the α -PbO₂ modification plays the role of a skeleton that conducts the current throughout the plate volume and provides mechanical support to the active material. This difference in electrochemical activity of the two PbO₂ species is one of the factors responsible for the long cycle life of the lead–acid cell.

12.5.2. Influence of Formation Parameters on its Efficiency and on the α - to β -PbO₂ Ratio in PAM

Ikari et al. [12–14] and Dodson [15] have investigated the influence of formation parameters on the efficiency of the formation process (% PbO₂ formed) and on the proportion between the α - and β -PbO₂ modifications formed in the active material.

We will discuss some of the obtained results below.

(a) Influence of paste density on formation efficiency

Figure 12.16 shows the content of PbO₂ (in %) in PAM obtained on formation of positive plates at a current density of 7.2 mA cm⁻² in H₂SO₄ solution of 1.135 rel. den. at 60 °C, as a function of initial paste density [15].

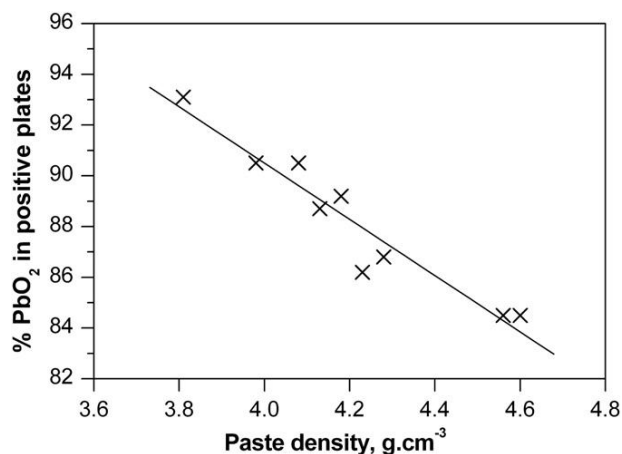


Figure 12.16:

Formation efficiency (% PbO₂ in PAM) as a function of initial paste density [15].

With increase of paste density the efficiency of PAM formation decreases linearly. The processes of formation depend on the pore system and the mean pore radius as well as on the thickness of the branches in the cured paste. While the former two factors are responsible for the dynamics of the movement of ion flows and H₂O in the plate interior, the third feature determines what part of the paste branches would be accessible by the H₂O and H⁺ ion flows for the reactions of oxidation to proceed.

Wet chemical analysis of the composition of PAM has evidenced that the content of PbO₂ in the active material is always less than 95%. Lead dioxide has been found to contain a certain amount of low-valency Pb³⁺ and Pb²⁺ ions. This makes the oxide non-stoichiometric, PbO_(2-x). Various values for x have been cited in the literature. Table 12.1 presents some of these values for PAM obtained at different temperatures [16].

Figure 12.17 shows the changes in α -PbO₂ content in PAM obtained from cured pastes of different densities formed at a current density of 7.2 mA cm⁻² in H₂SO₄ solutions of three different relative densities: 1.10, 1.15 and 1.25 [15]. The data in the figure suggest the following conclusions: with increase of paste density the content of α -PbO₂ in PAM increases. The amount of α -PbO₂ in the formed PAM depends also on the concentration of the H₂SO₄

Table 12.1: Stoichiometric coefficients of lead dioxide in PAM [16].

Temperature (°C)	PbO _n
20	PbO _{1.90}
40	PbO _{1.96}
55	PbO _{1.94}
70	PbO _{1.96}

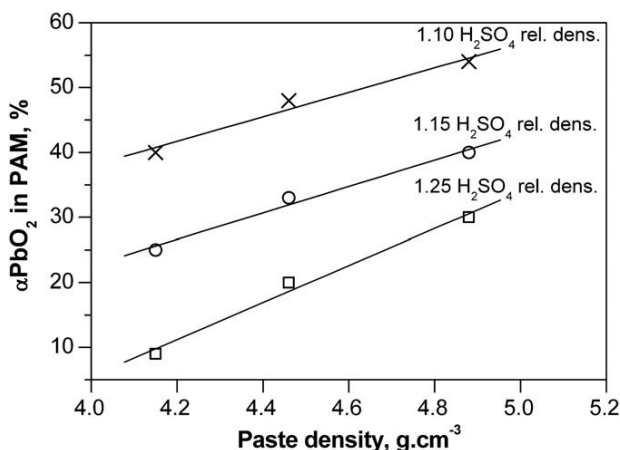


Figure 12.17:

Influence of paste density on the content of α - PbO_2 in PAM formed at $I = 7.2 \text{ mA cm}^{-2}$ in H_2SO_4 solutions of three different relative densities [15].

solution in which the formation process is conducted. With increase of H_2SO_4 concentration the amount of α - PbO_2 formed in PAM decreases.

(b) Influence of formation current density on the α/β - PbO_2 ratio

Figure 12.18 presents the ratio α - to β - PbO_2 in PAM vs. current density on formation of plates produced with pastes of two different densities and formed at 43°C in H_2SO_4 solutions of three relative densities [15].

The figure illustrates the correlations between the three parameters: I , d_{paste} and $C_{\text{H}_2\text{SO}_4}$. At $d = 4.70 \text{ g cm}^{-3}$, the ratio α/β - PbO_2 is between 1 and 2, i.e. the α - PbO_2 modification predominates. With increase of the current density of formation, more H^+ ions are generated and their concentration in the paste pores increases, the pH of the solution in the pores decreases and formation of β - PbO_2 starts instead of α - PbO_2 . The proportion α/β - PbO_2 in PAM formed from the same paste ($d = 4.70 \text{ g cm}^{-3}$) decreases when the acid concentration in the electrolyte is increased, for example from 1.15 to 1.25 rel. den. (Fig. 12.18). The current density has a similar effect on the ratio α/β - PbO_2 in PAM as described above. The curve α/β - PbO_2 ratio vs. formation current shifts to lower values of the α/β - PbO_2 ratio when the current density is increased.

Figure 12.18 also provides data about the formation of PAM from a paste with 3.91 g cm^{-3} density. This paste is highly porous thus allowing the H_2SO_4 solution to penetrate deep into the plate interior. The reactions of paste sulfation proceed at a high rate, which results in the formation of large amounts of PbSO_4 , which is then converted into β - PbO_2 . Hence, the ratio α/β - PbO_2 is between 0.03 and 0.05 at 1.25 rel. dens. H_2SO_4 .

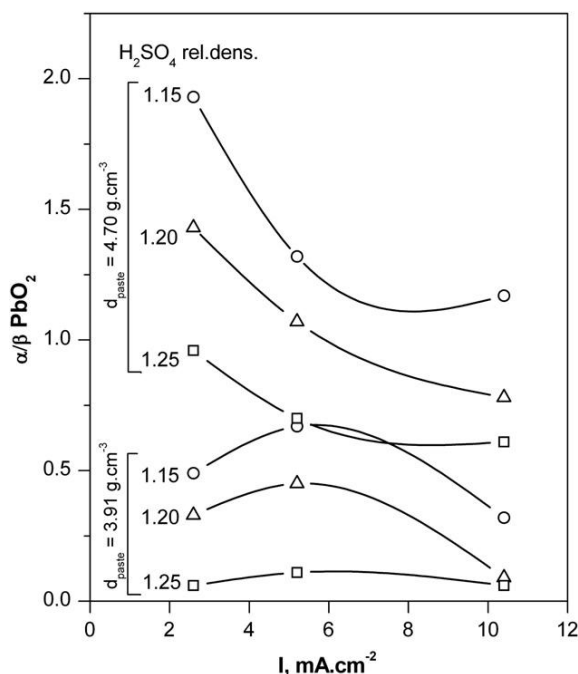
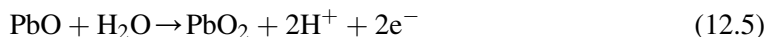


Figure 12.18:

$\alpha/\beta\text{-PbO}_2$ ratio in PAM formed from pastes of two different densities in H_2SO_4 solutions of three relative densities as a function of formation current [15].

How is the proportion between α - and $\beta\text{-PbO}_2$ in PAM influenced by the current density of formation? At low current densities (e.g. $2.5 \text{ mA}\cdot\text{cm}^{-2}$), small amounts of H^+ ions are generated in the paste pores, which do not lead to formation of $\beta\text{-PbO}_2$ from PbO . However, the plate needs more time to be formed. During this prolonged formation time, sulfation of PbO proceeds and large amounts of PbSO_4 will be formed, which will then be oxidized to $\beta\text{-PbO}_2$. By increasing the rate of formation (i.e. at higher I), the time for formation is shortened and less PbSO_4 will be formed. Consequently, the $\alpha/\beta\text{-PbO}_2$ ratio will increase. This increase will continue until generation of H^+ ions in the cured paste pores reaches a level at which PbO is converted to $\beta\text{-PbO}_2$. Figure 12.18 evidences that the critical value of I is about $5 \text{ mA}\cdot\text{cm}^{-2}$. On further increase of current density, the $\alpha/\beta\text{-PbO}_2$ ratio depends on I , i.e. on the amount of generated H^+ ions.

As a rule, formation of α - or $\beta\text{-PbO}_2$ is related to particular precursors, PbSO_4 yields $\beta\text{-PbO}_2$, whereas $\alpha\text{-PbO}_2$ originates from PbO . Formation of α - or $\beta\text{-PbO}_2$ species depends on the concentration of H^+ ions in the solution in which the electrochemical reaction proceeds. So $\beta\text{-PbO}_2$ may form also from PbO by the reaction



if the amount of H^+ ions generated in the pore solution is so high that the threshold pH is reached above which formation of $\beta\text{-PbO}_2$ starts.

It follows from all above said that the ratio $\alpha/\beta\text{-PbO}_2$ in PAM is determined by a complex relationship between formation current density, cured paste density and H_2SO_4 concentration of the formation electrolyte.

(c) Influence of temperature on the efficiency of formation and on the $\alpha/\beta\text{-PbO}_2$ ratio

The efficiency of the formation process (% PbO_2 in PAM) is presented in Fig. 12.19 as a function of temperature for three different paste densities. The formation process is conducted in 1.15 relative density H_2SO_4 solution with $I = 2.6 \text{ mA cm}^{-2}$.

At low temperatures, the efficiency of formation is low and depends very strongly on the cured paste density. With temperature increase the efficiency increases, too, and is less dependent on paste density. The temperature range for the formation process, generally accepted in the battery practise, is between 30 and 50 °C. Some battery manufacturers extend this temperature range to 60 °C. At formation temperatures of between 40 and 50 °C, the efficiency of the process is high and the density of the cured paste has but a small effect.

Figure 12.20 presents the dependences of the $\alpha/\beta\text{-PbO}_2$ ratio in PAM on formation temperature for three paste densities. Formation is conducted at 2.6 mA cm^{-2} in H_2SO_4 solution of 1.15 rel. den.

With increase in temperature the $\alpha/\beta\text{-PbO}_2$ ratio increases, too. This is an indication that the kinetic difficulties during formation of $\alpha\text{-PbO}_2$ crystallites have decreased. Such difficulties may be related to the formation of $\alpha\text{-PbO}_2$ nuclei, the diffusion of H^+ ions and H_2O molecules, etc. The above described effect of temperature seems to be exhausted at higher temperatures (60 °C and above). The higher the paste density the smaller the amount of H_2SO_4 that reaches the plate core to react with the cured paste there and form PbSO_4 . Hence, the ratio $\alpha/\beta\text{-PbO}_2$ increases.

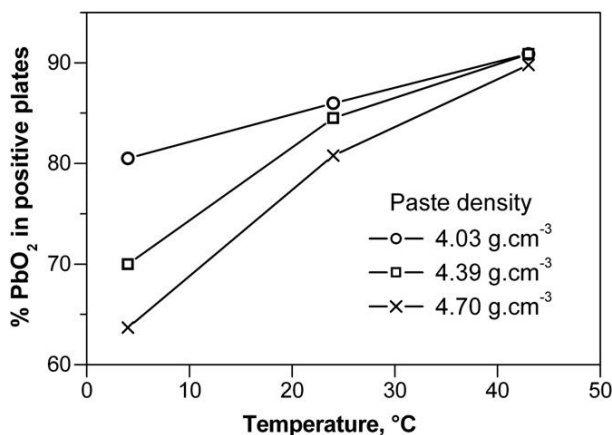


Figure 12.19:
Influence of temperature on formation efficiency [15].

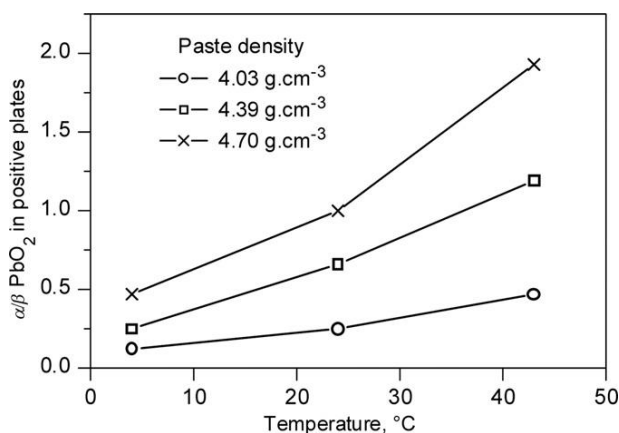


Figure 12.20:

α/β -PbO₂ ratio in PAM formed from pastes of three different densities as a function of formation temperature [15].

12.6. Criteria Indicating End of Formation

The following are the several basic criteria by which we can judge about the end of the formation process:

- the electrolyte concentration does not change over a period of 2 h;
- the rate of gas evolution does not change over a period of 2 h;
- if the negative plate is scratched with a fingernail, a metallic track appears;
- the positive active mass is black to dark brown in colour, hard and not subject to peeling;
- the most reliable criterion is the chemical analysis — the plates are completely formed when PAM contains 88–92% PbO₂ and NAM contains 92–94% Pb; actually, the positive active mass contains non-stoichiometric lead dioxide with the formula PbO_{1.88}–PbO_{1.96}, which implies that part of PAM contains lower-valency lead oxide.

For more comprehensive characterisation of PAM, it is necessary to determine the α/β -PbO₂ ratio and to measure the porosity and pore volume distribution by radius for both active materials. Of course, all these measurements are performed when designing the formation algorithm for each particular battery type.

12.7. Influence of Current-Collector Surface on Formation of PbSO₄ Crystals at Grid/PAM Interface

It has been established that on cycling of tubular positive plates with die-cut strap grids (SGTP) or of positive plates with expanded grids with flat ribs, a rapid capacity loss is observed (the PCL-1 effect) [17]. The reason for this capacity loss is the formation of groups of PbSO₄

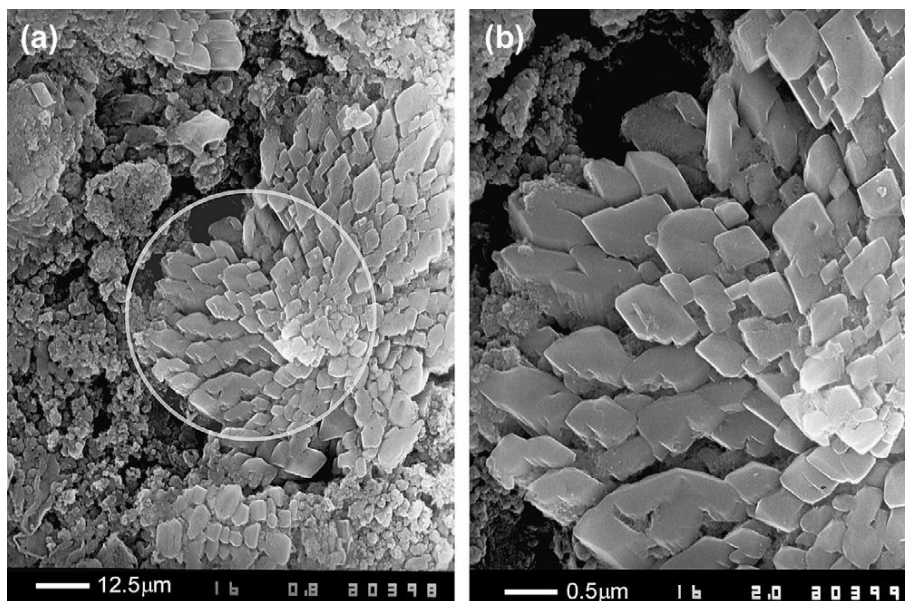


Figure 12.21:

Scanning electron micrograph of: (a) groups of PbSO_4 crystals formed in a layer close to the current-collector with smooth surface; (b) closer view of this PbSO_4 crystal layer [17].

crystals in the layer of the PAM that contacts the current-collector (Fig. 12.21). These PbSO_4 crystals are not oxidized to PbO_2 during charge. Hence, even though the PAM is in good health, the plates have low capacity and power.

What causes this phenomenon? The smooth metal surface encourages the processes of discharge to proceed at a uniform rate in a layer close to the grid/PAM interface, as a result of which large plate-like PbSO_4 crystals are formed in this layer (Fig. 12.21). These crystals ‘eat up’ and interrupt the branches of the PAM skeleton, and consequently their number at the interface (i.e. in the AMCL) decreases, which impairs the contact of the PAM with the current collector. On battery charge, the PbSO_4 crystals are not oxidized to PbO_2 because of the interrupted branches and the impeded transport of H_2SO_4 in the PAM.

A model for the grid/PAM interface of a plate with smooth metal surface is presented in Fig. 12.22a. Through roughening of the metal surface of rolled Pb–Sn–Ca or Pb–Ca grids (or straps), the formation of groups of plate-like PbSO_4 crystals can be prevented. Such roughening can be achieved by various techniques, as follows.

- (a) Through mechanical treatment of the grid or strap current collector.
- (b) Through subjecting the battery to reverse polarization for 30–45 min before formation [17]. As a result of this procedure, lead is deposited irregularly on the smooth metal surface of the positive grids and hence causes roughening of the latter (Fig. 12.22b).

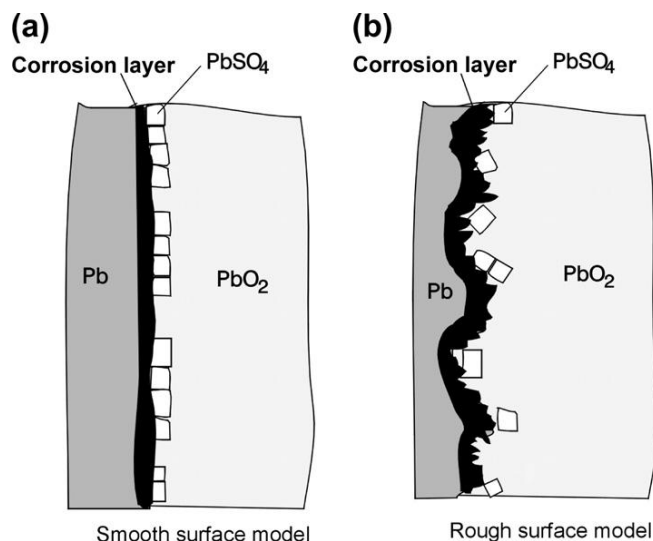


Figure 12.22:

Models for current-collector surface profiles, and PbSO₄ crystals formed on (a) smooth surface and (b) rough surface.

After such pre-treatment, the connections of the battery poles to the power source terminals are reversed and formation proper starts. Test results for batteries that have been formed employing an algorithm that includes reverse polarization prior to formation are given in Fig. 12.23. The capacity curve is similar to that for batteries with cast grids with rough surfaces.

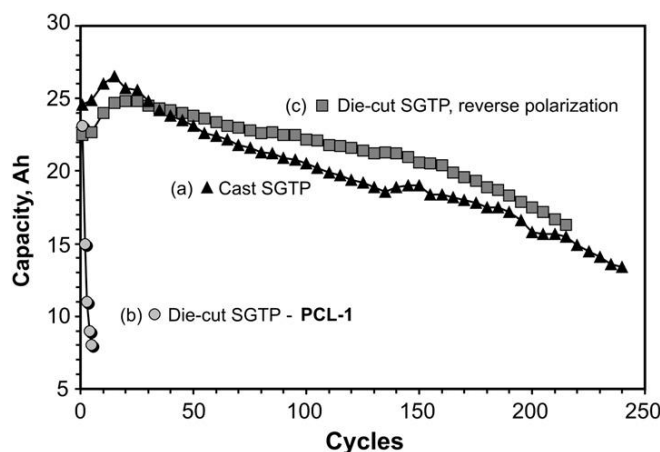


Figure 12.23:

Capacity curves for STrap grid tubular positive plates (SGTP): (a) cast strap grids with smooth surface; (b) die-cut strap grids with smooth surface (PCL-1 effect) and (c) die-cut strap grids with rough surface obtained after reverse-current treatment prior to formation proper [17].

12.8. Method for Shortening the Duration of the Formation Process

12.8.1. Accelerated Formation Through Electrolyte Re-Circulation

This method is used for container formation of high-amperehour cells and batteries for industrial, heavy duty, truck and automotive applications. Several installations of the Italian company OMI-NBE [18] and of the German company Inbatec [19] are currently operative in the battery industry.

Acceleration of the formation process is limited by two main parameters: heat effects and gas evolution. The heat effects during the formation process can be expressed by the equation:

$$Q_{\text{cell}} = Q_{\text{el.r.}} + Q_{\text{ch.r.}} + Q_{\text{Joule}} \quad (12.6)$$

where $Q_{\text{el.r.}}$ represents the heat effects of the electrochemical reactions that proceed at the two types of plates, $Q_{\text{ch.r.}}$ stands for the heat effects of the chemical reactions in the cell, and Q_{Joule} is the Joule heat. $Q_{\text{ch.r.}}$ depends on the content of PbO and basic lead sulfates in the paste, and on the concentration of H_2SO_4 . With increase of current density, the generated Joule heat increases and so does the heat evolved or absorbed by the electrochemical reactions in the cell. The released heat causes the temperature in the cell to rise and it may exceed the technological upper limit of 50°C if the formation current is increased further. And this should be avoided, of course. In order to prevent undesirable and uncontrolled temperature increase, the heat exchange of the cell (battery) with the surroundings should be accelerated. One possible way to achieve this is to remove the heated electrolyte from the cells and replace it with cooled H_2SO_4 solution of the same concentration. Thus, the formation current density may be increased substantially to an upper limit that depends on the rate of electrolyte re-circulation and on cell voltage.

With increase of formation current density the polarization (voltage) of the cell increases, i.e. the potentials of the two types of plates rise. They may reach values higher than the evolution potentials of the $\text{H}^+|\text{H}_2$ and $\text{H}_2\text{O}|\text{O}_2$ electrodes. Consequently, the rates of O_2 and H_2 evolution increase, i.e. greater volumes of gas are evolved per unit time. Adsorbed gas layers form on the surface of the lead and lead dioxide active materials, which increase the ohmic resistance of the cell and its polarization, and hence, the energy consumption for battery formation increases, too. The formed gas phase should be carried out of the cell, which can also be achieved by electrolyte re-circulation.

In order to ensure electrolyte re-circulation with no loss of electrolyte, the system cells- H_2SO_4 tanks-electrolyte circulation facilities should be a closed system. The gas absorbed by the circulation electrolyte is removed from the solution and passes through an exhaust air scrubber to eliminate the acid fumes before it is let out in the atmosphere. In this way, the electrolyte re-circulation system plays a dual role: first, it accelerates the formation process thus shortening the duration of the technological procedure, and secondly, eliminates the hazardous effect of the process on human health and on the environment.

12.8.2. Conceptual Block Scheme of Electrolyte Re-Circulation Process Employed to Accelerate Formation

Concentrated H_2SO_4 solution is supplied in tank trucks and is transferred into storage tanks close to the formation room. The concentrated H_2SO_4 solution (1.84 rel.dens.) has to be diluted before being used for battery formation. Formation of batteries/cells is conducted in diluted electrolyte of e.g. 1.10 rel. den. At the end of the formation process, before the batteries are dispatched for sale, this electrolyte is replaced by a more concentrated H_2SO_4 solution of 1.28 rel. den., which is the electrolyte concentration for normal battery operation.

The number and capacity of acid storage tanks (of 1.10 and 1.28 rel.dens.) in the formation area depend on the number of batteries and cells to be formed. The concentrated H_2SO_4 solution from the storage tanks is diluted to 1.10 or 1.28 rel. den., respectively, using de-mineralized (deionised) water. The process of acid dilution is associated with generation of substantial amounts of heat, which causes the temperature of the two acid solutions to rise. So both solutions pass through an acid cooling system before being poured into the respective formation electrolyte tanks, each solution in a separate tank. Figure 12.24 shows a conceptual block scheme of the installation for electrolyte re-circulation during the formation process. The figure features the storage tanks for the 1.10 rel. dens. H_2SO_4 solution (T_1) and for the acid solution of 1.28 rel. dens. (T_2).

First, the cells (batteries) are filled with H_2SO_4 solution of 1.10 rel. den. For the purpose, valve 2 for Tank 1 is opened, while valves 1, 3 and 4 remain closed. The formation electrolyte

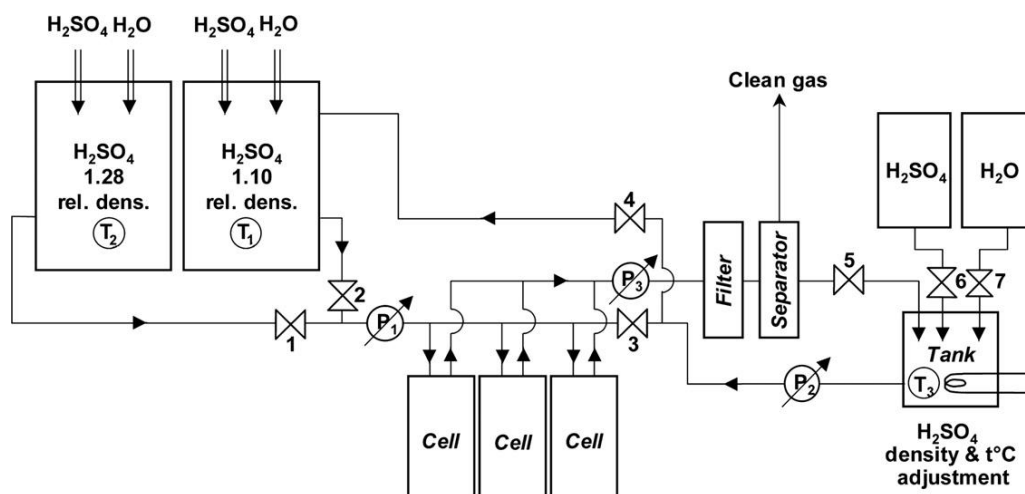


Figure 12.24:

Conceptual block scheme of the installation for electrolyte re-circulation during the battery formation process.

is pumped into the cells set to formation. When all cells (batteries) are filled with electrolyte, valve 2 is closed. Then valves 3 and 5 are opened. The current is switched on and the formation process starts. The electrolyte contained in the cells is pumped out, passes through a filter to remove any paste and/or active mass particles. Then the acid solution passes through a separator (exhaust air scrubber) to remove (under vacuum) the gases (H_2 and O_2) contained in it. The thus purified and gas-free solution is then pumped into another small tank, T_3 , for adjustment (correction) of acid concentration and temperature to the specified technological levels, through addition of H_2O or H_2SO_4 , and cooling or heating as necessary. Valve 3 is opened to ensure free electrolyte circulation within the closed circuit cells-filter-gas-separator-electrolyte adjustment tank-cells. When 85–88% degree of formation of the positive plates is reached, the formation electrolyte is replaced with H_2SO_4 solution of 1.28 rel. den. from tank T_2 . For the purpose, valves 1 (for tank T_2) and 4 (for tank T_1) are opened, and valve 3 is closed. Now replacement of the formation electrolyte (1.10 rel.dens) with the working electrolyte (1.28 rel.dens.) starts. The formation electrolyte is pumped out of the cells which passes through the separator, the gas filter and the acid adjustment tank T_3 , and, instead of being poured into the cells, it is discharged into tank T_1 where H_2SO_4 solution of 1.10 rel. den. is stored. This electrolyte circulation step continues until the electrolyte concentration in the cells reaches 1.28 rel. den. Further formation continues until 90–93% PbO_2 content in PAM is achieved. This is the criterion for completion of the cell formation process. The electrolyte level in the cells is measured and adjusted if necessary. The formed batteries (cells) are replaced by a new batch of non-formed batteries (cells), which are connected to the respective inlet and outlet pipes. The acid concentration in the storage tank T_1 is adjusted to 1.10 rel. den. through addition of H_2O or H_2SO_4 as necessary before formation of the next batch of cells (batteries) starts.

The electrolyte re-circulation system is a fairly complex hydrodynamic facility, including numerous pipes, conduits, valves, pumps, etc. Through the use of such an installation, however, the duration of the technological process of formation can be reduced to 6–10 h, depending on the ampere-hour capacity of the cells (batteries) to be formed. Moreover, the hygienic conditions in the formation room are improved substantially. On the other hand, connecting the cells (batteries) to all these pipes and conduits is done manually and is a very labour consuming process requiring special organisation of the workers charged with the task. So it is reasonable to employ this method for formation of high-capacity cells and batteries, where the classical (conventional) technological procedure of formation is too long. This formation method saves time, but increases the energy consumption for both the hydraulic system and the formation process itself.

The whole operation cycle of this complex hydrotechnical equipment is fully computer-controlled, accounting for the specificity of the processes that occur during the different formation stages, as described in this chapter. Thus, high efficiency of the formation process and adequate quality of the formed cells and batteries is guaranteed.

This method is still in its juvenile age, but it certainly has a future, as it shortens the duration of one of the longest technological processes in the manufacture of lead–acid batteries.

References

- [1] H. Bode, in: R.J. Brodd, K. Kordesch (Eds.), *Lead-acid batteries*, John Wiley, Electrochem. Soc., New York, USA, 1977, p. 251.
- [2] M. Dimitrov, M. Stoycheva, L. Bogdanova, D. Pavlov, ALABC Project no. P-001.4, Final report (2003).
- [3] D. Pavlov, *J. Power Sources* 53 (1995) 9.
- [4] S. Ruevski, G. Papazov, D. Pavlov, Annual report 1998, CLEPS-BAS.
- [5] M.J. Weighall, *J. Power Sources* 116 (2003) 219.
- [6] S. Ruevski, Annual report 1992, CLEPS-BAS.
- [7] H. Chen, Y. Wei, Y. Luo, S.H. Duan, *J. Power Sources* 59 (1996) 59.
- [8] Ch. Ressel, *Batteries Intl.* 3 (1990) 24.
- [9] R. Kiessling, *J. Power Sources* 33 (1991) 275.
- [10] G. Papazov, D. Pavlov, Annual report 2006, IEES-BAS.
- [11] V.H. Dodson, *J. Electrochem. Soc.* 108 (1961) 406.
- [12] S. Ikari, S. Yoshizawa, S. Okada; Japan, *J. Electrochem. Soc.* 27 (1959) E186–189.
- [13] S. Ikari, S. Yoshizawa, S. Okada; Japan, *J. Electrochem. Soc.* 27 (1959) E223–227.
- [14] S. Ikari, S. Yoshizawa, S. Okada; Japan, *J. Electrochem. Soc.* 27 (1959) E247–250.
- [15] V.H. Dodson, *J. Electrochem. Soc.* 108 (1961) 401.
- [16] R.H. Greenburg, F.B. Finan, B. Agruss, *J. Electrochem. Soc.* 98 (1951) 474.
- [17] G. Papazov, D. Pavlov, B. Monahov, Proc. vol. II, 4th ALABC members & contractors Conference, Scottsdale, AZ, USA, April 1999, p. 425.
- [18] www.OMI-NBE.com
- [19] www.inbatec.de

This page intentionally left blank

Battery Storage and VRLA Batteries

This page intentionally left blank

Processes After Formation of the Plates and During Battery Storage

13.1. State of Battery Plates After Formation

Within the period of time between plate formation and the final manufacturing stages, the plates undergo different technological operations. Depending on the particular production technology, these operations may involve removing the plates from the formation tank, washing, treatment in various conditioning solutions, drying, storage of the plates in warehouses, assembling the plates in batteries, etc. All these operations may cause capacity and energy loss as a result of self-discharge and passivation phenomena in the formed plates. The specific impact of these processes on battery energy loss during subsequent storage depends on the state of the battery. Dry-charged batteries suffer the most substantial energy losses during the manufacturing stages after formation, while the wet-charged batteries are less affected. The reverse situation is observed during battery storage.

The formation of a lead–acid battery represents its first charge. This is followed by different conservation procedures aimed at retaining this charge. Lead–acid batteries are produced and offered to the battery dealers in two states: (1) wet-charged, filled with electrolyte and charged, i.e. ready for use, or (2) in a dry-charged state without electrolyte. The manufacturing technology and the production costs for the two types of batteries differ, which ensures different periods of battery storage without significant decline or total loss of their initial discharge characteristics.

- (1) *Wet-charged batteries.* These batteries are manufactured by the simplest production technology, but have the shortest shelf-life (of between 3 and 8 months). Formation of the plates is performed in assembled batteries filled with sulfuric acid solution (container formation). Two main technological processes are employed for this type of formation as follows:
 - *Two-shot formation process.* The plates are formed in cells in a battery filled with H_2SO_4 solution of 1.15–1.10 relative density which serves as the formation electrolyte. After formation, the battery is set to a high current test discharge for 20 s, then it is recharged and the electrolyte is replaced with more concentrated solution of 1.30–1.32 relative density. This highly concentrated solution is diluted by the residual formation electrolyte in the plates and separators, and thus the required final electrolyte concentration of 1.28 relative density is reached.

- *One-shot formation process.* The plates are formed in assembled batteries filled with sulfuric acid solution of 1.23–1.24 relative density. When the basic lead sulfates and PbSO_4 in the paste are transformed into active masses, H_2SO_4 is produced and the formation acid reaches the required concentration for normal battery operation. The thus formed batteries are subjected to a final test by passing a high current for 20 s and monitoring the stability of the discharge voltage at that. The batteries are then recharged for 0.5–1 h. The acid concentration is measured after the formation and adjusted, if necessary. This is the least expensive manufacturing method, but the batteries will have a somewhat shorter cycle life. These batteries should be stored at 20–25 °C. Depending on the grid alloy used, they have a shelf-life of about 2–3 months when with Pb–Sb grids, or 6–8 months when with Pb–Ca–Sn grids, respectively.
- (2) *Dry-charged batteries.* The plates are formed in tanks and after drying under appropriate conditions, they are assembled in cells (batteries). Dry-charged batteries are least sensitive towards the storage temperature and have the longest shelf-life (up to 2 years). They are ready for use after filling with electrolyte of 1.26–1.28 relative density and soaking (1–2 h for traction batteries or 20 min for SLI batteries). If stored for a period longer than the specified shelf-life time, the battery should be charged before use.

The lead–acid battery is an unstable system. The main problems related to battery storage are (a) to identify the nature of the processes that occur during storage and (b) to reduce the rate of these processes and thus extend the duration of the safe shelf-life.

The storage time of lead–acid batteries, i.e. the period of time that elapses between manufacturing of the battery and the beginning of its service life, depends on the type of battery, the distance between battery user and manufacturer, the time between manufacturing of the battery and sale of the vehicle, etc. These factors determine the state of battery storage, filled with electrolyte and charged or dry-charged. Battery shelf-life and the optimum storage conditions depend on the specific battery chemistry as well as on the different additives used by the different manufacturers to optimise their performance. It is possible to outline some general recommendations about storage, but it is best to consult the manufacturers' specifications and recommendations.

The next section of this chapter will concentrate mainly on the energy losses observed during the different technological operations involved in the manufacture of dry-charged batteries.

13.2. Dry-Charged Batteries

13.2.1. Processes that Occur in the Positive Plates During Drying. Thermopassivation

Battery manufacturers have encountered a rather strange phenomenon during manufacture of dry-charged batteries, namely the discharge voltage of the battery decreased abruptly with

increase of the drying temperature. Three temperature regions have been identified with regard to positive plate behaviour on discharge [1,2]:

- (1) $25\text{--}80\text{ }^{\circ}\text{C}$ – *low temperature region*. The plates retain their energy, in terms of both mean discharge voltage and discharge time.
- (2) $80\text{--}220\text{ }^{\circ}\text{C}$ – *thermopassivation region*. When these plates are assembled into batteries, the discharge voltage of the cells decreases sharply without affecting the discharge time. This phenomenon has been termed ‘thermopassivation’. Thermopassivated plates retain their capacity, but the energy and power of the battery are reduced [1,2].
- (3) *Above $250\text{ }^{\circ}\text{C}$ – thermal disintegration region*. Depending on the crystal modification of PbO_2 in the formed positive active mass and the thermal treatment conditions during the subsequent drying process, oxygen is evolved from the oxide leading to a reduction of the stoichiometric coefficient. Within this temperature region, dramatic thermopassivation is accompanied by a decrease in capacity.

Thermopassivation is measured by the difference between the discharge potential of thermopassivated and unpassivated positive plates. Thermopassivation is a result of a solid-state reaction between the Pb grid and the PbO_2 corrosion layer at temperatures higher than $80\text{ }^{\circ}\text{C}$, which leads to formation of a layer of non-stoichiometric PbOn ($n < 1.5$) at the grid/PAM interface. This oxide is a semiconductor with high resistance which depends on the value of n . This layer is responsible for the high polarization of the positive plates during discharge and charge.

Figure 13.1 shows discharge curves for positive plates dried at 75° , 110° , 130° or $220\text{ }^{\circ}\text{C}$ [1]. For comparison, the discharge curve of undried plates is also given (marked with $25\text{ }^{\circ}\text{C}$). The discharge time is equal for all plates, i.e. the quantity of electricity delivered by the plates is

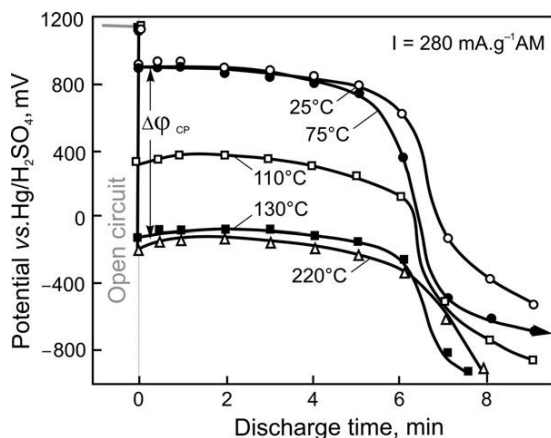


Figure 13.1:

Changes in potential of plates (dried at different temperatures) during discharge with a current density of $280\text{ mA per gram active mass}$ in H_2SO_4 solution of 1.28 relative density [1].

identical. $\Delta\phi_{cp}$ is the thermopassivation (measured at 30 s discharge). The thermopassivation during charge and discharge has different values. Hence, it is considered cathodic ($\Delta\phi_{cp}$) during discharge and anodic ($\Delta\phi_{ap}$) during charge.

The changes in internal resistance of dry-charged cells with plates dried at different temperatures are presented in Fig. 13.2 [3,4]. Curve A shows the resistance vs. drying temperature dependence for cells with thoroughly washed plates, and curve B, for plates after only rinsing off the acid. The data in the figure indicate that the temperature in the drying oven should be limited so that the plate surface temperature would not exceed 80 °C.

It has been established that thermopassivation of the positive plates is a result of changes in composition of the lead oxide corrosion layer [1]. This is a very thin film formed during the formation process and is composed mostly of PbO_2 . When the plates are heated to above 80 °C, Pb of the grid reacts with PbO_2 via a solid-state reaction yielding non-stoichiometric PbO_n . When the stoichiometric coefficient decreases below a critical value ($n < 1.5$), the resistance of the corrosion layer increases significantly, which causes thermopassivation of the plates.

As evident from Fig. 2.21 in Chapter 2 of this book, oxides with stoichiometric coefficients ≤ 1.4 have high ohmic resistance. Thus, a high-resistance interface layer forms between the active mass and the grid, which reduces the energy and power output of the battery during discharge. However, this layer does not affect the total amount of lead dioxide contained in the formed positive active mass. Hence, the discharge time of passivated and unpassivated plates

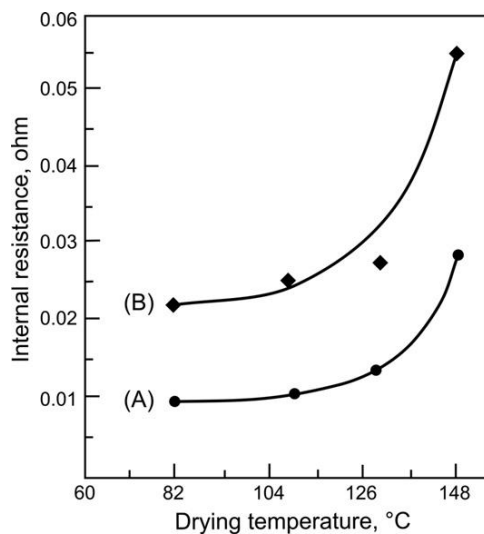


Figure 13.2:

Internal resistance of dry-charged batteries as a function of plate drying temperature. Curve (A): cells with thoroughly washed plates; curve (B): cells with plates after only rinsing off the acid [4].

is the same (Fig. 13.1). Only the internal resistance of the positive plates changes, leading to a decline in discharge potential and thus eventually in energy output.

If thermopassivation is a result of changes in composition of the corrosion layer, then the grid alloy composition will affect the semiconductor properties of the oxides in this layer through the dopants formed as a result of oxidation of the grid alloying additives. The latter's ions will modify the electrical properties of the oxides in the corrosion layer (Table 13.1) [5,6].

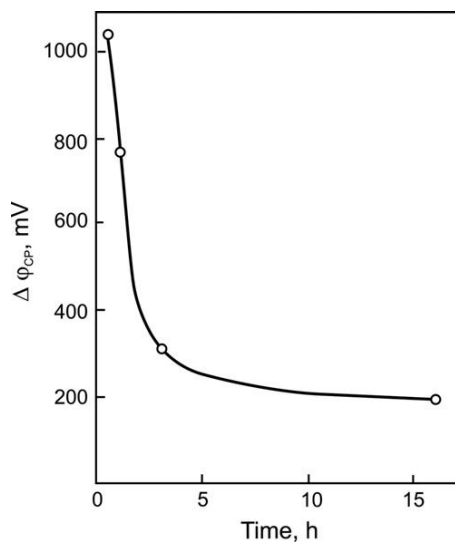
The influence of the reactions between H_2SO_4 and the corrosion layer on thermopassivation has been investigated. Figure 13.3 illustrates the correlation of cathodic thermopassivation and time of stay of the plates in 1.28 relative density H_2SO_4 solution on open circuit [1]. Depassivation processes occur during the time of stay of the plates in the H_2SO_4 solution. A battery with thermopassivated positive plates left for 24 h in 1.28 relative density H_2SO_4 on open circuit restores, though not completely, the energy and power lost during the high-temperature drying process. Probably, as a result of the interaction of H_2SO_4 with the lead oxides in the corrosion layer, the non-stoichiometric oxide is transformed into a higher valency oxide (which is conductive) and a lower valency oxide forming PbSO_4 . The high valency modification of the non-stoichiometric oxide seems to prevail, which leads to increase of the electroconductivity of the corrosion layer and thus the thermopassivation is reduced to some extent.

The thermopassivation effect is completely reversed after charging.

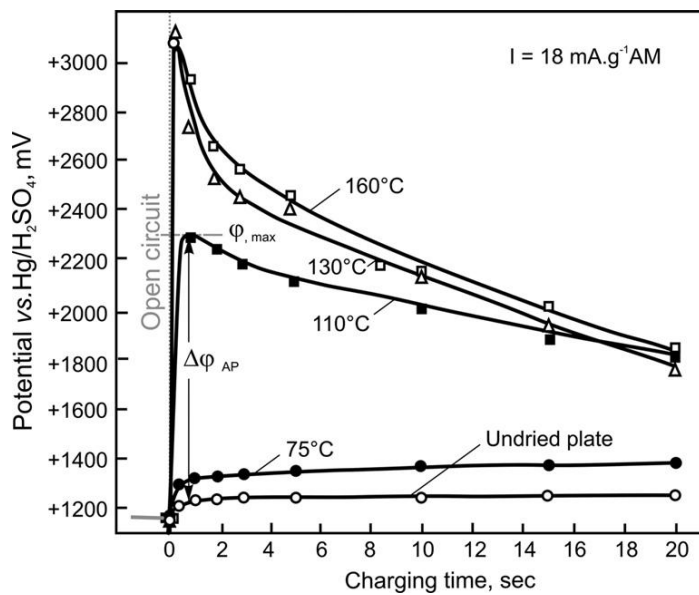
Figure 13.4 shows the potential curves during charge at a current density of 18 mA per gram active mass for thermopassivated and unpassivated plates [1]. The anodic thermopassivation decreases with increase of the quantity of electricity passed. During anodic polarization, oxygen is evolved and penetrates into the corrosion layer, thus oxidizing it. The stoichiometric coefficient of the oxide increases reducing the electrical resistance of the corrosion layer and thus the thermopassivation, too.

Table 13.1: Cathodic thermopassivation data.

Grid Alloy Composition	Plate Drying Temperature ($^{\circ}\text{C}$)	Duration of Drying (min)	Cathodic Thermopassivation (mV)	Reference
Pb	130, 175	60	160, 280	[5,6]
Pb-6%Sb	130	60	1050	[6]
Pb-5%Sb-0.3%As-0.4% Cu-0.01%Ag	130	60	760	[6]
Pb-0.07%Ca-0.3%Sb	130	60	160	[6]
Pb-2.5%Sb	175	60	970	[5]
Pb-5%Sb-0.1%As	175	60	1040	[5]
Pb-2.7%Sb-0.2%As-0.5% Cu-0.2%Sn-0.002%S	175	60	470	[5]

**Figure 13.3:**

Cathodic thermopassivation vs. dwell time of plates in H_2SO_4 solution of 1.28 relative density. Grids cast from Pb–6 wt% Sb alloy [1].

**Figure 13.4:**

Potential-time curves for thermopassivated and unpassivated plates during charging at 18 mA g^{-1} active mass [1].

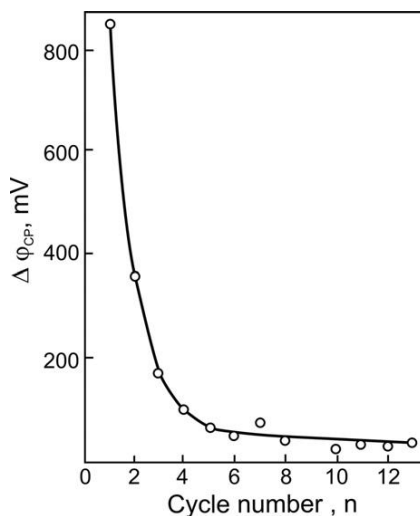


Figure 13.5:

Cathodic thermopassivation vs. number of charge/discharge cycles. Grids cast from Pb–6 wt% Sb alloy [1].

During cycling, thermopassivation decreases continuously and stops altogether after 15–20 cycles (Fig. 13.5) [1]. The oxide corrosion layer obtained during formation is very thin and it is readily reduced during the subsequent drying procedure, thus the plate gets thermopassivated. The corrosion layer grows on charge/discharge cycling. Figure 13.5 shows that the thermopassivation decreases with increase of the corrosion layer thickness on cycling.

Despite its reversibility, thermopassivation reduces significantly the energy output of the battery during the first cycle. Therefore, thermopassivation is carefully avoided by drying the plates in oxygen-containing atmosphere under conditions that do not allow the plate temperature to rise above 80 °C. Usually, low-temperature drying equipment, or tunnel ovens, is used with an adequate temperature and plate flow-rate control.

13.2.2. Methods for Drying Negative Plates After Formation

Here again, only the processes that occur during manufacture of dry-charged batteries will be discussed. The technological stages involved are washing the plates with water to remove the formation electrolyte, followed by drying under conditions completely different from those used for the positive plates. Positive plates should be dried in oxygen atmosphere to avoid energy and capacity loss. In contrast, negative plates are dried by methods that exclude oxygen from the drying atmosphere. Examples of such methods are discussed below.

(a) *Vacuum drying*

The washed negative plates are loaded in a pressure chamber equipped with heaters. The latter cause the temperature of the plates to rise above the boiling point of water. The pressure chamber is equipped with a condenser unit where the water vapours are liquefied and drained out. When the pressure chamber is loaded with plates, a vacuum pump is turned on and, after a definite vacuum level is reached, the heaters are turned on, too. The plates are dried for quite a long time (20–24 h) and when no more water condense forms, heating is stopped and the cooling system is turned on. When the temperature in the chamber reaches room temperature, the vacuum pump is stopped. This method is efficient, but too slow and expensive.

(b) *Drying in an inert gas atmosphere*

There are different variants of this process. One of them uses a tunnel oven with several temperature zones. After formation and washing to remove the sulfuric acid, the plates are arranged, apart from one another, on a conveyor. The latter passes first through a water seal (which closes the zone with the inert gas) and then moves on to the first hot zone with inert gas (nitrogen, carbon dioxide or argon) heated to 160°–180 °C. It is in this zone that the major part of the water evaporates from the plates. The plate temperature should not exceed 70°–80 °C to prevent expander disintegration. If the temperature in the oven rises to higher values, the time of stay of the plates in this temperature zone should be shorter. Then the plates move on to the second zone (compartment) with lower temperature, where the remaining moisture is evaporated and to the last two zones where they are cooled to room temperature. To remove the water from the inert gas, the latter is passed through a condenser system to condense the vapours to water. The third and fourth zones of the tunnel dryer are equipped with a cooling system, which cools the plates to temperatures close to room temperature. The oxygen level is monitored throughout the whole closed drying system, it should not exceed 1%.

Another variant of the oxygen-free drying method involves oxygen from the air into a gas combustion process (Tiegel process). In this process, the plates are arranged, at equal distances from one another, in cassettes and the latter are loaded into a chamber equipped with a gas combustion system (burner). Atmospheric oxygen is consumed by the combustion process forming CO₂ and other exhaust gases. These gases, together with the nitrogen from the air, are heated to very high temperatures and are blown into the chamber as a stream that circulates round the plates and causes the moisture to evaporate from them. Then, the stream of inert gases is passed through a heat exchanger where the water vapours are liquefied. A sensor monitors the oxygen level in the chamber and controls the combustion process so as to keep this level below 1.0%. This is a relatively fast and efficient drying method.

(c) *Contact drying with superheated steam*

There are two variants of this method: low-pressure drying and high-pressure drying. This method is employed mostly in small battery plants or workshops. The superheated steam

drying system consists of a fixed and a moveable (hinged) platen between which piles of several plates are placed. The platens are preheated to a very high temperature and are pressed against the plates. Consequently, the water contained in the plates evaporates and surrounds them with water vapour which isolates them from contact with the air during the drying process. When no more water vapour evaporates from the plates, heating continues for 2–3 min more so that the plates are fully dried. The drying units are mounted on a carousel which rotates with a pre-set speed. The contact drying process is fairly labour consuming. Moreover, to prevent wetting of plates after drying, some moisture inhibitors (anti-wetting agents) are introduced in the paste, which covers the surface of the dried plates and thus prevent them to re-absorb water again after the drying process. The moisture inhibitors should be carefully selected to avoid any health hazards. This drying method has but a limited application.

(d) *Drying of negative plates treated with inhibitors of lead oxidation (anti-oxidants)*

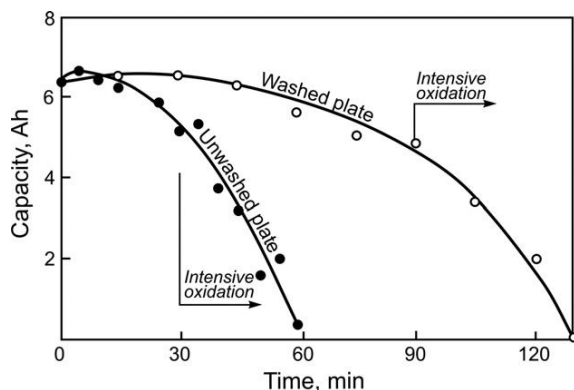
The formed plates are washed with water to remove the H_2SO_4 and are then immersed in a solution containing a suitable oxidation inhibitor for about an hour. Then the plates are dried at a high temperature. Thanks to the technological simplicity and the favourable cost parameters of this drying method, it has found fairly wide application in the battery industry. The main process parameters that need to be monitored and controlled are the drying temperature (between 60 and 180 °C), the hot air flow rate (from 2 to 6 ms^{-1}) and the duration of drying.

An analysis of the PbO distribution across the plate cross-section shows that the oxidation process proceeds mostly in the surface layers when alpha-oxynaphthoic acid is used as oxidation inhibitor and the hot air flow rate is high ($> 2 \text{ ms}^{-1}$). At drying temperatures above 130 °C, the organic additives to the negative plate (expander and inhibitor) disintegrate. Hence, the duration of high-temperature drying of the negative plates should be determined by the temperature of the hot air flow and should be shorter when higher temperatures are employed [11].

13.2.3. Processes That Occur in the Negative Plates Between the Technological Procedures of Plate Formation and Drying

Certain processes occur during the period of time that elapses after the formed plates are taken out of the formation tank and before they are immersed in the water tank for washing, as well as during the interval between plate washing and the subsequent drying in the oxygen-free unit. During the former period, the pores of the active mass are filled with diluted H_2SO_4 solution, while during the latter period, they are flooded with water. Hence, two different patterns of sponge lead oxidation proceed. In both cases, however, the processes are exothermic and the temperature of the plates increases.

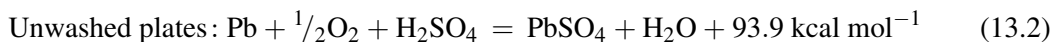
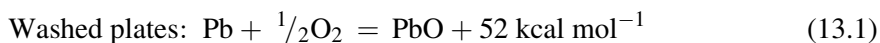
Iliev *et al.* [7,8] have investigated the interaction of the formed plates with air before and after they are washed with water to remove the H_2SO_4 . For the purpose, washed and unwashed

**Figure 13.6:**

Discharge capacity vs. exposure time for washed and unwashed SLI plates in air atmosphere at 25 °C [7].

SLI plates were kept in contact with air for different periods of time. The obtained kinetic curves of oxidation of the plates by the air are presented in Fig. 13.6. After reaching a definite critical temperature and moisture content, a vigorous oxidation or ‘burning’ of the plates commences. This phenomenon is quite similar to the processes observed during curing of the pasted plates. At the end of this period of rapid oxidation, the active mass contains 50–60% sponge lead and up to 40–50% lead oxide and lead sulfate. This composition of the negative active mass yields only a very low capacity, and often none at all.

The latent period after which a rapid oxidation of the active mass starts is about 30 min exposure to air for unwashed plates, and 90 min for the rinsed ones, respectively. This difference can be explained by the different thermal effects of the respective chemical reactions that proceed in the plates:



The more intense heat generation of reaction (13.2) causes the temperature and moisture in the plates to reach more quickly the critical values at which vigorous oxidation starts.

The sponge lead in the formed plates is oxidized also when the plates are washed with running water by the oxygen dissolved in it. Hence, many battery manufacturers restrict the washing time to maximum 1.5 h. Plates can remain in slightly acidic medium, or water, for several days with only a slight decrease in charge retention. The heaviest capacity losses may occur during the subsequent drying process. At high drying temperatures (up to 150 °C), lead will react even with trace amounts of oxygen in the drying oven. An intense oxidation also takes place if damp plates are removed from the drying equipment at temperatures higher than 35 °C.

13.2.4. Inhibitors of Lead Oxidation

In order to reduce the rate of lead oxidation, routine manufacturing practises recommend the use of oxidation inhibitors. These are added to retard the oxidation of lead during the technological procedure of plate drying as well as during battery storage and operation.

Inhibitors are introduced into the negative active material by two methods: (1) as additives to the paste during its preparation; in this case they slow down the oxidation of lead in the negative paste during curing, but has a weak effect on the subsequent technological processes; or (2) after formation of the plates they are washed with water to rinse off the sulfuric acid and are then immersed in an inhibitor containing solution for a definite period of time (about an hour), and only after that are set to drying. Table 13.2 summarises some of the commonly used lead oxidation inhibitors.

An example of inhibitor treatment of negative plates to prevent oxidation of the sponge lead in the active mass after formation is as follows: the washed plates are immersed in a 10–12 wt% solution of boric acid with addition of 1.0–1.5 wt% salicylic acid. The plates are left in this solution for about an hour and are then dried in a drying oven at a temperature of about 130 °C.

An example of the introduction of inhibitor into the paste is to add 0.2 wt% (vs. the leady oxide) meta-aminophenol and then continue with the routine technological procedures.

Inhibitor addition must be carefully controlled since overdosing may cause plate passivation, poor charge acceptance and increased polarization. If the amount of inhibitor is insufficient, it will have practically no effect on the rate of lead oxidation by atmospheric oxygen.

Inhibitors are adsorbed onto the lead surface isolating it from contact with atmospheric oxygen. So, they act as a higher potential barrier for the reaction between lead and oxygen,

Table 13.2: Lead oxidation inhibitors (anti-oxidants) for dry-charged plates.

Inhibitors added to paste	Inhibitors in solutions for soaking charged plates before drying
Stearic acid (0.8 wt%) [4]	Boric acid
Alpha-oxynaphthoic acid 91/0 wt%) [4]	Combination of boric acid and phenol [4]
Polymerised resins containing 10–80 wt% abietic acid (0.2 wt%) [4]	Combination of boric acid and salicylic acid [7]
Non-additive motor oils, e.g. 30 W grade (1 litre per tonne) [4]	Resorcinol and pyrogallol [4,11]
Lanolinic acid [9]	Cresol, sorbitol
Colophonium [9]	Anisaldehyde [12]
Meta aminophenol (3-aminophenol) [10]	Salicylaldehyde [12]

and thus reduce substantially the rate of this reaction. However, the organic component of the expander, too, is adsorbed onto the lead surface and it will affect the influence of the oxidation inhibitor and vice versa. Hence, the type and amount of inhibitor to be used should be selected taking into account also the type and amount of expander in the negative active material. The two additives should be selected in such a way as to mutually enhance each other's influence rather than impede it. Only then would both additives exhibit fully their beneficial effect(s) on the structure and performance of the lead active mass.

Inhibitors exert long-term effects: they not only suppress the oxidation of the plates during drying, but also protect the dry plates until they are assembled into batteries. If a dry-charged battery is not adequately sealed, inhibited plates will have better resistance to lead oxidation during storage. Batteries containing inhibitors are 2–5 times less affected by self-discharge both during storage and for some time during their service life. The use of inhibitors is especially beneficial in countries with warm climate, because it retards the self-discharge processes during battery storage at high temperatures.

13.2.5. Quality Control Monitoring During Manufacture of Dry-charged Batteries

The quality of the plates for dry-charged batteries should be monitored during the production process by measuring definite control parameters at least once a day. Only if the measured parameters meet the respective requirements, can these plates be assembled into batteries. The control parameters subject to inspection include the following:

- (a) Moisture content in the positive and negative plates, and in the separators. The maximum allowable moisture content is 0.2% for the positive plates and below 0.05% for the negative plates and the separators.
- (b) Lead oxide content in the positive and negative plates. The content of PbO in the negative plates can serve as a measure of the efficiency of the inhibitor used.

Besides monitoring the above plate parameters during the manufacturing process, battery activation tests should be performed at least once a week. This test includes the following steps: fill the battery with electrolyte and, after an idle period of 20 min, start it with a current of $I = 3 C_{20}$ A and then measure the time until a voltage of 6.0 V is reached. Using a cadmium or a silver sulfate reference electrode, the potentials of the positive or negative plates are measured to determine which of them are capacity limiting. During this discharge test the battery voltage at the 8th s should not be lower than 9.5 V (for 12 V batteries). This test is indicative of the ability of a battery to start a car 20 min after its activation, i.e. filling with electrolyte, with no preliminary (boost) charge. Such tests are mandatory also for batteries stored for more than 3 months in the manufacturer's or the dealer's storehouse.

13.2.6. Processes During Storage of Dry-charged Batteries

Processes that occur in the positive plates

Iliev and Pavlov [8] have investigated the characteristics of positive and negative plates of dry-charged batteries stored at $25 \pm 5^\circ\text{C}$ for 2 years. The cells were dismantled and the capacity and energy characteristics of the positive and negative plates were determined after assembling them in new cells with fresh counter electrodes. The cells were filled with H_2SO_4 electrolyte of 1.28 relative density, and after 30 min, the discharge characteristics were measured. A high-rate discharge test was carried out aimed to determine the extreme performance characteristics of the plates. Some of the batteries of the test batch were charged and then set to a discharge test in an effort to evaluate the reversibility of the processes during storage. These cells were also subjected to high-rate discharge.

Figure 13.7 presents the obtained discharge transients for the cells assembled with positive dry-charged plates. After storage, the discharge voltage declined dramatically and the discharge time decreased, too. A 5 min refreshing charge with a current $I = 0.1 C_{20}$ A was sufficient to increase the discharge voltage of the positive plates by 0.4 V. During this treatment, the capacity of the plates was not affected. After a 20 h charge, the discharge voltage of the plates was almost completely restored and the capacity improved substantially.

This behaviour of the positive plates indicates that two types of processes occur during storage: (1) passivation processes, which reduce the discharge voltage of the plates, and (2) self-discharge

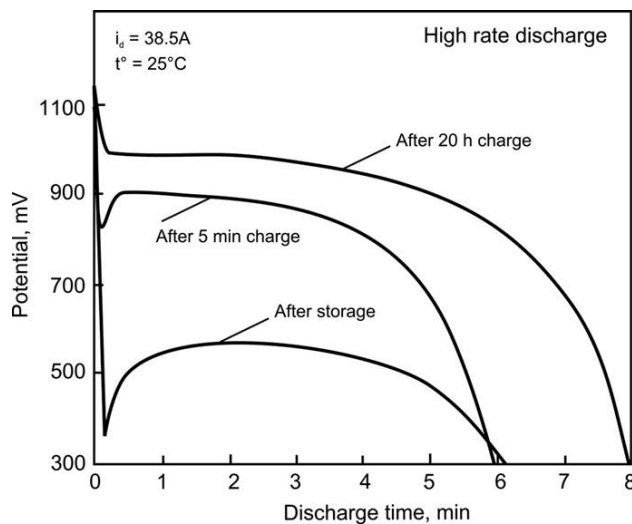


Figure 13.7:

Discharge transients for positive plates of dry-charged batteries after 2 years of storage; discharge current $3.5 C_{20}$ A [8].

processes, which reduce their capacity. The characteristics of the positive plates after storage are very similar to those of thermopassivated plates. During battery storage, some reactions have proceeded between the metallic lead of the grids and the lead dioxide in the corrosion layer as a result of which non-stoichiometric lead oxide(s) PbO_n ($n < 1.5$) have formed. The ohmic resistance of the corrosion layer has increased substantially. The shorter discharge time is due to the reduced PbO_2 content in the positive active mass. This process is related to partial decomposition of the lead dioxide to PbO_n with evolution of oxygen. The reduced number of Pb^{4+} ions in the active material is responsible for the decline in positive plate capacity, which is observed in Fig. 13.7.

When the passivated plates are subjected to charging, a depassivation process starts (Fig. 13.7). This is related to the oxidation of PbO_n in the corrosion layer to a higher valency oxide or to PbO_2 . The latter oxides are highly electroconductive and only a 5 min boost charge is sufficient to increase the cell voltage by 0.4 V. For the capacity of the positive plates to increase, however, some 20 h of charge are needed. During this period of time, the non-stoichiometric PbO_n reacts with H_2SO_4 forming PbO_2 and PbSO_4 . The latter is oxidized during the charge reaction and the positive plates restore most of their capacity (Fig. 13.7).

Processes that occur in the negative plates

Figure 13.8 shows the high-rate discharge transients for negative plates from dry-charged batteries after 2 years of storage [8]. During storage, the processes that occur in the negative plates reduce their capacity, but do not affect the discharge voltage.

New cells are assembled with plates taken out of the batteries after 2-year storage and fresh counter-electrodes. These cells are charged with increasing amounts of electricity (Q_{ch}) in an

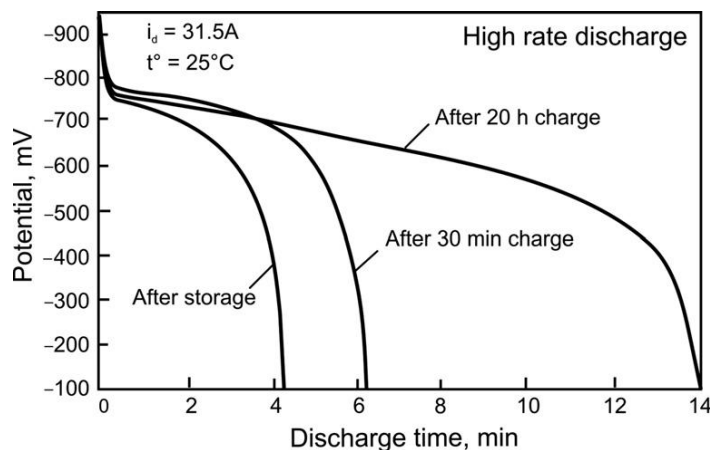


Figure 13.8:

Discharge transients for negative plates of dry-charged batteries after 2 years of storage; discharge current 3.5 C 20 A [8].

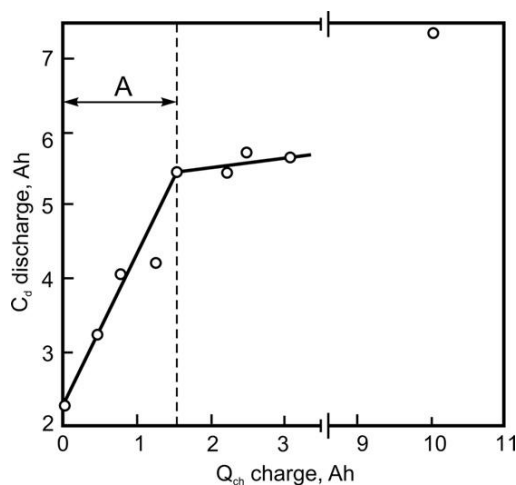


Figure 13.9:

Quantity of electricity charged into the negative plates after 2 years of storage vs. amount of electricity delivered during the subsequent discharge [7].

effort to determine whether the self-discharge processes during storage are accompanied by passivation phenomena, too. The discharge capacity (C_d) of each cell is experimentally determined and the quantity of electricity used for charging the plates (after 2-year storage) is evaluated. Figure 13.9 presents the ratio between the two electric charges [8].

During period 'A', each Ah charged into the battery yields a 4 Ah increase in plate capacity. This is too great an increase and is in contradiction with Faraday's law. It can be concluded therefore that during storage, the negative dry-charged plates undergo not only self-discharge processes, but passivation as well. The observed passivation phenomenon has been ascribed to exclusion of part of the active mass from the discharge process, and the depassivation is a result of re-involvement of this part of the active mass into the discharge process again.

Dry-charged cells, although hermetically sealed, always contain moisture above 0.2–0.5%. During the time of storage, oxygen is evolved at the positive plates, a process which is enhanced in humid atmosphere. This oxygen sustains a certain rate of oxidation of Pb to PbO. If H_2SO_4 in the plates is not completely washed off, PbO will react with the residual acid in the pores to form $PbSO_4$. Where does the passivation process take place? The negative active mass structure is built of (a) a *skeleton*, which serves as a current-collector for all parts of the active mass and provides mechanical support to the lead crystals which participate in the current-generation process and (b) a *secondary (energetic) structure*, which consists of separate small lead crystals attached to the skeleton structure. These crystals are oxidized during discharge and restored during charge. Their amount determines the capacity of the plate.

A model for the passivation of the negative plates has been proposed [8]. During storage, the surface of the lead crystals, as well as their interface with the skeleton, is subjected to oxidation by oxygen evolved from the positive plates. As a result of this process, the electronic contact between the secondary crystals of the energetic structure and the skeleton is either reduced (impaired), or completely disrupted by the formed PbO . Thus, part of the secondary structure, although not oxidized, is excluded from the current-generation process during discharge. As the time of storage increases, ever more secondary lead crystals are excluded from the discharge process and the plate capacity declines. Moreover, there are zones in the skeleton structure with very small cross-section, e.g., the connections between the individual branches. These parts may be oxidized by the evolved oxygen and thus large parts of the lead active mass may be excluded from the electro-conductive network of the skeleton, despite the fact that they contain high amounts of unoxidized lead.

During battery charging, the lead oxide and lead sulfate located between the secondary lead crystals and the skeleton are reduced to Pb . The electronic contact between the skeleton and the lead crystals which have been excluded from the discharge process is restored. The PbSO_4 and PbO which isolate part of the skeleton structure are also reduced. Thus, the electrical system of the skeleton is restored, which leads to an increase in plate capacity greater than the accepted charge during the charging process (Fig. 13.9). When the above processes are completed, further increase in plate capacity follows Faraday's law (Fig. 13.9).

Separator. The separators of dry-charged batteries are not affected during storage.

13.2.7. Summary

The processes that proceed in dry-charged batteries during storage depend strongly on the moisture content in the plates and separators. At moisture contents up to 0.2%, these processes proceed at a low rate, but at 0.6–1.0% moisture levels, the energy losses of the plates increase. To keep down the moisture level and thus increase the shelf-life of dry-charged batteries, some manufacturers add a certain amount of silica-gel desiccant to each cell.

As evident from the above exposition, the technological processes employed in the manufacture of the two types of plates for dry-charged batteries are specific and require strict control of the technological parameters to ensure long shelf-life. The above described technology was introduced at the time when lead–antimony alloys were predominantly used for the production of plate grids. The wet-charged batteries assembled with such grids had a shelf-life of only 2–3 months. If this storage time was exceeded, the plates suffered so severe self-discharge processes and heavy sulfation that the batteries could not reach the required performance parameters even after boost charging and had to be withdrawn from the market and sent for recycling. This forced battery manufacturers to adopt the dry-charged technology in their battery plants. This technology made it possible for battery dealers to offer their customers fully charged batteries meeting the standard performance requirements. On the other hand, the

transportation of dry-charged batteries was cheaper and safer than of wet-charged batteries filled with electrolyte. Moreover, the dry-charged technology allowed battery manufacturers to produce and keep in store large amounts of batteries and thus be able to respond quickly to any momentary or seasonal increase in market demands for ample amounts of batteries of different types (for different applications).

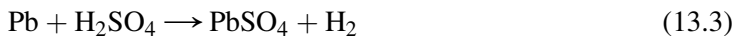
With the introduction of lead–calcium alloys for the manufacture of battery grids, and of improved control over the purity of primary and secondary lead for the production of lead alloys and leady oxides, the self-discharge issue during battery storage was resolved. Maintenance-free wet-charged batteries were launched, which were very well accepted and preferred by both battery dealers and users. The share of this new type of wet-charged batteries has increased at the expense of reduced production of dry-charged batteries. Lately, production of dry-charged batteries has been limited to stand-by batteries with long shelf-life.

The next section of this chapter will discuss the processes that occur during storage of wet-charged batteries.

13.3. Wet-Charged Batteries

13.3.1. Processes That Occur During Storage of Wet-charged Batteries

Figure 13.10 presents a segment of the E/pH diagram of the $\text{Pb}|\text{H}_2\text{SO}_4|\text{H}_2\text{O}$ equilibrium electrode system within the $\text{Pb}|\text{PbSO}_4$ electrode potential region. At $\text{pH} = 1$, the electrochemical systems $\text{Pb}|\text{PbSO}_4$ and $\text{H}_2\text{O}|\text{H}_2$ form on the Pb electrode with a potential difference of $\Delta\phi_{\text{sd}} = 257$ mV. According to thermodynamics, this potential difference will initiate oxidation of lead to lead sulfate and the released electrons will react with H^+ ions to form hydrogen molecules (Fig. 2.8 in Chapter 2). These reactions can be represented by the following overall equation:



The elementary reactions forming the above system ($\text{Pb}|\text{PbSO}_4||\text{H}_2\text{O}|\text{H}_2$), as well as the electrochemical and physicochemical steps involved (e.g. Pb^{2+} ion transfer, electron transfer, diffusion and adsorption of H^+ and SO_4^{2-} ions, chemical reactions between SO_4^{2-} and Pb^{2+} ions, etc.), proceed at different rates, whereby the slowest reaction determines the overall rate of the above process. It has been established that the reaction of hydrogen evolution on the Pb surface is strongly impeded and a higher polarization (overpotential) should be applied to the lead electrode for this reaction to proceed. This means that the above electrode system (13.3) is kinetically limited. Hence, hydrogen will be evolved on the Pb electrode only at potentials considerably more negative than the equilibrium potential of the $\text{Pb}|\text{PbSO}_4$ electrode. Without external polarization, only under the action of the potential difference of 257 mV, reaction

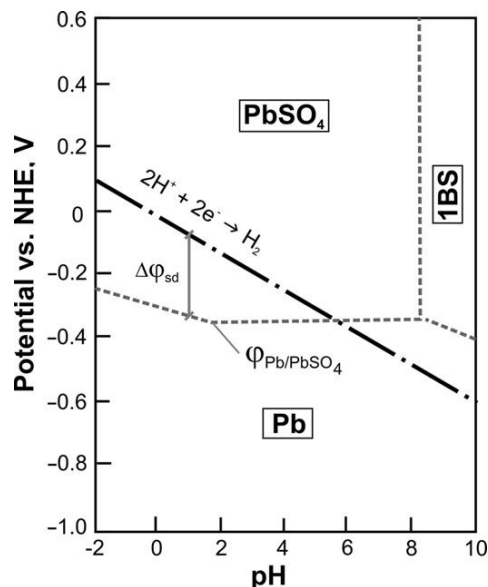
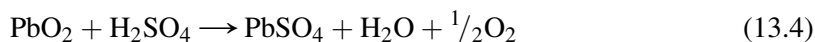


Figure 13.10:

Segment of the E/pH diagram within the Pb/PbSO₄ electrode potential region.

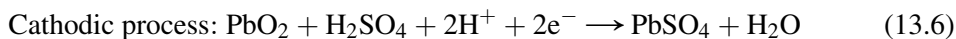
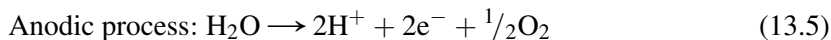
(13.3) will proceed on the Pb electrode immersed in H₂SO₄ solution at a negligibly low rate. This is actually a process of electrode self-discharge. If, however, the lead electrode contains impurities (or additives) of elements which facilitate the hydrogen evolution reaction to commence at a lower overpotential, the self-discharge reactions will proceed at significant rate.

A similar picture is also observed on the PbO₂ surface. At low pH values, the electrode system PbO₂|PbSO₄ || H₂O|O₂ forms (Fig. 13.11). At pH = 1, the potential difference of this system is $\Delta\phi_{sd} = 472$ mV. According to the laws of thermodynamics, at this potential difference evolution of oxygen and formation of PbSO₄ should be expected to proceed by the following overall reaction:



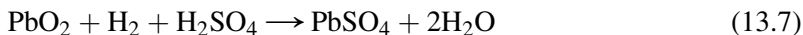
The elementary electrochemical, physicochemical and chemical processes involved in the above overall reaction are strongly impeded and some of them proceed at a very slow rate. Oxygen evolution has been found to commence at very high overpotentials. Hence, PbO₂ is reduced to PbSO₄ but very slowly on the PbO₂ electrode surface and it is the rate of the oxygen evolution reaction that determines the self-discharge of the PbO₂|PbSO₄ electrode. If the PbO₂ active material contains impurities with electronic conductivity which lower the overpotential of oxygen evolution, the latter reaction will proceed at a higher rate and hence increase the self-discharge of the PbO₂|PbSO₄ electrode.

to the potential of the $\text{Pb}|\text{PbO}_2|\text{PbSO}_4$ electrode. The electrochemical reactions which proceed in this system can be represented by the following electrochemical equations:



The cathodic process involves sulfuric acid, so one of the parameters which affect the self-discharge rate of the positive plates is the H_2SO_4 concentration. The latter's influence was followed by measuring the amount of evolved oxygen when a 1.5 g sample of $\beta\text{-PbO}_2$ was immersed in H_2SO_4 solutions of different concentrations (Fig. 13.12) [13,14]. The rate of the self-discharge processes on the PbO_2 surface increases with increase of acid concentration, this increase being most significant at H_2SO_4 solutions of concentrations higher than 1.14 g cm^{-3} .

It has also been established that the hydrogen evolved by the self-discharge processes on the negative plates can be oxidized on the positive plates via the following reaction [15–18]:



The above reaction, however, proceeds at a very low rate. This may be due to the low solubility of hydrogen in sulfuric acid solution, which decreases further with increase of the acid concentration in the solution [19]. Oxidation of hydrogen on the positive plates is part of the complex set of self-discharge reactions which take place on positive plates during storage of wet-charged lead–acid batteries.

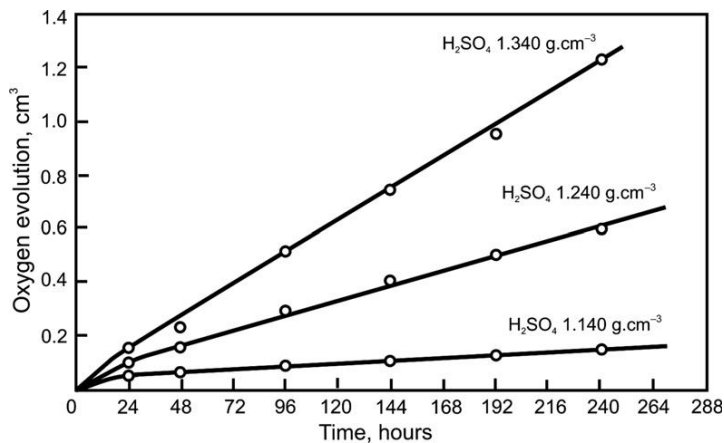


Figure 13.12:

Oxygen evolved from samples of 1.5 g $\beta\text{-PbO}_2$ at 30°C vs. time of stay in sulfuric acid solutions of different concentrations [13].

13.3.3. Influence of Additives to the Positive Grid Alloy on the Processes During Storage and on the Performance Parameters of Wet-charged Batteries

The second important factor with a strong influence on the self-discharge of the positive plates is the grid alloy composition, i.e. the type and content of alloying additives. On corrosion of lead–antimony positive grids, antimony dissolves in the pores of PAM and is adsorbed onto or/and incorporated into the structure of the PbO_2 active mass. The oxygen reaction (13.5) proceeds at lower overpotentials on these PbO_2 formations (active centres), thus accelerating the self-discharge of the positive plates. Similar effect has been observed also with copper, nickel, cobalt, silver and other alloying additive, too [15,16].

This is not the case with lead–calcium alloys, however, as illustrated clearly by the data in Fig. 13.13 [16]. The self-discharge of the plates was evaluated by measuring the amount of lead sulfate formed via reaction (13.6) in the lead dioxide active material of plates with lead–antimony or lead–calcium grids, after open-circuit stay (storage) for 16 weeks at 35 °C. The cells under test had been filled with H_2SO_4 electrolytes of different concentrations so as to follow the influence of acid concentration, too. The sulfation data for active material alone, with no grid or separator, are also given in the figure for comparison.

The grid alloy composition exerts a strong effect on the self-discharge processes. At H_2SO_4 concentrations lower than 1.10 g cm^{-3} , the self-discharge rate of the plates with Pb–Ca grids increases with decrease of acid concentration, whereas that of the plates with Pb–Sb grids decreases. The latter plates suffer the fastest self-discharge at H_2SO_4 concentration of 1.12 g cm^{-3} . At 1.28 acid relative density, the self-discharge rate of the plates with Pb–Ca grids is twice slower than that of the Pb–Sb plates. The slowest self-discharge rate is measured

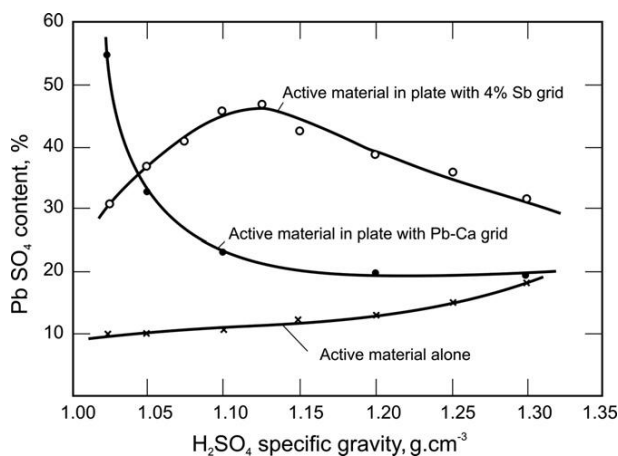


Figure 13.13:

Analytically determined lead sulfate content (in wt%) in positive active material, after storage of plates, or active material alone, for 16 weeks at 35 °C [14].

for the active material without grid. This indicates that there is a transfer of alloying additives from the grid to the lead dioxide active material, which affects the processes that take place in the positive active mass.

When Pb—Sb grid alloys were substituted with Pb—Ca alloys, in an attempt to reduce or eliminate the need for battery maintenance and thus promote production and sale of wet-charged batteries, a strange phenomenon was observed, namely batteries rapidly lost capacity on cycling because of limited discharge of the positive plates (Fig. 13.14). This phenomenon was called ‘premature capacity loss’ (PCL) [20]. In search of the reasons for this phenomenon, it has been established that apart from its beneficial effect on the mechanical and casting properties of the lead alloys and its negative influence on the self-discharge processes, antimony also affects the electrochemical and physicochemical processes that occur on the positive plates.

Investigations were performed, with the financial support of the Advanced Lead—Acid Battery Consortium (ALABC), aimed to identify which structural components of the plate were affected by antimony in the grid alloy.

The following model study was conducted with the aim to identify and localise the phenomena which promote premature capacity loss of the plate [21]. Model plates were prepared with one lead and one Pb—4.5 wt% Sb subgrids attached to one another with epoxy resin (Fig. 13.15). Each of the subgrids had a separate current-collector through which cycling of the plate could be conducted. Deep discharge cycling was performed (down to 100% DOD) at 47% utilisation of the positive active material, i.e. under conditions that facilitated strongly the PCL effect.

Figure 13.16 presents the capacity vs. cycle curves for cells assembled with one positive plate (with lead and Pb—4.5wt% Sb subgrids) and two negative plates. Cycling was performed in two ways: (a) one of the cells was cycled through the lead subgrid and the other one through the Pb—Sb subgrid; (b) one cell was cycled through the lead subgrid first and then through the

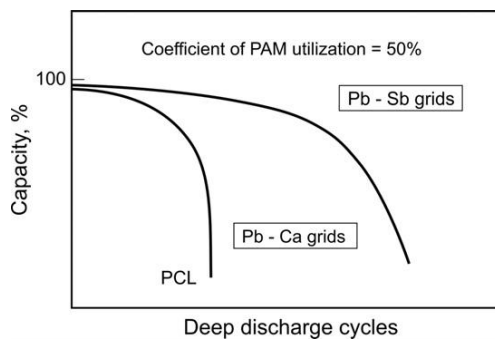


Figure 13.14:

Capacity of batteries with lead—calcium or high-antimony lead grids on cycling; a demonstration of the early capacity decline of batteries; PCL = premature capacity loss.

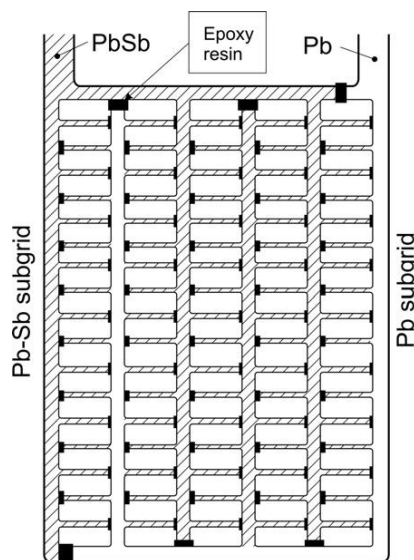


Figure 13.15:

Design of a positive grid with lead and lead–antimony subgrids [21].

Pb–Sb counterpart, while the other cell was cycled through the Pb–Sb subgrid first, and after 12 cycles, through the lead subgrid.

The results presented in Fig. 13.16a show that, during the first few cycles, both cells have the same capacity. This suggests that the PAM structure of each of the subgrids is sufficiently branched and capable of delivering the current to every point in the PAM. When cycling is performed through the lead subgrid, the life of the battery is limited to 12 cycles. When the Pb–Sb subgrid is used, however, the plate preserves its capacity for more than twice as many cycles. This means that, when the grid is made from pure lead, the capacity is determined by the properties of both the corrosion layer (CL) and its interfaces with the grid and the PAM. The same conclusion was also reached when the discharge was conducted consecutively (Fig. 13.16b,c).

The properties of the corrosion layer, and of its interfaces, depend strongly on the additives to the grid alloy (in this case, antimony). Antimony affects the corrosion layer in such a way that it does not limit the discharge of the active mass, so the latter exhibits its full capacity. This phenomenon is known as ‘antimony-free effect’.

Finally, the experimental results for the double subgrids indicate that the PbO_2 active mass is ‘healthy’, despite that the plate reaches the end of its cycle life when discharged through the lead subgrid. If cycling is continued through the Pb–Sb subgrid, the same PbO_2 active mass exhibits its full capacity for many more cycles.

What is the mechanism by which the corrosion layer exerts such a strong influence on battery performance?

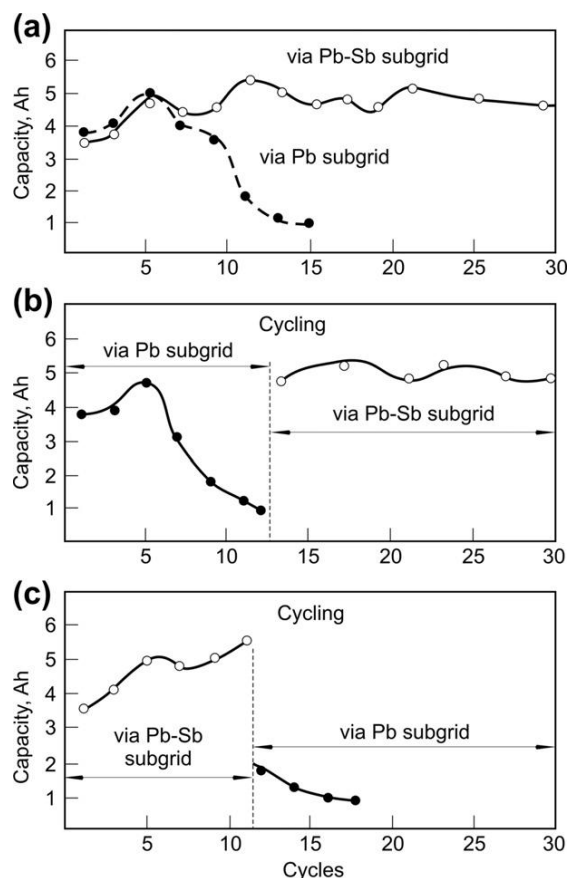
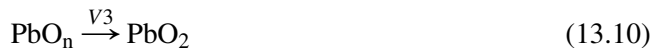


Figure 13.16:

Capacity changes on cycling of positive plates: (a) through the lead or lead-antimony subgrids; (b) first through the lead subgrid, then through the lead-antimony subgrid; (c) first through the lead-antimony and then through the lead subgrid [21].

During battery operation, the metal grids of the positive plates are oxidized both by the evolved oxygen and by self-discharge processes. As a result of this the corrosion layer grows in thickness. The phase composition of the CL is determined by the following reactions [22,23]:



where V_1 , V_2 and V_3 are the rates of the respective reactions.

It has been established, through scanning electron microscopy (SEM), that the CL is built of agglomerates and particles of various sizes and shapes. Their composition depends on the ratio between the rates of the above reactions, namely $V_1:V_2:V_3$. Thus:

- (i) when $V_1 > V_2$, a distinct PbO sublayer is formed and the electrode system is of the type $\text{Pb}|\text{PbO}|\text{PbO}_n|\text{PbO}_2$; as PbO has a high ohmic resistance, the electrode is passivated;
- (ii) when $V_1 < V_2$, the electrode system $\text{Pb}|\text{PbO}_n|\text{PbO}_2$ is formed; PbO_n has low ohmic resistance and hence the electrode is electrochemically active; the positive battery plate is a system of this type.

It has been established that the corrosion layer formed at +0.85 V (vs. $\text{Hg}|\text{Hg}_2\text{SO}_4$ electrode) on the Pb–Sb electrode has a higher electron conductivity than on pure lead [23,24]. This is due to the incorporation of antimony in the structure of the lead oxides $\text{Pb}_{(1-x)}\text{Sb}_x\text{O}$, $\text{Pb}_{(1-x)}\text{Sb}_x\text{O}_n$ and $\text{Pb}_{(1-x)}\text{Sb}_x\text{O}_2$ [25]. It has also been found (Fig. 4.25) that Sb accelerates the reaction of PbO oxidation to PbO_2 by shifting the onset of this reaction to more negative potentials. So antimony eliminates the PCL effect on cycling.

Despite the above discussed positive effects of antimony, battery manufacturers tend to avoid the use of Sb as grid alloying additive and thus make the battery maintenance-free and suitable for storage in the wet-charged state. As a first step, the content of antimony in the grid alloy was reduced to below 2.0 wt%. This resulted in poor charge acceptance of the positive plates. The charging voltage had to be increased to compensate for the impaired charge efficiency. This, however, accelerated the grid corrosion processes and lead to the formation of a thicker tet-PbO layer at the grid/PAM interface and hence passivation of the positive plates [26]. Giess has established that addition of 0.2–0.4 wt% Sn to the alloy for positive grids prevents formation of tet-PbO in the corrosion layer at Sn contents of up to 1.5 wt% [27]. This means that tin facilitates the oxidation of tet-PbO to PbO_2 .

Our team, in collaboration with the research group of Prof. M. Maya (Italy), investigated the influence of Sn on the rate of oxidation of PbO to PbO_n [28]. Figure 13.17 presents a series of potentiodynamic sweeps of Pb and Pb–0.5 wt% Sn electrodes in the dark. The polarization was performed in the dark to rule out photooxidation of PbO. The serial sweep number is encircled. The arrows mark the start of the oxidation reaction. The voltammograms for the pure Pb electrode are presented by dashed lines, while those for the Pb–Sn electrodes are marked by continuous lines [28]. The data in the figure show that Sn lowers the onset potential of the oxidation reaction and accelerates the rate of PbO oxidation to PbO_n .

Figure 13.18 illustrates the relationship between the potential at which the oxidation reaction starts and the number of successive sweeps [28]. Tin lowers this potential by approximately 0.2 V. This effect is probably due to the action of tin ions incorporated in the oxide.

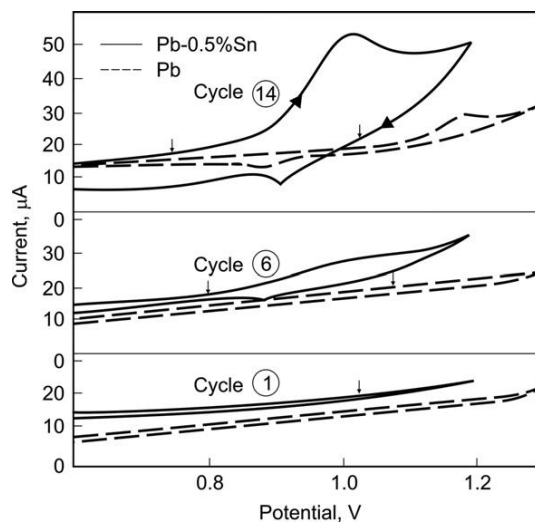


Figure 13.17:

First, sixth and fourteenth voltammograms for pure Pb and Pb–0.5 wt% Sn electrodes on polarization up to 1.3 V. The arrows mark the start of PbO oxidation. Sweep rate 10 mV s^{-1} [28].

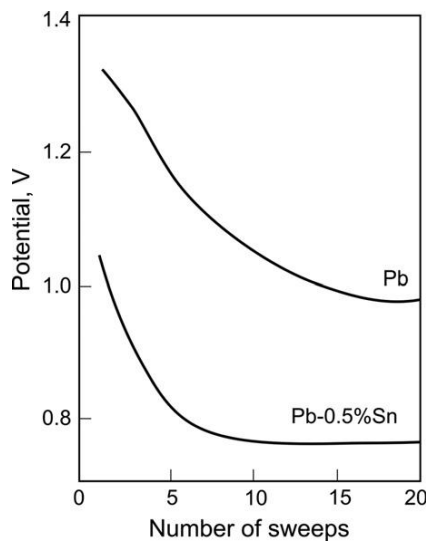


Figure 13.18:

Potential at which PbO oxidation starts as a function of the number of sweeps for Pb and Pb–0.5 wt% Sn electrodes [28].

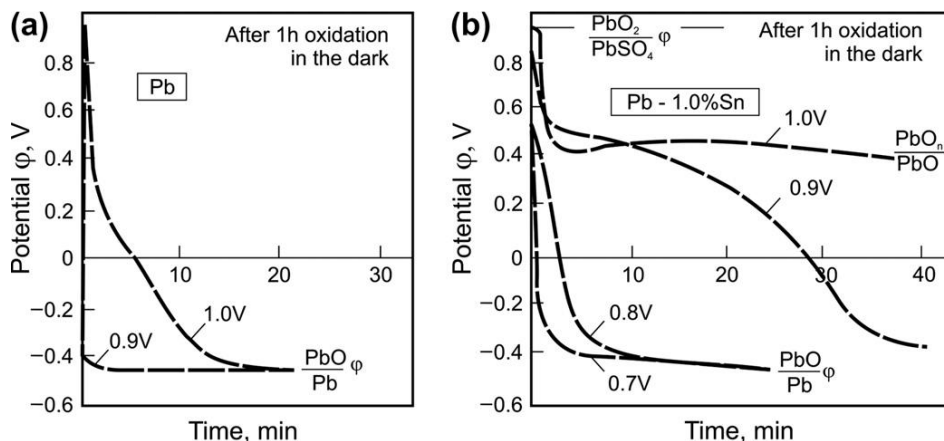


Figure 13.19:

Potential decay of Pb and Pb–1.0 wt%Sn electrodes after 1 h of oxidation at constant potential [28].

Does this effect occur from the beginning of PbO formation? To answer this question, Pb and Pb–Sn electrodes were oxidized for one hour at a constant potential in the high positive potential region. Then, the circuit was open and the potential transients were recorded. Figure 13.19 shows these transients.

When the oxidation of the Pb electrode is conducted at up to +0.9 V (vs. Hg|Hg₂SO₄ electrode), on opening the circuit the potential drops to a plateau coinciding with the equilibrium potential of the Pb|PbO electrode. This means that PbO does not undergo oxidation up to the above potential.

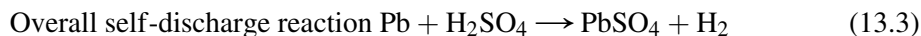
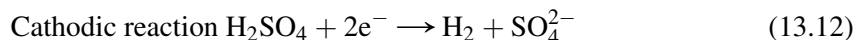
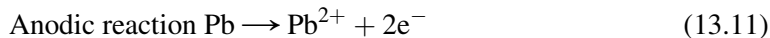
When the Pb–1.0 wt%Sn electrode is oxidized at +0.8 V (vs. Hg|Hg₂SO₄ electrode), the transient features a potential arrest on open circuit. After oxidation at higher potentials, a plateau appears at about +0.5 V on open circuit. This plateau has to be distinguished from the PbO₂ plateau at 0.9 V after oxidation at 1.0 V.

A semiconductor mechanism was proposed for the electrocatalytic action of tin on the oxidation of PbO to PbO_n and PbO₂. Tin has substituted antimony as an additive to the alloys for lead–acid battery grids. It is added in considerably lower concentrations than Sb and in combination with calcium which improves the mechanical properties of the alloys. Thus the interface problem of lead–calcium grids was resolved and the way was open for the manufacture of maintenance-free wet-charged batteries.

As evident from Fig. 4.41 in Chapter 4 of this book, when Pb–Ca–Sn positive grids contain up to 1.8 wt% Sn, no tet-PbO layer forms in the corrosion layer. That is why the positive grids for all types of maintenance-free valve-regulated lead–acid batteries are cast from lead alloys with 0.05–0.07 wt% Ca and 1.5–1.7 wt% Sn content.

13.3.4. Processes That Occur in the Negative Plates During Storage of Wet-charged Batteries

The reactions that proceed in the negative plates of wet-charged batteries on storage can be represented by the following equations:



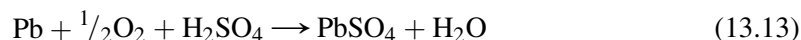
The electromotive force of the self-discharged cell $\text{Pb}|\text{H}_2|\text{H}_2\text{SO}_4||\text{PbSO}_4|\text{Pb}$ can be determined from the equation:

$$E = E_0 - \frac{0.059}{2} \lg a_{\text{H}^+}^2 \cdot a_{\text{SO}_4^{2-}} \quad (13.E1)$$

That is E depends on the sulfuric acid concentration. The rate of the cathodic reaction (13.12) is very slow, because of the very high overpotential of hydrogen evolution on lead electrode of high purity grade. And it is the reaction of hydrogen evolution that exerts the strongest influence on the rate of the self-discharge process, i.e. it practically determines this rate.

The lead–acid battery industry uses low-antimony and lead-calcium-tin alloys which contain other additives or impurities as well. Antimony, in particular, lowers significantly the overpotential of hydrogen evolution and thus accelerates the self-discharge of the negative plates. In order to avoid this, battery manufacturers have substituted lead-antimony alloys for the negative grids with lead–calcium or lead–calcium–tin alloys. The positive grids are commonly cast from low-antimony lead alloys. Hence, batteries with different positive and negative grids are called ‘hybrid batteries’. The major part of the antimony ions produced by the corrosion of the positive grids are retained in the lead dioxide active mass, but then after a certain period of time, these ions diffuse to the negative plates and are reduced there. This leads to accelerated self-discharge and water loss during charge. In order to alleviate this effect, specially designed separators have been introduced which absorb antimony ions and thus less antimony is reduced on the negative plates. So battery engineers and manufacturers are trying hard to prevent lowering of the overpotential of hydrogen evolution and thus reduce the self-discharge and water loss of the battery.

The second reaction that accelerates the self-discharge processes of the negative plates in wet-charged batteries is the oxidation of lead by the oxygen evolved by the self-discharge processes at the positive plates. This oxidation of the lead active mass can be represented by the following equation:



The above reaction of oxygen reduction and lead oxidation is a fast process. Hence, the diffusion of oxygen from the positive to the negative plates is the rate limiting step in this reaction. It is this elementary process of the self-discharge that is affected by the separator. The latter slows down the diffusion of oxygen, the extent of this effect depending on the pore system and the chemical composition of the separator. The influence of battery separator on the self-discharge processes that take place on the negative plates has been studied by wrapping formed plates in different separators and immersing them in sulfuric acid solutions of 1.25 relative density, with or without addition of $0.1 \text{ g L}^{-1} \text{ Sb}_2(\text{SO}_4)_3$ [16]. The obtained results are presented in Fig. 13.20.

The amount of PbSO_4 formed as a result of the self-discharge of the negative plates is determined after different periods of time. The data in the figure show that (a) antimony accelerates significantly the rate of the self-discharge processes and (b) spun glass or microporous rubber separators retard notably the self-discharge of the negative plates. During the open-circuit stay of wet-charged batteries, the product of the self-discharge reaction, PbSO_4 , slowly covers the surface of the lead active mass and hence the rate of the self-discharge decreases gradually with time. This is an insignificant decrease, however, because the lead sulfate recrystallizes into big PbSO_4 crystals.

Figure 13.21 illustrates the changes in discharge performance of the negative plates after storage [8]. It can be seen from the data in the figure that the capacity of the wet-charged

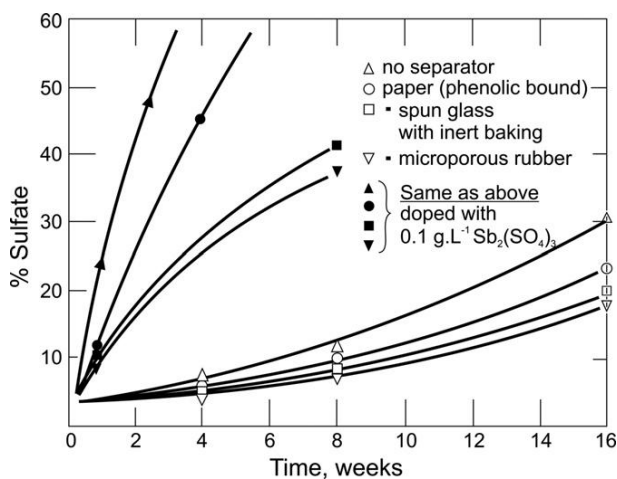


Figure 13.20:

Influence of different separators on the self-discharge of single negative plates immersed in H_2SO_4 solution of 1.25 relative density at 35°C . Separators used: Δ no separator; \circ paper (phenolic-bound); \square spun glass with inert baking; ∇ microporous rubber. The self-discharge rates in H_2SO_4 solution of 1.25 relative density, doped with $0.1 \text{ g L}^{-1} \text{ Sb}_2(\text{SO}_4)_3$, are marked by black symbols.

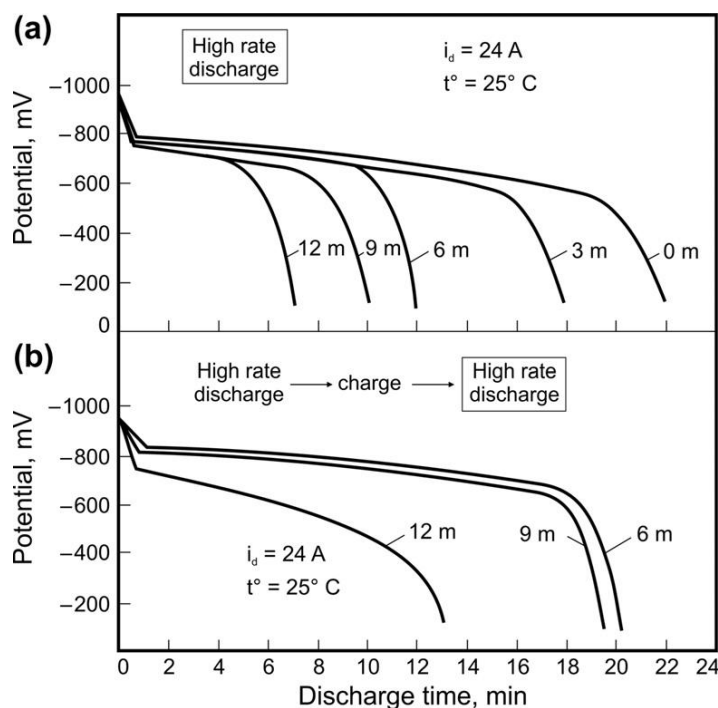


Figure 13.21:

Changes in electric parameters of negative plates during storage: (a) discharge transients for the plates after storage; (b) discharge transients for the same plates after 20 h charge.

negative plates declines, while the discharge voltage is almost unaffected. The figure shows also the discharge transients for the same cells after an overcharge of up to 150% of their rated capacity. When stored for less than 6 months, the plates restore completely their capacity after charging. Only the batteries stored for 1 year do not recover their capacity, probably as a result of processes that have irreversibly altered the NAM structure.

The chemical composition of the active mass after 1 year of storage contains about 5% PbO and 10% PbSO_4 , and the discharge curves for these plates feature a marked decline in capacity (Fig. 13.21). This experimental finding provides evidence that, besides the self-discharge processes, certain structural changes occur as well, as a result of which part of the secondary energetic structure is excluded from the current generation process. These changes include (a) recrystallization of the small PbSO_4 particles into big PbSO_4 crystals with low solubility in H_2SO_4 solution and (b) degradation of the expander organic component contributing to the growth (in thickness) of the lead dendrites, thus precluding the formation of small lead crystals of the secondary structure with high surface which would allow the delivery of high currents on discharge.

Iliev and Pavlov have shown that PbSO_4 particles precipitate in the pores of the separator during battery storage [8]. Electron micrographs of a separator taken out of a fully charged

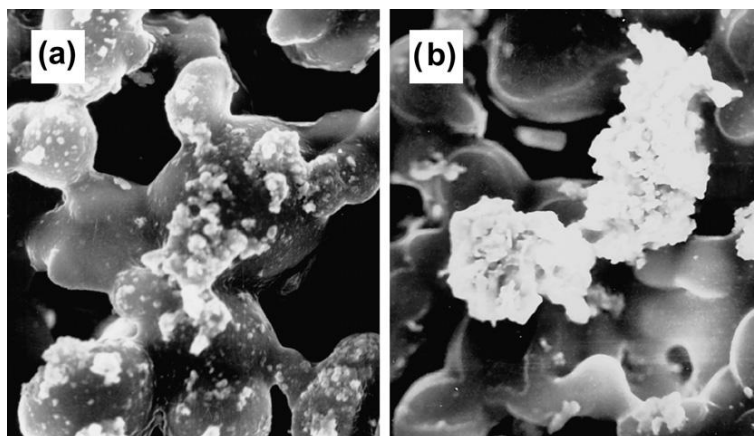


Figure 13.22:

Scanning electron micrographs of a separator from a wet-charged battery after 9 months of storage. Separator surface facing: (a) positive plate; (b) negative plate.

battery after 1 year of storage are presented in Fig. 13.22. Lead sulfate nuclei are clearly seen in the separator pores, especially on the separator surface facing the negative plate. Accumulation of PbSO_4 crystals in the separator is an irreversible process which has a disastrous effect on the cycle life and capacity performance of the battery.

The structural changes in the negative plates could be suppressed, to a great extent, by retarding the self-discharge of wet-charged batteries. This could be achieved by adding inhibitors of the self-discharge reactions to the negative paste. A list of such inhibitors is presented in Table 13.2. This technique has proved efficient and has found wide application.

The second requirement, which is critical for the reversibility of the structural changes of NAM, is that the negative grids are cast from lead-calcium or lead-calcium-tin alloys. Under the above conditions, wet-charged batteries undergo considerably slow self-discharge, which guarantees sufficiently long shelf-life.

The third major factor that affects the self-discharge processes in wet-charged batteries is the storage temperature. It should not exceed 25–30 °C.

A further requirement for safe storage of wet-charged batteries is to isolate completely the access of atmospheric oxygen to the cells. Oxygen from the air may penetrate into the battery both via defective valves and also, though very slowly, through the walls of the polymer battery container, if inappropriately designed and/or made of unsuitable material.

By observing all the above technological requirements in the manufacture of the positive and negative plates, and in the design of battery components (containers and valves), battery manufacturers have been able to produce and launch on the market wet-charged batteries for various applications.

References

- [1] D. Pavlov, S. Ruevski, *J. Electrochem. Soc.* 126 (1979) 1100.
- [2] D. Pavlov, S. Ruevski, *Proc. 28th Meeting ISE, Electrochem. Power Sources*, Varna, Bulgaria, 18 September 1977, p. 97.
- [3] E.G. Tiegel, *LEAD'68 Edited proceedings 3rd international conference on Lead*, Venice, Italy, Pergamon Press, Oxford, 1969, p. 191.
- [4] J.E. Manders, *J. Power Sources* 19 (1987) 189.
- [5] N. Anastasijevic, J. Garche, K. Wiesener, *J. Power Sources* 7 (1982) 201.
- [6] S. Ruevski, D. Pavlov, *Annual report 1979; CLEPS, Bulg. Acad. Scis.* (1979); Sofia, Bulgaria.
- [7] V. Iliev, S. Ruevski, D. Pavlov, *Annual report 1980; CLEPS, Bulg. Acad. Scis.* (1980); Sofia, Bulgaria.
- [8] V. Iliev, D. Pavlov, *J. Electrochem. Soc.* 129 (1982) 458.
- [9] H. Bode, in: R.J. Brodd, K.V. Kordesch (Eds.), *Lead-acid batteries*, John Wiley & Sons, New York, USA, 1977, p. 278.
- [10] S. Ruevski, V. Iliev, D. Pavlov, *Bulg. Patent No.* 52833/1982.
- [11] M.A. Dasoyan, I.A. Aguf, *Fundamentals of lead-acid battery design and manufacturing technology*, Energia, Leningrad, 1978, p. 127 (in Russian).
- [12] M. Saakes, P.J. van Duin, A.C.P. Ligtvoet, D. Schmall, *J. Power Sources* 47 (1994) 149.
- [13] P. Ruetschi, J. Sklarhuck, R.T. Angstadt, *Electrochim. Acta* 8 (1963) 333.
- [14] P. Ruetschi, *J. Power Sources* 2 (1977/78) 3.
- [15] R.T. Angstadt, C.J. Venuto, P. Ruetschi, *J. Electrochem. Soc.* 109 (1962) 177.
- [16] P. Ruetschi, R.T. Angstadt, *J. Electrochem. Soc.* 105 (1958) 555.
- [17] K.R. Bullock, D.H. McClelland, *J. Electrochem. Soc.* 123 (1976) 327.
- [18] B.K. Mahato, E.Y. Weissman, E.C. Laird, *J. Electrochem. Soc.* 121 (1976) 13.
- [19] P. Ruetschi, *J. Electrochem. Soc.* 114 (1967) 301.
- [20] A.F. Hollenkamp, *J. Power Sources* 36 (1991) 567.
- [21] M.K. Dimitrov, D. Pavlov, *J. Power Sources* 46 (1993) 203.
- [22] D. Pavlov, *J. Power Sources* 46 (1993) 171.
- [23] T. Laitinen, K. Salmi, G. Sundholm, B. Monahov, D. Pavlov, *Electrochim. Acta* 36 (1991) 605.
- [24] M.P.J. Brennan, B.N. Stirrup, N.A. Hampson, *J. Appl. Electrochem.* 4 (1974) 49.
- [25] D. Pavlov, B. Monahov, G. Sundholm, T. Laitinen, *J. Electroanal. Chem.* 305 (1991) 57.
- [26] D. Pavlov, *J. Power Sources* 48 (1994) 179.
- [27] H. Giess, in: K.R. Bullock, D. Pavlov (Eds.), *Advances in lead-acid batteries*, Vol. 84-14, *Proc. Electrochem. Soc. Inc*, N.J., USA, 1984, p. 241.
- [28] D. Pavlov, B. Monahov, M. Maya, N. Peanzzi, *J. Electrochem. Soc.* 136 (1989) 27.

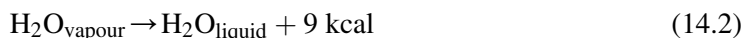
Methods to Restore the Water Decomposed During Charge and Overcharge of Lead—Acid Batteries. VRLA Batteries

After the introduction of lead—calcium—tin alloys in the manufacture of the grids for lead—acid batteries and the use of inhibitors to the hydrogen reaction on the negative plates, the wet-charged battery technology found wide application in the battery industry. The charging voltage was limited and these batteries were considered to be maintenance free. Their service life, however, depended very much on strictly observing the conditions of charging, especially the maximum charging voltage limit. Battery engineers and manufacturers began looking for methods to recombine the hydrogen and oxygen gases evolved during battery charge and overcharge into water again. Thus, the water loss problem would be resolved, too. Water loss of the cell leads to an increase of the H_2SO_4 electrolyte concentration and hence to passivation of the positive plates. Three principal techniques have been developed for the recombination of hydrogen and oxygen to water, and these will be discussed further in this chapter.

14.1. Recombination of Hydrogen and Oxygen into Water Using Catalytic Plugs

The progress of power industry, telecommunication technology and military equipment during the past decades has increased the need for ample amounts of reserve (back up) energy and power. The cheapest source of reserve (back up) power is the lead—acid battery. Hence, production of stationary lead—acid cells with high capacity for use in multicell arrays for standby operation has increased significantly. However, the maintenance of these batteries, i.e. to monitor and sustain the necessary electrolyte level in the cells, requires highly skilled and trained personnel, and is fairly expensive. The first attempts to resolve this problem were aimed at recombining hydrogen and oxygen by the use of a catalytic plug. This technique found a wide application and was rapidly developed during the 1950s and through the 1970s.

It was based on the following chemical reaction:



Both the chemical reaction (14.1) and the phase transition (14.2) are exothermic processes and a considerable amount of heat is generated, which poses a serious problem to designers and engineers, namely how to evacuate the heat released within the small volume of the catalytic plug. If the rate of the reaction between hydrogen and oxygen increases abruptly, the temperature in the plug may reach values of up to 430 °C, i.e. the ignition point of the gas mixture, and an explosion may occur. In order to prevent this to happen, a number of various catalytic plug designs have been developed. Three of these are presented in Fig. 14.1 [1–4].

The basic principles taken into account in the design of catalytic plugs include the following:

- To provide high catalyst surface for the reaction between hydrogen and oxygen to proceed, and to rapidly return the recombined water back to the electrolyte so as to sustain high efficiency of the catalyst.
- To ensure intense heat exchange between the catalytic plug and the ambient atmosphere, so as to prevent overheating of the plug and ignition of the gas mixture.
- To restrict the catalytic reaction to proceed up to a definite temperature, lower than the ignition point of the H_2/O_2 mixture, and if this temperature limit is exceeded to vent out the unreacted hydrogen and oxygen gases to the ambient atmosphere and thus prevent further temperature rise; when the maximum temperature limit is reached, an electric signal is sent to the charging device to reduce the charging current and thus it slows down the evolution of hydrogen and oxygen, or to stop charging altogether.

The efficiency of the catalytic plug depends mostly on the type of catalyst used. Generally, metals of the platinum group (platinum, palladium, ruthenium) are used for the purpose. Oxygen and hydrogen are adsorbed onto the catalyst surface and a series of chemical reactions proceed between them, with the formation of a number of intermediate products (H_2O_2 , OH^- and others), until water is formed at the end. For this recombination reaction to proceed at a high rate, the catalyst should have a high surface. It is therefore deposited onto a carrier with a high surface and resistance to high temperatures. The very first catalyst carrier used was asbestos, which was later substituted for $\gamma-Al_2O_3$, vitreous silicate (SiO_2), and lately some types of carbon have proved to be very efficient catalysts of this reaction.

The catalyst efficiency is measured by the ratio of the volume of restored (recombined) water in the plug vs. the volume of the decomposed water. Watanabe and Yonezu have determined the gas recombination efficiency of some catalyst materials as a function of the overcharge current [5]. Figure 14.2 shows the obtained results.

It is evident from the data in the figure that the highest efficiency in recombining hydrogen and oxygen to water is observed when palladium is used as a catalyst. The platinum–ruthenium catalyst exhibits the lowest catalytic activity.

For a full recombination of hydrogen and oxygen by the chemical reaction (14.1), the two gases should be evolved in a stoichiometric proportion in the cell (2:1). This ratio is sustained in the

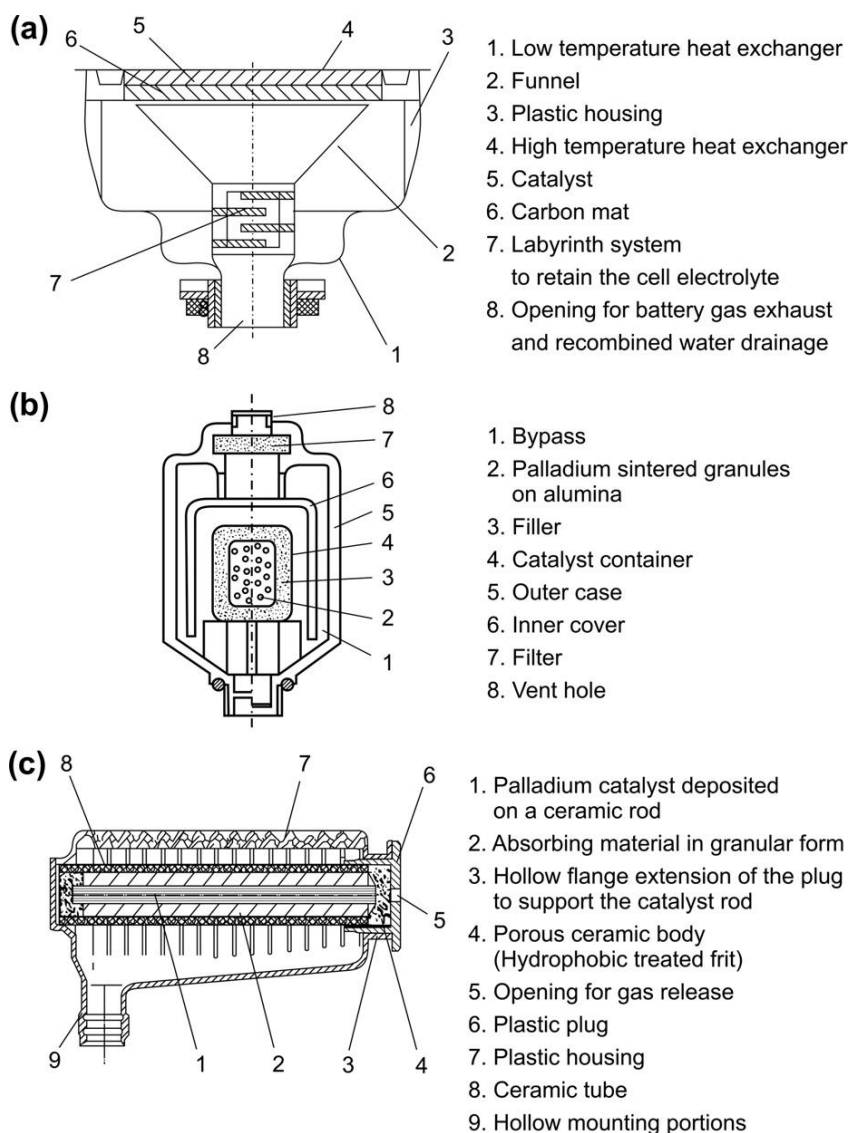


Figure 14.1:

(a) Catalytic plug from VARTA [1]; (b) Catalytic plug from Japan storage battery [2]; (c) Aquagen catalytic plug from Hoppecke [3,4].

battery when fully charged and during the period of overcharge. This is not the case, however, when the battery has been cycled, discharged and is in the process of charge. Under these conditions, oxygen evolution starts on the positive plates when the battery reaches 70% state of charge (SOC). The evolved oxygen increases the pressure in the cells above the critical level and when it is vented out results in water loss. When the cell (battery) is charged to 92–95% SOC, a reaction of hydrogen evolution starts on the negative plates. The evolved hydrogen and oxygen

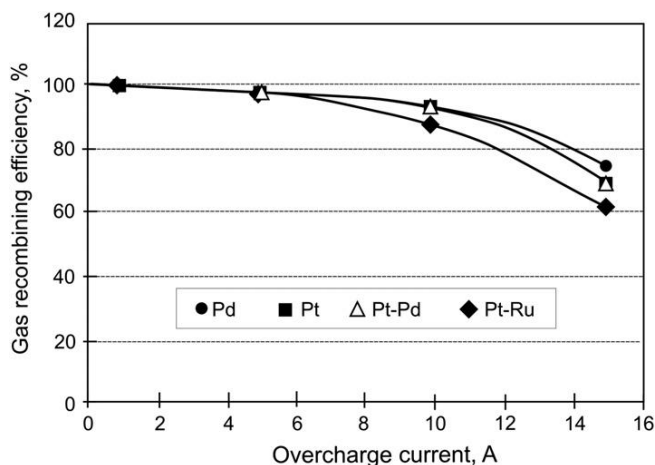


Figure 14.2:

Oxygen and hydrogen recombination efficiencies for different catalyst plugs as a function of overcharge current [5].

gases form a H_2/O_2 mixture in the space above the active block. This gas mixture enters the catalytic plug where the recombination reaction proceeds. With increase of the hydrogen content in the mixture the rate of this reaction increases to reach a maximum value when a stoichiometric ratio between the amounts of the two gases is reached. This process leads to a increase of the generated heat and hence causes the temperature in the plug to rise. The heat exchange between the catalytic plug and the surrounding medium is intensified until a stationary rate of the recombination reaction, and hence a stationary plug temperature, is reached.

The reaction between hydrogen and oxygen produces water. The latter covers the surface of the catalyst and thus retards the reaction of water recombination. To avoid the formation of a water film on the catalyst surface, the catalyst carrier is treated with a hydrophobic substance, e.g. PTFE (polytetrafluoroethylene or teflon). The condensed water runs down draining paths back into the cell. The plug may be fitted with a stopper as well to prevent the H_2SO_4 electrolyte to get into the plug and to deactivate the catalyst.

When the plate grids were cast from alloys containing above 6.0 wt% of Sb or above 0.2 wt% of As, at cell voltages higher than 2.40 V, stibine (SbH_3) or arsine (AsH_3) formed on the negative plates. These gases reacted with the catalyst and poisoned it. Various methods were proposed to remove SbH_3 and AsH_3 from the H_2/O_2 gas mixture. The introduction of lead–calcium–tin alloys for the manufacture of the grids has proved to be the most effective solution to the above problem.

Sometimes, hydrogen sulfide (H_2S) is generated on the negative plates by the reduction of sulfur-containing particles. The latter may be obtained under extreme conditions of charging. Hydrogen sulfide has a strong poisoning effect on the catalyst. Absorbents of H_2S may be introduced on the gas path to the catalyst if there is a probability of such processes to occur.

Catalytic plugs have undergone significant development and improvement in terms of both construction and functional efficiency, as well as with regard to reliability and safety of operation. At present, catalytic plugs are highly efficient and reliable, but fairly expensive, too. Their increased application in remote area and photovoltaic battery systems calls for further improvement of these devices.

14.2. Recombination of Hydrogen and Oxygen to Water on Auxiliary Catalytic Electrodes

This method is based on electrochemical reduction of oxygen in a closed oxygen cycle (COC) and electrochemical oxidation of hydrogen in a closed hydrogen cycle within the cell. The above electrochemical reactions proceed on auxiliary catalytic electrodes partially immersed in the electrolyte and connected by means of electronic devices (ED) to the negative electrode (for oxygen reduction) and to the positive electrode (for hydrogen oxidation), respectively. A schematic diagram of a lead–acid cell with auxiliary catalytic electrodes is presented in Fig. 14.3.

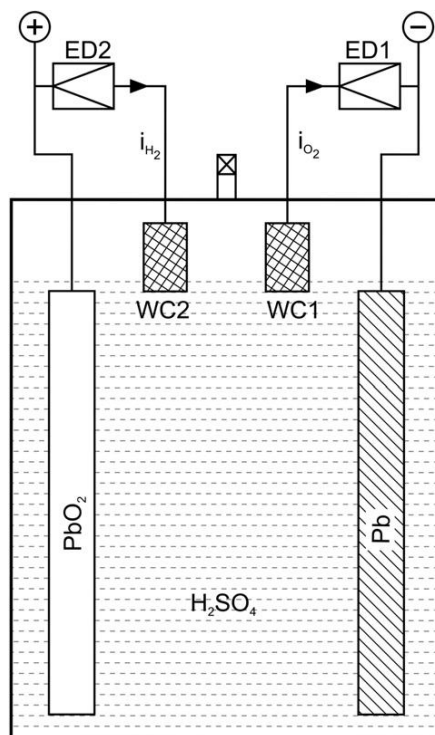


Figure 14.3:
Experimental lead–acid cell with auxiliary electrodes with tungsten carbide (WC) used as catalyst. ED1 and ED2 are electric devices [10].

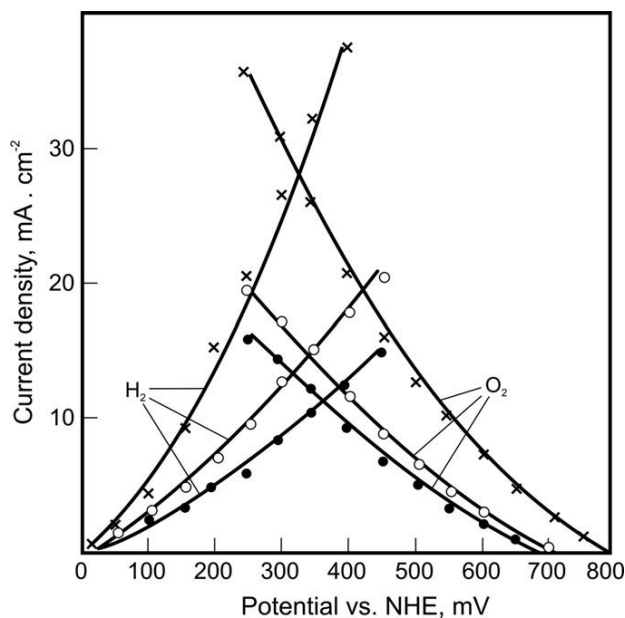


Figure 14.4:

Volt-ampere characteristics of H_2 and O_2 reactions on partially immersed electrodes containing different catalysts: (•) WC (200 mg cm^{-2}); (o) WC + C ($200 \text{ mg cm}^{-2} + 10 \text{ mg cm}^{-2}$); (x) C + Pt ($100 \text{ mg cm}^{-2} + 6 \text{ mg cm}^{-2}$). Temperature 30°C ; H_2SO_4 with 1.28 rel.dens. [11].

The auxiliary electrodes intended to facilitate the reduction of oxygen comprise of, for example, carbon–teflon porous mass catalyzed with silver [6,7] or phthalocyanine [8]. Ruetschi and Ockermann have established that both hydrogen oxidation and oxygen reduction can proceed on the same auxiliary electrode [9]. In our institute, we developed auxiliary catalytic electrodes with tungsten carbide (WC) or a mixture of WC and active carbon as catalyst [10–12]. Figure 14.4 presents the volt-ampere curves of the hydrogen and oxygen reactions on partially immersed auxiliary electrodes with different catalysts: WC alone, or WC plus active carbon (WC+C), or platinum (Pt) [10–12].

The data in the figure indicate that the catalytic activity of the WC+C electrode towards oxygen reduction is commensurate with its activity towards hydrogen oxidation. Active carbon added to the WC enhances the electrode's catalytic activity with regard to both reactions. Electrodes catalyzed with Pt are twice more efficient than the WC and WC+C electrodes, but they are much more expensive as well. Hence, we focused our attention on the WC+C catalytic electrodes. Further in this chapter, we will discuss the behaviour of WC-based auxiliary catalytic electrodes during operation of 12 V/82 Ah cell.

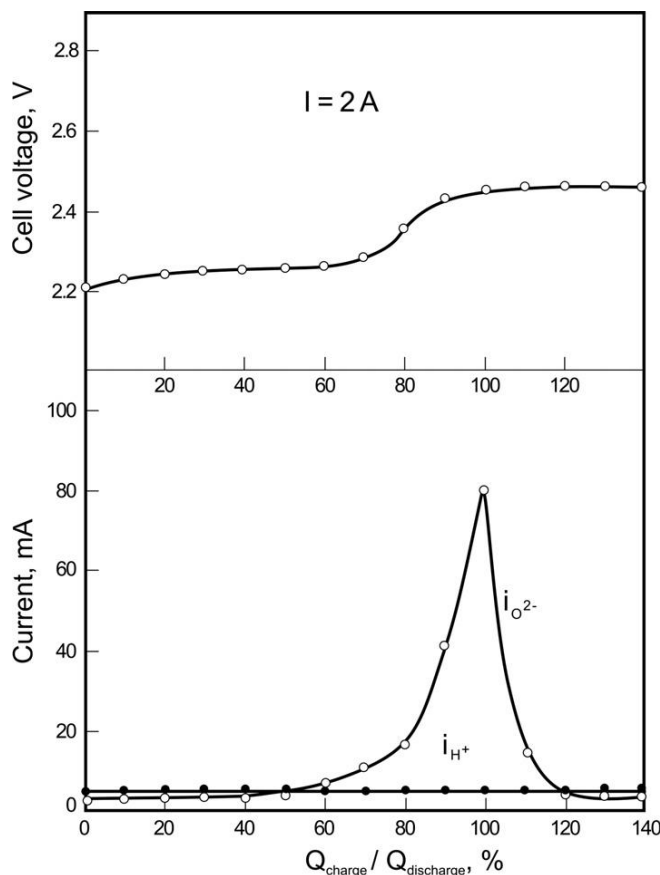


Figure 14.5:

Changes in cell voltage and oxygen and hydrogen currents during charge [12].

14.2.1. Cell Charge

Figure 14.5 illustrates the changes in cell voltage and in the current of the oxygen and hydrogen reactions during charge [12]. Following a partial discharge, the cell was charged with a current of 2 A and the cell voltage, as well as the currents on the WC1 and WC2 electrodes were measured. During cell charge, the current in the outer circuit is distributed as follows:

$$I = (I_{\text{Pb}} + I_{\text{H}_2})_{\text{Pbplate}} + (i_{\text{O}_2})_{\text{WC1}} \quad (14.3)$$

$$I = (I_{\text{PbO}_2} + I_{\text{O}_2})_{\text{PbO}_2\text{plate}} + (i_{\text{H}_2})_{\text{WC2}} \quad (14.4)$$

At the beginning of charge, no hydrogen nor oxygen is evolved:

$$I_{\text{H}_2} = 0$$

and

$$I_{O_2} = 0$$

Since the resistance of the electronic devices ED1 and ED2 is high, the entire current is utilized for charging the plates. When the positive plates reach 70% SOC, oxygen evolution starts, i.e. $(I_{O_2})_{PbO_2 \text{ plate}} > 0$ and the total current I is distributed as follows:

$$I = (I_{PbO_2} + I_{O_2})_{PbO_2 \text{ plate}} \quad (14.5)$$

$$I = (I_{Pb})_{Pb \text{ plate}} + (i_{O_2})_{WC1} \quad (14.6)$$

The current of the oxygen reaction $(i_{O_2})_{WC1}$ increases (Fig. 14.5).

When the negative plates are charged to 95% SOC, hydrogen evolution starts and $(I_{H_2})_{Pb \text{ plate}} > 0$. The total current of the negative plates is distributed as follows:

$$I = (I_{Pb} + I_{H_2})_{Pb \text{ plate}} + (i_{O_2})_{WC1} \quad (4.3)$$

The generated hydrogen recombines with part of the evolved oxygen on the WC1 and WC2 electrodes, whereby the current I_{O_2} decreases.

When the PbO_2 and Pb plates are fully charged, the charge currents become $I_{Pb} = 0$ and $I_{PbO_2} = 0$. In this case:

$$I = (I_{H_2})_{Pb \text{ plate}} + (i_{O_2})_{WC1} \quad (14.7)$$

$$I = (I_{O_2})_{PbO_2 \text{ plate}} + (i_{H_2})_{WC2} \quad (14.8)$$

Figure 14.5 shows that after reaching full charge, the currents $(i_{O_2})_{WC1}$ and $(i_{H_2})_{WC2}$ are very low, which indicates that the total amount of hydrogen and oxygen has recombined on the WC1 and WC2 electrodes.

The above equations are valid for the case when hydrogen and oxygen are produced in stoichiometric amounts. However, about 1–2% of the evolved oxygen diffuses through the corrosion layer on the positive grid and oxidizes the grid metal, thus the stoichiometric ratio between hydrogen and oxygen is disturbed. This leads to slow accumulation of hydrogen in the cell. To prevent increase of the gas pressure in the cell, the latter should be furnished with a valve which opens at a given pressure and lets the gases out of the cell.

As can be seen in Fig. 14.5, the maximum appears in the $(i_{O_2})_{WC1}$ curve always at the end of charge. This peculiarity in the behaviour of the oxygen reaction current may find practical application, namely the WC1 electrode can be used as a sensor indicating the end of charge. The obtained electric signal can be transmitted to the control unit of the charging device for the latter to reduce or stop the charging current.

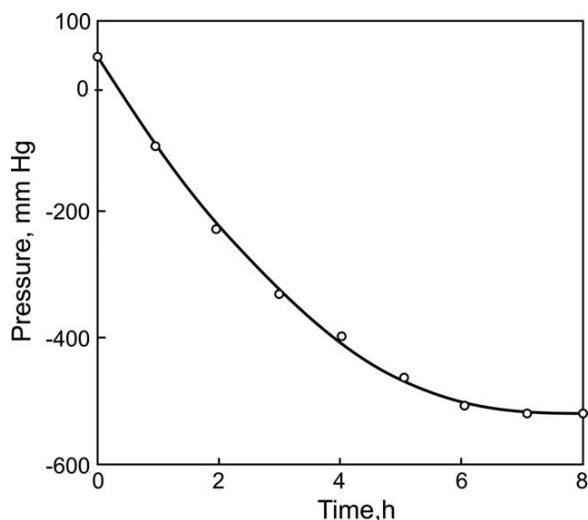


Figure 14.6:
Changes in cell pressure during discharge [12].

14.2.2. Cell Discharge

During discharge, evolution of hydrogen and oxygen on the Pb and PbO₂ electrodes stops and the gases which are already released continue to recombine on the WC1 and WC2 electrodes, which leads to decrease in gas pressure in the cell and eventually to formation of vacuum. To avoid gas leakage into the cell, in our tests the cell was placed in a sealed chamber. The pressure in the chamber and the hydrogen and oxygen currents (i_{H_2} and i_{O_2}) flowing through the WC1 and WC2 electrodes were measured. The changes in cell pressure during discharge are presented in Fig. 14.6.

It can be seen that after 6 h, a high vacuum is created (500 mm Hg), which is sustained throughout the subsequent discharge. No changes in the i_{H_2} and i_{O_2} currents are observed. It was established that, under the action of the vacuum formed during discharge, the pores of the WC1 and WC2 electrodes were filled with electrolyte, as a result of which the catalytic activity of the two electrodes declined. It is, therefore, essential that a safety valve is mounted in the cell lid that will let air into the cell when the vacuum reaches a value of 30 mm mercury.

14.2.3. Open Circuit

When, during overcharge, the current is switched off, hydrogen and oxygen evolution stops, but the processes of recombination on the catalytic electrodes continue. The pressure in the cell decreases, as during discharge. Moreover, due to the potential differences between the Pb and WC1 electrodes, respectively the PbO₂ and WC2 electrodes, self-discharge processes may

occur in the cell. The negative plates are most affected by the self-discharge processes as a result of which hydrogen is evolved.

Tests of high-capacity stationary cells with auxiliary catalytic electrodes were conducted at a number of battery plants, but on grounds of certain technical and economical considerations, this method of recombination of hydrogen and oxygen has not found wide practical application in the battery industry.

14.3. Valve-Regulated Lead–Acid Batteries (VRLAB)

14.3.1. General Principles of VRLAB Design and Operation

The general principle of operation of valve-regulated lead–acid batteries can be summarized as follows:

- Water decomposition at the positive plates results in evolution of O_2 and formation of H^+ ions.
- O_2 and H^+ ions diffuse to the negative plates through gas and electrolyte channels in the separator.
- Reaching the negative plates, oxygen is reduced and reacts with hydrogen ions to form water.
- The thus produced water diffuses through the separator to the positive plates, thus restoring the water decomposed by electrolysis.

The above processes form the so-called closed oxygen cycle (COC). The latter reduces substantially the water loss during charge and overcharge of the battery, making it maintenance-free.

There are two basic technologies employed in VRLA batteries depending on the type of separator used and the electrolyte state:

- (1) *Batteries with absorptive glass mat (AGM)*, in which the electrolyte is absorbed by the AGM separator. Absorptive glass mat comprises up to 85% borosilicate glass microfibres with a length of 1–2 mm and 15% polymer fibres (polyethylene, polypropylene, etc.) used as reinforcement binders. The glass fibres are hydrophilic and absorb electrolyte, whereas polymer fibres provide mechanical strength to the separator as well as partial hydrophobicity, which facilitates the formation of gas channels.

At the beginning of operation of this type of VRLA battery, 95% of the AGM pores are filled with electrolyte and the remaining 5% form gas channels along which the oxygen flows between the two plates. With time of cycling, the battery loses water and the saturation of the AGM separator with electrolyte gradually decreases to 90%, then to 85%, etc. Consequently, the efficiency of the COC increases, which, however, is associated with thermal problems and leads eventually to capacity decline.

- (2) *Batteries with gelled electrolyte (gel batteries)*, in which the electrolyte is immobilized in the form of a xotropic gel of SiO_2 and Al_2O_3 particles, several nanometers in diameter. An additional polymer separator, like the ones used in flooded batteries, separates the positive from the negative plates. At the beginning of operation of gel batteries, they behave like flooded batteries (with liquid electrolyte) and lose water. As a result of this water loss, the gel shrinks and cracks are formed in it. These cracks provide open paths for the oxygen evolved at the positive plates to reach the negatives and thus the COC starts to operate, as a result of which the water loss stops. The mechanism of operation of the COC in VRLA batteries is the same, irrespective of the type of separator system used (AGM or gel/separator).

The cells in VRLA batteries have a pressure relief valve (instead of the gas vent in flooded batteries) which sustains a definite pressure in the gas space above the active block comprising plates and separators. The reaction of oxygen reduction at the negative plates significantly reduces the oxygen gas pressure in this part of the active block. A diffusion gradient forms in the active block, which directs the oxygen flow towards the negative plates. The pressure relief valve is, therefore, a mandatory component in the construction of valve-regulated lead–acid batteries.

In this chapter, we will focus our attention mostly on VRLAB with AGM separator. In the 1970s, McClelland and Devitt invented the first valve-regulated lead–acid cell with electrolyte immobilized in microporous glass mat with gas channels in the AGM and a safety valve mounted on the cell lid, and thus forced the COC to proceed within the active block [13]. Figure 14.7 presents a schematic diagram of the transport of oxygen, H^+ ions and water between the two

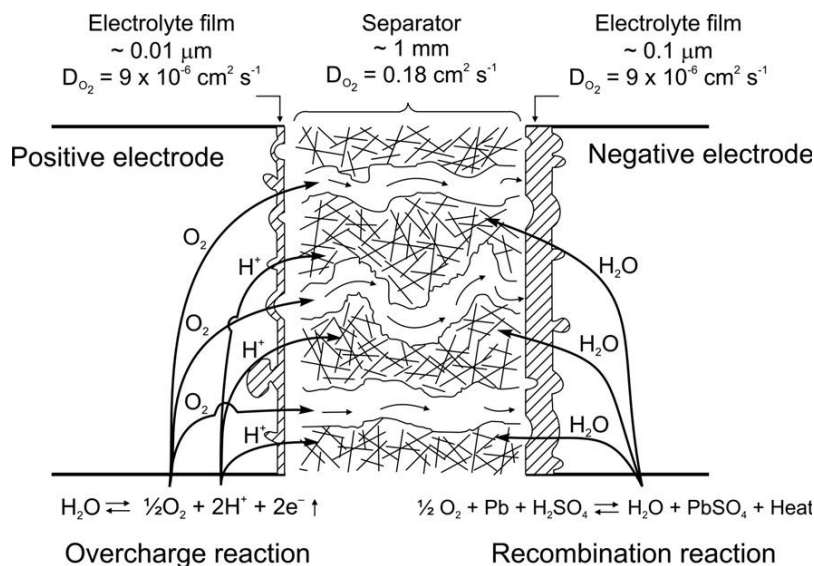


Figure 14.7:

Schematic representation of the internal COC in a valve-regulated lead–acid cell [14].

plates of opposite polarity [14]. The oxygen flows move along two paths: (1) along the open gas channels through the AGM separator and (2) dissolved in the electrolyte, moves along electrolytic channels filling pores of a definite diameter. The diffusion coefficient of oxygen in the gas channels is six orders of magnitude higher than the oxygen diffusion coefficient in the electrolyte. Hence, the flow of oxygen dissolved in the electrolyte is ignored as being negligibly small.

Further, in this chapter we will discuss the processes that occur in a VRLA battery: (a) during charge between 70% and 95% SOC, when the battery is charged and the COC operates; and (b) during overcharge, when the reactions of the COC mostly proceed.

14.3.2. Reactions that Proceed in VRLA Cells During Charge and COC

Figure 14.8 presents schematically the electrochemical reactions involved in the charge process and in the COC in a VRLA cell between 70% and 95% SOC. The reactions are stoichiometric so as to preserve the electroneutrality of the cell. The total cell current I is distributed between the two types of reactions as follows: (1) $(1-\theta)I$ is the current utilized for charging the cell and (2) θI is the current of the reactions involved in the COC. These are the basic processes that take place during cell charging with operating COC. Besides these reactions, the other processes occur as well, at a very low rate are as follows:

- *Positive grid corrosion.* The oxygen evolved on the positive plates penetrates through the interface grid/active material and oxidizes the lead alloy of the positive grid (see Chapter 2.11, p. 91). The rate of this process depends on grid alloy composition, cell temperature, positive plate potential and battery duty.
- *Corrosion of negative plate lugs and connecting strap.* In flooded batteries, these components of the negative active block are wet or partially immersed in electrolyte. This thin

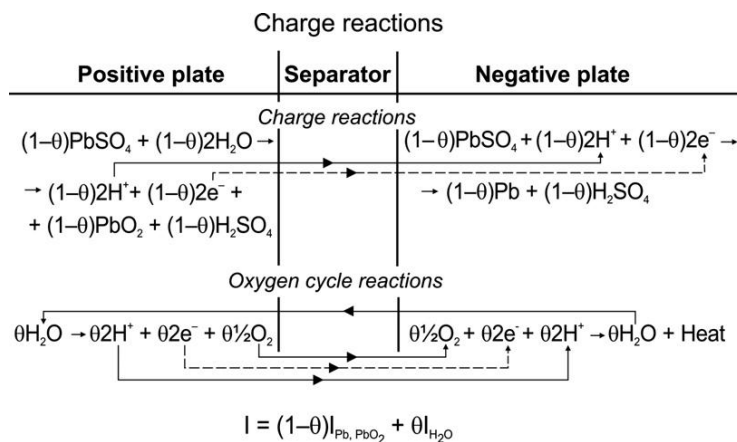


Figure 14.8:

Schematic representation of the electrochemical reactions that proceed in a VRLA cell during charge and those involved in the COC.

electrolyte film is electroconductive, so the potential of these components is close to that of the negative plates, hence the plate lugs and the strap are cathodically protected [15]. In VRLA batteries, the electrolyte is absorbed in the AGM separator and the strap and lugs of the negative plates are exposed to oxygen containing atmosphere, conditions facilitating greatly the corrosion processes. The straps for lead–acid batteries are commonly cast from Pb-0.8/2.5 wt% Sn alloys. A description of the corrosion of VRLAB straps is provided in Chapter 4.6 (p. 199) of this book. The process of strap and plate lug corrosion consumes part of the oxygen that would otherwise take part in the COC, which leads to certain, though minimum, water loss.

- *Oxidation of the organic expander component (lignosulfonate).* When exposed to oxygen attack at temperatures higher than 40 °C, the rate of lignosulfonate disintegration is accelerated considerably, which leads to the formation of CO₂ and H₂O. With time of polarization, the concentration of CO₂ in the gas mixture increases. Part of these gases are vented out to the atmosphere, which results in the loss of oxygen and water.
- *Hydrogen evolution.* Although, theoretically, no hydrogen evolution is expected to occur within the above SOC range (70–95%), and hence the balance of the reactions in Fig. 14.8 should remain unaffected, this is not always the case in practice. There are certain impurities in the grid alloys or in the electrolyte which deposit on the surface of the negative plates forming active centres of lower overpotential of hydrogen evolution. Hence, generation of hydrogen starts in these centres, though, at a low rate. Consequently, the balance of the reactions in Fig. 14.8 is disturbed, which results in (though small) water loss. This effect of hydrogen evolution on the negative plates can be alleviated by its oxidation, even at a low rate, on the positive plates, thus forming a hydrogen cycle [16–18].
- *Reduced electrolyte stratification.* In flooded batteries, gravitation causes the formation of vertical layers of different electrolyte concentration (i.e. electrolyte stratification). This creates potential differences between the top and bottom parts of vertical cells [19] and leads eventually to slow self-discharge processes. In VRLA batteries, the electrolyte is immobilized, which allows the cells to be positioned (mounted) horizontally as well. Thus, the degree of electrolyte stratification is reduced substantially and hence the service life of the cells is extended.

Having made this overview of the processes that occur in VRLA cells during charge, we can distinguish four groups of zonal processes that deserve to be discussed in more detail. These are (a) processes on the positive plates; (b) processes on the negative plates; (c) transport processes through the separator and (d) thermal processes in VRLAB.

14.3.3. Behaviour of the Positive Plates in VRLABs During Charge and Oxygen Cycle

Figure 14.8 presents a scheme of the basic reactions that proceed on the positive plates at between 70% and 95% SOC. It is interesting to disclose the mechanism of these two

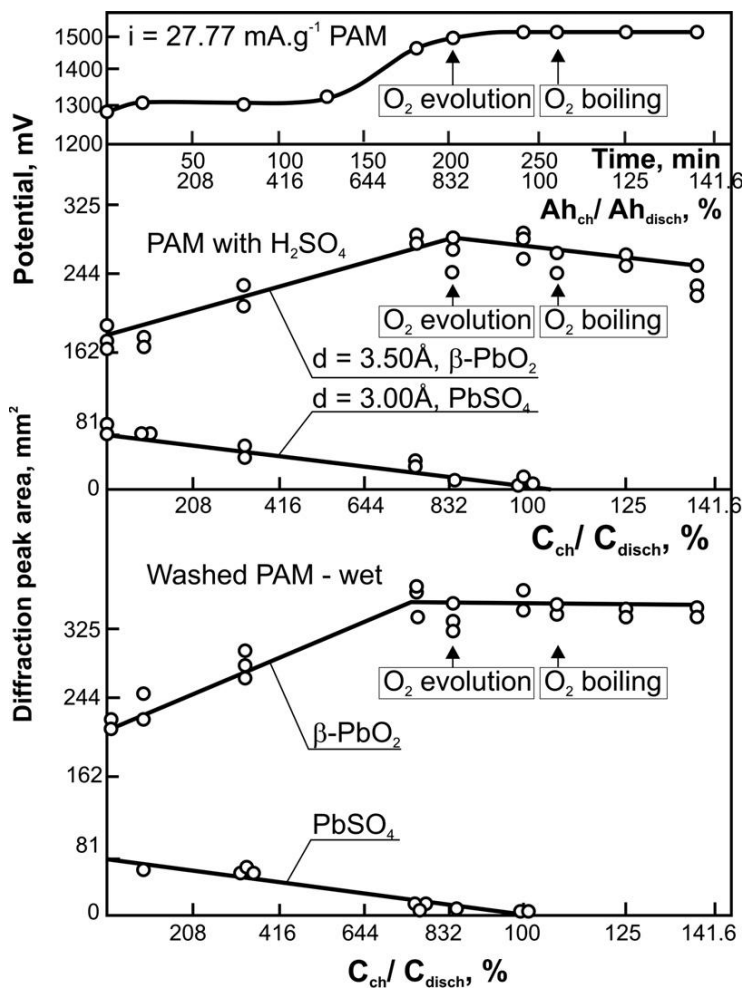


Figure 14.9:

Changes in positive plate potential and in intensity of the diffraction lines for $\beta\text{-PbO}_2$ (3.50 Å) and for $PbSO_4$ (3.00 Å) during charge [20].

types of reactions (charge reactions and COC reactions) and to establish how they are interrelated.

Our research team investigated these processes employing X-ray diffraction analysis in combination with potential measurements of the positive plates vs. $Hg|Hg_2SO_4$ reference electrode [20]. The changes in crystallinity of the lead dioxide active material (PAM) were followed during charge and discharge of cells with one positive and two negative plates. Samples were taken from the positive active material and X-rayed, as taken out of the cell with H_2SO_4 solution on it, and then the solution was washed away with water. Figure 14.9 shows the

changes in positive plate potential and in intensity of the characteristic diffraction lines for β -PbO₂ (3.50 Å) and for PbSO₄ (3.00 Å) during cell charge. The abscissa represents both the real time in minutes and the SOC. The latter is expressed by the ratio between the quantity of electricity that has passed during charge vs. the quantity of electricity obtained during the previous discharge, C_{ch}/C_{disch} .

The following conclusions can be drawn from the data in the figure:

- The PbSO₄ diffraction line intensity decreases linearly with time, the slope being the same for the two types of measurements, up to the 240th minute of charge. This is a period that corresponds to full oxidation of the PbSO₄ formed during the preceding discharge.
- The intensity of the PbO₂ diffraction line changes following Faraday's law, until reaching 65–75% SOC. In this region, a visible evolution of oxygen takes place, and at 108% SOC, oxygen is released vigorously all over the plate surface in the form of 'boiling'. Peters *et al.* [21] have established that at above 70–80% SOC, the charge acceptance decreases in a rather complex manner. Oxygen evolution could be expected to reduce the slope of the curve PbO₂ diffraction line intensity vs. charge time, but this curve should keep rising as PbO₂ formation goes on. Figure 14.9 shows, however, that the intensity of the β -PbO₂ line stops growing. This may mean that, after reaching 65–75% SOC, further charging yields only amorphous PbO₂. That is hardly the case. More probably, oxygen is sorbed both by the newly forming PbO₂ particles and by the already formed ones, and destroys parts of the β -PbO₂ crystal lattice. Oxygen sorption by PbO₂ particles was studied and demonstrated by Ruetschi *et al.* [22] and by Kabanov *et al.* [23].

In the samples with H₂SO₄ solution, the crystal zones of the newly forming PbO₂ particles at 65–75% SOC cannot compensate for the increased amorphization caused by the incorporation of oxygen into the particles formed before the cell reaches 65–75% SOC. In the washed active mass, the two processes are compensated and hence the curve is parallel to the abscissa.

Influence of O₂ on the crystallinity of PbO₂ particles. The charged cell was left on open circuit for 1 h, then a charging current of 5 A was switched on for 40 min and the circuit was open again. Samples were taken all the time and X-rayed when taken out of the cell, still wet with H₂SO₄. The results from these analyses are presented in Fig. 14.10 [20].

When the circuit was open, the electrode (plate) potential decreased, while the intensity of the X-ray diffraction line for PbO₂ increased. On closing the circuit, the intensity decreased again and the potential rose. Since the plate was fully charged, the current was utilized entirely for oxygen evolution. Consequently, the variations in the diffraction line intensities are due to release of oxygen from the PbO₂ particles when the current was switched off and its re-entering the PbO₂ particles, when the current was switched on again. With increase of the amount of oxygen incorporated in the particles, their amorphous zones grow, which leads to increase in electrode polarization, i.e. in active material specific resistance.

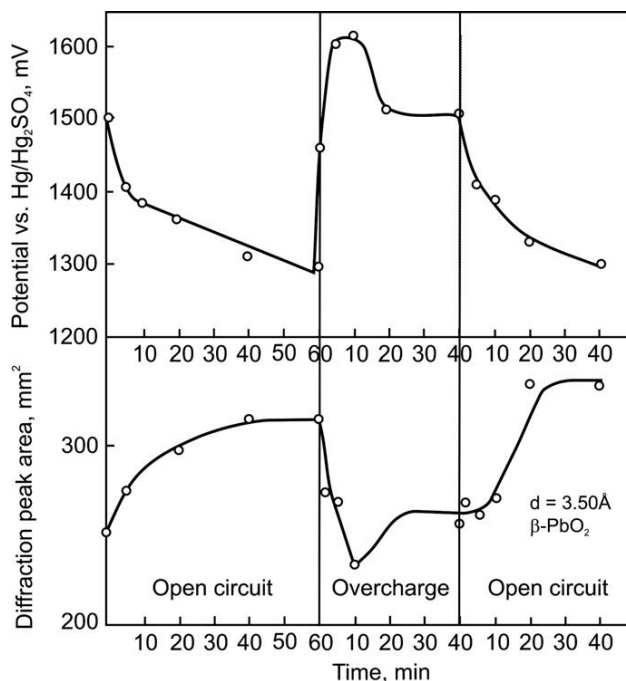


Figure 14.10:

Behaviour of positive plate potential and intensity of the diffraction line for $\beta\text{-PbO}_2$ (3.50 \AA) at open circuit and during overcharge [20].

A mechanism of the reactions of oxygen evolution was proposed in references [24] and [25], and is discussed in more detail in Chapter 2.10.3 (p. 89) of this book.

14.3.4. AGM Separator and Transport Processes Between the Positive and Negative Plates

Structure and functions of the AGM separator

In flooded batteries, the primary function of the microporous separator is to isolate the plates with opposite polarity and prevent electronic contact between them, while at the same time to ensure high ionic conductivity and thus allow ionic flows to move freely between the plates. The AGM separator used in VRLA batteries has a number of additional functions such as the following:

- It absorbs the electrolyte (the third active material in the battery) and thus immobilizes it.
- Provides gas transport channels of relatively large pores for the diffusion of oxygen and thus facilitates the operation of the COC.
- Provides ion transport channels along which ionic fluxes can pass between the two types of plates for the redox reactions to proceed, i.e. ensures high ionic conductivity.

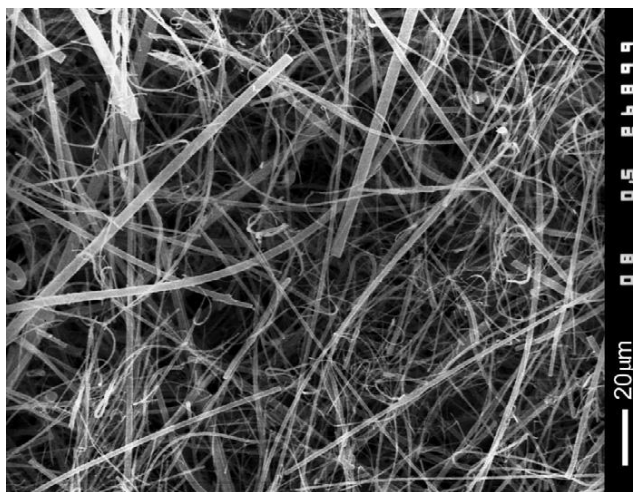


Figure 14.11:
Scanning electron micrograph (SEM) of AGM separator.

- Being under compression in the active block, the AGM separator minimizes the adverse effect of the pulsation of the positive active material on cycling [26], by constraining the expansion of PAM in volume.

Figure 14.11 shows a scanning electron micrograph (SEM) of an AGM separator sample. It comprises fibres of different thickness (fibre diameters from 0.1 to 10 μm) with a length of between 1 and 2 mm, made of chemical grade borosilicate glass. The proportion between the different fibres determines the balance between the different functions of the separator and its price. The fibres are hydrophilic and absorb the electrolyte. Finer fibres (i.e. fibres with smaller diameters) have higher surface and form pores of smaller radii in the separator, but are more expensive. AGM separators contain also between 15 and 18% polymer fibres of polypropylene, polyethylene, etc., which are added to reinforce the mechanical strength of the separator, but also (due to their partial hydrophobicity) to facilitate the formation of gas channels and to reduce the separator price. The AGM separator has an anisotropic structure, which is a result of the technology of its manufacture, similar to the paper making technology. This structure is characterized by pore diameters of between 2 and 4 μm in the x – y plane of the separator sheet and pore sizes of between 10 and 30 μm in the direction perpendicular to the separator x – y plane [27]. The small pores in the x – y plane have the function to distribute the electrolyte across the separator thickness and to sustain the wicking rate when the separator is partially saturated with electrolyte. The large pores form the open gas channels.

Table 14.1 summarizes the effects of fibre diameter on the technical characteristics of the AGM separator [27].

Table 14.1: Influence of fibre diameter on separator characteristics.

Fibre diameter (μm)	0.1	0.5	1.0	2.0	5.0	10.0
Fibre length (m kg^{-1})	4.7×10^{10}	1.9×10^9	4.7×10^8	1.2×10^8	1.9×10^7	4.7×10^6
(m m^{-3})	1.1×10^{13}	4.5×10^{11}	1.1×10^{11}	2.8×10^{10}	4.5×10^9	1.1×10^9
Surface area ($\text{m}^2 \text{kg}^{-1}$)	14 800	2960	1480	741	296	148
($\text{m}^2 \text{m}^{-3}$)	3.5×10^6	7.1×10^5	3.5×10^5	1.8×10^5	7.1×10^4	3.6×10^4
Pore size	\rightarrow		Increasing	\rightarrow		
Tensile strength	\rightarrow		Decreasing	\rightarrow		
Cost	\rightarrow		Decreasing	\rightarrow		

Gas transport through the AGM separator

The transport of oxygen from the positive plates, where it is evolved, to the negative plates, where it is reduced, is realized through the following stages.

First, microbubbles of oxygen are formed in the pores of PAM filled with electrolyte. The microbubbles then coalesce into discrete gas bubbles which gradually displace the electrolyte from the plate pores towards the separator. The separator pores are filled with electrolyte. The gas bubbles reach the plate surface. Small amounts of the oxygen gas dissolve in the electrolyte, the major part of the gaseous oxygen phase remaining in the form of gas bubbles at the interface plate/separator. The AGM separator has a non-homogeneous structure, hence the oxygen gas accumulates at those sites on the AGM surface with lower fibre density (loose structure) or where there are some voids between the separator and the plate (tubular electrodes/AGM).

Percolation of the oxygen gas into the separator is facilitated by more intimate contact between the glass mat surface and the surface of the positive plate. This is achieved by applying compression to the active block. There are two possible mechanisms of this process:

- (1) At low compression of the active block, the gas accumulated at the interface plate/AGM separator will increase in volume. Under the action of gravitation, the gas flow will be directed vertically. The electrolyte has three times higher density than that of the gas, so it will push the gas upwards to the gas space above the active block. Thus, oxygen will leave the active block. The rate of this vertical gas flow depends on the current flowing through the cell, the electrolyte temperature and the service condition of the cell (i.e. new or after long service).
- (2) At high compression of the active block, the separator is pressed tightly against the plate and the gas bubbles enter the separator. They move in the horizontal direction trying to crease gas channels in the separator. The glass mat structure has a non-uniform density and the gas bubbles will penetrate into the zones of lower fibre density. Hence, the gas flow may occasionally move in the direction not only parallel to the separator surface, but also perpendicular to it. However, the primary gas flow direction is through the AGM separator towards the negative plate where the gas pressure is the lowest and

the pressure gradient pushes the oxygen gas flow in this direction. Under this pressure, the gas flow displaces the electrolyte from the separator pores and thus forms gas channels. When these uninterrupted gas channels are formed, the transport of oxygen between the positive and the negative plates is accelerated.

In the manufacture of AGM separator materials for VRLA batteries, the thickness is quoted (measured) under a controlled standard pressure of 10 kPa. To improve the separator contact with the plates, the plate groups (active blocks) are compressed so as to reduce the separator thickness by about 25%. In tall stationary batteries, this compression is sustained by fastening the active blocks (plate groups) with polymer tapes before inserting them into the battery container.

Pore system of the AGM separator

The performance characteristics of a VRLA cell depends greatly on the capillary properties of the AGM separator, i.e. its ability to keep all pores along the separator height filled with electrolyte and to prevent drainage of acid which would lead to electrolyte stratification. These properties of the AGM separator are related to its structure and especially to the pore size distribution. A comprehensive study of the structure of AGM separators was performed by Culpin [28]. He conducted wicking measurements of AGM separators made of a mixture of fine and coarse glass fibres. Strips of these separators were held vertically with their lower ends immersed in H₂SO₄ solution of 1.28 rel. dens. and the time of electrolyte wicking to different heights was measured. The wicking rates (height/wicking time) for AGM separators containing 0%, 10%, 50% or 100% fine fibres are presented in Fig. 14.12.

A well-pronounced linear relationship is observed. By employing Washburn equation and subsequent theoretical processing, Culpin came to the Laplace equation:

$$P = \frac{2\gamma \cos \theta}{r} \quad (14.9)$$

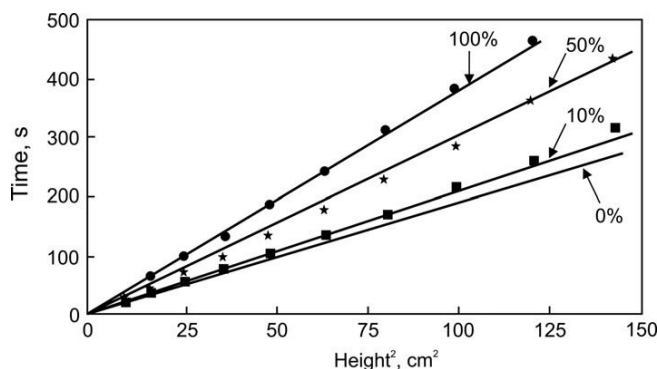


Figure 14.12:

Effect of fibre mix on wicking characteristics; percentage of fine fibres as shown [28].

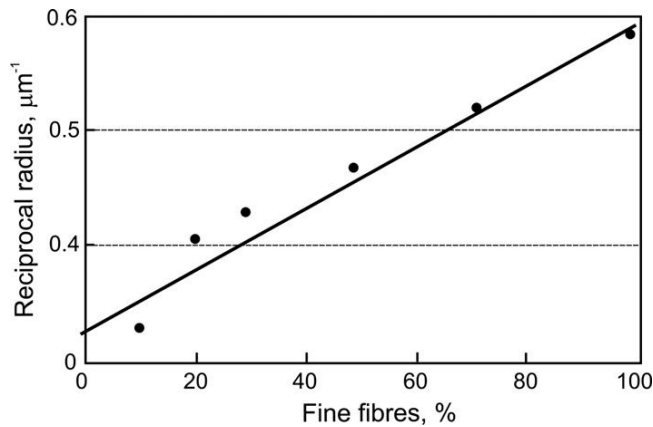


Figure 14.13:
Effect of fibre mix on capillary pressure [28].

where P is the capillary pressure, r is the pore radius, γ is the interfacial tension and θ is the contact angle. Figure 14.13 shows the relationship between the reciprocal pore radius and the percent content of fine fibres (diameter $< 1 \mu\text{m}$) in the AGM mix. This dependence indicates that there is a linear relationship between capillary pressure and fibre size in a two-component AGM mix. Thus, by altering the proportion between fine and coarse fibres in the mix it is possible to produce AGM material of pre-defined pore size structure.

Figure 14.14a shows the pore size distribution by diameter for an AGM separator sample, as obtained by low-pressure intrusion methods [29].

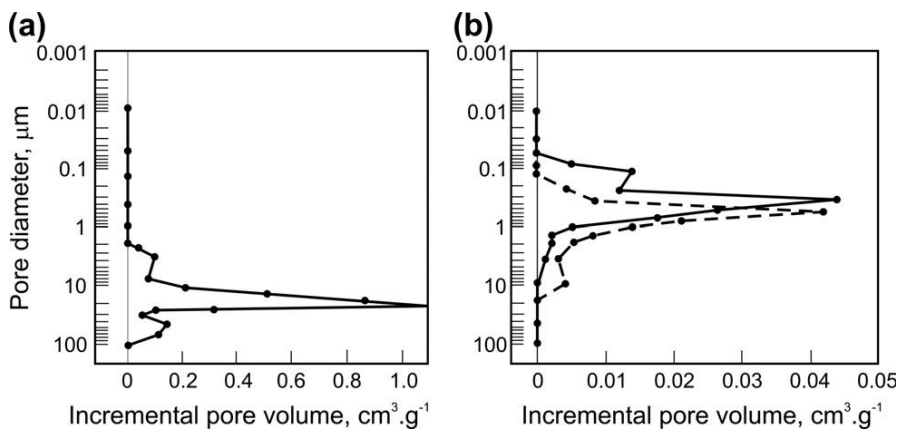


Figure 14.14:
Pore size distribution in (a) glass microfibre separator; (b) (---) positive and (—) negative active materials [29].

As evident from Fig. 14.14a, about 90% of the pore volume consists of pores with diameters between 10 and 24 μm . These are mainly pores in the z plane. About 5% of the large pores have diameters within the range from 30 to 100 μm , and a small percentage of the pores are $< 10 \mu\text{m}$ in diameter. In the VRLA cell, the pore system of the AGM separator is in close contact with the pore systems of the two types of plates. The pore size distribution by diameter for positive and negative active materials is presented in Fig. 14.14b [29]. But there are small differences in pore size distribution between the two plates. For new, fully formed plates, 80% of the porosity of the active materials is due to pores with diameters smaller than 1 μm . These are values considerably lower than the median pore diameter of the AGM separator. Within a compressed active block, the AGM separator is pressed against the plates, thus an intimate contact is ensured between the two surfaces. After the cell is evacuated, it is filled with electrolyte, the latter being absorbed first in the plate pores and then in the separator. The AGM separator should be 96% saturated with electrolyte according to the technological specification.

When the plates start gassing, the electrolyte is pushed out of the plate pores and is readily absorbed into the pores of the separator, thus the latter is fully saturated. On switching off the current, the gas leaves the plate pores and electrolyte is re-absorbed in these pores from the separator. Thus, only the largest diameter pores in the AGM separator remain empty, while the plate pores are again filled with electrolyte. So the parameter 'electrolyte saturation' holds mainly for the AGM separator.

Figure 14.15 shows the changes in volume porosity of an AGM sample with a basic weight of 225 g m^{-2} , as a function of applied pressure (up to 138 kPa). Porosity is defined as the ratio (as a percentage) of void volume to total volume of AGM [30].

The AGM porosity changes insignificantly under the action of the above pressure. The battery container should have very thick walls to resist to such a high pressure. Hence, the volume porosity is affected but slightly by the pressure applied on the x – y separator plane [30].

Why does pressure exert such a small effect on separator porosity? The glass mat structure comprises fibres lying at random, but predominantly in the x – y plane of the AGM sheet, with

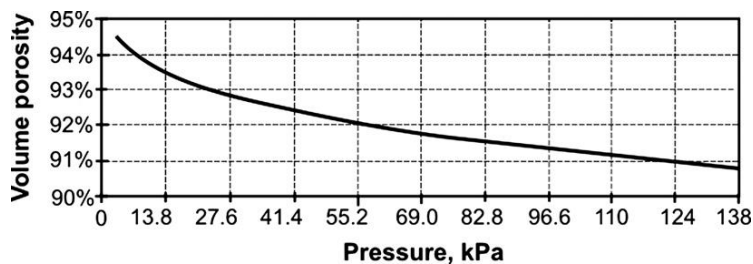


Figure 14.15:
Separator porosity as a function of pressure [30].

the largest pores in the z -direction perpendicular to the x - y plane. Compression of the sheet would be expected to have weak effect on pore size in the z -direction. This was actually confirmed by Culpin in reference [28]. This is not the case, however, with the pore size in the x - y direction. These pores change significantly under pressure. Thus, a 15% compression yields a 50% reduction in pore diameter [31].

Critical gas pressure for electrolyte displacement from the AGM pores

In VRLA batteries, reduction of oxygen at the negative plates is a diffusion controlled process and depends on the degree of electrolyte saturation of the AGM separator. Because of the high gas/liquid interfacial tension, the contact area of the glass fibres with the gas phase should be very small. Hence, the pores with small diameter (i.e. with large surface) will be filled with electrolyte first at the expense of the larger pores. With increase of the AGM saturation, the larger pores are filled with electrolyte, too. At 90% saturation, the largest separator pores are full and the remaining 10% of gas form separate bubbles in the AGM which do not play a notable role in the transport of oxygen through the separator [29]. Consequently, oxygen diffusion proceeds through the liquid and the diffusion flow is small. At 60% saturation, oxygen diffuses through the gas phase and the oxygen cycle operates at a rate three orders of magnitude higher than that at 90% saturation. The situation is different in a compressed active block, where the evolved oxygen gas has a greater volume than that of the water which produced it and, hence, a gas pressure is created in the separator pores, which grows when electric current flows through the cell until a critical pressure is reached, which displaces the electrolyte from the larger pores and open gas channels form between the positive and the negative plates. If we assume that the pores in the separator are cylindrical, with a contact angle of the H_2SO_4 electrolyte on glass equal to zero, then movement of the gas in the pores will start

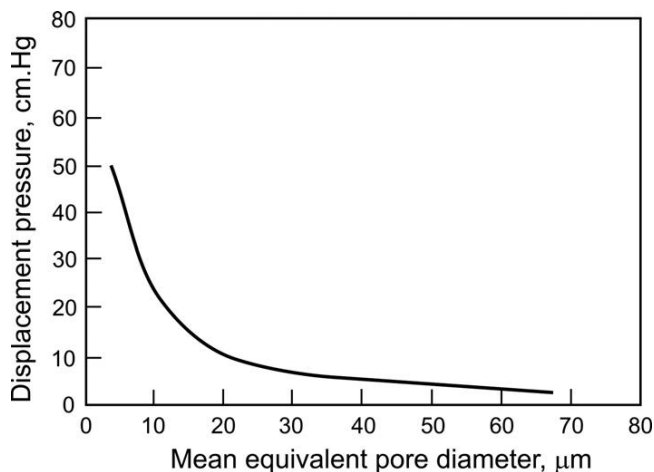


Figure 14.16:
Critical displacement pressure vs. mean pore diameter [29].

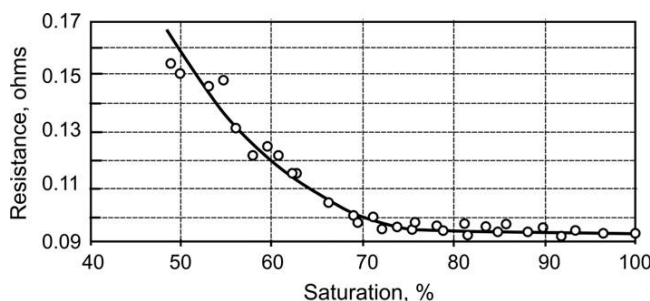


Figure 14.17:

Cell internal resistance as a function of separator saturation (H_2SO_4 density 1.28 g ml^{-1}) [30].

when the pressure at the separator surface becomes greater than the capillary pressure (see Eq. 14.7). The critical pressure required to displace electrolyte for different pore diameters, at a surface tension of $\gamma = 75 \text{ dyne cm}^{-1}$, is shown in Fig. 14.16 [29].

For AGM with high electrolyte saturation, a capillary pressure of 9 cm Hg (1.8 psi) is needed for the gas to flow through pores of $20 \text{ }\mu\text{m}$ diameter and a higher pressure is required to displace the electrolyte from the smaller pores.

It follows from all above said that the separator saturation with electrolyte exerts a very strong influence on the rate and efficiency of the COC in VRLA batteries.

AGM separator saturation and electrical resistance of the VRLA cell

It can be generally assumed that, during operation of the VRLA cell, electrolytic and gas channels form in the microporous AGM separator. The electric current is carried by ionic flows moving along the electrolytic channels. Therefore, the ratio between the two types of channels in the separator exerts a strong influence on the electrical resistance of the cell and hence on its discharge power. The proportion of electrolytic and gas channels in the AGM separator depends on its saturation with electrolyte. It is interesting to determine the saturation level below where the cell resistance increases. Figure 14.17 shows this relationship as obtained by Crouch and Reitz [3] with the help of a 1 kHz impedance bridge. A pressure of 10 kPa was applied to the active block.

The curve in the figure shows that down to 80% saturation of the AGM, the resistance remains constant and low. At saturations below 80%, it increases rapidly to reach a 40% higher value at 60% saturation than that at 80% saturation level.

The transition point to higher resistance depends on the diameter of the fibres in the AGM (which affects the median radius and the surface of the pores), on the pressure applied to the active block and on the separator thickness. It has been established that 1.5 mm thick AGM separator absorbed with H_2SO_4 electrolyte of 1.28 rel. dens. has a specific resistance of $20 \text{ m}\Omega\cdot\text{cm}^2$ [30]. This is a relatively low resistance.

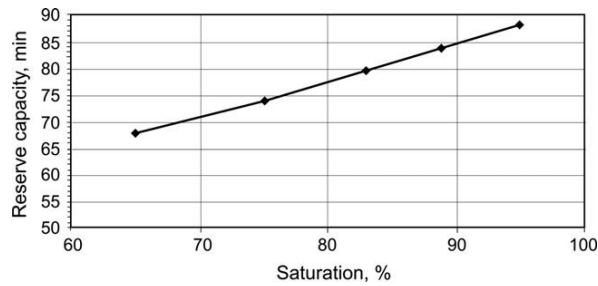


Figure 14.18:

Effect of cell saturation on reserve capacity at 25 A [32].

Correlation between cell saturation with electrolyte and its capacity and electrical characteristics

Valve-regulated lead–acid batteries operate under conditions of slight deficiency of H_2SO_4 electrolyte as a result of which, on deep discharge, the concentration of the H_2SO_4 in the plate pores drops down to very low values and thus it may become the capacity limiting active material. In an attempt to compensate partially for the H_2SO_4 shortage, many VRLA battery manufacturers use H_2SO_4 solutions with concentrations higher than 1.28 rel. dens. Elevated H_2SO_4 concentrations, however, cause passivation of the positive plates and capacity decline. It is therefore not recommended.

On the other hand, saturation affects the electrical resistance of the cell, i.e. the influence of discharge current on cell capacity increases.

Figure 14.18 illustrates the effect of cell saturation on its reserve capacity on discharge with a current of 25 A [32]. The reserve capacity is a linear function of saturation at low discharge currents.

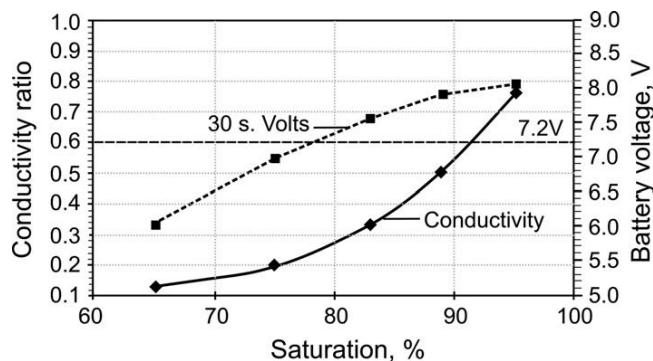


Figure 14.19:

Effect of saturation on high rate capacity. Notes: Results are for a 12 V battery. Conductivity ratio is the battery conductivity compared to the conductivity at 100% saturation. The 30 s voltage refers to the battery discharged at the rated cold cranking current at -18°C . After 30 s on discharge the requirement is that the battery voltage be in excess of 7.2 V [32].

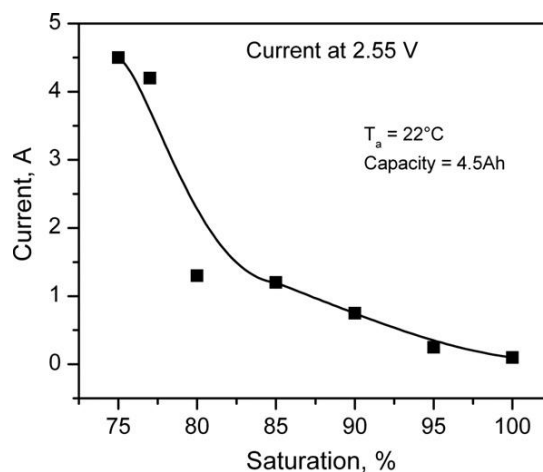


Figure 14.20:

The steady state currents at 2.55 V, $T_a = 22^\circ\text{C}$, at different saturations [33].

Figure 14.19 shows the relationship between battery voltage at the 30th s of discharge with the rated cold cranking current at -18°C [32]. The requirement is that the battery voltage should be in excess of 7.2 V. The obtained results show that this requirement is met down to 78% cell saturation. Another finding is that the dependence of the 30th s voltage on saturation is not a linear relationship for discharge at low temperatures and high currents. This behaviour of the battery may be related to its conductivity as a function of saturation. The conductivity is represented in Fig. 14.19 as a ratio between the battery conductivity at a given saturation to the conductivity at 100% saturation. The data in the figure indicate also that, above 78% saturation, the battery conductivity increases and so does its voltage.

Figure 14.20 presents the changes in cell current at 2.55 V as a function of saturation at 22°C [33].

At this voltage and at saturations higher than 80%, the cell current increases by 3.5 A with 10% decrease in cell saturation. When the saturation drops below 80%, the current rises rapidly, probably, because new gas channels are opened between the positive and negative plates, facilitating oxygen diffusion to the negative plates where it is electrochemically reduced. In order to verify this conjecture, volt-ampere tests of model 4.5 Ah cells with saturations between 75% and 77% were conducted at 22°C . The obtained results are presented in Fig. 14.21 [33].

Up to 2.45 V, a relatively low current flows through the cell. At 2.48 V, the current increases abruptly. This is obviously related to the onset of oxygen evolution at the positive plates and its diffusion to the negatives along available free gas channels in the AGM separator at 75–77% saturation. For this high current to flow through the cell, besides the rate of oxygen transport between the two plates, another important parameter is the transport of H^+ ions along the electrolytic channels between the plates (Fig. 14.8).

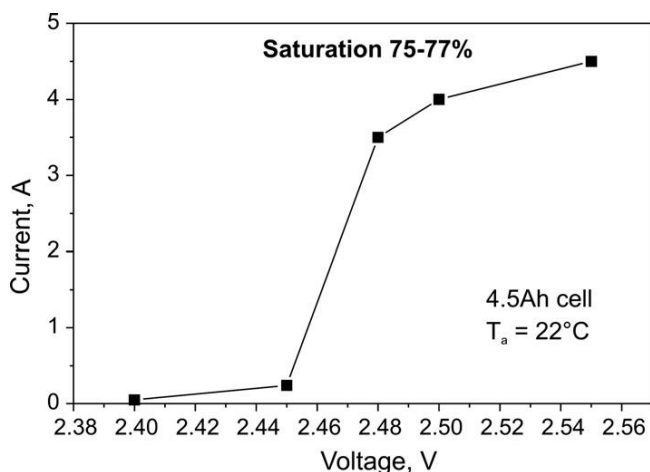


Figure 14.21:

Cell current vs. applied voltage for 4.5 Ah cells with 75–77% saturation polarized at 22°C [33].

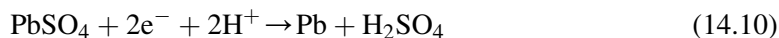
The experimental data in Fig. 14.21 indicate that the diffusion of hydrogen ions does not impede the operation of the oxygen cycle. Due to the high mobility of H^+ ions, even the reduced number of electrolytic channels (75%) suffice to sustain high rate of the electrochemical reaction of oxygen reduction.

Having reviewed the transfer of oxygen and hydrogen ions between the positive and negative plates, let us now discuss the processes of reduction of oxygen at the negative plates.

14.3.5. Charge Processes at the Negative Plates of VRLA Batteries and COC

General picture of the processes of charge, overcharge and COC at the negative plates of VRLABs

During charge of a VRLA battery, the only reaction that proceeds at the negative plates, up to 70% SOC of the battery, is the charge reaction (Fig. 14.8):



Within this SOC region, only one electrode system, $Pb|PbSO_4|H_2SO_4$, is operating. The behaviour of this electrode was discussed in Chapter 2.3 (p. 47) of this book.

When the SOC of the valve-regulated lead–acid battery exceeds 70%, a reaction of water decomposition with evolution of oxygen starts at the positive plates, parallel to the basic charge reaction: $PbSO_4 \rightarrow PbO_2$. The evolved oxygen passes through gas channels in the AGM separator reaching the negative plates where it is reduced via two reactions:





Thus, a second electrochemical system, $\text{O}_2|\text{H}_2\text{O}$, forms at the negative plate (Fig. 14.8). This system will affect both the potential of the plates and the charge processes that take place there.

When the SOC of the negative plates reaches 92–95%, a reaction of hydrogen evolution starts on the lead surface, i.e. a third electrode system forms.



The behaviour of the hydrogen electrode on polarization of the lead surface was discussed in Chapter 2.4 (p. 56) of this book.

When the plates are fully charged, operation of the first electrode system stops and the processes of oxygen reduction and hydrogen evolution start at different rates. So, during charge of a VRLA cell, from one to three electrode systems are operating, depending on the SOC of the cell.

Oxidation of hydrogen at the positive plates is a slow process. The evolved hydrogen remains in the cell and causes the gas pressure above the active block to increase, thus retarding the oxygen reaction. When the gas pressure exceeds a certain critical value, the cell valve opens and lets the gas mixture of hydrogen and oxygen out to the surrounding atmosphere. The cell loses water. The amount of vented out gas mixture depends on the voltage applied to the cell or on the charging current.

Thermal phenomena during operation of the COC

Let us examine the phenomena that occur during constant voltage polarization at 2.40 V of a partially charged VRLA cell [34]. Figure 14.22 presents a full picture of the changes in all six measured parameters (current, cell voltage, positive and negative plate potentials, temperature and gassing rate). After 1 h of polarization, the potential of the positive plates passes through a small maximum, while that of the negative plates passes through a small minimum.

During this A period, the cell is charged and when the positive plate potential, φ^+ , reaches its maximum, a reaction of oxygen evolution starts. With increase of the quantity of electricity charged into the cell, the latter is fully charged and the rate of oxygen evolution increases. This leads first to the formation of gas bubbles in the positive active material and in the AGM separator, while at the negative plates, reactions of hydrogen evolution and of partial reduction of oxygen start.

After 2.5 h of polarization, open gas channels form between the positive and the negative plates, and the COC becomes the dominating process. The oxygen reaction is accelerated and hence the cell current starts to increase. The heat released by the reactions of oxygen reduction causes the cell temperature to rise. The potential of the positive plates decreases, while that of negatives increases. Besides the reduction of oxygen, hydrogen is also evolved at the negative plates. The reaction of oxygen reduction produces more heat and the temperature in the cell increases further.

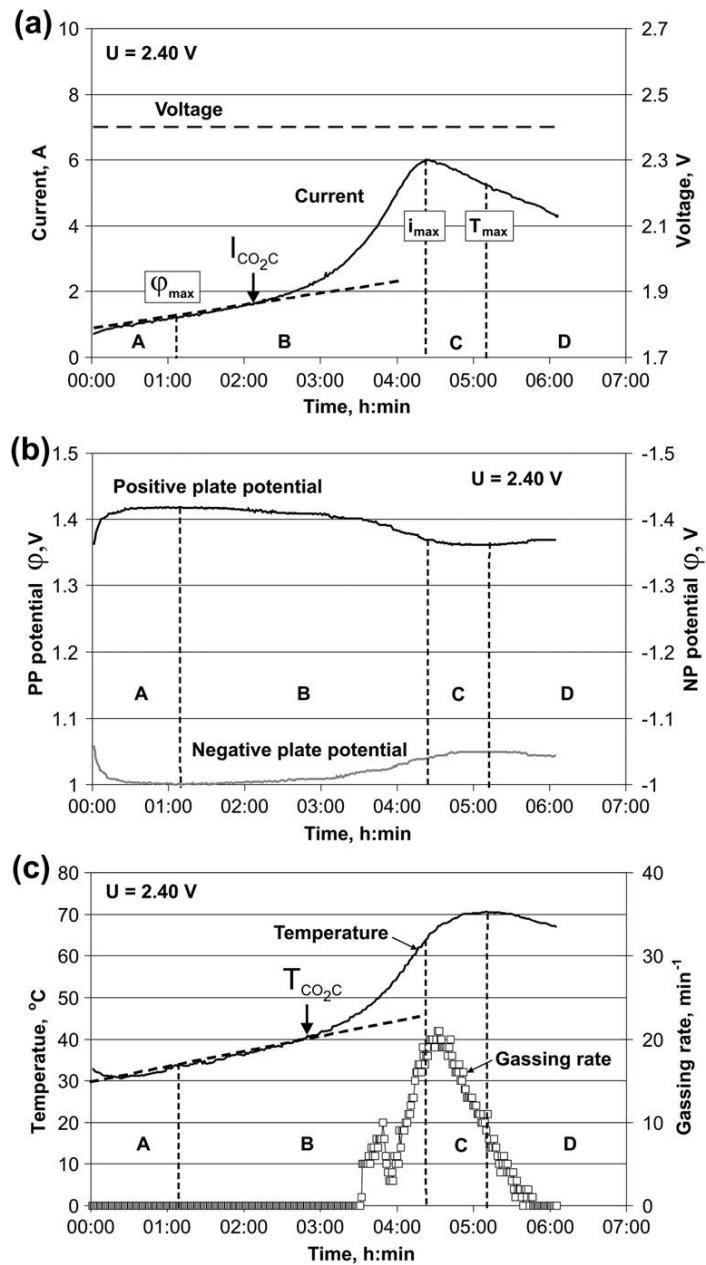


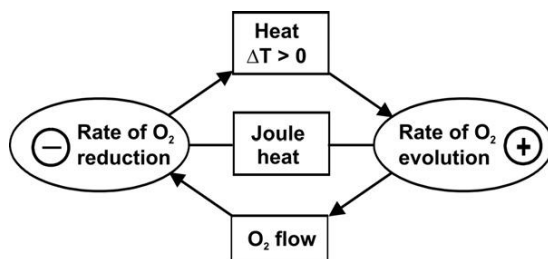
Figure 14.22:

Polarization of a VRLA cell at 2.40 V. The thermal runaway (TRA) phenomenon is manifested by changes in (a) current and voltage; (b) positive and negative plate potentials; (c) cell temperature and gassing rate [34].

The oxygen evolved at the positive plates is not entirely reduced at the negatives and, together with the evolved hydrogen, it causes the gas pressure in the cell to rise until, after 3.5 h of polarization, the cell valve opens and lets the gases out, i.e. the cell starts gassing. Part of the heat generated by the reactions in the cell is carried away with the vented gas flow to the surrounding atmosphere. The elevated temperature in the cell creates a temperature gradient between the cell and the surrounding medium, and the heat dissipates out of the cell to the surroundings. When higher current flows through the cell more Joule heat is produced, which is the second source of increased heat generation in the cell. With increase of the temperature in the cell, the latter's heat exchange with the surroundings is intensified. At higher temperatures, the overpotential of oxygen evolution is reduced and hence the latter reaction is accelerated. However, the oxygen flow to the negative plates is limited by the capacity of the gas channels in the AGM separator to transfer this flow. Consequently, non-recombined hydrogen and oxygen gases leave the cell. The rate of oxygen reduction is retarded and the cell current reaches a maximum. The temperature rise continues for some more time due to the heat generated by the Joule effects and by the reactions at the negative plates, but it is accompanied by intense heat release from the cell. The accelerated reaction of water decomposition at the positive plates causes the concentration of the H_2SO_4 electrolyte in and near these plates to increase, which leads to their partial passivation. The rate of the oxygen evolution reaction is retarded, the cell current decreases and so does the gassing rate, too. The cell temperature passes through a maximum and begins to decrease thereafter. This slows down the reduction of oxygen and hence less heat is generated by this reaction. The cell tends to reach a steady state at which the amount of heat generated in the cell becomes equal to the heat dissipated to the surroundings and thus the cell temperature and cell current remain constant.

Figure 14.22 indicates that there exists a correlation between cell current and temperature. The heat generated in the cell causes its temperature to rise, which lowers the overpotential of oxygen evolution and thus accelerates this reaction. The higher temperature increases the rate of the oxygen transport to the negative plates and consequently the rate of the oxygen reduction at the negatives, too. The latter reaction generates more heat, which causes the cell temperature to rise further. Thus, during the period between $I_{\text{CO}_2\text{O}}$ and T_{max} (Fig. 14.22), there is a self-accelerating interrelation between the reactions of the oxygen cycle, as illustrated in Fig. 14.23 [35]. This phenomenon was called 'thermal runaway'.

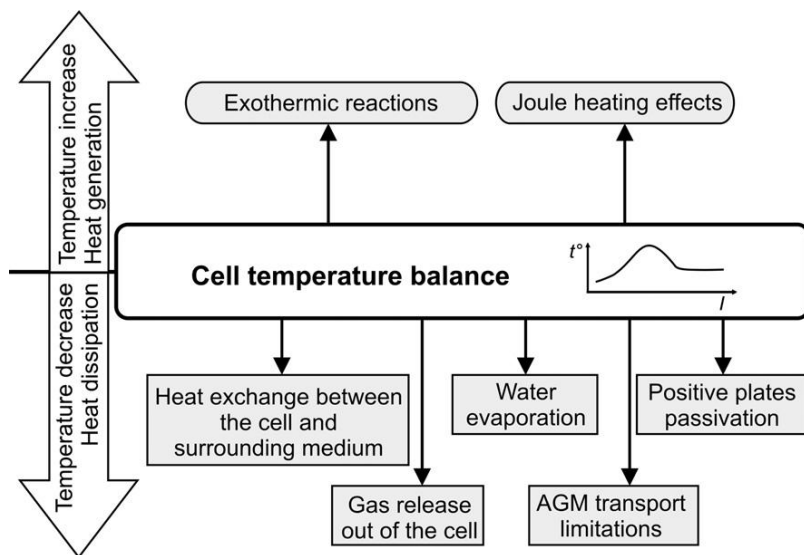
A general picture of the thermal phenomena responsible for changes in cell temperature during operation of the COC is presented in Fig. 14.24. The figure shows the processes which cause temperature rise and those which reduce the temperature in the cell. These processes are in dynamic state. At the beginning of cell polarization, the phenomena causing the temperature to increase (i.e. exothermic reactions, Joule effects) are predominating, as a result of which the cell temperature rises rapidly. However, the elevated temperature and the high cell current intensify the heat exchange of the cell with the surrounding medium, the gassing rate increases

**Figure 14.23:**

Schematic representation of the processes at the two electrodes which are in positive (self-accelerating) interrelation.

and so does the rate of water evaporation, etc. Thus the thermal effects of the two types of processes begin to compensate each other and, after a certain period of time, the cell gets into a steady state.

The maximum temperature of normal operation of a lead–acid battery is 60 °C. Above this temperature, the rates of expander decomposition in the negative plates and of grid corrosion in the positives increase significantly. The evaporation of water from the cell is also accelerated. It is therefore essential that operation of the COC should not lead to thermal runaway with temperature rise above the upper limit value of 60 °C.

**Figure 14.24:**

A general scheme of the phenomena responsible for changes in cell temperature during operation of the COC.

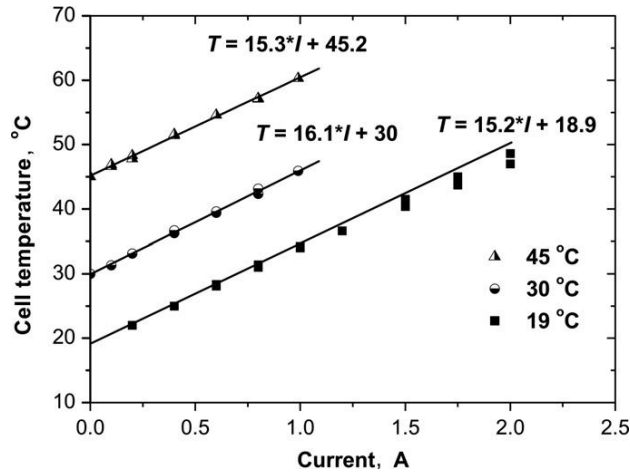


Figure 14.25:

Cell temperature as a function of applied current at quasi-steady state conditions under free air convection [36].

A series of galvanostatic polarization experiments with stepwise increase of the current were performed aimed to determine the quasi-stationary characteristics of the system at each current step [36]. In order to evaluate the heat exchange between the cell and the surrounding medium, the latter was sustained constant. The T vs. I dependences were studied at three ambient temperatures: 19 °C, 30 °C and 45 °C. The obtained results are presented in Fig. 14.25 [36].

The experimental data in the figure show that the cell temperature is a linear function of applied current

$$T = T_0 + b I \quad (14.14)$$

Where T_0 is the temperature of the cell at $I = 0$ (for our experiments it corresponds to the ambient temperature, $T_0 = T_a$) and b is the slope of the curve. The slopes of the three straight lines are almost the same: $b = 15.2 \text{ KA}^{-1}$, 16.1 KA^{-1} and 15.3 KA^{-1} at 19 °C, 30 °C and 45 °C, respectively. The very close values of b for the three experiments indicate that the mechanism of heat generation within the cell does not change and the temperature rise is a direct result of current increase.

The temperature rise with increase of the applied current within the period marked with B in Fig. 14.22 depends on (a) ambient temperature, (b) applied cell voltage, (c) AGM separator type (it determines the maximum oxygen flow that can be transferred between the plates) and (d) cell container design and material (they determine the heat transfer coefficient of the cell). By appropriate selection of the above parameters the temperature rise during operation of the COC can be limited to 60 °C.

Types of currents flowing between the positive and negative plate in a VRLA cell

The above described general picture of the processes that occur at the positive and negative plates of a VRLA cell would not be complete if the processes of positive grid corrosion are omitted.

During overcharge of a VRLA cell, the oxygen evolved by the electrochemical reaction at the positive plates is distributed as follows: the major part of this oxygen diffuses to the negative plates and is reduced there, another part oxidizes the grids of the positive plates and a third part is vented out of the cell. In each electrochemical system, the sum of the rates of the cathodic reactions should be equal to the sum of the anodic reaction rates, in order to preserve the electroneutrality of the cell. Under the above conditions, the following currents will flow through the VRLA cell:

$$[i_{O_2} - i_{gc} - i_{O_{2out}} + i_{H_2CHC} + i_{H_{2out}}]^+ = [i_{O_2R} + i_{H_2}]^- \quad (14.15)$$

where i_{gc} is the current generated by the grid corrosion reaction, i_{H_2CHC} is the current of hydrogen oxidation at the positive plates, i_{O_2R} is the current of oxygen reduction at the negative plates.

The conditions of cell polarization can be selected so that no oxygen nor hydrogen would leave the cell, i.e. $i_{O_{2out}} = 0$ and $i_{H_{2out}} = 0$. In this case:

$$[i_{O_2} - i_{gc} + i_{H_2CHC}]^+ = [i_{O_2R} + i_{H_2}]^- \quad (14.16)$$

Evolution of hydrogen can be suppressed by addition of appropriate inhibitors to the negative active material. Then, the amount of water lost will be equal to the amount of oxygen involved in the corrosion reaction. Since the corrosion current is too low, VRLA batteries will need no maintenance for years of service.

Mechanism of the oxygen reduction at the negative plates

(a) *Electrochemical mechanism of O_2 reduction (Fig. 14.26)*

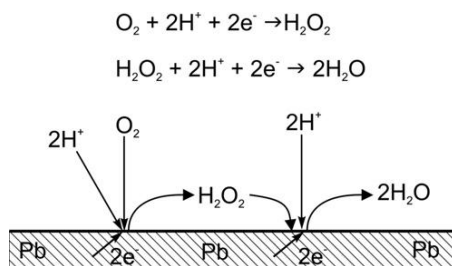
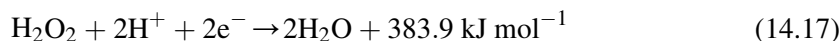


Figure 14.26:

Schematic representation of the electrochemical reactions of oxygen reduction with formation of hydrogen peroxide as an intermediate product.

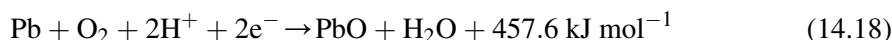
It has been established that reduction of oxygen on the lead electrode surface proceeds in two stages, whereby hydrogen peroxide is formed as an intermediate product. The reactions involved in this mechanism are electrochemical and can be represented by the following equations:



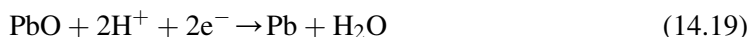
In this mechanism, the lead surface plays the role of a source of electrons. The reaction is exothermic and significant amount of heat is generated. The end product of the above two reactions is water, which diffuses to the positive plates.

(b) *Reduction of oxygen with formation of PbO as an intermediate product (Fig. 14.27)*

Lead is readily oxidized (via a chemical reaction) by atmospheric oxygen in humid medium. The lead electrode surface is negatively charged and there are negligible concentrations of SO_4^{2-} ions, or none at all, on this surface. Hence, a chemical reaction of Pb oxidation proceeds, involving one atom of the oxygen molecule, while the other atom participates in an electrochemical reaction of reduction.



Since the electrode surface on which the above reaction proceeds is highly cathodically polarized, the PbO formed is reduced to lead through an electrochemical reaction:



Thus, PbO is an intermediate product formed by a chemical reaction of oxygen reduction, which is then reduced to Pb through an electrochemical reaction. If we sum up the two reactions, we will see that the water decomposed to evolve oxygen at the positive plates is restored at the negative plates via reactions of different nature.

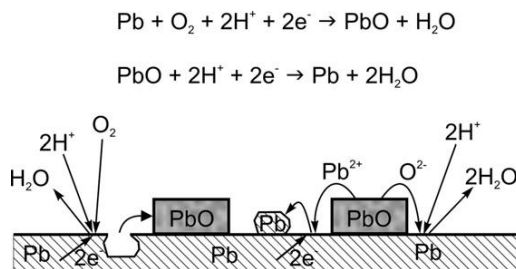


Figure 14.27:

Schematic representation of the reactions of oxygen reduction with oxidation of lead and formation of PbO as an intermediate product.

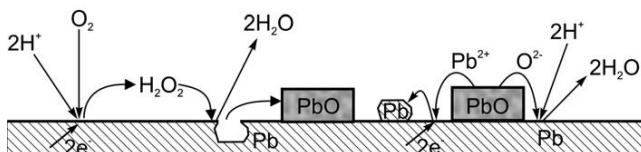
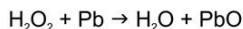
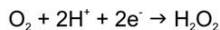
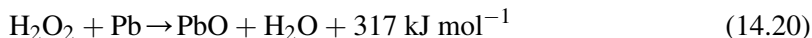


Figure 14.28:

Schematic representation of the reactions of oxygen reduction with formation of H_2O_2 and PbO as intermediate products.

(c) *Reduction of oxygen with formation of H_2O_2 and PbO as intermediate products (Fig. 14.28)*

In this mechanism, the electrochemical reaction of H_2O_2 formation (reaction 14.11) proceeds first on the lead surface. Hydrogen peroxide is a strong oxidant and oxidizes the lead surface via the following chemical reaction:



On the cathodically polarized surface, PbO is readily reduced to Pb via the electrochemical reaction (14.19) as a result of which water is formed, too.

(d) *Reduction of oxygen with formation of H_2O_2 , PbO and PbSO_4 as intermediate products (Fig. 14.29)*

In this mechanism, the hydrogen peroxide formed by the electrochemical reaction oxidizes the lead surface first via the chemical reaction (14.20) yielding PbO . If, for

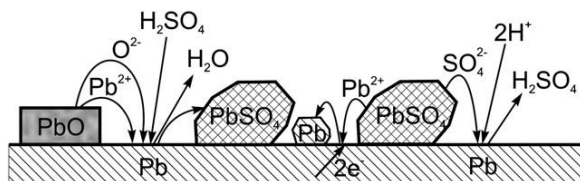
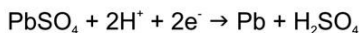
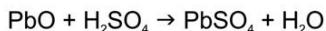
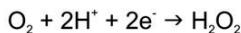


Figure 14.29:

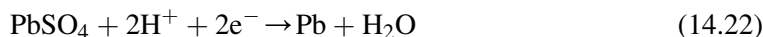
Schematic representation of the reactions of oxygen reduction with formation of H_2O_2 , PbO and PbSO_4 as intermediate products.

some reason, there is H_2SO_4 on the lead surface, it reacts with PbO according to the reaction



The above reaction is in competition with the electrochemical reaction (14.19).

The lead sulfate formed on the highly cathodically polarized surface will be reduced to Pb via the reaction



So, reduction of oxygen at the lead surface may proceed via four different mechanisms involving different chemical reactions. Which of these mechanisms will be the dominating one(s) depends on the local conditions in the pores of the negative active material: ion concentration, pH of the solution filling the pores, temperature and gas phase pressure.

All above mechanisms have one process in common, namely the oxygen molecules have to reach the lead surface. And the latter is covered by a thin liquid film. The processes that occur during the transport of oxygen molecules through the liquid film and the latter's behaviour have been studied by Kirchev *et al.* [37]. A schematic representation of a cross-section through a pore in the negative active material is presented in Fig. 14.30.

The surface of the lead particles surrounding the pore is covered by a thin liquid film in which the oxygen molecules have to dissolve and diffuse to the lead surface, where they are

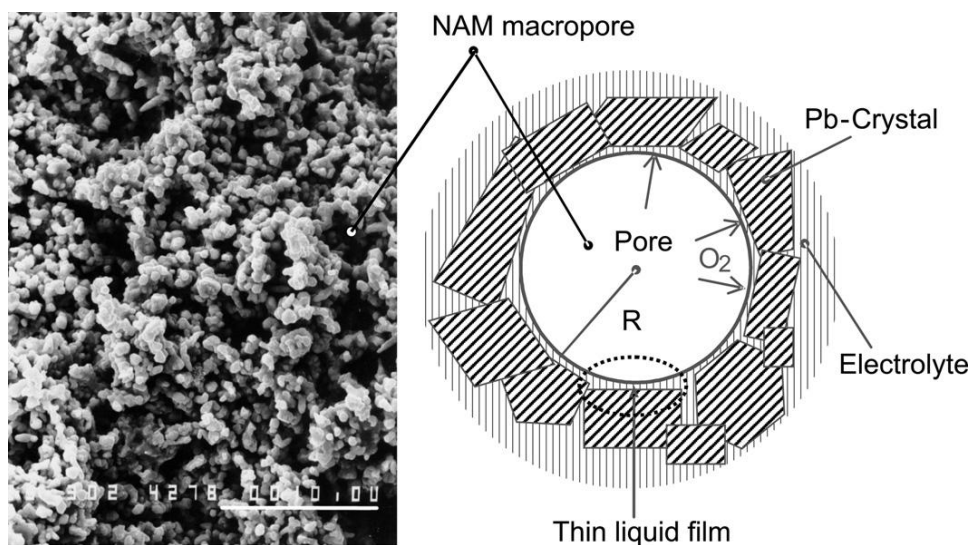


Figure 14.30:

Micrograph of an open gas pore in NAM and a scheme of the cross-section through the NAM pore [37].

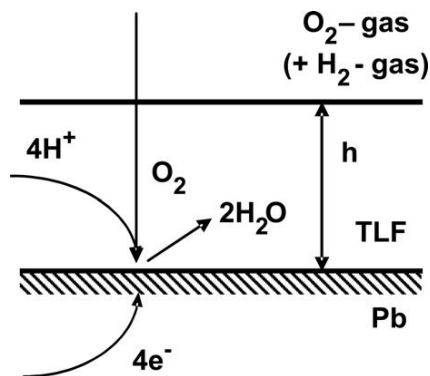


Figure 14.31:

Schematic representation of the electrochemical mechanism of oxygen reduction in active centres at the phase boundary metal/thin liquid film (see point (a) in Section “Mechanism of the oxygen reduction at the negative plates” chapter) [37].

reduced via one of the above discussed mechanisms. The diffusion coefficient of O_2 in the solution is within the range $1/2 \times 10^{-5} \text{ cm}^2 \text{ s}^{-1}$, depending on the acid concentration.

Figure 14.31 shows a scheme of the electrochemical mechanism of oxygen reduction at the interface metal/thin liquid film [37].

Reactions (14.11) and (14.12) are integrated in the scheme. h is the thickness of the thin liquid film. Khomskaya *et al.* have established that diffusion of oxygen through the liquid film wetting the surface of the lead crystals surrounding the pore is the slowest stage in the COC [38]. This conjecture has been supported by Maja *et al.* [39–41]. Oxygen transport to the negative plates and oxygen reduction at the surface of these plates have been studied, employing mathematical models and computer simulations, first by Bernardi and Carpenter [42], and later by Newman and Tiedemann [43] and Gu *et al.* [44].

Summary

This chapter made an overview of the main techniques employed to suppress the effect of the side reactions of water decomposition through catalytic recombination of H_2 and O_2 to water (catalytic plugs) or through operation of a COC (VRLAB). These methods have reduced, or even eliminated, the need for battery maintenance, as a result of which maintenance-free batteries are gaining ever increasing share of the battery production nowadays.

References

- [1] K. Ledjeff, A. Winsel, J. Power Sources 8 (1982) 215.
- [2] M. Nonoguchi, K. Ando, Progress in Batteries and Solar Cells 1 (1978) 128.
- [3] K. Lahme, G. Sassmannshausen, US Patents 4,048,387 (1977) and 4,129,687 (1978).

- [4] B. Riegel, E. Cattaneo, in: J. Garche (Ed.), *Encyclopedia of Electrochemical Power Sources*, vol. 4, Elsevier B.V, 2009, p. 735.
- [5] H. Watanabe, K. Yonezu, *Progress in Batteries and Solar Cells* 2 (1979) 153.
- [6] P. Ruetschi, J.B. Ockerman, *J. Electrochem. Soc.* 116 (1969) 1222.
- [7] P. Ruetschi, US Patent 2,951,106 (1960).
- [8] H. Reber, *Bosch Tech. Ber.* 3 (Aug. 1970).
- [9] P. Ruetschi, J.B. Ockerman, *Electrochem. Technol.* 4 (1966) 383.
- [10] G. Papazov, I. Nikolov, D. Pavlov, T. Vitanov, *Bull. Electrochem.* 6 (1990) 255.
- [11] I. Nikolov, G. Papazov, D. Pavlov, T. Vitanov, V. Naidenov, *J. Power Sources* 31 (1990) 69.
- [12] G. Papazov, I. Nikolov, D. Pavlov, T. Vitanov, P. Andreev, M. Bojinov, *J. Power Sources* 31 (1990) 79.
- [13] D.H. McClelland, J.L. Devitt, US Patent 3,862,861 (1975).
- [14] R.F. Nelson, *Proceeding of 4th Intl. Lead-Acid Battery Seminar*, International Lead Zinc Research organization, Inc, San Francisco, USA, 1990, p. 31.
- [15] D. Pavlov, M. Dimitrov, G. Petkova, H. Giess, C. Gnehm, *J. Electrochem. Soc.* 142 (1995) 2919.
- [16] B.K. Maha, E.Y. Weissman, E.C. Laird, *J. Electrochem. Soc.* 121 (1974) 13.
- [17] E.A. Khomskaya, N.F. Gorbacheva, N.Y. Lyzlov, I.A. Aguf, *Elektrokhimiya* 21 (1985) 156.
- [18] M. Maja, N. Penazzi, *J. Power Sources* 31 (1990) 115.
- [19] F. Mattera, D. Desmettre, J.L. Martin, Ph. Malbranche, *J. Power Sources* 113 (2003) 400.
- [20] D. Pavlov, I. Balkanov, T. Halachev, P. Rachev, *J. Electrochem. Soc.* 136 (1989) 3189.
- [21] K. Peters, A.I. Harrison, W.H. Durant, in: D.H. Collins (Ed.), *Power Sources* 2, Pergamon Press, Oxford, 1968, p. 1.
- [22] P. Ruetschi, J. Ockerman, R. Amlie, *J. Electrochem. Soc.* 107 (1960) 325.
- [23] B.N. Kabanov, E.S. Weisberg, I.L. Romanova, E.V. Krivolapova, *Electrochem. Acta* 9 (1964) 1197.
- [24] D. Pavlov, B. Monahov, *J. Electrochem. Soc.* 143 (1996) 3616.
- [25] D. Pavlov, B. Monahov, *J. Electrochem. Soc.* 145 (1998) 70.
- [26] D. Pavlov, E. Bashtavelova, *J. Electrochem. Soc.* 133 (1986) 241.
- [27] M.J. Weighall, in: J. Garche (Ed.), *Encyclopedia of Electrochemical Power Sources*, vol. 4, Elsevier B.V, 2009, p. 715.
- [28] B. Culpin, *J. Power Sources* 53 (1995) 127.
- [29] K. Peters, *J. Power Sources* 42 (1993) 155.
- [30] D.A. Crouch Jr., J.W. Reitz, *J. Power Sources* 31 (1990) 125.
- [31] B. Culpin, J.A. Hayman, in: L.J. Pearce (Ed.), *Power Sources* 2, International Power Sources Symposium, Leatherhead, UK, 1986, p. 45.
- [32] B. Culpin, in: J. Garche (Ed.), *Encyclopedia of Electrochemical Power Sources*, vol. 4, Elsevier B.V, 2009, p. 705.
- [33] M. Dimitrov, B. Drenchev, D. Pavlov, Yi Ding, S. Zanardelli, *Proceedings of 44th Power Sources Symposium*, Las Vegas, USA, June 2010, p. 83.
- [34] D. Pavlov, B. Monahov, A. Kirchev, D. Valkovska, *J. Power Sources* 158 (2006) 689.
- [35] D. Pavlov, *J. Power Sources* 64 (1997) 131.
- [36] D. Valkovska, M. Dimitrov, T. Todorov, D. Pavlov, *J. Power Sources* 191 (2009) 119.
- [37] A. Kirchev, D. Pavlov, B. Monahov, *J. Power Sources* 113 (2003) 245.
- [38] E.A. Khomskaya, N.F. Gorbacheva, N.B. Tolochkov, *Elektrokhimiya* 16 (1980) 56.
- [39] M. Maja, N. Penazzi, *J. Power Sources* 25 (1989) 99.
- [40] M. Maja, N. Penazzi, *J. Power Sources* 25 (1989) 229.
- [41] S. Bodoardo, M. Maja, N. Penazzi, *J. Power Sources* 55 (1995) 183.
- [42] D.M. Bernardi, M.K. Carpenter, *J. Electrochem. Soc.* 142 (1995) 2631.
- [43] J. Newman, W. Tiedemann, *J. Electrochem. Soc.* 144 (1997) 3081.
- [44] W.B. Gu, G.Q. Wang, C.Y. Wang, *J. Power Sources* 108 (2002) 174.

This page intentionally left blank

Calculation of the Active Materials in a Lead–Acid Cell

This page intentionally left blank

Calculation of the Active Materials for Lead–Acid Cells

15.1. Basic Units of Electricity and Equivalents for Electricity and Mass

The measurement unit of electric charge is *coulomb* (C). One coulomb is the amount of electric charge carried by a current of 1 A flowing for 1 s through the cross-section of an electric conductor ($1\text{ C} = 1\text{ A/s}$). This unit is very small for the application of electrochemical power sources. Therefore, the unit ampere-hour (Ah) is adopted instead. One hour consists of 3600 s. Hence, $1\text{ Ah} = 3600\text{C}$.

Michael Faraday has established that when 96,487 C of electricity pass through an electrochemical cell, one gram of equivalent mass is formed or dissolved at the electrodes through the electrochemical reaction. This quantity of electricity is assumed as measurement unit of electricity and is named as faraday (F). One gram equivalent of a given element is equal to its atomic weight divided by the number of valences that change during the electrochemical reaction. For compounds, the molecular weight is used instead of the atomic weight. For simplicity, the value of 1 F is assumed to be $F \approx 96,500\text{C}$.

Let us express the quantity of electricity (electric charge) of 1F in Ah:

$$Q = 96,500/3600 = 26.80\text{ Ah g}\cdot\text{eq}^{-1}$$

This measurement unit of electricity (electric charge) is a basic unit used in calculating the amounts of active materials needed for an electrochemical power source to deliver a given capacity.

Now let us determine the electrochemical equivalent weights per Ah of the basic active materials in a lead–acid cell.

15.2. Electrochemical Equivalent Weights of Active Materials in a Lead–Acid Cell per Ah of Electric Charge (Electricity)

15.2.1. Pb|PbSO₄ Electrode

The atomic weight of Pb is equal to 207.21 g. Two electrons of each Pb atom take part in the electrochemical reactions of charge or discharge in a lead–acid cell (LA cell). The equivalent weight of Pb, $g_{\text{Pb}}^{\text{eq}}$, is equal to:

$$g_{\text{Pb}}^{\text{eq}} = 207.21/2 = 103.61\text{ g}$$

Let us determine the electrochemical equivalent weight of Pb per Ah. We will denote as δ^0 the electrochemical equivalent weight per Ah of a given active material (δ_{Pb}^0 , $\delta_{\text{PbO}_2}^0$ or $\delta_{\text{H}_2\text{SO}_4}^0$).

$$\delta_{\text{Pb}}^0 = 103.61/26.8 = 3.866 \text{ g Pb Ah}^{-1}$$

When 1Ah of electricity flows through the LA cell, 3.866 g Pb are oxidized at the negative plates during discharge or released during charge of a LA cell.

15.2.2. $\text{PbO}_2|\text{PbSO}_4$ Electrode

The molecular weight of PbO_2 is equal to 239.21g. Two electrons of each PbO_2 molecule take part in the electrochemical reactions of charge or discharge at the $\text{PbO}_2|\text{PbSO}_4$ electrode. The equivalent weight of PbO_2 is:

$$g_{\text{PbO}_2}^{\text{eq}} = 239.21/2 = 119.605 \text{ g.}$$

The electrochemical equivalent weight of PbO_2 per Ah is:

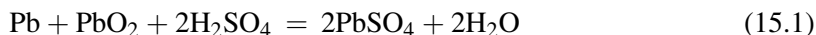
$$\delta_{\text{PbO}_2}^0 = 119.605/26.8 = 4.463 \text{ g PbO}_2 \text{ Ah}^{-1}$$

When 1Ah of electricity flows through the LA cell, 4.463 g PbO_2 are reduced to PbSO_4 at the positive plates during discharge or released during charge.

15.2.3. H_2SO_4 Solution

Sulfuric acid has a molecular weight of 98.08g and is divalent. Hence, its gram-equivalent weight is $g_{\text{H}_2\text{SO}_4}^{\text{eq}} = 98.08/2 = 49.04 \text{ g.}$

In the lead–acid cell, electrochemical reactions proceed at the two electrodes, which can be presented by the following general equation:



2 g equivalents of H_2SO_4 take part in the above reaction, when 26.8Ah flow through the cell.

The electrochemical equivalent weight of H_2SO_4 per Ah is:

$$\delta_{\text{H}_2\text{SO}_4}^0 = (2 \times 49.04)/26.8 = 3.66 \text{ g H}_2\text{SO}_4 \text{ Ah}^{-1}$$

When 1Ah of electricity flows through the cell, 3.66 g H_2SO_4 react at the two electrodes.

The proportion by weight of active materials in a lead–acid cell that take part in the electrochemical reactions during cell operation is:

$$\text{Pb} : \text{PbO}_2 : 2\text{H}_2\text{SO}_4 = 207.21 : 239.21 : 2 \times 98.08$$

The weights of PbO_2 and H_2SO_4 vs. the weight of Pb give:

$$\text{PbO}_2 : \text{Pb} = 1.154 \quad \text{H}_2\text{SO}_4 : \text{Pb} = 0.947$$

So the proportion by weight of the active materials ($\text{NAM} : \text{PAM} : \text{H}_2\text{SO}_4$) that take part in the charge or discharge reactions, when electricity flows through a LA cell, is:

$$\text{NAM} : \text{PAM} : \text{H}_2\text{SO}_4 = 1.00 : 1.154 : 0.947$$

15.3. Parameters Accounting for the Degree of Active Material Utilization During Current Generation and Correlation Between These Parameters

The active materials formed at the two types of electrodes (plates) comprises of two structural elements:

1. *Energetic structure, G_e* . It takes part in the charge–discharge processes. The calculations of the active materials and of the electric charges presented in Section 15.2 refer to the energetic structure only.
2. *Skeleton structure, G_s* . It provides mechanical support to the energetic structure and has electron conductivity, thus allowing it to conduct the current throughout the plate volume.

The total weight (G) of the positive or negative active material in a cell is equal to:

$$G = G_e + G_s$$

All calculations of the active materials are made using the value of G .

There are three parameters used for calculating the actual amount of active material needed for producing a cell of a given capacity.

1. *Active mass utilization coefficient, (η)*. This coefficient gives the share (by weight) of the energetic structure in the total amount of positive or negative active mass per cell:

$$\eta = G_e / G \quad \eta < 1$$

The amount of NAM or PAM per cell of a given capacity (C) is calculated by the following formulae:

$$G_e = C\delta^o$$

$$G = C\delta^o / \eta \quad [\text{g cell}^{-1}]$$

The parameter active mass utilization coefficient has the most clear physical meaning, namely what part of the whole active material is involved in the current generation and current accumulation processes.

2. *Active mass weight coefficient per Ah, (β)*. The active mass weight coefficient accounts for the actual amount of PAM or NAM (in grams) that would deliver 1Ah of capacity on discharge.

$$\beta = G/C \quad [\text{g Ah}^{-1}]$$

The β value is determined experientially for each particular technology of positive or negative active mass production. It depends on battery type as well.

3. *Specific capacity of PAM or NAM per kg active mass, (σ)*. It is equal to the reciprocal value of β :

$$\sigma = C/G \quad [\text{Ah kg}^{-1}]$$

and gives the Ah capacity that can be delivered by 1 kg of PAM or NAM.

During the design process, one of the above parameters is used to calculate the necessary amounts of active materials for a particular battery type.

The correlation between η , β and σ for positive and negative plates is presented in (Fig. 15.1). Thus, at $\eta_{\text{PAM}} = 50\%$ utilization of PAM, β_{PbO_2} is 8.75 g PbO₂ per Ah and σ_{PbO_2} is 112 Ah per kg PAM. For the negative plates: at $\eta_{\text{NAM}} = 45\%$ utilization of NAM, β_{Pb} is 8.55 g Pb per Ah and σ_{Pb} is 118 Ah per kg NAM.

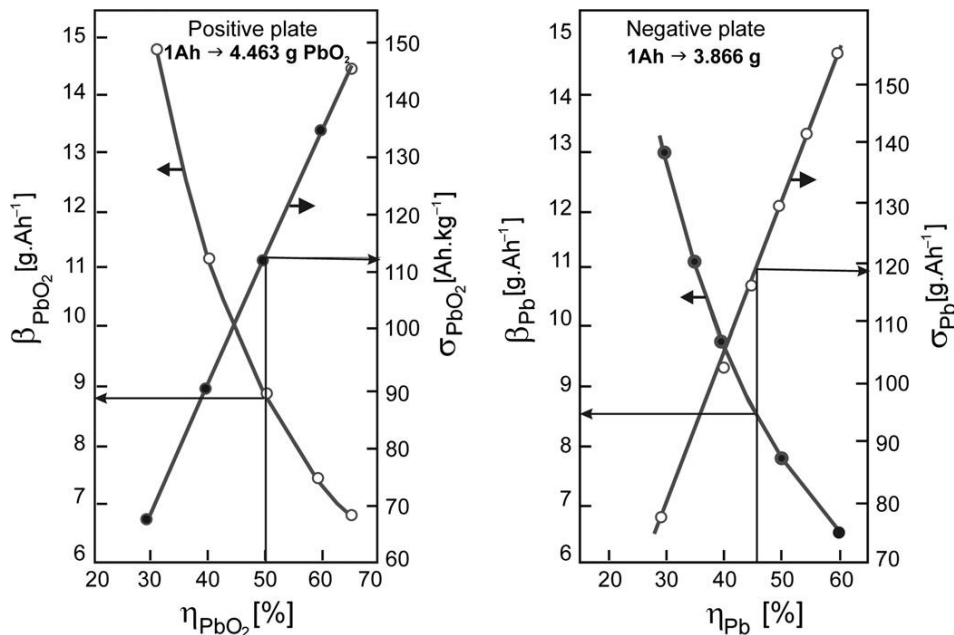


Figure 15.1:
Correlation between η [%], β [gAh⁻¹] and σ [Ahkg⁻¹].

Table 15.1: Specific energy, weight coefficients per Ah (β) and specific capacity per kg active mass (σ) for different battery types [1].

Battery Type	Specific Energy		β and σ Coefficients			
	Wh kg ⁻¹	Wh L ⁻¹	PbO ₂		Pb	
			β_{PbO_2} g Ah ⁻¹	σ_{PbO_2} Ah kg ⁻¹	β_{Pb} g Ah ⁻¹	σ_{Pb} Ah kg ⁻¹
SLI (20h rate)	30–40	75–100	10–7.7	100–130	8.7–6.5	115–154
Traction cell (5h rate)	25–32	60–100	16.7–11.1	60–90	12.5–10.0	80–100
Stationary battery: Flooded	20–28	35–60	16.7–10.0	60–100	12.5–10.0	80–100
VRLAB (60Ah)	21–31	45–85	15.2–11.4	66–90	12.5–7.2	80–140

Table 15.1 presents the value ranges for the specific capacity per kg active mass (σ) for PAM and NAM, and the weight coefficients (β) per Ah for the basic types of commercial lead–acid batteries: SLI, traction and stationary. The table also gives the respective specific energies (by volume and weight).

All these values have been experientially determined and they meet definite performance characteristics requirements specified for the particular battery type/application. The variation in β and σ values for a given battery type is due to differences in the technology of plate manufacture, battery design and general or specific application requirements.

15.4. Amount of H₂SO₄ in a Lead–Acid Cell

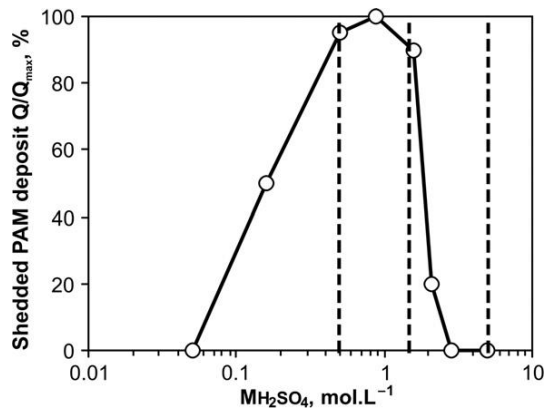
The amount of H₂SO₄ per cell should be calculated so that after cell discharge part of H₂SO₄ would remain unreacted to conduct the current during the subsequent charge.

It has been established that H₂SO₄ influences the electrochemical activity of PbO₂ on one hand and the solubility of PbSO₄ on the other hand (see Chapter 3).

As discussed in Chapter 3, PbO₂ is electrochemically active at H₂SO₄ concentrations between 0.5 and 5.0 M. So this is the acceptable range within which the concentration of H₂SO₄ solution in the battery may vary on charge and discharge.

On cycling a PbO₂|PbSO₄ electrode in H₂SO₄ solutions of different concentration, part of the PbO₂ and PbSO₄ particles shed off. Figure 15.2 presents the experimentally determined amounts of lead dioxide active mass that sheds off vs. the maximum amount of shed off PAM at different H₂SO₄ concentrations [2].

Intense PAM shedding is observed between 1.5 and 0.06 M in H₂SO₄ concentrations. Hence, to guarantee long battery cycle life, the concentration of H₂SO₄ in the battery during discharge should not drop below 1.5 M, which corresponds to 1.10 relative density. So the working

**Figure 15.2:**

Amount of PbO_2 that sheds off at different H_2SO_4 concentrations [2].

concentration region of H_2SO_4 in the cell is between 1.5 and 5.0 M , i.e. from 1.10 to 1.25 relative density.

Table 15.2 summarises the H_2SO_4 electrolyte concentration regions suggested by M. Barak for the different types of batteries in the charged state [3].

H_2SO_4 is an active material. The electrochemical equivalent of H_2SO_4 solutions (in ampere-hours per litre of solution) within the concentration region from 1.25 to 1.10 relative density can be found in Fig. 3.6. It is evident from the data in the figure that 5.0 M $\text{H}_2\text{SO}_4 \text{ L}^{-1}$ (1.25 rel. dens.) has an electrochemical equivalent of 117 Ah; 1.5 M H_2SO_4 (i.e. 1.10 rel. dens.) has an electrochemical equivalent of 45 Ah. Thus, from 1L of H_2SO_4 solution with 1.25 relative density, almost 3.5 M H_2SO_4 take part in the electrochemical reactions at the Pb and PbO_2 electrodes, delivering 72 Ah of electricity.

This quantity of electricity referred to the total quantity of electricity that can be produced by the reaction involving 5.0 M H_2SO_4 (117 Ah) gives the maximum utilization of H_2SO_4 in the LA cell:

$$\eta_{\text{H}_2\text{SO}_4} = 72/117 = 61.5\%$$

Table 15.2: Concentration of H_2SO_4 electrolytes for various battery applications [3].

Battery Type		r.d., at 25°C	$\text{H}_2\text{SO}_4 \text{ (g L}^{-1}\text{)}$	Ah L^{-1}
1.	Starter battery, SLI	1.27–1.28	460–488	125–131
2.	Tropical battery, SLI	1.24	404	110
3.	Traction battery: flat and tubular	1.25–1.28	423–480	115–131
4.	Stationary battery: Planté type	1.21	351	95
	Flat plates	1.22	390	102
5.	Discharged batteries: depending on discharge rate	1.14–1.08	233–120	63–33

During normal operation of a lead–acid cell, 72 Ah of electricity can be generated by the discharge reactions at the two types of electrodes per 1L of H_2SO_4 solution with 1.25 relative density, and the utilization of H_2SO_4 is 61.5%.

This is, in brief, the basic knowledge to be used for calculating the amounts of active materials needed for the production of a lead–acid cell.

15.5. An Example for Calculating the Active Materials in a 50Ah SLI Cell at $\eta_{\text{PAM}} = 50\%$ and $\eta_{\text{NAM}} = 45\%$

15.5.1. PAM

The specific electrochemical equivalent weight of PbO_2 is $\delta_{\text{PbO}_2}^0 = 4.463 \text{ g PbO}_2 \text{ Ah}^{-1}$. For a 50 Ah cell:

$$G_{\text{PbO}_2}^e = 50 \times 4.463 = 223.15 \text{ g PbO}_2.$$

The above amount of PbO_2 ($G_{\text{PbO}_2}^e$) comprises only the energetic structure of PAM, which will take part in the electrochemical reaction of discharge. In order to calculate the total PAM weight, we should also take into account the skeleton structure of PAM, which does not participate in the reaction.

We can calculate the weight of PAM (G) in an SLI cell at $\eta_{\text{PAM}} = 50\%$ by dividing the weight of the energetic structure of PAM (223.15 g) by the utilization coefficient:

$$G_{\text{PAM}} = 223.15/0.50 = 446.30 \text{ g PAM cell}^{-1}$$

The weight coefficient (β) for this SLI cell is:

$$\beta_{\text{PbO}_2} = 446.30/50 = 8.93 \text{ g PAM Ah}^{-1}$$

15.5.2. NAM

The specific electrochemical equivalent weight of Pb is $\delta_{\text{Pb}}^0 = 3.866 \text{ g Pb Ah}^{-1}$.

For a 50 Ah cell the weight of NAM which participates in the electrochemical reactions is:

$$G_{\text{Pb}} = 50 \times 3.866 = 193.3 \text{ g Pb}.$$

At $\eta_{\text{NAM}} = 45\%$ for SLI batteries: $G_{\text{NAM}} = 193.3/0.45 = 429.6 \approx 430 \text{ g Pb cell}^{-1}$ and $\beta_{\text{Pb}} = 430/50 = 8.6 \text{ g Pb Ah}^{-1}$.

H_2SO_4

The volume and weight of H_2SO_4 solution (1.25 rel. dens.) in the cell are calculated in the following way. Seventy-two amphere-hour are delivered by 1000 mL H_2SO_4 with 1.25 relative density, hence 50 Ah will be delivered by:

$$V_{\text{H}_2\text{SO}_4} = (50 \times 1000)/72 = 694.5 \text{ mL H}_2\text{SO}_4(1.25 \text{ rel.dens.})\text{cell}^{-1}$$

$$G_{H_2SO_4} = 694.5 \times 1.25 = 868.05 \text{ g H}_2\text{SO}_4(1.25 \text{ rel.dens.})\text{cell}^{-1}$$

The volume coefficient of H_2SO_4 (1.25 rel. dens.) per Ah is:

$$\beta_{V_{H_2SO_4}} = 694.5/50 = 13.89 \text{ ml H}_2\text{SO}_4(1.25 \text{ rel.dens.})\text{Ah}^{-1}$$

$$\beta_{G_{H_2SO_4}} = 13.89 \times 1.25 = 17.36 \text{ g H}_2\text{SO}_4(1.25 \text{ rel.dens.})\text{Ah}^{-1}$$

So a 50 Ah lead–acid cell should contain:

$$\text{PAM} = 446 \text{ g(at } \eta_{\text{PAM}} = 50\%)$$

$$\text{NAM} = 430 \text{ g(at } \eta_{\text{NAM}} = 45\%)$$

$$\text{H}_2\text{SO}_4 = 694 \text{ mL}(C_{H_2SO_4} = 1.25 \text{ g cm}^{-3})$$

The above amounts of active materials will guarantee normal operation of the cell.

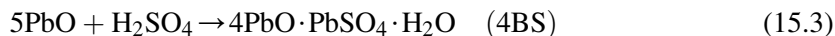
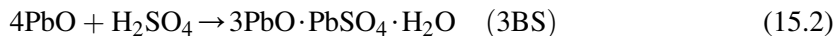
15.6. An Exemplary Calculation of Paste Composition

15.6.1. Calculation of the Content of Solid Phases in the Paste

Let us calculate the solid phase composition of a paste prepared with the following initial materials:

- LO containing 80 wt% PbO and 20 wt% Pb, i.e. 1 kg LO contains 800 g PbO and 200 g Pb;
- H_2SO_4 vs. LO ratio of 6% by weight, i.e. 60 g H_2SO_4 per 1 kg LO;
- H_2SO_4 solution with specific density 1.40 or 1.18 kgL^{-1} ;
- in order to obtain paste with a density of 4.10 gcm^{-3} , 200 mL of liquid (H_2SO_4 solution + H_2O) should be used per 1 kg LO.

The chemical reactions of formation of 3BS and 4BS are:



For calculating the composition of the paste we need to know the molecular weights of 3BS, 4BS, PbO, H_2SO_4 and H_2O , as well as the atomic weight of Pb. These are given in Table 15.3.

Calculation of the paste composition per 1 kg LO will be performed in three steps. The first step determines how many grams of 3BS will be formed when 60 g H_2SO_4 are used per 1 kg LO. 98.08 g H_2SO_4 mixed with PbO yield 990.8 g 3BS. Hence, 60 g H_2SO_4 yield:

$$G_{3\text{BS}} = (60 \times 990.8)/98.08 = 606.1 \text{ g 3BS per 1000 g LO}$$

Table 15.3: Molecular weights and molar volumes of active mass constituents [4].

Material	Molecular Weight (gmol^{-1})	Density (kgL^{-1})	Molar Volume ($\text{cm}^3\text{mol}^{-1}$)
Pb (metal)	207.19	11.341	18.25
PbO (tetragonal)	223.19	9.35	23.9
Pb ₃ O ₄	685.57	9.1	75.3
α -PbO ₂	239.19	9.8	24.3
β -PbO ₂	239.19	9.5	25.15
3PbO·PbSO ₄ ·H ₂ O	990.83	6.5	152
4PbO·PbSO ₄	1196.01	8.1	149
PbSO ₄	303.25	6.3	48.2
H ₂ O	18.0154	0.995	18.0
H ₂ SO ₄	98.08		

60 g H₂SO₄ mixed with 1 kg LO yield 606 g 3BS.

The next step in the calculation is to determine how many grams of PbO remain unreacted in the LO. For this purpose, we deduct the amount of PbO involved in the formation of 3BS from the total amount of PbO in the initial LO. It can be seen from the chemical reaction of 3BS formation that 1 mole of 3BS is formed out of 4 moles of PbO or 990.8 g 3BS are formed from 892.8 g PbO. Then, 606 g 3BS will be formed from:

$$G_{\text{PbO}}^{(3\text{BS})} = (892.76 \times 606) / 990.83 = 546 \text{ g PbO}$$

LO with 80% degree of oxidation is used. If we deduct from 800 g PbO (contained in the LO) 546 g PbO that react with H₂SO₄, we obtain 254 g PbO that remain unreacted (free) in the paste.

Hence, according to the above calculations, the paste should contain the following amounts of solid phase components:

$$3\text{BS} = 606 \text{ g}$$

$$\text{PbO} = 254 \text{ g}$$

$$\text{Pb} = 200 \text{ g}$$

$$\text{Total} = 1060 \text{ g}$$

The extra 60 g over 1000 g are the H₂SO₄ that has reacted with PbO to form 3BS.

The above paste composition is obtained, provided the whole amount of H₂SO₄ reacts to form 3BS and no other compounds (e.g. hydroxides) are produced.

In the calculations so far we have not taken into account the amount of water that transforms the solid components into paste.

15.6.2. Calculation of the Volumes of H_2SO_4 and H_2O Solution Needed for Paste Preparation

During the process of paste preparation, H_2SO_4 solution and water are used to achieve the desired paste density. The next step in the calculation is to determine the amounts of H_2SO_4 solution and of water that should be introduced into the paste mixer so as to obtain a paste density of 4.10 g cm^{-3} . Let us again make the calculations for 1 kg of LO.

In the battery manufacturing industry, pastes are usually prepared using H_2SO_4 solutions with density within the range from 1.40 to 1.18 g cm^{-3} . We will use this exemplary calculation for the upper and lower limit concentrations. In order to calculate how many mL of H_2SO_4 solution with the above relative density should be used for paste preparation, we need to know how many moles of H_2SO_4 are contained in the above solutions. These data can be found in most chemical reference books. Let us use Table 3.1.

According to the data in Table 3.1, at 25°C 1L of H_2SO_4 solution with density 1.40 g cm^{-3} contains 7.221 moles of H_2SO_4 , whereas H_2SO_4 with density 1.18 g cm^{-3} contains 3.042 moles of H_2SO_4 per litre.

In our exemplary calculation, we use 60 g H_2SO_4 per 1 kg LO. When dividing 60 g H_2SO_4 by the molecular weight of H_2SO_4 (98.08 g), we obtain that 1 kg LO reacts with 0.61 moles of H_2SO_4 . Based on the above data we can determine the volume of H_2SO_4 solution and water that should be added to the paste.

Now let us perform the calculation for H_2SO_4 solution with density 1.40 g cm^{-3} . In this case, 1000 mL of solution will contain 7.22 moles of H_2SO_4 . Then, 0.61 M H_2SO_4 will be contained in:

$$V_{\text{H}_2\text{SO}_4}^{1.4} = (0.61 \times 1000)/7.221 = 84.50 \text{ mL } \text{H}_2\text{SO}_4 \text{ solution}(1.40 \text{ g cm}^{-3})$$

In order to obtain a paste with a density of 4.10 g cm^{-3} , 200 mL of H_2SO_4 solution and water should be added per 1 kg LO. Hence, 84.5 mL H_2SO_4 with density 1.40 g cm^{-3} and 115.5 mL H_2O should be used for preparation of the paste.

Let us now repeat the above step of the calculation for the case when H_2SO_4 solution with density 1.18 g cm^{-3} is used. One litre of this solution contains 3.04 moles of H_2SO_4 . So 0.61 moles of H_2SO_4 , needed to react with 1 kg LO, will be contained in:

$$V_{\text{H}_2\text{SO}_4}^{1.18} = (0.61 \times 1000)/3.042 = 200.5 \text{ mL } \text{H}_2\text{SO}_4 \text{ solution}(1.18 \text{ g cm}^{-3})$$

There is no need to add water during paste preparation when mixing 1kg LO with 200.5 mL H_2SO_4 solution of 1.18 g cm^{-3} density in order to obtain a paste with density 4.10 g cm^{-3} .

Summarising the results of the above calculations the following recipe for 3BS paste preparation can be formulated: 1 kg leady oxide (LO) with 80% degree of oxidation and

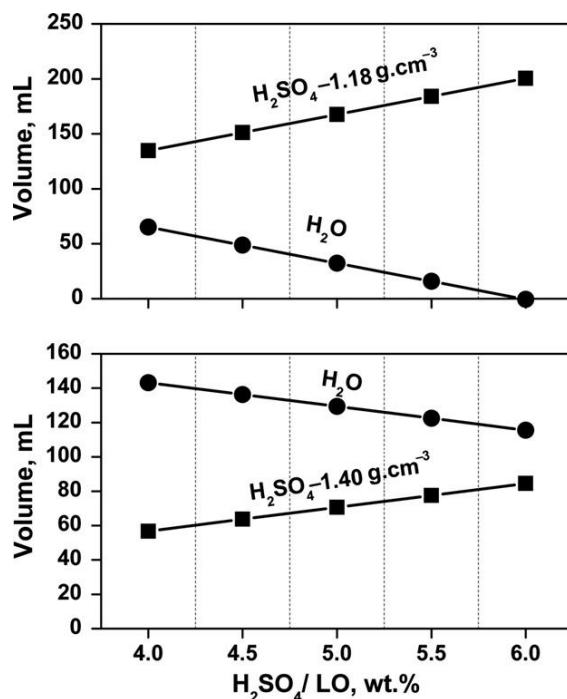


Figure 15.3:

Volumes of H₂SO₄ solution (1.40 or 1.18 gcm⁻³) and of H₂O to be used for paste preparation for various H₂SO₄/LO ratios.

H₂SO₄/LO = 6% by weight should be mixed with 200 ml H₂SO₄ solution with density 1.18 gcm⁻³ or with 84.5 ml of H₂SO₄ solution (1.40 g cm⁻³) plus 115.5 mL of H₂O, so as to produce paste with density 4.10 gcm⁻³. During the process of paste preparation the temperature should not exceed 50 °C in order to obtain 3BS phase.

Figure 15.3 shows the correlation between the volumes of water and H₂SO₄ solution (1.18 or 1.40 gcm⁻³) for various H₂SO₄/LO ratios.

For H₂SO₄/LO < 6 wt% (H₂SO₄ density 1.18 gcm⁻³), beside the calculated quantity of H₂SO₄ solution also a certain amount of water should be added.

When H₂SO₄ solution with 1.40 gcm⁻³ density is used, the volume of water to be added in order to achieve the desired paste density is greater than the volume of H₂SO₄ solution. In this case water is added first and then the H₂SO₄ solution.

15.7. Measuring of Electrode Potentials

The EMF of a cell (battery) is measured on open circuit. The open circuit voltage (OCV) depends on acid concentration and temperature of the cell or battery. However, these

parameters are not uniform throughout the cell volume during its operation. Electrolyte concentration and temperature gradients are created during cell (battery) charge and discharge. Moreover, during overcharge, hydrogen is incorporated into the negative lead plates, while the positive lead dioxide plates absorb oxygen. These processes change the potentials of the positive and negative plates, as well as the EMF of the cells. Therefore, measuring the EMF should be performed only after the cell voltage does not change any longer with time. Otherwise, the OCV will depend not only on acid concentration and temperature, but also on time. Thus, for example, if the measured cell voltage preserves its value unchanged for 1 h, it can be assumed that this is the real EMF of the cell. It has been established that this stationary value is reached after about 8 hours and, in some cases, even slower.

The potentials of the two electrodes of the lead–acid cell are measured vs. a reference electrode. Thus, the lead–acid cell turns into a three-electrode cell. During measuring the potential of the two electrodes of the LA cell, the reference electrode should not be polarized, i.e. its potential should remain constant. The most common reference electrodes are hydrogen, cadmium, mercury-mercurous sulfate and silver-silver sulfate electrodes. Cadmium sticks are widely used in industrial quality control laboratories to measure the electrode potentials of the manufactured batteries. Cadmium does not form poorly soluble cadmium sulfate, which is the reason why during the measurement the electrolyte in the cell absorbs a few Cd ion impurities that do not affect the performance of the battery, however.

The Hg/Hg₂SO₄ reference electrode is used mainly in research laboratories and in applications where precise measurement of the electrode potentials of the LA cell is required. Hg/HgSO₄ electrode is offered as commercial reference electrode for laboratory purposes.

The potentials of the Hg/Hg₂SO₄ reference electrode vs. a standard H₂/H⁺ electrode are presented in Table 15.4 for various sulfuric acid solutions [5]. Table 15.5 gives the

Table 15.4: Data for the Hg|Hg₂SO₄ electrode in sulfuric acid solutions of different concentrations at 30 °C.

H ₂ SO ₄ Concentration			Hg Hg ₂ SO ₄ Potential (V)	
mol L ⁻¹	mol kg ⁻¹	pH	vs. H ₂ H ⁺ in same solution	vs. SHE at pH = 0
0.01	0.01	1.8	0.785	0.679
0.10	0.10	1.03	0.737	0.676
0.50	0.51	0.48	0.696	0.668
1.00	1.04	0.20	0.674	0.662
4.20	5.05	−0.48	0.592	0.620
10.0	17.9	−1.2	0.467	0.538

Table 15.5: Potentials of the mercury-mercurous sulfate reference electrode vs. $\text{H}_2|\text{H}^+$ electrode at different sulfuric acid concentrations and temperatures.

Temp. (°K)	0.1003 M	0.1745 M	0.3877 M	0.5530 M	0.9776 M	1.872 M	3.911 M	5.767 M	7.972 M
$\phi \text{ Hg} \text{Hg}_2\text{SO}_4 \text{ vs. } \text{H}_2 \text{H}^+ \text{ in the same } \text{H}_2\text{SO}_4 \text{ solution (V)}$									
278.16	0.739	0.725	0.706	0.697	0.681	0.658	0.620	0.595	0.560
288.16	0.738	0.725	0.704	0.695	0.679	0.656	0.617	0.587	0.557
298.16	0.738	0.724	0.702	0.694	0.677	0.653	0.614	0.585	0.555
308.16	0.737	0.723	0.702	0.692	0.674	0.651	0.611	0.582	0.553
318.16	0.737	0.722	0.700	0.690	0.672	0.648	0.608	0.579	0.550
328.16	0.736	0.721	0.698	0.688	0.670	0.645	0.606	0.576	0.548

potentials of the $\text{Hg}/\text{Hg}_2\text{SO}_4$ electrode vs. a H_2/H^+ electrode in the same solution. Potential measurements are performed at different temperatures and different sulfuric acid concentrations [6].

Recently, thanks to the works of Ruetschi [7,8], the $\text{Ag}/\text{Ag}_2\text{SO}_4$ reference electrode has found application in the laboratory practice for measuring the electrode potentials of the lead–acid cell. The solubility of Ag_2SO_4 in H_2SO_4 is relatively high and Ag accelerates the self-discharge processes at the two electrodes. With the introduction of a micro-fibre glass plug in the $\text{Ag}/\text{Ag}_2\text{SO}_4$ electrode construction, the diffusion of Ag^+ ions into the solution of the cell was strongly impeded, which made the $\text{Ag}/\text{Ag}_2\text{SO}_4$ electrode applicable in the laboratory practice. Figure 15.4 shows schematic of the construction of the $\text{Ag}/\text{Ag}_2\text{SO}_4$ reference electrode proposed by Ruetschi [7].

Figures 15.5 and 15.6 present the calculated electrode potentials of the Pb/PbSO_4 and $\text{PbO}_2/\text{PbSO}_4$ electrodes vs. the above four types of reference electrodes [7]. The data in the figures evidence that the potential of the $\text{Ag}/\text{Ag}_2\text{SO}_4$ reference electrode is by 0.038 V more positive than that of the $\text{Hg}/\text{Hg}_2\text{SO}_4$ reference electrode. This difference is independent of the H_2SO_4 concentration. The thermodynamically calculated electrode potentials are in close agreement with the experimentally measured values.

To avoid formation of a diffusion potential between the cell electrolyte and the reference electrode electrolyte, the two solutions should be of the same acid concentration. If this is not the case, the value of the concentration potential (E_D) should be calculated from the following equation:

$$E_D = t + 0.029 \lg(a_1/a_2)$$

The diffusion potential (E_D) is measured between two reference electrodes of the same material, one of which is filled with solution of the same H_2SO_4 concentration as that of the electrolyte in the cell, and the solution in the other one is equal to that of the reference electrode

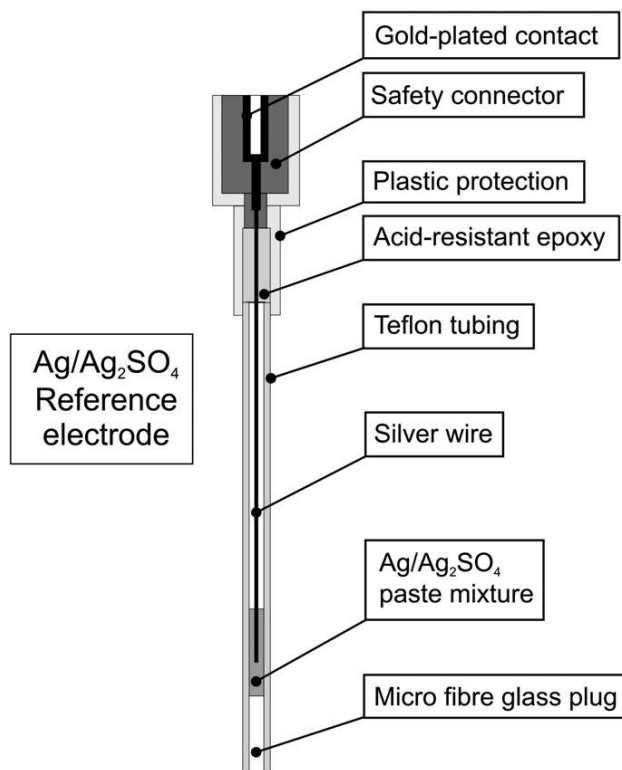


Figure 15.4:
Construction of silver-silver sulfate reference electrode [7].

against which the potential is measured. t_+ is the transport number of H^+ ions, which are the most mobile of all ions and hence, the two solutions will exchange mainly these ions. The transport number t_+ depends on the acid concentration [9] and its value may vary between 0.75 and 0.82. SO_4^{2-} ions also diffuse between solutions of different concentrations. Their transport number $t_- = 0.25$ to 0.18. The electrode in the more concentrated solution is positively charged and that in the more diluted solution is negatively charged.

Diffusion potential is also created between the electrolyte concentrations near the positive and the negative battery plates on charge and discharge [10]. A certain period of time is needed to equalize the H_2SO_4 concentration between the two plates before measuring the EMF of the cell. The duration of this time period depends on the particular cell design.

A diffusion potential also develops between the H_2SO_4 solution in the top and bottom parts of cell (vertical electrolyte stratification) [11]. This potential should also be taken into consideration when measuring the EMF of the cell or battery, i.e. the measurement should be performed after levelling of the acid concentration by height of the cell (battery).

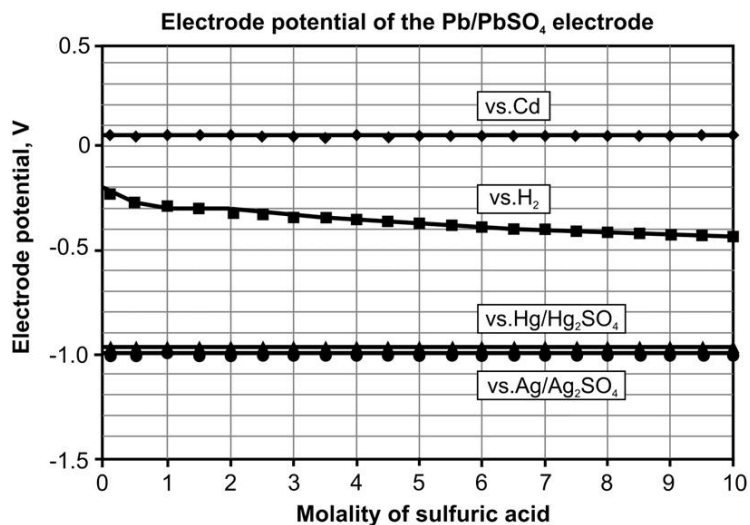


Figure 15.5:
Calculated potentials of the Pb|PbSO₄ electrode vs. different reference electrodes, as a function of sulfuric acid concentration [7].

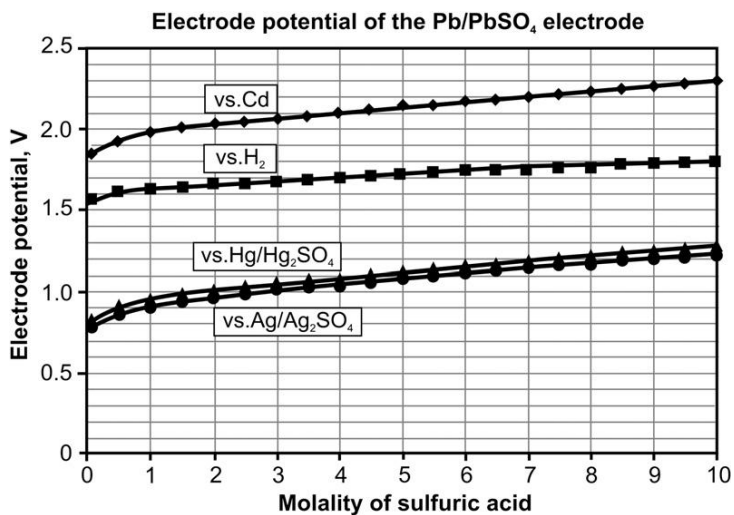


Figure 15.6:
Calculated potentials of the PbO₂|PbSO₄ electrode vs. different reference electrodes, as a function of sulfuric acid concentration [7].

References

- [1] D. Berndt, Maintenance-free batteries, Research Studies Press Ltd., John Wiley & Sons, New York, USA, 1993, p. 45.
- [2] D. Pavlov, A. Kirchev, M. Stoycheva, B. Monahov, J. Power Sources 137 (2004) 288.
- [3] M. Barak, Electrochemical power sources, Peter Peregrinus Ltd., Stevenage, UK, 1980, p. 158.
- [4] H. Bode, Lead-acid batteries, John Wiley & Sons, New York, USA, 1977, p. 13.
- [5] P. Ruetschi, R.T. Angstadt, J. Electrochem. Soc. 111 (1964) 1323.
- [6] W.H. Beck, K.P. Singh, W.F.K. Wynne-Jones, Trans. Faraday Soc. 55 (1959) 331.
- [7] P. Ruetschi, J. Power Sources 113 (2003) 363.
- [8] P. Ruetschi, J. Power Sources 116 (2003) 53.
- [9] A. Hammouche, E. Karden, I. Walter, R.W. De Donker, J. Power Sources 96 (2001) 106.
- [10] D. Pavlov, V. Naidenov, S. Ruevski, V. Mircheva, M. Cherneva, J. Power Sources 113 (2003) 209.
- [11] F. Mattera, D. Desmetre, J.L. Martin, Ph. Malbranche, J. Power Sources 113 (2003) 400.

Epilogue

Science generates knowledge.

Knowledge is the power that creates and drives the development of technology.

Technology makes products for use by people and society.

How I Found Myself in the Realm of the Lead-Acid Batteries?

Sometimes man's life is determined by random events.

I was working in the Institute of Physical Chemistry at the Bulgarian Academy of Sciences when in 1962 I was sent to specialization in *the Laboratoire Curie, Institut du Radium* in Paris. Professor Moïse Haïssinsky, the director of the laboratory there, set me a task of determining the adsorption of cesium ions on thorium oxide. During the investigation I found out that contrary to expectations when introducing thorium oxide in a diluted solution of cesium ions the concentration of cesium ions increases. This showed that the surface of thorium oxide was positively charged and repulsed cesium ions, generating a volume free of cesium ions in the solution. On my departure to Bulgaria, professor Haïssinsky said to me: 'Detchko, I recommend you to investigate the anodic processes in electrochemistry. You go well with oxides. These processes are complex and their models are hard to elaborate. This is the reason why scientists avoid them at present.'

When I returned to the Institute of Physical Chemistry I shared professor Haïssinsky's advice with professor Rostislav Kaishev, the director of the Institute and renowned scientist with great contributions in the area of phase formation and crystal growth. Our director offered me a theme: 'Start with the anode oxidation of lead in sulfuric acid. It is interesting to find out how the electrochemical processes are modified when forming a new phase of compound on the surface of the metal. These processes are related with batteries as well. Now we are building battery plants and the Academy should establish the scientific potential for this industry.'

The first potentiostatic studies of anodic oxidation of lead in sulfuric acid solution gave very interesting results and inspired me in such a way that I did not leave the lead-acid batteries for the rest of my life.

Soon within Bulgarian Academy of Science, the Central Laboratory for Electrochemical Power Sources (CLEPS) was established. At that time Professor Evgeni Budevsky undertook the establishment and management of the department of new electrochemical power sources, while I undertook the department

of development of lead-acid batteries. I gathered students in chemistry and physics, who had graduated with honors from the universities in Sofia. I determined the department's purposes of investigations as follows:

- Disclosure of the mechanisms of electrochemical and chemical processes, which take place in the production technology of plates (electrodes) of lead-acid batteries. These studies were important both for theory and practice.
- Disclosure of the structures of batteries' active masses and their organization in transforming chemical energy into electrical and vice versa during batteries' charge and discharge. The electrochemical power source is living through the reversibility of the plate's structural elements. The efficiency of this power source depends on these elements as well.

Gradually our work progressed. We published our results in international scientific journals. All of us learned from the diversity of the processes and we discovered their mechanisms. The significant knowledge we had gained provoked us to discuss our experience with colleagues from around the world, who were working in the field of lead-acid batteries. Therefore, our department organized the First International Conference on Lead-Acid Batteries, called LABAT, in June 1989, Varna, Bulgaria. The world was still divided, but all participants in the conference felt as one family with common interests. We found out that many of us work for the establishment of science in the technology for production of lead-acid batteries and for the increase of its efficiency. This has brought us spiritually closer. LABAT conferences had their international life and until now they had eight editions.

As my professional career approaches its end during the last few years I have written this book aiming to help more effectively further development of science and production of lead-acid batteries.

As mentioned earlier I am very grateful to the two great scientists — professor Moïse Haïssinsky and academician Rostislav Kaishev — who paved the way for my professional development.

Comments and suggestions from readers of this book are welcome.

Appendices

Appendix 1. Thermodynamic Data for Lead Compounds. H. Bode, Lead-Acid Batteries, John Wiles & Sons, Inc., New York, USA, 1977, p. 366, 367

Material	ΔH° (10^3 J/mol)	ΔG° (10^3 J/mol)	S° (10^3 J/mol)	C_p (10^3 J/mol)
3PbO·PbSO ₄	−1626.7	−1427.5	340.6	
PbO·PbSO ₄	−1152.7	−1016.3	217.4	150.2
2PbO·PbSO ₄	−1358.5	−1202.6	318.6	196.2
4PbO·PbSO ₄	−1882.1	−1595.3	435.6	287.9
3PbO·PbSO ₄ ·H ₂ O		−1668.5		
5PbO·2H ₂ O		−1407.5		
PbO·0.4H ₂ O		−281.5		
Pb(OH) ₂	−514.63	−420.91	87.86	
PbSO ₄ rhombic	−919.94	−813.20	148.57	103.21
PbO tet	−218.99	−188.95	66.52	45.82
PbO orthorhomb	−217.32	−187.90	68.70	45.77
H ₂ O fluid	−285.83	−237.18	69.92	75.29
H ₂ SO ₄ fluid	−813.99	−690.10	156.90	138.91
Pb ²⁺ aq.	1.67	−24.39	10.46	
HPbO ₂ [−] aq.		−338.48		

Appendix 2. X-Ray Powder Diffraction Data for Battery Phases Pb R.J. Hill, J. Power Sources 9 (1983) 55

2 θ	<i>d</i> -Spacing	<i>I</i> / <i>I</i> ₀	<i>h</i>	<i>k</i>	<i>l</i>
31.27	2.858	100.0	1	1	1
36.26	2.475	50.3	0	0	2
52.22	1.750	34.6	0	2	2

α -PbO

2 θ	<i>d</i> -Spacing	<i>I</i> / <i>I</i> ₀	<i>h</i>	<i>k</i>	<i>l</i>
17.64	5.024	2.6	0	0	1
28.62	3.117	100.0	0	1	1

(Continued)

2θ	d -Spacing	I/I_0	h	k	l
31.83	2.809	31.6	1	1	0
35.72	2.512	11.3	0	0	2
45.63	1.987	15.7	0	2	0
48.59	1.872	25.2	1	1	2
54.76	1.672	30.4	1	2	1

 β -PbO

2θ	d -Spacing	I/I_0	h	k	l
15.03	5.890	4.9	1	0	0
22.12	4.015	3.2	1	1	0
29.08	3.068	100.0	1	1	1
30.32	2.946	24.9	2	0	0
32.60	2.745	21.6	0	2	0
37.81	2.377	16.7	0	0	2
45.12	2.008	15.0	2	2	0
49.21	1.850	12.3	2	0	2
50.77	1.797	11.7	0	2	2
53.10	1.723	18.9	3	1	1

 Pb_3O_4

2θ	d -Spacing	I/I_0	h	k	l
14.20	6.232	11.3	1	1	0
24.31	3.658	2.8	0	2	1
26.35	3.380	100.0	1	2	1
27.14	2.283	5.1	0	0	2
28.63	3.115	13.1	2	2	0
30.76	2.904	37.8	1	1	2
32.09	2.787	48.7	1	3	0
34.03	2.632	26.2	0	2	2
36.74	2.444	2.2	2	3	0
39.30	2.291	4.2	2	3	1
39.86	2.260	5.6	2	2	2
44.54	2.033	10.1	1	4	1
46.02	1.971	11.1	2	4	0
47.48	1.913	19.0	1	2	3
49.81	1.829	23.7	0	4	2
52.06	1.755	25.5	3	3	2
52.93	1.728	2.3	1	5	0

$\alpha\text{-PbO}_2$

2θ	$d\text{-Spacing}$	I/I_0	h	k	l
23.25	3.823	21.6	1	1	0
28.47	3.133	100.0	1	1	1
30.03	2.973	8.5	0	2	0
32.74	2.733	17.4	0	0	2
34.30	2.612	19.3	0	2	1
35.97	2.495	11.6	2	0	0
40.55	2.223	8.7	1	1	2
45.02	2.012	7.3	0	2	2
47.53	1.911	6.5	2	2	0
49.43	1.842	15.4	2	0	2
49.43	1.842	12.6	1	3	0
50.55	1.804	17.5	2	2	1

$\beta\text{-PbO}_2$

2θ	$d\text{-Spacing}$	I/I_0	h	k	l
25.40	3.504	100.0	1	1	0
31.98	2.796	95.2	0	1	1
36.23	2.477	28.4	0	2	0
49.09	1.854	68.1	1	2	1
52.16	1.752	14.7	2	2	0
54.12	1.693	8.1	0	0	2

$\text{PbO} \cdot \text{PbSO}_4$

2θ	$d\text{-Spacing}$	I/I_0	h	k	l
13.90	6.371	16.0	0	0	1
14.29	6.198	16.1	2	0	0
14.96	5.922	11.3	2	0	$\bar{1}$
17.12	5.179	3.0	1	1	0
20.02	4.435	16.9	1	1	$\bar{1}$
24.02	3.705	11.7	2	0	1
24.04	3.702	5.4	1	1	1
25.31	3.519	10.6	3	1	$\bar{1}$
26.65	3.345	100.0	3	1	0
28.01	3.186	8.7	0	0	2
30.13	2.966	75.0	1	1	$\bar{2}$
30.19	2.960	23.0	4	0	$\bar{2}$
31.17	2.869	17.3	3	1	$\bar{2}$
31.37	2.852	35.3	0	2	0

(Continued)

2θ	d -Spacing	I/I_0	h	k	l
34.63	2.590	2.7	2	2	0
34.93	2.569	4.7	2	2	$\bar{1}$
36.24	2.479	14.7	5	1	$\bar{1}$
36.94	2.433	13.6	2	0	2
37.42	2.403	5.2	4	0	1
38.32	2.349	6.4	2	0	$\bar{3}$
39.55	2.279	4.6	6	0	$\bar{1}$
39.65	2.273	5.8	5	1	0
39.90	2.259	14.7	2	2	1
40.34	2.236	6.6	6	0	$\bar{2}$
41.52	2.175	3.4	3	1	$\bar{3}$
42.55	2.125	3.7	0	2	2
43.83	2.066	7.5	6	0	0
44.10	2.054	24.3	4	2	$\bar{2}$
45.99	1.073	5.4	6	0	$\bar{3}$
47.56	1.912	7.3	5	1	1
49.23	1.851	14.8	2	2	2
49.26	1.850	9.9	1	1	3
49.35	1.847	5.4	7	1	$\bar{2}$
49.61	1.838	4.6	4	2	1
49.67	1.835	2.3	1	3	$\bar{1}$
50.33	1.813	2.2	2	2	3
51.81	1.765	4.4	4	0	$\bar{4}$
51.97	1.760	5.5	6	2	$\bar{2}$
52.71	1.737	4.2	2	0	$\bar{4}$
53.03	1.727	11.5	3	3	0
54.50	1.684	3.9	8	0	$\bar{1}$
54.89	1.673	4.6	6	2	0
55.08	1.667	12.7	1	3	$\bar{2}$
55.61	1.653	5.1	5	1	$\bar{4}$
55.72	1.650	2.4	3	3	$\bar{2}$

 $3PbO \cdot PbSO_4 \cdot H_2O$

2θ	d -Spacing	I/I_0	h	k	l
9.0	9.826	60	1	0	0
14.1	6.281	10	0	1	0
15.4	5.754	20	1	1	0
18.1	4.901	10	2	0	0
20.9	4.250	15	2	1	0
24.1	3.693	2	1	0	2
24.7	3.604	4	0	0	2
25.1	3.548	5	$\bar{2}$	1	0

(Continued)

2θ	d -Spacing	l/l_0	h	k	l			
26.7	3.339	2	2	0	2			
27.0	3.302	2	3	0	1			
27.4	3.255	100	3	0	0			
28.5	3.132	45	3	1	0	$\bar{1}$	0	2
31.0	2.885	10	2	2	0			
31.5	2.840	7	$\bar{1}$	2	0	2	2	1
32.0	2.797	2	3	0	2			
32.9	2.722	5	$\bar{3}$	0	1	3	$\bar{1}$	1
33.2	2.698	10	$\bar{3}$	1	0			
36.0	2.495	15	3	2	0			
36.7	2.449	10	4	0	0			
36.8	2.442	5	$\bar{2}$	2	0			
36.9	2.436	2	4	1	0			
38.4	2.344	2	1	1	3			
38.9	2.315	2	4	0	2			
41.8	2.161	4	$\bar{3}$	0	2			
42.0	2.151	3	$\bar{1}$	2	2	2	$\bar{2}$	2
42.1	2.146	2	$\bar{4}$	$\bar{1}$	1			
43.4	2.085	3	3	$\bar{2}$	1	0	3	0
43.6	2.076	15	$\bar{3}$	2	0			
44.0	2.058	5	2	3	0	4	$\bar{1}$	2
44.8	2.023	2	5	0	1			
46.0	1.073	10	5	0	0			

$4PbO \cdot PbSO_4$

2θ	d -Spacing	l/l_0	h	k	l			
10.7	8.286	10	1	1	0			
12.1	7.314	4	0	0	1			
14.3	6.194	4	0	1	1			
15.4	5.754	3	2	0	0			
16.2	5.471	2	$\bar{1}$	1	1			
16.3	5.438	4	1	1	1			
17.1	5.185	2	2	1	0			
20.8	4.271	4	$\bar{1}$	2	1			
26.8	3.327	2	1	1	2			
27.1	3.290	6	1	3	1	$\bar{3}$	1	1
27.6	3.232	100	2	3	0			
28.7	3.110	45	$\bar{2}$	0	2			
29.2	3.058	45	2	0	2			
29.7	3.008	2	$\bar{2}$	1	2	$\bar{1}$	2	2
31.0	2.885	30	4	0	0			
33.6	2.667	45	0	3	2			

(Continued)

2θ	d -Spacing	I/I_0	h	k	l			
34.4	2.607	3	$\bar{1}$	3	2	4	0	2
34.8	2.578	2	$\bar{3}$	3	2	$\bar{3}$	1	2
35.0	2.564	2	3	1	2			
36.6	2.455	2	2	4	1	$\bar{4}$	2	2
46.0	1.973	18	4	4	1	$\bar{4}$	3	2
46.5	1.953	14	0	6	0			
46.7	1.945	20	4	3	2			
49.9	1.828	10	6	1	1			

 $PbSO_4$

2θ	d -Spacing	I/I_0	h	k	l
16.46	5.386	2.3	1	1	0
20.81	4.269	72.3	1	0	1
20.93	4.244	28.4	0	2	0
23.33	3.813	51.1	1	1	1
24.56	3.625	19.9	1	2	1
25.58	3.482	28.0	2	0	0
26.71	3.338	82.5	0	2	1
27.69	3.222	66.8	2	1	0
29.68	3.010	100.0	1	2	1
32.35	2.767	37.9	2	1	1
33.17	2.701	44.1	0	0	2
34.20	2.622	9.9	1	3	0
37.32	2.409	17.5	2	2	1
39.55	2.279	18.5	0	2	2
40.27	2.240	4.8	3	1	0
41.10	2.196	6.4	2	3	0
41.70	2.166	27.3	1	2	2
42.35	2.134	5.2	2	0	2
43.73	2.070	45.3	2	1	2
43.76	2.069	50.1	3	1	1
44.54	2.034	35.1	2	3	1
44.64	2.030	33.6	1	4	0
45.95	1.975	22.3	0	4	1
47.69	1.907	3.7	2	2	2
48.38	1.881	7.1	1	3	2
50.88	1.795	18.7	3	3	0
52.49	1.743	7.5	1	0	3
52.56	1.741	2.1	4	0	0
53.32	1.718	2.6	2	4	1
53.67	1.708	4.2	1	1	3
53.74	1.706	8.5	4	1	0

(Continued)

2θ	d -Spacing	I/I_0	h	k	l
53.82	1.703	8.2	3	3	1
55.43	1.658	6.9	0	2	3
55.73	1.649	2.6	1	5	0

$2PbCO_3 \cdot Pb(OH)_2$

2θ	d -Spacing	I/I_0	h	k	l			
11.3	7.830	5	0	0	3			
19.9	4.462	60	1	0	1			
20.9	4.250	60	0	1	2			
24.7	3.604	90	1	0	4			
27.1	3.290	90	0	1	5			
33.0	2.714	20	1	0	7			
34.2	2.622	100	1	1	0	0	0	9
36.1	2.488	30	0	1	8			
39.9	2.259	10	0	2	1			
40.4	2.233	50	2	0	2			
42.6	2.122	30	0	2	4			
43.1	2.099	20	1	0	10			
44.3	2.045	30	2	0	5			
48.3	1.884	20	0	2	7			
49.1	1.855	30	1	1	9			

This page intentionally left blank

Index

A

Absorptive glass mat (AGM), 14,
35, 407, 576, 582, 588
in lead-tin alloys, 200
pore system, 412
separators, 582, 582, 583, 585,
589
structure, 582
AC1, 339f, 338
Acetophenones, 141–142
Acid spray treatment, 303f, 304f
Active block, 127–128
Active mass
electrolyte stratification and, 146
lead dioxide and, 174
Active mass connecting layer
(AMCL), 205, 508–509,
515
Active mass formation, 501. *See*
also Negative active mass;
Positive active mass
algorithms for, 517f, 519f, 509,
511, 512, 513, 516
cell voltage in, 506f
changes in, 510f, 514f, 514f,
515f, 518f
charging v, 509
end of, 525
H₂SO₄ in, 501
initial stages of, 505
plate capacity and, 504
processes after, 535
shortening, 528
technological parameters, 503
temperature in, 524f, 501
Active materials
calculation of, 607

electrochemical equivalent
weights, 607
in NAM, 613
in PAM, 613
utilization, 609
Additives, 311. *See also* Carbon
additives
defined, 311
electro-conductive, 351
to electrolytes, 138
graphite, 332f, 333, 326t
grid alloying, 475, 555
to lead-antimony alloys, 165
to lead-calcium-tin alloys, 195
to NAM, 326t
for negative plates, 311
to pastes, 348
to positive plate, 350, 353
Advanced Lead-Acid Battery
Consortium, 398
Age hardening, 155–156, 159–160
kinetic, 160
lead-calcium-tin alloys, 187f
Aged state, 188
AGM. *See* Absorptive glass mat
Air curing, 397, 398t
Aldehydes, 141–142
Aluminium, 144t
in grid casting, 184f
in lead-calcium alloys, 183
in lead-calcium-tin alloys, 199
solubility of, 185f, 184
AMCL. *See* Active mass
connecting layer
Ammonium (NH₄), 120t
Ampere hours, 128t
Anderson, 61, 68
Anisaldehyde, 350

Anodic corrosion, 96
Anodic oxidation
elementary processes of, 49
stoichiometric coefficient of, 95f
Anodic polarization, 44
Pb/PbO₂/H₂SO₄ electrode
system, 84
schematic representation of, 46f
Antimony (Sb), 143, 120t, 144t,
476t. *See also* Lead-
antimony alloys
corrosion layer and, 177
corrosion resistance and, 164f
creep resistance and, 164f
lead dioxide active mass
structure and, 174
melting point, 158f
oxygen overpotential and, 169f
solubility of, 156f
in tubular electrode specific
capacity, 176f
Aron, Hermann, 12
Arsenic (As), 120t, 144t, 153
lead dioxide active mass
structure and, 174
in lead-antimony alloys, 165,
166t
As. *See* Arsenic
Auxiliary catalytic electrodes, 571
Axion Power International, 26

B

Ball-mill, 13
air flow rate, 232
air humidity, 233
Barton pot v, 236f, 233, 235t
conical, 231f
developments in, 236

- Ball-mill (*Continued*)
 drum rotation speed, 232
 feed rate, 232
 free lead content in, 246f
 with low temperature oxidation, 231
 particle size distribution from, 245f
 reactivity of leady oxides from, 241f
 SEM micrographs of, 234f
 temperature in, 232
 test cell with, 249f
- BaPbO₃. *See* Barium plumbate
- Barium, 143, 144t
 in lead-calcium-tin alloys, 195
 UTS and, 195f
- Barium plumbate (BaPbO₃), 351
- Barium sulfate (BaSO₄), 312, 343
 concentration of, 347f
 lead sulfate and, 343
 NAM and, 345f, 345
 structure of, 345f, 343
- Barton, George, 13, 227
- Barton pot, 13
 air flow rate, 229
 ball-mill v, 236f, 233, 235t
 developments in, 236
 free lead content in, 246f
 humidity in, 229
 melting pot temperature, 229
 with moderate temperature oxidation, 227
 molten lead feed rate, 229
 parameters, 229
 particle size distribution from, 245f
 reactivity of leady oxides from, 241f
 reactor temperature, 229
 schematic of, 228f
 SEM micrographs of, 230f
- Barytes, 344–345
- Basic lead sulfate paste, 15
- BaSO₄. *See* Barium sulfate
- Batteries. *See also specific types*
 acid purity requirements for, 120t
 active masses, 16
 assembly, 109
 component weight, 106t
 energy costs, 23t
 main characteristics of, 22t
 processes after formation, 535
 straps, 152
 voltage, 126f, 126
- Beckquerel, Edmond, 7
- Bell Laboratory, 14
- Belt-type pasting machine, 302f
- Benzaldehyde, 141–142, 350
- Benzene, 141–142, 350
- 2-benzimidazolethiol, 349
- Benzoic acid, 141–142, 350
- Binders, 357
- Bismuth, 143, 144t
 lead dioxide active mass
 structure and, 174
 in lead-calcium-tin alloys, 198
- Blanc Fix, 344–345
- Bode, H, 15–16
- Boric acid, 140
- Borregaard LignoTech, 320
- Bréquet Company, 11
- Bullock, 34
- Butler, 73
- ## C
- Cadmium, 143, 144t, 153
- Calcium, 143, 144t, 384. *See also*
 Lead-calcium alloys;
 Lead-calcium-tin alloys
- Calcium sulfate (CaSO₄), 357
- Capillary pressure, 586f
- Carbon additives, 332f, 312–313, 325, 326t
 NAM and, 325, 333, 337
 particle size, 338
- Carbon fibres, 352
- Carbon suspensions, 141
- Carbonization, 276
- Carboxy methyl cellulose (CMC), 208, 348, 356
- CaSO₄. *See* Calcium sulfate
- Catalytic plugs, 569f, 567
- CCA test, 292
 cranking time on, 293f
 initial capacity, 293f
- Cell discharge, 574
- Cell saturation, 590f, 589, 589
- Cerium, 143, 144t
- Charge transfer, 336f
- Charge voltage
 electromotive forces and, 123
 HRPSOC and, 335f
- Charge-discharge cycles, 430f
- Chloride, 120t
- Chloride lead oxide mill, 231f
- Chloride Motive Power, 306
- Chlorine, 119–121, 143, 144t
- Chromium, 144t
- CMC. *See* Carboxy methyl cellulose
- Coarse dendritic cast, 171f
- Cobalt, 143, 144t
- Colloidal silica, 140
- Composite colloid, 141
- Comptes Rendus, 4
- Concast process, 153
- Conductive polymers, 352
- Conical ball-mill, 231f
- Contact ovens, 304
- Contact surface resistance, 207f
- Container formation, 407
- Continuous drum-casting process
 (Concast process), 153
- Continuous plate production
 process, 209f, 208
- Continuous process drying ovens,
 304–305
- Conventional rectangular plate,
 204f
- Copper (Cu), 120t, 144t, 153, 173
- Copper-stretch-metal (CSM)
 negative grids, 217
- Cork powder, 208
- Corrosion currents, 102f
- Corrosion layer, 149, 427f, 425
 antimony and, 177
 formation, 384, 426f, 460f, 505
 lead-calcium-tin alloys and,
 388f, 386
 PAM interface, 504
 paste crystals in, 389
 structure, 386, 437, 460
- Corrosion rates, 183f
- Corrosion resistance
 antimony and, 164f
 of lead-antimony alloys, 162
 of lead-calcium-tin alloys, 191
- Corrosion transients, 201f
- Coulomb, 607

Creep resistance, 181, 188
 antimony and, 164f
 of lead-antimony alloys, 162
 CSM. *See* Copper-stretch-metal
 negative grids
 Cu. *See* Copper
 Cu₃As, 173–174
 Curie, Pierre, 10
 Curing. *See* Plate curing
 Current curve, 46f, 48f
 Current-collector surface, 527f,
 525
 Current-conducting structure, 327
 Cycle life, 131f
 DIN, 321f
 grid thickness and, 197f
 H₂SO₄ and, 132f
 in HRPSOC, 337
 NAM and, 496
 of positive plates, 276, 558f
 of red lead, 286t
 of SLI batteries, 441f
 soaking and, 429
 voltage determining, 322f
 Cycle number, discharge capacity
 v, 249f
 Cyclic voltammograms, 50f, 560f
 H₂SO₄, 69f
 for lead electrodes, 67f
 for lead sulfate, 316f
 during oxidation of PbO, 68–70
 shape of, 70
 in sulfuric acid, 69f
 Cylindrical tube cross section, 216f,
 217f

D

Density
 of lead dioxide, 73t
 of leady oxides, 242
 packed, 242
 paste, 287
 paste, critical values, 289
 paste, parameters, 288
 poured, 242
 powder, 290f
 soaking and, 419f
 sulfuric acid, 119f, 127f, 124t
 Depth-of-discharge (DOD),
 145–146

Devitt, John, 14–15
 3-5 Diamino benzoic acid, 349
 Differential scanning calorimetric
 (DSC) measurements, 439f,
 438
 Differential thermogravimetric
 (DTG) curves, 424f
 DIN cycle life, 321f
 Discharge capacity, 249f, 441f,
 544f
 DOD. *See* Depth-of-discharge
 n-dodecylamine, 349
 Donnan equilibrium potential, 55
 Dry-charged batteries, 536
 internal resistance, 538f
 storage of, 547
 Drying ovens
 contact, 304
 continuous process, 304–305
 tunnel, 304
 DSC. *See* Differential scanning
 calorimetric measurements
 DSL Dresden Material-Innovation
 GmbH, 213
 DTG curves. *See* Differential
 thermogravimetric curves
 Dynel flock, 356–357, 348

E

Ebonite, 14
 Edison, Thomas, 11
 Electrical conductivity, 63
 Electrical resistivity, 137
 Electricity, basic units of, 607
 Electrochemical oxidation, 66
 Electro-conductive additives, 351
 Electrode. *See specific types*
 Electrode potentials, 617
 Electrolytes, 588, 589
 additives to, 138
 contaminants in, 142
 filling techniques, 413f, 411
 gelled, 576
 H₂SO₄ as, 117
 re-circulation, 528, 529
 reservoir, 127–128
 soaking and, 414f
 stratification, 146, 144, 379
 Electrolyte-tight seating ring,
 105f

Electromotive force, 123
 Elliptical tube cross section, 216f,
 217f
 Energetic structure, NAM, 327
 E/pH diagram, 38, 552f, 553f
 European Norm, 107t
 Eutectic phase, 171f
 Expanded metal plate, 204f
 Expander, 311
 charge process and, 319
 compositions of, 347, 347t
 in discharge process, 318
 effect of, on electrochemical
 processes, 315
 grid alloy composition and, 327f
 hydrogen and, 321
 lead sulfate and, 315
 in negative active mass, 493
 negative plate performance and,
 319
 in negative plates, 311
 oxygen and, 321
 pastes and, 274f, 265
 stability, 324
 structural units of, 324f
 temperature and, 324
 tetrabasic lead sulfate and, 272
 three-component, 20
 EZE-Skitan, 323f, 322

F

FAER. *See* First anodic electro-
 chemical reaction
 Faraday, Michael, 29
 Faraday's law, 104, 126
 Fauré, Camille, 12, 13
 Fe. *See* Iron
 Felt mat, 204f
 Fibres, 348
 carbon, 352
 diameter, 584t
 graphite, 352
 polymer, 313
 Fillers, 357
 Film thickness, 74f
 Firefly Energy, 26
 First anodic electrochemical
 reaction (FAER), 91
 Flat-plate batteries, 108
 Float current, 170f

Flooded batteries, 21, 35, 108
 acid stratification in, 145f
 formation options, 411
 purity specifications in, 238t
 sulfuric acid in, 125

FORAFAC 1033D, 142

Freudenberg formulas, 314f

Furukawa Battery Co, 195

G

Galvanostatic oxidation, 52f

Gastornix parisiensis, 7

Gates Corporation, 14–15

Gautherot, N, 3

Gel-crystal structure, 17, 469

Gel-electrolyte batteries, 35

Gibbs free energy, 30–31

Gibbs-Helmholtz equation,
 42–43

Gladstone, 12

Grain diameter, 187f

Grain refinement, 173f, 181f

Gramme, Zénobe, 11

Graphite additives, 332f, 326t
 NAM and, 333, 337

Graphite fibres, 352

Gravity filling, 412–413

Grids, 149

Grid alloy composition

 additives, 475, 555

 expander efficiency and, 320

Grid casting, 108

 alloys used for, 152t

 aluminium in, 184f

 tubular-plate batteries, 111

Grid design principles, 204f, 202

Grid expanding process, 210f

Grid hot cracking, 170

Grid pasting, 108, 253

 for SLI batteries, 303

 technological scheme for, 300

Grid plate, 105f

Grid/spine casting, 207

H

H₂/H⁺, on Pb surface, 56

H₂O/O₂ electrode system, 86

H₂SO₄. *See* Sulfuric acid

H₃PO₄. *See* Phosphoric acid

HADI Maschinenbau GmbH, 208

Hammond Expanders, 299–300

Haring, 14

High charge acceptance, 138

High-rate partial state of charge
 (HRPSoC), 142, 326

 cell charge voltage during, 335f

 cycle life, 337

H-region, 129, 130, 132–133

HRPSoC. *See* High-rate partial
 state of charge

Hybrid electric vehicles, 23, 326

 energy demands of, 24f

 full, 23

 micro, 24

 mild, 23

 plug-in, 24

Hydration, 276

Hydrocarbonates, 391f, 389

Hydrogen, 573f

 expander and, 321

 recombination, 567

Hydrogen evolution, 579

 inhibitors of, 313, 349

 at negative plates, 349

 overpotential of, 169f

 rate, 57f

 reaction, 168

Hydrogen over-voltage, 56,
 138–139

Hydrolyzed lignin, 296

Hydrophobic channels, 349

I

i-layer, 433f, 433

Inert gas atmosphere, 542

Inorganic compounds, 139

Intermediate lead oxides, 61

Iron (Fe), 120t, 144t, 153

Isotope-labelled sulfur, 147

IUPAC Compendium of Chemical
 Terminology, 117

J

Jache, Otto, 14

Jenatzy, Camille, 12

K

Kameyama, 71

Kinetic curves, 82f

Kirchoff, Charles, 11

Kugelhaufen theory, 15

L

Lead (Pb)

 anodic corrosion of, 91

 anodic oxidation of, 49

 anodic polarization of, 44

 cyclic voltammograms, 68–70

 electrochemical oxidation of, 47

 formation, 492t

 free, 377, 378

 grain structure of, 163f

 H₂/H⁺ on surface, 56

 oxidation inhibitors, 545, 545t

 oxidation of, 60f, 276, 377, 380,
 381, 491t, 560f

 potential decay, 561f

 pseudo-cubic, 61, 62f

 purity specifications, 152, 153t,
 238

 rhombic, 61–62

 stationary, 315f

 Tet, 61, 224, 275f, 267

 tetragonal, 272–273

 thermal oxidation, 225

 unoxidized, 379f, 380f

 yellow, 224f

Lead alloys, 149

 for grid casting, 152t

 industry requirements to, 149

 mechanical properties, 149

 properties of, 151f

Lead dioxide (PbO₂), 37, 278, 581,
 612f

 active mass, 17, 78, 174

 aggregates, 458f

 amorphization of, 78

 anodic corrosion of, 91

 antimony and, 174

 arsenic and, 174

 binders, 475

 bismuth and, 174

 composition of, 74t

 corrosion layer growth, 91

 crystal lattice, 88

 density of, 73t

 diffusion into, layer, 87

 electrochemical reactions in,
 473, 519

- electrode potential, 32
 electrode system, 45
 film thickness, 74f
 formation of, 69f, 136, 446t
 gel-crystal forms of, 469
 gel-zone of, 79
 H_2SO_4 and, 133
 hydration of, 78
 over-voltage on, 86
 oxygen coverage of, 87
 oxygen evolution, 89
 oxygen over-voltage of, 88f
 in PAM, 411f, 522f, 525f, 520, 521t
 passivation, 138
 physico-chemical properties of, 71
 polymorphism, 71
 positive plates and, 519
 potentials, 177
 potentials of, as function of solution pH, 77f
 potentials of, as function of temperature, 77f
 powder densities, 290f
 preparation of, 75, 75
 ratios, 525f, 520, 522, 524
 SEM of, 456f, 470f
 semiconductor properties, 74
 stability of, 102
 stoichiometry of, 73
 structure, 79
 surface hydration of, 81
 transmission electron micrograph of, 471f, 472f
 unit cells, 71f
 X-ray diffraction of, 68
 zones, 454f
- Lead electrode**
 cyclic voltammograms of, 67f
 cycling of, 135f
- Lead oxide (PbO), 36, 223, 600f**
 chloride, mill, 231f
 conductivity of, 63
 crystal modification of, 240
 cyclic voltammogram, 68–70
 growth, 59
 H_2SO_4 and, 265f, 260, 271, 367, 462
 after illumination, 66f
- inhibitors, 313
 intermediate, 61
 lead sulfate electrode system, 45, 46
 modification, 266, 272
 molar volume of, 60
 nano-structure, 248
 orthorhomb, 223, 266
 physical properties, 223
 powders, 248f
 test cell with, 249f
 tetragonal, 272–273
- Lead sulfate (PbSO_4), 36**
 alkalization of solution in pores of, 52
 barium sulfate and, 343
 changes in, 431f
 crystal layer, 49, 422f, 461f
 distribution, 487f
 electrochemical oxidation of, 84–85
 expander and, 315
 formation of, 525
 H_2SO_4 and, 133
 membrane, 139
 membrane destruction, 70f
 morphology, 420f
 NAM and, 494f
 pH curve, 259f
 physical characteristics of, 255t
 pores with membrane dimensions in, 56
 SEM of, 51f, 70f, 488f, 490f, 526f
 solubility of, 136, 137f, 138
 stability regions for, 255t
 structure of, 318f, 343t
 technological applicability of, 279
 thermal effects of formation of, 258t
 tribasic pastes, 258
 voltammograms for, 316f
 wide pores in, 56
 zones, 454f
- Lead sulfate electrode, 35–36, 45, 30**
- Lead-acid battery**
 active materials in, 129
 applications of, 21
- cycle life, 131f, 132f
 development, 11
 first applications of, 12
 in HEVs, 25
 invention, 3
 lead compounds in manufacture of, 36
 maintenance problem, 14
 maximum initial capacity, 131f
 new developments in, 23
 position of, 22
 technological processes, 13, 408f, 407
 technological schemes for manufacture of, 108
 in twentieth century, 13
 types of, 21
- Lead-acid cell**
 cut-away cell of, 105f
 design, 105
 electromotive force of, 123
 energetic structure, 105
 skeleton, 105
 specific energy of, 104
 temperature and, 42
 voltage, 124f
- Lead-antimony alloys, 153, 557f**
 additives to, 165
 arsenic in, 165, 166t
 for casting straps, 155
 cooling rate, 160f
 corrosion resistance of, 162
 creep resistance of, 162
 development of, 154
 equilibrium phase diagram of, 155
 hardness of, 159f, 158
 high-antimony, 154–155
 history, 153
 low-antimony, 155
 medium-antimony, 154–155
 microstructure of, 155
 properties of, 157
 silver in, 167, 166t
 tin in, 167, 166t
 yield strength, 161
- Lead-calcium alloys, 178, 556f**
 aluminium addition to, 183
 concentration of calcium in, 179

- Lead-calcium alloys (*Continued*)
corrosion rate, 183f
equilibrium phase diagram of, 180
grain refinement in, 181f
history of, 178
low-calcium, 179
mechanical properties of, 181
medium-calcium, 179
- Lead-calcium grids, 14
- Lead-calcium-tin alloys, 110, 211, 185
additives, 195
age hardening of, 187f
aluminium in, 199
barium in, 195
bismuth in, 198
conclusions about, 194
corrosion layer and, 388f, 386
corrosion resistance of, 191
electrochemical properties of, 193
grain diameter, 187f
mechanical properties of, 187
mechanical properties of cast, 189f
mechanical properties of wrought, 190f
micrographs of, 186f
microstructure of, 185, 385f
plate curing and, 384
ratios in, 386t
silver in, 197
test alloys, 197t
- Lead-tin alloys, 199
AGM in, 200
corrosion transients in, 201f
mechanical properties of, 199t
selenium in, 202
sodium sulfate in, 200
- Leady oxide, 152
battery performance
characteristics, 247
cells produced with, 247
characteristics of, 238
chemical composition of, 240
cycling behavior of, 249f
environmental issues, 247
manufacture, 108
microscopic analysis, 243
nephelometric analysis, 243
particle size distribution, 245f
pastes prepared from, 281
production, 13, 227
purity of, 238
reactivity of, 241f, 234–236
sedimentation analysis, 243
stability of, 245
surface area, 241
- Leadly oxides
packed density of, 242
particle size distribution, 243
poured density of, 242, 243t
real density of, 242
- Lewis, T, 34
- Light scattering methods, 243
- Lignins
Freudenberg formulas for, 314f
hydrolyzed, 296
M, 296–297
structure, 313
- Lignosulfonate, 312, 579
- Linear voltammetric sweeps, 177f
- Linklater furnace, 237f
- Liquid/particle system, 288f, 287
- Lithium, 143, 144t
- Lithium-ion, 23t
- Lithium-polymer, 23t
- M**
- MAC Engineering and Equipment Company, 302
- Macropores, 465–467
- MAGM. *See* Modified AGM membrane
- Main transport system, 465–467
- Maintenance-free batteries, 21, 35
- MALs. *See* Maximum acceptable levels
- Manganese (Mn), 143, 120t, 144t
- Manufacturing, 108
- MARACELL E, 317
- Maschinenfabrik Gustav Eirich, 291, 300–301
- Mass, basic units of, 607
- Maximum acceptable levels (MALs), 239t
- McClelland, Donald, 14–15
- Me/PbO₂ electrode, 75
- Mercury, 143, 144t
- Mercury-mercurous sulfate, 66, 618t, 619t
- Micropores, 468f, 465–467
- Microporous separator, 105f
- Minimum water loss, 138–139
- Mn. *See* Manganese
- Modified AGM membrane (MAGM), 128–129
- Molar volumes, 615t
- Molecular weights, 615t
- Molybdenum, 143, 144t
- Monobasic lead sulfate (PbO-PbSO₄), 36, 280
oxidation of, 41
- Motive power batteries, 21
- Multitube positive plate, 214f
- Multi-valent ions, 119
- N**
- Na₂PbO₂, 75–76
- Na₂SO₄. *See* Sodium sulfate
- NAM. *See* Negative active mass
- Nano-structured lead oxide, 248
cycling behavior of, 249f
- Nanotubes, 357
- National lead pool operation, 151f
- Negative active mass (NAM), 17, 247, 312
active materials in, 613
additives to, 326t
barium sulfate and, 345f, 345
carbon additives and, 325, 333, 337
current-conducting structure, 327
cycle life and, 496
electrochemical behavior of, 338
energetic structure of, 327, 497f
expander in, 493
formation, 483f, 484f, 486
formation of, 509
graphite additives and, 337
hydrophobic channels, 349
lead sulfate and, 494f
median pore radius of, 332f
microstructure of, 330f, 331f, 340f
open gas pore in, 601f
SEM micrographs of, 327f, 498f

- structure of, 495f, 486, 496
 surface area of, 333f
 three-component expander for, 20
- Negative plates, 562
 additives, 311
 capacity of, 323f
 charge reactions of, 336
 cross-section, 485f
 discharge transients, 548f
 drying, 541, 543, 543
 equilibrium potentials in, 481
 expander in, 311, 319
 formation, 543
 in H_2SO_4 , 563f
 hydrogen evolution at, 349
 oxygen reduction at, 598
 pack, 105f
 performance, 319
 phase composition changes in, 482f
 pore structure, 492
 reactions in, 482
 SEM of, 489f, 489f
 state of, after formation, 535
 storage, 564f, 562
 tribasic lead sulfate for, 299f, 299
 of VRLA batteries, 592, 598
 zonal processes, 484
- Negative pole, 105f
- Nephelometric analysis, leady oxide, 243
- Nernst equation, 86
- NH_4 . *See* Ammonium
- Ni. *See* Nickel
- Nickel (Ni), 143, 120t, 144t, 153
- Nickel-cadmium, 23t
- Nickel-metal hydride, 23t
- Nicotinic acid, 349
- Nitrogen, 119–121
- Noble metals, 119
- N-region, 129, 132–133
- Nucleants, 172
- O**
- Octahedral, 72f
- OCV. *See* Open-circuit voltage
- Open-circuit voltage (OCV), 137, 575
- Orthorhomb-PbO, 223, 266
- Ovens. *See* Drying ovens
- Overcharge current, 570f
- Oxidation
 anodic, 95f, 49
 electrochemical, 66
 electrochemical, of Pb, 47
 galvanostatic, 52f
 of lead, 60f, 276, 377, 380, 381, 491t, 560f
 of monobasic lead sulfate, 41
 paste moisture and, 378f, 377, 377
 of PbO-PbSO_4 , 41
 photo-electrochemical, 64
 plate curing and, 379f
 potentiostatic, 66
 thermal, 225
 of tribasic lead sulfate, 41
- Oxidized graphite, 141
- Oxmaster, 301
- Oxygen, 60, 573f, 581
 expander and, 321
 overpotential, 169f
 recombination, 567
 reduction, 599f, 600f, 598
 vacancies, 387
- Oxygen evolution, 89, 93, 554f
 over-voltage of, 138–139
 polarization curves of, 99f
 reaction, 168
 tin and, 193f
- Ozone, 353
- P**
- PAM. *See* Positive active mass
- PASP. *See* Polyaspartate
- Paste(s), 253, 616. *See also*
 Additives
 additives to, 348
 adhesion, 396f, 396f, 395
 amorphous components, 274
 belt-type machine for, 302f
 capacity and, 277f
 carbonization of, 276
 composition, 614
 consistency, 295f, 296f
 corrosion layer and, 389
 crystal morphology of, 261f, 260, 263
 cycle dependencies and, 277f
- density, 287, 374f
 density critical values, 289
 density parameters, 288
 expander added to, 274f, 265
 fundamentals of, 253
 general requirements to, 286
 H_2SO_4 and, 277
 hydration of, 276
 leady oxide, 281
 mixer, 302
 moisture content, 378f, 377
 negative, 265
 oxidation and, 378f, 377
 phase composition of, 260f, 267f, 269f, 273f, 275f, 253, 255, 260, 428f
 pore system evolution, 445
 red lead, 281
 residual free lead oxidation in, 377
 SEM pictures of, 264f, 284f, 417f, 418f
 slurry preparation, 282f
 stirring, 266f, 267f
 temperature of, 269f
 tetrabasic lead sulfate, 268, 374f, 375f
 tribasic lead sulfate, 258, 374f, 375f
 XRD patterns, 256f, 262f
- Paste preparation, 108, 257, 367
 block scheme of, 301f
 equipment for, 297, 300
 kinetics of, 258
 sequence of procedures, 297
 technological scheme for, 300f
 technology of, 286
 thermal effects during, 258
- Pasted-plate batteries, 109f
- Pb. *See* Lead
- Pb^{2+} , 54f, 53
- Pb_3O_4 . *See* Red lead
- $\text{Pb}_{24}\text{O}_{48}$, 78
- $\text{Pb}/\text{H}_2\text{SO}_4/\text{H}_2\text{O}$ system, 37, 31t
 chemical reactions in, 38t
 electrochemical reactions
 proceeding in, 39t
 E/pH diagram for, 38

- Pb/H₂SO₄/H₂O system
(*Continued*)
thermodynamic characteristics
of, 31t
- PbO. *See* Lead oxide
- PbO₂. *See* Lead dioxide
- PbO(OH)₂, 84
- PbO₂|PbSO₄ electrode, 608
- 3PbO-PbSO₄-H₂O. *See* Tribasic lead sulfate
- 4PbO-PbSO₄. *See* Tetrabasic lead sulfate
- PbO/H₂SO₄/H₂O system
reactions for, 254t
thermodynamics of, 253
- PbO-PbO₂, 61–62
- PbO-PbSO₄. *See* Monobasic lead sulfate
- Pb/PbO₂/H₂SO₄ electrode system
anodic polarization of, 84
electrochemical behaviour of, 76
equilibrium potentials, 76
polarization of, 89–90
potential of, 93
temperature dependence, 77
- Pb/PbO₂/PbSO₄ electrode system, 71
current curve, 85f
electrochemical behaviour of, 76
equilibrium potential, 76
potential curve, 85f
- Pb/PbO/PbSO₄ electrode system, 55, 59
electrochemical oxidation of, 66
photo-activation, 64
photo-electrochemical oxidation of, 64
- Pb|PbO|PbSO₄|H₂SO₄, 19
- Pb|PbSO₄ electrode, 53, 607, 621f, 621f
- Pb/PbSO₄/H₂SO₄ electrode system, 47
- PbSO₄. *See* Lead sulfate
- Peukert dependencies, 292, 399f, 398–399
- Phenolic groups, 322f, 321
- Phosphoric acid (H₃PO₄), 139, 358
- Phosphorus, 143, 144t
- Photo-activation
light pulses during, 65f
- Pb/PbO/PbSO₄, 64
- Photo-electrochemical oxidation, 64
- Planté, Francis, 6f, 5–7
- Planté, Gaston, 4, 29
biography of, 5
personality of, 8
- Planté, Leopold, 5–7
- Plate curing, 108, 363
accelerating, 402
air, 397, 398t
basic processes during, 363f
in chamber, 398
equipment, 401
fundamentals, 364
hard porous mass formation, 364
lead-calcium-tin alloys and, 384
oxidation and, 379f
oxygen vacancies during, 387
phase composition in, 364
pore radius, 373f
pore volume, 393f
size distribution diagrams, 373f
structure in, 369f, 423f
surface area in, 371, 376t
technology of, 397
tetrabasic lead sulfate, 400, 402
time, 379f, 381f
tribasic lead sulfate, 400, 401
- Plate drying
atmosphere in, 394
negative, 541, 542, 543
process, 392
stages of, 394f
vacuum, 542
water and, 395f
- Plate formation, 109
- Polyaspartate (PASp), 142
- Polyethylene, 14
bottom bar, 214f
- Polymer emulsions, 141
- Polymer fibres, 313
- Polymorphism, 71
- Polyolefin, 355–356
- Poly(N-vinylpyrrolidone) polymers (PVP), 142
- Polypropylene, 14
- Polyvinyl alcohol (PVA), 141
- Positive active mass (PAM), 78, 132, 206f
- active materials in, 613
conductivity, 354t
corrosion layer interface, 504
crystal zones, 81
formation of, 448f, 444, 509
gel zones, 81
hydration and, 475t
lead dioxide in, 411f, 522f, 525f, 520, 521t
macrostructure, 464
microstructure, 464
plate capacity and, 469f, 478f, 462
pore volume, 466f, 467f
proton-electron mechanism, 83
reaction pores, 465
SEM of, 464f, 465f
specific capacity of, 217f
structure, 466f, 463
TEM of, 80f
tetrabasic lead oxide and, 278–279, 444
volume of, 83
washing, 83
- Positive cell connection, 105f
- Positive electrode, 42f
- Positive grid corrosion, 578
- Positive plate, 105f, 536
additives, 350, 353
capacity, 248f, 469f, 478f, 462, 520f
changes in, 536, 580f
cycle life of, 276, 558f
discharge transients for, 547f
equilibrium potentials in, 443
formation of, 350, 443
lead dioxide and, 519
performance of, 248
reactions during formation of, 446
tetrabasic lead sulfate for, 298f, 299, 453, 457
tribasic lead sulfate for, 298f, 297
in VRLA batteries, 579, 598
- Positive tubular plates
filling, 305
manufacture of, 305
- Potential curves, 48f
Pb/PbO₂/PbSO₄, 85f
- Potential/pH diagram

with marked regions of battery operation, 42f
 for Pb-H₂SO₄-H₂O system, 31t
 Potential/time curves, 53
 Potentiostatic oxidation, 66
 Pourbaix diagram, 76
 P-region, 129, 129, 132–133
 Premature capacity loss, 15, 179
 Printex, 328f, 327–329
 Proton-electron mechanism, 83
 Pseudo-cubic PbO, 61
 unit cells of, 62f
 Punched grid, 211f
 PVA. *See* Polyvinyl alcohol
 PVP. *See* Poly(N-vinylpyrrolidone) polymers

Q

Quebraco, 323f, 322
 Quinones, 320

R

Reaction pores, 465–467
 REAX 80C, 317
Recherches sur l'électricité (Planté), 8
 Rectangular grids, 203f
 Recycling, 151
 Red lead (Pb₃O₄), 224, 280, 352
 cycle life of, 286t
 decomposition, 285
 H₂SO₄ and, 285f
 in linklater furnace, 237f
 pastes prepared from, 281
 production of, 237
 Rheostatic machine, 7–8
 Rhombic PbO, 61–62
 Ritter, Johann, 4f, 3
 Robinson, 34
 Rotating ring disc electrode, 70

S

SAER. *See* Second anodic electrochemical reaction
 Sb. *See* Antimony
 Scanning electron microscope (SEM), 17, 50, 583f
 of ball-mill, 234f
 of Barton pot oxides, 230f

of lead dioxide, 456f, 470f
 of lead sulfate, 488f, 490f, 526f
 of lead sulfate layer, 51f, 70f
 of NAM, 327f, 498f
 of negative plate, 489f, 489f
 of PAM, 464f, 465f
 of pastes, 264f, 284f, 417f, 418f
 Schonbein, 3
 Scott volumeter, 242
 Se. *See* Selenium
 Second anodic electrochemical reaction (SAER), 91
 Sedimentation analysis, leady oxide, 243
 Selective semipermeable membranes, 55
 Selenium (Se), 120t, 153, 202, 172
 Self-discharge processes, 49f, 85
 SEM. *See* Scanning electron microscope
 Semi-blocks, 106
 Semi-suspension technology
 tetrabasic lead sulfate, 291
 water in, 291t
 Separators, 565f, 550, 582
 AGM, 582, 582, 583, 585, 589
 fibre diameter in, 584t
 porosity, 587f
 structure, 582
 Shimadzu, G, 13, 231
 Siemens, Wilhelm, 11
 Silver, 100f, 98–99, 99, 143, 144t
 in lead-antimony alloys, 167, 166t
 in lead-calcium-tin alloys, 197
 Silver-silver sulfate, 620f
 Sinsteden, Wilhelm, 4
 SLI batteries (starting, lighting, ignition), 21
 cycle life of, 441f
 grid pasting, 303
 Slurry, 282f
 SnO₂. *See* Tin dioxide
 SnSO₄, 140–141
 SO₂. *See* Sulfur dioxide
 Soaking, 363, 407
 central layer and, 422
 changes during, 425
 cycle life and, 429

density and, 419f
 DSC measurements, 439f, 438
 electrolyte concentration during, 414f
 H₂SO₄ and, 409
 intermediate layer and, 420
 outer layer and, 420
 pore volume distribution after, 425f
 tetrabasic lead sulfate, 413, 428, 431, 434
 zonal processes during, 419
 SOC. *See* State-of-charge
 Sodium silicate, 208
 Sodium sulfate (Na₂SO₄), 141, 200, 359
 Solubility, 254f
 Solution molality, 127f
 Sonnenschein, 14
 Special purpose batteries, 21
 Specific energy, 611t
 Specific gravity, 117
 Stability regions, 255t
 State-of-charge (SOC), 25
 Stationary batteries, 21
 Stationary voltage, 46f
 Steady-state corrosion rate, 92
 Steady-state current, 48, 591f
 Steady-state potential, 47
 Sterns, 68
 Stokes, 34
 Storage, 535
 negative plates in, 562
 Strap grid tubular plate construction, 216f
 Strems, 61
 Structural stabilizers, 348
 Sulfur, 119–121, 172
 isotope-labelled, 147
 Sulfur dioxide (SO₂), 120t
 Sulfuric acid (H₂SO₄), 47, 110, 117, 427f, 553, 608, 616, 617f, 618t
 absorption, 83
 in active mass formation, 501
 active medium-concentration, 133
 activity coefficients for, 34t
 adsorption of, 78

Sulfuric acid (H_2SO_4) (*Continued*)
 amount of, 611
 anodic polarization of Pb in, 44
 battery cycle life and, 132f
 battery performance and, 136
 cell capacity and, 126
 concentration of, 409f, 409, 502f, 612t, 619
 conductivity of, 121
 cyclic voltammograms in, 69f
 diagrammatic summary of influence of, 137f
 dissociation of, 121
 electrical resistance of, 123f, 121–122
 electrochemical equivalents for, 128t
 as electrolytes, 117
 in flooded batteries, 125
 lead oxide and, 265f, 260, 271, 367, 462
 lead-acid cell voltage and, 124f
 mass fraction and density for, 124t
 molality, 43f
 negative plates in, 563f
 oxidation of lead in, 60f
 passive high-concentration, 133
 passive low-concentration, 134
 pastes and, 295f, 296f, 277
 PbO_2 and, 133
 PbSO_4 and, 133
 phase composition and, 133, 413
 purity of, 118, 120t
 red lead and, 285f
 relative concentrations, 118t
 relative density, 119f
 soaking and, 409
 solution density v, 127f
 solution molality v, 127f
 tetrabasic lead sulfate and, 451
 utilization, 130f, 132f
 water absorption and, 240
 water systems, 124t
 X-ray diffraction analysis of concentrations, 134

Superheated steam, 542
 Swan, Joseph, 11

T

Tafel curve, 57
 Tafel equation, 56, 86
 Tafel plot, 57f
 Tafel slope coefficient, 86
 Tank formation, 407
 TDA activated carbons, 340f, 341f
 Tellurium, 143, 144t
 TEM. *See* Transmission electron micrographs
 Temperature, 597f
 in active mass formation, 524f, 501
 balance, 596f
 in ball-mill, 231, 232
 Barton pot, 227, 229
 coefficient, 43
 effect of, on lead-acid cell, 42
 expander stability and, 324
 of pastes, 269f, 378
 in $\text{Pb/PbO}_2/\text{H}_2\text{SO}_4$ electrode system, 77
 tetrabasic lead sulfate and, 270
 Temperature-transformation-time diagram (TTT), 188f
 Terminal posts, 152
 Tet- PbO , 61, 224, 275f
 formation of, 267
 unit cells of, 62f
 Tetrabasic lead sulfate (4PbO-PbSO_4), 41, 37
 bonding, 390f
 conversion, 368, 457f
 curing schedule, 400, 402
 expanders and, 272
 formation of, 268, 462f
 H_2SO_4 and, 451
 hydrated, 436f, 440f
 kinetics of, 268, 272
 PAM particles and, 278–279, 444
 particle size, 371
 pastes, 268, 374f, 375f
 phase composition of, 271f, 434t, 455f

pore volume distribution, 372f, 447f
 positive plates and, 298f, 298f, 299, 453, 457
 preparation of, 299
 semi-suspension technology, 291
 soaking, 413, 428, 431, 434
 structure, 368, 434, 459f
 sulfation rates, 436f, 431, 432
 surface areas, 392f, 437
 temperature and, 270
 XRD patterns, 366f
 Tetragonal elementary cell, 72
 Tetragonal PbO , 272–273
 Thermal oxidation, 225
 Thermal runaway phenomenon, 594f
 Thermopassivation, 540f, 540f, 541f, 536
 Thomas, 14
 Three-component expander, 20
 Ti_4O_7 . *See* Titanium oxide
 Tin, 143, 144t. *See also* Lead-calcium-tin alloys
 calcium and, 384
 in lead-antimony alloys, 167, 166t
 oxygen evolution and, 193f
 Tin dioxide (SnO_2), 351, 343t
 Titanium oxide (Ti_4O_7), 354, 351, 343t
 Transmission electron micrographs (TEM), 79
 of lead dioxide, 471f, 472f
 of PAM particles, 80f
 Tribasic lead sulfate ($3\text{PbO-PbSO}_4\text{-H}_2\text{O}$), 37
 bonding, 391f
 conversion of, 368
 curing schedule, 401f, 400
 for negative plates, 299f, 299
 oxidation of, 41
 PAM and, 466f
 pastes, 374f, 375f
 phase composition, 386t
 for positive plates, 297
 preparation of, 297, 299
 structure, 371f, 368
 sulfation rates, 431

Tribe, 12
 TTT. *See* Temperature-transformation-time diagram
 Tubular electrodes, 290f
 Tubular plate designs, 216f
 Tubular plate filling, 307f, 305
 Tubular positive plates, 213
 Tubular-plate batteries, 110f, 111, 204f
 curing, 111
 filling, 111
 preparation, 111
 spine and grid casting, 111
 Tunnel ovens, 304

U

UFC. *See* Ultra-fine carbon
 Ultimate tensile strength (UTS), 161
 barium and, 195f
 Ultra-fine carbon (UFC), 141
 Uninterruptible power supply (UPS), 206–207
 UPS. *See* Uninterruptible power supply
 UTS. *See* Ultimate tensile strength

V

Vacuum drying, 542
 Vacuum method, 412–413
 Valve adapter, 105f

Valve-regulated lead-acid (VRLA) batteries, 107, 178–179, 576, 578, 589
 formation options, 411f, 411
 MALs in, 239t
 negative plates of, 592, 598
 polarization, 594f
 positive plates in, 579, 598
 Vanadium, 143, 144t
 Vanilline, 350
 VARTA, 569f
 Volckmar, Ernest, 12
 Volta cell, 3
 Volt-ampere characteristics, 572f
 Voss, E, 15–16
 VRLA batteries. *See* Valve-regulated lead-acid batteries

W

Water
 absorption, 240
 decomposition, 168
 electrolysis, 143
 lead oxidation and, 380
 loss, 14
 plate drying and, 395f
 restoring, 567
 in semi-suspensions, 291t
 Weight coefficients, 611t
 Wet-charged batteries, 535, 565f, 551, 553, 562

Wheatstone, 3
 White dendrites, 157f
 Wicking characteristics, 585f
 WIRTZ Manufacturing Company, 212, 384

X

XPS. *See* X-ray photoelectron spectroscopy
 X-ray diffraction (XRD), 44–45, 94–95
 H₂SO₄, 134
 lines, 416f
 of pastes, 256f, 262f
 of PbO₂, 68
 relative intensity of, 44f
 for tetrabasic lead sulfate, 366f
 X-ray photoelectron spectroscopy (XPS), 81
 X-ray powder diffraction, 257
 XRD. *See* X-ray diffraction

Y

Yellow PbO, 224f
 Yield strength, 161

Z

Zinc (Zn), 143, 120t, 144t, 153
 Zn. *See* Zinc

This page intentionally left blank